

NAT'L INST. OF STAND & TECH



A11107 264299

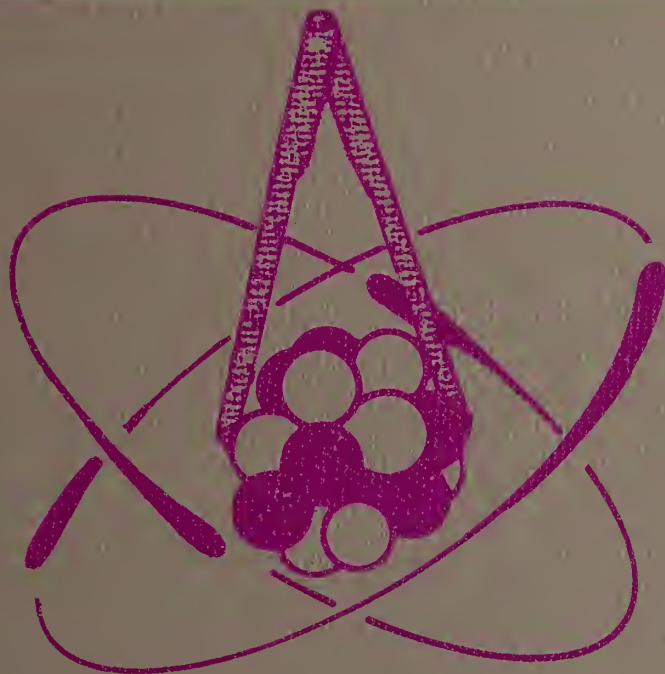
NBS  
PUBLICATIONS



# NBS SPECIAL PUBLICATION 425

Volume II

U.S. DEPARTMENT OF COMMERCE / National Bureau of Standards



## NUCLEAR CROSS SECTIONS AND TECHNOLOGY PROCEEDINGS OF A CONFERENCE









NOV 26 1975

761116

# Nuclear Cross Sections and Technology

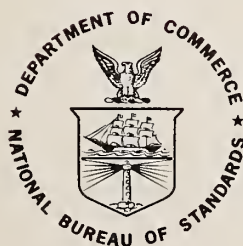
## Volume II

Proceedings of a Conference  
Washington, D.C.  
March 3-7, 1975

Edited by

R. A. Schrack and C. D. Bowman

Center for Radiation Research  
National Bureau of Standards  
Washington, D.C. 20234



U.S. DEPARTMENT OF COMMERCE, Rogers C. B. Morton, Secretary

U.S. NATIONAL BUREAU OF STANDARDS, Ernest Ambler, Acting Director

Issued October 1975

## Library of Congress Cataloging in Publication Data

Conference on Nuclear Cross Sections and Technology,  
Washington, D.C., 1975  
Nuclear Cross Sections and Technology.  
(NBS Special Publication; 425)  
Conference sponsored by the Reactor and Shielding Division of  
the American Nuclear Society and others.  
Includes Indexes.  
Supt. of Docs. No.: C 13.10:425  
1. Cross Sections (Nuclear physics)—Congresses.  
2. Cross Sections (Nuclear physics)—Standards—Congresses.  
I. Schrack, Roald A. II. Bowman, Charles E., 1935- III.  
American Nuclear Society. Reactor and Shielding Division.  
IV. Title. V. Series: United States. National Bureau of Stand-  
ards. Special publication; 425.  
QC100.U57 no. 425 [QC794.6.C7] 389'.08s [539.7'5] 75-619216

## National Bureau of Standards Special Publication 425

Nat. Bur. Stand. (U.S.), Spec. Publ. 425, 553 pages (Oct. 1975)

CODEN: XNBSAV

U.S. GOVERNMENT PRINTING OFFICE  
WASHINGTON: 1975

---

For sale by the Superintendent of Documents, U.S. Government Printing Office  
Washington, D.C. 20402 - Price \$19.45 per 2 vol. set sold in sets only  
Stock Number 003-003-01461-3



## FOREWORD

The development of new energy sources is one of the critical problems facing our society, and the use of nuclear energy is expected to grow rapidly in the coming decades. Thus, the recent Conference on Nuclear Cross Sections and Technology was a most timely event. I think that the Conference successfully met its goal of summarizing the present status of nuclear cross sections and technology, discussing future cross section needs and exchanging information between nuclear scientists and engineers. The National Bureau of Standards has long been involved in the development of nuclear science and technology. While the generation of measurement techniques and the publication of nuclear data are important activities, so is the sponsorship of and participation in conferences such as this one. It is through the publication of these conference proceedings that we will continue widening the forum of interchange.

Ernest Ambler  
Acting Director

## PREFACE

These are the proceedings of the Nuclear Cross Sections and Technology Conference held at the Shoreham Americana Hotel in Washington, D.C., March 3-7, 1975. It might be considered as the fourth in a series of conferences formerly entitled "Neutron Cross Sections and Technology" or as the first of a new series of conferences of a broader scope. The list of participants and the table of contents indicate the success of the conference in attracting representatives of many disciplines and countries.

The conference was sponsored by the Reactor and Shielding Division of the American Nuclear Society, the Nuclear Physics Division of the American Physical Society, the International Union of Pure and Applied Physics, the National Bureau of Standards, and the United States Energy Research and Development Administration. The purpose of the conference was to provide a forum for the exchange of information related to the use by technology of nuclear data and techniques. The great majority of technological contributions reflects the current needs and interests of the fields of reactor technology and biomedicine. Scientific contributions to the conference deal with the development of nuclear standards and the measurement of cross sections. Included are papers on measurement techniques and experimental results, as well as data evaluation and analysis. The reader is directed to the summary paper in session JA for a more detailed evaluation of the conference.

The papers are printed in the proceedings as they were received from the authors and in the order in which they were presented in the sessions and in the Bulletin of the American Physical Society, Series II Volume 20, pp. 132-177 (1975). For convenience we have preserved the conference notation for the sessions. In a few cases manuscripts were not submitted by the authors. The following papers

for which abstracts appeared in the Bulletin were not submitted: BA-3, BB-17, CB-8, CB-9, EB-12, HB-1, HB-18, and HB-24. Several papers have been added at the end of some sessions that arrived after the deadline for the Bulletin.

To speed the publication of the proceedings, all papers were submitted by the authors in camera-ready form. We are greatly indebted to the authors and all those who assisted in the preparation of the manuscripts. Their efforts have made it possible to get the proceedings in print much more rapidly than would otherwise be the case. To make the proceedings more useful we include, as well as a table of contents, an author index, a list of participants, and a CINDA index of subject matter. We would like to thank Dr. Norman Holden of Brookhaven National Laboratory for the preparation of the CINDA index.

When commercial equipment, instruments and materials are mentioned or identified in this proceedings it is intended only to adequately specify experimental procedure. In no case does such identification imply recommendation or endorsement by the National Bureau of Standards, nor does it imply that the material or equipment identified is necessarily the best available for the purpose.

We wish to express our appreciation for the financial support from the U. S. Energy Research and Development Administration and the National Bureau of Standards which made the publication possible.

The Editors gratefully acknowledge the assistance of the National Bureau of Standards Office of Technical Information and Publications and the extensive secretarial assistance of Mrs. Julia Marks, Mrs. Lois Gallahan, and Mrs. Linda Cline.

R. A. Schrack  
C. D. Bowman

#### ABSTRACT

These proceedings are the compilation of 221 papers presented at the Conference on Nuclear Cross Sections and Technology held in Washington, D.C. on March 3-7, 1975. The Conference summarized the present status of nuclear cross sections and technology and discussed future cross section needs. Special emphasis is placed on reactor technology and biomedical applications of nuclear science and the measurement of standard cross sections.

Key words: Biomedical; Conference; cross section; nuclear; standards; technology.





# TABLE OF CONTENTS

<u>Contents, Volume I</u>	<u>Page</u>
Foreword . . . . .	III
Preface . . . . .	IV
Abstract . . . . .	V
Table of Contents . . . . .	VII through XVII
Conference Personnel . . . . .	XVIII
Session Chairmen . . . . .	XIX
Papers from Sessions AA through FA — Pages 1 through 468	

<u>SESSION AA: FISSION REACTORS I</u>	<u>Page</u>
AA 1. Opening Remarks, by W. W. Havens, Jr. . . . .	1
AA 2. Neutron Cross-Section Needs, by H. J. C. Kouts . . . . .	3
AA 3. The Light Water Reactor Industry—Nuclear Data Needs, by V. O. Uotinen, J. D. Robertson, and J. S. Tulenko . . . . .	7
AA 4. Radioactive-Nuclide Decay Data in Science and Technology, by C. W. Reich and R. G. Helmer . . . . .	14
AA 5. Radioactive Decay Heat Analyses, by R. E. Schenter and F. Schmittroth . . . . .	21
AA 6. Sensitivity of the Afterheat from <sup>235</sup> U and <sup>239</sup> Pu Thermal Fission To Errors In Fission Product Nuclear Data, by C. Devillers, B. Nimal, C. Fiche, J. P. Noëi, J. Blachot, and R. de Turreil . . . . .	29

<u>SESSION BA: FISSION REACTORS II</u>	
BA 1. Significance of Nuclear Data on Neutron Monitoring of an LMFBFR, by N. C. Paik . . . . .	39
BA 2. Fast Reactor Safety, by R. Avery . . . . .	45
BA 4. After PHENIX, What Is the Importance of Nuclear Data Programs for Fast Breeder Reactor Development?, by J. Y. Barre, J. Bouchard, and J. P. Chaudat . .	51

<u>SESSION BB: INSTRUMENTS AND TECHNIQUES</u>	
BB 1. NE-213 Neutron Spectrometry System for Measurements to 15 MeV, by R. H. Johnson, B. W. Wehring, and J. J. Dorning . . . . .	62
BB 2. Absolute Calibration of Neutron Detectors in the 10-30 MeV Energy Range, by J. A. Cookson, M. Hussian, C. A. Uttley, J. L. Fowler, and R. B. Schwartz . . . . .	66
BB 3. A Thick Target Measurement Technique for Determining Nuclear Reaction Rates, by N. A. Roughton, M. J. Fritts, R. J. Peterson, C. J. Hansen, and C. S. Zaidins . . . . .	69
BB 4. A Black Detector for 250 keV—1000 keV Neutrons, by G. P. Lamaze, M. M. Meier, and O. A. Wasson . . . . .	73
BB 5. Detector Calibration with an Associated Particle Apparatus, by M. M. Meier, A. D. Carlson, and G. P. Lamaze . . . . .	75
BB 6. Use of Gas Proportional Counters for Neutron Flux Monitors at the NBS Linac, by O. A. Wasson . . . . .	78
BB 7. Fission Cross Section Measurements on Short-Lived Alpha Emitters, by J. W. T. Dabbs, N. W. Hill, C. E. Bemis, and S. Raman . . . . .	81

<u>SESSION BB (Continued)</u>	<u>Page</u>
BB 8. Systematic Discrepancy in Photoneutron Cross Sections for Medium and Heavy Nuclei, by T. Tomimasu and S. Sugiyama . . . . .	83
BB 9. The 2-keV Filtered Beam Facility at the NBS Reactor, by I. G. Schroder, R. B. Schwartz, and E. D. McGarry . . . . .	89
BB 10. The Rensselaer Intense Neutron Spectrometer, by R. C. Block, R. W. Hockenbury, D. S. Cramer, E. Bean, and R. E. Slovacek . . . . .	93
BB 11. A Modular Minicomputer Multiparameter Data Gathering and Virtual Memory Operating System for the NBS Neutron Standards Program, by R. A. Schrack, H. T. Heaton II, and D. Green . . . . .	97
BB 12. TUNL Fast Neutron Cross Section Facility, by D. W. Glasgow, F. O. Purser, J. C. Clement, G. Mack, K. Stelzer, J. R. Boyce, D.H. Epperson, H. H. Hogue, E. G. Bilpuch, H. W. Newson, and C. R. Gould . . . . .	99
BB 13. A Facility for Studying Neutron-Induced Charged Particle Reactions, by F. P. Brady, N. S. P. King, M. W. McNaughton, J. F. Harrison, and B. E. Bonner . . . . .	103
BB 14. After-Pulse Suppression for 8850 and 8854 Photomultipliers, by G. P. Lamaze, J. K. Whittaker, R. A. Schrack, and O. A. Wasson . . . . .	106
BB 15. A Secondary Standard Neutron Detector for Measuring Total Reaction Cross Sections, by K. K. Sekharan, H. Laumer, and F. Gabbard . . . . .	108
BB 16. Facilities for Cross Section Measurements Using Na-D Photoneutron Sources, by J. C. Robertson, M. C. Davis, and J. C. Engdahl . . . . .	112
BB 18. A 25-keV Neutron Beam Facility at NBS, by E. D. McGarry and I. G. Schroder . . .	116

#### SESSION CA: MICROSCOPIC DATA AND TECHNIQUES

CA 1. New Experimental Techniques and Results in Neutron Spectroscopy, by C..D. Bowman . . . . .	119
CA 2. Measurement, Analysis, and Implications of the Fission Cross Sections of the Important Fissionable Isotopes, by M. S. Moore . . . . .	129
CA 3. Neutron Capture Cross Section Measurement Techniques, by R. E. Chrien . . . . .	139
CA 4. Nuclear Models and Data for Gamma-Ray Production, by P. G. Young . . . . .	149
CA 5. Techniques for the Determination of Neutron Induced Charged Particle Reactions, by H. Liskien . . . . .	156

#### SESSION CB: BENCHMARKS AND SENSITIVITIES

CB 1. Integral Measurements to Test Shielding Cross Sections, by L. Harris, Jr., J. C. Young, N.A. Lurie, D.K. Steinman, S. J. Friesenhahn, D. E. Bryan, W. E. Gober, and L. Schänzler . . . . .	161
CB 2. Evaluation, Uncertainty Estimation and Adjustment of Capture Cross Sections for Fission Product Nuclei, by H. Gruppelaar, J. B. Dragt, A. J. Janssen, and J. W. M. Dekker. . . . .	165
CB 3. Integral Test of Cross Sections Using Neutron Leakage Spectra from Spheres of Iron, Niobium, Beryllium, and Polyethylene, by R. H. Johnson, J. J. Dornig, and B. W. Wehring . . . . .	169
CB 4. Uncertainties and Correlations in Evaluated Data Sets Induced by Use of Standard Cross Sections, by R. W. Peelle . . . . .	173

<u>SESSION CB (Continued)</u>	<u>Page</u>
CB 5. Shielding Benchmark Experiments and Sensitivity Studies in Progress at Some European Laboratories, by G. Hehn, M. Mattes, W. Matthes, R. Nicks, and H. Rief . . . . .	177
CB 6. Assessment of Neutron Group Constants for Iron and Stainless Steel Through Measurements and Analyses of Energy and Space Distributions of Neutrons in Test Assemblies, by I. Kimura, K. Kobayashi, Shu A. Hayashi, S. Yamamoto, H. Nishihara, M. Ando, S. Kanazawa, and M. Nakagawa . . . . .	184
CB 7. ENDF/B Dosimetry Cross Section File Benchmark Neutron Flux-Spectral Uncertainties, by W. N. McElroy . . . . .	189
CB 10. Fission Product Gamma-Ray and Photoneutron Spectra, by M. G. Stammatelatos and T. R. England . . . . .	193

#### SESSION DA: MANAGEMENT OF THE ACTINIDES

DA 1. Safeguards Against Theft or Diversion of Nuclear Materials, by T. B. Taylor . .	199
DA 2. Fission Theory and Actinide Fission Data, by A. Michaudon . . . . .	202
DA 3. Nuclear Data for Actinide Recycle, by E. J. Hennelly . . . . .	214
DA 4. (n,f) Cross Sections for Exotic Actinides, by J. B. Wilhelmy, H. C. Britt, A. Gavron, E. Konecny, and J. Weber . . . . .	218
DA 5. A Study of the $^{233}\text{U}$ - $^{232}\text{Th}$ Reactor as a Burner for Actinide Wastes, by S. Raman, C. W. Nestor, Jr., and J. W. T. Dabbs . . . . .	222
DA 6. A Consistent Set of Transplutonium Multigroup Cross Sections, by R. W. Benjamin, V. D. Vandervelde, T. C. Gorrell, and F. J. McCrosson . . . . .	224
DA 7. Measurement of the Neutron Capture Cross Sections of the Actinides, by L. W. Weston and J. H. Todd . . . . .	229

#### SESSION DB: CROSS SECTIONS AND FLUX STANDARDS

DB 1. Measurements of the $^6\text{Li}$ and $^{10}\text{B}$ Partial Cross Sections from 1 to 1500 keV, by S. J. Friesenhahn, V. J. Orphan, A. D. Carlson, M. P. Fricke, and W. M. Lopez . . . . .	232
DB 2. An Absolute Measurement of the $^6\text{Li}(n,\alpha)$ Cross Section at 964 keV, by W. P. Stephany and G. F. Knoll . . . . .	236
DB 3. Angular Anisotropy in the $^6\text{Li}(n,\alpha)^3\text{H}$ Reaction at 25 keV, by I. G. Schroder, E. D. McGarry, G. de Leeuw-Gierts and S. de Leeuw . . . . .	240
DB 4. Neutron Total Cross Section of $^6\text{Li}$ from 10 eV to 10 MeV, by J. A. Harvey and N. W. Hill . . . . .	244
DB 5. Observation and Analysis of Elastic Neutron Scattering from $^{12}\text{C}$ , by R. J. Holt, A. B. Smith, and J. F. Whalen . . . . .	246
DB 6. Fission Spectrum Neutrons for Cross Section Validation and Neutron Flux Transfer, by J. Grundl and C. M. Eisenhauer . . . . .	250
DB 7. Fundamental Integral Cross Section Ratio Measurements in the Thermal-Neutron Induced $^{235}\text{U}$ Fission Neutron Spectrum, by A. Fabry, J. A. Grundl, and C. Eisenhauer . . . . .	254
DB 8. Interlaboratory Comparison of Absolute Fission Rate and $^{238}\text{U}$ Capture Rate Measurements in the Mol- $\Sigma$ Secondary Intermediate-Energy Standard Neutron Field, by M. Pinter, W. Scholtyssek, P. Fehsenfeld, H. A. J. Van der Kamp, W. H. J. Quaadvliet, A. Fabry, G. and S. de Leeuw, F. Cops, J. A. Grundl, D. Gilliam, and C. Eisenhauer . . . . .	258

<u>SESSION DB (Continued)</u>	<u>Page</u>
DB 9. Manganese Bath Systematic Effects in Measurements of $\bar{\nu}$ and $\eta$ , by J. R. Smith . .	262
DB 10. Absolute $^{235}\text{U}$ Fission Cross Section for $^{252}\text{Cf}$ Spontaneous Fission Neutrons, by H. T. Heaton II, J. A. Grundl, V. Spiegel, Jr, D. M. Gilliam, C. Eisenhauer . . .	266
DB 11. Fission Cross Section Ratios in the $^{252}\text{Cf}$ Neutron Spectrum ( $^{235}\text{U}$ : $^{238}\text{U}$ : $^{239}\text{Pu}$ : $^{237}\text{Np}$ ), by D. M. Gilliam, C. Eisenhauer, H. T. Heaton II, and J. A. Grundl . . . . .	270
DB 12. Measurement of Cross Sections for Threshold Reactions Induced by $^{252}\text{Cf}$ Spontaneous Fission Neutrons, by W. G. Alberts, J. Bortfeldt, E. Günther, K. Knauf, M. Matzke, G. Rassel, V. Siegel, and K. F. Walz . . . . .	273
DB 13. Absolute Neutron Flux Determination in Fast Neutron Spectra, by I. Schouky, S. Cierjacks, P. Brotz, D. Gröschel, and B. Leugers . . . . .	277
 <u>SESSION EA: CROSS SECTIONS AND FLUX STANDARDS</u>	
EA 1. Thermal Parameters of the Fissile Isotopes, by Bowen R. Leonard, Jr. . . . .	281
EA 2. The Third IAEA Evaluation of the 2200 m/s and 20°C Maxwellian Neutron Data for $^{235}\text{U}$ , $^{238}\text{U}$ , $^{239}\text{Pu}$ and $^{241}\text{Pu}$ , by H. D. Lemmel . . . . .	286
EA 3. Neutron Cross Section Standards and Flux Determinations Above Thermal Energies, by A. D. Carlson . . . . .	293
EA 4. R-Matrix Analysis of the Light Element Standards, by G. M. Hale . . . . .	302
 <u>SESSION EB: EVALUATION AND CALCULATION OF CROSS SECTIONS OF NONFISSIONABLE MATERIALS</u>	
EB 1. Computer-Readable "Nuclear Data Sheets", by W. B. Ewbank . . . . .	309
EB 2. Recent Evaluation for the German Nuclear Data Library KEDAK-3, by B. Goel, H. Küsters, and F. Weller . . . . .	313
EB 3. Description of the ENDF/B-IV Silicon Evaluation Energy Distributions of Outgoing Particles, by D. Larson . . . . .	317
EB 4. Evaluation of Fission Product Nuclear Data for 28 Important Nuclides, by S. Igarasi, S. Iijima, M. Kawai, T. Nakagawa, Y. Kikuchi, K. Maki, and H. Matsunobu . . . . .	320
EB 5. Evaluated Decay-Scheme Data for the ILRR Program, by R. G. Helmer and R. C. Greenwood . . . . .	324
EB 6. Development of a Two-Step Hauser-Feshbach Code with Precompound Decays and Gamma-Ray Cascades—A Theoretical Tool for Cross Section Evaluations, by C. Y. Fu . . . . .	328
EB 7. Neutron Cross Sections and Their Uncertainties Obtained from Nuclear Systematics, by S. Pearlstein . . . . .	332
EB 8. Level Density Calculation for Deformed Nuclei, by J. P. Felvinci, D. Cacuci, and E. Melkonian . . . . .	335
EB 9. Odd-Even Fluctuations in Neutron Strength Functions, by G. J. Kirouac . . . . .	338
EB 10. Statistical Estimation of Physical Quantities in Thermal- and Fast-Neutron-Induced Fission, by T. Yamamoto and K. Sugiyama . . . . .	342
EB 11. Theoretical Estimates of $(n,\gamma)$ Cross Sections for 6-15 MeV Neutrons, by G. Longo and F. Saporetti . . . . .	346
EB 13. Reaction Mechanisms in the High Energy Tail of the 14 MeV $^{56}\text{Fe}(n,n')$ -Process, by H. Jahn, C. H. M. Broeders, and I. Broeders . . . . .	350



<u>SESSION EB (Continued)</u>	<u>Page</u>
EB 14. Calculations of $(n,\alpha)$ Rates for Iron Group Materials, by F. M. Mann and Z. E. Switkowski . . . . .	354
EB 15. Parametric Fit of the Total Cross Section of $^{45}\text{Sc}$ , by B. A. Magurno and S. F. Mughabghab . . . . .	357
EB 16. Neutron Capture Mechanism in Light and Closed Shell Nuclides, by B. J. Allen, J.W. Boldeman, M.J. Kenny, A.R. deL. Musgrove, Hla Pe and R.L. Macklin.....	360
EB 17. Radiation Shielding Information Center Data Activities, by R. W. Roussin, B. F. Maskewitz, and D. K. Trubey . . . . .	363
EB 18. Evaluation of the Resonance Parameters and Capture Cross Section for Chromium Up to 600 keV, by D. Abramson, J. C. Bluet and P. Fardeau . . . . .	367

SESSION FA: REACTOR PHYSICS; TRANSPORT AND SENSITIVITY

FA 1. Representation of Neutron Cross Sections in the Unresolved Resonance Region, by G. de Saussure and R. B. Perez . . . . .	371
FA 2. Helium Production in Reactor Materials, by E. P. Lippincott, W. N. McElroy, and H. Farrar IV . . . . .	375
FA 3. Fast Reactor Fission Yields for $^{233}\text{U}$ , $^{235}\text{U}$ , $^{238}\text{U}$ , $^{239}\text{Pu}$ , and Recommendations for the Determination of Burnup on FBR Mixed Oxide Fuels, by W. J. Maeck, . . . .	378
FA 4. Effects of Nuclear Data Uncertainties upon LMFBR Fuel Cycle Characteristics, by R. D. McKnight, L. G. LeSage, and J. M. Christenson . . . . .	385
FA 5. The Sensitivity of $k_{\text{eff}}$ of Metallic Assemblies to the Parametric Representation of the Fission and the Inelastic Scattering Spectra, by H. Nissimov and J. J. Wagschal . . . . .	389
FA 6. Comparison of Doppler Broadening Methods, by D. E. Cullen, C. R. Weisbin, R. Q. Wright, and J. E. White . . . . .	392
FA 7. Burnup Calculations for the KWO Reactor, by D. C. Lutz . . . . .	398
FA 8. Fission Product Nuclear Data Obtained by Use of an On-Line Mass Spectrometer, by P. L. Reeder, J. F. Wright, and R. A. Anderl . . . . .	401
FA 9. Differential Cross Sections and Integral Data: the ENDF/B-4 Library and "Clean" Criticals, by J. J. Wagschal, A. Ya'ari, and Y. Yeivin. . . . .	405
FA 10. Neutron Attenuation in Normal and Ilmenite Concretes, by R. J. Adams and K. H. Lokan . . . . .	409
FA 11. Analysis of the BNL $\text{ThO}_2$ - $^{233}\text{U}$ Exponential Experiments, by D. Dabby . . . . .	415
FA 12. Tabular Cross Section File Generation and Utilization Techniques, by D. E. Cullen, Odelli Ozer, and C. R. Weisbin . . . . .	419
FA 13. Neutron Energy Spectrum Controlled Blanket for Fast Breeder Reactor, by L. H. Tang. . . . .	422
FA 14. Use of Monte Carlo Method in the Estimation of Fast Neutrons Leaked Through a Concrete-Paraffin Shielding, by L. S. Chuang and K. C. Wong . . . . .	426
FA 15. A Comparison of Air-Over-Ground Transport Calculations Using Different Cross Sections, by J. C. Saccenti and W. A. Woolson . . . . .	431
FA 16. The Sensitivity of Neutron Air Transport to Nitrogen Cross Section Uncertainties, by A. Niiler, W. B. Beverly, and N. E. Banks . . . . .	436
FA 17. Monte Carlo Studies of the Effect of Cross Section Characteristics on Fast Neutron Penetration in Iron, by L. P. Ku and H. Goldstein . . . . .	440

<u>SESSION FA (Continued)</u>	<u>Page</u>
FA 18. Neutron-Coupled Gamma-Ray Cross-Section Requirements for Gas-Cooled Fast Breeder Reactors, by M. Nagel and R. J. Cerbone . . . . .	444
FA 19. Cross Section Preparation for the Continuous-Energy Monte Carlo Code VIM, by R. E. Prael . . . . .	447
FA 20. A Comparison of VIM and MC <sup>2</sup> --2--Two Detailed Solutions of the Neutron Slowing-Down Problem, by R. E. Prael and H. Henryson, II . . . . .	451
FA 21. Decay Heat Analysis for an LMFBR Fuel Assembly Using ENDF/B-IV Data, by G. W. Morrison, C. R. Weisbin, and C. W. Kee . . . . .	455
FA 22. A Two Dimensional Cross Section Sensitivity Analysis of Iron In a Concrete Shield, by T. E. Albert and G. L. Simmons . . . . .	459
FA 23. GCFR Benchmarks: Experiments and Analysis, by S. Seth, W. Heer, M. Jermann, C. McCombie, E. Ottewitte, R. Richmond, and P. Wydler . . . . .	464

# Contents, Volume II

Papers from Sessions FB through JA — Pages 469 through 970

## SESSION FB: VARIOUS APPLICATIONS OF NUCLEAR DATA

FB 1. Biomedical Application of Shortlived Positron Emitting Isotopes, by P. Meyer, E. Behrin, R. Frank, R. Holub, and C. E. McJilton . . . . .	469
FB 2. Energy-Dependent Pion Mean Free Path Length for Star Formation, by C. Werntz and C. W. Lucas, Jr. . . . .	472
FB 3. Spectrum and Shielding Measurements and Calculations of Neutrons Produced by 800 MeV Protons, by L. R. Veaser, G. J. Russell, E. D. Arthur, P. A. Seeger, W. F. Sommer, D. M. Drake, R. G. Fluharty, and R. F. Bentley . . . . .	476
FB 4. Nuclear Data for Assessment of Activation of Scintillator Materials During Spaceflight, by C. S. Dyer, J. I. Trombka and S. M. Seltzer . . . . .	480
FB 5. Proton Scattering for Analysis of Atmospheric Particulate Matter, by K. R. Akselsson, J. W. Nelson, and J. W. Winchester . . . . .	484
FB 6. Use of Elastic Scattering Cross Section Anomalies for Depth Profiling Helium and Hydrogen Isotopes in Solids, by R. S. Blewer . . . . .	488
FB 7. Spallation Cross Sections and the LAMPF Medical Radioisotope Program, by B. R. Erdal, P. M. Grant, V. R. Casella, A. E. Ogard, and H. A. O'Brien, Jr. . . . .	492
FB 8. Feasibility of Neutron-Gamma Techniques for Field Analysis of Fresh Concrete, by M. C. Taylor, J. R. Rhodes, and D. L. Bernard . . . . .	496
FB 9. Cross Section Requirements for Industrial Gauging Applications, by B. Y. Cho and T. P. Sheahan . . . . .	500
FB 10. Li, Be and B Production in Proton-Induced Reactions: Implications for Astrophysics and Space Radiation Effects, by C. T. Roche, R. G. Clark, G. J. Methews, and V. E. Viola, Jr. . . . .	504
FB 11. Long Lived Isotope Production Cross Sections from Proton Bombardment of Rhenium, by A. J. Armini and S. N. Bunker . . . . .	509
FB 12. A Need for (p,n) Cross Sections for Selected Targets at Lower Energies, by H. S. Ahluwalia . . . . .	512
FB 13. The Measurement of Thermal Neutron Constants of the Soil; Application to the Calibration of Neutron Moisture Gauges and to the Pedological Study of Soil, by Ph. Couchat, C. Carre, J. Marcesse, and J. Le Ho . . . . .	516

SESSION GA: VARIOUS APPLICATIONS OF NUCLEAR DATA	Page
GA 1. Medical Uses of Nuclear Data, by R. S. Tilbury, R. E. Bigler, L. Zeitz, and J. S. Laughlin . . . . .	520
GA 2. Medical Use of Fast Neutrons in Radiotherapy and Radiography, by D. K. Bewley. .	527
GA 3. Biomedical Radiation Transport Calculations as an Application of Nuclear Data, by R. G. Alsmiller, Jr. . . . .	533
GA 4. Geochemical Mapping of the Moon by Orbital Gamma Ray Spectroscopy, by Robert C. Reedy . . . . .	540
SESSION GB: CROSS SECTIONS MEASUREMENTS ON FISSIONABLE ISOTOPES	
GB 1. A Measurement of the Fission Cross Section of $^{235}\text{U}$ from 1 keV to 1 MeV, by J. B. Czirr and G. S. Sidhu . . . . .	546
GB 2. The Average Number of Prompt Neutrons, $\bar{\nu}_p$ , from Neutron Induced Fission of $^{235}\text{U}$ Between 0.2 and 1.4 MeV, by F. Käppeler and R. -E. Bandl . . . . .	549
GB 3. Monte Carlo Analysis of Direct Measurements of the Thermal $\eta$ (.025 eV) for $^{233}\text{U}$ and $^{235}\text{U}$ , by J. J. Ullo and M. Goldsmith . . . . .	553
GB 4. Monte Carlo Analysis of Manganese Bath Measurements of $\eta$ of $^{233}\text{U}$ and $^{235}\text{U}$ Using Thermalized Neutrons, by M. Goldsmith and J. J. Ullo . . . . .	557
GB 5. Parameters of the Subthreshold Fission Structure in $^{240}\text{Pu}$ , by G. F. Auchampaugh and L. W. Weston . . . . .	560
GB 6. Measurement of the $^{239}\text{Pu}$ Fission Cross-Section and its Ratio to the $^{235}\text{U}$ Fission Cross-Section in the Energy Range from 1 keV to 1 MeV, by D. B. Gayther. .	564
GB 7. A Measurement of the $^{238}\text{U}/^{235}\text{U}$ Fission Cross Section Ratio, by M. S. Coates, D. B. Gayther, and N. J. Pattenden . . . . .	568
GB 8. Precision Measurement of Prompt Fission Neutron Spectra of $^{235}\text{U}$ , $^{238}\text{U}$ , and $^{239}\text{Pu}$ , by P.I. Johansson, B. Holmqvist, T. Wielding . . . . .	572
GB 10. Spin Determination of Resonances in $^{235}\text{U}$ , by G. A. Keyworth, C. E. Olsen, J. D. Moses, J. W. T. Dabbs, and N. W. Hill . . . . .	576
GB 11. Quantum Numbers of Low Lying Neutron Resonances in U-235, by J.P. Felvinci, E. Melkonian and W.W. Havens, Jr. . . . .	580
GB 12. KeV Capture Cross Section of $^{242}\text{Pu}$ , by R. W. Hockenbury, A. J. Sanislo, and N. N. Kaushal . . . . .	584
GB 13. Spontaneous Fission Decay Constant of $^{238}\text{Pu}$ , by R. Gay and R. Sher . . . . .	587
GB 14. Neutron-Induced Fission Cross Sections of $^{233}\text{U}$ , $^{234}\text{U}$ , $^{236}\text{U}$ , and $^{238}\text{U}$ with Respect to $^{235}\text{U}$ , by J. W. Behrens, G. W. Carlson, and R. W. Bauer . . . . .	591
GB 15. On Sub-Barrier Fission in $^{238}\text{U}$ , by J. A. Wartena, H. Weigmann, and E. Migneco . . . . .	597
GB 16. Capture-To-Fission Ratio of $^{235}\text{U}$ from the Measurement of Low-Energy $\gamma$ -Rays, by F. Corvi and P. Giacobbe . . . . .	599
GB 17. The $^{241}\text{Pu}$ Neutron Induced Fission Cross Section from 0.01 eV to 50 eV and its Normalization, by C. Wagemans and A. J. Deruytter . . . . .	603
GB 18. Intermediate Structure in the keV Fission Cross Section of $^{235}\text{U}$ , by E. Migneco, P. Bonsignore, G. Lanzano, J. A. Wartena, and H. Weigmann . . . . .	607
GB 19. Energy Spectrum of Delayed Neutrons from Photo-Fission of $^{238}\text{U}$ , by S. Iwasaki, K. Yana, S. Sato, K. Sano, M. Hagiwara, and K. Sugiyama . . . . .	611
GB 20. $^{235}\text{U}$ Fission Cross Section Measurements Relative to Neutron-Proton Scattering, by G. S. Sidhu and J. B. Czirr . . . . .	615
GB 21. Measurement of the $^{238}\text{U}$ Capture Cross Section Shape in the Neutron Energy Region 20 to 550 keV, by R. R. Spencer and F. Kaeppler . . . . .	620



GB 22.	Intermediate Structure in the $^{238}\text{U}$ Neutron Capture Cross Section, by R. B. Perez and G. de Saussure . . . . .	623
GB 23.	A Direct Comparison of Different Experimental Techniques for Measuring Neutron Capture and Fission Cross Sections for $^{239}\text{Pu}$ , by R. Gwin, L. W. Weston, J. H. Todd, R. W. Ingle, and H. Weaver . . . . .	627
GB 24.	Fast Neutron Fission Spectrum Measurements of $^{235}\text{U}$ at 0.52 MeV Incident Neutron Energy, by P. I. Johansson and J. M. Adams . . . . .	631
GB 25.	The Fission Cross Section of $^{235}\text{U}$ for Na-Be Photoneutrons, by G. M. Gilliam and G. F. Knoll . . . . .	635
GB 26.	The Total Cross Section and the Fission Cross Section of $^{241}\text{Am}$ in the Resonance Region, Resonance Parameters, by H. Derrien and B. Lucas . . . . .	637
GB 27.	Structures in $^{232}\text{Th}(n,f)$ and $^{238}\text{U}(n,f)$ Cross Sections, by J. Blons, C. Mazur, and D. Paya . . . . .	642

## SESSION HA: FUSION

HA 1.	Nuclear Data Needs for Fusion Reactor Design, by D. Steiner . . . . .	646
HA 2.	Model Calculations as One Means of Satisfying the Neutron Cross Section Requirements of the CTR Program, by Donald G. Gardner . . . . .	651
HA 3.	Energy from Charged Particle Reactions Among Light Nuclei, by T. A. Tombrello. . . . .	659
HA 4.	A Survey of Fast-Neutron Induced Reaction Cross-Section Data, by S. M. Qaim . . . . .	664
HA 5.	A Quantitative Assessment of CTR Cross Section Needs, by S. A. W. Gerstl, D. J. Dudziak, and D. W. Muir . . . . .	674
HA 6.	A Sensitivity Study of Data Deficiencies, Weighting Functions, and 14 MeV Neutron Source Spectrum Effects in a $^{238}\text{U}$ Fueled Fusion-Fission Hybrid Blanket, by B. R. Leonard, Jr., U. P. Jenquin, D. L. Lessor, D. F. Newman, and K. B. Stewart . . . . .	680
HA 7.	Advanced Fuels for Nuclear Fusion Reactors, by J. Rand McNally, Jr. . . . .	683
HA 8.	A Study of the $^6\text{Li}(n,\alpha)t$ Reaction Between 2-10 MeV, by C. M. Bartle . . . . .	688
HA 9.	Absolute Cross Sections for Neutrons from $^6\text{Li} + d$ Reactions at Energies Between 0.2 and 0.9 MeV, by A. J. Elwyn, R. E. Holland, F. J. Lynch, J. E. Monahan, and F. P. Mooring . . . . .	692
HA 10.	Cross Section Measurements for Charged Particle Induced Reactions on $^6\text{Li}$ , by C. R. Gould, J. M. Joyce, and J. R. Boyce . . . . .	697
HA 11.	Phase Shift Analysis of nD, nT, DD, DT, TT, $\alpha$ D and $\alpha$ T Cross Sections, by Carla Abulaffio and Asher Peres . . . . .	701
HA 12.	$^{238}\text{U}$ Pulsed Sphere Measurements and CTR Fusion-Fission Blanket Calculations, by C. Wong, J. D. Anderson, R. C. Haight, L. F. Hansen and T. Komoto . . . . .	704
HA 13.	The $^{94}\text{Nb}(n,\gamma)^{95}\text{Nb}$ , $^{95m}\text{Nb}$ Reaction for the CTR Reactor Technology Program, by P. J. Persiani, E. M. Pennington, Y. D. Harker, and R. L. Heath . . . . .	708
HA 14.	Production Cross Sections of Some Micro and Millisecond Isomers with 14.8 MeV Neutrons, by G. N. Salaita and P. K. Eapen . . . . .	712
HA 15.	Reactivities for Two-Component Fusion Calculations, by G. H. Miley and H. H. Towner . . . . .	716
HA 16.	Application of Bondarenko Formalism to Fusion Reactors, by Patrick D. Soran and Donald J. Dudziak . . . . .	722

## SESSION HB: NEUTRON CROSS SECTION MEASUREMENTS ON NONFISSIONABLE MATERIALS

HB 2.	Neutron Cross-Section Measurements on $^{236}\text{U}$ , by L. Mewissen, F. Poortmans, G. Rohr, J. Theobald, H. Weigmann, and G. Vanpraet . . . . .	729
-------	---	-----



HB 3.	p-Wave Assignment of $^{238}\text{U}$ Neutron Resonances, by F. Corvi, G. Rohr, and H. Weigmann . . . . .	733
HB 4.	Neutron Resonance Parameters of $^{238}\text{U}$ , by Y. Nakajima, A. Asami, M. Mizumoto, T. Fuketa, and H. Takekoshi . . . . .	738
HB 5.	Evidence for Structure in the Sequence of S-Wave Levels in $^{238}\text{U}$ , by E. Melkonian, J. P. Felvinci, and W. W. Havens, Jr. . . . .	742
HB 6.	Total Neutron Cross Section Measurements on Gross Fission Products, by H. G. Priesmeyer and U. Harz . . . . .	744
HB 7.	High Resolution Total Neutron Cross-Section in the $^{54}\text{Fe}$ and $^{56}\text{Fe}$ , by M. S. Pandey, J. B. Garg, J. A. Harvey and W. M. Good . . . . .	748
HB 8.	Thick Sample Transmission Measurement and Resonance Analysis of the Total Neutron Cross Section of Iron, by S. Cierjacks, G. Schmalz, R. Töpke, R. R. Spencer, and F. Voss . . . . .	754
HB 9.	Gamma-Ray Production Measurements Due to Interactions of Neutrons with Elements Required for Nuclear Power Applications and Design, by G. T. Chapman, J. K. Dickens, T. A. Love, G. L. Morgan and E. Newman . . . . .	758
HB 10.	Cross Sections for the Production of Low Energy Photons by Neutron Interactions with Fluorine and Tantalum, by J. K. Dickens, G. L. Morgan, and F. G. Perey . . . . .	762
HB 11.	Spectral Gamma Ray Production Cross Section Measurements from Threshold to 20 MeV, by V. C. Rogers, V. J. Orphan, C. G. Hoot, V. V. Verbinski, D. G. Costello, and S. J. Friesenhahn . . . . .	766
HB 12.	Fourteen-MeV, Neutron-Induced Gamma-Ray Production Cross Sections for Several Elements, by E. D. Arthur, D. M. Drake, M. G. Silbert, and P. G. Young . . . . .	770
HB 13.	The Low Energy Total Cross Section of $^{36}\text{Ar}$ , by S. F. Mughabghab and B. A. Magurno . . . . .	774
HB 14.	Neutron Cross Sections of $^{59}\text{Ni}$ , by G. J. Kirouac and H. M. Eiland . . . . .	776
HB 15.	Neutron Resonance Spectroscopy at Nevis Laboratories, by G. Hacken, H. I. Liou, J. Rainwater, and U. N. Singh . . . . .	780
HB 16.	Threshold Photoneutron Spectroscopy of Nuclei Near $A = 140$ , by R. J. Holt and H. E. Jackson . . . . .	784
HB 17.	Analyzing Powers of the $^6\text{Li}(\bar{n}, t)^4\text{He}$ Reaction, by Munawar Karim and J. C. Overlay . . . . .	788
HB 19.	Neutron-Absorption Cross Section of $^{22}\text{Na}$ , by R. Rundberg, M. F. Elgart, H. L. Finston, E. T. Williams, and A. H. Bond, Jr. . . . .	792
HB 20.	Evidence for Valence Neutron Capture in S-Wave Neutron Capture in $^{36}\text{Ar}$ and $^{54}\text{Fe}$ , by S. F. Mughabghab . . . . .	795
HB 21.	Neutron Resonance Spectroscopy. $^{209}\text{Bi}$ , by U. N. Singh, J. Rainwater, H. I. Liou, G. Hacken, and J. B. Garg . . . . .	799
HB 22.	Measurement of Neutron Capture Cross Sections Near 24 KeV, by N. Yamamuro, T. Doi, T. Hayase, Y. Fujita, K. Kobayashi, and R. C. Block . . . . .	802
HB 23.	Fluctuations in the Neutron Strength Function, by C. M. Newstead . . . . .	806
HB 25.	Measurements of Thermal Neutron Cross Sections for Helium Production in $^{59}\text{Ni}$ , by J. McDonald and N. G. Sjöstrand . . . . .	810
HB 26.	Differential Cross Sections for the 0.847-MeV Gamma Ray from Iron for Incident Neutrons of 8.5, 10.0, 12.2, and 14.2 MeV, by D. M. Drake, L. R. Veaser, Manfred Drog, and Gary Jensen . . . . .	813
HB 27.	High Energy $\gamma$ -Ray Transitions of $^{56}\text{Fe}$ Resonances in the Energy Range 7-70 keV, by H. Beer, R. R. Spencer and F. Käppeler . . . . .	816

HB 28.	Excitation Functions of the (n,2n) Reactions on $^{12}\text{C}$ and $^{238}\text{U}$ , by A. Ackermann, B. Anders, M. Bormann and W. Scobel . . . . .	819
HB 29.	Incoherent Neutron Scattering Cross-Sections as Determined by Diffuse Neutron Scattering Techniques, by W. Schmatz, G. Bauer, and M. Löwenhaupt . . . . .	823

## SESSION IA: BENCHMARKS AND SENSITIVITIES

IA 1.	Cross Section and Method Uncertainties: The Application of Sensitivity Analysis to Study Their Relationship in Computational Benchmark Problems, by C. R. Weisbin, E. M. Oblow, J. Ching, J. E. White, R. Q. Wright, and J. Drischler . . . . .	825
IA 2.	Benchmark Experiments for Nuclear Data, by E. M. Bohn, R. E. Maerker, F. J. McCrosson, R. J. LaBauve, B. A. Magurno, and R. E. Schenter . . . . .	834
IA 3.	Estimated Uncertainties in Nuclear Data -- An Approach, by F. G. Perey . . . . .	842
IA 4.	A Survey of Computer Codes Which Produce Multigroup Data from ENDF/B-IV, by N. M. Greene . . . . .	848

## SESSION IB: MEASUREMENTS OF NEUTRON CROSS SECTIONS OF NONFISSIONABLE MATERIALS

IB 1.	Measurement of (n,2n) and (n,3n) Cross-Sections for Incident Energies Between 6 and 15 MeV, by J. Fréhaut and G. Mosinski . . . . .	855
IB 2.	Excitation Curve for the Production of $^{115}\text{In}^m$ by Neutron Inelastic Scattering, by D. C. Santry and J. P. Butler . . . . .	859
IB 3.	Inelastic Neutron Excitation of the Ground State Rotational Band of $^{238}\text{U}$ , by P. Guenther and A. Smith . . . . .	862
IB 4.	Differential Elastic and Inelastic Scattering of 9-15 MeV Neutrons from Carbon, by F. O. Purser, D. W. Glasgow, H. H. Hogue, J. C. Clement, G. Mack, K. Stelzer, J. R. Boyce, D. H. Epperson, S. G. Buccino, P. W. Lisowski, S. G. Glendinning, E. G. Bilpuch, H. W. Newson, and C. R. Gould . . . . .	866
IB 5.	Neutron Inelastic Scattering Cross Sections in the Energy Range 2 to 4.5 MeV, by M. A. Etemad . . . . .	871
IB 6.	The Absolute Polarization of Fast Neutrons Elastically Scattered from Light Nuclei, by F. W. K. Firk, J. E. Bond, G. T. Hickey, R. J. Holt, R. Nath, and H. L. Schultz . . . . .	875
IB 7.	Inelastic Scattering of Fast Neutrons from $^{103}\text{Rh}$ , by D. Reitmann, E. Barnard, D. T. L. Jones, and J. G. Malan . . . . .	879
IB 8.	ORNL Neutron Scattering Cross Section Measurements from 4 to 8.5 MeV: A Summary, by W. E. Kinney and F. G. Perey . . . . .	883
IB 9.	Differential Elastic Scattering Cross Sections of Sulphur for 14.8 MeV Neutrons by Surface of Revolution Technique, by A. M. Ghose, A. Chatterjee, and S. Nath . . . . .	886
IB 10.	Differential Cross Sections for Carbon Neutron Elastic and Inelastic Scattering from 8.0 to 14.5 MeV, by G. Haouat, J. Lachkar, Y. Patin, J. Sigaud, and F. Cocu . . . . .	889
IB 11.	Level and Decay Schemes of Even-A Se and Ge Isotopes from (n,n' $\gamma$ ) Reaction Studies, by J. Sigaud, Y. Patin, M. T. McEllistrem, G. Haouat, and J. Lachkar . . . . .	893
IB 12.	Symmetry Effects in Neutron Scattering from Isotopically Enriched Se Isotopes, by J. Lachkar, G. Haouat, M. T. McEllistrem, Y. Patin, J. Sigaud, and F. Cocu . . . . .	897
IB 13.	Fast Neutron Capture and Activation Cross Sections, by W. P. Poenitz . . . . .	901

<u>SESSION IB (Continued)</u>	<u>Page</u>
IB 14. Fission Product Capture Cross Sections in the keV Region, by R. W. Hockenbury, H. R. Knox, and N. N. Kaushal . . . . .	905
IB 15. Integral Capture Cross-Section Measurements in the CFRMF for LMFBR Control Materials, by R. A. Anderl, Y. D. Harker, E. H. Turk, R. G. Nisle, and J. R. Berreth . . . . .	908
IB 16. Radiative Capture of Neutrons in the keV Region, by R. C. Greenwood, R. E. Chrien, and K. Rimawi . . . . .	912
IB 17. Measurement of the $\gamma$ -Ray Production Cross Sections from Inelastic Neutron Scattering in Some Chromium and Nickel Isotopes Between 0.5 and 10 MeV, by F. Voss, S. Cierjacks, D. Erbe, and G. Schmalz . . . . .	916
IB 18. Measurement of 24.3 keV Activation Cross Sections with the Iron Filter Technique, by K. Rimawi and R. E. Chrien . . . . .	920
IB 19. Radiative Capture Gamma Rays from the Reaction $^{208}\text{Pb}(n,\gamma)^{209}\text{Pb}$ for 11-MeV Incident Neutrons, by D. M. Drake, E. D. Arthur, I. Bergqvist, D. K. McDaniels, and Philip Varghese . . . . .	923
IB 20. $\gamma$ -Ray Spectra from $\ell=1$ Neutron Capture Near 24 keV, by K. Rimawi and R. E. Chrien . . . . .	926
IB 21. Shape Analysis and Width Correlation Studies Based on Neutron Capture Data for $^{56}\text{Fe}$ , $^{58}\text{Ni}$ , $^{60}\text{Ni}$ and $^{61}\text{Ni}$ , by F. H. Fröhner . . . . .	929
IB 22. $\gamma$ Ray Production Cross Sections for Neutron Inelastic Scattering from Cr, Ni, $^{92}\text{Zr}$ , and $^{94}\text{Zr}$ from 3 to 6 MeV, by G. Tessler and S. S. Glickstein . . . . .	934
IB 23. Scattering of Neutrons by Nitrogen and Oxygen from 5.0 to 9.3 MeV, by D. L. Bernard and M. C. Taylor . . . . .	938
IB 24. Deformation Effects in Neutron Scattering from the Sm Isotopes, by M. T. McEllistrem, J. Lachkar, G. Haouat, Ch. Lagrange, Y. Patin, R. E. Shamu, J. Sigaud, and F. Coçu . . . . .	942
IB 25. Small Angle Scattering of Fast Neutrons, by W. Bucher, C. E. Hollandsworth, and J. E. Youngblood . . . . .	946
IB 26. Elastic and Inelastic Differential Neutron Scattering Cross Sections for $^{238}\text{U}$ from 0.9 - 2.7 MeV, by J. J. Egan, G. H. R. Kegel, G. P. Couchell, A. Mittler, B. K. Barnes, W. A. Schier, D. J. Pullen, P. Harihar, T. V. Marcella, N. B. Sullivan, E. Sheldon, and A. Prince . . . . .	950
IB 27. Absolute Measurements of Neutron Radiative Capture Cross Sections for $^{23}\text{Na}$ , Cr, $^{55}\text{Mn}$ , Fe, Ni, $^{103}\text{Rh}$ , Ta, $^{238}\text{U}$ in the keV Energy Range, by C. Le Rigoleur, A. Arnaud, and J. Taste . . . . .	953
IB 28. Capture Cross Section of $^{197}\text{Au}$ Between 10 keV and 500 keV, by E. Fort and C. Le Rigoleur . . . . .	957
IB 29. Self Shielding Factor Measurements for Natural Iron and $^{23}\text{Na}$ Between 24 keV and 160 keV at 300° K, by A. Arnaud, C. Le Rigoleur and J. P. Marquette . . . . .	961

SESSION JA: ROUNDTABLE DISCUSSION OF THE SIGNIFICANCE AND ACCOMPLISHMENTS OF THE CONFERENCE

E. P. Wigner and J. L. Fowler . . . . .	964
B. Rose . . . . .	965
J. J. Schmidt . . . . .	967
List of Registrants . . . . .	971
Author Index . . . . .	979
CINDA Type Subject Index . . . . .	982

#### PROGRAM COMMITTEE

W. W. Havens, Jr., Chairman -- Columbia University  
R. S. Caswell -- National Bureau of Standards  
F. Feiner -- General Electric Corporation  
H. Goldstein -- Columbia University  
D. Harris -- Los Alamos Scientific Laboratory  
D. J. Horen -- Oak Ridge National Laboratory  
H. Jackson -- Argonne National Laboratory  
D. A. Lind -- University of Colorado  
S. Pearlstein -- Brookhaven National Laboratory  
F. Perey -- Oak Ridge National Laboratory  
C. Preskitt -- Intelcom Radiation Technology  
J. S. Robertson -- Brookhaven National Laboratory  
A. B. Smith -- Argonne National Laboratory  
D. Steiner -- Oak Ridge National Laboratory

#### INTERNATIONAL ADVISORS TO THE PROGRAM COMMITTEE

S. W. Cierjacks -- Karlsruhe  
W. G. Cross -- Atomic Energy of Canada, Ltd.  
A. S. Divatia -- Bhabha Atomic Research Centre  
R. Joly -- Saclay  
B. Rose -- Harwell  
J. J. Schmidt -- IAEA  
K. Tsukada -- Japan Atomic Energy Research Institute  
L. N. Usachev -- Obninsk

#### ARRANGEMENTS

E. H. Eisenhower, National Bureau of Standards

SESSION CHAIRMEN

SESSION AA: OPENING SESSION, FISSION REACTORS I  
W. W. Havens, Jr.

SESSION BA: FISSION REACTORS II  
F. Feiner

SESSION BB: INSTRUMENTS AND TECHNIQUES  
A. B. Smith

SESSION CA: MICROSCOPIC DATA AND TECHNIQUES  
H. Jackson

SESSION CB: BENCHMARKS AND SENSITIVITIES  
D. Harris

SESSION DA: MANAGEMENT OF THE ACTINIDES  
D. J. Horen

SESSION DB: CROSS SECTIONS AND FLUX STANDARDS  
L. Stewart

SESSION EA: CROSS SECTIONS AND FLUX STANDARDS  
R. S. Caswell

SESSION EB: EVALUATION AND CALCULATION OF CROSS SECTIONS OF  
NONFISSIONABLE MATERIALS  
F. Perey

SESSION FA: REACTOR PHYSICS; TRANSPORT AND SENSITIVITY  
H. Goldstein

SESSION FB: VARIOUS APPLICATIONS OF NUCLEAR DATA  
J. I. Trombka

SESSION GA: VARIOUS APPLICATIONS OF NUCLEAR DATA  
J. S. Robertson

SESSION GB: CROSS SECTIONS MEASUREMENTS ON FISSIONABLE  
ISOTOPES  
M. Moore

SESSION HA: FUSION  
J. M. Williams

SESSION HB: NEUTRON CROSS SECTION MEASUREMENTS ON NONFISSIONABLE  
MATERIALS  
V. Orphan

SESSION IA: BENCHMARKS AND SENSITIVITIES  
S. Pearlstein

SESSION IB: MEASUREMENTS OF NEUTRON CROSS SECTIONS OF  
NONFISSIONABLE MATERIALS  
R. Lane

SESSION JA: CRITIQUE AND SUMMARY LESSON  
H. Jackson







P. Meyer and E. Behrin  
Lawrence Livermore Laboratory  
Livermore, California 94550

R. Frank, R. Holub and C. E. McJilton  
University of Washington  
Seattle, Washington 98105

Radioactive nitrogen, oxygen and ozone have been used for dynamic lung-function studies on live dogs with an Anger positron camera. In particular an attempt was made to determine the feasibility of this method to study early functional changes caused by ozone.

(Radioactive tracers; Anger positron camera, lung function)

### Introduction

Ozone has been identified as a significant component of ambient air pollution where atmospheric photochemical activity occurs. The importance of ozone,<sup>1</sup> ( $O_3$ ), as a toxicant has been investigated and several of its effects have been defined, although the mechanism is still uncertain.<sup>2</sup>

The results of this research have led, in part, to an interest in where the ozone is taken up in the respiratory system. At present the distribution of the ozone-uptake throughout the airways is unknown.

By tagging ozone with an  $^{15}O$  isotope, actual sites of  $O_3$ -uptake may be discovered.

More information as to the effects of ozone on the lung function can possibly be obtained by the use of  $^{13}N$  tracers in a breathing gas. Nitrogen is not usually soluble in the blood, stays in the lungs until recirculated and, labeled with a  $^{13}N$  tracer its distribution can provide a useful image of a lung. Using radioactive Nitrogen periodically, functional changes in the respiratory system due to, for instance, ozone may perhaps be detected early.

The  $^{13}N$  and  $^{15}O$  isotopes were produced by bremsstrahlung from the 100 MeV Livermore Electron Accelerator (Linac) via  $^{14}N(\gamma, n)^{13}N$  and  $^{16}O(\gamma, n)^{15}O$ .<sup>3,4</sup> Thresholds for these reactions are 10.4 MeV ( $^{14}N$ ) and 15.7 MeV ( $^{16}O$ ). Both isotopes decay by positron emission with half lives of 10 min. and 2 min., respectively. After irradiation, the tracer gas was pumped to the anesthetized, mechanically ventilated animal which was placed between the two detector crystals of the positron camera. The camera detects the two .51 MeV annihilation gamma rays in coincidence and stores the information in the memory of an on-line PDP-15 computer. Data transfer from the computer to a magnetic drum is initiated breath by breath so that, in principle, single breath studies can be made, the quality depending primarily on the level of activity of the gas.

### Radioactive Gas Production

A stainless steel bottle of 2 liters volume, located downstream behind the tantalum bremsstrahlung target of the Linac, was pressurized with pure  $O_2$  and irradiated with  $\gamma$ -rays of about 30 MeV end-point energy having a typical bremsstrahlung spectrum. To minimize the production of  $^{11}C$  from the reaction  $^{16}O(\gamma, n)^{11}C$  it was desirable to keep the maximum  $\gamma$ -ray energy near the 26.5 MeV threshold for this reaction. After an irradiation time of about 2 half-lives (4 minutes) the exposed gas, now a mixture of

$O_2$ ,  $^{*}O_2$ ,  $O_3$  and  $^{*}O_3$ , (the astericks refer to molecules with an  $^{15}O$  atom) has nearly reached saturation activity. Since there is no way to differentiate between the decay of  $^{*}O_2$  or  $^{*}O_3$  it was necessary to eliminate the activated oxygen. This was accomplished by passing the mixture through an ozone trap of silica gel at dry-ice temperature ( $-78^{\circ}C$ ). After collecting sufficient amounts of ozone, the trap was flushed with clean oxygen to remove all  $^{*}O_2$ , then heated to release the ozone which then was mixed with air to the desired concentration, lppm or 5ppm, for an animal exposure.

Similarly,  $^{*}N_2$  was produced by using  $N_2$  as a target gas to which clean oxygen was added after irradiation.

### Anger Positron Camera<sup>5</sup>

The camera's operation depends on detecting, in coincidence, the two back-to-back gamma rays from a positron-electron annihilation and thus defining a line between the two detector crystals along which the event took place. Many events allow then, in principle to determine the point or points of intercept and thus the location of the source of activity.

The Livermore camera<sup>6</sup> consists of two identical detector heads, each with 37 photomultiplier tubes mounted on a 40 cm dia. NaI-crystal of 1.25 cm thickness (Figs. 1a,b). Each head derives position information, i.e. where on the X-tal the gamma rays hit, from a precision-capacitor network coupled with the P.M.T.-outputs. These outputs are sampled, digitized and stored on a high-speed drum by the PDP-15. The camera heads can also be used independently as scintillators with position sensitivity. Maximum count-rate capability is  $2 \times 10^5$  positron events per second.

Annihilation pairs are ordered into a 100 x 100 matrix permitting, in principle, a spatial resolution of about .3 cm. In practice, the camera's point-source resolution is only about 1.5 cm. However, the extrapolated range<sup>7</sup> of the  $^{15}O$ -positron ( $E_{max} = 1.74$  MeV) in lung tissue of density  $\bar{\rho} .23g/cc$  is about 3.5 cm and the resolution is thus limited by this fact. For the  $^{13}N$ -positron the max. range is somewhat shorter.

During collection, data is displayed on an oscilloscope with four brightness levels controlled by the PDP-15. Hard-data-output is available in graphical form as well as in a digital map, giving the number of annihilation events versus matrix location. Corrections for decreased counting efficiency near the edges of the detectors can be applied as a function of

camera radius. All data shown below has been corrected accordingly.

### Discussion

The experiments described here were performed on an 18 lb. beagle resting on its back between the two detector crystals of the camera so that the lung was centrally located. During an exposure, the dog was forced to breathe from a reservoir filled with air and tagged nitrogen or ozone. A teflon lined pump (to minimize decomposition of the ozone) served to control the breathing rate. The procedure was to image the lung by first administering a mixture of 80%  $^{15}\text{N}_2$  and 20%  $\text{O}_2$  (Fig. 2). The activated nitrogen is well suited for this purpose since it does not enter significantly into the pulmonary bloodstream, hence remains in the airways until ventilated with clean air. This ventilation was followed by an exposure with a 1ppm ozone-air mixture, lasting 300 inspirations or approximately 10 minutes. After ventilation the dog was again put on  $^{15}\text{N}_2$  (Fig. 3). Then a 5ppm ozone concentration in air was administered (Fig. 4) and a third nitrogen run (Fig. 5) completed this sequence.

Fig. 2, 3, 4 and 5 represent some typical results in the form of computer graphics, showing the distribution of annihilation activity for a particular plane between the detector heads of the camera, integrated over about 150 inspirations. The original 100 x 100 matrix is compressed into a 64 x 64 array for practical reasons. Left and right lungs are characterized by two peaks (Fig. 2) with a depression just forward of these indicating the location of the heart with only a low level of  $^{15}\text{N}_2$ -activity. Just below the focal plane, appearing diffused, is the trachea. By choosing a different focal plane the trachea, having a diameter a little more than 1 cm, can be brought out somewhat more clearly.

Fig. 4 shows a 5ppm ozone exposure. The peak in the animal's trachea near the camera edge appears to indicate some preferred ozone absorption in the upper region of this airway. It should be pointed out however, that the specific activity of the ozone-air mixture is quite low to begin with, because the ratio of activated ozone to normal ozone achieved to date is only about  $10^{-9}$ . In addition, the chemical separation of  $^{15}\text{O}_2$  and  $^{15}\text{O}_3$  after irradiation and prior to administration to the dog, takes perhaps 3 half-lives (6 minutes) before counting can actually begin; this results in relatively low counting statistics for the ozone exposures. On the other hand, the  $^{15}\text{N}_2$ , having a 10 minute half-life and requiring in general no chemistry, poses no such problems. Combining the results of pre- and post-ozone nitrogen runs, Fig. 2 shows a symmetric  $^{15}\text{N}_2$  distribution. Following the 1ppm ozone treatment, the nitrogen activity observed in Fig. 3 indicates a reduced ventilation in the right lung wing which further decreased after the administration of the 5ppm ozone concentration (Fig. 5). Considerably more detail is obtained from the digital maps for which there is no room here, but the graphical data representation suffices to show that regional functional changes can be detected. More recent experiments have provided better quality of information, i.e. more detail, by improved experimental procedures and higher specific gas activities. In addition, promising results have been obtained from blood perfusion measurements using

$^{15}\text{C}^{18}\text{O}_2$  and  $\text{H}_2^{18}\text{O}$  tracers.

It is clear that the most important single factor limiting quality of detail that can be obtained with a positron camera is the range of the positrons in matter of interest, i.e. animal or human tissue, bone, blood, etc. It has been pointed out above that the maximum range (3-4 cm) of the highest energy positron from  $^{15}\text{O}$  in lung tissue is considerably larger than the intrinsic resolution (1.5 cm) of the camera. We are planning to investigate the quantitative effect of particle range on the camera resolution for biologically important isotopes.

**Acknowledgments:** The authors thank Don Freeman of Livermore for ably preparing the software that generates the graphic data displays, and C. D. Bowman, E. Goldberg and R. E. Yoder for suggesting this project and for many helpful discussions.

### References:

- 1a) Watanabe, S., Frank, R., and Yokoyama, E.: Acute Effects of Ozone on Lungs of Cats. I. Functional. *Amer. Rev. Resp. Dis.* 108:1141-1151, 1973.
- 1b) Yokoyama, E., and Frank, R.: Respiratory uptake of ozone in dogs. *Arch. Environ. Health* 25: 132-138, 1972.
- 2) Mueller, Peter K. and Hitchcock, M.: Air Quality Criteria. Toxicological Appraisal For Oxidants. Nitrogen Oxides and Hydrocarbons. *J. Air Poll. Control Assoc.* 19 (1): 670-678 (1969).
- 3) McNeill, K. G.: Photonicuclear Reactions in Medicine. *Physics Today*, April 1974.
- 4) Meyer, P.: Ozone Tagging for Biomedical Purposes Proc. Int'l. Conf. on Photonicuclear Reactions and Applications, Asilomar, CA, 1973 (Berman, B. L. ed.).
- 5) Anger, H. O., *Rev. Sci. Instr.* 29, 27 (1958).
- 6) Behrin, E.: Positron/Scintillation Camera Data Acquisition and Display System. UCRL-51288, September, 1972.
- 7) Evans, R. D.: *The Atomic Nucleus*. McGraw-Hill, 1955, p. 625.

<sup>†</sup>Work supported in part by the U.S. Atomic Energy Commission and the National Institute for Occupational Safety and Health, Public Health Service, Department of Health, Education and Welfare, OH 00340-06



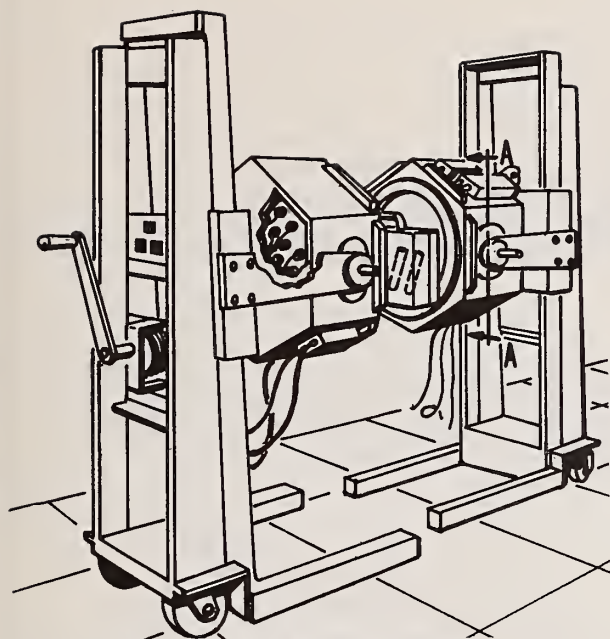


FIG. 1a, POSITRON CAMERA

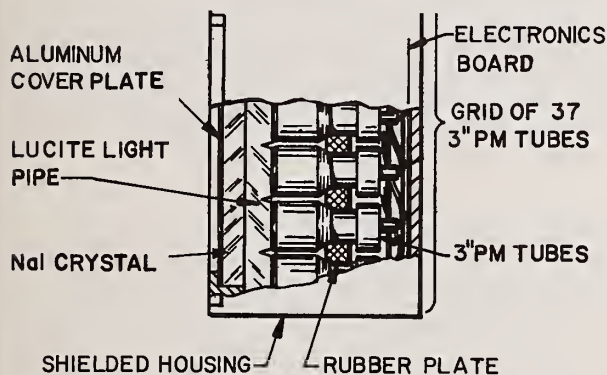


FIG. 1b, POSITRON CAMERA, DETAIL A-A

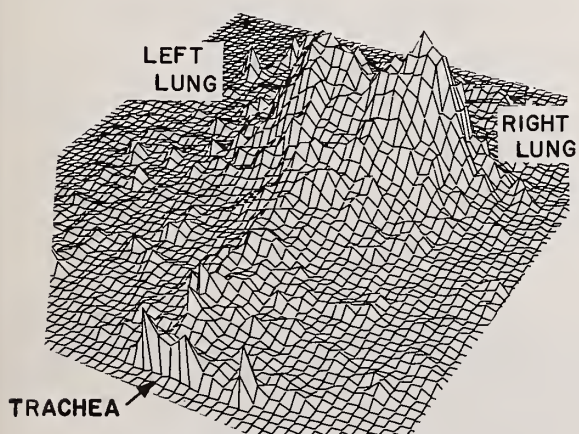


FIG. 2, NITROGEN UPTAKE  
PRE-OZONE EXPOSURE

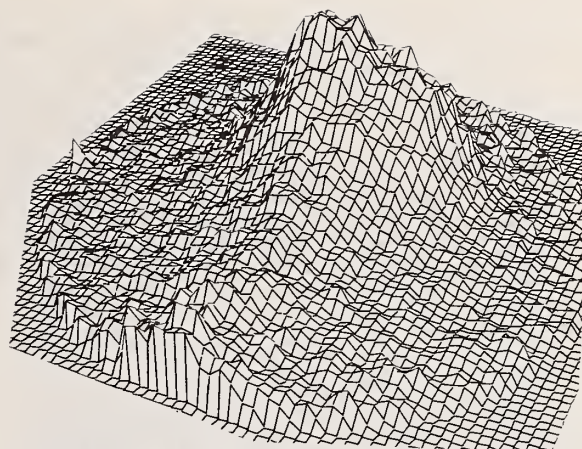


FIG. 3, NITROGEN UPTAKE  
POST 1PPM OZONE EXPOSURE

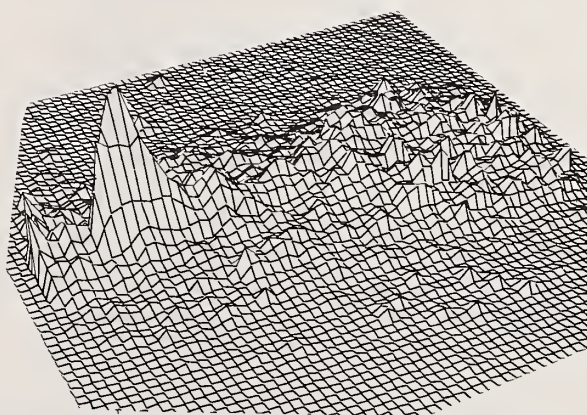


FIG. 4, 5PPM OZONE UPTAKE

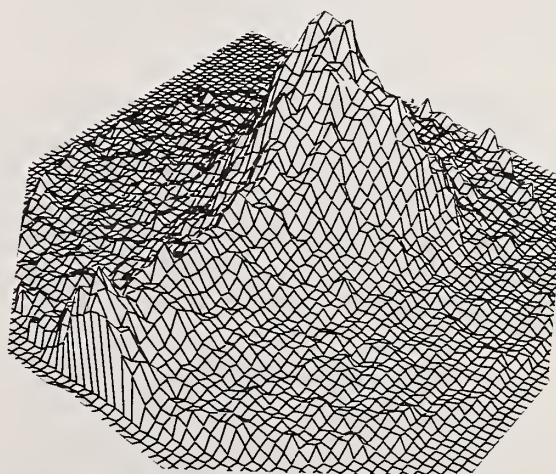


FIG. 5, NITROGEN UPTAKE  
POST 5PPM OZONE EXPOSURE

C. Werntz\* and C. W. Lucas, Jr.\*  
Catholic University of America  
Washington, D.C. 20017

Through the use of a simple model in which true absorption of a pion in flight by a nucleus is treated analogously to collisional broadening in optics, the energy dependent mean free path for star formation in water is calculated. Besides the absorption cross section, the cross sections for elastic and inelastic scattering are presented.

### Introduction

Beams of negative pi mesons are soon to be used in radiation therapy for cancer victims. The property of these elementary particles which makes their use seem promising<sup>1</sup> is the process of absorption by atomic nuclei after coming to rest and being captured into Bohr orbits. Transferring their rest mass energy to the nucleus results in the formation of nuclear stars, the name deriving from the multiple tracks of ionizing particles radiating from the absorbing nucleus, seen, for example, in nuclear emulsions. Since negative pions interacting with protons produce neutrons much of the energy is lost in the form of non-ionizing radiation. In fact, only about 30 MeV is deposited as localized energy.<sup>2</sup>

A pion passing through condensed matter loses energy by making ionizing collisions with atomic electrons (the usual  $dE/dx$ ), by elastic and inelastic collisions with the atomic nuclei, and by absorption - this is the process we have already called star formation. Boyd<sup>3</sup> pointed out the possible importance of in flight star formation and Li et al.<sup>4</sup> have presented explicit equations which enable one to calculate the equivalent biological dose arising from star formation. Their starting point is an attenuation length for  $\pi^-$  in water of  $Z_0 = 46$  cm. with which a fit to the integral range curve is obtained. While the authors state that approximately 25% of this attenuation is due to elastic scattering  $Z_0$  is effectively taken to be the attenuation length due to star formation in their subsequent calculations.

The actual absorption length of pions in matter is an uncertain quantity.<sup>5</sup> In this paper we present a theoretical determination of the star formation cross section as a function of energy in complex nuclei. By applying it to  $^{16}O$  we are able to calculate an energy dependent attenuation length in water. (Pions cannot be absorbed by a single proton.) We find that star formation in flight is significantly reduced as compared to Ref. 4.

### Pion Optical Potential

Due to the strong interaction of pions and nucleons the lower energy levels of pionic atoms are shifted. Since strong absorption occurs they are also broadened compared to their usual electro-magnetic widths. Both phenomena can be explained by the in-

troduction of an optical potential<sup>6</sup> which when inserted into a Klein-Gordon equation leads to complex energy values. A recent potential that has been fit to a massive amount of X-ray spectra is due to Backenstoss.<sup>7</sup>

$$V = -\frac{2\pi}{m\pi} [b_0 \rho(\vec{r}) + i \text{Im } B_0 \rho^2(\vec{r}) - \vec{r} \cdot (c_0 \rho(\vec{r}) + C_0 \rho^2(\vec{r})) \vec{V}] \quad (1)$$

$$C_0 = -4\pi c_0^2/3 + i \text{Im } C_0$$

In multiple scattering theory the coefficients of terms linear in  $\rho(\vec{r})$ , the nuclear density, are combinations of iso-spin pi-nucleon amplitudes evaluated at zero energy.<sup>6</sup> The terms quadratic in the density came from either multiple scattering with the nucleus being excited between scatterings, the  $c_0^2$  term, or from two nucleon absorption of the pion, the imaginary terms involving  $\text{Im} B_0$  and  $\text{Im } C_0$ .

At higher energies the  $b_0$  and  $c_0$  terms are still well defined in terms of free pion-nucleon amplitudes but the energy behavior of the  $\rho^2$  terms has not hertofore been estimated. Most treatments are restricted to a linear density dependence so that elastic and inelastic nuclear scattering alone are being taken into account - no true absorption of the pion occurs. We obtain a representation for the  $\rho^2$  terms at all energies by postulating absorption takes place through the collisional deexcitation of a  $\Delta 33$  inside the nucleus through interaction with a second nucleon.

Retaining for p-waves only the 3,3 channel, the parameter  $c_0$  is given by

$$c_0 = \frac{4 \exp(i\delta_{33}) \sin \delta_{33}}{3\kappa^3} \quad (2a)$$

$$\exp(i\delta_{33}) \sin \delta_{33} = \frac{\Gamma/2}{(\epsilon_R + \Delta - \epsilon\pi) - i\Gamma/2} \quad (2b)$$

For free pion-nucleon scattering one can fit<sup>8</sup> the phase shift with  $\Delta=0$ , and

$$\Gamma \equiv \Gamma_e = \frac{4m\pi}{\epsilon_R + \epsilon\pi} M\gamma^2 P(\kappa a) \quad (3)$$

The resonant energy  $\epsilon_R$  and the pion energy  $\epsilon\pi$  are evaluated in the pion-nucleon CM and  $c_0$  should be obtained from a Fermi average over the nucleon motion. Inside a nucleus we postulate that the shift is

$$\Delta = \Delta a(\epsilon\pi) \rho(r) = \Delta a(m\pi) \frac{(\epsilon_R - \epsilon\pi)}{(\epsilon_R - m\pi)} \rho(r) \quad (4)$$



and

$$\Gamma = \Gamma_e + \Gamma_a(\epsilon\pi) \rho(r) \quad (5)$$

$$\Gamma_a(\epsilon\pi) = \Gamma_a(m\pi) \frac{(\epsilon\pi - B_2)^{1/2}}{(m\pi - B_2)^{1/2}}$$

The square root factor comes from the density of final states of the final nucleon pair and  $B_2$  is the binding energy of the two nucleons in the residual nucleus.

We evaluate the shift and absorption width from the pionic atom potential,  $\epsilon\pi = m\pi$ .

$$\exp(i\delta_{33}) \sin \delta_{33} \rightarrow \frac{\Gamma_e/2}{\epsilon_R - \epsilon\pi} \left[ 1 - \frac{(\Delta a - i\Gamma_a/2) \rho(\vec{r})}{\epsilon_R - \epsilon\pi} \right] \quad (6)$$

Comparing to Eqs. (1) and (2), we get

$$\Gamma_a(m\pi) = \frac{2\text{Im}C_0}{C_0} (\epsilon_R - m\pi), \quad (7)$$

$$\Delta_a(m\pi) = \frac{R_e C_0 - 4\pi/3 C_0^2}{C_0}$$

We have added a term  $R_e C_0$  to the expression for  $\Delta_a$  above since the nucleon-nucleon interactions in the media create both energy shifts and absorptions.<sup>9</sup> One other point is worth noting. Since all p-waves other than the 3,3 have been ignored, the free width  $\Gamma_e$  must be adjusted to give the proper threshold value for  $C_0$ .

$$C_0 = \lim_{k \rightarrow 0} \frac{1}{2k^3} \frac{\Gamma_e}{\epsilon_R - \epsilon\pi} \quad (8)$$

The parameters in our theory are

$$\text{Im } B_0 = + 0.04 m\pi^{-4}, \quad C_0 = +.21 m\pi^{-3}$$

$$R_e C_0 = +.078 m\pi^{-6}, \quad \text{Im}C_0 = +.078 m\pi^{-6} \quad (9)$$

$$B_2 = 27 \text{ MeV}, \quad \epsilon_R = 1.91 m\pi$$

The values of  $b_0$  were taken from the pion-nucleon phase shifts.

### Pion-Nucleus Cross Sections

The elastic differential cross section for scattering of a  $\pi^-$  on  $^{12}\text{C}$  at an energy of interest, 62.0 MeV, is shown in Fig. 1.

The total elastic cross section is obtained from the phase shifts by use of

$$\sigma_{el} = 4\pi \sum_l (2l+1) |f_l|^2 \quad (10)$$

$$f_l = \exp(2i\delta_l) \frac{\exp(i\delta_l) \sin \delta_l}{k}$$

The inelastic (nuclear excitation) and absorption cross sections are estimated separately by observing that the imaginary part of the optical potential is (aside from the small  $\text{Im}B_0$  term)

$$\text{Im } V = \frac{+2\pi}{\epsilon\pi} \frac{1}{3k^3} \frac{\vec{v} \cdot \rho(\vec{r}) (\Gamma_e^2 + \Gamma_e \Gamma_a \rho(\vec{r})) \vec{v}}{(\epsilon_R + \Delta - \epsilon\pi)^2 + \Gamma^2/4} \quad (11)$$

$$= \text{Im } V_{ee} + \text{Im } V_{ea}$$

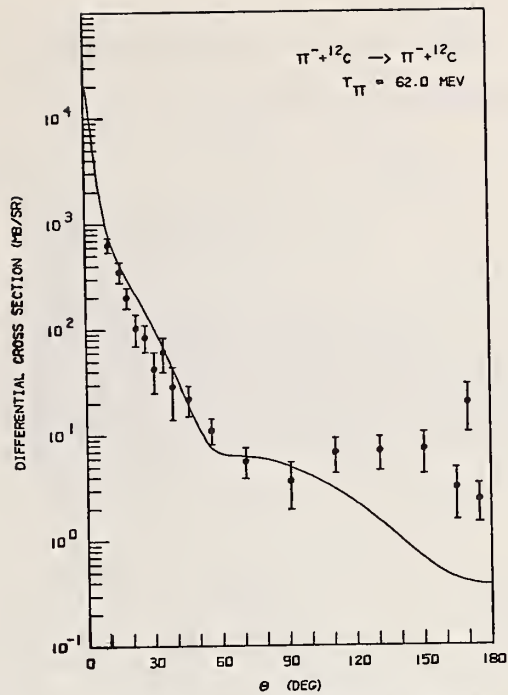


Fig. 1. Theoretical differential cross section for  $\pi^-$  scattering from  $^{12}\text{C}$  compared to data of Ref. 10.

In general, the difference between the total and elastic cross sections caused by an imaginary potential can be calculated from the expression

$$\sigma_{tot} - \sigma_{el} = -\frac{2}{v} \int d\vec{r} \psi^{(+)*} \text{Im} V \psi^{(+)} \quad (12)$$

where the  $\psi^{(+)}$  are the scattering solutions to the wave equation. Our ansatz is that the inelastic and absorption cross section can be calculated separately from

$$\sigma_{inel} = -\frac{2}{v} \int d\vec{r} \psi^{(+)*} \text{Im} V_{ee} \psi^{(+)}$$

$$\sigma_{ab} = -\frac{2}{v} \int d\vec{r} \psi^{(+)*} \text{Im} V_{ea} \psi^{(+)} \quad (13)$$

$$v = k/E\pi$$

The expressions in Eq. (13) are plausible because the inelastic excitation of a nucleus occurs following the scattering of a pion from a nucleon with the momentum distribution of the nucleon overlapping with that of the excited state. On the other hand, absorption depends on the presence of a new process represented by  $\Gamma_a$ .

The program was checked by requiring

$$\sigma_{tot} = \sigma_{el} + \sigma_{inel} + \sigma_{ab} \quad (14)$$

$$\sigma_{tot} = \frac{4\pi}{k} \text{Im } f(0)$$

<sup>12</sup> Our total and elastic cross section for  $^{12}\text{C}$  turn out to be about 15% too small<sup>11</sup>, so one can expect the  $^{16}\text{O}$  results to be similarly too low. The four calculated cross sections for  $^{16}\text{O}$  are shown in Fig. 2.



### Dose Contributions of Pion States

Li et. al.<sup>4</sup> calculated the dose due to star formation from the formula

$$D_S(z,r) = \left| \frac{dN_\pi(z)}{dz} \right| \times E_S \times D_{ms}(z,r) \quad (15)$$

$$N_\pi(z) = N_\pi(0) \exp(-z/z_0) \frac{1}{1 + \exp\left(\frac{z - R_0}{z_1}\right)}$$

where  $E_S$  is the average energy liberated, from an in flight star,  $D_{ms}(z,r)$  is a function that describes the lateral spread of the pencil pion beam, and  $N_\pi(z)$  is the number of pions that penetrate to a depth  $z$ . As mentioned before they used  $Z_0 = 46$  cm for  $H_2O$ .

With an energy dependent absorption cross section

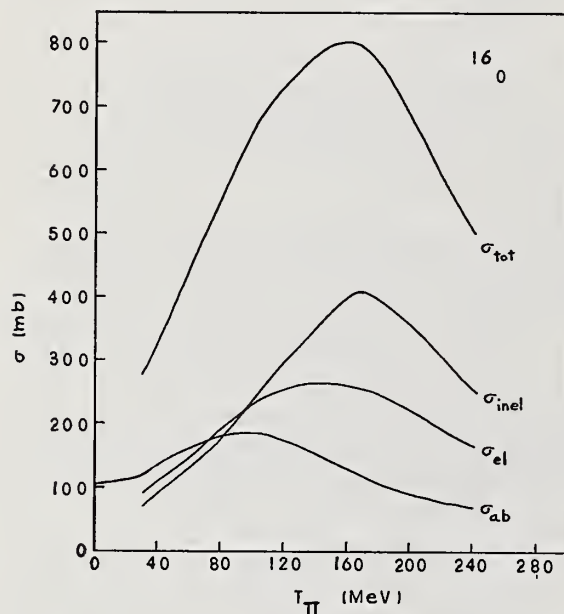


Fig. 2. Theoretical total, elastic, inelastic, and absorption (star formation) cross sections in  $^{16}O$ .

$$N_\pi(E) = \exp(-\alpha(E))$$

$$\alpha(E) = - \frac{N_{AV}}{A} \int_{E_0}^E dE \frac{\sigma_{ab}(E)}{dE/dz} \quad (16)$$

where straggling has been omitted and  $dE/dz$  is the mass stopping power.<sup>12</sup> Using the tables of Barkas and Berger<sup>12</sup> and the cross section from Figures 2 the attenuation of pions has been calculated and is compared to that of Li et. al.<sup>4</sup> in Table I for 75 MeV incident  $\pi^-$ . One sees that if the present

Energy (MeV)	Depth (cm)	$\alpha(E)$ ( $10^{-2}$ )	$e^{-\alpha(E)}$	$e^{-Z/Z_0}$
65	4.0	2.0	.98	.92
55	8.0	3.8	.96	.84
45	12.0	5.2	.95	.77
35	15.3	6.4	.94	.72
25	18.0	7.2	.93	.68
15	20.5	7.8	.92	.64
5	21.3	7.9	.92	.63

Table I. Attenuation due to star formation by 75 MeV incident negative pions in water. The present calculation is compared to the results of Ref. 4.

calculation is correct, attenuation due to star formation has been over estimated in Ref. 4. This result agrees better with the work of Turner et. al.<sup>13</sup> where about 85% of incident pions are estimated to stop and the discrepancy may be made up by large angle elastic and inelastic scattering.

For further comparison we calculate the star dose or linear energy transfer (LET) for a pion going through water. We simplify Eq. (15) to

$$D_S(z) = \frac{1}{Z_0} \exp(-Z/Z_0) (30 + E/3) \quad (17)$$

and for the energy dependent cross section use

$$D_S(E) = \frac{N_{AV}}{A} \rho \sigma_{ab}(E) (30 + E/3) \quad (18)$$

For water  $A = 18$  gms,  $\rho = 1$  gm/cm<sup>3</sup>, and besides the 30 MeV share of the pion rest mass energy 1/3 of its kinetic energy has been estimated to go into ionization energy. The results are shown in Table 2. Once again our theory leads to significantly smaller values than in Ref. 4.

E	$\sigma_{ab}(E)$ (mb)	Z(E) (cm)	LET (MeV/cm)	LET <sup>4)</sup> (MeV/cm)
75	175	0.	0.32	1.20
65	167	4.0	0.28	1.03
55	153	8.0	0.24	0.88
45	136	12.0	0.20	0.75
35	125	15.3	0.16	0.65
25	113	18.0	0.14	0.57
15	104	20.5	0.11	0.49
5	102	21.3	0.10	0.43

Table 2. Linear energy transfer in water due to in flight star formation. Present theory compared to Ref. 4. LET values near end of track are unrealistic since some pions will stop and all of the stopping pions create stars.

### References

\*Supported in part by Office of Naval Research  
<sup>†</sup>Present address: Smithsonian Science Information Exchange, Inc., Washington, D.C. 20036

1. P.H. Fowler and D.H. Perkins, Nature **189**, 524 (1961).
2. P.H. Fowler and V.M. Mayes, Proc. Phys. Soc. **92**, 377 (1967).

3. D. Boyd, High Energy Physics Laboratory Report No. HEPL-TN-71-1, Stanford University.
4. G.C. Li, D. Boyd, and H. Schwettman, High Energy Physics Laboratory Report No. HEPL-668, August 1972, Stanford University.
5. R.R. Silbar, "Quasi Elastic Scattering and the Absorption of Pions in Nuclear Matter", preprint.
6. M. Ericson and T.E.O. Ericson, Annals of Physics 36, 323 (1966).
7. G. Backenstoss, Annual Review of Nuclear Science 20, 467 (1970).
8. L.D. Roper, R.M. Wright, and B.T. Feld, Phys. Rev. 138, B190 (1965).
9. C.B. Dover, Annals of Physics, (N.Y.) 79, 441 (1973).
10. H. Byfield, J. Kessler, and L.M. Lederman, Phys. Rev. 86, 17 (1952).
11. F. Binon, P. Duteil, J.P. Garron, J. Gorres, L. Hugon, J.P. Peigneux, C. Schmist, M. Speghel, J.P. Stroot, Nucl. Phys. 17B, 168 (1970).
12. "Tables of True Energy Losses and Ranges of Heavy Charged Particles"; Walter H. Berkas and Martin J. Berger, NASA SP-3013, Washington, D.C. 1964.
13. J.E. Turner, J. Dutrannois, H.A. Wright, R.N. Hamm, J. Baarli, A.H. Sullivan, M.J. Berger, and S.M. Seltzer, Rad. Res. 52, 229 (1972).

SPECTRUM AND SHIELDING MEASUREMENTS AND CALCULATIONS  
OF NEUTRONS PRODUCED BY 800 MeV PROTONS\*  
L. R. Veesser, G. J. Russell, E. D. Arthur,  
P. A. Seeger, W. F. Sommer, D. M. Drake,  
R. G. Fluharty, and R. F. Bentley  
Los Alamos Scientific Laboratory  
Los Alamos, NM 87544

Measurements were made to check: (a) calculation of the neutron flux produced by 800-MeV protons on a cylinder of depleted uranium, and (b) computations of the energy-dependent neutron flux as a function of thickness for a rectangular shield surrounding the target. A proton recoil spectrometer was used to measure neutron fluxes from the shield between 300 keV and 7 MeV. Agreement has been obtained between the proton recoil data and Monte Carlo calculations for shields composed of steel and gypsum for thicknesses between 0.48 m and 1.37 m. Agreement is good at most angles for energies above 1 MeV.

[ SHIELDING,  $^{238}\text{U}(p, xn)$ ,  $E_p = 800$  MeV; measured neutron spectra;  
deep penetration of neutrons in Fe + H shield;  
angular dependence; Analysis by Monte Carlo ]

### Introduction

Measurements of neutron spectra produced by medium energy protons striking heavy metal targets indicate that such reactions can be used to make an intense neutron source with relatively few photons emitted as by-products.<sup>1-3</sup> This experiment was done to provide information for the design and use of the Weapons Neutron Research Facility (WNR), a neutron time-of-flight facility now being built at the Clinton P. Anderson Meson Physics Facility (LAMPF) at the Los Alamos Scientific Laboratory. Neutrons will be obtained at WNR by impinging the 800-MeV LAMPF proton beam onto a depleted uranium target.

Shielding needs for medium and high energy accelerators are often determined by Monte Carlo calculations.<sup>4</sup> For WNR, however, it was felt that the limited space available for shielding, the large thicknesses needed, and the high energies of the particles for which the shielding must be effective made necessary an experimental verification of the calculations.

### Uranium Spectrum

Two continuous-energy Monte Carlo codes were used to compute the neutron leakage spectra from 800-MeV protons striking a 30 mm-diam x 250 mm-long depleted (0.2 wt%  $^{235}\text{U}$ ) uranium cylinder. The Nucleon Meson Transport Code<sup>5</sup> (NMTC) was used to transport all particles with energies above 20 MeV, and lower energy neutrons were transported using the Neutron Monte Carlo Code<sup>6</sup> (MCNG). To enhance the capabilities of NMTC, the versatile MCNG geometry package was incorporated into it.<sup>4</sup>

Protons were assumed to strike the target uniformly in a 15 mm-diam spot centered on the axis of the cylinder. The calculations indicate that for each incident proton, 18 neutrons are emitted from the target, and 87% of the neutrons emerge from the first 150 mm of the cylindrical surface. Figure 1 summarizes the calculated neutron leakage from the uranium target. The high energy neutrons (>100 MeV) are strongly forward peaked, while low energy neutrons are nearly isotropically distributed.

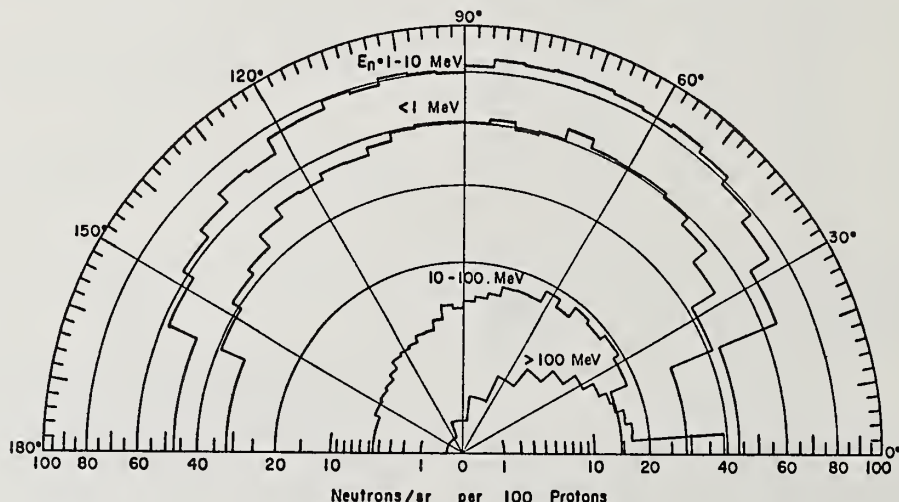


Fig. 1. Calculated angular distribution, for 4 energy groups, of neutrons emitted from a 30 mm-diam by 250 mm-long depleted uranium target for 800-MeV protons incident along axis in the 0° direction and uniformly spread over a 15 mm-diam spot. Note the strong forward distribution for neutrons having energies above 100 MeV.



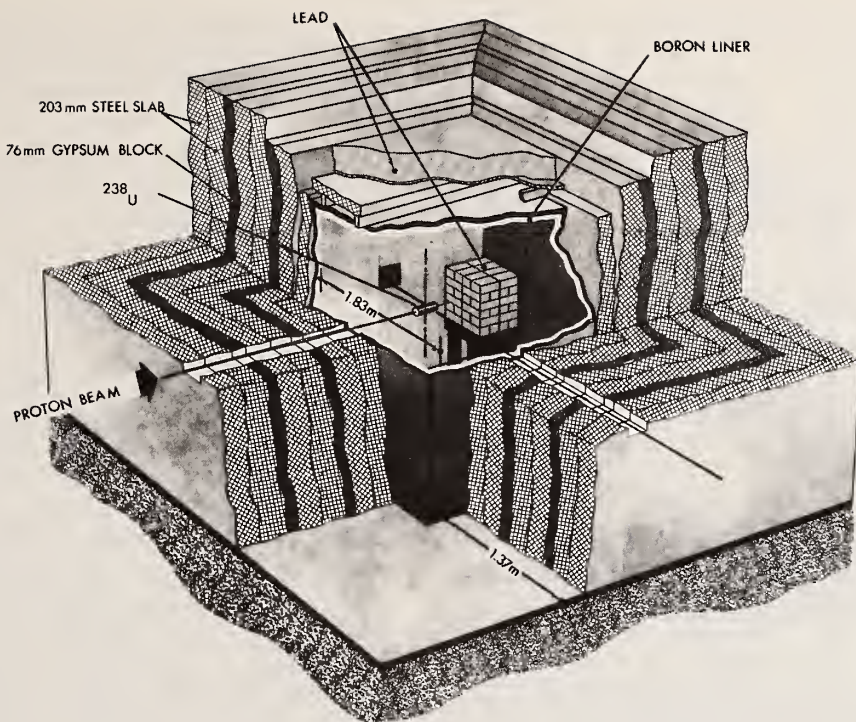


Fig. 2. Schematic of the uranium target and shield around it. To measure thinner shields, layers of steel and gypsum were removed from the outside. The hole at 90° to the proton beam was used to measure the source spectrum and was filled with lead for the shielding measurements. The pile of lead bricks inside the shield served as a secondary beam stop to prevent protons from penetrating the shield if they missed the target during tuning.

The calculation was checked at 90° to the proton beam by measuring the neutron spectrum using time-of-flight methods. Although more high energy neutrons were measured than the calculation indicates, the computed spectrum was used as the neutron source for the remaining Monte Carlo computations, partly to reproduce design methods and partly for convenience.

#### Shielding Results

A large shield, shown in Fig. 2, was built around the target. The shield consisted of three 406 mm-thick layers of steel separated by 76 mm of gypsum ( $\text{CaSO}_4 \cdot 2\text{H}_2\text{O}$ ). The inside of the shield was lined with 38 mm of boron-loaded polyethylene. Although the uranium target was longer than the range of the 800-MeV protons, a lead beam stop was required to keep the proton beam from penetrating the back shield wall during beam tuning.

Iron, which has a relatively large neutron inelastic scattering cross section, efficiently reduces the number of high energy neutrons. However, there are "windows" where the total cross section is very small (e.g., near 24 keV and between 100 and 800 keV). To prevent neutrons of these energies from leaking out of the shield, the layers of gypsum were used between the iron layers. Gypsum was chosen because it was available and convenient to use; in the final design

of WNR, the hydrogenous material will be magnetite concrete.

The Monte Carlo programs used in calculating the neutron spectrum from the uranium target were also used to transport particles through the shield. In addition, a routine was written to allow splitting of the high energy particles as they progressed through the shield.<sup>4</sup> Figure 3 shows the results of the transport calculations for neutrons penetrating one side of the shield parallel to the target. The angle-integrated neutron intensity incident upon the shield wall is depicted in Fig. 3 as well as the leakage-neutron intensity from four thicknesses of shield. The effects of neutron-streaming through the iron "windows" and the degradation of these neutrons by the gypsum are apparent.

Measurements of the neutrons between 0.5 and 7 MeV emerging from the shield were made at several angles using a 51 mm-diam by 51 mm-long NE-213 liquid scintillator as a proton recoil spectrometer. An Elron Model PSD-N-1 pulse shape discriminator identified and rejected pulses from gamma rays. Known response functions<sup>7</sup> were used in a least structures unfolding program<sup>8</sup> to calculate neutron spectra from the neutron pulse height spectra.

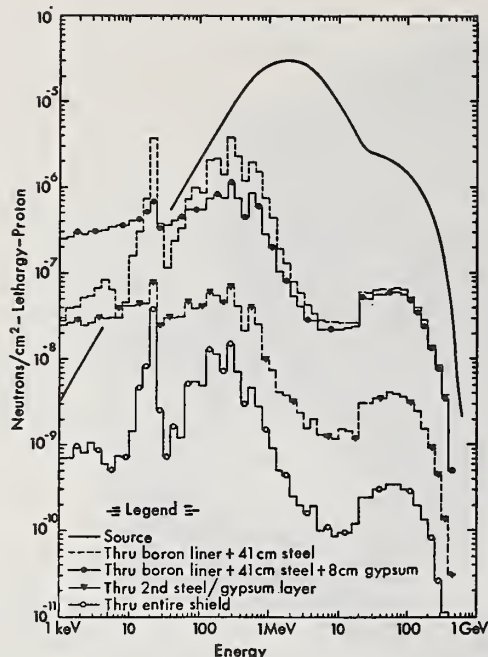


Fig. 3. Calculated neutron intensity incident upon the side of the shield parallel to the axis of target, and the leakage-neutron intensity from four shield thicknesses. Iron does most of the shielding. Note the effects of neutron-streaming through the iron cross section "windows" and the degradation of these neutrons by the gypsum.

Neutron spectra for thinner shielding were obtained by removing the outer layer of steel and repeating the spectrum measurements. Finally, a layer of gypsum and a second layer of steel were removed to permit a third spectrum measurement.

Because of the large numbers of high energy gamma rays emerging from the shields, particularly for the thinner shielding, the pulse shape discrimination did not work well at high energies. Consequently, meaningful results were not obtained for neutrons above 7 MeV.

In Fig. 4 the measurements are compared with the calculations at 0, 20, and 41°. The "thin," "medium," and "thick" notation refers to the relative thicknesses of the shielding mentioned above. Uncertainties in the measurements are about 30%. Above 2 MeV the uncertainty is essentially statistical, while at lower energies the major uncertainty arises from using response functions which were measured for a somewhat smaller (46 mm-diam by 46 mm-long) detector than was used here.

At 0 and 20°, the calculations are systematically higher than the measurements at all energies except for the thin shield at 0°. For this latter run it is possible that the detector was positioned where it could be struck by neutrons leaking through cracks in the shield. For 41°, the measurements and calculations seem to agree above 1 MeV, but the calculations are again higher at low energies. Although the 41° results are lower than the forward angle data for a given shield thickness, it should be remembered that neutrons emerging at 41° had to travel a longer path because of the rectangular shape of the shield.

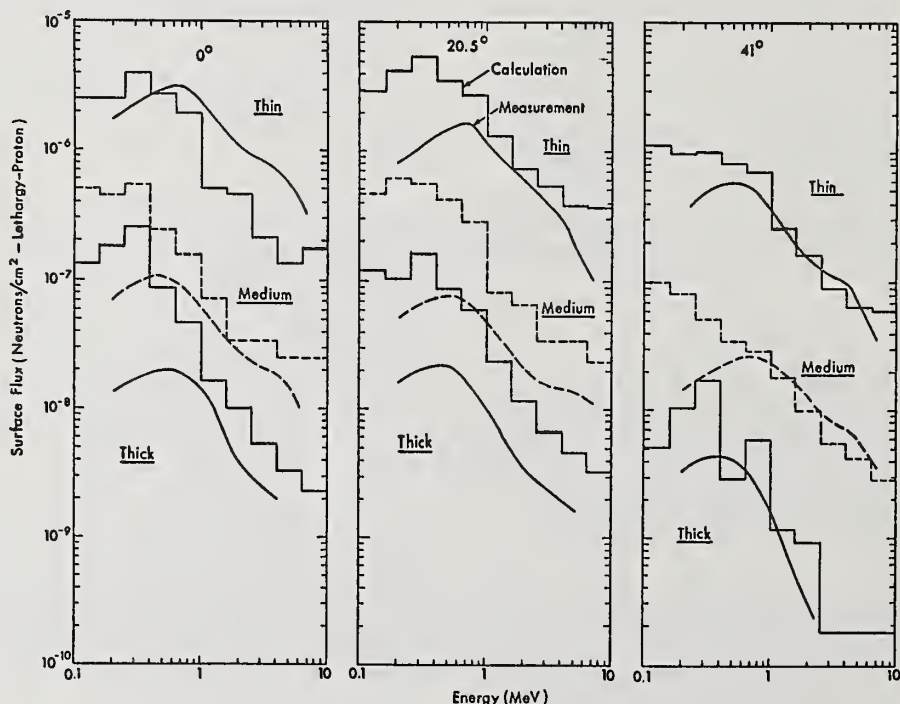


Fig. 4. Shielding results at 0, 20, and 41°. The histograms are calculations, and the smooth curves show the measurements. Uncertainties in the measurements are about 30%.



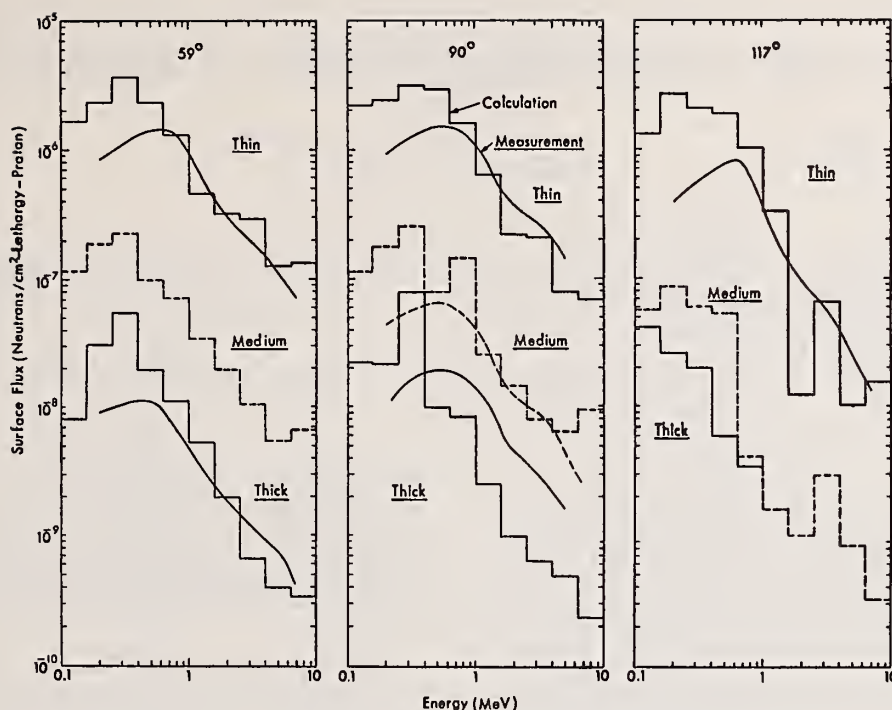


Fig. 5. Shielding results at 59, 90, and 117°. The histograms are calculations, and the smooth curves show the measurements. Uncertainties in the measurements are about 30%.

Figure 5 compares measurements with calculations for 59, 90, and 117°. Agreement is very similar to the 41° cases; it is reasonably good above 1 MeV, but at lower energies the calculations are again higher than the experimental results. A thick-shield measurement at 135° looks qualitatively similar to the results shown here. The 90° thick-shield measurement, which is higher than the calculations, probably is in error because the hole used to check the 90° source spectrum was not plugged completely for the thick-shield measurements.

### Conclusions

The results of the shielding measurements indicate that the Monte Carlo calculations of NMTC and MCNG will do an adequate job of predicting needed shielding thicknesses. Where the calculations are not in agreement with the measurements, below 1 MeV and at forward angles, they appear to overestimate the neutron flux through the shield.

Although high-energy shielding results are not available from this experiment, it is known that NMTC underestimates the number of high energy particles produced at large angles by the proton beam.<sup>2</sup> We therefore expect more large angle scattering of high energy neutrons in the iron shield than is predicted by NMTC, and consequently less penetration through the shield. Although the calculated source does not contain enough high energy neutrons, the increased attenuation in a thick shield will eventually compensate because the attenuation is exponential while the source error is multiplicative.

\*Work performed under the auspices of the USERDA.

- <sup>1</sup>J. S. Fraser, J. S. Hewitt, and J. Walker, "Neutron Spectra and Angular Distribution Produced by 1 GeV Protons on a Thick Lead Target," paper presented at the Congress-Canadian Association of Physicists, Sherbrooke, Quebec, Canada (1966), Gmelin Institute Number 66-221-4.
- <sup>2</sup>R. Madey and F. M. Waterman, Phys. Rev. **C8**, 2412 (1973).
- <sup>3</sup>L. R. Veaser, R. R. Fullwood, A. A. Robba, and E. R. Shunk, Nucl. Instr. and Meth., **117**, 509 (1974).
- <sup>4</sup>R. G. Fluharty, P. A. Seeger, D. R. Harris, J. J. Koelling, and O. L. Deutsch, "Transport of Neutrons Induced by 800-MeV Protons," in Nuclear Data in Science and Technology, **1**, IAEA, Vienna, 607 (1973).
- <sup>5</sup>W. A. Coleman and T. W. Armstrong, "The Nucleon-Meson Transport Code NMTC," Oak Ridge National Laboratory Report ORNL-4606 (1970).
- <sup>6</sup>E. D. Cashwell, J. R. Neergard, W. M. Taylor, and G. D. Turner, "MCN: A Neutron Monte Carlo Code," Los Alamos Scientific Laboratory Report LA-4751 (1972).
- <sup>7</sup>V. V. Verbinski, W. R. Burrus, T. A. Love, W. Zobel, N. W. Hill, and R. Textor, Nucl. Instr. and Meth., **65**, 8 (1968).
- <sup>8</sup>A. A. Robba and L. R. Veaser, "A Least-Structures Unfolding Code," Los Alamos Scientific Laboratory Report LA-5088 (1972).

C. S. Dyer\* and J. I. Trombka  
 NASA, Goddard Space Flight Center  
 Greenbelt, MD 20771  
 and  
 S. M. Seltzer  
 National Bureau of Standards  
 Washington, DC 20234

\*NAS/NRC Resident Research Associate

A calculation is outlined which predicts energy-loss spectra observed in detector materials due to the decay of radioactive nuclides which are produced by particle irradiation in spaceflight. The input decay schemes and cross-section requirements are described. Examples are given from the Apollo gamma-ray spectrometer experiments.

(Activation; scintillators; spacecraft, gamma-rays; background; spallation; computation, decay-schemes; cross-sections; Apollo)

### Introduction

Radioactivity induced in detector and spacecraft materials by cosmic ray and trapped protons is a major source of background in gamma-ray remote sensing spectroscopy and astronomy measurements for the photon range from 20 KeV to 20 MeV. This spectral band promises important new results with implications for cosmology and antimatter in the universe. However, at present, spectral features and their implications are in a state of controversy because of uncertainties in allowing for radioactivity (see Ref. 1 for details). Future developments in this field require an accurate activation model in order that detector design and location may be optimized and data accurately corrected.

While spacecraft effects may be considerably reduced by active-shielding or extension of spectrometers on long booms, the problem of activation of the central detector element results in an unavoidable background. Detailed calculation of the activation of such systems is therefore important. Here the remainder of the spacecraft is considered only in terms of its influence on the incident particle flux.

Activation of NaI scintillator due to passage through trapped proton regions was first observed on OSO-1 by Peterson<sup>2</sup>. Early attempts were made to explain the data in terms of one or two isotopes produced by the capture of secondary neutrons. Since that time, activation has been observed in all the OSO gamma-ray experiments and has been shown to contain a complex superposition of half-lives<sup>3</sup>. An explanation of these observations was offered by Dyer and Morfill<sup>4</sup> who suggested that for such thin slab cases ( $\sim 10 \text{ gm cm}^{-2}$ ) direct spallation interactions of protons would be the dominant activating mechanism. This work used the results of 155 MeV irradiation of CsI and predictions based on Rudstam formula cross-section estimates used in conjunction with approximations to the energy-loss spectra of the decaying nuclides. From this work, and studies by Fishman<sup>5</sup> using 600 MeV irradiation of NaI, it was shown that the activation acquired in equilibrium with the cosmic ray flux could contaminate gamma-ray data in the MeV region. These predictions have since been borne out by gamma-ray spectrometers carried on the Apollo missions, which show additional effects due to secondary neutrons produced in the heavy spacecraft.

### Computation Scheme for Induced Activity

A computation scheme is under development based on the method given in Dyer and Morfill<sup>4</sup> but using

improved input data and computational techniques. The scheme, which is illustrated in Fig. 1, may be conveniently divided into two parts. On the one side, there is the problem of determining the energy-loss spectra of the relevant radioactive products when they decay inside the detector itself. On the other side, the rate of isotope production and decay must be calculated.

The energy-loss spectra are computed using a photon transport code which samples the decay schemes stochastically in order to allow for gamma-gamma and particle-gamma coincidences. In this code, the radioactive species are distributed uniformly throughout the crystal. For the majority of isotopes,  $Q < 4 \text{ MeV}$ , and it is only necessary to follow photon transport. A more elaborate version of the code may be used to follow electrons and photons and their secondaries for the few more energetic decays of interest. Examples of response functions are given in Figs. 2 and 3 which show the decay of  $\text{I}_{124}$  and  $\text{Na}_{24}$  inside a  $7 \text{ cm} \times 7 \text{ cm NaI}$  crystal. The underlying continuum is due to  $\beta$ -branches while line features result from electron-capture decay modes. It is worth noting that the line features are shifted in energy by coincidence with the K-shell X-ray. Accurate decay scheme data are required for this code. In view of the large number of isotopes which must be included it is of the utmost value to have decay scheme data available in computer-readable form. A limited amount of data have been incorporated in this way using computer cards from the Oak Ridge Nuclear data file<sup>6</sup>.

The isotope production side requires good spallation cross-section estimates. Trapped radiation effects are dominated by protons in the energy range 20-200 MeV and cross-sections for  $(p, xn)$ , peripheral, and spallation interactions are required. For cosmic-ray energies in excess of 1 GeV, both the fission and light fragmentation regions are important. The semi-empirical formulae of Silberberg and Tsao<sup>7</sup> cover all these cases and are used as the basic data set. Intra-nuclear cascade codes provided by Bertini et al.<sup>8</sup> have been used as an alternative data set in the spallation region. At present, sixty isotopes, for which the cross-section exceeds 10 mb, have been incorporated into the calculation for NaI. These are adequate for trapped radiation effects but cover only about one-half of cosmic ray activation, although the major line features should be reproduced. Energy-loss spectra from these species extend up to about 4 MeV. The contribution of light fragments (e.g.,  $\text{B}_{12}$ ,  $\text{Be}_{11}$ ,  $\text{Li}_8$ ) has also been assessed and shows a possible contribution to gamma-ray count-rates in the 10 to 15 MeV region. So far, the fission region has not been studied. It is possible

FIG. 1

# FLOW DIAGRAM OF SPALLATION ACTIVATION COMPUTATION

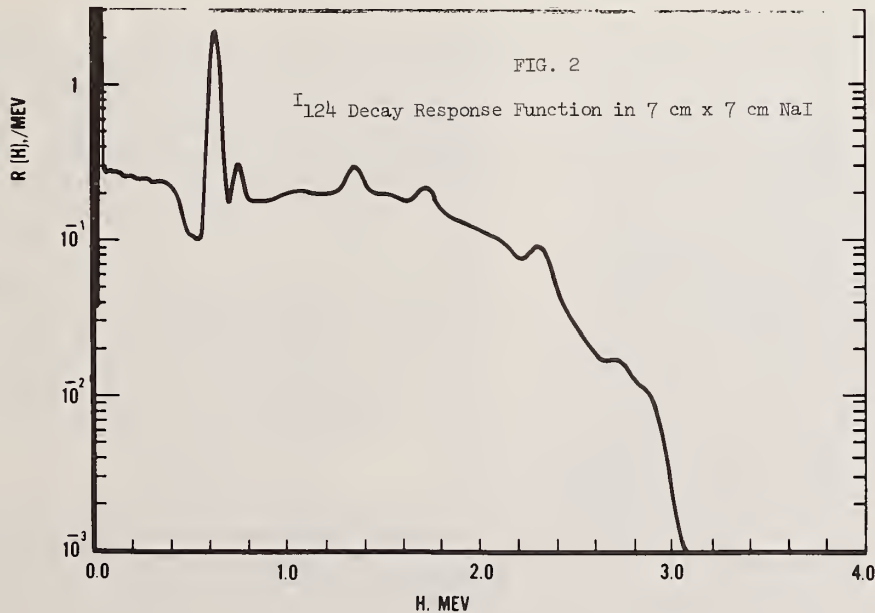
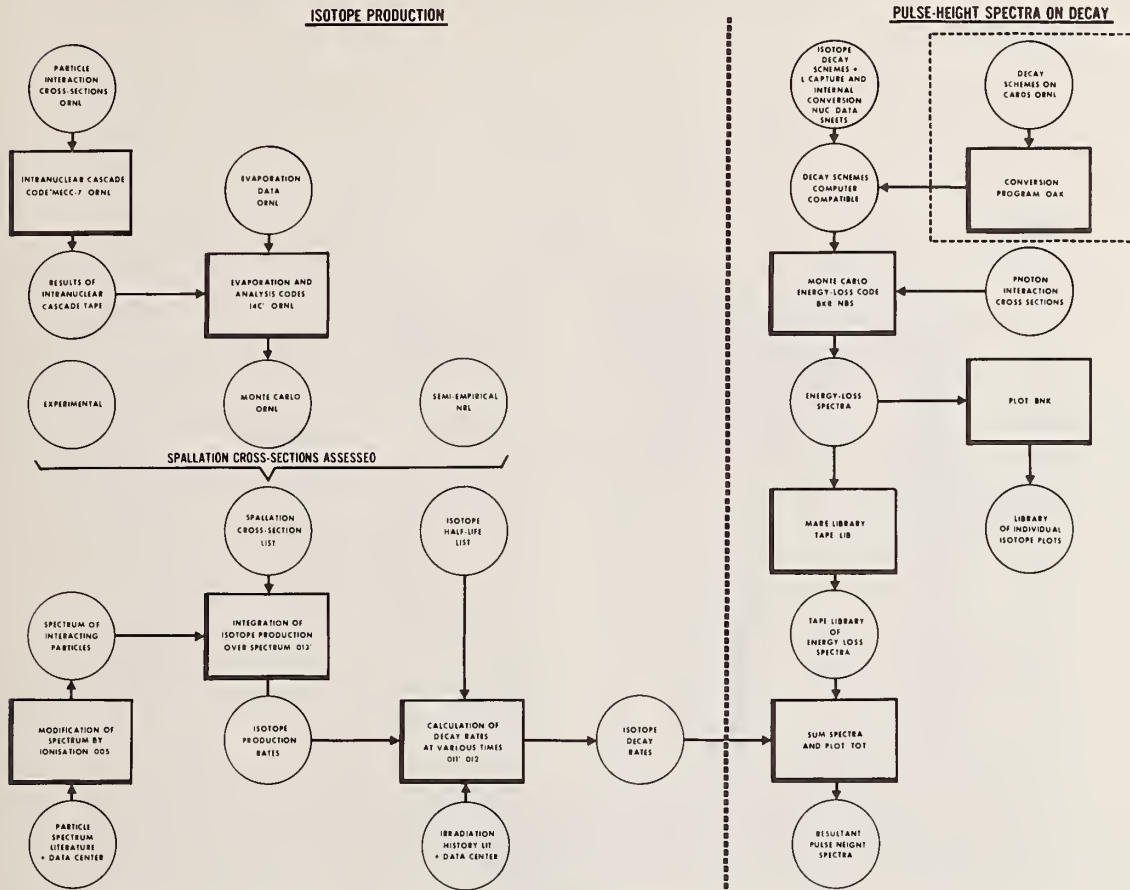
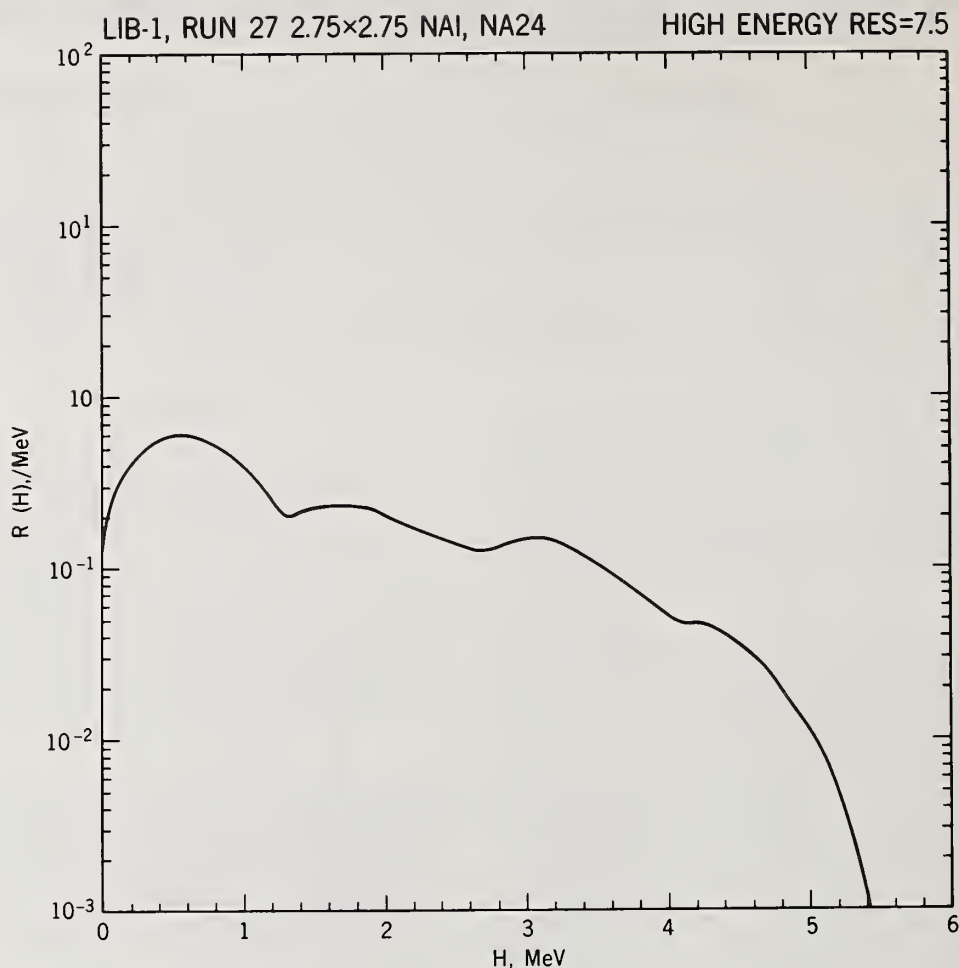




FIG. 3



that these products fill in a smooth contribution from 4 to 10 MeV.

Clearly these calculations require careful comparison with controlled monoenergetic beam irradiation studies. So far, only the limited data outlined above have been obtained for half-lives in excess of 1 minute. In equilibrium with cosmic rays, all half-lives down to the direct particle veto pulse width ( $\sim 10 \mu\text{s}$  for NaI) can contribute. Irradiations are planned to study these species and provide further data. These results used in conjunction with the response functions can be used to improve the cross-section estimates. In the immediate future, intrinsic Germanium will be studied in addition to NaI and CsI.

At present the computation scheme includes modification of the particle spectra by ionization loss but not secondary particle production. The production side may be interfaced with codes which simulate such cascades. In this case, which is required for heavy spacecraft, neutron cross-sections are also required.

#### Apollo Detector Activation

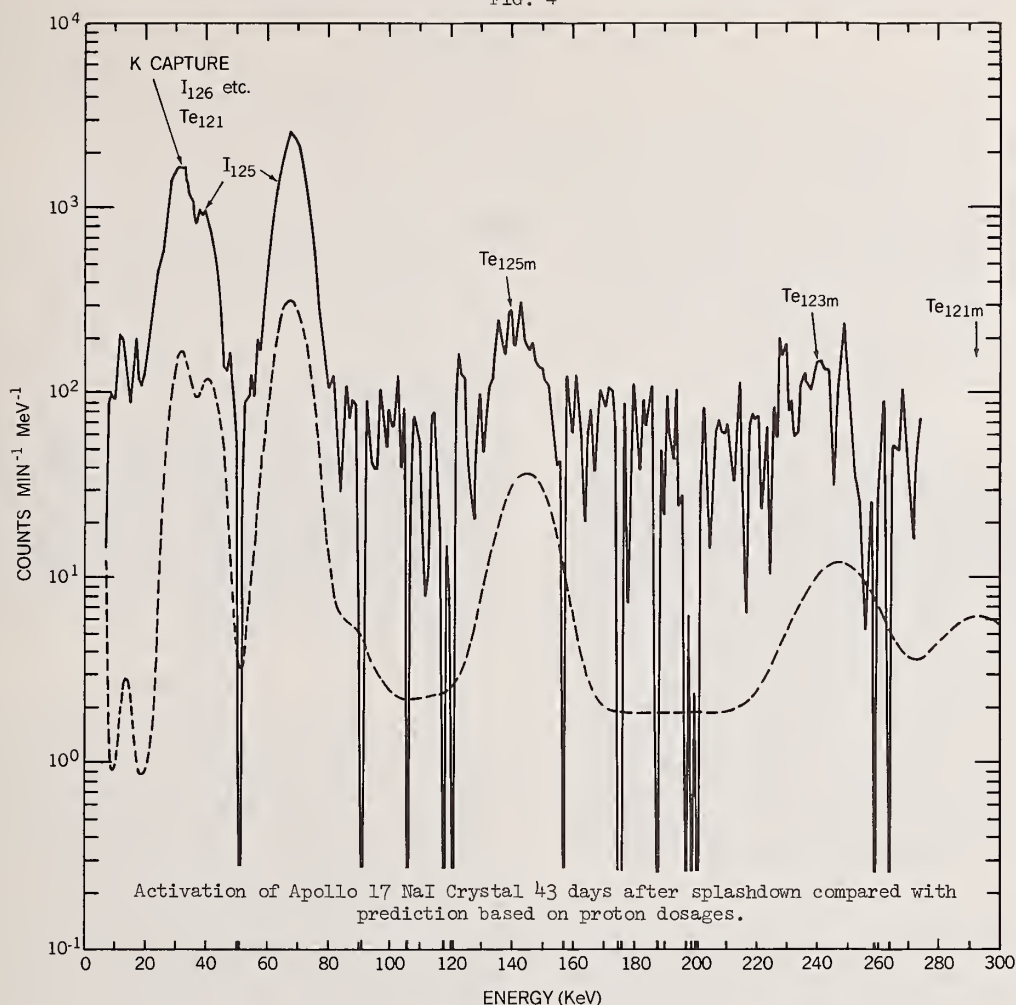
A 7 cm x 7 cm NaI(Tl) detector crystal was used to perform gamma-ray measurements on the Apollo 15 and 16

missions.<sup>9</sup> In order to obtain further information on activation, an identical detector was returned to earth from Apollo 17. This crystal has shown a higher rate of activation than would be expected from proton interactions alone, as can be seen in Fig. 4 in which the activation observed after 43 days is compared with a prediction based on known proton dosages. Certain isotopes were monitored using a 4 $\pi$ -coincidence technique and the results are compared with predictions below:

Isotope	Landing Decay Rate (per min.)	Prediction
Na <sub>22</sub>	$2.6 \pm 1.4$	0.4
Na <sub>24</sub>	$100.0 \pm 40$	Implies thermal neutrons
I <sub>124</sub>	$300.0 \pm 80$	25
I <sub>126</sub>	$300.0 \pm 150$	38

The Na<sub>24</sub> result implies a mission-average flux of  $1.5 \text{ cm}^{-2} \text{ s}^{-1}$  for thermal neutrons ( $< 1 \text{ eV}$ ). The other results may be explained by a flux of 20-100 MeV neutrons of about  $5 \text{ cm}^{-2} \text{ s}^{-1}$ . Clearly neutron production is important in heavy spacecraft and neutron

FIG. 4



cross-sections at all energies are required together with codes to assess their production and transport. In the Apollo in-flight data, background was reduced by extension of the detector on a 7.6m boom. For detectors located within heavy spacecraft prompt gamma-ray production by neutrons will also be important and these cross-sections will be required for detector materials.

#### Summary of Nuclear Data Requirements

Particle cross-sections of nearly every conceivable sort are required for detector materials Na, Cs, I, and Ge. Nuclear decay schemes in computer-readable form are a great asset in this calculation. In addition, neutron production and transport codes applied to heavy spacecraft are extremely important in assessing shielding possibilities and deciding between lightweight and heavyweight detector systems.

#### References

1. Gamma-Ray Astrophysics, (F. W. Stecker and J. I. Trombka, ed.) NASA SP-339, U. S. Gov't. Printing Office, Washington, D. C.
2. Peterson, L. E., 1965, J. Geophys. Res. 68, 5633.
3. Dennis, B. R., Suri, A. N., and Frost, K. J., 1973, Astrophys. J., 186, 97.
4. Dyer, C. S., and Morfill, G. E., 1971, Astrophys. and Space Sci., 19, 359.
5. Fishman, G. J., 1972, Astrophys. J., 171, 163.
6. Ewbank, W. B., 1975, E B.1, These Proceedings.
7. Silberberg, R., and Tsao, C. H., 1973, Astrophys. J., Supp. 25, 315.
8. Bertini, H. W., Guthrie, M. P., and Hermann, O. W., O. W., 1971, ORNL-RSIC, CCC-156.
9. Metzger, A. E., Trombka, J. I., Peterson, L. E., and Arnold, J. R., 1973, Science, 179, 800.



Proton scattering has been applied to the problem of elemental quantitative analysis of air particulate matter. Elements up through chlorine may be resolved using 16 MeV protons incident upon targets up to about 1 mg/cm<sup>2</sup> in thickness. Using the FSU Super FN Tandem Accelerator and a large area solid state proton detector, an analysis can be performed in several minutes. Combination of this technique with proton induced X-ray emission analysis provides a means of quantitative analysis for all elements. These accelerator based methods are being applied to studies of the composition of air particulate matter in diverse locations such as St. Louis, Mo.; Los Angeles, Ca.; several cities in Florida; and Bermuda.

\*This research was supported in part by the U.S. Environmental Protection Agency, Grants R-803913 and R-802132, and the National Science Foundation for accelerator operations support.

(proton scattering; quantitative analysis; air particulate matter)

### Introduction

Direct measurement of the most abundant elemental constituents of atmospheric aerosol particle size fractions is important in relating aerosol particle physics theory to the variation of chemical composition with particle size. The former depends on physical interactions leading to particle coagulation and removal from the atmosphere, which are functions of particle mass,<sup>1</sup> and the latter is important in describing the transport of specific chemical substances in the atmosphere, many of which are of practical public health importance.<sup>2</sup> The direct measurement of the most abundant constituents, carbon, nitrogen, and oxygen, however, is difficult by most analytical techniques and in practice is almost never attempted in atmospheric research requiring large numbers of separate elemental analyses. Therefore, full advantage has not been taken of our present understanding of the physics of aerosols in accounting for the occurrence of chemical components of aerosol particles.

The present research is directed toward developing a sensitive and rapid technique for determining the light elements up to sulfur and chlorine in non-volatile components of aerosol particle size fractions by

proton elastic scattering analysis, PESA.<sup>3-5</sup> Elements sulfur and heavier can be determined by proton induced X-ray emission, PIXE,<sup>6-8</sup> and the two methods in combination should provide a determination of all elemental constituents which contribute significantly to the total aerosol particle mass. The present paper presents evidence that this approach is feasible, and the two techniques can be applied to the same atmospheric samples by proton bombardment in a Van de Graaff accelerator.

### Experimental

The experimental arrangement is similar to that used in our previous reports.<sup>3-5</sup> A collimated proton beam of 16 MeV is used as an optimum of high enough energy to provide resolution of protons elastically scattered by isotopes of adjacent elements up to chlorine and of low enough energy to be stopped completely in the available Si detector of 1500 micron depletion depth. The detector used in the present study is 6 mm x 50 mm active area collimated by a 1 mm elliptical curve running the length of the detector, so as to accept a narrow range of backscattered proton energies from each target nuclide at the 120° detector angle and still have a large enough effective detector surface area to

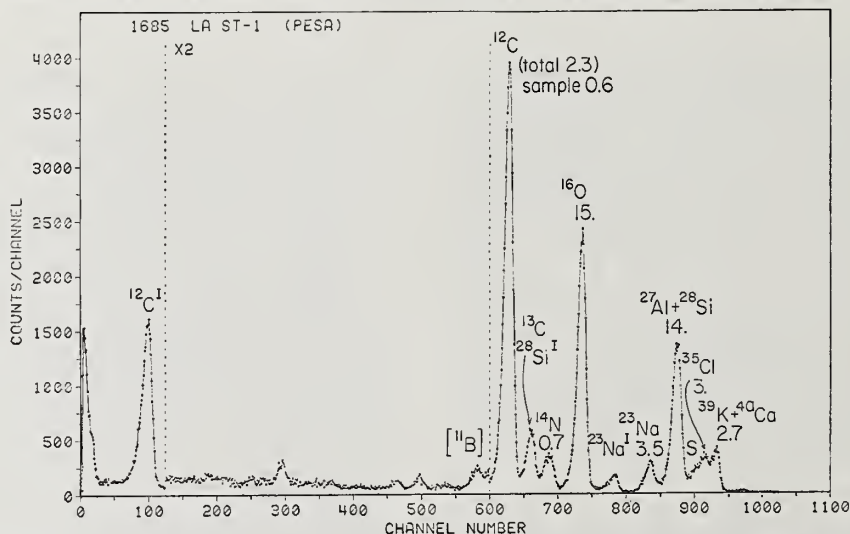


Fig. 1 Proton scattering spectrum for 16 MeV protons incident upon an air particulate sample from the coast north of Los Angeles, California. This sample was obtained from 1.1 m<sup>3</sup> of air using a single orifice cascade impactor. The numbers above each peak are the mass of that element in micrograms per cubic meter of air.

assure good counting efficiency for small aerosol particle samples in the target position. The detector is located outside the vacuum system of the scattering chamber, and scattered protons pass through a 1/4-mil (6.25  $\mu\text{m}$ ) Mylar window and about 2 mm of air before entering the detector, causing negligible loss of resolution in comparison with other factors in the arrangement.

### Results

Figure 1 presents the elastically scattered proton spectrum from a sample of aerosol particles greater than 4  $\mu\text{m}$  aerodynamic diameter collected during a 16 hour period along a coastal location near Los Angeles, September 1974. The sample is stage 1 of a cascade impactor<sup>9</sup> operating at a 1 liter/min air flow rate, representing 1.1  $\text{m}^3$  total air volume, and the sample is supported by polystyrene film of thickness  $\sim 100 \mu\text{g}/\text{cm}^2$ . Figure 2 is an X-ray spectrum produced by bombardment of the same sample with 3.75 MeV protons and detection in a Si(Li) detector. At the present time the PIXE procedure is precisely calibrated<sup>8</sup> permitting routine quantitative analysis, and the PESA procedure is undergoing calibration verification. The sample from stage 1 is large and has a diameter of about 2 mm and the beam was collimated to about 1.5 mm. Thus, not all of the sample was analyzed. The numbers

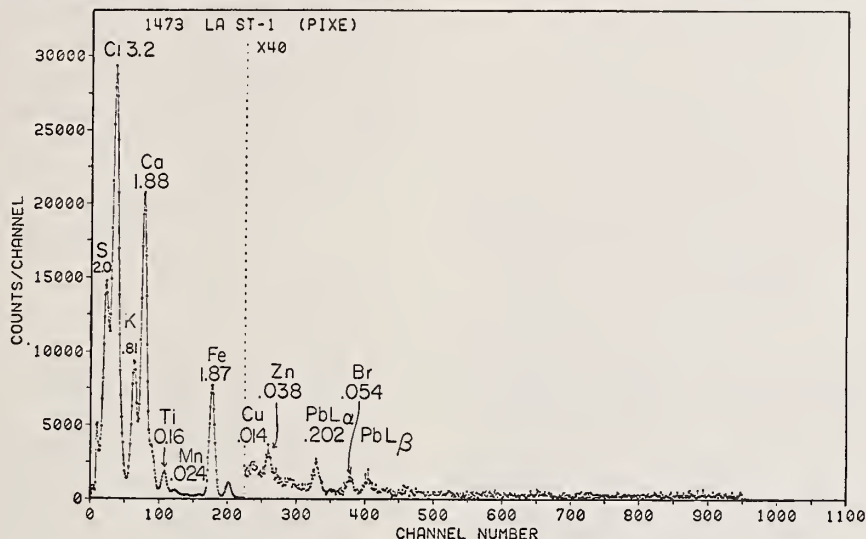


Fig. 2 Proton induced X-ray emission analysis of the same air particulate sample as shown in Fig. 1. Numbers above each peak are the mass of that element in micrograms per cubic meter of air.

of micrograms of each element given in Fig. 1 have been calculated after normalizing the PESA Ca + K value to that of PIXE, supposing the elements have the same distribution in the sample. It is seen that the sample size for PESA analysis is sufficient for detection of most elements from carbon to calcium and still small enough not to cause proton energy dispersion and loss of resolution. The sample size is also adequate for detection of about ten elements by PIXE.

Figure 3 presents the distribution of seven elements with particle size for a sample collected during a 72 hour period in October 1973 by cascade impactor from a tower in Bermuda.<sup>10</sup> This analysis, performed before the absolute PESA calibration was quantified, represents concentrations of S, Cl, and Ca by PIXE and concentrations of C, N, O, and S by PESA with normalization of S to the PIXE value all stages. Carbon values are approximate owing to uncertainties in polystyrene backing thickness. The particle size distribution

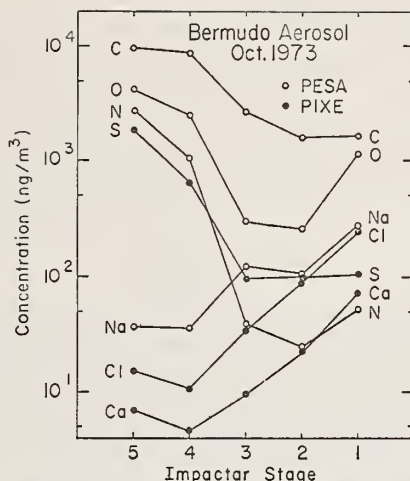


Fig. 3 Size fraction analysis of a Bermuda aerosol sample using proton elastic scattering analysis (PESA) for C, N, O, and S, and proton induced X-ray emission analysis (PIXE) for S, Cl, and Ca. Impactor stages 5 through 1 represent particles of equivalent aerodynamic diameters 0.25-0.5, 0.5-1, 1-2, 2-4, and  $>4 \mu\text{m}$ , respectively.

show high large particle abundances for Na, Cl, and Ca, which may originate from sea water dispersion, and high small particle abundances for much of the N, S, and O, where composition of  $(\text{NH}_4)_2\text{SO}_4$  is expected, and for some of the carbon. The combination of PESA and PIXE appears to be valuable for presenting enough elemental data to suggest chemical composition relationships such as these. PIXE alone would be insufficient.

Because of the special interest in measurements of nitrogen and sulfur related to the atmospheric chemistry of these elements, test bombardments have been carried out on targets which could serve as standards. Figure 4 shows the scattering spectrum for Kapton film, a material with a precisely known atomic ratio  $\text{O}/\text{N} = 2.5$ . The spectrum is simple and the elements are clearly resolved and can be readily analyzed by suitable computer programs. This material provides a convenient means to determine the relative N/O



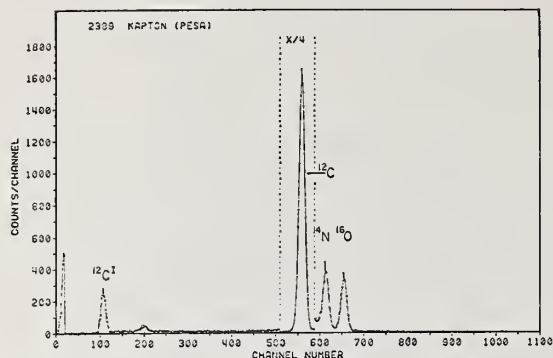


Fig. 4 Proton scattering spectrum for 16 MeV protons incident upon a 7.5  $\mu\text{m}$  thick Kapton film.

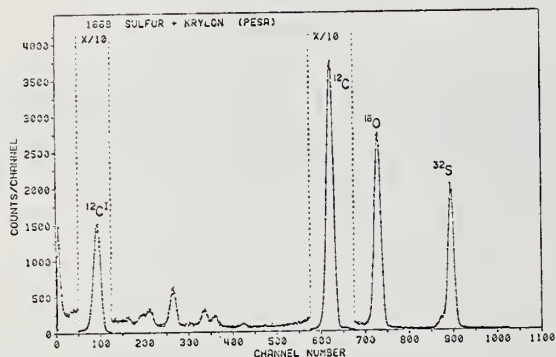


Fig. 5 Proton scattering spectrum for 16 MeV protons incident upon a sulfur target. The target was prepared by vacuum evaporation of elemental sulfur onto a Mylar backing and then over sprayed with Krylon to stabilize the sulfur to bombardment in vacuum.

scattering cross sections. Figure 5 shows the scattering spectrum for elemental sulfur on Mylar, with Krylon binder. The elastic scattering cross section for sulfur is dominant over lower energy inelastic proton groups in the spectrum. Our identification of peaks between channels 100 and 600 is not yet complete, but a few inelastic sulfur scattering peaks are apparently present and may be useful in quantitative resolution of spectra from complex mixtures as may be encountered in analysis of environmental samples. Current emphasis on high quality analyses of particulate sulfur in atmospheric samples, because of its pollution significance, makes it desirable to have alternate methods for sulfur determination. PESA and PIXE can both be applied to sulfur determination in the same samples.

High quality elemental analyses may be produced providing the proton scattering cross section is not highly sensitive to variables in a routine procedure and providing that variations in sample composition and thickness do not degrade the spectrum to the point of not being able to resolve the elemental constituents. As exemplified by Fig. 1, impactor sampling time may readily be chosen for obtaining a sample of size large enough for detection of elements by PESA and small enough to permit their resolution. It should be pointed out that thick samples tend to cause proton energy dispersion, not proton particle loss, and some dispersion can be tolerated if adjacent energy peaks can be resolved. In contrast, PIXE and any other X-ray methods for elemental analysis are vulnerable to X-ray attenuation at low X-ray energies, and this makes determination of elements lighter than sulfur uncertain if the required

sample self-absorption corrections are large. Thus, in many practical cases, determinations of elements in the region of sulfur by both PIXE and PESA offer a decided advantage over determinations by one method alone.

In order to define the sensitivity of the PESA method to instrumental variables, measurements of effective cross section with angle and proton energy have been made. Figure 6 shows how the relative cross section varies with scattering angle for  $^{12}\text{C}$ ,  $^{16}\text{O}$ , and  $^{32}\text{S}$ . (These are relative values only. The variation of effective cross section at  $120^\circ$  with mass number of nuclides  $^7\text{Li}$  to  $^{40}\text{Ca}$  has been given in Fig. 9 of reference 5.) Figure 6 indicates that the sulfur cross section varies imperceptibly over a broad angle interval from  $100^\circ$  to  $135^\circ$ , oxygen has a gentle minimum centered about  $118^\circ$ , and carbon decreases almost monotonically with angle from  $100^\circ$  to  $135^\circ$ , being relatively flatter around  $120^\circ$  than angles greater or less than this. For convenience in our experimental arrangement and for the least practical sensitivity to variations in scattering angle, we have chosen  $120^\circ$  for most of our further calibration experiments. This choice of angle also affords a relatively high carbon cross section and permits precise carbon measurements where subtraction of backing material contribution is required. We also note that more forward angles suffer from apparently less satisfactory peak to background ratios, and the peaks are kinematically more closely spaced. These and other practical considerations for the resolution of elemental constituents in environmental samples indicate that the optimum angle chosen for analysis is not a trivial problem and should be explored with great care. At present, our choice of  $120^\circ$  appears to be a good one.

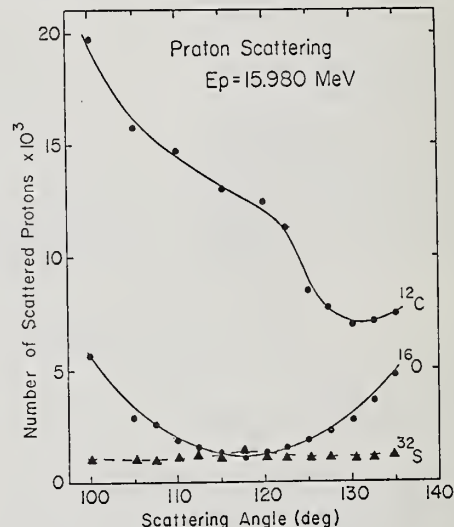


Fig. 6 Differential cross section in arbitrary units versus scattering angle for three isotopes. The lines through the points are guides for the eye.

Figure 7 shows relations calculated which influence the resolution which can be achieved for  $^{12}\text{C}$  and  $^{35}\text{Cl}$ . The angle subtended by the detector is determined by the width of the elliptical curve which forms the collimator of our detector face, currently about  $1^\circ$ . Since the intrinsic detector resolution is in the region of 40 keV, it is desirable to keep additional energy dispersion due to detector angle well below this value. This is especially true if resolution of  $^{27}\text{Al}$  and  $^{28}\text{Si}$  is to be achieved, as we consider necessary in atmospheric aerosol studies.

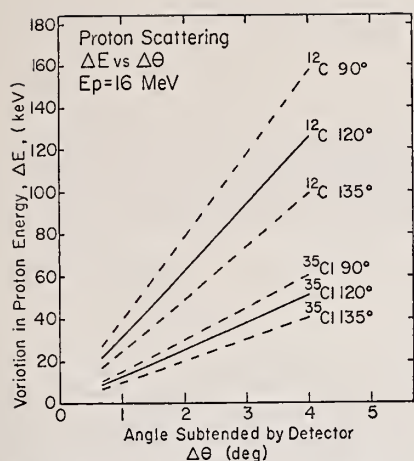


Fig. 7 Variations in scattered proton energy versus angle subtended by the proton detector. In the analysis system at FSU, angles between 1 and 2 degrees are employed.

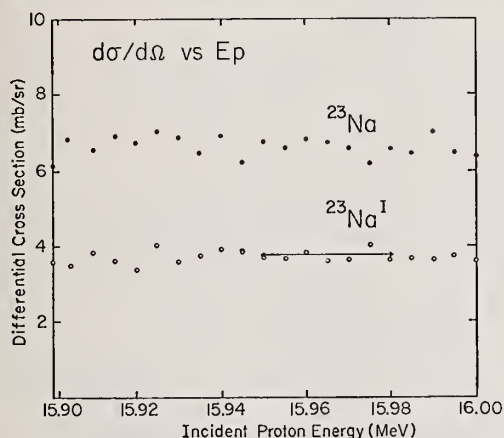


Fig. 8 Excitation functions for the ground and first excited states of  $^{23}\text{Na}$  over the range of interest for the FSU analysis system. The lack of structure is desirable in that quantitative analyses do not depend upon sample thickness. The line indicates 30 keV, the maximum sample thickness analyzable with good resolution.

Finally, Fig. 8 shows the differential scattering cross section as a function of proton energy for  $^{23}\text{Na}$  as measured from a  $60 \mu\text{g}/\text{cm}^2$  Na Cl sample. The uncertainty in the repeatability of the proton energy scale was  $\pm 10$  keV. Data for the two major peaks observed in the sodium spectrum, elastic scattering from the ground state and inelastic scattering to form the first excited state, are given for a range of energy. This range is several times greater than we anticipate will be caused by extreme variations in sample thickness which can be accepted and still give the energy resolution required for a successful analysis for individual elements. Normally, no thickness greater than that equivalent to a 30 keV energy loss would be accepted, and neither sodium cross section is found to vary over this range. Also, it is seen from Fig. 8 that tedious energy calibration procedures of the incident proton energy are not necessary for sodium measurements. Clearly, such tests must be carried out for every

element for which analysis is attempted. For those we have completed to date, similar results have been found, indicating no difficulties are foreseen due to cross section sensitivity to this effect. It is also fortunate that the ratio of cross sections for the elastic and inelastic groups of scattered protons from sodium is constant with energy, because then both groups can be used in the quantitative analysis for sodium in complex mixtures by straightforward computer fitting programs.

### Conclusions

Experiments performed to date indicate that proton elastic scattering analysis can be a practical, rapid, and sensitive means of elemental analysis when applied to atmospheric aerosol samples. It has inherent simplicity, relative freedom from interference between elements present in the sample, and potential for automated nondestructive analysis. In combination with PIXE, PESA has the capability for determining all elemental constituents of aerosol samples that contribute significantly to the total aerosol mass, a capability which is unique in contrast to alternative analytical techniques. Future research and development of PESA should be directed to detailed cross section measurements of the nuclides of interest over the range of variables of energy, angle, and other parameters encountered in practical elemental analysis. An effort should be made to develop computer hardware and software which will automate the procedure so that analyses can be carried out in minutes or less of time and data can be handled readily for interpretation. Finally, the PESA technique should be field tested extensively so that relationships in elemental composition of environmental samples revealed by the technique can be evaluated. Such evaluations may indicate directions for further improvement of the technique.

### References

- 1C. E. Junge, Air Chemistry and Radioactivity, Academic Press, New York, 1963.
- 2T. B. Johansson and J. W. Winchester, Proc. 2nd Int. Conf. Nucl. Meth. Environ. Res., Columbia, Mo. July 1974 (in press, Tech. Info. Center, USAEC, Oak Ridge, Tenn.).
- 3J. W. Nelson et al., IEEE Trans. Nucl. Sci. **NS21**, 618 (1974).
- 4J. W. Nelson and D. L. Meinert, Advances in X-Ray Analysis **18** (1975) (in press, Plenum).
- 5J. W. Nelson et al., Proc. 3rd Conf. on Applications of Small Accelerators, Denton, Texas, Oct. 1974 (in press, USAEC Tech. Info. Center).
- 6T. B. Johansson et al., Nucl. Instr. & Meth. **84** (1970) 141.
- 7T. B. Johansson et al., Advances in X-Ray Analysis **15** p. 373 (Plenum Press, 1972).
- 8T. B. Johansson et al., (accepted Anal. Chem.).
- 9R. I. Mitchell and J. M. Pilcher, Indus. and Engr. Chem. **51**, 1039 (1959).
- 10D. L. Meinert, M.S. thesis, The Florida State University, June 1974 (unpublished).



USE OF ELASTIC SCATTERING CROSS SECTION ANOMALIES FOR DEPTH PROFILING  
HELIUM AND HYDROGEN ISOTOPES IN SOLIDS\*

Robert S. Blewer  
Sandia Laboratories  
Albuquerque, New Mexico 87115

A proton elastic scattering technique is described which makes possible direct accurate depth profile measurements of light element isotopes (deuterium, tritium, helium, etc.) in metal or insulator hosts. Several examples of the application of this technique to current problems are given in the fields of energy research and neutron generator target evaluation.

(Proton; elastic; scattering; range; depth; migration; diffusion; helium; deuterium; oxide)

### Introduction

One of the most useful and widely practiced surface analytical techniques to derive from the field of elastic cross section measurements is Rutherford Ion Backscattering Spectrometry (RIBS). This technique provides a means of nondestructively probing the near-surface composition of materials, particularly thin film and surface layer systems. Numerous examples of its use have been published.<sup>1</sup> The ease of its application relies on the simplicity of elastic scattering kinetics and the predictability of elemental elastic scattering cross sections (Rutherford's Law). However, the application of RIBS has been restricted principally to systems in which the atomic number of the impurity or surface film atom is higher than that of the host or substrate. Thus, systems with low Z impurities have not been amenable to analysis because of the unfavorable ratio of elastic scattering yields which exist for low Z atoms in higher Z hosts. This paper describes a proton elastic scattering technique which has been found to be capable of profiling low Z atom depth distributions in a variety of metals and insulators with detection sensitivities as great as 0.5 at. %.

The success of the method rests partly on the existence of an elastic yield for protons incident on helium which greatly exceeds the Rutherford value in the range of 2.5 MeV incident proton energy.<sup>2,3</sup> Because a similar enhancement in elastic scattering cross section exists for 2.5 MeV protons incident on the other low Z elements (D, <sup>3</sup>He, Li, O, C, etc.), the technique is capable of simultaneously profiling the other light elements which may be present in the sample.

In the following sections the proton elastic scattering technique will be described and an in-depth illustrative example of its use given. The final section will contain a general discussion of other fields in which the technique is being applied.

### Proton Backscattering Technique

The proton backscattering method for depth profiling light atom species in the near surface region of solids differs from the conventional Rutherford backscattering in two important respects: (1) use of a proton analysis beam (rather than a helium ion beam) of sufficient energy that the Coulomb barrier for low Z target atoms is partially penetrated and nuclear elastic scattering occurs, providing a large enhancement (over the Rutherford value) to the elastic scattering cross section of the light atoms in the target, and (2) use of a thin foil target mounted on a "beam catcher" device that traps the portion of the incident beam which scatters from surfaces beyond the foil. The latter provision prevents thick target low energy protons which are encountered in conventional backscattering techniques from reaching the detector except for those scattered from (low Z) atoms within the foil itself. This reduces the thick target background to near zero and leaves a clear (energy) field

\*Work supported by US ERDA.

for the observation of low Z species that are present in the foil.

In Figure 1 is illustrated a schematic view of the experimental arrangement. A monoenergetic 2.0 MeV to 2.5 MeV proton beam is directed perpendicularly to the surface of the foil sample which has been mounted on the beam catcher device whose purpose was described above. The beam itself is generated by a conventional 2.5 MeV Van de Graaff accelerator. The dimensions of the beam catcher and the positioning of the Faraday cup are such that even protons which are scattered at 180° at the rear of the catcher and then repenetrate the foil are not able to enter the detector unless they scatter at precisely 16° in the foil on their second passage through it. A silicon surface barrier detector with 8 keV energy resolution for 2.5 MeV protons is used with pulse shaping and amplifying electronics to register the energy of protons incident on its surface in a multichannel analyzer. Protons which are backscattered at kinematically unique energies from low Z atoms in the target are thus registered by the multichannel analyzer in energy intervals characteristic of the mass of the atoms in the target from which the protons backscattered. In this manner a spectrum is generated.

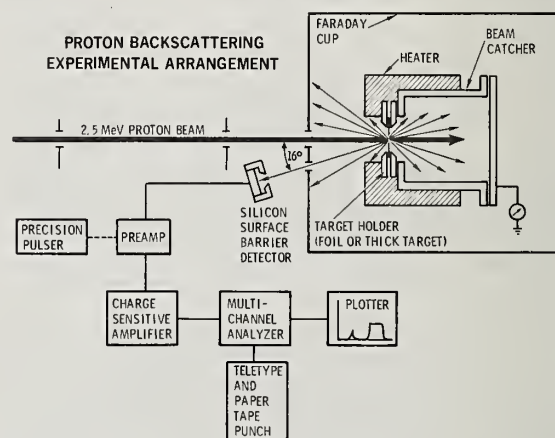


Figure 1: Schematic of proton backscattering method.

In Figure 2 is illustrated the output of the multichannel analyzer (with the "channels" axis converted to backscattered proton energy). The spectrum is actually that from a thick copper target implanted with  $1 \times 10^{17}$  <sup>4</sup>He ions/cm<sup>2</sup> at 100 keV. A carbon surface layer exists on the target which results in an observable peak at the energy determined by the laws of conservation of momentum and energy, as being appropriate for a collision of a 2.0 MeV proton and a carbon atom at 164° (denoted "C"). Note that a small peak which should exist at the characteristic energy for protons backscattered from helium atoms in the target cannot be clearly distinguished above the thick target background.



The spectrum which would be obtained for a foil target is also indicated in the figure. For a properly aligned beam catcher and foil sample the thick target yield is reduced to near zero, leaving the small helium peak observable above the background. Moreover, the He peak is well separated from the metal foil peak so that no deconvolution of the spectrum is necessary (for foils up to 10  $\mu\text{m}$  in thickness). Also, backscattering peaks from other low Z elements in the foil are sufficiently separated in energy from each other to be easily observed above the uniform low background.

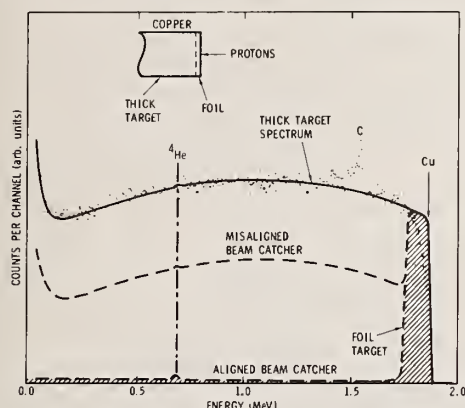


Figure 2: Backscattering spectra for thick and thin targets.

Figure 3 illustrates the foregoing point. The energy position at which each of several low Z elements would appear is indicated in the figure. The uppermost spectrum exhibits the scattering peak produced only by backscattering events from metal atoms in the foil itself. The center spectrum shows the additional peak produced if the foil contains surface implanted helium. If, in addition, the foil is deuterided and has front and rear surface oxide layers, their presence can be observed in the lowermost spectrum at the kinematically appropriate positions. Note that because

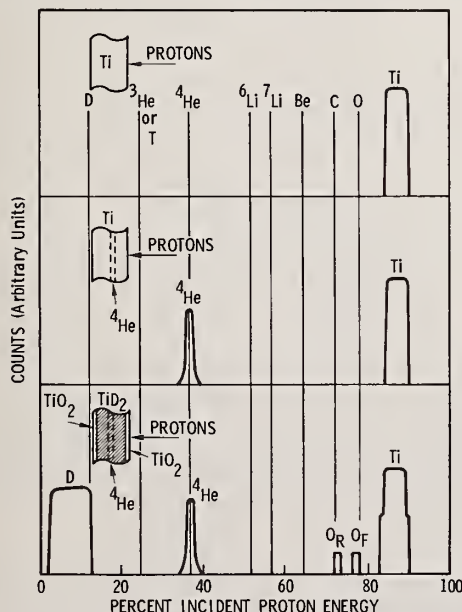


Figure 3: Appearance of spectra with several low Z constituents.

there is a significant difference between characteristic backscattering energies for low Z atoms, each of these low Z elements is resolved from the others so that the concentration and depth distribution of each can be observed independently of the others.

Further experimental details of the technique have been published previously.<sup>4,5</sup> The reader is referred to the references for more information.

#### Illustrative Example: Behavior of Helium and Deuterium in Titanium

Titanium is a hydrogen occluding metal that has received attention as a potential collector material in controlled thermonuclear reactors, and has also been used (in hydride form) as the target in intense neutron sources. In view of these applications, the behavior of helium and hydrogen isotopes in titanium hydrides is of great interest, especially at elevated temperatures. The proton backscattering technique is particularly appropriate for a study of a system involving both D and He (and, as will be seen later, oxygen) because, as mentioned previously, one can observe the depth distribution of each of these elements simultaneously and the sequential changes in their respective depth distribution which occur at higher temperatures.

In order to determine the migration and release characteristics of helium implanted in titanium metal, a 2.5  $\mu\text{m}$  titanium foil was implanted at room temperature to a fluence of  $4 \times 10^{17}$  He/cm<sup>2</sup> at an energy of 50 keV. When analyzed by proton backscattering, the "as implanted" distribution was observed to be symmetric (approximately Gaussian) with a mean depth of 2610  $\text{\AA}$ , which agrees (to within 100  $\text{\AA}$ ) with the theoretical projected range calculations of Brice.<sup>6</sup> The sample was subjected to in situ vacuum annealing treatments at temperatures of 200°C, 330°C, 440°C, 540°C and 600°C.

In Figure 4 is exhibited a plot of the volume concentration of helium remaining in the foil after each anneal. Shown as an inset is the size, shape and mean depth of the helium distribution at each temperature, relative to the as-implanted depth and height. The amount of helium retained in the foil (area under the He peak) remained essentially constant in magnitude up to 330°C, indicating that very little of the implanted helium was released up to this temperature. After the 440°C anneal, a significant decrease in the peak area occurred, but the width (and mean depth) of the distribution was constant, a behavior which is contrary to

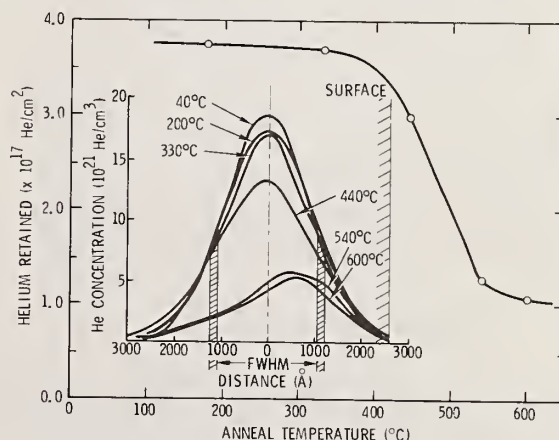


Figure 4: Helium release from Ti metal versus temperature.<sup>7</sup>

that expected if the escape of helium occurred via Fickian diffusion, where gas would be released by a net spreading of the distribution until one wing intersected the foil surface. Since the width (FWHM) of the distribution stayed essentially constant, it appears that up to this temperature the helium has neither diffused into the area nearer the surface which contains residual radiation damage from the implantation process, nor has it diffused deeper into the foil into areas which contain no radiation damage. This suggests that radiation enhanced diffusion is not a factor in this experiment at room temperature or up to 440°C.

Further significant release occurred as a result of the 540°C anneal and, for the first time, the mean depth of the distribution seemed to decrease though no significant spreading of the distribution toward the surface occurred. An additional anneal at 600°C resulted in very little additional He release, thus abruptly interrupting the rate of decrease in helium content of the foil with increasing temperature. An explanation for these last two observations (mean depth shift and He release behavior) will be given together with the discussion of the titanium deuteride results below.

In order to determine the effect of inclusion of hydrogen isotopes in the lattice on the behavior of implanted helium in the host (and also to determine what effect, if any, the presence of helium in the lattice has on the release characteristics of hydrogen isotopes), helium was implanted into a  $\sim 2.9 \mu\text{m}$  titanium deuteride film deposited on a thin W foil and then subjected to vacuum annealing up to 575°C. Implant conditions (fluence, implant energy, implant temperature) and anneal conditions were equivalent to those which existed for the implanted titanium metal experiments so that the results of the two systems could be compared.

The proton backscattering spectrum of the helium implanted titanium deuteride film before and after annealing is exhibited in Figure 5. Note the large energy separation between the D and He peaks (species which differ only by two AMU) allowing clear observation of the depth distribution of both isotopes. Thirty minute anneals were performed at temperatures of 150°C, 200°C, 275°C, 325°C, 400°C, 475°C and 575°C.

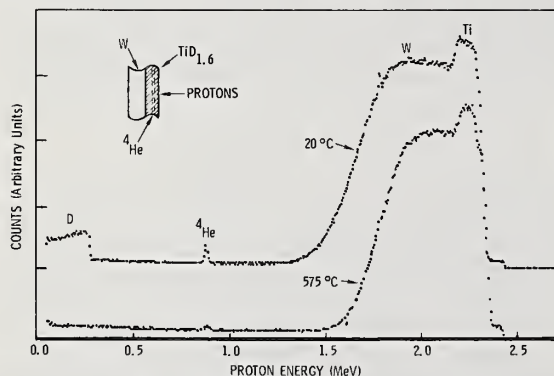


Figure 5: Spectra of helium implanted  $\text{TiD}_{1.6}$  before (upper trace) and after anneal.

The portion of the spectrum containing the deuterium peak is shown in more detail in Figure 6 for both room temperature and elevated temperature runs. The points shown correspond to the counts (backscattered protons) per channel (i.e. per energy interval) versus channel number (backscattered proton energy). Actual depth profiles differ from the spectra in Figure 6

when the effect of stopping cross-section changes with energy are included. The channel at which one would expect (kinematically) to observe protons backscattered from front surface deuterium is indicated in the figure, but no significant concentration of deuterium is observable in the first 1000 Å of the film (because of a surface oxide layer).

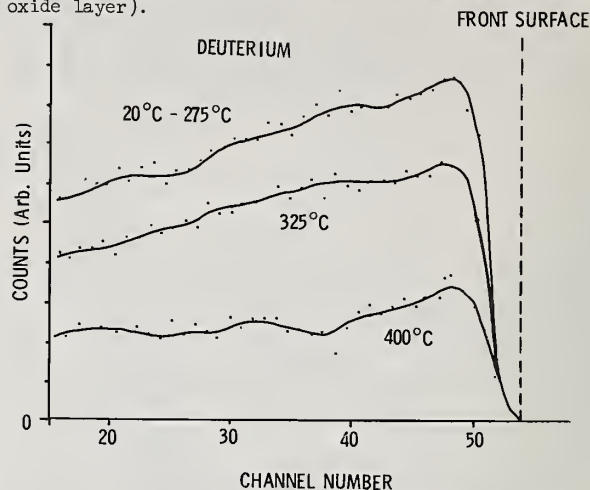


Figure 6: Deuterium peak spectra for several anneal temperatures.

No change in the room temperature spectrum was observed before and after helium implantation. Likewise the spectrum remained essentially unchanged after 30 minute anneals at 150°C, 200°C and 275°C. However, after a 325°C anneal, the area under the D peak was reduced 25% and after a 400°C anneal, it was reduced 75% from the room temperature value. No measurable amount of deuterium still remained in the film after a 475°C anneal. It is noteworthy that the implanted helium layer (in the vicinity of channels 42-46) had no consistent influence on the deuterium distribution either at room temperature or at elevated temperatures. The phenomenon of trapping of deuterium at damage centers in other materials has been studied recently by other workers using channelling techniques.<sup>8</sup>

The spectrum of implanted helium in the titanium deuteride film is similar to that of Figure 4. The distribution was symmetric, as was the case for implanted titanium metal, except for a slight indication of a small tail toward the surface. The helium profile remained in the "as implanted" position up to 400°C. After a 475°C, 30 minute anneal, more than half of the implanted helium was released. Moreover, part of the distribution appeared to shift toward the surface. A scanning electron microscope examination of the surface showed, however, that the film surface had spalled in large patches, partially exposing a portion of the analyzing proton beam to the implanted layer.<sup>7</sup> This resulted in a proton backscattering spectrum which has the appearance of two overlapping depth profiles. This does not, however, indicate migration of helium to the surface. Instead, the helium release can be explained by the formation and rupture of bubbles which form at the end-of-range.<sup>4</sup> At temperatures above 500°C, helium release seemed to be inhibited by a thick surface oxide layer.

Helium release from implanted titanium deuteride appears to be identical to the behavior observed in helium implanted titanium metal, as shown in Figure 7. Points from the implanted metal anneal sample follow precisely the same locus as those for helium



implanted titanium deuteride. Much of the deuterium in the deuteride sample has already been released at 400°C, when helium outgassing begins. Titanium deuteride exhibits a tetragonal crystal structure whereas titanium metal is hexagonal. Therefore, it is evident that a change in the crystal structure of the host lattice is not sufficient in the case of this material to release the implanted helium from the lattice, as has been observed with inert gas implanted semiconductors. Moreover, since the helium is released at 400°C from the metal-plus-deuteride sample in exactly the same way as it was for the pure titanium sample, one must conclude that helium in the dihydride phase makes no significant contribution to the total of helium which is being released.

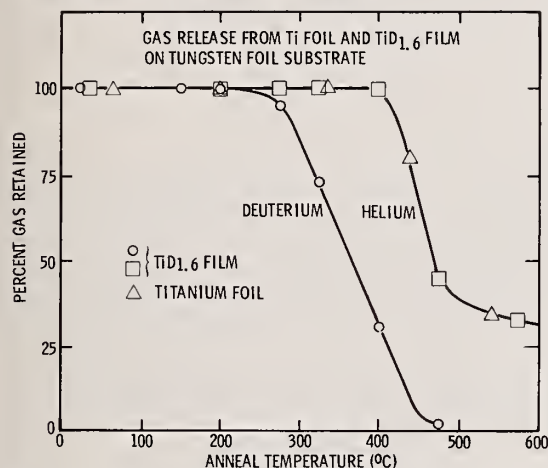


Figure 7: Percent He and D released vs temperature in Ti and TiD<sub>1.7</sub>.

In both the metal and metal deuteride samples, helium release is retarded above 475°C. From the proton backscattering spectra, it is evident that vigorous surface oxidation occurs at this temperature and above, even in a 10<sup>-6</sup> torr to 10<sup>-7</sup> torr vacuum. The helium-bearing layer is enveloped by oxide in the case of the metal (where the oxide peak could be unambiguously resolved) and likely also in the case of the deuteride so that further helium release is inhibited. This observation is a case in point of the advantage of being able to observe the presence and depth distribution of low Z elements in the foils other than those of primary concern.

#### Other Applications

In several fields of energy research, materials problems have been identified which are directly concerned with the behavior of light elements in metals and insulators:

(1) As stated in the previous section, fusion reactor first walls will face severe implantation fluxes of D, T, and <sup>3</sup>He. Moreover, tritium implanted in the first wall will generate <sup>3</sup>He in the lattice of the first wall material by radioactive decay. Several investigators have shown the adverse surface erosion effects caused by He implantation into metals and metal hydrides.<sup>9</sup> The influence of intense neutron bombardment on the host lattice is another complicating factor. The proton elastic scattering technique described in this paper seems ideal for studies concerned with evaluating the "as implanted" disposition

and migrational behavior of these low Z species in various materials under consideration as first wall candidates.<sup>7</sup>

(2) As natural gas and petroleum sources dwindle, increased consideration is being given to the "Hydrogen Economy" concept, particularly in view of the low pollution potential. Transport of gaseous or liquid hydrogen in pipelines or tankers revives concern about hydrogen embrittlement of metals. Protective coatings and the basic nature of hydrogen permeation and diffusion in metals is an area that needs additional research. The use of metal hydrides as a stable storage medium for hydrogen isotope fuels is also being given wide consideration. Proton backscattering has much to offer as an investigative tool in this area, too.

(3) Interest in intense neutron sources has been running high recently both as a means of performing material testing programs for CTR applications and as another tool in the medical fight against cancer. The most intense neutron source now available (located at the Livermore Lawrence Laboratory) utilizes an accelerated deuterium ion beam incident on a titanium tritide target (T(d,n)<sup>4</sup>He reaction). Tritium in deeper parts of the foil does not or cannot diffuse into the near surface region as the source operation depletes the near surface supply.<sup>10</sup> For this reason, the targets have very limited life. Thus, the behavior of deuterium implanted into the target by an energetic accelerator beam and the diffusion of tritium in the target from the beginning of target use is of interest in applications such as this. Studies in this area using the proton backscattering technique have also now been initiated by the author.

#### References

1. See, for example, Ion Beam Surface Layer Analysis, J. W. Mayer and J. F. Zeigler, ed., Elsevier (Lausanne), 1974.
2. G. Freier, E. Lampi, W. Sleator, and J. H. Williams, Phys. Rev. **75** (1949) 1345.
3. L. R. Mervine, R. C. Der, R. J. Fortner, T. M. Kavanagh and J. M. Khan, LLL Report URCL-73087, 1971.
4. R. S. Blewer, Application of Ion Beams to Metals, S. T. Picraux, E. P. EerNisse and F. L. Vook, ed., Plenum Press, New York (1974) 557.
5. R. S. Blewer, J. Nucl. Mat. **53** (1974) 268.
6. D. K. Brice, Rad. Eff. **11**, 227 (1971) and private communication, Dec., 1973.
7. R. S. Blewer, Technology of Controlled Nuclear Fusion, Vol. II, USAEC-CONF-740402, U. S. Dept. of Commerce, Wash., D.C. (1974) 525.
8. R. A. Langley, S. T. Picraux, and F. L. Vook, Proc. Hyd. Econ. Miami Energy Confr., Plenum Press, New York (1975).
9. Ion Surface Interaction, Sputtering and Related Phenomena, R. Behrisch, ed., Gordon and Breach (New York), 1973, pp. 199-246.
10. J. C. Davis and J. D. Anderson, J. Vac. Sci. Tech. (to be published).

B. R. Erdal, P. M. Grant, V. R. Casella, A. E. Ogard, and H. A. O'Brien, Jr.  
University of California, Los Alamos Scientific Laboratory  
Los Alamos, New Mexico 87544

The intense beam of medium-energy protons (600 to 800 MeV) from the LAMPF accelerator will be used to prepare multi-curie quantities of radioisotopes of value in diagnostic and therapeutic nuclear medicine. Thin-target cross section measurements of spallation-induced reactions represent a significant segment of the LASL Medical Radioisotope Research Program, as these data provide a basis for calculating specific radioisotope yields in thick targets, evaluating potential isotopic interferences, and monitoring hot-cell operations. Recent measurements include the cross sections (cumulative yields) of  $^{123}\text{I}$ ,  $^{127}\text{Xe}$ ,  $^{82}\text{Sr}$ , and  $^{43}\text{K}$  formed in the interaction of 800-MeV protons with La, Mo, and V targets; they are reported to be  $51 \pm 3$  mb,  $51 \pm 7$  mb,  $24.5 \pm 0.8$  mb, and  $5.4 \pm 0.3$  mb, respectively. Comparison with previous results at 590 MeV are made, and quantity and product quality estimates are presented for biomedical isotopes under the irradiation conditions expected to prevail at LAMPF.

(Nuclear Reactions; La, Mo, V(p, spallation); E = 800 MeV; Measured  $\sigma$ ; Isotope Production; Nuclear Medicine)

### Introduction

Upon reaching full design objectives, the Clinton P. Anderson Meson Physics Facility (LAMPF) at the Los Alamos Scientific Laboratory will produce a beam of  $800 \pm 3$  MeV protons with an average current of one particle-milliampere.<sup>1</sup> Of this total beam intensity, approximately 0.5 mA is estimated to be available at the main accelerator beam stop for radioisotope production. A Medical Radioisotope Research Program<sup>2</sup> is studying the utilization of this residual beam of medium-energy protons for the production of significant amounts of nuclides of importance in the health sciences.

The present research goals of this program include investigations of fundamental cross sections (production capability), radiochemical recovery and purification techniques, and biomedical generator development for isotopes produced via spallation reactions in massive targets (8 cm in diameter x 2.5 cm thick). The radionuclides of initial interest to the program are  $^{123}\text{I}$  and  $^{127}\text{Xe}$  from La targets, the  $^{82}\text{Sr}$ - $^{82}\text{Rb}$  system from Mo targets, and  $^{43}\text{K}$  from V targets.  $^{123}\text{I}$  is of use in diagnostic nuclear medicine as a desirable (much lower radiation dose to the patient) substitute for the presently-used  $^{131}\text{I}$  isotope in thyroid imaging and function studies, as well as in iodine-labelled radio-pharmaceutical investigations.<sup>3,4</sup>  $^{127}\text{Xe}$  has the potential to replace  $^{133}\text{Xe}$  in studies of pulmonary function and brain imaging,<sup>3,5</sup> while both  $^{82}\text{Rb}$  and  $^{43}\text{K}$  are of value for circulation and perfusion examinations and for myocardial imaging.<sup>3,6</sup> Radioanalytical separation schemes have been developed in this laboratory for each of these isotopes to effect a quantitative recovery and isolation from numerous other spallation products, and work has also been done on a  $^{82}\text{Sr}$ - $^{82}\text{Rb}$  nuclidic generator.<sup>7-11</sup>

The experimental determination of thin-target cross sections of spallation-induced reactions is an important aspect of the Medical Radioisotope Program. These data allow an estimation of specific radionuclide yields in thick targets, an evaluation of potential isotopic interferences in a given product (e.g.,  $^{42}\text{K}$  in  $^{43}\text{K}$  and  $^{85}\text{Sr}$  in  $^{82}\text{Sr}$ ), and a check on hot-cell operations.

The basis for cross section determinations by charged-particle activation is Eq. (1),

$$A_0 = \lambda N_0 = N \sigma I S \quad (1)$$

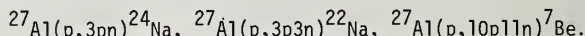
in which  $A_0$  is the activity (in dps) at the end of the

irradiation producing  $N_0$  transmuted atoms of decay constant  $\lambda$ .  $N$  is the number of target nuclei per  $\text{cm}^2$  in the beam,  $\sigma$  is the cross section or probability of reaction (in units of  $\text{cm}^2$ ), and  $I$  is the beam intensity in particles/sec.  $S$  is the dimensionless saturation factor and equal to  $(1 - e^{-\lambda T})$ , where  $T$  is the duration of the irradiation.  $N$  is related to the target thickness  $X$  (in  $\text{g}/\text{cm}^2$ ) through Eq. (2), in terms of Avogadro's constant, the atomic weight ( $M$ ) of the target element, and the fractional isotopic abundance ( $f$ ) of the specific stable nuclide which undergoes the nuclear reaction of interest:

$$N = (6.022 \times 10^{23}) X f / M \quad (2)$$

For the medium-energy spallation processes in the elemental targets under consideration here,  $f$  is taken to be 1.0.

In practice, the beam intensity ( $I$ ) is measured through one or more well-known monitor reactions. For this work, we use high-purity Al as a monitor foil and the following three transformations as monitor reactions:



### Experimental

#### Irradiations

Bombardments of experimental packets with 800-MeV protons were made in the LAMPF Nuclear Chemistry Area B targeting station. The irradiation durations usually ranged from approximately 0.5 to 2  $\mu\text{A}\cdot\text{hr}$  of integrated intensity, depending upon the thickness of the targets under study.

Each packet contained a number of 1.268-cm diameter monitor, target, and recoil-catcher foils. Elemental Al, with a purity of 99.997% and thickness 26  $\mu\text{m}$ , was used for beam monitors and forward and backward recoil catchers. A catcher foil was placed both upstream and downstream of each target to determine recoil loss corrections, and monitors were situated likewise to measure any loss of beam intensity upon traversal of the experimental packet. All Al monitors were, of course, fully compensated. High-purity ( $\geq 99.9\%$ ) elemental targets of La, Mo, and V were irradiated, and an entire packet was sandwiched together and maintained at a constant position in the proton beam with an external holder. While each packet contained a single La and Mo foil, three adjacent V targets were incorporated. In this way, the cross sections for nuclides such as  $^{24}\text{Na}$ ,  $^{22}\text{Na}$ , and  $^7\text{Be}$ , which are also produced in and recoil from the Al catchers,



could be determined by analyzing the central V target.

Two independent bombardments were performed. In the first, the thickness of each of the targets was approximately 0.05 mm, while in the second 0.25 mm was typical. Such a procedure allowed the study of individual cross sections as a function of target thickness in order to correct for any possible production via secondary reactions.

#### Radioactivity Analysis

Following the bombardment, an irradiated packet was taken apart, the individual monitors, targets, and recoil catchers were mounted on separate aluminum counting plates in a constant geometry, and the various foils were then sequentially counted for several months by gamma-ray spectrometry. Counting positions on the spectrometer system were previously efficiency-calibrated and well-characterized through the use of U. S. National Bureau of Standards and International Atomic Energy Agency reference gamma sources.

The detector was a closed-end coaxial, cylindrical Ge(Li) crystal of approximately  $76 \text{ cm}^3$  active volume. Detector specifications at the  $^{60}\text{Co}$  1332.51 keV photo-peak were 14.0% relative efficiency, 2.07 keV FWHM resolution, and 41:1 Peak/Compton Ratio. Spectra were acquired in 4096 channels of a pulse-height analyzer at a total system gain of approximately 0.5 keV/channel. Individual gamma spectra were recorded on magnetic tape, and they were then transferred to an optical photostore system at the Los Alamos Central Computer Facility for permanent storage.

#### Data Reduction

The spectra were analyzed with the code GAMANAL<sup>12</sup> on a CDC-7600 computer. Output from this program provided energy and activity information on all statistically significant photopeaks in the spectra.

Isotopic assignments of detected gamma rays were made by GAMANAL from nuclear data (half-lives, gamma energies, and photon intensities) contained in our own gamma-ray library. Nuclidic identifications were based upon considerations of both half-life and gamma-ray multiplicity correlations, and this routine also estimated the disintegrations per minute and number of atoms ( $N_0$ ) present at the end of bombardment for each isotope encountered.

The nuclear constants employed for the calculations in this study are presented in Table 1. Cross sections at 800 MeV for the three Al monitor reactions were taken from the adopted values recommended in a study which evaluated all the existing experimental data.<sup>13</sup>

#### Results and Discussion

The spallation cross sections (cumulative yields) measured at 800 MeV are presented in Table 2, along with values at 590 MeV previously reported by O'Brien.<sup>2</sup> The 800-MeV numbers are weighted averages derived from many repetitive counts of the irradiated targets and monitors, but the reported cross sections are based only upon the  $^{22}\text{Na}$  and  $^7\text{Be}$  monitor reactions in Al. While these monitors gave comparable results, cross sections calculated relative to  $^{24}\text{Na}$  production were observed to be consistently 10-20% smaller. Although this is the correct direction for possible secondary interferences in this monitor reaction [primarily from the fast-neutron induced  $^{27}\text{Al}(n,\alpha)^{24}\text{Na}$  reaction], our results are not compatible with the expected secondary rate, nor did we observe any appreciable differences in thick-target vs. thin-target experiments. Other investigators at this laboratory have had similar problems, and present thinking attributes the discrepancy to the values of the reference Al cross sections.

While the recommended<sup>13</sup>  $\sigma$  of 10.75 mb for  $^{24}\text{Na}$  production is consistent with that given by Cumming,<sup>22</sup> if this number is correct then both the  $^{22}\text{Na}$  and  $^7\text{Be}$  cross sections must be high by the same relative amount. We plan to study this problem experimentally in the future.

The errors given in the 800-MeV data in Table 2 are one standard deviation of our individual experimental values, including a 3% uncertainty in the detector efficiency calibration. They do not encompass any uncertainties in the monitor cross sections, however.

#### Conclusions

A wealth of practical information can be garnered from the experimental results presented in Table 2. The very energetic beta and gamma radiations emitted during  $^{42}\text{K}$  decay render this radionuclide unsuitable for many diagnostic applications because of both excessive radiation doses to the patient and imaging difficulties using conventional collimators and medical scanners. While  $^{43}\text{K}$  is a much more desirable isotope, the amount of  $^{42}\text{K}$  contamination in the product is an important concern to the nuclear physician.

For example, one supplier presently produces  $^{43}\text{K}$  in a high-flux nuclear reactor by the (n,p) reaction on  $^{43}\text{Ca}$  in enriched (61%  $^{43}\text{Ca}$ ) CaO targets.<sup>23</sup> In a typical operation, after irradiating 0.4-0.6 g of material for about 66 hours, a total of approximately 50 mCi (0.085 mCi/mg of CaO) of  $^{43}\text{K}$  is generated. After processing and shipping, about 24 mCi of  $^{43}\text{K}$  with a 10-12%  $^{42}\text{K}$  content can be delivered. Unfortunately, the current high cost is a deterrent to the widespread utilization of this isotope.

Using the 800-MeV cross section data of Table 2 and the conditions of future LAMPF operating parameters, one can estimate the quality and quantity of the  $^{43}\text{K}$  produced at this facility. Such a study is presented in Table 3 as a function of product decay time and degree of saturation of  $^{43}\text{K}$  during irradiation. It can be seen that six days after the end of bombardment (EOB), nearly a curie of  $^{43}\text{K}$  will be available with a  $^{42}\text{K}/^{43}\text{K}$  ratio of approximately 6-7%. Hopefully, the availability of such large amounts of this activity will stimulate increased applications among the biomedical community.

The relative positioning of targets in the proton beam is also indicated by the data in Table 2. The Isotope Production Facility at LAMPF will accommodate a total of nine target stringers (remote-insertion devices), each capable of positioning a 2.5-cm thick target in the beam. From the absolute values of the  $^{43}\text{K}$  cross sections as well as from the  $^{43}\text{K}/^{42}\text{K}$  cross-section ratios, it is evident that  $^{43}\text{K}$  is produced more efficiently and enhanced relative to  $^{42}\text{K}$  using 800-MeV protons compared to 600-MeV protons. This information suggests the placement of V targets in upstream positions in the stringer array, before appreciable energy degradation of the beam occurs. Similar considerations apply to the Mo targets, where a factor of 1.6 increase in  $^{82}\text{Sr}$  yields can be expected at the higher energy. Production of radioiodine and radioxenon activities from La targets, on the other hand, seems to be as efficient at 600 MeV as at 800 MeV, and may even be slightly enhanced at the lower energy. Consequently, beam positioning should not be a critical factor for these isotopes.

The data of Table 2 also indicate that large amounts of  $^{85}\text{Sr}$  will be present as an isotopic

impurity in the  $^{82}\text{Sr}$  product. This is not of the same concern as the  $^{42}\text{K}$  contamination in  $^{43}\text{K}$  since the  $^{82}\text{Rb}$  decay product is the species of interest for clinical use, however. While the radiostrontium activities will not be directly injected, additional shielding requirements for the  $^{82}\text{Sr}$ - $^{82}\text{Rb}$  generator must be considered. The factor of 2 advantage in cross section and factor of 2.6 advantage in half-life that  $^{85}\text{Sr}$  enjoys over  $^{82}\text{Sr}$  imply that, even after the  $^{82}\text{Sr}$  decays to non-useful levels, significant amounts of  $^{85}\text{Sr}$  will remain. Recovery of this activity for strontium tracer studies could prove an additional benefit to scientific investigation.

Of course, many more nuclides than the ones considered here are produced in the nuclear interactions of 800-MeV protons. Cross sections for these isotopes will be reported in detail elsewhere at a later date, along with a number of forward/backward recoil ratios and related quantities. Such cross-section measurements form an important data base upon which future production capabilities can be established. The estimates presented here graphically illustrate that the unique combination of particle energy and beam intensity at LAMPF can be effectively utilized to provide a source of nuclear materials of significant importance to nuclear medicine.

#### Acknowledgments

This work was performed under the auspices of the United States Atomic Energy Commission with partial support from the American Cancer Society Research Grant No. DT-23A and Associated Western Universities.

#### References

1. L. Rosen, Proc. Nat. Acad. Sci. USA **70**, 603 (1973).
2. H. A. O'Brien, Jr., Proceedings of the Symposium on Practical Applications of Accelerators, LA-5535-C (CONF-730849), 1973, pp. 93-107, 133-134.
3. E. L. Saenger, Proceedings of the Symposium on Practical Applications of Accelerators, LA-5535-C (CONF-730849), 1973, pp. 5-21.
4. V. J. Sodd, Proceedings of the Symposium on Practical Applications of Accelerators, LA-5535-C (CONF-730849), 1973, pp. 47-62.
5. P. B. Hoffer, P. V. Harper, R. N. Beck, V. Stark, H. Krizek, L. Heck, and N. Lembares, J. Nucl. Med. **14**, 172 (1973).
6. Y. Yano and H. O. Anger, J. Nucl. Med. **9**, 2 (1968); **9**, 412 (1968).
7. H. A. O'Brien and A. Ogard, J. Nucl. Med. **14**, 635 (1973).
8. P. M. Grant, M. Kahn, and H. A. O'Brien, Jr., J. Inorg. Nucl. Chem., in press.
9. V. R. Casella, LA-5830-T, Ph.D. Thesis (1974).
10. H. A. O'Brien, Jr., A. E. Ogard, and P. M. Grant, Proceedings of the First World Congress of Nuclear Medicine, CONF-740926, 1974, pp. 1485-1489.
11. P. M. Grant, B. R. Erdal, and H. A. O'Brien, Jr., J. Nucl. Med., in press.
12. R. Gunnink and J. B. Niday, UCRL-51061 (1971-1972).
13. J. Tobaillem, C.-H. de Lassus St-Genies, and L. Leveque, CEA-N-1466(1) (1971).
14. M. J. Martin and P. H. Blichert-Toft, Nuclear Data Tables **A8**, 1 (1970).
15. R. L. Auble, Nuclear Data Sheets **B7**, 363 (1972).
16. R. L. Auble, Nuclear Data Sheets **B8**, 77 (1972).
17. G. Erdtmann and W. Soyka, JUL-1003-AC (1973).
18. A. Artna, Nuclear Data Sheets **B1**, 103 (1966).
19. S. Raman and J. J. Pinajian, Nucl. Phys. **A125**, 129 (1969).
20. P. M. Endt and C. Van der Leun, Nucl. Phys. **A214**, 1 (1973).
21. D. Barr, personal communication, LASL Group CNC-11 internal half-life values (1974).
22. J. B. Cumming, Ann. Rev. Nucl. Sci. **13**, 261 (1963).
23. T. A. Butler, ORNL, personal communication (1974):

TABLE 1. NUCLEAR DATA FOR CROSS SECTION DETERMINATIONS

Nuclide	Half-Life	Major $E_\gamma$ in keV (Photons/100 Decays)	800-MeV Proton $\sigma$ in Al (mb)	Reference
$^{123}\text{I}$	13.2 h	159.0(0.829), 346.6(0.0010), 440.4(0.0035), 505.6(0.0026), 529.0(0.0105), 538.5(0.0027)	-	14
$^{123}\text{Xe}$	2.08 h	148.9(0.486), 178.1(0.148), 330.2(0.0850), 899.6(0.024), 1093.4(0.028), 1113.1(0.016), 1807.3(0.0124)	-	15
$^{127}\text{Xe}$	36.41 d	57.60(0.0122), 145.22(0.0372), 172.10(0.200), 202.84(0.582), 374.96(0.175)	-	16,17
$^{82}\text{Sr}$	25.0 d	Daughter gammas only.	-	18
$^{82}\text{Rb}$	1.25 m	698.4(0.0014), 776.6(0.134), 1395.2(0.0047)	-	19
$^{85}\text{Sr}$	64.5 d	513.97(0.9928)	-	14
$^{43}\text{K}$	22.3 h	220.7(0.043), 372.9(0.85), 396.4(0.11), 404.9(0.0039), 593.6(0.10), 617.1(0.79), 990.0(0.0064), 1022.0(0.023)	-	20
$^{42}\text{K}$	12.36 h	312.4(0.0018), 1524.7(0.179)	-	14
$^{24}\text{Na}$	15.00 h	1368.55(1.00), 2754.10(0.9985)	10.75	13,14
$^{22}\text{Na}$	2.60 y	1274.54(0.9995)	16.3	13,14
$^7\text{Be}$	52.93 d	477.56(0.103)	6.4	13,14,21

TABLE 3. PROJECTED LAMPF  $^{43}\text{K}$  YIELDS AND  $^{42}\text{K}$  IMPURITY LEVELS FROM V TARGETS AS A FUNCTION OF DECAY TIME AND  $^{43}\text{K}$  SATURATION. (ASSUMPTIONS:  $E_p^+ = 800$  MeV,  $I = 500$   $\mu\text{A}$ ,  $X_V = 15.1$  g/cm<sup>2</sup>)

		$^{43}\text{K}$ Saturation Factor			
Time		0.50	0.70	0.90	0.98
EOB	$^{43}\text{K A}_0$ (Ci)	41	57	73	80
	$^{42}\text{K A}_0$ (Ci)	130	160	170	180
EOB+5d	$^{43}\text{K A}$ (mCi)	980	1400	1800	1900
	$^{42}\text{K A}$ (mCi)	150	190	210	210
	$^{42}\text{K}/^{43}\text{K}$ (%)	16	14	12	11
EOB+6d	$^{43}\text{K A}$ (mCi)	460	650	830	910
	$^{42}\text{K A}$ (mCi)	39	49	54	55
	$^{42}\text{K}/^{43}\text{K}$ (%)	8.5	7.6	6.5	6.1
EOB+7d	$^{43}\text{K A}$ (mCi)	220	310	390	430
	$^{42}\text{K A}$ (mCi)	10	13	14	14
	$^{42}\text{K}/^{43}\text{K}$ (%)	4.7	4.1	3.6	3.3
EOB+8d	$^{43}\text{K A}$ (mCi)	100	150	190	200
	$^{42}\text{K A}$ (mCi)	2.7	3.3	3.7	3.7
	$^{42}\text{K}/^{43}\text{K}$ (%)	2.6	2.3	2.0	1.8

TABLE 2. SPALLATION CROSS SECTIONS WITH 800-MeV PROTONS---CUMULATIVE YIELDS OF RADIOISOTOPES OF INTEREST TO NUCLEAR MEDICINE.

Target	Nuclide	$\sigma$ at 800 MeV (mb)	$\sigma$ at 590 MeV <sup>2</sup> (mb)
La	$^{123}\text{I}$	$51 \pm 3$	$57 \pm 9$
	$^{123}\text{Xe}$	---	$36 \pm 5$
	$^{127}\text{Xe}$	$51 \pm 7$	$53 \pm 11$
Mo	$^{82}\text{Sr}$	$24.5 \pm 0.8$	$15 \pm 3$
	$^{85}\text{Sr}$	$50 \pm 2$	---
V	$^{43}\text{K}$	$5.4 \pm 0.3$	$3.8 \pm 0.8$
	$^{42}\text{K}$	$11.8 \pm 0.5$	$8.9 \pm 3.6$



A technique has been developed which employs two neutron sources ( $^{252}\text{Cf}$  and  $^{238}\text{Pu-BE}$ ) and three NaI(Tl) detectors to determine the H, Ca, Si and C content of calcareous aggregate concrete in its plastic state. These elements are indicative of the water, cement, fine aggregate and coarse aggregate components which along with air entrainment are key factors in strength determination. Results are presented which demonstrate the feasibility of the technique for analysis of typical samples in a total time of the order of 10 minutes.

(Neutrons; gamma-rays; analysis; concrete; feasibility; application)

### Introduction

Nuclear cross section data plays an important role in the development of new analytical instrumentation, especially in the early stages when the feasibilities of several alternative techniques must be investigated. Precise, extensive data are not usually required, but they should be of sufficient quality to permit accurate assessment of competing source-detector combinations and configurations. This paper illustrates the sequence of steps involved and the role that nuclear data plays in a typical feasibility study.

### Statement of the Problem

One of the most important problems in Civil Engineering is that of quality assurance of concrete, particularly in large military or civil construction projects such as bridges, dams, silos and aircraft runways. Quality is based on the strength of the hardened concrete, when it may be too late or too expensive to rectify mistakes. The strength potential of fresh concrete is a function of the cement and water content, bulk density and degree of air entrainment. All these quantities except cement content can be measured on-site prior to concrete placement. However, no satisfactory method exists for field measurement of the most vital quantity, cement content. One recent attack on this problem has resulted in the development of a radioisotope backscatter probe for cement content measurement.<sup>1</sup> The probe measures mean atomic number which is correlated with cement/aggregate ratio. The X-ray backscatter approach suffers from two disadvantages which have prevented its effective application. These are 1) sensitivity to variations in aggregate composition, particularly an inability to distinguish calcareous aggregate from cement and 2) heterogeneity errors due to the small penetration of X-rays or low energy gamma-rays compared with the particle size of coarse aggregate.

The use of neutron excitation of characteristic gamma-rays for elemental analysis offers unique advantages over X-rays for concrete analysis. The main advantages are: 1) ability to determine cement content of all types of concrete independent of type or mixture and 2) insensitivity to particle size and heterogeneity due to the high degree of penetration of gamma-rays compared with sample volume and the maximum particle size of the coarse aggregate.

Aggregates can vary widely in composition from quartz (e.g., river sand fines) to limestone. Fine aggregates are usually siliceous but coarse

aggregates can equally well be siliceous or calcareous depending on local availability. Nuclear techniques of analysis measure elemental concentration so it is important to establish a definite correlation between the quantities required and certain elemental concentrations or ratios. Earlier work by Iddings, et al. has shown that the cement content can be determined by activation analysis for completely siliceous aggregates.<sup>2</sup> However, this breaks down when some of the aggregate is calcareous.

The only element unique to calcareous aggregate is carbon, so the chosen technique must be able to monitor carbon content. Assuming, therefore that 1) cement contains a known ratio of calcium to silicon, 2) siliceous aggregate is characterized by a certain silicon content and 3) calcareous aggregate is characterized by a certain carbonate content, then it is possible to uniquely determine the cement content in the presence of an unknown siliceous to calcareous aggregate ratio by measuring the concentrations of carbon, calcium and silicon.

### Investigation of Candidate Techniques

#### Basic Requirements

The key signature elements, in order of importance, are H, Ca, Si and C, with the possibility of substituting Al for C in some instances. Elements of secondary interest are Fe and Mg. The desired experimental accuracy in a total analysis time of the order of 10 minutes is 2% or better on all measurements. With these criteria in mind, an investigation into the feasibility of various nuclear techniques was conducted.

#### Possible Nuclear Reactions

The only practicable reaction available for measuring carbon content is fast neutron inelastic scattering,  $^{12}\text{C}(n,n'\gamma)^{12}\text{C}$ . The  $^{12}\text{C}$  nucleus has a relatively large cross section for excitation to its 4.43 MeV excited state which decays promptly, with emission of a 4.43 MeV gamma-ray. The incident neutrons must have an energy above 5 MeV to exceed the threshold for production of this characteristic gamma ray. Fast neutron inelastic scattering also yields characteristic gamma radiation with many other elements, including calcium (main gamma energy 3.75 MeV), silicon (main gamma energy 1.78 MeV), oxygen (main gamma energy 6.13 MeV), iron and aluminum.

Thermal neutron capture (n,γ) reactions produce gamma-rays which are characteristic of the product nucleus and indicative of the capturing element. The hydrogen 2.22 MeV capture gamma-ray, for example, is quite intense and serves as a good elemental

\*Work supported by Army Corps of Engineers.

\*\*Present address: University of Southwestern Louisiana.



signature. Silicon and calcium also have fairly intense unambiguous capture gamma-rays at 3.54 MeV and 6.42 MeV respectively. However, the main capture gamma-ray from carbon at 4.95 MeV is very weak and an unlikely elemental signature.

As a result of both fast and thermal neutron reactions the sample can become radioactive. Characteristic gamma-rays from activation can be measured after the source is switched off or removed. Relevant reactions are  $^{48}\text{Ca}(n,\gamma)^{49}\text{Ca}$ , half-life 8.8 mins, gamma energy 3.1 MeV;  $^{28}\text{Si}(n,p)^{28}\text{Al}$  and  $^{27}\text{Al}(n,\gamma)^{28}\text{Al}$ , half-life 2.3 mins, gamma energy 1.78 MeV;  $^{27}\text{Al}(n,p)^{27}\text{Mg}$ , half-life 9.5 mins, gamma energies 0.84 and 1.01 MeV;  $^{16}\text{O}(n,p)^{16}\text{N}$ , half-life 7.14 sec, gamma energy 6.13 MeV;  $^{56}\text{Fe}(n,p)^{56}\text{Mn}$ , gamma energies 0.85 and 1.81 MeV, half-life 2.58 hrs;  $^{24}\text{Mg}(n,p)^{24}\text{Na}$ , gamma energies 1.37 and 2.75 MeV, half-life 15 hours.

#### Summary of Feasibility and Selected Technique

A qualitative summary of the results of a detailed investigation into various neutron-gamma techniques for determination of key signature elements in concrete constituents is presented in Table 1.<sup>3</sup> The conclusion drawn from this study was that no simple technique combining one neutron source and one gamma-ray detector was suitable for the determination of all four primary elements. Thus, it becomes necessary to employ a more complex procedure which combines two or more of these techniques in one instrument.

Resultant losses in simplicity can be offset by gains in flexibility. This approach has been demonstrated previously as a means for determination of Ca, Si and Al in cement for on-stream process control.<sup>4</sup>

An evaluation of possible combined techniques has shown that the preferred combination is a dual source, multiple analysis procedure employing a  $^{252}\text{Cf}$  source for thermal neutron, prompt gamma and activation reactions and a  $^{238}\text{Pu-Be}$  source for fast neutron, prompt gamma and activation reactions. This approach provides the flexibility of having all possible neutron-gamma analytical processes combined into one instrument.

#### Detailed Investigation of Selected Technique

##### Experimental Procedure

A mock-up of a dual-source system was constructed by using two neutron sources ( $^{252}\text{Cf}$  and  $^{238}\text{Pu-Be}$ ) and three 5 in. x 5 in. NaI(Tl) detectors. Spectra were collected on a 1024 channel analyzer. The basic steps in the analysis procedure were:

- 1) Irradiate a 4 kg sample of wet concrete with a partially thermalized 185 microgram  $^{252}\text{Cf}$  source for 5 min. During this time obtain a hydrogen count from the prompt 2.22 MeV gamma peak;
- 2) Transfer the sample to an activation counting cell remote from the source and count for 5 min. after a 1 min. delay. This procedure gives a silicon peak at 1.78 MeV and a calcium peak at 3.09 MeV;
- 3) Irradiate another 4 kg sample of wet concrete with fast neutrons from a  $^{238}\text{Pu-Be}$  source for 500 sec. During this time obtain a carbon count from the prompt 4.43 MeV peak and a silicon count from the prompt 1.78 MeV peak.

Each step involves certain assumptions which must hold, and potential pitfalls which must be avoided, to insure accurate results.

Table 1

Summary of Neutron-Gamma Methods for Concrete Analysis

Element	Importance	Technique	Reaction	Source	Detector	Gamma Energy (MeV)	Comments
Hydrogen	Primary	Thermal neutron capture	$\text{H}(n,\gamma)\text{D}$	$^{252}\text{Cf}$	NaI(Tl)	2.22	Best method.
					Ge(Li)	2.22	Better resolution, but less sensitive and more expensive.
		Fast neutron capture	$\text{H}(n,\gamma)\text{D}$	Pu-Be 14 MeV	NaI(Tl)	2.22	Less sensitive than thermal capture.
					NaI(Tl)	2.22	Least sensitive method.
Carbon	Primary	Thermal neutron capture	$^{12}\text{C}(n,\gamma)^{13}\text{C}$	$^{252}\text{Cf}$	Ge(Li)	4.95	Very low intensity.
		Neutron inelastic scattering	$^{12}\text{C}(n,n')^{12}\text{C}$	$^{252}\text{Cf}$	NaI(Tl)	4.43	Very low intensity due to source spectrum.
				Pu-Be	NaI(Tl)	4.43	Best method provided source is well shielded.
					Ge(Li)	4.43	Offers no advantage due to Doppler broadening of gamma peak.
				14 MeV	NaI(Tl)	4.43	Interference from $^{16}\text{O}(n,n',\alpha)^{12}\text{C}$ for n energies > 12.5 MeV.
Silicon	Primary	Thermal neutron capture	$^{28}\text{Si}(n,\gamma)^{29}\text{Si}$	$^{252}\text{Cf}$	Ge(Li)	3.53	Requires large expensive source.
		Neutron activation	$^{28}\text{Si}(n,p)^{28}\text{Al}$	$^{252}\text{Cf}$	NaI(Tl)	1.78	Works well with source unmoderated.
				Pu-Be	NaI(Tl)	1.78	Works very well - ~ 0.1% precision.
				14 MeV	NaI(Tl)	1.78	Works very well - ~ 0.1% precision.
		Neutron inelastic scattering	$^{28}\text{Si}(n,n')^{28}\text{Si}$	Pu-Be	NaI(Tl)	1.78	Works reasonably well.
				14 MeV	NaI(Tl)	1.78	Works reasonably well.
Calcium	Primary	Thermal neutron capture	$^{40}\text{Ca}(n,\gamma)^{41}\text{Ca}$	$^{252}\text{Cf}$	Ge(Li)	6.42	Requires large expensive source.
		Neutron activation	$^{48}\text{Ca}(n,\gamma)^{49}\text{Ca}$	$^{252}\text{Cf}$	NaI(Tl)	3.09	Works well.

The combination of intense neutron sources, large, efficient NaI(Tl) detectors and large samples, required in order to achieve adequate sensitivity, results in count rates in excess of  $10^4$  counts per second. These high count rates cause deadtime losses in the data acquisition system which, unless accounted for, can cause serious errors in quantitative analysis. This problem is particularly critical when the collection of three independent spectra at different count rates is involved, even though the desired result is a relative concentration. This necessitates an independent measurement of the true analysis time (live-time) for each of the three measurements.

Background subtraction is very important in Steps 1 and 3 because neutrons scattered from the sample constitute a significant portion of this background. The background intensity will change with sample composition, especially silicon content. Since the statistical error in the net count is determined by the sum of the peak and background counts and since the net count in each peak channel diminishes rapidly with distance from the central channel (approximately a Gaussian distribution), there is an optimum number of channels which will yield a minimum statistical error. In previous investigations, a near optimum choice has been found to be the channels across the full-width at half-maximum (FWHM) of the peak together with an equivalent number of background channels.

#### System Calibration

A set of calibration curves were obtained for the mock-up system by using mixtures of pure samples of  $H_2O$ ,  $SiO_2$  and  $CaCO_3$ . These materials were chosen for standards preparation because of their known elemental composition. However, they are not ideally suited for simulation of wet concrete because they are not totally representative of the ingredients. In particular, they contain no aluminum, which may influence the determination of silicon by activation with  $^{252}Cf$ . However, if aluminum interference is a significant problem for  $^{252}Cf$  determination of silicon, a second determination of silicon with  $^{238}Pu$ -Be by neutron inelastic scattering is independent of

aluminum content and can be used in place of the first. Also, these two silicon determinations can be used for normalization when simultaneous irradiations of separate samples are made. A third and most accurate calibration for silicon could be obtained by counting the  $^{28}Al$  activity following  $^{238}Pu$ -Be irradiation.

#### Analysis of Typical Samples

Following calibration, two samples of concrete were prepared using locally available aggregates and Type I cement, and analyzed. In a preliminary investigation the coarse aggregate was found to contain both siliceous and calcareous components. Samples of this aggregate were analyzed using Step 3 above and were found to contain  $47\% \pm 3\% CaCO_3$  and  $53\% \pm 3\% SiO_2$ .

Based upon this aggregate composition, an analysis of the concrete was made for which the results are given in Table 2. The "Standard Deviation" column is the statistical error on the concentrations while the "% Error" column is the relative difference between weighed and measured amounts. Because of its silicon and calcium content, the large uncertainties in coarse aggregate composition are propagated to the fine aggregate and cement determinations. However, the accuracy and precision of these measurements is considered to be encouragingly good at this stage of development.

Significant improvements in accuracy and/or analysis time are considered to be possible through careful shield and geometry optimization and by use of somewhat larger sources.

#### Conclusions

This feasibility study has shown that while no single neutron source technique is capable of determining all four primary signatures, H, C, Si, and Ca for plastic concrete, it is possible to employ a combination of techniques which will meet the analytical requirements. In order to evaluate the combined source method for routine analysis, a prototype laboratory instrument is under development. This instrument will be evaluated by the U. S. Army Construction Engineering Research Laboratory.

Table 2

#### Concrete Analysis Data

Component	Weighed Amount	Source	Elemental Signature	Measured Amount	Standard Deviation	% Error
<u>Sample No. 1</u>						
Water	8.7%	$^{252}Cf$	H	8.5%	0.15%	2.2%
Cement	21%	$^{252}Cf$	Ca	21.8%	0.8%	3.8%
Fine Aggregate	25.3%	$^{252}Cf$	Si	26.6%	1.1%	5.1%
Coarse Aggregate	45%	$^{238}Pu$ -Be	C	43.1%	2.3%	4.2%
<u>Sample No. 2</u>						
Water	8.7%	$^{252}Cf$	H	8.8%	0.15%	1.1%
Cement	12.3%	$^{252}Cf$	Ca	14.5%	0.8%	17.9%
Fine Aggregate	36%	$^{252}Cf$	Si	38.4%	1.1%	6.7%
Coarse Aggregate	45%	$^{238}Pu$ -Be	C	41.9%	2.3%	6.7%

#### Acknowledgements

The authors wish to acknowledge the support of the U. S. Army Construction Engineering Research Laboratory and thank Mr. Paul Howdysshell for laying the ground rules for the feasibility study and providing timely advice on concrete analysis procedures and requirements.

#### References

1. Berry, P. F. and T. Furuta, 1969-1970, "Radio-isotope X- and Gamma-Ray Methods for Field Analysis of Wet Concrete Quality", Technical Reports ORO-3842-1, -2 and -3 (U. S. Atomic Energy Commission).
2. Iddings, F. A. et al., 1969, "Nuclear Techniques for Cement Determination", Highway Research Record No. 268, pp. 118-130.
3. Taylor, M. C., 1973, "A New Method for Field Analysis of Plastic Concrete--Feasibility Study", U. S. Army Construction Engineering Laboratory, Report No. CERL-TR-M-64.
4. Taylor, M. C. and J. R. Rhodes, February 1974, "Analyzing Process Streams by Neutron Activation - A Dual Source Technique", Instrumentation Technology, 21, pp. 32-35.



# CROSS SECTION REQUIREMENTS FOR INDUSTRIAL GAUGING APPLICATIONS

B. Y. Cho and T. P. Sheahan  
*Industrial Nucleonics, Columbus Ohio 43202*

We use nuclear isotopes for gauging and control of industrial products. The use of recycled materials have made paper, steel, plastic, etc., into ever-changing composite media, forcing us to update calibrations empirically. This paper lists those areas of research that would benefit our work. Specifically, we need: differential cross sections for electrons scattered from most common elements, as a function of energy below 3.6 MeV; Monte Carlo calculations that simulate isotopic sources (Kr-85, Sr-90/Y-90) interacting with common materials; phenomenological models or empirical expressions that coalesce scattering formulas and Monte Carlo results into forms usable for gauge design.

(Industrial gauging; multiple scattering; Monte Carlo calculations; isotopes)

## I. Introduction

For over 25 years, the scattering of electrons with MeV energies has been exploited in the control of industrial processes<sup>1</sup>. The cornerstone of this activity is the  $\beta$ -gauge, a term loosely applied to the various combinations of an isotopic source (emitting electrons or photons), a sample of some material to be measured, and a detector<sup>2</sup> such as a scintillation counter, proportional counter or ionization chamber. Up to the present time, the development of such gauges has been highly empirical, indeed artwork.

With the advent of modern computational techniques, it is possible in principle to design gauges using Monte Carlo calculations of the response of the detector system to the source when a sheet of material intervenes. This paper tries to stimulate the basic research (both theoretical and experimental) that is needed to put such design efforts on a firm footing. We need to know cross sections to much higher accuracy than has been generally available in the literature.

In section II, an overview is given of the way in which a  $\beta$ -gauge is used<sup>3</sup> in industrial process control. Section III cites specific problems related to cross sections. These are provided to improve the perspective of the potential researcher, and hopefully will lead to more valuable contributions in the long run. Section IV lists the specific needs that we foresee, but our list may be incomplete. Section V tells what would be accomplished by having better cross section data.

## II. Industrial Process Control

Many industrial products (paper, plastic, rolled metals, etc.) are produced in sheet form by machines running at high speed (perhaps 60 m/sec). The machines require feed-forward and feedback control systems to regulate their speed and the amount of raw materials used. Such control systems necessarily include gauges to measure essential properties of the finished material. The most important measurement is usually the *basis weight*, defined as density times thickness, with units of mass per unit area. A  $\beta$ -gauge performs this measurement, frequently in the configuration shown schematically in Fig. 1. Ionization chambers are the most common detectors.

The basis weight of the process material is determined by measuring the attenuation of the initial beam. The source emission is partially absorbed and scattered by the source window and the dust accumulated on it. The radiation is further scattered by air before it reaches the sample. Since the sample will scatter the radiation significantly, its distance to the detector influences the intensity reaching the detector window. During an on-line measurement, we cannot afford the luxury of manipulating the samples and fixing the sample position relative to the measurement instrument. Even the positions of the source

and the detector relative to each other cannot often be fixed accurately enough.

When the  $\beta$ -gauge senses the process material to be too heavy, the line speed is increased or the raw material input is reduced; and when the material is too light, the countermanding controls are applied. In this way the product becomes more uniform than it would be without control. Assuming the production goal permits some tiny percentage of rejects, the average basis weight may be reduced when the system is controlled. Such action saves raw materials, increases throughput, and reduces the energy demand per unit of product. For example, it required 10,000 Joules to produce this page from a tree.

There are 3 major isotopes used for most industrial applications: Kr-85 ( $\beta$ ,  $E_{\max} = 0.7$  MeV), Sr-90/Y-90 ( $\beta$ ,  $E_{\max} = 2.3$  MeV), and Am-241 ( $\gamma$ , 60 KeV). Other less frequently used isotopes include  $\gamma$ -emitters Co-60 and Cs-137,  $\beta$ -emitters Ru-106 and Pm-147, X-ray<sup>4</sup> emitters Fe-55 and Cd-109, and bremsstrahlung generators H-3, C-14, Pm-147 and Sr-90/Y-90. Considerations of packaging integrity, emitted energy spectrum, and lifetime dominate the choice of source in any particular case<sup>3</sup>. For example, packaging requirements make it impossible to use the familiar C-14  $\beta$  spectrum ( $E_{\max} = 156$  KeV) directly. Similarly, possible applications of neutrons<sup>5</sup> are very limited due to industrial shielding demands.

The materials being measured (paper, plastic, glass, rubber, aluminum, steel) are typically composed of the lighter, most common elements. Aside from stainless steels, most industrial products seldom contain significant fractions of heavier elements. When they do appear, it is typically as a pigment added to

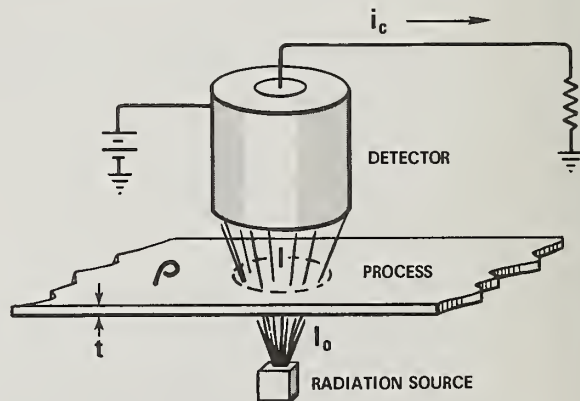


Figure 1. Typical  $\beta$  - gauge configuration. An alternate arrangement is to have both source and detector on the same side and collect backscattered radiation.



plastic or paper;  $\text{PbCrO}_4$  is an example. Thus our interest in better cross sections focuses on interactions between a few sources and the lighter elements.

### III. Use of Cross Section Data

The attenuation of photons or electrons from an isotopic source passing through any medium is approximately exponential<sup>6</sup>. The intensity reaching the detector is usually written

$$I = I_0 \Omega_S \Omega_D \exp(-\mu \rho t), \quad (1)$$

where  $I_0$  is the source strength,  $\Omega_S$  and  $\Omega_D$  are solid angles subtended by the source and detector as seen from the material,  $\mu$  is the effective average mass absorption coefficient,  $\rho$  is the density of the medium and  $t$  is its thickness. However, Eq. (1) is not precise enough to be used in process control of industry, where control algorithms demand 0.1% accuracy. Not surprisingly, semilog plots of  $I$  vs.  $\rho t$  show marked excursions from linearity on this scale. At the design stage, values of  $\mu$  need to be known within 1 or 2% if we are to build a gauge that can be calibrated to yield 0.1% reproducibility.

Most  $\gamma$  sources are monoenergetic, but their absorption cross sections vary with the chemical constituency of the medium<sup>3</sup>. By contrast,  $\beta$  sources have Fermi-distributed energies<sup>7</sup>, none of which are exponentially attenuated. The approximate validity of Eq. (1) is a result of the actual scattering and the emitted energy spectrum. The rigorous equivalent of Eq. (1) must be written

$$I = \int_0^{E_{\max}} I_0(E) \Omega_S(E) \Omega_D(E) f[\mu(E), \rho t] dE, \quad (2)$$

where  $I_0(E)$  denotes the Fermi distribution and  $f[\mu(E), \rho t]$  is the monoenergetic scattering. The energy dependence of the solid angle factors accounts for the effect of thin steel windows, attenuation in air, and variation of the detector efficiency with energy. All of these influences must be included if the precise behavior of the measurement system is to be calculated. The absence of accurate cross section data has precluded any calculation of the form (2).

The empirical and very delicate adjustment of the geometrical factors continues to be the principal design criterion of a  $\beta$ -gauge system; the difference between good and bad gauges is dominated by geometrical considerations such as the horizontal or vertical misalignment of the source and detector with respect to each other. The availability of good scattering cross section data would help to alleviate this empiricism. One specific example illustrates this point: Fig. 2 shows the sensitivity to vertical motion of the sheet of material, known as *pass-line flutter*. Four scattering events are portrayed; with the sheet close to the source, two of these deflections miss the detector; with the sheet close to the detector, all four are collected. Mathematically this may be expressed by generalizing Eq. (2) to include integration over a certain scattering volume which can vary in location. If we know the angular distribution of scattered electrons at various energies, we could calculate the extent of such flutter effects for various choices of geometrical factors, and thereby minimize the flutter-sensitivity of the measurement system.

Similar examples abound. Dirt collects on the windows and is wiped off intermittently; the density of air in the source-detector gap varies with temperature of the material; the composition of the material changes hourly as diverse recycled materials are fed into the hopper. The effect of all these uncontrollables must

be minimized at the design stage. Without the basic cross section data, the task is purely empirical. Moreover, there is no predictive capability to account for the possible introduction of other factors in the future.

Beyond the task of helping to eliminate nuisance effects, better cross section data would be most valuable in choosing the *desired* operating range of the gauging system. Collimating the emitted or received beam, choosing or shaping energies, and barricading certain geometrical regions all contribute to shaping the curve of signal attenuation vs. basis weight. Reverting to Eq. (1), this means that geometrical tricks can alter the effective absorption coefficient  $\mu$ . Because industrial process control generally is concerned with *percent* deviations of the product, the goal is to build a gauge that is sharply responsive over the range of basis weights being manufactured. We define *process resolution* as the percent change in the process material per unit change in transmittance. When the attenuation is approximately exponential, this becomes

$$\frac{d(\rho t)}{\rho t} / d\left(\frac{I}{I_0}\right) = -\frac{\exp(-\mu \rho t)}{\mu \rho t}, \quad (3)$$

which has a minimum at  $\mu \rho t = 1$ . It is desirable to straddle this minimum; for example, in Fig. 3 we see that when the basis weight of the process material falls within the limits shown by the dashed vertical lines, the system should be geometrically designed to yield  $\mu = \mu_3$ . Moderately accurate cross section data for small-angle scattering is needed to facilitate such design calculations. Incidentally, because of the poor process resolution, we stay out of the thickness region where straggling is important.

Composition effects in a  $\beta$ -gauge become important when high accuracy is sought. The textbook approximations  $\mu \propto Z^{1/2}$  for  $\beta$ 's and  $\mu \propto Z^{4.5}$  for  $\gamma$ 's are not accurate enough to account for  $Z$ -dependence. Dirt on the windows, always a minor nuisance, would be easier to correct for if cross section variations with atomic number were well known.

### IV. Specific Needs

In order to use a solid theoretical foundation in designing and calibrating gauges, substantial improvement in cross section data is a prerequisite. This section lists the most significant needs that we foresee.

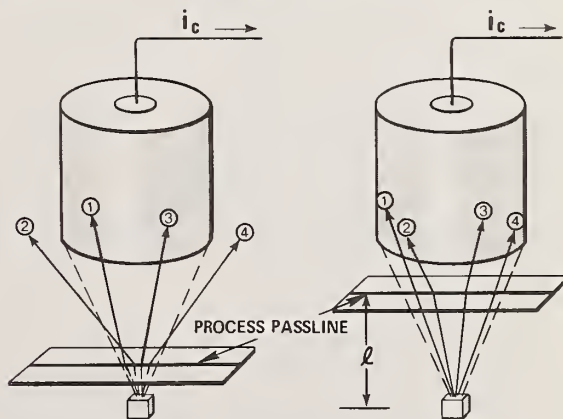


Figure 2. The effect of pass-line flutter on the measurement. In each case the 4 scattering events are identical. At left, only 2 events are detected; at right, all 4 are detected.

# RESOLUTION CURVES

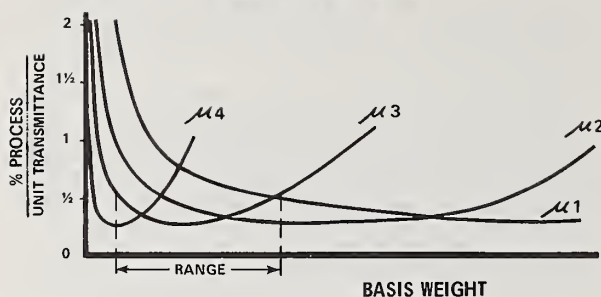


Figure 3. Variation of process resolution with mass-attenuation coefficient  $\mu$ . For any given range of basis weights (vertical dashed lines), there is an optimum value of  $\mu$  ( $= \mu_3$  here) that gives the most sensitive measurement.

The monoenergetic  $\gamma$  sources often have an interaction with matter dominated by photoelectric absorption. Even for scattering-dominated applications, various means of correction schemes (such as "build-up" factors) are established. The problems are generally simpler (at least from the theoretical viewpoint) than for  $\beta$  applications, and sufficient information is documented<sup>8</sup> for convenient use by the nuclear instrumentation industry. The Klein-Nishina formula for incoherent scattering and the Rayleigh formula for coherent scattering are sufficiently accurate to reduce the problem to one of determining atomic form factors  $F(q, Z)$  and  $S(q, Z)$ , defined<sup>9</sup> in the usual way. As more and more Hartree-Fock calculations<sup>10</sup> are done, cross sections determined in this way become ever more accurate.

For the application of  $\beta$  radiation, there is a significant amount of information scattered in the literature, but in a form that is not very convenient for our purposes. For example, several NASA-sponsored programs 11-13 helped to design protection for astronauts in the Van Allen belts, but this work was not extended into cases relevant to industry. The specific needs for industrial on-line measurement application can be delineated into 4 broad categories. Table I summarizes these needs.

## 1. Differential Cross Sections:

All our applications are sufficiently thick that the multiple scattering condition<sup>6</sup> holds. Moliere<sup>14</sup> theory is known to be accurate in computing multiple scattering of electrons. However, it requires a significant amount of machine computation to obtain differential angular cross sections. The chosen energy range (0.03 to 3.6 MeV) reflects the negligible penetrating power of electrons below 30 KeV and the maximum energy of  $\beta$ s from Ru-106. The step sizes reflect the rapid variation in range at low energies. Energies above 2.3 MeV ( $= E_{\text{max}}$  for Sr-90/Y-90) are less important than lower energies. The elements of interest are simply those found in metal windows, air and common industrial products.

## 2. Monte Carlo Calculations:

The presence of upper and lower boundaries on all process materials obstructs the use of scattering models valid in continuous media, and necessitates computational modeling<sup>15</sup>. The energy spectrum, beam and target conditions cited in Table I span the range of popular gauge designs. At the present time, results of Monte Carlo computations<sup>16</sup> (as well as experimental measurements<sup>13</sup>) are available for various materials. However, this data is difficult to use since it is in

TABLE I

## Calculations Needed for $\beta$ -Gauge Design

- Differential angular cross sections of multiple  $\beta$  scattering processes, with input parameters of:  
Energy Range: 30 to 700 KeV at 30 KeV steps  
0.7 to 3.6 MeV at 0.1 MeV steps  
Elements: H, Be, C, N, O, Si, P, S, Ar and common metals
- Monte Carlo calculations of transmission through and reflection from various target materials, with input parameters of:  
Energy Spectrum: Kr-85 and Sr-90/Y-90  
Incident Beam Configurations:  
A. Pencil beam with angles 0 - 30° from normal  
B. Cone-shaped beam with half-angles of 0 - 30° at 5° steps.  
Target thickness range: 0.02 to 10 Kg/M<sup>2</sup>  
Materials: C<sub>6</sub>H<sub>10</sub>O<sub>5</sub>, CH<sub>2</sub>, Aluminum, Steel, Brass  
Output: # of  $\beta$ s at each energy & each polar angle
- Outputs from 1 and 2 cast into empirical expressions
- Other phenomenological descriptions of the interaction between  $\beta$ s and sheet material.

partially-integrated form, *i.e.*, energy spectral data integrated over the angles, and the angular distribution data integrated over the energy spectrum. Of course, it would become excessively voluminous if both angular and spectral information were listed separately. Also, a vast number of Monte Carlo case histories are needed for the results to be statistically meaningful.

## 3. Empirical Formulas:

To avoid tabulating voluminous data, the Monte Carlo results should be put into some form of empirical expressions. For example, Moliere theory gives a Gaussian distribution of multiple-angle scattering with the *rms* angle definable by the thickness and the atomic number of the target material. Similarly, some Monte Carlo results have been coalesced into explicit formulas. One empirical expression of monoenergetic  $\beta$  transmission is due to Mar<sup>17</sup>:

$$T(E - m_0, Z, \rho t) = \exp \left\{ - \left[ \frac{0.63(E - m_0) Z^{-0.23}}{\rho t^{0.848}} \right] - 7(Z - 3.25)^{-0.24} \right\}, \quad (4)$$

where  $E$  and  $m_0$  are total and rest energies of the electron in MeV,  $Z$  is the atomic number of the target, and  $\rho t$  is the basis weight of the target. However, a combination of the Moliere angular theory and the empirical curve fitting for the energy spectrum has not yet been done, to our knowledge. This type of analytical and empirical expression, extended to include both angular and spectral cross-sections with  $\beta$  energy spectra of Kr-85 and Y-90, would be exactly what we need.

## 4. Phenomenological Models:

There are cases in which we need only approximate transmission or reflection information, but in a reasonably simple form. Such information would provide guidelines for design perturbations. Thus an empirically designed gauge could be correctly modified with the aid of approximate expressions. The fourth category of Table I is directed toward that situation.



To illustrate this point, recall that industrial on-line applications never have target thicknesses larger than that which attenuates the radiation by 95%. With this restriction, the energy spectrum of Kr-85 and Y-90 sources will be reasonably well conserved<sup>6</sup>, enormously simplifying the problem. Therefore, it is conceivable that some relatively simple phenomenological expression of the interaction process may result in predictions accurate enough for design modifications. A fluid mechanical analog applies here: just as the Monte Carlo method is the equivalent of Lagrangian motion<sup>15</sup>, consideration of the electron flux at one point is the equivalent of Eulerian motion.

This type of analysis has been used in the treatment of transmission and reflection of optical beams by Kubelka and Munk<sup>18</sup>, with results that often<sup>19</sup> resemble the exact results of radiative transport<sup>20</sup> theory. Hopefully, an equally valid model can be found for electrons transmitted and reflected from sheet material. The empirical expression (4), in conjunction with a Gaussian angular distribution, may be a good starting point for such an investigation.

Experimental verification of the theoretical calculations is very desirable. The simplest experiments to do are also the most useful: measure angular and energy distributions of electrons transmitted and reflected from sheets of process material when Kr-85 or Sr-90/Y-90 sources are used. The conditions specified by item 2 of Table I state the experimental arrangement needed. At first, the target materials should be pure substances, to connect with the theoretical work. Later, targets should be standard industrial products such as newsprint, polyethylene, 304 stainless steel, etc. The most difficult aspect of such experiments will be preserving (or retrieving) the energy spectrum emerging from the process material when using any of the commonplace nuclear detectors.

Finally, we need to have each result (theoretical or experimental) accompanied by an appraisal of its applicability, wherein statements about numerical precision are supplemented by analysis of the assumptions and limitations inherent in the model used.

#### V. Design of Better Gauges

Once the specific needs of Table I are met and verified experimentally, we will immediately have a much better predictive capability with which to approach industrial gauging. Empiricism in  $\beta$ -gauge design would be mitigated. Knowing how the process material influences the incident radiation would leave us with the task of designing source collimation and detector geometry so as to optimize performance of the gauge under the typical conditions described in section III. This is still a sizable task, and quite possibly another echelon of Monte Carlo calculations would be performed by the gauge designer to simulate the cumulative behavior of the source, process material, geometrical components, and detector.

Of particular interest here is the case where recycled materials constitute a substantial fraction of the input stock: composition effects must be predicted and eliminated through clever geometrical manipulation of the effective mass-attenuation coefficient  $\mu$ . We can do this for the photon spectrum from a man-made X-ray machine<sup>21</sup>, but it is much more difficult to shape the response of a detector to the  $\beta$  energy spectrum<sup>22</sup>. Of course, electrons are much less Z-dependent in their scattering than photons, so the composition problem is not as pressing.

Phenomenological models would be quite useful for real time processing of data. Ten years ago industrial gauges used piecewise-linear approximations of empirical calibration curves to convert signal to basis weight via analog electronics. Today minicomputers

routinely evaluate polynomials that represent the calibration curves when processing on-line data. As microprocessors assume more of the computational burden, it will shortly be possible to update calibrations for every change in the process material. Time constraints prevent the employment of Monte Carlo results for such updates, but empirical formulas or phenomenological models can certainly be used.

A comparison is warranted between this suggested work and other previous calculations of electron penetration through matter. The NASA calculations were concerned with shielding, and hence the numerical results were used only as minimum guidelines in the design of space capsules; therefore numerical precision was not crucial. In contrast, the industrial application outlined here demands much greater refinement, with cross sections accurate to  $\pm 1\%$ . By no means does this imply that only calculations of ultra high accuracy are worth doing. Rather, we believe that a continuing exchange of information between scientists doing basic studies and those doing gauge design will rapidly lead to an understanding of what is really important for improving industrial measurements.

#### References

1. N.N. Shumilovskii & L.V. Mel'ttser, *Radioactive Isotopes in Instrumentation and Control*, Transl. by R. F. Kelleher (Macmillan, New York: 1964)
2. W.J. Price, *Nuclear Radiation Detection* (McGraw Hill, New York: 1964)
3. H.J. Evans, *Isotopes and Rad. Techn.* 7, 381 (1970)
4. R.J. Pfeifer, B.Y. Cho & O.L. Utt in *Applications of Low Energy X and  $\gamma$  Rays*, Ed. by C.A. Ziegler (Gordon & Breach, New York: 1971) p. 115
5. H. Goldstein, *Fundamental Aspects of Reactor Shielding* (Addison-Wesley, Reading, Mass.: 1959)
6. R.D. Evans, *The Atomic Nucleus* (McGraw-Hill, New York: 1955)
7. H.A. Enge, *Introduction to Nuclear Physics* (Addison Wesley, Reading, Mass.: 1966)
8. E. Storm & H.I. Israel, "Photon Cross Sections from 0.001 to 100 MeV for Elements 1 through 100", Los Alamos Scientific Laboratory Report LA-3753 (1967)
9. A.H. Compton & S.K. Allison, *X-Rays in Theory and Experiment*, Second Edition (VanNostrand, Princeton: 1935)
10. e.g., see R.T. Brown, *Phys. Rev. A* 5, 2141 (1972)
11. M.J. Berger & S.M. Seltzer "Energy Spectra and Angular Distributions of Electrons Transmitted through Sapphire Foils", NBS report # NASA-SP-3008 (1964)
12. K.F. Kopal & A.J. Cohen "Empirical Equations for Electron Backscattering Coefficients", NASA report N65-27274 (1965)
13. W.E. Dance, W.J. Rainwater & D.H. Rester "Investigation of Electron Interaction in Matter" LTV Report # NASA CR-1194 (1968)
14. G. Moliere, *Z. Naturforsch.* 3a, 78 (1948)
15. M.J. Berger, "Monte Carlo Calculation of the Penetration and Diffusion of Fast Charged Particles", in *Methods in Computational Physics*, Vol I, Ed. by B. Alder *et al.* (Academic Press, New York: 1963)
16. W.C. Dickenson & E.M. Lent, "Calculation of Forward Bremsstrahlung Spectra from Thick Targets", Lawrence Radiation Laboratory Report TID-4500, UC-34 (June 1968)
17. B.W. Mar, "Electron Shielding for Space Vehicles" *American Nuclear Society Transactions* 7, 322 (1964)
18. P. Kubelka & F. Munk, *Z. Tech. Physik* 12, 593 (1931)
19. L.F. Gate, *Applied Optics* 13, 236 (1974)
20. S. Chandrasekhar, *Radiative Transfer* (Dover, New York: 1960)
21. B.Y. Cho, O.L. Utt & R.J. Pfeifer in ref. 4, p. 105
22. J.R. Dukes *et al.* "Composition-Insensitive  $\beta$  Ray Gauging System", U.S. Patent #3087061 (1963)

manuscript typed by Lin Taylor



LI, BE AND B PRODUCTION IN PROTON-INDUCED REACTIONS:  
IMPLICATIONS FOR ASTROPHYSICS AND SPACE RADIATION EFFECTS\*  
C. T. Roche,<sup>†</sup> R. G. Clark,<sup>††</sup> G. J. Methews and V. E. Viola, Jr.  
Department of Chemistry  
University of Maryland  
College Park, Maryland 20742

Cross sections for the production of mass 6 to 11 isobars from proton spallation of carbon targets have been measured at bombarding energies of 45, 55, 60, 65, 75 and 100 MeV. The results of these measurements and similar studies by other groups are used to test theories of Li, Be and B nucleosynthesis. The measured abundance ratios for  ${}^7\text{Li}/{}^6\text{Li}$ ,  ${}^{11}\text{B}/{}^{10}\text{B}$ , Li/Be and B/Li can be reproduced using measured cross sections and models which propose interstellar proton fluxes  $\phi(E)$  of the form  $(m c^2 + E)^{-2.6}$ ,  $E^{-\gamma}$  ( $\gamma \approx 1.5$ -2.0) or  $E^{-3}$  for  $E > 30$  MeV, if a substantial amount of  ${}^7\text{Li}$  is synthesized via some other source. The cross sections for formation of Li, Be and B are also of importance because of possible high LET effects in biological material exposed to cosmic radiation. Our measurements are compared with calculated cross sections that have been used to estimate LET effects.

[Nuclear Reactions  ${}^{12}\text{C}(p,L)$ ; L = Li, Be, B; E = 45-100 MeV; measured  $\sigma(E)$  for A = 6, 7, 9, 10, 11. Astrophysical production of Li, Be and B.

### Introduction

During the past two decades considerable experimental and theoretical effort has been devoted to understanding the processes responsible for the production and propagation of the elements lithium, beryllium and boron (LiBeB) in various astrophysical environments. The low cosmic abundance of these elements<sup>1</sup> relative to their heavier neighbors carbon, nitrogen, and oxygen (CNO/LiBeB  $\approx 10^6$ ) suggests and independent origin for LiBeB. The principle mechanism for nucleosynthesis of most elements lighter than iron is believed to be thermonuclear reactions in stellar interiors.<sup>2</sup> However, due to the instability of LiBeB nuclei at temperatures and densities found in stellar interiors, non-equilibrium processes are generally invoked to explain their formation. These reactions are thought to occur in low-density astronomical environments where LiBeB isotopes are produced by high energy endoergic reactions between  ${}^1\text{H}$  and  ${}^4\text{He}$  ions and heavier nuclei such as  ${}^{12}\text{C}$ ,  ${}^{14}\text{N}$  and  ${}^{16}\text{O}$  (CNO). This hypothesis is strengthened by the fact that the LiBeB/CNO ratio found in cosmic rays is much larger than in representative solar system material.<sup>3</sup> The major theories accounting for the origin of LiBeB have recently been reviewed by Reeves<sup>4</sup> and Audouze and Tinsley.<sup>5</sup> Among the proposed non-equilibrium sources of LiBeB are (1) interaction of galactic cosmic rays with the interstellar gas,<sup>6</sup> (2) reactions initiated at the stellar surface during the early stages of evolution,<sup>7</sup> and (3) formation in pulsating<sup>8</sup> or exploding stars.<sup>9</sup>

In order to examine the validity of the above theories, cross section information for the production of LiBeB from CNO targets is necessary. Extensive data are currently available for proton bombarding energies below 45 MeV.<sup>10,11</sup> Data also exist above 100 MeV, where the excitation functions become independent of bombarding energy.<sup>12-16</sup> This paper presents cross section data for 45-100 MeV proton bombardment of carbon, where several of the LiBeB excitation functions reach their maxima. Our results are combined with those obtained at other energies<sup>10-16</sup> in order to test current theories of LiBeB synthesis.

In addition, the data will be discussed in relation to the extended exposure of biological material to interstellar proton fluxes. Current predictions of radiological damage due to LET effects rely largely upon theoretically derived cross sections.<sup>17</sup> In

the 50-100 MeV region the theoretical cross sections and energy spectra may be in substantial error, resulting in erroneous estimations of biological damage due to cosmic and stellar proton radiation.

### Experimental Measurements

These experiments were performed at the University of Maryland Cyclotron Laboratory using proton beams of 45.0, 55.0, 60.0, 65.0, 75.0 and 100.0 MeV. Targets were spectroscopically pure carbon films<sup>18</sup> of thicknesses 113  $\mu\text{g}/\text{cm}^2$  and 50  $\mu\text{g}/\text{cm}^2$ , determined by weight with an uncertainty of  $\pm 10$  percent. LiBeB fragments produced in these reactions were detected by means of a semiconductor counter system which combined time-of-flight mass identification (TOF) with  $\Delta E$ -E particle identification (PI).

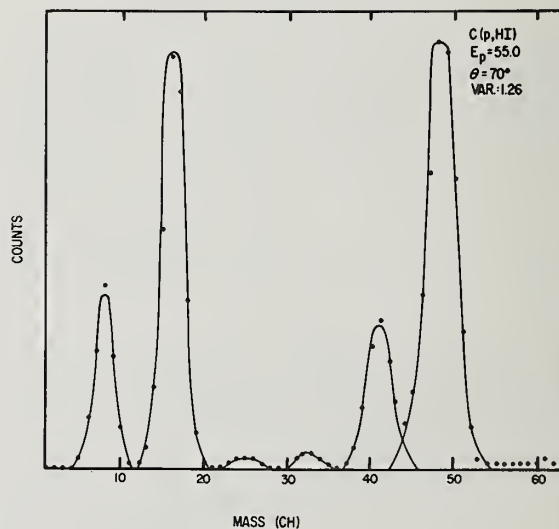


Figure 1. Mass spectrum for A = 6 to 11 isobars formed in reactions between 55-MeV protons and carbon. Measurement performed at an angle of 70 deg with respect to the beam axis. Solid lines represent Gaussian fitting routine used to extract cross-section information.

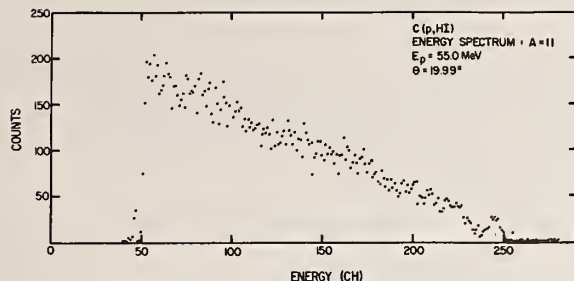


Figure 2. Energy spectrum for  $A = 11$  fragments produced in reactions of 55-MeV protons with carbon. Measurement performed at an angle of 20 deg with respect to the beam. Spectrum below channel 50 is cut off due to instrumental effects

The detector telescope was placed at a distance of 35 cm from the target and consisted of three silicon surface barrier detectors of thicknesses 30  $\mu\text{m}$ , 500  $\mu\text{m}$  and 500  $\mu\text{m}$ , respectively.<sup>19</sup> The fragment time-of-flight relative to the cyclotron radio-frequency was measured with the 30  $\mu\text{m}$  detector (the first detector in the array). The second detector (500  $\mu\text{m}$ ) was sufficiently thick to stop the most energetic  ${}^6\text{Li}$  produced. Both of these detectors were calibrated with alpha particle sources and a precision pulse generator. For fragments which penetrated the first detector the combined energy signals of the first two detectors gave the total energy for  $\text{Et}^2$  mass calculations and the  $\Delta E$ - $E$  information for particle identification. The third detector acted as an event veto for energetic light particles produced in these reactions.

The time-of-flight technique identifies a product's mass by measuring its total energy ( $E$ ) and flight time ( $t$ ) relative to the cyclotron radiofrequency oscillator. Time resolution of the beam bursts were the order of 1 ns. Using this technique, we are able to identify masses via the relation  $M \propto \text{Et}^2$ . In recent measurements mass identification has been successfully extended to product energies as low as about 0.1 MeV/nucleon. This has significantly reduced the uncertainty in extrapolating the low-energy portion of the energy spectrum in order to account for the entire cross section. Since on an astrophysical time scale ( $\sim 10^9$  years) all mass chains which include stable LiBeB nuclides decay to a single stable isotope ( ${}^6\text{Li}$ ,  ${}^7\text{Li}$ ,  ${}^9\text{Be}$ ,  ${}^{10}\text{B}$  and  ${}^{11}\text{B}$ ), mass identification is sufficient for the problem of LiBeB synthesis. On the other hand, for estimation of space radiation effects and better understanding of the mechanism of these nuclear reactions, individual isotope identification is valuable. Thus, by combining the PI and TOF techniques we are able to obtain an accurate estimate of the elemental production cross sections and also extract relative information on the contributions of individual nuclides.

### Experimental Results

Data acquisition and analysis were performed with an IBM 360/44 on-line computer. Mass information for each bombarding energy and detector angle was obtained from a two-dimensional correlation between total energy ( $E$ ) and the quantity  $\text{Et}^2$ , proportional to mass. Projection onto the  $\text{Et}^2$  axis gave a mass spectrum for the products shown in Fig. 1. A mass resolution (FWHM) of about 0.4 amu was achieved.

Projection onto the energy axis gives a set of mass-separated energy spectra, an example of which is shown in Fig. 2. A low-energy cutoff in  $dN/dE$  was observed in all spectra due to instrumental effects. Recent experiments have shown that these spectra become flat in the energy region below about 0.5 MeV/nucleon and then decrease as zero energy is approached. For spectra reported here extrapolation of the low-energy region was taken to be the average contents of the channels directly above the experimental cutoff, multiplied by the number of extrapolated channels. An uncertainty of one-half this value is included in the error estimates. This problem was most severe for the heaviest masses measured.

At each bombarding energy differential cross sections ( $d\sigma/d\Omega$ ) were measured at angles between 10 and 150 degrees. The angular distributions for 55-MeV protons is shown in Fig. 3. Integration of the angular distributions yields the total cross section results given in Table I. The total errors combine counting statistics, low-energy extrapolations and uncertainties due to target thickness, angle and flight-path measurements. The excitation functions shown in Figure 4 compare the present data with lower-energy measurements of Davids, et al.<sup>10</sup> All excitation functions are seen to reach a maximum well below 100 MeV, except perhaps for  ${}^9\text{Be}$ . Comparison of our 100-MeV cross sections with higher energy data (Refs. 12-16) indicate that the excitation functions are essentially flat beyond this energy. The data are in good general agreement with the calculations of Bernas,<sup>7</sup> although the measured  $A = 6$  excitation function has a somewhat larger magnitude and peaks at a higher energy than the

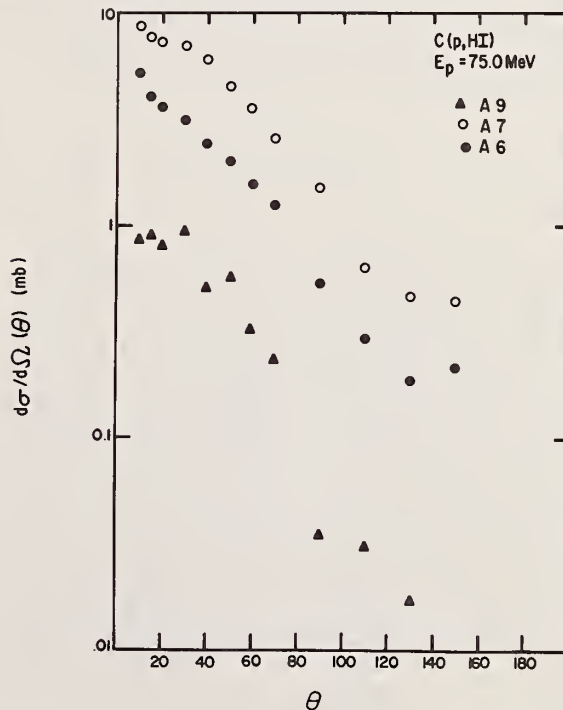


Figure 3. Laboratory angular distributions for  $A = 6$ , 7 and 9 fragments produced in reactions of 75-MeV protons with carbon.



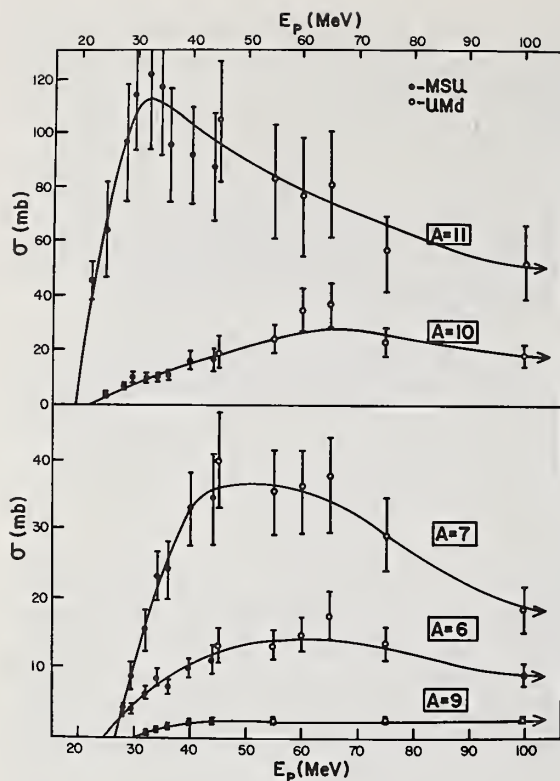


Figure 4. Excitation functions for production of  $A = 6, 7, 9, 10$  and  $11$  in reactions between protons and carbon. Solid points are data from Ref. 10. Results are in good general agreement with other data (Refs. 11-16).

TABLE I. Total Production Cross Sections

Mass Energy	6	7	9
45.0	13.3±2.7	39.9±7.4	--
55.0	13.4±2.5	35.6±6.4	2.3±0.6
60.0	14.9±2.8	34.1±6.5	--
65.0	17.6±3.5	36.2±7.1	--
75.0	13.6±2.5	29.4±5.6	2.6±0.6
100.0	11.0±1.5	21.7±3.1	2.8±0.5

Mass Energy	10	11
45.0	28.6±6.6	104.6±2.4
55.0	23.8±5.7	81.5±20.9
60.0	34.5±8.0	75.9±22.4
65.0	36.3±8.1	80.0±18.9
75.0	22.6±5.4	55.3±14.3
100.0	21.8±3.0	68.1±9.0

calculations predict. The higher energy  $A = 11$  cross sections also are not in good agreement with Ref. 7.

Comparisons with the calculations of Ref. 17 are discussed in section on Applications of Data (B).

Particle identification was obtained from a  $\Delta E \cdot E$  correlation matrix. The data were processed in similar fashion to the TOF methods; however, a much larger low-energy extrapolation is required to obtain isotopic ratios. For this reason and the fact that PI data have only been acquired at 55.0 and 100 MeV, we do not discuss these data here.

### Applications of the Data

#### A. Nucleosynthesis of LiBeB

In any successful theory of nucleosynthesis it is necessary to reproduce the natural isotopic and elemental abundance ratios of the principal species in question, specifically  ${}^7\text{Li}/{}^6\text{Li} = 12.5$ ,  ${}^{11}\text{B}/{}^{10}\text{B} = 4.1$ ,  $\text{Li}/\text{Be} = 0.7 - 7$  (Ref. 19). These values are obtained from studies of meteorites and spectroscopic studies of stars and gas clouds. The values of the  ${}^7\text{Li}/{}^6\text{Li}$  and  ${}^{11}\text{B}/{}^{10}\text{B}$  isotopic ratios are universally accepted. However, the elemental abundances, especially that for boron, are subject to uncertainties which arise from our insufficient understanding of the chemical processes which have altered the interstellar gas from which the solar system condensed.

Theories of LiBeB nucleosynthesis via non-equilibrium processes may be classified as either autogenic or galactogenic. Autogenic models assume that each star generates its own LiBeB via  ${}^1\text{H}$  and  ${}^4\text{He}$  reactions with CNO. Similarities in the LiBeB abundance ratios observed in widely separated stars are accounted for by postulating that nucleosynthesis occurs during an early period of stellar condensation.<sup>20</sup> The  ${}^1\text{H}$  and  ${}^4\text{He}$  particle flux is assumed to be described by a spectrum of the form  $\phi(E) \propto E^{-\gamma}$ , where  $E$  is the particle kinetic energy. For the solar light particle flux,  $\gamma \approx 3$ . The principal difficulty encountered in the autogenic models is that the energy requirements for production of the observed amounts of LiBeB are unrealistically high for stars in this phase of evolution.<sup>21</sup> Galactogenic theories propose that LiBeB result from the interaction of cosmic rays with interstellar material.<sup>6</sup> Thus, these elements are inherited by a star when it condenses from the interstellar medium. The energy spectrum which characterizes the galactic cosmic ray flux is uncertain below 1 GeV and very poorly understood below 100 MeV because of solar modulation. A spectrum shape of the form  $\phi(E) \propto (E + Mc^2)^{-2.6}$  is usually assumed, which contains many more high energy particles than for the autogenic models. Recently, it has been suggested that the true cosmic ray flux may be considerably richer in low energy particles than previously thought.<sup>22,23</sup>

Production rates for LiBeB are obtained from the relation

$$dN_L/dt = \sum_i n_i \sum_j \int_{E_0}^{\infty} \phi_j(E) \sigma_{ijL}(E) dE$$

where  $L$  represents the isotopes  ${}^6\text{Li}$ ,  ${}^7\text{Li}$ ,  ${}^9\text{Be}$ ,  ${}^{10}\text{B}$  and  ${}^{11}\text{B}$ ;  $n_i$  is the relative number of target nuclei, of type  $i$ , usually taken to be  $\text{C}/\text{N}/\text{O} \equiv 3/1/5$ ;  $\phi_j(E)$  is the incident particle flux for particle  $j$ ,  $\text{H}/\text{He} = 10/1$ , and  $\sigma_{ijL}(E)$  is the cross section for formation of product  $L$  from target  $i$  bombarded by particle  $j$ , given as a function of energy from the threshold energy  $E_0$  to infinity. By comparing calculated ratios of the various isotopes and elements, it is not necessary to integrate over time in order to examine the results, assuming  $\text{C}/\text{N}/\text{O}$  is time independent. In Table II the



production ratios of interest here are tabulated for several assumptions concerning  $\phi(E)$  and for C/N/O ratios that should bracket the real conditions.

TABLE II. LiBeB Production Ratios as a Function of Various Assumptions Concerning Spectra of Particle Flux,  $\phi(E)$ , where  $W = (Mc^2)$ . The Target Ratio was C/N/O = 3/1/5.5  $P$  for  $\phi(E) \propto W^{-2.6}$  and 3/1/5 for all other cases.

Particle Spectrum $\phi(E)$	Production Ratios			
	${}^7\text{Li}/{}^6\text{Li}$	${}^{11}\text{B}/{}^{10}\text{B}$	Li/Be	B/Li
$W^{-2.6}$	1.4	2.0	15.3	1.2
$E^{-1.5}$	1.7	3.5	11.9	3.3
$E^{-3}$	2.4	9.5	17.4	9.5
$E^{-4.5}$	3.6	33.4	25.5	35.0
$E^{-3}$ ( $E > 30$ MeV)	1.7	3.8	8.3	3.4

It is clear from examination of Table II that no single set of circumstances will successfully reproduce the cosmic abundances for LiBeB. The most obvious conclusion to be derived from the model calculations is that under no conditions can realistic values for  ${}^7\text{Li}/{}^6\text{Li}$  and Li/Be ratios be obtained, and that the B/Li ratio is reasonable only if the enhanced boron abundance<sup>9</sup> is accepted. A reasonable  ${}^{11}\text{B}/{}^{10}\text{B}$  ratio is obtained for  $\gamma \approx 1.5$ -2 and for the galactic cosmic ray flux. In order to account for the discrepancies involving lithium ratios, one must conclude that processes other than those described here are major sources of  ${}^7\text{Li}$  in the universe. A number of supplemental mechanisms have been postulated that will produce additional  ${}^7\text{Li}$  but no appreciable amounts of the other LiBeB isotopes.<sup>4</sup> Among these are: (1) formation during the "Big Bang"; (2) production of  ${}^7\text{Be}$  in helium flares in the cores of certain types of Red Giant stars; (3) production in supernovae; and (4) the cosmic ray reactions  $\alpha(\alpha, p){}^7\text{Li}$  and  $\alpha(\alpha, n){}^7\text{Be}$ . Of these, the Big Bang or supernova seem most plausible.

If one assumes that (1) approximately 80 percent of the  ${}^7\text{Li}$  in nature is produced via supplemental mechanisms, and (2) the remaining  ${}^6\text{Li}$ ,  ${}^7\text{Li}$ ,  ${}^9\text{Be}$ ,  ${}^{10}\text{B}$  and  ${}^{11}\text{B}$  results from one of the non-thermal processes described previously, then reasonable agreement with the experimental abundance ratios can be obtained. For either the galactic cosmic ray flux or  $\gamma \approx 1.5$ -2, the corrected ratios become:  ${}^7\text{Li}/{}^6\text{Li} = 12.5$  (by definition),  ${}^{11}\text{B}/{}^{10}\text{B} \approx 4$ , Li/Be  $\approx 60$  and B/Li  $\approx 0.8$ . Similar satisfactory results can be found for a proton flux of the form ( $E > 30$  MeV)  $\propto E^{-3}$  and  $\phi(E > 30 \text{ MeV})$  approximately zero, again assuming supplemental  ${}^7\text{Li}$  production. This latter situation presumably approximates the conditions which exist in high temperature solar flares. On the other hand, if the new B/Li ratio<sup>9</sup> of B/Li  $\approx 7$  is correct, then more complicated mechanisms must be proposed to enhance this ratio without altering the  ${}^{11}\text{B}/{}^{10}\text{B}$  ratio. In particular, this condition appears to demand a large flux of low energy particles. This would lead to a much more complex picture for LiBeB nucleosynthesis than has been previously postulated.

#### B. Space Radiation Effects

The cross section data obtained in this work

also have an important application in estimating the biological damage that may be experienced by astronauts during prolonged space flights. Because carbon, nitrogen and oxygen are the primary constituents of biological material, the interactions induced by solar and cosmic ray protons--which have ranges up to several cm in such a medium--are of considerable biophysical interest. The LiBeB recoil nuclei formed in  $p + \text{CNO}$  reactions are characterized by high ionization densities in matter relative to other components of the space radiation field. Hence, the LET (energy loss per unit path length in matter) is large for LiBeB recoils, implying greater localized damage in the stopping medium.

Previous attempts to determine the effects of high LET recoil ions on biological material have included both exposures of plastics on space flights, as well as comparison with calculations based upon theoretical estimates of the reaction cross sections and energy spectra.<sup>24</sup> The calculated LET values have relied on Monte Carlo calculations for the nuclear reaction parameters.<sup>17</sup> In Table III the calculated results for the total cross sections at 55 and 100 MeV are compared with the experimental values obtained here.

TABLE III. Comparison of Calculated<sup>17</sup> and Experimental Cross Sections. Values from calculations of Harp are listed as  $\sigma_H$ , those from Bertini are given as  $\sigma_B$  and experimental values as  $\sigma_{\text{exp}}$ .

A	55 MeV			100 MeV		
	$\sigma_H$	$\sigma_B$	$\sigma_{\text{exp}}$	$\sigma_H$	$\sigma_B$	$\sigma_{\text{exp}}$
6	8.9	19.7	13.4	6.9	11.5	11.0
7	--	2.6	35.6	--	2.0	21.7
9	1.7	0.3	2.3	2.4	0.8	2.8
10	22.0	62.9	23.8	19.2	38.4	21.8
11	56.5	99.6	81.5	58.7	75.4	68.1

One observes that the calculations are approximately correct for A = 6 and 11. In addition, the yield of mass 9 is so low that it is not an important consideration here. The most noticeable deviations are noted for A = 7 which is greatly underproduced in the calculations and A = 10 which is too abundant in the Bertini calculation. Radioactivity and particle identification measurements both show that  ${}^7\text{Be}$  is an important component of the A = 7 yield. Hence, to first order these two effects tend to cancel out in calculation of the LET values. However, it is also noted that the calculated energy spectra appear to be too rich in low-energy particles compared to the experimental dN/dE results. With the availability of experimental cross sections, angular distributions and energy spectra, it should now be possible to obtain much more realistic calculations of the LET effects due to the passage of LiBeB recoils through biological material.

#### Acknowledgements

The authors wish to thank W. G. Meyer for his many contributions to this work. We also acknowledge Pamela Schuster, Dr. R. N. Yoder and the University of Maryland Cyclotron staff for their assistance in performing the experiments. The cooperation of

Dr. S. B. Curtis in familiarizing us with the space radiation aspects of this work is also gratefully acknowledged.

# References

\*Work supported by U. S. ERDA

†Present address: Argonne National Laboratory,  
Argonne, Illinois

††Present address: Federal Energy Agency,  
Washington, D. C.

1. A. G. W. Cameron, "Origin & Distribution of the Elements," ed. by Lott. Aherns (Pergamon Press, Oxford, 1968), p. 130.
2. E. M. Burbidge, G. R. Burbidge, W. A. Fowler, and F. Hoyle, Rev. Mod. Phys. 29, 547 (1957).
3. V. L. Ginzberg, "The Origin of Cosmic Rays," (Bordon & Breach, N. Y., 1969).
4. H. Reeves, Ann. Rev. Astrophys. 12, 437 (1974).
5. J. Audouze and B. Tinsley, Ap. J. 192, 487 (1974).
6. H. Reeves, W. A. Fowler, and F. Hoyle, Nature 226, 727 (1970).
7. R. Bernas, E. Gradsztajn, H. Reeves and E. Schatzman, Ann. de Physique 44, 426 (1967).
8. R. J. Talbot and W. D. Arnett, Nature Phys. Soc. 229, 150 (1971).
9. A. G. W. Cameron, S. A. Colgate, and L. Grossman, Nature, 243 209 (1973).
10. C. N. Davids, H. W. Laumer, and S. W. Austin, Phys. Rev. C1, 270 (1970); H. W. Laumer, S. M. Austin, L. M. Panngabean, and C. M. Davids, Phys. Rev. C8, 483 (1973).
11. W. W. Jacobs, D. Bodansky, D. Chamberlin and D. L. Oberg, Phys. Rev. C9, 2134 (1974).
12. M. Jung, C. Jacquot, C. Baixeras-Aiquabella, R. Schmitt, H. Braun, Phys. Rev. C1, 435 (1970).
13. P. Fontes, C. Perron, J. Lestringuez, F. Yior, and R. Bernas, Nucl. Phys. A165, 405 (1971).
14. R. Bernas, E. Gradsztajn, E. Epherre, R. Klapisch, and F. Yiou, Phys. Lett. 15, 147 (1965).
15. J. Audouze, M. Epherre, and H. Reeves, Nucl. Phys. A97, 144 (1967).
16. G. M. Raisbeck, J. Lestringuez and F. Yiou, Phys. Rev. C6, 685 (1972).
17. H. Bertini, Oak Ridge National Laboratory, and George Harp, Los Alamos Scientific Laboratory, private communication of cross section calculations.
18. Carbon films were purchased from Yissum Development Corp., Israel.
19. Low energy cross-sections ( $E \leq 75$  MeV) were measured by the time-of-flight technique. A 75  $\mu$ m thick detector and a flight path of 67 cm were used in these experiments.
20. W. K. Bonsack, and J. L. Greenstein, Ap. J. 131, 83 (1960).
21. C. Ryter, H. Reeves, E. Gradsztajn and J. Audouze, Astron. and Ap. 8, 389 (1970).
22. S. Ramadurai and S. Biswas, Astron. & Space Sci. 30, 187 (1974).
23. W. R. Webber and J. A. Lezniak, Astron. & Space Sci. 30, 361 (1974).
24. E. V. Benton, S. B. Curtis, R. P. Henke and C. A. Tobias, Health Physics 23, 149 (1972).

# LONG LIVED ISOTOPE PRODUCTION CROSS SECTIONS FROM PROTON BOMBARDMENT OF RHENIUM

A. J. Armini and S. N. Bunker  
Simulation Physics, Inc.  
Burlington, MA 01803

The production cross reaction of long lived isotopes produced by proton bombardment of rhenium has been measured between 15 and 160 MeV. A set of stacked graphite disks impregnated with rhenium was used as a target. The data have been used to calibrate a high temperature graphite thickness gauge.

(cross sections; rhenium; proton; excitation function)

Graphitic materials have found wide application for use at high temperatures above 2000°C. Frequently the ambient conditions are such that significant erosion of the graphite occurs. In some applications it is necessary to know the change in graphite dimensions as erosion progresses. Such cases include rocket exhaust nozzles and heatshields.

A simple technique for producing a graphite thickness gauge is to irradiate the material with a well-collimated beam of protons. As shown in Figure 1, a gamma detector will exhibit a decrease in count rate as material is eroded away. This change in total count rate can be calibrated against the length of the tube of activity in the graphite. Advantages of this type of approach are as follows:

1. erosion is measured over an area equal to the diameter of the proton beam which can be made quite small.
2. a significant decrease in required activity results compared to activating the entire part with neutrons.
3. divergence of a proton beam penetrating matter is small over most of the range.
4. the original graphite material is unchanged by the irradiation.

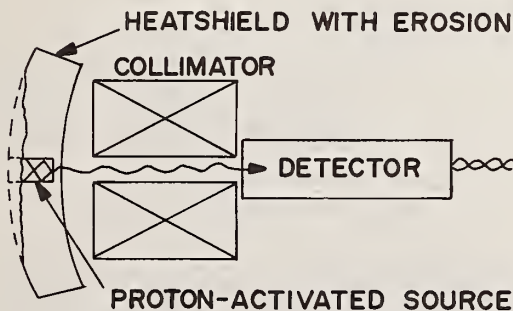


Figure 1.

Proton Activated Thickness Gauge Layout.

The most straight-forward reaction for activating graphite is  $p(C^{12}, pn\alpha)Be^7$  (53 d). This is a well known reaction whose excitation function is shown in Figure 2. However, in the present application the residual nucleus,  $Be^7$ , is insufficiently refractory. The beryllium tracer was found to migrate out of a porous block of graphite by gaseous diffusion at about

2300 - 2400°C. At this temperature beryllium carbide decomposes. A more refractory radioactive tracer is required.

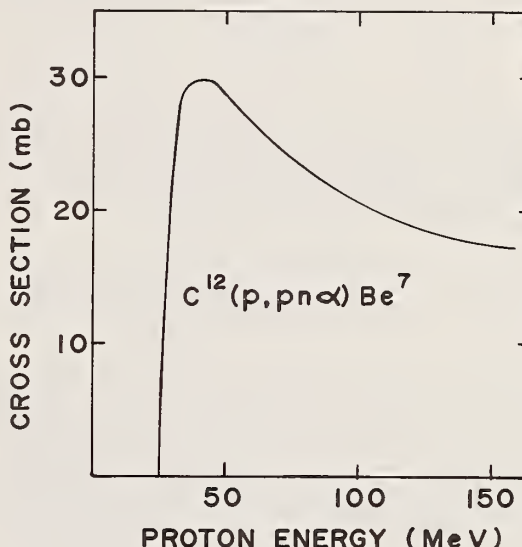


Figure 2.

Beryllium-7 Production in Carbon.

Several very refractory metals also have high (p, xn) activation cross sections leading to isotopes with long half lives ( $30 < T_{1/2} < 200d$ ). Experiments indicated that for naturally occurring refractory materials, the highest total production cross sections could be obtained with the element rhenium. Rhenium is a metal next to tungsten in the periodic table and is somewhat more refractory than carbon. Three isotopes are produced by proton bombardment of natural rhenium. The primary reactions are listed below:

Parent Isotopes	Reaction	Daughter (after $\beta$ decay)
$Re^{185}$	$p, 3n$	$Re^{183}$ (70d)
$Re^{185}$	$p, pn$	$Re^{184}$ (38d)
$Re^{187}$	$p, 3n$	$Re^{185}$ (94d)
$Re^{187}$	$p, 5n$	$Re^{183}$ (70d)
$Re^{187}$	$p, p3n$	$Re^{184}$ (58d)

All other reactions producing these isotopes have small cross sections and are difficult to separate in the excitation function data.



Excitation functions are most conveniently measured using the stacked foil method. However, the large neutron build up caused by (p, xn) reactions in a rhenium foil stack can create discrepancies in the activation cross section. This is especially apparent at the end of the range for protons where neutron-induced activity can exist at a significant percentage of that from protons. Therefore, a target stack was fabricated which contained rhenium in highly diffuse quantities imbedded in a low Z material. This was accomplished chemically by impregnating thin porous graphite disks with a water solution of rhenium heptoxide. The water was subsequently evaporated off and the remaining rhenium heptoxide was converted to metal by reduction in hydrogen.

The disks showed a typical mass increase of 3 weight percent. The actual amount of metal in each disk was determined by neutron activation analysis using the  $\text{Re}^{185}(\text{n}, \gamma)\text{Re}^{186}$  (90 hr.) reaction. Mass was determined by comparison to a thin rhenium foil standard irradiated simultaneously. The samples varied in rhenium mass from 2.75 to 3.65 wt. %. X-rays were made of each disk to confirm uniformity of impregnation.

A stack of rhenium-impregnated graphite disks was irradiated at both the Brookhaven proton linear accelerator (160 MeV) and at the Crocker Laboratory cyclotron in Davis, California (65 MeV). Two irradiations at high and low incident beam energies were performed due to the energy straggling that would occur at the end of the range for the 160 MeV beam.

No effort was made to accurately measure the total beam current. The absolute activity was determined by normalization to the  $\text{Cl}^{35}(\text{p}, \alpha\text{p})\text{S}^{32}$  reaction whose cross section has been accurately measured.<sup>1,2</sup>

The cross sections for production of the long lived isotopes by all possible reactions are shown in Figures 3, 4, and 5. The various contributing reaction thresholds have been indicated. Figure 6 shows the  $\text{Re}^{187}(\text{p}, 3\text{n})$  reaction corrected in cross section to correspond to 100% isotope abundance. The (p, 3n) reaction exhibits a magnitude and shape consistent with other elements in this mass region.

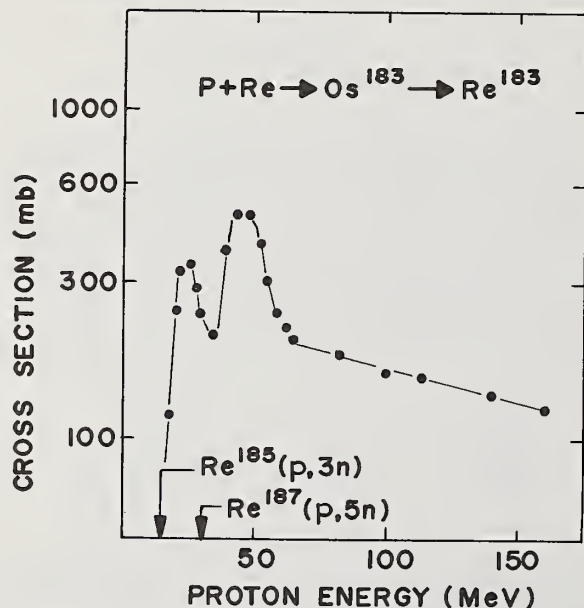


Figure 3. Rhenium-183 Production in Rhenium.

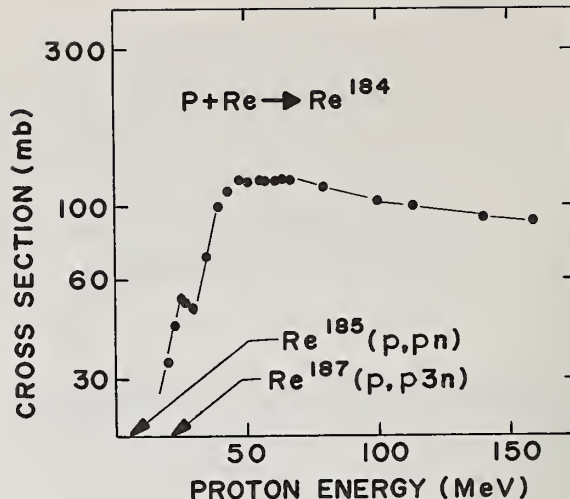


Figure 4.

Rhenium-184 Production in Rhenium.

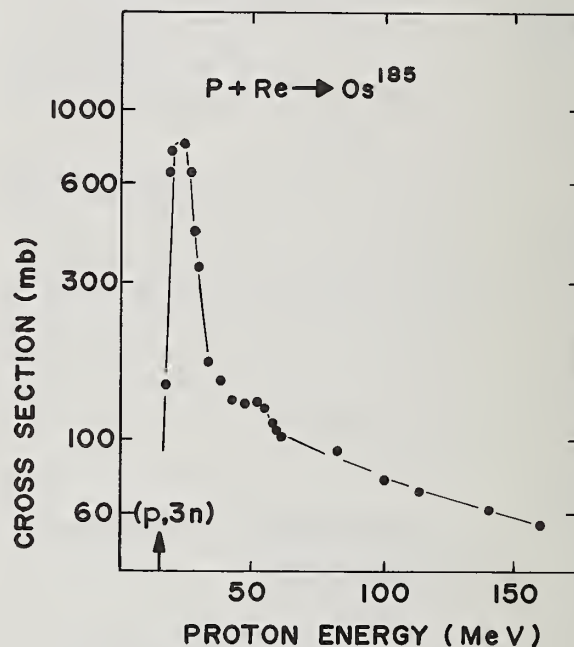


Figure 5.

Osmium-185 Production in Rhenium.

An experimental erosion measurement was required to confirm the cross sections and test the accuracy. This consisted of bombarding a 4" stack of rhenium-loaded graphite disks at the Brookhaven Linac. The energy of the beam was adjusted in steps to deposit more protons at locations corresponding to the greatest distances from the detector. This resulted in a fairly linear dependence of count rate versus erosion depth.

A test setup was constructed to measure the amount of thickness loss versus predictions based on the measured cross sections. The setup consists of a set of stacked activated disks viewed by a well-collimated gamma detector. In the application being simulated, space and weight were at a premium. Thus, a CdTe detector was used as a counter. Such a detector is capable

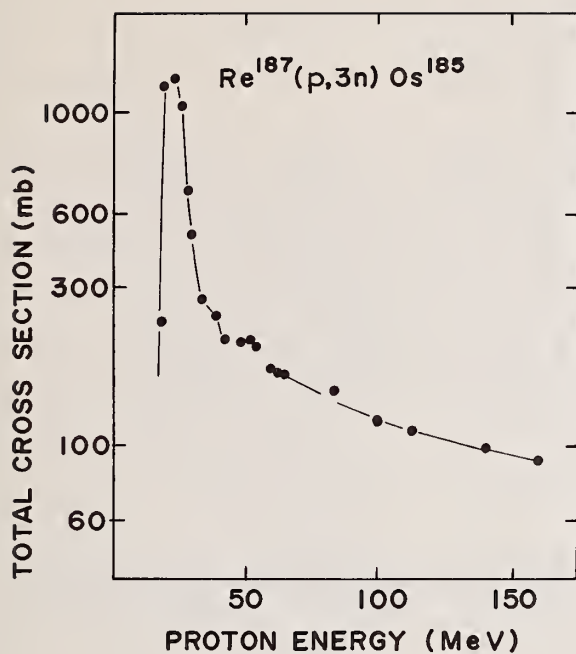


Figure 6.

Osmium-185 Production From Rhenium-187.

of room temperature operation and can be fabricated in a small unit. Figure 7 shows the results obtained. Correlation within 5% was obtained in all cases.

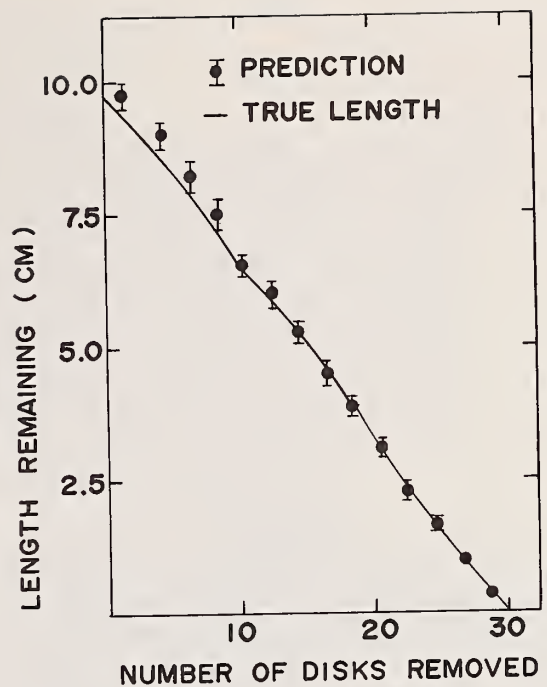


Figure 7.

Thickness Gauge Test Results.

This method of measuring erosion will be used in a number of applications requiring the measurement of the thickness of graphitic heatshields in real time. Two primary candidates are the measurement of the diameter for the throat nozzle of a rock engine and the thickness of the heatshield that protects an object re-entering the atmosphere from space.

#### References

- <sup>1</sup>C. Brun, et. al., J. Phys. Radium, 23, 371, (1962).  
C. B. Fulmer, Phys. Rev., 154, 1005, (1967).
- <sup>2</sup>A. J. Armini, et. al., SAMSO TR 71-197, PARS Program Final Report, Vol. 1.

H. S. Ahluwalia  
Department of Physics and Astronomy  
The University of New Mexico  
Albuquerque, New Mexico 87131

We have argued elsewhere<sup>4,5</sup> that protons of energy  $\lesssim 10$  MeV are probably accelerated, in the active regions on the sun, for several days, following a solar flare. These protons must undergo nuclear interactions with the constituents of the solar atmosphere producing, among other things, neutrons. Being electrically neutral the neutrons are not affected by the solar or interplanetary magnetic fields. So they should be observable when the active regions lie on the earth-sun line. No solar neutrons have been detected so far.<sup>14-25</sup> We think that the reason for this null-result is that the energy response of most of the detectors used, peaks at too high an energy ( $\sim 100$  MeV). Recent discovery of solar deuterons<sup>26</sup> indicates that the solar neutrons probably have lower energies. They are probably produced in (p,n) reactions involving C,N,O,Ne,Mg,Si,S,Ca,Fe, etc. The available cross sections, in the energy range 3.4 MeV to 30 MeV, certainly bear out this expectation for Fe. The cross sections for some other elements are as yet unknown. Our conclusions are presented and the urgent need for the determination of the (p,n) cross sections for other elements is discussed.

(nuclear reactions; solar flares; neutrons; protons; acceleration mechanisms)

### Introduction

The discovery that the sun is an intermittent source of energetic protons was made nearly thirty years ago by Forbush<sup>1</sup> who noticed a close time association between the unusual worldwide ground level increases in cosmic ray hard-component (muons) and large solar flares. Solar protons with energy as large as 50 GeV may have been observed, following a class 3+ solar flare of 23 February 1956.<sup>2</sup> This spectacular event is unique, however. Usually the solar proton energy ( $E_p$ ), in such events, lies in the range: 400 MeV  $\lesssim E_p \lesssim 4$  GeV. The frequency of occurrence of these events is nevertheless quite small; less than thirty ground level enhancements (GLE) have been observed during over thirty years of observations with different types of detectors. With the advent of the space age came the discovery that the sun more commonly emits protons with energies in the range: 0.5 MeV  $\lesssim E_p \lesssim 100$  MeV,<sup>3</sup> which are prevented from reaching the ground level by absorption in the atmosphere of the earth. These protons can therefore only be observed directly by detectors placed on high flying balloons or satellites and space probes or indirectly by observing the so-called polar cap absorption events.

It is commonly believed that transient acceleration mechanisms are somehow set up in the solar active regions during the solar flares which generate energetic protons and other nuclei in a one shot operation. Numerous attempts made along these lines have not produced a generally acceptable flare model, so far. We have suggested elsewhere<sup>4,5</sup> that the acceleration mechanism(s) might be long-lived rather than impulsive in character. It appears however that one might have to find satisfactory answers to several crucial questions before any detailed model of acceleration mechanism(s) can begin to emerge. For example, where exactly is the location of the acceleration mechanism(s) in the solar atmosphere? Does the efficiency of the mechanism(s) remain the same throughout its lifetime? What determines the upper cut-off in the observed energy spectrum of the solar protons? Are any differential aspects involved? For example, are all the different energetic particle species (p, e, $\alpha$ , light and heavier nuclei) generated in a single step or in several successive steps, one leading to another, etc.? It is the feeling of this author that at least part of the information needed to answer some of the above questions must come from our understanding of a wide variety of nuclear interactions of energetic protons with the constituents of the solar atmosphere. A better overall understanding of the uncertainties that exist at the present time will indeed contribute

significantly towards developing the science of solar meteorology which might one day make it possible to forecast solar activity, in a reliable manner, on a long-term basis.

### Solar Neutrons

Active regions on the sun are seats of strong ( $\sim 1000$  G) magnetic field. Solar flares always occur in the active regions.<sup>6</sup> A weak magnetic field also pervades the interplanetary medium. Biermann *et al.*,<sup>7</sup> were the first to point out that some of the energetic protons, which give rise to a GLE on arriving at the orbit of the earth, must undergo nuclear interactions in the solar atmosphere producing neutrons, among other things. Neutrons have a mean life of about 1000 seconds and carry no electrical charge. Therefore they are not restrained by the magnetic fields in the solar atmosphere or in the interplanetary medium. One should therefore observe energetic neutrons at the time of a GLE, provided enough are emitted in the forward directions, i.e., away from the sun.

Quantitative calculations (involving different boundary conditions) have been carried out by Biermann *et al.*,<sup>8</sup> Hess,<sup>9</sup> Chupp,<sup>9,10</sup> and Lingenfelter *et al.*<sup>11-13</sup> These calculations predict a measurable flux of high energy solar neutrons at the orbit of the earth. Unfortunately these calculations consider the event of 23 February 1956 as fairly typical in terms of fluxes and energies of the parent protons involved. As we have stated above, the event of 23 February 1956 is unique. Also in the most refined of the above calculations,<sup>13</sup> high energy protons ( $E_p \gtrsim 100$  MeV) are made to interact with lighter nuclei (H,He,C,N,O,Ne) in the solar atmosphere -- pp interaction is not an important contributor for  $E_p \leq 300$  MeV. These calculations thus make optimistic predictions for the fluxes of high energy solar neutrons (mean energy  $\sim 100$  MeV) at the orbit of the earth. Many experimenters have tried to verify these predictions. The pertinent information related to their detectors and the results obtained by them are summarized in Table 1.

Nearly all the experiments have only resulted in defining upper limits for the solar neutron fluxes. Two of the measurements<sup>15,21</sup> where claims of a definite discovery have been advanced, some questions have been raised as to whether the large observed fluxes might not be the result of the methods of analysis or undetected instrumental trouble of some kind.<sup>17</sup> Anyway the large fluxes have not been confirmed by subsequent experiments which claim to have better signal



TABLE 1  
Quiet-Time Flux of Solar Neutrons

Literature Reference	Detector type	Detector Response Characteristics				Location of Experiment	Upper Limit on Solar Neutron Flux $m^{-2} sec^{-1}$
		Energy Range MeV	Energy of Maximum Response MeV	Detection Efficiency at Max. %	Average $A_p$		
Haymes (1964) <sup>14</sup>	Proton recoil (Balloon)	1-14	3	18	25	Brownwood, Texas	$\lesssim 200$
Apparao et al (1966) <sup>15</sup>	Nuclear Emulsions (Balloon)	20-160	?	?	4	Hyderabad, India	$450 \pm 60$
Bame & Asbridge (1966) <sup>16</sup>	Proton recoil (Vela 1,2,3)	0.1-10	5	?	?	outer space	$\lesssim 100$
Hess & Kaifer (1967) <sup>17</sup>	BF <sub>3</sub> Counter (OSO-1)	0.01-10	?	?	?	outer space	$\lesssim 20$
Webber & Ormes (1967) <sup>18</sup>	Proton recoil (Balloon)	>100	?	10	5	Tucuman, Argentina	$\lesssim 24$
Wolcott (1968) <sup>19</sup>	Proton recoil (Balloon)	30-130	65	$\sim 1$	5	Alamagordo, New Mexico	$\lesssim 28$
Heidbreder et al (1970) <sup>20</sup>	Proton recoil (Balloon)	100-400	100	1	19	Palestine, Texas	$\lesssim 12.5$
Daniel et al (1971) <sup>21</sup>	Proton recoil (Balloon)	50-500	?	?	4	Hyderabad, India	$\lesssim 1500$
Eyles et al (1971) <sup>22</sup>	Proton recoil (Balloon)	50-350	200	1.5	10	Kampala, Uganda	$\lesssim 30$
Cortellesa et al (1971) <sup>23</sup>	Proton recoil (Balloon)	10-200	75	14	6	Gap & Aire-sur-L'Adour, France	$\lesssim 55$
Leavitt et al (1972) <sup>24</sup>	Proton recoil (OSO-6)	20-200	100	0.01	?	outer space	$\lesssim 4$
Lockwood et al (1973) <sup>25</sup>	Proton recoil (OGO-6)	1-20	1	?	?	outerspace	$\lesssim 18$

to noise ratios. The lowest upper limit on the flux of high energy solar neutrons comes from the satellite experiment of Leavitt et al.<sup>24</sup> Their flux value of  $\lesssim 4 m^{-2} sec^{-1}$  should be compared with the value of  $30 m^{-2} sec^{-1}$  predicted by Lingenfelter et al.,<sup>12</sup> on theoretical grounds, for neutrons in the energy range:  $30 MeV \lesssim E_n \lesssim 40 MeV$ . Leavitt et al., value is an order of magnitude lower. In fact all the experiments listed in Table 1, with the exception of the two singled out above for a comment, are consistent with a null hypothesis. It should be noted though that none of the observations were made coincident in time with a large solar flare. It is not difficult to understand why. Solar flares are, in general, hard to predict and the task of the experimentalists becomes all the more formidable when one plans to select epochs involving solar flares which will be accompanied by a GLE. The prediction made by Biermann et al.,<sup>7</sup> therefore remains unverified in the strictest sense. Some of the observations were made however following a small scale solar activity<sup>21</sup> or a larger flare.<sup>15,16,19,20,22</sup> However no GLE was observed either before or during the time that observations were being made. Note also that the average value of the geomagnetic index  $A_p$  is quite small for all experiments, indicating that geomagnetic field was not significantly disturbed. The null result thus seems to suggest only that there is no steady state flux of high energy solar neutrons near the orbit of the earth, above the noise level of the detectors. One need not conclude, however, that neutrons are not produced in the solar atmosphere.

Recently Chupp et al.,<sup>26</sup> have reported the discovery of 2.224 MeV  $\gamma$ -ray line, characteristic of

neutron capture by hydrogen to form a deuteron, during the large solar flares of August 4 and 7, 1972. The clear implication is that at least low energy neutrons must also be present in the solar atmosphere at these times. Interestingly enough GLEs were also observed on these two dates.<sup>27</sup> Unfortunately, however, no neutron detectors were aloft and hence no neutrons of solar origin were actually detected! Reppin et al.,<sup>28</sup> estimate that a neutron detector with an energy range of:  $10 MeV \lesssim E_n \lesssim 100 MeV$  would have detected a flux of about 20 neutrons  $m^{-2} sec^{-1}$  on August 4 and a flux of 30-50 neutrons  $m^{-2} sec^{-1}$  on August 7, 1972, during the solar flares.

#### Total Neutron Production Cross Sections

Figure 1 shows the elemental abundances in the solar corona relative to a hydrogen abundance of  $10^6$ , as given by Pottasch.<sup>29</sup> Note that the elements Mg, Si, S, Fe are about as abundant as are N or Ne. The four elements together are about 1/6 as abundant as are the elements C, N, O, Ne together.

The (p,n) cross section data in the energy range: Threshold  $\lesssim E_p \lesssim 300 MeV$ , for various elements, are sparse, sketchy, and widely scattered in the literature. One has to make do with small pieces of information after considerable literature search. This process, to say the least, is extremely time consuming. In Figure 2 are plotted some cross section data for He, C, N, O, and Fe. For some elements the cross sections for neutron production are as close as total as can be, for example the curve for N contains data not only for (p,n) reactions but also for (p,pn) and (p,2p2n) type reactions. Similarly the curve for O is made up

of (p,pn), (p,2p2n), (p,3p3n) and (p,5p5n) reaction cross sections. So far as we can tell the same data

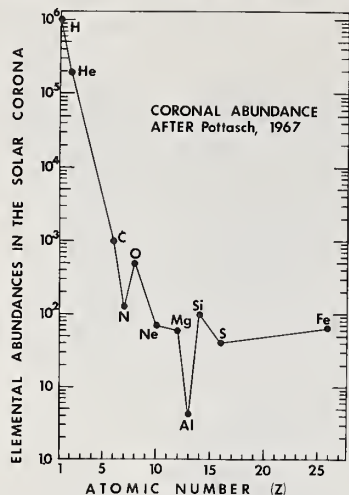


FIGURE 1

were used by Lingenfelter et al.,<sup>11-13</sup> to calculate the yield of neutron in p-HeCNO reactions except that their calculations extended up to 10 GeV. We wish to draw attention to the curve for Fe which is made up of cross sections for (p,n), (p,pn), (p,2n), (p,2p2n) type reactions as given by Jenkins and Wain.<sup>30</sup> The portion of the curve between 40 MeV and 370 MeV is defined by just two extreme points and so is unreliable. However the following two points stand out quite clearly.

1) In the intermediate energy range i.e., 20 MeV  $\lesssim E_p \lesssim 200$  MeV, iron contributes as many as or more neutrons as do C, N, and O together. This fact permits one to speculate that if neutrons contributed by Mg, Si, and S are just as large as that from Fe then Fe, Mg, Si, S group must be considered a significant contributor to the total number of neutrons produced on the sun even if they are only 1/6 as abundant as C, N, O, Ne group in the solar corona. This group has been totally ignored in the calculations of Lingenfelter et al.

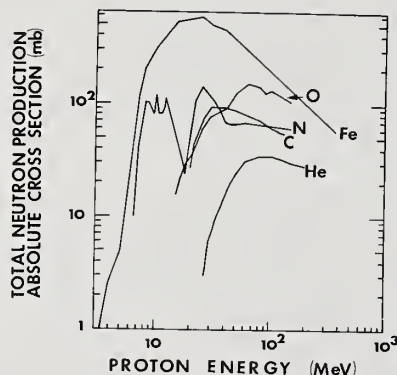


FIGURE 2

2) In the low energy region, i.e.,  $E_p < 20$  MeV, which was not explored by Lingenfelter et al., the possibilities are quite promising. For one thing contribution by N and Fe is quite large, whereas He contributes no neutrons at all. Also we have recently become aware of the work of Blaser et al.,<sup>31</sup> who have

investigated excitation functions of (p,n) reaction involving several elements, in the energy range: Threshold  $\leq E_p \leq 6.8$  MeV. Those of interest to us are C, O, and Mg. They report several resonances for which the (p,n) cross sections rise to several tens, and in some cases to several hundreds, of millibarns. This indicates to us that the sun may indeed be a source of low energy neutrons in a steady state or for several tens of hours after a large or a medium sized solar flare. A large fraction of such neutrons could decay on their way to earth, e.g., a 2 MeV solar neutron has less than 1 in 1000 chances to make it to the orbit of the earth. This expectation has a very logical basis. We refer here to our suggestions<sup>4,5</sup> that the sun might continue to accelerate, at least, low energy protons ( $E_p \lesssim 10$  MeV) for several tens of hours after the visible traces of the optical solar flare have vanished. This indicates that the best experimental strategy would be to mount a neutron detector on a spacecraft headed towards the sun. The peak response of such a detector should be at low enough energy. If neutrons are detected, a  $r^2$ -type increase in their flux towards the sun would of course confirm their solar origin. On the other hand if no neutrons are detected this would imply that the acceleration of protons takes place fairly high up in the solar corona so that cross section requirements for neutron production are not satisfied and of course no neutrons are then produced. This conclusion will only be valid if a proton detector on the same spacecraft records an increasing flux of low energy protons, as the spacecraft gets closer to the sun.

### Conclusions

The following conclusions may be drawn from our study.

1. We have presented and analyzed detailed evidence in support of our earlier suggestion<sup>31</sup> that the sun may be a source of low energy neutrons in a steady state or for several tens of hours after a large or medium size solar flare. We suggest that it is probably futile to search for solar neutrons periodically in the vicinity of the earth, as has been done so far. On the other hand information of great value to solar physics can be obtained by mounting a neutron as well as a proton detector on a space probe launched toward the sun.

2. It is pointed out that experimental information on total neutron production cross sections by protons with different elements is sketchy, sparse, and widely scattered in the literature. It is therefore strongly recommended that someone should undertake the task of collecting all the available information in one place. Perhaps this could be done quite competently at the Oak Ridge National Laboratory.

3. It appears that the energy region: Threshold  $\leq E_p \leq 10$  MeV has not been explored in sufficient detail experimentally so far as (p,n) type reactions, involving light and medium nuclei, are concerned. A systematic experimental study should be undertaken to identify all the resonances precisely. This would prove extremely useful in designing an optimum space experiment to detect low energy neutrons of solar origin.

### Acknowledgements

I am grateful to Professor Bernard Cohen of the University of Pittsburgh for drawing my attention to the work of Blaser et al. This research is supported in part by the NASA-Goddard Space Flight Center under P.C. #680-8177.

### References

1. Forbush, S.E., Phys. Rev. **70**, 771, 1946.

2. Sarabhai, V., Duggal, S.P., Razdan, H., and Sastry, T.S.G., Proc. Ind. Acad. Sci. 43A, 309, 1956.
3. McCracken, K.G., and Rao, U.R., Space Sci. Rev. 11, 155, 1970.
4. Ahluwalia, H.S., J. Geophys. Res. 74, 1230, 1969.
5. Ahluwalia, H.S., Twelfth International Conference on Cosmic Rays, Hobart. Conference Papers (Univ. of Tasmania) 2, 468, 1971.
6. Kuiper, G.P., The Sun, Vol. 1 in the Solar System Series. Published by the University of Chicago Press, Chicago, 1953.
7. Biermann, L., Haxel, O., and Schuster, A., Z. Naturforsch. 6a, 47, 1951.
8. Hess, W.M., Proc. Fifth InterAmerican Seminar on Cosmic Rays, La Paz, 1, 17, 1962.
9. Chupp, E.L., AAS-NASA Symposium on the Physics of Solar Flares, Greenbelt, (ed. W.N. Hess), NASA SP-50, 445, 1963.
10. Chupp, E.L., Space Sci. Rev. 12, 486, 1971.
11. Lingenfelter, R.E., Flamm, E.J., Canfield, E.H., and Kellman, S., J. Geophys. Res. 70, 4077, 1965a.
12. Lingenfelter, R.E., Flamm, E.J., Canfield, E.H., and Kellman, S., J. Geophys. Res. 70, 4087, 1965b.
13. Lingenfelter, R.E., and Ramaty, R., High Energy Nuclear Reactions in Astrophysics, (ed. B.S.P. Shen), W. A. Benjamin Press, New York, 99, 1967.
14. Haymes, R.C., J. Geophys. Res. 69, 853, 1964.
15. Apparao, M.V.K., Daniel, R.R., Vijayalakshami, B., and Bhatt, V.L., J. Geophys. Res. 71, 1781, 1966.
16. Bame, S.J., and Asbridge, J.R., J. Geophys. Res. 71, 4605, 1966.
17. Hess, W.N., and Kaifer, R.C., Solar Phys. 2, 202, 1967.
18. Webber, W.R., and Ormes, J.F., J. Geophys. Res. 72, 3387, 1967.
19. Wolcott, J.H., Ph.D. Dissertation submitted to the University of New Mexico, 1968.
20. Heibredner, E., Pinkau, K., Reppin, C., and Schonfelder, V., J. Geophys. Res. 75, 6347, 1970.
21. Daniel, R.R., Joseph, G., Lavakare, P.J., and Sunderrajan, R., J. Geophys. Res. 76, 3152, 1971.
22. Eyles, C.J., Linney, A.D., and Rochester, G.K., Twelfth International Conference on Cosmic Rays, Hobart. Conference Papers (Univ. of Tasmania) 2, 462, 1971.
23. Cortellessa, P., Benedetto, P., and Paizis, C., Solar Phys. 20, 474, 1971.
24. Leavitt, C.P., Robb, D.S., and Young, F., Bull. Am. Phys. Soc. 17, 687, 1972.
25. Lockwood, J.A., Ifedili, S.O., and Jenkins, R.W., Solar Phys. 30, 183, 1973.
26. Chupp, E.L., Forrest, D.J., Higbie, R.R., Suri, A.N., Tsai, C., and Dunphy, P., Nature 241, 333, 1973.
27. Tanskanen, P.J., Kananen, H., and Blomster, K.A., Collected Data Reports on August 1972 Solar Terrestrial Events, World Data Center A, Report UAG-28 (part 2), p.415, 1973.
28. Reppin, C., Chupp, E.L., Forrest, D.J., and Suri, A.N., Thirteenth International Conference on Cosmic Rays, Denver. Conference Papers (Univ. of Denver) 2, 1577, 1973.
29. Pottasch, S.R., Bull. Astron. Inst. Netherlands, 19, 113, 1967.
30. Jenkins, I.L., and Wain, A.G., J. Iorgan. Nucl. Chem. 32, 1419, 1970.
31. Blaser, J.P., Boehm, F., Marmier, P., and Scherrer, P., Helv. Phys. Acta, 24, 465, 1951.
32. Ahluwalia, H.S., Thirteenth International Conference on Cosmic Rays, Denver. Conference Papers (Univ. of Denver) 2, 1576, 1973.



APPLICATION TO THE CALIBRATION OF NEUTRON MOISTURE GAUGES AND TO THE PEDOLOGICAL STUDY OF SOIL

Ph. COUCHAT<sup>+</sup>, C. CARRE<sup>++</sup>, J. MARCESSE<sup>+</sup>, J. LE HO<sup>+++</sup>

+ Département de Biologie, Service de Radioagronomie

CEN Cadarache, B.P. n°1, 13115-Saint-Paul-lez-Durance, France

++ DPRMA, CEN Fontenay-aux-Roses, B.P. n°6

92260 - Fontenay-aux-Roses, France

+++ DPRMA/SECPR, CEN Cadarache, B.P. n°1,  
13115- Saint-Paul-lez-Durance, France

The neutronic method for measuring the water content of soils is more and more used by agronomists, hydrogeologists and pedologists. On the other hand the studies on the phenomena of slowing down and diffusion process have shown a narrow relation between the thermal absorption ( $\Sigma_a$ ) and diffusion ( $\Sigma_d$ ) constants and the thermal flux developed in the soil around a fast neutron source like Am-Be. Then, the authors present two original applications of the direct measurement of  $\Sigma_a$  and  $\Sigma_d$ .

The method described consists in the measurement, in a cube of graphite with an Am-Be source in the middle, on one side of the perturbation of the thermal flux, obtained by the introduction of 300 g of soil, and on the other side of the transmitted thermal flux measured through the same sample of soil, on a side of the cube.

After calibrating the device, these two parameters give  $\Sigma_a$  and  $\Sigma_d$  which are easily introduced in the calibration equation of neutron moisture gauge. Also these two values are useful for the pedologists because  $\Sigma_d$  is connected to clay content in the soil and  $\Sigma_a$  is connected to the type of clay by the way of rare earth contents.

(Key words : thermal neutron constants, soil, neutron moisture gauge, calibration, pedology)

### Introduction

For the soils and rocks, the use of the principles and experiments related to the neutron diffusion is now well established seeing that in 1945 Brummer for the first time proposed the neutronic measurement of soil water. Then a great diversification took place on one hand in the field of study which ranges from geology to agronomy, on the other hand with regards to the neutronic techniques which ranges from the life time of neutron to neutronography. But undoubtedly the methods derived from the measurement of fast, epithermal and thermal flux developed around a fast neutron source in the soil is by far the most interesting ; it is especially employed with thermal flux that are easily measured<sup>1</sup>. The description of its principles was made with the aid of the previous nuclear reactor studies.

Then it is paradoxal to observe that the neutronic method was accepted by soil physicists with great difficulty. This is an example that, still 30 years after its introduction, the neutronic measurement of the soil water content is not very conveniently calibrated<sup>2</sup>. It is unnecessary to seek the reason for this difficulty in a nonexistent technological complexity in measuring thermal flux. On the other hand it evidently appears that the main hindrance is the heterogeneity of the chemical composition of soils and rocks. Face this problem the researcher attempted to determine for each medium, the relation between the measured flux and the desired variable (soil water content or rock porosity). Although it allows to give a response for the studied case, this approach was quickly recognized as unable to give a generalization of the results and consequently to calibrate neutron moisture meters. With the intent to answer this so put question, we have proposed the direct measurement of intrinsic

neutronic parameters of dry soils and rocks samples. This approach on the other side of previous methods, in very useful not only to solve the calibration of neutron moisture meters but also to give new means to characterize soils and rocks.

#### 1. The neutronic soil constants.

In the chemical composition of soils and rocks, it is usual to distinguish the main elements, the hydrogen and the trace elements. Outside oxygen, the fundamental constituent elements are silicium, aluminium, iron, titanium and manganese ; they are expressed by their respective oxydes. Hydrogen, important element because this neutronic properties, is present as constituent mineral water or hydroxyl ions. We can measure it by its equivalent water obtained by an oxydation at 1000°C during one hour and called here by extension constituent water. This there is a relation between this constituent water and the SiO<sub>2</sub> percentage for several different soils. The elements as trace elements and neutronicly important are essentially Boron, Lithium and certain rare earths like Samarium, Gadolinium, Europium. He should be remember that their analysis is delicate and very imprecise compared with their great interaction with the neutrons.

In connection with neutronic constants, it is possible to separate neutron slowing down, thermalization and thermal diffusion. On the other hand in order to take into account particular neutronic properties of soil hydrogen, we study these constants with using this element as a variable.

The slowing down process being defined by the slowing down power  $\Sigma_s$  and the fast transport neutron cross section, we can show that the soil water is the main parameter for the slowing-down and that the others soil elements, nearly exclusively the major ones, arise

in the fast transport definition (fig.1) with the second order. The thermalization stage can be ignored without error in this type of soil neutronic measurement. During the thermal diffusion process, the water remains the predominant term concerning the  $\Sigma_d$  diffusion parameter, the major elements essentially arising by the  $\text{SiO}_2$ . Then we observe, as showed on figure 2, a narrow relation for several soils between  $\Sigma_d$  and the constitutive water. On the other hand thermal absorption is strongly dependent on the amount of trace elements particularly (Boron) and there is no relation between  $\Sigma_a$  absorption parameter and soil constitutive water (fig.3).

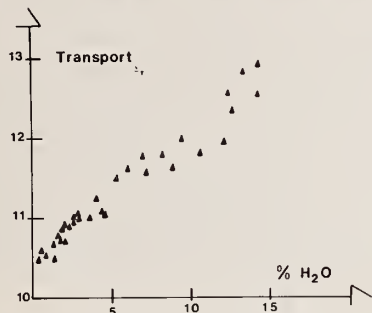


Fig.1 - Fast transport neutron cross section ( $\text{mm}^2/\text{g}$ ) versus constitutive soil water content

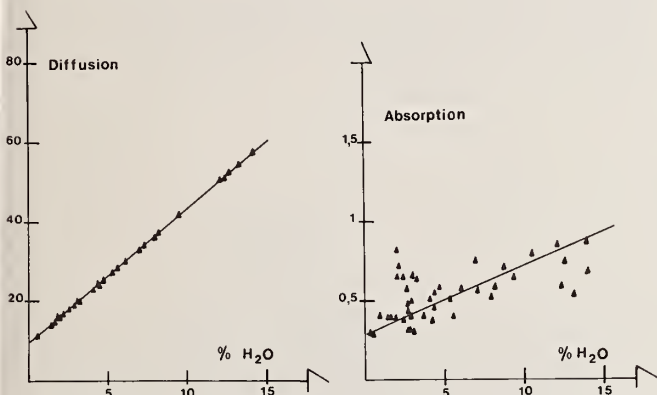


Fig.2 - Thermal diffusion ( $\text{mm}^2/\text{g}$ ) versus soil water content.

Fig.3 - Thermal absorption ( $\text{mm}^2/\text{g}$ ) versus soil water content.

Then it appears from this consideration that, neutronically, a soil could be well defined for the slowing down and thermal diffusion if we know the constitutive water content and the trace elements. The accuracy of this definition is given by that of the correlation which exists between constitutive water and fast transport. Then we can turn over the proposition and, that is an important point, we can say that the knowledge of  $\Sigma_a$  and  $\Sigma_d$  is sufficient to neutronically define the soil if we are interested in the measurement of thermal flux which arises around a fast neutron source ; the accuracy of the assessment thus established will be connected to variability of the influence on the fast transport of the constitutive water, influence balanced by the relation between fast neutron flux and fast transport.

## 2. The measurement of thermal diffusion constants $\Sigma_a$ and $\Sigma_d$ in the soils and rocks.

A standard method to measure the thermal absorption of any sample (method non still used for the soils consist in introducing the sample in an equilibrium nuclear reactor and to move periodically sample. We measure in a certain point the neutronic flux modulation spreading in the whole reactor with the assistance of an ionization chamber. The fundamental of the signal is proportional to sample absorption : this is the amplitude oscillation method. The phase oscillation method is based on the fact that an oscillatory sample gives in a nuclear reactor simultaneously a modulation spreading everywhere and a perturbation measurable only near the sample. By judiciously putting the detector, we show that the loch of phase between the obtained signals with two samples of different capture is proportional to the difference of neutron absorption cross section<sup>3</sup>.

Thus we have determined the absorption cross section of several dry ( $105^\circ\text{C}$  during 24 h) soils ; the measurement is taken by comparing with a silice sample which is the main constitutive part of soil. With this measurement, we observe on one hand a systematic discrepancy between the values measured and calculated from the known chemical composition, which does mean that the trace elements are badly known to be used to calculate thermal neutron diffusion ; on the other hand we note the lack of relation between  $\Sigma_a$  and  $\Sigma_d$ .

Such a measurement of neutronic constants is long and expensive ; thus a new method is proposed. It requires a graphite pile of the same kind as the BOREAL device<sup>4</sup> : a thermal neutron flux arises in the pile from an several curies Am-Be source. A thermal flux detector measures the perturbation introduced by a soil sample placed between the detector and the source. Another detector measures on a side of the pile the thermal neutron beam transmitted through the same soil sample. We obtain two count rates dependently on  $\Sigma_a$  and  $\Sigma_d$  and we calculate from these after a previous calibration, the thermal neutronic soil constants.

## 3. The calibration of neutron moisture meter.

We have seen that soils and rocks have, because of their chemical composition, a great variety of neutronic behaviour which can be seen in the large range of  $\Sigma_a$  and  $\Sigma_d$ . This has a direct consequence on the neutron moisture gauges the principle of which consists of relating the measurement of a thermal flux around a fast neutron source, introduced with a tube in the soil, to the water content of this soil. The so obtained relation is not unique and depends on the chemical composition and the bulk density of soil<sup>5</sup>. This is moreover shown by classical experimental calibration which gives the correlation between a water content measured by burning the soil at  $105^\circ\text{C}$  during 24 h and the count rate : from one soil to another the calibration curves that can be considered as straight lines for classical devices have a slope which have a 40% range, and the absolute measurement is obtained with an accuracy of ten volumetric points (pure water represents 100 volumetric points and a saturated soil 40 volumetrics points).

A solution was proposed which consisted in determining the calibration curve from a model describing the slowing down and the thermal diffusion by soil chemical composition<sup>6,7</sup>. As a matter of fact, this method is advantageous, compared with merely experimental calibration, for the interpretation and the extent of results ; the error of determination from the calculation of the neutronic constants, of soils



gives the calculated calibration curve be obtained with an accuracy of 12,5%.

The theory shows, however, that it is possible to write the count rate of the neutronic gauge under the form :

$N = (\alpha\rho_d + \beta) H_V + \gamma\rho_d + \delta$  where  $H_V$  is volumetric moisture  $\rho_d$ , bulk density,  $\alpha$   $\beta$   $\gamma$  and  $\delta$  specific constants of the soil depending upon the chemical composition ;  $\alpha$  and  $\beta$  define the slope's curve, and  $\gamma$  and  $\delta$  its origin ordinate. This representation besides enables to notice on fig.4 that, when we pass from a clay soil (small percentage of  $SiO_2$ ) to a sandy soil, the  $\rho_d$  influence on the slope of calibration ( $\alpha$ ) increases ; whereas, the  $\rho_d$  influence on origin ordinate decreases ; on the other hand we notice that the correlation between  $SiO_2$  and the calibration curve is very large, which excludes the calibration from knowledge of only major elements.

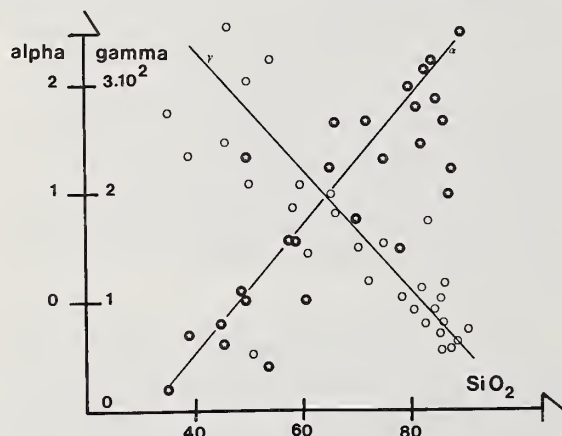


Fig.4 - Neutron moisture gauge calibration curve parameters ( $\alpha$ ,  $\bullet$  -  $\beta$ ,  $\circ$ ) versus percentage of  $SiO_2$ .

Because the  $\Sigma_a$  and  $\Sigma_d$  define entirely the slowing down and thermal diffusion, except on the second order fast transport, the thermal flux is also itself entirely defined and consequently,  $\alpha$ ,  $\beta$ ,  $\gamma$  and  $\delta$  parameters. We have calculated the variation of  $\alpha$  versus  $\Sigma_a$  and  $\Sigma_d$  for a matrix of sandy soil with consecutively added type absorber (Gadolinium) and added constitutive water. We observe, according to the published calibration curves, that the influence on the slope decreases in the same manner when the soil has a larger clay content (greater v constitutive water content and traces elements). With using all the correlations between  $\Sigma_a$ ,  $\Sigma_d$  and  $\alpha$   $\beta$   $\gamma$   $\delta$  in a large range of soils, we notice that the fast transport imprecision has a small influence on the obtained calibration curve. Then the  $\Sigma_a$  and  $\Sigma_d$  values entirely define the soil calibration curve by giving univocally  $\alpha$   $\beta$   $\gamma$  and  $\delta$ .

Therefore the proposed calibration method is the following<sup>8</sup> : on a 300 g soil sample, we measure with graphite pile,  $\Sigma_a$  and  $\Sigma_d$ . A small computer program give  $\alpha$   $\beta$   $\gamma$   $\delta$ . The thermal diffusion is directly given by  $\Sigma_a$  and  $\Sigma_d$  ; the slowing down is obtained from the constitutive water content issued from  $\Sigma_d$  and we improve the accuracy by using for  $\Sigma_{tr}$  the values of several reference soils distributed from the constitutive water. Calcareous soil is treated separately for the  $CO_3Ca$  content above ten percent. The accuracy of obtained calibration curve is directly related to that of  $\Sigma_a$  and  $\Sigma_d$ . The influence on the calibration curves passes through the relation between this two constants

and the parameters of calibration curve. If  $\Sigma_a$  varies in the range of 10% the slope  $\Pi$  varies in the range of 4% and the absolute measurement of volumetric content of 4% to 30 volumetric points ; in the case of  $\Sigma_d$ , for a variation of 10%, the variations are respectively of 1% and 10%. Then, by the direct measurement method the precision obtained on the calibration curve are of respectively + 1,2% for  $\Pi$  and 1,2% for absolute values due to  $\Sigma_a$  and 0,68% for  $\Pi$  and 3,4% for absolute water contents due to  $\Sigma_d$ .

#### 4. Neutronic soil characterization.

Besides the calibration of neutron moisture gauges, the  $\Sigma_a$  and  $\Sigma_d$  measurement gives to hydrogeologists an information about the neutronic homogeneity of the soil at the scale of an experimental agricultural soil or a watershed. We remark that the soil is more depth homogeneous than could be predicted by chemical analysis : this is a favorable point for the using of neutron moisture gauges. In the case of the sandy loam soil of Cadarache, taken as example, we could note that the dispersion of  $\Sigma_a$  is not more than four percent on all the cultivated plot. On the other hand we often observe an increase of  $\Sigma_a$  near the soil surface which can be reach twenty-five percent and is perhaps derived from trace elements in the soil. These results were corroborated by activation analysis.

This relation between soil chemical composition, and neutronic constants gave on the idea of exploiting the  $\Sigma_a = f(\Sigma_d)$  diagram. On the figure 5 we observe that the image-points are not randomly distributed ; they are brought together in relation to the sample site. It is possible easily to distinguish on this diagram a soil of Bouaké from a soil of Nancy. These collections are representative of the granulometry and

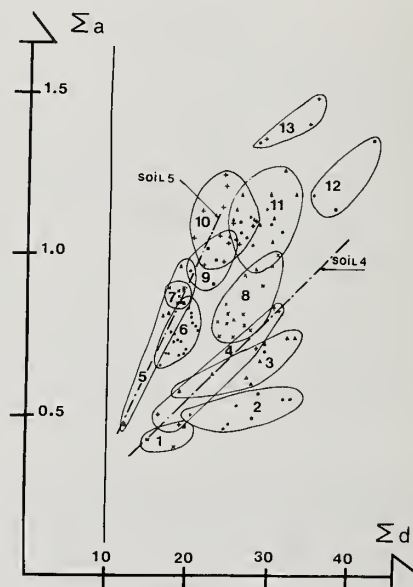


Fig.5 - Neutronic characterization of soils with  $\Sigma_a$  versus  $\Sigma_d$ .  
Origin of soils : Ivory Coast (1 Adiopodoumé, 2 Gagnoa, 3 Bouaké), Niger (4 Tillabery), France (5 Tarascon, 6 Cadarache, 8 Lunel, 9 Grenoble, 10 Lalèze, 13 Nancy), Belgium (7 Gembloux), Algeria (11 El Khemis), Tunisia (12 Ben Nasseur).



mineralogy of the soil ; for example, we can see that a soil obtained with great  $\Sigma_d$  and small  $\Sigma_a$  will be richer in clay than a soil with small  $\Sigma_d$  and great  $\Sigma_a$ . Generally, it is possible to detect a tendency when the increase of  $\Sigma_d$  is followed by an increase of  $\Sigma_a$  and means that we pass from a sandy soil to a clayey one ; this tendency is the reflection of the granulometry and mineralogy variation.

On the other hand, if we observe in an accurate manner a site, it is possible to see that the obtained points are on a straight line. This is the case, for example, with Tillabery and Tarascon soil ; we then say that these points correspond to two soils which are mineralogically different ; the excursion on this straight line is only dependent on granulometry. Thus if we obtain a narrow correlation between  $\Sigma_a$  and  $\Sigma_d$  for a group of points, these points are representative of a same mineralogic soil. In addition let us consider the point obtained for a  $\Sigma_d$  value which correspond to the diffusion of waterless soil (see fig.1) ; the  $\Sigma_a$  value of this point is representative of the clayless part of soil and give us an information on this part : for example, we distinguish between ferralitic soil (Bouaké) and siliceous soil (Grenoble). Figure 6 shows

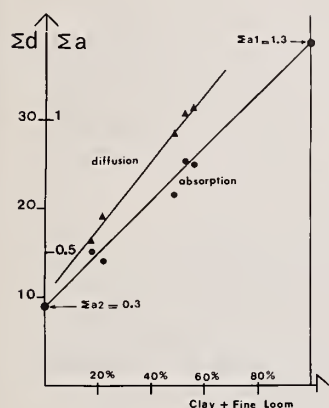


Fig. 6 - Diffusion and absorption cross sections of soil n°4 Tillabery versus clay + fine loam (< 20  $\mu$ m) percentage.

that is is possible, in certain cases, to consider the soil as composed of two granulometric parts : the clayed one < 20  $\mu$ m ( $\Sigma_{a1}$ ,  $\Sigma_{d1}$ ) and the sandy one ( $\Sigma_{a2}$ ,  $\Sigma_{d2}$ ). Thus the excursion on the  $\Sigma_a = f(\Sigma_d)$  curve is significative of the < 20  $\mu$ m variation. Finally, because the variation of  $\Sigma_d$  depends upon constitutive water we can say that the different variation of  $\Sigma_a$  ( $\Delta\Sigma_a$ ) with relation to  $\Sigma_d$  ( $\Delta\Sigma_d$ ) would be related with the type of clay (kaolinite, montmorillonite,...).

#### Conclusion

The direct measurement of  $\Sigma_a$  and  $\Sigma_d$  soil parameters allows the interpretation of the obtained results by thermal flux near a fast neutron source introduced in the soil. We have shown that this measurement also ensures an adequate neutron moisture gauges calibration. A simple measuring device with a graphite pile is presented.

Besides the neutron humidimeter calibration, we show the profit it is possible to obtain from the neutronic soil characterization also to assess their neutronic heterogeneity on an experimental plot (using of neutron humidimeter) also to obtain a quick classification of a soil useful for the pedologist in a  $\Sigma_a = f(\Sigma_d)$  diagram.

We have only stressed one of the important aspects of direct neutronic applications in the field of the problems set by hydrologists or pedologists. We have also to quote as an example the "in situ" determination of the slope of calibration curve of neutron moisture gauges by a double measurement of thermal and epithermal fluxes ; in the same manner, we can cite the use of neutronography for non destructive evaluation of the space-time evolution of roots. Then the gamma-neutron method, from a device with a Thallium source and a thermal neutron detector, was used to measure the D<sub>2</sub>O content in the soil water and to know dispersion movement.

As can be seen, the agronomist as the pedologist can expect numerous services from neutronic method. We have here some new technics at this crossing of the agronomy and the neutronic method that could be called "Neutronoagronomy".

#### References

1. Van Bavel, Nielsen Jr. Davidson, Calibration and characterization of two neutron moisture probes, Soil Sci. Soc. Am. Proc. 25, 329-34, 1961
2. Cameron J.C., Couchat Ph. and al, Neutron moisture gauges, Technical report n°112 AIEA, Vienne 1970
3. Carré J.C., Vidal R., Mesure des sections efficaces et des intégrales de résonances par la méthode d'oscillation, Confer. sur Constantes Nucléaires, Nuclear Data for reactor, vol.I, 479-494, IAEA Vienna, 1967
4. Carré J.C., Letour C., Empilement Boréal pour le contrôle de la teneur en bore d'échantillons d'alliage bore-aluminium, Revue Phys. Appl., 267)272, nov.1971
5. Cohen O.P., A procedure for calibrating neutron probes in the field, Israël Journal of Agricultural Research 14, n°4, 169-78, 1964
6. Couchat Ph., La détermination de la courbe d'étalonnage de l'humidimètre à neutrons à partir de l'analyse chimique des sols, Isotopes and Radiation techniques in soil physics, AIEA, Istanbul 1967
7. ØLGAARD P.L., On the theory of neutronic method for measuring water content. Riso Report n°97, 65
8. Couchat Ph. Mesure neutronique de l'humidité des sols Thèse d'Etat, Toulouse 1974

Nuclear data is used in modern medicine in a myriad of ways. Activation cross sections are used in the calculation of radioisotope production rates for both neutron and charged particle activation. The radioisotopes so produced are used in diagnostic nuclear medicine for the early detection of disease and for therapy either by external radiation or by internal radiation. The calculation of radiation dose from internally administered radioisotopes involves a knowledge of the decay scheme, mode and energy of decay, internal conversion coefficients, x-ray fluorescent and Auger electron yields. The decay scheme of radioisotopes including parent-daughter equilibria is essential knowledge for their accurate assay and for the understanding of radioisotope generators. Range-energy relationships for neutrons of various energies, charged particles, gamma-rays and electrons are also necessary for therapy and dose considerations. Applications to in vivo neutron activation analysis and photon absorptiometry for bone mineral measurement are also considered. An attempt is made to briefly describe these applications and to point out where more basic nuclear data measurements would be helpful.

(Activation cross-sections, in vivo neutron-activation analysis, radiation dose, bone mineral, therapy)

#### Activation Cross-Sections

Neutron activation cross-sections of the elements at thermal energies (n, $\gamma$  reactions) have been very carefully measured and are well documented<sup>1</sup>. At neutron energies up to 15 MeV activation cross-section measurements are less complete but compilations of existing data have been made and unknown cross-sections have been estimated<sup>2</sup>.

Many radionuclides are produced for medical use in nuclear reactors, and the activation cross-sections for these reactions are well known. The (n,p) and (n, $\alpha$ ) reactions and enriched isotopes are also used to produce some of the more rare radionuclides<sup>3</sup>. The knowledge of neutron activation cross-sections is essential to the calculation of expected yields, and the present status of nuclear data for this purpose is by and large adequate. Nuclear data, such as activation or production cross-sections, and/or decay scheme data is frequently generated as a result of an investigation into the production of a radionuclide for some other purpose.

Charged particle activation cross-sections are much less well known, and their precision of measurement is probably, in general, less than thermal neutron activation cross-sections. Compilations of charged particle activation cross-sections have been made but they are not at all complete<sup>4</sup>. Many attempts have been made to estimate charged particle cross-sections from empirical data and to use these to calculate thin and thick target yields from the elements for simple charged particle nuclear reactions<sup>5</sup>. However the results are probably no more accurate than factors of 2 to 10 and this is unsatisfactory<sup>6</sup>. The above calculations are made assuming the compound nucleus mechanism of nuclear reactions to be operative, and this seems to be a reasonable approximation.

For higher energy accelerators such as the linear accelerators at Brookhaven National Laboratory (200 MeV protons) and Los Alamos Scientific Laboratory

(800 MeV protons) calculations have been made of the yields of radioisotopes by spallation reactions<sup>7</sup>. Such calculations are essential for the justification of such programs as BLIP (Brookhaven Linear Isotope Producer) and LAMPF (Los Alamos Meson Production Facility) and seem to be the best, if not the only way, of producing useful quantities of certain radionuclides eg. Xe-127, or of producing them in high enough radionuclidic purity e.g. I-123<sup>8,9</sup>.

In the United States there seems to be a clear distinction between commercial production of radionuclides and those national laboratories and hospitals with their own production facilities. The law which seems to be in operation, favors the commercial companies, in that they can petition the government to stop government supported institutions from making radionuclides in competition with industry. Cyclotron installations in U.S. medical installations have tended to be small, low energy units, whereas in Europe and Japan they have been higher energy machines, more versatile for radionuclide production and with the potential for neutron therapy. Table I lists cyclotron installations in medical institutions throughout the world and Table II the particles accelerated and their energies. In the U.S.A., government supported labs confine themselves to research and industry confines itself largely to commerce. As an example of the type of radionuclides being produced by a small medical cyclotron in the U.S.A. for research purposes, Table III gives yields and other data for the Sloan-Kettering Institute (SKI) cyclotron a model CS-15, the first machine built by the Cyclotron Corporation. This model is no longer available from the Cyclotron Corporation, as subsequent purchasers have realized the limitations of a low energy machine and as the CS-22 or CS-30 models became available for a relatively small increase in cost.

\*This work supported in part by NCI Grant CA-08747 and AEC Contract AT(11-1)-3521.

TABLE I. MEDICAL CYCLOTRONS

Location	Manufacturer (model)	Installation
Hammersmith Hospital, London, U.K.	Medical Research Council	1955
Mallinckrodt Institute of Radiology, St. Louis	Allis-Chalmers	1965
Massachusetts General Hospital, Boston	Allis-Chalmers	1967
Sloan-Kettering Institute for Cancer Research, New York	Cyclotron Corp. (CS-15)	1967
Argonne Cancer Research Hospital, Chicago	Cyclotron Corp. (CS-15)	1969
Service Hospitalier Frédéric Joliot, Orsay, France	Thompson-CSF (compact)	1971
University of California, Los Angeles	Cyclotron Corp. (CS-22)	1971
Institut für Nuklearmedizin, Heidelberg, F.R. Germany	A.E.G. (compact)	1972
Mount Sinai Hospital, Miami	Cyclotron Corp. (CS-30)	1972
University of Tokyo, Tokyo, Japan	Cyclotron Corp. (CS-30)	1973
Medizinische Hochschule, Hanover, Germany	Scanditronix (MC-20)	1973
Institute of Radiological Sciences, Chiba, Japan	Thompson-CSF (70)	1974
University of Liège, Liège, Belgium	Thompson-CSF (compact)	1974
Klinikum Essen, Germany	Cyclotron Corp. (CS-30)	1974

TABLE II. SPECIFICATIONS OF CURRENTLY AVAILABLE COMMERCIAL CYCLOTRONS

		CS-22*	CS-30*	CV-28*	CV-40*	CV-70*	Actitron†	Th-CSF(70)†	MC-20‡
Maximum beam energy (MeV)	p	22	26	24	36	60	19	70	20
	d	12	15	14	20	35	11	35	10
	$^3\text{He}$	31	39	36	52	93	28	93	27
	$\alpha$	24	30	28	40	70	22	70	20
External beam current ( $\mu\text{A}$ )	p	50	60	70	45	30	70	20	100
	d	50	100	100	80	50	70	40	100
	$^3\text{He}$	50	70	70	60	38	50	—	50
	$\alpha$	50	50	50	80	40	50	—	50
Internal beam current ( $\mu\text{A}$ )	p	100	500	500	500	—	—	—	—
	d	100	500	500	500	—	—	—	—
	$^3\text{He}$	100	150	150	150	—	—	—	—
	$\alpha$	100	100	100	100	—	—	—	—

\*Cyclotron Corp. (U.S.).

†Thompson-CSF (France).

‡Scanditronix (Sweden).



TABLE III. YIELDS OF RADIONUCLIDES WITH THE S.K.I. CYCLOTRON

Radionuclide	Half-life	Decay gamma energy (keV)	Target <sup>a</sup>	Production reaction	Product chemical form	Yield at E.O.B. <sup>b</sup>		Impurities <sup>d</sup> (%)
						$\mu\text{Ci}/\mu\text{A}$ per h	mCi achieved after 1 h <sup>c</sup>	
<sup>11</sup> C	20 m	511	N <sub>2</sub> <sup>f</sup>	p, $\alpha$	HCN CO <sub>2</sub>	19000	300	-
<sup>13</sup> N	10 m	511	CO <sub>2</sub> <sup>f</sup>	d, n	N <sub>2</sub> NH <sub>3</sub>	3200	100	-
<sup>15</sup> O	2 m	511	N <sub>2</sub> <sup>f</sup>	d, n	O <sub>2</sub>	4600	150	-
<sup>18</sup> F	110 m	511	H <sub>2</sub> O	<sup>3</sup> He, p	F <sup>-</sup>	6 x 10 <sup>3</sup>	200	Negligible
<sup>30</sup> P	2.5 m	511, 2240	Al	( $\alpha$ , n)	PO <sub>4</sub> <sup>3-</sup>	10000	10	-
<sup>43</sup> K	22 h	$\beta^-$ , 370+	Ar <sup>e</sup>	<sup>4</sup> He, n	K <sup>+</sup>	10	0.3	-
<sup>48</sup> Cr	23 h	300, 120	Ti	<sup>3</sup> He, 2n	CrO <sub>4</sub> <sup>2-</sup>	1.5	0.03	<sup>51</sup> Cr (25)
<sup>51</sup> Cr	28 d	320	V	p, n	-	340	3.4	-
<sup>52</sup> Fe	8 h	165	Cr	<sup>3</sup> He, 3n	Fe <sup>2+</sup>	0.7	0.1	Negligible
<sup>67</sup> Ga	78 h	184, 296	Zn	p, n	Ga <sup>3+</sup>	77	3.8	( <sup>66</sup> Ga)
<sup>67</sup> Ga	78 h	184, 296	Zn	d, n	Ga <sup>3+</sup>	30	1.5	( <sup>69m</sup> Zn)
<sup>73</sup> Se	7.1 h	360	Ge	<sup>3</sup> He, 2n	SeO <sub>3</sub> <sup>2-</sup> SeO <sub>4</sub> <sup>2-</sup>	250	5	Negligible
<sup>81</sup> Rb	4.7 h	190, 450	NaBr	<sup>3</sup> He, 3n	Rb <sup>+</sup>	35	0.3	-
<sup>82m</sup> Rb	6.3 h	780, 620	NaBr	<sup>3</sup> He, 2n	Rb <sup>+</sup>	70	0.7	-
<sup>111</sup> In	2.8 d	173, 247	Cd	p, n	In <sup>3+</sup>	150	7.5	<sup>114m</sup> In (3)
<sup>121</sup> I	2.0 h	210	Sb	<sup>3</sup> He, 3n	I <sup>-</sup>	110	5	<sup>123</sup> I (2)
<sup>123</sup> I	13 h	160	<sup>123</sup> Te (77%)	p, n	I <sup>-</sup>	4000	20	<sup>124</sup> I (0.7)
<sup>123</sup> I	13 h	160	Sb	<sup>3</sup> He, 3n	I <sup>-</sup>	24	1.2	<sup>124</sup> I (5)
<sup>127</sup> Cs	6.2 h	410, 125	NaI	<sup>3</sup> He, 3n	Cs <sup>+</sup>	43	0.4	-
<sup>167</sup> Tm	9.7 d	208	<sup>167</sup> Er (91%)	p, n	Tm <sup>3+</sup>	38	0.4	-
<sup>197</sup> Hg	65 h	70	Au	p, n	Hg <sup>2+</sup>	36	2	-
<sup>197m</sup> Hg	24 h	135	Au	p, n	Hg <sup>2+</sup>	23	1	-
<sup>206</sup> Bi	6.2 d	70-1720	Pb	p, n	Bi <sup>3+</sup>	100	5	<sup>207</sup> Bi (0.02)

<sup>a</sup> Target is "thick" and of natural isotopic abundance unless otherwise indicated.<sup>b</sup> E.O.B. = end of bombardment.<sup>c</sup> Yields achieved in practice for a beam current that the target would withstand.<sup>d</sup> As a percentage of the given radionuclide at E.O.B.<sup>e</sup> Not a thick target.<sup>f</sup> For a flowing gas target.

A large variety of nuclear data has been used in establishing current methods of neutron activation analysis in man in the living state. Future methods and improvements will depend to a large extent upon an expansion of this knowledge. Basically the human body can be looked upon as a thick, rather bulky target by usual nondestructive analysis methods. It is definitely not homogeneous and therefore requires relatively uniform irradiation if quantitative information regarding its elemental make up is to be achieved. The human cannot be expected to sit in a fixed position for a long period so that the radiation source must be sufficiently intense to provide the required irradiation within a reasonable time frame. Biological damage must be kept to a minimum in order that the radiation exposure can be medically justified.

Neutron sources must be evaluated with regard to their source strength, energy distribution, changes in neutron energy distribution and flux attenuation with depth in biological media, radiation dose, angular distribution, etc. An estimate of expected target content variation must be made. Each potential reaction for assay must be evaluated for possible interferences, detection method sensitivity, minimization of dose requirements and relative cost factors.

The neutron activation analysis technique receiving the largest amount of attention in the past has involved thermal neutron activation in the whole body<sup>10-16</sup>. A quantitative measure of changes in calcium due to bone related disease as a function of progression and the response to therapeutic management has been the primary goal. These studies have also demonstrated a capability to measure sodium and chlorine by thermal neutron activation and nitrogen and phosphorus by the  $^{14}\text{N}(n,2n)^{13}\text{N}$  and  $^{31}\text{P}(n,2n)^{30}\text{P}$  reactions. Partial body measurements *in vivo* have been carried out for the determination of iodine in the thyroid<sup>17</sup>; phosphorus in bone<sup>18</sup>; and calcium, sodium and chlorine in bone<sup>19-21</sup>. Capture gamma-ray analysis has been demonstrated to be effective for measuring calcium and chlorine at a local bone site<sup>20</sup> and for measuring total body hydrogen<sup>22</sup>.

A more recent method for measuring calcium *in vivo* involves fast neutron activation of calcium-40. The  $(n,\alpha)$  reaction yields  $^{37}\text{Ar}$ , an inert gas, which is extracted from expired breath following irradiation. This method has been shown to be feasible in small animals<sup>23</sup>. A very low radiation dose requirement has been demonstrated for humans and a number of argon-37 exhalation rate experiments performed<sup>24,25</sup>. The use of the respiratory mechanism to extract the induced radioactivity from the target allows the argon-37 to be assayed with very high counting efficiency; however, the extraction of argon-37 from the body must be shown to be reproducible within a few percent if this method is to have value in the management of patients with metabolic bone disease.

### Radiation Dosimetry of Internally Deposited Radionuclides

The Society of Nuclear Medicine has established a Medical Internal Radiation Dose Committee (MIRD) to prepare authoritative references in the field of

absorbed-dose estimation resulting from the diagnostic use of radiopharmaceuticals. Pamphlets containing this information, including the physical, nuclear and anatomical data needed for these calculations, are published in a series as supplements to the Journal of Nuclear Medicine<sup>26</sup>. The work of this committee is expected to continue in the years to come due to the continuing development of new radiopharmaceuticals and the development of better physical data and computational techniques. Supplement Number 2 of this series, "Radionuclide Decay Schemes and Nuclear Parameters for use in Radiation-Dose Estimation" by L.T. Dillman describes the methods whereby nuclear decay data are used as input information to calculate the intensities and respective energies of all radiations emitted in alpha emission, electron or positron emission, electron capture and internal conversion of gamma rays.

The accuracy of nuclear decay scheme data is usually not limiting in the estimate of radiation absorbed dose, primarily because of uncertainties in the biological distribution data and in the inherent statistical uncertainty associated with the Monte-Carlo technique for calculating effective absorbed fractions. Further, there is normally a considerable variation from individual to individual in biological distribution, organ size and location, and in the effects of age and disease states on these parameters. The lack of a direct method for measuring radiation absorbed dose within living tissues necessitates continued refinements in all areas contributing to uncertainties. Many radionuclides currently undergoing study for their diagnostic utility do not have accurately known nuclear decay parameters and since a number of others are being considered for their use as pharmaceuticals of radiotherapeutic value, the accuracy of much nuclear data will require further improvement. The use of an internally deposited radionuclide to perform useful radiation therapy puts a much higher demand upon overall accuracy requirements.

### Radiation Therapy

Although x-rays were used therapeutically within a year following their discovery in 1895, the basis of such use for the next 50 years was essentially empirical and drastically limited by the energies available. With the development of the betatron, followed by that of the linear accelerator and the production of cobalt-60 in large quantities, it became possible to use energetic x-rays and electrons to deposit radiation energy in a controlled manner. The quantitative use of these radiations has required both atomic and nuclear data. Realistic planning of radiation treatment now requires not only accurate localization of the target volume but automatic computation methods to handle the large number of calculations necessary to compute the deposition of energy. This in turn has required attenuation and scattering data for various tissue constituent elements for different energies of both x-rays and electrons. One of the remaining problems with respect to the loss of energy by ionizing and exciting collisions as handled by the original Bethe-Bloch expression is the contribution of small energy losses below the ionization limits involved in conventional energy loss expressions. More precise data are needed, particularly with respect to interpretation of biological response to radiations of both low and high linear energy transfer characteristics.

Similar considerations apply with even more force to the computation of energy loss in tissue



element situations by the absorption of heavier particles such as negative pi-mesons. In the computation of resultant dose distributions in inhomogeneous structures of different elements more experimental data are necessary on the cross-sections of the nuclear reactions involved, and the absorption of the consequent radiations following nuclear disintegration.

Better data are also needed with regard to the use of internally located radionuclides. Radioactive materials are deliberately used internally, both by metabolic localization and by mechanical insertion and implantation. Internally employed sources include radium-226, radon-222, iridium-192, iodine-125, cobalt-60, cesium-137 and californium-252. The computation of dose in many instances still rests on calculations based on decay schemes. Some inadequacy in this situation is represented, for instance, by the different values of the exposure rate constant for iridium-192. These range, currently, from four to nearly six  $\frac{\text{R cm}^2}{\text{h-mCi}}$ , depending on which

handbook is employed and which decay scheme is utilized. Experimental measurements have been employed for many of the internal radioactive source arrangements, but for computation of dose distributions resulting from complex geometrical arrangements there is some need for better absorption, attenuation and scattering data. In the case of  $^{252}\text{Cf}$ , used for therapy as implants one is concerned not only with the absorption of the fission neutron spectrum but also with the concomitant gamma ray component, whose proportion increases rapidly with distance from the source in tissue.

#### Photon Absorptiometry for Bone Mineral Measurement

The photon absorptiometry technique for the *in vivo* measurement of bone mineral content does not use nuclear data in the actual measurement, but nuclear data is important in understanding the method and in attempting to correlate theoretical calculations with experiment.

The single energy photon technique of Cameron<sup>27</sup> has proven to be a noninvasive, and precise technique for evaluating mineral content of human extremity bones, with only local radiation dose to the subject of a few millirads. The method uses a linear or rectilinear scanning device which measures, by photon counting techniques, the transmission of a well collimated beam of monochromatic, or nearly monochromatic, X or  $\gamma$ -rays obtained from radioactive sources such as  $^{125}\text{I}$ ,  $^{241}\text{Am}$ ,  $^{153}\text{Gd}$ ,  $^{244}\text{Cm}$  or  $^{145}\text{Pm}$ . The single energy constant-thickness method involves positioning the limb to be scanned in a sample box filled with soft-tissue-equivalent material such that a constant thickness is presented to the collimated beam as the source and detector are moved.

For this physical arrangement, and assuming a two component system of bone and soft tissue or soft tissue equivalent material, the photon attenuation equations yield the following expressions<sup>28</sup> for bone mineral content (BMC):

$$\text{BMC (g/cm)} = \frac{\rho_B}{\mu_B - \mu_S} \delta \left\{ \sum_i \ln \left( \frac{I_0^*}{I_i} \right) \right\} = K L_1, \quad (1)$$

where  $\rho_B$  = density of bone mineral,  $\mu_B$  and  $\mu_S$  are the

linear absorption coefficients for bone mineral and soft tissue at the photon energy employed,  $\delta$  equals the scanning increment size,  $I_0^*$  is the transmitted intensity through the thickness of soft tissue and  $I_i$  is the transmitted intensity at the point where the bone mineral content is being evaluated. The use of available experimentally determined values for  $\rho_B$ ,  $\mu_B$  and  $\mu_S$  introduces errors because of the uncertainties involved. The density of the mineral portion of bone is known to vary by about

$\pm 5\%$ <sup>29</sup>. The determination of linear absorption coefficients with accuracies of a couple of percent for the actual components in human limbs is not trivial and the values obtained would vary with collimation and the degree of monochromaticity of the radiation employed. To overcome some of these errors, the proportionality factor  $K$  relating BMC (g/cm) and the "integral value",  $L_1 = \delta \left\{ \sum_i \ln \left( \frac{I_0^*}{I_i} \right) \right\}$ ,

is established for a particular set of instrumental values approximating that used in scanning the actual limb, in the form of a general linear equation by means of a scan to obtain  $L_1$  plus an ashing to determine the g/cm of bone mineral in the scanned section of an excised bone.

The major drawback in the single energy constant thickness approach as outlined above, is that the error due to the presence of adipose tissue, fat, cannot be determined *in vivo*<sup>30</sup>. The absorption in fat of  $^{125}\text{I}$  radiation ( $\sim 27$  keV) is about 60% of that of muscle or other soft tissue<sup>31</sup> and must be included as a third component for most human subjects. Dual energy techniques have been suggested as a means of overcoming this error. In one of these<sup>32</sup>, a dual source of 200 mCi  $^{125}\text{I}$  with 90 mCi of  $^{241}\text{Am}$  mounted above it is used as a single shielded source to give dual photon energies of about 27 keV and 60 keV. This dual energy constant-thickness approach has been shown theoretically to overcome the error due to fat<sup>32</sup>. Experimentally, it has been shown to adequately correct for the presence of the third component with circular cross-sectional shapes. It remains to be shown if one can obtain adequate accuracy in results for actual human limbs where highly irregular (non-circular) cross-sectional shapes are involved.

#### Acknowledgements

Tables I, II and III are reproduced with permission of the International Atomic Energy Agency, and appear in Symposium No. 171. Thanks are due to D. J. Silvester also for permission to use Tables I and II.

#### References

1. Goldberg, M.D., et al. Neutron Cross Sections and Resonance Parameters. Volumes I, IIA, IIB, IIC and III, Brookhaven National Laboratory, Report No. 325 and Supplements, 1962-1967.
2. Alley, W.E. and Lessler, R.M. Semiempirical neutron induced reactions cross sections. Report No. UCRL-50484 (Rev. 1) 1972.



3. Poggenburg, K.J. Neutron production at ORNL, Radioisotope Production Technology Development Meeting, pp. 12-24, Oak Ridge, Tenn.; U.S. AEC Report No. 700646, 2 June 1970.
4. McGowan, F.K., et al. Reaction list for charged particle induced nuclear reactions. Nuclear Data Section A-6, No. 4-6 and Sect. A-7, No. 1-2, 1969.
5. Lange, J. and Münzel, H. Estimation of unknown excitation functions for  $(\alpha, xn)$ ,  $(\alpha, pxn)$ ,  $(d, xn)$ ,  $(d, pxn)$  and  $(p, xn)$  reactions. KFK 767, 1968. Nuclear Research Center, Karlsruhe, also translated by J.J. Pinajian of ORNL.
6. Barbier, M. Compound nucleus reactions. Chapter IV in Induced Radioactivity, Am. Elsev., New York, 1969. See also Chapter II on Spallation Reactions.
7. Jaeger, U. and Münzel, H. Nuclear reactions induced by fast particles. Accuracy of the calculated activities. Nuclear Data in Science and Technology, Vol. II, pp. 475-482, Vienna, 1973.
8. Stang, L.G., Hillman, M. and Lebowitz, E. The production of radioisotopes by spallation. BNL 50195 (T-547), 1969.
9. Sodd, V.J., Scholtz, K.L. and Blue, J.W. Fe-52 production for medical use by 588 MeV proton irradiation of Mn, Co, Ni and Cu targets. Medical Physics 1:25-28, 1974.
10. Anderson, J., Osborn, S.B., Newton, D., Rundo, J., Salmon, L., and Smith, W.J. Neutron activation analysis in man in vivo. Lancet 2:1201-1205, 1964.
11. Chamberlain, M.J., Fremlin, J.H., Peters, D.K., and Philips, H. Total body calcium by whole body neutron activation: New technique for study of bone disease. Brit. Med. J. 2:581-583, 1968.
12. Palmer, H.E., Nelp, W.B., Murano, R. and Rich, C. The feasibility of in vivo neutron activation analysis of total body calcium and other elements of body composition. Phys. Med. Biol. 13:269-279, 1968.
13. Nelp, W.B., Palmer, H.E., Murano, R., Pailthorp, K., Hinn, G.M., Rich, C., Williams, J.L., Rudd, T.G., and Denney, J.D. Measurement of total body calcium (bone mass) in vivo with the use of total body neutron activation analysis. J. Lab. Clin. Med. 76:151-162, 1970.
14. Cohn, S.H., Dombrowski, C.S., and Fairchild, R.G. In vivo neutron activation analysis of calcium in man. Int. J. Appl. Radiat. and Isotopes 21: 127-137, 1970.
15. Cohn, S.H. and Dombrowski, C.S. Measurement of total-body calcium, sodium, chlorine, nitrogen and phosphorus in man by in vivo neutron activation analysis. J. Nucl. Med. 12:499-505, 1971.
16. McNeill, K.G., Thomas, B.J., Sturtridge, W.C., and Harrison, J.E. In vivo neutron activation analysis for calcium in man. J. Nucl. Med. 14:502-506, 1973.
17. Boddy, K., Hardin, M.R. and Alexander, W.D. In vivo measurement of the intrathyroidal iodine concentration in man by activation analysis. J. Clin. Endocr. Metab. 28:294-300, 1968.
18. Boddy, K. and Glaros, D. The measurement of phosphorus in human bone using radioactive neutron sources - a technique for partial body in vivo activation analysis. Int. J. Appl. Radiat. Isotopes 24:179-182, 1973.
19. Comar, D., Riviere, R., Maziere, B. and Kellershohn, C. in Proc. 9th Int. Symp. on Radioactive Isotopes in Clinical Medicine and Research (Munich: Urban and Schwarzenberg), pp. 431-437, 1970.
20. Comar, D., Riviere, R., Raynaud, C. and Kellershohn, C. in Proc. 8th Int. Symp. on Radioactive Isotopes in Clinical Medicine and Research (Munich: Urban and Schwarzenberg), pp. 186-194, 1968.
21. Catto, G.R.D., McIntosh, J.A.R., MacDonald, A.F., and MacLeod, M. Haemodialysis therapy and changes in skeletal calcium. Lancet, 1150-1152, May 26, 1973.
22. Rundo, J. and Bunce, L.J. Estimation of the total hydrogen content of the human body. Nature 210: 1023-1024, 1966.
23. Palmer, H.E. The feasibility of determining total body calcium in animals and humans by measuring <sup>37</sup>Ar in expired air after neutron irradiation. J. Nucl. Med. 14:522-527, 1973.
24. Bigler, R.E., Davis Jr., R., Evans, J.C., and Laughlin, J.S. Low dose human calcium assay in vivo via the <sup>40</sup>Ca(n, $\alpha$ ) reaction. In Proceedings Third National Conf. on Applications of Small Accelerators (Denton, Texas, Oct., 1974), U.S. Atomic Energy Commission.
25. Lewellen, T.K., Nelp, W.B., Palmer, N.E., Murano, R., Hinn, G.M. and Chestnut III, C.H. Argon-37 excretion in humans following total body neutron activation. J. Nucl. Med. 15: 511-512, 1974. (Abstract)
26. Medical International Dose Committee (MIRD), Pamphlets, J. Nucl. Med.; Suppl. No. 1 (1968), Nos. 2,3 (1969), No. 4 (1970) and No. 5 (1971).
27. Cameron, J.R. and Sorenson, J.A. Measurement of bone mineral in vivo: an improved method. Science 142:230-232, 1963.
28. Sorenson, J.A. and Cameron, J.R. A reliable in vivo measurement of bone mineral content. J. Bone and Joint Surgery 49-A:481-497, 1967.
29. Omell, K.A. Quantitative roentgenologic studies in mineral content of bone in vitro. Acta Radiol. Suppl. 41, pg. 25, 1957.
30. Zeitz, L. Effect of subcutaneous fat on bone mineral content measurements with the 'single-energy' photon absorptiometry technique. Acta Radiol. 11:401-410, 1972.

31. Spiers, F.W. Effective atomic number and energy absorption in tissue. Brit. J. Radiol. 19:52-63, 1946.
32. McDonald, J.M. and Zeitz, L. Dual energy absorptiometry technique for bone mineral content measurement. In: International Conf. on Bone Mineral Measurement, Chicago, 1973, DHEW Publ. No. (NIH) 75-683, 1974, pp. 88-99.

(Radiotherapy; tissue; dosimeter; radiography)

Over 400 patients have been treated with fast neutrons from a cyclotron at Hammersmith Hospital, London, using 16 MeV deuterons on beryllium. A large variety of malignant disease is included in this trial. A randomized trial of fast neutron therapy for cancer of the mouth and throat is in progress and preliminary results will be given. Fast neutron radiographs are often taken to check the positions of the fields used on the patients. These show no contrast from bone, but demonstrate only the presence of gas-filled cavities. As a diagnostic method, fast neutron radiography suffers from a number of disadvantages, the main ones being lack of sensitivity of the image-forming system and the hazard to the patient due to a large Quality Factor. Estimation of the absorbed dose given to different types of tissue is an important factor in the medical use of fast neutrons. More data are needed on the processes whereby fast neutrons impart energy to matter, particularly for neutrons above 15 MeV.

#### Radiotherapy with fast neutrons

At the present time the use of fast neutrons for the treatment of malignant disease seems one of the most hopeful applications of neutrons to the biomedical field. Nuclear data have many uses in connection with neutron radiotherapy, but before devoting resources to extending such data it is important to know whether this form of treatment is going to be only a nine-days wonder.

Fast neutrons were first used for radiotherapy in California between 1938 and 1943, the neutron beam being generated by some of the early cyclotrons built by Lawrence. The trial was not a success; in a lecture in 1947 Stone<sup>1</sup> wrote "Neutron therapy as administered by us has resulted in such bad late sequelae in proportion to the few good results that it should not be continued". As a result the method was not investigated again until 1966 when we began a fresh trial at the Hammersmith Hospital, London. This was based on radiobiological experiments which suggested a rationale for fast neutron therapy based on the oxygen effect: a fraction of the cells in many tumours is in a hypoxic condition and these cells are protected from the effects of irradiation by photons but to a lesser extent by neutrons. Looking back today to the early trial, it seems likely that the bad results were due to over-dosage, resulting partly from lack of knowledge of the radiobiological effects of treatments given in many fractions and partly from erratic operation of the cyclotrons which made it impossible to establish a safe and effective regime of treatment.<sup>2</sup>

At the Hammersmith Hospital we have now treated over 400 patients with advanced malignant disease in many sites using fast neutrons of mean energy 7.5 MeV. Many tumours which were not expected to respond well to radiotherapy have in fact regressed, without severe side effects<sup>3</sup>. To make an objective assessment however it is necessary to randomize the patients into two series, for treatment by photons or neutrons. We have been doing this for a selected group with advanced disease of the mouth and throat but with no known secondary spread at the time of randomization.

We have made a preliminary analysis of the results up to June 1974, as shown in Fig. 1. The number of patients are given across the top, and amount to about 50 on each side of the trial. Many entered the trial only a few months before the analysis, so the number available for assessment declines steadily with period of follow-up. There is a very clear and statistically significant difference between the two groups in terms of the proportion showing complete regression of the tumour in the treated area, based on clinical judgment.

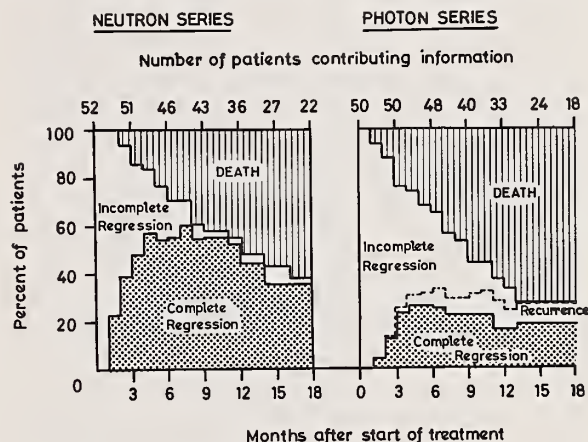


Fig. 1. Percentages of patients with persistent complete regression of tumours, regression followed by recurrence, incomplete regression or death according to interval since the start of treatment (Actuarial estimates).

In addition some of the tumours which regressed follow-treatment with photons subsequently recurred, whereas this has not yet happened to any of those which have regressed after treatment with neutrons. Relief of pain and ulceration has also been significantly better after treatment with neutrons. The proportion of patients surviving after neutron therapy is rather larger than that after treatment with photons, but here the difference is not statistically significant.

In a trial of two qualities of radiation it is important to know if any difference in response is really due to the quality rather than to a difference in quantity delivered. It is difficult to compare the biologically effective doses of two radiations which are as different as photons and fast neutrons. However, a wide range of doses was used in the photon series. The correlation between tumour regression and dose delivered in this series was very slight; when we included the best estimate we could make of the relative biological effectiveness of the neutron beam, it seems highly unlikely that the observed differences could have been due to delivery of different quantities of radiation. Another approach to this problem is through the reactions of normal tissues and the incidence of complications. These were similar in the two series, supporting the suggestion that there was no important quantitative difference between the doses given.



It seems therefore, from this interim analysis, that there is a real advantage to be gained from the use of fast neutrons instead of photons in the treatment of some kinds of advanced cancer. We cannot however foretell to what extent neutrons will be used for this purpose. Neutron therapy will probably always be a more expensive method than treatment with photons. Also new and different methods of treating cancer may be developed which would reduce the importance of any form of treatment with ionizing radiation.

#### Neutron spectra and penetration in tissue

In considering what kinds of nuclear data are needed for application in neutron therapy we need to know the neutron energy range of interest. The principal consideration is the penetration of the beam. Fig. 2 compares the penetration of various beams in unit density tissue<sup>4</sup>. The beam we have been using, produced by 16 MeV deuterons on beryllium, is not much better than a beam of 250 kVp X rays. Radiotherapy with photons was greatly improved when X ray units working at 250 kV were replaced by cobalt-60  $\gamma$  ray units and linear accelerators running at 4 - 10 MeV; to match the penetration given by these with neutrons it is necessary to accelerate deuterons to at least 30 MeV.

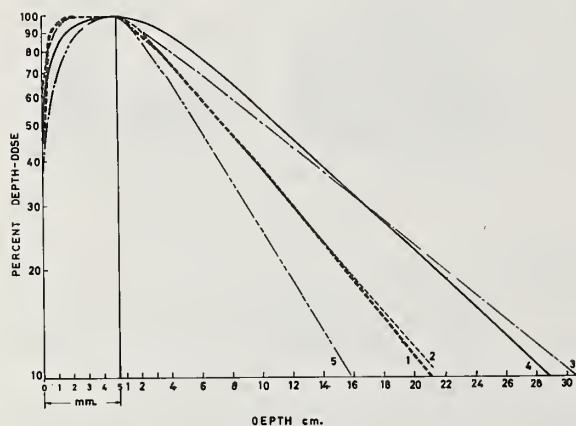


Fig. 2. Depth doses and build-up for a 5 x 5 cm field. The first 5 mm is shown on an expanded scale. Curve 1 -  $E_n = 7.5$  MeV, 120 cm f.s.d.; Curve 2 -  $E_n = 14$  MeV, 50 cm f.s.d.; Curve 3 - Co gamma rays, 80 cm f.s.d.; Curve 4 - neutrons from 30 MeV d on Be, 125 cm f.s.d. Curve 5 - 250 kVp X rays, 50 cm f.s.d.

Fig. 3 shows spectra of neutrons generated in the forward direction by deuterons of 16, 33 and 50 MeV on beryllium, drawn from the data of Meulders<sup>5</sup>. These show that increasing the deuteron energy from 33 to 50 MeV produces a relatively small increase in mean neutron energy. Nevertheless a cyclotron working at 50 MeV is now in use for neutron radiotherapy and preparatory work for the same purpose is in progress at other machines. There is therefore a current need for information on neutron interaction processes at least up to 50 MeV. At present there is a wealth of information at 14 - 15 MeV but a notable paucity at higher energies. Even if we consider neutron therapy at 14 - 15 MeV using a deuterium-tritium generator, there is need of more data at lower energies because the neutrons are degraded in energy as they pass through the patient.

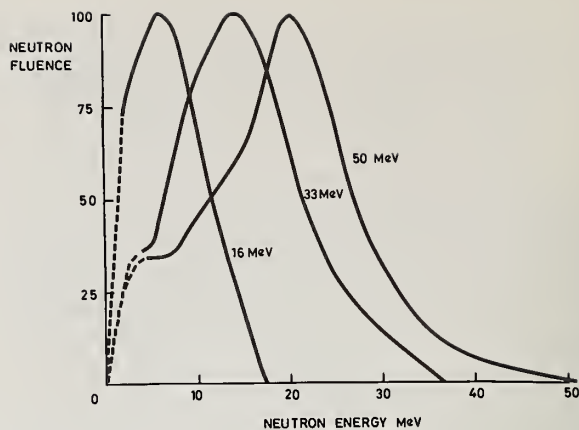


Fig. 3. Neutron spectra in the forward direction from deuterons on thick Be targets.

#### Kerma

The most immediate need is the calculation of Kerma per unit fluence in biological materials and in the materials of which dosimeters are made. Kerma is defined as the Kinetic Energy Released in the form of secondary charged-particles per unit Mass, and corresponds approximately to the old concept of first collision dose. The Kerma in a given material for a continuous spectrum of neutrons is given by

$$K = \int_0^{E_{\max}} \phi(E) \sum_L N_L \sum_J \sigma_{L,J}(E) \bar{E}_{L,J}(E) dE \quad \dots \quad (1)$$

where  $\phi(E)$  is the differential neutron fluence at  $E$ .

$N_L$  is the number of nuclei of species  $L$  per unit mass of the material concerned.

$\sigma_{L,J}(E)$  is the cross section for production of charged particles  $J$  from  $L$ .

$\bar{E}_{L,J}(E)$  is the mean initial kinetic energy of these charged particles.

Thus not only are the cross sections  $\sigma$  needed but also the information on the kinetic energy of the particles released. In the present instance only the mean energy is required, but often the energy spectrum of secondary particles is also wanted.

At the present time there are two main sources of tabulated data on Kerma, namely Bach and Caswell<sup>6</sup> who include only H, C, N and O up to 18 MeV, and Ritts et al<sup>7</sup> who include a number of other elements found in the human body but only up to 15 MeV. Table I gives information drawn from the literature on the composition of various types of tissue, together with values of Kerma calculated from the tables of Bach and Caswell<sup>6</sup> for the neutron spectrum produced by the cyclotron at Hammersmith Hospital and for 14 MeV neutrons. Small corrections were made for P, Ca and the other elements, but these account for only about one percent of the total Kerma. Sub-cutaneous fatty tissue suffers a substantially greater absorption of energy than do other soft tissues, while bone absorbs about half the energy per unit fluence. At higher neutron energies however the relative importance of hydrogen in absorbing energy from fast neutrons becomes smaller, while an increasing number of nuclear reactions occur in the other elements.

Lack of the relevant data prevents a calculation of Kerma for neutron beams of higher energy.

TABLE I

Type of Tissue	PERCENT OF ELEMENT						RELATIVE KERMA	
	H	C	N	O	(P (Ca	Others	14MeV $\bar{E}=7.5$ MeV	
ICRU muscle	10.2	12.3	3.5	72.9	0.2	0.9	100	100
TE plastic A-150	10.25	76.0	3.5	5.2	2.0	3.05	106	104
Muscle	10.3	15.0	3.0	70.5	1.2	-	101	101
Subcutaneous fatty tissue	11.9	49.6	-	38.5	-	-	118	118
Liver	11.0	4.1	1.2	82.5	-	1.2	105	106
Kidney	9.6	3.0	12.2	72.9	0.2	2.1	94	95
Brain	10.8	13.1	1.3	73.6	1.2	-	104	105
ICRU bone	6.4	27.8	2.7	41.0	21.7	0.4	69	66
Wet cortical bone	3.4	15.5	4.0	44.1	32.4	0.6	44	39

For neutron dosimetry it is convenient to use a conducting plastic to simulate tissue, with composition shown in the 2nd row of Table 1. Carbon has been used to replace almost all the oxygen in tissue. Ionization chambers are usually filled with a gas mixture simulating tissue, which also has carbon replacing oxygen. Up to 18 MeV the effect of this substitution is fairly small and is calculable, but at higher energies there is at present no published information. The measurement of dose from neutron beams generated by cyclotrons running at 30 or 50 MeV, using ionization chambers or calorimeters, is therefore subject to an unknown uncertainty.

#### Response of dosimeters

Calculation of Kerma is a special case of the calculation of response functions. For most purposes it is necessary to know more than the average energy of the emitted particles. For example the energy required to form an ion pair in an ion chamber varies with the energy of the recoil ion, particularly for ions heavier than protons. In general the response of an instrument to neutrons, relative to its response to  $\gamma$  rays, can be calculated by a fuller version of equation (1),

$$k_n = \frac{1}{K_t} \int_0^{\epsilon_{\max}} \phi(E) \sum_L N_L \sum_J \sigma_{L,J}(E, \epsilon) \epsilon f_J(\epsilon) d\epsilon dE \dots (2)$$

where  $k_n$  is the sensitivity of the instrument to neutrons relative to its sensitivity to  $\gamma$  rays, per unit energy absorbed in tissue in each case,

$K_t$  is the Kerma value for tissue

$\sigma_{L,J}(E, \epsilon)$  is the cross section for neutrons of energy  $E$  to produce recoils  $J$  from nuclei  $L$  with energies from  $\epsilon$  to  $(\epsilon + d\epsilon)$ .

$f_J(\epsilon)$  is the response of the dosimeter to particles of type  $J$  and energy  $\epsilon$  per unit energy absorbed in the dosimeter material, relative to its response to  $\gamma$  rays. The other symbols are as in equation (1).

For practically all effects used in dosimetry the response  $f_J(\epsilon)$  per unit energy absorbed is smaller for slow, densely ionizing particles than it is for energetic electrons. Ionization in hydrogenous gases is one example of this, as mentioned above. Others are the generation of thermoluminescent centres, pulse-heights from scintillators and semi-conductors, production of free radicals in organic substances and the yield of radiochemical reactions for example in the Fricke dosimeter. In principle the response of biological entities such as cells can be calculated in a similar way. Full data on types and energies of secondary charged particles are needed for calculations of this kind.

#### Neutron spectra in a tissue-equivalent medium

The spectra of Fig. 3 represent the fluence of neutrons coming from the machine. As the beam passes into the patient some of the neutrons are scattered and degraded in energy, while others, particularly those of lowest energy, are absorbed. The neutron spectrum in the patient depends not only on the incident spectrum but also on the area of the beam as it enters the body, the depth and the distance from the central axis.

The question is of some importance for neutron radiotherapy because the Relative Biological Effectiveness (RBE) of neutrons varies with neutron energy, reaching a maximum between 0.1 and 1 MeV<sup>9</sup>. This is different from the situation in conventional radiotherapy with photons since the variation in RBE of photons varies only by about 20% over the energy range of interest.

Fig. 4 compares the spectrum on the central axis at 10 cm deep in tissue to a field of area 80 - 90 cm<sup>2</sup> with the incident spectrum of neutrons from the cyclotron at Hammersmith. The incident spectrum was measured by Parnell<sup>9</sup> with a recoil proton telescope. The spectrum in the phantom was measured with activation and fission detectors while the calculated spectrum was kindly supplied by Dr. Grünauer using a transport method<sup>10</sup>. An increase in fluence of low-energy neutrons is shown both in the measurement and the calculation. In quantitative terms however the calculations give too great an attenuation of neutron dose with depth. Calculations of this kind require full information on the angular dependence of neutron scattering together with the energy loss, and perhaps the differences between measurement and calculation reflect lack of adequate data over the range of neutron energies concerned.

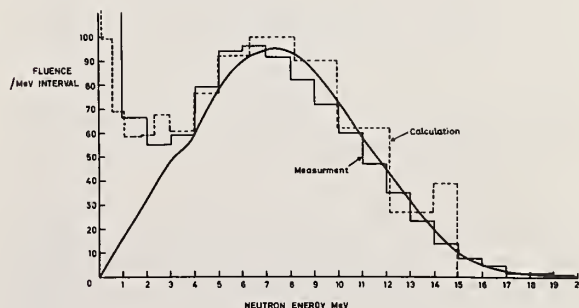


Fig. 4. Neutron spectra in a phantom by measurement and calculation, compared with the spectrum with no phantom present.



The radiation shielding round a neutron generator performs two functions, namely protecting the patient and staff from whole-body radiation while the beam is switched on, and limiting the dose-rate due to induced radioactivity after a treatment. The latter is important because after a treatment the staff have to work close to the neutron generator setting up the next patient.

Fig. 5 shows some measurements of attenuation in broad beams of neutrons generated by 16 and 42 MeV on beryllium. The measurements were made with pairs of ionization chambers so that the effect of  $\gamma$  rays could be eliminated. The chambers were placed at 120-130 cm from the target, while the materials under test were placed at 60 - 80 cm from the target using a neutron beam collimated to a diameter of 10-15 cm at the attenuator. The diagram shows clearly that as the deuteron energy is raised from 16 to 42 MeV the efficiency of iron as a shielding material remains nearly constant, while shielding based on hydrogenous materials becomes much less effective. Calculation is a more flexible approach than measurement to this problem. Calculation would make it easier to study a wide range of materials, to investigate the effects of heterogeneous shields and to indicate changes in the neutron spectrum as the beam passes through the shield. The latter may be of some importance as RBE varies with neutron energy as noted above. A high degree of accuracy is less important for this type of application than for those discussed earlier and perhaps approximate values for cross-sections obtained from nuclear models would be adequate.

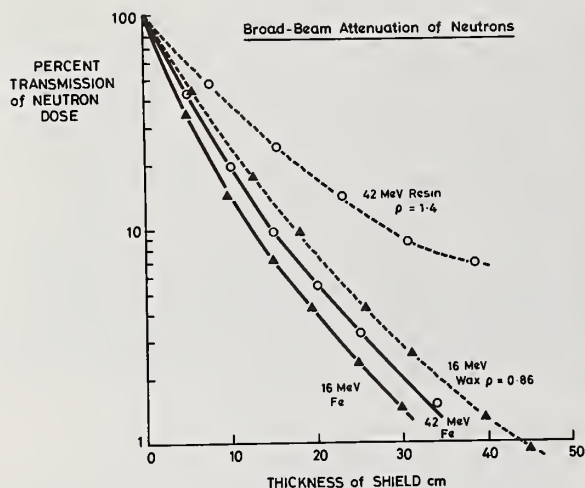


Fig. 5. Attenuation in iron and hydrogenous shields for neutrons generated by 16 and 42 MeV deuterons on Be.

Another advantage of calculation would be that the activation induced in the shield can be calculated at the same time. The stray radiation received by therapy radiographers while setting patients up for treatment is one of the factors limiting the number of patients who can be treated on our neutron beam.

#### Neutron Radiography

We have taken advantage of the exposure of patients on the fast neutron beam to make a short inves-

tigation of the potential value of fast neutron radiography<sup>11</sup>. Table I above gives the relative absorption of energy in various tissues, and shows that energy absorption per gm of bone is only about half that in soft tissue. As the density of bone is about two, energy absorption per unit volume is about the same in the two tissues. A smaller difference occurs between muscle and fat, and again the relative density reduces the difference in terms of energy absorption per unit volume. Thus one would expect fast neutron radiographs to show very little contrast. On the other hand air spaces might be visible even if partially obscured by bone on a normal X radiograph.

Figs. 6 and 7 compare neutron and X radiographs of a lateral view of the face and neck. The neutrogram was taken during a treatment session and the X radiograph was taken on a simulator used to check the positioning for treatment. As expected, the bones are completely invisible in the neutrogram. The corner of the field at F was shielded to protect the eye. The tongue, uvula and posterior pharyngeal wall are marked A, B and C, while pharyngeal and mastoid cavities are marked D and E. The patient was treated with carbonated wax as bolus to give a plane outline. Part of the bolus can be seen at G which lies just outside the patient's neck; the bolus is intended to attenuate neutrons to be the same extent as tissue, and it can be seen from the neutrogram that in practice the attenuations are not too different.

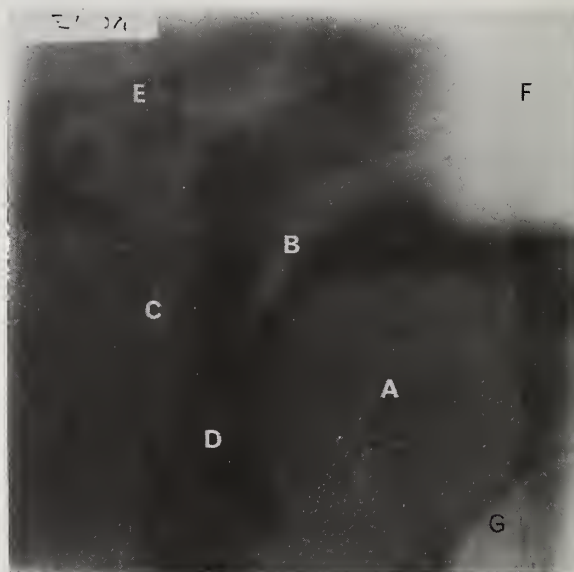


Fig. 6. Neutrogram of patient under treatment for carcinoma of floor of mouth. Red seal in salt screens, 5 rads to patient.

The technique we use for the neutrograms is to use standard X ray film with radiographic salt screens. Salt screens give greater contrast than that obtainable with a polythene radiator over the film to give recoil protons. It is convenient to leave the cassette in position during the whole of one session of treatment to one field; this is possible if one chooses the right combination of film and screen.

The presence of  $\gamma$  radiation in the neutron beam is a complicating factor as the film-screen combination is much more sensitive to  $\gamma$  radiation than it is to neutrons.





Fig. 7. X radiograph of same patient as Fig. 6, taken on therapy simulator.

Most of the  $\gamma$  radiation is produced by neutron interactions in the patient, probably mainly 2.2 MeV  $\gamma$  rays from thermal neutron capture in hydrogen. It produces a general fog on the neutrogram, obscuring detail. Attempts to remove the  $\gamma$  rays with lead screens of practicable thickness were unsuccessful. We therefore space the cassette 20 cm away from the patient. This also reduces the effects of scattered neutrons. The optimum spacing is a compromise because increasing the separation reduces fogging but also increases unsharpness due to the finite size of the source of neutrons which is up to 2 x 2 cm. The effect of  $\gamma$  rays could be eliminated completely by using the transfer method. In this method an image of radio-activity is formed on a metal plate which is put in contact with a photographic film after the exposure. Unfortunately the sensitivity of this method is inadequate (see below)

Fig. 8 shows a neutrogram of the chest of a patient with lung metastases from a carcinoma of the antrum. Again the bony skeleton is invisible. L is the left main bronchus close to the division of the trachea into the two main bronchi, while M is the medial margin of the right lung.

It is doubtful whether neutrograms of this kind can demonstrate any anatomy which cannot be demonstrated equally well or better with X rays, with suitable choices of kV and projection. For example shadowing by bone can be overcome by taking several radiographs from different directions, or by using more penetrating radiation (a higher kV).

However the main problem in fast neutron radiography is the large dose received by the patient. Table II shows the doses received by the skin of the patient at the entry point of the beam. The transfer method requires 200 times the exposure compared to a fast film in salt screens. Even the latter requires 100 times as much dose to the patient's skin as is needed for a conventional radiograph. In addition one must allow for the greater biological effectiveness of

TABLE II

Detection Method	Dose to skin of patient	
	Diagnostic X ray rad	Fast neutron rad rem
Transfer method Al screen + fast film	-	$10^3$ $10^4$
Fast film in salt screens	0.04	4 40
Hypothetical 10% efficiency	-	0.04 0.4

neutrons in comparison with photons. For radiation protection purposes this Quality Factor<sup>12</sup> is usually taken as 10, so that the effective dose to the patient's skin, measured in rem, is 1000 times that in a conventional radiograph<sup>14</sup>.



Fig. 8. Neutrogram (antero-posterior) of patient with lung metastases; 3.5 rads to patient.

The main reason for the poor showing of neutrons is the very low detection-efficiency of the film-screen combination which was designed for use with photons. On the other hand there is no obvious simple way in which a great improvement in detection efficiency can be obtained. A proton radiator (a sheet of polythene) placed behind the radiographic screen increases the sensitivity by less than a factor of two. The basic trouble is that a radiographic screen can be made from a material such as calcium tungstate which has a very high absorption coefficient for photons, whereas no such materials exist for fast neutrons. Detection based on thermal neutrons fails because the thermalised neutrons are diffused and carry no radiographic information. Use of a beam of thermal neutrons is only applicable to thin specimens, up to 2 cm thick, because of the scattering and poor penetration of thermal

neutrons.

An entirely new method of detecting fast neutrons is needed for this application. One possibility which has been suggested is a thick matrix of fine optical fibres. They should be of a hydrogenous material for efficient absorption of the fast neutrons, and should be efficient scintillators, the light output registering on the film. If some system of this kind could achieve a detection efficiency of 10%, compared to about 0.1% for the present method, the dose to the patient in terms of rad would be comparable to that occurring in conventional radiography (see table II). But in rems the dose would still be 10 times greater.

There is another problem in neutron radiography, namely statistical fluctuations in the image. Fig. 9 is an enlargement of two radiographs of a water filled model containing an empty, blind tube. Both were taken with identical fast film and salt screens, that on the left being a neutrogram and that on the right an X radiograph using X rays of mean energy 2.5 MeV. The neutrogram shows more contrast because the neutron beam was less penetrating than the X rays, but the picture is much grainier.

The cause of this effect lies in the interaction processes between the radiations and matter. X rays produce a diffuse field of secondary electrons which interact mainly with the intensifying screen, while neutrons produce recoil protons and heavier nuclei interacting with the film and the screen, and in which the deposition of energy is more localized, showing greater statistical fluctuation from point to point. As this is an inherent property of the radiation, use of a more sensitive method of image registration will not overcome the problem of spottiness in the image which will tend to become even more marked if the image can be formed by the absorption of fewer neutrons.

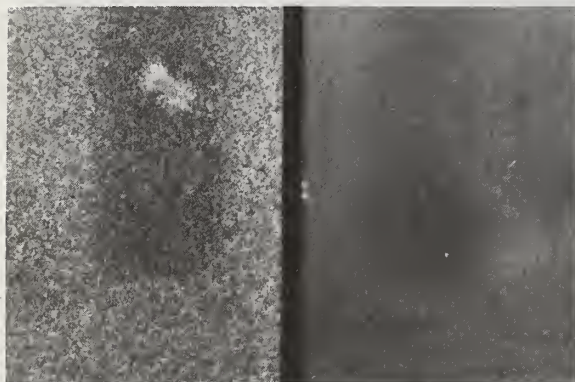


Fig. 9. Comparison of graininess in neutron (left) and X (right) radiographs. Red seal film in Ilford hv screens in both cases.

In view of these problems, I believe that further data on nuclear interactions will have little impact on the diagnostic use of fast neutron radiography. What is needed above all is a more sensitive method of registering the image, together with a smaller source of neutrons to limit geometrical unsharpness. However, even if these could be achieved, I doubt if the method would be of great medical value because the large

Quality Factor of neutrons makes the procedure radiologically hazardous, and because the pictures will almost inevitably be technically poorer than X radiographs. A lower neutron energy would increase the contrast but at the expense of a bigger dose at the entry surface. The future of neutron radiography in medicine perhaps lies more as an in-vitro test, for example the radiography with thermal neutrons of histological sections or other dead preparations in which deuterium might be exchanged with hydrogen<sup>13</sup>.

#### References

1. STONE, R.S. 1947. Amer. J. Roentgenol., 59, 771.
2. SHELINE, G.E., PHILLIPS, T.L., FIELD, S.B., BRENNAN, J.T. and RAVENTOS, A., 1971. Amer. J. Roentgenol., 111, 31.
3. CATTERALL, M., 1974. Cancer, 34, 91.
4. FOWLER, J.F. and BEWLEY, D.K., 1972. "Radiobiological Applications of Neutron Irradiation" IAEA, Vienna.
5. MEULDERS, J. Phys. Med. Biol. In Press.
6. BACH, R.L. and CASWELL, R.S., 1968. Radiation Research, 35, 1.
7. RITTS, J.J., SOLOMITO, M. and STEVENS, P.N., 1970. Oak Ridge National Laboratory, U.S. Atomic Energy Commission, ORNL-TM-2991.
8. HALL, E.J., ROSSI, H.H., KELLERER, A.M., GOODMAN, L. and MARINO, S., 1973. Radiation Research, 54, 431.
9. PARNELL, C.J., 1972. Brit. J. Radiol., 45, 452.
10. GRÜNAUER, F., 1972. Proc. 1st Symposium Neutron Dosimetry in Biology and Medicine, Munchen. EUR. 4896 d-f-e, p.511.
11. BEWLEY, D.K., CATTERALL, M. and PAGE, B.C., 1973. Brit. J. Radiol., 46, 24.
12. ICRP Publication 4, 1964. Pergamon Press.
13. BROWN, M. and PARKS, P.B., 1969. Amer. J. Roentgenol., 106, 472.
14. ROGERS, R.T. 1969. Brit. J. Radiol., 42, 511.



The extent to which transport calculations of biomedical interest for negatively charged pions, neutrons, protons, alpha particles, and heavier ions can presently be performed is reviewed.

(Radiotherapy; heavy particles; absorbed dose; cell survival; OER)

### Introduction

The potential advantages of using negatively charged pions, neutrons, protons, alpha particles, and heavier ions in cancer radiotherapy have been recognized for some time, and radiobiological experiments and therapeutic exposures with these radiation modalities are being carried out or will be carried out in the near future (see Ref. 1 and the references given therein). The physical properties and biological effects of these radiations are quite different from those of photons and electrons that are usually used in radiotherapy, and thus a large amount of physical and biological data must be accumulated before the manner in which these modalities can most effectively be used in radiotherapy can be determined. To aid in the design of experiments for accumulating these data and to aid in the interpretation of the experimental results, it would be very useful if accurate and general calculational methods were available to study the transport of the various particles and their nuclear-reaction products through matter. For biomedical applications, the charged nuclear-reaction products are of considerable importance since they determine quantities of biological interest, such as cell-survival probabilities, relative biological effectiveness (RBE), and oxygen enhancement ratios (OER). At the energies of interest ( $\leq 75$  MeV for negatively charged pions,  $\leq 50$  MeV for neutrons,  $\leq 150$  MeV for protons,  $\leq 600$  MeV for alpha particles, and  $\leq 7500$  MeV for neon ions), the available experimental differential particle-production cross-section data are very limited, and therefore, to a considerable extent, transport calculations must be based on theoretical cross-section data. In this paper, I will discuss the extent to which transport calculations for the various particles can presently be carried out.

### Differential Cross-Section Data

Charged particles, when they reach low energies (e.g.,  $\sim 25$  MeV for protons), may, to a good approximation, be assumed to come to rest without undergoing nuclear reactions, so in transporting charged particles through matter, one is primarily concerned with their nuclear reactions at the higher energies. Negatively charged pions are a slight exception to this statement since they are predominantly captured after coming to rest, but the reaction products from these captures may, to a reasonable approximation, be obtained from the same cross-section model that is used to treat the higher energy pion-nucleus nonelastic collisions<sup>2</sup> (see discussion and results given later in this section). Elastic nuclear collisions have only a small effect on the transport of high-energy charged particles through matter, so the nonelastic nuclear collisions of the charged particles will be of primary interest here. Due to their nonelastic interactions with nuclei, high-energy charged particles produce both low-energy ( $\leq 20$  MeV) and high-energy ( $\geq 20$  MeV) neutrons, and thus the nuclear interactions of such neutrons are of interest in the case of incident charged particles, as well as in the case of incident neutron spectra. At energies  $\leq 20$  MeV, the existing neutron cross-section libraries<sup>3,4</sup> are adequate for carrying out neutron

transport calculations, but, for biomedical applications where the charged-particle energy distributions produced by neutron-nucleus collisions are required, it is often necessary to supplement the data given in the libraries by theoretical considerations. At energies  $\geq 20$  MeV, there are ample experimental data for treating neutron-hydrogen collisions,<sup>5-7</sup> and neutron-nucleus elastic collisions can be treated using experimental data and optical-model calculations (e.g., see Refs. 8 and 9 and the references given therein).

For both neutrons and charged particles, there is very little information on particle production for non-elastic nuclear collisions at the higher energies ( $\geq 15$ -20 MeV), and thus this information must be obtained almost entirely from theoretical models. The most generally available source of the large amount of data needed in transport calculations is the intranuclear-cascade-evaporation model of nuclear reactions as implemented by Bertini *et al.*<sup>10</sup> in the code MECC-7. A detailed discussion of this model is beyond the scope of this paper, but such discussions, as well as many comparisons between calculated and experimental results for nucleon-nucleus and pion-nucleus collisions, will be found in Refs. 11-13. The model was originally intended to apply to nucleon- and pion-nucleus collisions and has been used most extensively for these types of collisions. Versions of the model which treat alpha-particle-nucleus<sup>14</sup> and heavy-ion-nucleus collisions have been developed,<sup>15,16</sup> but the results obtained for these types of incident particles must be considered very approximate. The power of the model lies in the fact that it gives estimates of the total nonelastic cross section, the energy and angular distribution of all emitted particles (neutrons, protons, positively and negatively charged pions, neutral pions, deuterons, tritons,  $^3\text{He}$ 's, and alpha particles), and the mass, charge, and kinetic-energy and excitation-energy distributions of the residual nucleus. The excitation energy of the residual nucleus is the total energy emitted in the form of photons. At the present time, the model does not give the spectra of these emitted photons. The model was intended to describe nucleon-nucleus and pion-nucleus collisions at energies  $\geq 50$  MeV, but, because of the lack of any other source of data, it has often been used in transport calculations at lower energies ( $\geq 15$  MeV) despite the fact that its use at these lower energies is dubious. Comparisons between calculated results obtained with the model and experimental data at these lower energies will be found in Refs. 17-19.

Comparisons between calculated results obtained with the intranuclear-cascade-evaporation model and the experimental data of Fowler<sup>20</sup> and Fowler and Mayes<sup>21</sup> for  $\pi^-$  capture in oxygen are shown in Figs. 1 and 2. Calculated results obtained with the intranuclear-cascade-evaporation model in several materials of biomedical interest have also been given by Armstrong and Chandler.<sup>22</sup> The major advantage of using negatively charged pions in radiotherapy is that a stopped  $\pi^-$  in tissue will, with high probability, be captured by one of the tissue nuclei and will produce a variety of particles. The effectiveness of particles in producing



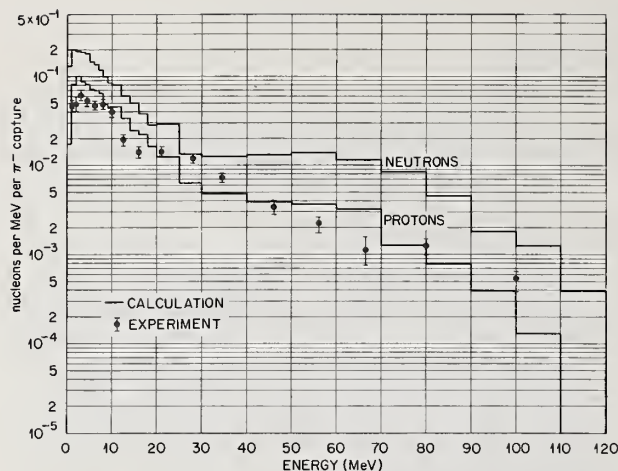


FIG. 1. Neutron- and proton-emission spectra from  $\pi^-$  capture in oxygen.

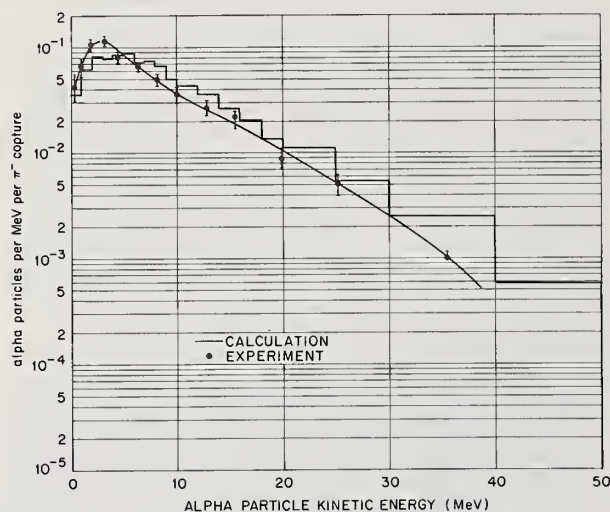


FIG. 2. Alpha-particle-emission spectra from  $\pi^-$  capture in oxygen.

damage in tissue is a function of type and energy of the particle, and, thus, to study calculationally the effects of  $\pi^-$  beams in tissue, it is important that the cross-section models used give a reliable estimate of the charged-particle spectra produced by these captures. In Fig. 1 the calculated energy spectrum of protons from  $\pi^-$  capture in oxygen is compared with the experimentally measured spectrum. The spectra are quite similar, but there are clear differences, particularly at the lower energies. Also shown in Fig. 1 is the calculated neutron spectrum. There are no experimental data on the neutron-emission spectrum from  $\pi^-$  captures in oxygen, but comparisons between calculated and measured neutron spectra from  $\pi^-$  captures in carbon and aluminum are given in Ref. 2, and results similar to those shown for protons in Fig. 1 are obtained. It should be noted that the neutron spectrum in Fig. 1 indicates that there is an appreciable number of high-energy neutrons produced by  $\pi^-$  captures in oxygen, and thus the transport of high-energy neutrons through tissue is an essential feature of the study of the effects of  $\pi^-$  beams in tissue. In Fig. 2 the calculated and

experimental alpha-particle spectra from  $\pi^-$  captures in oxygen are compared and are shown to be in approximate agreement. In general, it seems clear that more experimental and theoretical information concerning particle-emission spectra from  $\pi^-$  captures in nuclei is needed for biomedical applications.

#### Charged-Pion, Nucleon, and Alpha-Particle Transport Calculations

All of the results presented in this section were obtained with the nucleon-meson transport code HETC.<sup>23,24</sup> This code utilizes Monte Carlo techniques to simulate particle transport and takes into account charged-particle energy loss due to atomic ionization and excitation, multiple Coulomb scattering of incident charged particles, elastic and nonelastic neutron-nucleus collisions, nonelastic collisions of protons and charged pions with nuclei other than hydrogen, elastic and non-elastic nucleon and charged-pion collisions with hydrogen, pion and muon decay in flight and at rest, and negatively charged pion capture at rest. The intranuclear-cascade-evaporation model (see previous section) is used to treat particle production from pion-nucleus collisions at all energies and nucleon-nucleus collisions at energies  $> 15$  MeV. A detailed discussion of the manner in which the various physical processes are included in the code is beyond the scope of this paper, but such a discussion will be found in Refs. 25 and 26. The code HETC in its published form is operable for incident neutrons, protons, and pions at all energies of interest in radiotherapy and is capable of treating very general source-geometry configurations, including an essentially arbitrary phantom configuration. A version of the code to treat the transport of alpha particles and the nuclear-reaction products produced by alpha-particle-nucleus nonelastic collisions and alpha-particle-hydrogen elastic and nonelastic collisions has recently been written<sup>27,28</sup> and was used in producing the alpha-particle results presented later in this section.

The code HETC has been used to calculate the energy deposition in tissue by a variety of charged-pion, neutron, and proton beams,<sup>25,29-33</sup> and results obtained with the code have, in general, been found to be in good agreement with experimental data.<sup>30-32</sup> The usefulness of the code for biomedical applications is not only that it gives a reliable estimate of the absorbed dose as a function of position in a phantom but also that it gives a complete description of the type and energy distribution of the charged particles produced by nuclear interactions, and this information may be combined with cell-inactivation models, such as that of Katz *et al.*,<sup>34,35</sup> to predict quantities of biological significance. In the remainder of this section, calculated results obtained with HETC of both absorbed dose and cell-survival probabilities will be presented, and comparisons between calculated results and experimental data will be presented.

#### Absorbed Dose from an Incident Negatively Charged Pion Beam and Comparison with Experimental Data

Experimental data on the absorbed dose as a function of depth in a water phantom irradiated by a negatively charged pion beam with a mean momentum of 175 MeV/c (corresponding to a kinetic energy of 84 MeV) are available from Turner *et al.*<sup>36</sup> In the experiment, the pion beam was approximately elliptical in shape and was normally incident on one end of the water phantom. The absorbed dose was measured as a function of depth along the beam axis, using a detector 3 cm in radius. The momentum spread of the beam was not measured precisely but was estimated to be Gaussian with a standard deviation of 4.7 MeV/c. The experimental  $\pi^-$  beam was

contaminated with unmeasured numbers of negatively charged muons and electrons, and thus the measured absorbed-dose distribution contains contributions from these particles as well as from pions.

Using HETC for  $\pi^-$  and  $\mu^-$  transport and the electron-photon cascade code of Beck<sup>37</sup> for  $e^-$  transport, calculations have been carried out by Armstrong and Chandler<sup>31</sup> for comparison with the experimental data. Comparisons between calculated results, obtained using a different calculational procedure than that used by Armstrong and Chandler, and these experimental data have also been given by Turner *et al.*<sup>38</sup> In order to compare with the data, separate dose distributions from incident  $\pi^-$ ,  $\mu^-$ , and  $e^-$  beams were obtained, and the relative contributions of each type of particle to the measured absorbed-dose curve was determined by fitting the calculated results to the measured curve at three points. The comparison between the calculated results and the experimental data is shown in Fig. 3. Depths

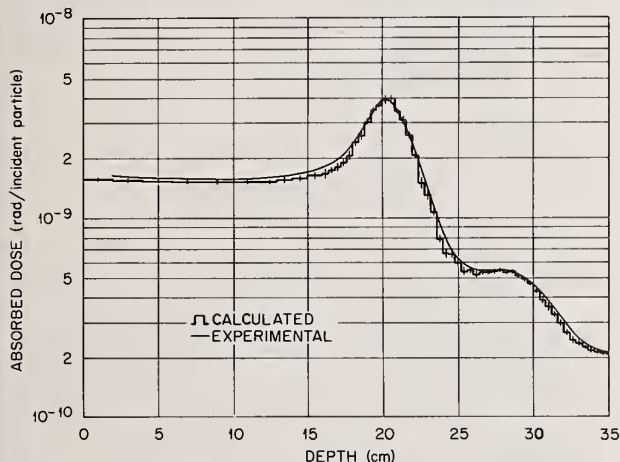


FIG. 3. Comparison of calculated and experimental absorbed dose from an incident  $\pi^-$  beam.

of 20.5, 28.5, and 35 cm were used to determine the relative number of each type of incident particle, so the calculated and experimental results must agree at these points. The calculations indicated that the beam was composed of 71%  $\pi^-$ , 13%  $\mu^-$ , and 16%  $e^-$ . The agreement between the calculated and experimental data in Fig. 3 is quite satisfactory, but the comparison is not definitive because of the fitting procedure needed to determine the beam contamination. Additional experimental data are required before the absolute validity of the calculations can be determined.

#### Calculated Cell-Survival Probabilities and Comparison with Experimental Data for Negatively Charged Pions

Katz *et al.*<sup>34,35</sup> have developed a model of cell inactivation. Basically, this model allows a prediction of the probability that a given cell type will survive in any known radiation field no matter how complex, provided that the parameters in the model are available. These parameters, which must be determined from experimental data, are dependent on cell type and on whether the irradiation is carried out under aerobic or anoxic conditions. Parameters are presently available for a few cell types. When negatively charged pions, nucleons, or alpha particles are incident on a tissue phantom, HETC provides an estimate of the energy distribution of each type of charged particle and photon as a function of position in the phantom, and this information may be combined with the cell-inactivation

model of Katz *et al.* to calculate the cell-survival probability as a function of position in the phantom. A detailed discussion of the manner in which such cell-survival probabilities may be calculated using HETC results has been given by Armstrong and Chandler.<sup>33</sup>

Experimental data on the spatial dependence of the cell-survival probability from an incident pion beam are not available at present for comparison with calculated results. There is, however, one experiment by Raju *et al.*<sup>39</sup> in which the survival of T-1 kidney cells was measured at a single location in the stopping region of a pion beam. The measurements were made by placing T-1 kidney cells in the peak dose region of a contaminated pion beam (65% pions, 10% muons, and 25% electrons) having a mean range of  $\approx 23 \text{ g cm}^{-2}$  in lucite. Experimental cell-survival probabilities taken under both anoxic and aerobic conditions are shown in Fig. 4 as a function of absorbed dose. The experimental data show considerable spread because the experiment had to be performed with a very low intensity beam.

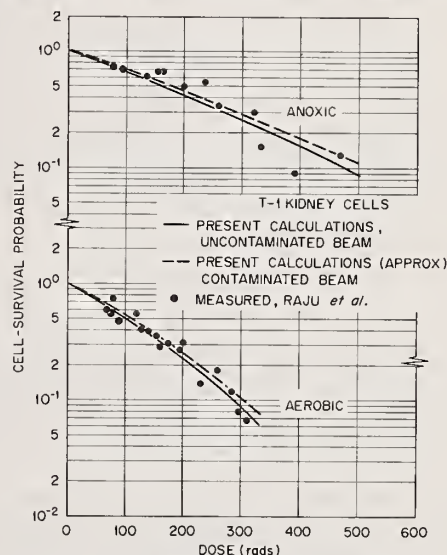


FIG. 4. Comparison of measured<sup>39</sup> and calculated<sup>33</sup> cell-survival probabilities in the capture region of a  $\pi^-$  beam.

Also shown in Fig. 4 are calculated results due to Armstrong and Chandler.<sup>33</sup> Calculations using the experimental beam could not be made because the momentum spread of the beam was not measured. The results of Armstrong and Chandler were obtained using a pion beam which produced approximately uniform pion captures over the depth interval of 12.5-17.5 cm and the radial interval of 0-2.5 cm in tissue. The results shown in the figure are the cell-survival probabilities averaged over this uniform capture region. While the conditions in the experiment and the calculations are not completely equivalent, they are sufficiently similar to permit a valid comparison. Armstrong and Chandler did not perform detailed calculations on the effects of the muon and electron contamination in the experimental beam, but they estimated the effects of these contaminants and found them to be small, as shown in Fig. 4. The agreement between the calculated and experimental data in Fig. 4 is quite satisfactory. Armstrong and Chandler<sup>33</sup> have obtained similar good agreement between calculated and experimental cell-survival probabilities for the case of a thin sample of T-1 kidney cells exposed to 14-MeV neutrons. Comparisons between calculated and experimental cell-survival probabilities are a much more stringent test



of the calculations than are comparisons between calculated and experimental absorbed doses because the heavier highly ionizing particles contribute very appreciably to the cell-survival probabilities, while they contribute only a small fraction of the absorbed doses.

#### Comparison of Calculated Results for Photons, Negatively Charged Pions, Neutrons, Protons, and Alpha Particles Incident on a Tissue Phantom.<sup>40</sup>

Calculated results are presented and compared for <sup>60</sup>Co photons, 15-MeV neutrons, neutrons from 35-MeV <sup>2</sup>H on Be, negatively charged pions, protons, and alpha particles. For each type of particle, the beam parameters have been chosen to be approximately those appropriate for the single-port irradiation of a small cylindrical volume centered about a depth of 15 cm in a 30-cm tissue slab. For both photons and neutrons, a point source at a "source-to-skin" distance,  $d_s$ , is assumed. For <sup>60</sup>Co photons,  $d_s = 80$  cm was used since this is a distance often used in clinical situations. In the case of 15-MeV neutrons which will be produced by D-T reactions, there will, with presently available sources, be an intensity problem, and a  $d_s$  of 100 cm is thought to be representative of the value that will be used clinically.<sup>41</sup> For neutrons from 35-MeV <sup>2</sup>H on Be,  $d_s = 125$  cm was used since this is the value often used with this neutron spectrum at the Naval Research Laboratory.<sup>42</sup> Both photons and neutrons were assumed to be emitted isotropically in a solid-angle interval defined by the polar angle  $\theta_s$  where the tangent of the angle  $\theta_s$  is defined to be

$$\tan \theta_s = \frac{1 \text{ cm}}{d_s + 15 \text{ cm}} .$$

For polar angles greater than  $\theta_s$ , all of the particles emitted by the sources are assumed to be completely removed by a collimator. The energy distribution of neutrons used in the calculations to represent the neutron spectrum produced by 35-MeV <sup>2</sup>H on Be is taken from the measurements of Theus *et al.*<sup>43</sup>

In the case of pions, protons, and alpha particles, the incident particles are assumed to be normally incident on the phantom. The incident beams in all cases are taken to be uniform over a circular area of 1 cm in radius and to be zero outside of this area. This is important because the results indicate that for negatively charged pions a 1-cm-radius beam may not be the optimum choice for irradiating a region of 1 cm in radius at a depth of 15 cm in the phantom. It is assumed that the incident charged-particle beams are free of contamination. This is particularly significant because the negatively charged pion beams that will be used in radiotherapy will be contaminated to some extent by both electrons and negatively charged muons, but since these beams are not yet available, the extent to which they will be contaminated is not known. The energy distributions of the incident proton, alpha-particle, and pion beams were determined to be those that would produce approximately a uniform absorbed dose over the region of 14-16 cm in the tissue phantom. The energy distributions used in the calculations are given in Ref. 40.

Cell-survival probabilities for both aerobic and anoxic T-1 kidney cells, averaged over the radial interval of 0-1 cm and the depth interval of 14-16 cm, are shown in Fig. 5 as a function of local dose for all of the incident particles considered. The abscissa in the figure is labeled "local absorbed dose" to emphasize that the curves give the cell-survival probabilities when the dose values, averaged over the indicated spatial intervals, are the same for all incident-particle types. For both aerobic and anoxic conditions,

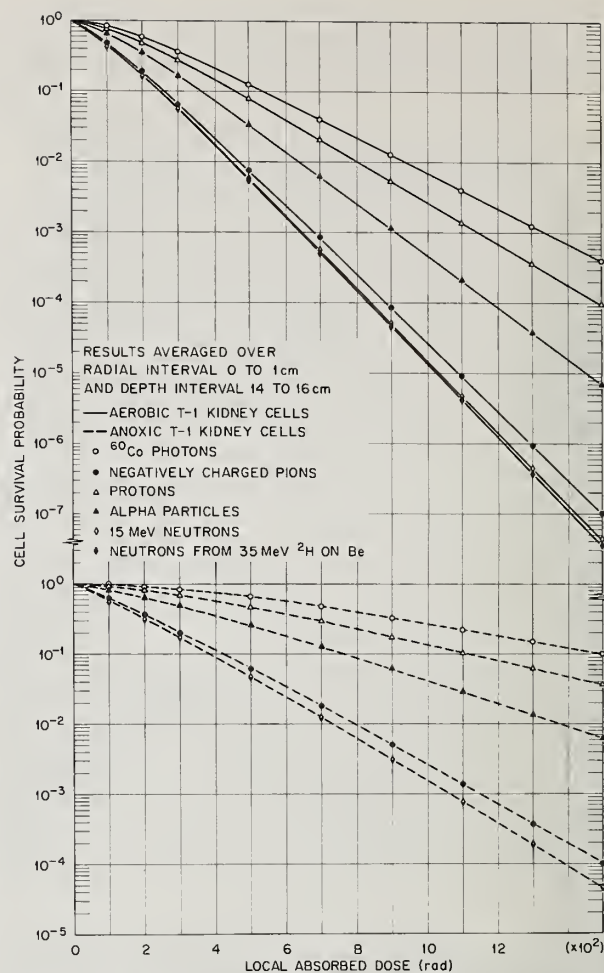


FIG. 5. Cell-survival probabilities for aerobic and anoxic T-1 kidney cells vs local absorbed dose for various incident particles. The results are averaged over the indicated spatial intervals. In the anoxic results, the two incident neutron beams give the same cell-survival probability, so only one curve appears for these particles.

the cell-survival-probability curves in Fig. 5 are very different for the various types of incident particles. The relative biological effectiveness, RBE, is a way of expressing the difference between the cell-survival-probability curve for a given type of incident particle and that for photons, and is defined to be the ratio of the absorbed dose due to photons that will produce a given cell-survival probability to the absorbed dose due to any other type of incident particle that will produce the same cell-survival probability. The RBE is a function of cell type, the cell-survival probability considered, the irradiation conditions considered (i.e., aerobic or anoxic), and varies as a function of position in the phantom.

For each type of particle considered, the cell-survival probability in Fig. 5 at a given dose is larger under anoxic conditions than under aerobic conditions; i.e., for a given type of irradiation and at a given dose level, well-oxygenated cells are more susceptible to damage than are poorly oxygenated cells. This effect is termed the "oxygen effect" and is usually expressed quantitatively as the oxygen enhancement ratio (OER)



which is defined for a given type of irradiation to be the ratio of the absorbed dose required to produce a given cell-survival probability under anoxic conditions to the absorbed dose required to produce the same cell-survival probability under aerobic conditions. The OER is a function of cell type, the cell-survival probability level considered, and varies as a function of position in the phantom.

From the curves in Fig. 5 and from similar curves for other spatial intervals, RBE and OER values may be obtained. RBE and OER values for all of the particle types considered here are given for various spatial intervals in Table I. The RBE for photons is, by definition, always unity. In the depth interval of 0-13 cm

TABLE I  
RBE and OER Values at 10% Survival Level for T-1 Kidney Cells  
Averaged Over the Indicated Spatial Intervals for  
Various Incident Particles

Depth Interval (cm)	Radial Interval = 0 - 1.0 cm					
	Negatively Charged Pions	Protons	Alpha Particles	15-MeV Neutrons	Neutrons from 35-MeV <sup>2</sup> H on Be	Photons
RBE for Aerobic Cells						
0 - 13	1.1	1.0	1.1	2.1	2.3	1.0
14 - 16	2.0	1.2	1.5	2.2	2.2	1.0
17 - 30	1.8	1.3	1.8	2.2	2.1	1.0
RBE for Anoxic Cells						
14 - 16	3.4	1.3	1.9	3.8	3.8	1.0
OER						
14 - 16	1.6	2.4	2.1	1.6	1.6	2.7

and the radial interval of 0-1 cm for aerobic cells, the RBE for charged particles is unity or only slightly greater than unity, while the RBE for neutrons is considerably larger than unity. In the depth interval of 14-16 cm and the radial interval of 0-1 cm, i.e., in the "irradiation volume," for both aerobic and anoxic conditions, the RBE for incident pions and neutrons is larger than is the RBE for incident protons and alpha particles, and the OER for incident pions and neutrons is smaller than is the OER for incident protons and alpha particles. For the two incident neutron spectra considered, the RBEs and OERs are approximately the same in the depth and radial intervals shown in the table.

In considering the results presented here, it must be understood that they are dependent on the irradiation conditions; i.e., the beam parameter, the volume to be irradiated, etc., and thus the comparisons cannot be assumed to be valid under other conditions. The cell-inactivation results presented are for a particular cell line, T-1 kidney cells, and since the response of cells to radiation is dependent on cell type, different results from those presented here might be obtained with a different cell line. Furthermore, the response of cells *in vivo* is influenced by many complex factors which are not taken into account in obtaining the results presented here, and therefore the results cannot in any quantitative way be applied directly to clinical radiotherapy.

#### Heavy-Ion Transport Calculations

Heavy-ion beams of sufficiently high energy to be of interest in radiotherapy, i.e., heavy-ion beams which have a range  $\sim 15$  g  $\text{cm}^{-2}$  in tissue, have been available for only a very short time, and, therefore, the experimental information concerning the nuclear reaction of such ions and the physical and biological effects of such beams is limited.<sup>44-46</sup> Nevertheless, calculated results based on the available nuclear-

reaction information have been obtained by several investigators<sup>47-49</sup> and have been shown to be in good agreement with experimentally measured absorbed-dose data<sup>48</sup> and cell-survival probabilities.<sup>49</sup>

In Fig. 6 a comparison between calculated and experimental absorbed-dose data is presented for 233-MeV/nucleon oxygen ions incident on water.<sup>46,48</sup> The calculated results include an estimate of the energy deposition by nuclear-reaction products as well as of the energy deposition by the primary ions. In the calculations, a collision mean free path of 19.4 cm, as measured by Maccabee and Ritter,<sup>46</sup> was assumed. The

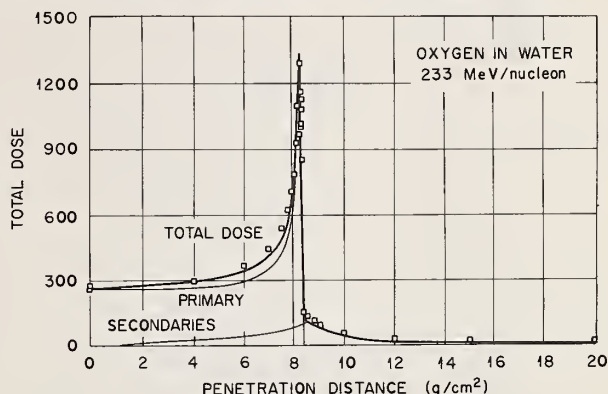


FIG. 6. Depth-dose curves for a 233-MeV/nucleon oxygen-ion beam in water. (The ordinate is normalized to the average LET per unit incident-particle fluence in  $\text{MeV cm}^2/\text{g}$ , so that the dose in rads can be obtained by multiplication of an ordinate value by the actual incident fluence in  $\text{No./cm}^2$  and the conversion factor  $1.60 \times 10^{-8}$  g rads/MeV.) (This figure is reprinted from Ref. 46 with permission.)

nuclear-reaction products which are transported are assumed to be emitted in the same direction and to have the same velocity as the incident ion making the collision. The fragmentation parameters, i.e., the probabilities that a particle of a given type be emitted from a nonelastic collision, were taken to be 0.21 for C, 0.21 for N, 0.07 for B, 0.07 for Be, 0.07 for Li, 0.19 for He, and 0.19 for H. The probabilities for N, C, and B were taken from the experimental work of Maccabee and Ritter<sup>46</sup> and the other probabilities were obtained by fitting the experimental absorbed-dose data in Fig. 6. In addition to the nuclear-reaction products that are transported, it was assumed in the calculations that at each collision 30 MeV is deposited locally. The agreement between the calculated and experimental data is quite good. The nuclear-reaction products contribute only a small amount to the absorbed dose at depths which are less than the range of the incident ions.

In Fig. 7 comparisons are given between calculated and experimental cell-survival probabilities for 278-MeV/nucleon nitrogen ions incident on polyethylene.<sup>49</sup> Results are given for two different incident-particle currents. The assumptions in the calculations are similar to those discussed above, but the fragmentation parameters were derived from cosmic-ray data and Monte Carlo methods were used. The cell-survival calculations were carried out using the cell-inactivation model of Katz *et al.*<sup>34,35</sup> The calculated results were obtained using survival parameters for T-1 kidney cells, while the experiment was performed with Chinese hamster M3-1 cells, but this difference is not thought to have any appreciable effect on the comparisons. The calculated and experimental results are in reasonable agreement at

all depths.

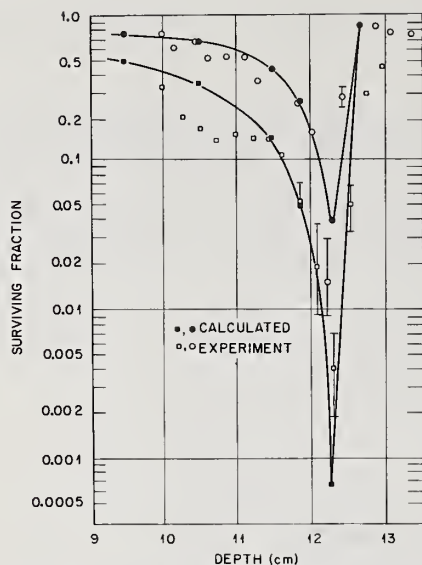


FIG. 7. Comparison of predicted cell-survival profiles for exposure to  $2.2 \times 10^7$  nitrogen ions per square centimeter (solid circles) and  $4.5 \times 10^7$  nitrogen ions per square centimeter (solid squares) with experimentally determined survival profiles for the same incident exposures (open circles and squares). (This figure is reprinted from Ref. 49 with permission.)

\*This research was funded by the Energy Research and Development Administration under contract with the Union Carbide Corporation.

<sup>1</sup>Proc. Conf. on Particle Accelerators in Radiation Therapy, October 2-5, 1972, Los Alamos Scientific Laboratory, Los Alamos, New Mexico, LA-5180-C, 1973.

<sup>2</sup>M. P. Guthrie, R. G. Alsmiller, Jr., and H. W. Bertini, Nucl. Instr. Meth. **66**, 29 (1968); with erratum, Nucl. Instr. Meth. **91**, 669 (1971).

<sup>3</sup>O. Ozer and D. Garber, National Cross Section Center, BNL Report No. BNL-17541, 1973.

<sup>4</sup>R. W. Roussin, Radiation Shielding Information Center, ORNL Report No. ORNL-RSIC-34, Vol. 1, 1972.

<sup>5</sup>Wilmot N. Hess, Rev. Mod. Phys. **30**, 368 (1958).

<sup>6</sup>Hugo W. Bertini, Phys. Rev. **131**, 1801 (1963); with erratum, Phys. Rev. **138**, AB2 (1965).

<sup>7</sup>V. S. Barashenkov, Interaction Cross Sections of Elementary Particles, 1966, Israel Program for Scientific Translation, Jerusalem, 1968.

<sup>8</sup>F. D. Becchetti, Jr. and G. W. Greenlees, Phys. Rev. **182**, 1190 (1969).

<sup>9</sup>C. M. Perey and F. G. Perey, Atomic Data and Nuclear Data Tables **13**, 293 (1974).

<sup>10</sup>H. W. Bertini, M. P. Guthrie, and O. W. Hermann, ORNL Report No. ORNL-4564, 1971.

<sup>11</sup>H. W. Bertini, ORNL Report No. ORNL-3383, 1963.

<sup>12</sup>H. W. Bertini, Phys. Rev. **188**, 1711 (1969).

<sup>13</sup>H. W. Bertini, Phys. Rev. C **6**, 631 (1972).

<sup>14</sup>T. A. Gabriel, R. T. Santoro, and R. G. Alsmiller, Jr., Nucl. Sci. Eng. **44**, 104 (1971).

<sup>15</sup>H. W. Bertini *et al.*, ORNL Report No. ORNL-TM-4134, 1974.

<sup>16</sup>H. W. Bertini, T. A. Gabriel, and R. T. Santoro, Phys. Rev. C **9**, 522 (1974).

<sup>17</sup>R. G. Alsmiller, Jr. and O. W. Hermann, Nucl. Sci. Eng. **40**, 254 (1970).

<sup>18</sup>Hugo W. Bertini, Phys. Rev. C **5**, 2118 (1972).

<sup>19</sup>F. E. Bertrand and R. W. Peelle, Phys. Rev. C **8**, 1045 (1973).

<sup>20</sup>P. H. Fowler, Proc. Phys. Soc. **85**, 1051 (1965).

<sup>21</sup>P. H. Fowler and V. M. Mayes, Proc. Phys. Soc. **92**, 377 (1961).

<sup>22</sup>T. W. Armstrong and K. C. Chandler, Nucl. Instr. Meth. **118**, 515 (1972).

<sup>23</sup>W. A. Coleman and T. W. Armstrong, ORNL Report No. ORNL-4606, 1970.

<sup>24</sup>K. C. Chandler and T. W. Armstrong, ORNL Report No. ORNL-4744, 1972.

<sup>25</sup>R. G. Alsmiller, Jr., T. W. Armstrong, and W. A. Coleman, Nucl. Sci. Eng. **42**, 367 (1970).

<sup>26</sup>T. W. Armstrong, R. G. Alsmiller, Jr., K. C. Chandler, and B. L. Bishop, Nucl. Sci. Eng. **49**, 82 (1972).

<sup>27</sup>T. W. Armstrong, K. C. Chandler, and J. Barish, J. Geophys. Res. **78**, 2715 (1973).

<sup>28</sup>R. T. Santoro, R. G. Alsmiller, Jr., and K. C. Chandler, Nucl. Sci. Eng. **52**, 124 (1973).

<sup>29</sup>T. W. Armstrong, R. G. Alsmiller, Jr., and K. C. Chandler, Phys. Med. Biol. **18**, 830 (1973).

<sup>30</sup>T. W. Armstrong and B. L. Bishop, Radiat. Res. **47**, 581 (1971).

<sup>31</sup>T. W. Armstrong and K. C. Chandler, Radiat. Res. **52**, 247 (1972).

<sup>32</sup>R. G. Alsmiller, Jr. and J. Barish, Med. Phys. **1**, 51 (1974); with erratum to be published.

<sup>33</sup>T. W. Armstrong and K. C. Chandler, Radiat. Res. **58**, 293 (1974).

<sup>34</sup>R. Katz, S. C. Sharma, and M. Homayoonfar, Chap. 6 in Topics in Radiation Dosimetry, Suppl. 1 to Radiation Dosimetry, edited by Frank A. Attix (Academic, New York, 1972).

<sup>35</sup>Robert Katz and S. C. Sharma, Nucl. Instr. Meth. **111**, 93 (1973).

- <sup>36</sup>J. E. Turner *et al.*, Proc. Intl. Congress on Protection Against Accelerator and Space Radiation, Vol. 1, p. 231, April 26-30, 1971, CERN, Geneva, Switzerland, CERN 71-16.
- <sup>37</sup>Harold L. Beck, USAEC Health and Safety Laboratory Report No. HASL-213, 1969.
- <sup>38</sup>J. E. Turner *et al.*, Radiat. Res. 52, 229 (1972).
- <sup>39</sup>M. R. Raju *et al.*, Brit. J. Radiol. 45, 178 (1972).
- <sup>40</sup>R. G. Alsmiller, Jr., *et al.*, Radiat. Res. 60, 369 (1974).
- <sup>41</sup>Proc. of Workshop on High Intensity Neutron Generators, June 17, 1972, USAEC Nevada Operations Office, Las Vegas, Nev.
- <sup>42</sup>Middle Atlantic Neutron Therapy Association (MANTA) Progress Report, subm. by C. C. Rogers, M.D., Virginia Commonwealth University, Medical College of Virginia, Richmond, Va., 1973.
- <sup>43</sup>R. B. Theus *et al.*, Appendix v of Middle Atlantic Neutron Therapy Association (MANTA) Progress Report, subm. by C. C. Rogers, M.D., Virginia Commonwealth University, Medical College of Virginia, Richmond, Va., 1973.
- <sup>44</sup>"Heavy Ion Acceleration," Science 174, 1121 (1971).
- <sup>45</sup>H. H. Heckman *et al.*, Phys. Rev. Letters 28, 926 (1972).
- <sup>46</sup>H. D. Maccabee and M. A. Ritter, Radiat. Res. 60, 409 (1974).
- <sup>47</sup>S. B. Curtis, W. R. Doherty, and M. C. Wilkinson, National Aeronautics and Space Administration Report No. NASA CR-1469, 1969.
- <sup>48</sup>J. T. Lyman, Lawrence Berkeley Laboratory, as quoted by Maccabee and Ritter.<sup>46</sup>
- <sup>49</sup>K. G. Vosburgh, Science 174, 1125 (1971).



Robert C. Reedy

University of California, Los Alamos Scientific Laboratory  
Los Alamos, New Mexico 87544

Chemical compositions of the surfaces of the moon and certain planetary bodies can be determined by orbital  $\gamma$ -ray spectroscopy. The major sources of  $\gamma$ -ray lines (and of radionuclides) in the moon are the decay of the primordial radioelements (U, Th, and  $^{40}\text{K}$ ) and nuclear reactions induced by the bombardment of the moon by cosmic-ray particles. The major cosmogenic  $\gamma$ -ray lines are produced by neutron nonelastic scattering and neutron capture reactions. The fluxes of  $\gamma$ -ray lines expected from the moon for each major source have been calculated. Gamma-rays from the moon were measured by  $\gamma$ -ray spectrometers during the Apollo 15 and 16 missions. The preliminary analysis of the data show that O and Si vary little over the moon's surface, that Mg, Fe, and Ti have higher concentrations in the maria than in the lunar highlands, and that the radioelements are significantly more abundant in and near the western nearside maria than in the rest of the moon.

(Lunar  $\gamma$ -rays; lunar chemistry; radioelements; cosmic-ray reactions; non-elastic scattering; neutron capture)

### Introduction

The exploration of the solar system has progressed considerably in recent years and will continue actively in the future. Although ground-based observations and terrestrial research have contributed to recent advances, information obtained from spacecraft missions to the moon, Venus, Mars, Mercury, and Jupiter has increased significantly our knowledge about planetary bodies. The age of space exploration has expanded the number of fields active in solar system research to a wide range of disciplines. Nuclear techniques are frequently used and have played an important role in remote determinations of the chemical composition of the moon, i.e., the gamma-ray spectrometers in lunar orbit on Apollo 15 and 16<sup>1</sup> and on Luna 10<sup>2</sup> and the alpha-particle back-scatter experiments on Surveyor spacecraft.<sup>3</sup> This paper discusses the use of gamma-ray spectroscopy in mapping the chemistry of the surface features of certain planetary bodies.

### Cosmic-Ray Reactions in the Moon

All bodies in the solar system are bombarded by energetic cosmic-ray particles. If a planetary body does not have a thick atmosphere or a strong magnetic field, the cosmic-ray particles penetrate the body's surface and produce gamma rays which can escape and be observed by orbital gamma-ray spectrometers. The measured intensities of certain gamma-ray lines can be used to infer the abundances of various elements in the surface layers of the planet. In addition to the moon, such measurements could be used to determine the chemical composition of Mars, Mercury, an asteroid, or a planetary satellite.

The primary cosmic-ray particles in the vicinity of the earth have been measured by numerous satellite experiments. There are two main types of energetic cosmic rays: the galactic cosmic rays (GCR), high-energy particles (energies of the order of GeV) from outside the solar system whose intensities vary only slowly over a solar cycle, and the solar cosmic rays (SCR), energetic particles (energies of the order of MeV) which are emitted irregularly from the sun during certain solar flares. Most of the GCR particles incident on the earth interact in the atmosphere. The earth's magnetic field shields the earth from most of the solar cosmic rays (except at the magnetic poles).

### Radionuclides Produced in the Moon

Much of our present knowledge about the interactions of cosmic rays with planets having negligible atmospheres and magnetic fields comes from measurements of radionuclides in returned lunar samples. Table 1 lists most of the radionuclides observed in lunar

samples and the major reactions which produce them. The types of reactions producing radionuclides include high-energy spallation reactions, low-energy threshold reactions induced by protons, neutrons, and alpha-particles, and neutron-capture reactions. A detailed discussion of the production of radionuclides in the moon is given by Reedy and Arnold.<sup>4</sup> Measurements of activities as a function of depth in the moon have been reported by Finkel et al.<sup>5</sup> for several SCR-produced radionuclides and by Imamura et al.<sup>6</sup> and Wahlen et al.<sup>7</sup> for a couple of GCR-produced radionuclides. The activity of SCR-produced radionuclides decreases rapidly with depth in the moon. The reactions are induced by the "primary" protons or alpha particles before they are stopped by ionization energy losses in the moon. The GCR-produced radionuclides are made to depths of

TABLE 1  
RADIONUCLIDES MEASURED IN LUNAR SAMPLES

Nuclide	Important Reactions
$^3\text{H}$ , $^7\text{Be}$ , $^{10}\text{Be}$ , $^{14}\text{C}$	$0(p, X)$
$^{22}\text{Na}$	$\text{Mg}(p, X)$ , $\text{Al}(p, X)$ , $\text{Si}(p, X)$
$^{26}\text{Al}$	$^{27}\text{Al}(p, pn)$ , $^{27}\text{Al}(n, 2n)$ , $\text{Si}(p, X)$
$^{36}\text{Cl}$	$\text{Ca}(p, X)$ , $\text{Fe}(p, X)$
$^{37}\text{Ar}$	$^{40}\text{Ca}(n, \alpha)$
$^{39}\text{Ar}$	$^{40}\text{Ca}(n, 2p)$ , $^{39}\text{K}(n, p)$
$^{44}\text{Ti}$	$\text{Fe}(p, X)$
$^{46}\text{Sc}$	$\text{Ti}(n, pxn)$ , $\text{Fe}(p, X)$
$^{48}\text{V}$	$^{48}\text{Ti}(p, n)$ , $\text{Fe}(p, X)$
$^{53}\text{Mn}$	$^{56}\text{Fe}(p, \alpha)$ , $\text{Fe}(p, X)$
$^{54}\text{Mn}$	$\text{Fe}(p, X)$ , $^{54}\text{Fe}(n, p)$
$^{55}\text{Fe}$	$^{56}\text{Fe}(n, 2n)$ , $^{56}\text{Fe}(p, pn)$ , $^{54}\text{Fe}(n, \gamma)$
$^{56}\text{Co}$	$^{56}\text{Fe}(p, n)$
$^{58}\text{Co}$	$^{56}\text{Fe}(\alpha, pn)$ , $^{58}\text{Fe}(p, n)$
$^{59}\text{Ni}$	$^{56}\text{Fe}(\alpha, n)$ , $^{58}\text{Ni}(n, \gamma)$
$^{60}\text{Co}$	$^{59}\text{Co}(n, \gamma)$
$^{81}\text{Kr}$	$\text{Sr}(p, X)$ , $\text{Zr}(p, X)$

TABLE 2  
CHEMISTRIES OF RETURNED LUNAR SOILS  
MAJOR ELEMENTS (WEIGHT PERCENT)

Element	Average Moon	Apollo 11 E. Mare	Apollo 12 W. Mare	Apollo 14 "KREEP"	Apollo 16 Highland	Chondrite (Meteorite)
O	42.5	41.6	42.6	44.2	45.0	35.0
Mg	5	4.6	6.3	5.6	3.3	14.4
Al	10	7.1	6.8	9.2	14.4	1.3
Si	21	20.0	21.4	22.5	21.1	18.0
Ca	9	8.6	7.2	7.6	11.2	1.4
Ti	1.5	4.6	1.7	1.0	0.34	0.08
Fe	10	12.3	12.0	8.0	4.0	25
Σ (major)	99.0	98.8	98.0	98.1	99.34	95.18
Natural Radioelements (ppm)						
K	1200	1150	1800	4300	960	860
Th	2.0	2.1	8	14	2.1	0.04
U	0.5	0.55	2	4	0.58	0.013

MINOR AND IMPORTANT TRACE ELEMENTS (ppm)

Element	Apollo 11 E. Mare	Apollo 12 W. Mare	Apollo 14 "KREEP"	Apollo 16 Highland	Chondrite (Meteorite)
Na	3200	3200	4700	3500	6800
P	600	1200	2100	500	1000
S	1000	800	1000	600	23000
Cr	1950	2900	1300	750	2500
Mn	1600	1700	1000	540	2600
Ni	240	160	400	450	13000
Sr	170	200	190	180	10
Zr	320	500	800	170	30
Ba	170	300	1000	130	5
Sm	14	20	27	6	0.23
Gd	17	22	35	7	0.34

several meters. Most GCR reactions are induced by secondary neutrons, since about 10 neutrons are produced by each incident GCR particle.

#### Lunar Chemical Compositions

The chemical compositions of some of the soils returned by various Apollo missions are given in Table 2. Volatile elements, such as the rare gases, hydrogen, and water, are extremely rare in the returned lunar samples. There are three main chemical systems which have been observed in lunar samples. The mare regions (Apollo 11 and 12) are composed mainly of basaltic rocks and fragments which have high abundances of iron and titanium. The lunar highlands (Apollo 16) are made of "anorthositic" fragments with high concentrations of aluminum and calcium. The soils of the Apollo landing sites in the western part of the lunar nearside (Apollo 14) have considerable amounts of a trace-element rich component dubbed "KREEP" (K-potassium, Rare Earth Element, and Phosphorous). The approximate average composition of the lunar surface is also given in Table 2 and will be used below in discussing the gamma-ray fluxes expected from the moon. The ordinary chondrite, a common class of meteorite, represents a chemical composition not yet encountered on the moon, but which could be an asteroidal or planetary surface composition.

#### Calculated Lunar Gamma-Ray Line Fluxes

The main sources of gamma-ray lines from the moon are the decay of the natural radioelements (K, Th, and U), prompt neutron-induced reactions (nonelastic scattering and neutron capture), and the decay of GCR- and SCR-produced radionuclides. The flux expected for each gamma-ray line from the lunar surface was calculated by integrating over depth the product of the source term for the line and the probability that the photon would escape from the moon without undergoing an interaction. The source term for gamma-ray lines resulting from the

decay of natural radionuclides is the yield of the line per disintegration of the parent nucleus ( $^{40}\text{K}$ ,  $^{232}\text{Th}$ , or  $^{238}\text{U}$ ) times the disintegration rate of the parent. The major lines from the decay of natural radioelements are given in Table 3. For lines which result from cosmic-ray interactions, the source term is the rate for the production of that line. For threshold reactions, the production rate is calculated by integrating over energy the product of the differential flux of particles and the excitation function for the reaction.<sup>4</sup> For neutron-capture reactions, the results of a neutron-transport calculation by Lingenfelter et al.<sup>8</sup> for the moon were used to obtain the source terms. The details of the flux calculations are discussed by Reedy et al.<sup>9</sup>

#### SCR-Induced Radioactivity

Because solar flares which produce large fluxes of energetic SCR particles occur only a few times a year during the solar maximum part of a solar cycle and almost never occur during the solar minimum periods, only those lines which result from the decay of relatively long-lived radionuclides (half-lives of about a month or more) need be considered. During an SCR event, the high intensity of energetic charged particles would saturate an actual detector system and make the detection of gamma rays almost impossible. A mission shortly after a large solar flare would observe SCR-produced radionuclides with half-lives as short as the time elapsed since the flare (e.g., 16-day  $^{48}\text{V}$ ). The dominant gamma-ray-emitting radionuclides produced by solar particles in the moon are  $^{22}\text{Na}$ ,  $^{26}\text{Al}$ ,  $^{54}\text{Mn}$ , and  $^{56}\text{Co}$  (the last two would be observed mainly during periods of solar maximum). Usually the strongest SCR-induced line is the 1.809 MeV line from  $^{26}\text{Al}$  (153



TABLE 3  
MAJOR  $\gamma$ -RAY LINES FROM THE DECAY OF  
NATURAL RADIOELEMENTS  
(Average Lunar Composition)

Parent Element	Source	$E_{\gamma}$ (MeV)	Photons/ ( $m^2$ sec)
K	$^{40}K$	1.461	413
Th	$^{208}Tl$	2.614	382
Th	$^{228}Ac$	1.593	37
Th	$^{228}Ac$	0.967	131
Th	$^{212}Ac$	0.911	146
Th	$^{212}Bi$	0.727	40
Th	$^{208}Tl$	0.583	161
U	$^{214}Bi$	2.204	37
U	$^{214}Bi$	1.764	113
U	$^{214}Bi$	1.120	90
U	$^{214}Bi$	0.609	188

photons/ $m^2$  sec for an average lunar surface composition).

#### Neutron Capture

For a  $1\text{ cm}^2$  column in the moon, there are about 17 neutrons produced by GCR particles. Most of the neutrons are produced by evaporation from excited nuclei, ( $\pi, n$ ) reactions, and knock-on reactions.<sup>8</sup> A large number of these neutrons escape from the moon or are nonelastically scattered. Many neutrons are slowed sufficiently that they can only elastically scatter or be captured by ( $n, \gamma$ ) reactions. The moon is a relatively poor moderator for neutrons, being composed mainly of silicate minerals which have very little hydrogen. The neutron energy spectrum from 1 eV to almost 1 MeV is a power law with the approximate shape  $E^{-0.9}$ . Below 1 eV the neutron spectrum is sensitive to the temperature (which varies considerably between lunar day and night) and the macroscopic cross section for the medium.<sup>8</sup> These variations in spectral shape affect only those nuclei whose neutron-capture excitation functions differ significantly from "1/v" below 1 eV, such as  $^{157}Gd$ , which has a large resonance at 0.03 eV.

TABLE 4  
MAJOR NEUTRON CAPTURE  $\gamma$ -RAY LINES  
(Average Lunar Composition)

Source	$E_{\gamma}$ (MeV)	Yield/ Capture	Photons/ ( $m^2$ sec)
$^{27}Al(n, \gamma)$	7.724	0.30	39
$Al(n, \gamma)^{28}Al$	1.779	1.00	47
$^{28}Si(n, \gamma)$	4.934	0.61	95
$^{28}Si(n, \gamma)$	3.540	0.66	81
$^{40}Ca(n, \gamma)$	6.420	0.36	49
$^{40}Ca(n, \gamma)$	1.943	0.80	46
$^{48}Ti(n, \gamma)$	6.761	0.40	108
$^{48}Ti(n, \gamma)$	6.418	0.28	73
$^{48}Ti(n, \gamma)$	1.382	0.82	70
$^{56}Fe(n, \gamma)$	7.645	0.22	150
$^{56}Fe(n, \gamma)$	7.631	0.24	163
$^{56}Fe(n, \gamma)$	6.019	0.08	48
$^{56}Fe(n, \gamma)$	5.921	0.08	48

For a "1/v" capturing nucleus, about 80% of the neutron captures occur at energies below 3 eV. The fluxes for gamma-ray lines resulting from neutron capture are given in Table 4 for an average lunar surface composition. Thermal neutron-capture gamma-ray yields are used for the elements whose neutron-capture excitation functions are approximately "1/v". Since the major elements are roughly "1/v", thermal gamma-ray yields are sufficient. However, gamma-ray yields for capture by resonances are important for certain minor elements (such as cobalt).

#### GCR-Induced Reactions

Several strong gamma-ray lines are produced by the decay of GCR-produced radionuclides. The more intense lines usually result from low energy reactions which produce short-lived isotopes, such as  $^{16}O(n, p)^{16}N$  and  $^{27}Al(n, \alpha)^{24}Na$ , although the gamma rays from the decay of the GCR-produced isotopes  $^{22}Na$  and  $^{26}Al$  are fairly strong. Since the cross sections for inelastic-scattering reactions are generally higher than those for other threshold reactions, prompt lines from ( $n, ny$ ) reactions are usually the most intense lines from the moon. In several cases ( $n, xy$ ) reactions where x is not a neutron can produce strong lines (e.g.,  $^{16}O(n, \alpha\gamma)^{13}C$  and  $^{40}Ca(n, p\gamma)^{40}K$ ). Since oxygen is the most abundant element in the moon (and the least interesting since its abundance varies by less than 10% in the lunar surface), it produces many strong gamma-ray lines.

Other intense lines result from  $2^+$  to  $0^+$  transitions in the even-even isotopes of the major elements (i.e.,  $^{24}Mg$ ,  $^{28}Si$ , and  $^{56}Fe$ ). The isotopes  $^{40}Ca$  and  $^{27}Al$  do not have any very intense lines, but have several major lines with about the same intensities. The nonelastic-scattering lines of titanium are relatively weak (compared to similar lines for the other major elements) because of its usually low abundance. (Titanium abundances are determined by measuring its neutron-capture lines.) The major GCR-produced lines for the major elements in the moon are listed in Table 5.

Excitation functions from threshold to about 20 MeV are needed for most ( $n, xy$ ) reactions for the major elements and for strong ( $n, xy$ ) lines for minor elements. Fairly good data exist for oxygen, aluminum, and iron at these energies and some data exist for the other major elements. Excitation functions generally are not available for such reactions with the minor lunar elements. A limitation to the calculation of the fluxes for ( $n, xy$ ) lines is that the differential flux of neutrons in the moon is not very well known for these energies. However, the relative fluxes of the lines can be well determined and are important in unfolding the experimental gamma-ray spectra.

#### Elemental Detection Sensitivities

The gamma-ray flux calculations indicate that there are good strong lines with which to determine the concentrations of the elements potassium, thorium, oxygen, silicon, and iron and fairly good lines for uranium, magnesium, and titanium. There are not strong lines for aluminum or calcium, although they have lines which could be resolved by solid-state gamma-ray spectrometers. These lines would also be expected from other planetary bodies such as Mars and Mercury. For Mars (and possibly comets and certain asteroids) the hydrogen neutron-capture line and the inelastic-scattering line from carbon could be observable. For a planetary object with a chondritic composition (cf. Table 2), gamma-ray lines from nickel and sulfur could be detectable.



TABLE 5  
MAJOR GCR-PRODUCED  $\gamma$ -RAY LINES VIA NONELASTIC  
SCATTERING AND RADIONUCLIDE DECAY  
(Average Lunar Composition)

Source	$E_\gamma$ (MeV)	Photons/(m <sup>2</sup> sec)
<sup>16</sup> O(n,n $\gamma$ )	7.117	160
<sup>16</sup> O(n,n $\gamma$ )	6.917	135
<sup>16</sup> O(n,n $\gamma$ )	6.129	415
<sup>16</sup> O(n,p) <sup>16</sup> N	6.129	45
<sup>16</sup> O(n,n $\alpha\gamma$ )	4.433	75
<sup>16</sup> O(n, $\alpha\gamma$ )	3.684	95
<sup>16</sup> O(n,n $\gamma$ )	2.743	78
<sup>22</sup> Na	1.275	56
<sup>24</sup> Na	2.754	107
<sup>24</sup> Na	1.369	72
<sup>24</sup> Mg(n,n $\gamma$ )	1.369	141
<sup>27</sup> Al(n,n $\gamma$ )	2.210	101
<sup>27</sup> Al(n,n $\gamma$ )	1.013	94
<sup>26</sup> Al	1.809	98
<sup>28</sup> Si(n,n $\gamma$ )	2.835	47
<sup>28</sup> Si(n,n $\gamma$ )	1.779	464
<sup>28</sup> Si(n,p) <sup>28</sup> Al	1.779	127
<sup>40</sup> Ca(n,n $\gamma$ )	3.737	38
<sup>56</sup> Fe(n,n $\gamma$ )	1.238	50
<sup>56</sup> Fe(n,n $\gamma$ )	0.847	207

#### Apollo Gamma-Ray Experiment

Gamma rays from the moon were measured during the Apollo 15 and 16 missions using a 7.0 cm by 7.0 cm

NaI(Tl) crystal and associated electronics.<sup>10</sup> The instrument was mounted at the end of a boom and was deployed 7.6 m from the Apollo Service Module during normal operation. The Command-Service Module was in a circular orbit about 100 km above the lunar surface. The lunar surface resolution of the experiment was about 100 km. During the return trips to the earth, cosmic gamma-ray fluxes<sup>11</sup> and various backgrounds from the instrument and spacecraft<sup>12</sup> were determined. Other investigators for this experiment include J. R. Arnold and L. E. Peterson, University of California at San Diego, J. I. Trombka, Goddard Space Flight Center, and A. E. Metzger, Jet Propulsion Laboratory.

A spectrum obtained from the Apollo 16 mission over the western maria is shown in Fig. 1. Spectra were also accumulated for other lunar regions. Preliminary unfolding of these spectra indicated that almost all of the variation of the count rate for the energy interval of 0.55 to 2.75 MeV was due to the decay of the natural radioelements. These counting-rate results (reported by Metzger et al.<sup>1</sup>) showed that the lunar highlands and the far side (except for the region around the crater Van de Graaff) are low in natural radioactivity and that the western maria have the highest concentrations of the naturally radioactive elements.

#### Spectrum Unfolding

The gamma-ray spectra accumulated over various lunar regions were first processed by subtracting the contributions of the cosmic gamma-ray fluxes and of gamma-rays from the spacecraft and the instrument from the total pulse-height spectra. Most of the gamma rays escaping from the moon are continua produced by various scattering and other mechanisms (e.g.,  $\pi^0$  decay or bremsstrahlung) in the moon. Only the detector response to the major gamma-ray lines which escape from the moon without undergoing interactions were used in the unfolding of the data to determine the chemical composition. A continuum was subtracted from the data to get the pulse-height spectrum for the discrete line

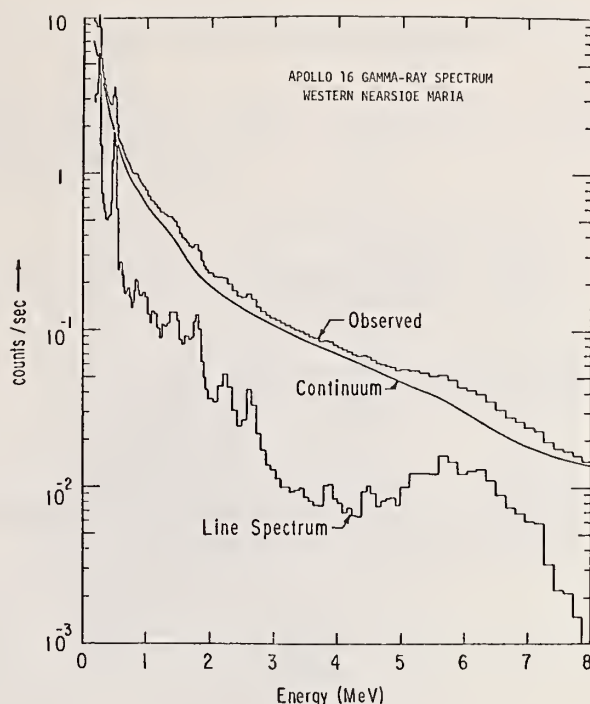


Fig. 1. Pulse-height spectrum from Apollo 16, 270-minute accumulation for 1° to 73° W. Top curve-transmitted data; middle curve-estimated pulse-height spectrum of continuum; bottom curve-net line spectrum.

spectrum. This spectrum was then transformed by the method of weighted least squares utilizing functions which characterize the detector response to gamma rays in the range of 0.5 to 10 MeV. All the lines for each element were grouped together as a single monoenergetic component in the unfolding operation. Several iterations were performed, with a continuum estimated for the first iteration and a continuum determined for successive iterations by subtracting the discrete line contributions (determined in the previous iteration) from the lunar pulse-height spectrum and then smoothing the difference. After several iterations, a continuum which gave consistent results for all regions was obtained and was used for the final iteration. (A special continuum for the natural radioelements was separately determined and included in these calculations.)

The results for the final unfolding of the discrete-line pulse-height spectrum for all of the Apollo 15 lunar data are shown in Fig. 2. The results for calcium and aluminum are poor because neither element has a major line of sufficient intensity which is isolated from other strong lines to give good abundance results. Since the library intensities for the major elements were determined using theoretical cosmic-ray production rates, their final chemical abundance values were obtained by normalizing the unfolding results for each region with the corresponding ratio of the Apollo 11 soil values to the results for the region of Mare Tranquillitatis overflown by the Apollo 15 mission. Corrections were also applied for the effects of the macroscopic neutron-capture cross section of the lunar surface regions on the neutron-capture rates. The results for thorium and <sup>40</sup>K were not changed since their gamma-ray fluxes can be calculated without the use of any models for their source terms.

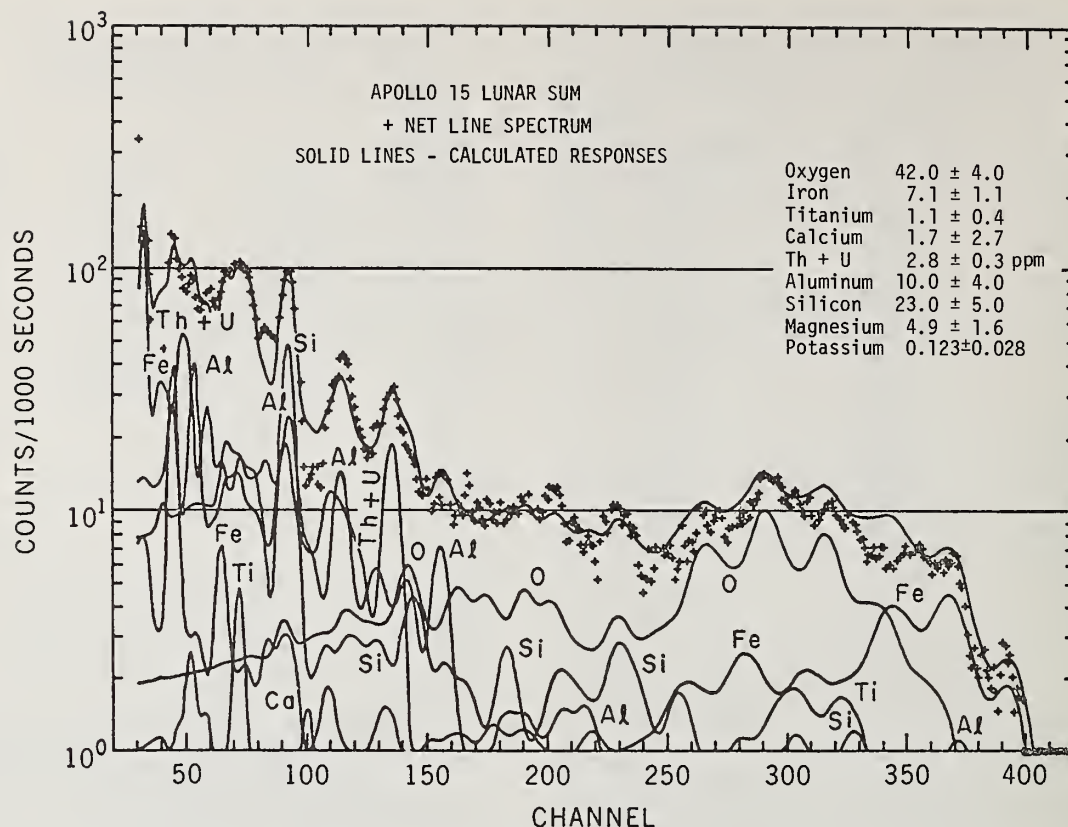


Fig. 2. The net line spectrum for all Apollo 15 lunar data after continuum subtraction. (The scale is 19 keV/channel.) The contributions are shown for each element. (Results are given in weight percent.) The responses for Mg and  $^{40}\text{K}$  are not shown.

The concentrations of thorium, potassium, iron, magnesium, and titanium were reported by Metzger et al.<sup>13</sup> for 28 lunar regions. The results for silicon and oxygen showed little variation over the moon and their abundance values were fixed in the data unfolding. The results for regions near other landing sites are consistent with returned samples and the two missions gave reasonable agreement in a lunar region overflowed by both missions. Iron, magnesium, and titanium were found to be more abundant for the maria than for highland regions. The highest concentrations of potassium, thorium, and uranium were in the western regions of the near side. The ratio K/Th varies, being the highest for regions of low natural radioactivity. The region around the crater Van de Graaff (near 180° on the far side) was found to be unique among all the regions overflowed by the two missions, having highland values for iron, titanium, and magnesium, but values of thorium and potassium considerably higher than the other highland regions.

#### Future Work

The gamma-ray fluxes expected from the moon are being recalculated using more recent cross-section measurements for photon production by nonelastic-scattering reactions and gamma-ray yields for thermal and resonance neutron captures. These fluxes will be used in unfolding the present Apollo data and in planning future gamma-ray spectrometer missions. The natures of the backgrounds from the spacecraft, instrument, and the detector crystal are being investi-

gated. The background due to the activation of the crystal material is being studied both theoretically and experimentally. Dyer et al.<sup>12</sup> have calculated the spallation activation of scintillator crystals. A NaI(Tl) crystal was flown on the Apollo 17 mission and was recovered and counted after splashdown<sup>14</sup> and a similar experiment will be performed on the Apollo-Soyuz Test Project mission. Several accelerator experiments are planned to simulate the effects of cosmic-ray bombardments of detector crystals and of the moon. The use of intrinsic germanium crystals is being studied for use on future missions. It is hoped that such advanced gamma-ray spectrometer systems will be flown on missions to determine the chemical compositions of Mars, Mercury, and regions of the moon not previously studied.

#### Acknowledgments

The author received invaluable assistance in his initial calculations of the lunar gamma-ray fluxes from Professor James R. Arnold. The Apollo gamma-ray results for the moon represents the collective efforts of the author and many others - in particular; Professor Arnold, Dr. Albert E. Metzger, and Dr. Jacob I. Trombka.

\*Work supported by the U.S.A.E.C. and by NASA.

# References

1. A. E. Metzger, J. I. Trombka, L. E. Peterson, R. C. Reedy, and J. R. Arnold, Science **179**, 800-803 (1973).
2. A. P. Vinogradov, Yu. A. Surkov, G. M. Chernov, F. F. Kirnozov, and G. B. Nazarkina, Cosmic Research USSR **5**, 741-753 (1967).
3. T. E. Economou, A. L. Turkevich, K. P. Sowinski, J. H. Patterson, and E. J. Franzgrote, Journal of Geophysical Research **75**, 6514-6523 (1970).
4. R. C. Reedy, and J. R. Arnold, Journal of Geophysical Research **77**, 537-555 (1972).
5. R. C. Finkel, J. R. Arnold, M. Imamura, R. C. Reedy, J. S. Fruchter, H. H. Loosli, J. C. Evans, A. C. Delany, and J. P. Shedlovsky, Proceedings of the Second Lunar Science Conference, Vol. 2, pp. 1773-1789, The M.I.T. Press, Cambridge (1971).
6. M. Imamura, R. C. Finkel, and M. Wahlen, Earth and Planetary Science Letters **20**, 107-112 (1973).
7. M. Wahlen, R. C. Finkel, M. Imamura, C. P. Kohl, and J. R. Arnold, Earth and Planetary Science Letters **19**, 315-320 (1973).
8. R. E. Lingenfelter, E. H. Canfield, and V. E. Hampel, Earth and Planetary Science Letters **16**, 355-369 (1972).
9. R. C. Reedy, J. R. Arnold, and J. I. Trombka, Journal of Geophysical Research **78**, 5847-5866 (1973).
10. Timothy M. Harrington, J. Howard Marshall, James R. Arnold, Laurence E. Peterson, Jacob I. Trombka, and Albert E. Metzger, Nuclear Instruments and Methods **118**, 401-411 (1974).
11. J. I. Trombka, A. E. Metzger, J. R. Arnold, J. L. Matteson, R. C. Reedy, and L. E. Peterson, The Astrophysical Journal **181**, 737-746 (1973).
12. C. S. Dyer, S. M. Seltzer, and J. I. Trombka, paper FB4 presented at this conference, Bull. Am. Phys. Soc. **20**, 155 (1975).
13. A. E. Metzger, J. I. Trombka, R. C. Reedy, and J. R. Arnold, Proceedings of the Fifth Lunar Science Conference, Vol. 2, pp. 1067-1078, Pergamon Press, New York (1974).
14. J. I. Trombka, R. L. Schmadebeck, M. Bielefeld, G. D. O'Kelley, J. S. Eldridge, K. J. Northcutt, A. E. Metzger, E. Schonfeld, L. E. Peterson, J. R. Arnold, and R. C. Reedy, Apollo 17 Preliminary Science Report, NASA Report SP-330, pp. 20-1 - 20-4 (1973).



A MEASUREMENT OF THE FISSION CROSS SECTION  
OF  $^{235}\text{U}$  FROM 1 keV TO 1 MeV<sup>†</sup>

J. B. Czirr and G. S. Sidhu  
Lawrence Livermore Laboratory  
Livermore, California 94550

(Fission;  $^{235}\text{U}$ ; measurement; ratio)

Introduction

We have measured the ratio of the  $^{235}\text{U}$  fission cross section to the  $^6\text{Li}$  (n,  $\alpha$ ) reaction for neutron energies from thermal to 1 MeV. This experiment is the third in a series which is designed to measure the relative fission cross section of  $^{235}\text{U}$  from thermal to 20 MeV. The first two experiments covered the energy range from 0.8- to 20-MeV, and used the n, p scattering reaction to measure the energy dependence of incident flux.<sup>1</sup>

Experimental Technique

The LLNL Linac provided a pulsed source of neutrons with energies from .01 eV to several MeV. Neutron energies were measured by time of flight over path lengths of 37m for the fission detector and 60m for the flux monitor. The fission detector consisted of a parallel plate ionization chamber with ten layers of 100  $\mu\text{g}/\text{cm}^2$   $^{235}\text{U}$  deposited on Al foils. Figure 1 shows the fission-chamber pulse-height spectrum obtained at 0.17 eV. The transmitted neutron spectrum was measured along the same flight path with a 1/2 mm-thick  $^6\text{Li}$ -glass scintillator. The two phototubes, which viewed the edges of the scintillator, were situated outside of the neutron beam in order to reduce neutron scattering. Figure 2 shows the experimental setup and a typical pulse-height spectrum. The background for both detectors was monitored continuously by the insertion of Na, Xe and Al or S resonance "foils" near the neutron source. <sup>10</sup>B foils were used to absorb low energy neutrons. The energy scale was obtained from the measured flight path and observed time of flight corresponding to the 5.903 $\pm$ 0.008 keV Al resonance. Pulse-height versus time-shift corrections were applied to the data above 100-keV neutron energy.

The data were recorded in a two-dimensional mode so that the bias levels for both detectors could be chosen during data analysis. The data were obtained in three energy regions. The first set of data, from 0.01 eV to 1.8 keV, was used to normalize the higher energy region to the thermal cross-section value. The fission cross section of  $^{235}\text{U}$  is taken to be 580 b at 0.0253 eV.<sup>2</sup>

The intermediate energy region, from 100 eV to 100 keV, was normalized to the low energy data in the overlap region from 100- to 1800 eV, using wide averaging intervals. The data are presented in Table 1 in two forms: 1)  $R_f/R_p$ , the ratio of the fission-chamber rate to the Li-glass detector rate, vs neutron energy. The raw data have been corrected for background, dead-time, Li-glass self attenuation, the presence of Al foils between the fission chamber and flux monitor, and scintillator efficiency enhancement due to neutron scattering from glass. This ratio is normalized to 1.0 in the 1.0-to 1.5-keV region. 2)  $\sigma_f$  is the normalized  $^{235}\text{U}$  cross section obtained from  $R_f/R_L$  and the ENDF/B-IV  $^6\text{Li}$  (n,  $\alpha$ ) cross section.

The high energy portion, from 100 keV to 1 MeV was obtained with 51  $\text{g}/\text{cm}^2$  of sulfur in the beam, in order to measure the background in this region. Because of current uncertainties in the  $^6\text{Li}$  (n,  $\alpha$ ) cross section above 100 keV, we report only  $R_f/R_L$  in this high energy region. The above-mentioned corrections were applied to the raw data and the results are listed in Table II. The ratio is normalized to 1.0 in the 50 to 75 keV energy group.

The major uncertainty which arises in the use of glass scintillators is due to the efficiency enhancement as a result of neutron scattering from oxygen. A high-precision measurement of this effect was made in an auxiliary experiment using two thicknesses of  $^6\text{Li}$  glass. The ratio of counting rates for the 0.139  $\text{g}/\text{cm}^2$  standard scintillator versus a 0.250  $\text{g}/\text{cm}^2$  scintillator was obtained from 20 keV to 1 MeV. This ratio was used to correct the thin-scintillator reaction rate to zero thickness, assuming a linear correction with thickness. Table III and Figure 3 present the results of this measurement. The tabulated factor applies to a scintillator thickness of 0.139  $\text{g}/\text{cm}^2$ . It should be noted that the enhancement due to scattering is 14% at 425 keV, even for the thin scintillator used.

Discussion

The tabulated  $^{235}\text{U}$  data are plotted in Figure 4 and compared with the ENDF/B-IV values.

The present ratio measurement extends from 100 eV to 1 MeV, with the cross section data from 100 eV to 100 keV normalized to the thermal value. The usefulness of the high energy data is limited by current uncertainties in the  $^6\text{Li}$  (n,  $\alpha$ ) cross section. The reliability of the data is enhanced by the use of a measured correction for scattering in a thin glass scintillator. With improved knowledge of the  $^6\text{Li}$  cross section, the fission cross section of  $^{235}\text{U}$  from 100 eV to 20 MeV could be normalized to the high-accuracy thermal cross section, using the three measurements in the current series.

References:

- 1) J. B. Czirr and G. S. Sidhu, Fission Cross Section of Uranium-235 From 3 to 20 MeV. To be published in Nuclear Science and Engineering.
- 2) G. C. Hanna, C. H. Westcott, H. D. Lemmel, B. R. Leonard, Jr., J. S. Story, and P. M. Attree, Atomic Energy Review, 7, 3 (1969).

Table I  
<sup>235</sup>U Fission Cross Section from 100 eV to 100 keV

E <sub>min</sub>	E <sub>max</sub>	R <sub>U</sub> /R <sub>L</sub>	σ <sub>U</sub>	Statistical Uncertainty (Standard Deviation)	Systematic* Error (r.m.s.)
0.10	0.20 keV	0.874	20.2	± 1.7%	± 2.2%
0.20	0.30	1.160	20.7	1.5	2.2
0.30	0.40	0.848	12.8	1.1	2.2
0.40	0.50	1.015	13.4	1.0	2.2
0.50	0.60	1.241	14.9	1.0	2.2
0.60	0.80	1.040	11.0	0.9	2.2
0.80	1.0	0.825	7.72	1.1	2.2
1.0	1.5	1.000	7.98	0.8	2.2
1.5	2.0	0.959	6.43	1.0	2.2
2.0	2.25	0.839	5.10	2.3	2.2
2.25	3.5	---	---	---	---
3.5	4.5	0.982	4.35	1.6	2.2
4.5	5.5	0.957	3.80	1.3	2.2
5.5	6.1	---	---	---	---
6.1	6.5	0.858	3.04	2.3	2.2
6.5	7.5	0.967	3.25	1.3	2.2
7.5	8.5	0.895	2.82	1.3	2.2
8.5	10	1.027	3.00	1.0	2.2
10	15	1.015	2.57	0.6	2.2
15	20	1.083	2.34	0.7	2.2
20	25	1.175	2.27	0.7	2.3
25	30	1.286	2.28	0.9	2.3
30	40	---	---	---	---
40	50	1.404	2.05	1.9	2.4
50	60	1.386	1.90	1.5	2.5
60	70	1.376	1.81	1.2	2.7
70	75	1.375	1.77	2.0	2.8
75	95	---	---	---	---
95	105	1.280	1.635	2.3	3.0

\*The systematic errors arise primarily from uncertainties in the shape of the <sup>6</sup>Li(n,α) cross section and in the thermal normalization uncertainty (± 2.1%). The systematic errors in the arbitrarily normalized ratio, R<sub>U</sub>/R<sub>L</sub>, are therefore considerably smaller than the statistical uncertainties at all energies.

Table II  
<sup>235</sup>U to <sup>6</sup>Li Reaction Rate Ratio from 0.1 to 1.0 MeV

E <sub>min</sub>	E <sub>max</sub>	R <sub>U</sub> /R <sub>L</sub>	Statistical Uncertainty (Standard Deviation)
50	75 keV	1.0	---
80	90	1.028	±3.0%
150	200	0.506	12.6
210	230	0.170	4.6
230	250	0.143	3.6
250	270	0.167	3.4
275	285	0.219	5.8
295	315	0.325	3.7
315	335	0.417	3.0
335	355	0.495	2.5
355	370	0.596	2.4
400	450	0.880	3.3
450	500	1.05	2.5
500	550	1.16	2.3
550	580	1.28	3.0
600	650	1.36	2.2
650	680	1.37	2.2
750	800	1.70	3.9
800	900	1.63	2.1
900	1000	1.94	3.0

Table III  
<sup>6</sup>Li-Glass-Scintillator Efficiency-Enhancement Factor(F)

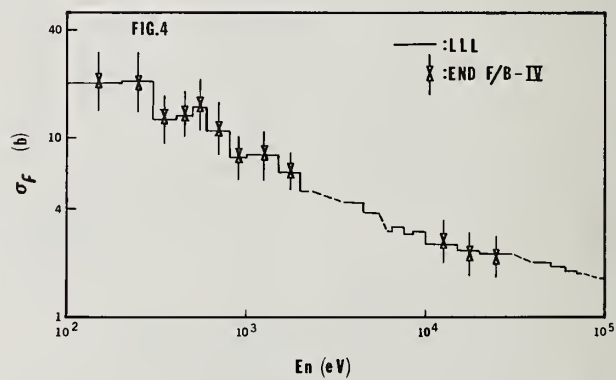
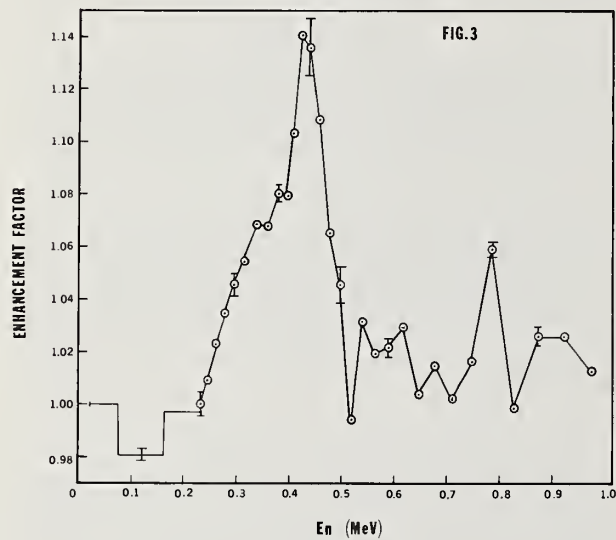
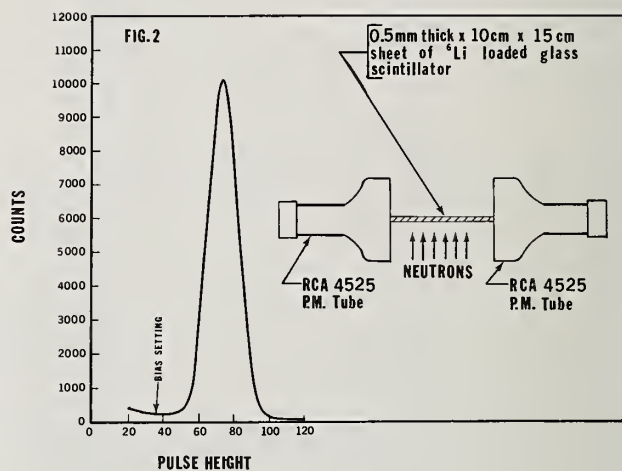
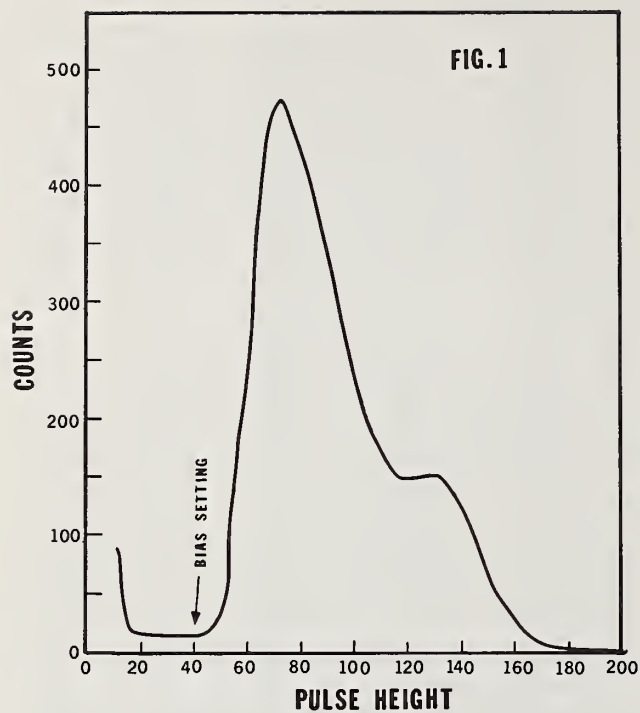
E <sub>min</sub>	E <sub>max</sub>	Ē	F*	Total error (r.m.s.)
20.8	73.3 keV	---	1.0	---
73.3	161	---	0.981	± 0.2 %
161	229	---	0.997	0.4
229	239	234 keV	1.000	0.5
239	253	246	1.009	0.5
253	269	261	1.023	0.5
269	286	277	1.035	0.5
286	305	295	1.046	0.5
305	325	314	1.054	0.3
325	348	337	1.068	0.3
348	373	360	1.068	0.4
373	386	380	1.081	0.3
386	401	394	1.079	0.3
401	416	409	1.104	0.7
416	432	424	1.140	1.1
432	450	441	1.136	1.1
450	467	458	1.108	1.1
467	486	478	1.066	1.1
486	507	497	1.045	0.7
507	529	518	0.995	0.3
529	552	540	1.031	0.4
552	577	564	1.020	0.4
577	603	590	1.022	0.4
603	631	617	1.029	0.4
631	662	647	1.004	0.4
662	694	678	1.015	0.3
694	729	712	1.002	0.3
729	766	748	1.017	0.3
766	807	787	1.059	0.3
807	852	829	0.998	0.4
852	899	875	1.026	0.4
899	951	924	1.026	0.4
951	1000	978	1.013	0.4

\*The enhancement factor has been normalized to 1.0 in the 20.8- to 73.3-keV region.

### Figure Captions

- Fig. 1. Fission-chamber pulse height spectrum at a neutron energy of 0.17 eV.  
 Fig. 2. <sup>6</sup>Li-glass detector pulse height spectrum at a neutron energy of 170 keV.  
 Fig. 3. Efficiency enhancement factor for 0.139 g/cm<sup>2</sup> <sup>6</sup>Li-glass detector.  
 Fig. 4. Fission cross section of <sup>235</sup>U from 100 eV to 100 keV. The dotted lines represent regions which were blanked out by resonance absorber foils.

†Work performed under the auspices of the U.S. Atomic Energy Commission.





F. Käppeler and R.-E. Bandl  
 Institut für Angewandte Kernphysik  
 Kernforschungszentrum Karlsruhe, Germany

For the clarification of existing discrepancies in the energy dependence of  $\bar{\nu}_p$  for  $^{235}\text{U}$  an experiment was performed which was based on a method independent of current techniques. A considerable reduction of background and correction problems was achieved by renouncing on an absolute measurement. Thus the resulting systematic uncertainty was 0.6 %. In the energy range between 0.2 and 1.4 MeV the shape of  $\bar{\nu}_p$  was measured at 22 points in steps of 50 keV with an average energy resolution of 3.3 %. Repetition of several runs with modified experimental conditions ensured the consistent reproduction of the results. It was found that  $\bar{\nu}_p$  of  $^{235}\text{U}$  shows distinct deviations of up to 2 % from a linear energy dependence.

(Number of prompt fission neutrons;  $^{235}\text{U}$ ;  $E_n = 0.2\text{--}1.4$  MeV; fast time-of-flight technique)

### Introduction

Due to its importance in reactor design the average number of prompt neutrons per fission,  $\bar{\nu}_p$ , emitted in (n,f)-reactions belongs to the most extensively investigated nuclear data<sup>1</sup>. In the energy range above 2 MeV the different measurements for  $^{235}\text{U}$  agree satisfactorily with each other. In the lower energy range, however, there are systematic discrepancies in the energy dependence of  $\bar{\nu}_p$ . The one authors<sup>2,3</sup> report a linear increase of  $\bar{\nu}_p$  with neutron energy while the others<sup>4-6</sup> find a distinct structure around 400 keV and some less pronounced deviations from the straight line dependence at higher energies. These discrepancies in  $\bar{\nu}_p$  are two or three times larger than the respective experimental uncertainties. As most of the data were taken with similar techniques it was felt that in this situation an additional measurement based on a technique independent of earlier work might help for clarification.

### Experimental Method and Arrangement

By contrast with most earlier measurements it was renounced on an absolute determination of  $\bar{\nu}_p$  because the main interest was concentrated on the energy dependence. With this restriction small detectors and fast

time-of-flight techniques could be chosen which allowed a considerable reduction of background and correction problems. A schematic view of the experimental arrangement is shown in Fig. 1. Neutrons were produced via the  $^7\text{Li}$  (p,n) reaction by bombardment with protons from the Karlsruhe 3 MV pulsed Van-de-Graaff-accelerator. The pulse width was 1 nsec and the average beam current about 20  $\mu\text{A}$  at a repetition rate of 5 MHz. The thickness of the metallic Li-targets was chosen such that the neutron energy spread  $\Delta E_n$  did not exceed 4 %. A collimator in the neutron flight path allowed to arrange three samples in the very same neutron flux at certain distances from each other. In this way scattered neutrons and fission neutrons from one sample did not influence the fission yield of the other samples. Due to the collimated neutron beam no corrections for neutrons scattered nearby the samples had to be made. It also shielded the fission neutron detector from the primary neutron flux which lowered the background count rate and increased the detector stability. The in-scattering from the collimator - a double tapered type according to Langsdorf<sup>9</sup> - was calculated to be less than 0.2 % even for neutron energies of 2 MeV.

As a consequence of the restriction to a shape measurement of  $\bar{\nu}_p$  the characteristic feature of the experiment was to detect fission neutrons and fission

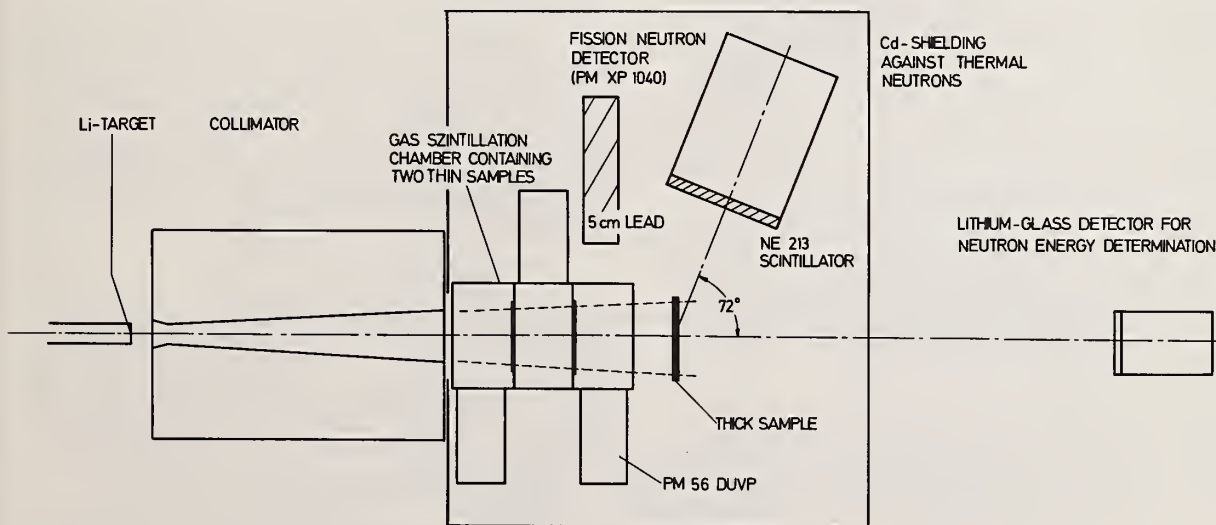


Fig. 1 Schematic view of the experimental arrangement

fragments independent of each other. Behind the collimator a gas scintillation fission counter was located containing two thin samples of  $^{235}\text{U}$  with flight paths of 56 and 63 cm respectively. This counter corresponds very closely to similar detectors reported earlier<sup>10</sup>. The chamber is divided by the samples into optically decoupled thirds each inspected by a 56 DUVP photomultiplier. The samples consist of uranium acetate layers of less than  $0.5 \text{ mg/cm}^2$  thickness electroplated onto thin backings of Vyns<sup>11</sup>. The mass determination was carried out by low geometry  $\alpha$ -counting.<sup>12</sup> A coincidence between two thirds was required for the registration of a fission event in order to eliminate  $\alpha$ -background. Both, samples and counter windows were thin enough not to attenuate the neutron flux by a measurable fraction ( $<0.1\%$ ). Thus, the same neutron flux to which the thin samples are exposed is seen by the thick sample which is located at a flight path of 74 cm. From this sample (a  $^{235}\text{U}$  metal disk of  $0.15 \text{ mm}$  thickness and  $70 \text{ mm}$  diameter) fission neutrons are recorded by a fission neutron detector. For all the samples the diameter was at least  $10 \text{ mm}$  larger than the extended collimator cone. The fission neutron detector placed at  $12.5 \text{ cm}$  distance from the sample was the same as used in an earlier measurement<sup>13</sup>. Pulse shape discrimination (PSD) against gamma radiation was performed by the zero cross over method<sup>14</sup>. Both detectors and the samples were shielded against slow, roomscattered neutrons by Cd-sheets to reduce the time-independent background. With a flight path of  $130 \text{ cm}$  from the target a  $^6\text{Li}$ -glass detector was mounted. It served for the neutron spectrum determination and as a monitor for the neutron yield.

#### Data Accumulation and Analysis

All data used for evaluation were recorded in a  $16 \text{ K}$  on-line computer while control data were stored in multichannel analyzers. Fig. 2 shows the spectra accumulated in the computer. These are the time-of-flight spectra of the three samples together with the pulse height distribution of the fission neutron detector for the maximum energy run at  $1363 \pm 35 \text{ keV}$ . This run was chosen because it is the most unfavorable case for the discrimination of the second neutron group from the  $^7\text{Li}(p, n\gamma)^7\text{Be}^*$ -reaction. Although the flight time difference for this second group is small due to the short flight path the overall time resolution of  $2.5 \text{ nsec}$  is sufficient for a clear separation. Except for the  $\gamma$ -peak caused by the proton burst at time zero no additional structure appears in the time-of-flight spectra, demonstrating the clean background conditions in a fast pulsed monoenergetic neutron flux. The pulse height distribution of the fission neutrons was taken because the electronic threshold was set at  $1.7 \text{ MeV}$  neutron energy where the spectrum is very steep. Therefore any spectrum shift had to be detected and corrected for in order to establish constant efficiency. This was achieved by a calibration procedure before and after each run which will be described later on. In addition the proper operation of the PSD was controlled permanently by recording the zero cross-over time distribution for fission neutrons in an extra multichannel analyzer. During each run also a time-of-flight spectrum with  $1.5 \text{ nsec/m}$  resolution was taken from the  $^6\text{Li}$ -glass detector to determine the neutron energy spread  $\Delta E_n$ .

From the experimental count rates (integrated peaks in the time-of-flight spectra)  $\bar{v}_p$  was derived in the following way: with the neutron flux,  $\phi$ , the fission cross section,  $\sigma_f$ , and the number of atoms per  $\text{cm}^2$ ,  $N_1$ , the count rate measured in the gas scintillation chamber can be written as

$$C_1 = \phi \cdot \sigma_f \cdot N_1 \cdot \epsilon_1 \cdot K_1 \quad (1)$$

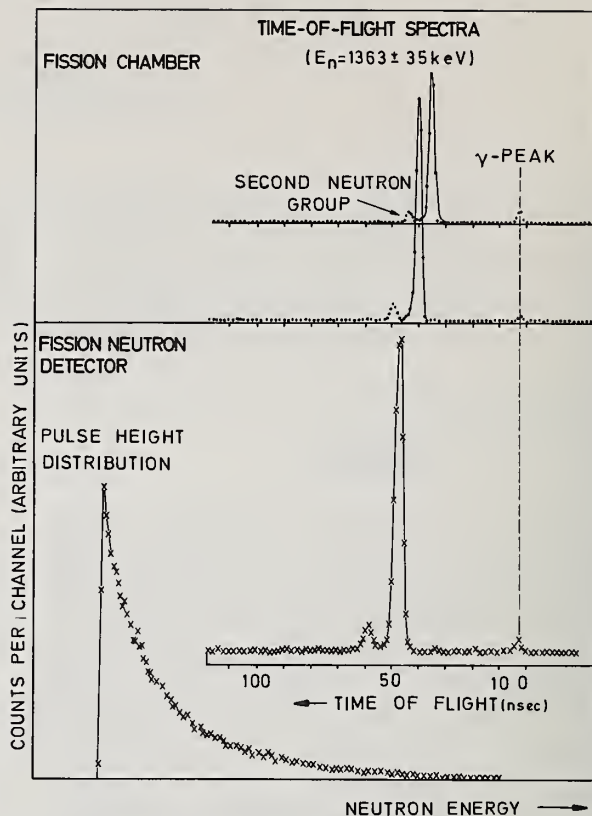


Fig. 2 Spectra used for analysis from a run at  $1363 \pm 35 \text{ keV}$  neutron energy.

where  $\epsilon_1$  denotes the efficiency and  $K_1$  a correction factor for fission events from other isotopes than  $^{235}\text{U}$ . The count rate of the fission neutron detector is obtained by

$$C_2 = \phi \cdot \sigma_f \cdot \bar{v}_p \cdot N_2 \cdot \epsilon_2 \cdot \frac{K_2}{K_R} \cdot \frac{1}{1+MS} \quad (2)$$

$N_2$  is the number of atoms per  $\text{cm}^2$  in the thick sample,  $\epsilon_2$  the efficiency of the fission neutron detector and  $MS$  the correction for multiple scattering.  $K_2$  accounts for fission neutrons from other isotopes than  $^{235}\text{U}$  and  $K_R$  for effects smaller than  $0.5\%$  such as the angular anisotropy of the fission neutrons and the self shielding of the thick sample. In the ratio of eqs. (1) and (2) the neutron flux cancels out and as no absolute values of  $\bar{v}_p$  are to be determined one gets

$$\bar{v}_p = \frac{C_2}{C_1} \cdot K_N \cdot K_{\gamma} \cdot (1 + MS) K_R \quad (3)$$

Now  $K_N$  is a normalization constant independent of neutron energy but sensitive to changes of the respective detector efficiencies. Therefore much care was devoted to the problem either to keep  $K_N$  extremely constant throughout the whole experiment or to correct for small shifts in the efficiencies.  $K_{\gamma}$  accounts for the contribution of other isotopes, mainly  $^{234}\text{U}$  and  $^{238}\text{U}$ .

#### Corrections and Background Considerations

In equation (3)  $K_N$ ,  $K_{\gamma}$ ,  $MS$  and  $K_R$  are corrections to the experimental count rates. The normalization constant  $K_N$  contains the detector efficiencies  $\epsilon_1$  and  $\epsilon_2$ .



While the efficiency of the fission chamber,  $\epsilon_1$ , was very stable, the fission neutron detector showed a smooth long term drift of its efficiency,  $\epsilon_2$ , which was entirely due to a gain shift of the photomultiplier. This was corrected for by introducing a virtual threshold which was determined by a calibration procedure.

Before and after each run a strong Am-Be neutron source was located at 3 m distance in a well defined position. The detected count rate ( $10^5$  cts in 1000 sec) can be used as a measure of the efficiency. As the spectra are different for neutrons from the Am-Be source and fission neutrons a fit to the respective amplitude spectra was performed using a Monte-Carlo-program<sup>15</sup> with the Am-Be spectrum of Geiger and van der Zwan<sup>16</sup> and a Maxwell distribution for the fission neutrons as input data. In this way a relation between the Am-Be calibration count rate and the detector efficiency was established with good accuracy. The reliability of the procedure was checked by repeating the measurement for a number of energies after the multiplier gain was changed artificially. Although this resulted in a 12 % change of the efficiency (over two times more than really observed) the corresponding results have been found in excellent agreement. The correction  $K_N$  includes also the hardening of the fission neutron spectrum with excitation energy according to Terrell<sup>17</sup>. In Table 1 the normalization constant  $K_N$  and the other corrections are listed together with the related uncertainties. As all these quantities are energy dependent only the maximum values are given for each case. The correction factor  $K_V$  which accounts for the isotopic impurities was determined using the fission cross section ratios  $\sigma_{fi}/\sigma_f$   $^{235}\text{U}$  and the respective  $\bar{v}_i$  values from the evaluation of Davey<sup>18</sup>. The multiple scattering corrections  $1/(1+MS)$  for the thick sample were calculated by means of a Monte-Carlo program<sup>19</sup> using the cross sections of Refs. <sup>20,21</sup>. Two minor corrections have been summarized by the factor  $K_R$ . These are the correction for

Type of correction		Max. Value (%)	Uncertainty (%)
Fission neutron detector efficiency; Increase of fragment temperature	$K_N$	5	0.5
Isotopic composition	$K_V$	1.5	<0.2
Multiple scattering	MS	1.5	<0.2
Self shielding; Fission neutron angular distr.	$K_R$	0.8	<0.2

Table 1 Corrections to the experimental count rates

self shielding of the thick sample and the correction for the change of the fission neutron angular distribution with excitation. At the end of this chapter some background considerations concerning the fission neutron detector have to be added. Time-correlated backgrounds in this detector may be due to  $\gamma$ -rays from fission and capture events or neutrons scattered in the sample. The influence of scattered neutrons was investigated with an 0.5 mm thick lead disk instead of the  $^{235}\text{U}$  sample. As was expected from the high threshold of 1.7 MeV, no neutrons from the direct flux were detected. The background from capture or fission  $\gamma$ -rays was measured with the thick sample located very close to the target thus allowing discrimination between fission neutrons and prompt  $\gamma$ -rays by time-of-flight. It was found that the  $\gamma$ -background is eliminated except for a rest of 0.6 % which is mainly due to fission  $\gamma$ -rays and therefore does not affect the result. A further estimate showed that the influence of fission neutrons scattered in the lead shielding on both the fission samples as well as the neutron detector is negligible.

#### Results and Discussion

The average number of prompt fission neutrons,  $\bar{v}_p$ , has been determined, for 22 energy points between

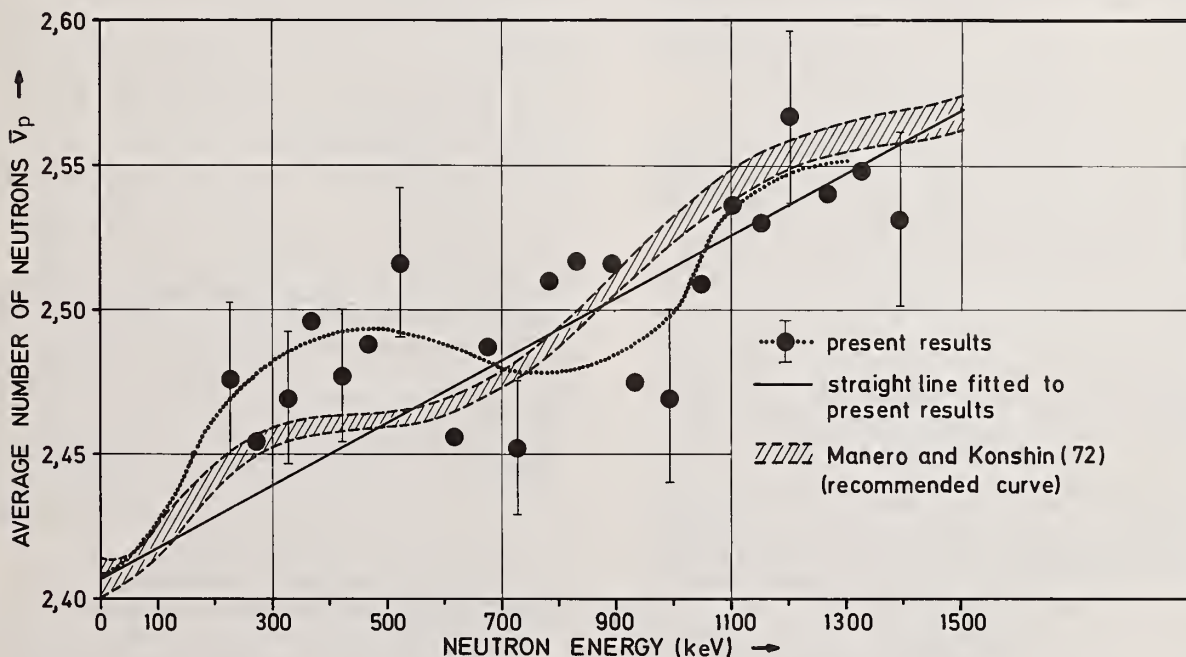


Fig. 3 Experimental results of  $\bar{v}_p$ . The dotted eye-guide line illustrates the deviations from a linear increase with excitation energy.



0.2 and 1.4 MeV with an average energy spread of 3.3 %. The systematic uncertainty of the data due to background and corrections was 0.6 % while the counting statistics vary from 0.7 to 1.1 %. These uncertainties correspond to one standard deviation. By repeating several runs with modified experimental conditions it was ensured that the results could be reproduced in a consistent way within the quoted uncertainties.

As the present experiment was concentrated on the energy dependence of  $\bar{v}_p$ , the results had to be normalized for a comparison with the existing data. For that purpose the integral  $\int_{225}^{1363} \bar{v}_p dE$  with the  $\bar{v}$ -values recommended by Manero and Konshin (1) was used as an appropriate normalization constant. Fig. 3 shows the results in comparison with the recommended curve of Ref. (1). The error bars which are given for some of the points indicate the overall uncertainties. It is apparent that the experimental points are consistently higher between 200 and 500 keV. From 500 keV upward the experimental values agree well with the recommended curve except for the two points at 930 and 988 keV which are lower by twice the standard deviation. The dotted eye-guide line illustrates the experimental energy dependence and it is obvious that it corresponds closely to the curve of Ref. (1) although the structure is more pronounced in the present case. For comparison a linear least square fit to the data points was performed, starting with the thermal value of 2.407 as given in Ref. (1). The resulting straight line follows the equation

$$\bar{v}_p = 2.407 + (1.108 \pm 0.007) E_n (\text{MeV}). \quad (4)$$

The slope of  $0.108 \pm 0.007$  appears to agree well with the result of Boldeman and Walsh<sup>3</sup> who found  $0.114 \pm 0.008$ . However, by contrast with their work, the straight line is no satisfactory fit to the present results.

From an interpretation of the observed structure in  $\bar{v}_p$  no detailed conclusions on the fission process can be drawn, because the information contained in a quantity like  $\bar{v}_p$  is naturally an average of many components. But if a structure occurs in such an integral quantity it can be assumed that this was caused by a rather strong effect of one of the components and therefore should show up for related quantities as well. The energy dependence of  $\bar{v}_p$  is interpreted by the equation for the total energy release in fission

$$E_T = \bar{E}_K + \bar{E}_v + \bar{E}_\gamma. \quad (5)$$

$\bar{E}_K$  means the average total kinetic energy of the fragments,  $\bar{E}_v$  is the average total fragment excitation energy carried off by neutrons and  $\bar{E}_\gamma$  is the average total  $\gamma$ -ray energy. With the assumption that  $\bar{E}_\gamma$  is constant in this range of excitation energy and  $\bar{v}_p$  is proportional to  $\bar{E}_v$  one would expect an anticorrelation between  $\bar{v}_p$  and  $\bar{E}_K$  from equation (5). An indication for such a behaviour can be seen from kinetic energy data of fission fragments which are compiled in the work of Boldeman and Walsh (Ref. (3)). This again suggests that the influence of the various fission channels is responsible for the observed structure in  $\bar{v}_p$ .

For further investigations it may be of interest to separate the various fission channels - for example by the fragment angular anisotropy - in order to establish more detailed information about the distribution of the compound excitation energy on  $\bar{E}_K$ ,  $\bar{E}_v$  and  $\bar{E}_\gamma$ .

#### Acknowledgement

The authors wish to thank R. Schlüter for his help with the Monte Carlo calculations and A. Ernst

who performed the computer connection of the experiment. They are also indebted to the entire Van-de-Graaff staff for their continuous help.

#### References

- (1) F. MANERO and V.A. KONSHIN, Atomic Energy Review 10, IAEA, Vienna (1972) p. 637.
- (2) V.G. NESTEROV, B. NURPEISOV, L.I. PROKHOROVA, G.N. SMIRENKIN and Yu. M. TURCHIN, Nuclear Data for Reactors, 2, IAEA, Vienna (1970) p. 167.
- (3) J.W. BOLDEMAN and R.L. WALSH, J. Nucl. Energy 24 (1970) 191.
- (4) Yu. A. BLYUMKINA, I.I. BONDARENKO, V.F. KUZNETSOV, V.G. NESTEROV, V.N. OKOLOVITCH, G.N. SMIRENKIN and Z.N. USACHEV, Nucl. Phys. 52 (1964) 648.
- (5) M.V. SAVIN, Yu. A. KHOKHLOV, Yu. S. ZAMYATNIN and I.N. PARAMONOVA, Nuclear Data for Reactors 2, IAEA, Vienna (1970) p. 157.
- (6) M. SOLEILHAC, J. FREHAUT, J. GAURIAN and G. MOSINKI, Nuclear Data for Reactors 2, IAEA, Vienna (1970) p. 145.
- (7) J.W. MEADOWS and J.F. WHALEN, J. Nucl. Energy 21 (1967) 157.
- (8) D.S. MATHER, P. FIELDHOUSE and A. MOAT, Phys. Rev. 133 (1964) B 1403.
- (9) A. LANGSDORF, Jr., in "Fast Neutron Physics I" Eds. J.B. Marion and J.L. Fowler, Interscience Publishers Inc., New York (1960), p. 721.
- (10) F. KÄPPELER, Neutron Standard Reference Data, IAEA, Vienna (1974) 213.
- (11) V. VERDINGH and K.F. LAUER, Nucl. Instr. Meth. 21 (1963) 161.
- (12) A. SPERNOL and O. LERCH, Nucl. Instr. Meth. 32 (1965) 224.
- (13) R.-E. BANDL, H. MIESSNER and F.H. FRÖHNER, Nucl. Sci. Eng. 48 (1972) 324, also KFK-1563, Kernforschungszentrum Karlsruhe (1973).
- (14) R.-E. BANDL, KFK-1458, Kernforschungszentrum Karlsruhe (1971).
- (15) R.E. TEXTOR and V.V. VERBINSKI, ORNL-4160 (1968); also R. SCHLÜFTER, priv. communication.
- (16) K.W. GEIGER and L. van der ZWAN, Int. Journal of Applied Radiation and Isotopes 21 (1970) 193.
- (17) J. TERRELL, Physics and Chemistry of Fission II, IAEA, Vienna (1965) p. 3.
- (18) W.G. DAVEY, Nucl. Sci. Eng. 32 (1968) 35.
- (19) R.-E. BANDL, KFK-IAK internal report 103/72, unpublished.
- (20) I. LANGNER, J.J. SCHMIDT and D. WOLL, KFK-750 (1968).
- (21) M.C. BERTIN, G. GROCHOWSKI, J. CELNIK, M.H. KALOS, H. FLESHER, J.H. RAY and E.S. TROUBETZKOY, United Nuclear Corporation-5099 (1964).

MONTE CARLO ANALYSIS OF DIRECT MEASUREMENTS  
OF THE THERMAL  $\eta$  (.025 eV) FOR  $U^{233}$  AND  $U^{235}$

J. J. Ullo and M. Goldsmith  
Westinghouse Electric Corporation  
Bettis Atomic Power Laboratory  
Pittsburgh, Pennsylvania 15122

In support of the LWER program, the manganese bath measurements of  $\eta$  of  $U^{233}$  and  $U^{235}$  at .025 eV were analyzed using Monte Carlo methods. The calculated values of  $\eta$ , including statistical, cross section, and experimental uncertainties, are  $\eta^{233} = 2.2993 \pm .0082$  and  $\eta^{235} = 2.0777 \pm .0064$ . The systematic corrections to the experiments were also studied in detail.

(Nuclear Reactions,  $U^{233}$ ,  $U^{235}$ , fission neutrons per absorption,  $\eta$ ,  $E = .025$  eV)

## I. Introduction

From the viewpoint of reactor physics, a significant discrepancy exists between direct measurements of  $\eta$  and values of  $\eta$  derived from  $\bar{\nu}$  measurements through the relation

$$\eta = \frac{\bar{\nu} \sigma_f}{\sigma_f + \sigma_c} = \frac{\bar{\nu}}{1 + \alpha}, \quad (1)$$

where  $\alpha$  is the ratio of the capture to fission cross sections.

The discrepancy becomes apparent through an examination of measurements of the average number of prompt fission neutrons,  $\bar{\nu}_p$ , of  $Cr^{252}$  which is used as a standard for thermal-neutron fission, especially for  $U^{233}$ ,  $U^{235}$ ,  $Pu^{239}$ , and  $Pu^{241}$ . Until recently, measured values of  $\bar{\nu}$  of  $Cr^{252}$  fell into two groups. Those based on liquid scintillator techniques<sup>(1,2)</sup> yielded values of  $\bar{\nu}_p = 3.78 \pm .03$ , whereas a value of  $3.713 \pm .015$  was obtained using a boron pile.<sup>(3)</sup> Other measurements employing manganese baths<sup>(4,5,6)</sup> as neutron detectors tend to support the boron pile determination. A recent measurement of  $\bar{\nu}_p$  of  $Cr^{252}$  by Boldeman<sup>(7)</sup> using a liquid scintillator yields a value of  $\bar{\nu}_p = 3.738 \pm .015$  ( $\bar{\nu}_p = 3.747 \pm .015$ ) which is almost midway between the other two sets of values.

The two direct measurements of  $\eta$ <sup>(8,9)</sup> are consistent with  $\bar{\nu}_p$  of  $Cr^{252}$  of 3.78, which is more than 1% higher than the mean of all the nubar measurements. This is a serious difference, and the practice has been to reduce  $\eta$  values to produce a set of compromise  $\eta$ -nubar values<sup>(10)</sup>.

Since there are no a priori grounds for settling the  $\eta$ -nubar discrepancy, one is led to consider detailed neutronic analysis of the experiments. This paper reports such an analysis, using continuous energy Monte Carlo techniques, applied to the monoenergetic  $\eta$  measurements of Smith<sup>(8)</sup> for  $U^{233}$  and  $U^{235}$ . Since  $U^{235}$  is often used as a thermal-fission standard, the analysis of  $\eta$  of  $U^{235}$  is intended to offer further support of the present and previous analyses<sup>(11-13)</sup> of  $\eta$  of  $U^{233}$  in support of the LWER development program. An analysis of the thermal beam measurements of  $\eta$  by Macklin, et al.<sup>(9)</sup> is reported in another paper<sup>(14)</sup>.

## II. The Smith Measurement

Smith, et al.<sup>(8)</sup> measured for the first time the absolute value of  $\eta$  using monochromatic .025 eV and .057 eV neutrons. Using a technique similar to that of Macklin and deSaussure<sup>(9)</sup>, a manganese sulfate ( $MnSO_4$ ) bath was employed as a neutron detector. A collimated neutron beam, Figure 1, from the crystal spectrometer at the Materials Testing Reactor (MTR)

was directed onto a fissile sample, Figure 2, mounted at the center of the bath. The bath was contained in a cylindrical tank 42 inches in inside length and diameter. Fission neutrons arising from absorptions in the sample were captured in the surrounding bath. The resulting manganese activity was nearly proportional to the number of fission neutrons produced. In addition, the manganese activity was measured with the fissionable samples removed. The ratio of the two solution activities yields a value for  $\eta^*$ ,

$$\eta^* = \frac{\text{Manganese absorptions (Target In)}}{\text{Manganese absorptions (Target Out)}}. \quad (2)$$

The value of  $\eta$  is inferred from:

$$\eta = \frac{\eta^*}{\prod_{i=1}^{10} C_i}, \quad (3)$$

where the  $C_i$  are ten small systematic corrections. Most of these corrections are automatically accounted for in the Monte Carlo calculations described below. However, detailed calculations have been independently made for each correction. These will be separately discussed in Section IV.

## III. Computational Strategy

The actual arrangement and the corresponding Monte Carlo representation of Smith's experimental setup are depicted in Figure 1 and Figure 2. The strategy used to calculate  $\eta^*$ <sup>(11,12)</sup> consisted of three fixed-source Monte Carlo calculations. In the first, a monodirectional (along the beam tube) .025 eV source of neutrons impinged on the target foils. The beam diameter was 1 inch, as in the experiment. From this calculation was determined the distribution of the absorptions in the sample foils.

In the second calculation, the geometry remained unchanged, but a starting neutron source of unit strength was distributed among eight foil regions according to the distribution of the absorptions determined in the first calculation. The initial neutron energies were chosen from a  $U^{233}$  or  $U^{235}$  fission spectrum. (Sensitivities to the mean energy,  $\bar{E}$ , of the spectrum are discussed later.) Essential results from this calculation are the manganese absorptions per initial fission neutron as well as the fraction of starting source neutrons that cause secondary fission events due to fast multiplication, in which neutrons cause an additional fission before leaving the sample foil, and slow multiplication, in which neutrons are reflected back from the bath to cause additional fissions.

In the third problem, the target foils were removed and the monodirectional .025 eV source of neutrons



identical to that of the first problem was allowed to impinge on the  $MnSO_4$  bath. From this, the  $Mn$  absorption per beam neutron was determined for the target-out configuration.

In Table 1, some of the results of these three Monte Carlo calculations are summarized together with the statistical probable errors. The number of secondary neutrons produced through the fast effect and indirect multiplication was determined by editing the number of fissions per starting fission neutron over two energy groups. The first of these extended from 10 MeV to 5.53 keV, and the second from 5.53 keV to 0 eV. An effective value of  $\bar{\nu}$ , the average number of neutrons per fission, was determined for the first group from

$$\bar{\nu}(1) = \frac{\int \nu(E) \Sigma_f(E) \phi(E) dE}{\int \Sigma_f(E) \phi(E) dE}, \quad (4)$$

where  $\phi(E)$  is the fission spectrum employed. This yielded  $\bar{\nu}(1) = 2.7661$  for  $U^{233}$  and  $\bar{\nu}(1) = 2.7622$  for  $U^{235}$ . In either case, a Maxwellian form of the fission spectrum with  $T = 1.323$  MeV was used. For the second group, values of  $\bar{\nu}(2) = 2.4959$  and  $\bar{\nu}(2) = 2.4188$  were assumed for  $U^{233}$  and  $U^{235}$ , respectively. The number of second-generation fission neutrons produced is given by

$$B_2 = \bar{\nu}(1)F(1) + \bar{\nu}(2)F(2). \quad (5)$$

From the definition of  $\eta^*$ , the ratio  $\eta^*/\eta_{2200}$  can be determined from the quantities in Table 1,

$$\begin{aligned} \frac{\eta^*}{\eta_{2200}} &= \frac{A_1 \eta_{2200} A_2 + A_1 \eta_{2200} A_2 \bar{B}_2 + B_1}{A_3 \eta_{2200}} \\ &= \frac{A_1 A_2 (1 + \bar{B}_2)}{A_3} + \frac{B_1}{A_3 \eta_{2200}}, \end{aligned} \quad (6)$$

where to account for third and higher generations,  $\bar{B}_2 = B_2/(1 - B_2)$ .

The three quantities in the numerator of the first ratio are respectively the manganese absorptions per beam neutron resulting from  $U^{233}$  or  $U^{235}$  thermal fissions, fast fission and indirect multiplication, and scattering of incident beam neutrons from the target.

Inserting values from Table 1 into Equation (6) yields values for the ratio  $\eta^*/\eta_{2200}$  for  $U^{233}$  and  $U^{235}$ , which are summarized in Table 2 along with Smith's experimental results. Values assumed for  $\eta_{2200}$  were those of ENDF-4, where  $\eta_{2200}^{233} = 2.2972$  and  $\eta_{2200}^{235} = 2.0728$ . Our calculated ratios are in almost perfect agreement with Smith's experimental values. One verifies from Equation (6) that  $\eta^*/\eta_{2200}$  is essentially independent of the assumed value of  $\eta_{2200}$ , since

$$\frac{\partial(\eta^*/\eta_{2200})}{\partial \eta_{2200}} \approx .001. \text{ Employing the measured values, } \eta_{\text{expt.}}^{233} = 2.364 \pm .005 \text{ and } \eta_{\text{expt.}}^{235} = 2.086 \pm .004, \text{ one}$$

obtains the calculated values of  $\eta$  shown in Table 3. Again, the calculated values of  $\eta$  are in excellent agreement with those of Smith, et al. It should be emphasized that the error associated with our calculated values of  $\eta$  include statistical, cross section, and experimental uncertainties at one standard deviation. The total cross section sensitivity is discussed in Section V.

#### IV. Systematic Corrections To The Data

The ratio of solution activities with and without fissile samples present is close to the true value of  $\eta$ . Smith, et al. used ten systematic corrections, ranging from less than .1% to slightly greater than 3%, to deduce the value of  $\eta$ . In the previous section, the calculated ratios of  $\eta^*/\eta_{2200}$  determine the total cor-

rection factor in Equation (3),  $\prod_{i=1}^{10} C_i$ .

In Table 4, we list the separate corrections and our calculations of their individual magnitudes.

All of the calculated corrections in Table 4, except for the corrections due to scattering, cadmium wrap effects, and parasitic reactions, agree with those deduced by Smith at the 1 $\sigma$  level.

It is believed that the discrepancy in the parasitic reactions correction is due to our using more recent cross section data for oxygen and sulfur. However, in both the  $U^{233}$  and  $U^{235}$  cases, the smaller correction for parasitic absorption is almost compensated by larger corrections for cadmium wrap effects and scattering yielding an overall correction factor,  $\prod_{i=1}^{10} C_i$ , which is in good agreement with the value of  $\eta^*/\eta_{2200}$  in Table 3.

#### V. Cross Section Sensitivities

To the maximum extent possible, the nuclear data used in the Monte Carlo calculations were those employed in ENDF-4. The  $U^{233}$  cross sections were taken directly from the ENDF-4 evaluation done by Steen<sup>(13,15)</sup> with the thermal parameters (at .025 eV) given by  $\sigma_{\text{Tot}} = 686.32$  barns,  $\sigma_c = 46.165$  barns, and  $\sigma_f = 528.25$  barns. In the  $U^{235}$  case, the .025 eV cross sections were  $\sigma_{\text{Tot}} = 703.16$  barns,  $\sigma_c = 98.38$  barns, and  $\sigma_f = 589.28$  barns. For the resonance data of  $U^{235}$ , the ENDF-4 single-level resonance parameters were replaced with the multi-level parameters of deSaussure<sup>(16)</sup> from .625 eV to 60 eV. The resonance integrals above .625 eV were  $I_f = 261.24$  barns and  $I_v = 135.84$  barns.

The important cross sections in the bath were those of hydrogen and manganese. Hydrogen cross sections were those from the ENDF-4 files, whereas the manganese was obtained from ENDF-3 files. At .025 eV, the absorption cross section of  $Mn$  was 13.35 barns, the same as in ENDF-4. Our manganese absorption integral above .625 eV was 14.263 barns vs. 14.213 barns in ENDF-4. This difference is well within the uncertainties assumed when assessing the sensitivity of  $\eta^*/\eta_{2200}$  to uncertainties in this absorption integral. The sulfur cross sections were prepared from BNL-325<sup>(17)</sup>, and were the same as those used in Reference 11. At .025 eV, the sulfur absorption cross section was .523 barns, and the absorption integral above .625 eV was .498 barns. In the case of oxygen, the cross sections were taken from ENDF-4.

Using our Monte Carlo results, the sensitivities of the ratios for  $\eta^*/\eta_{2200}$  to various cross section and nuclear data uncertainties were calculated. The components of the total sensitivity for each ratio are shown in Table 5 along with the assumed variations.

The quoted uncertainties in the calculated values of  $\eta$  in Table 3 include the above total cross section sensitivities.

#### VI. Conclusions

The monoenergetic  $\eta$  measurements of Smith, et al. have been subjected to detailed nucleonic analysis using continuous energy Monte Carlo methods. Our results (Table 3) clearly support previous interpretations of Smith's measurements. In addition, the errors assigned to our results, which include statistical, cross section, and experimental uncertainties, are smaller than those in Reference 8. All of the systematic corrections in the experiments have been studied in detail, and except for the corrections due to scattering, cadmium wrap effects, and parasitic reactions, agree with those deduced by Smith at the 1 $\sigma$  level. However, the total



correction factors,  $\prod_{i=1}^{10} |C_i|$  in Table 4, are in good agreement with the ratios for  $\eta^*/\eta_{2200}$  in Table 2.

For the case of  $U^{233}$ , the analyses of the monoenergetic eta of Smith and the thermal beam eta of Macklin (13,14), yield results which are highly consistent but disparate with the values of eta derived through  $Cf^{252}$  nubar measurements. Essentially, the same can now be said for  $U^{235}$  since, prior to this study, no extensive reanalysis of the  $U^{235}$  data had been attempted. The calculated ratio of  $\eta_{233}/\eta_{235}$  at .025 eV (Table 3) with good statistics (cross section uncertainties, except those of  $U^{233}$  and  $U^{235}$ , have no effect on this ratio) strengthens the interpretation of the present analysis and previous analyses of  $\eta_{233}$ , and lends further support to the eta of  $U^{233}$  used in the LWER program.

### References

1. I. Asplund-Nilsson, H. Condé, and N. Starfelt, Nucl. Sci. Eng. 16, 124, (1963).
2. J. C. Hopkins and B. C. Diven, Nucl. Phys., 48, 433, (1963).
3. D. W. Colvin and M. G. Sowerby, "Proc. IAEA Symp. Physics and Chemistry of Fission," Salzburg, II, 25, (1965).
4. P. H. White and E. J. Axton, J. Nucl. Energy, 22, 23, (1968).
5. E. J. Axton, A. G. Bardell, and B. N. Adric, EANDC(UK)-110, p. 70, National Physical Lab, (1969).
6. A. DeVolpi and K. G. Porges, Phys. Rev., C1, 683, (1970).
7. J. W. Boldeman, Nucl. Sci. Eng., 55, 188, (1974).
8. J. R. Smith, S. D. Reeder, and R. G. Fluhrty, "Measurements of the Absolute Value of Eta for  $U^{233}$ ,  $U^{235}$ , and  $Pu^{239}$  Using Monoenergetic Neutrons," IDO-17083, (1966).
9. R. L. Macklin, G. deSaussure, J. D. Kington, and W. S. Lyon, Nucl. Sci. Eng., 8, 210, (1960).
10. E. J. Axton, Contributions to the EANDC Topical Conference - Nov. 29, 1972, P. Ribon Ed., EANDC(E)-154, 20.
11. J. A. Mitchell and C. J. Emert, "Evaluation of Eta for  $U^{233}$  at .025 eV Using Monte Carlo," Proc. 3rd Conf. Neutron Cross Sections and Technology CONF-710301, Vol. 2, p. 605, August (1971).
12. S. Milani, C. J. Emert, and N. Candelore, "An Evaluation of Eta for  $U^{233}$  at .025 eV Using the RECAP-4C Monte Carlo Program," WAPD-TM-772, September 1968.
13. N. M. Steen, "A Revision of the  $U^{233}$  Thermal Parameters," WAPD-TM-1052, September 1972.
14. M. Goldsmith and J. J. Ullo, "Monte Carlo Analysis of Manganese Bath Measurements of Eta of  $U^{233}$  and  $U^{235}$  Using Thermalized Neutrons," Bull. Am. Phys. Soc., Vol. 20, 2, p. 158, 1975.
15. N. M. Steen, "An Evaluation of the Neutron Reaction Cross Sections and Fission Spectrum of  $U^{233}$  for ENDF/B," WAPD-TM-691, December 1969.
16. G. deSaussure, et al., "Multilevel Analysis of the  $U^{235}$  Fission and Capture Cross Sections," ORNL-TM-3707, March 1972.
17. S. F. Mughabghab and D. I. Garber, BNL-325, EANDC(US)-183/L, (1973).

Table 1

Definition of Calculated Quantities and Results

	$U^{233}$	$U^{235}$
<b>Step 1</b>		
$A_1 = U^{233}$ or $U^{235}$ absorptions per .025 eV beam neutron	.992002 ± .000765	.991242 ± .000706
$B_1 =$ Manganese Absorptions per .025 eV Beam Neutron due to Scattering	.001529 ± .000022	.001618 ± .000022
<b>Step 2</b>		
$A_2 =$ Manganese Absorptions per Initial Fission Neutron	.327378 ± .000171	.327543 ± .000211
$F(1) =$ Second Generation Fissions Between 5.53 keV and 10 MeV	.015815 ± .000176	.008647 ± .000124
$F(2) =$ Second Generation Fissions Between 0.0 eV and 5.53 keV	.006274 ± .000319	.005290 ± .000205
<b>Step 3</b>		
$A_3 =$ Manganese Absorptions per Initial .025 eV Beam Neutron (Target Out)	.336473 ± .000102	.336473 ± .000102

Table 2

	Calculation	Smith
$(\frac{\eta^*}{\eta_{2200}})^{233}$	1.0281 ± .0018*	1.0287 ± .0045
$(\frac{\eta^*}{\eta_{2200}})^{235}$	1.0040 ± .0018*	1.0034 ± .0021

\*Statistical uncertainties only.

Table 3

	Calculated	Smith's Deduced Value
$\eta_{233}$	2.2993 ± .0083*	2.298 ± .009
$\eta_{235}$	2.0777 ± .0064*	2.079 ± .010
$\frac{\eta_{233}}{\eta_{235}}$	1.1067 ± .0052	1.105 ± .005

\*Includes Monte Carlo, cross section, and experimental uncertainties.

Table 4  
Systematic Corrections for  $\sigma_{fs}$  of  $U^{233}$  and  $U^{235}$

Effect	Calculated Value for $U^{233}$	Calculated Value for $U^{235}$
1) Fast Multiplication	$1.0278 \pm .0025$	$1.0146 \pm .0013$
2) Indirect Multiplication and Cadmium Wrap Effects	$.9921 \pm .0013$	$.9826 \pm .0011$
3) Scattering	$.9946 \pm .0012$	$.9941 \pm .0012$
4) Transmission	$.9993 \pm .0001$	$.9995 \pm .0001$
5) Structural Absorption a) Open Beam b) Fission Neutrons	$1.0112 \pm .0006$ $.9982 \pm .0003$	$1.0112 \pm .0006$ $.9982 \pm .0003$
6) Leakage	$.9976 \pm .0012$	$.9977 \pm .0011$
7) Duct Streaming	$.9996 \pm .0001$	$.9997 \pm .0001$
8) Mn Resonance Absorption	$1.0100 \pm .0010$	$1.0100 \pm .0010$
9) High Energy Absorption in O and S	$.9978 \pm .0002$	$.9977 \pm .0002$
10) Impurities	$.9999 \pm .0010$	$.9998 \pm .0010$
$\prod_{i=1}^{10} C_i =$	$1.0279 \pm .0036$	$1.0047 \pm .0028$

Table 5  
Cross Section Sensitivities

Effect	Assumed Variation	Variation in $(\eta/\eta_{2200})^{233}$	Variation in $(\eta/\eta_{2200})^{235}$
U Fast Cross Sections	5%	.00233	.00124
Fission Neutron Mean Energy	0.5%	.00050	.00050
Mn Resonance Integral	2.7%	.00071	.00070
Mn Thermal Absorption Cross Section	1.0%	.00025	.00026
Hydrogen Thermal Absorption Cross Section	0.5%	.00025	.00025
Sulfur and Oxygen Fast Cross Sections	10%	.00022	.00022
Total = $\sqrt{\sum_{i=1}^6 (\delta_i^2)}$		.00253	.00158

# SMITH EXPERIMENT

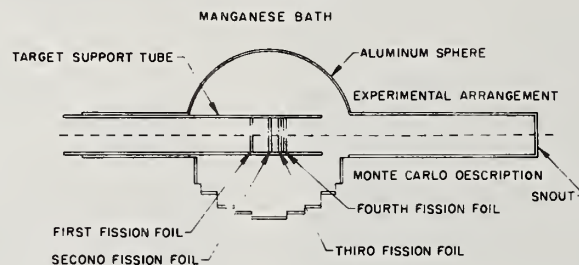


FIGURE 1

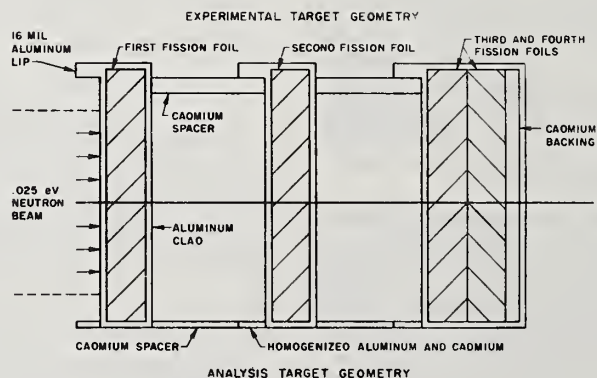


FIGURE 2



OF  $^{233}\text{U}$  AND  $^{235}\text{U}$  USING THERMALIZED NEUTRONS

M. Goldsmith and J. J. Uitto  
Westinghouse Electric Corporation  
Bettis Atomic Power Laboratory  
Pittsburgh, Pennsylvania 15122

Monte Carlo analysis of the ORNL manganese bath measurements of eta of  $^{233}\text{U}$  and  $^{235}\text{U}$  at 2200 m/sec yields:  $\eta_{2200}^{233} = 2.3019 \pm 0.0086$ , and  $\eta_{2200}^{235} = 2.0746 \pm 0.0078$ . The analysis was confirmed by calculating measured quantities used by the experimentalists in their determinations of  $\eta_{2200}$ .

(Nuclear Reactions,  $^{233}\text{U}$ ,  $^{235}\text{U}$ ; fission neutrons per absorption, eta,  $E=0.0253\text{eV}$ )

### I. Introduction

Manganese bath measurements of  $\eta$ , the number of fission neutrons produced per absorption, are direct and absolute but their accuracy has customarily depended upon the evaluation of a considerable number of small corrective factors.<sup>1),2)</sup> In the present study, Monte Carlo methods have been used to analyze the measurements of  $\eta$  of  $^{233}\text{U}$  and  $^{235}\text{U}$  made by Macklin et al.<sup>2)</sup> at the Oak Ridge National Laboratory. The Monte Carlo extraction of  $\eta_{2200}$ , the 2200 m/sec value of eta, implicitly accounts not only for all corrective factors but also for any correlations which may exist between them. Detailed comparisons of our analysis with those of previous workers will be presented in Section IV.

The Oak Ridge experiment analyzed here employed thermalized reactor neutrons as a source and to that extent is not as clean a measurement of  $\eta_{2200}$  as is the Idaho experiment<sup>1)</sup> in which monochromatic neutrons were used. A thermalized source experiment, however, has the obvious advantage that one may use it to test proposed representations of the energy dependence of  $\eta$ .

### II. The Oak Ridge Experiment

In the Oak Ridge measurements of  $\eta$ , neutrons emanate from a reactor, are thermalized in a tank of  $\text{D}_2\text{O}$ , and pass through a collimator into the center of a manganese bath one meter in diameter. The thermal component of the beam, defined by cadmium difference, is first made to activate the bath directly. In a second set of experiments the beam is absorbed in a U target whose fission neutrons activate the bath. The ratio of the target-in to target-out activations caused by the thermal component of the source is numerically close to  $\eta_{2200}$  and is referred to as  $\eta^*$ . Details of the target geometry and of the beam monitoring and counting techniques used in the measurement of  $\eta^*$  are given in Reference 2.

### III. Determination of Eta

Monte Carlo calculations were made using a program written by N. Candelore and R. C. Gast. The range from 5 keV to 10 MeV was spanned by 3000 energy points and inelastic scattering treated explicitly. Elastic scattering by hydrogen was treated exactly, while that by other nuclides was described using four Legendre components in the center of mass system. Between 5 keV and 0.625 eV, the range over which resonance cross sections were generated from either single or multilevel parameters, 26,000 energy points were used. At energies between 0.625 eV and 10 eV, scattering by hydrogen was approximated as that due to free protons at an effective temperature of 0.121 eV; below 0.625 eV the detailed ENDF scattering law was employed.

Insofar as possible, cross sections used in our analysis were taken from the ENDF-4 files. With regard to the resonance data for  $^{235}\text{U}$ , however, the procedures used by us to edit capture and fission events are incompatible with the negative background cross sections used in the ENDF file.  $^{235}\text{U}$  resonance cross sections were therefore generated from the multilevel parameters derived by deSaussure et al.<sup>3)</sup> Sulfur cross sections, negligibly different from those of Reference 4, were generated from data in BNL-325.<sup>4)</sup>

The determination of  $\eta_{2200}$  required three pairs of Monte Carlo calculations. The first set consisted of calculations in which the collimated neutron beam impinged on the target oriented a) as in Figure 1, and b) so that the beam was incident upon the cadmium backing foil. We shall refer to these calculations as the target-in U-Cd and Cd-U problems, respectively. The Al shell surrounding the target was approximated as in Reference 4. The homogenization of Cd and Al shown in Figure 1 preserved Cd mass and changed the surface to mass ratio of the spacers by less than 1%. An analytic representation of the source spectrum was generated by the method of Reference 6 using a Maxwellian temperature of 0.0273 eV, the value calculated for the center of the  $\text{D}_2\text{O}$  bath<sup>2)</sup> using a multigroup discrete ordinate program written by L. Eisenhart.

From the target-in problems were edited:

- $A_1$  = Fraction of a beam neutron absorbed in uranium,
- $B_1$  = Fraction of a beam neutron absorbed in manganese,
- $C^{(i)}$  = Number of initial fission events in each of twelve uranium foil regions.

In the second pair of Monte Carlo calculations, the U-Cd and Cd-U fission start problems, fission neutrons were born in the U foil regions. Spatial weights were proportional to the  $C^{(i)}$  and starting energies chosen from a Maxwellian fission spectrum whose mean energy was 1.98 MeV. The fission start problems yield:

- $A_2$  = Fraction of a fission source neutron absorbed in manganese, and
- $B_2$  = Second generation fission neutrons per fission source neutron.

The number of third and higher generation neutrons, which comprise less than 0.1% of the fission neutrons, was obtained analytically.

The third set of Monte Carlo calculations corresponded to the target-out experiments and yielded:

- $A_3$  = Fraction of a beam neutron absorbed in Mn when the bath is exposed directly to the collimated neutron beam, and
- $A_3^f$  = Fraction of a beam neutron absorbed in Mn when the beam impinges on a 20-mil Cd foil target.



In terms of the parameters edited from the three sets of Monte Carlo problems, one has

$$\frac{\eta^*/\eta_{2200} - D'A_2'(1+B_2') + (B_1-B_1')/\eta_{2200}}{(A_3 - A_3')} \quad (1)$$

where D is the number of first generation fission neutrons per beam neutron divided by  $\eta_{2200}$ , the ENDF value of  $\eta_{2200}$ .  $B_2$  is the number of second and higher generation fission neutrons per beam neutron, and, with the obvious exceptions of  $A_3$  and  $A_3'$ , unprimed and primed quantities refer to U-Cd and Cd-U calculations, respectively.

In order to determine the sensitivity of  $(\eta^*/\eta_{2200})$  to cross section uncertainties, we considered the following plausible variations: U fast cross sections, + 5%; U thermal absorption cross sections, + 1%; U thermal scattering cross sections, + 10%; Mn resonance integral, + 2.7%; Mn thermal absorption cross section, + 1%; hydrogen thermal absorption cross section, + 5%; mean energy of fission spectrum, 0.5%; and S and O fast cross sections, 10%. Uncertainties in the beam source spectrum were taken from Reference 6. The composite cross section uncertainties in  $(\eta^*/\eta_{2200})$  were found to be + 0.0025 and + 0.0018 for U233 and U235, respectively.

Equation 1, together with the combined cross section and Monte Carlo uncertainties, gave

$$\begin{aligned} (\eta^*/\eta_{2200})^{233} &= 1.0059 \pm .0037, \text{ and} \\ (\eta^*/\eta_{2200})^{235} &= 0.9937 \pm .0036 \end{aligned} \quad (2)$$

in which the uncertainties quoted are standard deviations. Dividing the measured values of  $(\eta^*)^2$  by the quantities of Equation 2, one obtains

$$\eta_{2200}^{233} = 2.3019 \pm .0086, \text{ and } \eta_{2200}^{235} = 2.0745 \pm .0079. \quad (3)$$

The excellent agreement of these values with those obtained in References 2 and 6 is displayed in Table 1. It is interesting to note that none of the analyses of the Oak Ridge experiment have led to values of  $\eta_{2200}$  which are significantly different from those obtained originally by the experimentalists themselves. The extent to which this is fortuitous is considered in the next section.

#### IV. Examination of Previous Analyses

In their original determination of  $\eta_{2200}$  from  $\eta^*$ , Macklin et al.<sup>2)</sup> used ten corrective factors whose product was taken to be  $\eta^*/\eta_{2200}$ . The Monte Carlo evaluation of these factors is important from two points of view: Some of the corrections are based on measurement and test the accuracy of the Monte Carlo analysis. Other corrections employed approximations which are tested by the Monte Carlo analysis.

Comparisons of our calculations with those of previous workers are given in Tables 2 and 3. In each case the correction is the ratio of  $(\eta^*/\eta_{2200})$  to the value this parameter would have if the physical effect in question were absent. The denominator of the correction for the energy dependence of  $\eta$ , for example, is  $(\eta^*/\eta_{2200})_{\eta=\text{Const}}$  and is obtained by setting  $D=A_1\eta_{2200}$  and  $D'=A_1'\eta_{2200}$  in Equation 1. The evaluation of the fast effect, in which fission neutrons cause additional fissions before leaving U foils, and the evaluation of the correction for indirect multiplication, in which fission neutrons which have escaped from the foils return to cause additional fissions, were evaluated with the aid of an additional pair of fission start problems in which the target was surrounded by a black non-scattering shroud. One notes from the last two lines of Tables 2 and 3 that the overall effect of correlations is less than the uncertainty, + 0.004, in  $\eta^*/\eta_{2200}$ .

The only serious discrepancies among the results of these tables involve the Oak Ridge determination of the Mn resonance absorption correction and the  $^{233}\text{U}$  energy dependence and transmission correction. In both cases, this is due to improvements in cross sections in the years since Reference 2 appeared.

#### V. Conclusion

Manganese bath measurements of  $\eta_{2200}$  have repeatedly been opened to question because of the numerous corrections which were used to extract  $\eta_{2200}$  from  $\eta^*$ . In the present investigation, we have evaluated  $\eta^*/\eta_{2200}$  by Monte Carlo calculations which implicitly account for these corrections. Further, we have re-evaluated each of the corrections, used by previous workers, and constructed  $\eta^*/\eta_{2200}$  from them. Values of  $\eta^*/\eta_{2200}$  obtained by the two methods agree within 0.2% for both  $^{233}\text{U}$  and  $^{235}\text{U}$ . We conclude that the Oak Ridge measurements imply that  $\eta_{2200}^{233} = 2.302 \pm .009$  and  $\eta_{2200}^{235} = 2.075 \pm .008$ . These values are in good agreement with all previous analyses of both the Oak Ridge and Idaho experiments.

#### References

1. J. R. Smith, S. D. Reeder, and R. G. Fluharty, IDO-17083, February 1966.
2. R. L. Macklin, G. deSaussure, J. D. Kington, and W. S. Lyon, Nuc. Sci. and Eng., 8, 210 (1960).
3. G. deSaussure, R. B. Perez, and W. Kolar, ORNL-TM-3707, March 1972.
4. J. A. Mitchell and C. J. Emert, Proc. 3rd Conf. Neutron Cross Sections and Technology, CONF-710301 (Vol. 2), p. 605, August 1971.
5. S. F. Mughabghab, et al., BNL-325, Third Ed., Vol. 1, Brookhaven National Laboratory, June 1973.
6. N. M. Steen, WAPD-TM-1052, September 1972.
7. J. J. Ullo and M. Goldsmith, "Monte Carlo Analysis of Measurements of Eta of  $^{233}\text{U}$  and  $^{235}\text{U}$  Using Monochromatic Neutrons," Bull. Am. Phys. Soc., Vol. 20, 2, p. 158, 1975.

Table 1

Manganese Bath Determinations of  $\eta_{2200}$ 

Measurement	Analysis	$\eta_{2200}^{233}$	$\eta_{2200}^{235}$
Oak Ridge Expt. (Ref. 2)	Present Work	$2.3019 \pm .0086$	$2.0745 \pm .0079$
	Macklin, et al. (Ref. 2)	$2.296 \pm .010$	$2.077 \pm .010$
	Steen (Ref. 6)	$2.2982 \pm 0.0094$	--
Idaho Expt. (Ref. 1)	Saith, et al. (Ref. 1)	$2.298 \pm .009$	$2.079 \pm .010$
	Ullo and Goldsmith (Ref. 7)	$2.299 \pm 0.008$	$2.078 \pm .006$
	Mitchell and Emert (Ref. 4)	$2.296 \pm 0.007$	--
	Steen (Ref. 6)	$2.2956 \pm .0073$	--
	(ENR-4)	(2.2966)	(2.0728)

Table 2

Contributions to  $(\eta^*/\eta_{2200})^{233}$ 

Correction	Present Work	Macklin, et al. (Ref. 2)	Steen (Ref. 6)
(Energy Dependence of $\eta$ )	$(0.9946 \pm .0013)^*$	(-1)	--
( $U^{233}$ Transmission)	$(0.9868 \pm .0004)$	(-.988)	--
1. Energy Dependence and $U^{233}$ Transmission	$0.9815 \pm .0014$	$0.9876 \pm .0016$	$0.9809 \pm .0007$
2. Fast Effect	$1.0272 \pm .0024$	$1.033 \pm .0020$	$1.0297 \pm .0031$
(Indirect Multiplication)	$(1.0103 \pm .0007)$	--	--
(Cd Absorption of Fission Neutrons)	$(0.9815 \pm .0004)$	--	--
(Al Absorption of Fission Neutrons)	$(0.9979 \pm .0002)$	--	--
3. Indirect Multiplication + Cd Absorption + Al Absorption of Fission Neutrons	$0.9897 \pm .0008$	$0.9891 \pm .0020$	$.9920 \pm .0004$
4. Scattering and Total Target Transmission	$0.9979 \pm .0013$	$0.9976 \pm .0012$	$0.9966 \pm .0008$
5. Mn Resonance Absorption	$1.0111 \pm .0007$	$1.0052 \pm .0005$	$1.0092 \pm .0005$
6. Al Absorption of Non-Fission Neutrons (target-out experiment)	$1.0069 \pm .0007$	$1.0060 \pm .0015$	--
7. Duct Streaming	$0.9996 \pm .0001$	$0.9997 \pm .0001$	--
8. Fast Neutron Leakage	$0.9974 \pm .0003$	$0.9973 \pm .0015$	--
9. High Energy O and S Absorption	$0.9975 \pm .0005$	$0.9942 \pm .0005$	$0.9969 \pm .0004$
10. Sample Impurities	$0.9999 \pm 0.0013$	$0.9999 \pm 0.0013$	--
$\sum_{i=1}^{10} c_i^2 + (\sum_{i=1}^{10} sc_i^2)^{\frac{1}{2}}$	$1.0080 \pm .0036$	$1.0089 \pm .0043$	--
$\eta^*/\eta_{2200}$ (Eq. 2)	$1.0059 \pm .0037$	--	--

\*Uncertainties quoted are standard deviations which include both Monte Carlo and cross section uncertainties.

Table 3  
Contributions to  $(\eta^*/\eta_{2200})^{235}$ 

Physical Effect	Component of $\eta^*/\eta_{2200}$	
	Present Work	Macklin, et al. (Ref. 2)
(Energy Dependence of $\eta$ )	$(0.9946 \pm 0.0013)$	--
( $U^{235}$ Transmission)	$(0.9889 \pm .0004)$	--
1. Energy Dependence and $U^{235}$ Transmission	$0.9837 \pm .0014$	$0.9859 \pm .0025$
2. Fast Effect	$1.0183 \pm .0017$	$1.0182 \pm .0013$
(Indirect Multiplication)	$(1.0073 \pm .0010)$	--
(Cd Absorption of Fission Neutrons)	$(0.9808 \pm .0007)$	--
(Al Absorption of Fission Neutrons)	$(0.9980 \pm .0002)$	--
3. Indirect Multiplication + Cd and Al Absorption of Fission Neutrons	$0.9860 \pm .0012$	$0.9883 \pm .0020$
4. Scattering and Total Target Transmission	$0.9959 \pm .0013$	$0.9985 \pm .0008$
5. Mn Resonance Absorption	$1.0111 \pm .0007$	$1.0052 \pm .0005$
6. Al Absorption of Non-Fission Neutrons	$1.0069 \pm .0007$	$1.0060 \pm .0015$
7. Duct Streaming	$0.9996 \pm .0001$	$0.9997 \pm .0001$
8. Fast Neutron Leakage	$0.9974 \pm .0003$	$0.9973 \pm .0015$
9. High Energy O and S Absorption	$0.9975 \pm .0005$	$0.9942 \pm .0005$
10. Sample Impurities	$0.9998 \pm 0.0030$	$0.9998 \pm 0.0030$
$\sum_{i=1}^{10} c_i^2 + (\sum_{i=1}^{10} sc_i^2)^{\frac{1}{2}}$	$0.9957 \pm .0043$	$0.9927 \pm .0052$
$\eta^*/\eta_{2200}$ (Eq. 2)	$0.9937 \pm .0036$	--

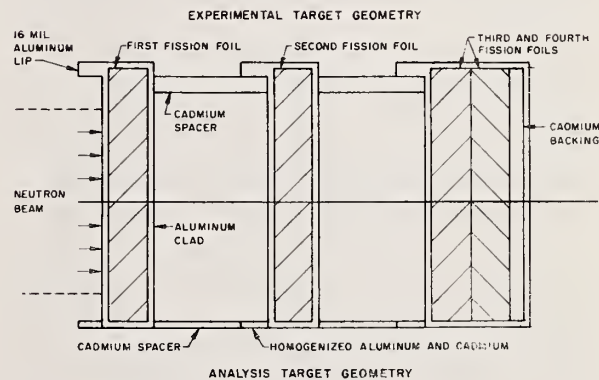


FIGURE 1



George F. Auchampaugh  
Los Alamos Scientific Laboratory  
Los Alamos, New Mexico 87544

Lawrence W. Weston  
Oak Ridge National Laboratory  
Oak Ridge, Tennessee 37830

The neutron subthreshold fission cross section of  $^{240}\text{Pu}$  has been measured from 500 eV to 10 000 eV using the Oak Ridge Electron Linear Accelerator neutron facility. A total of 82 fission widths were obtained from area and shape analysis of those resonances which define the class II states at  $\approx 782$  eV,  $\approx 1406$  eV,  $\approx 1936$  eV, and  $\approx 2700$  eV. The average square of the coupling matrix element for the first three class II states is  $4.08 \pm 1.63$  eV<sup>2</sup>. The average class II fission width is  $2.47 \pm 0.96$  eV. Approximately 22 clusters of class I resonances were observed below 10 keV, which results in a value of  $450 \pm 50$  eV for the average class II level spacing. Assuming parabolic inner and outer barriers, the following barrier parameters were obtained:  $V_{A-Bn}/\hbar\omega_A = 0.59 \pm 0.06$  and  $V_{B-Bn}/\hbar\omega_B = 0.54 \pm 0.06$ .

$$[^{240}\text{Pu}(n,f); 500 \text{ to } 10,000 \text{ eV}; \Gamma_{f\lambda'}, \Gamma_{f\lambda''}^{\text{II}}, \langle H_{\lambda',\lambda''}^2 \rangle]$$

### Introduction

The existence of narrow intermediate structure is a well-known feature in the subthreshold region of the neutron-induced fission cross sections of nuclei in the mass region  $234 \leq A \leq 244$ .<sup>1-3</sup> Lynn<sup>4</sup> and Weigmann<sup>5</sup> ascribe the observed intermediate structure to coupling between the compound nuclear states corresponding to the ground-state deformation of the nucleus "class I", and the "class II" states in the secondary minimum of the double-humped fission barrier.<sup>6</sup> The separation between the clusters of strong fission resonances ( $D_{\text{II}} \gg D_{\text{I}}$ ) provides information on the level density of states in the secondary minimum. A detailed analysis of the structure within each cluster provides information on the coupling matrix elements  $H_{\lambda',\lambda''}$  between the class II state,  $\lambda''$ , and the class I states,  $\lambda'$ , and on the fission width,  $\Gamma_{f\lambda''}^{\text{II}}$ , of the class II state. The averages  $\langle \langle H_{\lambda',\lambda''}^2 \rangle \rangle_{\text{II}}$  and  $\langle \Gamma_{f\lambda''}^{\text{II}} \rangle_{\text{II}}$  over many class I states (denoted by  $\langle \rangle_{\text{I}}$  for a fixed  $\lambda''$ ) and class II states (denoted by  $\langle \rangle_{\text{II}}$ ) can be related to the penetrabilities through the inner and outer barriers, respectively.

According to Lynn,<sup>4</sup> the  $H_{\lambda',\lambda''}^2$  for the  $\lambda''$  state will fluctuate according to a Porter-Thomas distribution.<sup>7</sup> Also,  $\langle H_{\lambda',\lambda''}^2 \rangle_{\text{I}}$  and  $\Gamma_{f\lambda''}^{\text{II}}$  will fluctuate strongly from one state to another. Therefore, to study the coupling mechanism for a given nucleus requires measuring a large number of  $H_{\lambda',\lambda''}^2$  and  $\Gamma_{f\lambda''}^{\text{II}}$ .

We report in this paper on a measurement of the subthreshold neutron-induced fission cross section of  $^{240}\text{Pu}$  and on the analysis of the intermediate structure of the first three class II states in the system  $^{240}\text{Pu}+n$ .

### Experimental Details

For the  $^{240}\text{Pu}(n,f)$  measurement the Oak Ridge Electron Linear Accelerator was operated at power levels up to 25 kW for 8-ns-wide pulses at a repetition

rate of 1000 pulses per second. A 20.0-m flight path was used for the measurement.

Data were taken on samples of  $^{240}\text{Pu}$ ,  $^{239}\text{Pu}$ , and  $^{238}\text{U}$ . The pressed sample of  $^{240}\text{Pu}$  was made from a mixture of approximately 12 g of S and 10.23 g of  $\text{PuO}_2$  (98.47% isotropic enrichment), and the pressed sample of  $^{239}\text{Pu}$  from a mixture of 5.33 g of  $\text{Pu}$  (98.91%) metal and 1.07% by weight Al. The  $^{238}\text{U}$  (99.99%) sample was in metallic form. The diameter of the samples was 7.62 cm and that of the neutron beam 10.2 cm. The samples were oriented at  $45^\circ$  to the incident neutron beam direction. At  $45^\circ$  they had atom/barn thicknesses of 0.000692 ( $^{240}\text{Pu}$ ), 0.000409 ( $^{239}\text{Pu}$ ), and 0.00738 ( $^{238}\text{U}$ ).

Two NE-213 liquid scintillators (10 cm in diameter by 5-cm thick) mounted on 12.7-cm-diameter photomultipliers (58 AVP) were used as gamma-ray and fission-neutron detectors. They were aligned perpendicular to the neutron beam direction, diametrically opposite each other, 5.5 cm from the center of the sample.

Pulse-shape discrimination (PSD) of the Forte-type<sup>8</sup> was used on the signals from each detector to tag the neutron and gamma-ray pulses. A 1.3-cm-thick disk of lead was inserted in front of each detector to reduce the effects of the intense gamma flash from the machine.

The fission neutron efficiency was about 5.5% per detector per fission event. The fission gamma-ray efficiency was about 1.5% for both detectors per fission event. These were determined by detecting the fission neutrons and fission gamma rays from the spontaneous fission of  $^{240}\text{Pu}$  using for the spontaneous fission half life  $1.4 \times 10^{11}$  y.<sup>9</sup> The neutron efficiency was low enough to suppress effects due to multiple neutron detection, as evidenced by the fact that the ratio of coincidence to single events between the two detectors was less than 1%.

The neutron and gamma-ray time-of-flight (TOF) spectra from each detector, as well as the neutron coincidence TOF spectrum, were stored simultaneously in separate regions of the fast-disk storage device attached to the Oak Ridge SEL810B computer system. In addition, a measurement of the neutron spectrum shape was made using a  $^{10}\text{B}$  parallel plate ionization chamber which was inserted in the neutron beam upstream of the

\*Work done under the auspices of the U.S. Energy Research and Development Administration.



sample position. The diameter of the  $^{10}\text{B}$  deposit was 7.62 cm. Therefore it saw the same neutron beam as the other samples. All data were taken with channel widths of 16 ns (500 to 1300 eV) and 8 ns (1300 to 10 000 eV). Data above 10 keV were not analyzed due to spectrum distortion effects caused by the gamma flash.

### Data Reduction

We corrected the neutron TOF spectra of  $^{240}\text{Pu}$  and  $^{239}\text{Pu}$  for gamma-ray events, tagged as neutron events in the PSD circuit, by subtracting from each neutron TOF spectrum a fraction,  $K$ , of the corresponding gamma-ray TOF spectrum. Since the fission cross section of  $^{238}\text{U}$  is essentially zero in the low-eV region, the neutron TOF spectrum should contain no true fission neutron events.  $K$  was obtained from ratios of the  $^{238}\text{U}$  resonance areas in the gamma-ray TOF spectrum to the corresponding ones in the neutron TOF spectrum.  $K$  was checked against that obtained from a few selected capture-only resonances in  $^{240}\text{Pu}$ . The two values of  $K$  agreed within the errors calculated for each  $K$ . This implies that the detectors were not sensitive to the differences between the  $^{238}\text{U}$  capture gamma-ray spectrum and the  $^{240}\text{Pu}$  or  $^{239}\text{Pu}$  capture plus fission gamma-ray spectra. The effect this correction had on the determined fission widths was less than 10%.

The corrected neutron TOF  $^{240}\text{Pu}$  data were converted to cross section by dividing by the  $^{10}\text{B}$  spectrum. The  $^{10}\text{B}$  spectrum was normalized in the interval from 600 to 1000 eV by the corrected  $^{239}\text{Pu}$  data using the ENDF/B-IV evaluated  $^{239}\text{Pu}$  fission cross section.<sup>10</sup> The fission neutron efficiency for  $^{240}\text{Pu}$  was set equal to that for  $^{239}\text{Pu}$  ( $\bar{\nu}_{\text{n}}^{239} \approx \bar{\nu}_{\text{n}}^{240}$ ).

### Results and Analysis

The final  $^{240}\text{Pu}$  fission cross section shown in Fig. 1 represents a sum of all singles data from both detectors and coincidence data. Approximately 22 clusters of resonances are visible below 10 keV. The class II level spacing  $D_{\text{II}}$  is  $450 \pm 50$  eV (Wigner distribution error  $\pm \sqrt{0.273 D^2/N}$ ).

The results of an area and shape analysis of these data are presented in Table I. Multiple scattering and self-shielding effects are less than 2% and are ignored. The thin sample approximation is used for all but the strongest fission resonances. The neutron widths labeled (a) are taken from the total cross-section measurement by Kolar et al.<sup>11</sup> The parameters labeled with a (b) are obtained from a shape fit to the data using the code MULTI.<sup>12</sup> The neutron widths of the strongest fission resonances are allowed to vary since they are quoted with very large errors in the total cross-section measurement.<sup>11</sup> Our final values of  $\Gamma_{\text{n}}^{\text{O}}$  fall within the quoted errors. A satisfactory fit to the doublet at 1405 eV cannot be achieved unless the neutron widths for these two resonances are allowed to vary. The 1936-eV resonance which appears to have most of the fission strength for the 1936-eV cluster is not seen in the total cross-section measurement. For the 2700-eV cluster the resonances are not sufficiently resolved to permit a

meaningful shape fit. It is unlikely that the perturbed class II state (for weak coupling the resonance with most of the fission strength) has been found for this cluster since the fission and neutron widths for the 2695-eV resonance, which has the largest fission width, do not have the same properties of the other three class II states, namely,  $\Gamma_{\text{f}}(2695) \sim 1/15 \langle \Gamma_{\text{f}\lambda}^{\text{II}} \rangle$  and  $\Gamma_{\text{n}}^{\text{O}}(2695) \sim 66 \langle \Gamma_{\text{n}\lambda}^{\text{O}} \rangle$ . For this reason the remaining analysis ignores the 2700-eV data.

A plot of  $\Gamma_{\text{f}}$  vs  $E$  reveals that the widths of the envelopes of the intermediate structure are less than  $D_{\text{I}} = 14.67$  eV.<sup>11</sup> The neutron widths given in Table I for the 782-eV and 1936-eV resonances are, on the average,  $\sim 1/10 \langle \Gamma_{\text{n}}^{\text{O}} \rangle$ : the fission widths are  $\approx \Gamma_{\text{f}}^{\text{II}}$ . The neutron widths of the doublet cannot be included in this comparison if the class II state is degenerate. In this case, the acquired neutron width of the class II state,  $\Gamma_{\text{n}\lambda}^{\text{O}}$ , is approximately 1/2 that of the unperturbed class I neutron width,  $\Gamma_{\text{n}}^{\text{OI}}$ ; if  $\Gamma_{\text{n}}^{\text{OI}}$  is large, then  $\Gamma_{\text{n}\lambda}^{\text{O}}$  will be large. These two properties of the structure require that  $\langle H_{\lambda, \lambda'} \rangle$  and  $\langle \Gamma_{\text{f}}^{\text{II}} \rangle \ll D_{\text{I}}$ . Therefore, the fission width of a class I resonance, in the uniform picket-fence model, is given by

$$\Gamma_{\text{f}\lambda} = \frac{\langle H_{\lambda, \lambda'}^2 \rangle \Gamma_{\text{f}\lambda}^{\text{II}}}{(E_{\lambda} - E^{\text{II}})^2 + (W/2)^2 + WD_{\text{I}}/2\pi} + \langle \Gamma_{\text{f}\lambda}^{\text{b}} \rangle,$$

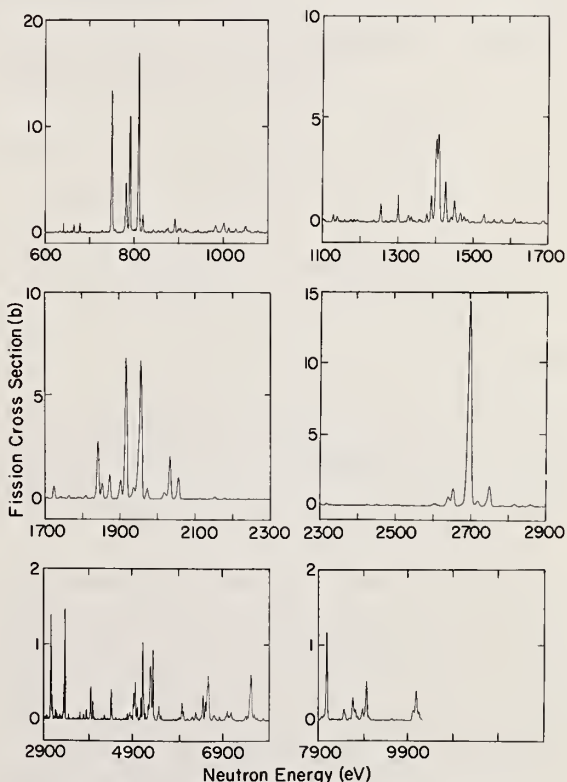


Fig. 1 -  $^{240}\text{Pu}$  subthreshold fission cross sections from 500 to 10 000 eV.

TABLE I

<sup>240</sup>Pu+n CLASS I RESONANCE PARAMETERS

E (eV)	$\Gamma_n^a$ (meV)	$\Gamma_f$ (meV)	E (eV)	$\Gamma_n^a$ (meV)	$\Gamma_f$ (meV)	E (eV)	$\Gamma_n^a$ (meV)	$\Gamma_f$ (meV)
608	0.92 ± 0.06	0.06 ± 0.05	1002	3.10 ± 0.16	1.12 ± 0.08	1724	2.01 ± 0.16	2.16 ± 0.16
632	0.53 ± 0.05	0.44 ± 0.09	1042	0.39 ± 0.06	1.13 ± 0.20	1742	0.60 ± 0.10	0.83 ± 0.16
637	0.46 ± 0.05	0.17 ± 0.06	1073	3.34 ± 0.17	0.31 ± 0.05	1764	1.23 ± 0.11	0.65 ± 0.09
665	7.64 ± 0.31	0.48 ± 0.05	1099	2.54 ± 0.26	0.25 ± 0.05	1841	2.93 ± 0.21	10.70 ± 0.74
678	1.00 ± 0.07	0.78 ± 0.08	1129	1.49 ± 0.09	0.70 ± 0.08	1853	0.80 ± 0.13	4.15 ± 0.55
712	0.050 ± 0.023	0.80 ± 0.90	1134	0.20 ± 0.06	0.60 ± 0.3	1873	1.79 ± 0.16	4.91 ± 0.39
743	0.037 ± 0.026	3.0 ± 34.0	1143	1.20 ± 0.08	0.12 ± 0.04	1901	4.80 ± 0.29	3.0 ± 0.1 <sup>b</sup>
750	2.49 ± 0.12	12.70 ± 0.95	1159	0.65 ± 0.06	0.28 ± 0.07	1917	0.82 ± 0.14	70.0 ± 1.0 <sup>b</sup>
759	0.22 ± 0.03	1.42 ± 0.59	1185	4.57 ± 0.23	0.30 ± 0.06	1936	0.045 ± 0.005 <sup>b</sup>	2200 ± 600 <sup>b</sup>
779	0.007 ± 0.015 <sup>b</sup>	10 to 100 <sup>b</sup>	1191	3.33 ± 0.17	0.34 ± 0.06	1944	0.18 ± 0.11	1.8 ± 0.4 <sup>b</sup>
782.4	0.130 ± 0.002 <sup>b</sup>	1450 ± 400 <sup>b</sup>	1208	1.81 ± 0.11	0.13 ± 0.05	1950	1.87 ± 0.17	6.3 ± 0.10 <sup>b</sup>
791.4	0.85 ± 0.05	12.5 ± 0.4 <sup>b</sup>	1236	0.32 ± 0.06	0.59 ± 0.16	1957	5.90 ± 0.36	25.0 ± 0.20 <sup>b</sup>
811.0	7.52 ± 0.35	11.6 ± 0.1 <sup>b</sup>	1255	2.17 ± 0.13	1.79 ± 0.13	1973	1.53 ± 0.17	1.80 ± 0.10 <sup>b</sup>
820.3	3.84 ± 0.19	1.10 ± 0.02 <sup>b</sup>	1301	6.79 ± 0.35	1.47 ± 0.10	2016	1.17 ± 0.17	2.64 ± 0.29
846	0.35 ± 0.03	0.93 ± 0.14	1329	10.13 ± 0.51	0.84 ± 0.06	2034	2.25 ± 0.21	9.79 ± 0.77
855	1.64 ± 0.09	0.30 ± 0.05	1345	0.71 ± 0.08	0.47 ± 0.09	2056	1.51 ± 0.17	5.73 ± 0.51
876	0.47 ± 0.04	0.96 ± 0.13	1363	0.20 ± 0.08	0.70 ± 0.60	2154	0.31 ± 0.15	2.28 ± 1.00
891	3.16 ± 0.15	1.32 ± 0.09	1377	1.74 ± 0.12	1.10 ± 0.10	2178	(1.83 ± 0.18)	0.36 ± 0.07
904	0.73 ± 0.05	0.67 ± 0.08	1389	0.38 ± 0.07	5.0 ± 0.2 <sup>b</sup>	2577	0.94 ± 0.19	0.48 ± 0.14
909	2.62 ± 0.13	0.06 ± 0.04	1402.2	0.22 ± 0.01 <sup>b</sup>	2000 ± 200 <sup>b</sup>	2639	8.29 ± 0.83	5.22 ± 0.29
915	1.19 ± 0.07	0.56 ± 0.07	1408.5	0.23 ± 0.01 <sup>b</sup>	1500 ± 200 <sup>b</sup>	2652	0.71 ± 0.16	14.46 ± 2.95
943	4.00 ± 0.18	0.32 ± 0.05	1426	0.97 ± 0.10 <sup>b</sup>	5.3 ± 0.1 <sup>b</sup>	2695	6.64 ± 0.50	164 ± 18
958	2.31 ± 0.16	0.19 ± 0.05	1430	0.4 ± 0.2 <sup>b</sup>	1.6 ± 0.3 <sup>b</sup>	2719	0.78 ± 0.19	5.29 ± 0.92
971	2.58 ± 0.13	0.41 ± 0.05	1450	1.67 ± 0.14	3.42 ± 0.27	2741	3.38 ± 0.34	1.74 ± 0.35
979	0.23 ± 0.05	1.10 ± 0.20	1466	0.55 ± 0.09	2.71 ± 0.42	2750	1.95 ± 0.25	11.17 ± 1.10
			1484	(0.24 ± 0.08)	1.70 ± 0.80	2819	0.78 ± 0.19	1.98 ± 0.36
					- 0.40	2845	2.94 ± 0.30	0.69 ± 0.11
			1576	3.18 ± 0.19	0.51 ± 0.06	2860	0.51 ± 0.21	2.81 ± 0.85
			1610	0.87 ± 0.10	1.12 ± 0.14			
			1688	0.80 ± 0.10	1.07 ± 0.15			

<sup>a</sup>Parameters from Ref. 11.

<sup>b</sup>Parameters obtained from the shape fitting code MULTI (Ref. 12).

where  $W = 2\pi \frac{\langle H_{\lambda',\lambda''}^2 \rangle}{D_I}$  and  $\langle \Gamma_{f\lambda'}^b \rangle$  is the average class

I fission width for direct penetration through both barriers.

The values of  $\langle H_{\lambda',\lambda''}^2 \rangle$  and  $\Gamma_{f\lambda''}^{II}$  given in Table II are obtained from fitting the step function

$$\Sigma(E_{\lambda'}) = \sum_{\lambda''} \Gamma_{f\lambda''}^{II}, \text{ vs } E_{\lambda'}, \text{ with the function}$$

$\bar{\Sigma}(E) = \bar{\Sigma}^b + 1/\pi \tan^{-1} \left( \frac{E - E_{\lambda''}^{II}}{W/2} \right)$ , as suggested by Lane,<sup>13</sup> for each cluster separately. A satisfactory fit is obtained to the 782-eV and 1939-eV clusters with and without the background term,  $\bar{\Sigma}^b$ . The errors given reflect the extremes of these two conditions.

The 1405-eV doublet represents an excellent textbook example of near degeneracy [ $(E_{\lambda'}^I - E_{\lambda''}^{II})/2H_{\lambda',\lambda''} < 1$ ] between an unperturbed class II state,  $E_{\lambda''}^{II}$ , and an unperturbed class I state,  $E_{\lambda'}^I$ . If we ignore the other levels in the cluster then the unperturbed parameters of the two-level system are completely determined;  $\Gamma_n^{OI} = 0.45$  meV,  $\Gamma_f^{II} = 3500$  meV,  $E_1^I = 1405.7$  eV,  $E_2^{II} = 1405.0$  eV, as well as  $H_{12}^2 = 9.91$  eV.<sup>2</sup>

TABLE II

<sup>240</sup>Pu+n CLASS II RESONANCE PARAMETERS

E (eV)	$\langle H_{\lambda',\lambda''}^2 \rangle$ (eV) <sup>2</sup>	$\Gamma_{f\lambda''}^{II}$ (eV)
782	2.24 ± 0.23	1.6 ± 0.4
1406	4.67 ± 2.33	3.5 ± 0.4
1936	5.37 ± 3.27	2.3 ± 0.6

The fit to the 1405-eV integral data using the function  $\bar{\Sigma}(E)$  is too sensitive to the fission widths of the doublet to yield a value of  $\langle H_{\lambda',\lambda''}^2 \rangle$  which fits the wings of the data well. The estimate of  $\langle H_{\lambda',\lambda''}^2 \rangle$  given in Table II is obtained from an "eyeball" fit to the data.

The average values of  $\langle \Gamma^{\dagger} \rangle \equiv \Gamma_{f\lambda''}^{II}$  and  $\langle \Gamma^{\dagger} \rangle \equiv 2\pi \langle H_{\lambda',\lambda''}^2 \rangle / D_I$  are related to the penetrabilities through the inner and outer barriers, respectively. If we describe these barriers by parabolas, then the heights of the inner,  $V_A$ , and outer,  $V_B$ , barriers can be calculated from the following formulas,

$$2\pi \frac{\langle \Gamma^{\dagger} \rangle}{D_{II}} = \left\{ 1 + \exp \left[ \frac{2\pi}{\hbar\omega_A} (V_A - E_n) \right] \right\}^{-1}$$

and

$$2\pi \frac{\langle \Gamma^\uparrow \rangle}{D_{II}} = \left\{ 1 + \exp \left[ \frac{2\pi}{\hbar\omega_B} (V_B - B_n) \right] \right\}^{-1},$$

where  $B_n$  is the neutron binding energy and  $\hbar\omega_{A,B}$  the curvature parameters of the barriers. The inner and outer barrier heights given in Table III are calculated using reported values of  $\hbar\omega_{A,B}$ .<sup>14</sup> The agreement between  $V_A$  and  $V_B$  of Ref. 14 and our values is remarkable considering that we are dealing with an s-wave barrier and they are dealing with an average over many angular momentum barriers.

We would like to acknowledge the assistance provided by J. D. Moses in the analysis of the coupling matrix element distributions.

TABLE III

<sup>240</sup>Pu+n BARRIER PARAMETERS

Inner Barrier

$$\langle \Gamma^\uparrow \rangle = 1.75 \pm 0.70 \text{ eV}$$

$$V_A - B_n / \hbar\omega_A = 0.59 \pm 0.06$$

$$V_A = 5.89 \pm 0.09 \text{ MeV}$$

$$\hbar\omega_A^a = 1.10 \pm 0.10 \text{ MeV}$$

$$V_A^a = 6.25 \pm 0.20 \text{ MeV}$$

Outer Barrier

$$\langle \Gamma^\uparrow \rangle = 2.47 \pm 0.96 \text{ eV}$$

$$V_B - B_n / \hbar\omega_B = 0.54 \pm 0.06$$

$$V_B = 5.54 \pm 0.03 \text{ MeV}$$

$$\hbar\omega_B^a = 0.55 \text{ MeV}$$

$$V_B^a = 5.50 \text{ MeV}$$

<sup>a</sup>Ref. 14.

References

1. E. Migneco and J. P. Theobald, Nucl. Phys. A112, 603 (1968).
2. D. Paya, H. Derrien, A. Fubini, A. Michaudon, and P. Ribon, "Nuclear Data for Reactors" (IAEA, Vienna, 1968), Vol. II, p. 128.
3. G. D. James, Nucl. Phys. A123, 24 (1969).
4. J. E. Lynn, United Kingdom Atomic Energy Research Establishment report AERE-R 5891 (1968).
5. H. Weigmann, Z. Phys. 214, 7 (1968).
6. V. M. Strutinsky, Nucl. Phys. A95, 420 (1967).
7. C. E. Porter and R. G. Thomas, Phys. Rev. 104, 483 (1956).
8. M. Forte, International Conf. on Peaceful Uses of Atomic Energy, A/Conf. 15/P/1514, Geneva (1958).
9. C. M. Lederer, J. M. Hollander, and I. Perlman, Table of Isotopes, 6th Ed., John Wiley & Sons, Inc., New York (1967).
10. ENDF/B-IV MAT 1264 distributed in 1974.
11. W. Kolar and K. H. Böckhoff, J. of Nucl. Energy 22, 299 (1968).
12. G. F. Auchampaugh, Los Alamos Scientific Laboratory report LA-5473-MS (1974).
13. A. M. Lane, J. E. Lynn, and J. D. Moses, Nucl. Phys. A232, 189 (1974).
14. B. B. Back, H. C. Britt, Ole Hansen, B. Leroux, Phys. Rev. C10, 1948 (1974).



D. B. Gayther

Nuclear Physics Division, A.E.R.E., Harwell, Didcot, Oxon., U.K.

The cross-section for the  $^{239}\text{Pu}(n,f)$  reaction has been measured on the Harwell 45 MeV linac using the time-of-flight method. Fission events were recorded by detecting the prompt neutrons and the incident neutron flux spectrum was measured with a detector which was calibrated against two standard detectors. The cross-section was normalised in the 10 to 30 keV energy interval to agree with the recent evaluation of Sowerby et al. Comparison with this evaluation shows agreement to within 5% at energies above a few keV. The agreement with the ENDF/B-IV evaluation is generally within 4% throughout the complete energy range. A similar comparison is made for the ratio of the  $^{239}\text{Pu}$  and  $^{235}\text{U}$  fission cross-sections, obtained from the present measurement, and a previously published measurement of the  $^{235}\text{U}(n,f)$  cross-section made with the same equipment.

(Fission; cross-sections;  $^{239}\text{Pu}$ ;  $^{235}\text{U}$ ; measured; neutrons; 1 keV - 1 MeV)

### Introduction

A knowledge of the fission cross-section of  $^{239}\text{Pu}$  is essential to fast reactor technology, and yet in the important energy region from 30 keV to several MeV few direct measurements of this quantity have been published, and these have been mainly restricted to measurements at 'spot' energies made with electrostatic machines or neutron sources. The discovery of large fluctuations in the cross-section in the keV region<sup>1</sup> emphasises the need for new measurements to be made at continuous energies using the time-of-flight technique.

This paper reports the results of a measurement of the  $^{239}\text{Pu}(n,f)$  cross-section made on the Harwell 45 MeV linac using the time-of-flight technique. The measurements were made with the same apparatus and were taken in the same period of time as previously published measurements of the  $^{235}\text{U}(n,f)$  cross-section<sup>2</sup>. The relative cross-sections measured for both reactions were normalised to average values in the 10 to 30 keV energy range obtained from the recent UK evaluations of Sowerby et al.<sup>3</sup>. The ratio of the average  $^{239}\text{Pu}(n,f)$  and  $^{235}\text{U}(n,f)$  cross-section was also derived from the measurements. The measurements are compared with other recent measurements and the UK and ENDF/B-IV evaluations.

### Experimental Method

The experimental method will be summarised since it has been described in detail previously<sup>2</sup>.

The fission yields and the incident neutron spectrum were measured using the time-of-flight technique with the detectors placed alternately at the same position on a 100 m flight path of the linac. The nominal overall experimental resolution for all measurements was 1.7 ns/m. The same collimation system was used throughout to give a beam 8 cm in diameter at the detector position.

#### The fission detector

Fission events were detected by observing the prompt fission neutrons in one or more of four NE213 proton recoil detectors placed around the sample but out of the incident beam. Gamma rays from neutron capture or inelastic scattering were rejected by pulse-shape discrimination. The measurements extended upwards in energy to 1 MeV, and the detection of scattered neutrons in this range was prevented by setting the electronic bias of each detector to reject all neutrons with energies below 1 MeV. The four detectors were placed at 90° to the incident beam.

With the particular arrangement used, the

efficiency for detecting fission neutrons was low, and the observed fission yield per neutron incident on a thin sample was accurately proportional to  $\bar{\nu} p \sigma_f$ , where  $\bar{\nu}$  is the average number of prompt neutrons per fission and  $\sigma_f$  is the fission cross-section.

Measurements were made on two 7.9 cm diameter samples of  $^{235}\text{U}$  containing respectively  $1.08 \times 10^{-3}$  and  $3.8 \times 10^{-3}$   $^{235}\text{U}$  atoms/b and one 5.1 cm diameter sample of  $^{239}\text{Pu}$  containing  $1.2 \times 10^{-3}$   $^{239}\text{Pu}$  atoms/b. The plutonium sample was in alloy form containing 1% by weight of Al and was clad in Al of wall thickness 0.13 mm. The plutonium sample also contained 0.7% by weight of  $^{240}\text{Pu}$  and a small correction (<0.8%) was made to the observed fission yields above 200 keV to allow for its presence. Corrections for other fissile isotopes in the samples were unnecessary.

### Spectrum measurement

The incident neutron spectrum at the 100 m station was measured with a calibrated boron-vaseline plug detector. This consisted of a 7 cm diameter boron-vaseline cylinder placed coaxially in the beam and surrounded by four NaI crystals which detected the 478 keV gamma-rays from the  $^{10}\text{B}(n,\alpha\gamma)^7\text{Li}$  reaction.

The relative neutron detection efficiency of the detector as a function of energy was determined by calibration against the 'black' detector of Coates et al.<sup>4</sup> from 1 to 700 keV using the linac 300 m flight path, and from 68 keV to 2 MeV against the Harwell long counter<sup>5</sup> using the pulsed Van de Graaff IBIS. No attempt was made to determine the absolute efficiency, and the relative efficiency curves obtained from the two calibrations were normalised in the region of overlap.

### Background determination

The backgrounds in all the time-of-flight measurements were determined with the 'black' resonance filter technique, using samples of Mn, Al and  $\text{SiO}_2$ . The background points between the 2.38 keV Mn resonance and the 440 keV oxygen resonance were fitted by a power law in flight time which was used to extrapolate beyond this energy range. The time-dependent component of background determined in this way did not exceed 5% of the true open beam counts in any of the measurements, and in the regions of extrapolation its value was always less than 2% of the open counts.

### Data Analysis

#### Corrections

Following the standard corrections for background and count loss in the time-of-flight measurements, three further corrections were required in order to

obtain the fission cross-sections.

Energy dependence of fission detector efficiency. The efficiency of the system for detecting fission neutrons varies with the energy of the neutron beam incident on the sample due to the effects of changes in the prompt neutron energy and angular distributions.

1. The fission neutron detectors consisted of cylindrical glass cells, 12.5 cm diameter and 7.6 cm thick, containing the NE213 liquid scintillator. The neutrons entered the plane surfaces of the cells. Each pulse height discriminator was adjusted to allow the detection of only those neutrons with energy greater than about 1.5 MeV. With this arrangement, calculation showed that as the temperature of the prompt neutron spectrum rises so the efficiency of detection increases. Since the effect was small, the neutron spectrum was represented by a Maxwellian with a temperature determined by the energy dependence of  $\bar{v}_p$  through the Terrell relationship<sup>6</sup>. The correction was negligible for both nuclei at incident energies below 100 keV. At higher energies, the detection efficiency increases with increasing neutron energy, the correction at 1 MeV being 0.7% for <sup>235</sup>U and 0.9% for <sup>239</sup>Pu.

2. In the energy range under consideration, both nuclei exhibit a forward-backward peaked anisotropy of emission with respect to the direction of the incident beam. If all the prompt neutrons are assumed to be emitted from the fully accelerated fragments, then they also will show a similar but smaller anisotropy; recent evidence suggests this assumption to be reasonable<sup>7,8</sup>. Since the fragment anisotropy generally increases with increasing incident neutron energy, there will be a corresponding decrease in fission detection efficiency for a detector placed at 90° to the beam. The correction for this effect was estimated by supposing all the fission neutrons to be emitted isotropically in the fragment rest systems, making due allowance for the 1.5 MeV detection bias and the angular resolution of the detectors. In the case of <sup>235</sup>U the correction was negligible below 200 keV and reached a maximum value of 1.4% at 1 MeV. The correction for <sup>239</sup>Pu increased from zero at 50 keV to a maximum value of 1% at 1 MeV.

Sample thickness effects. Since the measurements are not absolute, the only concern is with the effect of sample thickness on the relative shapes of the measured cross-sections.

The corrections for multiple scattering and self-shielding in the <sup>235</sup>U samples were treated with a Monte Carlo code<sup>9</sup> and used average cross-sections from the UK Nuclear Data Library. The results of these calculations, which have been described previously<sup>2</sup>, showed that for the thicker of the two samples the overall correction for sample thickness changes by about 2% between 1 keV and 1 MeV. For the thinner sample the net correction changes by less than 1% throughout the energy range. These calculations did not include the increase in fission yield produced by fission neutrons and inelastically scattered neutrons. The effect of such 'multiple reactions'<sup>10</sup> on the shape of the cross-section measured for the thicker sample was estimated to be less than 1%, and no correction for these effects was applied.

No correction was applied to the <sup>239</sup>Pu measurements, since experimental evidence<sup>11</sup> shows that this is not necessary for a measurement of the relative cross-section with the sample thickness used.

The energy dependence of  $\bar{v}_p$ . In deriving the fission cross-section from the directly observed quantity,  $\bar{v}_{pof}$ , the evaluations of Mather and

Bampton<sup>12,13</sup> were used to allow for the energy dependence of  $\bar{v}_p$ .

TABLE I. ESTIMATED SYSTEMATIC ERRORS IN THE MEASUREMENTS

Contribution	Error (%)	
SPECTRUM MEASUREMENT	$2\frac{1}{2} - 3\frac{1}{2}$	
FISSION MEASUREMENTS	Pu-239	U-235
Detector efficiency	0 - $\frac{1}{2}$	0 - $\frac{1}{2}$
Background determination	1 - $1\frac{1}{2}$	0 - $1\frac{1}{2}$
Sample thickness correction	1	1
$\bar{v}_p(E)$	1	1
TOTAL SYSTEMATIC ERROR IN MEASURED CROSS-SECTION	$3\frac{1}{2} - 4$	3 - 4
TOTAL SYSTEMATIC ERROR IN MEASURED CROSS-SECTION RATIO Pu-239/U-235	$2\frac{1}{2} - 3$	

## Errors

Estimated systematic contributions to the standard deviation errors in the measurements are given in Table I. The errors are generally dependent on energy, and where appropriate the table shows the error limits for the present range of incident neutron energy. The largest contribution comes from the spectrum measurement, and this includes uncertainties in the relative efficiencies of the standard detectors (both  $\sim \pm 2\%$ ), uncertainties in the calibration of the boron-vaseline plug detector ( $\pm 2$  to  $3\%$ ) and uncertainties in the actual spectrum measurement itself ( $\sim \pm 1\frac{1}{2}\%$ ). The uncertainties in the fission measurements include contributions from the energy-dependence of the detector efficiency, the determination of the time-dependent background, and the correction for sample thickness effects. The error for the energy-dependence of  $\bar{v}_p$  was taken from the two evaluations<sup>12,13</sup>.

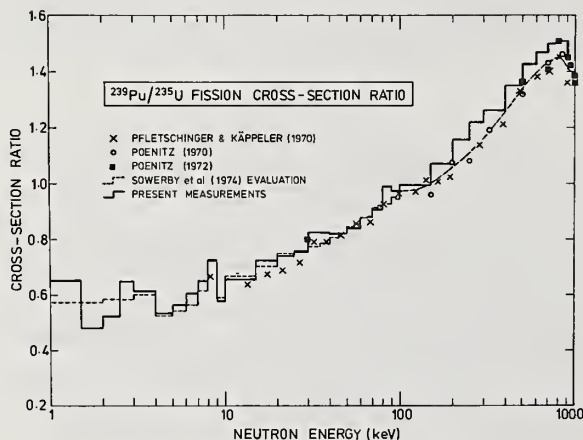
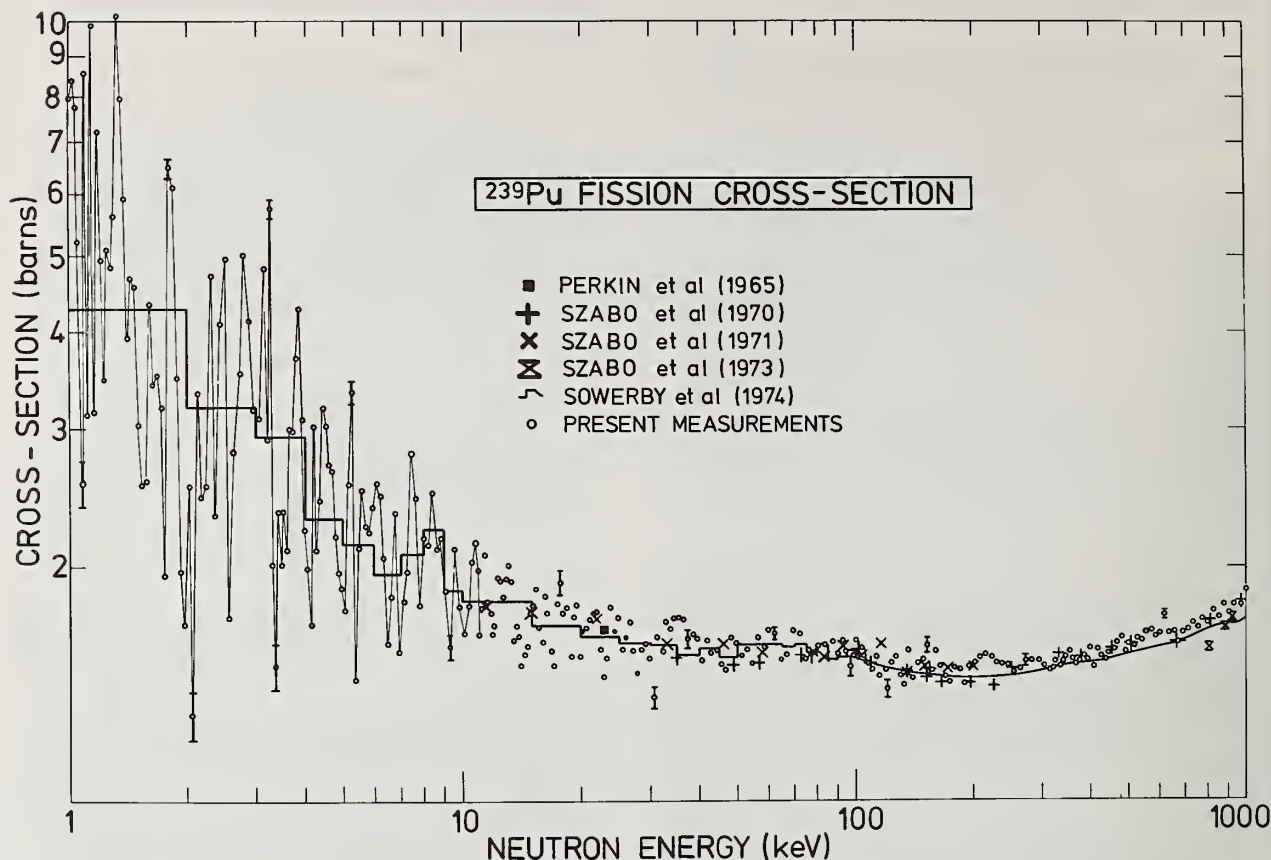
## Results

The results of the measurements are shown in the two figures and Table II. The measured relative cross-sections were normalised to give average values in the 10 to 30 keV energy range in agreement with the UK evaluations, namely 2.349b for the <sup>235</sup>U average fission cross-section and 1.6775b for the <sup>239</sup>Pu average fission cross-section. The standard deviation errors in the table include the systematic errors given in Table I for <sup>239</sup>Pu and in the earlier publication<sup>2</sup> for <sup>235</sup>U, combined with the small statistical errors associated with the chosen energy intervals. No error is included for the normalisation. In the normalisation region, the UK evaluation assigns errors of 3.9% and 4.0% to the <sup>235</sup>U and <sup>239</sup>Pu fission cross-sections respectively.

In the figure showing the <sup>239</sup>Pu cross-section, the statistical errors alone are shown at selected points. The observed structure below 30 keV is in excellent agreement with earlier measurements<sup>11,14</sup>. The spot-point measurements of Perkin et al<sup>15</sup> and Szabo et al<sup>16,17,18</sup> are shown for comparison.

The <sup>239</sup>Pu/<sup>235</sup>U fission cross-section ratio is shown in comparison with other recent measurements. For the sake of clarity only alternate energy points are shown from the measurements of Pfletschinger and Kämpfeler<sup>19</sup>. The data of Pfletschinger and Kämpfeler at energies below 150 keV are based on time-of-flight





measurements using a 'white' neutron source, and unlike spot-point measurements should represent the true average behaviour of the cross-sections in this region. The relative shape of the present cross-section ratio agrees to within  $\pm 3\%$  with that of Pfletschinger and Käppeler, throughout the complete energy range, if both measurements are normalised in the 10 to 30 keV interval.

#### Comparison with Evaluations

The comparisons are shown in Table III.

#### The $^{239}\text{Pu}(n,f)$ cross-section

Throughout most of the energy range the general shape of the ENDF/B-IV cross-section is in remarkably good agreement with the measurements. This evaluation predicts an average cross-section in the 10 to 30 keV normalisation interval which is 2.2% greater than the UK value. If we subtract 2.2% from the first column of differences in the table, thus normalising the measurements to the ENDF/B-IV evaluation in the 10-30 keV interval, it can be seen that only in a few energy bins does the difference exceed the estimated uncertainty in the measurement of  $3\frac{1}{2}$  to 4%.

At energies above 10 keV the difference between the UK evaluation and the measurements generally lies within the experimental uncertainty, although above 100 keV the evaluation consistently predicts a lower cross-section. Below 10 keV the agreement with this evaluation is not as good.

#### The $^{239}\text{Pu}/^{235}\text{U}$ fission cross-section ratio

Comparison with the present results shows that the ENDF/B-IV ratio generally rises less rapidly with increasing energy. The overall difference in shape above 10 keV is not much greater than the experimental uncertainty of  $\pm 3\%$ , but at lower energies the differences in shape are more significant. The good overall agreement between the measured  $^{239}\text{Pu}$  fission cross-section and this evaluation shows that the inferior agreement with the measured cross-section ratio at energies below 10 keV can be attributed to differences between the measured and evaluated shapes of the  $^{235}\text{U}$  fission cross-section.



TABLE II. THE MEASURED AVERAGE FISSION  
CROSS-SECTIONS OF PU-239 AND  
U-235 AND THEIR RATIO

Energy Interval (keV)	Cross-section (barns)		Cross-section ratio Pu-239(n,f)/ U-235(n,f)
	Pu-239(n,f)	U-235(n,f)	
1-1.5	5.672+0.233	8.679+0.356	0.654+0.014
1.5-2	3.417+0.137	7.084+0.283	0.482+0.011
2-2.5	3.109+0.124	5.961+0.232	0.522+0.013
2.5-3	3.541+0.142	5.484+0.208	0.646+0.016
3-4	3.097+0.118	5.045+0.187	0.614+0.015
4-5	2.391+0.091	4.474+0.157	0.534+0.013
5-6	2.278+0.084	4.048+0.134	0.563+0.014
6-7	2.047+0.076	3.379+0.108	0.606+0.016
7-8	2.130+0.079	3.280+0.102	0.649+0.018
8-9	2.222+0.082	3.071+0.095	0.724+0.020
9-10	1.820+0.067	3.153+0.098	0.577+0.018
10-15	1.773+0.062	2.702+0.081	0.656+0.015
15-20	1.709+0.060	2.359+0.071	0.724+0.017
20-25	1.650+0.058	2.237+0.067	0.738+0.018
25-30	1.579+0.055	2.095+0.063	0.754+0.018
30-40	1.632+0.057	1.978+0.059	0.825+0.020
40-50	1.552+0.054	1.893+0.057	0.820+0.020
50-60	1.570+0.055	1.866+0.056	0.841+0.020
60-70	1.596+0.056	1.815+0.054	0.879+0.021
70-80	1.572+0.055	1.733+0.054	0.907+0.022
80-90	1.593+0.057	1.612+0.052	0.988+0.025
90-100	1.545+0.057	1.588+0.052	0.973+0.026
100-150	1.496+0.054	1.505+0.051	0.994+0.024
150-200	1.480+0.055	1.383+0.047	1.070+0.026
200-250	1.513+0.056	1.306+0.044	1.158+0.028
250-300	1.497+0.057	1.227+0.042	1.220+0.031
300-400	1.511+0.056	1.196+0.041	1.263+0.033
400-500	1.558+0.059	1.153+0.040	1.351+0.035
500-600	1.619+0.063	1.134+0.041	1.428+0.039
600-700	1.648+0.064	1.122+0.043	1.469+0.041
700-800	1.681+0.066	1.122+0.044	1.498+0.042
800-900	1.744+0.068	1.156+0.045	1.509+0.044
900-1000	1.783+0.070	1.218+0.049	1.464+0.042

The UK evaluated cross-section ratio is generally smaller than the measured ratio, but this is just a matter of normalisation. The overall shape of the evaluation is in better agreement with the measurements than is the ENDF/B-IV evaluation.

#### Acknowledgments

The author would like to thank Dr. J. E. Lynn for his encouragement, and members of the Linac group who helped to run the equipment and analyse the data. He is also grateful to Dr. Sol Pearlstein of the NNCSC for letting him have relevant ENDF/B-IV listings and average cross-sections.

#### References

- Patrick B. H., James G. D., Phys. Lett. 28B, 258 (1968)
- Gayther D. B., Boyce D. A., Brisland J. B., Proc. 2nd IAEA Panel on Neutron Standard Reference Data, p.201, Vienna (1974)
- Sowerby M. G., Patrick B. H., Mather D. S., Annals Nuc. Sci. Eng. 1, 409 (1974)
- Coates M. S., Hart W., Rep. EANDC(UK)109AL (1969)
- Adams J. M., Ferguson A. T. G., McKenzie C. D., UKAEA Rep. AERE - R 6429 (1970)
- Terrell J., Physics and Chemistry of Fission, 2, 3, IAEA Vienna (1965)
- Skarsvåg K., Physica Scripta 7, 160 (1973)
- Nair S., Gayther D. B., UKAEA Prog. Rep. AERE-PR/NP21, 38 (1974)

TABLE III. COMPARISON OF PRESENT MEASUREMENTS  
WITH THE ENDF/B-IV AND UK EVALUATIONS

Energy Interval (keV)	DIFFERENCE BETWEEN EVALUATION AND MEASUREMENT (%)			
	Pu-239(n,f)		Pu-239(n,f)/ U-235(n,f)	
	ENDF/B-IV	UK	ENDF/B-IV	UK
1-2	+1.2	-6.1	+7.4	-0.7
2-3	+2.2	-4.0	+8.7	+0.2
3-4	-0.4	-5.6	+4.5	-2.1
4-5	+0.1	-3.8	+3.7	-2.0
5-6	-0.5	-6.4	+4.8	-4.0
6-7	+0.7	-4.5	-1.3	-7.2
7-8	-2.0	-2.8	+1.3	-5.5
8-9	-2.3	+0.2	-2.1	+0.2
9-10	+7.0	+2.4	+9.3	+2.0
10-15	+2.4	+1.9	+3.1	+1.7
15-20	+1.2	-1.7	+0.9	-3.0
20-25	+1.7	-1.3	+3.1	+1.4
25-30	+3.5	+1.1	+2.1	-0.1
30-40	-1.2	-4.1	-1.5	-5.7
40-50	+2.1	-0.1	+3.8	-0.9
50-60	+3.2	+1.3	+3.7	+1.0
60-70	+1.1	-0.7	+2.3	-0.3
70-80	+3.6	-0.1	+2.9	+1.0
80-90	-2.0	-2.4	-2.3	-6.4
90-100	+1.6	0.0	+0.4	-2.7
100-150	+4.4	-0.9	+3.4	-1.1
150-200	+0.8	-2.6	-0.8	-3.9
200-250	-1.9	-4.9	-3.0	-6.5
250-300	+0.6	-2.7	-4.8	-7.1
300-400	+2.2	-1.4	-0.8	-4.3
400-500	+1.1	-2.2	-2.4	-4.1
500-600	-1.6	-3.6	-3.7	-4.2
600-700	-1.1	-3.5	-3.0	-3.7
700-800	-0.2	-2.9	-0.9	-3.9
800-900	-2.9	-4.2	-2.6	-5.2
900-1000	-4.4	-5.1	-2.9	-4.2

- Lynn J. E., Moxon M. C., private communication (1967)
- Devaney J. J., Nuc. Sci. Eng. 51, 272 (1973)
- Schomberg M. G., Sowerby M. G., Boyce D. A., Murray K. J., Sutton D. L., Nuclear Data for Reactors I, 315, IAEA Vienna (1970)
- Mather D. S., Bampton P. F., Rep. EANDC(UK)132AL (1971)
- Mather D. S., Bampton P. F., UKAEA Rep. AWRE 086/70 (1970)
- Blons J., Nuc. Sci. Eng. 51, 130 (1973)
- Perkin J. L., White P. H., Fieldhouse P., Axton E. J., Cross P., Robertson J. C., J. Nucl. Energy, 19, 423 (1965)
- Szabo I., Fillipi G., Huet J. L., Leroy J. L., Marquette J. P., Proc. 1970 Argonne Symp. on Neutron Standards and Flux Normalization, 257 (1971)
- Szabo I., Fillipi G., Huet J. L., Leroy J. L., Marquette J. P., Proc. Conf. Neutron Cross-sections and Technology, 2, 573 (1971)
- Szabo I., Leroy J. L., Marquette J. P., Proc. 1973 Conf. on Neutron Physics, Kiev, 3, 27 (1974)
- Pfletschinger E., Kappeler F., Nuc. Sci. Eng., 40, 375 (1970)
- Poenitz W. P., Nuc. Sci. Eng. 40, 383 (1970)
- Poenitz W. P., Nuc. Sci. Eng. 47, 228 (1972)

The ratio of the neutron induced fission cross-sections of  $^{238}\text{U}$  and  $^{235}\text{U}$  have been measured in the energy range from 600 keV to 22 MeV using the time-of-flight method on the Harwell synchrocyclotron, at a nominal resolution of 0.5 ns/m. Fission fragments were detected in a gas scintillation chamber containing foils of each material mounted back-to-back and perpendicular to the incident beam. The measured cross-section ratio was normalised at 14 MeV to the ratio evaluated by Sowerby et al. The estimated standard deviation error in the ratio measurements is  $\pm 2\%$ . Comparison with other recent data shows reasonable agreement throughout most of the energy range.

(Cross-sections, fission, ratio,  $^{238}\text{U}$ ,  $^{235}\text{U}$ , measured, neutrons, 600 keV - 22 MeV)

### Introduction

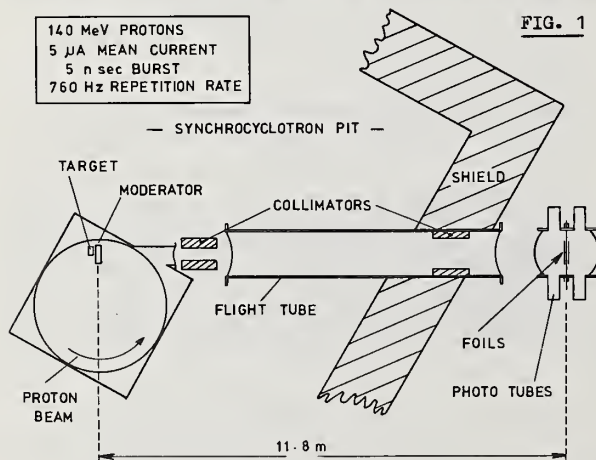
A measurement has been made of the  $^{238}\text{U}/^{235}\text{U}$  neutron induced fission cross-section ratio in the energy range from 600 keV to 22 MeV using the 12 m time-of-flight facility on the Harwell synchrocyclotron. The experiment was prompted by recent results from integral measurements, involving the  $^{238}\text{U}(n,f)$  cross-section, which could not be reconciled with the existing differential nuclear data. To give some idea of the size of the discrepancy, it was found necessary, in producing the UK adjusted data set, FGL 5, which is fitted to a range of integral measurements, to increase the  $^{238}\text{U}(n,f)$  cross-section by 11% above the UK nuclear data evaluation<sup>2</sup>. Although the agreement between the existing differential data seemed to preclude such a large adjustment, and other explanations of the discrepancy are possible, another measurement seemed desirable, particularly as relatively few measurements covered the entire energy range of fast reactor interest. The present measurement was specifically intended to give the detailed relative shape of the cross-section over this energy range. An accurate method of determining the incident neutron flux spectrum was not available, and the cross-section was measured as a ratio to the  $^{235}\text{U}$  fission cross-section. No attempt was made to determine the ratio absolutely and in order to compare our results with other experiments an arbitrary normalisation has to be made.

### Experimental Method

#### General

The arrangement of the experiment is shown schematically in Fig. 1. Pulses of neutrons of

5 ns duration (FWHM) were produced at a repetition frequency of 760 Hz by the 140 MeV proton beam from the



synchrocyclotron striking a tungsten target. The neutrons were moderated by a 2 cm thick layer of water contained in a thin-walled tantalum box, and the neutron beam was extracted at  $180^\circ$  to the incident proton beam to minimise the number of energetic neutrons produced in direct interactions. With this arrangement the neutron spectrum consisted essentially of an evaporation spectrum, together with a low energy tail with approximate form  $1/E^{0.8}$  below about 30 keV. The beam passed through thin Mylar windows and a short path length in air before reaching the detector; its shape was defined by brass collimators. The fission detector was placed at a distance of 11.8 m from the target in a heavily shielded underground tunnel.

#### The fission detector

This consisted of a gas scintillation chamber in which the fission fragments were detected. Both fissile materials were deposited to a thickness of  $0.5 \text{ mg/cm}^2$  on thin Al backings. The foils were 7.6 cm in diameter and were placed back-to-back at the centre of the chamber and perpendicular to the neutron beam. The chamber was divided optically in the plane of the foils, and each half was 'viewed' through quartz windows by two EMI 9816 photomultipliers. The detector was continuously flushed with a regulated mixture of He and  $\text{N}_2$  chosen to maximise the pulse amplitudes observed in the photomultipliers.

A pulse height analyser was used to continuously monitor the stability of the chamber and to establish discriminator bias levels. It was not found necessary to use coincidences between the two photomultipliers on each side of the chamber in order to make a clear separation between pulses due to fission fragments and those due to unwanted events.

#### Time-of-flight measurement

The synchrocyclotron instrumentation<sup>3</sup> provides a start pulse for timing purposes which is synchronised to the neutron burst to within  $\pm 1 \text{ ns}$ . The start pulse and the stop pulses derived from the detector electronics were fed to a digital time analyser with a basic channel width of 3.6 ns. The system was capable of accepting more than one stop pulse for each neutron burst, and the stop pulse information was fed through CAMAC units to a Honeywell DDP-516 computer. The events from both halves of the chamber were recorded simultaneously.

#### Treatment of Data

##### Correction for energy dependence of detector efficiency

1. At energies above a few MeV, the incident neutron momentum causes the fragments to be emitted



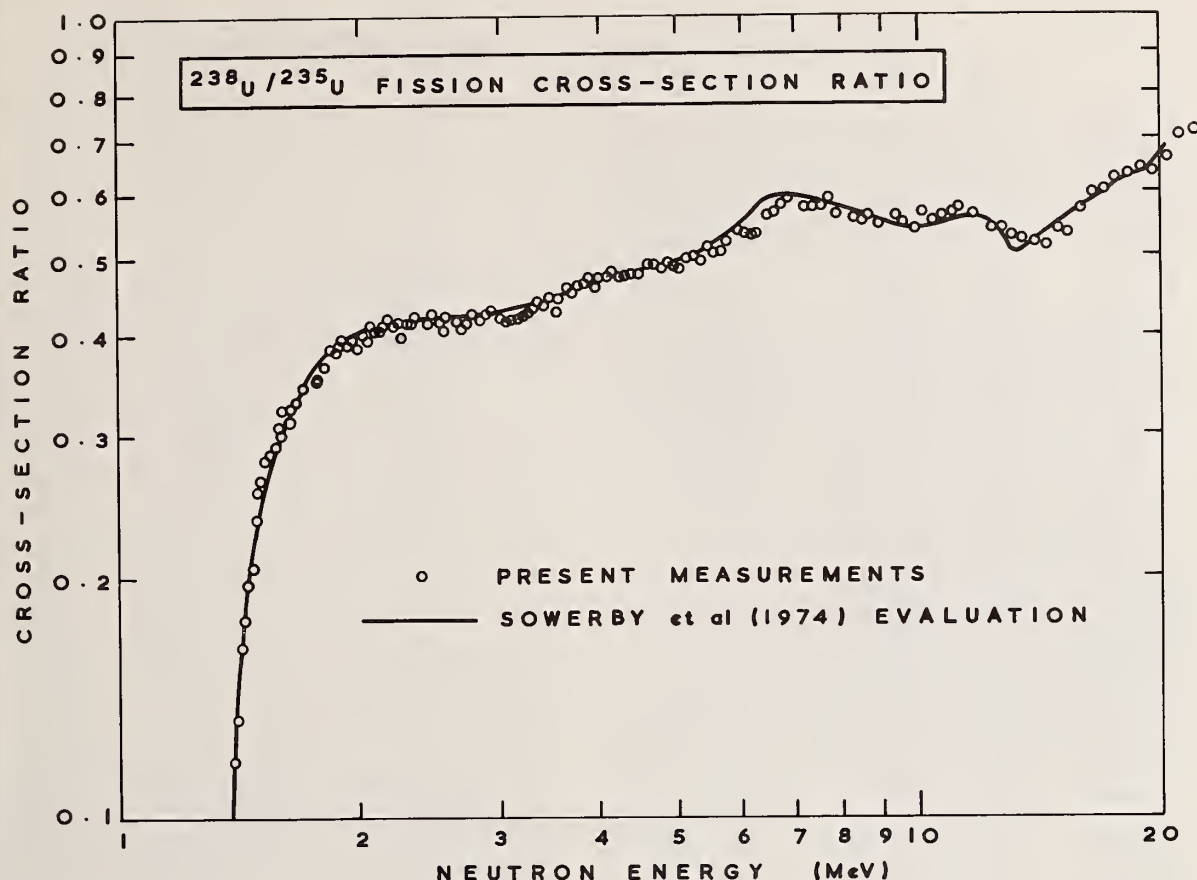


FIG. 2

preferentially in the forward direction by a significant amount, resulting in an increased detection efficiency for the side of the chamber remote from the neutron source. The change in efficiency is  $\sim 7\%$  at 14 MeV. The effect was eliminated by making measurements with the  $^{238}\text{U}$  and then the  $^{235}\text{U}$  foil facing the source and averaging the two sets of data.

2. The anisotropy of fragment emission with respect to the incident neutron beam (in the centre-of-mass system) is significantly different for the two samples; the  $^{238}\text{U}$  fragments exhibiting more forward peaking over most of the energy region than those from  $^{235}\text{U}$ . This effect is only important when the fragments are absorbed in thick foils. It was estimated that for the present foils, the difference in detection efficiency for the  $^{238}\text{U}$  and  $^{235}\text{U}$  fragments caused by the differing anisotropies would generally be less than 0.5%, and no correction was applied.

3. In making the measurements, the detector bias levels were chosen to exclude events produced by  $\alpha$ -particles from  $(n, \alpha)$  reactions in the thin Al windows of the chamber and the foil backings. This necessitated losing a significant fraction of fission events from each side of the chamber, and this could lead to a distortion of the results if the kinetic energy distributions are dependent on the excitation energy of the fissioned nucleus. However, the available evidence<sup>4</sup> indicates that the average

fragment kinetic energy changes by only  $\sim 0.5$  MeV when the incident neutron energy increases from thermal to over 15 MeV. Since, in any case, a cross-section ratio is measured, it has been assumed that the bias produces a negligible effect on the results.

#### Calibration of energy scale

The energy scale for the time-of-flight measurements was established by placing carbon samples in the neutron beam and observing the positions of the well-known resonances<sup>5</sup> above 2 MeV.

#### Background determination

The carbon samples also allowed an assessment to be made of the time-dependent background in the time-of-flight measurements. The conventional 'black' resonance technique, which is widely used at low energies, cannot be used in the present energy region. The method adopted relies on the resonance structure in the carbon total cross-section and makes use of comparing the resonance transmission shapes observed in the  $^{238}\text{U}$  and  $^{235}\text{U}$  sides of the chamber. The method does not depend on the absolute value of the carbon total cross-section. The analysis showed that the observed ratio measurements were consistent with a negligible time-dependent background effect, although the possibility of a  $\pm 2\%$  systematic error due to such a background cannot be precluded.



TABLE I. THE MEASURED U-238/U-235 FISSION CROSS SECTION RATIO

Energy (keV)	Ratio	Energy (keV)	Ratio	Energy (keV)	Ratio	Energy (keV)	Ratio	Energy (keV)	Ratio
0.21835E 05	0.727	0.61471E 04	0.536	0.28470E 04	0.414	0.16353E 04	0.308	0.10599E 04	0.0173
0.21001E 05	0.721	0.60209E 04	0.535	0.28070E 04	0.422	0.16179E 04	0.318	0.10692E 04	0.0151
0.20214E 05	0.676	0.58984E 04	0.543	0.27678E 04	0.424	0.16007E 04	0.299	0.10599E 04	0.0173
0.19470E 05	0.644	0.57797E 04	0.536	0.27295E 04	0.414	0.15838E 04	0.303	0.10508E 04	0.0149
0.18767E 05	0.658	0.56646E 04	0.512	0.26920E 04	0.408	0.15671E 04	0.289	0.10418E 04	0.0137
0.18101E 05	0.644	0.55528E 04	0.510	0.26552E 04	0.412	0.15508E 04	0.283	0.10329E 04	0.0135
0.17470E 05	0.638	0.54443E 04	0.514	0.26191E 04	0.411	0.15346E 04	0.277	0.10241E 04	0.0140
0.16872E 05	0.609	0.53390E 04	0.496	0.25838E 04	0.424	0.15188E 04	0.262	0.10155E 04	0.0143
0.16303E 05	0.608	0.52367E 04	0.501	0.25492E 04	0.403	0.15031E 04	0.253	0.10069E 04	0.0116
0.15763E 05	0.576	0.51373E 04	0.500	0.25153E 04	0.417	0.14877E 04	0.234	0.99847E 03	0.0134
0.15249E 05	0.537	0.50407E 04	0.486	0.24821E 04	0.424	0.14726E 04	0.204	0.99013E 03	0.0123
0.14760E 05	0.548	0.49468E 04	0.489	0.24495E 04	0.410	0.14577E 04	0.190	0.98189E 03	0.0124
0.14295E 05	0.517	0.48555E 04	0.496	0.24176E 04	0.415	0.14430E 04	0.173	0.97375E 03	0.0136
0.13850E 05	0.525	0.47667E 04	0.490	0.23862E 04	0.417	0.14285E 04	0.161	0.96572E 03	0.0138
0.13427E 05	0.533	0.46803E 04	0.492	0.23555E 04	0.422	0.14142E 04	0.130	0.95778E 03	0.0134
0.13022E 05	0.535	0.45963E 04	0.493	0.23254E 04	0.417	0.14002E 04	0.114	0.94994E 03	0.0134
0.12635E 05	0.549	0.45144E 04	0.483	0.22958E 04	0.412	0.13864E 04	0.0985	0.94220E 03	0.0155
0.12266E 05	0.545	0.44348E 04	0.479	0.22669E 04	0.396	0.13727E 04	0.0819	0.93455E 03	0.0132
0.11912E 05	0.561	0.43573E 04	0.477	0.22384E 04	0.417	0.13593E 04	0.0761	0.92699E 03	0.0121
0.11574E 05	0.572	0.42817E 04	0.475	0.22105E 04	0.416	0.13460E 04	0.0701	0.91953E 03	0.0128
0.11249E 05	0.578	0.42081E 04	0.472	0.21831E 04	0.419	0.13330E 04	0.0591	0.91215E 03	0.0113
0.10938E 05	0.571	0.41364E 04	0.485	0.21562E 04	0.409	0.13201E 04	0.0593	0.90487E 03	0.0127
0.10640E 05	0.571	0.40665E 04	0.490	0.21298E 04	0.408	0.13075E 04	0.0498	0.89767E 03	0.00957
0.10354E 05	0.559	0.39984E 04	0.474	0.21039E 04	0.403	0.12950E 04	0.0432	0.89055E 03	0.01038
0.10079E 05	0.572	0.39320E 04	0.457	0.20784E 04	0.409	0.12827E 04	0.0384	0.88352E 03	0.00739
0.98154E 04	0.546	0.38672E 04	0.473	0.20535E 04	0.394	0.12705E 04	0.0409	0.87658E 03	0.00788
0.95617E 04	0.559	0.38040E 04	0.466	0.20289E 04	0.399	0.12586E 04	0.0347	0.86971E 03	0.00661
0.93176E 04	0.572	0.37423E 04	0.460	0.20048E 04	0.387	0.12468E 04	0.0330	0.86293E 03	0.00579
0.90829E 04	0.564	0.36821E 04	0.452	0.19811E 04	0.399	0.12351E 04	0.0353	0.85622E 03	0.00531
0.88568E 04	0.552	0.36234E 04	0.456	0.19579E 04	0.397	0.12237E 04	0.0344	0.84959E 03	0.00525
0.86391E 04	0.569	0.35660E 04	0.444	0.19350E 04	0.390	0.12124E 04	0.0361	0.84304E 03	0.00463
0.84294E 04	0.556	0.35100E 04	0.428	0.19126E 04	0.392	0.12012E 04	0.0360	0.83657E 03	0.00364
0.82272E 04	0.565	0.34553E 04	0.444	0.18905E 04	0.383	0.11902E 04	0.0339	0.83017E 03	0.00407
0.80321E 04	0.577	0.34019E 04	0.438	0.18688E 04	0.378	0.11793E 04	0.0337	0.82384E 03	0.00457
0.78439E 04	0.573	0.33497E 04	0.437	0.18475E 04	0.381	0.11686E 04	0.0287	0.81758E 03	0.00401
0.76623E 04	0.597	0.32987E 04	0.432	0.18266E 04	0.365	0.11581E 04	0.0291	0.81139E 03	0.00366
0.74869E 04	0.580	0.32489E 04	0.429	0.18060E 04	0.352	0.11477E 04	0.0257	0.80528E 03	0.00360
0.73174E 04	0.578	0.32002E 04	0.421	0.17857E 04	0.354	0.11374E 04	0.0258	0.79923E 03	0.00430
0.71537E 04	0.581	0.31525E 04	0.420	0.17658E 04	0.348	0.11273E 04	0.0261	0.79325E 03	0.00365
0.69954E 04	0.602	0.31060E 04	0.417	0.17462E 04	0.346	0.11173E 04	0.0234	0.78734E 03	0.00328
0.68422E 04	0.596	0.30604E 04	0.408	0.17270E 04	0.331	0.11074E 04	0.0220	0.78150E 03	0.00314
0.66941E 04	0.587	0.30158E 04	0.419	0.17080E 04	0.345	0.10976E 04	0.0185	0.77572E 03	0.00272
0.65507E 04	0.574	0.29723E 04	0.423	0.16894E 04	0.326	0.10880E 04	0.0187	0.77000E 03	0.00190
0.64119E 04	0.564	0.29296E 04	0.430	0.16711E 04	0.328	0.10785E 04	0.0173	0.76402E 03	0.00221
0.62774E 04	0.546	0.28879E 04	0.424	0.16530E 04	0.322	0.10692E 04	0.0151	0.68943E 03	0.00145
								0.64371E 03	0.00097

### Isotopic impurities

The only significant corrections required for the presence of other isotopes in the foils were for the  $^{235}\text{U}$  content in the  $^{238}\text{U}$  foil (0.036%) and for the  $^{238}\text{U}$  content in the  $^{235}\text{U}$  foil (6.06%).

### Results and Comparison with Other Data

The data above 1.4 MeV are shown in Fig. 2 in comparison with the results of the most recent UK evaluation<sup>6</sup>. The present measurements were normalised to this evaluation at 14 MeV, where because of the many existing measurements, the evaluators are able to assign a comparatively low standard deviation error (s.d.) of  $\pm 2\%$  to their ratio. The error in making the normalisation is  $\pm 1.5\%$  (s.d.). The main experimental uncertainty arises from the time-dependent background and the estimated systematic error we have assigned to the data to allow for this is  $\pm 2\frac{1}{2}\%$  (s.d.). The statistical error on all the points shown in the figure is always less than  $\pm 2\%$  (s.d.). It can be seen that the overall agreement in shape is good, apart from a disagreement of  $\sim 5\%$  in the 6 to 7 MeV region where

the individual fission cross-sections and fragment angular distributions change abruptly.

The results at lower energies are shown in Fig. 3 together with other published data. The early values of Lamphere<sup>7</sup> have been re-normalised to agree with more recent measurements at higher energies following the suggestion of Sowerby et al<sup>6</sup>. The statistical errors on the experimental points increase at the lower energies, typical values being  $\pm 7\%$  (s.d.) at 1 MeV and  $\pm 20\%$  at 700 keV. It can be seen that our data agree well in the threshold region with the recent values of Stein et al<sup>8</sup> and Meadows<sup>9</sup> but disagree with the Lamphere values between 600 keV and 1.8 MeV. It is interesting to note the effect this discrepancy would have on the calculated counting rate of a  $^{238}\text{U}$ -fission chamber placed in a typical fast reactor spectrum. Taking a recently evaluated  $^{235}\text{U}$  fission cross-section<sup>6</sup> to derive  $^{238}\text{U}$  fission cross-sections from the two ratios and integrating between 600 keV and 1.8 MeV in the spectrum it is found that the rates would not differ by more than 0.5%.

Below 600 keV the measured cross-section ratio

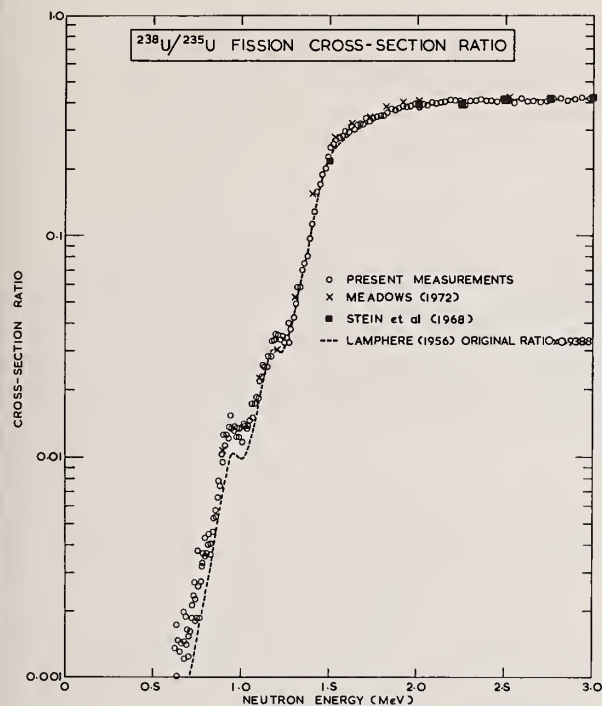


FIG. 3

becomes increasingly inaccurate due to the  $^{235}\text{U}$  content of the  $^{238}\text{U}$  fission foil (358 ppm) and meaningful results cannot be derived below 400 keV. In the energy interval 400 to 420 keV the ratio is  $0.0002 \pm 0.0001$  corresponding to a  $^{238}\text{U}$  fission cross-section of  $240 \pm 120$  b.

A data listing of Figs. 2 and 3 is given in Table I.

#### Acknowledgments

We should like to thank Drs. J. E. Lynn and A. E. Taylor for their encouragement. In operating the experiment we received considerable assistance from D. A. Boyce and J. B. Brisland of the Electron Linear Accelerator Group, and I. T. Belcher, P. H. Bowen, G. C. Cox and P. E. Dolley of the Synchrocyclotron Group.

#### References

1. Rowlands J. L., Dean C. J., MacDougall J. D., Smith R. W., Int. Symp. on Physics of Fast Reactors 3, 1133 Tokyo (1973)
2. Sowerby M. G., Patrick B. H., Mather D. S., UKAEA Rep. AERE - R 7273 (1973)
3. Pattenden N. J., Belcher I. T., Blair I. M., Bowen P. H., Cox G. C., Dolley P. E., McMurray W. R., UKAEA Rep. AERE - R 7425 (1973)
4. D'yachenko P. P., Kuz'minov B. D., Tarasko M. Z., Sov. J. Nuc. Phys., 8, No. 2, 165 (1969)
5. Cierjacks S., Proc. Argonne Symp. on Neutron Standards and Flux Normalizations, 190 (1971)
6. Sowerby M. G., Patrick B. H., Mather D. S., Annals of Nuc. Sci. & Eng. 1, 409 (1974)
7. Lamphere R. W., Phys. Rev. 104, 1654 (1956)
8. Stein W. E., Smith R. K., Smith H. L., Proc. Washington Conf. on Neutron Cross-sections and Technology 627 (1968)
9. Meadows J. W., Nuc. Sci. Eng. 49, 310 (1972)



P.I. Johansson, B. Holmqvist, T. Wiedling

Neutron Physics Laboratory

Atomic Energy Company

Studsvik, Nyköping, Sweden

and

L. Jéki

Central Research Institute for Physics

Budapest, Hungary

Prompt neutron spectra from fission of  $^{235}\text{U}$ , and  $^{239}\text{Pu}$  have been measured at incident neutron energies of 0.10, 0.18, 0.53 and 2.07 MeV. A major effort was made to obtain an accurate experimental determination of the efficiency and energy response function of the time-of-flight neutron detector in the energy range 0.15 to 15 MeV. The spectra have been analytically described by the so called Watt distribution, as well as with a Maxwell distribution. It is shown that the Watt relation gives a somewhat better description of the spectra than the Maxwell formula. The angular correlation between incident-neutrons and fission-neutrons was measured for  $^{235}\text{U}$  and  $^{238}\text{U}$  at an incident neutron energy of 2.07 MeV. The data indicate some slight anisotropies, being rather small or even negligible for  $^{235}\text{U}$  and somewhat more pronounced for  $^{238}\text{U}$ . The results show that the shape of the neutron energy distribution is independent of the angle of observation.

(Fast fission neutron spectra;  $^{235}\text{U}$ ;  $^{238}\text{U}$ ;  $^{239}\text{Pu}$ ; TOF-technique)

### Introduction

The status of the experimental knowledge of prompt fission neutron spectra of fertile and fissile isotopes was summarized by Wiedling<sup>1</sup> and by Grundl<sup>2</sup> at the symposium on Neutron Standards and Flux Normalization at Argonne in 1970. At the specialist meeting arranged by IAEA in 1971<sup>3</sup> regarding prompt neutron spectra the situation was further enlightened in several review papers. The general conclusion at the IAEA meeting was that the neutron distributions measured by various authors using the differential technique agree fairly well, within the expected experimental accuracy, for the isotopes  $^{235}\text{U}$  and  $^{239}\text{Pu}$  when judged by the fitting distributions used to interpret the experimental results. However, the measurements had usually been restricted to the neutron energy range 0.7 to 8 MeV of the fission spectrum which in fact comprises an energy range of about 15 MeV. The shapes of the prompt neutron fission spectra for  $^{235}\text{U}$  and  $^{239}\text{Pu}$  have also been determined recently by integral measurements by Fabry<sup>4</sup> and Grundl<sup>2</sup>. The results of the integral and differential measurements of  $^{235}\text{U}$  and  $^{239}\text{Pu}$  show, however, discrepancies which are larger than the experimental uncertainties. It is thus very important to make precision measurements of the fission spectra of these elements. For future work regarding such spectrum measurements Wiedling<sup>1</sup> proposed the fission neutron spectra of  $^{235}\text{U}$  and  $^{252}\text{Cf}$  to be used as standards, as was also suggested at the IAEA meeting<sup>3</sup>.

One comes to the conclusion, after an analysis of the results of previous measurements made by using the time-of-flight (TOF) method, that essential improvements must be made to experimental techniques and procedures. The detector sensitivity must be large and the background conditions optimized, giving large signal-to-background ratios. This has been accomplished in the present experiment by shielding of the detector and by use of an efficient pulse shape discrimination system. Efforts to optimize the experimental conditions have enabled measurements and analyses of the fission spectra with a high degree of accuracy in the energy interval 0.16 MeV to 15 MeV. It is also of primary importance to measure the neutron detector response function as accurately as possible as well as the detector energy calibration.

The ultimate goal of this project which has now been in progress for several years<sup>5-10</sup> is to measure the shape of the fission neutron spectrum of  $^{235}\text{U}$  with as high a degree of accuracy as possible with present day techniques. With this spectrum as a standard it would be comparatively easy to also measure the shapes of other fission neutron spectra, i.e.

$^{238}\text{U}$  and  $^{239}\text{Pu}$ . A comprehensive report regarding the details of this work is being prepared<sup>11</sup>.

### Experimental Method

The measurements were performed with the aid of a 6 MeV Van de Graaff accelerator delivering pulses of protons and deuterons of a width of about 1.5 ns at a repetition rate of 1 MHz.

The neutron TOF spectrometer included a liquid scintillator (NE213) neutron detector with pulse shape discrimination properties. The scintillators (2.5 cm and 5 cm thickness, 12.5 cm diameter) were coupled to low-noise photomultipliers (RCA 8854). The detectors were biased at neutron energies corresponding to 50 keV (the 2.5 cm scintillator) and 450 keV (the 5 cm scintillator).

The neutron flight path was 300 cm throughout the measurements. A heavy shield of lithium paraffin, iron and lead surrounded the scintillation detector. The shield was placed on an arm, movable on a horizontal circular track, with the sample positioned on the axis of rotation. The reproducibility of the detector position was better than 0.1 degree. This accuracy was necessary in order to make a careful calibration of the TOF spectrometer with respect to energy and efficiency by observing angular distributions from nuclear reactions. The relative neutron fluence was monitored with a directionally sensitive, collimated and shielded standard long counter.

### Measurements of the detector response function and energy calibration of the TOF spectrometer

An accurate determination of the fission neutron spectrum is dependent on a good knowledge of the relative detector efficiency. The proper method for determining the efficiency is to measure it under conditions identical with those used in the fission experiments. The relative efficiency function was thus measured in the following way. In the energy range 0.6 to 15 MeV the angular neutron yield from (n,p)-scattering was recorded at a number of primary neutron energies. The energies and scattering angles were chosen such that there were, for each incident neutron energy, at least two overlapping points on the efficiency curve for normalization purposes. Different sizes and shapes of polyethylene samples were used and the effects of multiple scattering caused by the finite size of a sample were considered. The primary neutrons were produced in the reactions  $\text{T}(p,n)^3\text{He}$ ,  $\text{D}(d,n)^3\text{He}$  and  $\text{T}(d,n)^4\text{He}$  using gas targets. The energy range 0.1 to about 3 MeV of the detector response function was determined for each de-



detector from measurements of the angular distribution of neutrons from the  $T(p,n)^3\text{He}$  reaction.

The TOF spectrometer was energy calibrated by observing direct neutrons from the reactions  $T(p,n)^3\text{He}$ ,  $^9\text{Be}(d,n)^{10}\text{B}$  and  $T(d,n)^4\text{He}$ . A range of energies of the bombarding particles was used, which made it possible to cover the energy range 0.1 to 15 MeV.

### Fission Spectrum Measurements

Fission neutron spectra of  $^{235}\text{U}$  and  $^{239}\text{Pu}$  were measured at the energies: 0.10, 0.18, 0.53 and 2.07 MeV. Angular distributions measurements were performed on fission spectra of  $^{235}\text{U}$  and  $^{238}\text{U}$  at 2.07 MeV incident energy. The samples used in the spectrum measurements were all of the same cylindrical shape having a height of 3.00 cm, an outer diameter of 1.80 cm and an inner diameter of 0.95 cm. The samples had the following compositions: " $^{235}\text{U}$ ", 93.3%  $^{235}\text{U}$ , 6.85%  $^{238}\text{U}$ ; " $^{238}\text{U}$ ", natural uranium; " $^{239}\text{Pu}$ ", 94%  $^{239}\text{Pu}$ , 6% Ga\*. The plutonium sample was canned in an aluminium container with a wall thickness of 0.5 mm.

The  $^7\text{Li}(p,n)^7\text{Be}$  reaction was used as a neutron source except in the 2 MeV measurement where the neutrons were produced by the  $T(p,n)^3\text{He}$ -reaction. The target thicknesses were 7 to 32 keV and 100 keV, respectively. The measurements were performed alternately with and without a fission sample in the scatterer position and with a tantalum sample. The spectra obtained with the tantalum scatterer were used to study the effect of sample scattered neutrons. The fission spectra of  $^{238}\text{U}$  and  $^{239}\text{Pu}$  were measured relative to that of  $^{235}\text{U}$ . When the plutonium sample was involved, the  $^{235}\text{U}$  and tantalum samples were put in a can of the same material and dimensions as the plutonium container.

A TOF spectrum recorded when irradiating  $^{235}\text{U}$  at 0.53 MeV incident neutron energy is shown in Fig. 1 (unfilled circles). The spectrum consists of the beautifully recorded fission neutron spectrum, well resolved from a gamma related peak and a superimposed low energy tail from elastic and inelastic events in the sample, i.e. at energies of 0.53 MeV and below. The very good signal-to-background ratio should also be noted. The background (filled circles), normalized to the same neutron fluence as that of the  $^{235}\text{U}$  spectrum, is also plotted in the figure. The background spectrum can be seen to be well independent of energy in the entire energy region.

\* CEN - SACLAY, GIF-sur-YVETTE, FRANCE

### Comments on Data Analyses and Corrections

When examining the time spectra of Fig. 1 it can be observed that there exists a small background effect which is not observed in the direct measurement of the background with no sample in the target position. The excess background has its origin in processes in the sample which cause the emission of delayed neutrons and gammas. It can be corrected for, since when inspecting the spectra it can be seen that this background is constant in the whole energy range. After background subtractions the time spectra were transformed to energy spectra and corrected for energy dependent neutron detector efficiency. The analyses of the fission spectra were restricted to energies above the incident neutron energies.

The effect of the finite size of the samples makes it necessary to consider neutron attenuation and multiple scattering. The size dependence has been investigated for  $^{238}\text{U}$  samples of different dimensions. The shapes of the fission spectra were found to agree within the accuracy of the measurements. One may thus be allowed to draw the conclusion that attenuation and multiple scattering may not have much influence on the spectrum shapes. The fission spectra of  $^{235}\text{U}$  and  $^{239}\text{Pu}$  will probably not either be influenced by multiple effects.

The spectra of  $^{235}\text{U}$  and  $^{239}\text{Pu}$  which were recorded at 0.53 MeV incident energy were analyzed in the energy range 0.6-15 MeV but those measured at 0.10 and 0.18 and 2.07 MeV were, because of intensity reasons, analyzed only in the intervals 0.1-3, 0.3-3 and 2.5-10 MeV, respectively. The spectra of each isotope were combined into a single spectrum extending from 0.16 to 15 MeV. The spectrum for  $^{235}\text{U}$  is shown in Fig. 2. The experimental accuracy is depicted by the error bars. This measurement has been made with extraordinary efforts with regard to the extension of the spectrum energy range, precision in energy calibration, counter efficiency calibration, counting statistics, background suppression and other error sources having major influence on the accuracy of the presented data.

### Numerical analysis of $^{235}\text{U}$ and $^{239}\text{Pu}$ data

The observed fission neutron spectra of  $^{235}\text{U}$  and  $^{239}\text{Pu}$  were interpreted in terms of the Watt and Maxwellian type distributions expressed by the relations  $\chi(E) \sim \exp(-AE) \sinh(BE)^{1/2}$  and  $\chi(E) \sim E^{1/2} \exp(-E/T)$  ( $E$  is the outgoing neutron energy and  $A$ ,  $B$  and  $T$  are constants). The numerical values of the constants were de-

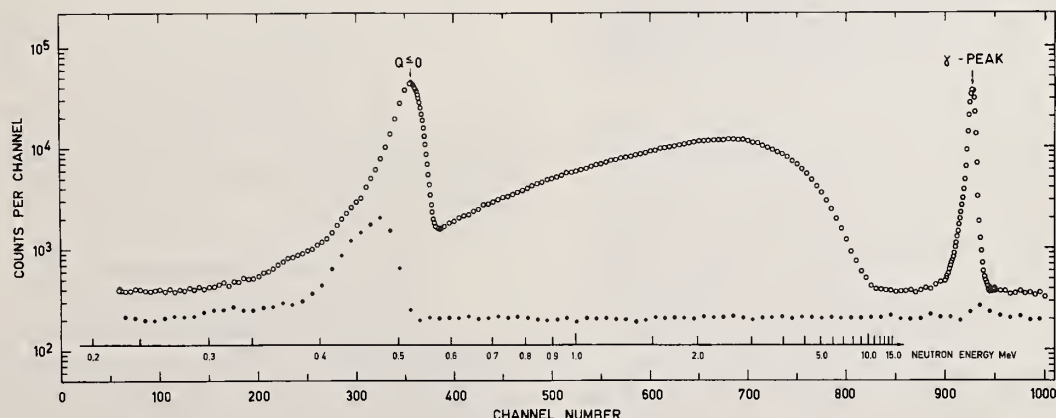


Figure 1. Time-of-flight spectrum of  $^{235}\text{U}$  (unfilled circles) recorded at an incident neutron energy of 0.53 MeV. Also shown is a spectrum (filled circles) observed with no sample in target position.

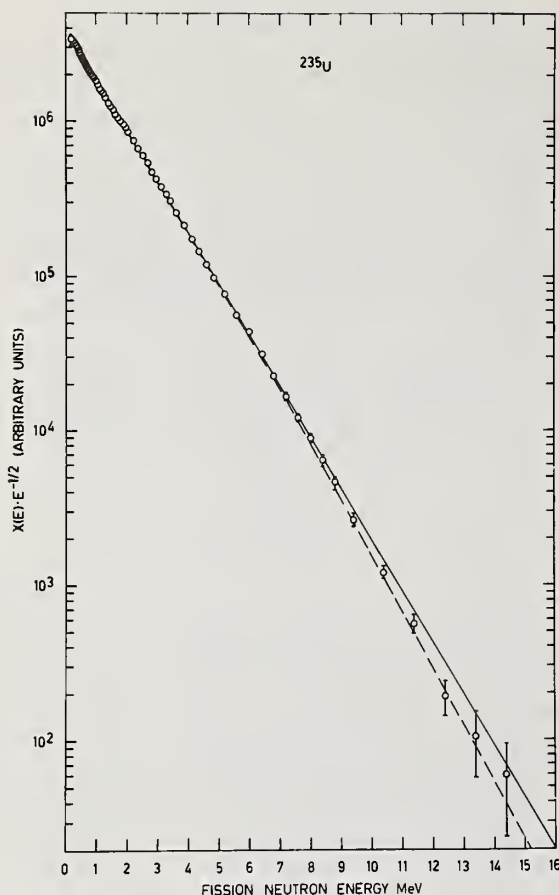


Figure 2. Fission neutron spectrum of  $^{235}\text{U}$ . The spectrum consists of data from measurements at 0.10, 0.18, 0.53 and 2.07 MeV incident neutron energies. The solid and dotted lines are the best fitted Maxwell and Watt distribution functions, respectively. (Table 1)

derived by a least squares fit procedure and a quantity  $\kappa^2$  defined as

$$\kappa^2 = n^{-1} \sum_{i=1}^n \frac{[N(E_i)_{\text{fit}} - N(E_i)_{\text{exp}}]^2}{\epsilon_i^2}$$

was chosen for judging the results.  $N(E_i)_{\text{exp}}$  is the relative number of measured neutrons per unit energy interval at the energy  $E_i$ ,  $N(E_i)_{\text{fit}}$  is the corresponding fitted value,  $\epsilon_i$  is the experimental error,  $n$  is the number of data points.

The parameter values of the fitting procedures are given in Table 1. Included in the table are also the mean energies of the spectra when calculated from the expressions  $E = A^{-1}(1.5 + 0.25B/A)$  (Watt) and  $E = 1.5 T$  (Maxwell). When judging the  $\kappa^2$ -values one observes that the  $^{235}\text{U}$ -spectrum seems to be well described by both functions. However, one gets a somewhat different picture from Fig. 3. This figure illustrates very nicely the quality of the fitting in showing the energy dependent ratio of the number of neutrons in the fission spectrum relative to that calculated from the fitted distribution function  $\chi_{\text{exp}}(E)/\chi_{\text{fit}}(E)$ . The deviation from unity of this ratio is remarkably small for the Watt distribution of  $^{235}\text{U}$  in the whole energy range 0.16 to 14 MeV. It is also clear that the Maxwell distribution describes the spectrum less well at high energies. Concerning the description of the  $^{239}\text{Pu}$  spectrum by Watt and Maxwell distribution functions, the  $\kappa^2$ -values give strong in-

dications of a preference for the Watt-distribution. This is also confirmed by the results of the  $\chi_{\text{exp}}(E)/\chi_{\text{fit}}(E)$  ratios (Fig. 3) which differ from unity for low as well as for large energies.

Table 1 Parameter values of Watt and Maxwell distributions fitted to the measured prompt fission neutron spectra of  $^{235}\text{U}$  and  $^{239}\text{Pu}$ .

Type of distribution	Energy interval MeV	Parameter	$\kappa^2$	Average energy $\bar{E}$ MeV
$^{235}\text{U}$ :				
WATT	0.16-15	A = $1.000 \pm 0.013$ B = $1.970 \pm 0.134$	0.544	1.992
MAXWELL	0.16-15	T = $1.318 \pm 0.030$	0.644	1.977
$^{239}\text{Pu}$ :				
WATT	0.3-15	A = $0.981 \pm 0.008$ B = $2.184 \pm 0.084$	0.234	2.096
MAXWELL	0.3-15	T = $1.383 \pm 0.010$	2.312	2.074

The conclusion is that the Watt distribution is to be recommended for the interpretation of the fission spectra of  $^{235}\text{U}$  and  $^{239}\text{Pu}$ .

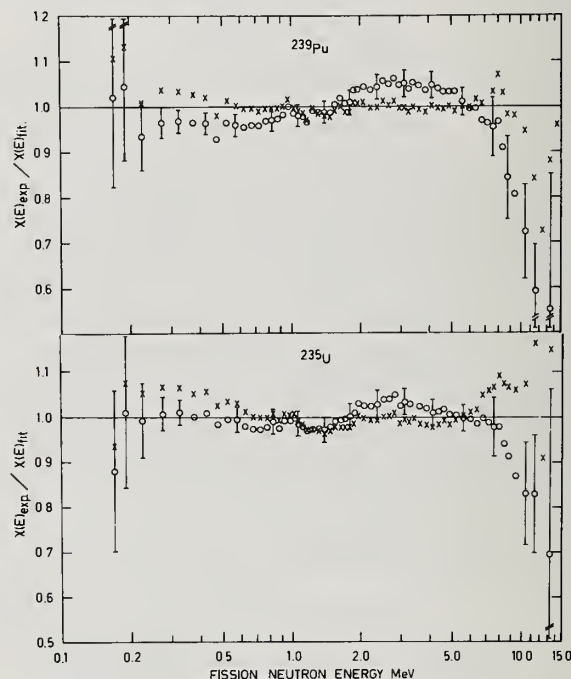


Figure 3. The ratio between the number,  $\chi_{\text{exp}}(E)$ , of neutrons of energy  $E$  in the observed fission spectrum and the neutron number,  $\chi_{\text{fit}}(E)$ , at the corresponding energy of the distribution function fitted to the experimental data points. x: Watt distribution, o: Maxwell distribution.

#### Angular Distribution Measurements of Prompt Fission Neutrons from $^{235}\text{U}$ and $^{238}\text{U}$

Measurements of important neutron cross sections are often repeated in order to get information regarding systematic errors. For such measurements it is desirable to use different experimental techniques. When the collection of fast neutron fission cross sections is concerned an attractive project is to measure such cross sections by neutron time-of-flight for fertile and fissile isotopes relative to the fission cross sections of  $^{235}\text{U}$ . For that purpose it is necessary to know

both the shape of the prompt neutron fission spectrum relative to that of  $^{235}\text{U}$  for the isotope in question and the angular distribution of the emitted neutrons. Knitter<sup>12</sup> has performed angular distribution measurements of prompt fission neutrons from  $^{238}\text{U}$  at incident energies 1.5, 1.9 and 2.3 MeV. The results indicated anisotropic distributions but the accuracy of the data does not allow one to draw any quantitative conclusions regarding the magnitude of the effect.

The yield of the prompt neutrons from  $^{235}\text{U}$  and  $^{238}\text{U}$  has been studied with respect to the angle between the incident neutrons and the outgoing neutrons at an incident neutron energy of 2.07 MeV. The angular range was from  $30^\circ$  to  $150^\circ$ . The measured fission spectrum distributions have been converted to an energy spectrum which was integrated and averaged over 500 keV intervals. The observed relative angular distributions are given in Fig. 4 for  $^{235}\text{U}$  and  $^{238}\text{U}$  with the energy of the emitted neutron as a parameter. Second

order Legendre polynomial fits to the angular distribution of neutrons in the energy interval 2.5 to 11 MeV are shown in the figure.

There are three important results of the distribution measurements: 1. The data indicate some slight anisotropies, being rather small or even negligible for  $^{235}\text{U}$  and somewhat more pronounced for  $^{238}\text{U}$ . 2. Within the experimental accuracy, there is no angle dependent effect on the shape of a fission neutron spectrum. 3. If the TOF-method is used to measure relative fission cross sections the angular distribution effects have to be considered.

#### References

- 1 T. Wiedling, Proceedings of a Symposium Neutron Standards and Flux Normalization, Argonne, October 21-23, 1970, p. 437.
- 2 J.A. Grundl, Proceedings of a Symposium Neutron Standards and Flux Normalization, Argonne, October 21-23, 1970, p. 417.
- 3 Prompt Fission Neutron Spectra 1972. Proceedings of Consultants' Meeting, IAEA Vienna 25-27 August 1971.
- 4 A. Fabry et al, Proceedings of Conference Nuclear Data for Reactors, Helsinki, 15-19 June, 1970. IAEA Vienna 1970, Vol. II, p. 535.
- 5 E. Almén, B. Holmqvist and T. Wiedling, Swedish Atomic Energy Company Report, AE-429, 1971.
- 6 E. Almén, B. Holmqvist and T. Wiedling, Proceedings of Conference Nuclear Data for Reactors, Helsinki, 15-19 June, 1970. IAEA Vienna 1970, Vol. II, p. 93.
- 7 P.I. Johansson, B. Holmqvist and T. Wiedling, Proceedings of Consultants' Meeting, IAEA Vienna 25-27 August 1971.
- 8 P.I. Johansson, B. Holmqvist and T. Wiedling, Contribution to the Cadarache Meeting, 21-23 June, 1972.
- 9 P.I. Johansson, Joint Linac Van de Graaff Seminar, Harwell, 24-26 September, 1973.
- 10 P.I. Johansson, B. Holmqvist and T. Wiedling, Proceedings of a Panel, Neutron Standard Reference Data, Vienna, 20-24 November, 1972. IAEA Vienna 1974, p. 327.
- 11 P.I. Johansson and B. Holmqvist, An Experimental Study of the Prompt Fission Neutron Spectrum Induced by 0.5 MeV Neutrons Incident on  $^{235}\text{U}$ , to be published.
- 12 H.H. Knitter, M. Coppola, M.M. Islam, N. Ahmed and B. Jay, Proceedings of a Consultants' Meeting, Prompt Fission Neutron Spectra, IAEA Vienna, 25-27 August, 1971. IAEA Vienna 1972, p. 41.

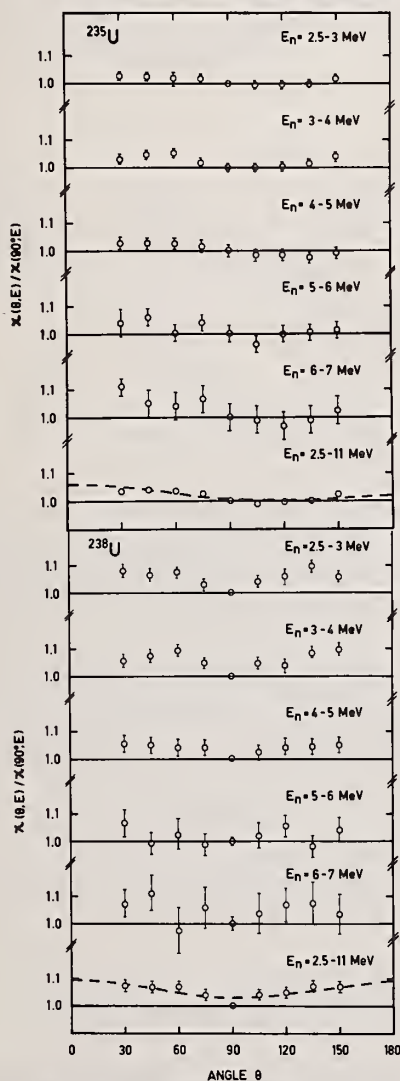


Figure 4. Angular distributions of fission neutrons from  $^{235}\text{U}$  and  $^{238}\text{U}$  measured at 2.07 MeV incident neutron energy. The distributions are given in 0.5 or 1 MeV energy intervals distributed in the range 2.5 to 7 MeV as well as for the interval 2.5 to 11 MeV.



J.W.T. Dabbs and N. W. Hill  
 Oak Ridge National Laboratory  
 Oak Ridge, Tennessee 37830

A polarized beam of neutrons and a polarized  $^{235}\text{U}$  target have been used to determine the spins of resonances below 150 eV. Most spins are assigned by inspection of the data; others by comparison with multilevel or single-level fits. Previously published data on fission fragment angular distributions, in conjunction with our spin assignments, indicate that two or more fission channels are available to each spin state. The ratio of symmetric to asymmetric fission appears to be uncorrelated with the resonance spin.

[ $^{235}\text{U}(n,f)$ ; J; polarized neutrons; polarized target; multilevel fits; fission channels]

## Introduction

The determination of spins of s-wave resonances in the  $^{235}\text{U}+n$  system induced by polarized neutrons on polarized targets has been reported by Keyworth et al.<sup>1</sup> for incident neutrons up to 60 eV. In this paper we present some results of a subsequent experiment which both confirm and extend the preliminary measurements, and we discuss some of the consequences in terms of the channel theory of fission.

## Experiment

This experiment was performed at the Oak Ridge Electron Linear Accelerator (ORELA) using polarization equipment designed and built at Los Alamos. A detailed description of the method has been given elsewhere<sup>2</sup> and only a brief discussion will be given here. The goal of the experiment is to assign resonance spins by comparing the neutron-induced fission cross sections of  $^{235}\text{U}$  for the cases for which the neutrons and the target nuclei have their spins aligned parallel and antiparallel. The experimental arrangement by which the required spin polarization was achieved is shown in Fig. 1. Bursts of neutrons from the linac pass through a sample of  $\text{La}_2\text{Mg}_3(\text{NO}_3)_{12} \cdot 24\text{H}_2\text{O}$  (LMN) cooled to about 10°K by thermal contact with superfluid helium. The protons in the water of hydration of the LMN are dynamically polarized. Because the cross section for (n,p) scattering through the singlet state is about 20 times greater than that for the triplet state, the transmitted neutrons are polarized parallel to the protons. The neutron polarization achieved in this experiment was  $f_n \approx 0.55$ . The direction of the neutron polarization was reversed by a slight ( $\sim 0.2\%$ ) change in the applied magnetic field.

The target was polarized in a second cryogenic system, a  $^3\text{He}$ - $^4\text{He}$  dilution refrigerator operated at a temperature of  $\sim 15$  mK. The enriched uranium was in the form of the ferromagnetic compound uranium monosulfide (US). The hyperfine field induced by a 10-kOe applied field resulted in a polarization of the  $^{235}\text{U}$  nuclei of the order  $f_N \approx 0.15$ .

Fission neutrons were detected in eight 10.8-cm-diam by 7.6-cm-thick liquid scintillators positioned at approximately 90° to the beam direction. Pulse-shape discrimination techniques were used to distinguish between neutrons and gamma rays. The data were

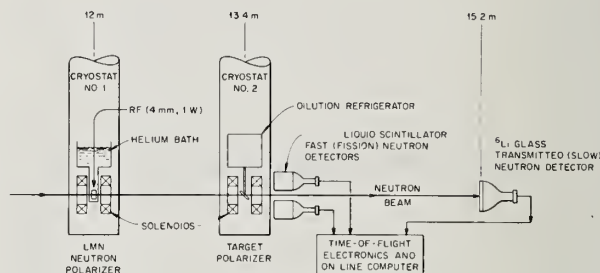


Fig. 1 - Schematic of the experiment.

taken in seven pairs of runs, each run being of about 22-hours duration. We were particularly careful to maintain experimental conditions as nearly identical as possible during corresponding spin-parallel, spin-antiparallel runs. Events were stored in four groups of 20 000 time-of-flight channels and later retrieved for analysis. The neutron beam was monitored with a thin lithium glass scintillator directly in the transmitted beam line. It should be noted that we are interested only in the change in the reaction rate when the relative spin direction of the incident neutron and target are reversed. The absolute cross section is unimportant to this experiment.

## Data Analysis

It is straightforward to show that the ratio of the reaction cross section when the neutron and target have their spins antiparallel to that when the spins are parallel is

$$R = \frac{[(I+1) - I f_n f_N] \sigma_+ + I(1 + f_n f_N) \sigma_-}{[(I+1) + I f_n f_N] \sigma_+ + I(1 - f_n f_N) \sigma_-} \quad (1)$$

In Eq. (1)  $f_n$  and  $f_N$  are, respectively, the magnitudes of the neutron and target polarizations, and  $\sigma_+$  and  $\sigma_-$  are the reaction cross sections for  $J = I \pm 1/2$ , where  $I$  is the spin of the target nucleus. For  $^{235}\text{U}$ ,  $I = 7/2$ . The only approximation in Eq. (1) is that  $\sigma_+$  is small, where  $n$  is the effective target thickness.

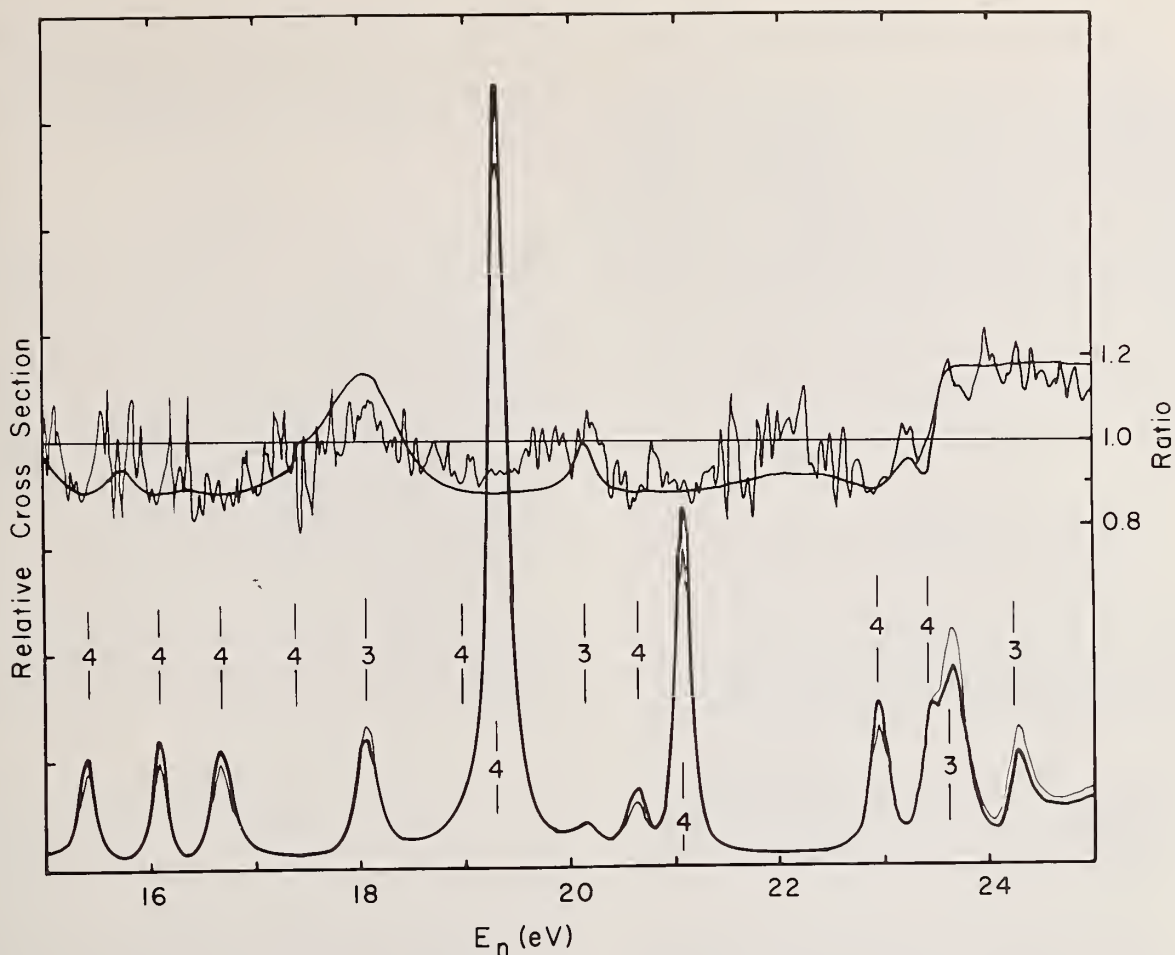


Fig. 2

A sample of the fission data. The heavier of the bottom curves is the spin parallel data. The rapidly fluctuating curve is the experimentally determined ratio. The smooth ratio curve is generated from Eq. (1), as explained in the text.

This is a very good approximation for this experiment ( $n \approx 6.18 \times 10^{-4}$  atoms/barn). Equation (1) is general and can be used to fit the shape of the experimentally determined ratio if the cross sections  $\sigma_{\pm}$  can be generated. Examples of this will be given below. If either  $\sigma_{+}$  or  $\sigma_{-}$  dominates the cross section, as is the case on resonance, then Eq. (1) becomes

$$R \approx \frac{1 - f \frac{f_n}{f_{nN}}}{1 + f \frac{f_n}{f_{nN}}} \quad (2)$$

with  $f = \frac{1}{I+1}$  if  $J = I + 1/2$

and  $f = -1$  if  $J = I - 1/2$ .

With this convention  $R > 1$  implies  $J = 3$ , and  $R < 1$  implies  $J = 4$ .

A representative sample of the low energy data is shown in Fig. 2. The lower curves were produced by merging all of the spin parallel (heavy line) and spin anti-parallel (lighter line) runs. The data were smoothed

in bins of four channels. The rapidly fluctuating curve is the ratio. Notice that while the fluctuations are large between resonances, they are small on resonance. The statistical uncertainty at 19.3 eV is 1.5%. At 15.4 eV, it is 4%. It is apparent that the spins of most of these resonances can be assigned immediately by inspection. The resonances at 15.4, 16.08, 16.68, 18.96, 19.3, 20.6, 21.07, and 22.94 eV clearly have  $R < 1$ , and thus  $J = 4$ . Resonances at 18.05, 23.63, and 24.25 eV have  $R > 1$ , and so  $J = 3$ . The spins of the resonances at 20.13 and 23.42 eV are not as easily assigned.

The solid ratio curve was generated using Eq. (1) and resonance parameters from a multilevel R-matrix fit to the  $^{235}\text{U}(n,f)$  and  $^{235}\text{U}(n,\gamma)$  data of de Saussure et al.<sup>3</sup> The fits were done with the multilevel, multi-channel search code MULT1, written by Auchampaugh.<sup>4</sup> Resonance spins were assigned on the basis of the polarization data. Two fission channels for each spin state were used in the fit. Note the following:

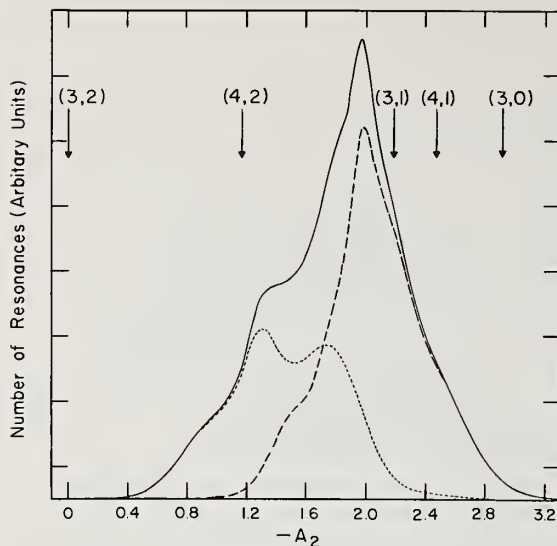


Fig. 3  
Weighted frequency distributions of  $A_2(\text{obs})$ . The solid curve includes all resonances. The dashed line indicates resonances with  $J = 4$ ; the dots indicate  $J = 3$ . The arrows indicate predicted  $A_2(J,K)$  values.

- (1) Not all sets of R-matrix parameters which give good fits to the fission and capture data give a good fit to the ratio. The polarization data ideally should be fitted simultaneously with the fission and capture data to provide a consistent set of parameters.
- (2) In spite of the fact that the fit is poor in detail, the spins of the small resonances at 20.13 and 23.42 eV can be assigned with confidence. The ratio near 20 eV is dominated by  $J = 4$  resonances, but rises to approximately 1 at the peak of the 20.13-eV  $J = 3$  resonance. The 23.4-eV resonance lies between regions dominated by  $J = 4$  and  $J = 3$ . The dip around  $R \approx 1$  is statistically significant, and is fit remarkably well by Eq. (2), assuming  $J = 4$  for the 23.4-eV resonance.
- (3) The dip at 17.5 eV in the data is probably significant. It shows up in the individual pairs of runs, as well as in these composite data. It probably is caused by a  $J = 4$  resonance which is not observed in either the (n,f) or the (n,y) data. This resonance was included in the fit to the fission and capture data and the result is the small "glitch" in the theoretical curve. The inclusion of one more level is of little importance, in view of the fact that as many as 50% of the levels may be missed.<sup>5</sup> If a much larger polarization effect could be obtained, however, say by increasing  $f_N$  sharply from about 15%, many of the missing levels might be found by this technique.

Spin assignments for most of the observed levels below approximately 60 eV have been made by the method outlined above, i.e., most assignments are made by inspection, and a theoretical curve based on Eq. (4) and multilevel fitting are used for the less obvious assignments. Above 60 eV multilevel fits are not used, but the same procedure can be followed using single-level resonance parameters. In this way we will assign

the spins of resonances below 150 eV. This is taken as an arbitrary upper energy limit of this first stage of data analysis; it is the highest energy for which widths are given in Ref. 6. No table of spin assignments is presented here. Spin assignments will be published after completion of the analysis.

### Discussion

It became clear from the results of the preliminary experiment<sup>2</sup> that, with one exception,<sup>7</sup> attempts to assign spins of neutron resonances in  $^{236}\text{U}$  by indirect methods were unsuccessful. The successful assignments of Corvi et al. were based on measurements of intensities of specific gamma rays fed by cascade from higher states. The intensities are expected to be  $J$ -dependent on general grounds, not on the basis of specific models. The success of Corvi et al. shows that such methods can work if enough care is taken in the measurements. However, it seems clear now that measurements of specific properties of the transition states are not, in general, reliable methods for assigning resonance spins. We elaborate below.

The angular distribution of fission fragments from neutron-induced fission of aligned  $^{235}\text{U}$  were first measured by Dabbs et al.<sup>8</sup> and, more recently with greater alignment and improved statistics, by Pattenden and Postma.<sup>9</sup> The form of the angular distribution is

$$W(\theta) = 1 + A_2 f_2 P_2(\cos \theta) + \dots \quad (3)$$

where  $f_2$  is the alignment parameter and  $A_2$  is determined by the angular momentum coupling. The  $A_2$  values of Pattenden and Postma are shown in Fig. 3 plotted in the form of a pseudohistogram, i.e., a function of the form

$$f(x) = \frac{1}{\sqrt{2\pi}} \int \frac{1}{\sigma_i} e^{-(x-x_i)^2/2\sigma_i^2} \quad (4)$$

The  $x_i$  represent measurements with statistical uncertainties  $\sigma_i$ . The solid curve in Fig. 3 includes both spin states. The dotted line represents resonances with  $J = 3$ , based on our spin assignments. The  $J = 4$  resonances are represented by the dashed line. The calculated values of  $A_2$  for various  $(J,K)$  values are also indicated in Fig. 3. The distribution for  $J = 4$  can be explained (i.e., reproduced in a Monte-Carlo calculation) by assuming that the  $K = 1$  channel is fully open, and that the  $K = 2$  channel is partially ( $\sim 1/4$ ) open. The (3,1) and (3,2) transition states, since they are lower- $J$  members of the same rotational bands, should lie lower in energy than the (4,1) and (4,2) states, respectively. The (3,1) and (3,2) channels should thus be open to at least the same degree as the (4,1) and (4,2) channels. In addition, the high  $A_2$  bump in the  $J = 3$  data is an indication that the (3,0) channel is at least partially open. Thus there seem to be two fission channels at least partially open for  $J = 4$ , and three for  $J = 3$ . Results of an analysis of the preliminary fission widths below 25 eV are consistent with this conjecture. The widths for  $J = 4$ , when fit with a chi-squared distribution of  $\nu$  degrees of freedom, give  $\nu = 1.27 \pm 0.33$ . For  $J = 3$ ,  $\nu = 2.04 \pm 0.65$ .



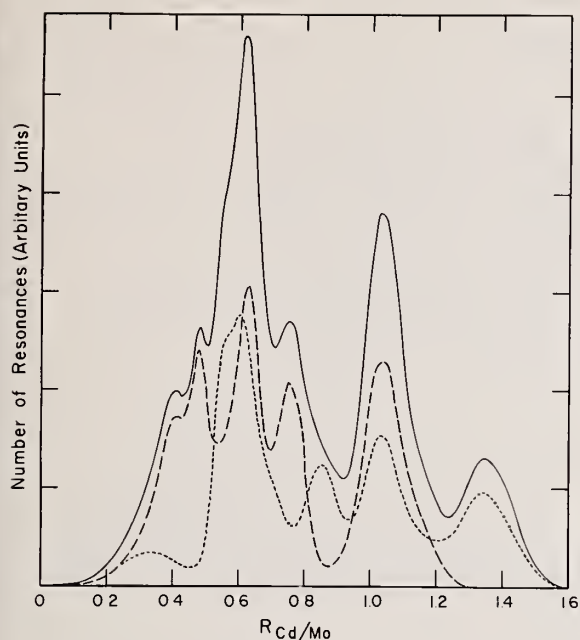


Fig. 4  
Weighted frequency distributions of the ratio of the resonance yield of  $^{115}\text{Cd}$  to  $^{99}\text{Mo}$ . The solid line indicates all resonances. The dashed line indicates  $J = 4$ ; the dots indicate  $J = 3$ .

In Fig. 4 we show a pseudohistogram of the ratio of symmetric to asymmetric fission as measured<sup>10</sup> by the relative yield of  $^{115}\text{Cd}$  to  $^{99}\text{Mo}$ . The three curves represent the frequency distributions for resonances of both spin states, and for resonances of  $J = 3$  and  $J = 4$  separately, based on our spin assignments. The composite distribution is bimodal, and it was surmised originally<sup>10</sup> that the two peaks might correspond to resonances of different spin. This is clearly not the case. The distributions for  $J = 3$  and  $J = 4$  are both bimodal. Presumably resonances of both spins contain admixtures of two or more transition states, and the distribution is dependent on  $K$ , which is mixed, rather than on  $J$ . It is surprising that the distributions for  $J = 3$  and  $J = 4$  are so similar, in view of the different  $K$  admixtures implied by the Pattenden and Postma data.

We feel that these results point to a need for two kinds of data. First, it is important to determine, if possible, the  $K$  admixture of the various resonances whose  $J$  is known. This could be done by improving the alignment experiment to the extent that higher order terms in the angular distribution could be determined. In addition, any experiment which measures resonance properties which can be related to the properties of the transition states is valuable. It is important to realize, however, that these properties are not, in general, determined by the spins of the resonances.

This work was conducted under the auspices of the U.S. Energy Research and Development Administration.

#### References

1. G. A. Keyworth, C. E. Olsen, F. T. Seibel, J.W.T. Dabbs, and N. W. Hill, *Phys. Rev. Letters* **31**, 1077 (1973).
2. G. A. Keyworth, J. R. Lemley, C. E. Olsen, F. T. Seibel, J.W.T. Dabbs, and N. W. Hill, *Phys. Rev. C* **8**, 2352 (1973).
3. G. de Saussure, R. Gwin, L. W. Weston, R. W. Ingle, R. R. Fullwood, and R. W. Hockenbury, Oak Ridge National Laboratory report ORNL-TM-1804 (1967).
4. G. F. Auchampaugh, Los Alamos Scientific Laboratory report LA-5473-MS (1973).
5. J. D. Garrison, to be published.
6. Brookhaven National Laboratory report BNL-325 (1973).
7. F. Corvi, M. Stefanon, C. Coceva, P. Giacobbe, *Nucl. Phys. A* **203**, 145 (1973).
8. J.W.T. Dabbs, C. Eggerman, B. Cauvin, A. Michaudon, and M. Sanche, *Proc. of the Second International Atomic Energy Symposium on Physics and Chemistry of Fission*, Vienna (1969), p. 321.
9. N. J. Pattenden and H. Postma, *Nucl. Phys. A* **176**, 225 (1971).
10. G. A. Cowan, B. P. Bayhurst, R. J. Prestwood, J. S. Gilmore, and G. W. Knobeloch, *Phys. Rev. C* **2**, 615 (1970).

J.P. Felvinci, E. Melkonian and W.W. Havens, Jr.  
Columbia University  
New York, New York 10027

Experiments were performed at ORELA to measure the low energy fission cross section of U-235. Times of flight of the neutrons causing fission and the fission fragment energy detected by a solid state detector were recorded event-by-event. Analysis of the data showed marked pulse height variation among resonances. Several of the large resonances were shown to be composites and the level density obtained is much higher than previously determined. The results were interpreted by the hypothesis that  $K$  is a good quantum number in the compound nucleus. This assumption and the systematic variation of the fission fragment energies among resonances enabled us to assign  $J$  and  $K$  quantum numbers to many levels. Three families of fission resonances were seen,  $J = 4^-$ ;  $K = 2$ ,  $J = 4^-$ ;  $K = 1$ , and  $J = 3^-$ ;  $K = 1$ . Our results have implications as to the accuracy of fission cross section measurements and to the calculation of cross sections in the unresolved energy region.

(Spins of  $^{235}\text{U}$  resonances from the  $(n,f)$  reaction possible interpretation)

Many attempts have been made in past years to determine the spins of the neutron resonances in  $^{235}\text{U}$ . Most of these measurements were of an indirect nature and yielded conflicting results. Recently, Keyworth et al<sup>1</sup>, using polarized neutrons on a polarized target, obtained many definitive spin values. The spins of the resonances are important in establishing the distribution of resonance parameters which are used to calculate the neutron cross sections in the unresolved energy region and also for the determination of possible interference effects between resonances of the same spin.

We have previously had indications of variations in the kinetic energy distributions<sup>2</sup> and have repeated these measurements with better fission fragment energy resolution and with lower background.

The experiment reported here has been performed at the Oak Ridge Electron Linear Accelerator (ORELA) using a flight path of 8.69 m. The machine repetition rate was 800 Hz and a Cd filter was used to prevent overlap neutrons from being detected, limiting the usable neutron energies to 0.4 eV to 1 keV. The  $^{235}\text{U}$  target thickness was 100  $\mu\text{g}/\text{cm}^2$ , which is a small fraction of the range of fission fragments. The 6.25  $\text{cm}^2$  area target was deposited on a 0.035 cm thick aluminum backing and was viewed by a 4  $\text{cm}^2$  area ORTEC heavy ion solid state detector at a distance of 2 cm from the target. The energy of one of the fission fragments and the time-of-flight (TOF) of the neutron causing the fission were recorded event by event on magnetic tape. The TOF system was a multiscaler with a basic time channel of 12.5 nsec, interfaced, together with a 256 channel analog-to-digital converter, to a PDP-8 computer. The event-by-event recording at the best time resolution of 12.5 nsec enabled us later to analyze the data in many different ways. In Fig. 1 the number of fission fragments counted in the neutron energy range 0.4 to 105 eV, is plotted against the channel number.

The initial step in the analysis consisted of forming energy histograms, in which the channel width was arranged to 1/4 of the combined Doppler and slowing down resolution broadening at each neutron energy. This method gave continuous cross section curves with the energy channel width a continuously changing quantity. The results were stored on a magnetic

drum as a 128 x 2048 array for 128 fragment energy and 2048 neutron energy channels. We could take then any pulse height cut and display the corresponding partial fission cross section as a function of neutron energy.

The divisions of pulse heights, used in this paper and shown in Fig. 1, were obtained by subdividing the total number of events into 15 groups, having approximately equal numbers of counts. The results for the first eight groups between neutron energies of 5 to 15 eV are plotted on Fig. 2. These groups correspond to pulse height regions where there is an approximate correspondence between the kinetic energy and the mass of the fragment. The lowest fragment energy correspond to the heaviest fragment and successively higher energies correspond approximately to lighter masses. In the high energy fission fragment peak there is no simple relation between energy and mass.

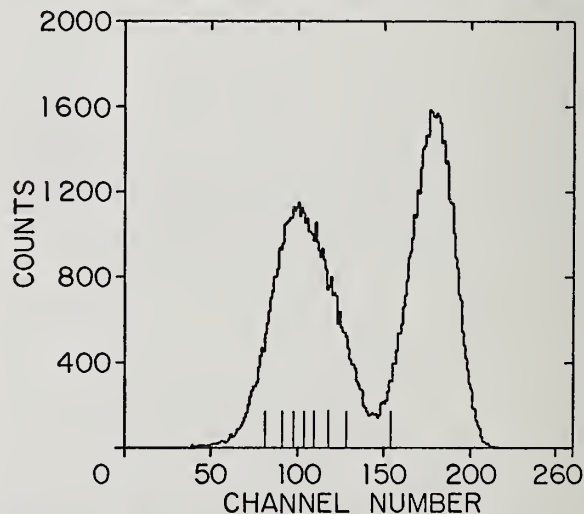


Figure 1. Number of fission fragments counted as a function of channel number. The lines bracket the regions which are sequentially plotted in Fig. 2.

Contingency tables<sup>3</sup> were also developed in selected neutron energy regions corresponding to these cuts,

giving a quantitative measure of statistically significant variations to complement the qualitative nature of the plots. These contingency tables were very large, typically having 15 columns of fragment energy and 50 rows of neutron energy. The  $\chi^2$  associated with them in certain neutron energy regions gave the probability of only  $10^{-4}$  that the fission fragment distributions were the same for all neutron energies.

Fig. 2 shows visible differences between the various cuts. Most of these differences are statistically significant and lead to the following conclusions:

- a) In many resonances, there is a systematic variation between the pulse height groups and this variation can be divided into three cases:
  - 1) Both the low energy region (curve 1) and the region corresponding to masses 130 and 136 (curves 6,7) excited;
  - 2) The medium energy in the low energy peak excited (curves 3,4,5);
  - 3) all energies equally excited.
- b) The spacing of the levels is smaller than seen previously; we resolve many resonances

into constituents which were previously considered to be single levels.

- c) The apparent interference effects seen in the fission cross section are in many cases due to several single levels which are selectively populated by different pulse height cuts.
- d) The fact that we observe all fission fragments, coupled with the indication that the low energy group has a different structure, would suggest possible, if small, biases in other types of measurements, e.g. those using ionization- and spark-chambers and/or those using thick  $^{235}\text{U}$  samples<sup>4</sup>.

It is also noted that the additional splitting of levels observed here is much more apparent in the partial fission cross sections than in the totalized fission cross section. This explains in part why these "new" resonances have not been seen previously. These considerations may explain the confusion in the spin determinations by the various methods which may be sensitive to different characteristics of the capture and the fission process. To understand these results we suggest a possible interpretation which is

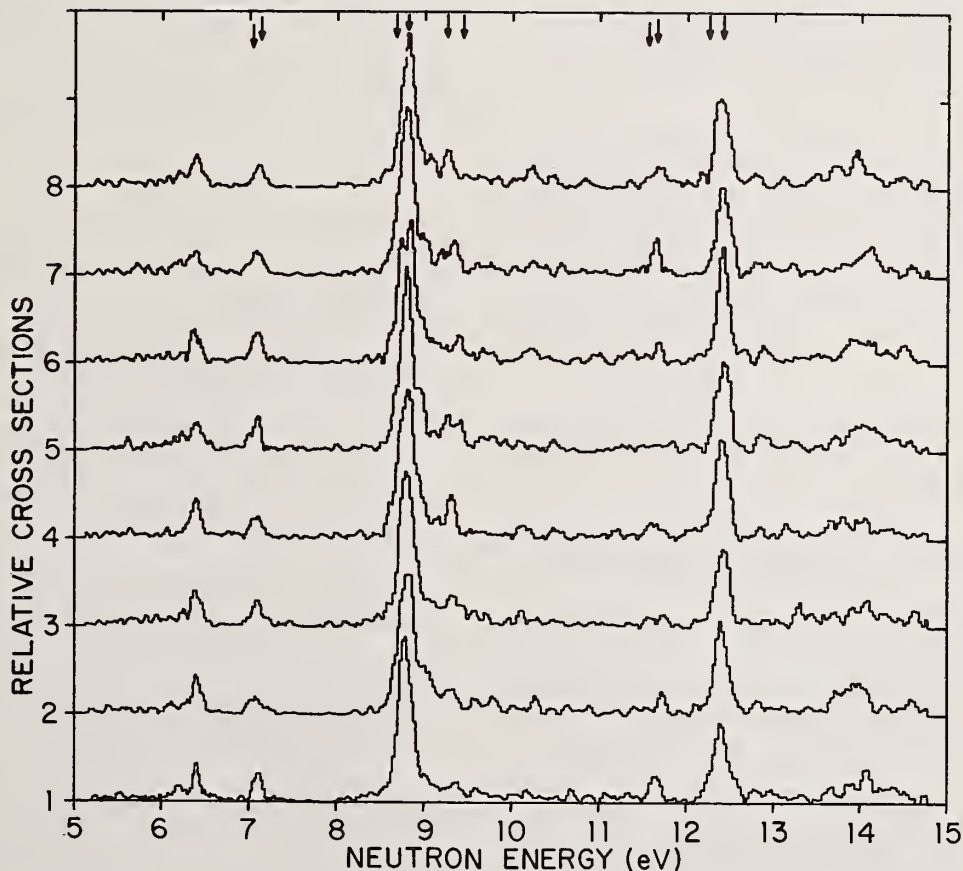


Figure 2. Relative partial fission cross sections of  $^{235}\text{U}$  from 5 eV to 15 eV incident neutron energy. The eight curves correspond to the eight pulse height cuts indicated in Fig. 1. The data were smoothed by fitting a quintic polynomial through nine adjacent points. This smoothing was found to be the best compromise between eliminating statistical noise and conserving the structure of the curves. Arrows indicate the five resonance groups which have been considered single levels in the past.



pure speculation at this point, but supported by certain amounts of circumstantial evidence.

It is well known that deformed nuclei in the rare earth and the actinide regions have definite rotational bands built on states of different characteristic collective vibrations. When a low energy neutron is captured by these nuclei, the compound nucleus will have an excitation energy between 5 and 7 MeV. It has been assumed, in the past, that at these excitations all of the short range correlations between the nucleons responsible for the collective motion are destroyed and that collective motion no longer exists.

We make the basic assumption here that, even at this high excitation energy, the compound nucleus maintains a collective motion, so that the quantum number  $K$  (the projection of the total angular momentum,  $J$ , on the nuclear symmetry axis) is conserved during the lifetime of the compound state. The ground state of the target nucleus has a definite  $(J, K)$  value with  $K = J$ ; i.e. the total angular momentum is aligned with the nuclear symmetry axis and no net collective rotation exists. Since we are considering only s-wave neutrons here, the addition of a neutron does not add angular momentum to the compound nucleus, and the probability of forming a compound nucleus for  $K$  less than  $J$  will be reduced corresponding to the degree of difference. Once formed, the compound nucleus will tend to maintain its initial collective state, resisting the exchange of vibrational motion for rotational motion.

The compound state formed will thus be in one of the few possible states with definite  $(J^P, K)$  quantum numbers and having definite but different amounts of energy of collective motion. On each of these collective (mostly vibrational) excitations will be built a sequence of levels based on the incoming energy minus the energy tied up in collective excitation. The spacing of these different sequences will be determined by the location of the vibrational band; the higher it is above the ground state, the larger will be the level spacing.

For the ground state of the  $^{235}\text{U}$  nucleus,  $J = (7/2)^-$  and  $K = 7/2$ . Consequently in  $^{236}\text{U}$  we expect to see only the  $(4^-, 4)$ ,  $(4^-, 3)$ ,  $(3^-, 3)$ , and  $(3^-, 2)$  states; the probability for the formation of the other possible states will be small.

The  $K = 3^-$  band is a composite of  $K = 1^-$  and  $K = 2^-$  bands and lies 1.2 MeV above the ground state of  $^{236}\text{U}$ . The  $K = 4^-$  band is a composite of  $K = 2^-$  and  $K = 2^+$  bands and lies approximately 2.0 MeV above the ground state. Level density calculations using an exponential dependence on energy give a factor of 3 increase for this 0.8 MeV energy difference. If it is assumed that the strength functions are of comparable magnitude for the different spin states, it follows that the  $(4^-, 4)$  levels will have a larger average  $g_n^0$  because of their larger average spacing.

The consequence of this larger  $\langle g_n^0 \rangle$  is that most of the large levels observed would have  $n(4^-, 4)$  quantum numbers and be widely separated, while the valleys of the cross section curve and the shoulders of the large levels would be populated with a higher density of levels corresponding to the  $(3^-, 3)$ ,  $(4^-, 3)$ , and  $(3^-, 2)$  quantum numbers, the other possibilities having small probability of formation. These effects are in the entrance channel.

In the exit channel, small changes in  $K$  are much more likely than large changes, consistent with the above assumption. As an example, the  $(n, \gamma)$  process will have additional selection rules operating on the change of the  $K$  quantum number, limiting the number of possible transitions, especially the ones to the ground state rotational band. Capture gamma ray experiments by Kane<sup>5</sup> and by Graves et al<sup>6</sup> indicate that the transitions to the ground state band are indeed considerably hindered.

The fission process presents a special case. As the nucleus becomes more elongated while maintaining its  $K$  quantum number, more energy is tied up in deformation. At the top of the fission barrier only about 1.0 MeV will be available as excitation energy. Both the  $K = 3^-$  and  $K = 4^-$  bands lie above this fission barrier and are thus energetically unavailable for fission to occur. The nucleus then will try to fission through one of its constituents, which are below the barrier, in the case of  $K = 3^-$  through  $K = 1^-$ , in the case of  $K = 4^-$  through  $K = 2^-$ . (It has to be the negative parity band because parity is conserved in the process). The  $(3^-, 2)$  state is already below the barrier and so we should expect large fission widths but small  $g_n^0$  for these levels, making them hard to observe.

The argument given above is consistent with the observation of only three of the four probable transitions resulting in fission, i.e. we do not observe the  $(3^-, 2)$  case. The results of Pattenden and Postma<sup>7</sup> who did not observe this state either, but did observe the  $(4^-, 1)$ ,  $(3^-, 1)$ , and  $(4^-, 1)$  states would corroborate our argument. The work of Keyworth et al<sup>1</sup> indicates that most of the large levels in fission have spin 4. We claim that they most likely have  $K = 2$ .

In Table I we list many, but not all, of the resonances observed between 0.4 and 40 eV incident neutron energy together with the assigned spin  $J$  and  $K$  quantum numbers. Where available, the  $J$  values obtained by Keyworth et al and the  $A_2$  coefficients of Pattenden and Postma are also included. The quantum numbers of Table I were obtained from a search for consistency between the three groups identified by us, the spin determinations of Keyworth et al and the measured  $A_2$  coefficients. These assignments equate our group (1) with  $(3^-, 1)$ , group (2) with  $(4^-, 1)$ , and group (3) with  $(4^-, 2)$ . It is to be noted that the  $(3^-, 1)$  resonances thus identified seem to correspond to divisions where the mass of one of the fragments is at or slightly above one of the doubly magic shells of  $A = 78$  and  $A = 132$ .

When we include all the levels observed in  $^{235}\text{U}$ , we obtain a level spacing of about 0.3 eV, which is slightly smaller than that suggested by Garrison<sup>8</sup>. In order to check on these results, we performed level density calculations based on a model by Ericson<sup>9</sup>, which gave very reasonable agreement with our observations. We report on these calculations and results in a separate paper to this conference<sup>10</sup>.

These tentative spin assignments coupled with the suggestion of higher level densities should affect the calculations of the cross sections in the unresolved energy region. Possible pulse height effects in some experiments may cause errors in the real fission cross section in this energy region and could be responsible for some discrepancies between microscopic and integral measurements.

In the low energy region very accurate measurements of fission cross sections cannot assume the absence of pulse height effects and thus discrepancies between measurements using different techniques may be expected.

TABLE I

$E_0$ (eV) <sup>c</sup>	J <sup>a</sup>	A <sub>2</sub> <sup>b</sup>	$E_0$ (eV)	J	K	$E_0$ (eV) <sup>c</sup>	J <sup>a</sup>	A <sub>2</sub> <sup>b</sup>	$E_0$ (eV)	J	K	$E_0$ (eV) <sup>c</sup>	J <sup>a</sup>	A <sub>2</sub> <sup>b</sup>	$E_0$ (eV)	J	K
1.135	4	-1.79	1.07 1.10 1.15	4 4 3	1 2 1	14.51	3	-1.49	14.5 14.8	3 4	1 1	22.94	4	-2.36	22.7 22.8 22.9 23.0 23.1	4 3 4 4 3	1 1 1 1 1
3.145	3	-1.76	3.10 3.20	3 4	1 2	15.40	4	-2.32	15.3 15.4 15.5	3 4 3	1 1 1						
3.163	4	-2.16	3.50 3.60 3.65	4 4 3	1 1 1	16.08	4	-2.06	16.0 16.1	3 4	1 2	24.25	3	-1.65	24.0 24.2	3 4	1 2
4.85	4	-1.91	4.80 4.90	4 4	1 2	16.68	4	-2.50	16.5 16.6 16.7 16.8 17.1 17.4	4 3 4 3 4 3	1 1 1 1 1 1	32.07	4	-2.06	31.2 31.7 31.8 32.0 32.1	3 4 3 4 4	1 1 1 1 2
6.21	3	-1.06	6.10 6.28	3 4	1 1							33.53	4	-2.32	33.5 33.6	4 3	1 1
6.39	4	-1.87	6.35 6.40 6.65 6.80	4 4 3 3	1 2 1 1	18.05	3	-1.80	17.8 17.9 18.1 18.2	3 4 4 3	1 1 2 1				34.0	3	1
7.08	4	-2.52	7.05 7.15	4 3	1 1	18.96	4	-	18.9 19.0	3 4	1 1	34.39	4	-1.56	34.4 34.5 34.8 34.9	4 3 4 3	2 1 1 1
8.78	4	-1.96	8.70 8.80	3 4	1 2	19.30	4	-2.00	19.2 19.3 19.5 19.6	4 4 4 3	1 2 1 1	35.20 35.3 35.78	3 3 -	-1.09 -1.09 -1.09 -	35.2 35.3 35.8	4 3 3	2 1 1
9.28	4	-1.99	9.25 9.40	4 3	1 1							38.36	4	-1.11	38.2	4	2
10.18	4	-2.08	10.12 10.20	4 3	1 1	20.13	-	-1.10	20.0 20.2	3 3	1 1	39.41	4	-1.88	39.1 39.2 39.4	3 4 4	1 1 2
11.66	4	-2.02	11.63 11.70	3 4	1 1	20.62	4	-2.62	20.5 20.7	4 3	1 1						
12.39	3	-1.29	12.10 12.25 12.40 12.50	4 3 4 3	1 1 2 1	21.07	4	-2.12	21.0 21.2 21.3	4 4 3	2 1 1						
12.85	4	-2.10	12.83	3	1												

<sup>a</sup> See ref. 1.

<sup>b</sup> See ref. 7.

<sup>c</sup> BNL - 325

Assigned J and K quantum numbers to selected  $^{235}\text{U}$  resonances. The resonances selected were those where statistical significance could be claimed.

#### References

- 1 G.A. Keyworth, et al., Phys. Rev. Lett. **31**, 1077 (1973)
- 2 E. Melkonian and G.K. Mehta, Physics and Chemistry of Fission, Vol. II, 355 (1965): IAEA, Vienna. J.P. Felvinci and E. Melkonian, Proceeding of the Third Conference of Neutron Cross Sections and Technology. - CONF - 710301, Vol. 2, 855 (1971). J.P. Felvinci and E. Melkonian, Transactions of the ANS, **19**, 420, (1974).
- 3 K.A. Brownlee, Statistical Theory and Methodology in Science and Engineering. John Wiley, N.Y., 1960, pp. 155.
- 4 F. Cohensedgh, et al., Transactions of the ANS, **19**, 420 (1974).
- 5 W.R. Kane, Phys. Rev. Lett., **25**, 953 (1970).
- 6 R.G. Graves, et al., Phys. Rev. C **8**, 781 (1973).
- 7 N.J. Pattenden and H. Postma, Nucl. Phys. A **167**, 225 (1971).
- 8 J.D. Garrison, Phys. Rev. Lett., **29**, 1185 (1972).
- 9 T. Ericson, Nucl. Phys. **6**, 62 (1958).
- 10 J.P. Felvinci, D. Cacuci, and E. Melkonian, Paper EB8, Nuclear Cross Sections and Technology, Washington, D.C. 1975.

\* Research supported in part by the U.S. Atomic Energy Commission.



The neutron capture cross section of  $^{242}\text{Pu}$  has been measured from 5 to 70 keV. The high-low bias method was used to distinguish between capture and fission events. Transmission experiments were also made in the resonance region. A normalization method was developed using the absorption and transmission data from six resonances. Using an average s-wave radiation width of 22 meV, an s-wave strength function of  $1.16 \times 10^{-4}$  and our measured capture cross section, we have determined p-wave contributions to the  $^{242}\text{Pu}$  capture cross section below 70 keV.

(Capture; normalization; strength functions)

### Introduction

The neutron capture cross section of  $^{242}\text{Pu}$  is of interest to the LMFBR program due to the substantial buildup of this isotope and its effect on the breeding ratio. A few measurements have been made to determine resonance parameters and the fission cross section<sup>1,2,3,4</sup>. For  $^{242}\text{Pu}$ , capture measurements require a simultaneous fission measurement because of the sub-threshold fission contribution.

### Experimental Apparatus

The high-low bias technique<sup>5,6</sup> was used to separate capture and fission components of the  $^{242}\text{Pu}$  absorption cross section from 20 eV to 70 keV. A 1.25m diameter liquid scintillator on the 25m flight path was used for the absorption experiments. The RPI LINAC was operated at 500 pps with a pulse width of 117 ns. The incident neutron flux was determined by a  $^{10}\text{B}$ -NaI detector at 28.3m. Neutron transmission measurements, using the same  $^{10}\text{B}$ -NaI detector, were made in the region below a few hundred eV. The data for all the experiments were accumulated in a PDP-7 on-line computer using a channel width of 0.0625 usec. Black resonance filters (S, Al, Na and Co) were kept in the neutron beam to determine the time-dependent background at 111, 35, 2.85 and 0.132 keV, respectively. A metallic  $^{242}\text{Pu}$  sample was prepared by Oak Ridge National Laboratory and doubly encapsulated in aluminum. The sample mass was 7.765 grams. The  $^{242}\text{Pu}$  content was 92.55%. An identical Al blank was used.

### Analysis

The high-low bias method has been described elsewhere<sup>5,6</sup> and only a brief summary is given here. The difference between capture and prompt fission gamma ray response in the large liquid scintillator is used to separate capture and fission events. By recording data taken simultaneously at two gamma ray biases, the capture and fission cross sections are determined from the following expressions:

$$\sigma_c(E_i) = \frac{L(E_i) - \frac{\eta_f}{\epsilon_f} H(E_i)}{N\varphi(E_i) \left[ \eta_c - \frac{\eta_f}{\epsilon_f} \epsilon_c \right]} \quad (1)$$

$$\sigma_f(E_i) = \frac{H(E_i) - \frac{\epsilon_c}{\eta_c} L(E_i)}{N\varphi(E_i) \left[ \epsilon_f - \frac{\epsilon_c}{\eta_c} \eta_f \right]} \quad (2)$$

where:  $\eta_c, \eta_f$  = spectrum fractions from 3-6 MeV for capture and fission events, respectively  
 $\epsilon_c, \epsilon_f$  = spectrum fractions from 6-15 MeV for capture and fission events  
 $L(E_i), H(E_i)$  = net, deadtime corrected counts in channel  $i$  for low and high bias data.  
 $\varphi(E_i)$  = absolute neutron flux in channel  $i$   
 $N$  = sample thickness, atoms/barn.

Equations 1 and 2 assume that self-shielding corrections have been made.

The spectrum fraction ratios  $\eta_c/\eta$  and  $\epsilon_c/\eta$  are determined from the ratio of hi-to-low data for five resonances (where  $\eta = \eta_c + \epsilon_c$ ). These ratios were constant, within statistics, thus showing that the fission width in each resonance is much less than the radiation width. The spectrum fractions  $\eta_f$  and  $\epsilon_f$  were determined from previous data<sup>6</sup> and assumed that the fission spectra is the same for  $^{242}\text{Pu}$  and  $^{252}\text{Cf}$ . The capture cross section is insensitive to the precise value of  $\eta_f$  and  $\epsilon_f$  since the fission component is much smaller than the capture contribution.

### Normalization

The present sample was too thin for previous<sup>6</sup> normalization techniques and only those resonances for which the neutron width was not small compared to the radiation width were observed in the transmission data. However,  $g\Gamma_n$  could be determined from the transmission data for five resonances using the Harvey-Atta code<sup>7</sup> (Table 1). Using these values of  $g\Gamma_n$  and an average radiation width of 0.0226 eV<sup>4</sup>, the capture area,  $A_\gamma$ , was calculated using a Monte Carlo code.<sup>8</sup>

An expression for the integrated net capture counts over a resonance and the flux  $\varphi(E)$  can be written: ( $M$  = scattering correction)

$$\int N_\gamma dE = \eta\varphi(E_0) \int [N\sigma_c(E) + M] dE \quad (3)$$



$$\int N_Y dE = \eta\phi(E_0)A_Y \quad (4)$$

and substituting the experimentally measured quantities for the integral in (4):

$$\eta\phi(E_0) = \frac{\sum_i N_Y(E_i)\Delta E_i}{A_Y} \quad (5)$$

where:  $\sum_i$  = sum net capture events over the resonance  
 $\Delta E_i$  = energy increment per channel  
 $A_Y$  = calculated capture area

The relative neutron flux,  $R(E)$ , is determined and for each of the five resonances, the quantity,  $\eta\phi(E)/R(E)$  was calculated. This ratio should be the same for all five resonances if the values of  $g\Gamma_n$  and  $\Gamma_\gamma$  are correct since the relative flux,  $R(E)$ , accounts for the flux shape. The average value of the ratio was used for absolute flux normalization.

The sensitivity of this normalization to the assumed radiation width was studied by repeating the calculation using  $\Gamma_\gamma = 0.030$  eV (an increase of 36%). The results of this study and the additional calculation of  $\eta\phi(E)/R(E)$  for the 232.9 eV resonance, where  $\Gamma_n \ll \Gamma_\gamma$  supported the choice of  $\Gamma_\gamma = 0.0226$  eV. (The resonance at 232.9 eV was seen only in capture.)

#### Estimate of Precision

The uncertainty in absolute normalization is composed of (1) the standard deviation of the net resonance counts and (2) the uncertainty in  $\Gamma_n$  derived from the transmission data for the five normalizing resonances. The % standard deviation of the net resonance counts is less than 1%. The uncertainty in  $\Gamma_n$  ranges from  $\pm 3$  to  $\pm 5\%$ . The total uncertainty of the absolute normalization is then  $\pm 3\%$  where the number of resonances used has been factored into the error calculation.

The standard deviation of the relative flux is  $\pm 3\%$ . The capture statistics, channel by channel, varies from  $\pm 10\%$  to  $\pm 15\%$ . Grouping the data reduces the uncertainty to  $\pm 2\%$  to  $\pm 4\%$ . The overall statistical uncertainty of the averaged data in the keV is then about  $\pm 4\%$ .

#### Results

The keV capture and fission cross sections were determined using equations (1) and (2). The keV fission cross section was found to be quite small relative to the high spontaneous fission background. The  $^{242}\text{Pu}$  capture cross section, (corrected for the impurity Pu contribution) is shown in Fig. 1. The gaps are due to the black filters used for background determination. The average capture cross section was calculated using the theory of Lane and Lynn.<sup>9</sup> Various values for  $\bar{D}$ , the average level spacing, and the s-wave ( $S^0$ ) and p-wave ( $S^1$ ) strength functions were assumed in attempts to fit the experimental results.

Above 27 keV, the p-wave contribution is about three times larger than the s-wave, thus increasing the sensitivity to the p-wave parameters. The final set of values are;  $\Gamma_\gamma = 0.0226$  eV,  $S^0 = 1.16 \times 10^{-4}$  and  $\bar{D} = 13$  eV and the calculated cross section is shown in Fig 1. Further adjustment of the parameters is possible since these quantities occur as products or ratios but  $S^1 = 2.5 \times 10^{-4}$  is adequate.

Table 2 gives the averaged experimental capture cross section for the range 6 to 70 keV.

Table 1  
Neutron Widths

Energy (eV)	$\Gamma_n$ (meV) (this work)	$\Gamma_n$ (meV) (Ref. 4)
205.0	$48 \pm 2.0$	$52 \pm 3$
273.8	$15.1 \pm 0.8$	$16.6 \pm 0.5$
303.7	$17 \pm 0.8$	$17.8 \pm 0.8$
332.6	$91 \pm 3.0$	$70 \pm 15$
382.4	$36 \pm 2.$	$54 \pm 5$

Table 2  
KeV Capture Cross Section

Energy (keV)	$\sigma_{n\gamma}$ (bn)	Energy (keV)	$\sigma_{n\gamma}$ (bn)
6-8	1.22	22-24	0.86
8-10	1.19	24-26	0.73
10-12	1.13	26-28	0.75
12-14	1.00	28-30	0.74
14-16	0.91	40-50	0.50
16-18	0.84	50-60	0.40
18-20	0.82	60-70	0.36
20-22	0.79		

#### References

1. G. F. Auchampaugh, J. A. Farrell and D. W. Bergen, Nucl. Phys., A171, 31 (1971)
2. D. W. Bergen and R. R. Fullwood, Nucl. Phys., A163, 577 (1971).
3. T. E. Young and S. D. Reeder, Nucl. Sci. Eng., 40, 389 (1970).
4. F. Poortmans, et al., Nucl. Phys., A207, 342 (1973).
5. R. Gwin, L. W. Weston, G. deSaussure, R. W. Ingle, J. H. Todd, F. E. Gillespie, R. W. Hockenbury and R. C. Block, Nucl. Sci. Eng., 45, 25 (1971).
6. R. W. Hockenbury, W. R. Moyer and R. C. Block, Nucl. Sci. Eng., 49, 153 (1972).
7. S. E. Atta and J. A. Harvey, "Numerical Analysis of Resonances," ORNL-3205, Oak Ridge National Laboratory (1964).
8. J. G. Sullivan, G. F. Warner, R. C. Block and R. W. Hockenbury, Rensselaer Polytechnic Institute (1969)(unpublished).
9. A. M. Lane and J. E. Lynn, Proc. Phys. Soc., A70, 557 (1957).

\* Sponsored by U.S.A.E.C. Contract AT(11-1)-3058.

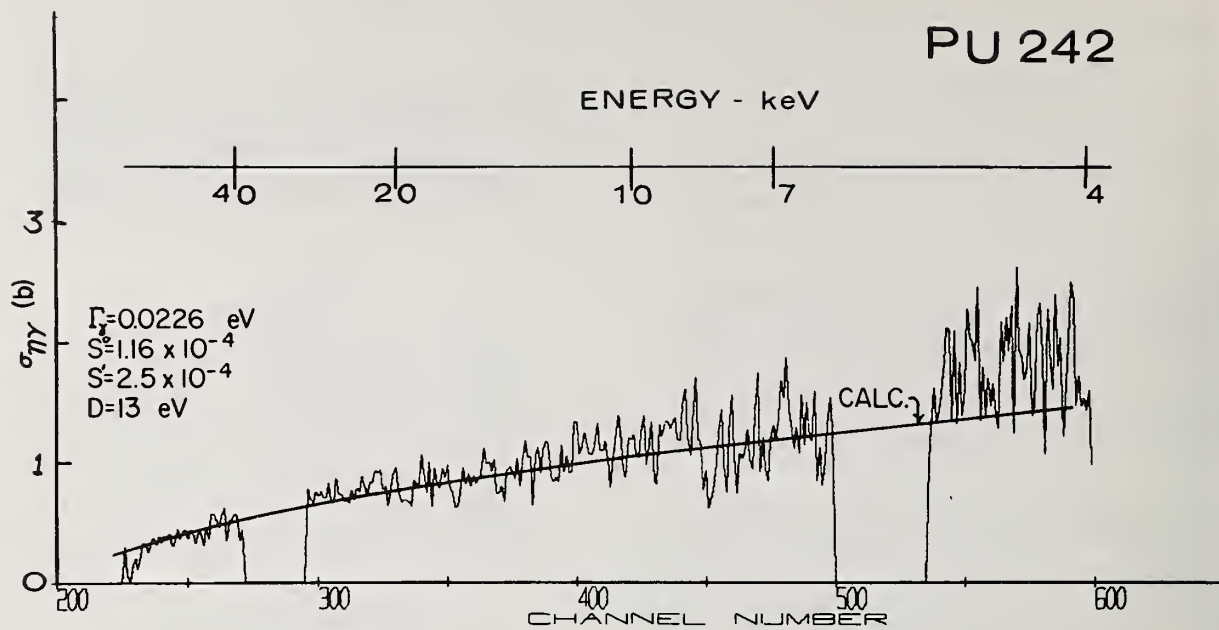


Fig. 1 Experimental and Calculated Capture Cross Section of  $^{242}\text{Pu}$

# SPONTANEOUS FISSION DECAY CONSTANT OF PLUTONIUM-238

R. Gay and R. Sher  
Stanford University  
Stanford, California 94305

The spontaneous fission decay constant of plutonium-238 was measured by two methods: fission-track counting in mica and coincidence counting of the fission fragments in solid-state detectors. The efficiency of the mica track detector was determined by thermal column irradiation of the plutonium source-mica detector assembly and subsequent counting of tracks arising from plutonium-239 fission. The coincidence counting result was combined with a determination of the  $\text{Pu}^{238}$  alpha emission rate of the sample to obtain the spontaneous fission decay constant. The results of the two methods were  $\lambda_{\text{sf}} = (4.75 \pm 0.12) \times 10^{-19} \text{ sec}^{-1}$  and  $(4.9 \pm 0.4) \times 10^{-19} \text{ sec}^{-1}$ , respectively.

(Spontaneous fission; decay constant; coincidence counting; track recorders; Plutonium-238; safeguards data)

## Introduction

A precise knowledge of the spontaneous fission decay constant of plutonium-238 is of interest both as required physics data in the study of nuclear structure and fission theory and as required data in the field of nuclear materials assay.

With the advent of fast breeder reactors and plutonium recycle in the 1980's, all plutonium isotopes will be produced in greater quantities than ever before. Because of the highly toxic and potentially strategic nature of these materials, very careful scrutiny will be required to ensure that none is lost or stolen during use, shipment or handling. Many current techniques for assay of these isotopes require accurate knowledge of the radioactive decay properties involved.

Although the spontaneous fission decay rate of  $\text{Pu}^{238}$  had been measured by four experimenters<sup>1,2,3,4</sup>, the high ratio of alpha to spontaneous fission decay, on the order of  $5 \times 10^8$ , limited the earlier methods used to few total fission counts and resultant poor statistical accuracy. This is because the total specific alpha activity of the source had to be kept small enough to reduce the probability of counting pile-up alpha pulses to a negligible level. The most recent measurement by Hastings and Strohm at Mound Laboratory<sup>4</sup> was based on a total of 1600 fission counts and therefore achieved greater accuracy than any of the previous experimenters. In the present effort, improvement is made upon all these past results by utilizing two independent techniques, previously unused for the measurement, which surmount the alpha-to-fission back-ratio difficulty, although in one case the measurement was still limited by poor statistics.

## Track Measurement Technique

For the purpose of the spontaneous fission-rate measurement by track detectors, a 1 mg,  $10 \text{ cm}^2$  ( $0.1 \text{ mg/cm}^2$ ) source containing 90.14%  $\text{Pu}^{238}$ , 9.21%  $\text{Pu}^{239}$ , and small amounts of other plutonium isotopes was obtained from Oak Ridge National Laboratories. The source material was electro-deposited on a 0.010-inch nickel backing. The quoted isotopic abundances are as supplied by the vendor and have not been independently verified.

Electro-deposited sources are known to be non-uniform, with source thickness especially low at the edges<sup>5,6</sup>. The effects of this source non-uniformity can be partially counteracted by employing an annular mask between the mica and the source material to absorb fission fragments emitted from the edges of the source while leaving the central region of the source directly exposed to the mica detector.

The mask selected for the experiment was  $68 \text{ mg/cm}^2$  lead, with a 0.5-inch inside diameter. The heavy Pb atoms are poor neutron absorbers and should not measurably perturb the neutron flux in thermal-column irradiations. Fig. 1 indicates the source arrangement.

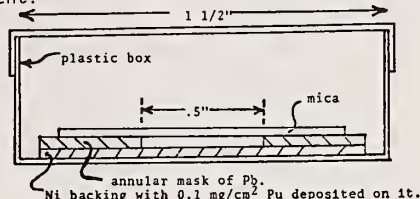


Fig. 1. Schematic of source arrangement

A Bausch and Lomb microscope with 20x oculars and a 20x dry objective was used for track counting. One eyepiece is inscribed with cross-hairs and a square. When counting, the mica foil, mounted on a calibrated stage, is moved continuously in one direction. The tracks appear to move horizontally across the field of view and are counted as they pass the center cross-hair. Only tracks that are within the bounds of the square are counted. Any track intersecting the top boundary of the square is counted, while tracks touching the bottom line are not. In this manner all tracks on the foil are counted. Successive horizontal sweeps are made, covering the entire area of the mica foil. Care must be taken when moving from one scan to the next that the scanning path is displaced exactly one field of view. This is done by locating a spot or track on the bottom line of the square and turning the stage dial so that the spot is moved to a corresponding position on the top line.

The source non-uniformity implies self-absorption in the thick regions and makes the absolute track-registration efficiency unknown and difficult to determine. However, the method employed eliminates the need for knowing this efficiency.

## Decay-Constant Calculation

In order to eliminate the need for knowing the track-registration efficiency of the source-SSTR combination, two exposures of mica to the  $\text{Pu}^{238}$  source were required. The first exposure recorded the spontaneous fission-track registration rate, and the second recorded tracks from fissions caused by a thermal neutron irradiation of the plutonium. Spontaneous fissions occurring during the second exposure form a background which must also be accounted for.



The number of tracks recorded from spontaneous fissions in the Pu-238 may be expressed as

$$(\text{tracks})_{sf} = \epsilon N^{238} \lambda_{sf} t_{sf}, \quad (1)$$

where  $\epsilon$  is the track-registration efficiency of the source-SSTR combination,  $N^{238}$  is the number of Pu-238 atoms exposed to the mica,  $\lambda_{sf}$  is the spontaneous fission decay constant of Pu-238, and  $t_{sf}$  is the exposure time.

The number of tracks recorded during a thermal neutron irradiation is

$$(\text{tracks})_{irr} = \epsilon \left[ \sum_f^{239} + \sum_f^{238} \right] \phi_{th} t_{irr} + \epsilon N^{238} \lambda_{sf} t_{con},$$

where  $\sum_f^{239}$  and  $\sum_f^{238}$  are the thermal neutron fission cross sections of Pu-239 and Pu-238, respectively,  $\phi_{th}$  is the thermal neutron flux,  $t_{irr}$  is the irradiation time, and  $t_{con}$  is the time during which the mica is in contact with the plutonium, which necessarily must be greater than  $t_{irr}$ .

The track-registration efficiency may be eliminated by dividing Eq. (2) by Eq. (1):

$$\frac{(\text{tracks})_{irr}}{(\text{tracks})_{sf}} = \frac{\left[ \sum_f^{239} + \sum_f^{238} \right] \phi_{th} t_{irr} + N^{238} \lambda_{sf} t_{con}}{N^{238} \lambda_{sf} t_{sf}}$$

Rearranging,

$$\frac{(\text{tracks})_{irr}}{(\text{tracks})_{sf}} = \left[ \frac{N^{239}}{N^{238}} g_f \sigma_f^{239} + \sigma_f^{238} \right] \frac{\phi_{th} t_{irr}}{\lambda_{sf} t_{sf}} + \frac{t_{con}}{t_{sf}},$$

where  $\sigma_f$  represents the microscopic (2200 m/sec) fission cross section, and  $g_f$  is the appropriate g factor for Pu-239. The g-factor for Pu-238 is assumed equal to unity. Solving for  $\lambda_{sf}$ ,

$$\lambda_{sf} = \frac{\left[ \frac{N^{239}}{N^{238}} g_f \sigma_f^{239} + \sigma_f^{238} \right] \frac{\phi_{th} t_{irr}}{t_{sf}}}{\frac{(\text{tracks})_{irr}}{(\text{tracks})_{sf}} - \frac{t_{con}}{t_{sf}}}. \quad (3)$$

If it is desired to express this result in terms of spontaneous fission half-life, this may be calculated by

$$T_{sf} = \frac{0.693}{\lambda_{sf}}. \quad (4)$$

#### Experimental Procedure

The thermal neutron irradiations were made in the thermal column of the University of California's TRIGA reactor at Berkeley. The neutron flux ( $\phi_{th}$ ) was determined by absolute gold-foil counting performed by the Stanford University Health Physics Department. Cadmium-covered gold foils were used in preliminary runs to ensure that the epi-thermal neutron flux was negligible. No cadmium was used in final measurements, since its effect on the neutron flux in the source region was unknown.

It was at first suspected that, due to a non-linear effect in counting technique, the recorded spontaneous fission decay rate was dependent upon the track density (tracks/cm<sup>2</sup>) of the mica foil being counted. To eliminate any such non-linearities, the exposures were made so as to yield approximately equal values of  $(\text{tracks})_{irr}$  and  $(\text{tracks})_{sf}$ . A systematic investigation later showed the track-counting efficiency ( $\epsilon$ ) to be in fact independent of the track density.

Since the track-counting efficiency reaches a broad maximum at the etching time and temperature used, its variation from foil to foil is not expected to be a problem. To be certain that etching conditions are the same, the mica foils from both exposures were etched simultaneously in the same HF solution. Also, to ensure accurate counting, the tracks were counted by different observers. Different individuals seem to count with different efficiencies ( $\epsilon$ ), but their results all led to calculated values of the spontaneous fission decay rate which were in agreement.

#### Results

Two separate runs of the measurement were made to verify the consistency of the method. Each run included both a spontaneous fission and a thermal neutron exposure of a mica-source combination. Two different observers counted the fission tracks of the first run. As shown on Table 1, the observers did not agree on the absolute number of tracks on a given mica foil; but the calculated spontaneous fission decay constants are in close agreement. The foils of the second run were counted by a third observer to further guard against any individual counting bias. As can be seen, the results of the second run agree satisfactorily with those of the first run.

Table 1

Run	$\phi_{th}$ (1/cm <sup>2</sup> -sec)	Observer	$(\text{tracks})_{irr}$	$(\text{tracks})_{sf}$	$\lambda_{sf} t_{sf}$ (sec)	$T_{sf}$ (yr)
I	$2.75 \cdot 10^5$	A	21,581	25,989	$4.75 \cdot 10^{-19}$	$4.63 \cdot 10^{10}$
		B	22,141	26,529	$4.72 \cdot 10^{-19}$	$4.66 \cdot 10^{10}$
II	$2.39 \cdot 10^5$	C	20,378	25,706	$4.78 \cdot 10^{-19}$	$4.60 \cdot 10^{10}$

The recommended final result from this measurement is

$$\lambda_{sf} = 4.75 \pm 0.12 \times 10^{-19} \text{sec}^{-1};$$

or in terms of half-life,

$$T_{1/2} = 4.63 \pm 0.12 \times 10^{10} \text{ years}.$$

The quoted uncertainty is based upon the combination of the individual uncertainties associated with each of the terms in Eq. (3). The uncertainties assumed for the fission cross sections were those given in BNL:325:  $\sigma_f^{239} = 742 \pm 3$  barns and  $\sigma_f^{238} = 16.5 \pm 0.5$  barns. No uncertainty was associated with the isotopic ratio or the g-factor of Pu-239 as these should be less than that of  $\sigma_f^{239}$ . In the absence of information about the behavior of  $\sigma_f^{238}$  with increasing energy, its g-factor was taken as unity. Fortunately,  $\sigma_f^{238}$  forms only a small percentage of the total fission cross section, so its contribution to the total error is small.

Errors in the measured time values were assumed negligible. The largest source of error for the experiment was that contributed by the thermal flux. A 2% uncertainty was associated with the experimentally determined flux value. Sources of error in this value are: counting statistics (1%), mass of the Au foil, calibration of the counter and spatial perturbation of the flux caused by the lead mask and the gold foils. Statistical uncertainties were included in the track-counting results.

### Coincidence Counting Measurement

The second measurement technique used is coincidence counting of fission fragments with silicon surface-barrier semiconductor detectors. This method achieves high alpha fission discrimination by combining energy discrimination with coincidence timing.

### Experimental Apparatus

In order to achieve coincidence counting of the fission fragments, Pu-238 foils are required which are thin compared to the range of fission fragments; they are mounted on a backing which is also thin. For this measurement, four Pu-238 foils of thickness less than  $5 \mu\text{g}/\text{cm}^2$  mounted on Ni backings of  $\sim 200 \mu\text{g}/\text{cm}^2$  were obtained. The largest foil contained a total mass of approximately  $5 \mu\text{g}$  of Pu-238. Since the range of a fission fragment in nickel is on the order of  $5 \text{ mg}/\text{cm}^2$ , a fragment should not be lost in this backing. Some fragment energy loss in the source backing ( $\sim 5 \text{ MeV}$ ) does occur, however.<sup>7,8</sup>

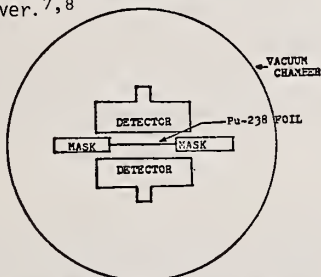


Fig. 2. Experimental Counting Set-up

The Pu-238 foil to be counted was placed in a vacuum chamber with detectors mounted on either side, as shown in Fig. 2. Two  $300 \text{ mm}^2$  Ortec Series "F", heavy ion, silicon surface-barrier detectors were used for the measurements. A Nuclear Equipment Corporation Model 336 preamplifier was used to amplify the signals from each detector. The pulses were then shaped by differentiation and integration in amplifiers. The pulses from one detector were delayed approximately  $3 \mu\text{sec}$  by utilizing the delayed output terminal of the amplifier.

These pulses were fed into EG&G TD101/n differential discriminators operating in the integral discrimination mode so that only pulses of amplitude greater than a set threshold level were passed. Most of the alpha pile-up was eliminated here. The discriminator outputs were input to a time-to-pulse-height converter, whose output was displayed on a RIDL 20-02 400-channel analyzer.

The peak on the analyzer spectrum, occurring at a pulse height representing approximately three microseconds, represents true coincidence or fission events. The off-peak counts are due to accidental coincidences. Fig. 3 is a block diagram of the system.

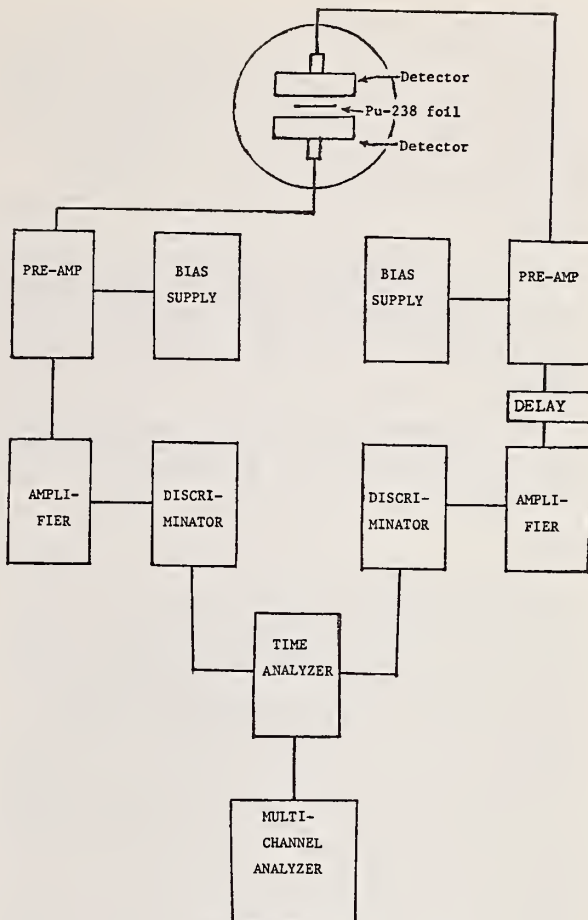


Fig. 3. Electronics Block Diagram

### Counting Efficiency

The geometrical counting efficiency for the source-detector arrangement used is required in order to obtain the absolute fission rate. This may be calculated since the geometry is known. The singles or alpha-counting efficiency is different from the coincidence or fission-counting efficiency as it is possible for one fragment of a given fission to intercept a detector while the other fragment of the fission misses the other detector. A Monte Carlo calculation was used to determine the counting efficiencies of the detectors. This technique was required because of the difficulty of analytically accounting for the effect of the source mask. The calculation was based on the assumptions that any particle which hits the detector registers a count, and that there is no scattering in of particles to the detector from surrounding structures such as the source mask. The no-scattering assumption is quite accurate for the fission fragments, as their mass is large compared to the mask nuclei (Al).<sup>9</sup> Additional assumptions are that particles are emitted isotropically, that fission fragments from the same fission fly in opposite directions, and that the source is uniform.

The Monte Carlo calculation proceeded as follows. First the position (radius), vertical angle, and azimuthal angle are selected for the first particle, using three random numbers generated by a random number generator subroutine. Using these three values,



the program first determines if the particle intercepts the detector. If so, the program then determines if the source mask was missed by the particle. A hit is registered if both of the above tests are passed; otherwise a miss is recorded. This procedure is repeated for each additional case considered. The counting efficiency is then equal to the number of hits divided by the number of trials. A detailed description of the Monte Carlo program is provided in reference 10.

Because of count-rate limitations, the alpha rate of the source had to be determined in a lower geometry than that used for the coincidence measurement. Hence, the plutonium source-mask combination was mounted in a position 21 mm below the detector for the alpha-rate measurement.

The Monte Carlo calculated efficiencies of 44.8% for coincidence counting and 12.4% for lower-geometry alpha counting were then used in the calculation of the spontaneous fission decay constant.

### Results

The measurement was performed with a source of thickness  $\sim 1 \mu\text{g}/\text{cm}^2$ . This source was counted in the coincidence geometry for 208 hours, yielding the time-analyzer multi-channel output histogram shown in Fig. 4. The total number of fissions was determined by subtracting the off-peak or accidental coincidence count rate (found by averaging channels 0-200 and 300-400) from the total number of counts to yield 123 fissions.

The alpha rate of the source was measured in the lower-geometry position (21 mm from the detector) to be  $11,700 \pm 150$  per second.

Since the counting efficiencies were known for both the coincidence and alpha measurements, the spontaneous fission half-life may be calculated by the following relationship:

$$T_{1/2}^{\text{Sf}} = T_{1/2}^{\alpha} \frac{N_{\alpha}}{N_{\text{f}}}$$

where  $T_{1/2}$  is the appropriate partial half-life and  $N_{\text{f}}$ ,  $N_{\alpha}$  are the spontaneous fission and alpha-source disintegration rates.

### References

- <sup>1</sup>Segre, E., Phys. Review, Vol. 86, No. 1 (1951).
- <sup>2</sup>Jaffey, A. H., and A. Hirsch, ANL-4286, (1949).
- <sup>3</sup>Druin, V. A., V. P. Pereilyin and G. I. Khlebnikov, Soviet Phys. JETP, Vol. 13, No. 5 (1961).
- <sup>4</sup>Hastings, J. D., and W. W. Strohm, J. Inorg. Nucl. Chem., Vol. 34, 25-28 (1972).
- <sup>5</sup>Gold, R., R. J. Armani and J. H. Roberts, Nuc. Sci. and Engr., 34, 13-32 (1968).
- <sup>6</sup>Roberts, J. H., R. Gold and R. J. Armani, "Spontaneous Fission Decay Constant of U-238," Phys. Rev., Vol. 174, No. 4 (1968).
- <sup>7</sup>Northcliffe, L. C., and R. F. Schilling, "Range & Stopping Power Tables for Heavy Ions," Nuclear Data Tables, A7, 233-463 (1970).
- <sup>8</sup>Kahn, S., R. Harman and V. Forgue, Nuc. Sci. & Engr., 23, 8-20 (1965).
- <sup>9</sup>Engelkemeir, D., Phys. Rev., Vol. 146, No. 1, p. 304 (1966).
- <sup>10</sup>Gay, R., "Spontaneous Fission Decay Constant of Pu-238", Ph.D. thesis, Mechanical Engr. Dept., Stanford U. (1975).

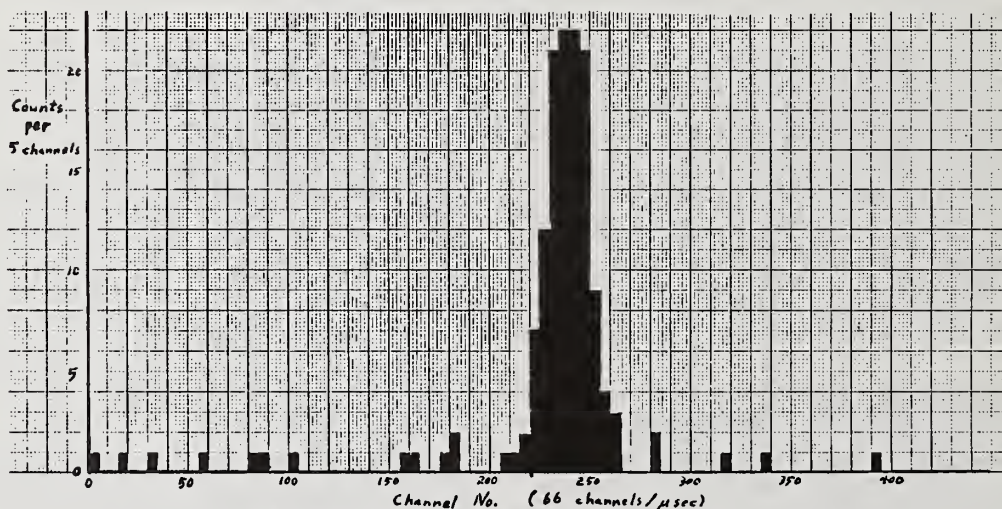


Fig. 4. Histogram of time analyzer output



# NEUTRON-INDUCED FISSION CROSS SECTIONS OF $^{233}\text{U}$ , $^{234}\text{U}$ , $^{236}\text{U}$ , AND $^{238}\text{U}$ WITH RESPECT TO $^{235}\text{U}^*$

J. W. Behrens, G. W. Carlson, and R. W. Bauer  
Lawrence Livermore Laboratory, University of California  
Livermore, California 94550

Ratios of the neutron-induced fission cross sections of  $^{233}\text{U}$ ,  $^{234}\text{U}$ ,  $^{236}\text{U}$ , and  $^{238}\text{U}$  relative to  $^{235}\text{U}$  and of  $^{238}\text{U}$  relative to  $^{233}\text{U}$  were measured with fission ionization chambers at the LLL 100-MeV electron linear accelerator. The time-of-flight technique was used to measure the cross section ratios as a function of neutron energy from 0.1 to 30 MeV, except for the  $^{233}\text{U}:$  $^{235}\text{U}$  and  $^{238}\text{U}:$  $^{233}\text{U}$  ratios, which were measured from 0.001 to 30 MeV, and 1 to 30 MeV, respectively. The continuous energy spectrum of the neutron source allowed us to cover the entire energy range of each ratio in one measurement. The threshold cross section method was used to normalize the ratios independent of other cross section measurements. Typical energy resolutions of the data are 5% at 20 MeV and 1.5% at 1 MeV. Most of the data have counting uncertainties smaller than 4%. Systematic errors are discussed, and current results are compared with previous measurements.

(Fission cross section ratios; uranium isotopes —  $^{233}\text{U}$ ,  $^{234}\text{U}$ ,  $^{235}\text{U}$ ,  $^{236}\text{U}$ ,  $^{238}\text{U}$ ;  
0.001 to 30 MeV; linear accelerator; time-of-flight technique)

## Introduction

The history of neutron-induced fission cross section measurements in the keV and MeV range on the relatively long-lived isotopes of uranium ( $^{233}\text{U}$ ,  $^{234}\text{U}$ ,  $^{235}\text{U}$ ,  $^{236}\text{U}$ , and  $^{238}\text{U}$ ) spans more than 20 years.<sup>1-17</sup> In spite of the large effort that has been expended, there are still gaps in the MeV energy range where experimental data for some of the isotopes are lacking. For the isotopes measured, there are regions of inconsistencies where different data sets disagree. The most complete and accurate set of cross sections for this group of isotopes is for  $^{235}\text{U}$ .

We measured the ratios of the fission cross sections of  $^{233}\text{U}$ ,  $^{234}\text{U}$ ,  $^{236}\text{U}$ , and  $^{238}\text{U}$  relative to  $^{235}\text{U}$ . The continuous energy spectrum of neutrons produced by the LLL 100-MeV linac made it possible to use the time-of-flight technique in the energy range from 0.001 to 30 MeV in one continuous measurement. Data for the threshold isotopes  $^{234}\text{U}$ ,  $^{236}\text{U}$ , and  $^{238}\text{U}$  are usable only above 0.1 MeV. The  $^{238}\text{U}:$  $^{233}\text{U}$  ratio was measured from 1 to 30 MeV to provide part of the normalization for the  $^{233}\text{U}:$  $^{235}\text{U}$  ratio. Our ratios fill gaps where no data existed. These data will provide better definition of the cross section vs energy curves.

The normalization is a probable cause of many discrepancies between different sets of cross section ratio data. A related problem, which can seriously limit the accuracy of the final results, is the determination of the relative masses of fissionable samples.

To normalize our ratios we followed a procedure we call the threshold cross section method. In this method determination of the normalization is an integral part of the measurement and can provide results with uncertainties less than 1% for each ratio involving a threshold isotope.

## Experiment

### Neutron Source and Detectors

The ratio measurements were made with fission chambers at the 34.25-m station of the 250-m time-of-flight tube at the LLL 100-MeV linac. The linac was operated at 1440 Hz with an electron pulse width of 10 ns to produce neutrons in a water-cooled-tantalum target.

Our fission detectors are parallel plate ionization chambers of modular design placed back-to-back in a pressure vessel with the foils oriented perpendicular to the incident neutron beam. Table 1 gives the areal densities and isotopic compositions of the fissionable materials used in the chambers.

Details of the fission chambers, electronics, and data acquisition system have been reported.<sup>18-20</sup>

TABLE 1. ISOTOPIC COMPOSITIONS AND AREAL DENSITIES OF FISSIONABLE MATERIALS.

Isotope	Isotopic Composition Mass Number (at.%)					Areal Density (g/m <sup>2</sup> )
	233	234	235	236	238	
$^{233}\text{U}$	99.99+			0.001		2.7
$^{234}\text{U}$	0.005	99.84	0.10	0.05	0.01	3.0
$^{235}\text{U}$		0.03	99.91	0.02	0.04	2.9
$^{236}\text{U}$			0.0025	99.99+		1.9
$^{238}\text{U}$			0.0006		99.99+	3.1
$^{235}\text{U}$ , $^{234}\text{U}$		60.16	39.78	0.04	0.06	2.2
$^{235}\text{U}$ , $^{236}\text{U}$		0.01	30.44	69.51	0.04	3.0
$^{235}\text{U}$ , $^{238}\text{U}$		0.01	25.35	0.01	74.63	3.8
$^{233}\text{U}$ , $^{238}\text{U}$	12.69				87.31	3.8

\*Work performed under the auspices of the U. S. Energy Research & Development Administration.

The gamma flash from the tantalum target was our main timing reference. Gamma rays cause signals with a pulse height distribution similar to the distribution for neutron-induced fission. Some of the signals arise from photo-fission events. The similarity of the two distributions means that the gamma- and neutron-induced signals cross the discriminator level at almost the same average time relative to the starting times of the signals. We located the center time of the gamma flash to within  $\pm 1.5$  ns for each fission chamber by splitting its counts evenly between two time-of-flight channels. We verified the gamma flash timing to within about 10 ns by measuring the location of the 2.079-, 2.819-, and 6.295-MeV resonances of carbon.<sup>21</sup>

The resolution of our experiment is determined by the resolution of the fission chamber system ( $\leq 9$  ns) and the pulse width of the electron pulses striking the tantalum target ( $\sim 10$  ns). Taken in quadrature, these two components result in a resolution of about 13 ns. Data are reported with a minimum time per channel of 16 ns, which corresponds to 5.4% energy resolution at 20 MeV and 1.5% at 1 MeV at the 34.25-m time-of-flight station. Uncertainty in flight path and finite target and detector thickness result in a loss of resolution that is small compared to the above two components. Our time-to-energy conversion includes the relativistic correction.

#### Threshold Cross Section Method

We use the term threshold cross section method to describe the way we obtained the normalization for our fission cross section ratios of threshold to non-threshold isotopes.<sup>22</sup> In this method the nonthreshold isotope is mixed with the threshold isotope to make the fissionable coating for one chamber. This mixed chamber is measured and compared to the measurements of a chamber containing the pure nonthreshold isotope. The resulting ratio may be written as:

$$R(E) = \frac{\beta_m N_t}{\beta_p N_{nt}} \left( \frac{\sigma_t(E)}{\sigma_{nt}(E)} + \eta \right),$$

where  $R(E)$  is the ratio of fission counts as a function of neutron energy from the two chambers,  $\beta_m$  and  $\beta_p$  are the efficiencies of the mixed and pure fission chambers,  $N_t$  is the number of atoms of the threshold isotope,  $N_{nt}$  is the number of atoms of the nonthreshold isotope in the pure chamber,  $\eta$  is the ratio of atoms of the nonthreshold isotope to threshold isotope in the mixed chamber, and  $\sigma_t(E)$  and  $\sigma_{nt}(E)$  are the fission cross sections whose ratio is to be determined.

At energies where the ratio  $\sigma_t(E)/\sigma_{nt}(E)$  is negligible, the ratio of counts  $R(E)$  is a constant  $Q$ . This constant, together with the measured value of  $\eta$ , gives the ratio of effective numbers of atoms, i.e.,  $(\beta_m N_t)/(\beta_p N_{nt}) = Q/\eta$ . This ratio normalizes the cross section ratio as follows:

$$\frac{\sigma_t(E)}{\sigma_{nt}(E)} = \eta \left( \frac{R(E)}{Q} - 1 \right). \quad (1)$$

Corrections are made for the nonzero fission cross sections of the threshold isotopes in determining  $Q$ .

We used four mixed chambers in the experiment. The atom ratios were determined by groups at Livermore and Los Alamos Scientific Laboratory using mass spectrometric methods. These measured atom ratios are compared in Table 2. An accuracy of  $\pm 0.25\%$  has been determined for each of the values of  $\eta$ .

These mixed fission chambers allow us to determine the  $^{238}\text{U}:^{235}\text{U}$ ,  $^{236}\text{U}:^{235}\text{U}$ ,  $^{234}\text{U}:^{235}\text{U}$ , and  $^{238}\text{U}:^{233}\text{U}$  ratios as a function of neutron energy without normalizing to other cross section measurements. For normalization purposes we chose energy intervals for each cross section ratio and formed averages by weighting the values of the individual ratios in their 16-ns time-of-flight channels with the energy width of the channel. Table 3 gives the threshold method ratios, the energy intervals over which they were averaged, and the contributions to the uncertainty from  $\eta$ ,  $Q$ , and  $R$  as defined in Eq. (1). In each case the statistical errors of  $R$  and  $Q$  are larger than the uncertainty in the atom ratio  $\eta$ .

The basic limitation of the threshold method is that the ratios obtained have large uncertainties when the ratio becomes small compared to the mixed chamber atom ratio. Therefore the  $^{234}\text{U}:^{235}\text{U}$ ,  $^{236}\text{U}:^{235}\text{U}$ , and  $^{238}\text{U}:^{235}\text{U}$  ratios were also measured with a chamber containing a pure sample of the threshold isotope.

All of the pure chamber data were normalized to the values shown in Table 3, which were obtained from the mixed chambers. In all cases the shapes of the data from the pure chambers and mixed chambers agreed within the experimental accuracy.

#### Corrections and Errors

Most of our data have statistical counting errors of less than 4%. A number of effects contributed

TABLE 2. MASS SPECTROMETER MEASUREMENTS OF  $\eta$ .

Main Isotopes	LLL		LASL		$\eta \pm \delta\eta$
	Samples Analyzed	Average $\eta$	Samples Analyzed	Average $\eta$	
$^{235}\text{U}, ^{234}\text{U}$	4	0.6603	3	0.6621	$0.6611 \pm 0.0017$
$^{235}\text{U}, ^{236}\text{U}$	5	0.4378	3	0.4384	$0.4380 \pm 0.0011$
$^{235}\text{U}, ^{238}\text{U}$	7	0.3397	5	0.3391	$0.3395 \pm 0.0008$
$^{238}\text{U}, ^{233}\text{U}$	3	0.1455	3	0.1451	$0.1453 \pm 0.0004$

TABLE 3. NORMALIZATION VALUES OBTAINED USING THE METHOD OF THRESHOLD CROSS SECTIONS.

Ratio	Energy Range (MeV)	Threshold Method Ratio	Breakdown of Uncertainties		
			$\eta$	$Q$	$R$
$^{234}\text{U}:^{235}\text{U}$	0.50-2.50	$1.089 \pm 0.012$	0.0030	0.0098	0.0068
$^{236}\text{U}:^{235}\text{U}$	0.90-2.50	$0.5707 \pm 0.0064$	0.0012	0.0047	0.0042
$^{238}\text{U}:^{235}\text{U}$	1.75-4.00	$0.4405 \pm 0.0040$	0.0010	0.0022	0.0032
$^{238}\text{U}:^{233}\text{U}$	1.75-4.00	$0.3005 \pm 0.0025$	0.0008	0.0016	0.0017



systematic errors to our experimental results. These effects are summarized in Table 4. The estimate of energy dependence in detector efficiency was obtained from a study of the pulse height distributions of the detectors as functions of energy.<sup>20</sup>

TABLE 4. SYSTEMATIC ERRORS IN THE RATIOS EXPERIMENT.

Effect	Error Size	Correction Made	Resultant Uncertainty in Ratios
Electronic deadtime	2% max	Yes	<0.01% (negligible)
Accidental coincidences between detectors	1% max	Yes	<0.2%
Neutron scattering in aluminum foils etc.	4% max 0.4% typical	Yes	0.8% max 0.08% typical
Out-of-time neutron background (measured by black resonance absorber technique)	<0.1%	No	<0.1%
Time independent background from amplifier noise and alpha pileup	~15% max <0.1% typical	Yes	0.6% max <0.01 typical
Energy-dependent detector efficiency	<0.5%	No	<0.5%
Impurities in isotopic samples	~10% max effect in $^{238}\text{U}/^{235}\text{U}$ ratio at 0.1 MeV	Yes	5% in $^{238}\text{U}/^{235}\text{U}$ ratio at 0.1 MeV, negligible almost everywhere else

### Results and Comparisons

#### $^{238}\text{U}/^{235}\text{U}$ Ratio

The data of Meadows<sup>16</sup> (0.898 to 5.33 MeV) agree well with our results for the  $^{238}\text{U}/^{235}\text{U}$  ratio (Figs. 1, 2, and 3). There is also good agreement with the data of White and Warner<sup>10</sup> at their three points (2.25, 5.4, and 14.1 MeV) and with the data of Poenitz and Armani<sup>15</sup> at 2.0, 2.5, and 3.0 MeV. Furthermore, our data are in general agreement with the value of Jarvis<sup>1</sup> at 2.5 MeV and the data of Grundl<sup>11</sup> (1.68 to 8.07 MeV). The data of Stein, Smith, and Smith<sup>12</sup> (1.50 to 5.00 MeV) follow the shape of our data, but they have a normalization about 4% lower than ours. The original data of Lamphere<sup>2</sup> (0.7 to 3.0 MeV) have a different shape than our data and are 5% higher from 2 to 3 MeV. Below 1.5 MeV, the Lamphere data dip below our values; however, the data of Meadows<sup>16</sup> are in general agreement with our results in this same region.

#### $^{236}\text{U}/^{235}\text{U}$ Ratio

In Fig. 4, the  $^{236}\text{U}/^{235}\text{U}$  ratio data of Lamphere<sup>2</sup> agree with our results; however, the data of Stein, Smith, and Smith<sup>12</sup> are about 4% lower than our results. The White and Warner<sup>10</sup> values (1 to 14 MeV) are also lower than our ratios.

#### $^{234}\text{U}/^{235}\text{U}$ Ratio

Our data for the  $^{234}\text{U}/^{235}\text{U}$  ratio (Fig. 5) are in good agreement with White, Hodgkinson, and Wall<sup>8</sup> at 0.127, 0.312, and 0.505 MeV, Lamphere<sup>2</sup> (0.5 to 3 MeV), Lamphere<sup>7</sup> (0.050-1.326 MeV), and White and Warner.<sup>10</sup>

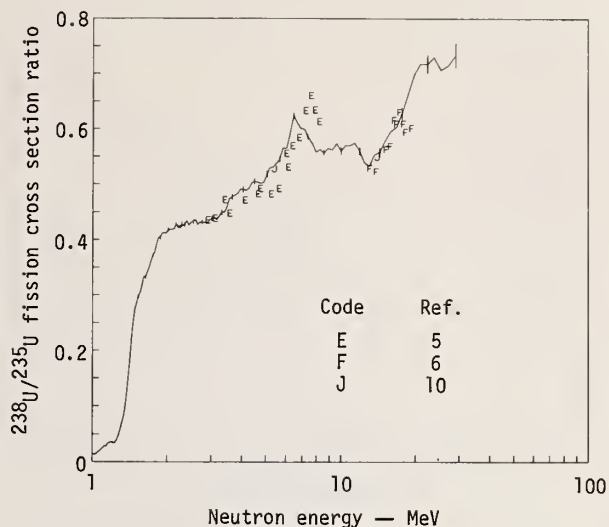


Fig. 1. Ratio of the  $^{238}\text{U}$  to  $^{235}\text{U}$  fission cross sections in the energy range 1 to 30 MeV. Present work is shown by the line that has segments connecting the individual points. Statistical error bars are shown on every fourth point.

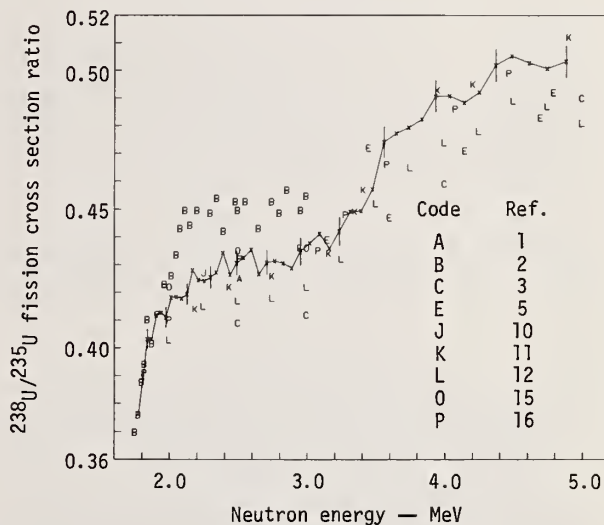


Fig. 2. Ratio of the  $^{238}\text{U}$  to  $^{235}\text{U}$  fission cross sections in the energy range 1.75 to 5.00 MeV. Present work is given by x's which are connected by line segments to guide the eye. Some of the statistical error bars are included.

#### $^{233}\text{U}/^{235}\text{U}$ Ratio

Our results (Figs. 6, 7, and 8) agree well with those of Pfletschinger and Kappeler<sup>14</sup> for the



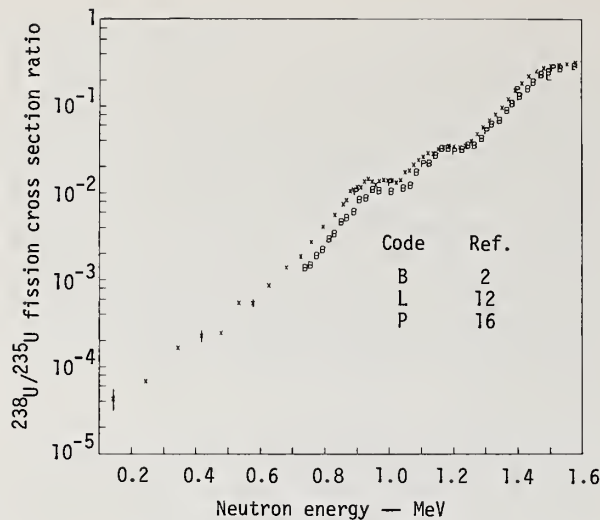


Fig. 3. Ratio of the  $^{238}\text{U}$  to  $^{235}\text{U}$  fission cross sections in the energy range 0.1 to 1.6 MeV. Present work is given by x. Some of the statistical error bars are included.

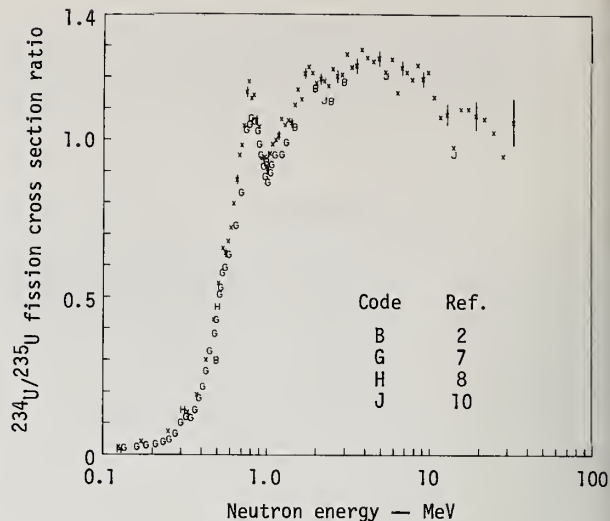


Fig. 5. Ratio of the  $^{234}\text{U}$  to  $^{235}\text{U}$  fission cross sections in the energy range 0.1 to 30 MeV. Present work is given by x. Some of the statistical error bars are included.

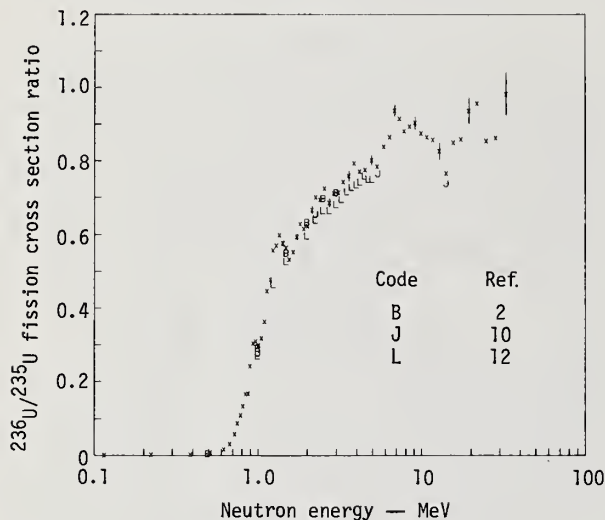


Fig. 4. Ratio of the  $^{236}\text{U}$  to  $^{235}\text{U}$  fission cross sections in the energy range 0.1 to 30 MeV. Present work is given by x. Some of the statistical error bars are included.

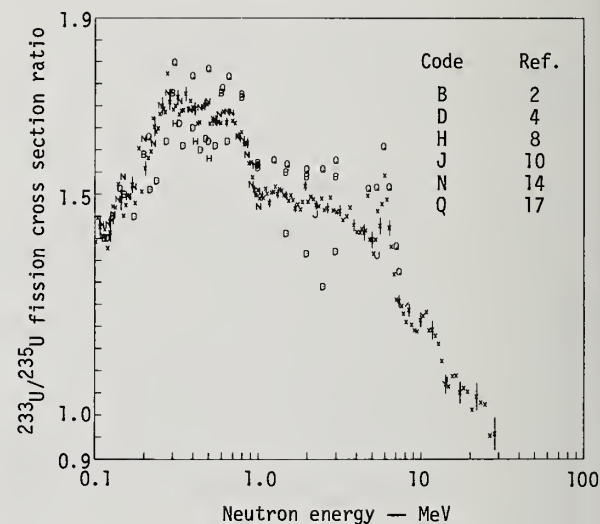


Fig. 6. Ratio of the  $^{233}\text{U}$  to  $^{235}\text{U}$  fission cross sections in the energy range 0.1 to 30 MeV. Present work is given by x. Some of the statistical error bars are included.

$^{233}\text{U} : ^{235}\text{U}$  ratios over the range of their experiment (0.005 to 1 MeV). We also agree well with White and Warner.<sup>10</sup> The results of Meadows<sup>17</sup> (0.144 to 7.1 MeV) follow the shape of our data, but have a normalization about 5% higher than ours. From 0.001 to 0.02 MeV we find structure in the ratio which, in part, is from  $^{235}\text{U}$ . It appears very difficult to get a detailed  $^{233}\text{U}$  cross section from  $^{233}\text{U} : ^{235}\text{U}$  ratio measurements in this region.

As a consistency check the  $^{233}\text{U} : ^{235}\text{U}$  ratio was also obtained by computer fitting smooth curves to our

$^{238}\text{U} : ^{235}\text{U}$  and  $^{238}\text{U} : ^{233}\text{U}$  results and forming the ratio of these smooth curves. This ratio is compared to the  $^{233}\text{U} : ^{235}\text{U}$  data in Fig. 8.

#### $^{238}\text{U} : ^{233}\text{U}$ Ratio

Our results for the  $^{238}\text{U} : ^{233}\text{U}$  ratio (Fig. 9) agree very well with those of Smith, Henkel, and Nobles.<sup>3</sup> The data of Allen and Ferguson<sup>4</sup> fall 5 to 10% lower than our values.

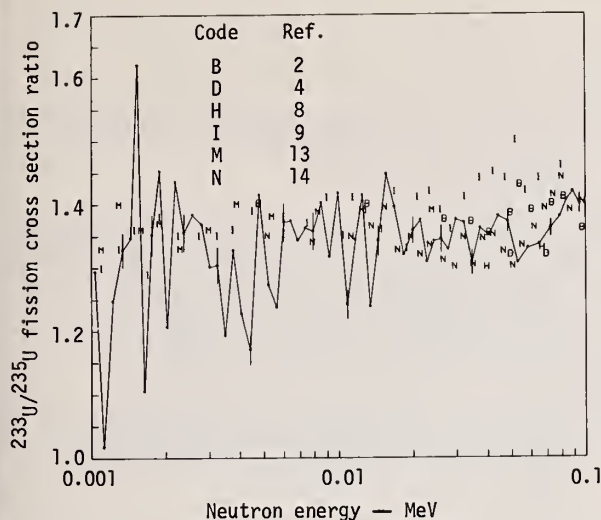


Fig. 7. Ratio of the  $^{233}\text{U}$  to  $^{235}\text{U}$  fission cross sections in the energy range 0.001 to 0.1 MeV. Present work is shown by the line of segments connecting the individual points. Statistical error bars are shown on every fourth point.

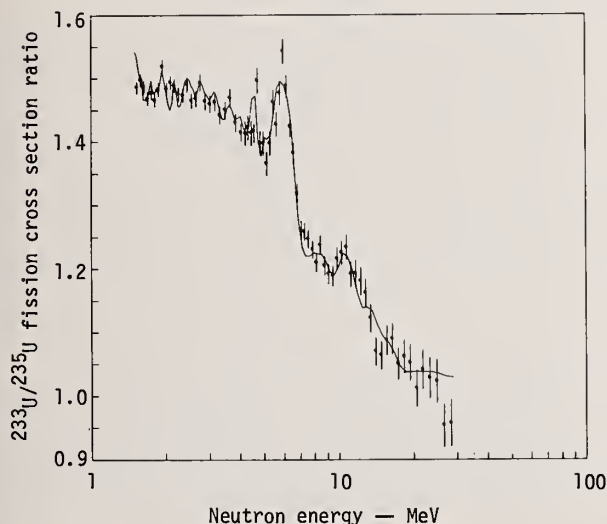


Fig. 8. Ratio of the  $^{233}\text{U}$  to  $^{235}\text{U}$  fission cross sections in the energy range 1.5 to 30 MeV. Present work is given by points. The statistical error bars are shown on each point. The line is the  $^{233}\text{U}$  to  $^{235}\text{U}$  ratio obtained by computer fitting smooth curves to our  $^{238}\text{U}$  to  $^{235}\text{U}$  results (Figs. 1 through 3) and  $^{238}\text{U}$  to  $^{233}\text{U}$  results (Fig. 9) and forming the ratio of these smooth curves.

#### Summary

Figures 1 through 9 present our results for the neutron-induced fission cross section ratios involving

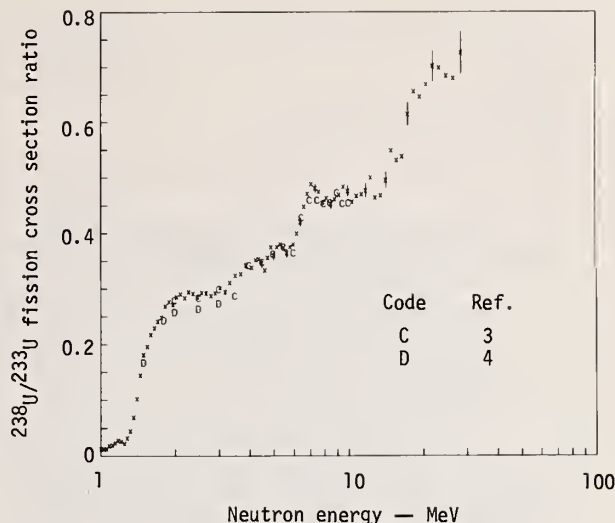


Fig. 9. Ratio of the  $^{238}\text{U}$  to  $^{233}\text{U}$  fission cross sections in the energy range 1 to 30 MeV. Present work is given by x. Some of the statistical error bars are included.

five isotopes of uranium ( $^{233}\text{U}$ ,  $^{234}\text{U}$ ,  $^{235}\text{U}$ ,  $^{236}\text{U}$ , and  $^{238}\text{U}$ ) measured continuously over a relatively wide energy range. Normalization of our ratios was obtained by applying the threshold cross section method. The comparison of our results with previous data sets demonstrates the advantage of a continuous measurement over a wide energy range in defining the cross section ratios as a function of energy.

The results presented in this paper supersede those reported in our preliminary report.<sup>19</sup> Data in tabular form will be made available upon request.

#### Acknowledgments

We wish to acknowledge the continued interest in our experiments expressed by R. L. Wagner, J. D. Anderson, and C. D. Bowman. We are indebted to E. Ables, A. Watanabe, and K. Kramer for their efforts in constructing the experimental apparatus; to J. W. Magana and J. C. Walden for handling the high purity isotopes; and to R. S. Newbury of Livermore and J. H. Capps of Los Alamos Scientific Laboratory for the mass spectrometric analyses.

#### References

1. G. A. Jarvis, Fission Comparison of  $\text{U}^{238}$  and  $\text{U}^{235}$  for 2.5 MeV Neutrons, Rept. LA-1571, Los Alamos Scientific Laboratory (1953).
2. R. W. Lamphere, Phys. Rev. **104**, 1654 (1956).
3. R. K. Smith, R. L. Henkel, and R. A. Nobles, Bull. Am. Phys. Soc. **2**, 196 (1957).
4. W. D. Allen and A. T. G. Ferguson, Proc. Phys. Soc., London, **70A**, 573 (1957).

5. S. P. Kalinin and V. M. Pankratov, in Proc. 2nd U.N. Int. Conf. on P.U.A.E., vol. 16, 1958, p. 136.
6. B. Adams, R. Batchelor, and T. S. Green, J. Nucl. Energy **14**, 85 (1961).
7. R. W. Lamphere, Nucl. Phys. **38**, 561 (1962).
8. P. H. White, J. G. Hodgkinson, and G. J. Wall, in Proc. Symp. Physics and Chemistry of Fission, Salzburg, vol. 1, 1965, p. 219.
9. R. D. Albert, Phys. Rev. **142**, 778 (1966).
10. P. H. White and G. P. Warner, J. Nucl. Energy **21**, 671 (1967).
11. J. A. Grundl, Nucl. Sci. Eng. **30**, 39 (1967).
12. W. E. Stein, R. K. Smith, and H. L. Smith, in Phys. Soc. Conf. Neutron Cross Section Techn., Washington, D.C., Rept. CONF-680307, 1968, p. 627.
13. W. K. Lehto, Nucl. Sci. Eng. **39**, 361 (1970).
14. E. Pfletschinger and F. Kappeler, Nucl. Sci. Eng. **40**, 375 (1970).
15. W. P. Poenitz and R. J. Armani, J. Nucl. Energy **26**, 483 (1972).
16. J. W. Meadows, Nucl. Sci. Eng. **49**, 310 (1972).
17. J. W. Meadows, Nucl. Sci. Eng. **54**, 317 (1974).
18. J. W. Behrens, Preparation of Fission Foils for Fission Ionization Chambers Using A Painting Technique, Rept. UCRL-51476, Lawrence Livermore Laboratory (1973).
19. J. W. Behrens and G. W. Carlson, High-Energy Measurements of Neutron-Induced Fission Cross Section Ratios Involving  $^{233}\text{U}$ ,  $^{235}\text{U}$ ,  $^{238}\text{U}$ , and  $^{239}\text{Pu}$  Using the Method of Threshold Cross Sections, Rept. UCID-16548, Lawrence Livermore Laboratory (1974, preliminary).
20. G. W. Carlson, M. O. Larson, and J. W. Behrens, Measurements of the Energy Dependence of the Efficiency of Fission Chambers, Rept. UCRL-51727, Lawrence Livermore Laboratory (1974).
21. H. T. Heaton II, J. L. Menke, R. A. Shrack, and R. B. Schwartz, Nucl. Sci. Eng. **56**, 27 (1975).
22. J. W. Behrens, Determination of Absolute Fission Cross Section Ratios Using the Method of Threshold Cross Sections, Rept. UCRL-51478, Lawrence Livermore Laboratory (1973).

#### NOTICE

"This report was prepared as an account of work sponsored by the United States Government. Neither the United States nor the United States Atomic Energy Commission, nor any of their employees, nor any of their contractors, subcontractors, or their employees, makes any warranty, express or implied, or assumes any legal liability or responsibility for the accuracy, completeness or usefulness of any information, apparatus, product or process disclosed, or represents that its use would not infringe privately-owned rights."



ON SUB-BARRIER FISSION IN  $^{238}\text{U}$   
 J. A. Wartena and H. Weigmann  
 Central Bureau for Nuclear Measurements  
 Geel, Belgium  
 and  
 E. Migneco  
 Istituto di Fisica Nucleare and INFN  
 Catania, Italy

Sub-barrier fission in  $^{238}\text{U}$  has first been observed by R. Block et al.<sup>1</sup>, using ionization chambers for fission fragment detection. In the present measurements a liquid scintillator was used to detect prompt fission neutrons. Thereby, with a sample of 250 g of  $^{238}\text{U}$ , neutron time-of-flight measurements could be performed at a 30 m flightpath with a nominal resolution of 1.3 nsec/m. The result of the present investigation is a full confirmation of the findings of Block et al.<sup>1</sup>. This includes a confirmation, by high resolution data, of the fact that the resonances at 721.0 eV and 1210.7 eV contribute most strongly to the observed fission in the two sub-barrier structures at low neutron energies. Their fission widths are found to be  $(0.85 \pm 0.13)\text{meV}$  and  $(0.25 \pm 0.05)\text{meV}$ , respectively (assuming  $\Gamma_\gamma = 23\text{ meV}$ ). For most of the other resonances in these two structures only upper limits for the fission widths are obtained.

### Introduction

Recently, R. Block et al.<sup>1</sup> reported on the detection of sub-barrier fission in  $^{238}\text{U}$ . The measurements of Block et al. were done by fission fragment detection, using an ionization chamber loaded with totally 660 mg of  $^{238}\text{U}$ . This small amount of sample material necessitated measurements at a rather short neutron flight path of 10 m, thus with only moderate neutron energy resolution.

In the present paper we report on a measurement of sub-barrier fission in  $^{238}\text{U}$  which was done with a liquid scintillator to detect prompt fission neutrons. This technique has the advantage that a sample of 250 g of  $^{238}\text{U}$  could be used and thereby the measurements could be performed at a 30 m neutron flight path with a nominal resolution of 1.3 nsec/m, corresponding to an energy resolution of 0.7 and 1.5 eV at 720 eV and 1210 eV neutron energy, respectively. On the other hand, prompt neutron detection has the disadvantage that the detector has a sensitivity for capture events of  $\sim 10^{-3}$  of its fission sensitivity. Thus one is encountered with a large background from capture and a lower limit of  $\sim 20\text{ }\mu\text{eV}$  is set for the determination of fission widths.

The purpose of the present measurement was 1) to confirm the existence of sub-barrier fission in  $^{238}\text{U}$  and 2) to check, by a high resolution measurement, the identification made by Block et al., of the 721.0 eV and 1210.7 eV resonances as those which contribute most strongly to the observed fission in the two sub-barrier structures at low neutron energies.

### Experimental Details

Some of the experimental parameters have already been mentioned. The liquid scintillator detector has been described earlier<sup>2</sup>. The sample was a 250 g disk of metallic U depleted to 0.2%  $^{235}\text{U}$ .

There were two main sources of background: The more important one is due to capture in  $^{238}\text{U}$  as mentioned above. It has been measured separately by taking a time-of-flight spectrum under conditions identical to the main run but with the pulse shape discriminators of the detectors set to detect capture. The second source of background is fission in the  $^{235}\text{U}$  present in the sample. Again, this background has been measured separately with a  $^{235}\text{U}$  sample in the beam.

Normalization of the observed fission yield has

been done by comparison to the yield obtained from low energy resonances (8 eV to 32 eV) in  $^{235}\text{U}$ .

### Results

The present measurements covered the neutron energy range from 5 eV to 5 keV.

Fig. 1 shows a spectrum of the fission yield as a function of neutron energy between 650 and 1300 eV. The two background contributions discussed above have already been subtracted. The two strong fission resonances at 721.0 eV and 1210.7 eV are clearly visible and a few minor resonances are also indicated.

A resonance analysis which takes into account resonance self-shielding as well as multiple scattering effects, has yielded fission widths of the strongest resonances and upper limits for the fission widths of weaker resonances. They are listed in table 1 together with the respective fission areas  $A_f$  (or their upper limits) for known s-wave resonances in two neutron energy intervals around 720 eV and 1210 eV. Resonances which have definitely been assigned as p-waves<sup>3</sup> are not included in table 1 because they would not belong to the same doorway structure to which the s-wave resonances belong. The fission widths of the two main resonances at 721.0 eV and 1210.7 eV have been obtained under the assumption that  $\Gamma_\gamma = 23\text{ meV}$ . That would be correct in a weak coupling situation ( $\Gamma^\downarrow \ll \Gamma^\uparrow$ ) but in an intermediate coupling situation ( $\Gamma^\downarrow \gg \Gamma^\uparrow$ ) one expects  $\Gamma_\gamma$  of the main resonances to be smaller: If, e.g., these resonances would be  $\approx 70\%$  class II, with  $\Gamma_\gamma(\text{II}) \approx 4\text{ meV}$ , one would have  $\Gamma_\gamma \approx 9\text{ meV}$  and their fission widths would be about  $360\text{ }\mu\text{eV}$  and  $130\text{ }\mu\text{eV}$ , respectively.

As seen from the table, by far the largest contribution to the total fission areas of the two sub-barrier fission structures is due to the resonances at 721.0 eV and 1210.7 eV. For the first structure it is also obvious that the 721.0 eV resonance has by far the largest fission width. For the 1210.7 eV resonance the same is, with respect to the second structure, not entirely certain but rather probable, too. The last column of table 1 gives for both sub-barrier structures, the upper limit for the quantity  $\Sigma \Gamma_{\text{f}}^\downarrow$ . This quantity is of interest as it is related  $\mu_{\text{uf}}$  to the penetrability of the higher (more exactly, the less penetrable) one of the two fission barriers, where again the question of relative barrier heights is linked to the question of coupling conditions.

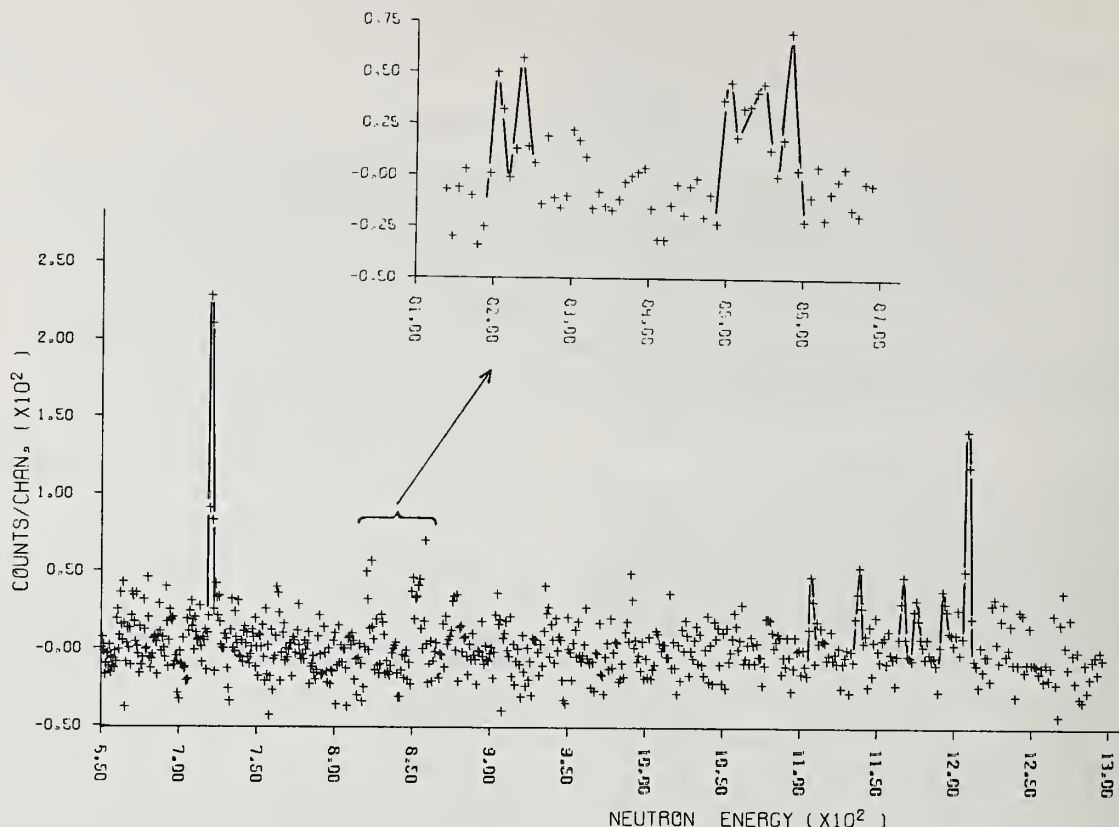


Table 1: Fission widths of known s-wave resonances in the two sub-barrier fission structures

$E_{\text{res}}$ (eV)	$A_f = 2\pi^2 \chi^2 \frac{g\Gamma_n \Gamma_f}{\Gamma}$ ( $10^{-3}$ b.eV)	$\Gamma_f$ ( $\mu\text{eV}$ )	$\Sigma \Gamma_{\mu f}$ ( $\mu\text{eV}$ )
660.7	< 130	< 25	< 1420
692.4	< 110	< 30	
707.8	< 70	< 25	
721.0	$260 \pm 40$	$850 \pm 130$	
729.7	< 30	< 120	
755.6	< 25	< 200	< 1070
764.3	< 50	< 40	
1108.9	$50 \pm 20$	$24 \pm 10$	
1139.5	$130 \pm 50$	$40 \pm 15$	
1159.2	< 20	< 100	
1167.0	$70 \pm 40$	$25 \pm 15$	
1176.5	$60 \pm 30$	$23 \pm 12$	
1194.1	$70 \pm 30$	$25 \pm 12$	
1210.7	$200 \pm 40$	$250 \pm 50$	
1232.6	< 30	< 400	
1244.0	< 60	< 20	
1266.5	< 35	< 20	
1272.2	< 50	< 30	

The situation with respect to this question is not entirely clear. The smallness of the neutron widths of the 721.0 eV and 1210.7 eV resonances might be looked at as suggesting an intermediate coupling situation, however capture  $\gamma$ -ray measurements<sup>4</sup> are in contra-

diction with such an assumption. A more complete discussion of these questions may be found in ref.<sup>4</sup>.

Finally, also in agreement with the data of Block et al.<sup>1</sup>, besides of the two structures around 720 and 1210 eV, some fission is observed around 820 and 850 eV neutron energy (see fig. 1). However, part of this fission strength seems to be not concentrated at energies of known s-wave resonances in <sup>238</sup>U, although the present data are not sufficiently accurate to make any firm statement with respect to this point. No resonance analysis has been attempted in this neutron energy region. No further appreciable fission strength has been found in the energy range covered by the present experiment.

#### References

1. R. C. Block, R. W. Hockenbury, R. E. Slovacek, E. B. Bean, and D. S. Cramer, Phys. Rev. Lett. **31** (1973) 247.
2. M. G. Cao, E. Migneco, J. P. Theobald, J. A. Wartena and J. Winter, Journ. Nucl. Energy **22** (1968) 211.
3. F. Corvi, G. Rohr and H. Weigmann, contributed paper to this conference.
4. H. Weigmann, G. Rohr, T. van der Veen and G. Vanpraet, Proc. 2<sup>nd</sup> Intern. Sympos. on Neutron Capture Gamma Ray Spectroscopy and Related Topics, Petten (N. H.), 1974, paper nr. 18.



# CAPTURE-TO-FISSION RATIO OF $^{235}\text{U}$ FROM THE MEASUREMENT OF LOW-ENERGY $\gamma$ -RAYS

F. Corvi and P. Giacobbe

Central Bureau for Nuclear Measurements

2440 Geel, Belgium

and

Comitato Nazionale per l'Energia Nucleare

Bologna, Italy

A new technique of  $\alpha$ -determination is presented, consisting of measuring with a Ge(Li)-detector low-energy  $\gamma$ -ray spectra following neutron absorption in  $^{235}\text{U}$ , as a function of neutron energy. A relative value of  $\alpha$  can then be deduced assuming that the intensity of a given capture (fission)  $\gamma$ -ray is proportional to the average capture (fission) cross-section. Such an assumption is thoroughly discussed in the text. More specifically,  $\alpha$  was taken proportional to the ratio between the intensity of the 642 keV capture transition and those of the fission  $\gamma$ -rays at 352 keV and 1280 keV. Average  $\alpha$ -values with statistical errors less or equal to  $\pm 5\%$  were determined for 20 intervals in the range 86 eV - 31.6 keV.

(NUCLEAR REACTIONS  $^{235}\text{U}(n, f)$  and  $^{235}\text{U}(n, \gamma)$ ,  $E = 86 \text{ eV} - 31.6 \text{ keV}$ ; measured capture-to-fission ratio. Enriched target).

## Outline of the Method

Relatively few direct measurements of the capture  $^{1-3}$  cross-section of  $^{235}\text{U}$  or alternatively of its capture-to-fission ratio  $^{4,5}$   $\alpha$  have been performed in the eV to keV region: this is due to the inherent difficulty of measuring the capture rate in a fissile nucleus due to contamination of fission  $\gamma$ -rays. In order to develop a completely new method of  $\alpha$ -determination, we measured the low-energy  $\gamma$ -ray spectra from neutron absorption in  $^{235}\text{U}$  as a function of neutron energy, with a high resolution Ge(Li)-detector. In such spectra, very few lines belong to the low-energy part of the  $\gamma$ -cascade following neutron capture while the great majority comes from the  $\gamma$ -decay of fission fragments. If one assumes that the intensities of the formers are proportional to the average capture rate and those of the latter to the average fission rate, then  $\alpha$  can be evaluated from the ratio of the intensity of a capture line to that of a fission line. Complete discrimination between capture and fission is thus achieved by the amplitude analysis. The new method was applied to the determination of  $\alpha$  of  $^{235}\text{U}$  in twenty neutron energy intervals selected by time of flight in the range 86 eV - 31.6 keV. The experiment was carried out at the 90 MeV Geel electron linac.

From a  $\gamma$ -ray spectrum corresponding to a given neutron energy interval  $\Delta E$ , one can deduce the ratio  $R$  between the peak area  $A_c$  of a capture line to the area  $A_f$  of a fission line. In the thin sample approximation  $R$  can be written:

$$R = \frac{A_c}{A_f} = \frac{\epsilon_c P_c}{\epsilon_f P_f} \frac{\int_{\Delta E} \sigma_\gamma(E) \Phi(E) dE}{\int_{\Delta E} \sigma_f(E) \Phi(E) dE} \quad (1)$$

$$= \frac{\epsilon_c P_c}{\epsilon_f P_f} \alpha^*$$

where  $\epsilon_c$  and  $\epsilon_f$  are the photo-peak efficiencies of the two  $\gamma$ -rays,  $P_c$  and  $P_f$  are the average intensities of the capture and fission line per capture and fission event respectively, and  $\Phi(E)$  is the neutron flux. It must be stressed that the quantity  $\alpha^*$  defined in (1) is not exactly the capture-to-fission ratio but rather the ratio of the integrated capture and fission cross section weighted over the neutron flux. Since the moderated neutron source used in this experiment had a flux  $\Phi(E) \sim E^{-0.90}$ , the quantity  $\alpha^*$  can be written:

$$\alpha^* = \frac{\int_{\Delta E} \sigma_\gamma(E) \cdot E^{-0.90} dE}{\int_{\Delta E} \sigma_f(E) \cdot E^{-0.90} dE} \quad (2)$$

It follows from (1) that  $R$  provides a relative measurement of  $\alpha^*$  as long as  $P_c/P_f$  can be considered constant as a function of neutron energy. As far as the constancy of  $P_c$  is concerned, it has been shown  $^{6-8}$  that the population of the low-lying states following neutron capture, and hence the intensity of the  $\gamma$ -transitions de-exciting them, depends considerably on the spin and parity of the initial capture state. As compound states of different  $J$  and  $\pi$  are formed, the value of  $P_c$  depends on the actual contribution to the capture rate of each spin and parity in the given energy interval:

$$P_c = \frac{\sum_{J, \pi} P_c(J, \pi) < \sigma_\gamma(J, \pi) >^*}{\sum_{J, \pi} < \sigma_\gamma(J, \pi) >^*} \quad (3)$$

where the  $< \sigma_\gamma >^*$  are similar to the numerator of the right-hand side of eq. (2), i. e. they are integrated partial capture cross-sections weighted over the neutron flux. Obviously, the sum is limited to those  $J, \pi$  values reachable by s-wave or p-wave neutron absorption in  $^{235}\text{U}$ . These values are:  $J^\pi = 3^-, 4^-$  for s-waves and  $J^\pi = 2^+, 3^+, 4^+, 5^+$  for p-waves.

The reasons which can affect the constancy of  $P_c$  against neutron energy are threefold:

- a) the limited number of resonances in a given interval: the relative values of  $< \sigma_\gamma(J, \pi) >^*$  may vary, due to statistical fluctuations in the number of resonances of given spin and parity as well as in their neutron and fission widths.
- b) possible non-statistical variations of  $< \Gamma_f(J, \pi) >$  due to intermediate structure effects in the fission cross-section  $^{9,10}$  of  $^{235}\text{U}$ , may also influence  $< \sigma_\gamma(J, \pi) >^*$  and eventually the  $P_c$  value.
- c) the p-wave contribution to the sum of eq. (3) increases with energy going from a negligible amount in the eV region up to a value comparable to the s-wave capture at 30 keV.

All such causes of uncertainty in the interpretation of the results will be discussed in detail in the third section.



As regard to  $P_f$ , it is first of all important to notice that the  $\gamma$ -rays of interest here belong obviously to fission fragments of high yield, i. e. those produced in asymmetric fission. Now, there is no evidence that the yields of such fragments vary appreciably with quantum numbers or with neutron energy, at least in the eV to keV range. In any case, possible variations of  $P_f$  should be small<sup>11</sup> and should be considered a minor effect as compared to the well-established and important changes of  $P_c(J, \pi)$  with the spin. For this reason, we will neglect them in the following discussion.

#### Experiment and Data Analysis

The measurements were performed on a 30 m flight path. The sample was a 12 cm metallic uranium disc containing  $^{235}\text{U}$  enriched to 93.1%. Its thickness was  $7.8 \cdot 10^{-4}$  atoms of  $^{235}\text{U}$ /barn, so that the thin-sample hypothesis is justified in almost all of the considered energy range. Gamma rays in the range 246 - 1513 keV were detected with a 70 cm<sup>3</sup> coaxial Ge(Li) detector. Apart from a  $^{10}\text{B}$  filter absorbing slow neutrons from previous cycles, also black-resonance filters of Co and Na were continuously kept in the neutron beam, in order to monitor the background at different time of flights. The effective relative energy resolution  $\Delta E/E$  varied from about 0.003 at low energy up to 0.01 at 30 keV. The widths of the neutron energy intervals were chosen so as to yield statistical errors of the ratios  $R$  smaller or equal to 5%. The bidimensional recording system used is briefly described in ref. 12. The lowest energy part of the spectrum corresponding to the neutron energy interval 200 - 300 eV is plotted in fig. 1: the  $\gamma$ -ray at 642 keV is the well-known capture transition de-exciting the 687 keV state of  $^{236}\text{U}$ . As a matter of fact, this is the only capture line which is resolved and strong enough to be measurable in the whole neutron energy range analysed. On the other hand, the two  $\gamma$ -rays at 352.3 keV and 1279.8 keV were selected in order to give a measure of the fission counting rate: such transitions which probably correspond to  $\gamma$ -decay of isomeric states belonging to  $^{100}\text{Zr}$  and  $^{134}\text{Te}$  fis-

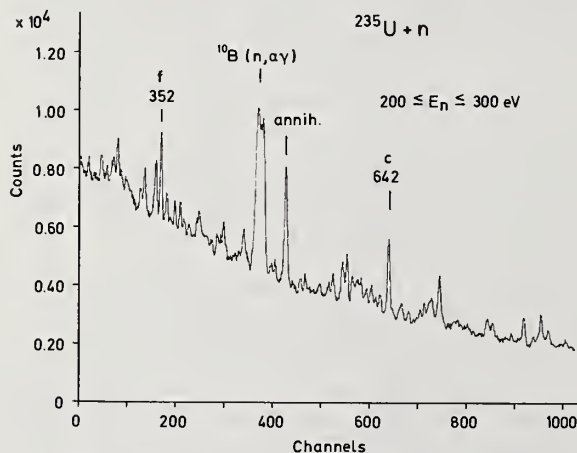


Fig. 1: Spectrum of  $\gamma$ -rays in the range 246 - 880 keV corresponding to the neutron energy interval 200 - 300 eV. Two out of three  $\gamma$ -rays used for  $\alpha$ -determination are indicated.

sion fragments<sup>13</sup> have half-lives equal to 21 ns and 164 ns, respectively<sup>14</sup>. Since the shortest time-of-flight interval considered was 0.625  $\mu\text{s}$ , no correction was necessary for the 21 ns  $\gamma$ -ray; for the other line, a time shift of the same magnitude as the half life was taken into account in order to compensate approximately for the delay.

The peak areas were evaluated by fitting the spectra with the GAFIT computer code<sup>12</sup> in suitable ranges around the  $\gamma$ -rays of interest: examples of such fits are given in fig. 2, where vertical bars indicate all peaks which had to be introduced in order to obtain a satisfactory fit. The background was measured at about 2.85 keV, 0.132 keV and in the region 2.86 - 0.88 eV: background corrections were found negligible for the two fission  $\gamma$ -rays. On the contrary, the capture transition had to be corrected from overlapping with the 641.3 keV  $\gamma$ -ray following  $\beta$ -decay of the fission product  $^{142}\text{La}$  with  $t_{1/2} = 92.5$ .<sup>5</sup> The relative contribution of such  $\gamma$ -ray, which is obviously constant with time of flight, reached a maximum value of 12% in the lower neutron energy region.

Finally, it was verified that the ratio between the intensities of the two fission  $\gamma$ -rays is constant over the whole energy range considered: their peak areas were then summed in order to reduce the final statistical errors.

#### Systematic Errors and Corrections

As already pointed out in the first section, the change of  $P_c$  of eq. (3) with neutron energy may come from two sources: fluctuations of the ratio  $x = \langle \sigma_{\gamma}(4^-) \rangle / \langle \sigma_{\gamma}(3^-) \rangle$  between the two average partial capture cross-sections of s-wave interaction; increase of p-wave contribution with energy. Change of  $x = \langle \sigma_{\gamma}(4^-) \rangle / \langle \sigma_{\gamma}(3^-) \rangle$ . Neglecting p-wave interaction and the weighting over the neutron flux, eq. (3) can be written:

$$P_c(l=0) = \frac{P_c(3^-) \langle \sigma_{\gamma}(3^-) \rangle + P_c(4^-) \langle \sigma_{\gamma}(4^-) \rangle}{\langle \sigma_{\gamma}(3^-) \rangle + \langle \sigma_{\gamma}(4^-) \rangle} =$$

$$= P_c(3^-) \frac{1 + \beta x}{1 + x} \quad (4)$$

where  $\beta = P_c(4^-) / P_c(3^-)$

In the absence of any experimental information, the ratio  $\beta$  was deduced from a Monte Carlo simulation of the  $\gamma$ -ray cascade<sup>8</sup>, using the  $^{236}\text{U}$  level scheme given by Ottmar et al.<sup>15</sup>. The result is  $\beta = 0.64 \pm 0.07$ . For  $x$  values not far from unity, it follows then from eq. (4):

$$\frac{\Delta P_c(l=0)}{P_c(l=0)} \approx -0.1 \frac{\Delta x}{x} \quad (5)$$

One may then conclude that  $P$  is relatively insensitive to changes in the cross-section ratio  $x$ . One reason for the non-constancy of  $x$  is the limited number of resonances in a given interval: the magnitude of such an effect can be calculated if one knows the resonance spacing, the average neutron, gamma and fission widths and their distribution. The relative error in  $P_c$  coming from this source was found to be about 3% for  $\Delta E = 100$  eV intervals and less than 1% for intervals above 3 keV. Because of its statistical origin, this error was composed quadratically with that due to counting statistics.

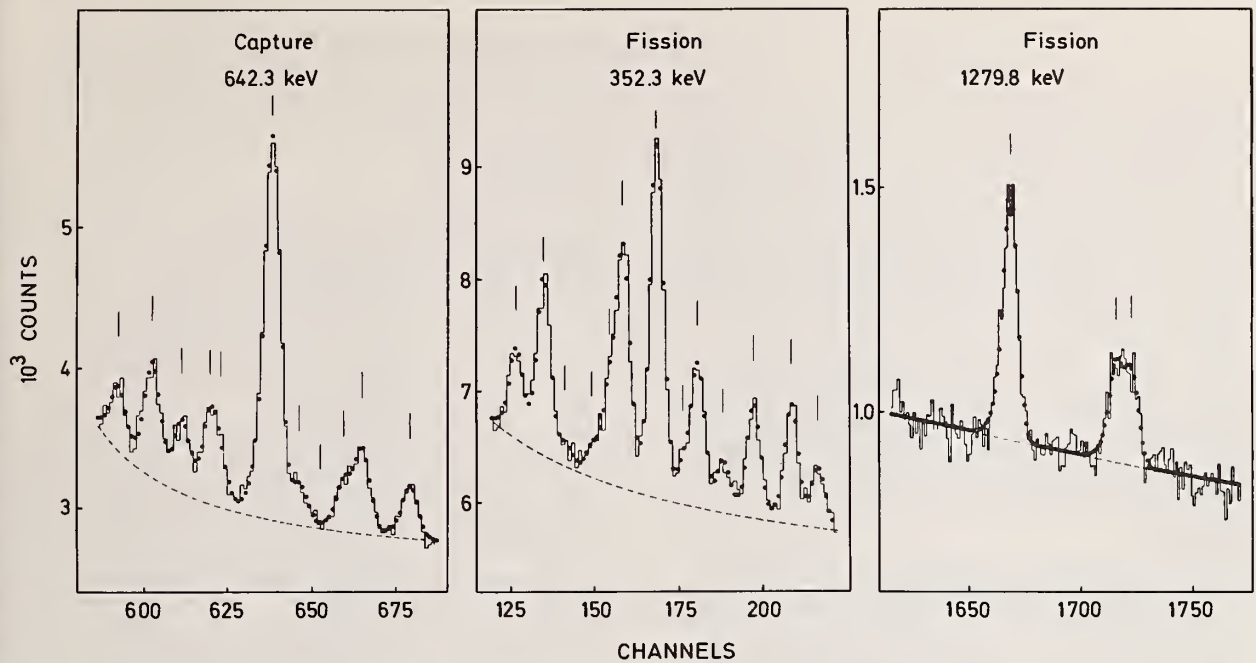


Fig. 2: Examples of fits of the three peaks of interest, taken from the spectrum corresponding to the interval 200 - 300 eV. The fit is represented by dots.

Concerning possible fluctuations of  $x$  due to intermediate structure in the fission cross-section of  $^{235}\text{U}$  as reported in refs. 9 and 10, the effect is not known enough to allow to fix an upper limit for the possible systematic error involved. It seems however that such a structure has a width considerably smaller than the intervals chosen in the present work above 3.5 keV. In fact, the value of  $x$  above such an energy is remarkably constant, as shown in fig. 3, suggesting that an averaging over a possible structure has already taken place in each interval. In view of this, and of eq. (5), the change in  $P_c$  due to such an effect should be negligible, at least above 3.5 keV.

Correction for p-wave capture. Eq. (1) can be written

$$\alpha^*(E) = \frac{\epsilon_f P_f}{\epsilon_c P_c(l=0)} \frac{R(E)}{f_p(E)} \quad (6)$$

where  $f_p(E)$  is the p-wave correction defined by:

$$f_p = 1 - \frac{1 - P_c(l=1) / P_c(l=0)}{1 + \langle \sigma_\gamma(l=0) \rangle / \langle \sigma_\gamma(l=1) \rangle} \quad (7)$$

Here also the weighting over the neutron flux is neglected by replacing  $\langle \sigma \rangle^*$  with  $\langle \sigma_\gamma \rangle$ . The quantity  $f_p$  can be evaluated by Monte Carlo simulation of the  $\gamma$ -cascade and by the knowledge of the different partial cross-sections contributing to p-wave capture. Some quantities such as the average fission widths for  $J^\pi = 2^+, 3^+, 4^+, 5^+$  are not known experimentally and they had to be estimated from the corresponding s-wave values and the knowledge of the energy positions of the saddle point transition states of same spin and parity 16.

The calculated correction is only  $\pm 2\%$  at 30 keV in spite of the fact that p-wave capture at such an energy contributes more than 1/3 of the total capture rate. However, in view of the large uncertainties in the parameters used in the calculation, the estimated error

is larger than the correction, being  $\pm 4\%$  in the upper energy interval and less than  $\pm 2\%$  below 10 keV. This contribution to the error was simply added to the statistical error because of its systematic character.

### Results

Absolute  $\alpha^*$  values can in principle be obtained from the experimental  $R$  values of eq. (1) if one knows the quantity  $K = \epsilon_c P_c / \epsilon_f P_f$ : unfortunately, neither  $P_c$  nor  $P_f$  are known with sufficient precision to yield reliable capture-to-fission ratios. Another possibility would be to derive  $K(J, \pi)$  from the measurement of  $R(E_0)$  in isolated resonances of known spin:

$$K(J, \pi) = \frac{\Gamma_f(E_0)}{\Gamma_\gamma(E_0)} R(E_0) \quad (8)$$

Knowledge of  $K(3^-)$ ,  $K(4^-)$  and of  $\langle \sigma_\gamma(3^-) \rangle$ ,  $\langle \sigma_\gamma(4^-) \rangle$ , would yield the  $K$  value to be used in the average region. This procedure meets with the following difficulties: the  $\Gamma_f(E_0)$  values given by different evaluations of  $^{235}\text{U}$  resonance parameters 17, 18 disagree considerably; moreover, the average capture cross-sections per spin state are not precisely known. In view of all this, it was simply decided to normalize the present results to the average  $\alpha$ -value of Perez et al. 3 in the range 200 - 1000 eV. The final data and associated errors are listed in the first two columns of table 1 and displayed in fig. 3, together with the results of ref. 3. Below 1 keV, there is an excellent agreement between the two sets of data. In the third column of table 1 are listed values of the average capture cross-section obtained from the present data (assuming  $\alpha^* = \langle \sigma_\gamma(E) \rangle / \langle \sigma_f(E) \rangle$ ) and from the fission integrals given by Perez et al. 3 below 1 keV and by Wagemans 19 above 1 keV. The errors were calculated by composing those of  $\alpha^*$  with a 3% estimated uncertainty in the case of ref. 3 and a 5% uncertainty in the case of ref. 19.



## Conclusions

High resolution  $\gamma$ -ray spectroscopy provides an elegant way of discriminating between capture and fission reactions. Moreover, the selective nature of this technique drastically reduces the background produced by neutron interactions in materials other than the  $^{235}\text{U}$  foil. In spite of the inherent low detector efficiency, the measurement yielded reasonable statistical errors up to 30 keV. A critical and detailed investigation of the degree of confidence of the assumptions on which the method is based, resulted in a surprisingly small correction for the p-wave contribution. The main drawback of the method consists in the difficulty of normalizing the results in the resonance region or at thermal. In spite of its relative nature, the measurement can be of use because the energy region investigated has a considerable overlapping with that covered in Van de Graaff experiments.

## References

1. Van Shi-Di et al., Proc. Symp. Physics and Chemistry of Fission, Salzburg, p. 287, IAEA, Vienna (1965).
2. G. de Saussure et al., ORNL-TM-1804 (1967).
3. R. B. Perez et al., Nucl. Sci. Engn., **52** (1973) 46.
4. J. B. Czirr and J. S. Lindsey, Proc. Int. Conf. Nuclear Data for Reactors, **I**, 331, IAEA, Vienna (1970).
5. M. A. Kurov et al., Atomnaya Energiya, **30** (1971) 258.
6. W. P. Pönitz, Z. Physik **197** (1966) 262.
7. K. J. Wetzel and G. E. Thomas, Phys. Rev. **C1** (1970) 1501.
8. C. Coceva, P. Giacobbe, F. Corvi and M. Stefanon, Nucl. Phys. **A218** (1974) 61.
9. R. B. Perez et al., Nucl. Sci. Engn. **55** (1974) 203.
10. E. Migneco et al., Intermediate Structure in the keV Fission Cross Section of  $^{235}\text{U}$ , this Conference.
11. P. Popa et al., Nucl. Sci. Engn. **39** (1970) 50.
12. F. Corvi, M. Stefanon, C. Coceva and P. Giacobbe, Nucl. Phys. **A203** (1973) 145.
13. F. Horsch, Proc. Int. Conf. on Properties of Nuclei far from the region of  $\beta$ -Stability, Geneva CERN 70-30, Vol. 2 (1970) 917.
14. W. John et al., Phys. Rev. **C2** (1970) 1451.
15. H. Ottmar, P. Matussek and I. Piper, Proc. Second Int. Symp. on Neutron Capture Gamma Ray Spectroscopy, Petten (1974) p. 417.
16. J. E. Lynn, The Theory of Neutron Resonance Reactions, Clarendon Press, Oxford (1968).
17. J. Krebs, G. Le Coq, J. P. L'Heriteau and P. Ribon, Proc. Third Conf. on Neutron Cross Sections and Technology, Knoxville, Vol. 1 (1971) p. 410.
18. G. de Saussure, R. B. Perez and W. Kolar, ORNL-TM-3707 (1972).
19. C. Wagemans, private communication.

Table 1: Values of  $\alpha^*$  in the range 0.086 - 31.6 keV. In the third column are listed values of  $\langle \sigma_{\gamma}(E) \rangle$  calculated from the present capture-to-fission ratios and the fission integrals of refs. <sup>3</sup> and 19.

Energy Interval (keV)	$\alpha^*$	$\langle \sigma_{\gamma}(E) \rangle$ (barns)
0.086 - 0.114	0.694 $\pm$ 0.044	
0.15 - 0.2	0.497 $\pm$ 0.025	
0.2 - 0.3	0.417 $\pm$ 0.017	8.72 $\pm$ 0.41
0.3 - 0.4	0.471 $\pm$ 0.020	6.28 $\pm$ 0.33
0.4 - 0.5	0.343 $\pm$ 0.017	4.78 $\pm$ 0.28
0.5 - 0.6	0.284 $\pm$ 0.015	4.42 $\pm$ 0.27
0.6 - 0.7	0.389 $\pm$ 0.021	4.56 $\pm$ 0.28
0.7 - 0.8	0.406 $\pm$ 0.022	4.58 $\pm$ 0.28
0.8 - 0.9	0.510 $\pm$ 0.032	4.24 $\pm$ 0.29
0.9 - 1.0	0.621 $\pm$ 0.039	4.76 $\pm$ 0.33
1.0 - 1.24	0.460 $\pm$ 0.020	3.81 $\pm$ 0.25
1.24 - 1.45	0.341 $\pm$ 0.018	2.54 $\pm$ 0.18
1.45 - 1.86	0.410 $\pm$ 0.022	2.51 $\pm$ 0.18
1.86 - 2.51	0.453 $\pm$ 0.024	2.49 $\pm$ 0.18
3.46 - 4.64	0.389 $\pm$ 0.026	1.74 $\pm$ 0.15
4.64 - 6.78	0.372 $\pm$ 0.025	1.27 $\pm$ 0.11
6.78 - 10.1	0.401 $\pm$ 0.024	1.21 $\pm$ 0.09
10.1 - 14.8	0.400 $\pm$ 0.028	1.03 $\pm$ 0.09
14.8 - 21.8	0.375 $\pm$ 0.029	0.83 $\pm$ 0.09
21.8 - 31.6	0.399 $\pm$ 0.037	0.84 $\pm$ 0.09

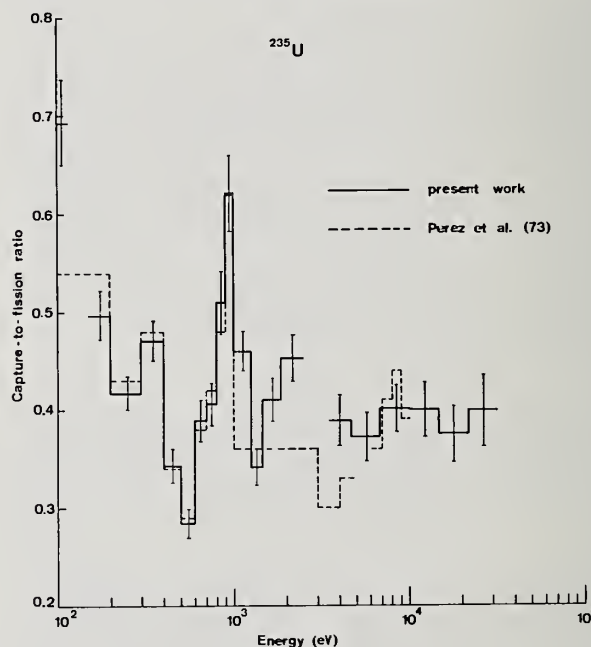


Fig. 3: Comparison between the capture-to-fission ratios of the present work and those of ref. 3. Vertical bars represent our total errors.



THE  $^{241}\text{Pu}$  NEUTRON INDUCED FISSION CROSS SECTION FROM 0.01 eV to 50 eV  
AND ITS NORMALIZATION

C. Wagemans<sup>+</sup>  
S. C. K. / C. E. N.  
2400 Mol, Belgium  
A. J. Deruytter<sup>++</sup>  
Central Bureau for Nuclear Measurements  
2440 Geel, Belgium

The neutron induced fission cross-section of  $^{241}\text{Pu}$  has been measured at an 8 m flightpath of the CBNM Linac (from 50 eV to below thermal energy) with respect to the  $^{10}\text{B}(n, \alpha)^7\text{Li}$  cross-section. Several fission integrals were calculated as well as the 20.44°C Westcott factor  $g_f = 1.046 \pm 0.006$ . Special attention is given to normalization problems.

( $^{241}\text{Pu}$  fission cross-section, normalization, Westcott  $g_f$ -factor)

### Introduction

Although the neutron induced fission cross-section of  $^{241}\text{Pu}$  is needed for the calculation of the reactivity and the Doppler coefficient of nuclear reactors containing highly irradiated fuel, only few measurements of this quantity are available until now. Moreover in the eV-region discrepancies up to about 40 percent exist between the different measurements. Also in the energy region below 1 eV the situation remains rather confused since there are no very precise  $\sigma_f$ -data available, which strongly influences the accuracy of the normalization of  $\sigma_f$  as well as the precision of the Westcott  $g_f$ -factor<sup>1</sup>.

For these reasons a remeasurement of the fission cross-section of  $^{241}\text{Pu}$  in the neutron energy region from 0.01 eV to 50 eV, with special attention to normalization problems was fully justified. These measurements were performed under conditions similar to those of our previous  $\sigma_f$ -measurements of  $^{233}\text{U}$ ,  $^{235}\text{U}$  and  $^{239}\text{Pu}$ , i. e. by a direct comparison of the fission rate and the  $^{10}\text{B}(n, \alpha)$  rate of a back-to-back  $^{241}\text{Pu}$ - $^{10}\text{B}$  foil using the  $1/v$ -behaviour of the  $^{10}\text{B}(n, \alpha)^7\text{Li}$  reaction cross-section 2, 3, 4.

### Apparatus

The measurements were performed at an 8 m flightpath of the CBNM-Linac. Fast neutrons produced by bombarding a mercury-cooled uranium target with the 70 MeV electron beam were slowed down by two 4 cm thick polyethylene slabs placed above and below the target. Furthermore concentric lead rings were mounted around the target to reduce the  $\gamma$ -ray flash and the contribution of the very fast neutrons to the spectrum.

The collimation system and the experimental arrangements were already described 2, 3. The fission fragments as well as the  $^{10}\text{B}(n, \alpha)$ -particles were detected by Au-Si surface barrier detectors placed outside the neutron beam. After amplification and discrimination fast signals produced by the  $^{10}\text{B}(n, \alpha)^7\text{Li}$  and  $^{241}\text{Pu}(n, f)$  reactions were fed into two halves of a 4096-channel time-of-flight analyser, which is linked to an IBM 1800 computer.

### Measurements

Two series of measurements of the fission cross-section were performed with a large region of overlap for the cross-normalization.

<sup>+</sup> NFWO, University of Gent and SCK/CEN, Mol

<sup>++</sup> Present address: INW, University of Gent, Belgium

1. In the first series we went down from 20 eV to 0.01 eV in order to normalize our measurements to the 2200 m/s reference cross-section. Large burst widths ( $\approx 1 \mu\text{sec}$ ) were used to obtain a sufficiently high counting rate with the low repetition frequencies needed to avoid overlapping of successive bursts.
2. In the second series we wanted a better resolution; so burst widths of 20 ns were used. Here we covered the energy region from 0.15 eV to 50 eV.

Background laws were established by means of black resonance neutron filters.

The  $^{10}\text{B}$  deposit is an elemental boron layer prepared by evaporation in vacuum. Its thickness is  $104 \mu\text{g}/\text{cm}^2$  with an isotopic enrichment of 92%. The  $^{241}\text{Pu}$  layer ( $1.08 \text{ mg}/\text{cm}^2$ ) was prepared at CBNM by the electro-spraying of plutoniumacetate on a 0.2 mm thick aluminium disk. The isotopic composition of the plutonium at the moment of the electro-spraying was:

$^{238}\text{Pu}$	0.011 atom%
$^{239}\text{Pu}$	1.046 atom%
$^{240}\text{Pu}$	3.657 atom%
$^{241}\text{Pu}$	93.432 atom%
$^{242}\text{Pu}$	1.854 atom%

### Results and Discussion

The treatment of data has been done in the same way as described in 2. The relative fission cross-section curve obtained from the first series of measurements was normalized to  $\sigma_f^0(0.0253 \text{ eV}) = 1019 \pm 8 \text{ barn}$ <sup>5</sup> via a linear least squares fit of  $\sigma_f \sqrt{E}$  from 0.02481 eV to 0.02586 eV. The fission cross-section curve obtained from the second series of measurements is normalized to the fission integral from 3 eV to 12 eV obtained from the first series. Figure 1 shows the fission cross-section from 3 to 20 eV obtained in this way (uncorrected for  $^{239}\text{Pu}$ ). The fission cross-section in the energy region below 1 eV (corrected for the  $^{239}\text{Pu}$  contribution) is shown in figure 2.

Based on these data the Westcott  $g_f$ -factor was calculated, which yielded <sup>6</sup>

$$g_f(20.44^\circ\text{C}) = 1.046 \pm 0.006$$

in good agreement with most measurements and evaluations<sup>5</sup>.

We also calculated several fission- and resonance integrals. In Table 1 our values of the fission integrals are compared with previous results. All these data were obtained from the NEA Neutron Data Compilation Centre, Saclay (France). When examining this table we find that differences up to about 40% exist between the different integrals. These differences can

partly be explained by examining the normalization procedures applied in the different measurements. Table 2 shows that these procedures are all different and sometimes not very accurate.

To reduce the contribution of inaccurate normalizations to the overall discrepancies, we propose a common normalization procedure based on a convenient fission integral with a sufficiently high counting rate and a numerical value nearly unaffected by timing errors (i. e. one with very small cross-sections at its limits). We found that the absolute fission integral

$$\int_{12 \text{ eV}}^{20 \text{ eV}} \sigma_f(E) dE = 1368 \pm 13 \text{ barn. eV}$$

obtained from these measurements is rather convenient. Such a renormalization is only able to remove a part of the discrepancies. Some discrepancies due to other systematic effects remain.

The measurements reported here were performed at CBNM Geel in the frame of the SCK/CEN Mol - CBNM Euratom association (contract number EUR/C/4146/67 f).

## References

1. H. Lemmel, C. Westcott, Journ. Nucl. En. 21 (1967) 417.
2. A. Deruytter, C. Wagemans, Journ. Nucl. En. 25 (1971) 263.
3. A. Deruytter, C. Wagemans, Journ. Nucl. En. 26 (1972) 293.
4. A. Deruytter, C. Wagemans, Nucl. Sci. & Engr. 54 (1974) 423.
5. H. Lemmel, this Conference (paper EA 2).
6. C. Wagemans, A. Deruytter, Ann. of Nucl. Sci. & Engr. (in press).
7. J. Blons, H. Derrien, A. Michaudon, Third Conf. on Neutron Cross Sections and Technology (Knoxville) 1 (1971) 836.
8. E. Migneco, J. Theobald, J. Wartena, Nucl. Data for Reactors (Helsinki) 1 (1969) 437.
9. O. Simpson et al., Conf. on Neutron Cross Sections and Technology, (Washington) 2 (1966) 910.
10. G. James, Nucl. Phys. 65 (1965) 353.
11. M. Moore et al., Phys. Rev. 135 (1964) B 945.
12. Y. Adamchuk et al., Proc. Int. Conf. on Peaceful uses of atomic energy (Geneva) 4 (1956) 216.
13. J. Blons et al., Nucl. Data for Reactors (Helsinki) 1 (1969) 469.
14. H. Hennies, Nucl. Data for Reactors (Paris) 2 (1966) 333.
15. G. James, Nucl. Data for Reactors (Helsinki) 1 (1969) 267.

Table 1:  $^{241}\text{Pu}$  fission integrals  $\int_{E_1}^{E_2} \sigma_f(E) dE$  (barn. eV)

Energy interval (eV)	This work	Blons <sup>7</sup>	Migneco <sup>8</sup>	Simpson <sup>9</sup>	James <sup>10</sup>	Moore <sup>11</sup>
3.0- 4.9	361.1	347.8	358.1		357.9 351.5	315.4
4.9- 8.0	871.6	882.0	898.2		868.8 885.9	847.6
8.0- 9.0	239.9	235.8	236.8		243.8 227.6	247.2 221.0
9.0-12.0	311.4	303.3	320.0		302.8 334.9	320.8 302.1
12.0-14.0	290.0	273.5	286.7		281.5 286.7	299.6 282.6
14.0-17.4	942.0	927.7	902.2		958.2 861.3	951.8 924.2
17.4-20.0	136.3	133.7	139.9		145.7 151.2	171.1 146.8
20.0-25.0	234.5	217.5 242.4	238.5	204.6	224.9 250.0	232.1 248.4
25.0-27.2	285.9	270.0 272.1	272.7	245.0	277.1	293.5 270.9
27.2-30.0	324.2	313.2 314.4	316.7	278.5	348.6	329.3 372.3
30.0-36.1	335.3	321.7 320.3	322.4	265.9	360.2	327.8 346.2
36.1-44.0	272.7	252.1 253.1	242.7	206.5	254.3	276.3 264.9
44.0-52.0	(333)	314.4 306.8		289.7	309.0	405.9 426.0
12.0-20.0	1368.3	1334.9	1328.8		1385.4 1299.2	1422.5 1353.6

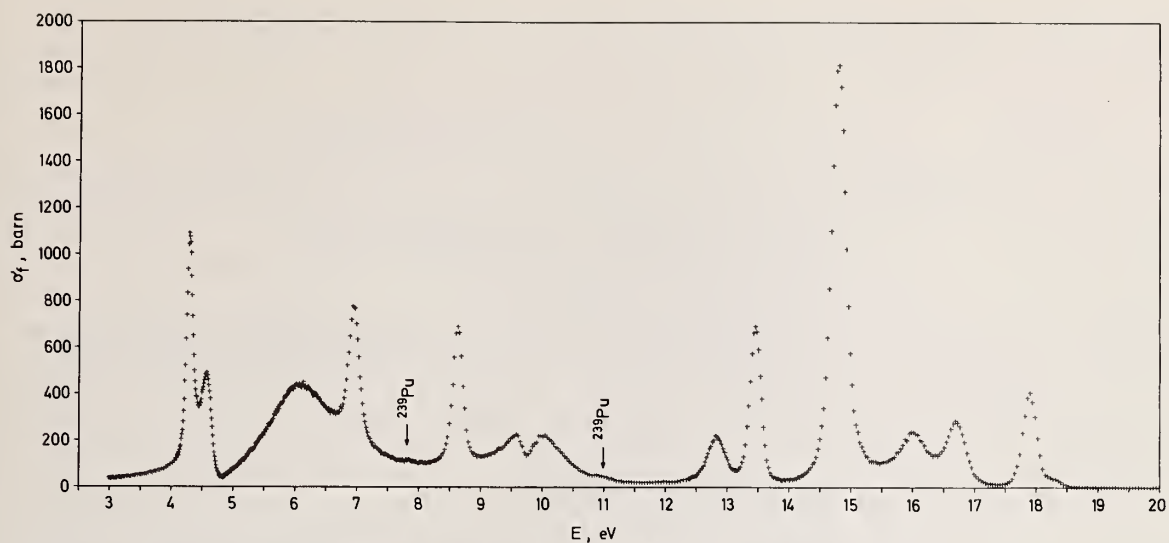


Figure 1: Neutron induced fission cross-section for  $^{241}\text{Pu}$  in the energy region 3 - 20 eV

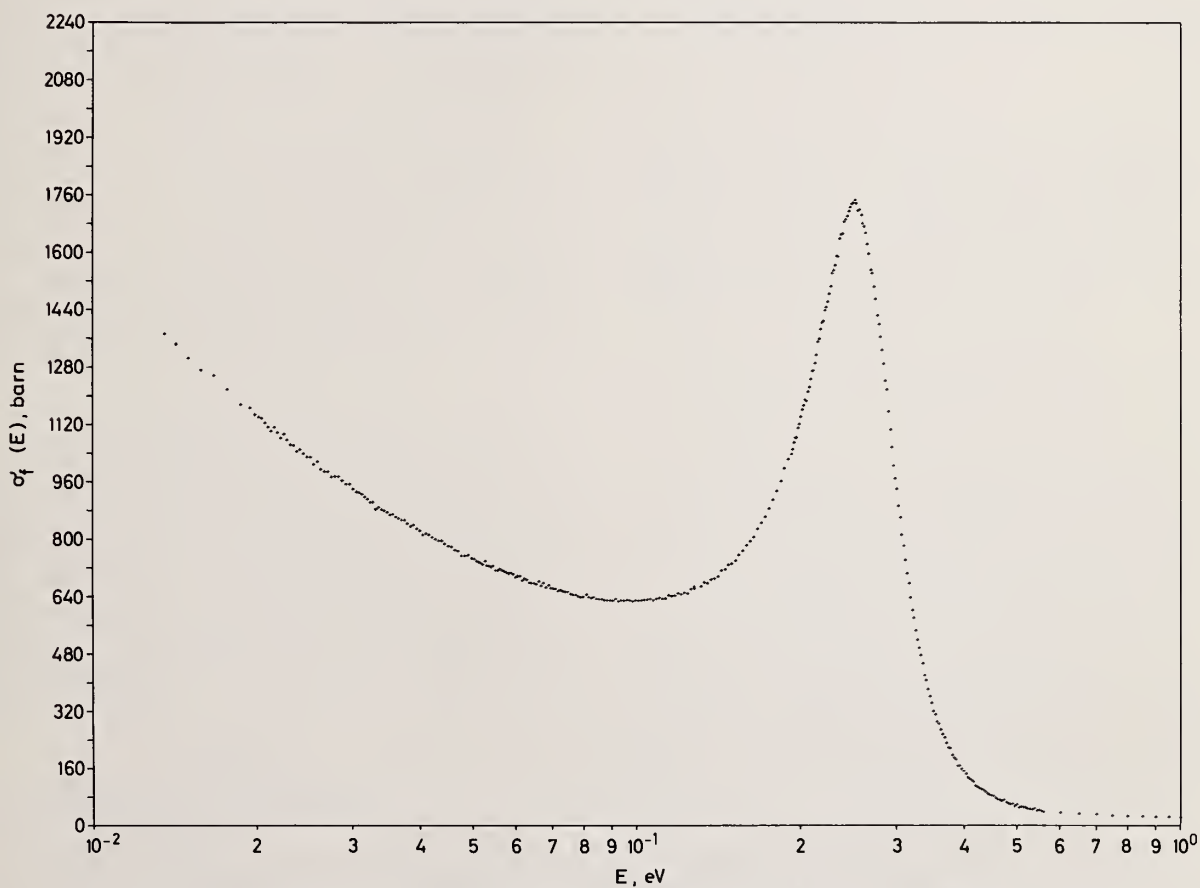


Figure 2: Low-energy neutron induced fission cross-section for  $^{241}\text{Pu}$  (corrected for  $^{239}\text{Pu}$ )



Table 2: Comparison of the normalization methods applied in some  $\sigma_f$  - measurements of  $^{241}\text{Pu}$

References	Normalization Method
Adamchuk et al. <sup>12</sup>	$\sigma_f$ normalized at 0.025 eV to $\sigma_f^0 = 950$ b. Chopper measurement (6.05 m flight path). Important $^{239}\text{Pu}$ contribution (8%).
Moore et al. <sup>11</sup>	$\sigma_f$ normalized at a peak-value of 406 b for the 6 eV resonance. Linac measurement (10.56 m flight path).
James <sup>10</sup>	$\sigma_f$ normalized at 0.0253 eV to $\sigma_f^0 = 1010$ b via a linear least-squares fit of $\sigma_f \sqrt{E}$ from 0.02 eV to 0.05 eV. Linac measurement (5 m and 15 m flight path).
Migneco et al. <sup>8</sup>	$\sigma_f$ normalized to $\int_{4.65 \text{ eV}}^{10 \text{ eV}} \sigma_f(E) \frac{dE}{E} = 193.6 \text{ b}$ (Hennies <sup>14</sup> ). Linac measurement (30.617 m flight path).
Blons et al. <sup>13</sup>	$\sigma_f$ normalized to the values of $\sigma_0 \Gamma_f$ for the 15.95 eV and 16.66 eV resonances as given by Stehn et al. (BNL 325). Linac measurement (10.89 m flight path).
Blons et al. <sup>7</sup>	$\sigma_f$ normalized to $\int_{20 \text{ eV}}^{70 \text{ eV}} \sigma_f(E) dE = 2367.5 \text{ b} \cdot \text{eV}$ (James <sup>15</sup> ) Linac measurement (10.89 m and 50.07 m flight path).
This measurement	$\sigma_f$ normalized to $\sigma_f^0 = (1019 \pm 8) \text{ b}$ . via a linear least-squares fit of $\sigma_f \sqrt{E}$ from 0.02481 to 0.02586 eV. Linac measurement (8.1 m flight path).

E. Migneco, P. Bonsignore, G. Lanzanò

Istituto di Fisica Nucleare, Università di Catania  
 Istituto Nazionale di Fisica Nucleare - Sezione di Catania  
 Centro Siciliano di Fisica Nucleare e di Struttura della Materia, Catania, (Italy)

J. A. Wartena and H. Weigmann

Central Bureau of Nuclear Measurements, Geel Belgium

The relative fission cross section of  $^{235}\text{U}$  has been measured up to 200 KeV with a nominal resolution of 1.0 ns/m, using a thin foil plastic scintillator detector. The data have been analysed in order to detect nonstatistical effects due to intermediate structure. Statistical tests which have been applied to this fission and similar total cross section data include calculations of the auto-correlation function and Wald-Wolfowitz tests on the cross-section and on the autocorrelograms. The comparison of the results indicates the presence of intermediate structure effects in fission cross-section which may be interpreted on the basis of the double-humped deformation potential.

### Introduction

Recent experiments (Ref.<sup>1</sup>) indicate the presence of large fluctuations in the KeV fission cross-section of  $^{235}\text{U}$ . We have measured this cross-section between 1 and 200 KeV using the C.B.N.M. Linac as pulsed neutron source with a nominal resolution of 1 ns/m and a thin plastic scintillator detector. The results confirm the presence of fluctuations. To interpret this effect in terms of intermediate fission states it is necessary to compare the fission and total cross-sections and to apply statistical tests to both sets of data. This paper reports a statistical study consisting in a serial correlation coefficients analysis and a Wald-Wolfowitz test applied to the present fission data and to the total cross section data of Böckhoff et al. (Ref.<sup>2</sup>).

### Experimental details

Two very thin (0.0025 cm) NE102A plastic scintillator foils of large area (16 cm x 16 cm) have been used as fission fragment detector (Ref.<sup>3</sup>). Coincidence techniques applied to the signals of the two photomultipliers which view the detectors allow to discriminate fission fragments against alphas and other background. The detector has high efficiency ( $\sim 50\%$ ) and is insensitive to the  $\gamma$ -flash. A flight path of 30 m with channel and burst widths of 20 ns have been used.

### Analysis

#### Serial correlation coefficients

This analysis is similar to that applied by Cao et al. (Ref.<sup>4</sup>) to the  $^{235}\text{U}$  at lower energy and by C.D. James et al. (Ref.<sup>5</sup>) to  $^{239}\text{Pu}$ . In the present case the data available extend from 780 eV to 200 KeV for fission and from 6 KeV to 200 KeV for total cross-section. The

sequence

$$A_j(W) = \int_{(j-1)W}^{(j+1)W} \left[ \frac{\sigma_f \sqrt{E}}{\langle \sigma_f \sqrt{E} \rangle} - 1 \right] dE \quad (1)$$

is calculated for energy interval  $W$  varying from 50 eV to 1 KeV. For a given  $W$  the maximum energy limit is imposed by the energy resolution. In a first calculation the value  $\langle \sigma_f \sqrt{E} \rangle$  was taken averaging over the entire range of analysis. The serial correlation coefficient is defined as:

$$R_K(W) = \frac{\text{COV}[A_j(W); A_{j+K}(W)]}{\left[ \text{Var } A_j(W) \cdot \text{Var } A_{j+K}(W) \right]^{\frac{1}{2}}} \quad (2)$$

In Fig. 1 the  $A_j$  sequences of  $\sigma_f \sqrt{E}$  and  $(\sigma_T - 11.2) \sqrt{E}$  [barn.  $\sqrt{\text{eV}}$ ] are shown in the energy range from 6 to 20 KeV. The  $\sigma_f$  appears more structured. The serial correlation coefficients for total and fission cross-section in the same energy interval are displayed in Fig. 2 (a) and (b) and in Fig. 3 (a) and (b) respectively for  $W=100$  eV and  $W=300$  eV. It can be seen that the correlograms for  $\sigma_f$  show a strongly fluctuating nonstatistical behaviour with a correlation full width of about 700 eV while the  $\sigma_T$  correlograms are indicating long range correlation, practically a slope in the cross section. The Wald-Wolfowitz test (Ref.<sup>6</sup>) applied to the correlograms of Fig. 2 (a) and (b), gives a significance level  $P(U)=3.6 \times 10^{-2}$  and  $1.6 \times 10^{-6}$  respectively. This is a very strong indication of intermediate structure in the fission channel even if the significance level has not been determined by randomization (Ref.<sup>6</sup>).

This features are identical in all correlograms calculated from 6 to 20 KeV with W ranging from 50 eV to 500 eV. If in the calculation of the correlation coefficients is used an energy dependent mean  $\langle \sigma_f(E) \sqrt{E} \rangle_\Delta$  and  $\langle (\sigma_T - 11.2) \sqrt{E} \rangle_\Delta$  averaged over an interval,  $\Delta = 10$  KeV, large compared with the correlation width, the fission cross-section correlogram (Fig. 4a) shows again a strong non-statistical behaviour similar to that of Fig. 2(a) with  $P(U) = 7 \times 10^{-4}$ , while the total cross-section correlograms Fig. 4(b) become fully statistical,  $P(U) = 0.5$ . If the  $\Delta$  value is comparable with the correlation width, e.g.  $\Delta = 900$  eV all nonstatistical effects are effaced in the  $\sigma_f$  correlogram (Fig. 5).

Therefore the  $\langle \sigma_f \sqrt{E} \rangle_\Delta$  for  $\Delta = 900$  eV;  $W = 100$  eV (Fig. 6a) is representative for the intermediate structure effects in the  $^{235}\text{U}$  fission cross section. In Fig. 4 and 5 the correlation coefficients are not divided by square root of the variances, therefore are not normalized to 1.

The intermediate structure spacing and widths cannot be directly deduced from the oscillation in the correlogram (Ref. <sup>7</sup>), but a comparison of  $\langle \sigma_f \sqrt{E} \rangle_\Delta$  and  $\langle (\sigma_T - 11.2) \sqrt{E} \rangle_\Delta$  [Fig. 6(a) and (b)] may suggest which structures are responsible for the non-statistical effects in  $\sigma_f$ .

In the range 6-20 KeV there are 4 or 5 of these structures indicated with an arrow. If we extend the range of analysis for  $\sigma_f$  from 6 to 40 KeV the correlogram pattern, obviously, changes as new structures are analyzed, but the non-statistical effect is still present,  $P(U) = 10^{-13}$ , and the correlation width remain almost constant.

#### Wald-Wolfowitz test on the cross-section

We have also tried an analysis consisting in the application of the Wald-Wolfowitz distribution free statistic (Ref. <sup>8</sup>) to the values

$$\frac{\sigma \sqrt{E} - \langle \sigma \sqrt{E} \rangle_\Delta}{\langle \sigma \sqrt{E} \rangle_\Delta}$$

for total and fission cross-section. A "run" is defined as an unbroken sequence of observed quantities lying above or below the median. The probability distribution of the total number of runs U has been calculated by Wald and Wolfowitz (Ref. <sup>8</sup>) together with the significance level  $P(U)$ .

We aspect that for  $\Delta$  values smaller or comparable with the structure widths the mean curve will follow the intermediate structures and the points will be statistically distributed around the mean, while for larger values of  $\Delta$  the mean curve will be smothered and the points will be distributed nonstatistically with a reduced number of "runs".

In Fig. 7 (a) and (b) is plotted the significance level  $P(U)$ , in function of  $\Delta$ , of the fission and total cross-section for  $W = 100$  and 300 eV. One can see that in both cases the test gives a very high significance level for fission at  $\Delta > 1.5$  KeV, while for the total cross-section  $P(U)$  remain almost constant and not significant ( $W = 100$  eV) or only slightly non-statistical ( $W = 300$  eV).

This results confirms the presence of intermediate structures in the fission cross-section between 6-20 KeV with a width smaller than 1.5 KeV in agreement with the results of the correlation analysis.

A further study on randomly generated mock-up cross-section is running.

#### References

- 1) B.U. Patrick, M.G. Sowerby and M.G. Schomberg J. Nucl. Energy, 24 (1970) 269  
J.R. Lemley, G.A. Keyworth and B.C. Diven, Nucl. Sc. Eng. 43 (1971) 281  
C.D. Bowman, M.L. Stelts and R.J. Baglan Proc. Conf. Nuclear Data for Reactors, Hel-sinky, Vol. II, pag. 65. IAEA Vienna (1970)  
R.B. Perez, G. De Saussure, E.G. Silver, R.W. Ingle and H. Weaver, Nucl. Sci. Eng. 55 (1974) 203.
- 2) K.M. Böckhoff, A. Dufrasne, G. Rohr and Weigmann, J. Nucl. Energy, 26 (1972) 91.
- 3) K.M. Böckhoff, E. Migneco, J. Theobald and J. Wartena, Nucl. Instr. Meth. 45 (1966) 233.
- 4) M.G. Cao, E. Migneco and J. Theobald, Phys. Lett., 27B (1968) 409.
- 5) B.M. Patrick and G.D. James, Phys. Lett. 28B (1968) 258.
- 6) G.D. James, Nucl. Phys. A170 (1971) 309.
- 7) P.B. Perez, G. de Saussure and M.N. Moore, Physics and Chemistry of fission (IAEA, Vienna 1969) 283.
- 8) A. Wald and J. Wolfowitz, Ann. Math. Stat. 11 (1940) 147.



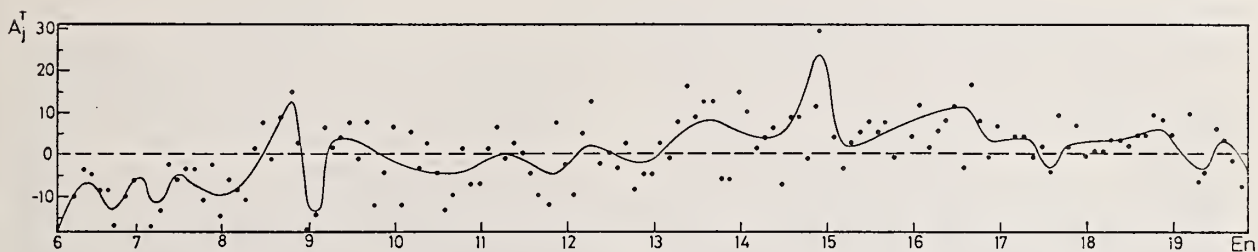
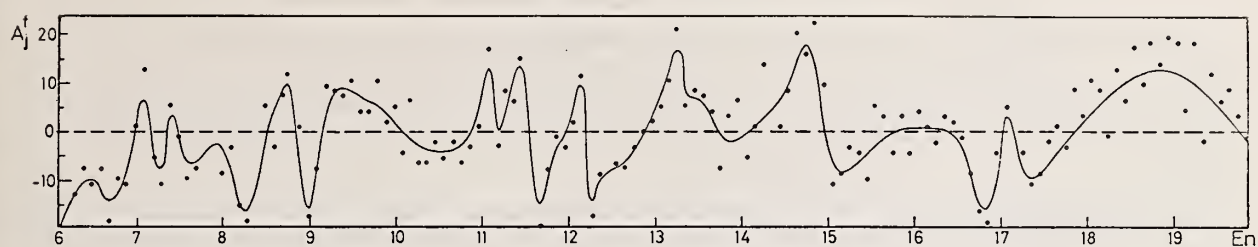


Fig.1

$\Delta C_T^{235} U+n$  En from 6 to 20KeV

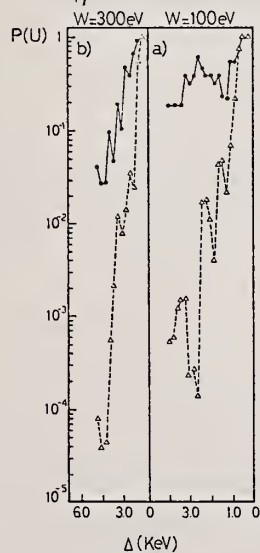


Fig.7

$^{235}U(n, total); W=100eV$  En: 6-20KeV  $P(U)=36 \times 10^{-2}$   $^{235}U(n, f); W=100eV$  En: 6-20KeV  $P(U)=16 \times 10^{-6}$

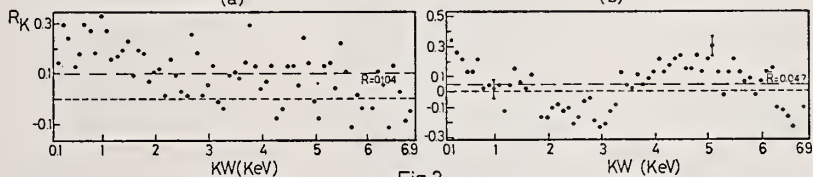


Fig.2

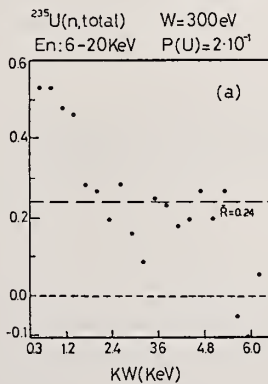
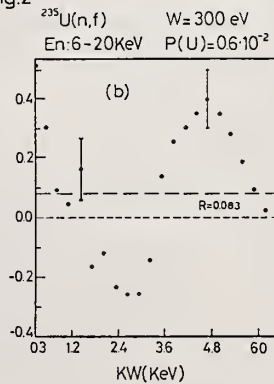


Fig.3



$W=100 \text{ eV} \quad \Delta=900 \text{ eV}$

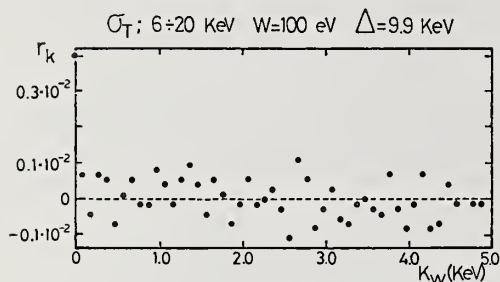
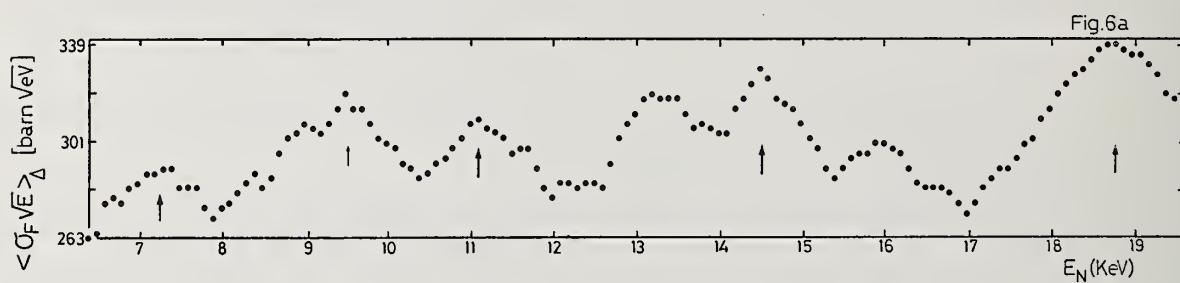
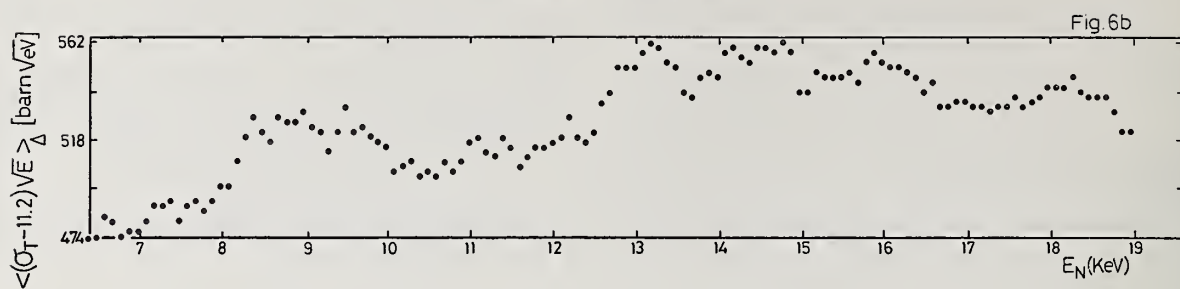


Fig. 4b

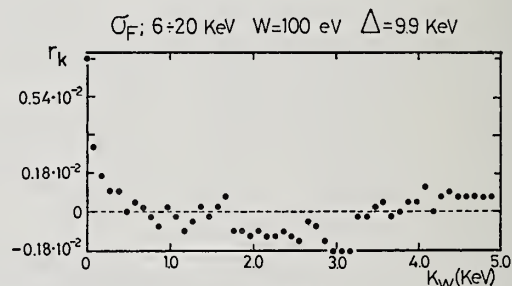


Fig. 4a

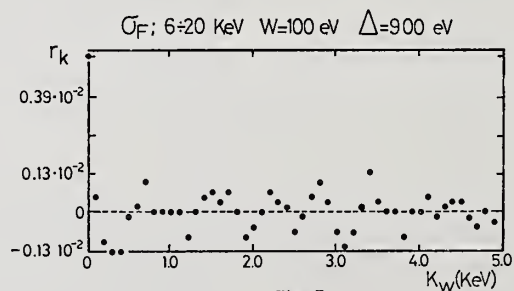


Fig. 5

S. Iwasaki, K. Yana, S. Sato, K. Sano, M. Hagiwara and K. Sugiyama  
Department of Nuclear Engineering, Tohoku University, Sendai, Japan

Energy spectrum of the second group delayed neutrons ( $T_{1/2} = 22$  sec.) from photo-fissions of  $^{238}\text{U}$  has been obtained using a time-of-flight technique between beta-particles and neutrons. Experimental results show a fine structure in the spectrum. The six prominent peaks of energies; 200-, 240-, 280-, 380-, 540- and 750-keV are observed.

[ Fission;  $^{238}\text{U}(\gamma, f)$ ; delayed neutron; group 2; energy spectrum,  $\beta$  - n time-of-flight ]

### Introduction

There was no report for several years, after the measurements of the energy spectrum of the delayed neutrons by Burgy et al.<sup>1</sup>, Bonner et al.<sup>2</sup>, and Batchelor and Hyder<sup>3</sup>. In the last years, several experimental results on the energy distributions of the delayed neutrons from neutron-induced fissions in  $^{235}\text{U}$  and other fissile nuclides have been reported<sup>4-10</sup>, because of requirements from nuclear engineering, nuclear safeguards, and an interest on nuclear energy level structure far off the beta-stability line. Shalev and Cuttler<sup>5</sup> have found a clear fine structure on the energy distribution of the delayed neutrons emitted from  $^{137}\text{Xe}$  of which precursor is  $^{137}\text{I}$ . There have been, however, no experimental data on the energy spectrum of the delayed neutrons from photo-fissions. In the present work, measurement is carried out on the delayed neutrons of the "group 2" which has the half-life of 22 sec., resulting from the photo-fissions of  $^{238}\text{U}$ , in which a fast time-of-flight technique is used for obtaining the energy spectrum of the neutrons in coincident with the beta-particles emitted at the decay of the precursors.

### Experimental Procedures

The neutron detector is a 5 in. dia. and 15 mm thick disk of the NE-213 liquid scintillator encapsuled in a glass vessel covered by aluminium foil reflector, and mounted on the XP-1040 photomultiplier. The beta-particle detector is a 20 mm dia. and 1 mm thick disk of the NE-102A plastic scintillator mounted on the RCA 8575 photomultiplier. The neutron detector is located 30 cm horizontally from sample. The beta-particle detector is located just behind the sample. The time intervals between coincided events in the two detectors

are measured with time-of-flight electronics shown in Fig. 1. A signal from the neutron detector is used as start pulse at the time-to-amplitude converter, and a delayed signal from the beta-particle detector is used as stop pulse at the converter, because of the intense counting on the beta-particle detector. The output pulse of the converter is fed to the linear gate which is opened by the neutron signal passed from discrimination unit of the neutrons and the gamma-rays. This  $n$  -  $\gamma$  discrimination unit is shown by a dotted line in Fig. 1. A method that the risetime-to-height converter which is a leading-edge time pickoff circuit consisting of two pulse-shaping networks and an amplitude comparator<sup>11</sup> is adopted.

The system was checked by neutrons and gamma-rays emitted from  $^{252}\text{Cf}$  source, in advance of the actual

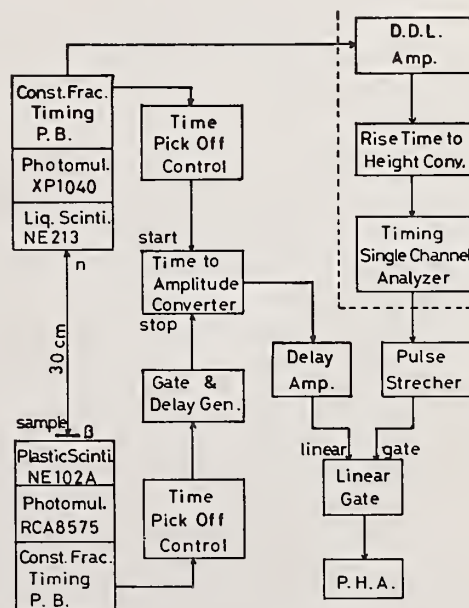


FIG. 1. Schematic diagram of electronic system.



measurement. The time resolution of 3 nano-sec. for this time-of-flight electronics is obtained at FWHM of a  $\gamma$ - $\gamma$  coincidence peak in the time spectrum using the annihilation gamma-rays from  $^{22}\text{Na}$  source.

A number of samples which are 50 mg of natural uranium oxide are prepared. Each sample is put between aluminium foil folded in half of 50  $\mu\text{m}$  thick. Irradiations of the samples are carried out by the Bremsstrahlung of the maximum energy 60 MeV at the electron linac of Tohoku University, using a pneumatic transfer device. The irradiation-counting cycle which is irradiation for 60 sec., cooling for 20 sec. and counting for 100 sec. was decided from a result of the decay calculation as in Fig. 2. The values of 14.7 MeV-neutron-fission for  $^{238}\text{U}$  obtained by East and

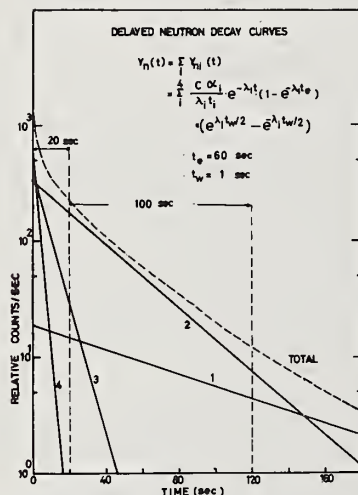


FIG. 2. Calculated decay curve for the each group of delayed neutrons which is used to time relation of irradiation-counting cycle.

Keepin<sup>12</sup>. Two series of the measurement are performed; consisting of 45 and 66 runs which means that, for example, neutron counts from forty-five samples are accumulated in the first series, which are irradiated and counted in order.

The time spectrum of the neutrons and gamma-rays which is the amplitude distribution in the output of the risetime-to-height converter was measured actually for the irradiated samples of thirty-five in preliminary measurement, in order to confirm an operation of the n- $\gamma$  discrimination unit. This result is shown in Fig. 3. Since the energy of most delayed neutrons is not so high, the separation of the peaks of neutrons and gamma-rays is not good, but the discrimination is acting in effective.

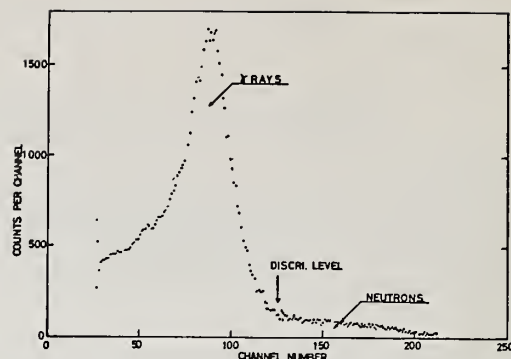


FIG. 3. The n- $\gamma$  discrimination time spectrum obtained from output of the risetime-to-converter for the irradiated uranium samples.

The time-of-flight spectrum of the delayed neutrons from the irradiated samples is shown in Fig. 4. The peak caused from the gamma-rays is also seen at the time-zero point, but the peak height is remained in small. If no n- $\gamma$  discrimination is performed, it would be impossible to obtain any meaningful result, because of very large peak from the intense gamma-rays. The neutron detecting system consisted of the NE-213 liquid scintillator and the n- $\gamma$  discrimination did make it possible, in contrast with a normal plastic scintillator.

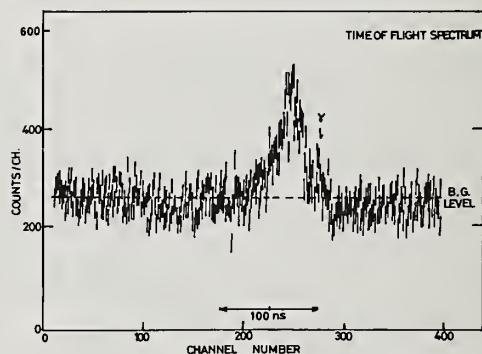


FIG. 4. Time-of-flight spectrum of the delayed neutrons from the photo-fission of  $^{238}\text{U}$ .

## Results and Discussions

The time spectrum such as Fig. 4 is converted to the energy spectrum for each series of the measurement, and corrected for the detection efficiency of the neutrons at various energies. The relation of discrimination bias level and the efficiency is calculated by the Monte Carlo method, as shown in Fig. 5. The

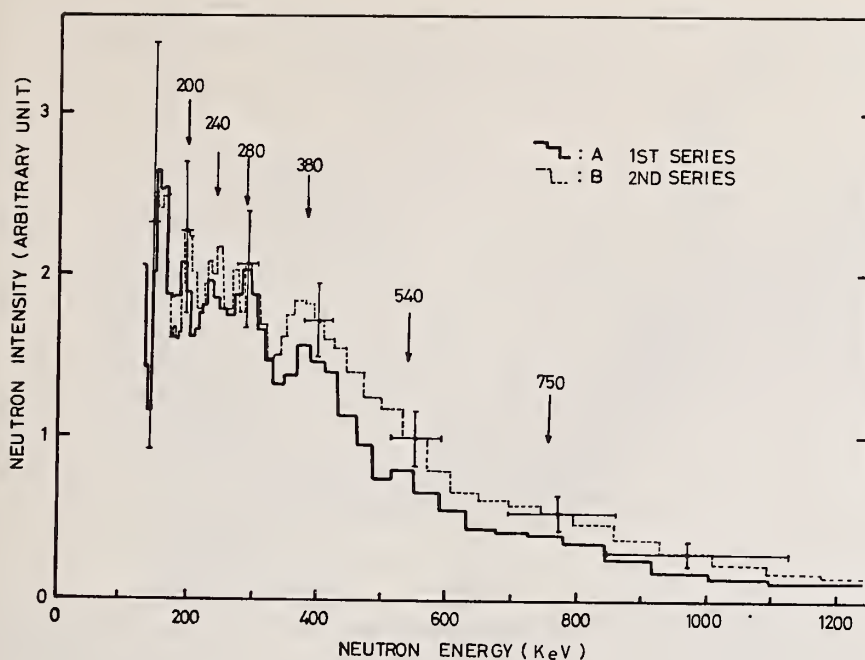


FIG. 6. Energy spectrum of delayed neutrons group 2 resulted from the photo-fission of  $^{238}\text{U}$ .

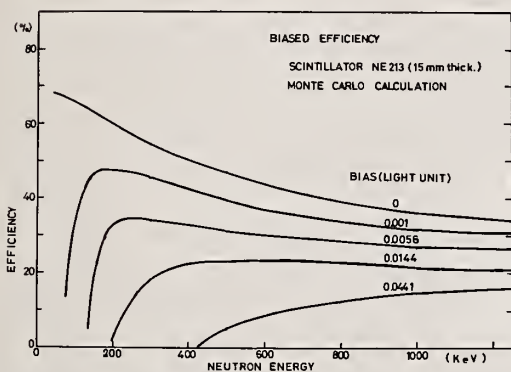


FIG. 5. Calculated efficiency for the neutron detection varying the discrimination bias level.

accurate correction for the neutron detector is very difficult because the determination of the relation between discrimination level and neutron energy is impossible for the thin organic scintillator using normal method using the Compton edge caused by the gamma-rays of definite energy. The efficiency correction for the beta-particles is also difficult because of its unknown momentum distributions. This makes it impossible to determine the absolute or relative yield of the delayed neutrons. In despite of the matter, it is worthwhile to see the fine structure on the energy spectrum shown in Fig. 6. At the present result, the prominent peaks having energies of 200-, 240-, 280-, 380-, 540- and 750-keV are assigned. Result on each series of measurement

is shown separately for confirming the reproducibility.

For comparison, the previous results by several authors<sup>5,6,9</sup> for the group 2 delayed neutrons from  $^{238}\text{U}$  are shown in Fig. 7 with the present result that data of the first and second series measurement are summed up. Table 1 presents the energies of peaks reported by above four authors and Sloan and Woodruff<sup>10</sup> whose work was made for group 2 delayed neutrons resulted from the thermal-neutron fission of  $^{235}\text{U}$ . It is noted that  $^{137}\text{I}$  is main precursor of group 2. The values on the results by Fieg<sup>8</sup> is taken from a compilation by Cox<sup>13</sup>.

In Fig. 7, these four results show approximately similar shape except for low energy region and 425-keV or 630-keV valley on the result by Shalev and Cuttler<sup>9</sup>.

The 380-keV peak is in completely agreement with each other. It may be concluded that the neutrons above energy of 350-keV are belonging to the group 2, and those concentrated to the energy region between 350-keV and 630-keV.

It is interesting to note that there is remarkable difference between the result by Shalev and Cuttler<sup>9</sup> and other authors in the low energy region, as mentioned above. The delayed neutrons caused from the precursor  $^{137}\text{I}$  show prominent peak at 270-keV and low intensity peak at 155-keV, and some humps and a few separated peaks are appeared on the Fieg's result and the present data, respectively, below 350-keV. Whereas the intensity of neutrons below 350-

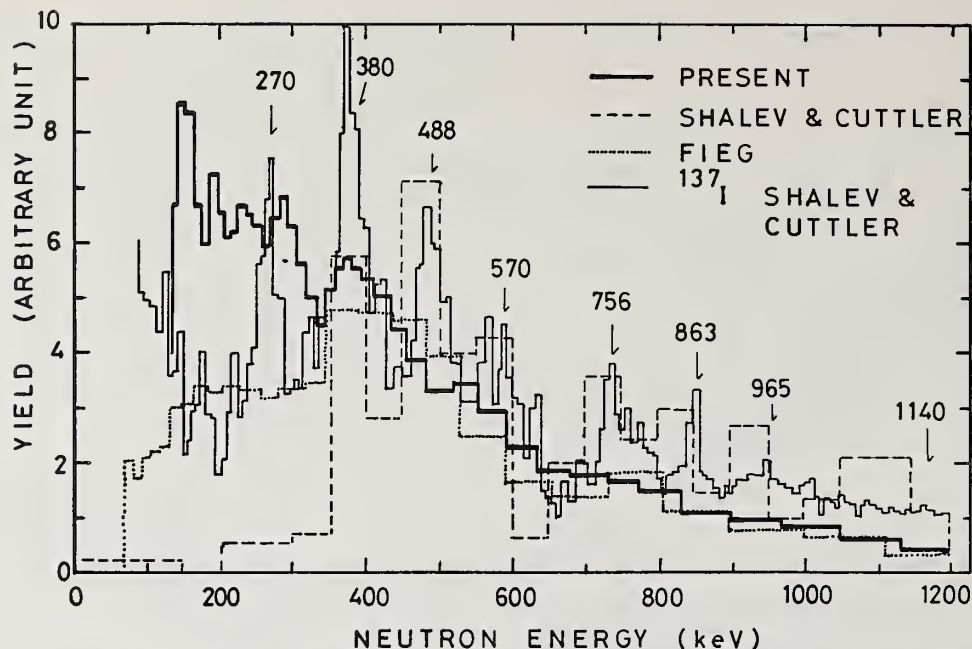


FIG. 7. Comparison of some experimental data on the energy spectrum of the group 2 delayed neutrons from the fission on  $^{238}\text{U}$  obtained by Shalev and Cuttler<sup>5,9</sup>, and Fieg<sup>8</sup>, and present authors.

keV is very low on the data by Shalev and Cuttler<sup>9</sup>. The reasons of these differences are not definite so far. More precise measurement should be made in future. It should be noted that a suitable corrections for the detection efficiencies and the mixing from the competing reaction ( $\gamma, nf$ ) and/or ( $n, f$ ) by the neutrons emitted from photo-reaction in  $^{238}\text{U}$ .

The authors would like to express their deep appreciation to Drs. M. Yagi and K. Kondo for valuable suggestion and cooperation during the experiments. They also thank the linac crew for the operation.

#### References

- <sup>1</sup>M. BURG, L. A. PARDUE, H. B. WILLARD, and E. O. WOLLEN, Phys. Rev., **70**, 104 (1946)
- <sup>2</sup>T. W. BONNER, S. J. BAME and J. E. EVANS, Phys. Rev., **101**, 1514 (1965)
- <sup>3</sup>R. BACHELOR and H. R. McK. HYDER, J. Nucl. Energy, **3**, 7 (1956)
- <sup>4</sup>E. T. CHULICK, P. L. REEDER, C. E. BEMIS and E. EICHLER, Nucl. Phys., **A168**, 250 (1971)
- <sup>5</sup>S. SHALEV and J. M. CUTTLER, Trans. Am. Nucl. Soc. **14**, 373 (1971)
- <sup>6</sup>S. SHALEV and G. RADSTAM, Phys. Rev. Letters, **25**, 687 (1972)
- <sup>7</sup>N. G. CHRYSOCHOIDES, J. N. ANOUSIS, C. A. MITSONIAS and D. C. PERRICOS, J. Nucl. Energy, **25**, 551 (1971)
- <sup>8</sup>G. FIEG, J. Nucl. Energy, **26**, 585 (1972)
- <sup>9</sup>S. SHALEV and J. M. CUTTLER, Nucl. Sci. Eng., **51**,

TABLE I. Prominent peak energies on the energy spectra of the group 2 delayed neutrons in keV.

$^{238}\text{U}$ GROUP 2  PRESENT	$^{137}\text{I}$  SHALEV AND RADSTAM	$^{238}\text{U}$ GROUP 2  SHALEV AND CUTTLER	$^{235}\text{U}$ GROUP 2  FIEG	$^{235}\text{U}$ 25 sec. IRRADI. SLOAN AND WOODRUFF
200	(155)		150	130
240			230	160
280	270 (325)		340	200
380	380 (425) (460)	367	380	240
540	488 570 685	460 485	440 500 530	280
750	756 863 965 1140	730 840 940 1135		350
				450
				750

52 (1973)

<sup>10</sup>W. R. SLOAN and G. L. WOODRUFF, Nucl. Sci. Eng. **55**, 28 (1974)

<sup>11</sup>S. KINBARA and T. KUMAHARA, Nucl. Instr. Methods, **67**, 261 (1969)

<sup>12</sup>L. V. EAST and G. R. KEEPIN, Proc. Second IAEA Symp. Physics and Chemistry of Fission, p.647 (1969)

<sup>13</sup>S. A. COX, ANL/NDM-5 (1974)



G. S. Sidhu and J. B. Czirr  
Lawrence Livermore Laboratory, University of California  
Livermore, California 94550

Energy dependence of the fission cross section of <sup>235</sup>U with respect to the n-p scattering reaction was measured for neutron energies from 0.8 to 20 MeV. The LLL linac target was used as the pulsed neutron source; neutron energies were measured by time-of-flight technique. A <sup>235</sup>U ion chamber was designed and operated to make the fission detection efficiency independent of the angular distribution of fission fragments. The neutron flux monitor consisted of an annular polyethylene radiator with a shielded proton recoil detector. Data in the energy range from 3 to 20 MeV were obtained with a 3.3 mg/cm<sup>2</sup> radiator; a 0.31 mg/cm<sup>2</sup> radiator was used for the range from 0.8 to 4 MeV. Both sets of data were normalized to yield the average fission cross section value of 1.198 b in the overlapping region from 3 to 4 MeV. Total error in the relative <sup>235</sup>U(n, f) cross section is  $\pm 1\%$  below 7 MeV,  $\pm 2\%$  at 14 MeV, and  $\pm 6\%$  at 20 MeV.

(U<sup>235</sup> fission cross section; neutron energy 0.8 to 20 MeV;  
relative to n-p scattering; linac source)

### Introduction

The potential use and broad scope of applications of the <sup>235</sup>U neutron fission cross section are hampered by the current level of uncertainty<sup>1</sup> in the knowledge of the cross section. In the energy region above 1 MeV, absolute measurements of the fission cross section have always required some changes in experimental conditions when going from one neutron energy to another. We followed the proposal of Bowman<sup>2</sup> to measure the <sup>235</sup>U(n, f) cross section to a precision of 1% in the energy range from thermal to 20 MeV, by using a linac source and the time-of-flight method to cover wide regions of energy simultaneously.

This paper describes our measurement of the energy dependence of the <sup>235</sup>U(n, f) cross section relative to n-p scattering in the energy region from 0.8 to 20 MeV. The portion of these data from 3 to 20 MeV were obtained and reported earlier.<sup>3</sup> The region from 0.8 to 4 MeV was measured with identical geometry but reduced n-p scattering foil thickness. The two sets of data were then normalized in the overlapping region to the fission cross section value<sup>4</sup> of 1198 mb at 3.5 MeV. The experimental accuracy below 14 MeV is 1 to 2%; therefore this cross section may now serve as a standard for flux measurements from 0.8 to 14 MeV.

### Experimental Procedure

A white spectrum of neutrons was obtained from the tantalum target of the LLL linac operating in the 10-ns pulse width mode. The neutron beam was collimated to sizes appropriate for our detectors. The fission detector and the flux monitor were located at 37.63 and 60.41 m, respectively, from the neutron source along the same flight path. The reaction rate vs time-of-flight data for each detector was taken for a selected portion of the neutron energy spectrum during each run.

The detectors used for this experiment separate the signal pulse height from the system noise sufficiently well to avoid the problems associated with

extrapolating into the noise region. Our neutron flux monitor<sup>5</sup> consisted of an annular polyethylene (CH<sub>2</sub>) radiator foil at the downstream end of a 45-cm-long, 6.35-cm-diameter lead shield and a 2-mm-thick 3.5-cm diameter Si(Li) semiconductor detector 10 cm further down the beam path, along the shield axis (Fig. 1). The effective outer diameter of the radiator foil was defined by the collimated beam to be about 13 cm and the inner diameter was defined by the lead shield. A 3.3-mg/cm<sup>2</sup> CH<sub>2</sub> foil thickness was used to obtain data from 3 to 20 MeV and a 0.31 mg/cm<sup>2</sup> foil was used for the data from 0.8 to 4 MeV.

The fission detector was a parallel plate ion chamber with five <sup>235</sup>U-loaded, 7-mg/cm<sup>2</sup>-aluminum foils interspaced at 1-cm intervals with blank aluminum

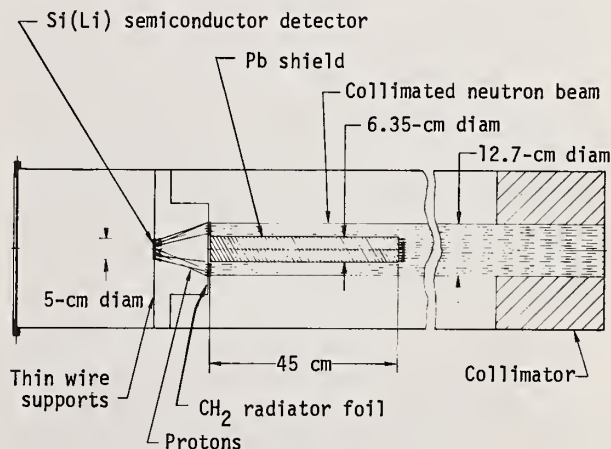


Fig. 1. Experimental configuration for neutron flux measurement.

\*This work was performed under the auspices of the U. S. Energy Research & Development Administration.

foils. The only other chamber material in the neutron beam was the 0.5-mm-thick-aluminum wall of the cylindrical chamber, which presented an unvarying mass when the chamber was rotated in the beam (Fig. 2). To minimize possible effects of the variation of fission fragment anisotropy on detection efficiency, the  $^{235}\text{U}$  deposit thickness was limited to  $0.1 \text{ mg/cm}^2$  on each surface of a loaded foil.\* To compensate for the anisotropy effect resulting from residual absorption of fragments in the deposit, the fission chamber was positioned at several angles with respect to the neutron beam during different runs. The resulting fission data were assigned weights (corresponding to the surface area of a sphere as a function of angle), which, according to Ref. 6, make the fission fragment loss in the deposit independent of fragment anisotropy. For the 0.8- to 4-MeV runs the fission chamber foils were positioned arbitrarily at  $40^\circ$  to the neutron beam because the maximum angular distribution effects in the 3- to 20-MeV runs were found to be comparable to the statistical errors.

To eliminate gamma flash, the signals from both detectors were gated off for the duration of the gamma flash. Nevertheless neutron pulse counting began at energies well above the regions of interest. The signals following the gates were processed to obtain time-of-flight (with reference to the linac target pulse) and pulse height information for every reaction event in two detectors. The pulse height for each time channel was indispensable for the analysis of proton recoil data because the bias for the pulse height spectrum for any time channel could be chosen only after the accumulated data were observed (see Fig. 3). For the fission chamber, pulse height vs time data was used to check the validity of the fixed bias (Fig. 4). The energy calibration for all runs was made in a separate run with respect to the  $2077 \pm 2 \text{ keV}$  resonance in carbon by comparing with appropriate markers. The fission detector marker was the  $527 \pm 2 \text{ keV}$  lead resonance; the flux monitor marker was the gamma flash for the 3- to 20-MeV runs and the lead resonance for the 0.8 to 4-MeV runs.

The pulse height bias and background for the proton recoil detector were determined the same way as for the foreground. As reported in Ref. 3, the major portion of background arises from neutrons scattered off the lead shield into the recoil detector. This was discovered by replacing the  $\text{CH}_2$  radiator with a carbon foil, then without any foil, and finally by covering the detector with a barrier plate and changing foils. The background was found to be about 4% near 15 MeV, and only 0.5% near 6 MeV. Below 1 MeV it rose sharply to 10% at 0.8 MeV. We estimated the fission chamber background to be less than 0.1% of the signal in the entire region from 0.8 to 20 MeV, therefore we did not subtract it.

#### Data Analysis

The proton recoil data were corrected for the time-shift vs pulse height variation errors measured in a separate run. This correction was unnecessary for the fission data. The variation of fission detection efficiency as a function of neutron time-of-flight was

\*The  $^{235}\text{U}$  deposit covered a 10-cm-wide 18-cm-high area on the 15 by 25 cm foil; the neutron beam at the chamber was 18 cm wide and 13 cm high. Thus the effective  $^{235}\text{U}$  mass exposed to the beam was about 130 mg.

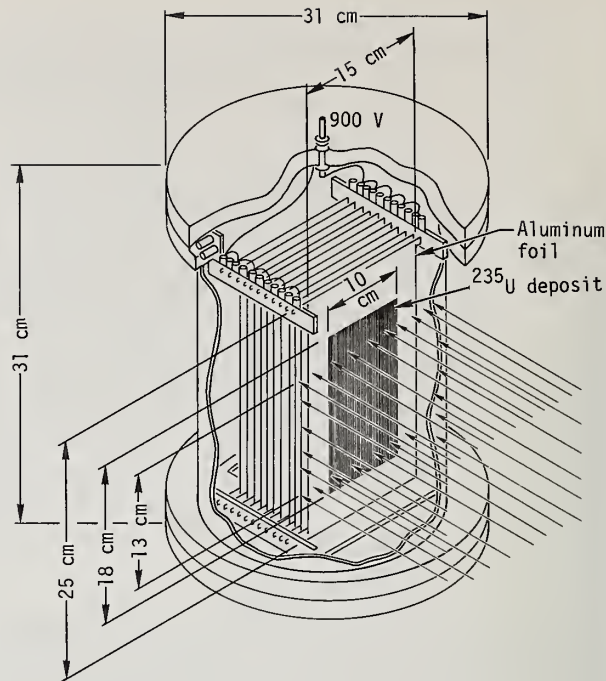


Fig. 2. Parallel plate ion-chamber with constant efficiency for fission detection.

measured by mixing the fission pulses with larger pulses from a pulser and observing the variation from randomness of the pulses above the fission pulse height. The fission data were corrected for this efficiency variation. The correction for the flux monitor was negligible. All rates were corrected for deadtime of the counting equipment.

The energy dependence of the fission cross section was computed from the corrected rates according to the formula

$$\sigma_f(E) = k \frac{R_f}{[R_\phi - B_\phi]} \sigma_{np} \cdot \text{AFM},$$

where  $R_f$  is the measured fission rate,  $R_\phi$  is the flux monitor foreground rate,  $B_\phi$  is the background rate,  $A$  is the  $n$ - $p$  angular distribution correction to the recoil detector efficiency based on Ref. 7,  $\sigma_{np}$  is the  $n$ - $p$  scattering cross section,<sup>8</sup>  $F$  is the correction for the time variation of fission detection efficiency, and  $M$  is the correction for the absorption of neutrons from the middle of the fission chamber to the radiator foil. All corrections except the normalization constant  $k$  are energy dependent functions.

The ratio of reaction rates  $R_f / (R_\phi - B_\phi) F \cdot M$  with an average value of 1.0 for the data between 3 and 4 MeV is presented in Table 1, column 2. This is the unnormalized ratio of  $^{235}\text{U}(n, f)$  and  $n$ - $p$  scattering cross sections and need not be revised as better cross section data become available. Column 3 contains the relative  $^{235}\text{U}(n, f)$  cross section again normalized to 1.0 while the fission cross section normalized to the average value of 1198 mb between 3 and 4



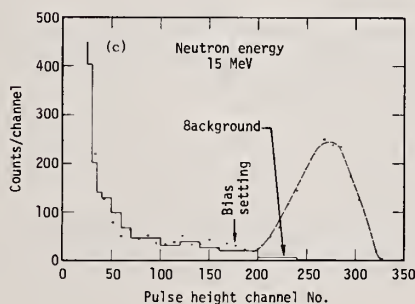
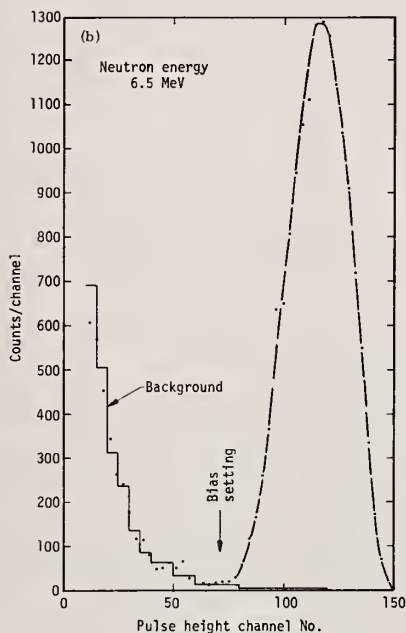
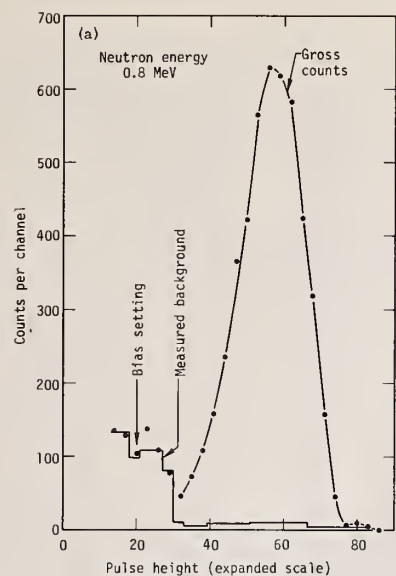


Fig. 3. Proton recoil pulse height spectra for incident neutron energies of 0.8, 6.5, and 15 MeV.

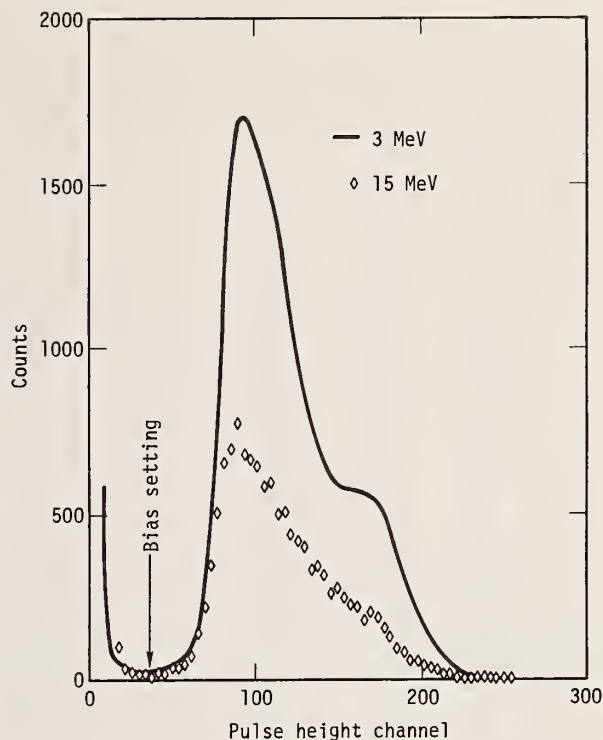


Fig. 4. Fission chamber pulse height spectra for 3 and 15 MeV incident neutrons.

MeV is presented in column 4. Columns 5 and 6 contain the total statistical and the rms sum of systematic errors (see Ref. 3).

### Discussion of Results

Although our measurements over the two energy regions were made separately, the detector geometry for the two sets of data was similar. The relative nature of the data and their normalization to one absolute value in the overlapping region between 3 and 4 MeV make the data in effect, a single continuous measurement from 0.8 to 20 MeV. The measurements are not subject to the errors usually predominant in absolute determination of flux, geometry, mass composition and detector efficiency. Other systematic errors are small because of the simplicity and good pulse height response of our detector systems. These measurements have the disadvantage of being dependent on other data for normalization for the time being. We at LLL are attempting to extend the relative fission measurements to thermal energies and eventually all our data may be normalized with respect to the thermal fission cross section. Since the  $^{235}\text{U}(n, f)$  cross section has been measured relative to the best known standard, i.e., the  $n\text{-p}$  scattering reaction, the fission cross section may now be used as a standard for flux measurements from 0.8 to 14 MeV (where the error rises from 1% to 2%) subject to the limitation of the absolute normalization error. Our data are presented along with some other measurements<sup>9-13</sup> for comparison in Fig. 5. Differences among various measurements are more significant at higher energies than at lower energies.



Table 1.

Neutron energy <sup>a</sup> (MeV)	$\frac{R_f}{R_\phi}$	$\sigma$ fission (relative)	$\sigma$ fission (normalized)	Statistical uncertainty std. dev.	Systematic error (rms)	Neutron energy <sup>a</sup> (MeV)	$\frac{R_f}{R_\phi}$	$\sigma$ fission (relative)	$\sigma$ fission (normalized)	Statistical uncertainty std. dev.	Systematic error (rms)
0.754	0.382	0.902	1.08	$\pm 1.0\%$	$\pm 0.5\%$	4.60	1.140	0.950	1.14	$\pm 1.0\%$	$\pm 0.3\%$
0.786	0.396	0.915	1.10	1.0	0.5	4.72	1.146	0.938	1.12	1.0	0.3
0.819	0.403	0.909	1.09	0.8	0.5	4.85	1.153	0.927	1.11	1.0	0.3
0.855	0.424	0.932	1.12	0.8	0.5	4.98	1.177	0.929	1.11	1.0	0.3
0.894	0.451	0.971	1.16	0.8	0.5	5.11	1.175	0.911	1.09	1.0	0.3
0.935	0.465	0.980	1.17	0.8	0.5	5.25	1.192	0.906	1.09	1.0	0.3
0.979	0.495	1.014	1.21	0.8	0.5	5.39	1.218	0.908	1.09	1.0	0.4
1.026	0.510	1.020	1.22	0.8	0.5	5.54	1.223	0.894	1.07	1.0	0.4
1.077	0.512	0.999	1.20	0.8	0.5	5.70	1.238	0.886	1.06	1.0	0.4
1.132	0.537	1.020	1.22	0.8	0.5	5.87	1.274	0.893	1.07	1.0	0.4
1.191	0.578	1.033	1.24	0.8	0.4	6.04	1.384	0.949	1.14	1.0	0.4
1.254	0.562	1.011	1.21	0.8	0.4	6.22	1.526	1.024	1.23	0.9	0.4
1.323	0.580	1.016	1.22	0.8	0.4	6.40	1.698	1.114	1.34	0.9	0.4
1.398	0.606	0.028	1.23	0.8	0.4	6.60	1.870	1.198	1.44	0.9	0.5
1.479	0.628	1.038	1.24	1.0	0.4	6.81	2.048	1.282	1.54	0.9	0.6
1.568	0.657	1.046	1.25	0.8	0.4	7.02	2.189	1.337	1.60	0.9	0.7
1.665	0.689	1.060	1.27	0.9	0.4	7.25	2.362	1.408	1.69	0.9	0.8
1.771	0.707	1.050	1.26	0.9	0.4	7.48	2.516	1.462	1.75	1.0	0.8
1.887	0.744	1.068	1.28	0.9	0.4	7.73	2.640	1.494	1.79	1.0	0.9
2.015	0.779	1.081	1.30	1.0	0.4	7.99	2.760	1.521	1.82	1.0	0.9
2.157	0.799	1.069	1.28	1.0	0.4	8.27	2.844	1.525	1.83	1.1	0.9
2.315	0.829	1.063	1.27	1.1	0.4	8.55	2.915	1.519	1.82	1.1	0.9
2.490	0.863	1.055	1.26	1.2	0.4	8.86	2.986	1.511	1.81	1.2	0.9
2.99	0.948	1.043	1.25	0.9	negligible	9.18	3.045	1.496	1.79	1.2	0.9
3.05	0.949	1.032	1.24	0.9	negligible	9.52	3.110	1.482	1.78	1.3	1.0
3.12	0.960	1.031	1.24	0.9	negligible	9.88	3.28	1.516	1.82	1.3	1.0
3.18	0.955	1.012	1.21	0.9	negligible	10.25	3.37	1.509	1.81	1.3	1.0
3.24	0.964	1.008	1.21	0.9	negligible	10.66	3.42	1.480	1.77	1.3	1.1
3.32	0.961	0.991	1.19	0.9	negligible	11.08	3.56	1.487	1.78	1.4	1.1
3.40	0.972	0.990	1.19	0.9	negligible	11.53	3.63	1.462	1.75	1.5	1.1
3.47	0.995	0.999	1.20	0.9	negligible	12.01	3.82	1.482	1.78	1.6	1.1
3.55	1.000	0.990	1.19	0.9	negligible	12.52	4.09	1.528	1.83	1.6	1.1
3.63	1.013	0.988	1.18	0.9	negligible	13.06	4.44	1.596	1.91	1.7	1.0
3.71	1.039	1.000	1.20	1.0	negligible	13.64	4.87	1.680	2.01	1.8	1.0
3.80	1.039	0.985	1.18	1.0	negligible	14.26	5.23	1.730	2.07	1.9	1.0
3.89	1.060	0.989	1.19	1.0	negligible	14.93	5.47	1.732	2.08	2.0 <sup>b</sup>	1.0
3.98	1.068	0.982	1.18	1.0	negligible	15.64	5.75	1.739	2.08	3.7 <sup>b</sup>	1.1
4.07	1.086	0.983	1.18	1.0	$\pm 0.1\%$	16.40	5.75	1.660	1.99	3.8 <sup>b</sup>	1.1
4.17	1.098	0.978	1.17	1.0	0.1	17.22	5.92	1.627	1.95	3.9 <sup>b</sup>	1.1
4.27	1.093	0.958	1.17	1.0	0.2	18.11	6.19	1.616	1.94	3.4 <sup>b</sup>	1.1
4.38	1.102	0.950	1.15	1.0	0.2	19.07	6.63	1.639	1.96	4.1 <sup>b</sup>	1.2
4.49	1.131	0.959	1.14	1.0	0.3	20.10	7.25	1.696	2.03	6.2 <sup>b</sup>	1.2

<sup>a</sup>Each listed energy represents the value at the middle of a time-of-flight bin width of 16 ns except that below 3 MeV the bin width is 64 ns.

<sup>b</sup>The error is the calculated standard deviation or the observed average deviation from the mean, whichever is larger.

By using our experimental method, precision of the measurements up to 14 MeV could be improved to 1% without inordinately long accelerator time. Data above 20 MeV could be obtained with appropriate choices of radiator thickness, detector location, etc. It may be possible to go somewhat lower than 0.8 MeV if the radiator-to-recoil-detector distance is increased to reduce the maximum angle of detected recoils and if a thinner proton recoil detector is used so as to minimize background.

### References

1. M. Moore, Proc. Symp. Neutron Standards and Flux Normalization, CONF 701002, U. S. Atomic Energy Commission, (1971) p. 509.
2. C. D. Bowman, Proposal for Fast Fission Measurements, p. 251, *ibid*.
3. J. B. Czirr and G. S. Sidhu, to be published Nuclear Science and Engineering.
4. W. P. Poenitz, Nucl. Sci. and Eng. **53**, 370 (1970).
5. G. S. Sidhu and J. B. Czirr, Nucl. Instrum. Methods **120**, 251 (1974).
6. D. L. Banner and J. B. Czirr, Nucl. Instrum. Methods **108**, 355 (1973).
7. J. C. Hopkins and G. Breit, Nucl. Data Tables, U. S. Atomic Energy Commission **A9**, 137 (1971).
8. L. Stewart, R. J. La Bauve, and P. G. Young, Evaluated Nuclear Data for Hydrogen with ENDF/BII Format, LA 4574, Los Alamos Scientific Laboratory (1971).
9. G. E. Hansen, private communication.
10. R. K. Smith, G. E. Hansen, and S. McGuire, unpublished data based on correcting and re-normalization of data from R. K. Smith, R. L. Hambel, and R. A. Nobles, Bull. Am. Phys. Soc. **2**, 196 (1957).
11. V. M. Pankratov, Sov. At. Energy **14**, 167 (1963).
12. P. H. White, J. Nucl. Energy **19**, 325 (1965).
13. I. Szabo, J. L. Leroy, J. P. Marquette, Soviet National Conference on the Physics of Neutrons, Kiev, May 1973.

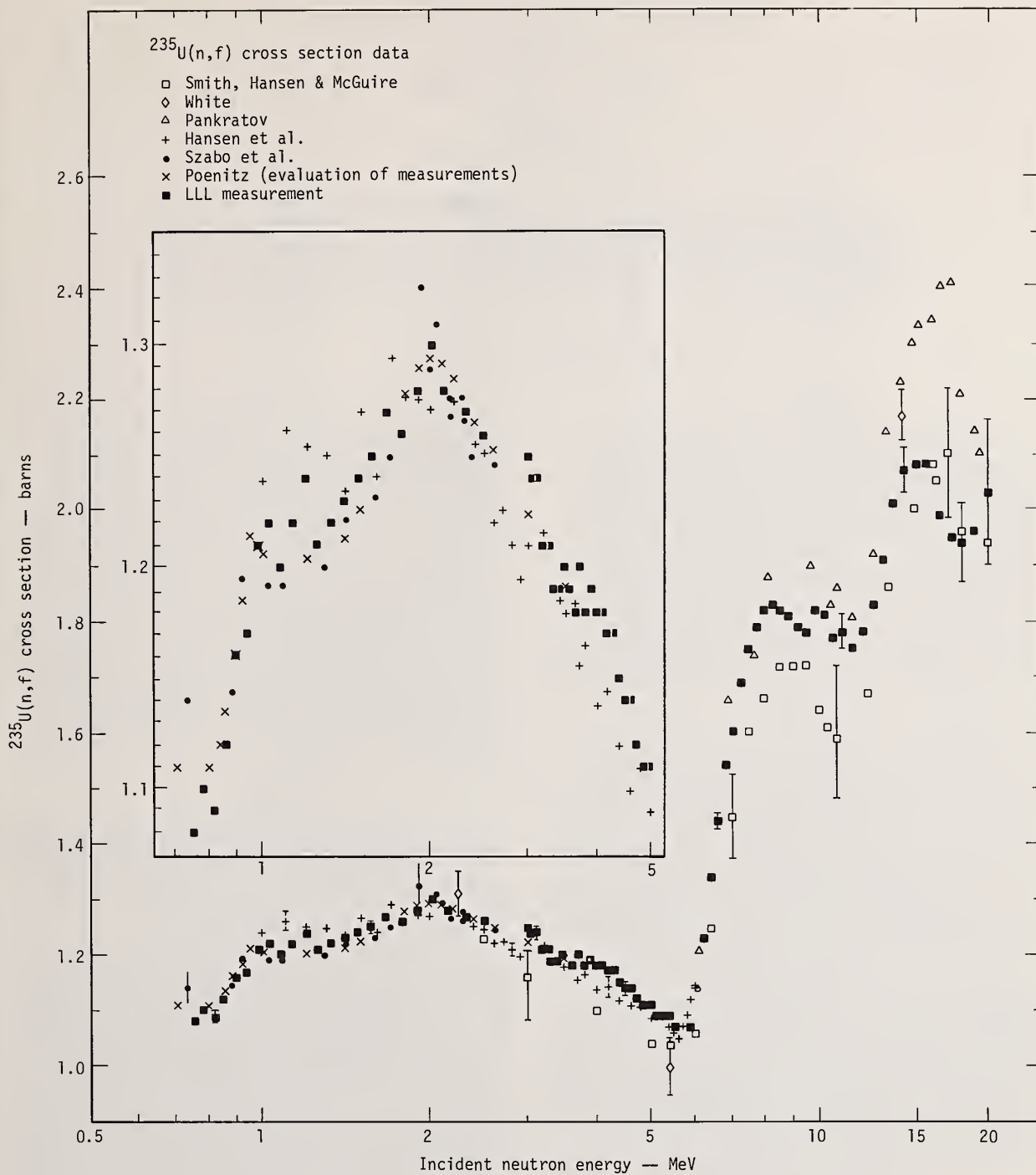


Fig. 5.  $^{235}\text{U}$  fission cross section data. Inset shows low-energy portion on expanded scale.

MEASUREMENT OF THE  $^{238}\text{U}$  CAPTURE CROSS SECTION SHAPE  
IN THE NEUTRON ENERGY REGION 20 TO 550 keV\*

R. R. Spencer  
Oak Ridge National Laboratory†  
Oak Ridge, Tennessee 37830  
and  
F. Kaeppler  
Kernforschungszentrum  
Karlsruhe, West Germany

The Karlsruhe 800  $\lambda$  liquid scintillator detector and 3 MV pulsed Van de Graaff were used to measure the shape vs. neutron energy of the  $^{238}\text{U}$  capture yield relative to a gold capture sample and relative to  $^{235}\text{U}$  fission. The resulting cross section shape computed from the gold capture cross section is consistent with that computed from a recent evaluation of the  $^{235}\text{U}$  fission cross section. Below 100 keV a significant intermediate structure is observed which corresponds to that in recent ORNL data.

( $\sigma_Y(^{238}\text{U})$  shape,  $E_n = 20\text{--}550$  keV)

### Introduction

The lack of agreement in the value and shape of the neutron capture cross section of  $^{238}\text{U}$  below 100 keV obtained in three recent high resolution time-of-flight measurements<sup>1-3</sup> suggests that further measurements of this important cross section may be of value. Since all three of the above mentioned experiments were carried out using linac produced neutrons it would seem that a measurement with the pulsed Van de Graaff making use of the  $^7\text{Li}[p,n]^7\text{Be}$  reaction for neutron production might provide a degree of experimental independence and in that way resolve previous difficulties. For example, the Van de Graaff technique has no interfering gamma flash and, due to the very fast time-of-flight method employed, background considerations are different and less complex.

The present measurements of the  $^{238}\text{U}$  capture yield were carried out using an 800  $\lambda$  liquid scintillator tank and the Karlsruhe, 3MV, pulsed Van de Graaff. Both a standard gold capture sample and a  $^{235}\text{U}$  fission chamber were employed as flux monitors in an attempt to obtain a partially independent verification of the measured capture yield shape. The gold reference technique has the advantage that at least some errors and corrections cancel to a high degree in this ratio measurement, while  $^{235}\text{U}$  offers one of the best studied cross sections for the neutron energy region under consideration. Due to the low binding energy for the neutron- $^{238}\text{U}$  system and the relatively high threshold for capture gamma-ray detection (2-2.5 MeV) required in the tank, the present measurements were considered to be a shape determination only and a supplemental experiment is planned to provide an "absolute" normalization. This will consist of calibrating a Moxon-Rae capture detector with gold and  $^{238}\text{U}$  samples in a thermal neutron beam at the Karlsruhe FR-2 Reactor and subsequent measurements with the same geometry at selected high energy points using monochromatic neutrons produced by the Van de Graaff.

### Experimental Detail

The shape measurements were carried out using a thick lithium target to produce a "white" neutron spectrum for energies below 300 keV and thin lithium targets giving "monochromatic" neutrons at higher energies. A 1-mm-thick sample of 99.76% purity  $^{238}\text{U}$ , a 1 mm thick gold sample and a carbon sample for background determination were cycled into the detector at intervals determined by the proton beam integrator. Flight paths for all samples were 203.3 cm. A  $^{235}\text{U}$ , gas scintillation, fission chamber operated with a flowing mixture of 85% Ar-15%  $\text{N}_2$  was placed in the

collimated neutron beam before the scintillator tank. This chamber was carefully adjusted so that its two  $^{235}\text{U}$  foils covered the entire beam. The  $^{235}\text{U}$  was electrosprayed onto thin VYNS backings.<sup>4</sup> Thus both fission fragments were observed in coincidence to discriminate completely against the natural  $\alpha$ -activity of the foils. Flight paths to the two fission foils were 92.15 and 98.75 cm. For the low energy (20-200 keV energy) run the accelerator was pulsed at a 500 kHz repetition rate, 1.66 MHz for a 200-300 keV run, and for the monochromatic neutron runs a 2.5 MHz rate was used. Capture events were stored in 256 channel (time) by 12 channel (pulse height) arrays and fission events for each sample were stored into 512 time channels. The scintillator tank is optically divided into quarters so that it was possible to carry out a "Voter" coincidence whereby a routing pulse was generated if simultaneous pulses occurred in any two of the quarters. Both "Voter" and "Non-voter" events were stored separately.

### Results

The "Voter" coincidence yields were used to derive the cross section ratios which are summarized in Tables I and II. Below 200 keV the gold-referenced data (Table I) were averaged over 10 and 20 keV intervals correspond to those required to obtain reasonable statistics in the  $^{235}\text{U}$  fission chamber. Due to the large uncertainty of the tank efficiency for  $^{238}\text{U}$  capture detection (at least  $\pm 10\%$ ) the data were normalized to a value of 200 mb for the interval 90-100 keV. This is the value reported in an evaluation of Sowerby et al.<sup>5</sup> Below 200 keV neutron energy the gold cross section of Kompe<sup>6</sup> was used to derive a  $^{238}\text{U}$  capture cross section. Above 200 keV a recent measurement of Le Rigoleur et al.<sup>7</sup> was used which agrees well with the data of Ref. 6 in the region above 80 keV where the two overlap. Recent measurements of Macklin et al.,<sup>8</sup> which are normalized by means of the "black resonance" technique at 4.9 eV, are in very good agreement ( $\sim \pm 3\%$ ) with data of Refs. 6 and 7 over the whole region and therefore add justification to the use of these particular experimental data. The data of Table I were corrected for tank detection of fission events from the 1/4%  $^{235}\text{U}$  impurity in the  $^{238}\text{U}$  sample. Calculations of the ratio of  $^{238}\text{U}$  to gold resonance self-protection and multiple scattering gave a constant result to within 0.3% over the whole energy range and were therefore neglected.

Table II shows the results of the  $^{235}\text{U}$  fission chamber referenced data. Again a normalization of 200 mb was chosen for the  $^{238}\text{U}$  capture in the 90-100 keV interval and, in addition, the  $^{235}\text{U}$  fission cross section evaluation of Sowerby et al.<sup>5</sup> was used. These



TABLE I. Gold Reference

E (keV)	$\frac{\sigma_Y(^{238}\text{U})}{\sigma_Y(^{197}\text{Au})}$	Std. Dev. (statistics) %	$\sigma_Y(^{197}\text{Au})$ mb	$\sigma_Y(^{238}\text{U})$ mb	Estimated $\frac{\Delta\sigma_Y}{\sigma_Y}(^{238}\text{U})$ ±%
20-30	0.8542	0.4	667	570	11
30-40	0.8704	0.3	546	475	11
40-50	0.8856	0.3	467	413.5	11
50-60	0.7823	0.4	409	320	11
60-70	0.7263	0.4	377	274	11
70-80	0.6635	0.4	357	237	11
80-90	0.6543	0.4	328	215	11
90-100	0.6430	0.5	311	200	10
100-120	0.6202	0.3	295	183	11
120-140	0.6015	0.4	277	167	11
140-160	0.5728	0.4	269	154	11
160-180	0.5694	0.5	258	147	11
180-200	0.5510	0.5	254	140	11
180-223	0.5689	1.0	251	143	11
223-264	0.5607	1.0	232	130	11
264-309	0.6104	1.0	216	132	11
317-373	0.6816	0.5	174	119	11
387-431	0.7872	0.5	158	124	11
423-467	0.7851	0.5	146	115	11
438-483	0.9092	0.5	142	129	11
483-529	1.0115	0.5	134.5	136	11
508-564	1.0735	0.5	125	134	11

data have been corrected for multiple scattering and resonance self-protection in the  $^{238}\text{U}$  sample, for the air scattering of the path between the fission chamber and the sample, and for the effect of the 1/4%  $^{235}\text{U}$  impurity.

#### Estimated Error

Since the estimated error given in Tables I and II is dominated by the 10% uncertainty assumed for the normalization value, a more detailed discussion of the remaining errors is necessary. For the gold-referenced result we get the following additional errors:

- (1) Uncertainty in shape of gold reference cross section: 3% to 0% from 20 keV to the normalization point and increasing to ~5% at 500 keV.
- (2) Uncertainty in background subtraction: 3% (20-30 keV), <1% (30-200 keV), 3% (200-300 keV), negligible for thin Li target runs (300-550 keV).
- (3) Resonance self-protection and multiple scattering: 3%.
- (4) Variation with neutron energy of spectrum fractions: 1.5%.
- (5) Uncertainty in flux averaging by sample cycling: <1% (20-200 keV), 2% (200-550 keV).
- (6) Uncertainty in counting loss correction: .5%.
- (7) Statistical uncertainty: given in Table I.

For the  $^{235}\text{U}$ -referenced results the following errors were estimated:

- (1) Uncertainty in reference cross section: 4.5-6.5%.
- (2) Uncertainty in background subtraction: same as for gold-referenced result.

- (3) Resonance self-protection and multiple scattering: 1%.

- (4) Variation of spectrum fraction: 1%.

- (5) Statistical uncertainty (dominated by fission chamber counts): given in Table II.

- (6) Uncertainty in air scattering correction: <.5%.

- (7) Uncertainty in counting loss correction: 1%.

#### Intermediate Structure

Comparison of the present gold-referenced results with that of de Saussure et al.<sup>3</sup> below 100 keV showed very good agreement in the  $^{238}\text{U}$  capture cross section shape. In addition, a significant intermediate structure in the cross section is confirmed. Figure 1 shows the present data and a replot of the high resolution data of Ref. 3 averaged to give the same energy intervals as the present measurements. The present results were normalized 5.4% higher for this plot. As can be seen in the figure, the correspondence between the two data sets is quite good.

#### Conclusions

Below 100 keV the shapes of the  $^{238}\text{U}$  capture cross section derived from both a gold reference cross section and a  $^{235}\text{U}$  fission cross section as reference are in excellent agreement with that observed in Ref. 3, are in fair agreement with Ref. 1 and deviate markedly from that of Ref. 2 below 50 keV. Within the errors of the reference cross sections used and with the presently chosen normalization, the data are in reasonable accord with activation measurements of Ryves et al.<sup>3</sup> in

TABLE II.  $^{235}\text{U}$  Fission Reference

E (keV)	$\frac{\sigma_Y(^{238}\text{U})}{\sigma_f(^{235}\text{U})}$	Std. Dev. (statistics) %	$\sigma_f(^{235}\text{U})$ mb	$\sigma_Y(^{238}\text{U})$ mb	Estimated $\frac{\Delta\sigma_Y}{\sigma_Y} (^{238}\text{U})$ ±%
20-30	0.2476	4	2148.3	532	12
30-40	0.2342	4	2010.7	471	12
40-50	0.2159	4	1908.4	412	12
50-60	0.1694	4	1871.4	317	12
60-70	0.1581	4	1808.8	286	12
70-80	0.1421	4	1714.1	243.5	12
80-90	0.1279	4	1681.0	215	12
90-100	0.1225	4	1632.2	200	10
100-120	0.1200	4	1542	185	12
120-140	0.1165	4	1493	174	12
140-180	0.1123	5	1424	160	13
180-223	0.1106	5	1343	148	13
223-264	0.1102	5	1295	143	13
264-309	0.0969	4	1262	122	12
317-373	0.0948	4	1223	116	12
387-431	0.0932	4	1180	110	12
423-467	0.0964	4	1162	112	12
438-483	0.1013	3	1155	117	12
483-529	0.1085	4	1134	123	12
508-564	0.1083	2	1126	122	12

The region of 157 keV and 231 keV. Below 100 keV, an intermediate structure is observed which could be of significance particularly in activation measurements of the capture cross section with 24 and 30 keV neutrons.

#### References

\*Work performed at Kernforschungszentrum, Karlsruhe.

†Operated by Union Carbide Corporation for the Energy Research and Development Administration.

1. M. C. Moxon, "The Neutron Capture Cross Sections of  $^{238}\text{U}$  in the Energy Region 0.5 to 100 keV," AERE-R-6074, U.K. Atomic Energy Authority, Harwell (1969).
2. S. J. Friesenhahn, et al., "The Neutron Capture Cross Sections of Molybdenum, Tantalum and  $^{238}\text{U}$ ," GA 10194, General Atomic (1970).
3. G. de Saussure, et al., Nuclear Science and Engineering 51, 385 (1973) and ORNL-TM-4059, Oak Ridge National Laboratory (1973).
4. V. Verdingh and K. F. Lauer, Nucl. Instr. Meth. 21, 16 (1963).
5. M. G. Sowerby, B. H. Patrick and D. S. Mather, AERE-R 7273, U.K. Atomic Energy Authority, Harwell (1973).
6. D. Kompe, Nucl. Phys. A 133, 513 (1969).
7. C. Le Rigoleur, et al., CEA-N-1662 (1973).
8. R. L. Macklin, et al., to be published in Phys. Rev. C, April 1975.
9. T. B. Ryves, et al., J. Nucl. Energy 27, 519 (1973).

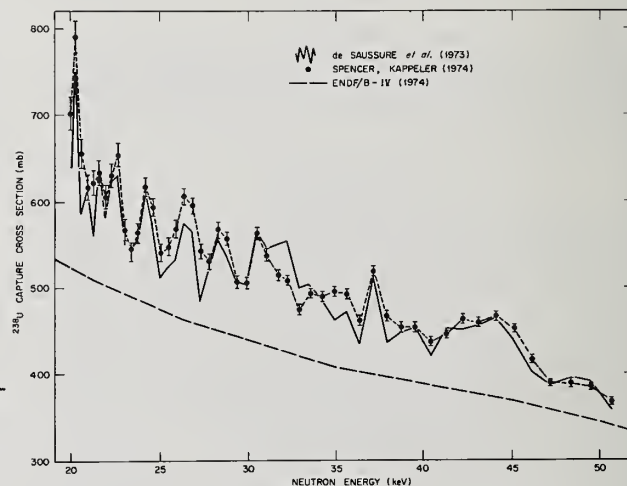


Fig. 1. Intermediate Structure in  $\sigma_Y(^{238}\text{U})$ .

R. B. Perez and G. de Saussure

Oak Ridge National Laboratory  
Oak Ridge, Tennessee 37830

Recent measurements of the  $^{238}\text{U}$  neutron capture cross section show large fluctuations in the unresolved resonance region. To test whether or not the observed long-range fluctuation of the neutron capture represent departures from the compound nuclear model, the Wald-Wolfowitz runs and correlation tests were applied to the  $^{238}\text{U}$  neutron capture data obtained at ORELA. The Wald-Wolfowitz runs test deals with the statistic,  $R$ , which is the number of unbroken sequences of data points above or below a given reference line. This statistic is to be compared with the expected value of runs  $E(R) \pm \sigma(R)$  arising from randomly distributed data. In the correlation test we have computed the first serial correlation coefficient of the data as well as its expected value and variance for a set of random data. In both tests one computes the probability,  $P$ , for the given statistical entity to depart from its expected value by more than  $\epsilon$  standard deviations. Both tests confirm the presence of intermediate structure between 5 and 100 keV. The range of the structure far exceeds the width of the experimental resolution and level widths.

(  $^{238}\text{U}$  capture cross section; intermediate structure; doorway states)

### Introduction

There is considerable experimental evidence of large fluctuations of the  $^{238}\text{U}(n,\gamma)$  cross section in the unresolved resonance region.<sup>1,2</sup> Similar structure was first reported by Kopsh, Cierjacks, and Kirouac<sup>3</sup> in the total  $^{238}\text{U}$  neutron cross section between .5 and 4.35 MeV. These observed fluctuations are wider than the sharp resonances associated with the compound nucleus levels and narrower than the broad structure due to the energy dependence of the penetration coefficients. They represent departures from the statistical nuclear model in localized energy regions, hence forming an intermediate structure, rather unexpected in the framework of the compound nucleus model.

Intermediate structure in the fission cross section of various fissile nuclei is by now well known,<sup>4-7</sup> as well as its interpretation<sup>8,9</sup> in terms of Strutinsky's double humped barrier.<sup>10</sup>

Although subthreshold fission yields have been found in the case of the  $^{238}\text{U}$  nucleus,<sup>11</sup> The fact that both the capture and total  $^{238}\text{U}$  cross sections exhibit intermediate structure leads one to hypothesize that the observed structure is indeed due to nuclear dynamics phenomena in the entrance (neutron) channels, such as "doorway" states.

The problem of extracting the intermediate structure from the observed cross section has been given considerable attention in the past.<sup>13</sup> James<sup>14</sup> and Moore<sup>15</sup> were the first to introduce the use of nonparametric statistics<sup>16</sup> for the detection of intermediate structure in the fissile nuclei. Extensive studies in this field have been also performed by Baudinet-Robinet and Mahaux.<sup>17</sup> We present here the results of some statistical tests performed on the  $^{238}\text{U}(n,\gamma)$  cross section in which the Wald-Wolfowitz<sup>16</sup> nonparametric statistics were utilized.

### Statistical Treatment of the $^{238}\text{U}$ Capture Cross Section

The Wald-Wolfowitz<sup>16</sup> runs and correlation tests were applied to the  $^{238}\text{U}$  neutron capture data obtained at ORELA.<sup>1</sup> The Wald-Wolfowitz runs test deals with the statistic,  $R$ , which is the number of unbroken sequences of data points above or below a given reference line. This test evaluates the expected number of runs  $E(R)$  from randomly distributed data, as well as the corresponding variance  $\sigma^2(R)$ . It is then shown that the ratio

$$\epsilon_R = [|R - E(R)| - 1/2]/\sigma(R)$$

follows a normal probability distribution. The evaluation of the test proceeds by computing the probability,  $P(\epsilon_R)$ , that a ratio equal or larger than  $\epsilon_R$  could arise from the sampling of random data.

The Wald-Wolfowitz correlation test is based on the computation of the usual autocorrelation function of the data with some modification, so that "end effects" are mitigated. Wald and Wolfowitz also give the distribution of the correlation function for random data. The end result of this test is the ratio  $\epsilon_c$ , between the particular serial correlation coefficient obtained from the actual data and its value for a set of random data, as well as the probability  $P(\epsilon_c)$ .

The  $^{238}\text{U}(n,\gamma)$  cross section obtained at ORELA (40 m flight station) was averaged over energy intervals varying from 600 eV up to 3 keV in the region between 5 and 100 keV. The lower value of 600 eV is about six times the total experimental and Doppler resolution of the measurement at 100 keV. These data were then fitted to an average cross section (with s-wave and p-wave contributions) according to the expression

$$\begin{aligned} \langle \sqrt{E} \sigma_\gamma(E) \rangle &= g_1 \frac{A_0}{\langle \Gamma_0(E_n) \rangle} R_{0n}^\gamma(E_n) + \left( \frac{\rho^2}{1 + \rho^2} \right) \\ &\times A_1 \left[ g_1 \frac{R_{1n}^\gamma(E_n)}{\langle \Gamma_1(E_n) \rangle} + g_2 \frac{R_{2n}^\gamma(E_n)}{\langle \Gamma_2(E_n) \rangle} \right] \end{aligned} \quad (2)$$

where

$$A_0 = (4.125 \times 10^6) \langle \Gamma_\gamma \rangle S_0$$

( $S_0$  = s-wave strength function)

$$A_1 = (4.125 \times 10^6) \langle \Gamma_\gamma \rangle S_1$$

( $S_1$  = p-wave strength function)

$$\langle \Gamma_0(E_n) \rangle = \langle \Gamma_\gamma \rangle + (E_n)^{1/2} \langle \Gamma_{0n}^0 \rangle$$

$$\langle \Gamma_1(E_n) \rangle = \langle \Gamma_\gamma \rangle + \left( \frac{\rho^2}{1 + \rho^2} \right) (E_n)^{1/2} \langle \Gamma_{1n}^0 \rangle$$

$$\langle \Gamma_2(E_n) \rangle = \langle \Gamma_\gamma \rangle + \left( \frac{\rho^2}{1 + \rho^2} \right) (E_n)^{1/2} \langle \Gamma_{2n}^0 \rangle$$

$$\rho = 1.8473 \times 10^{-3} (E_n)^{1/2}, \text{ and}$$

$g_0, g_1, g_2$  = statistical weight factors.



Table 1. Input Nuclear Parameters for the Average Cross Section Calculation and the Resulting s-wave and p-wave Strength Functions.

J	$\ell$	$g_J$	$\Gamma_{0n}^{(a)}$ (eV)	$\Gamma_{1n}^{(a)}$ (eV)	$\Gamma_{2n}^{(a)}$ (eV)	Strength Function ( $\times 10^{-4}$ )
1/2	0	1	.0021	-	-	1.31
1/2	1	1	-	.00298	-	1.72
3/2	1	2	-	-	.00164	1.72

<sup>a</sup>ENDF/B-IV values (ref 19) with  $\langle \Gamma_Y \rangle = .0235$  eV.

The average radiation width,  $\langle \Gamma_Y \rangle$ , and the neutron widths for the s-wave and p-wave components,  $\langle \Gamma_{0n} \rangle$ ,  $\langle \Gamma_{1n} \rangle$ , and  $\langle \Gamma_{2n} \rangle$ , are given in Table 1. The statistical fluctuation factors  $R_{0n}^Y$ ,  $R_{1n}^Y$ , and  $R_{2n}^Y$  (ref 18) were computed at each neutron energy. The values obtained for the  $S_0$  and  $S_1$  strength functions are also given in Table 1. These values are higher than the ENDF/B-IV<sup>19</sup> values of  $S_0 = 1.05 \times 10^{-4}$  and  $S_1 = 1.57 \times 10^{-4}$  reflecting the higher values for the  $^{238}\text{U}$  capture cross section obtained at ORELA and the assumed  $\langle \Gamma_Y \rangle = .0235$  eV.

The fit obtained from Eq. (2) is shown in Fig. 1 (with some statistical error flags at selected points). Also shown in the figure is the mock-up  $^{238}\text{U}(n, \gamma)$  cross section computed by Monte-Carlo techniques on the basis of the ENDF/B-IV<sup>19</sup> average resonance parameters and s-wave strength function. The mock-up cross section data were also fitted by Eq. (2) with only the s-wave contribution. Inspection of Fig. 1 already reveals quite a deal of structure of the cross section about its average value for the experimental data, as compared with the "good" fit in the case of the capture cross section computed on the basis of the statistical nucleus model.

The average cross section fit was utilized as the reference line for the Wald-Wolfowitz runs test. For the correlation test the data were divided through by the average fit to remove the correlation bias introduced by the energy dependence of the s-wave and p-wave penetration factors.

The results of the statistical tests are given in Table 2. Both tests show that there is a probability of less than  $10^{-5}$  for the average ratio  $\langle \epsilon_c \rangle = 5.1$  and less than  $10^{-4}$  for the average ratio  $\langle \epsilon_R \rangle = 4.1$  to occur from the sampling of random data. Essentially, the Wald-Wolfowitz nonparametric statistics test whether or not a given sample exhibits longer correlations than the expected from a set of random data. When applied to the mock-up cross section and averaged over energy intervals larger than the level widths, the results of Table 2 merely indicate that the compound nuclear model behaves from the viewpoint of correlation length similarly to a set of random data. Hence, the present results are to be interpreted as showing the presence of long-range correlations which represent departures from the compound nucleus model.

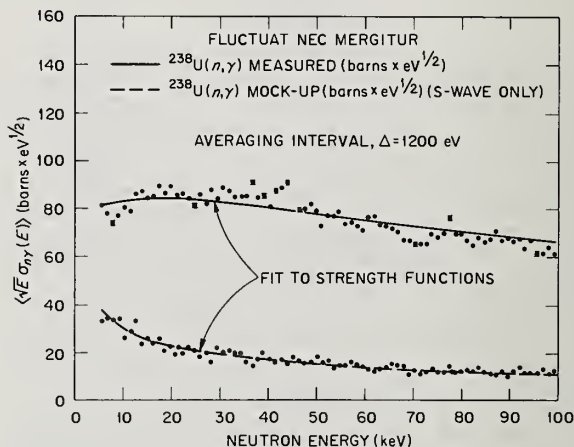


Fig. 1. Fit of the  $^{238}\text{U}(n, \gamma)$  Cross Section Measured and Mocked-up to the strength functions.

Table 2. Results of the Wald-Wolfowitz Correlation and Runs Tests for the Measured and Mockup  $^{238}\text{U}$  Capture Cross Section

Width (keV)	Capture (Measured)				(Capture (Mockup))			
	$\epsilon_c$	$P(\epsilon_c)$	$\epsilon_R$	$P(\epsilon_R)$	$\epsilon_c$	$P(\epsilon_c)$	$\epsilon_R$	$P(\epsilon_R)$
.6	5.9	$<10^{-5}$	4.5	$<10^{-5}$	.52	.60	.03	.98
.9	6.1	$<10^{-5}$	3.9	$2.7 \times 10^{-3}$	.20	.60	.96	.34
1.0	5.9	$<10^{-5}$	4.6	$<10^{-5}$	.37	.71	.68	.50
1.2	6.2	$<10^{-5}$	5.6	"	.65	.52	.34	.73
1.5	5.3	$<10^{-5}$	4.8	"	.31	.76	.002	.99
1.8	2.2	$2.7 \times 10^{-2}$	3.6	$<2.7 \times 10^{-3}$	.97	.33	1.11	.27
2.0	4.9	$<10^{-5}$	3.8	"	.22	.82	1.2	.23
3.0	3.9	$2.7 \times 10^{-3}$	1.8	$7.2 \times 10^{-2}$	1.1	.27	.006	.99

## Theoretical Interpretation

The fact that intermediate structure has been observed in both the  $^{238}\text{U}$  capture and total cross sections strongly favors the "door-way" states hypothesis. These short-lived states at the entrance channel interact via a residual interaction with the compound nucleus states. It can be shown<sup>20</sup> that the  $(n,\gamma)$  T-matrix component is given by

$$T_{n\gamma} = i \sum_{\lambda} \frac{g_{\lambda n} \Gamma_{\lambda\gamma}^{1/2}}{D_{\lambda}(E) - \phi_{\lambda}(E)}, \quad (3)$$

with the complex neutron width given by

$$g_{\lambda n} = \Gamma_{\lambda n}^{1/2} \left[ 1 - \sum_{\mu} \left( \frac{\Gamma_{\mu n}}{\Gamma_{\lambda n}} \right)^{1/2} \left( \frac{W_{\lambda\mu}}{D_{\mu}} \right) \right], \quad (4)$$

and

$$\phi_{\lambda}(E) = \sum_{\mu} \frac{|W_{\lambda\mu}|^2}{D_{\mu}}, \quad (5)$$

where

$$D_{\lambda} = (E_{\lambda} - E) + \frac{i}{2} \Gamma_{\gamma}, \quad (6)$$

$$D_{\mu} = (E_{\mu} - E) + \frac{i}{2} \Gamma_{\mu}, \quad (7)$$

$$W_{\lambda\mu} = \text{residual interaction (eV)}, \quad (8)$$

and the other symbols have the usual meaning. The sub-index,  $\lambda$ , goes over the compound nucleus states, and the subindex,  $\mu$ , classifies the "doorway" states.

On the basis of the previous results (valid only for  $|W_{\lambda\mu}/D_{\mu}| \ll 1$ ) the average cross section is again given by Eq. (2) in which the s-wave and p-wave strength functions are multiplied by the energy-dependent "modulation" factors  $M_0(E)$  and  $M_1(E)$ , respectively, where

$$M_{\ell}(E) = \left( 1 + \sum_{\mu} |D_{\mu}|^{-4} A_{\mu}^{\ell} \right) / \left( 1 + \sum_{\mu} |D_{\mu}|^{-2} B_{\mu}^{\ell} \right) \quad (9)$$

$$A_{\mu}^{\ell} = \frac{1}{2} \left[ \Gamma_{\mu}^{(\ell)} \right]^2 \Gamma_{0\mu n}^{(\ell)} \left\langle \frac{|W_{\lambda\mu}|^2}{\Gamma_{\lambda n}^{(\ell)}} \right\rangle_{\text{compound nucleus}} \quad (\text{eV}^4) \quad (10)$$

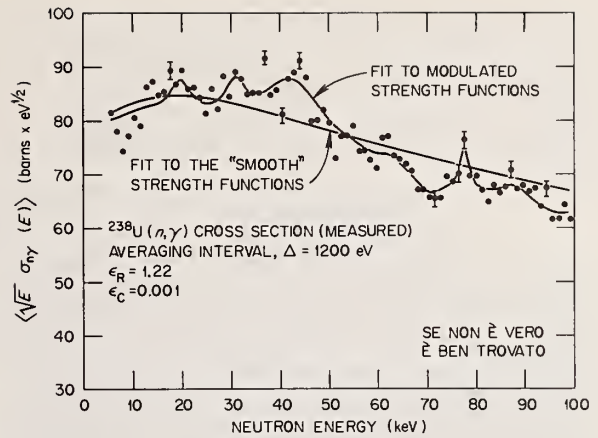


Fig. 2. Fit of the  $^{238}\text{U}(n,\gamma)$  Cross Section Measured to the Modulated Strength Function.

$$B_{\mu}^{\ell} = \Gamma_{\mu}^{(\ell)} \left\langle \frac{|W_{\lambda\mu}|^2}{\Gamma_{\lambda}^{(\ell)}} \right\rangle_{\text{compound nucleus}} \quad (\text{eV}^2) \quad (11)$$

$\ell = 0, 1$ ,

and the brackets indicate an average over the compound nucleus states. The neutron widths  $\Gamma_{0\lambda n}^{(\ell)}$  and  $\Gamma_{0\mu n}^{(\ell)}$  are reduced neutron widths and the total level widths  $\Gamma_{\lambda}^{(\ell)}$  and  $\Gamma_{\mu}^{(\ell)}$  are computed at the level energies.

These modulation factors arise from the fact that the interaction between the compound nucleus states and the doorway states "modulates" both the neutron widths and the average level spacing.

A cavalier attempt has been made to extract the main features of the intermediate structure by fitting the average cross section of Eq. (2) with "modulated" strength functions. Although one expects both the s-wave and p-wave strength functions to be modulated, we arbitrarily changed only the s-wave contribution. The results of this procedure are shown in Fig. 2 together with the "smooth" strength function fit. The goodness of fit, expressed in terms of the chi-square test, improved by a factor close to 100 between the "smooth" and "modulated" fits. The modulated fit was then used as the reference line for the Wald-Wolfowitz runs test. For the correlation test, the data were divided by the modulated fit. The results of both statistical tests are given in Table 3 and indicate that the intermediate

Table 3. The Wald-Wolfowitz Runs and Correlation Tests for the  $^{238}\text{U}(n,\gamma)$  Cross Section After Removal of the Intermediate Structure.

Width (keV)	$\epsilon_R$			$\epsilon_c$		
	Mock-up	Exp. (a)	Reduced (b)	Mock-up	Exp. (a)	Reduced (b)
.6	.03	4.5	.40	.52	5.9	.64
.9	.96	3.9	.60	.20	6.1	.15
1.0	.68	4.6	.03	.37	5.9	.44
1.2	.34	5.6	.001	.65	6.2	1.22
1.5	.002	4.8	.72	.31	5.3	.15
1.8	1.11	3.6	1.64	.97	2.2	.08
2.0	1.2	3.8	.003	.22	4.9	.64
3.0	.006	1.8	.006	1.1	3.9	1.1

<sup>a</sup>Measured  $^{238}\text{U}(n,\gamma)$  cross section.

<sup>b</sup>Measured  $^{238}\text{U}(n,\gamma)$  cross section after removal of the intermediate structure.

structure had been adequately described. The assignment of the doorway levels to the s-wave strength function only prevents one from giving too much credibility to the level parameters obtained for the intermediate structure. The present results tend, however, to indicate an average level spacing of around 9 keV and reduced neutron widths averaging 40 eV.

### Conclusions

The two statistical tests applied to the measured  $^{238}\text{U}(n,\gamma)$  cross sections give, with a high significance level, strong support to the presence of intermediate structure in the neutron capture of the  $^{238}\text{U}$  nucleus. Although we cannot exclude the possibility for at least a fraction of this structure originating from sub-threshold fission phenomena, the presence of large local fluctuations in the  $^{238}\text{U}$  total cross section<sup>3</sup> gives support to the presence of doorway states in the reaction entrance channel.

From the theoretical results referred to here, one concludes that the intermediate structure [see Eq. (9)] is due not only to local enhancements of the reaction widths, but also to rapid fluctuations of the average level spacing.

The Wald-Wolfowitz correlation and runs tests are also valuable in connection with the fitting of the intermediate structure as they can be used as an "added" goodness of fit test.

As we have discussed earlier, not too much physical significance can be attached to the level locations and widths of the detected doorway levels. However, fits, like the ones described here, do afford a method of representing the average behavior of the  $^{238}\text{U}$  capture cross section in the unresolved region. This may prove valuable for reactor calculations.<sup>21</sup>

Studies similar to this should be applied to high resolution measurements of capture cross section in other elements such as thorium, gadolinium, and other nonfissile uranium isotopes, in order to ascertain whether there is a systematics that can be deduced regarding intermediate structure phenomena. In this regard one should mention the work of Macklin<sup>22</sup> who also showed the presence of intermediate structure in the gold capture cross section.

### Acknowledgment

The authors would like to thank Professor H. Feshbach for several illuminating discussions.

### References

- \* Research sponsored by the Energy Research and Development Administration under contract with the Union Carbide Corporation.
- <sup>1</sup>G. de Saussure *et al.*, *Nucl. Sci. Eng.* 51, 385 (1973).
- <sup>2</sup>R. R. Spencer and F. Kappeler, *Proc. Specialist Meeting on Resonance Parameters of Fertile Nuclei,  $^{232}\text{Th}$ ,  $^{238}\text{U}$ ,  $^{240}\text{Pu}$ , and  $^{239}\text{Pu}$* , Saclay, May 1974 (to be published).
- <sup>3</sup>D. Kopsch, S. Cierjacks, and G. J. Kirouac, *Sec. Conf. on Nuclear Data for Reactors*, vol. 2, 1970, IAEA.
- <sup>4</sup>D. Paya *et al.* *Proc. Dubna Conf.*, 1968, SMNF 624/68.
- <sup>5</sup>E. Migneco and J. P. Theobald, *Nucl. Phys.* A112, 603 (1968).
- <sup>6</sup>B. H. Patrick *et al.*, *J. Nucl. Energy* 24, 269 (1970).
- <sup>7</sup>C. D. Bowman *et al.*, *Sec. Conf. on Nuclear Data for Reactors*, vol. 2, 1970, IAEA.
- <sup>8</sup>H. Weigmann, *Zeitschrift fur Physik* 214, 7 (1968).
- <sup>9</sup>J. E. Lynn, AERE-R5891, Sept. 1968.
- <sup>10</sup>V. M. Strutinsky, *Nucl. Phys.* A95, 420 (1967).
- <sup>11</sup>M. G. Silvert and D. W. Bergen, *Phys. Rev. C* 4, 200 (1971). Also R. C. Block *et al.* *Phys. Rev. Letters* 31, 247 (1973).
- <sup>12</sup>H. Feshbach, A. K. Kerman, and R. H. Lemmer, *Ann. Phys.* (N. Y.) 41, 230 (1967).
- <sup>13</sup>R. B. Perez *et al.*, *Symp. Phys. and Chemistry of Fission*, SM-122/21, p. 283, 1969, IAEA.
- <sup>14</sup>G. D. James, *Nucl. Phys.* A170, 308 (1971).
- <sup>15</sup>M. S. Moore, *Statistical Properties of Nuclei*, ed. J. B. Garg, Plenum, New York, 1972, p. 55.
- <sup>16</sup>A. Wald, and J. Wolfowitz, *Annals Math. Stat.* 11, No. 2 (1940). Also *Documenta Geigy, Scientific Tables, Geigy Pharmaceuticals*, ed. K. Diem, Ardsley, New York.
- <sup>17</sup>Y. Baudinet-Robinet and C. Mahaux, *Phys. Rev. C*, 9, 723 (1974).
- <sup>18</sup>J. J. Schmidt, KFK120 (EANDC-E-35U), B43 (1966).
- <sup>19</sup>CSEWG, ENDF/B-IV completed in July 1974.
- <sup>20</sup>R. B. Perez and G. de Saussure, work in preparation.
- <sup>21</sup>C. R. Weisbin, private communication, 1975.
- <sup>22</sup>R. L. Macklin *et al.*, *Phys. Rev. C*, to be published, April 1975.



A DIRECT COMPARISON OF DIFFERENT EXPERIMENTAL TECHNIQUES FOR MEASURING  
NEUTRON CAPTURE AND FISSION CROSS SECTIONS FOR  $^{239}\text{Pu}^*$

R. Gwin, L. W. Weston, J. H. Todd, R. W. Ingle, and H. Weaver

Oak Ridge National Laboratory  
Oak Ridge, Tennessee 37830

A comparison of the results of two different experimental methods of measuring the neutron absorption and fission cross sections for  $^{239}\text{Pu}$  is made. These measurements were normalized at thermal energy and extend to 200 keV. The ratio of the neutron capture to fission cross section for  $^{239}\text{Pu}$  derived in these two experiments is shown to be in good agreement.

( $^{239}\text{Pu}$ ; fission, absorption; measurement; comparison; cross sections)

### Introduction

Measurements of the neutron absorption  $\sigma_a$  and neutron fission  $\sigma_f$  cross sections, and thereby the neutron capture  $\sigma_c$  cross section, have been performed at ORNL using two different techniques. These experiments covered the neutron energy region from 0.02 eV to 200 keV and represent a part of the experimental program on  $^{239}\text{Pu}$  at ORNL. Two different techniques were used to serve as a guide for further experimentation at ORNL and to provide a measure of confidence in the measurements of  $\sigma_c/\sigma_f$ .

Several aspects of the two experiments were essentially the same, such as the measurement of the neutron flux; however, the performance and analysis of these experiments were independent as well as the techniques for observing fission and absorption events. The values  $\sigma_a$ ,  $\sigma_f$ , and  $\sigma_c/\sigma_f$  derived in these experiments are given in this paper along with the respective values from ENDF/B-IV MAT-1264.<sup>1</sup> Also included are the values  $\sigma_c/\sigma_f$  for  $^{239}\text{Pu}$  from the evaluation of Sowerby and Konshin.<sup>2</sup>

### Similarities in the Two Experiments

Both of the experiments described in this paper were performed at ORNL using the Oak Ridge Electron Linear Accelerator (ORELA) to produce the source of neutrons in bursts from 5 to 30 nsec wide. The energy of the neutrons was measured by the time-of-flight technique. The neutron flux was measured in each experiment using a parallel plate (pulse) ionization chamber filled with  $\text{BF}_3$ . The prescription for the  $^{10}\text{B}(n,\alpha)$  cross section used to extract the energy dependence of the neutron flux was that given in ENDF/B-III and was the same as that suggested by Sowerby and Patrick.<sup>3</sup> The energy range 0.02 eV to 200 keV was covered in one run in both experiments; this approach eliminates the problems encountered in internormalizing runs obtained under different experimental conditions and which cover a common but narrow energy interval. Normalization of the present data sets was performed in the thermal energy region using values of  $\sigma_f$  and  $\sigma_a$  from ENDF/B-III for  $^{239}\text{Pu}$ .

### Description of the Two Experimental Methods

One experiment (method 1) was performed flight path of about 20 m. A 3-in. diameter  $^{239}\text{Pu}$  sample having a mass of 0.24 g/cm<sup>2</sup> was used. Fission events were recorded using pulse-shape discrimination to detect fission neutrons and a separate detector "total energy detector" (similar to a Moxon-Rae detector) was used to measure the prompt gamma rays following neutron absorption in the sample. In the other experiment (method 2), the  $^{239}\text{Pu}$  (0.03 g/cm<sup>2</sup>) was contained in a multi-plate pulse ionization chamber. A large liquid scintillator was used with a 40 m flight

path to detect the prompt gamma rays resulting from neutron absorption in the sample, and pulses from this scintillator system in coincidence with pulses from the fission chamber were defined as fissions.

Auxiliary experiments were performed to test various features of the experiments. For example, the neutron (pulse-shape discrimination) detector was run in coincidence with the  $^{239}\text{Pu}$  fission chamber in a series of measurements.<sup>4</sup> Also, measurements of the neutron flux were made using  $^6\text{Li}$  glass.

### Presentation of the Data

The table shows the average values of  $\sigma_a$ ,  $\sigma_f$ , and  $\sigma_c/\sigma_f$  derived from the two independent experiments. Also shown are the cross sections from ENDF/B-IV and the values  $\sigma_c/\sigma_f$  for  $^{239}\text{Pu}$  taken from the evaluation of Sowerby and Konshin. In comparing the data shown in the table an average difference refers to the sum over a number of energy intervals of the percent difference between the values divided by the number of intervals. In the cases shown in the table where explicit results for  $\sigma_c$  and  $\sigma_f$  are not given values of  $\sigma_c/\sigma_f$  for larger intervals than those in the table are obtained using  $\sigma_a$  from ENDF/B-IV along with the appropriate  $\sigma_c/\sigma_f$  to yield  $\sigma_c$  and  $\sigma_f$  for each subinterval. These latter values of  $\sigma_c$  and  $\sigma_f$  are then averaged over the large interval. The uncertainties shown for  $\sigma_f$  and  $\sigma_a$  in the table for method 2 represent the precision of the experiments. For  $\sigma_c/\sigma_f$  the uncertainties shown include the known uncertainties except those due to errors in the cross sections below 0.4 eV used in the normalization. An examination of the table shows that the results  $\sigma_c/\sigma_f$  from the two experiments overlap within their uncertainties, and in fact about 70% of the results for method 1 fall within the uncertainty shown for method 2.

The results of two experiments for  $\sigma_f$  and  $\sigma_a$  agree within 0.7% and 0.3%, respectively, for the neutron energy range from 0.1 to 1.0 keV, and the average difference between the two results for  $\sigma_f$  and  $\sigma_a$  are 1.9% and 2.9%, respectively. Above 1 keV the neutron cross sections obtained in method 1 are about 4% lower than those derived in method 2. This is thought to be due to difficulties in the measurement of the neutron flux for method 1 at the time of these experiments.

For the 28 intervals shown in the table, the present two experimental values of  $\sigma_c/\sigma_f$  have an average difference of about 6%. A comparison of the average values of  $\sigma_c/\sigma_f$  obtained in the present experiments for the intervals 0.1 to 1, 1 to 10, and 10 to 100 keV shows that they differ by 2.3, 1.5, and 2.3%, respectively, and the results for method 2 are higher in each

Average Neutron Cross Sections for  $^{239}\text{Pu}$ , 0.1 to 200 keV

$$\bar{\sigma} = \frac{\int_{E1}^{E2} \sigma(E) dE}{E2 - E1}$$

E1 - E2 (keV)	Method 2 (a)				Method 1 (b)				Sowerby and Konshin		ENDF/B-IV Mat 1264	
	$\bar{\sigma}_f$ barns	$\bar{\sigma}_a$ barns	$\bar{\sigma}_c/\bar{\sigma}_f$ (d)	$\bar{\sigma}_c/\bar{\sigma}_f$ (d)	$\bar{\sigma}_f$ barns	$\bar{\sigma}_a$ barns	$\bar{\sigma}_c/\bar{\sigma}_f$ (d)	$\bar{\sigma}_c/\bar{\sigma}_f$ (d)	$\bar{\sigma}_f$ barns	$\bar{\sigma}_a$ barns	$\bar{\sigma}_c/\bar{\sigma}_f$ (d)	$\bar{\sigma}_c/\bar{\sigma}_f$ (d)
0.1 - 0.2	17.96 ± .04	33.66	0.87 ± .015	.871 ± .052	18.41	34.45	.871 ± .052	.845 ± .077	18.20	34.97	.845 ± .077	.92
0.2 - 0.3	17.90 ± .05	34.69	0.94 ± .010	.927 ± .056	17.77	34.24	.927 ± .056	.912 ± .094	17.50	34.67	.912 ± .094	.98
0.3 - 0.4	8.48 ± .03	18.31	1.16 ± .014	1.15 ± .069	8.43	18.12	1.15 ± .069	1.15 ± .099	8.54	18.07	1.15 ± .099	1.12
0.4 - 0.5	9.40 ± .05	13.56	0.44 ± .013	.426 ± .026	8.47	13.50	.426 ± .026	.483 ± .058	9.67	14.04	.483 ± .058	.45
0.5 - 0.6	15.46 ± .09	26.54	0.72 ± .040	.718 ± .043	15.64	26.87	.718 ± .043	.704 ± .069	15.73	27.10	.704 ± .069	.72
0.6 - 0.7	4.55 ± .03	11.57	1.54 ± .040	1.488 ± .089	4.38	10.90	1.488 ± .089	1.673 ± .133	4.57	11.29	1.673 ± .133	1.47
0.7 - 0.8	5.34 ± .07	10.52	0.97 ± .017	.890 ± .053	5.54	10.47	.890 ± .053	.973 ± .087	5.55	10.68	.973 ± .087	.93
0.8 - 0.9	5.10 ± .03	9.30	0.82 ± .025	.790 ± .047	5.02	8.99	.790 ± .047	.778 ± .101	5.20	9.50	.778 ± .101	.83
0.9 - 1.0	7.83 ± .14	13.23	0.70 ± .026	.675 ± .041	8.02	13.43	.675 ± .041	.717 ± .077	8.11	13.81	.717 ± .077	.70
1 - 2	4.52 ± .02	8.31	0.84 ± .013	.802 ± .048	4.45	8.02	.802 ± .048	.927 ± .093	4.60	8.37	.927 ± .093	.82
2 - 3	3.32	6.63	1.00	.972 ± .058	3.25	6.41	.972 ± .058	1.108 ± .103	3.40	6.76	1.108 ± .103	.99
3 - 4	3.04	5.24	0.72 ± .066	.738 ± .043	2.95	5.13	.738 ± .043	.895 ± .086	3.08	5.42	.895 ± .086	.76
4 - 5	2.37 ± .01(e)	4.44	0.87 ± .040	.831 ± .050	2.35	4.30	.831 ± .050	.821 ± .079	2.41	4.88	.821 ± .079	.86
5 - 6	2.32 ± .02(e)	4.23(e)	0.82 ± .046(e)	.807 ± .048	2.13	3.85	.807 ± .048	.867 ± .084	2.27	4.14	.867 ± .084	.82
6 - 7	2.05 ± .02	3.68	0.79 ± .040	.745 ± .045	2.01	3.51	.745 ± .045	.816 ± .086	2.06	3.65	.816 ± .086	.77
7 - 8	2.11 ± .01	3.45	0.64 ± .022	.642 ± .038	2.03	3.33	.642 ± .038	.629 ± .073	2.09	3.44	.629 ± .073	.65
8 - 9	2.28 ± .01	3.51	0.54 ± .022	.537 ± .032	2.06	3.17	.537 ± .032	.575 ± .064	2.17	3.35	.575 ± .064	.54
9 - 10	1.92 ± .02	2.97	0.55 ± .022	.606 ± .036	1.76	2.83	.606 ± .036	.617 ± .067	1.95	3.08	.617 ± .067	.58
10 - 20	1.78 ± .02	2.63	0.48 ± .022	.486 ± .029			.486 ± .029	.466 ± .05	1.77	2.64	.466 ± .05	.50
20 - 30	1.64 ± .02	2.22	0.35 ± .018	.332 ± .066			.332 ± .066	.373 ± .04	1.67	2.26	.373 ± .04	.36
30 - 40	1.61 ± .01	2.09	0.30 ± .041	.247 ± .049			.247 ± .049	.296 ± .03	1.61	2.07	.296 ± .03	.28
40 - 50	1.54 ± .02	1.94	0.26 ± .020	.254 ± .051			.254 ± .051	.242 ± .03	1.59	2.01	.242 ± .03	.27
50 - 60	1.66 ± .01	2.03	0.23 ± .020	.220 ± .044			.220 ± .044	.206 ± .03	1.62	2.06	.206 ± .03	.26
60 - 70	1.62 ± .03	1.99	0.23 ± .025	.215 ± .043			.215 ± .043	.182 ± .025	1.61	1.99	.182 ± .025	.23
70 - 80	1.64 ± .04	1.95	0.19 ± .025	.200 ± .040			.200 ± .040	.165 ± .025	1.63	1.97	.165 ± .025	.21
80 - 90	1.52 ± .02	1.85	0.22 ± .030	.138 ± .028			.138 ± .028	.159 ± .03	1.56	1.88	.159 ± .03	.21
90 - 100	1.54 ± .06	1.80	0.17 ± .045					.160 ± .03	1.57	1.82	.160 ± .03	.16
100 - 200	1.61 ± .02	1.86	0.15 ± .010	.148 ± .030			.148 ± .030	.170 ± .028	1.53	1.74	.170 ± .028	.14

(a) Fission chamber plus large liquid scintillator.

(b) Solid sample, "total energy detectors," and fast-neutron detection.

(c) Experimental precision,  $S^2 = \frac{1}{N(N-1)} \sum_{i=1}^N (x_i - \bar{x})^2$

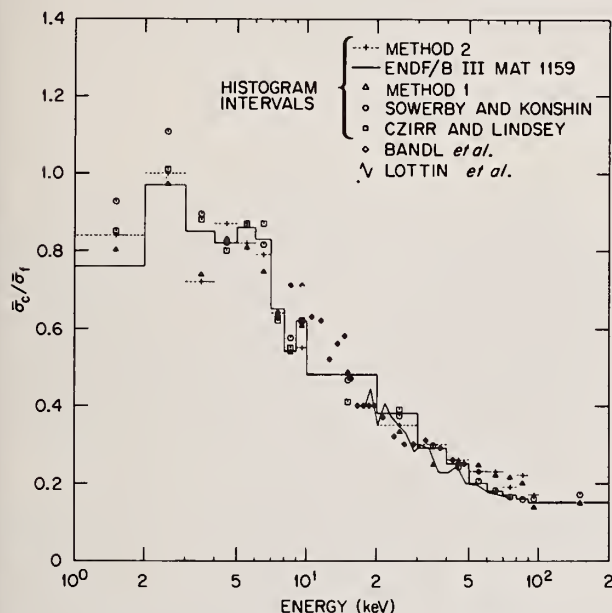
(d) Includes all known experimental errors.

(e) The aluminum resonance at 5.9 keV perturbs the measurement at this energy.



interval. The ENDF/B-IV values for  $^{239}\text{Pu}$ , MAT 1264 were based in part upon the data obtained in the present two experiments.

The relation of the present results for  $\bar{\sigma}_c/\bar{\sigma}_f$  for  $^{239}\text{Pu}$  and other experimental data can be summarized by comparing them with the results obtained in the evaluation of Sowerby and Konshin. From 0.1 to 40 keV the average difference between the present values (either set for  $\bar{\sigma}_c/\bar{\sigma}_f$  of  $^{239}\text{Pu}$  and those of Sowerby and Konshin is about 7%. For the energy intervals 1 to 10 keV and 50 to 100 keV, the present average values of  $\bar{\sigma}_c/\bar{\sigma}_f$  are 10% lower and 17% higher, respectively, than those obtained by Sowerby and Konshin.



Ratio of  $\bar{\sigma}_c/\bar{\sigma}_f$  for  $^{239}\text{Pu}$ , 1.0 to 200 keV.

The figure shows a plot of  $\bar{\sigma}_c/\bar{\sigma}_f$  for  $^{239}\text{Pu}$  obtained in the present two experiments along with those derived by Sowerby and Konshin. Experimental values measured by Czirr and Lindsey,<sup>5</sup> Bandl et al.,<sup>6</sup> and Lottin et al.<sup>7</sup> are also shown on the figure. Values from ENDF/B-III, MAT 1159 are also shown in the figure. Note that the earlier version (III) of ENDF/B shown in the figure follows very closely the results of the evaluation of Sowerby and Konshin above 10 keV and both of these data sets are systematically lower than the results of the present two experiments. These two above evaluations follow the experimental values of Lottin above 50 keV. Earlier measurements of  $\bar{\sigma}_c/\bar{\sigma}_f$  by Hopkins and Diven<sup>8</sup> (not shown in the figure) yield a value of .15 for  $\bar{\sigma}_c/\bar{\sigma}_f$  for  $^{239}\text{Pu}$  at about 60 keV, which supports the two evaluations shown in the figure. The data of Bandl et al. were normalized in the energy region from 40 to 50 keV and thus provide information on the energy dependence of  $\bar{\sigma}_c/\bar{\sigma}_f$  only.

#### Summary

The neutron cross sections  $\bar{\sigma}_f$  and  $\bar{\sigma}_a$  and especially the ratio  $\bar{\sigma}_c/\bar{\sigma}_f$  for  $^{239}\text{Pu}$  obtained by these two experiments agree to within a few percent over the

energy range of the experiments. In addition, these two results for  $\bar{\sigma}_c/\bar{\sigma}_f$  for  $^{239}\text{Pu}$  have been shown to be in good accord with the results of other measurements as reflected in the evaluation by Sowerby and Konshin.

Many factors influence the choice of detector systems for the simultaneous measurement of neutron capture and fission cross sections. The authors conclude that for the pursuit of high accuracy measurements of  $\bar{\sigma}_c/\bar{\sigma}_f$  on  $^{239}\text{Pu}$  a fission chamber used in

conjunction with total energy detectors represents a logical choice at ORELA. The total energy detectors are small and can be easily moved from one flight station to another in order to optimize the experimental conditions. Although the detection efficiency of the large liquid scintillator is larger (about a factor of 10 to 20 in the present case) than that of the total energy detector, a gain in the efficiency of the total energy detector system can be made by using additional detectors.

In the present experiments the signal-to-time-dependent background ratio for the large liquid scintillator system is about a factor of 2 to 10 less than that observed for the total energy detector system. Some of the background in the large liquid scintillator can be reduced by the dividing of the tank into optically separated sections and requiring that at least two of these sections detect the event; however, this makes the detector more sensitive to changes in the capture gamma-ray cascade with neutron energy and it also decreases the efficiency of this detector. The design and mode of use of the total energy detector minimizes possible changes in its response as the capture gamma cascade changes.

A fission chamber is preferred for use because the fission detection efficiency can approach unity (~95% efficiency). As the efficiency for fission detection approaches unity, all the fission events are identified and capture is measured directly.

The direct measurement of the neutron capture rate simplifies the normalization of  $\bar{\sigma}_c$  and eliminates a large part of the uncertainty in  $\bar{\sigma}_c/\bar{\sigma}_f$  when this ratio departs from that used in the normalization. In order to achieve the large efficiency (~95%) for fission fragment detection, the thickness of the fissile isotope is limited to about 100  $\mu\text{g}/\text{cm}^2$  and for  $^{239}\text{Pu}$  considerations of the alpha particle decay rate limit the total amount of the isotope that can be used with a single detector system. The present fission chamber contained a total of 1.4 g of  $^{239}\text{Pu}$  and had an efficiency of about 50%. Investigations of signal-to-background ratios with the total energy detector show that measurements of  $\bar{\sigma}_c/\bar{\sigma}_f$  for  $^{239}\text{Pu}$  using 0.1 g quantities of the isotope are feasible.

#### References

\* Research sponsored by the Energy Research and Development Administration under contract with the Union Carbide Corporation.

<sup>1</sup>Evaluated Nuclear Data File (ENDF/B) of the National Neutron Cross Section Center. A detailed list of the evaluators for the particular isotope (defined with a Mat number, Mat 1159 for  $^{239}\text{Pu}$ , ENDF/B, Version III) is given in File 1 of the data tape. The ENDF/B data tape is available from National Neutron Cross Section Center. The average neutron cross sections from the ENDF/B tape used in the present work were obtained using the processing code SUPERTOG, R. Q. Wright et al., "SUPERTOG: A Program to Generate Five-Group Constants and Pu Scattering Matrices from ENDF/B," ORNL-TM-2679 (1969).



<sup>2</sup>M. G. Sowerby and V. A. Konshin, Atomic Energy Review 10, No. 4, 453 (1972).

<sup>3</sup>M. G. Sowerby et al., Proc. Conf. Nuclear Data for Reactors, vol. 1, p. 161 (1970), IAEA.

<sup>4</sup>L. W. Weston and J. H. Todd, Phys. Rev. C 10, 4, 1402 (1974).

<sup>5</sup>J. B. Czirr and J. S. Lindsey, Proc. Conf. Nuclear Data for Reactors, vol. 1, p. 331 (1970), IAEA.

<sup>6</sup>R. E. Bandl, H. Miessner, and Frohner, Nucl. Sci. Eng. 48, 329 (1972).

<sup>7</sup>A. Lottin et al., Proc. Conf. Fast Critical Experiments and Their Analysis, ANL-7320, Argonne, p. 22 (1966).

<sup>8</sup>J. C. Hopkins and B. C. Diven, Nucl. Sci. Eng. 12, 169 (1962).

and

J M Adams

Nuclear Physics Division, AERE Harwell, Didcot, Oxon, England

There exists a large number of measurements of the prompt fission neutron spectrum of  $^{235}\text{U}$ . The discrepancies in the results, however, indicate systematic errors which might be attributable to the different experimental equipment and facilities used at the various laboratories. This measurement is a collaboration between the Harwell Nuclear Physics Division and the Neutron Physics Laboratory in Studsvik. The purpose was to repeat measurements on  $^{235}\text{U}$  at Studsvik and Harwell. The experiments were performed on IBIS, the Harwell neutron time-of-flight facility and the experimental parameters of importance were chosen to be identical, viz the same incident neutron energy, detector angle, sample size and composition etc, and also the highly critical parameters, viz the neutron detector response function and the energy calibration of the neutron time-of-flight spectrometer, were obtained by using the same experimental technique and nuclear reactions.

(Prompt fission neutron spectrum; U-235; Fast neutron fission; T-O-F technique)

### Introduction

There is still considerable interest for fast reactor design purposes in a good knowledge of the shape of fission neutron spectra at the higher neutron energy end, i.e. above 8-10 MeV. Although fission neutron spectral measurements have been conducted in many laboratories over a period of several years, the majority of them do not contain information on the shape above 8-10 MeV. Some time ago a program of work was initiated at Harwell by Rose<sup>1</sup> with the main purpose of investigating the higher neutron energy end of the fission neutron spectra of  $^{235}\text{U}$ ,  $^{239}\text{Pu}$  and  $^{252}\text{Cf}$ .

The particular measurement being reported at this conference was carried out as a joint experiment between Harwell and Studsvik using IBIS, the Harwell 3 MeV pulsed Van de Graaff<sup>2</sup>. The reason for this joint venture arose as a result of discrepancies in the measurements of fission neutron spectra at the two laboratories, viz the work of Johansson et al<sup>3</sup> at Studsvik and that of Rose<sup>1</sup> at Harwell. The discrepancy that this measurement set out to resolve was primarily concerned with the shape of the fission neutron spectra above a neutron energy of 8-10 MeV. The Studsvik work indicated no radical departure from a Watt distribution description, whereas the Harwell work indicated a marked deviation which can best be expressed as an "excess" of neutrons with respect to Watt. A close examination of the techniques employed in the two laboratories provided no satisfactory explanation of the discrepancy.

### Experimental Details

#### Fast Neutron Detection

For this work a fast neutron scintillation detector was built comprising a 11.5 cm diam by 5 cm thick NE213 organic scintillator (supplied by Nuclear Enterprises (GB) Ltd) coupled to a 10 cm diam RCA 8854 photomultiplier (supplied by RCA (GB) Ltd). The detector was biased corresponding to the 60 keV  $\gamma$ -rays of a  $^{241}\text{Am}$  source (so-called Am bias), which is roughly equivalent to a neutron energy of around 450 keV - the exact equivalence being unimportant only the reproducibility of the bias itself. A second detector, comprising a 10 cm diam by 2.5 cm thick NE213 organic scintillator coupled to a 12.5 cm diam XP1040 photomultiplier (supplied by Mullerd Ltd), was employed for monitoring the target neutron production. For both detectors, conventional fast neutron time-of-flight techniques

were employed to record the data. A modified version<sup>4</sup> of the Harwell pulse shape discrimination (PSD) system was used in conjunction with the main detector to reduce both the prompt time dependent and random background  $\gamma$ -ray contribution. Additional monitoring included the use of a Harwell long counter<sup>5</sup> and current integration.

#### Detected Efficiency Response

The relative detector efficiency response as a function of neutron energy was measured by the scattering of monoenergetic neutrons from right cylindrical polythene and carbon samples. The monoenergetic neutrons were produced using the  $\text{T}(p,n)^3\text{He}$ ,  $\text{D}(d,n)^3\text{He}$  and  $\text{T}(d,n)^4\text{He}$  reactions and, in order to minimise the amount of multiple scatter, the size of the scattering samples were chosen appropriate to each neutron source. In all cases dimensionally identical polythene and carbon sample pairs were used and the hydrogen scattering contribution obtained by subtraction. Multiple scatter correction analysis<sup>6</sup> was carried out on the data but this did not radically alter the experimental shape of the detector efficiency response function. The corrected experimental data agreed fairly well with a Monte Carlo prediction<sup>7</sup> of the detector response as shown in fig 1, and the shape of this calculated curve was adopted for efficiency correction purposes in the analysis of the fission neutron spectrum.

#### Fission Neutron Spectrum Measurement

The actual measurement of the fission neutron spectrum was conducted using a right cylindrical solid sample of  $^{235}\text{U}$  (214 g, 96.5 % enriched) situated 11 cm from a 40 keV thick Li metal target. A proton beam of 2.27 MeV was used which led to the production of  $0.52 \pm 0.02$  MeV neutrons. The main detector (suitably shielded from the primary neutrons) was positioned at a flight path of 3 metres from the  $^{235}\text{U}$  sample and at  $90^\circ$  with respect to the direction of the proton beam onto the target. The monitor detector was positioned so as not to interfere with the main detector and aligned to look only at the primary neutrons from the target. In addition, a sample of Bi was also used to record the shape of the elastically scattered neutrons and the experimental data were recorded by cycling the samples, plus a background (i.e. no sample) position using an automatic sample changer. The electronic arrangement used enabled the automatic recording, for each of the 3 sample positions, of neutron



time-of-flight spectra plus the cumulative time  $\gamma$ -ray spectrum for the main detector and total time-of-flight spectra for the monitor. A total of 48 hours, corresponding to 30 hours of the  $^{235}\text{U}$  sample position, accelerator time was required to accumulate the  $^{235}\text{U}$  fission neutron spectrum shown in fig 2. As can be seen there is no "interference" from a large prompt  $\gamma$ -ray time peak with the high energy region of the fission neutron spectrum - the small time  $\gamma$ -ray peaks are as a result of " $\gamma$ -break through" ( $< 0.1\%$ ) from the PSD system used. The overall time independent background is flat, not only in the region shown, but also from the neutron spectra corresponding to the Bi and background positions, and corresponds to  $< 2\%$  of the maximum in the actual fission spectrum. In order to ensure that no time shifts were occurring during the long time required to accumulate the data, the contents of both multichannel analysis were output and the device cleared several times in the course of the experiment. In fact no time shifts were observed. The spectrum shown in fig 2 was obtained by the addition of several such spectra.

### Energy Calibration

It is also necessary to be able to calibrate the time scale of the spectrum in terms of neutron energy and this is perhaps the most crucial aspect of fission neutron spectral measurements. This becomes more important at the highest neutron energies since, although the time scale is linear, the time differences become increasingly smaller with increasing neutron energy. For the fission neutron spectrum it was necessary to have a good energy calibration up to  $\sim 16$  MeV, which is difficult to do satisfactorily with monoenergetic neutrons using IBIS. The method adopted for this work was to move the main detector to 0" with respect to the accelerated charged particle beam, maintaining the same flight-path of 3 metres, but measured now between the target and detector, and record, under otherwise the same experimental conditions, three (d,n) neutron time-of-flight spectra with neutron groups covering the desired energy range. Firstly, the  $^{10}\text{B(d,n)}^{11}\text{C}$  reaction at 3.059 MeV, which, with a reaction Q-value of 6.467 MeV, led to neutron groups ranging from 0.559 MeV to 9.490 MeV. Secondly, the  $^{11}\text{B(d,n)}^{12}\text{C}$  reaction at 1.959 and 2.912 MeV, which, with a reaction Q-value of 13.733 MeV, led to neutron groups ranging from 2.970 to 15.366 MeV and 1.409 to 16.413 MeV respectively. After the appropriate  $\gamma$ -time peak adjustments, this led to a calibration, in terms of neutron flight times per metre,  $\tau$ , for the fission neutron spectrum of

$$\tau = -0.1488 \times \text{CH} + 144.0883 \quad (1)$$

where CH is the channel number, and from which the energy of a particular channel can be readily obtained.

### Analysis

#### Experimental Data

The analysis of the  $^{235}\text{U}$  fission neutron spectrum was carried out using an adaptation of the computer program used at Studsvik. The spectrum was converted to energy channel by channel using the above relation (1), corrected for background and detector efficiency response, and then integrated in equal energy intervals of 0.5 MeV to obtain the number of neutrons per energy interval,  $N(E)$ , and  $N(E)/E^{1/2}$  where  $E$  is the average neutron energy in each interval. The result is shown in fig 3 as a function of  $N(E)/E^{1/2}$  against  $E$ .

### Interpretation

Two familiar forms are given in the literature to describe fission neutron spectra, viz (2) a Maxwellian distribution due to Terrell<sup>8</sup>, which can be written as

$$N(E) \propto E^{1/2} \exp(-E/T) \quad (2)$$

where  $T$  is the fission "temperature" and is related to the average fission neutron energy,  $\bar{E}$ , by

$$E = 1.5 T \quad (3)$$

or (4) a Watt distribution<sup>9</sup>, which can be written as

$$N(E) \propto \exp(-AE) \sinh(\sqrt{BE}) \quad (4)$$

where  $A$  and  $B$  are constants defining the shape of the distribution and are related to  $\bar{E}$  by

$$\bar{E} = (1.5 + 0.25 B/A)/A \quad (5)$$

### Result

Both forms of distribution were used to describe the experimental data as shown in fig 3. The Maxwellian distribution led to values of  $T = 1.330 \pm 0.009$  MeV and  $\bar{E} = 1.995 \pm 0.014$  MeV, whereas the Watt distribution formalism led to values of  $A = 1.077 \pm 0.012 \text{ MeV}^{-1}$  and  $B = 2.949 \pm 0.146 \text{ MeV}^{-1}$  with  $\bar{E} = 2.028 \pm 0.038$  MeV, for least squares fits to the data between 1 and 16 MeV neutron energies. By comparison, the Studsvik result (dotted in fig 3) for  $^{235}\text{U}$ , obtained for a fit between 0.16 and 15 MeV, agrees very well for the neutron distribution and the value of  $\bar{E}$ . The Studsvik results are  $A = 1.000 \pm 0.013 \text{ MeV}^{-1}$  and  $B = 1.970 \pm 0.134 \text{ MeV}^{-1}$  which lead to the mean energy  $\bar{E} = 1.993 \pm 0.040$  MeV.

At the present time no attempt has been made to subtract out the enormous elastic scattering neutron group, since the neutron bias was  $\sim 450$  keV and the incident neutron energy was 520 keV. It was not felt meaningful to attempt fits to lower neutron energies since the shape of the relative detector efficiency response peaks  $\sim 1$  MeV and this energy region is particularly susceptible to any slight variation of the electronic conditions. Also the primary objectives of this measurement were aimed at resolving discrepancies between existing measurements concerned with the high energy end of the spectrum.

### Discussion and Conclusions

Considerable trouble and effort was used throughout the experiment and subsequent analysis to reduce any potential source of error. A check on the sensitivity of the analysis to small changes in some of the parameters to find out if the result could be radically altered was carried out. The effect of artificially increasing and decreasing the amount of time independent background has negligible effect on the result for small changes. The shape of the relative detector efficiency response is more important, particularly at neutron energies below 2-3 MeV, but has little effect above  $\sim 10$  MeV. However, the major potential source of error concerns the energy calibration of the fission neutron spectrum itself. It has been found that it is necessary to directly calibrate the complete neutron energy range of interest and not merely to rely on an extrapolation as a result of specifically elastically scattering a whole range of monoenergetic neutrons under the same experimental conditions. For example, the energy calibration (1) corresponds to 0.1488



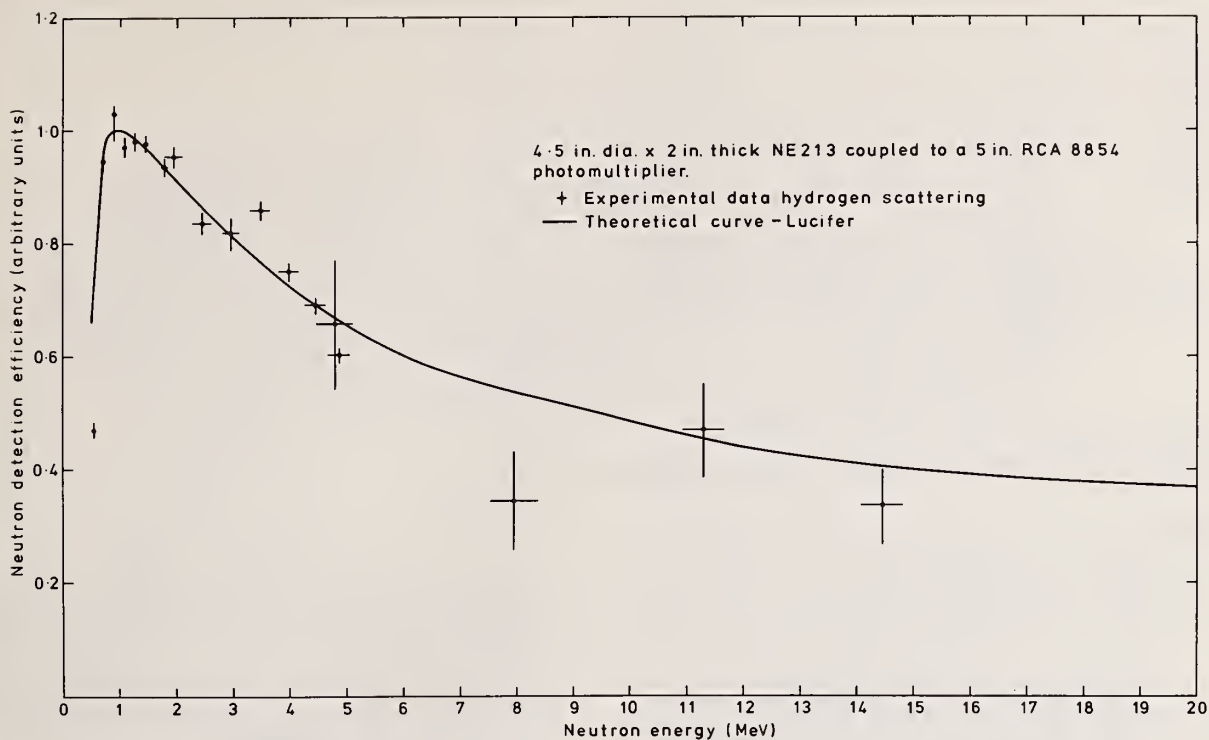


Fig 1 Fast neutron detection efficiency response ( $^{241}\text{Am}$  bias)

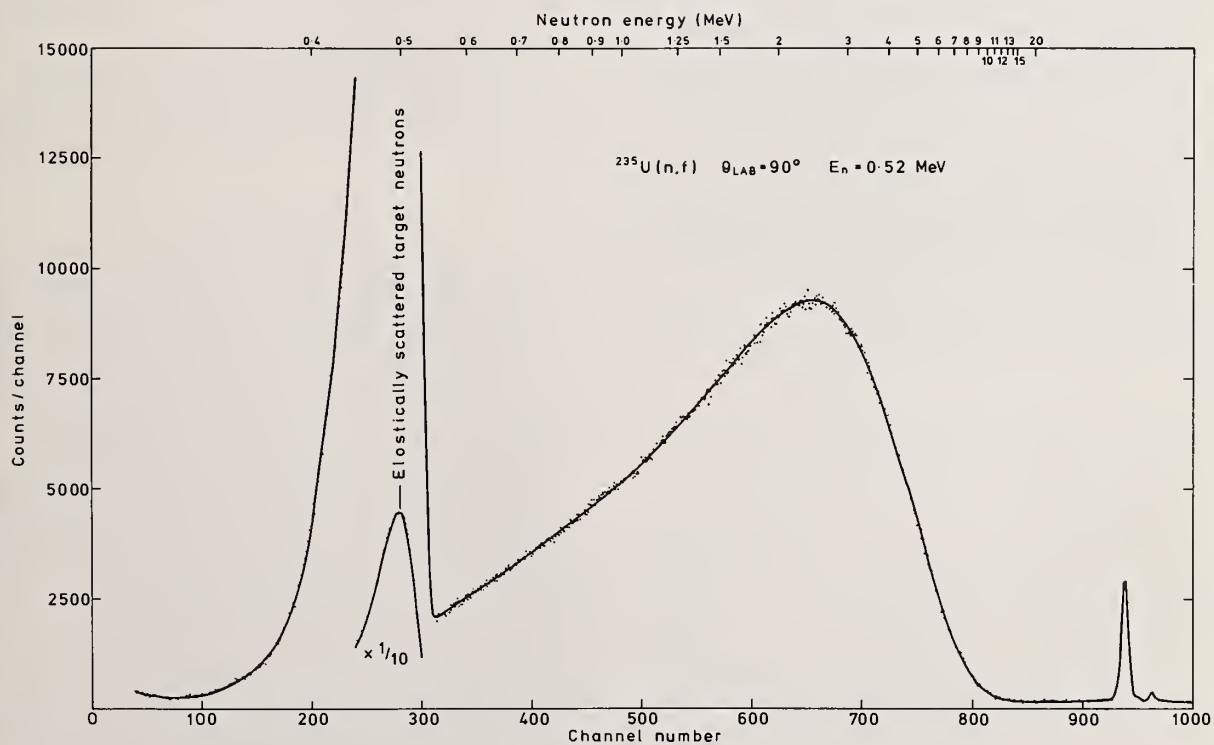


Fig 2 Fast neutron fission time-of-flight spectrum

ns/m/ch (or 0.45 ns/ch) leading to a channel difference of  $\sim 4$  keV around 1 MeV,  $\sim 46$  keV around 5 MeV,  $\sim 130$  keV around 10 MeV and  $\sim 250$  keV around 15 MeV, from which it is fairly obvious that it is not justifiable to extrapolate to higher energies a calibration obtained for lower neutron energies. Current investigation of the data of Rose would tend to suggest that it is mainly in the area of the energy calibration that his data differs from this present work and that done at Studsvik.

Although this paper only describes one measurement of the  $^{235}\text{U}$  fission neutron spectrum, the result is in close agreement with the Studsvik work. There is no evidence to indicate a departure from a Watt formalism at higher neutron energies.

#### Acknowledgements

The authors would like to thank both Dr A T G Ferguson (Harwell) and Dr T Wiedling (Studsvik) for making this joint experiment possible, and to Dr A T G Ferguson for making IBIS available for the measurement.

#### References

- 1 J L Rose, Ph D Work, unpublished
- 2 A T G Ferguson, Contemporary Physics, 5 (1964) 270-9
- 3 P I Johansson, B Holmqvist, T Wiedling and L Jéki, Precision measurement of prompt fission neutron spectra of  $\text{U}^{235}$  and  $\text{Pu}^{239}$ , A contribution to this conference
- 4 K Kandiah and G White, private communication
- 5 J M Adams, AERE-R6429
- 6 J B Parker, J N Towle, D Sams and P G Jones, Nuc Instr Meth 14 (1961) 1-12 and J B Parker, J H Towle, D Sams, W B Gilboy, A D Purnell and H T Stevens, Nuc Instr Meth 30 (1964) 77-87
- 7 R Batchelor, W B Gilboy, J B Parker, and J H Towle, Nuc Instr Meth 13 (1961) 70-82
- 8 J Terrell, Phys Rev 113 (1959) 527 and Proc of the Salzburg Symposium Vol II, p 3, IAEA, Vienna (1965)
- 9 B E Watt, Phys Rev 87 (1952) 1037

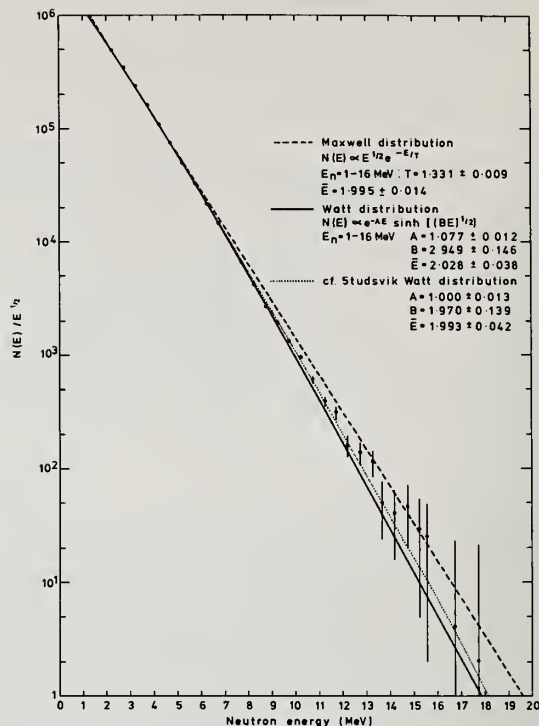


Fig 3  $^{235}\text{U}$  fission neutron spectrum

D. M. Gilliam and G. F. Knoll  
The University of Michigan  
Ann Arbor, Michigan 48105

The fission cross section of  $^{235}\text{U}$  for Na-Be photoneutrons has been measured with absolute flux determination. The neutron flux was determined absolutely (i.e., without significant dependence on other cross section data) by using a manganese bath to compare the photoneutron source with the standard source NBS-II. Fission counts were accumulated with the source positioned symmetrically between two identical detectors, all suspended in a low-albedo laboratory. Fission fragments passing through limited solid angle apertures were recorded on polyester track-etch films. Use of a projection microscope counting system allowed rapid measurement of track diameters, so that the smallest tracks could be distinguished reliably from background pits that were not much smaller in diameter. The masses of the  $\text{U}_3\text{O}_8$  deposits (7 mg each) were determined by microbalance weighings. After making a small correction for the calculated energy distribution of the source neutrons, a value for the fission cross section at 964 keV of  $1.21 \text{ barns} \pm 2.1\%$  (1.8% systematic and 1.0% random) is derived from the present measurement.

( $^{235}\text{U}$ ,  $^{24}\text{Na}$ ,  $^9\text{Be}(\gamma, n)$ , fission cross section, manganese bath, track-etch detector, NBS-II)

### Introduction

In the establishment of accurate cross section standards, it is highly desirable that two or more independent methods of absolute neutron flux determination be employed. Of the few known methods for measuring neutron fluxes absolutely, the total absorption method is one of the most accurate and most rigorously tested by interlaboratory comparisons. However, very few measurements of the  $^{235}\text{U}(n, f)$  cross section have utilized this method. The manganese bath was the total absorption device employed in the interlaboratory calibration of the standard source NBS-II, and a manganese bath was also employed in the present measurement for comparing the  $^{24}\text{Na}$ -Be photoneutron source with NBS-II.

Another feature that increases the independence of the present measurement from most others in the field is the track-etch fission counting.

Only a brief summary of the present measurement is given here, because a full description of this work will be published elsewhere<sup>1</sup>.

### Experimental Method

The neutron source in the present experiment consisted of a compressed sodium fluoride core (3 cm in diameter) surrounded by a spherical shell of beryllium (0.3 cm thick). Uniform activation of the sodium was achieved by positioning the irradiation package at the reactor mid-plane and slowly rotating the package during irradiation. The initial neutron yield was about  $3 \times 10^7$  neutrons/sec.

The fission rate measurement and the manganese bath source comparisons were carried out in a thick-walled concrete cell with a mean inside diameter of 4.2 m. All the interior surfaces of the cell were lined with a 5 cm layer of anhydrous borax to reduce the return of moderated neutrons into the experimental area. The manganese bath was drained during the fission rate measurement in order that the full advantage of the borax lining be realized.

At the center of the shielded cell, the photoneutron source was positioned symmetrically between two track-etch fission detectors as shown in Fig. 1. The source and detectors were supported by a light-weight tubular framework which was enclosed in a helium-filled drum 60 cm in diameter. The walls of the drum were of thin cadmium sheet, providing a second barrier against return of thermalized neutrons.

The total fission rate in the dual fission counters is insensitive to the position of the neutron source between them, so that an accurate measurement of the location of the highly radioactive photoneutron source was not necessary. The limited solid angle track collection was chosen instead of  $2\pi$  collection to avoid the difficulties of counting shallow tracks that would be formed by fragments emitted nearly parallel to the fissionable deposit. The helium atmosphere permitted use of the desired limited solid angle track accumulation without use of a heavy vacuum vessel, which would increase the neutron scattering correction. The timing of the track accumulation period was defined precisely by electrically actuated shutters that interposed between the fissionable deposit and the track-etch film. Three runs were made: two dual detector runs as illustrated in the figure with source-detector spacings of 5.1 cm and 9.2 cm, respectively, and a single-detector run with a 21.0 cm spacing.

The polyester track-etch films were etched in KOH to develop the tracks to an average diameter of about  $14 \mu\text{m}$ . A grid with line width of  $3 \mu\text{m}$  was ruled directly onto the etched samples to divide the exposed area into 1 mm squares for bookkeeping purposes. The maximum average density of the tracks was about  $16 \text{ mm}^{-2}$ . The tracks were counted manually on a projection microscope. A measurement of the track diameter distribution was carried out prior to counting each sample. The measured track diameter distribution was taken as the basis of the size criterion for distinguishing the smaller fission tracks from the larger background pits. Use of this quantitative criterion for marginal track

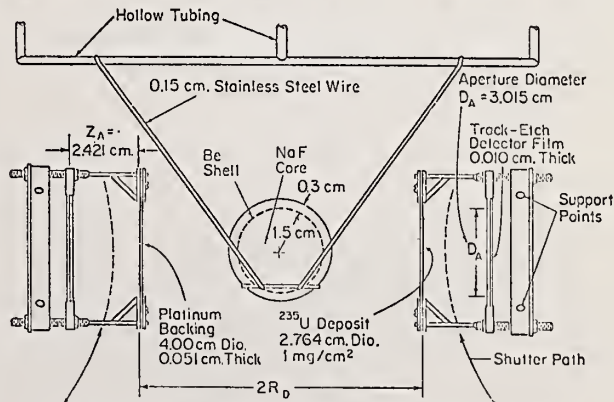


Figure 1. Detectors and photoneutron source.



rejection was found to improve the precision of repeated counts from about 1.5% to about 0.5%.

The comparison of the Na-Be photoneutron source and the standard source involved two unusual considerations: (1) the time-dependence of the Na-Be source, and (2) the production of photoneutrons by the natural deuterium content of the water of the manganous sulfate solution. A computer code was developed to unfold the time dependence of  $^{24}\text{Na}$  exponential decay,  $^{56}\text{Mn}$  activation, and the mixing delays in the bath-detector system. A saturated activity corresponding to the initial activity of the Na-Be source was computed from the counts accumulated in each 600 sec interval of the 30 hour activation-decay cycle. The computed saturated activity values were found to agree within the expectations of counting statistics over the entire cycle of activation and decay, including the decay period after the source was removed from the bath. The photoneutron production due to natural deuterium content in the bath was found experimentally to be  $(0.94 \pm .10)\%$  by insertion of a similar  $^{24}\text{Na}$  source which did not have a Be shell.

The masses of the  $\text{U}_3\text{O}_8$  deposits were determined by the supplier, the Isotope Target Laboratory at Oak Ridge National Laboratory, by means of microbalance weighings. The relative isotopic content was determined by mass spectrographic analysis, also performed by ORNL.

#### Corrections and Residual Uncertainties

The largest single uncertainty in the experiment was the  $\pm 1.12\%$  error associated with discrimination between background pits and the smallest fission fragment tracks. The next largest source of error was the  $\pm 0.92\%$  uncertainty in the detector efficiency arising from uncertainties in the angular distribution of fission fragment emission. The neutron yield of NBS-II was taken as the average of the results of four independent calibrations by NBS, BIPM, NPL, and ANL. An uncertainty of  $\pm 0.5\%$  in the average was estimated based on the agreement of the independent calibrations.

(This error estimate is the evaluation of the present authors, not a value certified by the calibrating laboratories.)

The deposit masses are uncertain to an estimated  $\pm 0.5\%$ . Since the deposits were massive (7 mg each) relative to the limits of accuracy of microbalance weighings (better than 10  $\mu\text{g}$ ), weighing accuracy is not the limiting factor. Furthermore, for properly fired deposits, stoichiometric imperfections are not expected to be able to cause errors exceeding 0.1% in the deposit masses. The  $\pm 0.5\%$  error estimate for the deposit masses is primarily an allowance for the possibility of contamination during the deposition and firing operations.

Other major sources of error were as follows: statistical errors in the track counts, 0.82%; geometrical uncertainties in source-detector spacing and deposit-aperture spacing, 0.60%; and error due to uncertainty in the  $^{24}\text{Na}$  half-life, 0.57%.

The total propagated uncertainty was 2.05% at the 67% confidence level.

#### Result and Conclusion

After correction for the energy distribution of neutrons scattered within the source, a  $^{235}\text{U}(n,f)$  cross section value of  $1.21 \text{ b} \pm 2.1\%$  was obtained corresponding to a neutron energy of 964 keV. Since 1970 five other absolute measurements of this cross section have been reported by Poenitz, Kaeppler, Gayther et al., Cramer, and Szabo et al. The values listed in the CSISRS file from these five measurements agree with the present result within  $\pm 1.0\%$ .

#### Reference

<sup>1</sup>D. M. Gilliam and G. F. Knoll. "An Absolute Determination of the  $^{235}\text{U}$  Fission Cross Section at 964 keV", Annals of Nuclear Science and Engineering, to be published.

THE TOTAL CROSS SECTION AND THE FISSION CROSS SECTION OF  $^{241}\text{Am}$   
IN THE RESONANCE REGION, RESONANCE PARAMETERS.

H. Derrien and B. Lucas

Département de Physique Nucléaire

CEN Saclay, BP 2, 91190 Gif-sur-Yvette, France

The  $^{241}\text{Am}$  total and fission cross sections have been measured in the resonance region, using the 60 MeV Saclay linac as a pulsed neutron source. The resonance parameters obtained by a single level shape analysis of the transmission data are given for 189 levels up to 150 eV neutron energy. The mean level spacing, corrected for 18 % of missed resonances in the 0 to 50 eV energy range, is  $(0.55 \pm 0.05)$  eV. The s-wave neutron strength function value, in the 0 to 150 eV energy range, is equal to  $(0.94 \pm 0.09)10^{-4}$ . The average radiation width obtained from 43 resonances is  $(43.77 \pm 0.72)$  meV. Only preliminary results of the fission experiment are available now ; 38 fission widths are given up to 32 eV neutron energy, with the average value  $\langle \Gamma_f \rangle \approx 0.23$  meV ; the statistical distribution of these fission widths corresponds to a  $X^2$  law with 4 degrees of freedom. An area analysis of the Los Alamos fission data<sup>1</sup> has also been done, from which we obtain 36  $\Gamma_f$  values in the 20 eV to 50 eV energy range ; the corresponding average value is :  $\langle \Gamma_f \rangle \approx 0.52$  meV ; the statistical distribution obeys to a  $X^2$  law with 15 degrees of freedom, in disagreement with the Saclay results.

(Neutron; total cross section;  $^{241}\text{Am}$ ; resonance parameters)

The Total Cross Section Measurement and Analysis

Experimental Conditions

The total cross section has been obtained up to 1 keV neutron energy from the transmission measurements of three sample thicknesses of americium oxyde :  $0.18 \text{ g/cm}^2$  ;  $0.63 \text{ g/cm}^2$  and  $(0.63 \pm 1.24) = 1.87 \text{ g/cm}^2$ . Three series of measurement were performed : the first at a 17 m flight path and the others at a 53 m flight path. The main characteristics of each series are given in the table 1. The best nominal resolution achieved was 0.8 ns/m.

Table 1

Energy range (eV)	Channel width (ns)	Electron burst width (ns)	Flight path length (m)	Sample thickness (g/cm <sup>2</sup> )
0.8-3.5	640	100	17.9	0.18, 0.63 and 1.87
3.5-8.8	320			
8.8-20	160			
20-27	80	100	53.4	1.87
27-90	80			
90-150	80			
150-1000	50	10	53.4	1.87

Method of Analysis

A shape analysis of the experimental data has been done up to 150 eV neutron energy by a least square fit (the code used is described in reference 2), which gives the energies, the neutron widths and the total widths of the resonances. In this shape analysis, the theoretical function is a sum of single level Breit-Wigner formulae broadened by a gaussian Doppler function and by a gaussian resolution. Such a formulation of the cross section gives a good representation of the resonance shape since the interferences in the fission channels are negligible (very small value of the fission widths). The Doppler width is taken equal to  $0.0209 \sqrt{E}$  (E energy of the incident neutron) with an accuracy better than 2 %. The parameters obtained by this analysis are given in table 2. In this table  $\Delta(2\Gamma_n)_1$  corresponds to the statistical error and  $\Delta(2\Gamma_n)_2$  to the systematic error due to the background evaluation ;  $\Delta(\Gamma_\gamma)$  is a statistical error.

Level Spacings

A number of 189 resonances is identified in the 0 to 150 eV energy range (including the resonances at 0.308 eV and 0.576 eV)<sup>3</sup>.

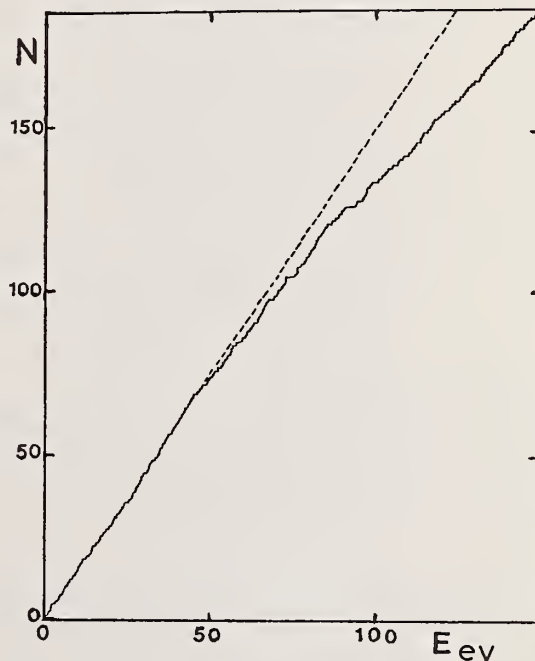


Fig. 1

Figure 1 shows the cumulative sum of the number of levels N versus the neutron energy E, in this energy range ; beyond 50 eV the variation of N is not linear ; there is a loss of resonances due to the increasing Doppler and resolution widths. So, a statistical study of the resonance parameters has to be limited to the 78 levels of the 0 to 50 eV energy range ; in this interval the observed mean spacing is equal to 0.65 eV.

Table 2

E (eV)	$2g\Gamma_n$ (meV)	$\Delta(2g\Gamma_n)_1$	$\Delta(2g\Gamma_n)_2$	$\Gamma_Y$ (meV)	$\Delta\Gamma_Y$ (meV)	E (eV)	$2g\Gamma_n$ (meV)	$\Delta(2g\Gamma_n)_1$	$\Delta(2g\Gamma_n)_2$	$\Gamma_Y$ (meV)	$\Delta\Gamma_Y$ (meV)
0.308	0.060	0.003				64.039	4.042	0.049	0.074	47.1	4.6
0.576	0.075	0.007				64.539	1.954	0.052	0.025	38.3	9.2
1.276	0.322	0.006	0.026	46.5	0.8	65.164	5.187	0.048	0.109	49.7	3.7
1.928	0.113	0.001	0.006	44.3	0.3	65.733	1.090	0.046	0.010	18.8	14.0
2.372	0.073	0.001	0.004	42.4	0.3	66.314	1.036	0.052	0.010	75.2	19.6
2.598	0.147	0.001	0.010	46.0	0.3	66.874	2.105	0.044	0.025	71.9	8.1
3.973	0.210	0.001	0.006	44.5	0.3	68.525	0.431	0.019	0.003		
4.968	0.175	0.001	0.004	43.8	0.4	69.585	1.116	0.051	0.013		
5.415	0.760	0.003	0.019	44.2	0.1	69.824	2.661	0.053	0.040		
5.800	0.002					71.253	0.583	0.085	0.006		
6.117	0.124	0.001	0.052	43.8	0.7	71.463	1.109	0.079	0.011		
6.745	0.028	0.001				71.841	1.034	0.025	0.010		
7.659	0.037	0.001				72.276	0.226	0.021	0.001		
8.173	0.108	0.001	0.001	42.7	1.2	74.969	0.481	0.020	0.004		
9.113	0.389	0.002	0.009	44.2	0.6	75.715	0.378	0.034	0.003		
9.851	0.406	0.002	0.009	43.9	0.6	75.943	0.515	0.027	0.003		
10.116	0.026	0.001				76.779	0.109				
10.403	0.326	0.002	0.005	42.4	0.8	78.191	1.486	0.099	0.015	10.3	17.4
10.997	0.413	0.002	0.006	46.5	0.8	78.551	1.179	0.105	0.011	60.8	26.0
11.583	0.016	0.001				79.555	0.730	0.023	0.005		
12.137	0.007	0.001				80.050	0.546	0.029	0.004		
12.879	0.131	0.001	0.001			80.393	0.588	0.029	0.004		
13.874	0.012	0.001				81.077	0.106	0.039			
14.360	0.071	0.002	0.001			81.458	1.042	0.081	0.008	104.6	35.0
14.682	2.482	0.011	0.075	40.3	0.5	82.089	1.454	0.054	0.015	26.7	14.0
15.689	0.244	0.003	0.003	39.3	2.9	82.900	0.439	0.024	0.003		
16.388	1.277	0.005	0.034	41.8	0.9	83.370	0.431	0.024	0.003		
16.849	0.646	0.004	0.012	41.2	1.5	84.006	1.456	0.027	0.015	38.1	8.7
17.729	0.391	0.004	0.006	37.3	2.4	84.685	2.141	0.044	0.022		
18.167	0.017					86.610	0.225	0.025	0.001		
19.445	0.213	0.003	0.002			87.481	0.126	0.029			
20.333	0.034					87.984	3.918	0.053	0.055	70.7	6.3
20.880	0.089	0.001				89.297	0.332	0.061	0.002		
21.740	0.081	0.003				89.602	2.364	0.093	0.024	86.7	16.1
22.748	0.069	0.003				93.412	6.296	0.055	0.115	53.7	4.0
23.079	0.417	0.012	0.005	42.2	6.0	94.610	0.754	0.030	0.006		
23.337	0.445	0.012	0.006	42.5	5.8	95.285	0.360	0.035	0.003		
24.192	1.304	0.007	0.028	39.2	1.5	95.686	2.663	0.041	0.034		
25.008	0.014	0.001	0.001			96.100	2.906	0.048	0.037		
25.634	1.258	0.008	0.025	37.6	1.7	96.460	2.834	0.052	0.035		
26.498	0.487	0.014	0.006	22.0	6.1	97.423	0.277	0.030	0.021		
26.669	0.217	0.010	0.004			98.356	0.265	0.030	0.001		
27.575	0.165	0.021	0.002			100.156	1.075	0.033	0.009		
27.726	0.509	0.029	0.006	70.6	8.8	101.598	2.825	0.058	0.028	51.1	10.0
28.355	0.570	0.009	0.008	44.7	3.7	102.555	0.248	0.035	0.001		
28.903	0.467	0.009	0.006	48.6	4.7	103.203	6.980	0.063	0.120	40.2	4.5
29.504	0.701	0.009	0.009	44.6	3.2	104.788	2.196	0.059	0.022	40.2	12.8
29.956	0.050					106.148	5.824	0.185	0.136		
30.822	0.150	0.010	0.002			106.396	3.352	0.180	0.054		
31.020	0.336	0.010	0.004			107.615	1.925	0.038	0.019		
31.251	0.996	0.019	0.015	42.6	4.2	109.824	3.256	0.144	0.042		
32.030	0.300	0.010	0.003	47.4	8.6	110.093	3.337	0.144	0.043		
33.510	0.060					111.170	0.374	0.059	0.003		
34.028	0.624	0.012	0.008	45.4	4.9	111.627	5.200	0.102	0.068	94.3	10.4
34.460	0.125	0.007				112.752	0.414	0.042	0.003		
34.928	0.612	0.012	0.006	42.8	5.4	113.280	0.300				
35.445	0.427	0.012	0.004	50.6	8.1	113.907	1.741	0.078	0.014	77.6	23.0
36.250	0.167	0.007	0.001			115.084	1.800	0.081	0.014	79.3	23.8
36.483	0.100					115.777	0.701	0.049	0.004		
36.979	2.995	0.017	0.075	52.0	1.5	116.396	2.623	0.081	0.023	42.0	15.6
38.366	2.260	0.015	0.044	47.0	2.0	117.656	0.030				
38.830	0.055					118.522	0.806	0.046	0.005		
39.617	1.275	0.020	0.020	40.2	4.2	119.823	2.237	0.131	0.022		
40.067	0.541	0.040	0.005	77.9	20.1	120.123	1.930	0.131	0.026		
40.396	0.948	0.034	0.012	66.0	8.6	121.982	3.216	0.138	0.033	36.9	19.0
41.298	0.084					122.662	3.893	0.222	0.040	64.2	27.6
41.791	0.355	0.009	0.003			123.283	3.534	0.166	0.035	56.3	20.5
42.130	0.150	0.009	0.001			124.946	1.640	0.054	0.013		
43.294	0.805	0.033	0.010	18.0	8.9	125.819	1.035	0.055	0.007		
43.574	0.582	0.035	0.006	36.2	13.6	126.441	2.035	0.057	0.017		
44.416	0.118	0.009				127.415	0.250				
44.921	0.074	0.009				127.994	1.688	0.056	0.013		
46.073	0.665	0.018	0.007	43.8	8.6	129.677	0.225		0.002		
46.566	0.371	0.018	0.003	22.8	14.0	130.720	1.358	0.072	0.009		
47.535	1.053	0.017	0.012	41.6	5.2	131.319	3.121	0.132	0.032	56.0	23.2
48.765	0.713	0.018	0.007	40.0	8.0	132.180	0.875	0.062	0.006		
49.332	0.220	0.011	0.002			132.754	1.180	0.059	0.008		
50.278	2.442	0.022	0.042	51.8	3.0	133.657	1.784	0.100	0.014	52.1	30.5
50.847	0.393	0.020	0.003	35.8	16.4	134.867	8.015	0.317	0.104		
51.934	1.385	0.021	0.017	50.2	4.9	135.449	4.131	0.348	0.042		
53.014	0.165	0.012	0.001			136.435	5.757	0.145	0.068	45.7	14.1
53.493	0.184	0.012	0.001			137.103	1.294	0.077	0.009		
54.407	0.073	0.012				137.613	1.628	0.064	0.012		
54.990	1.443	0.025	0.002	108.5	6.9	138.774	3.686	0.108	0.040	40.6	15.4
55.595	0.213	0.014	0.002			139.963	1.253	0.071	0.008		
55.945	1.432	0.034	0.018			140.498	2.436	0.073	0.021		
56.158	0.949	0.034	0.010			141.310	4.229	0.108	0.055		
57.372	4.146	0.029	0.082	81.0	2.7	141.520	3.256	0.106	0.039		
59.066	0.589	0.028	0.004	107.2	19.4	143.036	0.331	0.066	0.002		
60.045	0.285	0.017				144.869	1.421	0.068	0.010		
60.381	0.140	0.017	0.001			145.438	0.350				
61.258	1.672	0.044	0.017	74.7	9.6	146.436	1.739	0.070	0.012		
61.613	0.434	0.025	0.004			148.031	12.302	0.138	0.198		
62.549	0.222	0.016	0.001			149.141	3.926	0.076	0.039		
63.507	0.199	0.018	0.001								



Figure 2 shows the corresponding distribution of the level spacings ; the dashed line represents the Wigner distribution (two populations with spin and parity  $J^\pi = 2^-$  and  $J^\pi = 3^-$ ) normalized to the area of the experimental histogram. There is no agreement between the theoretical and the experimental distributions, which is an usual result for a nucleus with such a small level spacing ; the same kind of discrepancy is observed for  $^{233}\text{U}$ ,  $^{235}\text{U}$ ,  $^{241}\text{Pu}$ ,  $^{237}\text{Np}$  ... and is mainly due to the resonance overlap hiding the small resonances.

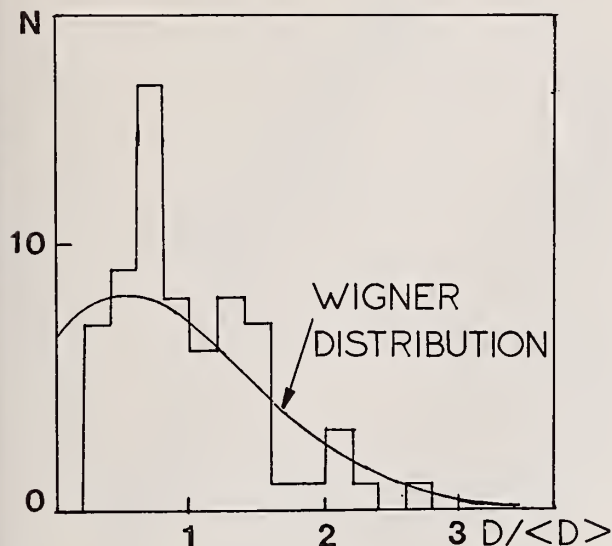


Fig. 2

#### Neutron Widths and S-Wave Strength Function

The distribution of the reduced neutron widths for resonances between 0 and 50 eV agrees relatively well with the Porter-Thomas law, if one assumes that about 15 % of levels are missed, corresponding to  $\Gamma_n^0$  values smaller than 0.1 times the mean value.

The strength function  $S_0$  is evaluated by the relation :

$$S_0 = \sum_{E_1}^{E_2} \frac{2g\Gamma_n^0(E)}{2(E_2 - E_1)} ;$$

the value obtained is not affected by the missed levels since in the shape analysis we take into account the total area of non resolved resonances. We obtain :  $S_0 = (0.75 \pm 0.12)10^{-4}$  in the 0-50 eV energy range and  $S_0 = (0.94 \pm 0.09)10^{-4}$  in the 0-150 eV energy range.

G.G. SLAUGHTER et al.<sup>4</sup> give a value of  $(1.1 \pm 0.2)10^{-4}$  from an area analysis of the total cross section as measured by BLOCK et al.<sup>5</sup>, up to about 45 eV. This value is significantly higher than ours ; the discrepancy is mainly due to three resonances or group of resonances (6.74 eV ; 9.17 eV and  $\approx 43$  eV) for which SLAUGHTER proposed  $\Gamma_n$  values about ten times greater than ours.

#### Capture Widths

The capture widths  $\Gamma_\gamma$  have been obtained for a large number of resonances by the relation :

$\Gamma_\gamma = \Gamma - 2g\Gamma_n$ , assuming that  $\Gamma_n$  and  $\Gamma_f$  are small enough. Up to 50 eV neutron energy the  $\Gamma_\gamma$  values are obtained with a relatively good accuracy ; beyond, the values are much more scattered, due to the facts that : i) the shape analysis cannot give accurate values of  $\Gamma$  when the Doppler and the resolution function widths are too large compared to  $\Gamma$  ; ii) the probability of observing unresolved resonances increases with energy, likewise the probability of observing abnormal large  $\Gamma$  values. The weighted average value in the 0 to 50 eV energy interval is :  $\langle \Gamma_\gamma \rangle = (43.77 \pm 0.72)$  meV, which is mainly due to the very accurate values in the 0 to 10 eV energy interval ; a correction of 0.20 meV has been applied to the average value to take into account the fission widths.

#### Attempt to Determine the Number of Missed Levels

The examination of the level spacing and neutron width distributions shows that 15 % to 20 % of levels are missed in the experimental cross section. A more precise evaluation of the number of missed levels has been done by a Monte-Carlo method. Table 3 shows the results obtained for 9 calculated cross sections in the 0 to 50 eV energy range, which are supposed to have the same statistical properties as  $^{241}\text{Am}$ .

Table 3

	N	D (eV)	N <sub>obs</sub>	D <sub>obs</sub> (eV)	$\frac{N-N_{obs}}{N}$
1	81	0.61	67	0.74	17 %
2	98	0.51	79	0.63	20 %
3	84	0.60	70	0.71	17 %
4*	88	0.57	74	0.67	16 %
5	89	0.56	74	0.67	16 %
6	102	0.49	80	0.62	22 %
7*	89	0.56	73	0.70	18 %
8*	95	0.53	75	0.67	21 %
9	91	0.54	72	0.68	21 %

N = number of levels for the calculated cross section.  
N<sub>obs</sub> = number of observed levels.

The cases n° 4, 7 and 8 have been particularly studied ; from a total number of 272 levels, 222 are observed, which means 18 % of missed levels ; the 50 non observed resonances correspond to 11 doublets (4 %) with large  $\Gamma_n^0$  values and 39 (14 %) with  $\Gamma_n^0$  values less than  $0.1 \langle \Gamma_n^0 \rangle$  ; 13 % of the missed level spacing are smaller than  $0.4 \langle D \rangle$ .

The conclusion is : the observed mean spacing has to be corrected for  $(18 \pm 4)$  % missed resonances ; then the right value of the average spacing would be :  $\langle D \rangle = (0.55 \pm 0.05)$  eV.

#### Fission Cross Section Measurements. Preliminary Results

##### Experimental Conditions

Due to the strong  $\alpha$  activity of  $^{241}\text{Am}$ , a fission fragment detector is not suitable for such measurement. We have built a new detector based on the fission neutron detection, using NE 213 as liquid scintillator. The  $\gamma$ -ray pulses are eliminated by a pulse shape discrimination method.<sup>6</sup> The rejecting rate for  $\gamma$ -ray pulses was 10<sup>5</sup>. An anti pile up system has been used and only isolated pulses in 1  $\mu$ s interval are taken into account. The detector has a cylindrical geometry and

contains 45 liters of liquid in 4 optically independent parts, each part being viewed by a XP 1040 photomultiplier. Internal shielding of lead and natural boron was used to protect against a large fraction of the  $\gamma$ -rays coming from the sample, and against neutrons thermalized in the liquid and backscattered. Due to the anti pile up system, the efficiency of the detector depends on the activity of the sample ; for  $^{241}\text{Am}$ , it is about 8 %. The energy threshold for the detection of fission neutrons is 800 keV, and the time resolution 5 ns.

The results given in this section concern only a preliminary experiment, for which the experimental conditions are those shown in Table 4.

Table 4

Energy range (eV)	TOF analyser width (ns)	Linac electron pulse width : 100 ns Frequency pulse : 500 Hz Sample thickness : 0.17 g/cm <sup>2</sup> Counting-rate : 10 fissions/h in the 5.4 eV resonance peak Experiment duration : 200 h
0.8-3.8	800	
3.8-9.7	400	
9.7-23.6	200	
26.6-86.7	100	
86.7-152	50	

### Results

The normalization has been done in relation to the BOWMAN results<sup>7</sup> (spark chamber measurement) which were normalized to the value of 3.13b at 0.025 eV neutron energy ; the resonance areas were compared for 11 levels up to 15 eV ; a good agreement can be obtained for 7 resonances, but not for the resonances at 3.97, 4.97, 6.12 and 9.11 eV for which the areas obtained from the parameters published by BOWMAN are about ten times smaller than ours. Nevertheless, there is no apparent discrepancy in the fission cross sections in the vicinity of these resonances. The origin of the disagreement has to be found in some mistake in the resonance analysis.

Table 5 - Fission widths from Saclay data.

E	$\Gamma_f$	E	$\Gamma_f$	E	$\Gamma_f$
1.28	0.37	10.12	0.16	24.19	0.14
1.93	0.08	10.40	0.06	25.63	0.29
2.37	0.18	10.99	0.13	26.50	0.05
2.60	0.17	12.88	0.06	26.67	0.19
3.97	0.16	14.68	0.27	28.36	0.16
4.97	0.44	15.69	0.10	28.90	0.16
5.42	0.63	16.39	0.11	29.50	0.10
6.12	0.42	16.85	0.32	31.25	0.22
6.74	0.22	17.73	0.30	32.03	0.28
7.66	0.10	19.44	0.03	36.98	0.51
8.17	0.12	21.74	0.27	38.37	0.30
9.11	0.18	23.08	0.27	39.62	0.23
9.85	0.95	23.34	0.17		

Table 5 shows the  $\Gamma_f$  values obtained for 38 resonances up to 32 eV ; these values were calculated by the relation :  $\Gamma_f = \Gamma_x(A_f/A_t)$  ;  $A_f$  and  $A_t$  are the fission and the total areas ;  $\Gamma$  and  $A_t$  correspond to the parameters of Table 2. The average fission width is :  $\langle \Gamma_f \rangle = 0.23$  meV. The integral distribution shown in figure 3 is well represented by a  $\chi^2$  law with 4 degrees of freedom. That means that there is a quite large

number of channels contributing to the  $^{241}\text{Am}$  sub-threshold fission, which is not impossible, since the  $^{242}\text{Am}$  compound nucleus is an odd-odd one.

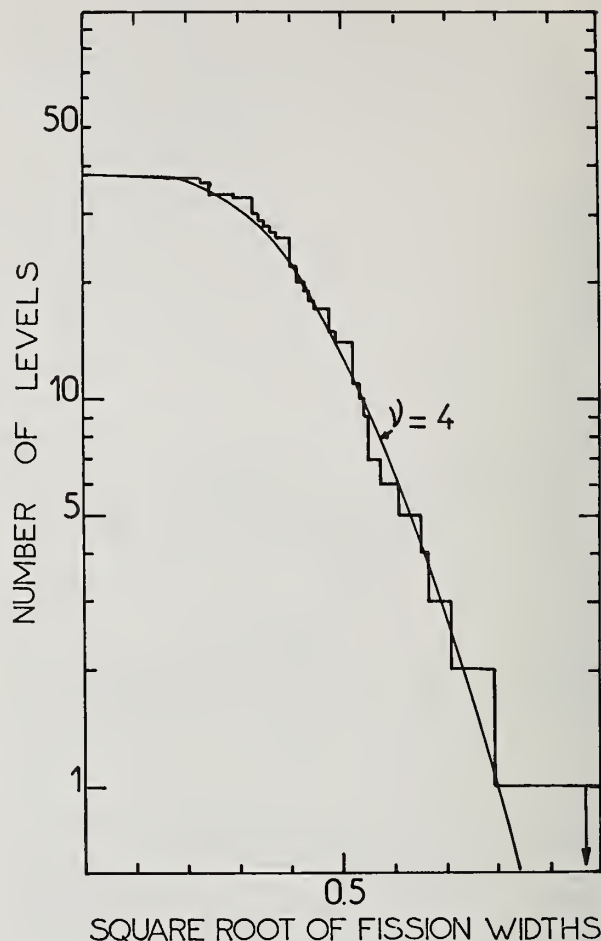


Fig. 3

### The Fission Widths Deduced of the Los Alamos Fission Cross Section<sup>1</sup> in the 20 eV to 50 eV Energy Range

No fission widths have been published up to now from the Los Alamos fission data. We have analysed these data (provided by the CCDN at Saclay) between 20 eV and 50 eV. Table 6 shows the fission widths we

Table 6 - Fission widths from Los Alamos data.

E	$\Gamma_f$	E	$\Gamma_f$	E	$\Gamma_f$
22.75	0.58	30.82	1.20	40.07	0.79
23.08	0.77	31.02	0.51	40.41	0.34
23.34	0.31	31.25	0.57	43.29	0.35
24.19	0.48	32.03	0.56	43.57	0.49
25.63	0.82	34.03	0.22	46.07	0.27
26.50	0.47	34.46	0.74	46.57	0.28
26.67	0.48	34.93	0.41	47.54	0.25
27.57	2.54	35.49	0.36	48.76	0.49
27.73	0.44	36.25	0.57	49.33	0.54
28.36	0.55	36.99	0.66	50.28	0.37
28.90	0.36	38.37	0.53	50.85	0.47
29.50	0.45	39.62	0.56	51.98	0.38

obtained for 36 resonances. The corresponding average value is :  $\langle \Gamma_f \rangle = 0.52$  meV, which is larger than the Saclay average value by a factor 2.3. The distribution of these fission widths is shown in figure 4 ; it corresponds to a  $\chi^2$  law with 15 degrees of freedom, not in agreement with the fission channel theory.

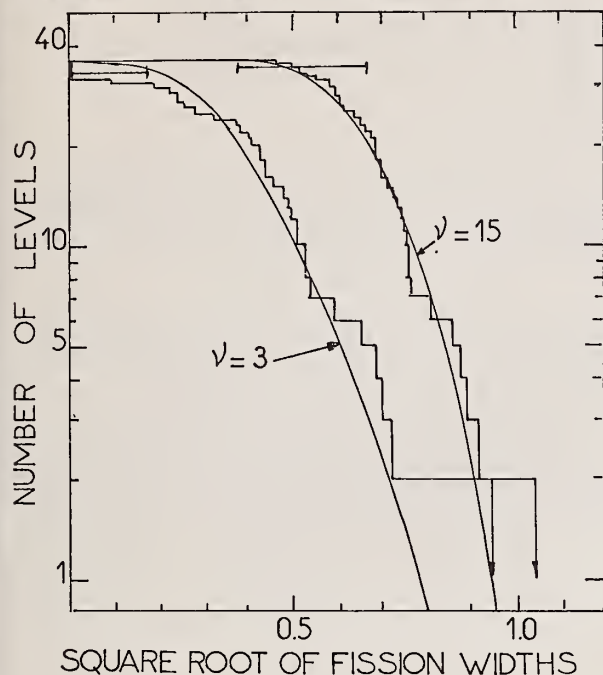


Fig. 4

The discrepancy between the average fission widths could be explained by a defect of normalization. As a matter of fact, the fission integral in the 22.5 eV to 28.7 eV energy range is equal to 2.32b-eV ; 2.80b-eV or 6.48b-eV when evaluated from Saclay, BOWMAN or Los Alamos data, which means that no severe discrepancy would appear in the average fission width if the Los Alamos results were renormalized to the Saclay or BOWMAN data. But such a renormalization will not change the shape of the Los Alamos fission width distribution ; particularly, the number of degrees of freedom will remain the same. Another explanation is a possible contamination by capture events in the Los Alamos experiment ; but to explain the observed discrepancy the contamination would be relatively important ; we have shown on the figure 4 how a correction of 0.30 meV on each fission width would modify the fission width distribution, which then would correspond to about 3 degrees of freedom. In this case, the Los Alamos measured cross section would be a mixing of 40 % fission and 60 % capture (in the average) ; however this capture contribution represents only 0.7 % of the total capture.

#### References

- 1 P.A. SEEGER et al., Nucl. Phys., 1967, A96, 605.
- 2 P. RIBON et al., Conf. AIEA sur les Données Nucléaires pour les Réacteurs, Paris 1966, CN 23/71.
- 3 BNL-325, 2th edition, supplément n° 2, vol. III.
- 4 G.G. SLAUGHTER et al., ORNL-3085, 1961.
- 5 R.C. BLOCK et al., ORNL-2718, 1959.
- 6 R.B. OWEN, AERE EL/R-2712, 1958.
- 7 C.D. BOWMAN et al., Phys. Rev., 1965, 137, B326.



The  $^{232}\text{Th}(n,f)$  and  $^{238}\text{U}(n,f)$  cross sections have been measured relative to that of  $^{235}\text{U}$  up to 6 MeV. The best energy resolution was 3 keV at 1.6 MeV. Below the fission threshold of  $^{238}\text{U}$ , intermediate structures are observed. In the  $^{232}\text{Th}(n,f)$  cross section, the broad vibrational resonances located above 1 MeV are resolved into sharp structures which are interpreted as rotational states. The angular anisotropy of fission fragments has been also measured in the same energy range. Thereby, values of K and J have been determined for each structure. The moment of inertia of  $^{233}\text{Th}$  in shape isomeric deformation has been deduced.

### Introduction

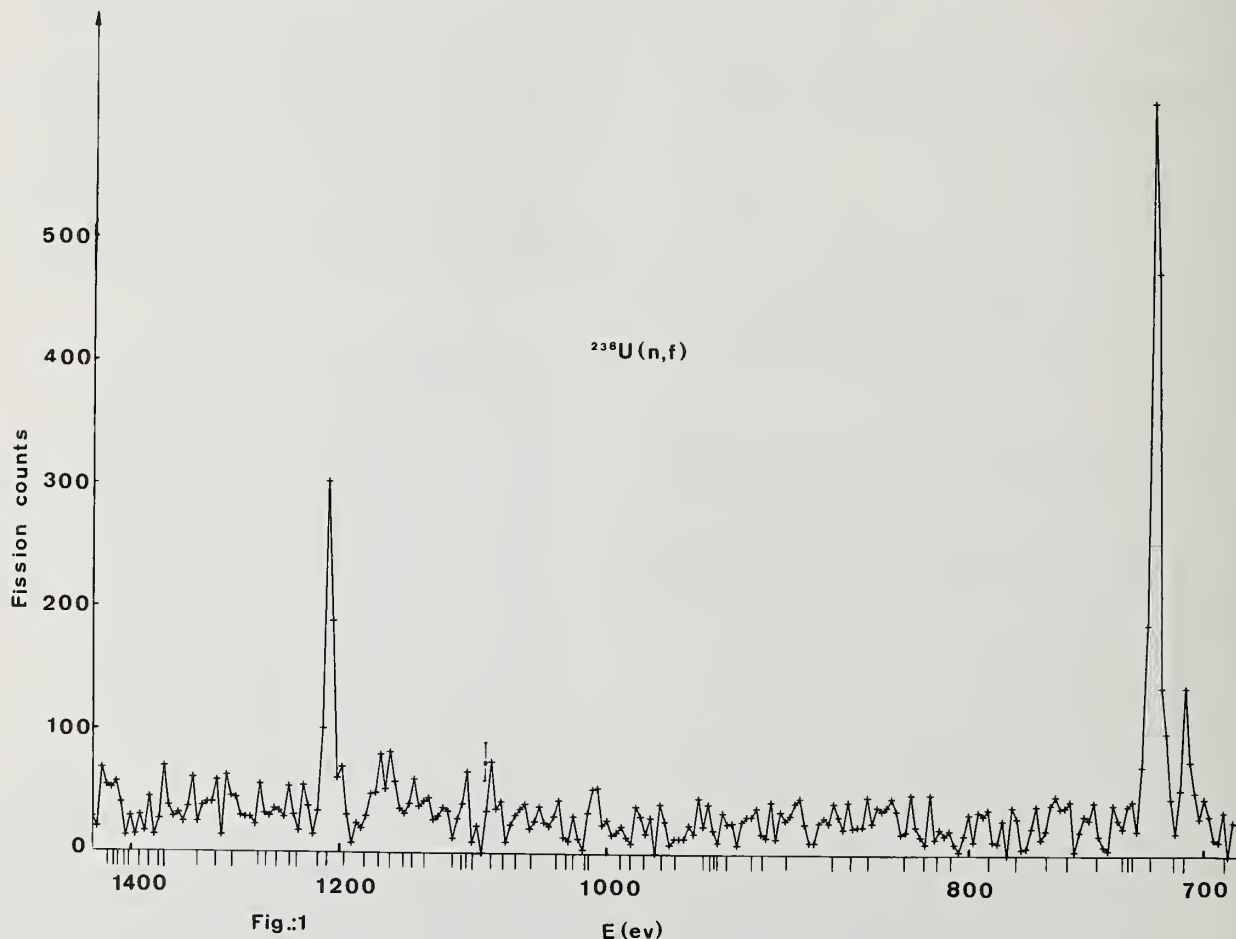
The last neutron measurements obtained with the 60 MeV Saclay linear accelerator before its closure, were used to determine fission cross sections of  $^{232}\text{Th}$ ,  $^{238}\text{U}$ ,  $^{243}\text{Am}$ ,  $^{237}\text{Np}$  and  $^{239}\text{Pu}$  relative to that of  $^{235}\text{U}$ , up to an energy of 6 MeV. The detector was a gas scintillator<sup>1</sup> divided into six optically independent cells containing a deposit of the isotope under study. In addition, one cell was equipped with an aluminium grid placed close by a layer of  $^{232}\text{Th}$ . The role of the grid was to stop the fission fragments emitted at an angle greater than  $\theta = 30^\circ$ , relative to the neutron direction, in order to measure the anisotropy of the fragments by comparison with a cell without grid. The transmission factor of the grid was 1/32.

Two sets of measurements were made : one, with a nominal resolution of 0.16 ns/m (51.9 m flight path) and one, with a nominal resolution of 0.27 ns/m (22.4 m flight path). The corresponding resolutions at 1.6 MeV were 3 keV and 6 keV respectively.

The data analysis is not completed yet. In this paper we will restrict ourselves to some outstanding features observed in the (n,f) cross sections of  $^{238}\text{U}$  and  $^{232}\text{Th}$ .

### Intermediate structure in $^{238}\text{U}(n,f)$

Block and al.<sup>2</sup> have reported an intermediate structure in the  $^{238}\text{U}$  fission cross section at 721 eV and 1211 eV. This effect is confirmed as seen in fig. 1. In the same figure we have indicated the position of



the neutron resonances. Although the statistics are barely sufficient, one observes about half of the known neutron resonances in this region. It can be seen also that the intermediate structure is not spread over many resonances as it is the case for  $^{237}\text{Np}$  or  $^{240}\text{Pu}$ . This would indicate that the widths of the class II states are of the same order or less than, the spacings of the levels in the first well. Other resonances are observed at 1684 eV, 2285 eV, 3230 eV, 4125 eV, 5250 eV, 7400 eV, 10710 eV, and 15140 eV.

In the threshold region many resonant structures appear, mainly at 337 keV, 618 keV, 793 keV, 899 keV, 921 keV, 960 keV and 1125 keV. The width of these structures is of the order of 20 keV, much larger than the ones observed in the resonance region. It is likely that many more structures exist around 1 MeV, but only those which are at energies where the cross-section does not increase very fast can be seen.

The near threshold fission of  $^{232}\text{Th}$

The  $^{232}\text{Th}$  fission cross section is known to present a broad resonance at 1.6 MeV and a smaller one at 1.7 MeV. Like in  $^{230}\text{Th}(n,f)$  cross section<sup>3</sup> it was anticipated that the shape of these resonances would be due to a rotational band built on a vibrational level but the previous attempt to resolve any fine structure has failed.<sup>4</sup> In our measurement with a 3 keV resolution, one observes, in particular, four well separated peaks at around 1.6 MeV and three others around 1.7 MeV (fig..2). The angular anisotropy of the fragments has also been measured and is shown in fig. 3 where the number of fissions detected in the cell with

the grid, relative to the number of fissions detected in the cell without grid, is plotted versus the neutron energy. The ratio has been corrected for the transmission coefficient of the grid. In fig. 3, one also indicates the calculated values of the ratio :

$$a(K,J) = \frac{\int_0^{30^\circ} W(K,J;\theta) \sin \theta d\theta}{\int_0^{90^\circ} W(K,J;\theta) \sin \theta d\theta}$$

where  $W(K,J;\theta)$  is the angular distribution corresponding to the quantum numbers  $K$  and  $J$ .

Resonances at 1.4 and 1.7 MeV have  $K = 1/2$  and resonances at 1.5 and 1.6 MeV have  $K = 3/2$  values. The following table gives the energies of the fine structures, as obtained by a least square fit on the cross section.

$\epsilon_o(J,K)$ (MeV)	1.415	1.429	1.444	1.504	1.517	1.534	1.556
J	1/2	3/2	5/2	3/2	5/2	7/2	9/2
K	1/2			3/2			
$\epsilon_o(J,K)$ (MeV)	1.579	1.592	1.609	1.637	1.711	1.724	1.748
J	3/2	5/2	7/2	9/2	1/2	3/2	5/2
K	3/2				1/2		

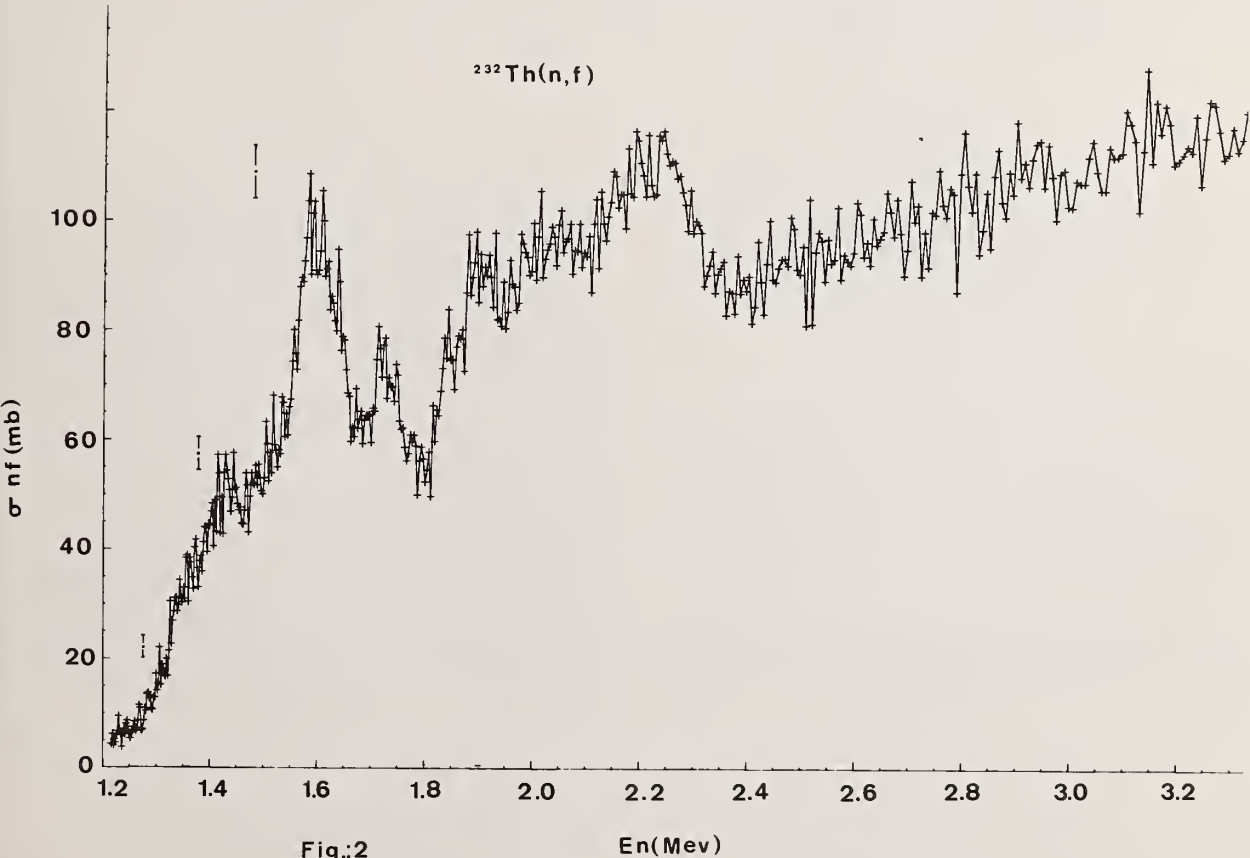


Fig.:2

En(Mev)

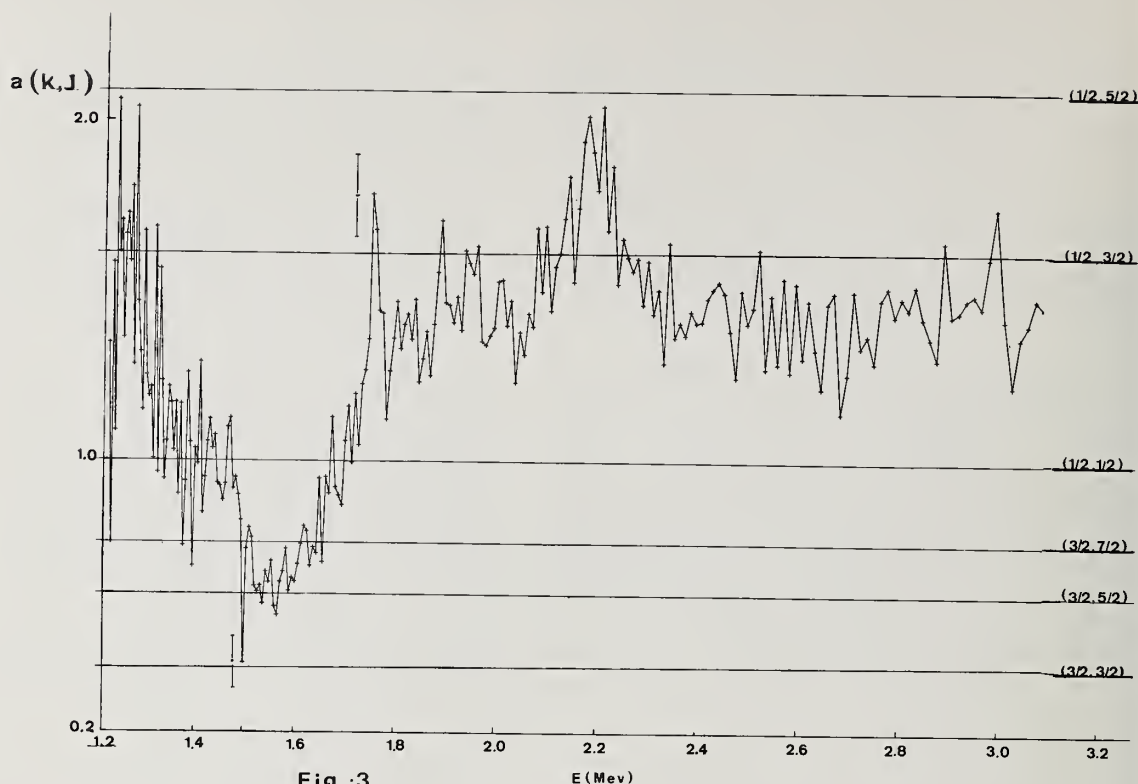


Fig.:3

These energies are in excellent agreement with the standard form for rotational bands :

$$\epsilon_o(J, K) = \epsilon_{oK} + \frac{\hbar^2}{2\mathcal{I}} |J(J+1) - K(K+1)| + \delta_{1/2, K} a(-1)^{J+1/2} (J+1/2)$$

where  $a$  is the decoupling parameter for  $K = 1/2$ .

The moment of inertia  $\mathcal{I}$  can be deduced from the energies of the rotational levels. For the  $K = 3/2$  bands, values of 2.5 and 2.8 are found for the parameter  $A = \hbar^2/2\mathcal{I}$  which is less than half of the usual value in the first well. For the  $K = 1/2$  bands, the effective moment of inertia is smaller with  $A = 3.9$  and 4.5, the decoupling parameters being  $a = 0.2$  and  $\sim 0.1$ .

The rotational levels can be fitted, both in position and in width, by the transmission coefficients of a double humped barrier, with reasonable parameters. For example, with the following parameters :

$$\begin{aligned} V_A &= 7.2 \text{ MeV} & \hbar\omega_A &= 0.8 \text{ MeV} \\ V_{II} &= 4.55 \text{ MeV} & \hbar\omega_{II} &= 0.5 \text{ MeV} \\ V_B &= 6.9 \text{ MeV} & \hbar\omega_B &= 0.56 \text{ MeV} \end{aligned}$$

The transmission coefficient shows a very broad peak at 1973 keV, a second one (10 keV wide) at 1612 keV and a third one (less than 1 keV wide) 430 keV lower. Around 1.1 MeV our statistic is too poor, but at 1306 keV, 1319 keV and 1343 keV we see three peaks with the same energy intervals as the three peaks of the rotational band located 405 keV above. In fig. 4 we have compared the fission-cross section with a calculated sum of transmission coefficients  $\sum_n a_n T_n(E)$  for a series of double humped barriers deduced from the one described above by translation along the  $V$  axis. The  $a_n$  coefficients have been chosen so that the shape of cross section is reproduced below 2 MeV. Although a more quantitative fit requires the use of the compound nucleus cross section, which is energy dependent, it is anticipated that, over a small energy range, the shape of the cross section is governed mainly by the transmission coefficients. As shown on fig. 4 a good qualitative agreement can be obtained.



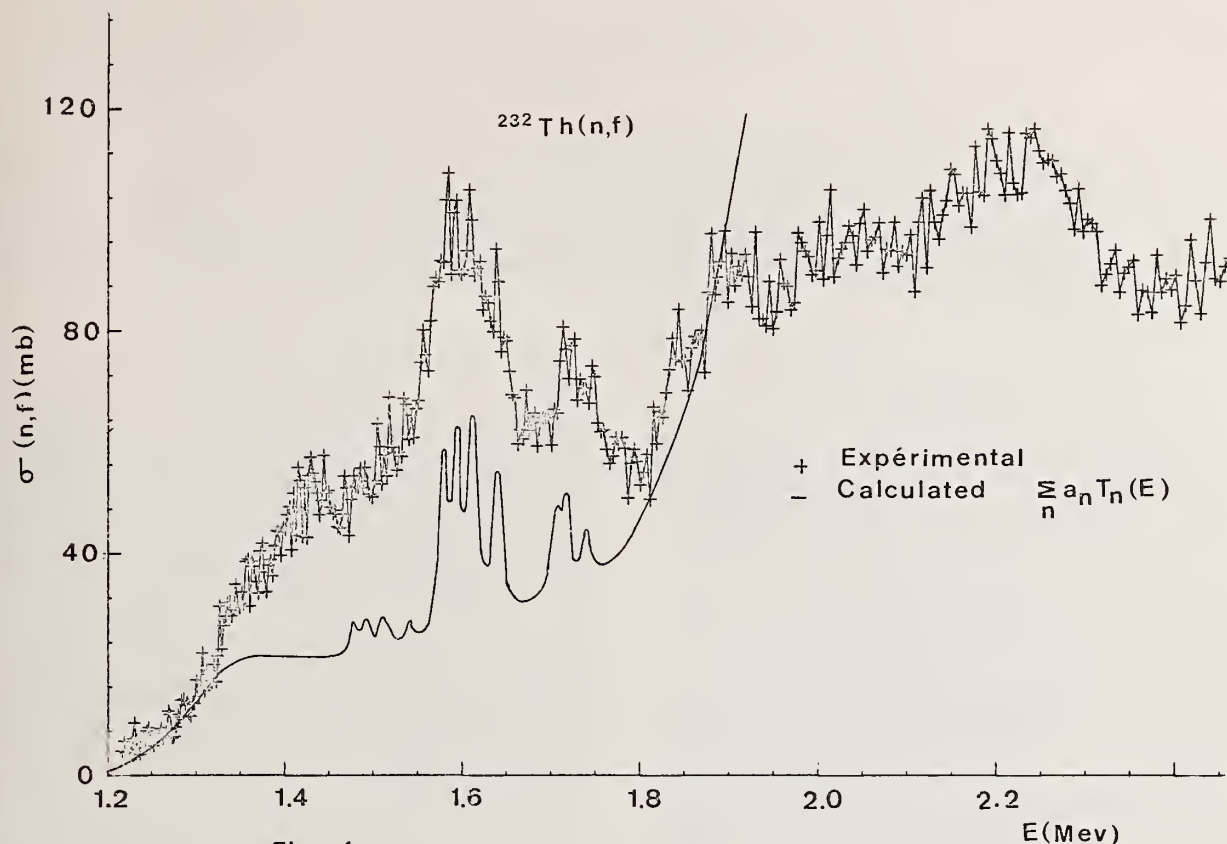


Fig.:4

#### Conclusion

Due to good energy resolution, we have been able to resolve many fine structures in the  $^{238}\text{U}(n,f)$  and  $^{232}\text{Th}(n,f)$  cross sections near the fission threshold. For  $^{232}\text{Th}$ , these fine structures have been identified as rotational bands built on vibrational levels. In the resonance region, intermediate structures have been observed for  $^{238}\text{U}$ . These measurements are intended to provide accurate fission cross sections up to 6 MeV. Data processing is in progress and the results will be published in the near future.

#### References

- 1 J. BLONS et al. Rev. Phys. appl. 4 (1969) 287.
- 2 R.C. BLOCK et al. Phys. Rev. Lett. 31 (1973) 247.
- 3 J.E. LYNN et al. AERE. R 6901 (1971).
- 4 E. KONECNY et al. Z. Physik, 251, (1972) 400.

## NUCLEAR DATA NEEDS FOR FUSION REACTOR DESIGN\*

Don Steiner

Oak Ridge National Laboratory  
Oak Ridge, Tennessee 37830

The nuclear data needs associated with the development of fusion as an energy source will be discussed in terms of seven areas of design application including: fusion fuel cycles, tritium breeding performance (for concepts based on the D-T fuel cycle), nuclear heating, radiation damage effects, induced activity, radiation shielding, and hybrid concepts. Dosimetry applications will also be considered. The areas of application described above will be related to specific types of nuclear data and to the programmatic requirements of the Controlled Thermonuclear Research effort. The paper concludes with a summary of recent activities relevant to CTR nuclear data needs.

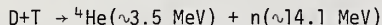
(Nuclear data for fusion; fusion reactor design)

### Introduction

The nuclear data needs associated with the development of fusion as a source of power are extensive and encompass nuclear data needs encountered in fission reactors, nuclear weapons, and accelerator programs. The purpose of this paper is to both elucidate and assess the nuclear data needs for fusion reactor design. These data needs will be discussed in terms of seven areas of application: 1) the fuel cycle, 2) tritium breeding, 3) nuclear heating, 4) radiation damage effects, 5) induced activity, 6) radiation shielding, and 7) hybrid concepts. The types of nuclear data required for each design application are summarized in Tables 1 and 2. The relevance of these design applications to experimental facilities projected for the U.S. Controlled Thermonuclear Research (CTR) Program during the next two decades is indicated in Table 3. The Fusion Test Reactor (FTR) will produce ~1-10 MW(t) and will operate within the time period ~1980-1985. The Experimental Power Reactor (EPR) will produce net electrical power and spans the time period ~1985-1995.

### The Fuel Cycle

The fusion reactions of primary interest are those involving the isotopes of hydrogen, D and T, and the helium isotope,  $^3\text{He}$ . Fuel cycles based on these isotopes produce substantial amounts of neutrons and require the handling of tritium. It has been suggested, [1,2] that higher-Z materials such as lithium, beryllium and boron be used as fusion fuels in order to provide fuel cycles which are essentially free of neutrons and tritium. However, the high-Z fuel cycles exhibit more demanding requirements for confinement and heating than do the low-Z fuel cycles. In this paper, the emphasis will be placed on the



fuel cycle because it is the most probable candidate for the initial phases of fusion power.

The accuracy of the  $\text{T}(\text{d},\text{n}){}^4\text{He}$  cross section in the energy range of interest (several KeV to several hundred KeV) appears adequate for current fusion studies. [3] However, there is no evaluated data set for this cross section which is of fundamental importance to the fusion effort. Therefore, it is recommended that an extensive evaluation of the  $\text{T}(\text{d},\text{n}){}^4\text{He}$  cross section be undertaken as soon as possible in order to insure that the most reliable data set be available for the program. It is further recommended that an evaluated nuclear data library be established for charged particle reactions of interest in fusion fuel-cycle analysis (including both low-Z and high-Z fuels).

Research sponsored by the Energy Research and Development Administration under contract with the Union Carbide Corporation.

### Tritium Breeding

A fusion power economy based on the D-T fuel cycle requires that tritium be bred in a blanket region surrounding the plasma. This requirement implies that lithium in some form must be present in the blanket since the only neutron-induced reactions which offer any promise for tritium breeding are  ${}^6\text{Li}(\text{n},\alpha)\text{T}$  and  ${}^7\text{Li}(\text{n},\alpha\text{n}')\text{T}$ . The  ${}^6\text{Li}(\text{n},\alpha)\text{T}$  reaction cross section varies inversely with neutron velocity below approximately 0.3 MeV. In any practical blanket, the  ${}^6\text{Li}(\text{n},\alpha)\text{T}$  reaction must compete with parasitic absorptions in structural materials. The  ${}^7\text{Li}(\text{n},\alpha\text{n}')\text{T}$  reaction has a threshold at about 2.8 MeV and, therefore, must compete with neutron downscattering processes, i.e., elastic scattering, inelastic scattering and  $(\text{n},2\text{n})$  reactions. Neutron multiplication resulting from  $(\text{n},2\text{n})$  reactions, to some extent, compensates for neutron losses due to parasitic absorption and leakage.

In addition to the breeding medium, the blanket will, in general, consist of structural material, coolant, and neutron moderator. In some designs, beryllium is included for neutron multiplication via  $(\text{n},2\text{n})$  reactions. The range of materials currently being considered for the various blanket functions is indicated in Table 4.

Cross-section sensitivity studies of tritium breeding in current fusion reactor blanket designs yield the following results: [4,5,6]

1. The status of the  ${}^6\text{Li}(\text{n},\alpha)\text{T}$  cross-section data appears adequate for accurate (of the order of ~1%) tritium-breeding calculations.
2. Uncertainties in the cross section and secondary neutron energy distribution of the  ${}^7\text{Li}(\text{n},\alpha\text{n}')\text{T}$  reaction attach uncertainties in the range of ~2-7% to the tritium breeding ratio. A re-evaluation of the relevant data in the energy range above ~10 MeV might provide a smaller uncertainty. Additional measurements may be required to reduce the uncertainty in the tritium-breeding ratio to the order of 1-2%.
3. Uncertainties in the cross section and secondary neutron energy distribution of the  $\text{Be}(\text{n},2\text{n})$  reaction can introduce uncertainties of the order of several percent in the tritium-breeding ratio. Additional measurements may be required to reduce this uncertainty.

### Nuclear Heating

All elastic and nonelastic interactions will result in the deposition of nuclear heat via the slowing down of the reaction products. Nuclear heat will also be deposited by the attenuation of secondary gamma rays. The major sources of these gamma rays will be nonelastic and radiative capture events. A detailed knowledge of



the secondary gamma-ray spectra is required for the thermal-hydraulic design of 1) the fusion reactor blanket and 2) the superconducting magnets which surround the blanket in some fusion reactor concepts. It is noted that as much as 30% of the total energy deposited within the blanket can arise from secondary gamma rays and that over 90% of the energy deposited within the superconducting magnet system can arise from secondary gamma rays. Secondary gamma-ray data are available for thermal capture events, but are generally lacking for epithermal capture and nonelastic events. Therefore, a measurement program in the energy range  $\sim 1$ -20 MeV is recommended in order to develop a secondary gamma-ray data base requisite to the needs of the fusion program.

#### Radiation Damage Effects

Experience with fission reactors indicates that neutron-induced atomic displacements and transmutations, especially gas production via  $(n,\alpha)$  and  $(n,p)$  reactions are important causes of deleterious radiation effects in materials. The correlation between neutron-induced phenomena and radiation damage effects are, at present, highly empirical and by no means definitive. Nevertheless, estimates of the atomic displacement and transmutation rates expected in fusion reactor materials are useful for: 1) anticipating the relevant damage effects and 2) planning radiation damage experiments.

Figure 1 compares the normalized neutron spectrum in the first wall of a fusion reactor blanket with that at the core center of the fission reactor EBR-II (Experimental Breeder Reactor II). Note that about 60% of both the fusion first-wall flux and the fission core center flux consists of neutrons with energies greater than  $\sim 0.3$  MeV. However, while nearly 25% of the neutron flux in the first wall consists of neutrons with energies greater than 10 MeV, there are very few neutrons with energies greater than 10 MeV in the fission reactor. Thus, the neutron-flux spectrum will be much harder in the first wall of the fusion reactor blanket than in a fission reactor. As a result of this, nonelastic reactions which are of little importance in introducing displacements in a fission reactor environment will be very significant sources of displacement in the first wall of a fusion reactor. Moreover, the cross sections for  $(n,\alpha)$  and  $(n,p)$  reactions are typically one-to-two orders of magnitude greater at incident energies of 10 MeV than at 5 MeV.

The available data base appears especially deficient with regard to the  $(n,\alpha)$  and  $(n,p)$  reactions. Therefore, it is recommended that the status of  $(n,\alpha)$  and  $(n,p)$  reactions be evaluated relative to the needs of the CTR Program. In particular, it is important to ascertain what role nuclear model calculations can play in satisfying some of these data needs.

#### Induced Activity

A knowledge of the magnitude and characteristics of the radioactive inventories induced in blanket structural materials is necessary in order to assess the technological requirements associated with system maintenance, reactor safety and radioactive waste disposal. The calculated level of induced activity generally falls in the range  $\sim 10^9$  to  $10^{10}$  curies for a 1000 MW<sub>e</sub> fusion reactor plant. It is emphasized that the level of activity by itself is not a meaningful measure of the technological problems associated with the radioactive inventories. Thus, the nuclear afterheat and the biological effects associated with the activation products must also be considered.

This design application requires data on activation cross sections, half-lives and decay schemes. Some

measurements will be required. However, it appears that model calculations can satisfy the majority of the near-term needs in this area.

#### Radiation Shielding

Radiation shielding will be required not only for personnel protection but also for protection of superconducting magnets. The effects of nuclear heating and radiation damage will require that a substantial amount of shielding be placed between the breeding blanket and the superconducting coils. The optimum choice of shielding materials and shield configuration will be determined by several cost factors including: 1) shield material costs, 2) magnet coil costs, and 3) refrigeration costs. In reactor design studies, coil shield thicknesses in the range about 50-100 cm have been proposed. These studies have, in general, been based on one-dimensional radiation transport calculations. The effects of penetrations and other geometrical irregularities will be very important in coil shield design and, therefore, multi-dimensional transport calculations will be required in any realistic shielding design. It is expected that the effects of nuclear data uncertainties will be extremely important in the coil shield design.

#### Hybrid Concepts

Hybrid concepts refer to those schemes in which the fusion neutrons are used to: 1) produce fissile material for subsequent use in fission reactions; 2) burn fertile and fissile material *in situ*; or 3) transmute long-lived radioactive wastes (in particular, the actinides) into short-lived radioactive wastes and stable isotopes. Such applications will require additional data on the fission and adsorption cross sections of the fertile and fissile materials and also of the actinides, especially at energies near 14 MeV. Also, improved data on secondary neutron spectra from nonelastic events in these materials will be required.

#### Neutron Dosimetry

In addition to the nuclear data requirements discussed above, the Controlled Thermonuclear Research Program will require accurate nuclear data in the area of neutron dosimetry. Neutron dosimetry applications for the CTR Program include: 1) the characterization of radiation environments for materials testing, and 2) the development of diagnostic tools for studying fusion reaction rates by means of analyzing the emitted neutrons.

In the near-term, it appears that foil-activation spectral-unfolding techniques will provide the principal dosimetric tool for the characterization of radiation environments employed in the CTR Materials Program. The CTR Materials Program is currently using fission reactors and the D-T Rotating Target Neutron Source (RTNS) at Livermore for its radiation damage studies. A great deal of effort has gone into dosimetry development for fission reactors; moreover, it appears that the dosimetry requirements for the RTNS, which produces a nearly monoenergetic beam of 14.8 MeV neutrons, are not too demanding. The CTR Program is also considering the use of deuteron-stripping neutron sources and spallation type neutron sources, such as the LAMPF beam-stop facility at LASL, for radiation damage studies. For such sources, the dosimetry requirements are much more demanding because of the rather broad spectrum of neutron energies produced.

#### Concluding Remarks

In order to develop a nuclear data base which will satisfy the needs of the fusion program, it appears that the major near-term effort should be directed



toward data evaluation and assessment. An experimental effort should also be initiated and, in the near term, secondary gamma-ray production data seem to be of high priority. In conclusion, it is useful to summarize some recent ERDA activities relevant to CTR nuclear data requirements.

The Division of Controlled Thermonuclear Research has initiated the following:

1. A CTR Evaluated Cross-Section Library is being established and will be maintained by the Radiation Shielding Information Center at Oak Ridge National Laboratory.

2. A program of nuclear data assessment, including sensitivity testing, has been undertaken in order to define quantitative requests for nuclear data measurements.

3. A dosimetry effort has been established under the auspices of the Dosimetry and Damage Analysis Center at Argonne National Laboratory.

The Division of Physical Research has supported the CTR nuclear data effort as follows:

1. The CTR Subcommittee of the U.S. Nuclear Data Committee has assembled a report entitled, "The Status of Neutron-Induced Nuclear Data for Controlled Thermonuclear Research Applications: Critical Reviews of Current Evaluations." [7] The purpose of this document is to provide a point of departure for evaluating the current data base relative to CTR applications.

2. The Division of Physical Research has initiated several measurements relevant to the CTR Program.

3. The U.S. Nuclear Data Committee will soon publish a data request list which includes 76 CTR requests. It is noted that the majority of these requests are for evaluations.

#### Acknowledgements

The author wishes to express his gratitude for the valuable input of N. D. Dudey (Argonne National Laboratory), B. R. Leonard (Pacific-Northwest Laboratory), J. R. McNally, Jr. (Oak Ridge National Laboratory), and L. K. Price (ERDA, Division of Controlled Thermonuclear Research).

#### References

1. J. R. McNally, Jr., "Fusion Chain Reactor Prospects and Problems," ORNL-TM-4575, Oak Ridge National Laboratory (1974).
2. T. Weaver, G. Zimmerman, and L. Wood, "Prospects for Exotic Fuel Usage in CTR Systems," UCRL-74191 (1972).
3. L. Stewart and G. M. Hale, "The  $T(d,n)^4\text{He}$  and  $T(t,2n)$  Cross Sections at Low Energies," LA-5828-MS USNDC-CTR-2, Los Alamos Scientific Laboratory (1975).

4. D. Steiner and M. Tobias, "Cross Section Sensitivity of Tritium Breeding in a Fusion Reactor Blanket: Effects of Uncertainties in Cross Sections of  $^6\text{Li}$ ,  $^7\text{Li}$  and  $^{93}\text{Ni}$ ," Nuclear Fusion 14, p 153 (1974).
5. R. G. Alsmiller, Jr., R. T. Santoro, J. Barish, and T. A. Gabriel, "Comparison of the Cross Section Sensitivity of the Tritium Breeding Ratio in Various Fusion Reactor Blankets," to be published in Nuclear Science and Engineering.
6. P. D. Soran, D. J. Dudziak, and D. W. Muir, "Effect of the  $\text{Be}(n,2n)$  Multigroup Treatment on Theta-Pinch Blanket Nucleonics," Proceedings of the First Topical Meeting of the Technology of Controlled Nuclear Fusion, April 16-18, 1974, San Diego, California, CONF 740402-P2.
7. D. Steiner (Compiled by), "The Status of Neutron-Induced Nuclear Data for Controlled Thermonuclear Research Applications: Critical Review of Current Evaluations," USNDC-CTR-1, Oak Ridge National Laboratory (1974).

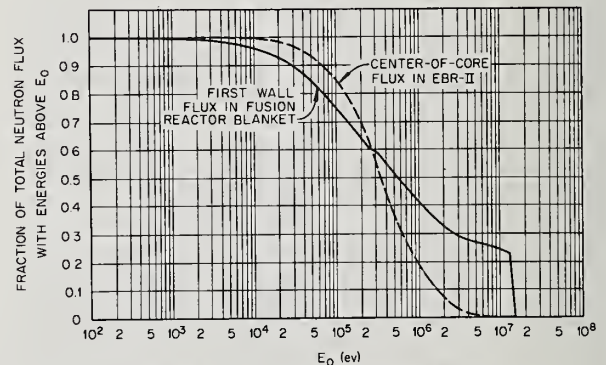


Fig. 1. The fraction of the total neutron flux with energies above  $E_0$ , as a function of  $E_0$ , for the neutron flux in the first wall of a fusion reactor blanket and at the center of the core of EBR-II.

Table 1. Nuclear Data Required for Design Applications

Data Type and Application	High Z		Fusion Reactions	Charged Particle	Photonuclear	$t_{1/2}$	Decay Schemes	Activation	Transmutation
	n, f	Other							
1. D-T Nuclear Reactions			X	X					
2. Alternate Fuel Cycles			X	X					
3. Nuclear Heating						X	X	X	
4. Radiation Damage									X
5. Induced Activity					X	X	X	X	
6. Radiation Shielding			X		X	X	X	X	
7. Hybrid Concepts	X	X						X	X

Table 2. Nuclear Data Required for Design Applications

Data Type and Application	Tritium Production	Elastic	Inelastic	n, 2n	n, p	n, d	n, $\alpha$	n, n', X	n, $\gamma$	n, X $\gamma$	n, n', $\gamma$
1. Tritium Production & Breeding	X	X	X	X							
2. Nuclear Heating	X	X	X	X	X	X	X	X	X	X	X
3. Radiation Damage Effects		X	X	X	X	X	X	X			
4. Radiation Shielding		X	X	X					X	X	X

Table 3. Design Applications Relevant to  
Experimental Facilities Projected for the US-CTR Program

Design Application	FTR <sup>a</sup>	EPR <sup>b</sup>
D-T Nuclear Reactions	X	X
Tritium Production		X
Nuclear Heating	X	X
Radiation Damage Effects		X
Induced Activity	X	X
Radiation Shielding	X	X

<sup>a</sup>Fusion Test Reactor (FTR).

<sup>b</sup>Experimental Power Reactor (EPR).

Table 4. Summary of Materials Being Considered  
for Blanket Applications

Application	Materials
Breeding	Liquid Lithium Molten Salts ( $\text{Li}_2\text{BeF}_4$ , LiF) Ceramic Compounds ( $\text{Li}_2\text{O}$ , $\text{Li}_2\text{C}_2$ ) Aluminum Compounds ( $\text{LiAl}$ , $\text{Li}_2\text{Al}_2\text{O}_4$ )
Structural	Refractory-Based Alloys (Nb, V, Mo) Iron-Based Alloys Nickel-Based Alloys Aluminum-Based Materials Carbon-Based Materials
Coolant	Liquid Lithium and Potassium Molten Salts Helium
Moderator	The Breeding Materials Graphite
Neutron Multiplication	Beryllium



MODEL CALCULATIONS AS ONE MEANS OF SATISFYING THE  
NEUTRON CROSS SECTION REQUIREMENTS OF THE CTR PROGRAM\*

Donald G. Gardner  
Lawrence Livermore Laboratory  
Livermore, CA 94550

A large amount of cross-section and spectral information for neutron-induced reactions will be required for the CTR design program. To undertake to provide the required data through a purely experimental measurement program alone may not be the most efficient way of attacking the problem. It is suggested that a preliminary theoretical calculation be made of all relevant reactions on the dozen or so elements that now seem to comprise the inventory of possible construction materials to find out which are actually important, and over what energy ranges they are important. A number of computer codes for calculating cross sections for neutron induced reactions have been evaluated and extended. These will be described and examples will be given of various types of calculations of interest to the CTR program.

[Cross-section calculations; statistical model codes; fast neutron reactions;  
radiation widths; gamma-ray production; isomers; applications to CTR.]

### Introduction

In a recent document<sup>1</sup> of the U.S. Nuclear Data Committee, entitled "Compilation of Requests for Nuclear Data", there are some 587 requests for information on various nuclear cross sections, of which over 100 came specifically from the AEC's Division of Controlled Thermonuclear Research (DCTR). In our opinion, only a small fraction of these requests will be satisfied in any reasonable length of time through an experimental program alone. Furthermore, these requests do not always specify the most important reactions or the most appropriate energy ranges. Finally, neutron reactions involving low abundance stable isotopes or even unstable species such as long-lived isomers or radioactive daughter products may be important in certain design considerations, and such reactions are inaccessible to normal experimental measurement in the laboratory.

It seems to us that the only approach that will get the job done is to make a preliminary theoretical calculation of all relevant reactions to find out which ones are actually important, and over what energy ranges they are important. This would then be followed by an experimental program to carefully measure only those reactions which are critical.

For certain engineering studies the calculated cross sections themselves might be sufficiently accurate, at least for preliminary evaluations, without further recourse to experiment. In a situation where there is a choice between otherwise comparable structural materials, calculations might show which material would cause the least problems. The calculated cross sections, when folded against estimated neutron flux histories from a CTR reactor, can show if unstable isotopes or isomers are important and to what extent deleterious daughter products will be produced and burned up. With regard to the experimental measurement program, the cross-section calculation can be used as a guide so that manpower is not wasted measuring relatively unimportant reactions and that important reactions are not overlooked.

### Nuclear Cross Section Codes

There are many different codes at Livermore of use in calculating nuclear reaction cross sections; however, we will restrict our discussion to the codes that we now have and are developing in Radiochemistry Division. Only the nuclear reaction codes will be discussed; no mention will be made of programs, such as nuclear structure codes, that may supply input information for our main programs.

\* Work performed under the auspices of the United States Atomic Energy Commission.

Our present codes comprise COMNUC<sup>2</sup> and CASCADE<sup>2</sup>, which are, respectively, a statistical model program and a program to calculate in detail the particle emission and fission competition occurring in a gamma-ray cascade; UHL<sup>3</sup>, another statistical model code used to compute isomer ratios; and FOURPLUS<sup>4</sup> and JUPITOR<sup>5</sup> which are coupled-channel, direct reaction codes. The codes were acquired during the past four-year period, and some have been extensively modified with the guidance of the original authors. Although we are still continuing the development of the codes, we feel at this time that they represent an exceptional facility for computing neutron-induced reaction cross sections in the neutron energy region from overlapping resonances up to perhaps 20 MeV.

Because of the exceptionally fine computer system at Livermore we are able to include in our calculations details and refinements that often are omitted. For example, the first compound nucleus population is computed for each  $J\pi$  spin and parity state, using optical model transmission coefficients, and the decay of each  $J\pi$  state is followed separately through all subsequent nuclei. At low energies, where only a few exit channels are available, the decay back to the target nucleus through the entrance channel is enhanced in COMNUC with a "correlation" correction, and again each  $J\pi$  state is considered separately. At each nucleus the gamma-ray emission in competition with particle decay and fission is considered. A combination constant temperature and Fermi gas level density may be used, and a simple yrast model is included so that unrealistically high spin states are not produced at low energies. Discrete nuclear levels may be included in all nuclei, as well as discrete fission channels where appropriate. This is vital for accurate calculations because level-density formulations cannot adequately represent the first 20 or so levels. In addition, the UHL code incorporates precompound evaporation of particles from the first compound nucleus. Both the UHL and the COMNUC - CASCADE codes calculate in great detail gamma-ray cascades. They are, to our knowledge, unexcelled in calculating reactions leading to isomers and reactions where gamma-ray cascades may be terminated by particle emission or fission before reaching the ground state.

Whenever the target nucleus is deformed it is necessary to calculate and correct for direct inelastic scattering reactions using the coupled-channel codes. The COMNUC code will accept reduced transmission coefficients from direct reaction codes, in order to properly compute the spin distribution in the first compound nucleus. The code will also accept

direct inelastic scattering cross sections and Legendre coefficients, and combine them with the compound nucleus evaporation results to give the complete inelastic scattering cross sections and angular distributions.

The codes COMNUC and UHL are compared in Table I. While they are both statistical model evaporation codes and while there are a number of differences between them they tend to complement each other. Neither code can do all calculations of interest to us, and each code was designed to do certain types of calculations better than the other code.

Table I. Comparison of current versions of statistical model codes at Livermore

Comment	COMNUC	UHL
1. Hauser-Feshbach with correlation correction	Yes	No
2. Moldauer's compound elastic "Q" correction	Yes	No
3. Built-in optical model program	Yes	No
4. Computes shape elastic and total cross sections	Yes	No
5. All possible cross sections always calculated	Yes	No
6. Entrance channel always neutrons	Yes	No
7. Level density formulation	Constant temperature plus Fermi gas	
8. Simple yrast level model	Yes	Yes
9. Discrete states in all nuclei considered	Yes	Yes
10. Computes angular distribution for discrete neutron channels	Yes	No
11. Calculates spectra of emitted particles	No	Yes
12. Precompound evaporation allowed	No	Yes
13. Gamma-ray competition with each compound nucleus	Yes	Yes
14. Maximum number of compound nuclei in evaporation sequence	3	6
15. Calculates gamma-ray spectra and gamma-ray production cross sections	No	Yes
16. Weisskopf and/or Brink-Axel energy dependence of the radiation width	Yes	Yes
17. Fission competition allowed	Yes	No
18. Direct and semi-direct neutron capture	Yes	No
19. Computes isomer populations	No	Yes
20. Accepts input from direct reaction codes	Yes	No

#### Cross-Section Calculations for the CTR Program

In a thermonuclear reactor the first wall material will face an incredibly intense, sustained radiation environment, and so radiation damage is likely to be a controlling engineering consideration in the reactor design. For the first wall this damage will be due mainly to elastic and inelastic neutron scattering and  $(n,2n)$  reactions from fast neutrons, while for low energy neutrons the  $(n,\gamma)$  reaction will be the main source of damage. For most first wall materials under consideration,  $(n,p)$  and  $(n,\alpha)$  reactions play a lesser role in displacement production, although blister production and embrittlement by hydrogen, and in particular by helium, may be a serious problem in the blanket components as well as the first wall. However, when it comes to heat deposition, in the cryogenic materials for example, it is the  $(n,p)$  and  $(n,\alpha)$  reactions, along with neutron capture, that become of major importance. Tritium production in the CTR is vital and this will be accomplished via neutron reactions on  $^6\text{Li}$ . However, only one neutron is produced per D-T reaction, which means that neutron multiplication through  $(n,2n)$  reactions is required. Shielding from both neutrons and gamma rays will be necessary to protect components and also to satisfy biological requirements. And then there is the problem of radioactivity produced in the reactor components. Here reliable data are essential for engineering, processing and storage design, not to mention the environmental aspects and public acceptance.

#### $(n,p)$ and $(n,\alpha)$ Reactions

With regard to the problems of hydrogen and helium embrittlement and energy deposition in structural materials, one could compute the excitation functions of these reactions for various materials such as niobium, vanadium or stainless steel, and point out which materials will cause the greatest problems. In Fig. 1 we compare an old calculation of an  $(n,\alpha)$  reaction on  $^{40}\text{Ca}$  with an experimental excitation function<sup>6</sup> measured about one year after the calculation was made. The agreement is quite satisfactory.

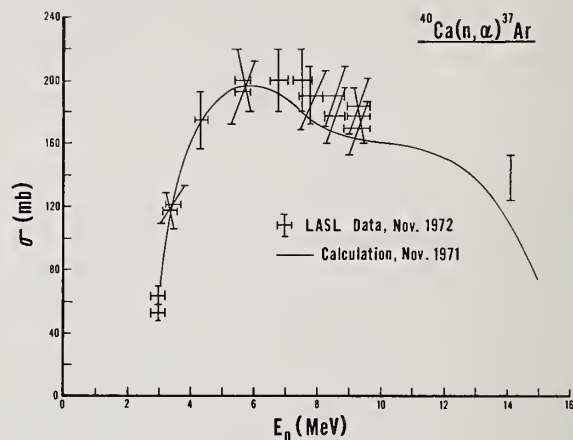


Fig. 1. Calculated and experimental values for the  $^{40}\text{Ca}(n,\alpha)^{37}\text{Ar}$  reaction.

It often happens that around 14 MeV in light materials the  $(n,pn)$  and  $(n,np)$  reactions are comparable to the  $(n,p)$  reaction in magnitude. Hence, measuring only the  $(n,p)$  reaction isn't sufficient. What one needs is the cross section for proton production by whatever means possible. To a lesser extent this is also true for  $\alpha$ -particle production, since  $(n,\alpha n)$  and  $(n,\alpha\alpha)$  reactions must often be considered as well as the  $(n,\alpha)$  reaction. Figs. 2 and 3 show rough calculations for proton and alpha-particle production from neutron reactions on the ground state of  $^{93}\text{Nb}$ . The calculations were made two years ago using global parameters for radiation widths, level densities and transmission coefficients. No attempt was made to adjust any parameters to fit experimental data. Similar calculations for  $^{51}\text{V}$  show that around 14 MeV the  $(n,p)$  and  $(n,pn)$  cross sections are quite similar, while the  $(n,np)$  cross section is about a factor of two greater than the sum of the  $(n,p)$  and  $(n,pn)$  cross sections.

Another common occurrence in such light materials is that neighboring isotopes of an element will have quite sizeable differences in the Q-values for  $(n,p)$  and  $(n,\alpha)$  reactions. For instance  $^{54}\text{Fe}$  and  $^{56}\text{Fe}$  have high thresholds for  $(n,p)$  and  $(n,\alpha)$  reactions whereas unstable  $^{55}\text{Fe}$  will undergo these reactions with thermal neutrons. The isotope  $^{50}\text{V}$  has considerably higher cross sections than does  $^{51}\text{V}$  for  $(n,p)$  and  $(n,\alpha)$  reactions for neutrons of a few MeV and lower. Therefore, the importance of rare stable isotopes or unstable species will depend on the energy spectrum and the fluence of neutrons to which they are exposed. Structural materials will be exposed to a sea of scattered,



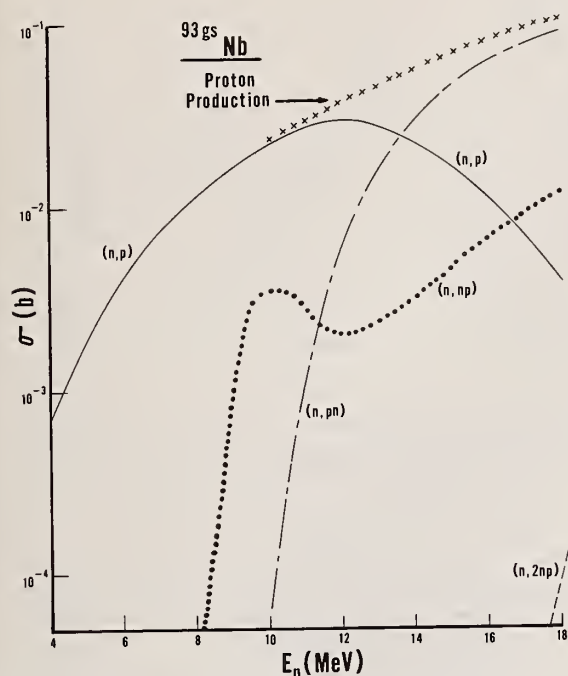


Fig. 2. Estimated proton production induced by neutrons on  $^{93}\text{Nb}$  ground state.

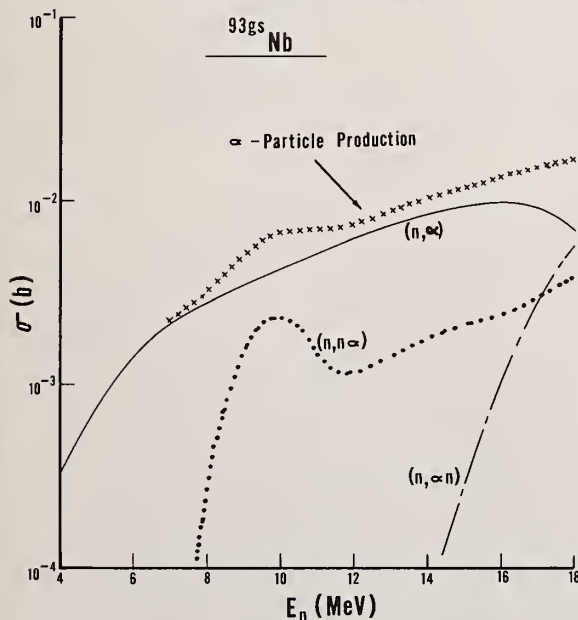


Fig. 3. Estimated helium production induced by neutrons on  $^{93}\text{Nb}$  ground state.

lower energy neutrons in addition to the primary spectrum of neutrons emitted by the plasma. Furthermore, the primary flux will tend to be normal to the surface of the first wall, while the scattered flux will have a full selection of incident angles and thus have a longer average path in the wall and other structural components. Hence, realistic calculations should be made over all neutron energies, not just at 14 MeV, to see if such rare or unstable species are important.

#### Gamma-Ray Production and Shielding

Gamma-ray production cross sections and the energy spectrum of the emitted gamma rays following most particle reactions can be computed, particularly in the gamma-ray energy regions below one MeV and above 5 MeV where the greatest experimental difficulties are encountered. In the latter range it is the transmission of the gamma-ray flux through shielding that is of concern, whereas for low-energy gamma rays it is usually the local deposition of energy resulting in ionization or heat that is important. To assist in local heating calculations one can also compute the conversion-electron, production cross section and energy spectrum.

Recently we have made calculations for  $^{181}\text{Ta}$  for neutrons up to 20 MeV in energy, and for  $^{197}\text{Au}$  for neutrons in the keV region. Fig. 4 presents some of our  $^{181}\text{Ta}$  results compared with experimental measurements from Oak Ridge.<sup>7</sup> Fig. 5 compares the calculated conversion electron spectrum following thermal neutron capture with some unpublished, relative measurements.<sup>8</sup> The latter were arbitrarily normalized at the point

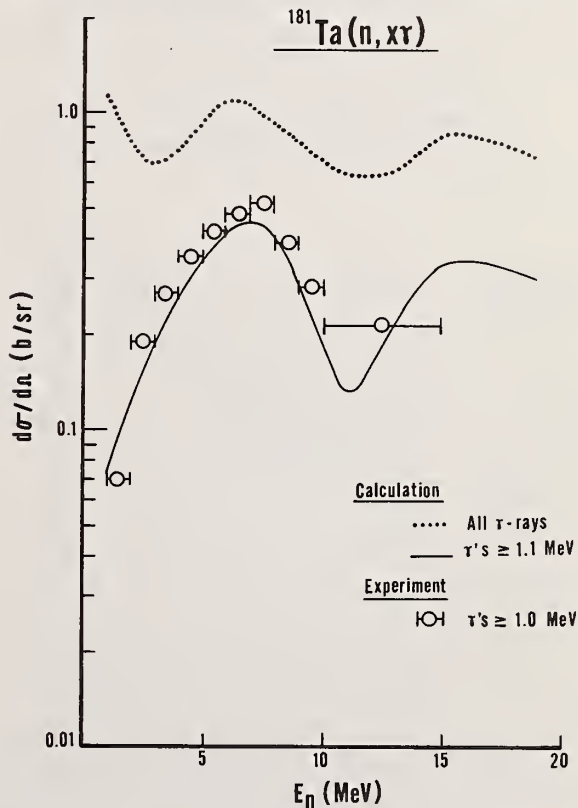


Fig. 4. Calculated and experimental values for gamma-ray production induced by neutrons on  $^{181}\text{Ta}$ .



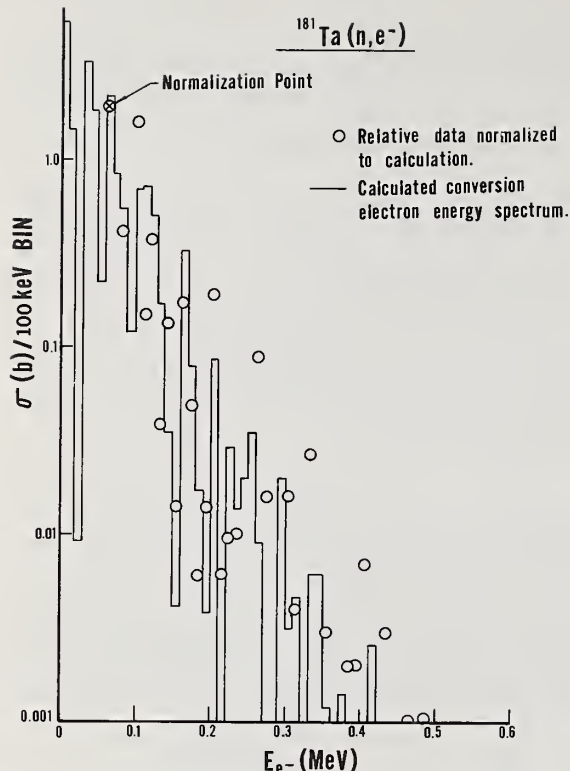


Fig. 5. Calculated conversion electron spectrum following thermal neutron capture on  $^{181}\text{Ta}$ , compared with normalized, relative experimental measurements.

shown so that the general trend of the data could be compared with the calculations. The calculated transitions have been grouped in 100-keV bins for clarity.

As an example of a calculation of the gamma-ray energy distribution following neutron capture, we show in Fig. 6 some recent results for  $^{197}\text{Au}$ . The calculation is in terms of photons/100 captures, and hence is quite insensitive to the magnitude of the radiation width employed. The data is that of Orphan.<sup>9</sup> We show the original, unnormalized data, and disregard the measurements for gamma rays below 2 MeV in energy. The EI gamma-ray strength function required to fit both the energy spectrum and the  $(n, \gamma)$  excitation function shown in Fig. 7 is displayed in Fig. 8. The general shape and magnitude agree with the strength functions extracted from other experimental data.<sup>10</sup> To obtain the indicated shape it was necessary to assume that the energy dependence of the radiation width corresponded to about 60% Brink-Axel, with a large, sharp decrease in the tail of the giant dipole resonance around 4 MeV, together with 40% "pigmy" resonance around 2.9 MeV. An almost equally good fit could be obtained with a combination of 30% Brink-Axel (with the same step) and 70% Weisskopf single particle energy dependence.

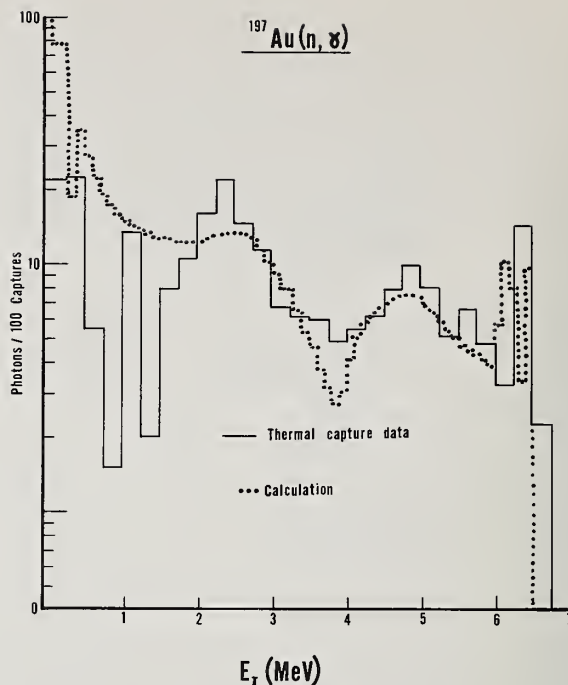


Fig. 6. Calculated and experimental values for the gamma-ray energy spectrum following thermal neutron capture by  $^{197}\text{Au}$ .

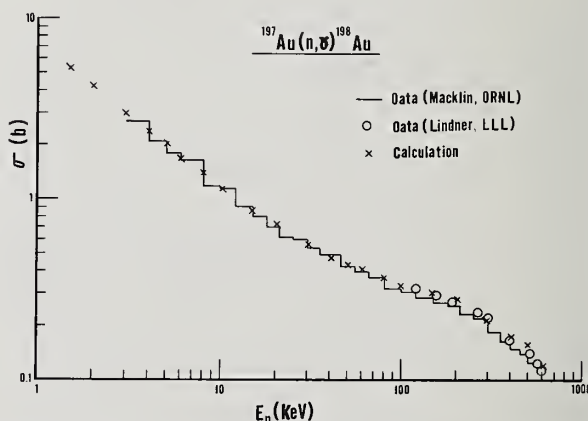


Fig. 7. Calculated and experimental values for the capture cross section of  $^{197}\text{Au}$ .

The step in the giant dipole tail amounted to about 95% decrease, and was necessary to reproduce the "excess" high-energy gamma rays in the capture spectrum. The same step is responsible for the fact that "excess" high-energy gamma rays do not appear in the spectrum following neutron inelastic scattering. When the same strength function is assumed for  $^{197}\text{Au}$  as was determined for  $^{198}\text{Au}$ , the results shown in Fig. 9 are obtained for the  $^{197}\text{Au}(n, n'\gamma)$  reaction. Even at

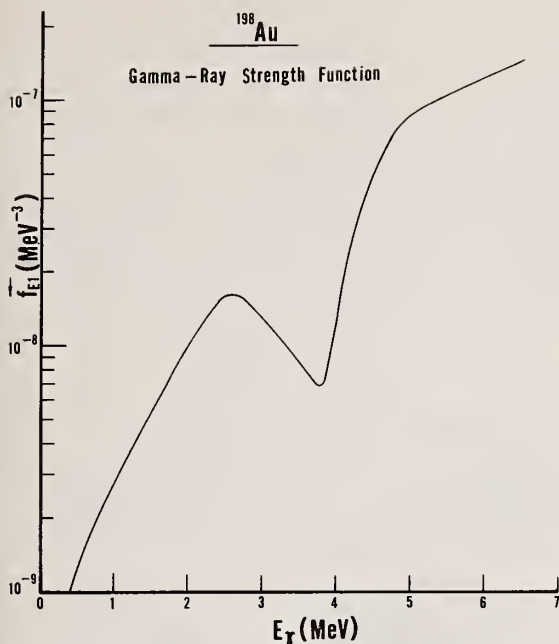


Fig. 8. Deduced gamma-ray strength function for  $^{198}\text{Au}$ .

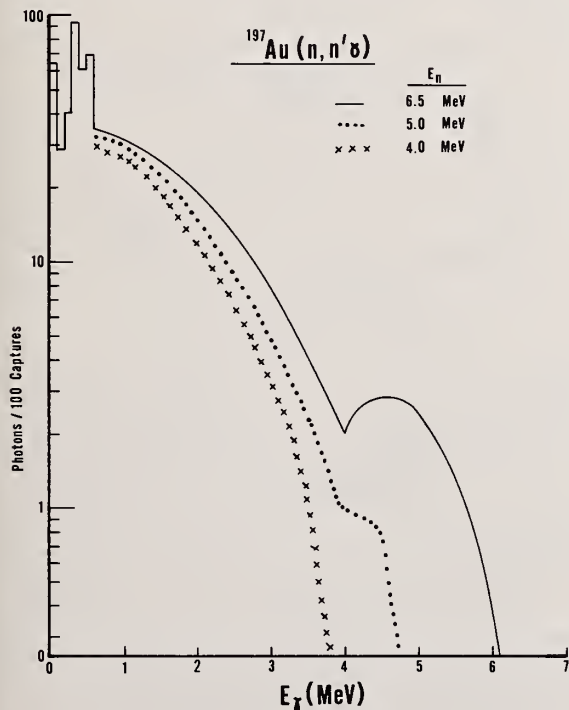


Fig. 9 Calculated gamma-ray spectrum following the inelastic scattering reaction on  $^{197}\text{Au}$ .

6.5 MeV, which corresponds to the neutron separation energy in  $^{198}\text{Au}$ , the high-energy bump is barely noticeable. The reason is that the  $(n,n')$  reaction will populate states in the target nucleus from zero up to

the center-of-mass energy of the incident particle. Only those states higher in energy than the step in the strength function can produce the high-energy bump, and it is only a small fraction of these states that actually will emit the required high-energy gamma rays. Clearly, the  $(n,n')$  gamma-ray spectrum will always be more skewed towards lower-energy transitions than the capture spectrum at an equivalent energy.

In the past we have used the approach of Stolovy and Harvey<sup>11</sup> to estimate unknown radiation widths. They suggest the semi-empirical relation

$$\overline{\Gamma}_\gamma = K A^{2/3} U^\alpha [D(U)]^\beta, \quad (1)$$

where  $A$  is the mass,  $U$  is the excitation energy corrected for pairing effects, and  $D(U)$  is the level spacing per spin state.

We have obtained values<sup>12</sup> for the constants  $K$ ,  $\alpha$ , and  $\beta$  by fitting 83 experimental radiation widths for nuclei from  $^{59}\text{Co}$  to  $^{246}\text{Cm}$ . For energies and level spacings in MeV units and for radiation widths in millivolts, good results are obtained with  $K = 0.0916$ ,  $\alpha = 3.50$ , and  $\beta = 0.256$ . Actually a slight improvement is effected if smaller ranges of elements are fitted separately. Our current parameter values are given in Table II, and the calculated radiation widths are compared with experiment in Fig. 10. The error flags merely indicate the spread in the reported experimental values for a few nuclei.

Table II. Parameter Values for the Stolovy-Harvey Radiation Width Expression.

Range	$K$	$\alpha$	$\beta$
$\leq 43$	0.19241	2.9955	0.20397
44-83	0.19745	2.9297	0.23454
$\geq 84$	0.087102	1.9449	0.052733

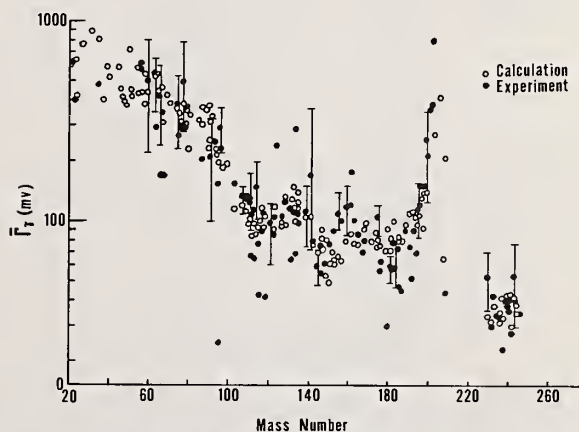


Fig. 10. Calculated and experimental values for average radiation widths.

We now feel, however, that it may be easier to develop systematics for estimating unmeasured gamma-ray strength functions, rather than the radiation widths themselves. This appears to be true at least for medium weight to heavy nuclei.

Some of the most accurate kinds of calculations that we can make involve neutron elastic and inelastic scattering reactions. For these we can compute the cross-sections, angular distributions, and the energy spectrum of the emitted neutron. Such information is of interest, for example, because these reactions are major producers of recoil target atoms, which, in turn, produce an important portion of the radiation damage in materials. Furthermore, the information is required for neutron shielding calculations, and for the estimation of radioactivity produced in structural materials.

As an example, we present some recent calculations made on  $^{235}\text{U}$ . The general situation is illustrated in Fig. 11, using the single-hump fission barrier approximation. In order to compute the inelastic scattering properly it is necessary to compute concurrently all reactions that can compete, and all calculations must be satisfactory. In this case the fission and gamma-ray competition are critically important, and because  $^{235}\text{U}$  is deformed the direct inelastic scattering to the ground state band must be

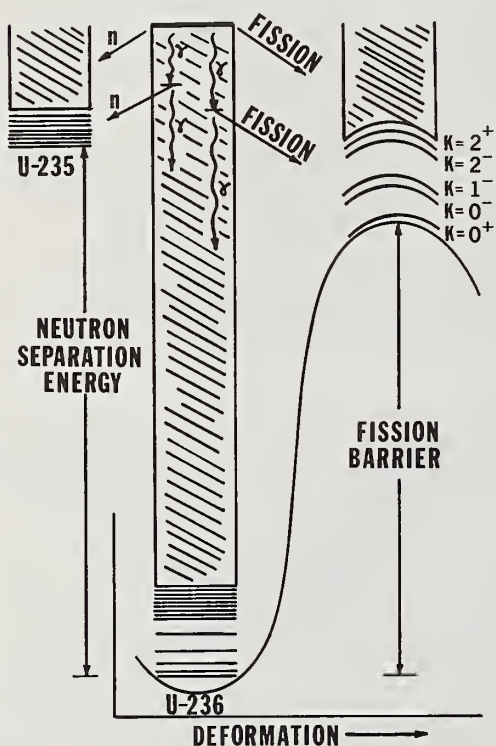


Fig. 11. Gamma-ray and fission competition to neutron inelastic scattering on  $^{235}\text{U}$ .

included. Nineteen discrete levels were included for  $^{235}\text{U}$ , twenty-five for  $^{236}\text{U}$ , and twenty discrete fission channels were used. Beyond these in each case a continuum of levels and fission channels was assumed. The discrete fission channels were taken as rotational bands built upon the vibrational bandheads shown in Fig. 11. The positions of these bandheads were

taken from the work of Britt, et al.,<sup>13</sup> and adjusted slightly to improve the fit to the ENDF/B-IV and the ENDF<sup>14</sup> evaluations. Moldauer's optical model parameters<sup>15</sup> were used to produce the neutron transmission coefficients. The total and fission cross sections appear in Fig. 12, while the elastic scattering and capture cross sections are given in Fig. 13. The angular distributions for the elastic scattering reaction, computed with a spherical potential for incident neutron energies of 0.2 and 0.5 MeV, are shown in Fig. 14. Finally, in Fig. 15 we present the calculated total inelastic scattering excitation function together with those for two of the levels in  $^{235}\text{U}$ .

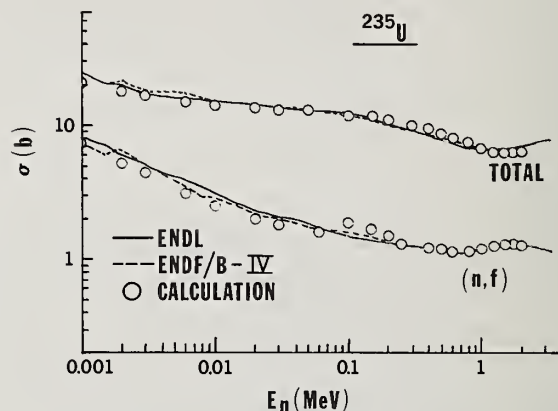


Fig. 12. Calculated and evaluated excitation functions for the neutron total and (n,fission) reactions on  $^{235}\text{U}$ .

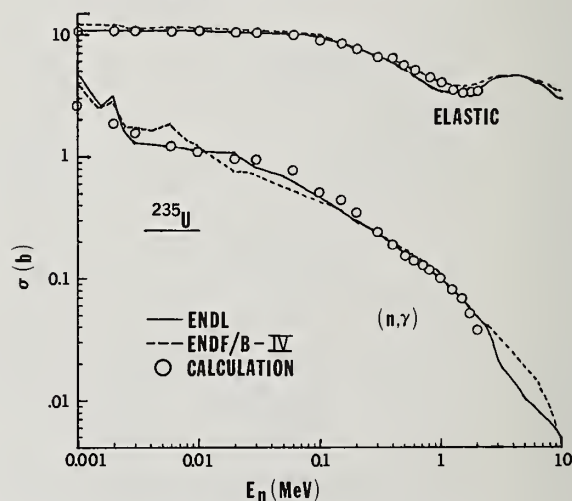


Fig. 13. Calculated and evaluated excitation functions for the neutron elastic scattering and capture reactions on  $^{235}\text{U}$ .

#### Radioactivity in Structural Materials

Radioactivity will be built up in the materials comprising a fusion reactor. Since the components must be replaceable when their damage approaches unsafe levels, it is important to know what levels of radioactivity may be anticipated in the various



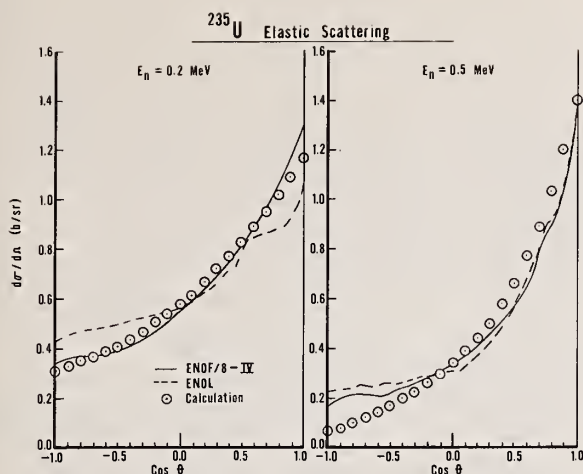


Fig. 14. Calculated and evaluated angular distributions for elastically scattered neutrons, at 0.2 and 0.5 MeV initial energy, on  $^{235}\text{U}$ .

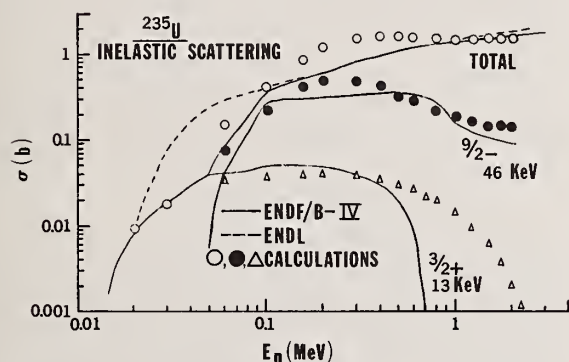


Fig. 15. Calculated and evaluated excitation functions for the total inelastic scattering reaction on  $^{235}\text{U}$ , and to two specific target levels.

components. Some components, such as the first wall, might have to be replaced every other year, while others might last 30 years or the anticipated life of a fusion reactor. Hence, not only the amount of radioactivity, but the activity as a function of operating time must be estimated.

The fast neutron flux from a fusion reactor will emphasize the importance of  $(n,2n)$  reactions, particularly where medium weight and heavy elements are involved. A relatively recent calculation for  $^{169}\text{Tm}$  is shown in Fig. 16, along with some Livermore measurements.<sup>16</sup> The high energy tail of the inelastic scattering reaction is due to precompound neutron evaporation plus the direct inelastic scattering.

Sometimes the radioactivity produced is due primarily to only one isomer in the daughter nucleus. In this case the gamma-ray cascade leading to the production of the isomer must be considered. Fig. 17 shows an old calculation for the production of the 4.5-hour isomer in  $^{115}\text{In}$ . The high-energy tail results from the assumption that the precompound evaporation of neutrons builds up to about 4% of the total

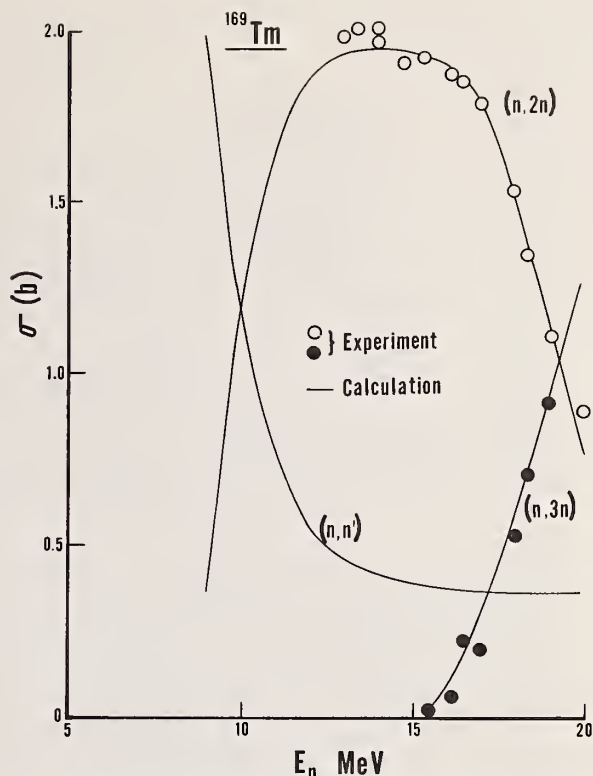


Fig. 16. Calculated and experimental values for the  $(n,2n)$  and  $(n,3n)$  reactions on  $^{169}\text{Tm}$ .

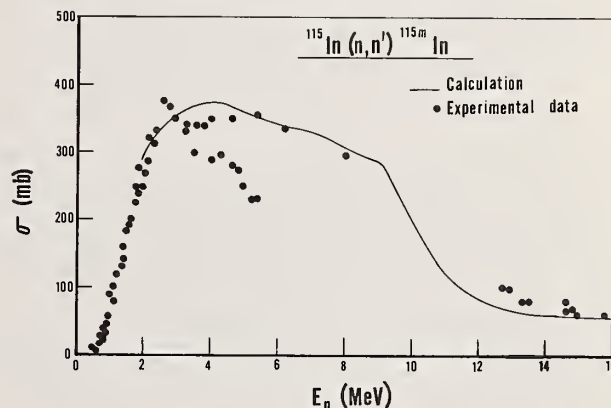


Fig. 17. Calculated and experimental values for the  $^{115}\text{In}(n,n')^{115m}\text{In}$  reaction.

neutron evaporation.

In many instances the amount of radioactivity likely to be produced could limit the choice of construction materials. For example, the 6-second positron emitter  $^{26m}\text{Al}$  produced by the  $(n,2n)$  reaction on  $^{27}\text{Al}$  might cause a problem in aluminum-based electrical insulators. Unfortunately there is about a factor of 30 discrepancy in the available experimental data. We have recently made the calculation, and in Fig. 18 we present our results both for the total  $(n,2n)$  reaction and for that fraction leading to the isomer. Our calculations are in fair agreement with the ENDF/B-IV estimate for the total  $(n,2n)$  reaction, and agree

better for the isomer production with Mani, *et al.*<sup>17</sup> than with Arnold.<sup>18</sup>

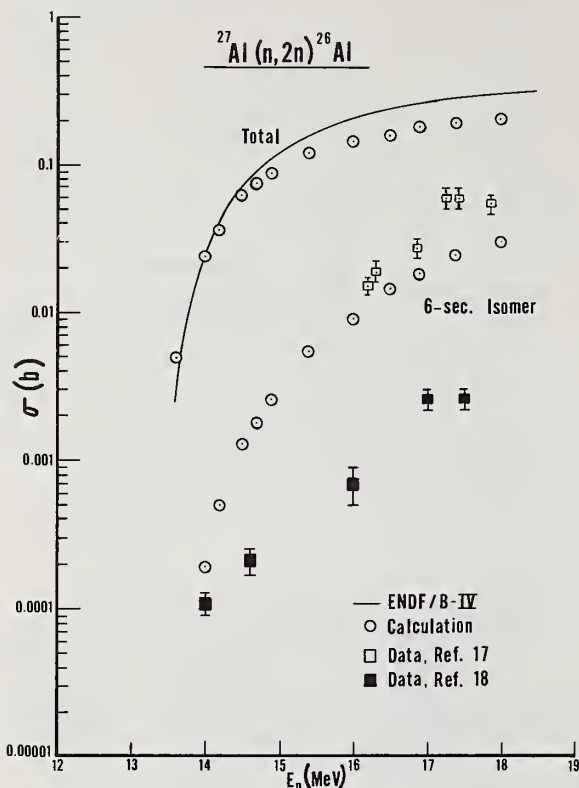


Fig. 18. Calculated excitation functions for the total (n,2n) reaction on  $^{27}\text{Al}$ , and for the production of the 6-second isomer in  $^{26}\text{Al}$ .

#### Accuracy of the Calculations

It is difficult to be quantitative about the accuracy that may be expected in any given case, because different reactions require different kinds of physical parameters as input. Our philosophy is that all reactions that occur concurrently must all be calculated satisfactorily before any of them can be trusted. If some information is available on any of the competing reactions, this will improve the accuracy of all calculations. Some reactions are inherently more difficult to calculate, and certain mass regions present more problems than others. However, a few rough generalizations may be made.

1. The total and elastic scattering reactions depend on optical model parameters. There are good sets available, for a spherical potential, that have been so adjusted to represent even deformed nuclei rather well. Finding parameters to be used with a deformed potential is far more difficult, but this is less important because the correction for direct inelastic scattering is usually less than 20% of the compound nucleus formation cross-section.
2. Inelastic scattering and (n, $\gamma$ ) reactions are dependent upon a good estimate of the first 15-25 levels in the target nucleus. We always use theoretical estimates of these levels to supplement the available experimental information. The levels in the A + 1

nucleus are of less importance, particularly for medium and heavy nuclei. However, for light nuclei, where most or all of the levels may be of one parity, the inclusion of these levels can affect the apparent energy dependence of the radiation width as the different partial waves come in. We always include precompound evaporation for neutron energies above a few MeV, although the effect is relatively small. The radiation width and its energy dependence can be estimated fairly well, and there is hope that this can be done even better with gamma-ray strength functions.

3. The (n,2n) reaction can usually be well represented, particularly for medium weight and heavy nuclei not susceptible to fission. For deformed nuclei the enhancement of the inelastic scattering at the expense of the (n,2n) reaction must be included.

4. For (n,p) and (n, $\alpha$ ) reactions at low energies it is more difficult to find satisfactory optical model parameters. Discrete level information is again quite important, and in the case of (n,p) reactions with light nuclei the precompound evaporation is very important.

5. Perhaps the most difficult situation involves fission. At low energies a shift in position of a discrete band of fission channels can be quite significant. Usually the density of fission channels at the saddle point exceeds the normal level density, and by as much as a factor of two in some cases. At high energies it becomes necessary to consider individually the (n,n' fission) and the (n,2n fission) reactions with gamma-ray and neutron competition. Except for fission isomers and subthreshold resonances related to levels in the second minimum, it is often adequate to use the single-hump barrier approximation in fission calculations.

#### Acknowledgments

We are particularly indebted to C. Dunford and M. Uhl, who supplied the original statistical model codes and guided their further development. At Livermore many people have contributed to the development of our codes and calculations. The assistance of the following people is gratefully acknowledged: J. Brownlee, A. Delucchi, C. Gatrousis, R. Lanier, N. Smith, G. Struble and J. Ferguson

#### References

1. L. Stewart, *et al.*, editors, LA-5252-MS (USNDC-6), 1973.
2. C. L. Dunford, AI-AEC-12931 (July, 1970).
3. M. Uhl, Acta Physica Austriaca **31** (1970) 245.
4. C. L. Dunford, unpublished computer program.
5. T. Tamura, ORNL-4152 (August, 1967).
6. Private communication, R. Prestwood, LASL.
7. G. L. Morgan, *et al.*, ORNL-TM-3702 (February 8, 1972).
8. P. Goudsmit, Thesis, Amsterdam University, 1969, NUIS-18536.
9. V. Orphan, *et al.*, GA-10248 (July 31, 1970).
10. G. Bartholomew, *et al.*, Advances In Nuclear Physics, Vol. 7, Chapter 4, Plenum Press, New York, 1973.
11. A. Stolovy and J. Harvey, Phys. Rev. **108** (1957) 353.
12. D. Gardner and C. Gatrousis, unpublished results.
13. H. Britt, *et al.*, Phys. Rev. **175** (1968) 1525.
14. R. Howerton, Lawrence Livermore Laboratory.
15. P. Moldauer, Nuclear Physics **47** (1963) 65.
16. D. Nethaway, private communication.
17. G. Mani, *et al.*, Nuclear Physics **19** (1960) 535.
18. D. Arnold, thesis, Dissertation Abstracts **26** (1965) 3525.



T. A. Tombrello  
California Institute of Technology  
Pasadena, California 91125

The copious production of neutrons in the "standard" CTR fuels has led to a renewed interest in proposals that various "exotic" fusion fuels be investigated. These fuels invariably involve reactions on lithium, beryllium, or boron isotopes in which most of the energy is liberated in the form of charged particles. Obtaining reaction cross sections at the appropriate energies or extrapolating the yield into inaccessible energy regions is, however, not always a straightforward procedure; and each reaction may require the development of new techniques. By means of selections from among such "exotic" fuel reactions, I shall show examples of experimental techniques for charged particle cross-section measurements at low energies and some techniques for extrapolation to still lower energies.

(NUCLEAR REACTIONS Discussion of the use of the  $d+d$ ,  $d+t$ ,  $d+{}^3\text{He}$ ,  $p+{}^6\text{Li}$ ,  $d+{}^6\text{Li}$ ,  $p+{}^9\text{Be}$ , and  $p+{}^{11}\text{B}$  reactions for CTR energy production.)

### Introduction

It is my intention in this paper to provide a brief survey of current ideas, problems, and data needs related to the use of nuclear reactions in controlled thermonuclear reactors. Though I shall be mainly concerned with questions related to nuclear reaction cross sections; problems of fuel cost, energy yield, build-up of radioactivity, etc. must be considered simultaneously to achieve a balanced perspective.

The present status of both magnetic confinement and laser driven fusion indicates that we are somewhere between two and three orders of magnitude away from the temperatures, densities, or confinement times that are necessary for useful CTR's. Thus, our current problems lie entirely in achieving these goals, thereby making the subject of this paper seem extremely premature. However, the construction of new fusion research facilities to test our current ideas involves lead times of 10-20 years; thus, even though we cannot see beyond the nearby obstacles, we need to face in parallel other difficulties that arise from radiation damage processes and fuel availability. Only if we have the required nuclear cross-section data in hand can we evaluate potential fuels and fuel cycles far enough in advance that decisions on second generation facilities can be made at an opportune time.

### Criteria for Fusion Fuels

It is quite clear that what one ultimately chooses as the optimum fusion fuel will represent a trade-off of many competing factors. A primary requirement is that one can find an exoergic nuclear reaction that has a high cross section at very low bombarding energies. From our knowledge of stellar element formation we know, however, that this requirement may also imply relative rarity. Thus, we must immediately think in terms of the cost of procuring this fuel and consider the possibility that it must be separated from other common isotopes of the same element.

Going beyond the questions of reaction rate and fuel cost, the nature of the reaction products of the fuel-burning reactions must also be taken into account. Obviously, we would like to minimize both the production of long term radioactivities and the structural damage that occurs through sputtering or through the interaction of fast neutrons with the reactor components. Such requirements involve a detailed study of the rate of radiation damage and the development of procedures by which radioactive by-products may be

safely handled. To use a currently fashionable analogy: we must consider not only the initial fuel cost but also the fuel's impact on the environment of the reactor.

Though the major part of the energy release is expected to occur at quasiequilibrium (equilibrium implying a well-defined temperature), one expects that non-equilibrium processes are also involved. Such processes arise mainly from nuclear reaction products that interact with the fuel before they are thermalized. Such effects play a large role in making possible some of the so-called "exotic" fuels. However, it is also expected that these processes allow the build up of unwanted radioactive species and thus must be evaluated from both points of view.

Because of the need for a high cross section at low temperature, we are necessarily limited in our choice of fuels to elements of low atomic number. This arises, of course, because of the Coulomb barrier between the charged particles in the fuel-burning reactions. This limitation also occurs due to rapid increase in the bremsstrahlung yield with atomic number. Cooling of the fuel by the escape of these x-rays requires that not only must the fuel be of low atomic number but also one must avoid the build-up of high-Z reaction products or contaminants. In magnetic confinement devices the major problem in the latter regard lies in the sputtering of metal ions from the reactor walls by energetic neutral atoms from the plasma; in laser-driven devices the shell of the pellet or microballoon must be chosen with this criterion in mind.

To summarize these points; our fuel and fuel reactions should be chosen to best reflect the following criteria:

- (1) The reaction cross section should be high at low energy and the reaction should have an appreciable energy release.
- (2) The fuel should be relatively cheap, require a minimum of preparation and be easily handled.
- (3) Reaction products should not lead to structural damage or to the buildup of long-lived radioactivities.
- (4) Elements with higher atomic numbers should be avoided because of their enhanced bremsstrahlung losses.

\*Supported in part by the National Science Foundation [GP-28027 and GP-43585].



Since we may for many years be limited to ignition temperatures corresponding to ion energies of 1-10 keV, criterion (1) takes on a special significance. Thus, you will hear no real enthusiasm from the people responsible for CTR development for any reaction other than  $d + t \rightarrow n + \alpha$  ( $Q = 17.6$  MeV). Because of the s-wave resonance at a center-of-mass energy of 60 keV and the lowest possible values of  $Z$ , this reaction has a rate that is orders of magnitude greater than its nearest competitor.<sup>1</sup> (See Fig. 1.) However, it is quite clear that an enormous price has been paid in terms of criteria (2) and (3). The tritium must be produced in nuclear reactors and it may be too expensive to consider as a fuel for anything but initial testing of first generation fusion reactors. In addition, tritium is radioactive and represents a significant handling problem. The neutrons from the reaction carry away 80% of the energy — leading to structural damage and further problems with induced radioactivity.

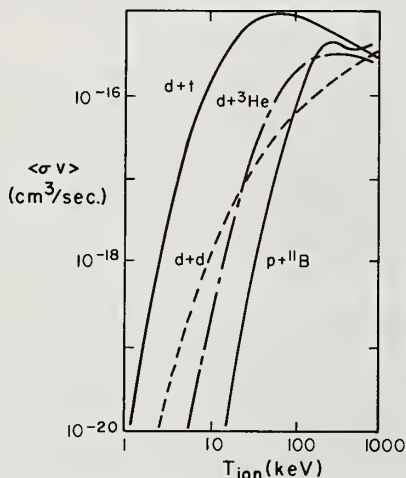
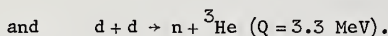
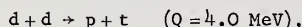


Fig. 1. The values of the reaction rate averaged over the Maxwell-Boltzmann distribution for the reactions induced by  $d + t$ ,  $d + d$ ,  $d + {}^3\text{He}$ , and  $p + {}^{11}\text{B}$ . The rate is plotted versus the temperature (in keV) of the interacting ions. (Taken from ref. 1.)

No one would seriously consider  $d + t$  as a fuel reaction unless the product neutrons were used to breed more tritium through  $n + {}^6\text{Li} \rightarrow t + \alpha$  ( $Q = 4.8$  MeV). Most present plans, however, consider an eventual shift to a pure deuterium fuel. This involves the primary reactions:

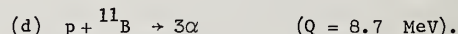
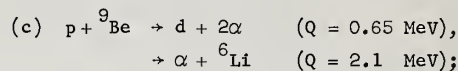
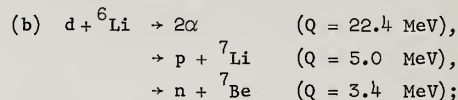
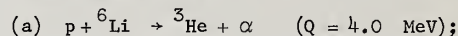


Subsequently, the tritium and  ${}^3\text{He}$  formed would also burn through  $d + t \rightarrow n + \alpha$  ( $Q = 17.6$  MeV) and  $d + {}^3\text{He} \rightarrow p + \alpha$  ( $Q = 18.4$  MeV). As shown in Fig. 1 the combined rate of the  $d + d$  reactions is very low compared to  $d + t$ , but at low energies  $d + d$  wins easily over other competitors. Though the same problems occur as with  $d + t$ , copious neutron production and the presence of tritium, neither is as serious for  $d + d$ .

$d + {}^3\text{He}$  would be a possible alternative to  $d + d$  if it were not for the cost of  ${}^3\text{He}$ . There is no breeding feature to this reaction and thus tritium would still

have to be separately produced to obtain more  ${}^3\text{He}$  fuel.

As the present technical difficulties are overcome we would expect that criteria (2) and (3) will assume increasing importance — especially when ignition temperatures above 100 keV can be attained. With this in mind, several proposals for second generation "exotic" fuels have been suggested.<sup>1-5</sup> The best possibilities appear to be:



Though  ${}^6\text{Li}$ ,  ${}^9\text{Be}$ , and  ${}^{11}\text{B}$  are all extremely rare in a cosmological sense, i.e., their large reaction cross sections insure their rapid destruction in stellar environments, they are relatively common on earth. For reasons of clarity, I have not put the curves for  ${}^6\text{Li}$  and  ${}^9\text{Be}$  in Fig. 1; for energies above 100 keV they are similar in form to that shown for  ${}^{11}\text{B} + p$ . For these temperatures (d) is better than (a), which in turn is better than (b) and (c). However, all have disadvantages: (d) has the highest bremsstrahlung losses and ignition temperature; (c) produces a deuteron which usually will produce a neutron in turn; (b) has a high neutron yield and a radioactive product,  ${}^7\text{Be}$ ; and (a) and (b) require the less common isotope of lithium.

It is obvious that with the possible exception of (d), there are many side reactions possible among the reaction products that also liberate energy and which must be carefully considered in a detailed evaluation. In addition, one must pay attention to reactions with other isotopes present. For example,  ${}^{10}\text{B}(p, \alpha){}^7\text{Be}$  ( $Q = 1.1$  MeV) will produce a radioactive product and thus the isotopic purity of the fuel may also have to be considered.<sup>6</sup>

#### Relevant Cross-Section Measurements

I shall not be able to discuss all these reactions, but shall choose examples that are typical of the techniques that may be required. With the exception of the small fraction of nonthermal processes, the nuclear reactions occur at energies that are low compared to the Coulomb barrier between the interacting ions. In this energy range the cross section is very energy dependent and can be written quite simply:

$$\sigma = \frac{S(E)}{E} \exp(-2\pi\eta),$$

where  $E$  is the center-of-mass energy and  $\eta = \frac{Z_1 Z_2 e^2}{\hbar v}$ .

The incident ions have mass numbers  $A_1$  and  $A_2$  and atomic numbers  $Z_1$  and  $Z_2$ . Removing the Gamow factor in this way usually leads to an  $S(E)$  that is slowly varying and which can be easily extrapolated to still lower energies. Often a slightly modified form of  $S$  is introduced that may further smooth its variation:

$$S(E) = \tilde{S}(E) \exp(-gE),$$

where 
$$g = \frac{2}{3\hbar} \left( \frac{2A_1 A_2}{(A_1 + A_2)} \frac{R^3}{Z_1 Z_2 e^2} \right)^{1/2} \quad \text{and}$$

R is the sum of the radii of the interacting ions.

Because the reaction cross section is varying rapidly, an accurate knowledge of its value can be obtained only if the beam energy and target energy loss are known very accurately. For this reason target thickness and composition, carbon build-up and absolute beam energy calibration are of crucial importance. One must include, for example, the variation of the cross section at different depths even in very thin targets.

For many years the measurements of the lithium reactions were notoriously unreliable because of the varying composition of the chemically active lithium targets. The solution adopted by Spinka et al.<sup>7</sup> was to use a differentially-pumped methane (CH<sub>4</sub>) target and a lithium beam. In this way a thin target of known density and composition could be obtained, and they could eliminate the uncertainties that plagued many of the earlier attempts. A cross sectional view of their scattering chamber is shown in Fig. 2, and the values of  $\tilde{S}(E)$  found for  ${}^6\text{Li}(p, {}^3\text{He}){}^4\text{He}$  are shown in Fig. 3 for data from refs. 7 and 8. In viewing this figure it would be very easy to assume that Spinka et al.<sup>7</sup> had been wasting their time because Gemeinhardt et al.<sup>8</sup> had more extensive data of comparable accuracy. However, before Spinka et al. established a reliable absolute cross section, there was no way to tell which of the many previous measurements were correct. (These previous data varied by a factor of at least two on both sides of the correct value.<sup>9</sup>)

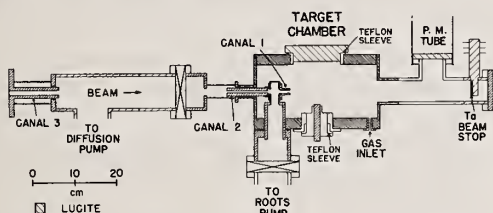


Fig. 2. The differentially-pumped target chamber of ref. 7. In this experiment the CH<sub>4</sub> target gas was bombarded with beams of  ${}^6\text{Li}$  and  ${}^7\text{Li}$ .

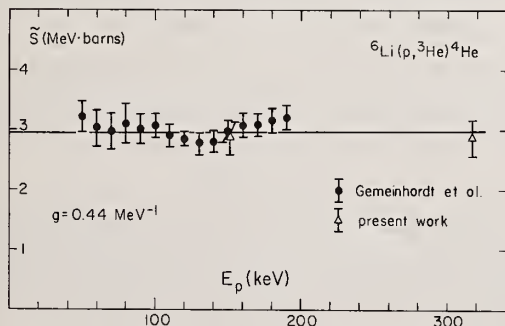


Fig. 3. The values of  $\tilde{S}$  versus proton bombarding energy for the  ${}^6\text{Li}(p, {}^3\text{He}){}^4\text{He}$  reaction. The Gemeinhardt et al. data are from ref. 8; the data labeled "present work" are from ref. 7. The quantities  $g$  and  $\tilde{S}$  are defined in the text.

Similar measurements have been made by Dwarakanath and Winkler for  ${}^3\text{He}({}^3\text{He}, 2p){}^4\text{He}$  using a recirculating,

differentially-pumped target.<sup>10</sup> Though the present low energy  ${}^6\text{Li}+d$  data look reasonable,<sup>11-13</sup> the accuracy of the absolute cross section could be established by using a recirculating, differentially-pumped deuterium target and a  ${}^6\text{Li}$  beam.

The  ${}^9\text{Be}+p$  reactions have recently been carefully measured for bombarding energies down to 30 keV.<sup>14</sup> Over the energy range of 300 keV to 30 keV the total cross section falls by five orders of magnitude, which required careful attention to target condition and the beam energy calibration. Fig. 4 shows the angular distribution coefficients for the  ${}^9\text{Be}(p, d){}^8\text{Be}$  reaction versus bombarding energy. Contrary to the usual expectation, the angular distributions become increasingly anisotropic as the energy is reduced. In ref. 14 this effect is attributed to interference between the 330-keV resonance and a level just below the  $p+{}^9\text{Be}$  threshold. However, an alternative (and perhaps more appealing) explanation is that a Coulomb pickup process provides the interfering amplitude instead of the bound state.<sup>15,16</sup> It is, of course, quite interesting that some nontrivial aspects of nuclear reaction theory survive in the few keV region.

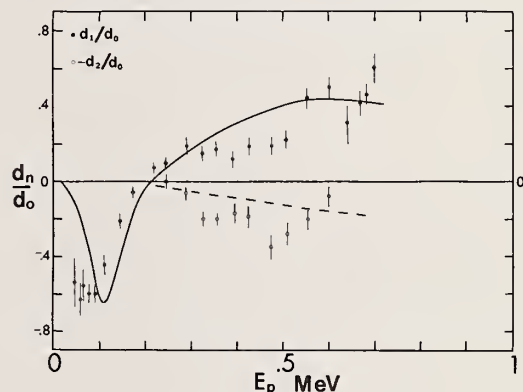


Fig. 4. The coefficients of a Legendre polynomial expansion of the deuteron center-of-mass angular distributions from  ${}^9\text{Be}(p, d){}^8\text{Be}$  (g.s.) plotted versus proton bombarding energy.  $\sigma(\theta) = d_0 + d_1 P_1(\cos\theta) + d_2 P_2(\cos\theta)$ . The solid and dashed lines are R-matrix fits to the data (ref. 14).

The S-factor for the  ${}^9\text{Be}+p$  reactions is given in Fig. 5, clearly showing the utility of extrapolating  $S$  instead of the cross section. The five decades of variation in  $\sigma$  have been reduced to a mere factor of five. Note that the presence of the tail of the 330-keV resonance requires a more elaborate extrapolation than that described at the beginning of this section; in the case of ref. 14 this was done using the R-matrix formalism.

The measurement of accurate total cross sections for the  ${}^{11}\text{B}(p, 3\alpha)$  reaction is made difficult not only by all the effects mentioned earlier but also by the fact that most of the yield involves the broad, first excited state of  ${}^8\text{Be}$ .<sup>17</sup> Thus, the alpha-particle spectrum is continuous and one must accurately determine the number of low energy reaction products. For the data shown in Fig. 6 this problem was overcome by RF pulsing the incident proton beam, which permitted the reaction products to be identified by comparing their energies and flight times from the target. Again, one should take note of the relevant energy range in which



the cross section must be measured. Even at the lowest energies shown, we are still talking about effective temperatures for a CTR that lie uncomfortably far in the future.

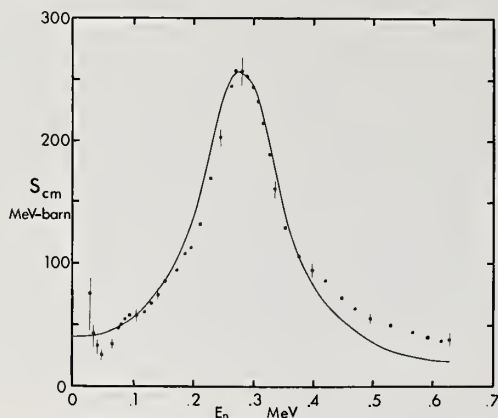


Fig. 5. The values of  $S$  for the sum of the  ${}^9\text{Be}(p,d)$  and  ${}^9\text{Be}(p,\alpha)$  reactions. The solid line corresponds to an R-matrix fit (ref. 14).

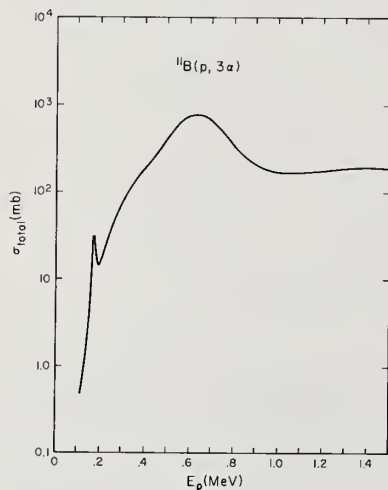


Fig. 6. The total cross section for  ${}^{11}\text{B}(p,3\alpha)$ . A smooth curve has been drawn through the many data points.

There is an interesting nonequilibrium process related to this reaction that serves as an excellent example of where cross-section measurements at higher energies may be important. In  ${}^{11}\text{B}(p,\alpha){}^8\text{Be}^*$  the decay of the 3 MeV, first excited state of  ${}^8\text{Be}$  produces many alpha particles with energies around 1.5 MeV. With this in mind we should look at the  ${}^{11}\text{B}(\alpha,p){}^{14}\text{C}$  ( $Q=0.8$  MeV) reaction, for it may represent an important contribution to the build-up of a long-lived radioactive product. Fig. 7 shows the total cross section for  ${}^{11}\text{B}(\alpha,p){}^{14}\text{C}$ . As luck would have it, there is a resonance near 1.5 MeV — just where it will do considerable harm.<sup>18,19</sup>

Another type of important nonequilibrium effect is caused by elastic scattering. For example, if one of the high energy alphas from  ${}^{11}\text{B}(p,3\alpha)$  strikes a proton, the recoiling proton will have a long range

and plenty of chance to interact at higher energies where the cross section is much larger. Thus, not all nonequilibrium effects are detrimental and in this case the burning of the fuel is enhanced.<sup>20</sup>

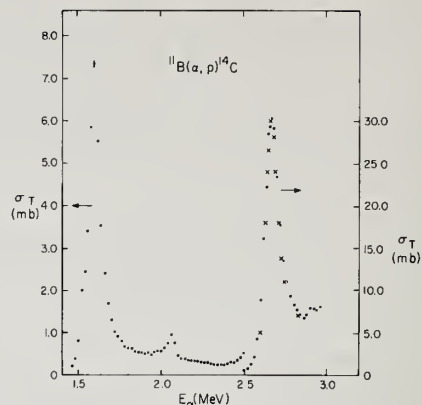


Fig. 7. The total cross section for  ${}^{11}\text{B}(\alpha,p){}^{14}\text{C}$  versus the alpha-particle bombarding energy. The dots are the data of ref. 18; the crosses are data from ref. 19.

#### Cross Section Needs

Probably more important to the reader than all my examples are the cases where the existing data should be improved. Some of the reactions I'll list are already under investigation in our laboratory, but much still remains to be done.

- 1) Of the primary fuels, the  ${}^6\text{Li}+d$  reactions are the least accurately known — especially for energies below 500 keV.
- 2) The cross section for  ${}^{10}\text{B}(p,\alpha){}^7\text{Be}$  stands in need of improvement for energies between 100 and 500 keV.
- 3) The low energy elastic scattering cross sections are in a sad state. Differential cross sections are needed for 0.5 to 3 MeV alpha particles and 0.5 to 2 MeV protons and deuterons on  ${}^6\text{Li}$ ,  ${}^9\text{Be}$ , and  ${}^{11}\text{B}$  targets. These data would be especially useful in determining the exact role played by nonequilibrium reactions.

It must be emphasized that the most frequently neglected region is that below 500 keV — but that is just the region where the data are relevant for application to CTR problems.

#### Acknowledgments

The author greatly appreciates the generosity of J. R. McNally, Jr. and T. A. Weaver for making available to him preprints of much of their recent work. Permission to include the preliminary data of R. Dayras and M. Lowry is also gratefully acknowledged.

#### References

1. T. Weaver, G. Zimmerman, and L. Wood, UCRL-74938 (1973)
2. R. F. Post, Nucl. Fusion Suppl., Part 1, 119 (1962).
3. J. R. McNally, Jr., *Nuclear Data in Science and Technology II*, IAEA, Vienna (1973) p. 41.
4. J. R. McNally, Jr., Nucl. Fusion **11**, 187, 554 (1971).



5. A. J. Elwyn, J. E. Monahan, and J. P. Schiffer, Nucl. Fusion 11, 551 (1971).
6. T. Weaver, G. Zimmerman, and L. Wood, URCL-74191 (1972).
7. H. Spinka, T. Tombrello, and H. Winkler, Nucl. Phys. A164, 1 (1971).
8. W. Gemeinhardt, D. Kamke, and C. von Rhöneck, Z. Phys. 197, 58 (1966).
9. J. Audouze and H. Reeves, Astrophys. J. 158, 419 (1968).
10. M. R. Dwarakanath and H. Winkler, Phys. Rev. C4, 1532 (1971).
11. C. C. Lee, J. Korean Phys. Soc. 2, 1 (1969).
12. F. Ajzenberg-Selove and T. Lauritsen, Nucl. Phys. A227, 1 (1974).
13. C. R. McClenahan and R. E. Segel, Phys. Rev. C11, 370 (1975).
14. A. J. Sierk and T. A. Tombrello, Nucl. Phys. A210, 341 (1973).
15. J. P. Schiffer, private communication (1973).
16. D. Novikoff, A. Sierk, and T. Tombrello, unpublished work (1974).
17. M. Lowry, M. Dwarakanath, and P. Batay-Csorba, work in progress.
18. R. Dayras and Z. E. Switkowski, Bull. Am. Phys. Soc. 20, 85 (1975).
19. L. L. Lee and J. P. Schiffer, Phys. Rev. 115, 160 (1959).
20. J. J. Devaney and M. L. Stein, Nucl. Sci. and Engin. 46, 323 (1971).

Sources of fast-neutrons and their spectra are discussed briefly. A critical survey of experimental techniques employed in studies of nuclear reactions (excluding fission) at  $E_n \geq 14$  MeV is presented. The recent experimental cross-section data are described concisely. Special attention is paid to the case of low-yield reactions, such as processes with trinucleon emission. A review of recently discussed cross-section systematics together with an outline of some of the theoretical implications is given.

(Fast neutrons; sources and spectra; non-elastic interactions; nuclear reactions; cross-section measurements; cross-section data and systematics; excitation functions)

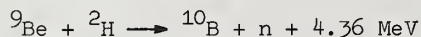
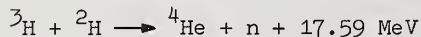
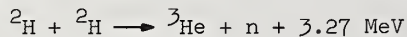
### Introduction

Measurements at various incident neutron energies of the total and scattering cross sections, together with the yield, energy spectrum and angular distribution of the emitted particles, yield useful information on nuclear forces, nuclear structure, reaction mechanisms etc. and provide a good way to test the applicability of various nuclear models. Furthermore, fast-neutron induced reaction cross-section data are finding increasing applications in several fields. The neutron data at 14 MeV are of prime interest for fusion technology.

This paper gives a brief survey of recent studies in the field of neutron cross-section measurements at 14 MeV and higher energies. The discussion is limited to the various components of the non-elastic interactions (excluding fission). Keeping in mind the need of data for applied purposes, in this survey the emphasis lies on experimental techniques and analysis of systematic trends in the data rather than on reaction theories and nuclear structure etc.

### Sources of Fast-Neutrons and their Spectra

The most intense available neutron sources are fission reactors and electron linear accelerators in which neutrons are produced by fission and photonuclear reactions, respectively. The average energies of the neutrons from both these sources, however, are well below 10 MeV. Fast neutrons can also be produced in the interactions of high-energy protons with various materials. The spectra of such neutrons extend to quite high energies. However, the most effective means of producing high-energy neutrons is the interaction of deuterons with deuterium, tritium and beryllium, giving rise to the following three nuclear reactions:



The neutron production cross sections in the forward direction for deuteron energies up to about 20 MeV, as summarized by Barschall<sup>1</sup>, are given in Fig. 1 and the average energies of the produced neutron<sup>1</sup> for various deuteron

bombarding energies in Fig. 2. It is evident that at low bombarding energies only the  $^3\text{H}(^2\text{H},n)^4\text{He}$  reaction has a large cross section. At higher energies the reaction  $^9\text{Be}(^2\text{H},n)^{10}\text{B}$  gives the highest yield. The increase with bombarding energy in the cross sections, and the decrease in the average neutron energy for the reaction  $^3\text{H}(^2\text{H},n)^4\text{He}$  is caused by the start of deuteron break-up which becomes the dominant mode above a deuteron energy of about 6 MeV.

Technology seems to be now sufficiently advanced to allow production of low-energy deuterons or tritons with ion currents up to a few amperes. However, the problem of dissipating hundreds of kW in a target of deuterium or tritium as well as maintaining a constant supply of neutrons are enormous. It seems that whereas the present day sources of fast-neutrons may suffice for many nuclear physics experiments, more intense sources are needed to study low-yield reactions and radiation damage phenomena similar to those anticipated in fusion reactor structural materials. The main efforts in overcoming these problems have been recently reviewed by Barschall<sup>1</sup>, and Csikai<sup>2</sup> has summarized the total neutron yields using various target compositions. The insulated core transformer system with a rotating tritium target at Livermore as well as the Los Alamos proposal of collisional interaction between intersecting beams of tritium ions and a supersonic jet of deuterium molecules are very promising. Construction of a high intensity neutron source at Jülich is also under discussion.

With low-energy deuterons only the  $^3\text{H}(^2\text{H},n)^4\text{He}$  reaction yields neutrons of energies above 13 MeV. This reaction in principle gives rise to monoenergetic neutrons whose energy depends on the energy of the accelerated deuterons as well as on the emission angle to the direction of bombarding deuterons, the anisotropy being less than 20 % at  $E_d < 400$  keV. If  $E_d = 200$  keV, at 90° the energy of the neutron is  $14.0 \pm 0.1$  MeV and the total angular variation of energy is  $E_n \sim 2$  MeV. In practice, however, due to scattering effects etc. in the immediate vicinity of the target, the spectra show much more spreads. Such effects have been recently estimated<sup>3-5</sup> in detail and it has been shown<sup>3</sup> that the calculated energy of neutrons from a sealed neutron generator tube depends also on the assumed  $^2\text{H}-^3\text{H}$  distribution ratio in the target.

Using deuterons of energies up to 4 MeV, neutrons of energies in the range of 13 to 19 MeV, depending on the angle of emission, can be obtained. Monoenergetic neutron beams above 19 MeV are difficult to get because deuterons of energies above 4 MeV show considerable break-up. This difficulty can be overcome by accelerating tritons rather than deuterons. However, due to health hazards associated with the acceleration of radioactive tritium, it has till now been only sparsely employed.

For the production of neutrons of energies above 10 MeV via  ${}^2\text{H}({}^2\text{H},n){}^3\text{He}$  and  ${}^9\text{Be}({}^2\text{H},n){}^{10}\text{B}$  reactions high energy deuterons are needed.

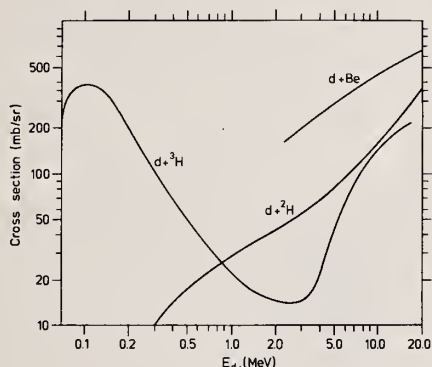


Fig. 1. Neutron production cross sections in the forward direction as a function of incident deuteron energy

However, since with increasing deuteron energy the break-up mode dominates, the neutron spectra cover a very broad range of energies. The energy spectra of the forward neutrons produced in bombardments of beryllium with deuterons of different energies, as given by Krivan and Münzel,<sup>6,7</sup> are reproduced in Fig. 3. The maximum intensity of the neutrons occurs at about one half of the incident deuteron energy. In the low-energy part of the spectrum an additional small peak occurs (not shown in Fig. 3) and is due to neutrons produced via evaporation effects. Elements other than Be have also been investigated but the neutron

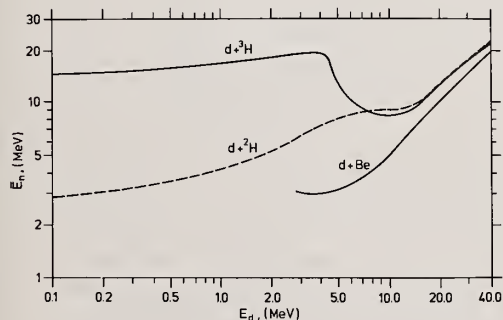


Fig. 2. Average energy of the neutrons from bombardments of thin targets with deuterons of varying energies

yields have been found to be much lower. In spite of the continuous shape of the neutron spectrum, using a high resolution time-of-flight spectrometer, such as the one at Karlsruhe,<sup>8,9</sup> it is possible to sort out neutrons of various energy groups and thus to determine the excitation functions with fairly good accuracies.

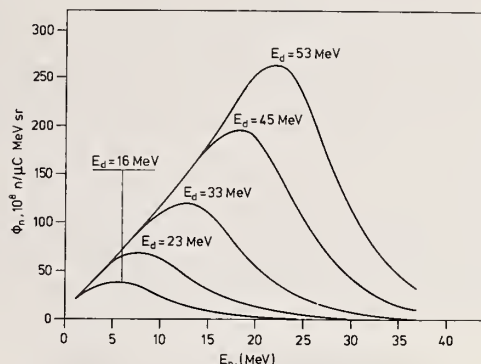


Fig. 3. Energy spectra of the forward neutrons produced in bombardments of beryllium with deuterons of different energies

#### Relative Contributions of Nuclear Reactions at 14 MeV

The relative contributions of the major components of the non-elastic interactions for elements with  $A > 40$  at 14 MeV, excluding fission which competes in the case of heavier nuclei, are roughly sketched out in Fig. 4. It is evident that the most common nuclear reactions are  $(n,\gamma)$ ,  $(n,n'\gamma)$ ,  $(n,2n)$ ,  $(n,p)$  and  $(n,\alpha)$ . Most of the studies so far have

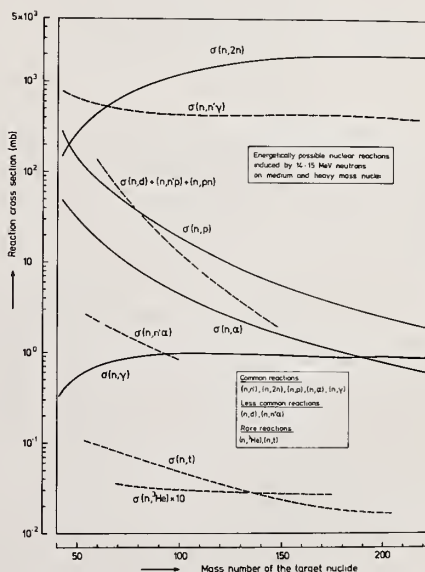


Fig. 4. Relative contributions of nuclear reactions induced by 14 MeV neutrons



concentrated in the investigation of those reactions. Certain less common reactions, however, like  $(n,n'p)$  and  $(n,n'\alpha)$  also have relatively high cross sections but still have not been looked for in any detail. The other reactions like  $(n,t)$ ,  $(n,^3\text{He})$ ,  $(n,2p)$ , and in heavier mass nuclei  $(n,3n)$ , are also energetically possible but are rare and need detailed investigations. A full discussion on the state of our knowledge on these reactions is given later but it seems appropriate here to mention that whereas in the lighter nuclei charged particle and neutron emission compete with each other, in the heavier mass region neutron emission is by far the most dominating process;  $(n, \text{charged particle})$  reactions in the heavy mass region are therefore difficult to investigate. At incident neutron energies higher than 14 MeV many more reaction channels are energetically possible, causing thereby high background problems. In general at higher energies the  $(n,xn)$  processes play the most dominating role.

### Techniques of Cross-Section Measurements

In cross-section measurements extensive use has been made both of the activation and spectrum methods. As discussed below, the two techniques have their own merits and limitations and are often complementary to each other.

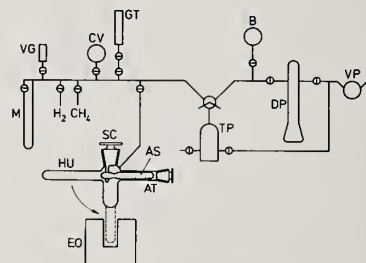
#### The Activation Method

The activation technique consists of off-line identification and quantitative determination of the reaction products by radiometric methods. In the case of stable and very long-lived products, if the cross section is very high, for the identification of the product mass spectrometric method may be applied.<sup>10</sup> In fast-neutron work, however, since the cross sections are not very high and the neutron sources are not very intense, this procedure so far has not been used. One relies therefore on the measurement of the radioactivity. Although all types of counting methods have been employed, in recent years with the use of high-resolution  $\text{Ge(Li)}$  detectors,  $\gamma$ -ray spectrometry is almost superseding all the other methods of counting (cf. 11-17). In work on elements consisting of several isotopes, use of enriched isotopes<sup>12,15,18,19</sup> and chemical separations<sup>15,18</sup> has led to higher precision.

The activation method is a relatively slow process and yields only an integral value of the cross section. No information on the differential cross sections or on the reaction mechanism is obtained. Nonetheless, in the case of simple reactions, like  $(n,p)$  and  $(n,\alpha)$ , the technique has a slight advantage over the spectrum method in that the contributions of  $(n,n'p)$  and  $(n,n'\alpha)$  reactions have not to be corrected for. The method is of special advantage in investigations of low-yield nuclear reactions like  $(n,t)$ ,  $(n,^3\text{He})$  etc., since the spectrum method is not sensitive enough to identify the low-abundance emitted particles. In this direction most of the studies in recent years have been carried out at Debrecen,<sup>20</sup> Jülich,<sup>21-25</sup> and Zagreb.<sup>26,27</sup> In particular at the Jülich Institute of Nuclear Chemistry extensive use of modern

radiochemical separations has been made.

A slight modification of the activation technique consists of accumulation and integral determination of the emitted particles rather than the reaction product; thus, for example,  $(n,\alpha)$  reaction on steel with reactor fast neutrons has been studied<sup>28</sup> using a high sensitivity gas mass spectrometric technique for the estimation of generated helium. Similarly in the case of  $(n,t)$  reactions, the emitted tritium was accumulated and identified off-line.<sup>20,25,29</sup> Separation of tritium was carried out by Qaim et al.<sup>29</sup> using the apparatus shown in Fig. 5. Quantitative estimation of tritium was effected using gas counting either in an anticoincidence circuit<sup>29</sup> or by a pulse shape discrimination procedure.<sup>30</sup>



Vacuum apparatus for the extraction of tritium from targets irradiated with fast neutrons

M	Monometer	ED	Electric oven
VG	Vacuum gauge	B	Bulb for carrier $\text{H}_2$
CV	Calibrating volume	TP	Tapler pump
GT	Gas counting tube	DP	$\text{H}_2$ -Diffusion pump
AT	Tube for introducing ampoule	VP	Vacuum pump
AS	Ampoule containing irradiated sample	SC	Stopcock with eccentric rod
HU	Heating unit		

Fig. 5. Sketch of vacuum apparatus used for isolation of tritium

#### The Spectrum Method

In this method the techniques employed differ from one reaction to another. Various types of reactions are therefore discussed individually.

**Radiative Neutron Capture.** For work with 14 MeV neutrons spherical telescopic scintillation pair spectrometer,<sup>31</sup> coincidence anti-coincidence pair spectrometer<sup>32</sup> as well as time-of-flight techniques<sup>33,34</sup> have been used. The fast neutron capture cross section is obtained by integrating the spectrum over the whole  $\gamma$ -ray energy. A drawback of the method appears to be that only transitions to the bound states are considered; the possible  $\gamma$ -ray branches to particle unstable states, which can subsequently decay by a further  $\gamma$ -ray transition, are not taken into consideration. It may, however, be added that, due to the smallness of the  $\gamma$ -ray widths compared to particle widths, the branching to unstable states should be relatively small.

**Neutron Inelastic Scattering and the  $(n,2n)$  Reaction.** For investigating neutron emission, time-of-flight techniques are employed in combination with large liquid scintillators as neutron detectors. At 14 MeV the  $(n,n')$  and  $(n,2n)$  reactions, and at higher energies

(n,xn) reactions, contribute to the spectrum, the relative contributions of which can be resolved by determining the angular correlations <sup>35,36</sup> between the various outgoing neutrons. At Livermore an extensive programme of work is underway on neutron spectra from bombardment of a variety of materials with pulsed 14 MeV neutron beams.<sup>36</sup> For the measurement of (n,2n) cross sections a watertank-method <sup>37</sup> has also been used. In this method the emitted neutrons are all thermalised prior to identification.

The (n,n'γ) reaction has also been investigated via the characterization of the associated prompt γ-lines.<sup>38,39</sup> The prompt γ-radiation and the neutrons emitted from the target irradiated with a pulsed 14 MeV neutron source are separated from each other using a short flight path and a Ge(Li) detector. Using a somewhat similar technique investigations up to a neutron bombarding energy of about 30 MeV have also been performed.<sup>9</sup>

(n,charged particle) Reactions. In studies on (n,p), (n,d), (n,t) and (n,α) reactions somewhat similar techniques have been employed. In order to minimize the absorption of the emitted charged particles thin targets have to be used and special shielding is needed for reducing the background. Although for the detection of charged particles nuclear emulsions,<sup>40,41</sup> thin CsI(Tl) crystals <sup>42,43</sup> as well as small semiconductor detectors <sup>44</sup> have been used, the more common technique seems to employ a counter telescope <sup>45-49</sup> consisting in general of two dE/dx proportional counters for measurement of the specific energy loss and one E scintillation or semiconductor detector for measuring the residual energy. At Tübingen, however, in studies of (n,α) reactions parallel plate avalanche counters have also been employed. A schematic diagram of such a telescope <sup>47</sup> is given in Fig. 6 and consists of two ΔE-parallel plate counters (PC 1 and PC 2), one Si-semiconductor detector (SD), and a third parallel plate counter (Veto) in front of the target which operates in anticoincidence to reduce the background.

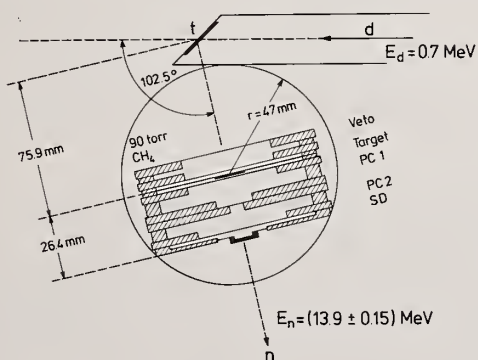


Fig. 6. Schematic diagram of a counter telescope employing parallel plate avalanche counters

At Karlsruhe a semiconductor telescope in combination with the time-of-flight facility is used for such studies. A typical spectrum

of the charged particles <sup>50</sup> from the neutron interaction with <sup>9</sup>Be is given in Fig. 7. The x-axis of the figure is defined by the relation

$$D = (E/\text{MeV} + 2)^{1.75} - (E_R/\text{MeV} + 2)^{1.75}$$

The helium nuclei <sup>4</sup>He and <sup>6</sup>He are separated completely and the hydrogen isotopes to better than 97 % for particles with energy distributions as given in the insert of Fig. 7. It is thus a very useful technique for investigating the energy and angular distributions of the emitted charged particles over the neutron energy range of 8 to 30 MeV.

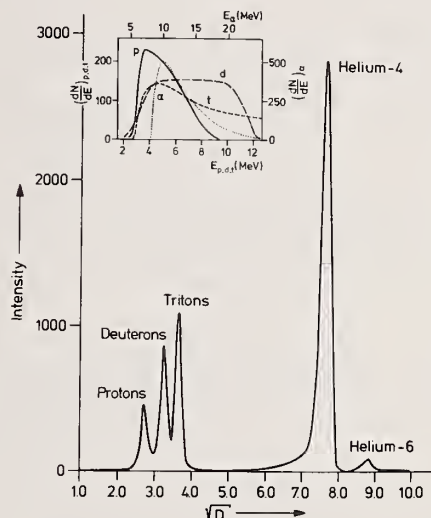


Fig. 7. Spectrum of charged particles from the neutron interaction with <sup>9</sup>Be measured in a Si-semiconductor detector telescope. The energy distributions of the charged particles involved are given in the insert

#### Experimental Cross-Section Data

Within the last few years a large number of measurements, mostly by the activation method at 14 - 15 MeV, have been reported. Due to the limited space available it is not possible to enumerate all of them here, hence only some selected works are discussed.

#### Cross-Section Data at 14 MeV

(n,2n), (n,p) and (n,α) Data. The data on these reactions in the energy range 13.9 to 15.1 MeV till January 1972 have been reviewed <sup>51-55</sup> and recommended cross-section values <sup>53-55</sup> have been given. Since then several measurements in various mass regions, including radioactive isotopes,<sup>56-60</sup> have been carried out. Among the works<sup>12,16-19,61-71</sup> on (n,2n) reactions, the investigations at Jülich <sup>16-19</sup> dealt with more than 55 nuclides of various elements, many of them being potential structural materials in fusion technology. The information published on (n,p) cross sections has been comparatively smaller.<sup>4,12,14,15,18,19,45,61,66,67,70,72-74</sup>



Some measurements on  $(n, \alpha)$  cross sections<sup>4,18,19</sup> have been carried out by the activation method. More extensive investigations, however, have been performed on the angular and energy distributions of the emitted  $\alpha$ -particles, e.g. on light nuclei at Tübingen,<sup>47,75</sup> on light and medium mass nuclei at Hamburg<sup>42,43</sup> and Rawalpindi,<sup>41</sup> and on heavy nuclei at Warsaw.<sup>44</sup> In the heavy mass region the spectrum of  $\alpha$ -particles<sup>44</sup> seems to be significantly shifted in the forward direction.

**(n,  $\gamma$ ) Data.** Recent measurements by the spectrum method have been carried out by Drake et al.,<sup>76</sup> Stamatelatos et al.,<sup>32</sup> Rigaud et al.,<sup>33</sup> Bergqvist et al.,<sup>34</sup> and Potokar et al.<sup>31</sup> Furthermore, in order to clarify the discrepancy between the results of activation and spectrum methods, activation measurements with improved target-sample arrangements have been repeated. Some of the authors<sup>77-80</sup> claim to have found good agreement between the results of two methods whereas Petö et al.<sup>81</sup> believe that the activation method definitely yields higher values except in the region of closed shells. A linear dependence of the apparent activation cross section on the target and sample thickness has been demonstrated<sup>81</sup> but according to Petö et al.<sup>81</sup> this does not explain the discrepancy fully.

**(n, n'  $\gamma$ ) Data.** Cross sections for the formation of several metastable states, with half-lives on the order of a few seconds, have been measured by the activation technique. These, however, are only partial cross sections. Using the spectrum method cross sections for several  $(n, n' \gamma)$  reactions have been obtained.<sup>35,36,38,39</sup>

**(n, d), (n, n' p) and (n, n'  $\alpha$ ) Data.** A survey of  $(n, d)$  reactions on very light nuclei has been given.<sup>82</sup> Very little information has been published on  $(n, n' p)$  and  $(n, n' \alpha)$  reactions. Cross sections have been measured using the activation technique for  $(n, n' p)$  reactions<sup>18,19,83</sup> on  $^{56}\text{Ni}$ ,  $^{84}\text{Sr}$ ,  $^{91,92}\text{Zr}$ ,  $^{92,96}\text{Mo}$ ,  $^{96}\text{Ru}$ ,  $^{106}\text{Cd}$ ,  $^{112}\text{Sn}$ ,  $^{142}\text{Ce}$  and  $^{183,184,186}\text{W}$ , and for  $(n, n' \alpha)$  reactions<sup>18</sup> on  $^{65}\text{Cu}$ ,  $^{70}\text{Zn}$ ,  $^{74}\text{Ga}$ ,  $^{76}\text{Ge}$  and  $^{99}\text{Tc}$ . The cross sections lie in the mb region.

**(n, t), (n,  $^3\text{He}$ ) and (n, 2p) Data.** Studies of  $(n, t)$  reactions on light nuclei have been carried out<sup>48,84,85</sup> by the spectrum method, mostly at Zagreb.<sup>48,84</sup> The angular distributions of tritons<sup>84</sup> from the  $(n, t)$  reactions on  $^{14}\text{N}$  and  $^6\text{Li}$  are shown in Fig. 8 and suggest that significant contributions from direct reactions, probably deuteron pick-up, are present. In the case of medium and heavy mass nuclei the information available till March 1972 has been summarized by Qaim and Stöcklin<sup>23</sup> who also reported<sup>18,23</sup> very careful measurements of a large number of  $(n, t)$  cross sections by activation and activity determination. Diksic et al.<sup>27</sup> later reported a few  $(n, t)$  cross sections and Biro et al.<sup>20</sup> investigated several  $(n, t)$  reactions by separation and  $\beta$ -counting of tritium. Although there are discrepancies in certain individual cases, the general conclusion from these studies is that the  $(n, t)$  cross sections for medium and heavy mass nuclei are quite small and amount to between 10 and 100  $\mu\text{b}$ .

The published information on  $(n, ^3\text{He})$  reactions till March 1973 has been reviewed

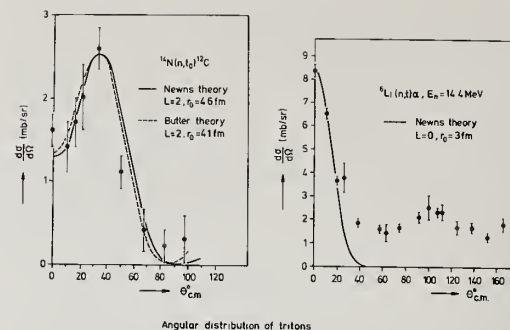


Fig. 8. Angular distributions of tritons produced in  $(n, t)$  reactions on  $^6\text{Li}$  and  $^{14}\text{N}$  at 14 MeV

by Qaim<sup>24</sup> who has described the first systematic study<sup>22,24</sup> on these reactions. Diksic et al.<sup>27</sup> have also reported a few  $(n, ^3\text{He})$  cross sections. In general the  $(n, ^3\text{He})$  cross sections at 14 MeV amount to a few  $\mu\text{b}$ .

In the case of  $(n, 2p)$  reactions, since the investigations of Lulic et al.<sup>26</sup> no further work has been reported.

#### Excitation Functions

The excitation functions of  $(n, 2n)$ ,  $(n, p)$  and  $(n, \alpha)$  reactions, mostly over the incident neutron energy up to 20 MeV, have been compiled by Bormann et al.<sup>55</sup> Some recent excitation function measurements over the energy range of 13 to 15 MeV deal with fast-neutron flux standards,<sup>86,87</sup>  $(n, 2n)$ ,  $(n, p)$  and  $(n, \alpha)$  reactions on medium and heavy mass nuclei,<sup>15,88</sup> and  $(n, 2n)$  reactions on heavy radioactive nuclei.<sup>58-60</sup> Excitation functions over the energy range up to about 20 MeV have been reported for  $(n, n' \gamma)$  reactions<sup>89</sup> on  $^{113}\text{In}$  and  $^{204}\text{Pb}$ ,  $(n, 2n)$  reactions<sup>68,71,89</sup> on  $^{46}\text{Ti}$ ,  $^{66}\text{Zn}$ ,  $^{113,115}\text{In}$  and  $^{197}\text{Au}$ , and  $(n, \alpha)$  reaction<sup>90</sup> on  $^{51}\text{V}$ . Using the time-of-flight technique excitation functions for a few  $(n, x)$  reactions over the energy range 11 to 30 MeV have also been measured.<sup>9,50</sup> In spite of these recent measurements the total available information on the excitation functions of reactions induced by neutrons above 15 MeV energy is still rather scanty and further measurements are needed.

#### Cross-Section Data with Break-up Neutrons

Krivan and Münzel<sup>6,7</sup> investigated on several nuclides  $(n, p)$ ,  $(n, \alpha)$  and  $(n, 2n)$  reactions induced with neutrons produced in the break-up of 33 and 53 MeV deuterons and constructed excitation functions empirically. With a view to investigating  $(n, t)$  reactions at a rather high reaction energy, Qaim et al.<sup>29</sup> recently carried out a systematic study employing radiochemical isolation and gas phase counting of tritium. In this work neutrons produced in the break-up of 53 MeV deuterons were used. Evidently the total information available in this field is still rather small.

#### Evaluated Cross-Section Data

In connection with reaction mechanism studies several theoretical methods have been



reported which describe the cross-section data more or less satisfactorily; e.g. semi-direct capture theory in the case of  $(n,\gamma)$  reactions, and statistical model calculations in the case of  $(n,n'\gamma)$ ,  $(n,2n)$ ,  $(n,p)$  and  $(n,\alpha)$  reactions. In the case of  $(n,p)$  and  $(n,\alpha)$  reactions contributions from pre-equilibrium emission processes have also been taken into account. On rare nuclear reactions like  $(n,t)$  and  $(n,^3\text{He})$ , especially in the medium and heavy mass regions, very little theoretical work has been done. Using the Hauser-Feshbach method Qaim et al<sup>91</sup> recently calculated  $(n,t)$  cross sections at 14.6 MeV on nuclei with  $A = 32 - 45$ . The dominant mode seems to be the statistical process.

Several formalisms and codes have been developed which are very successful in evaluating and predicting cross-section data. In this direction the work at Brookhaven and Livermore is worth mentioning.<sup>92,93</sup> In addition to these methods certain phenomenological formulae have been suggested as well as some systematic trends in cross sections have been analysed. The latter two methods are rather empirical but they do allow a quick estimation of unknown cross sections, although not with very high accuracies.

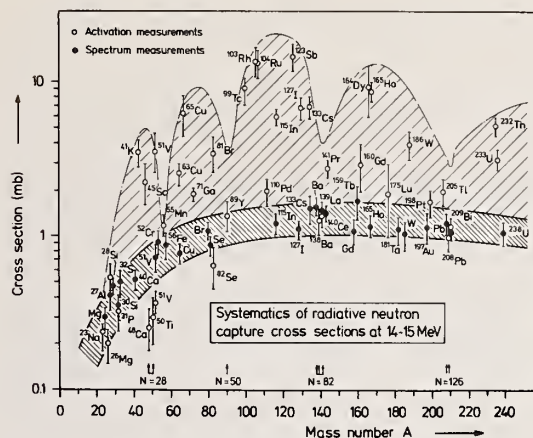
### Systematics of Reaction Cross Sections

#### Systematics of Cross-Section Data at 14 MeV

Although the systematics of reaction cross sections at 14-15 MeV have been investigated by several groups, in recent years most extensive investigations have been carried out at Jülich. It should, however, be mentioned that these studies are rather empirical since the cross-section data are not normalised to a constant reaction energy. Nonetheless, they are very useful for practical purposes and provide a method for quick prediction of unknown cross sections, in the case of common reactions like  $(n,2n)$ ,  $(n,p)$  and  $(n,\alpha)$ , where the data are relatively abundant, with errors of about 20 to 30 %, but for less common and rare reactions with lesser accuracies. A summary of the systematic trends observed in cross sections of various nuclear reactions is given below.

Systematics of  $(n,\gamma)$  Reaction Cross Sections. Using the method of Cvelbar et al<sup>94</sup> the total radiative neutron capture cross sections are shown as a function of  $A$  in Fig. 9. The results of the spectrum measurements show that the cross section increases up to a mass number of about 80 beyond which it is almost constant and approximately equal to 1 mb. Whereas in the region of magic neutron numbers the agreement between the results of activation and spectrum measurements is generally good, in between closed shells the discrepancies are maximum. Recent activation measurements with improved methods, however, tend to show that the discrepancies are not so high as in earlier works.

Systematics of  $(n,n'\gamma)$  and  $(n,2n)$  Reaction Cross Sections. The compilation of Csikai<sup>2</sup> on  $(n,n'\gamma)$  cross sections was updated and the total  $(n,n'\gamma)$  cross sections are plotted as a function of the asymmetry parameter  $(N-Z)/A$  in Fig. 10. Partial cross sections are omitted. Due to the paucity of data any detailed systematic trends



with increasing  $(N-Z)/A$  the cross section decreases slowly, possibly due to increasing competition from  $(n,2n)$  reaction.

The systematics of  $(n,2n)$  cross sections as described by Qaim<sup>16</sup> are given in Fig. 11. The steep rise in cross sections for nuclides with small  $(N-Z)/A$  is probably due to the decreasing thresholds for  $(n,2n)$  reactions on those nuclides. For nuclides with  $(N-Z)/A \geq 0.1$  the cross section increases only gradually till in the medium and heavy mass regions the  $(n,2n)$  reaction becomes the most dominating process.

Systematics of  $(n,p)$  and  $(n,\alpha)$  Reaction Cross Sections. The  $(n,p)$  cross-section data as a function of residual nuclear charge  $Z_R$  are shown<sup>95</sup> in Fig. 12. Apart from even-odd effects in the case of light nuclei, no systematic variations can be seen. In the case of

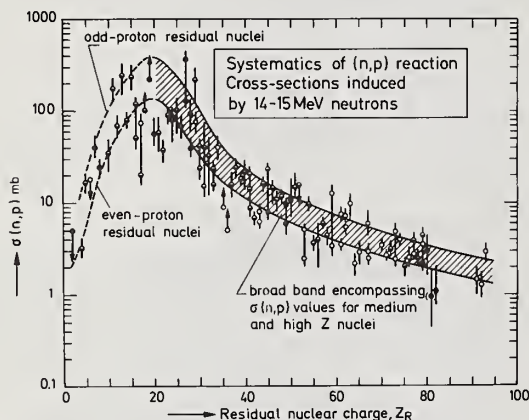


Fig. 12. Plot of 14 MeV  $(n,p)$  cross sections against proton number of the residual nucleus,  $Z_R$

$(n,\alpha)$  reactions no even-odd effects are found. The trend in  $(n,\alpha)$  cross sections for medium and heavy mass nuclei (Fig. 13) is similar to that for  $(n,p)$  cross sections. In the medium

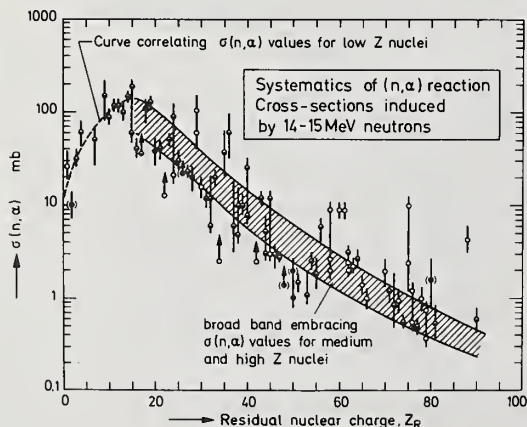


Fig. 13. Plot of 14 MeV  $(n,\alpha)$  cross sections against proton number of the residual nucleus,  $Z_R$

and heavy mass regions both the  $(n,p)$  and  $(n,\alpha)$  reaction cross sections decrease<sup>21,96</sup> with the increasing relative neutron excess  $(N-Z)/A$  of the target nucleus (Figs. 14 and 15).

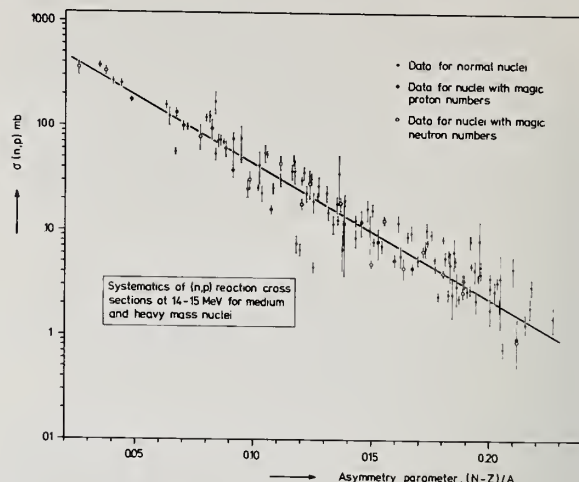


Fig. 14. Systematics of  $(n,p)$  cross sections at 14 MeV for medium and heavy mass nuclei

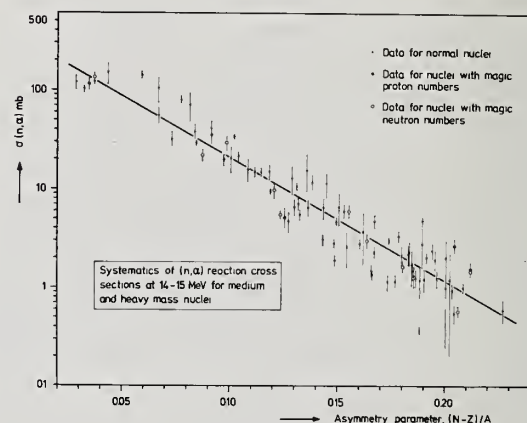


Fig. 15. Systematics of  $(n,\alpha)$  cross sections at 14 MeV for medium and heavy mass nuclei

This decrease in cross section with increasing  $(N-Z)/A$  is due to the increasing competition between charged particle and neutron emission.

Systematics of  $(n,t)$  and  $(n,^3\text{He})$  Reaction Cross Sections. The systematics of  $(n,t)$  cross sections, as described by Qaim and Stöcklin,<sup>18,21,23</sup> are shown in Fig. 16. The data based on both  $\gamma$ -spectrometric measurements<sup>18,23</sup> and  $\beta^-$ -counting of tritium<sup>20</sup> are shown. For medium and heavy mass nuclei the data which appeared to be very erroneous were discarded. For light nuclei the cross sections are rather high due to cluster formation which facilitates direct processes like deuteron pick-up and triton knock-out. In the case of elements with  $Z > 22$  the  $(n,t)$  cross sections decrease<sup>21-23</sup> with the increasing  $(N-Z)/A$



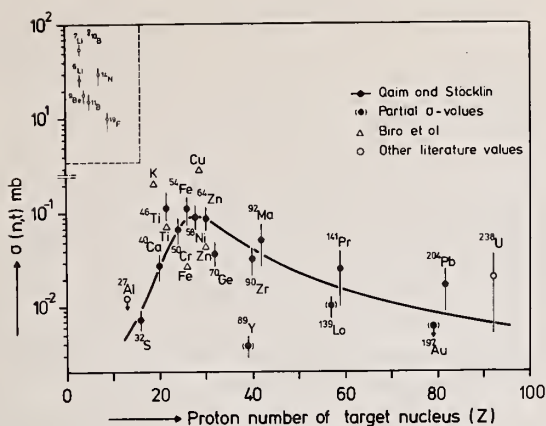


Fig. 16. Systematics of (n,t) cross sections at 14 MeV

and can be fitted with the empirical equation<sup>22</sup> given in Fig. 17. A somewhat similar trend is observed in the case of (n,<sup>3</sup>He) reactions (Fig. 18) though the decrease with increasing (N-Z)/A is less marked which suggests more contribution from direct processes.

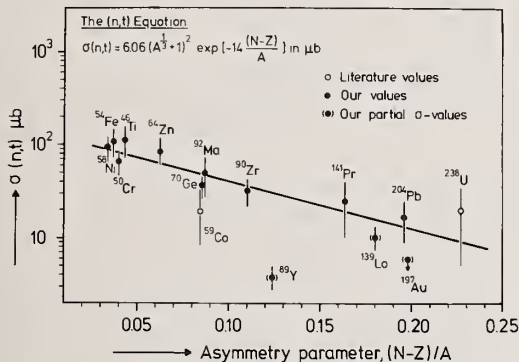


Fig. 17. 14 MeV neutron induced (n,t) reaction cross sections as a function of (N-Z)/A of target nuclei with Z > 22

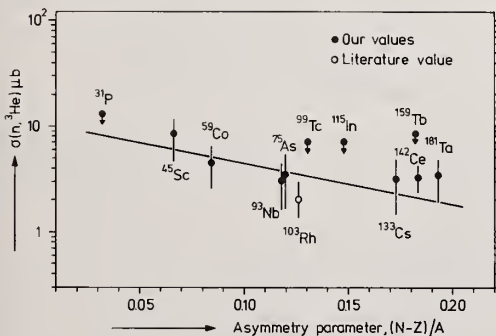


Fig. 18. (n,<sup>3</sup>He) reaction cross sections at 14 MeV for medium and heavy mass elements as a function of (N-Z)/A of the target nuclei

**Trends in Cross Sections for Other Reactions.** A survey of (n,d) reactions on light nuclei has been carried out<sup>82</sup> but no systematic trends in cross sections were reported. In the case of [(n,d)+(n,n'p)+(n,pn)] reactions Lu and Fink<sup>83</sup> noted that the cross section for the lightest isotope of each element decreases linearly with the increasing atomic number. Qaim and Graca<sup>19</sup> have shown recently that for adjacent isotopes of tungsten the cross section shows a dependence on (N-Z)/A. No further detailed analysis of trends in cross sections for this reaction or for (n,2p) and (n,n'α) reactions has been reported.

#### Systematics of (n,t) Reaction Cross Sections at $E_n \approx 22.5$ MeV

Qaim et al<sup>29</sup> investigated the systematics of tritium formation cross sections with fast neutrons produced via break-up of 53 MeV deuterons on Be. The cross sections lie between 3.5 and 5.5 mb for all the elements investigated over the Z range of 20-83. Only a slightly decreasing trend with the increasing Z of the target element has been observed.

#### Systematics of Excitation Functions

Krivan and Münzel<sup>6</sup> analysed some systematic trends in the excitation functions for (n,2n), (n,p) and (n,α) reactions. These are summarized in Fig. 19. Whereas with increasing Z the maximum cross section for the (n,2n) and (n,α) reaction increases, that for the (n,p) and (n,α) reaction decreases (Fig. 19 (A)). As is evident from Fig. 19 (B), for (n,2n) reactions the energy in excess of the Q-value at which the maximum of the excitation function occurs decreases only slightly with increasing Z. In the case of (n,p) and (n,α) reactions, on the other hand, this energy value increases, presumably due to increasing Coulomb barriers.

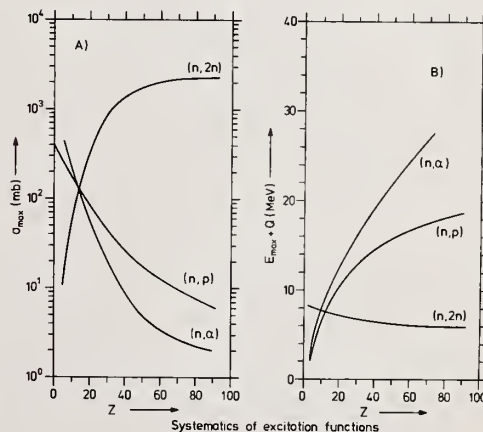


Fig. 19. Systematics of excitation functions of (n,2n), (n,p) and (n,α) reactions



## Conclusions

The techniques of cross-section measurements appear to be sufficiently advanced but more intense neutron sources are needed to study low-yield nuclear reactions and radiation damage phenomena similar to those anticipated in fusion reactor structural materials. Most of the reported cross-section data have been obtained at 14 MeV and deal mainly with  $(n, \gamma)$ ,  $(n, n'\gamma)$ ,  $(n, 2n)$ ,  $(n, p)$  and  $(n, \alpha)$  reactions. The latest data seem to attain the precision needed for fusion technology. The total information available on reactions like  $(n, d)$ ,  $(n, n'p)$ ,  $(n, n'\alpha)$ ,  $(n, t)$ ,  $(n, {}^3\text{He})$  etc. is rather small. The excitation functions in energy ranges in excess of 15 MeV have been investigated only in a few cases. The various calculational codes give data in good agreement with the experiment and the systematic trends discussed allow a quick estimation of unknown cross sections.

## Acknowledgements

It is a pleasure to thank G. Stöcklin, the Director of this Institute, for his active support of this research programme. The author is indebted to S. Bederka, M. Bormann, S. Cierjacks, J. Csikai, R. Haight, W. Herr, R.J. Howerton, S.E. Hunt, B. Karlik, N.A. Khan, V. Krivan, R.W. Loughheed, R. Michel, S. Mubarakmand, H. Münzel, D.R. Nethaway, A. Paulsen, O. Schult, I. Slaus, G. Staudt, H. Vonach, J. Walker and Z. Wilhelmi for providing the author with the latest published and unpublished works from their labs.

## References

- 1 H.H. Barschall, in "Nuclear Structure Study with Neutrons" (Editors J. Erö and J. Szücs, Plenum Press, London, 1974), p. 289.
- 2 J. Csikai, Atomic Energy Review 11, 415 (1973).
- 3 J. Wieldraaijer and H.R. Hoogerbrug, Nucl. Instr. Meth. 25, 119 (1971).
- 4 M. Schmidt-Hönow and W. Herr, Radiochim. Acta 17, 142 (1972).
- 5 R. Michel and H. Weigel, Radiochim. Acta, in press
- 6 V. Krivan and H. Münzel, J.inorg.nucl.Chem. 34, 2093, 2989 (1972).
- 7 V. Krivan and H. Münzel, J. Radioanalyt. Chem. 15, 575 (1973).
- 8 S. Cierjacks, in "Nuclear Structure Study with Neutrons" (Editors J. Erö and J. Szücs, Plenum Press, London, 1974), p. 299.
- 9 S. Cierjacks, KFK 1857 (1973).
- 10 H. Michael, A. Neubert and H. Nickel, Int. J. Appl. Rad. Isotopes 25, 183 (1974).
- 11 V.N. Levkovskii and O.I. Artem'ev, Sov. J. Nucl. Phys. 13, 525 (1971).
- 12 A.K. Hankla and R.W. Fink, Nucl. Phys. A180, 157 (1972).
- 13 D.R. Nethaway, Nucl. Phys. A190, 635 (1972).
- 14 W. Struwe and G. Winkler, Nucl. Phys. A222, 605 (1974).
- 15 T. Mavaddat, S.A. Rao and P.K. Kuroda, J.inorg.nucl.Chem. 36, 953 (1974).
- 16 S.M. Qaim, Nucl. Phys. A185, 614 (1972).
- 17 S.M. Qaim, Nucl. Phys. A224, 319 (1974).
- 18 S.M. Qaim and G. Stöcklin, Proc. 8th Symposium on Fusion Technology, Noordwijkerhout (The Netherlands) EUR 5182e, 939 (1974).
- 19 S.M. Qaim and C. Graca, Nucl. Phys., in press
- 20 T. Biro, S. Sudar and J. Csikai, Proc. Conf. Nucl. Structure Study with Neutrons, Budapest (1972), p. 130.
- 21 S.M. Qaim, R. Wölflle and G. Stöcklin, Proc. Conf. Chemical Nuclear Data, Canterbury, BNES (1971), p. 121.
- 22 S.M. Qaim, Proc. Conf. Nuclear Structure Study with Neutrons, Budapest (1972), p. 25.
- 23 S.M. Qaim and G. Stöcklin, J.inorg.nucl.Chem. 35, 19 (1973).
- 24 S.M. Qaim, J.inorg.nucl.Chem. 36, 239 (1974).
- 25 S.M. Qaim, R. Wölflle and G. Stöcklin, J. Radioanalyt. Chem. 21, 395 (1974).
- 26 S. Lulic, P. Strohal and I. Slaus, Nucl. Phys. A154, 273 (1970).
- 27 M. Diksic, P. Strohal and I. Slaus, J.inorg.nucl.Chem. 36, 477 (1974).
- 28 N.D. Dudey, S.D. Harkness and H. Farrar IV, Nuclear Applications and Technology 2, 700 (1970).
- 29 S.M. Qaim, R. Wölflle and G. Stöcklin, J.inorg.nucl.Chem. 36, 3639 (1974).
- 30 S. Sudar, L. Vas and T. Biro, Nucl. Instr. Methods 112, 399 (1973).
- 31 M. Potokar, A. Likar, F. Cvelbar, M. Budnar and E.R. Hodgson, Nucl. Phys. A213, 525 (1973).
- 32 M. Stamatelatos, B. Lawergren and L.J. Lidofsky, Nucl. Sci. Eng. 51, 113 (1973).
- 33 F. Rigaud, J.L. Irigaray, G.Y. Petit, G. Longo and F. Saporetti, Nucl. Phys. A176, 545 (1971).
- 34 I. Bergqvist, D.M. Drake and D.K. McDaniels, Nucl. Phys. A191, 641 (1972); A231, 29 (1974).
- 35 O.A. Sal'nikov, G.N. Lovchikova, G.V. Kotel'nikova, V.S. Nesterenko, N.I. Fetisov and A.M. Trufanov, Sov. J. Nucl. Phys. 12, 620 (1971).
- 36 L.F. Hansen, J.D. Anderson, P.S. Brown, R.J. Howerton, J.L. Kammerdiener, C.M. Logan, E.F. Plechaty and C. Wong, Nucl. Sci. Eng. 51, 278 (1973).
- 37 M. Häring, H. Vonach and E.J. Feicht, Z. Physik 244, 352 (1971).
- 38 W. Breunlich, G. Stengel and H. Vonach, Z. Naturf. 26a, 451 (1971).
- 39 F.S. Dietrich, M.C. Gregory and J.D. Anderson, Phys. Rev. C2, 973 (1974).
- 40 B. Antolkovic, Nucl. Instr. Meth. 100, 211 (1972).

- 41 N.A. Khan, S. Mubarakmand and M. Ahmad, Nucl.Phys. A202, 123 (1973) and (private communication).
- 42 M. Bormann, W. Schmidt, V. Schröder, W. Scobel and U. Seebeck, Nucl.Phys. A186, 65 (1972).
- 43 M. Bormann, D. Kaack, V. Schröder, W. Scobel and L. Wilde, Z.Physik 258, 285 (1973).
- 44 M. Jaskola, J. Turkiewicz, L. Zemlo and W. Osakiewicz, Acta Phys. Polonica B2, 521 (1971).
- 45 K.R. Alvar, Nucl.Phys. A195, 289 (1972).
- 46 M. Brendle, M. Möricke, G. Staudt and G. Steidle, Nucl.Instr.Meth. 81, 141 (1970).
- 47 H.J. Brede, Z.Physik 254, 364 (1972).
- 48 D. Miljanic, V. Valkovic, D. Rendic and M. Furic, Nucl.Phys. A156, 193 (1970).
- 49 J.P. Perroud, Ch. Sellem and J.F. Loude, Nucl.Instr.Meth. 115, 357 (1974).
- 50 L. Kropp and P. Forti, Nucl.Instr.Meth. 104, 381 (1972).
- 51 G. Eder, G. Winkler and P. Hille, Z.Physik 253, 335 (1972).
- 52 Z.T. Bödy, INDC (HUN)-10 (1973).
- 53 Z.T. Bödy and J. Csikai, Atomic Energy Review 11, 153 (1973).
- 54 V.L. Levkovskii, Sov.J.Nucl.Phys. 18, 361 (1974).
- 55 M. Bormann, H. Neuert and W. Scobel, in "Handbook on Nuclear Activation Cross Sections", Technical Reports Series No. 156, IAEA, Vienna (1974), p. 87.
- 56 S.M. Qaim, J.inorg.nucl.Chem. 35, 3669 (1973).
- 57 J.G. Kuhry and G. Bontems, Radiochem.Radio-analyt.Letters 15, 29 (1973).
- 58 J.R. Landrum, R.J. Nagle and M. Lindner, Phys.Rev. C8, 1938 (1973).
- 59 C.K. Paulson and E.J. Hennelly, Nucl.Sci. Eng. 55, 24 (1974).
- 60 R.W. Loughheed, Livermore (private communication).
- 61 S.S. Hasan, R. Prasad and M.L. Seghal, Nucl. Phys. A181, 101 (1972).
- 62 R. Mogharrab and H. Neuert, Atomkernenergie 19, 107 (1972).
- 63 A.A. Druzhinin, N.I. Ivanova and A.A. Lbov, Sov.J.Nucl.Phys. 14, 383 (1972).
- 64 D.V. Viktorov and V.L. Zyablin, Sov.J.Nucl. Phys. 15, 608 (1972).
- 65 G.N. Salaita and P.K. Eapen, J.inorg.nucl. Chem. 35, 2139 (1973).
- 66 J. Janczyszyn and L. Gorski, J.Radioanalyt. Chem. 14, 201 (1973).
- 67 S. Hlavac, J. Kristiak, P. Oblozinsky and I. Turzo, Int.Symp. Neutron Induced Reactions, Smolenice, Czechoslovakia (Sept. 1974).
- 68 S.K. Ghorai, R. Vos, J.R. Cooper and W.L. Alford, Nucl.Phys. A223, 118 (1974).
- 69 T.H. Kao and W.L. Alford, Nucl.Phys. A237, 11 (1975).
- 70 W. Mannhart and H. Vonach, Z.Physik, in press
- 71 A. Paulsen, Geel (private communication).
- 72 T. Tuurnala and V. Pursiheimo, Physica Scripta 5, 183 (1972).
- 73 N.C. Dyer and J.H. Hamilton, J.inorg.nucl. Chem. 34, 1119 (1972).
- 74 P. Holmberg, R. Rieppo, J.K. Keinänen and M. Valkonen, J.inorg.nucl.Chem. 36, 715 (1974).
- 75 H.J. Brede, Z.Physik 254, 375 (1972).
- 76 D. Drake, I. Bergqvist and D.K. McDaniels, Phys.Lett. 36B, 557 (1971).
- 77 M. Valkonen and J. Kantele, Nucl.Instr. Meth. 103, 549 (1972).
- 78 J. Vuletin, P. Kulisic and N. Cindro, Lett. Nuovo Cim. 10, 1 (1974).
- 79 K. Ponnert, G. Magnusson and I. Bergqvist, Physica Scripta 10, 35 (1974).
- 80 F. Rigaud, M.G. Desthuilliers, G.Y. Petit, J.L. Irigaray, G. Longo and F. Saporetti, Nucl. Sci.Eng. 55, 17 (1974).
- 81 G. Petö, J. Csikai, K.D.V. Long, S. Mukerjee, J. Banhalmi and Z. Miligy, Int.Symp. Neutron Induced Reactions, Smolenice, Czechoslovakia (Sept. 1974).
- 82 D. Miljanic and V. Valkovic, Nucl.Phys. A176, 110 (1971).
- 83 W. Lu and R.W. Fink, Phys.Rev. C4, 1173 (1971).
- 84 D. Rendic, in "Few Body Problems, Light Nuclei and Nuclear Interactions", Vol. II, Gordon and Beach, New York (1968), p. 485
- 85 J.P. Perroud and Ch. Sellem, Nucl.Phys. A227, 330 (1974).
- 86 R.A. Jarjis and S.E. Hunt, J.Radioanalyt. Chem. 16, 611 (1973).
- 87 R.A. Jarjis and S.E. Hunt, Int.J.Appl.Rad. Isotopes, in press
- 88 Y. Kanda, Nucl.Phys. A185, 177 (1972).
- 89 P. Decowski, W. Grochulski, J. Karolyi, A. Marcinkowski, J. Piotrowski, E. Saad and Z. Wilhelmi, Nucl.Phys. A204, 121 (1973).
- 90 A. Paulsen, R. Widera and H. Liskien, Atomkernenergie 22, 291 (1974).
- 91 S.M. Qaim, A. Fäßler, H.V. Klapdor and H. Reiss, to be published
- 92 R.J. Howerton, UCID-16376 (1973); UCRL-50400 Vol. 15, to be published
- 93 D.G. Gardner, Livermore (private communication).
- 94 F. Cvelbar, A. Hudoklin and M. Potokar, Nucl.Phys. A158, 251 (1970).
- 95 S.M. Qaim, Z.Naturf. 25a, 1977 (1970).
- 96 E. Havlik, Acta Physica Austriaca 34, 209 (1971).



S. A. W. Gerstl, D. J. Dudziak, and D. W. Muir  
Theoretical Division  
Los Alamos Scientific Laboratory  
University of California  
Los Alamos, New Mexico 87544

A computational method to quantitatively determine cross section requirements is described and applied to a particular CTR design project. In order to provide a rational basis for the priorities assigned to new cross section measurements or evaluations, this method includes a quantitative assessment of the uncertainty of currently available data, the sensitivity of important nuclear design parameters to selected cross sections, and the accuracy desired in predicting nuclear design parameters. Perturbation theory is used to combine estimated cross section uncertainties with calculated sensitivities to determine the variance of any nuclear design parameter of interest. Selected computational results are presented for a model of the Tokamak Fusion Test Reactor.

(Sensitivity, uncertainties, perturbation theory, fusion reactors, cross sections)

### Introduction

Upon applying nuclear data developed for fission reactor, nuclear weapon, or accelerator applications to fusion reactors, a need for more accurate neutron cross sections in the MeV range becomes immediately apparent.<sup>1</sup> Due to the large number of cross section data needed for fusion reactor design calculations it is clear that not all deficient data can be improved within a short time frame. Therefore, some reasonable criterion is sought to provide a rational basis for programmatic priority assignments for new cross section measurements or evaluations. We feel that such a criterion should be based on a quantitative assessment of the uncertainties of currently available data, the sensitivity of important nuclear design parameters to such cross sections, and the accuracy desired in predicting nuclear design parameters at various stages of an evolving fusion reactor design. The development of such a quantitative criterion for priority assignments to new cross section measurements and evaluations is an integral part of a CTR cross section assessment program now being pursued at LASL within the framework of recommendations of the CTR-Subcommittee of the U.S. Nuclear Data Committee.

It is obvious that the importance of a specific cross section for a specific fusion reactor design depends strongly on that particular design. Also, the accuracy of an existing cross section set may be fully satisfactory for the calculation of a certain design parameter  $R_A$  in a reactor design (A), while the same design parameter in another design (B),  $R_B$ , may be extremely sensitive to this particular cross section in question, so that its errors may introduce an unacceptably large uncertainty in  $R_B$ . This demonstrates that every cross section assessment task must be seen within the context of a given reactor design, and that any statement about the quality of a given cross section set must be related to its application. Such applications, however, may cover a generic class of designs. In this study we concentrate on cross section requirements for the presently highest priority CTR construction project, the Tokamak Fusion Test Reactor (TFTR), for which a preliminary design concept was made available by the Princeton Plasma Physics Laboratory<sup>2</sup> and Westinghouse.<sup>3,4</sup> The objective of the study is to identify any data deficiencies for TFTR nuclear design calculations early enough so that necessary new cross section measurements or evaluations can be performed in time to be available for final design calculations. The purpose of this paper is to demonstrate the application of this new, quantitative method to assess the cross section requirements for the TFTR project.

### Method of Analysis

Our goal is to calculate the effect of a given cross section uncertainty  $\Delta\Sigma$  on a specific nuclear design parameter of interest  $R$ ; or in other words, to predict the uncertainty  $\Delta R$  of a calculated integral parameter due to a given cross section uncertainty  $\Delta\Sigma$ . In the following we assume that the application of first-order perturbation theory is adequate.

Following a derivation by Perey,<sup>5</sup> we denote with  $(\Sigma_i)$  a set of group cross sections and with  $R$  any design parameter of interest which is calculated as the result of some transport calculation which uses the group cross sections  $(\Sigma_i)$ . Then we can write

$$R = R(\Sigma_i) \quad (1)$$

and calculate any change in  $R$  due to small changes  $\delta\Sigma_i$  in  $\Sigma_i$  as

$$\delta R \approx \sum_i \frac{\partial R}{\partial \Sigma_i} \delta \Sigma_i, \quad (2)$$

by using first-order perturbation theory. However, what we really want is the standard deviation of  $R$  derived from the statistical population of possible cross section values, which is defined as

$$\Delta R = \sqrt{E\{\delta R^2\}} = \sqrt{\text{Var}(R)}, \quad (3)$$

where  $\text{Var}(R)$  denotes the variance of the calculated parameter  $R$ .  $\text{Var}(R)$  is formally obtained as the expectation value of  $\delta R^2$  and may be written as

$$\begin{aligned} \text{Var}(R) &= E\{\delta R^2\} \\ &= E\left\{\sum_{i,j} \frac{\partial R}{\partial \Sigma_i} \frac{\partial R}{\partial \Sigma_j} \delta \Sigma_i \delta \Sigma_j\right\}, \end{aligned} \quad (4)$$

using Eq. (2). Since  $\partial R/\partial \Sigma_i$  and  $\partial R/\partial \Sigma_j$  are constants over the considered statistical ensemble, we can rewrite Eq. (4) as

$$\text{Var}(R) = \sum_{i,j} \frac{\partial R}{\partial \Sigma_i} \frac{\partial R}{\partial \Sigma_j} E\{\delta \Sigma_i \delta \Sigma_j\}. \quad (5)$$

The expectation value of the product of  $\delta \Sigma_i$  and  $\delta \Sigma_j$  is the definition of a matrix element of the covariance matrix for cross sections  $\Sigma_i$  and  $\Sigma_j$  over a joint probability density function  $f(\Sigma_i, \Sigma_j)$ :

$$\text{Cov}(\Sigma_i, \Sigma_j) \equiv E\{\delta \Sigma_i \delta \Sigma_j\}$$

\*Work performed under the auspices of the U. S. Energy Research and Development Administration.



$$= \iint_{-\infty}^{+\infty} f(\Sigma_i, \Sigma_j) \cdot (\Sigma_i - \hat{\Sigma}_i) (\Sigma_j - \hat{\Sigma}_j) d\Sigma_i d\Sigma_j, \quad (6)$$

where  $\hat{\Sigma}_i$  and  $\hat{\Sigma}_j$  are the expectation values of  $\Sigma_i$  and  $\Sigma_j$ , respectively. Inserting this definition (6) into Eq. (5) we obtain our final result

$$\text{Var}(R) = \sum_{i,j} \frac{\partial R}{\partial \Sigma_i} \frac{\partial R}{\partial \Sigma_j} \text{Cov}(\Sigma_i, \Sigma_j), \quad (7)$$

which is the basis for our quantitative data assessment program.

The diagonal elements of the covariance matrix,  $\text{Cov}(\Sigma_i, \Sigma_i)$ , are the usual (uncorrelated) cross section uncertainties expressed as the variance of  $\Sigma_i$ :

$$\begin{aligned} \text{Cov}(\Sigma_i, \Sigma_i) &= \text{Var}(\Sigma_i) \\ &\equiv E\{\delta \Sigma_i^2\} \\ &= \Delta \Sigma_i^2. \end{aligned} \quad (8)$$

Cross section variances have been compiled recently for a wide variety of CTR materials by the CTR Subcommittee of the USNDC.<sup>6</sup> The off-diagonal terms of the covariance matrix indicate correlations between the cross sections  $\Sigma_i$  and  $\Sigma_j$ .

The quantities  $\partial R / \partial \Sigma_i$  in Eq. (7) are the sensitivity coefficients which result from a sensitivity analysis of the particular transport problem of interest.<sup>7-9</sup> It is convenient and useful to define a relative sensitivity coefficient

$$P_{\Sigma_i} = \frac{(\partial R / R)}{(\partial \Sigma_i / \Sigma_i)}, \quad (9)$$

which is called a sensitivity profile for cross section  $\Sigma_i$  when  $i$  is the group index of a multigroup cross section set ( $\Sigma_i$ ).  $P_{\Sigma_i}$  can be interpreted as the fractional (percentage) change of the design parameter  $R$  per fractional (percentage) change of cross section  $\Sigma_i$ . The sensitivity profile for cross section  $\Sigma_i$  can be calculated from

$$P_{\Sigma_i} = \frac{\langle \phi^*, L_{\Sigma_i} \phi \rangle_i}{R}, \quad (10)$$

where  $\phi$  and  $\phi^*$  are the forward and adjoint angular fluxes of the problem in consideration, and  $L_{\Sigma_i}$  denotes that portion of the Boltzmann transport operator which contains the cross section  $\Sigma_i$ . The symbol  $\langle, \rangle_i$  indicates integrations over all angles and all spatial zones containing  $\Sigma_i$ . While the sensitivity profile for a certain cross section contains much valuable detailed information, it is also convenient to define an integral cross section sensitivity

$$S_{\Sigma} = \sum_i P_{\Sigma_i}, \quad (11)$$

which reduces the sensitivity information about the whole cross section set ( $\Sigma_i$ ) to one number.  $S_{\Sigma}$  can be interpreted as the percentage change of the design parameter of interest,  $(\partial R / R)$ , resulting from a simultaneous 1% increase of the group cross sections  $\Sigma_i$  in all energy groups  $i$  (assuming full correlation, i.e., a correlation coefficient of +1).

For convenience we transform our basic Eq. (7) into a form containing only fractional quantities. Inserting Eq. (9) into Eq. (7) and using Eq. (3) we obtain

$$\left(\frac{\Delta R}{R}\right)^2 = \sum_{i,j} P_{\Sigma_i} P_{\Sigma_j} \frac{\text{Cov}(\Sigma_i, \Sigma_j)}{\Sigma_i \Sigma_j}. \quad (12)$$

In Eq. (12) all cross section uncertainty information is contained in the relative covariance matrix elements  $\text{Cov}(\Sigma_i, \Sigma_j) / \Sigma_i \Sigma_j$  and all sensitivity information in the product of the profiles  $P_{\Sigma_i} P_{\Sigma_j}$ . It is seen from Eq. (10) that a sensitivity profile is highly problem-dependent and specific for a particular cross section  $\Sigma_i$  as well as a particular design parameter  $R$ . Hence, Eq. (12) combines the problem-dependent cross section sensitivities of a particular nuclear design with the basic cross section error information into a design-oriented quantity  $\Delta R / R$  which is of immediate use for the designer.

The predicted uncertainty  $\Delta R / R$  for a calculated design parameter  $R$  due to given uncertainties of a multigroup cross section set ( $\Sigma_i$ ) may be compared to a specified design criterion requiring a certain confidence limit for the parameter  $R$ . Such a confidence limit may be described as a maximum allowable standard deviation for the design parameter  $R$ ; say  $(\Delta R / R)_{\max, \text{crit.}}$ . Then three cases are possible:

$$a) \quad \Delta R / R < (\Delta R / R)_{\max, \text{crit.}} \quad (13a)$$

$$b) \quad \Delta R / R \approx (\Delta R / R)_{\max, \text{crit.}} \quad (13b)$$

$$c) \quad \Delta R / R >> (\Delta R / R)_{\max, \text{crit.}} \quad (13c)$$

For case (a) we conclude that the cross section set ( $\Sigma_i$ ) is adequate for the calculation of this particular design parameter in the underlying design, while in cases (b) and (c) we have identified situations where the cross section set is either marginal or grossly inadequate for this application. After such a deficient cross section set has been found, an inspection of the sensitivity profile  $P_{\Sigma_i}$  reveals in which energy range a cross section improvement should be attempted to contribute must to a reduction of  $\Delta R / R$ .

#### Upper Limits for $\Delta R / R$

In cases where no complete error files are available but rough error estimates can be obtained for the cross sections of interest, it is useful to determine upper limits for  $\Delta R / R$  based on calculated sensitivities and such rough error estimates. The term "rough" should indicate that either cross section correlations or energy dependencies or both are neglected when errors are estimated. Then certain conservative assumptions can be made about such correlations or energy dependencies to obtain upper limits for resulting response uncertainties  $\Delta R / R$ .

#### 1. Uncorrelated Cross Section Uncertainties

If cross sections  $\Sigma_i$  are assumed to be uncorrelated, then their uncertainties will also be uncorrelated, with the result that all off-diagonal elements of the covariance matrix vanish:

$$\text{Cov}(\Sigma_i, \Sigma_j)_{\text{uncorr.}} = \text{Cov}(\Sigma_i, \Sigma_j) \delta_{ij}. \quad (14)$$

Inserting Eq. (14) into Eq. (12) allows us to reduce the double sum to a single summation and we obtain with Eq. (8)

$$\left(\frac{\Delta R}{R}\right)_{\text{uncorr.}}^2 = \sum_i \left( P_{\Sigma_i} \frac{\Delta \Sigma_i}{\Sigma_i} \right)^2. \quad (15)$$

#### 2. Fully Correlated Cross Section Uncertainties

A more conservative assumption about group-wise cross sections  $\Sigma_i$  than being uncorrelated is to assume

a correlation of +1. This means that when a cross section in one specific energy group is increased by a certain amount, then the cross sections in all other groups are also increased by the same amount. Under this assumption all off-diagonal elements of the covariance matrix are fully determined by the diagonal elements alone:<sup>14</sup>

$$\text{Cov}(\Sigma_i, \Sigma_j)_{\text{corr.}(+1)} = \sqrt{\text{Cov}(\Sigma_i, \Sigma_i)} \sqrt{\text{Cov}(\Sigma_j, \Sigma_j)} \quad (16)$$

Inserting this into Eq. (12) and using again the notation of Eq. (8), we obtain

$$\left(\frac{\Delta R}{R}\right)_{\text{corr.}(+1)} = \left| \sum_i P_{\Sigma_i} \frac{\Delta \Sigma_i}{\Sigma_i} \right| \quad (17)$$

### 3. Energy Independent Cross Section Error Estimates

The simplest possible and most conservative error specification is to assume that all uncertainties in an entire cross section set are equal to the largest uncertainty in any of the individual cross sections, i.e.,

$$\frac{\Delta \Sigma_i}{\Sigma_i} = \text{const.} = \left(\frac{\Delta \Sigma}{\Sigma}\right)_{\text{max.}} \quad (18)$$

If we further assume the group-by-group errors to be fully correlated, we obtain the most conservative upper limit for  $\Delta R/R$ . Using a new definition for an always positive integral sensitivity [in contrast to  $S_{\Sigma}$  defined in Eq. (11)]:

$$\hat{S}_{\Sigma} = \sum_i |P_{\Sigma_i}| \quad (11a)$$

and inserting Eq. (18) into Eq. (17) we obtain

$$\left(\frac{\Delta R}{R}\right)_{\text{max.}} = \hat{S}_{\Sigma} \cdot \left(\frac{\Delta \Sigma}{\Sigma}\right)_{\text{max.}} \quad (19)$$

As long as the sensitivity profile  $P_{\Sigma_i}$  does not change sign (which is always the case in this study), it can be shown by comparing Eqs. (12), (17), and (19) that

$$\left(\frac{\Delta R}{R}\right) \leq \left(\frac{\Delta R}{R}\right)_{\text{corr.}(+1)} \leq \left(\frac{\Delta R}{R}\right)_{\text{max.}} \quad (20)$$

Then the largest upper limit for  $\Delta R/R$  is given by  $\left(\frac{\Delta R}{R}\right)_{\text{max.}}$ , if  $\left(\frac{\Delta \Sigma}{\Sigma}\right)_{\text{max.}}$  is the largest error expected in any group of the entire energy region of interest.  $\left(\frac{\Delta R}{R}\right)_{\text{corr.}(+1)}$  weighs the energy-dependent error estimates with the energy-dependent sensitivities, and  $\left(\frac{\Delta R}{R}\right)_{\text{uncorr.}}$  replaces the strong assumption of full correlation by the weaker assumption of no correlation at all. The last step to  $\Delta R/R$  via Eq. (12) allows individual terms of the double sum to have differing signs and thereby account for the possible cancellation or cumulation of errors. Therefore, while  $\left(\frac{\Delta R}{R}\right)_{\text{max.}}$  and  $\left(\frac{\Delta R}{R}\right)_{\text{corr.}(+1)}$  are real upper limits for  $\Delta R/R$ , the special case  $\left(\frac{\Delta R}{R}\right)_{\text{uncorr.}}$  does not constitute any limit to the real  $\Delta R/R$  from Eq. (12). The utility of the two different upper limits for  $\Delta R/R$  is recognized when a numerical comparison is made with the design criterion  $\left(\frac{\Delta R}{R}\right)_{\text{max, crit.}}$ . If it is found that Eq. (13a) is satisfied already with one of the upper limits for  $\Delta R/R$ , then a further uncertainty evaluation of that cross section set is not urgent for the design problem considered.

### Application and Results

The methodology outlined in the previous section has been applied to the nuclear design of the TFTR.<sup>4</sup> A preliminary one-dimensional computational model for neutronics calculations has been supplied by the

Princeton Plasma Physics Laboratory<sup>2</sup> and Westinghouse,<sup>3</sup> and is shown in Fig. 1, where  $R$  is the radial distance from the plasma centerline. Since the main objective of the TFTR is to demonstrate the scientific feasibility of a Tokamak fusion reactor, it is not required to breed tritium, and therefore does not employ a lithium blanket. The reactor is expected to operate in a pulsed mode yielding a maximum of 1 000 pulses per year, generating a maximum neutron fluence of  $1.4 \times 10^{15}$  fusion neutrons per  $\text{cm}^2$  per year on the first wall. Due to this low neutron fluence, radiation damage or nuclear heating problems are not of major concern. However, the activation of magnet coils, structural materials, and instruments is considered a major neutronics problem area, in particular the generation of long-living radioactive isotopes. Therefore, and for biological shielding reasons, a radiation shield is provided as close to the plasma as possible (Fig. 1). In cooperation with Princeton and Westinghouse we selected several threshold activation reactions in the structural steel (zones 9 and 11 in Fig. 1) and the main copper coil (zone 10 in Fig. 1) as important nuclear design parameters of interest (cf. Table I). Our objective is to estimate the uncertainties introduced in the calculation of these activation rates due to estimated errors in the neutron cross sections of the system. Of particular interest are uncertainties in the cross sections of the shield-zone 7, the composition of which is given in Table II.

TABLE I  
ACTIVATION REACTIONS OF INTEREST  
("Response")

1. In Steel:
  - $A_1 = \text{Fe54}(n,p)\text{Mn54}, \quad t_{1/2} = 303 \text{ d}$
  - $A_2 = \text{Mn55}(n,2n)\text{Mn54}, \quad t_{1/2} = 303 \text{ d}$
  - $A_3 = \text{Fe56}(n,p)\text{Mn56}, \quad t_{1/2} = 2.6 \text{ h}$
  - $A_4 = \text{Ni58}(n,p)\text{Co58}, \quad t_{1/2} = 71 \text{ d}$
2. In Copper:
  - $A_5 = \text{Cu65}(n,2n)\text{Cu64} \quad t_{1/2} = 12.9 \text{ h}$

In order to calculate the sensitivity coefficients  $\partial R / \partial \Sigma_i$  for Eq. (7) or, equivalently, the sensitivity profiles  $P_{\Sigma_i}$  for Eq. (12), we performed a forward transport calculation for the TFTR model of Fig. 1 and an adjoint for each of the 5 activation reactions listed in Table I, saving the angular fluxes  $\phi$  and  $\phi^*$ . All transport calculations were performed with the one-dimensional  $S_N$  code DTF-IV<sup>10</sup> in an  $S_8$  approximation using 20-group  $P_3$  neutron cross sections. This cross section set was generated from the first 20 groups of

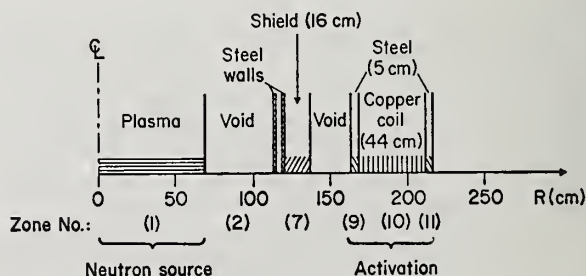


Fig. 1. One-dimensional computational model for TFTR cross section sensitivity analysis.



TABLE II  
SHIELD COMPOSITION  
("Perturbed Cross Section")

Lead-Borated-Polyethylene,  $\rho = 4.2 \text{ g/cm}^3$

Element	weight - %	at/barn'cm
H	1.8	0.0455
C	10.7	0.0225
Pb	80.0	0.0098
B	1.0	0.0023
$\emptyset$	6.5	0.0103

the DLC-2E 100-group set distributed by RSIC.<sup>11</sup> It covers neutron energies between 2.02 and 14.92 MeV, which is sufficient for the considered activation reactions. Cross sections for the activation reactions listed in Table I were taken from Ref. 12. The stored angular fluxes  $\phi$  and  $\phi^*$  from the transport calculations were then read into the LASL sensitivity code SENSIT-1D<sup>13</sup> to evaluate Eqs. (10), (11), and (12), and plot the sensitivity profiles of interest. In order to combine the sensitivity information with the cross section uncertainties, according to Eq. (12), the covariance matrices for the cross sections of interest ("perturbed cross sections") must also be read into SENSIT-1D. However, at present complete covariance matrices are available in ENDF/B only for three materials: N, O, and C. Therefore, cross section uncertainties had to be estimated for most of the materials in our design model and these estimates are still incomplete. We selected a few partial cross sections for which estimated covariance matrices have been produced and which serve here as illustrative samples.

As a basis for such selection we calculated the integral sensitivities, Eq. (11), of all five activation reactions to the total cross sections of all materials in the system and tabulate them in Table III. It is noted that all sensitivities are negative (except for

TABLE III

INTEGRAL SENSITIVITIES,  $S$ , OF THE RESPONSES,  $A_k$  (ACTIVATION REACTIONS), TO THE NEUTRON CROSS SECTIONS OF CERTAIN MATERIALS IN CERTAIN ZONES

Perturbed Cross Section	in Zone	RESPONSE				
		$A_1$ in Zone 9	$A_2$ in Zone 9	$A_3$ in Zone 9	$A_4$ in Zone 9	$A_5$ in Zone 10
$C_{Tot}$	7	-0.76	-0.67	-0.69	-0.68	-0.55
$C(n,n'3\alpha)$	7	-0.10	-0.12	-0.11	-0.09	-0.09
$Pb_{Tot}$	7	-1.30	-1.11	-1.14	-1.14	-0.91
$Pb(n,2n)$	7	-0.42	-0.46	-0.45	-0.39	-0.38
$\emptyset_{Tot}$	7	-0.26	-0.24	-0.24	-0.23	-0.19
$R_{Tot}$	7	-1.00	-0.70	-0.76	-0.82	-0.58
$Fe_{Tot}$	9	-0.72	-0.47	-0.53	-0.57	-0.88
$Fe_{incl. cont.}$	9	-0.09	-0.12	-0.14	-0.11	-0.22
$Cr_{Tot}$	9	-0.20	-0.13	-0.14	-0.15	-0.23
$Ni_{Tot}$	9	-0.13	-0.09	-0.09	-0.10	-0.16
$Mn_{Tot}$	9	-0.02	-0.01	-0.02	-0.02	-0.03
$Cu_{Tot}$	10	-0.05	-0.001	-0.006	-0.02	-1.96
$Cu_{Scat}$	10	+0.14	+0.09	+0.10	+0.11	+0.82

the scattering cross section of copper in the coil-zone 10) indicating that an increase in such cross sections would cause all of the considered activations to decrease. The largest sensitivity shown in Table III is that of  $A_5$  to  $Cu_{Tot}$  (viz., -1.96), which indicates that a 1% increase in the total cross section of copper would decrease the  $^{64}Cu$ -production in the coil by 1.96%. This and the other responses are even less sensitive to the total cross sections of the radiation shield materials (zone 7), resulting from the fact that this shield is relatively thin. Indeed, a hand calculation shows that the 16 cm of shield material corresponds to only 1.8 mean-free-path for the 14-MeV fusion neutrons originating in the plasma. Nevertheless, the uncertainties in these cross sections with marginal sensitivities still could be so high as to produce an undesirably large  $\Delta R/R$ .

For this paper we shall analyse in detail only the uncertainties in two partial cross sections of Pb and C. As shown in Table III as well as Table IV, the  $Pb(n,2n)$  cross section contributes about 32% to the sensitivity of the Pb total cross section, when the activation reaction  $Fe54(n,p)Mn54$  in the first structural steel-region (zone 9) is considered. Similarly, the  $C(n,n'3\alpha)$  cross section contributes 13% to the carbon total sensitivity. Therefore, an attempt was made to generate covariance matrices for these two partial cross sections.

Table IV gives the numerical values for the various upper limits for  $\Delta R/R$ , as well as  $\Delta R/R$  according to Eq. (12), depending upon the detail of available error information.<sup>6</sup> For example, uncertainties in the  $Pb(n,2n)$  cross section are estimated to be 15 to 50% in the energy range from 8 to 15 MeV (threshold energy  $E_{thres} = 7 \text{ MeV}$ ). Therefore, if a 50% uncertainty is assumed for the entire energy range of interest ( $E_{thres}$  to 15 MeV) then a maximum uncertainty of 21% can be expected in the calculated value for the  $Fe54(n,p)Mn54$  activation in steel-zone 9. However, a more realistic error estimate is the assumption of 15% error at 15 MeV increasing linearly to 50% at the threshold energy, which reduces  $\Delta R/R$  to 7.45% if the additional assumption is made that these cross section uncertainties are fully correlated among energy groups (which is considered correct for this case). Also given in Table IV is the  $\Delta R/R$  due to the estimated uncertainty of the  $Fe54(n,p)$  activation cross section itself, which constitutes no significant neutron transport effect but contributes to the overall  $\Delta R/R$  and must therefore be considered. Figure 2 shows the measured and recommended smoothed data for this reaction cross section and demonstrates a typical situation: in about half of the energy range of interest

TABLE IV

EFFECTS OF ESTIMATED ERRORS IN SELECTED COMPONENT CROSS SECTIONS IN TFTR SHIELD-ZONE 7, ON  $Fe54(n,p)Mn54$  ACTIVATION REACTIONS IN STEEL-ZONE 9 ( $A_1$ ). Question marks indicate missing cross section error data.

Pert. Cross Section in Shield-zone 7	Integral Sensitivity of $A_1$ , $S(\% \text{ per } \%)$	$\left(\frac{\Delta R}{R}\right)_{\max}^{\%}$	$\left(\frac{\Delta R}{R}\right)_{\max}^{\%}$	$\left(\frac{\Delta R}{R}\right)_{\text{corr}(\pm 1)}^{\%}$	$\left(\frac{\Delta R}{R}\right)_{\text{uncorr.}}^{\%}$	$\left(\frac{\Delta R}{R}\right)_{\text{uncorr.}}^{\%}$
$Pb_{Tot}$	- 1.30	4	5.2	5.2	3.15	?
$Pb_{Abs}$	- $5 \times 10^{-5}$	25	0.001	0.001	$< 10^{-3}$	?
$Pb_{scat.}$	- 1.30	?	?	?	?	?
$Pb(n,2n)$	- 0.42	50	21	7.45	---	7.45
$C_{Tot}$	- 0.76	4	3.04	2.93	1.9	?
$C_{Abs}$	- 0.07	25	1.75	0.53	0.28	?
$C_{scat.}$	-0.69	?	?	?	?	?
$C(n,n'3\alpha)$	- 0.10	50	5	2.05	---	2.05
$Fe54(n,p)$	+ 1.0	25	25	25	---	?



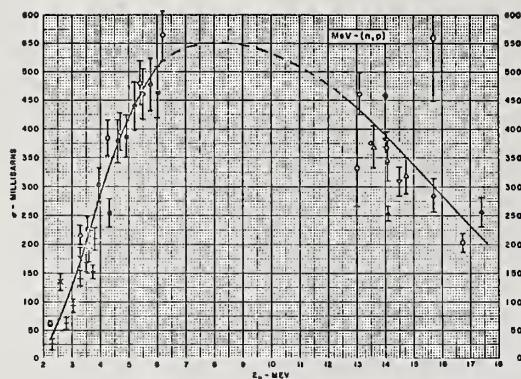
<sup>54</sup>Fe


Fig. 2. Uncertainties of measured Fe54(n,p)Mn54 reaction cross section (from BNL-325).

to our problem there exist no measured data at all. Therefore, an estimate of  $\Delta\Sigma/\Sigma = 25\%$ , fully correlated over the entire range from 2 to 15 MeV, appears realistic. This, of course, also gives a 25% uncertainty in the calculated Fe54(n,p) reaction rate, as included in Table IV. The question marks in Table IV indicate missing cross section error information.

In order to determine the cross section requirements for the entire TFTR nuclear design many tables of the type of Table IV have to be provided (for each design parameter of interest and each cross section set used in the nuclear model calculation). Then the calculated values for  $\Delta R/R$  must be compared with the specified design criterion according to Eqs. (13) to sift out those satisfying Eq. (13a). For the selected results shown in Table IV we conclude that if the Fe54(n,p)Mn54 activation rate in the first structural steel region must be predicted to better than 25% standard deviation then the accuracy of the Fe54(n,p) cross section must be improved, either by a re-evaluation or new measurements. If an even higher accuracy of the predicted activation  $A_1$  is desired (e.g., better than 7%) then the Pb(n,2n) cross section must also be improved. An improvement of the C(n,n' $\alpha$ ) cross section is only required if a very tight design criterion, e.g.,  $(\Delta R/R)_{\text{max, crit.}} < 2\%$ , were set for  $A_1$ . In order to determine at which neutron energy a new cross section measurement should be performed to give the largest benefit to the considered design problem, we look at the sensitivity profile. Figure 3 shows the sensitivity profile for the Pb(n,2n) cross section. It indicates that 76% of the integral sensitivity is due to the cross section in the highest energy group. Although the highest accuracy of 15% was estimated for the Pb(n,2n) cross section at this energy, it still contributes 64% of the total  $\Delta R/R$  due to all Pb(n,2n) cross section uncertainties, as shown in Fig. 4. This histogram plots the group-wise contributions to  $\Delta R/R$  for the case of fully correlated uncertainties

$$\left(\frac{\Delta R}{R}\right)_{\text{corr. (+1)}}^i = P_{\Sigma_i} \cdot \frac{\Delta\Sigma_i}{\Sigma_i}, \quad (21)$$

so that, according to Eq. (17),  $(\Delta R/R)_{\text{corr. (+1)}}$  is obtained as the linear sum of all terms of Eq. (21). Hence, from Fig. 4 we can conclude that an improvement of the Pb(n,2n) cross section in the first energy group, ranging from 13.5 to 14.9 MeV, would be more beneficial for the calculation of  $A_1$  than a similar improvement at any lower energy.

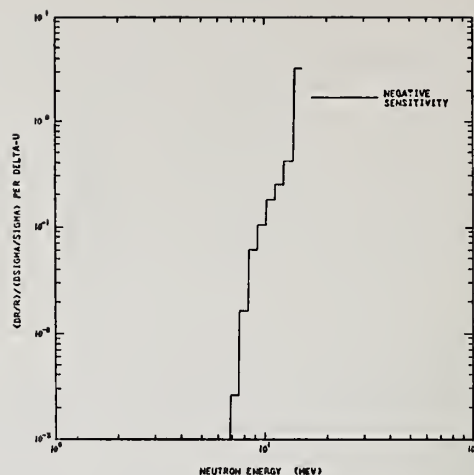


Fig. 3. Sensitivity of Fe54(n,p)Mn54-reaction rate in steel-zone 9 to Pb(n,2n) cross sections in shield-zone 7 of TFTR. The sensitivity profile is plotted per group width  $\Delta u$ . For all groups  $\Delta u = 0.1$ .

### Conclusion

We have demonstrated the applicability of a new quantitative method to assess cross section requirements by combining the results of a sensitivity analysis with estimated uncertainties of existing cross section data. The results of such quantitative assessment can be used in guiding priority assignments for new cross section measurements or evaluations. In addition, these results provide added confidence in cross section sets which have been found adequate for this application. Only selected results could be presented in this paper, partly due to the lack of complete cross section error files. Therefore, there is an immediate need for the establishment of estimated covariance data files for CTR materials. Such data are essential in order to

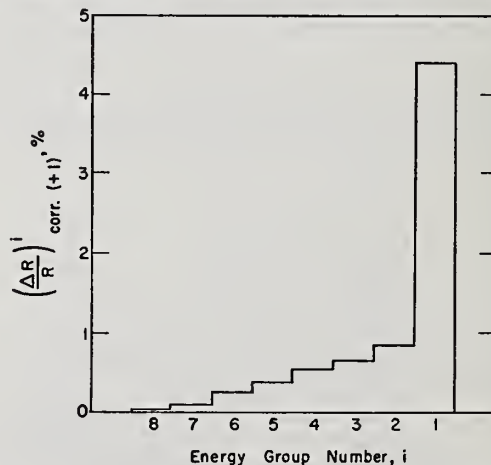


Fig. 4. Group-wise contributions to uncertainty of  $A_1$  in zone 9 due to estimated errors in Pb(n,2n) cross sections.

perform complete design-oriented cross section assessment tasks as outlined in this paper. However, the full information content as specified by the ENDF covariance file format<sup>5</sup> is not always necessary if rough, conservative error-estimates lead to acceptable upper limits of  $\Delta R/R$ . Therefore, the presently available ENDF covariance data, together with other estimated error information, have enabled us to draw some important conclusions regarding the adequacy of several existing cross section sets for TFTR applications. Many sensitivity profiles, similar to the sample shown in Fig. 3, and plotted automatically, have already added to our capability to identify areas for meaningful improvements in future cross section measurements and evaluations.

#### REFERENCES

1. D. Steiner, "Nuclear Data Needs for Fusion Reactor Design," this conference; and D. Steiner, N. D. Dudey, B. R. Leonhard, Jr., J. R. McNally, Jr., and L. K. Price, "Review of CTR Nuclear Data Requirements," Trans. Am. Nucl. Soc. 19, 457 (1974).
2. W. G. Price, Jr., Princeton University Plasma Physics Laboratory, private communication, December 7, 1974.
3. G. Gibson, Westinghouse Research and Development Center, private communication, February 6, 1975.
4. "TCT-Two-Component Torus," joint conceptual design study, performed by Plasma Physics Laboratory, Princeton, NJ, and Westinghouse Electric Corporation, Pittsburgh, PA, Vol. III, Sec. 6.1 (1974).
5. F. G. Perey, "Estimated Data Covariance Files of ENDF/B - Their Uses," presentation to the Cross Section Evaluation Working Group (CSEWG), Brookhaven, NY, June 1974.
6. D. Steiner, coordinator, "The Status of Neutron-Induced Nuclear Data for Controlled Thermonuclear Research Applications: Critical Reviews of Current Evaluations," USNDC-CTR-1 (1974).
7. S. A. W. Gerstl, "Second-Order Perturbation Theory and its Application to Sensitivity Studies in Shield Design Calculations," Trans. Am. Nucl. Soc. 16, 342 (1973); S. A. W. Gerstl and W. M. Stacey, Jr., "A Class of Second-Order Approximate Formulations of Deep Penetration Radiation Transport Problems," Nucl. Sci. Eng. 51, 339 (1973).
8. S. A. W. Gerstl, "The Application of Perturbation Methods to Shield and Blanket Design Sensitivity Analyses," AP/CTR/TM-28, Applied Physics Division, Argonne National Laboratory (1974).
9. D. E. Bartine, E. M. Oblow, and F. R. Mynatt, "Radiation-Transport Cross Section Sensitivity Analysis - A General Approach Illustrated for a Thermonuclear Source in Air," Nucl. Sci. Eng. 55, 147 (1974).
10. K. D. Lathrop, "DTF-IV, a FORTRAN-IV Program for Solving the Multigroup Transport Equation with Anisotropic Scattering," Los Alamos Scientific Laboratory report LA-3373 (1965).
11. "DLC-2/100G, 100 Group Neutron Cross-Section Data Based on ENDF/B," RSIC Data Library Collection, Radiation Shielding Information Center, HNL (1975).
12. D. W. Muir in "Applied Nuclear Data Research and Development Quarterly Progress Report, July 1 through September 30, 1974," edited by G. M. Hale, D. R. Harris, and R. E. MacFarlane, Los Alamos Scientific Laboratory report LA-5804-PR (1974).
13. S. A. W. Gerstl, "SENSIT-1D, A FORTRAN Code to Perform Cross Section and Design Sensitivity Analyses in One-Dimensional Geometries," Los Alamos Scientific Laboratory report, to be published.
14. W. C. Hamilton, "Statistics in Physical Science," Ronald Press, New York, NY, p. 31 (1964).



A SENSITIVITY STUDY OF DATA DEFICIENCIES, WEIGHTING FUNCTIONS,  
AND 14 MeV NEUTRON SOURCE SPECTRUM EFFECTS IN A  $^{238}\text{U}$  FUELED FUSION-FISSION HYBRID BLANKET  
B. R. Leonard, Jr., U. P. Jenquin, D. L. Lessor,  
D. F. Newman and K. B. Stewart  
Battelle-Northwest  
Richland, Washington 99352

Neutronic calculations have been made for a hybrid DT fusion reactor blanket in which the initial region is fueled with depleted uranium followed by lithium and graphite. The important parameters of the blanket are the tritium production, fissions,  $^{238}\text{U}$  captures, and thermal flux in the graphite. The sensitivity of these integral parameters was studied as a function of  $^{238}\text{U}$  region thickness and the  $^{238}\text{U}$  microscopic data used. In particular, the effect of modifying some improbable secondary neutron energy distributions of  $^{238}\text{U}$  on both versions III and IV of ENDF/B was calculated. Calculations were made for multigroup data obtained by collapsing over constant and  $E^{-1}$  weighting functions below the fusion peak. Results were also obtained for a narrow DT fusion neutron peak and for neutron source distribution resulting from an essentially exact calculation of a mirror plasma driven by 100 keV neutral  $^2\text{H}$  and  $^3\text{H}$ .

(Nuclear reactions,  $^{238}\text{U}$ , (n,n'), (n,2n), (n,3n) calculated sensitivity of secondary neutron energies to fusion blanket neutronics)

### Introduction

In previous work<sup>1,2</sup> Battelle-Northwest (BNW) has reported the results of the neutronic analyses of a fission hybrid blanket designed for a mirror fusion reactor. Nuclear data from ENDF/B-III was employed in these studies. We now report on a study which was designed to define uncertainties and improved estimates of the calculated neutronic performance parameters due to nuclear data deficiencies and related data handling and physical problems. Haight and Lee,<sup>3</sup> for example, have reported significant differences in neutronics parameters for calculations of a particular hybrid blanket for calculations employing ENDF/B-III and those using Lawrence Livermore Laboratory ENDL microscopic data. These calculated differences are assumed<sup>3</sup> to be primarily due to the known differences in the descriptions of neutron energy spectra of secondary neutrons from non-elastic reactions on iron<sup>4</sup> and uranium.<sup>5</sup> It is further known that the emission spectra of neutrons above 2 MeV from iron or uranium spheres<sup>6</sup> pulsed with a central 14 MeV neutron source are calculated much better with ENDL than with ENDF/B data. Since the first region of the hybrid blanket calculated by BNW was comprised primarily of iron and  $^{238}\text{U}$ , effects due to these data differences similar to those observed by Haight and Lee<sup>3</sup> may occur. In addition, Muir<sup>7</sup> has recently pointed out that the neutron emission spectra resulting from high-temperature isotropic Maxwellian DT plasmas are quite broad in energy distribution and can have significant impacts on calculated reaction rates for reactions which have significant variation with energy near 14 MeV. The mirror fusion reactor concept in which the leaky plasma is driven by 100 keV or higher<sup>1</sup> energetic neutrals produces plasma ion-energy distributions which are very similar to Maxwellian distributions with high characteristic temperatures.<sup>8</sup> Thus, the expected broad neutron source spectrum can impact on the calculated reaction rates and associated secondary neutron spectra in the mirror hybrid blanket. The broad source spectrum also raises questions of possible effects of: 1) assumptions used in the neutron spectrum used to obtain the multigroup data set, 2) the energy multi-group structure, and 3) the neutron source distributions used in the neutron balance calculation.

### Calculational Model

#### Description of the Hybrid Blanket

In the previously reported work,<sup>1</sup> the conceptual hybrid blanket consisted of inner and outer fissile blanket regions. The inner blanket region consisted of helium-cooled, depleted-uranium oxide and was called a convertor. Leakage neutrons from this region were used to drive a slightly-enriched HTGR lattice which (for lower energy neutrons) was largely decoupled from the convertor by an intervening thickness of lithium. The effects to be studied in the present work are dominated by events in the convertor region. Thus, in this study the HTGR thermal fission lattice has been replaced by graphite. This results in a blanket configuration similar to those reported by Lee<sup>9</sup> and by Haight and Lee.<sup>3</sup> Thus, the calculated neutronic parameters can be compared with the results of these studies. The basic blanket configuration is given in Table I.

Table I. Mirror Hybrid Blanket Description

Region	Thickness	Constituents	Density (at-b <sup>-1</sup> -cm <sup>-1</sup> )
1	3.5 m rad.	DT	0
2	5.0 m rad.	Vacuum	
3	t(cm)	Helium	0.000159
		St. steel	0.009935
		Oxygen	0.025734
		$^{238}\text{U}$	0.012828
		$^{235}\text{U}$	0.0000386
4	4.5 cm	$^6\text{Li}$	0.003317
		$^7\text{Li}$	0.04139
		SS	0.002524
		He	0.0000002
5	(188.5-t)cm	C	0.08123
6	7 cm	$^6\text{Li}$	0.003317
		$^7\text{Li}$	0.04139
		SS	0.002524
		He	0.0000002

The uranium in the convertor (region 3) is 0.3%  $^{235}\text{U}$ . The initial thickness of the convertor was 8.5 cm and this thickness was varied in the sensitivity calculations at the expense of the thickness of the graphite region.

### Calculational Methods

For the reference case, ENDF/B-III data were processed into a 27 energy group structure using a constant lethargy weighting function. Effective capture and fission cross sections obtained using the



GRANIT<sup>10</sup> and EGGNIT<sup>11</sup> codes were substituted into this set to account for spectral effects. All of the calculations reported in this study were performed for room temperature. Neutron balance calculations were performed using the ANISN<sup>12</sup> code in P<sub>3</sub>, S<sub>8</sub> approximation in spherical geometry with the 14 MeV neutron source distributed uniformly in the top energy group (1.5 - 14.92 MeV).

### Sensitivity Studies

#### ENDF/B <sup>238</sup>U Data

The ENDF/B-III description of <sup>238</sup>U, MAT-1158, used evaporation formula models to describe single distribution functions for the energy of secondary neutrons from (n,2n), (n,3n) and (n,n' $\gamma$ ) reactions. These distributions have been reevaluated to significantly increase the kinetic-energy of the outgoing neutrons, relative to the available energy, and are now similar to the descriptions on ENDL.<sup>5</sup> The cross sections and resultant average neutron energies for MAT-1158 and the BNW modification are compared on Table II for 14.07 MeV incident energy. The n,n' cross section was also reduced in magnitude and the difference added to the elastic cross section.

Table II. Description of Secondary Neutrons from U-238 for an Incident Neutron of 14.07 MeV Energy

Reaction	Cross Section (b)		Average Secondary Neutron Energy (MeV)	
	MAT-1158	BNW	MAT-1158	BNW
(N,2N) E <sub>1</sub>			1.03	1.50
E <sub>2</sub>			1.03	4.70
Total	0.824	0.824	2.06	6.20
(N,3N) E <sub>1</sub>			0.61	0.50
E <sub>2</sub>			0.61	0.50
E <sub>3</sub>			0.61	1.16
Total	0.505	0.505	1.83	2.16
N,N' Cont	0.325	0.0066	1.55	1.55
E <sub>1</sub>		0.045		12.58
E <sub>2</sub>		0.0525		11.57
E <sub>3</sub>		0.0525		10.57
E <sub>4</sub>		0.035		9.57
Total		0.1916		

The results of neutron balance calculations using the BNW modified <sup>238</sup>U data compared with the reference case are summarized on Table III for the important blanket parameters

Table III. Calculated Reactions per 14 MeV Source Neutrons

	ENDF/B-III	BNW Mod.	<sup>238</sup> U
Converter Thickness (cm)	8.5	8.5	12.0
Tritium Produced	1.040	1.065	1.053
Total Fissions	0.208	0.229	0.298
<sup>238</sup> U Captures	0.440	0.443	(Lost)
Graphite Thermal Flux	2.93	3.03	2.87

The differences in the integral quantities due to the <sup>238</sup>U data alone do not, in themselves, seem very large for the 8.5 cm thick converter. However, the calculations with a 12 cm thick converter show that the converter size can be significantly increased with this data set while still breeding tritium and decreasing the graphite thermal flux by only 2% relative to the ENDF/B-III 8.5 cm thick converter.

#### Mirror Neutron Source Spectrum

In order to evaluate the DT neutron source spectrum of the mirror fusion reactor, a computer program was written to make an essentially exact calculation of the neutron emission spectrum from tabulated ion-energy distributions as well as from Maxwellian distributions. Barr, et al<sup>8</sup> have reported a calculated ion-energy distribution for a mirror device in which the average injection energy was 100 keV. The calculated ion-energy distribution closely resembles a 100 keV Maxwellian. Our calculations using this ion-energy distribution yielded a neutron-energy distribution not greatly different from that of a 100 keV Maxwellian ion-energy distribution except for truncation of the wings of the distribution. The calculated neutron-energy distribution was centered at 14.2 MeV with a FWHM of 1.70 MeV with a significant contribution of neutrons above 15 MeV energy. Since the uranium files on ENDF/B-III terminated at 15 MeV we were forced to change to ENDF/B-IV cross sections in order to make calculations using this neutron source spectrum.

#### Sensitivity Studies Using ENDF/B-IV

In the remainder of the studies, all of the nuclear data were derived from ENDF/B-IV. The ENDF/B-IV <sup>238</sup>U, MAT-1262, descriptions for the secondary neutron energy distributions from (n,2n) and (n,3n) reactions were not changed from ENDF/B-III. Thus, these files were modified to contain the descriptions of our present evaluation. The ENDF/B-IV (n,n' $\gamma$ ) secondary neutron distributions were changed from ENDF/B-III. Since they are now similar to our evaluation they were not changed.

The energy group structure used in our calculations was modified to 30 groups, extended to 18.22 MeV, and given a finer mesh over the broad mirror neutron spectrum. Most of this source spectrum is now contained in 4 groups from 12.21- to 15.88 MeV. For mirror spectrum calculations, the neutron source was distributed in 6 energy groups in the ANISN calculations according to the fraction of the total source spectrum in each energy group.

**Weighting Functions.** Reference calculations were carried out using group cross sections derived using the calculated mirror neutron spectrum joined to a constant lethargy spectrum below 12 MeV. In order to study the effect of the broad spectrum mirror neutron-source, an alternate set of group cross sections was obtained for <sup>238</sup>U only in which the broad source spectrum was replaced by a 20 keV "line" source. As a further perturbation another <sup>238</sup>U group cross section set was calculated using the "line" source with a constant-flux weighting spectrum below the source. All of the line source calculations were made with all of the source neutrons in a single energy group (13.50-14.19 MeV) in ANISN.

**Results of ENDF/B-IV Calculations.** The results of the sensitivity studies described above are summarized in Table IV for the 8.5 cm thick converter.

Table IV. Calculated Reactions per 14 MeV Source Neutron Using ENDF/B-IV Data.<sup>a)</sup>

	Line Source <sup>b)</sup>		
	Mirror Source	Const $\phi(u)$	Const $\phi(E)$
Tritium Prod.	1.107	1.097	1.102
Total Fissions	0.236	0.233	0.235
<sup>238</sup> U captures	0.456	0.451	0.451
Graphite Flux	3.25	3.20	3.24

a) <sup>238</sup>U modified from ENDF/B-IV.

b) <sup>238</sup>U only weighting changed.

**Converter Thickness.** Calculations were also made for a 12 cm thick converter for the mirror source and for the line source with constant lethargy flux weighting. The relative differences in the calculated blanket parameters were only one percent or less.

**Comparison with Other Calculations.** Lee<sup>9</sup> has reported neutronic calculations for a natural uranium dioxide mirror hybrid blanket similar to the one studied here. The major differences in the two converters are that Lee's converter region contains lithium (Li/U = 0.39), different structural materials (Fe, Ni, Nb) at relatively lower concentrations (S/U = 0.43 vs S/U = 0.77), no voids (helium), and slightly more <sup>235</sup>U. In Table V the results of Lee's calculation (Table III of Ref. 9) are compared with the results of the mirror spectrum calculations of this study. The results are tabulated in reference to the equivalent <sup>238</sup>U atoms-b<sup>-1</sup> thickness of the converter.

Table V. Comparison of Two UO<sub>2</sub> Hybrid Blankets in Reactions per Source Neutron

Converter Thickness (at-b <sup>-1</sup> <sup>238</sup> U)	Lab	Tritium Produced	Total Fissions	<sup>238</sup> U Captures
0.154	BNW	1.09	0.305	0.69
0.154	Lee <sup>9</sup>	1.36	0.309	0.50
0.257	BNW	0.92	0.417	1.21
0.308	Lee <sup>9</sup>	1.00	0.484	1.20

Comparison of the two 0.154 at-b<sup>-1</sup> <sup>238</sup>U thickness blankets indicates that there are no great differences brought about by <sup>238</sup>U data or calculational techniques. The blanket model of Lee breeds tritium better because of <sup>7</sup>Li(n,n'T) $\alpha$  reactions in the converter region essentially at the expense of <sup>238</sup>U captures. The BNW blanket performance is worse than that calculated by Lee for the thicker blankets. This may be due to greater amounts of structural material and less <sup>235</sup>U in the BNW blanket design.

#### Summary and Conclusions

The sensitivity studies of this paper clearly indicate that this type of blanket is more sensitive to the description in the data files of the energies of secondary neutrons than to broadening of the neutron source spectrum. The cumulative uncertainty in the calculated integral parameters due to neutron source spectrum description and weighting functions used to derive multigroup data appears to be less than that due to the uncertainty in the proper description of these secondary neutron energy distri-

butions. The broad neutron-energy spectrum typical of the mirror fusion reactor appears not to have much impact on the important parameters of the system studied here. This conclusion, however, might not be valid if the descriptions of (n,2n) and (n,3n) reaction shapes near 14 MeV given in these data files are not good estimates. The broad spectrum certainly is expected to impact on other features of fusion reactor blankets not considered in the present study.

#### Acknowledgment

This paper is based on work performed under USAEC Contract AT(45-1)-1830.

#### References

1. W. C. Wolkenhauer, B. R. Leonard, Jr., A. M. Sutey and R. W. Moir, Proc. First Topical Conf. on Fusion Technology, San Diego, CONF-740402-P1, 238 (1974).
2. B. R. Leonard, Jr. and W. C. Wolkenhauer, IAEA Fifth Conf. on Plasma Physics and Controlled Fusion Research, Tokyo, 1974, in Publication.
3. R. C. Haight and J. D. Lee, Proc. First Topical Conf. on Fusion Technology, San Diego, CONF-740402-P1, 271 (1974).
4. L. F. Hansen, J. D. Anderson, P. S. Brown, R. W. Howerton, J. L. Kammerdiener, C. M. Logan, E. F. Plecharty, and C. Wong, Nucl. Sci. Engr. 51, 278 (1971).
5. R. J. Howerton and M. H. MacGregor, USAEC Report UCRL-51427 (1973).
6. J. L. Kammerdiener, USAEC Report UCRL-51232 (1972).
7. D. W. Muir, Proc. First Topical Conf. on Fusion Technology, San Diego, CONF-740402-P2, 166 (1974).
8. W. L. Barr, R. J. Burleigh, W. L. Dexter, R. W. Moir and R. R. Smith, USAEC Report UCRL-74636 (1973).
9. J. D. Lee, Proc. First Topical Conf. on Fusion Technology, San Diego, CONF-740402-P1, 223 (1974).
10. C. L. Bennett, USAEC Report BNWL-1634 (1971).
11. C. R. Richey, USAEC Report BNWL-1203 (1967).
12. W. W. Engle, Jr., USAEC Report K-1693 (1967).



Should magnetic confinement of hot plasma prove satisfactory at high beta ( $\beta \approx 0.2$ ), nuclear fusion fuels other than DT will be important in future fusion reactors. The prospect of the advanced fusion fuels DD and  ${}^6\text{LiD}$  in such fusion reactors appears very promising provided the system is large, well reflected and has a sufficiently high density and temperature (high beta). Steady state burning of DD can ensue in a 60 kG field, 5m radius reactor for  $\beta \gtrsim 0.1$  and wall reflectivity  $R_w = 0.9$ . The first generation thermonuclear reactions between D and D or  ${}^6\text{Li}$  produce the very active, energy-rich fuels t and  ${}^3\text{He}$  which exhibit a high burnup probability in very hot plasmas. Steady state burning of  ${}^6\text{LiD}$  has also been demonstrated theoretically for low concentrations of  ${}^6\text{Li}$ ; however, important features of the  ${}^6\text{LiD}$  system still need to be incorporated in the calculation. In particular, there is a need for new and improved nuclear cross section data on over 80 reaction possibilities.

(Advanced-Fuels; Fusion-Dynamics; DD;  ${}^6\text{Li}$ ; Reactivity-Coefficients; I-Layer)

Recent studies of the advanced fusion fuels DD and  ${}^6\text{LiD}$ <sup>1-3</sup> indicate that under certain conditions these fuels could prove superior to the DT fueled system. The conditions include: 1). stable, high- $\beta$  plasmas such as the I-layer nuclear dynamo ( $\beta = \Sigma \mu n k T / p^2 \gtrsim 0.2$ ); 2). large, dense and well reflected systems to reduce the synchrotron radiation losses; 3). some mechanism for feeding cold fuel deep into the plasma interior; and 4). particle loss processes significantly greater than classical diffusion permits. Other scientists are beginning to recognize the importance of the high- $\beta$  I-layer;<sup>2,4</sup> "Potentially even more fruitful in actual fusion reactors could be schemes in which the necessary ring currents are carried by very high energy ions."<sup>5</sup> The present paper lists the advantages which accrue to the advanced fuel systems and details the reactivity of such high- $\beta$  plasmas.

Some of the important advantages of the advanced fuels are: 1). there would be no dependence on a tritium breeding blanket or on neutron economy; 2). there would be cheap initial (and continuing) fueling costs (initial tritium fueling costs for DT reactors are about 75M\$ for a 10 kg T inventory); 3). significantly lower equilibrium concentration of tritium will be present in the plasma (e.g., 2% vs 50%); 4). reduced environmental hazards due to tritium leaks will apply because of the grossly reduced T inventory; 5). the fast neutron (14 MeV) flux is reduced by a factor of more than two; 6). a wider latitude is permitted in the choice of structural materials from the standpoint of fast neutron damage and induced radioactive after-heat; 7). a sodium based heat exchanger instead of a lithium blanket will increase the energy release on neutron capture by  $12.6/4.8 = 2.6$ ; 8). no chemical combustion hazard exists if the heat exchanger is based on chemically fixed sodium (e.g.,  $\text{Na}_2\text{CO}_3$  or NaOH in water); 9). there is a high burnup of tritium ( $\sim 80\%$ ) in steady state, high- $\beta$  plasma systems; 10). catalyzed DD or  ${}^6\text{LiD}$  burning of unburned tritium will further reduce the total tritium inventory; 11). increased energy release in charged particles improves the burn properties; and 12). all the neutrons are "free" and can be used for breeding  ${}^{235}\text{U}$  or  ${}^{239}\text{Pu}$  fuel for fission reactors (with increased energy amplification) or for other applications.

The present plasma reactivity code is an extension of that developed by Etzweiler, Clarke and Fowler<sup>6</sup> and now includes 15 reactions of a possible 80 reactions.<sup>7</sup> The reactions presently included in the code are  $d(t,n)\alpha + 17.6$  MeV,  $d(d,n){}^3\text{He} + 3.3$  MeV,  $d(d,p)t + 4.0$  MeV,

$t(t,2n)\alpha + 11.3$  MeV,  $d({}^3\text{He},p)\alpha + 18.4$  MeV,  $t({}^3\text{He},d)\alpha + 14.3$  MeV,  $t({}^3\text{He},n){}^5\text{Li} \rightarrow p + \alpha + 12.1$  MeV,  $t({}^3\text{He},p){}^5\text{He} \rightarrow n + \alpha + 12.1$  MeV,  ${}^6\text{Li}(p,{}^3\text{He})\alpha + 4.0$  MeV,  ${}^6\text{Li}(d,p){}^7\text{Li} + 5.0$  MeV,  ${}^6\text{Li}(d,p)t + \alpha + 2.6$  MeV,  ${}^6\text{Li}(d,n){}^7\text{Be} + 3.4$  MeV,  ${}^6\text{Li}(d,n){}^3\text{He} + \alpha + 1.8$  MeV,  ${}^6\text{Li}(d,\alpha)\alpha + 22.4$  MeV and the endothermic reaction  $t(p,n){}^3\text{He} - 0.8$  MeV which is evaluated in terms of the slowing down rates for energetic protons from  $d(d,p)t$  and  $d({}^3\text{He},p)\alpha$  reactions.<sup>1</sup> The  ${}^6\text{Li}(p_{\text{fast}}, {}^3\text{He})\alpha + 4.0$  MeV reaction is also treated as a beam-plasma type process as the energetic protons slow down in the fuel mix. Averaged  $\sigma v$  values are taken from Greene<sup>8</sup> or calculated from the literature as in the case of  ${}^6\text{Li}(p,{}^3\text{He})\alpha$ . Fig. 1 shows the temperature variation of  $\langle \sigma v \rangle Q_+$  summed over all channels,

where  $Q_+$  is the energy release in charged particles. At temperatures above 100 keV the advanced fuels become very competitive with the exotic fuels DT and D-He.

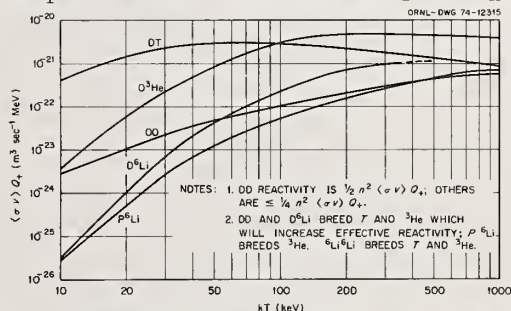


Fig. 1 Temperature dependence of reactivity parameters,  $\langle \sigma v \rangle Q_+$ , for all exothermic reaction channels. See notes for additional factors involved in evaluating reactivity of different fuels.

The particle and energy balance equations are described elsewhere<sup>1</sup> but include radiation dominated plasmas in closed (pulsed) systems and radiation damped plasmas in systems having particle losses and source feed terms. Both bremsstrahlung and synchrotron radiation terms are relativistically corrected. Except for the few beam-plasma reactions included the plasma is taken to have Maxwellianized electron and ion temperatures established by a dynamic equilibrium between the ions and the electrons resulting from the power input from the nuclear reactions, from the power



loss by radiation and particle escape and from the power loss to incoming cold-fuel feed. Synchrotron radiation is partially reduced by absorption in the plasma in large, dense and well reflected systems ( $R_\mu = 0.9$ ) and is found to be tolerable especially with "primed" fuels, i.e., fuels having a nearly equilibrium abundance of the active t and  $^3\text{He}$  such that the production rates of these energy-rich fuels are approximately equal to their burnup rates.

Fig. 2 illustrates schematically the burning characteristics of a DT fueled system. If a brute force ignition mode is used, such as injection in tokamaks, the plasma will ignite at about 6 keV and undergo a thermal runaway to the operating or burning temperature which may exceed 200 keV ( $\sim 2 \times 10^9 \text{K}$ ) at which point the charged particle nuclear power production equals the radiation (and particle power) losses. The burning temperature is then a stable operating temperature if the particle densities remain constant; however, in a closed, pulsed system the ashes eventually build up and the system gradually quenches due to the increased radiation losses as calculated for a pulsed DD system shown in Fig. 3 for which the burn time extends for about 200 sec.

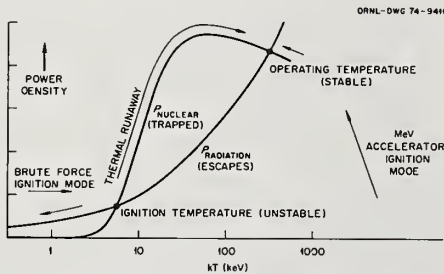


Fig. 2 Illustration of the thermal runaway of a radiation-dominated DT reactor above its ignition temperature of about 6 keV. Operating temperature is a "stable" operating point in terms of its negative temperature coefficient (but see text on positive density coefficient). Accelerator ignition mode discussed in Ref. 2.

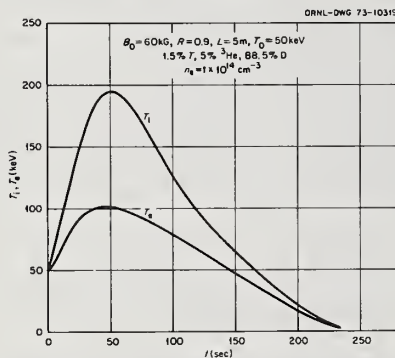


Fig. 3 Burn characteristics of a radiation dominated, pulsed burn, closed DD reactor.

Three new features have been recently introduced into the evaluations; namely, 1). the inclusion of an approximate nuclear elastic scattering energy flow correction, 2). the incorporation of a magnetic field correction to the Coulomb logarithm which reduces the electronic stopping power on the fast ions and, 3). the addition of catalyzed burning of t and  $^3\text{He}$  (feed

of cold t and  $^3\text{He}$  equal to their loss rates).

Figs. 4 and 5 illustrate the energy loss rate in a  $10^{20} \text{m}^{-3}$  density deuterium plasma due to the nuclear elastic collisions of different fast ions with deuterons.<sup>9</sup> Arbitrarily taking all nuclear elastic collision energy loss rates to be continuous rather than discrete functions one has  $dW/dt \approx -0.13 \times 10^{-20} W_1 n_2$ .

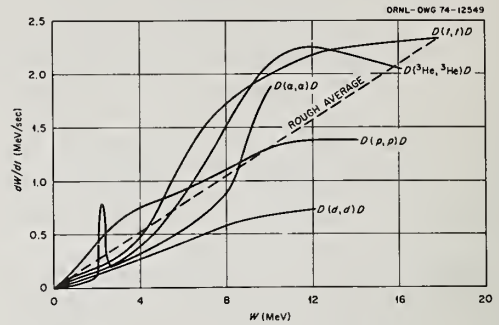


Fig. 4 Nuclear elastic collisional energy loss rate vs fast particle energy (after Devaney and Stein<sup>9</sup>). Deuteron density  $n_D = 10^{20} \text{m}^{-3}$ .

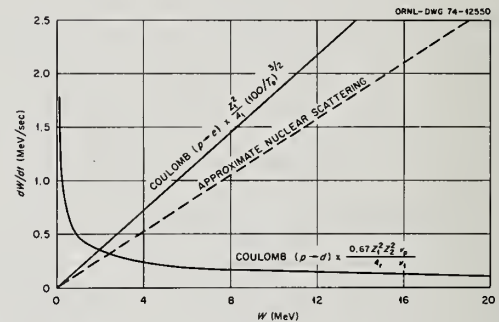


Fig. 5 Energy loss rates of fast particles due to nuclear elastic collisions with ions and due to Coulomb collisions with ions and electrons. An average curve is used for nuclear elastic collisions to give simple analytic expression for  $f_e$  (see text).

Plasma density:  $n_D = n_e = 10^{20} \text{m}^{-3}$

This gives for the energy flow from fast reaction products to plasma ions and electrons (see Ref. 10):

$$\frac{dW}{dt} = -\frac{2.5 W_1 Z_1^2}{\tau_s A_1} [1 + \gamma] - 0.13 \times 10^{-20} W_1 n_2$$

where  $W_1$  is the fast ion energy in keV,  $n_2$  is the total density of all plasma ions in  $\text{m}^{-3}$ ,  $Z_1$  and  $A_1$  are the charge and atomic number of the test ion. Following Rose,<sup>10</sup> one obtains for the fraction of the fast ion energy delivered to the plasma electrons,

$$f_e = \frac{\ln A_1 e}{30(1+NS)} \int_0^{\infty} \frac{1+NS+\gamma}{\gamma} \left[ \frac{(1+NS+\gamma)e^{-x} - \gamma}{1+NS} \right]^{2/3} dx$$

where

$$\tau_s = 1.25 \times 10^{18} \left( \frac{20}{\ln \Lambda_{1e}} \right) \frac{T_e^{3/2}}{n_e}$$

$$NS = 5.2 \times 10^{-22} \tau_s n_2 A_1 / Z_1^2$$

$$\gamma = \frac{57}{n_e} \sum_2 \frac{Z_2^2 n_2}{A_2} \frac{\ln \Lambda_{1i}}{\ln \Lambda_{1e}} \left( \frac{T_e A_1}{W_{10}} \right)^{3/2} \frac{A_1 + \bar{A}_2}{A_1} \frac{10}{6.5}$$

where  $\bar{A}_2$  is the average atomic mass number of the field ions and  $10(A_1 + \bar{A}_2)/6.5 A_1$  represents a slight reduced mass correction to Rose's  $\gamma$ .<sup>10</sup> The Coulomb logarithms are of the form  $\ln \Lambda = \ln (\lambda_D m v_t^2 2\alpha c / Ze^2 v_t)$ , where

$\lambda_D$ , the Debye length, is  $2.3 \times 10^4 \sqrt{T(\text{keV})/n(\text{cm}^{-3})}$ ,  $v_t$  is the velocity of the test particle, and  $\alpha = 1/137$ .

The effect of the magnetic field on the Coulomb logarithm<sup>11</sup> has been included by using  $v_t/\sqrt{2}\omega_{ce}$  (where  $\omega_{ce} = eB/mc$  = electron gyro-frequency) when it is less than  $\lambda_D$ . This reduction in the Coulomb logarithm results from long range binary collisions between fast ions and electrons because the electrons execute an  $E \times B$  drift about the test ion trajectory rather than a "free-fall" towards the test ion. The effect is more important for test ions than for test electrons ( $v_e \gg v_t$ ) and leads to a larger disparity between ion and electron temperatures. Fig. 6 shows the effects of including both nuclear elastic scattering corrections and Coulomb logarithm corrections in a magnetic field on a pulsed DD reactor "primed" with some initial  $t$  and  $^3\text{He}$  approximately equal to their concentrations during the burn period. The ignition temperature is taken as 50 keV. The peak ion temperature is about 80 keV higher when both nuclear elastic and  $\ln \Lambda(B)$  corrections are included.

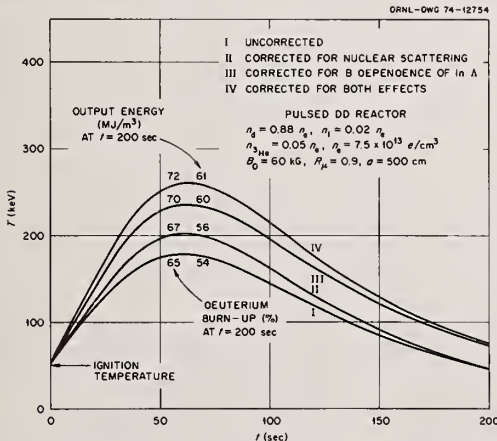


Fig. 6 Effects of nuclear elastic collisions and magnetic field corrected Coulomb logarithm on reactivity of a pulsed DD fusion reactor.

Figs. 7 and 8 illustrate the variation in the peak ion and electron temperatures as a function of the density of radiation-dominated, pulsed DD or  $D^6\text{Li}$  plasmas. Also given are the burn time to reach the peak ion temperature as well as the associated  $\beta (= \Sigma 8\pi n_k T / B^2)$ , the radiation power ( $P_{\text{RAD}}$ ), and the power in neutrons and blanket energy release ( $P_{\text{NAB}}$ ).

The important feature of Figs. 7 and 8 is that they reveal a positive density coefficient for a fusion

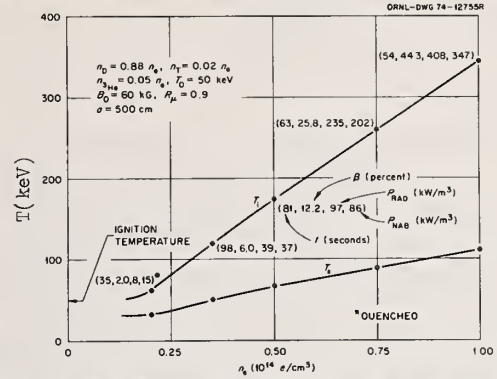


Fig. 7

Peak temperatures and other parameters as a function of the density of radiation-dominated, pulsed, closed DD fusion reactors ignited at 50 keV.  $R_\mu$  = wall reflectivity in infrared and microwave region,  $a$  = plasma radius.

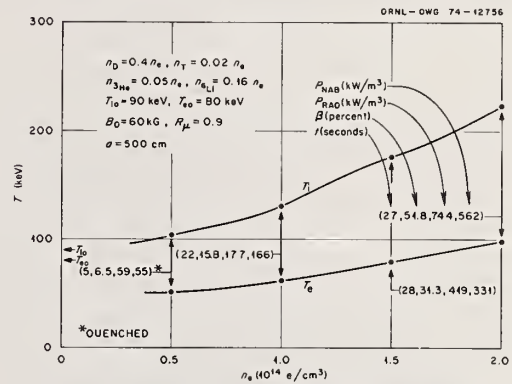


Fig. 8

Peak temperatures and other parameters as a function of the density of radiation-dominated, pulsed, closed  $D^6\text{Li}$  fusion reactors ignited at about 90 keV.

reacting plasma, i.e., any increase of density increases the net reactivity (the reaction power input goes as  $n^2$  whereas the synchrotron radiation losses vary only as  $n^{1/2}$ ). Thus, a fuel leak into such a system can lead to a nuclear excursion if cold fuel feed is realizable - this must then be compensated for by a positive feedback loop probably tied to the magnetic field since particle diffusion losses should increase with reduced magnetic confining field. Impurity feed such as ordinary hydrogen feed could also be used to control the plasma reactivity.

Note that at low densities which give beta's in the tokamak range ( $\leq 0.10$ ) these pulsed reactors will quench or just barely ignite. At high densities, and hence higher beta's the "primed" reactors ignite and burn very well. Both DD and  $D^6\text{Li}$  plasmas generate interesting power levels for pulsed mode operation at high beta's ( $\geq 0.20$ ). These high  $\beta$  values would necessitate a closed magnetic mirror configuration such as the proton E-layer<sup>12</sup> or the I-layer,<sup>2,4</sup> and possibly the ELMO Bumpy Torus,<sup>13</sup> all of which permit high average beta's. In the ion layers the magnetic mirror is closed by the self magnetic field produced by a transparent proton or ion ring-current perpendicular to the applied magnetic field.<sup>2,5,12</sup>

The I-layer nuclear dynamo system should also permit axial fuel feed deep into the plasma along the



magnetic axis as well as provide a strong divertor action outside the region of the closed flux lines.<sup>4,14</sup> Divertor action is necessary in steady state reactors for the removal of any impurities as well as the ashes and some of the unburned plasma. It may also provide a partial separation of electrical charges leading to the prospects of some direct energy conversion or even thrust.<sup>4,14</sup>

Steady state operation of the advanced fuel fusion reactors is now considered. The actual particle loss processes in fusion reactors are not well understood and may be weak (pseudo-classical losses), strong (Bohm or trapped particle losses) or perhaps controllable (charge exchange losses). To evaluate whether a fusion reactor might operate, in principle, as a steady state system we have provided for cold D or <sup>6</sup>LiD fuel feed in such a way as to maintain the plasma electron density and the deuteron density constant without specifying the actual physical nature of the loss or feed mechanisms.

Catalyzed burning is also included by eliminating any net tritium or <sup>3</sup>He losses, i.e., the source feed rates of cold t and <sup>3</sup>He are set equal to their hot particle loss rates. The effect of including source and loss terms is illustrated in Fig. 9 for which the source and loss terms were introduced at t = 30 sec in such a way as to maintain n<sub>e</sub> and n<sub>d</sub> constant. The plasma shifted quickly to a lower-temperature, steady-state operation with T<sub>e</sub> ≈ 81 keV, T<sub>i</sub> ≈ 186 keV and the plasma β = 27%. The particle confinement (or replacement) time required to maintain this steady state is 22.2 seconds. It should be noted that the feed of cold fuel ions and associated electrons and the loss of hot plasma ions and electrons cools the plasma but it does not cool it below an ignition temperature. Thus, from Fig. 1 the operating (or burning) temperature remains above the ignition (or quench) temperature even with cold particle feed and losses and a steady state burn behavior is ensured. The particle confinement time of 22.2 seconds for the case illustrated in Fig. 9 is many orders of magnitude shorter than classical or pseudo-classical particle diffusion times; thus, a strong instability-driven loss mechanism or controlled charge exchange losses can not only be permitted but is essential to steady state operation. Whether an appropriate loss process may exist in such high β systems must await careful experimentation and theoretical analysis.

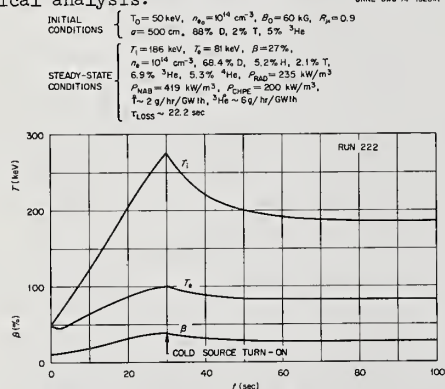


Fig. 9 Effect of turn-on of a source of cold D<sup>0</sup> feed and fixed losses 30 seconds after ignition of a DD fusion reactor. Source and losses are defined so as to maintain n<sub>e</sub> and n<sub>d</sub> constants. Catalyzed burning of T and <sup>3</sup>He ( $S_T = L_{nT}$ ;  $S_{^3\text{He}} = L_{n^3\text{He}}$ ;  $L = 1/\tau_{\text{LOSS}}$ ).

Note that in the steady-state, catalyzed DD reactor of Fig. 9 the equilibrium tritium concentration is only 2.1% whereas <sup>3</sup>He is at 6.9%. The power output in neutron energy release and blanket energy release (assumed only 4.8 MeV/n) is P<sub>RAD</sub> which with the radiation power output, P<sub>RAD</sub>, and NAB the leakage escape power in charged particles, P<sub>CHPE</sub> [= 1.5nk(T<sub>i</sub>+T<sub>e</sub>)/τ], gives 0.85 MW/m<sup>3</sup>, a quite respectable figure. Thus, a 5m radius spherical reactor of this type would then give P<sub>OUT</sub> ~ 400 MW (thermal) and a wall loading of P/A ~ 1.3 MW/m<sup>2</sup> at the plasma surface (5m) or ~ 0.7 MW/m<sup>2</sup> at 7m. Higher power production could be attained by increase of the plasma density (see Fig. 7).

The prospects of direct conversion of the charged particle escape power to electricity may be rather modest since it would involve only about 23% of the total energy release - the 77% fraction would require a thermal cycle. Thus, for 70% direct electrical conversion of the 23% for P<sub>CHPE</sub> the total thermal efficiency would be of order 23(0.70) + 77(0.35) ~ 43%.

Perturbation studies of the steady state, DD fueled reactor of Fig. 9 indicate that it has a negative temperature coefficient, which is very desirable; however, as mentioned earlier it does have a positive density coefficient which must be controlled by a positive feedback system involving power output sensors which control the magnetic field (or the feed of impurity atoms). It should be emphasized that the startup of any fusion reactor will necessitate very careful controls on the reactivity level since the walls may well be loaded with excess D and some T. Any thermal excursion of the plasma would lead to a thermal loading of the walls with a concomitant increase in gas release which may enhance the thermal runaway.

The prospects for steady state operation of D<sup>6</sup>Li fusion reactors are beginning to emerge at the present time and steady state D<sup>6</sup>Li reactors containing up to at least 21% <sup>6</sup>Li appear feasible (see Table I). The further improvement of the reactivity codes and the inclusion of many more reaction combinations may well reveal the operation of steady-state D<sup>6</sup>Li fueled plasmas having even higher concentration of <sup>6</sup>Li. It should be noted that stripped ions of <sup>6</sup>Li should have a high affinity for charge exchange with any H<sup>0</sup>, D<sup>0</sup> or T<sup>0</sup> atoms which enter the plasma and hence the <sup>6</sup>Li<sup>3+</sup> would help purge the plasma of the bound electrons since the Li<sup>2+</sup> so formed would be rapidly ionized.<sup>15</sup> There is an urgent need for the evaluation and accurate (~15%) measurement of the nuclear reaction cross sections for the many charged particle nuclear reactions involving <sup>6</sup>Li (and <sup>7</sup>Li and <sup>7</sup>Be) (see Price<sup>7</sup>). The production of a large I-layer type plasma will probably require a major development program on multi-MeV accelerators with steady state current outputs in excess of 10 mA (see Ref. 2).

I am greatly indebted to R. D. Sharp of the Computer Sciences Division at ORNL for many improvements to the Etzweiler, Clarke and Fowler code.



Table I. Plasma Parameters of Two Possible Steady-State, Advanced Fuel, Catalyzed Fusion Reactors\* (B = 60 kG, a = 500 cm, R<sub>c</sub> = 0.90)

Parameter	DD $1.0 \times 10^{14} \text{ e/cm}^3$	D <sup>6</sup> Li $2.0 \times 10^{14} \text{ e/cm}^3$
n <sub>e</sub>		
T <sub>i</sub>	186 keV	150 keV
T <sub>e</sub>	81 keV	75 keV
β	27%	40%
n <sub>p</sub> /n <sub>e</sub>	5.2%	4.2%
n <sub>d</sub> /n <sub>e</sub>	68.4%	44.0%
n <sub>t</sub> /n <sub>e</sub>	2.1%	1.4%
n <sub>3He</sub> /n <sub>e</sub>	6.9%	5.6%
n <sub>α</sub> /n <sub>e</sub>	5.3%	5.1%
n <sub>6Li</sub> /n <sub>e</sub>	---	9.3%
n <sub>7Li</sub> /n <sub>e</sub>	---	0.4%
n <sub>7Be</sub> /n <sub>e</sub>	---	0.1%
P <sub>RAD</sub>	235 kW/m <sup>3</sup>	514 kW/m <sup>3</sup>
P <sub>NAB**</sub>	419 kW/m <sup>3</sup>	765 kW/m <sup>3</sup>
P <sub>CHPE</sub>	200 kW/m <sup>3</sup>	190 kW/m <sup>3</sup>
τ (Conf. Time)	22.2 sec	18.9 sec
D thrupt	48 gms/hr/GWth	47 gms/hr/GWth
T thrupt	1.8 gm/hr/GWth	1.8 gm/hr/GWth
<sup>3</sup> He thrupt	6.0 gm/hr/GWth	7.2 gm/hr/GWth
14 MeV n rate	1.1x10 <sup>20</sup> n/s/GWth	1.2x10 <sup>20</sup> n/s/GWth
Total n rate	2.5x10 <sup>20</sup> n/s/GWth	2.6x10 <sup>20</sup> n/s/GWth

\* Presumes cold fuel feed and fixed losses to maintain n<sub>e</sub> and n<sub>d</sub> constant.

\*\* Assumes average 4.8 MeV/n energy release on neutron capture in blanket.

\*\*\* 1 gm tritium ~ 10<sup>4</sup> Curies. Maximum permissible losses to atmosphere ~ 10 Curies/day.

## References

- 1) J. Rand McNally, Jr., "Reactivity of Advanced Fusion Fuels," USAEC Report ORNL-TM-4647 (1974).
- 2) J. Rand McNally, Jr., "Fusion Chain Reactor Prospects and Problems," USAEC Report ORNL-TM-4575 (1974).
- 3) J. Rand McNally, Jr., "Advanced Fuels for Nuclear Fusion Reactors," Third Conference on Application of Small Accelerators, North Texas State University, Oct., 1974 (to be published).
- 4) J. Rand McNally, Jr., "Conjectures on Fusion Chain Reaction Cycles and the I-layer Configuration," USAEC Report ORNL-CF-64-8-9 (1964).
- 5) N. Rostoker and K. Moses, "The Application of High Current Relativistic Electron Beams in Controlled Thermonuclear Research," USAEC Report WASH-1286 (1974).
- 6) J. F. Etzweiler, J. F. Clarke, and R. H. Fowler, "Effect of Fuel Injection of a Cyclic β-limited Radiation Dominated Fusion Reactor," USAEC Report ORNL-TM-4083 (1974).
- 7) L. K. Price, "Nuclear Data Requests," USAEC letter to Fusion Technology Group, May 9, 1974.
- 8) S. L. Greene, Jr., "Maxwell Averaged Cross Sections for Some Thermonuclear Reactions on Light Isotopes," USAEC Report UCRL-70522 (1967).
- 9) J. J. Devaney and M. L. Stein, Nuclear Science and Engineering 46, 323 (1971).
- 10) D. J. Rose, Nuclear Fusion 9, 183 (1969).
- 11) J. Rand McNally, Jr., submitted to Nuclear Fusion.
- 12) Nicholas C. Christofilos, "Proton E-layer Astron for Producing Controlled Thermonuclear Reactions," U. S. Government Patent 3, 664, 921 (1972).
- 13) R. A. Dandl, H. O. Eason, A. C. England, G. E. Guest, C. L. Hedrick and J. C. Sprott, "The Elmo Bumpy Torus Experiment," USAEC Report ORNL-TM-3694 (1971).
- 14) J. Rand McNally, Jr., "Speculations on the Configurational Properties of a Fusing Plasma," Nuclear Fusion 12, 265 (1972).
- 15) J. Rand McNally, Jr., "Neutral Injection Heating of Tokamaks," USAEC Report ORNL-TM-4363 (1973).

\* Research sponsored by the U. S. Atomic Energy Commission under contract with the Union Carbide Corporation.

# A STUDY OF THE ${}^6\text{Li}(n,\alpha)\text{t}$ REACTION BETWEEN 2-10 MeV\*

C. Murray Bartle\*\*  
University of Wisconsin,  
Madison 53706, U.S.A.

Absolute  ${}^6\text{Li}(n,\alpha)\text{t}$  cross section measurements are reported between 2.16 and 9.66 MeV. The results agree with the Pendlebury evaluation. The possibility of unfolding angular distributions from the pulse-height distributions in  ${}^6\text{LiI}(\text{Eu})$  is investigated.

( ${}^6\text{Li}(n,\alpha)\text{t}$ ; 2-10 MeV; angular distribution)

## Introduction

A review of the  ${}^6\text{Li}(n,\alpha)\text{t}$  reaction below  $E_n = 1.7$  MeV was recently made by Uttley et al<sup>1</sup>. Above 1.7 MeV the total cross section has been evaluated by Pendlebury<sup>2</sup> and Uttley et al<sup>3</sup>. The reaction is employed as a primary standard for neutron flux measurement<sup>4</sup> and has important applications in the nuclear engineering field. These include the development of a  ${}^6\text{Li}$ -sandwich detector<sup>5</sup> to measure neutron spectra in fast-breeder reactors<sup>6,7</sup> and tritium breeding for the proposed D-T fusion reactors<sup>8</sup>. Therefore accurate cross sections for the reaction up to 14 MeV are needed.

At the present time there are serious discrepancies in previous data for neutron energies above 1 MeV. The recent evaluation of the total cross sections made by Uttley et al<sup>3</sup> is in very poor agreement with the earlier-obtained Pendlebury evaluation<sup>2</sup> which is the accepted data source<sup>9</sup>. Here, an attempt has been made to produce data of improved reliability through the utilization of the proven associated particle system developed at the University of Wisconsin<sup>10-13</sup>. A feature of this system is that the sources of experimental error are reduced through the inherent simplicity of the procedures involved. Strictly absolute neutron flux measurements are obtained through electronic techniques which involve counting the recoiling associated  ${}^3\text{He}$  ions within a carefully chosen experimental geometry. In this work the  ${}^6\text{Li}$  target is a  ${}^6\text{LiI}(\text{Eu})$  scintillator which has interesting response properties which yield information about the details of the  ${}^6\text{Li}(n,\alpha)\text{t}$  angular distributions.

## Total Cross Section Measurements

### Experimental Method

The experimental system, illustrated in fig.1 and discussed in detail elsewhere<sup>10</sup>, employs a  ${}^6\text{LiI}(\text{Eu})$  scintillator measuring 2.5cm in diameter and 1.3cm in depth<sup>#</sup>. This scintillator is positioned to encompass the electronically-collimated neutron beam following measurements of the beam profile<sup>14,15</sup>.

### Experimental Spectra

Typical spectra which show the broad  ${}^6\text{Li}(n,\alpha)\text{t}$  distribution are shown in fig.2. These events occur in time coincidence with the detected  ${}^3\text{He}$  ions. The timing resolution is typically 2ns. The timing constraint greatly reduces the observed experimental background, such as would arise, for example, from the

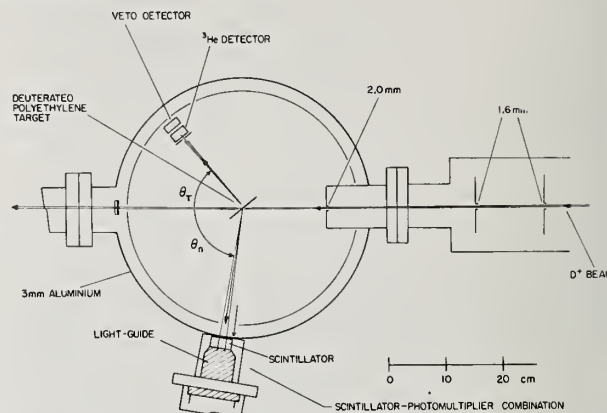


Fig.1. The experimental system. Typical experimental parameters are: beam current, 0.3μA; target thickness, 100μg/cm<sup>2</sup> and neutron flux, 100 /s.

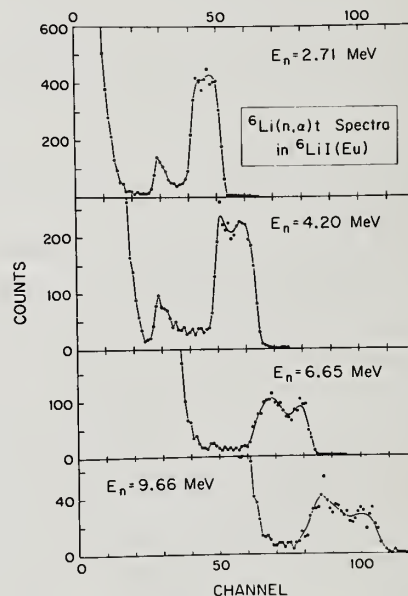


Fig.2. Typical spectra for monoenergetic neutrons incident on  ${}^6\text{LiI}(\text{Eu})$ .

\* Work supported in part by the U.S. Atomic Energy Commission.

\*\*AINSE Fellow - present address: School of Physical Sciences, ANU, A.C.T. 2600, Australia.

# Manufactured by Harshaw Chemical Co., Cleveland, Ohio.

reactions of thermal neutrons unavoidably present in the experimental environment. Reactions produced by energy degraded neutrons in the energy region where the cross section is large produce a low energy tail on the fast-neutron distribution. Slowing-down mechanisms include the  ${}^6\text{Li}(n,n){}^6\text{Li}$  and  ${}^6\text{Li}(n,\alpha)d$  reactions.

### Analysis

Cross sections for the reaction are calculated using a standard procedure<sup>10,15</sup>. In all 24 spectra were obtained in the energy range from 2.16 to 9.66 MeV in several running periods during which the neutron energies chosen were interwoven. A feature of the experiment is the individual independence of the calculated cross sections obtained. Small corrections arise from effects of neutron elastic and non-elastic processes occurring both outside and inside the scintillator which cause the neutron beam to be partially attenuated. A typical summary is given in table 1. Allowance is made for events contributed to the broad fast-neutron distribution by the appropriate proportion of the energy-degraded neutrons produced within the scintillator.

### Errors

The total cross section measurements are shown in fig.4. Of the typical uncertainty of  $\pm 3\%$  the component uncertainties are typically:  $\pm 2\%$  due to the effective beam attenuation correction (table 1);  $\pm 2\%$  due to the counting statistics;  $\pm 0.5\%$  in counting the  ${}^3\text{He}$  ions;  $\pm 0.5\%$  in the scintillator thickness and  $\pm 0.2\%$  in scintillator edge effects.

### Discussion

In fig.3, the measurements are compared with pertinent previous data. It is clear that the results of the present experiments strongly support the previous Pendlebury evaluation<sup>2</sup>. The measurements of Clements and Rickard<sup>16</sup> which are a basis for the recent evaluation by Uttley et al<sup>3</sup> do not agree with the present measurements. Apparently, the problem in the case of the measurements of ref:16 is primarily one of normalization. Since these measurements are normalized with the data of Coates et al<sup>17</sup> in the keV region, there are possibly undetermined uncertainties in this region. It would be informative, too, to investigate

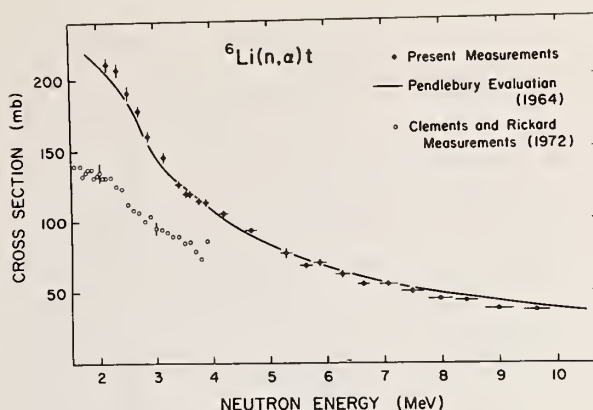


Fig.3. A comparison with earlier data. Horizontal error bars represent the energy spread of the incident neutrons. The present measurements are tabulated in Appendix 1.

the low energy tail exhibited by the fast-neutron  ${}^6\text{Li}(n,\alpha)t$  distributions from  ${}^6\text{LiI}(\text{Eu})$  with Monte Carlo methods. Such an analysis may affect the number of events attributed to the fast-neutron distribution although the adjustment should be small.

### Differential Cross Section Measurements

The difficulty in measuring  $(n,\alpha)$  differential cross sections is illustrated by the absence of data for the  ${}^6\text{Li}(n,\alpha)t$  reaction between 2.7 and 14 MeV<sup>18</sup>. Here, the possibility of unfolding angular distributions from  ${}^6\text{Li}(n,\alpha)t$  distributions in  ${}^6\text{LiI}(\text{Eu})$  is investigated.

### Resolution of the ${}^6\text{Li}(n,\alpha)t$ Distributions

As illustrated in the superimposed spectra in fig.4, the resolution of the  ${}^6\text{Li}(n,\alpha)t$  distribution for fast neutrons is much poorer than that for thermal

Table 1. Effective neutron beam attenuation

Source	4 MeV		8 MeV	
	correction (%)	error ( $\pm$ )	correction (%)	error ( $\pm$ )
Non-elastic events:				
outside scintillator	+1.1	0.6	+1.4	0.7
inside scintillator	+1.9	0.9	+1.5	0.8
Elastic events:				
inside scintillator				
(a) multiple scattering	-1.6	0.8	-1.6	0.8
(b) scattering on ${}^6\text{Li}$	+2.0	1.0	+2.0	1.0
outside scintillator	+1.7	0.2	+0.4	0.1
Net Correction	+5.1	1.7	+3.7	1.7



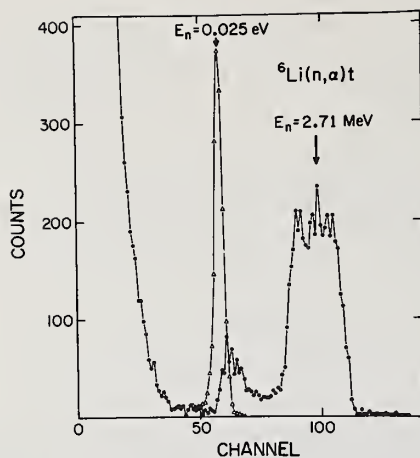


Fig. 4. Comparison of the  ${}^6\text{Li}(n,\alpha)t$  distributions produced by thermal and fast neutrons. The origin of the thermal neutrons is a Pu-Be source.

neutrons. This observation has been attributed by several groups<sup>19-21</sup> to the difference between the triton and  $\alpha$ -particle response in  ${}^6\text{LiI}(\text{Eu})$ . This is effective because, in the case of fast neutrons, large c.m. motion causes the emitted tritons and  $\alpha$ -particles to have a range of energies in the laboratory system. From reaction kinematics, the energy of each product particle is a linear function of the Cosine of the c.m. emission angle of the outgoing triton ( $\theta_{\text{cm}}$ ). Thus, if each product particle has a different linear response in  ${}^6\text{LiI}(\text{Eu})$  the total response from the simultaneous detection of both particles is in turn a linear of  $\text{Cos}(\theta_{\text{cm}})$ . Since the strength of this effect is proportional to the product of the particle and c.m. velocities the fast-neutron distributions are relatively broad as illustrated in fig. 4. Indeed, the eloquent observations made by Barschall and Kanner<sup>22</sup> and Barschall and Powell<sup>23</sup> in relation to the interpretation of recoil spectra in  ${}^4\text{He}$ -counters also apply to  ${}^6\text{Li}(n,\alpha)t$  distributions in  ${}^6\text{LiI}(\text{Eu})$ . With appropriate scaling the pulse-height distribution images the differential-cross-section curve plotted against  $\text{cos}\theta_{\text{cm}}$ .

#### Response Curves for ${}^6\text{LiI}(\text{Eu})$

Response curves are necessary to unfold the spectra. It is possible to derive these response curves by tracing the movement of the  ${}^6\text{Li}(n,\alpha)t$  distribution with neutron energy, assuming that kinematic broadening dominates the spectral width. These curves are based on the expected dominance of the response of the scintillator to the emitted triton<sup>21</sup>, particularly for forward emission. In fig. 5 the idealized line shapes corresponding to isotropic angular distributions clearly do not reproduce the experimental spectral shapes obtained. The unfolded angular distributions shown in fig. 6 exhibit a fluctuating behaviour.

#### Discussion

Preliminary results have been obtained. There are several interesting observations to be summarized here. First, for excitations of the  ${}^7\text{Li}$  system corresponding to  $E_n = 2.5$  and  $3.5$  MeV accentuated maxima and minima are observed. The agreement with the positions of the  $\frac{1}{2}^-$  and  $\frac{3}{2}^-$  states found previously<sup>24</sup> suggests a strong contribution through compound nucleus formation.

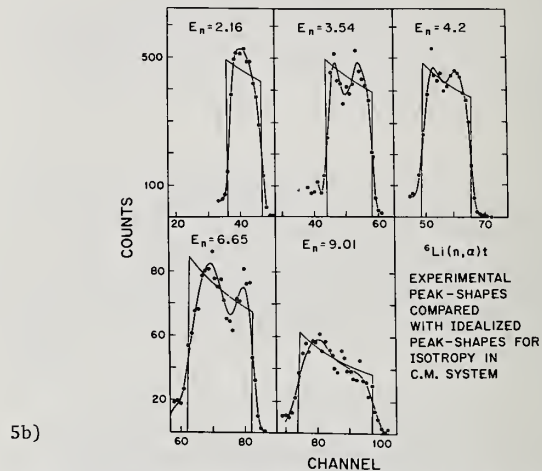
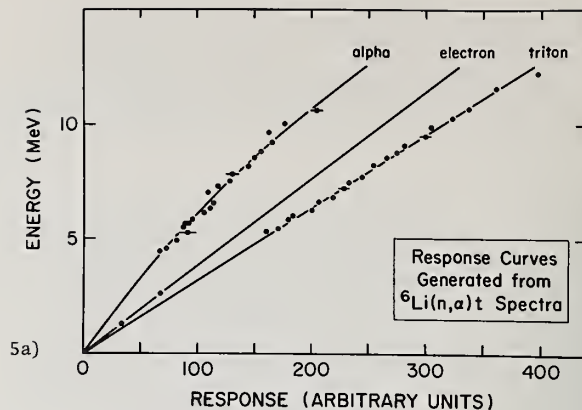


Fig. 5. Idealized spectrum shapes for isotropic triton distributions in c.m. (fig. 5b) are derived from response curves (fig. 5a) obtained from an analysis of the spectral-width of the experimental distributions

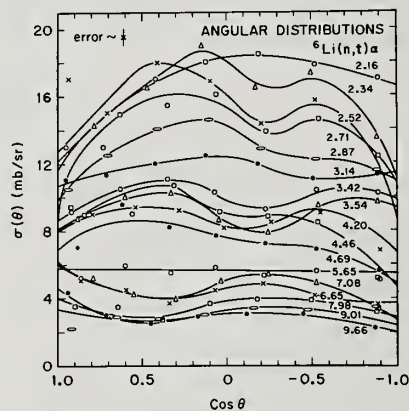


Fig. 6. Angular distributions for the emitted triton plotted in the c.m. system. Lines drawn through the points are a guide to the eye only. For clarity, other curves are not shown but are in similar agreement. The statistical error is indicated. Each point represents the average cross section over an increment of approximately 0.2 in  $\text{Cos}\theta$ .

At higher neutron energies a forward-peaked pattern is established in good agreement with the measurement of Valkovic et al.<sup>25</sup> at 14.4 MeV. Generally, the curves are in good agreement with the corresponding  ${}^6\text{Li}(p, {}^3\text{He})\alpha$  distributions<sup>26,27</sup> where the higher-energy data is described well by direct-mechanism codes<sup>27</sup>. There is a suggestion in fig.6 that there is a transition from the dominance of a compound-nucleus mechanism to a direct mechanism in the region of  $E_n = 5.65$  MeV. The study of the  ${}^6\text{Li}(n, \alpha)t$  angular distributions is continuing.

### Conclusions

A feature of the present experiment is the individual independence of the measurements which generate the  ${}^6\text{Li}(n, \alpha)t$  excitation function. Only small deviations from the predictions of the Pendlebury evaluation are found in this work. Thus, the recent evaluation of Uttley et al. which is normalized quite differently appears to be in error.

The broadening of the  ${}^6\text{Li}(n, \alpha)t$  distributions in  ${}^6\text{LiI}(\text{Eu})$  is due to a sensitivity to the reaction kinematics obtained through the differing response curves for the product particles. Angular distributions have been unfolded with apparently good reliability and provide new insight into the reaction mechanism.

### Acknowledgement

The author is indebted to Professor P.A. Quin and Dr D.T.L. Jones for their assistance during the experimental phases of this work.

### References

1. C.A. Uttley, M.G. Sowerby, B.H. Patrick and E.R. Rae, Neutron Standards and Flux Normalization (Argonne, 1971) p.80.
2. E.D. Pendlebury, AWRE 0-60/64 (1964).
3. C.A. Uttley, M.G. Sowerby and R. North, AERE-PR/NP 19 (1972).
4. D.J. Deruytter, Nuclear Data for Reactors (Helsinki, 1970) p.129.
5. I.C. Rickard, Nucl.Instr. 105 (1972) 397.
6. M.E. Lee and M.L. Awcock, Neutron Dosimetry I (Vienna, 1963) p.441.
7. S.K.I. Patterson and M.J. Stevenson, Proc. CEGB Conf.on Radiation Measurements in Nuclear Power (1966).
8. Wisconsin Tokamak Reactor Design, Univ.of Wisc., UWFD-68.
9. J.R. Stehn, NNCSC, BNL, private communication.
10. C.M. Bartle and P.A. Quin, Nucl.Instr. 121 (1974) 119.
11. C.M. Bartle and P.A. Quin, Nucl.Phys. A216 (1973) 90.
12. C.M. Bartle, Nucl.Instr. 117 (1974) 569.
13. C.M. Bartle, Nucl.Instr. in press.

14. C.M. Bartle, N.G. Chapman and P.B. Johnson, Nucl.Instr. 95 (1971) 221.
15. C.M. Bartle, P.B. Johnson and N.G. Chapman, Nucl.Phys. A220 (1974) 395.
16. P.J. Clements and I.C. Rickard, AERE-R 7075.
17. M.S. Coates, J. Hunt and C.A. Uttley, AERE-PR/NP 18 (1970/71).
18. USAEC Report BNL-400, 3rd edition.
19. B.D. Kern and W.E. Kreger, Phys.Rev., 112 (1958) 926.
20. R.B. Murray, Nucl.Instr. 2 (1958) 237.
21. T.R. Ophel, Nucl.Instr. 3 (1958) 45.
22. H.H. Barschall and M.H. Kanner, Phys.Rev., 58 (1940) 590.
23. H.H. Barschall and J.L. Powell, Phys.Rev., 96 (1954) 713.
24. F. Ajzenberg-selove and T. Lauritsen, Nucl.Phys. A227 (1974) 55.
25. V. Valkovic, I. Slaus, P. Tomas and M. Cerineo, Nucl.Phys. A98 (1967) 305.
26. J.M.F. Jeronymo, G.S. Mani and A. Sadeghi, Nucl. Phys. 43 (1963) 424.
27. M.F. Werby, M.B. Greenfield, K.W. Kemper, D.L. McShan and S. Edwards, Phys.Rev. C8 (1973) 106.

### APPENDIX

The  ${}^6\text{Li}(n, \alpha)t$  Cross Section

Mean neutron energy (MeV)	Energy width (keV) -FWHM	$\sigma_{n, \alpha}$
2.16	80	211 $\pm$ 5
2.34	100	207 $\pm$ 5
2.52	80	191 $\pm$ 5
2.71	120	178 $\pm$ 4
2.87	120	160 $\pm$ 4
3.14	120	145 $\pm$ 4
3.42	120	126 $\pm$ 3
3.54	140	119 $\pm$ 3
3.61	140	119 $\pm$ 3
3.77	140	114 $\pm$ 3
3.89	140	113 $\pm$ 3
4.20	160	105 $\pm$ 3
4.69	200	93 $\pm$ 2
5.30	240	77 $\pm$ 4
5.65	240	68 $\pm$ 2
5.89	240	70 $\pm$ 3
6.28	240	62 $\pm$ 3
6.65	240	55 $\pm$ 2
7.08	320	55 $\pm$ 2
7.51	400	50 $\pm$ 2
7.98	400	44.8 $\pm$ 1.4
8.44	400	43.2 $\pm$ 1.6
9.01	500	37.9 $\pm$ 1.4
9.66	500	36.3 $\pm$ 1.5



# ABSOLUTE CROSS SECTIONS FOR NEUTRONS FROM ${}^6\text{Li} + d$ REACTIONS AT ENERGIES BETWEEN 0.2 AND 0.9 MeV<sup>†</sup>

A. J. Elwyn, R. E. Holland, F. J. Lynch, J. E. Monahan, and F. P. Mooring  
Argonne National Laboratory, Argonne, Illinois 60439

Absolute differential and total cross sections in reactions of deuterons with  ${}^6\text{Li}$  have been measured for neutrons corresponding to the formation of  ${}^7\text{Be}$  in both its ground and its first excited state, and for the continuum neutrons involved in the breakup of  ${}^7\text{Be}$  at deuteron energies between 0.2 and 0.9 MeV. Discussion of the experimental procedure is presented. The results indicate that the breakup neutrons are a substantial portion of the total neutron production cross section in this reaction. The reaction rates of the various neutron production reactions are presented.

(Measured  $\sigma(\theta; E_d)$ ,  $\sigma_t(E_d)$  for  ${}^6\text{Li}(d, n){}^7\text{Be}$  reactions; measured  $\frac{d^2\sigma}{dE_n d\Omega}(\theta; E_d)$ ,  $\sigma_t(E_d)$  for  ${}^7\text{Be}$  breakup reaction;  $E_d = 0.2-0.9$  MeV).

## Introduction

It has been pointed out by McNally<sup>1</sup> and others<sup>2</sup> that knowledge of absolute reaction cross sections for the outgoing particles in nuclear reactions of deuterons with  ${}^6\text{Li}$  at energies between 100 keV and a few MeV is of importance to evaluate the prospects of fusion chain reactions in controlled thermonuclear research applications. Unfortunately, data for deuteron-induced reactions on the lithium isotopes reveal<sup>2</sup> substantial disagreement among the various existing measurements. For the case of neutron production in  $d + {}^6\text{Li}$  reactions only one absolute total cross section measurement (over a limited energy range) had been reported<sup>3</sup> prior to 1973.

As part of a program for determining reaction cross sections for various nuclear particles emitted in charged particle induced reactions on light nuclei we report here the results of a study of the outgoing neutrons in the bombardment of  ${}^6\text{Li}$  by 0.2–0.9-MeV deuterons. Differential and total cross sections for neutrons from the  ${}^6\text{Li}(d, n){}^7\text{Be}$  reaction, and for those associated with the breakup of  ${}^7\text{Be}$  were obtained. The present measurements supplement, in part, a recent report by McClenahan and Segel<sup>4</sup> who measured  ${}^6\text{Li}(d, n)$  cross sections from  $\sim 0.5-3.0$  MeV by a different technique.

## Experiment

The experiment was carried out at the ANL 4-MV Dynamitron accelerator equipped with a pulsed and bunched ion source. The  $\text{D}_3^+$  molecular ion beam was incident on thin ( $75-90 \mu\text{g}/\text{cm}^2$ ) targets of LiF (enriched to 99.3% in  ${}^6\text{Li}$ ) evaporated onto thick tantalum backings. The use of LiF rather than metallic lithium, which was possible since the number of neutrons that arise from  $(d, n)$  reactions on F are negligibly small for deuteron energies below 1-MeV, allowed the fabrication of very uniform stable films. The target was supported on an O-ring seal at the end of an aluminum can which also acted as a Faraday cup. A current integrator accurate to considerably better than 1% was utilized to ensure proper beam integration. A jet of compressed air cooled the target which was also rotated at about 1 rev/sec. The acceleration of the  $\text{D}_3^+$  molecular ion beam rather than the normal  $\text{D}_1^+$  ion made it possible to obtain low deuteron energies on target for the higher terminal

voltages at which more stable Dynamitron operating conditions prevailed.

In order to monitor the condition of the target during an experimental run and to measure the target thickness a thin layer of Au ( $\leq 10 \mu\text{g}/\text{cm}^2$ ) was evaporated over the LiF film and the spectrum of deuterons backscattered at  $177^\circ$  was recorded in a Si surface-barrier detector. This spectrum is shown in Fig. 1. The energy difference between the narrow peak which corresponds to deuteron scattering from the thin Au film, and the edge due to scattering from the thick tantalum backing is directly related to the energy loss of the deuteron beam in LiF. Target thicknesses obtained in this fashion agree very closely with determinations by more conventional techniques. The error of the measurement depends primarily upon the accuracy with which the rates of energy loss are known, and is probably less than 10%.

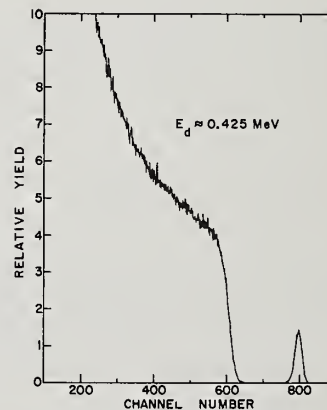


Fig. 1. Spectrum of deuterons scattered at  $177^\circ$  from "sandwich" target that consists of Au +  ${}^6\text{LiF}$  + Ta backing.

Differential cross sections for neutrons from the  ${}^6\text{Li}(d, n){}^7\text{Be}$  reaction and for those that arise from the breakup of  ${}^7\text{Be}$  into  ${}^3\text{He}$  and  ${}^4\text{He}$  were determined from time-of-flight measurements. Four detectors, each of which was a cylindrical stilbene scintillator 2.54 cm long and 5.08 cm in diameter directly coupled to an RCA-8575 photomultiplier, were used so that simultaneous measurements at four angles were possible. Each counter assembly was supported



by a wedge-shaped arm that could rotate about a pivot directly below the target position. The main features of the electronic instrumentation, which utilized pulse-shape  $\gamma$ -ray suppression, have been described previously.<sup>5</sup>

A typical time-of-flight spectrum is shown in Fig. 2. The flight path, 3.5 meters, was sufficient to resolve the neutron groups corresponding to the ground and first excited states of  $^7\text{Be}$ , the two sharp peaks on this spectrum. The broad peak corresponds to the continuous neutron distribution from the  $^7\text{Be}$  breakup reaction.

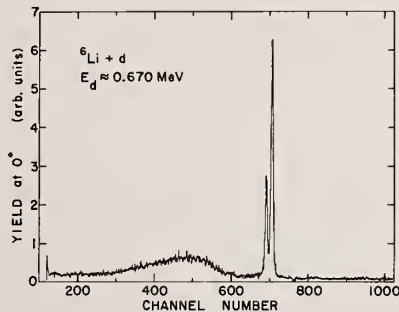


Fig. 2. Typical T.O.F. spectrum for neutrons emitted in  $d + ^6\text{Li}$  reactions at 3.5 m. flight path. Time dispersion is  $\sim 1$  ns/ch.

The absolute efficiency for one of the detectors is shown in Fig. 3. It was obtained from measurements of the  $0^\circ$  neutron yield in the  $^7\text{Li}(p,n)^7\text{Be}$  reaction for energies between 0.25 and 2.75 MeV by use of the recently published cross sections of Burke et al.<sup>6</sup> and Smith and Meadows,<sup>7</sup> and at a few higher energies (to 4 MeV) by measuring the ratio<sup>8</sup> of neutron- $^3\text{He}$  coincidences to total  $^3\text{He}$  counts in the  $\text{D}(d,n)^3\text{He}$  reaction. The solid curve of Fig. 3 represents a calculation<sup>9</sup> that takes into account the production of recoil protons by direct  $n$ - $p$  collisions in the stilbene scintillator as well as by proton collisions with neutrons scattered by one or more carbon atoms. The photomultiplier gains and other electronics settings were adjusted to give similar responses for all four detectors; differences in efficiency occurred mostly in the region of the detector threshold ( $\sim 0.3$  MeV). Accuracy of the absolute efficiencies is  $\sim 12\%$ , based predominately on the quoted<sup>6</sup> accuracy of the  $^7\text{Li}(p,n)$  cross sections and the uncertainty in target thickness.

Neutron backgrounds at the detectors were evaluated by use of a blank tantalum disc in place of the  $\text{LiF}$ -plus-tantalum targets. These measurements accounted well for beam-line related sources of neutrons. Backgrounds at the detectors associated with the  $^6\text{LiF}$  target itself were determined by intercepting the direct neutron beam with Lucite absorbers placed between the target and each detector; although such effects were small they were taken into account in the subsequent analysis of the data.

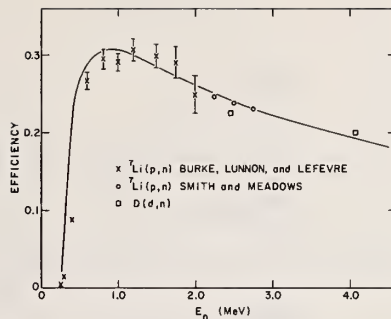


Fig. 3. Absolute neutron-detector efficiency as function of neutron energy.

The intensities of the neutron groups corresponding to the ground and first excited state of  $^7\text{Be}$  were found by summing the contents of the relevant channels and subtracting the background. Since the two groups were not completely resolved at most bombarding energies, an unfolding procedure<sup>10</sup> was used. Differential cross sections were obtained from these results after correction for detector efficiency by use of the measured target thickness and total integrated charge. Corrections for electronic dead time and other effects were determined (experimentally) or estimated to be less than 2% and were not made. For the continuum neutrons, corresponding to  $^7\text{Be}$  breakup, measured counts per channel were corrected for background and converted into differential cross section per unit energy interval. An example of such results is shown in Fig. 4. These distributions were then integrated from a neutron energy of 0.5 MeV, to the maximum neutron energy at which breakup can occur for each deuteron energy in order to obtain differential cross sections at each angle.

Angular distributions were determined at seven angles between  $0^\circ$  and  $149^\circ$  at each of a number of average deuteron energies between 0.204 and 0.880 MeV. Calibration of the energy scale of the accelerator gave deuteron energies accurate to  $\pm 0.005$  MeV.

### Results

Figures 5 shows center-of-mass differential cross sections as a function of angle at various bombarding energies for the  $^7\text{Be}$  ground state and 0.431-MeV first excited state neutrons, respectively. Total cross sections for each neutron group were obtained from the values of the coefficient  $B_0$  in an expansion of the differential cross section into a series of Legendre polynomials [i.e.

$$\frac{d\sigma}{d\Omega} = \sum_{L=0}^5 B_L P_L(\cos\theta)], \text{ and are displayed in Fig. 6 and Table I.}$$

Laboratory differential cross sections for all continuum neutrons with energy greater than 0.5 MeV are shown at a number of bombarding energies in Fig. 7. From the Legendre polynomial expansion of these, the total cross sections are obtained and displayed in Fig. 8 and Table I.

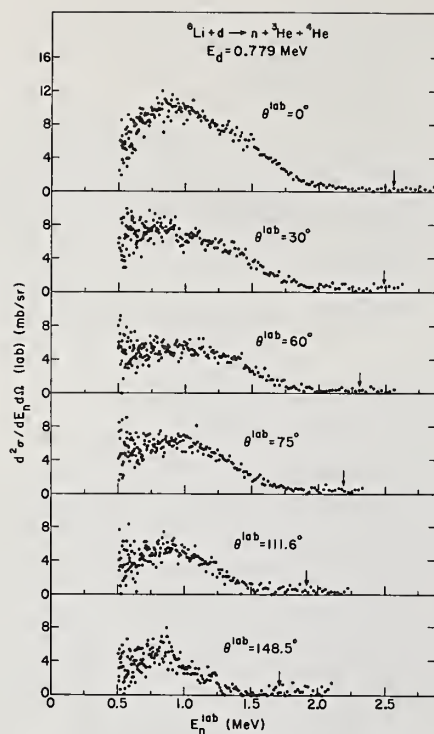


Fig. 4. Lab. differential cross sections per MeV as function of  $E_n$  at  $E_d = 0.779$  MeV for neutrons associated with  ${}^7\text{Be}$  breakup. The arrows indicate the max. value of  $E_n$  at which breakup neutrons can occur.

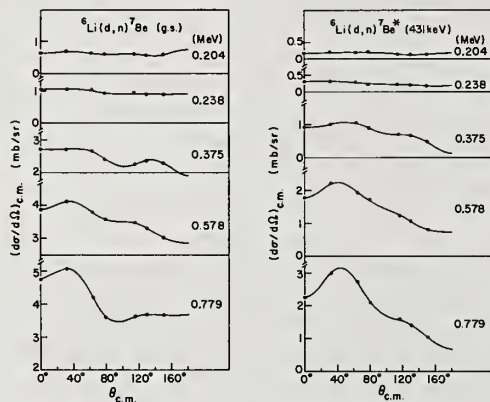


Fig. 5. C.M. differential cross sections as a function of angle for neutrons associated with the ground state and 431-keV state in the  ${}^6\text{Li}(d,n){}^7\text{Be}$  reaction at various deuteron energies. The curves represent Legendre polynomial fits.

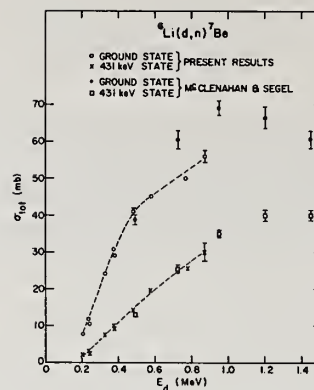


Fig. 6. Total cross section for the  ${}^6\text{Li}(d,n){}^7\text{Be}$  reaction as a function of  $E_d$ . The dashed curves are drawn to guide the eye.

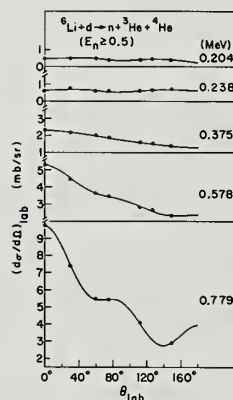


Fig. 7. Lab. differential cross sections as a function of angle for neutrons with  $E_n \geq 0.5$  MeV associated with  ${}^7\text{Be}$  breakup at various deuteron energies. The curves represent Legendre polynomial fits.

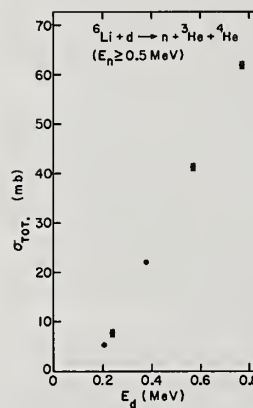


Fig. 8. Total cross section for neutrons with  $E_n \geq 0.5$  MeV associated with  ${}^7\text{Be}$  breakup as a function of  $E_d$ .

The relative uncertainties of the differential and total cross sections are indicated in Figs. 5–8 by the error bars (or the size of the data points). On the basis of the precision with which absolute efficiencies and target thicknesses were obtained, along with the statistical accuracy of the data, total cross sections for the  $(d,n)$  reaction should have absolute uncertainties of  $\sim 16\%$ . For the continuum neutrons this value

should be  $\sim 18\%$  because of larger uncertainties associated with the problems of proper background subtraction.

### Discussion

As indicated in Table I the neutrons associated with  ${}^7\text{Be}$  breakup contribute between 35 and 45% to the total neutron production cross section for  ${}^6\text{Li} + d$  reactions at deuteron energies 0.2–0.9 MeV. The importance of this contribution emphasizes the necessity of its inclusion in any quantitative evaluation of advanced fusion fuels containing  ${}^6\text{Li}$ .

This point stresses the utility of attempting to interpret the energy dependence of the measured continuum neutron distributions in terms of reaction mechanisms. While such efforts can clearly contribute to the understanding of the structure of light nuclei, a consistent interpretation of mechanisms that can produce a neutron in the final state will also allow the extrapolation from neutron detector threshold to zero neutron energy in order to obtain more complete total cross sections. In Fig. 9, the results of a preliminary calculation for a few individual contributions to three-body breakup processes are compared to the observed  $0^\circ$ -neutron distributions. As seen, the observations are qualitatively different from the spectra expected for a direct-breakup (i.e., one-step) mechanism. On the other hand, the calculation based on a sequential decay mechanism in which the s-wave Coulomb interaction between  ${}^3\text{He}$  and  ${}^4\text{He}$  in the final state is taken into account, appears quite promising. A more complete analysis, based on various final-state interactions, is currently in progress.

The reaction rate coefficients  $^{1,2} \sigma_t v$  for the  $d + {}^6\text{Li}$  reactions described in this report are shown in Fig. 10, along with the corresponding quantities for the  $d + T$  and  $d + D$  reactions. The feasibility of the use of  ${}^6\text{Li}$  as a fusion fuel should depend at least in part on the magnitude of the total reactivity for all exothermic reactions of deuterons with  ${}^6\text{Li}$ . Cross-section measurements for the charged particles emitted in these reactions at energies between 0.2 and 1.0 MeV is currently underway at ANL.

Table I

Total cross sections (in mb) for neutrons emitted in  $d + {}^6\text{Li}$  reactions.

$E_d$ (MeV)	$\sigma_t$ (g. s.)	$\sigma_t$ (431 keV)	$\sigma_t$ ( $E_n \geq 0.5$ MeV)
( $\pm 0.005$ )	( $\pm 16\%$ )	( $\pm 16\%$ )	( $\pm 18\%$ )
0.873	56.0	29.9	
0.779	49.9	25.5	61.7
0.578	45.0	19.5	41.2
0.482	41.2	14.6	
0.379	29.0	9.45	
0.375	30.4	10.1	22.1
0.328	24.3	7.78	
0.242	10.0	2.68	
0.238	11.8	3.12	7.64
0.204	7.67	2.16	5.29

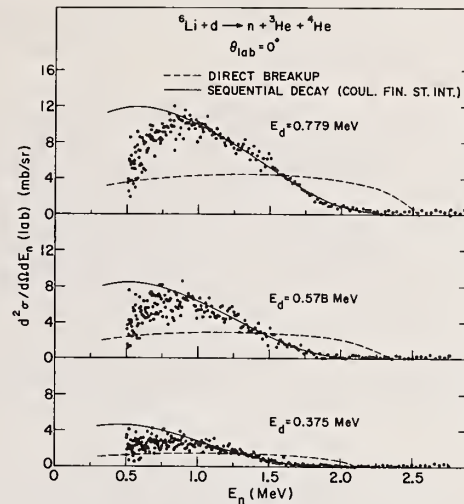


Fig. 9. Lab. differential cross sections per MeV as a function of  $E_n$  at  $\theta = 0^\circ$  for various deuteron energies compared to preliminary calculations for direct  ${}^7\text{Be}$  breakup (dashed curve) and for sequential decay with a Coulomb final state interaction between  ${}^3\text{He}$  and  ${}^4\text{He}$  (solid curve). The calculations were normalized to the data at neutron energies greater than 0.9 MeV.

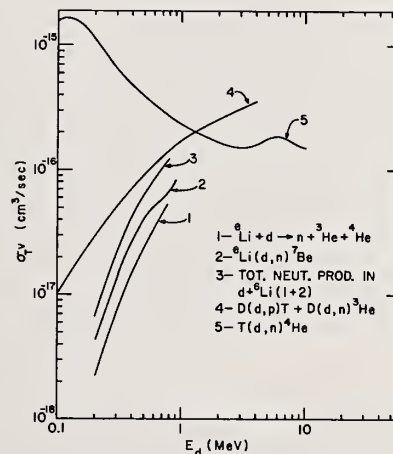


Fig. 10. Reaction rate coefficients  $\sigma_t v$ , where  $\sigma_t$  = total cross section and  $v$  = velocity of deuteron beam, as a function of  $E_d$ .



### References

<sup>†</sup>Work performed under the auspices of the U. S. Atomic Energy Commission.

<sup>1</sup>See, e.g., J. Rand McNally, Jr., "Fusion Chain Reactor Prospects and Problems," USAEC Report ORNL-TM-4575 (1974).

<sup>2</sup>V. S. Crocker, S. Blow, and C. J. H. Watson, "Nuclear Cross-Section Requirements for Fusion Reactions," Culham Laboratory Report #CLM-P240 (1970).

<sup>3</sup>F. Hirst, I. Johnstone, and M. J. Poole, Phil. Mag. 45, 762 (1954).

<sup>4</sup>C. R. McClenahan and R. E. Segel, Phys. Rev. C 11, 370 (1975).

<sup>5</sup>A. J. Elwyn, F. T. Kuchnir, J. E. Monahan, F. P. Mooring, and J. F. Lemming, Phys. Rev. C 6, 1730 (1972).

<sup>6</sup>C. A. Burke, M. T. Lunnnon, and H. W. Lefevre, Phys. Rev. C 10, 1299 (1974).

<sup>7</sup>J. W. Meadows and D. L. Smith, "Neutrons from Proton Bombardment of Natural Lithium," Argonne Nat'l. Lab. report ANL-7938 (1972).

<sup>8</sup>A. Chastel, M. B. Davis, C. M. Hoffman, M. N. Kreisler, and A. J. S. Smith, Nucl. Instrum. Methods 94, 493 (1971); R. Plasek, D. Miljanic, V. Valkovic, R. B. Liebert, and G. C. Phillips, Nucl. Instrum. Methods 111, 251 (1973).

<sup>9</sup>A. J. Elwyn, J. V. Kane, S. Ofer, and D. H. Wilkinson, Phys. Rev. 116, 1490 (1959).

<sup>10</sup>J. R. Comfort, "Manual of Data-Analysis Programs for Charged-Particle Reactions," ANL Physics Division Informal Report PHY-1970B (1970).

Investigations of proton, deuteron and helium induced reactions on  ${}^6\text{Li}$  are of importance in connection with the advantages of fusion reactor cycles involving only charged particles. The cross section data for many of these reactions are incomplete and poorly known. We report measurements of the absolute cross sections of the reactions  ${}^6\text{Li}(p,p)$ ,  ${}^6\text{Li}(p,{}^3\text{He})$  at  $E_p = 3-12$  MeV,  ${}^6\text{Li}(d,p)$ ,  ${}^6\text{Li}(d,\alpha)$  at  $E_d = 2.25-6$  MeV and  ${}^6\text{Li}({}^3\text{He},p)$  at  $E = 3-6$  MeV. Our data are combined with available information in the literature to determine reaction rate parameters as a function of the temperature of the reacting nuclei.

(NUCLEAR REACTIONS  ${}^6\text{Li}(p,p)$ ,  $(p,{}^3\text{He})$ ,  $({}^3\text{He},p)$ ,  $(d,p)$ ,  $(d,\alpha)$  measured  $\sigma(\theta)$ , deduced  $\sigma$  and  $\langle\sigma v\rangle$ )

### Introduction

Nuclear chain reactions involving only charged particles are of considerable interest at the present time in studies for controlled thermonuclear reactors.<sup>1</sup> If all the particles are charged, the reaction products may be confined magnetically thus maintaining most of the energy within the plasma. In contrast, of course, neutrons cannot be magnetically confined and much energy will be lost from a plasma in which substantial neutron production is taking place.

McNally *et al.*<sup>2</sup> have studied the reactivity of systems containing  $d$ - ${}^6\text{Li}$  and have identified the reactions among the  $p$ ,  $d$ ,  $t$ ,  ${}^3\text{He}$ ,  $\alpha$  and  ${}^6\text{Li}$  ions which are likely to make the largest contributions to energy production in the plasma. In 1970 Crocker, Blow and Watson<sup>3</sup> made a compilation of the results of a number of light mass reaction cross section measurements, including those for  ${}^6\text{Li}$  and  ${}^7\text{Li}$ . However, detailed evaluations of the performance of advanced fuel systems such as  $d$ - ${}^6\text{Li}$  are still hampered by a lack of knowledge of the absolute cross sections for reactions among the constituent ions. In this paper we summarize some recent and continuing work at Triangle Universities Nuclear Laboratory on the measurement of absolute cross sections for charged particle induced reactions on  ${}^6\text{Li}$ . In particular we report measurements for  $(p,p)$ ,  $(p,p')$ ,  $(p,{}^3\text{He})$ ,  $({}^3\text{He},p)$ ,  $(d,p)$  and  $(d,\alpha)$  reactions on  ${}^6\text{Li}$  and attempt to correlate our results with existing data in the literature. Most of these reactions have been studied in at least part of the energy range of interest, but frequently absolute cross sections were either not reported or were based on mutually inconsistent reference cross sections. We have tried to base all our absolute cross sections on one reference value; namely that for proton elastic scattering from  ${}^6\text{Li}$  at  $E_p = 6.868$  MeV and  $\theta_{\text{lab}} = 95^\circ$  as reported by Bingham *et al.*<sup>4</sup>

### Cross Section Results

#### ${}^6\text{Li}(p,{}^3\text{He})\alpha$

This reaction is of prime importance as a means of creating  ${}^3\text{He}$  in the plasma. The  $d({}^3\text{He},p)\alpha$  reaction, which is one of the main energy producing reactions in the  $d$ - ${}^6\text{Li}$  system, has a  $Q$  value of +18.4 MeV. The protons will lose energy in the plasma via elastic and inelastic collisions and one thus expects a continuum of proton energies in the system up to ~15 MeV. Our

measurements<sup>5</sup> for the  ${}^6\text{Li}(p,{}^3\text{He})\alpha$  reaction extended from  $E_p = 3$  to 12 MeV and are shown in Fig. 1. The cross section has a large resonance near 1.8 MeV and our results support the contention of Hooton and Ivanovich<sup>6</sup> that the cross section in the neighbourhood of this resonance is higher than has previously been supposed. Other data in Fig. 1 are from Werby *et al.*<sup>7</sup>, Spinka and Tombrello<sup>8</sup> and, more recently, Johnston and Sargood<sup>9</sup> in the region 0.5 to 1.2 MeV. These latter data were arbitrarily normalized to those of Ref. 6 at  $E_p = 1.0$  and 1.2 MeV.

#### ${}^6\text{Li}(p,p)$ , ${}^6\text{Li}$ , ${}^6\text{Li}(p,p')$ , ${}^6\text{Li}^*$

The first excited state of  ${}^6\text{Li}$  at 2.2 MeV is particle unstable and is a potentially important source of suprathermal  $d$  and  $\alpha$  particles in the plasma. On the basis of our results in Ref. 5 we concluded that our cross sections for elastic and inelastic proton scattering were 40% higher than those of Harrison and Whitehead<sup>10</sup> and Harrison<sup>11</sup>. In fact in Ref. 11, Harrison discusses relative normalizations among different experiments and indicates that other work by Tombrello and Parker<sup>12</sup> would probably yield a more reliable absolute normalization for his proton inelastic scattering data. This alternative normalization implies his cross section should be  $25 \pm 5\%$  higher. This is in only moderate agreement with our value of a  $40 \pm 10\%$  increase but subject to the errors in the measurements is not necessarily inconsistent. In Fig. 2 we show the data of Ref. 11 for the total cross section leading to the 2.2 MeV state in  ${}^6\text{Li}$  where we have increased the values by 40% in accordance with the normalization factor discussed above.

#### ${}^6\text{Li}({}^3\text{He},p)2\alpha$

This reaction has a high positive  $Q$  value (16.9 MeV) which makes it important from the point of view of energy deposition in the plasma. The  ${}^3\text{He}$  energies in the  $d$ - ${}^6\text{Li}$  system are low however and therefore the reaction is likely to be inhibited by the effect of the Coulomb barrier in the entrance channel. The work of Schiffer *et al.*<sup>13</sup> indicated that there were no strong resonances in the energy range 0.8 - 5 MeV. The three body final state in this reaction is actually reached by three possible channels:  ${}^6\text{Li}({}^3\text{He},p){}^8\text{Be}$ ,  ${}^6\text{Li}({}^3\text{He},\alpha){}^8\text{Li}$  and direct three body break up.  ${}^8\text{Be}$  and  ${}^8\text{Li}$  are of course particle unstable and immediately break up into  $2\alpha$  or  $\alpha + p$  respectively. Only reactions proceeding to the  ${}^8\text{Be}$

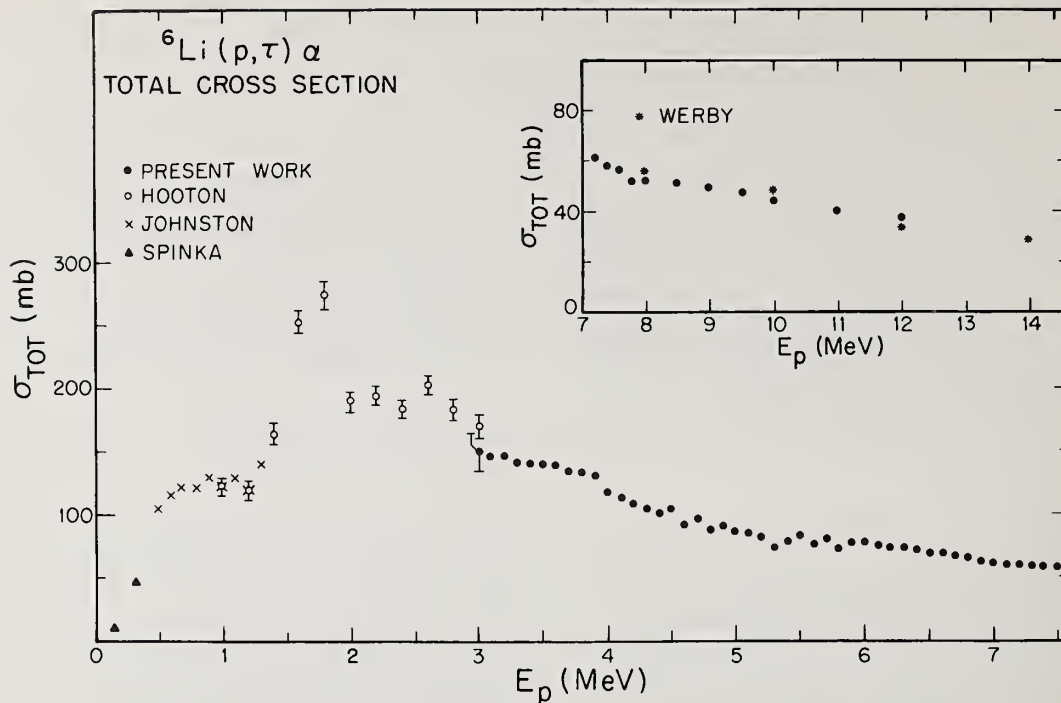


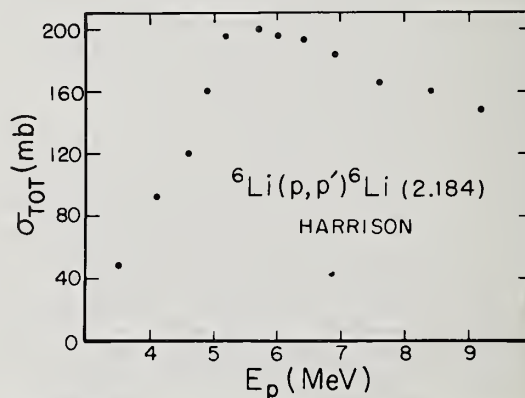
Fig. 1 Total cross section results for  ${}^6\text{Li}(p, {}^3\text{He})\alpha$  up to 14 MeV. Apart from the present work, the other measurements are from Refs. 6-9.

ground and first excited states yield discrete proton groups and these are the only channels for which absolute cross section measurements have been reported<sup>3,14</sup>. No estimates of the absolute magnitude of the continuum cross section have been given. Fig. 3 is a typical proton spectrum obtained at 5 MeV bombarding energy with stoppings foils in front of the detectors to remove all  ${}^3\text{He}$  and  $\alpha$  particles. As can be seen there is a substantial continuum present in the proton spectra and some care is therefore required in extracting yields to the 2.9 MeV first excited state of  ${}^8\text{Be}$ .

We parametrized the proton continuum by assuming it to be due solely to direct three body break up. The cross section is then determined by phase space considerations and is given, in the laboratory frame, by<sup>16</sup>

$$\frac{d^2\sigma}{d\Omega dE} = [E(\frac{8}{9}E_T - E_C)]^{\frac{1}{2}} \times A$$

where  $E$  is the laboratory proton energy at a laboratory angle  $\theta$ ,  $E_C$  the center of mass proton energy corresponding to  $E$ ,  $\theta$  and  $E_T$  is the total energy available in the center of mass ( $E_T = 18.9 + 0.667 \times E({}^3\text{He})$ ). The line in Fig. 3 is a best fit of the phase space expression to the experimental background and fixes the value of the quantity  $A$ . We find this



Erratum

Paper HA10 "Cross Section Measurements for Charged Particle Induced Reactions on  ${}^6\text{Li}$ " by C. R. Gould, J. M. Joyce, and J. R. Boyce.

"Absolute cross sections for the  ${}^6\text{Li}({}^3\text{He}, p){}^8\text{Be}$  reaction are incorrect due to a normalization error. The values shown in Fig. 4 should be increased by a factor of 2.1. The cross section results for the proton and deuteron induced reactions are not affected."



The large uncertainty in this latter case arises from the fact that the protons from reactions with the carbon backing obscure the low energy part of the proton continuum ( $E_p \leq 8$  MeV) and make it impossible to determine exactly how well the phase space expression fits the background in this region. The data of Schiffer *et al.*<sup>13</sup> and Fletcher *et al.*<sup>14</sup> are also shown in Fig. 4 and have been normalized to agree with our total cross sections at the energies where we have equivalent data. Our renormalization implies that the cross sections of Ref. 13 are about a factor three too high.

#### ${}^6\text{Li}(d,p){}^7\text{Li}$ , ${}^6\text{Li}(d,\alpha){}^3\text{He}$

The (d,p) reaction ( $Q = +5.0$  MeV) provides a means of regenerating energetic protons to continue  ${}^3\text{He}$  production via  ${}^6\text{Li}(p,{}^3\text{He})\alpha$ . The (d, $\alpha$ ) reaction has the highest  $Q$  value of all  ${}^6\text{Li}$  reactions (+22.4 MeV) and can thus be investigated simultaneously with the (d,p) reaction without the need for any particle identification. The reactions were studied in 250 keV steps from 2.25 MeV to 4 MeV and in 500 keV steps up to 6 MeV with particles detected at laboratory angles from  $20^\circ$  to  $160^\circ$ . Based on Legendre polynomial fits to the center of mass angular distributions, we obtain the total cross section results shown in Fig. 5 for the (d, $\alpha$ ) channel and for protons leading to the ground and first excited states of  ${}^7\text{Li}$ . For these deuteron induced cross section measurements, we used as our reference cross section the value of Ref. 1 quoted for  ${}^6\text{Li}(d,d)$  at 8 MeV bombarding energy and  $\theta = 70^\circ$ . We estimate the uncertainty in our cross section results to be  $\sim 15\%$ . Mclenahan and Segel<sup>17</sup> have recently studied both these reactions in some detail and have also summarized the results of previous investigations. Their absolute cross section results were determined by comparison to Rutherford scattering at very low energies and are shown in Fig. 5 as the open circles. Subject to their stated error of 15%, our values are in good agreement in the energy range 2-3.5 MeV. The (d, $p\alpha$ ) cross section results do seem to deviate systematically from each other more than the values for the other two channels however.

The (d, $\alpha$ ) reaction has two broad resonances around 1 and 4 MeV. The (d,p) reaction appears to be predominantly direct<sup>17</sup>, with both ground and first excited state cross sections decreasing smoothly at bombarding energies higher than about 1 MeV.

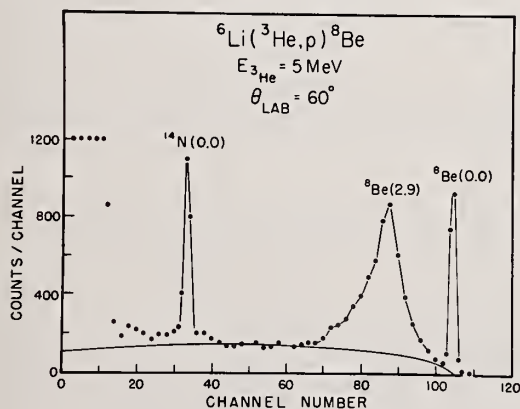


Fig. 3. The proton spectrum obtained at  $60^\circ$  for the  ${}^6\text{Li}({}^3\text{He},p)$  reaction at 5 MeV bombarding energy. Stopping foils remove  ${}^3\text{He}$  and  $\alpha$  particles from the spectrum.

#### Summary

Cross section results for a number of charged particle induced reactions on  ${}^6\text{Li}$  have been presented and correlated where possible with existing data in the literature. Our values are based on one reference cross section value and are believed to be accurate to  $\sim 15\%$ .

In order to estimate the energy release in a plasma the quantity of interest is the Maxwell averaged reaction rate parameter  $\langle\sigma v\rangle$ , as a function of the temperature of a plasma of the reacting ions<sup>18</sup>. Calculations of  $\langle\sigma v\rangle$  for deuteron induced reactions on  ${}^6\text{Li}$  have been presented by Greene<sup>19</sup>. Fig 6 shows the results of a calculation of  $\langle\sigma v\rangle$  versus  $kT$  for  $p$ - ${}^6\text{Li}$  and  ${}^3\text{He}$ - ${}^6\text{Li}$  systems. For the  $p$ - ${}^6\text{Li}$  system, the necessary cross sections required for the calculation were obtained by interpolating smoothly between the values of Fig. 1. For the  ${}^3\text{He}$ - ${}^6\text{Li}$  system there are no cross section data below 1 MeV and we therefore assumed that the  ${}^8\text{Be}$  cross sections would fall monotonically following the s wave Gamow form<sup>20</sup>,  $\sigma = S/E \exp[-B/E^{1/2}]$ . Here  $B = 108 \text{ keV}^{1/2}$  and  $S = 6410 \text{ keV-b}$  and  $15730 \text{ keV-b}$  respectively for the ground and 2.9 MeV states respectively. A contribution from the three body break up continuum was not included and there are clearly large uncertainties in the  $\langle\sigma v\rangle$  curve for the  ${}^3\text{He}$ - ${}^6\text{Li}$  system. Nevertheless the values do imply that the contribution of this reaction to the reactivity of a  $d$ - ${}^6\text{Li}$  fuelled plasma will be small even though the energy deposition per event is considerable.

\*Work supported in part by USAEC.

\*\*Summer visitor from East Carolina University.

#### References

1. J. Rand McNally, Jr., "Nuclear Data in Science and Technology," Proc. IAEA Conf., Paris 1973, 2, 41, International Atomic Energy Agency, Vienna (1973).
2. J. Rand McNally, Jr., R. D. Sharp, R. H. Fowler and J. F. Clarke, Nucl. Fusion **14**, 579 (1974).
3. V. S. Crocker, S. Blow and C. J. H. Watson, Nuclear Data for Reactors **1**, 67 (IAEA, Vienna (1970)).

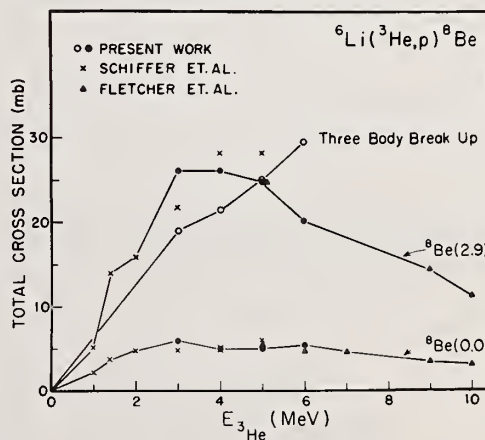


Fig. 4. Total cross section results for the  ${}^6\text{Li}({}^3\text{He},p)2\alpha$  reaction. Apart from the present work, other measurements are from Refs. 13, 14.

4. H. C. Bingham, A. R. Zander, K. W. Kemper, and N. R. Fletcher, Nucl. Phys., A173, 265 (1971).
5. C. R. Gould, R. O. Nelson, J. R. Williams and J. R. Boyce, Nucl. Sci. Eng. 55, 267 (1974).
6. B. W. Hooton and M. Ivanovich, "Neutron Physics Division Progress Report from the Period May 1, 1970-April 30, 1971," AERE-PR/NP 18, p. 37, United Kingdom Atomic Energy Authority, Harwell (1972). See also Ref. 1.
7. M. W. Werby, M. B. Greenfield, K. W. Kemper, D. L. McShan, and S. Edwards, Phys. Rev., C8, 106 (1973).
8. H. Spinka, T. A. Tombrello, and H. Winkler, Nucl. Phys. A164, 1 (1971).
9. G. P. Johnston and D. G. Sargood, Nucl. Phys. A224, 349 (1974).
10. W. D. Harrison and A. B. Whitehead, Phys. Rev. 132, 2607 (1963).
11. W. D. Harrison, Nucl. Phys. A92, 260 (1967).
12. T. A. Tombrello and P. D. Parker, Phys. Rev. 130, 1112 (1963).
13. J. P. Schiffer, T. W. Bonner, R. H. Davis and F. W. Prosser, Phys. Rev. 104, 1064 (1956).
14. N. R. Fletcher, J. D. Marshall and R. H. Davis, Nucl. Phys. 70, 471 (1965).
15. G. G. Ohlsen, Nucl. Inst. Meth. 37, 240 (1965).
16. C. R. Gould et al. (to be published).
17. C. R. Mclenahan and R. E. Segel, Phys. Rev. C11, 370 (1975).
18. D. J. Rose and M. Clark, Jr., Plasmas and Controlled Fusion, MIT Press, p. 81 Cambridge, Massachusetts (1961).
19. S. L. Greene, USAEC report UCRL-70522 (1967).
20. E. M. Burbridge, G. R. Burbridge, W. A. Fowler and F. Hoyle, Rev. Mod. Phys. 29, 548 (1957).

Fig. 6. Plot of the Maxwell averaged reaction rate parameter  $\langle\sigma v\rangle$  as a function of the temperature of the system,  $kT$ . See text for a discussion of the cross section data used.

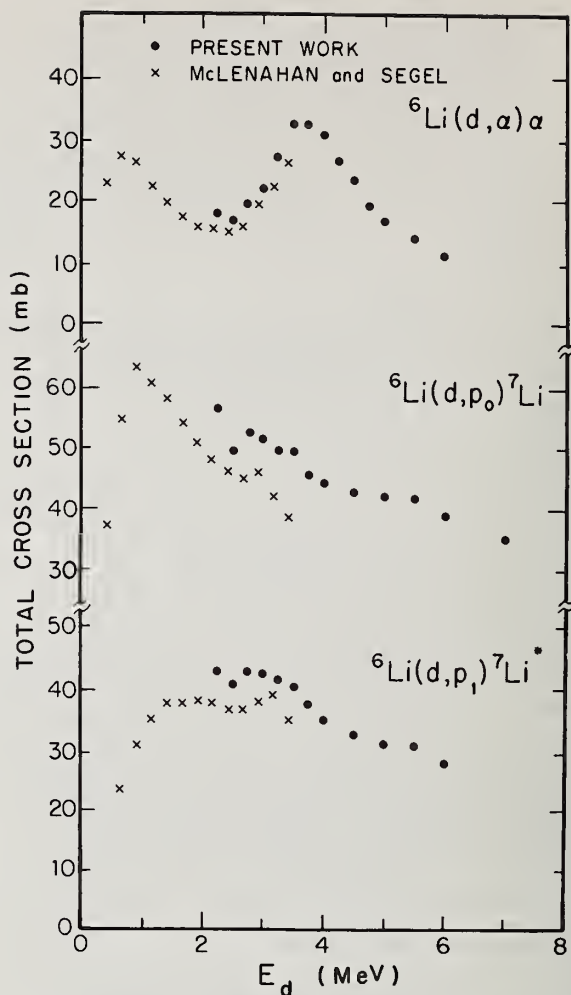
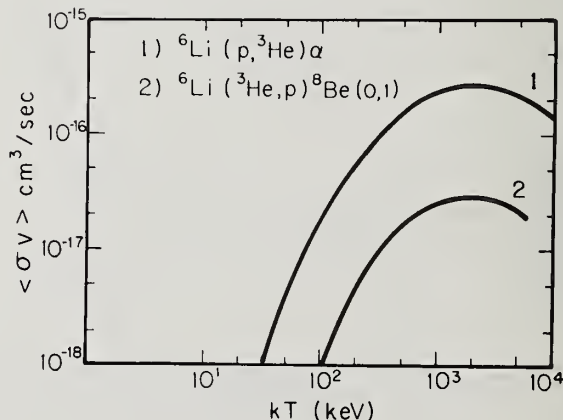


Fig. 5. Total cross section results for the (d,p) and (d,α) reactions on  ${}^6\text{Li}$  from the present work and from Ref. 17.



Explicit formulas are given for the elastic and inelastic cross sections of neutrons, deuterons, tritons and alpha particles. These formulas, obtained by a phase shift analysis, are the best fit to currently available experimental data, for all angles and energies up to 14 MeV.

(Cross sections; phase shifts; neutrons; deuterons; tritons; alpha particles)

### Introduction

Calculations on fusion in dense plasmas require a detailed knowledge of numerous elastic cross sections. Unfortunately, experimental data are often very sparse. In order to interpolate (in angle and energy) between available data, we have performed a phase shift analysis of the various elastic cross sections. No theoretical nuclear model was assumed. Our only guidelines were the following:

a) Phase shifts at each energy were usually assumed to depend only on the total spin  $S$  and orbital angular momentum  $\ell$ . However, for  $\alpha$ -D resonant scattering and  $\alpha$ -T scattering, we also introduced a  $j$ -dependence (see below).

b) At low energy, the phase shift  $\delta_\ell$  behaves as  $E^{\ell+1/2}$ . At higher energies, we write  $\text{tg} \delta_\ell = E^{\ell+1/2} f(E)$ , where  $f(E)$  is a rational function of  $E$  (usually a polynomial). It is convenient to fit  $\text{tg} \delta_\ell$ , rather than  $\delta_\ell$  itself, as a function of  $E$ , because the expressions  $e^{i\delta} \sin \delta = 1/(\cot \delta - i)$ , which appear in the cross sections, become rational functions of the parameters. This ensures considerable savings of computer time.

c) The number of partial waves needed, and the number of parameters for the energy dependence of each one, were found by trial and error. A formula was considered satisfactory when it reproduced the experimental data with errors comparable to the experimental errors. We endeavoured to find "satisfactory" formulas with as few parameters as possible.

All cross sections are given in barns per steradian in the c.o.m. system as functions of  $P_\ell(\cos \theta)$ . All energies are given in MeV in the laboratory system.

### Neutron - Deuteron

The n-D cross sections are well documented.<sup>1</sup> Above the breakup threshold (3.339 MeV) the (n,2n) channel has a cross section<sup>2,3</sup>

$$\sigma_{n,2n} = (E-3.339) (5.36783 \cdot 10^{-2} - 0.115396/E - 2.07008 \cdot 10^{-3} E)$$

where  $E$  is the energy of neutron.

The differential elastic cross section can be written in terms of the doublet and quartet phase shifts  $\delta_{\ell 2}$  and  $\delta_{\ell 4}$ . Below threshold<sup>4-7</sup> ( $E < 3.339$  MeV) we have

$$\frac{d\sigma}{d\Omega} = \frac{0.155572}{E} \left[ 2 \left| \sum_{\ell=0}^2 \frac{(2\ell+1)P_\ell}{\cot \delta_{\ell 4} - i} \right|^2 + \left| \sum_{\ell=0}^2 \frac{(2\ell+1)P_\ell}{\cot \delta_{\ell 2} - i} \right|^2 \right]$$

where

$$\begin{aligned} \text{tg} \delta_{04} &= [-3.75982 - 9.18518 \cdot 10^{-1} (E-3.339)] (E/3.339)^{1/2} \\ \text{tg} \delta_{02} &= [-4.79059 \cdot 10^{-1} + 5.49062 \cdot 10^{-1} (E-3.339)] (E/3.339)^{1/2} \\ \text{tg} \delta_{14} &= [2.51485 \cdot 10^{-1} - 3.31624 \cdot 10^{-1} (E-3.339)] (E/3.339)^{3/2} \\ \text{tg} \delta_{12} &= [-5.49470 \cdot 10^{-1} - 4.64498 \cdot 10^{-1} (E-3.339)] (E/3.339)^{3/2} \\ \text{tg} \delta_{24} &= [-3.57546 \cdot 10^{-3} + 2.25043 \cdot 10^{-1} (E-3.339)] (E/3.339)^{5/2} \end{aligned}$$

$$\text{tg} \delta_{22} = [5.17095 \cdot 10^{-2} + 3.54638 \cdot 10^{-1} (E-3.339)] (E/3.339)^{5/2}$$

Above threshold<sup>8-13</sup> ( $E > 3.339$  MeV) one must introduce the inelasticity factors  $\eta_{\ell 4}$  and  $\eta_{\ell 2}$ . The formula then becomes

$$\frac{d\sigma}{d\Omega} = \frac{0.155572}{E} \left[ 2 \left| \sum_{\ell=0}^2 \frac{(2\ell+1)P_\ell}{2} \left( 1 - \eta_{\ell 4} \frac{i - \text{tg} \delta_{\ell 4}}{i + \text{tg} \delta_{\ell 4}} \right) \right|^2 + \left| \sum_{\ell=0}^2 \frac{(2\ell+1)P_\ell}{2} \left( 1 - \eta_{\ell 2} \frac{i - \text{tg} \delta_{\ell 2}}{i + \text{tg} \delta_{\ell 2}} \right) \right|^2 \right]$$

where

$$\begin{aligned} \text{tg} \delta_{04} &= [-3.75982 + 8.69252 \cdot 10^{-2} (E-3.339)] (E/3.339)^{1/2} \\ \text{tg} \delta_{02} &= [-4.79059 \cdot 10^{-1} + 4.18254 \cdot 10^{-2} (E-3.339)] (E/3.339)^{1/2} \\ \text{tg} \delta_{14} &= [2.51485 \cdot 10^{-1} - 1.46593 \cdot 10^{-2} (E-3.339)] (E/3.339)^{3/2} \\ \text{tg} \delta_{12} &= [-5.49470 \cdot 10^{-1} + 8.80116 \cdot 10^{-2} (E-3.339)] (E/3.339)^{3/2} \\ \text{tg} \delta_{24} &= [-3.57546 \cdot 10^{-3} + 2.05239 \cdot 10^{-4} (E-3.339)] (E/3.339)^{5/2} \\ \text{tg} \delta_{22} &= [5.17095 \cdot 10^{-2} - 3.62048 \cdot 10^{-3} (E-3.339)] (E/3.339)^{5/2} \end{aligned}$$

and

$$\eta_{\ell m} = [1 - X_{\ell m} (E-3.339) (E-3.85646 \cdot 10^{-2} E^2 - 2.14977)]^{1/2}$$

where

$$\begin{aligned} X_{04} &= 1.89456 \cdot 10^{-2}, \quad X_{14} = 1.74255 \cdot 10^{-2}, \quad X_{24} = -1.72691 \cdot 10^{-2} \\ X_{02} &= 2.10000 \cdot 10^{-2}, \quad X_{12} = 2.06282 \cdot 10^{-2}, \quad X_{22} = 1.14229 \cdot 10^{-2} \end{aligned}$$

Since by definition  $\eta_{\ell m} < 1$ , the  $X_{\ell m}$  should be positive. The small violation of unitarity ( $X_{24} < 0$ ) is probably due to the arbitrary truncation at  $\ell = 2$ .

### Neutron - Triton

The n-T breakup data are extremely sparse<sup>14</sup>. The  $T(n,2n)$  threshold is 8.35 MeV and the  $T(n,3n)$  threshold 11.3 MeV. At 14.1 MeV the inelastic channel has a cross section  $\sigma_{ne} = (45 \pm 5) \cdot 10^{-3}$  barn and the upper limit for  $T(n,3n)$  is  $10^{-3}$  barn.

Although the elastic scattering is more adequately documented<sup>14-19</sup> the data hardly justify the introduction of inelasticity factors above threshold. Therefore we write a single expression for the elastic scattering cross section up to 14.1 MeV:

$$\frac{d\sigma}{d\Omega} = \frac{0.092244}{E} \left[ 3 \left| \sum_{\ell=0}^1 \frac{(2\ell+1)P_\ell}{\cot \delta_{\ell 3} - i} \right|^2 + \left| \sum_{\ell=0}^2 \frac{(2\ell+1)P_\ell}{\cot \delta_{\ell 1} - i} \right|^2 \right]$$

where  $\delta_{\ell 3}$  and  $\delta_{\ell 1}$  (the triplet and singlet phase shifts)<sup>4</sup> are given by

$$\begin{aligned} \text{tg} \delta_{03} &= [-6.54134 / (10.81013 - E)] E^{1/2} \\ \text{tg} \delta_{01} &= [-2.24628 / (5.00099 - E)] E^{1/2} \\ \text{tg} \delta_{13} &= (1.736229 \cdot 10^{-1} - 1.47844 \cdot 10^{-2} E) E^{3/2} \\ \text{tg} \delta_{11} &= (1.233168 \cdot 10^{-1} - 8.81344 \cdot 10^{-3} E) E^{3/2} \end{aligned}$$



$$\text{tg}\delta_{21} = (-2.96688 \cdot 10^{-3} + 1.78526 \cdot 10^{-4} E) E^{5/2}$$

The  $\ell = 2$  triplet phase shift  $\delta_{23}$  is very poorly defined by the data. It can be put equal to zero without affecting the quality of the fit.

### Deuteron - Deuteron

The cross sections for the exothermic D-D reactions  ${}^2\text{H}(d,n){}^3\text{He}$  and  ${}^2\text{H}(d,p){}^3\text{H}$  are well documented<sup>20,27</sup>. They can be written as

$$\sigma_{d,n} = (0.182039 + 0.203408 E - 0.0083589) \exp(-1.49426/\sqrt{E})/E$$

$$\sigma_{d,p} = (0.12193 + 0.181099 E - 0.00672257) \exp(-1.41385/\sqrt{E})/E$$

At very low energy these cross sections are dominated by the Gamow factors  $\exp(-C_i/\sqrt{E})$ . The numerical coefficients  $C_i$  have been considered as variational parameters and not held fixed at their theoretical values.

No inelastic factors are included in the differential elastic scattering cross section, because they are very close to 1. Moreover, we assume that spin dependence enters only via the parity of the wave function, i.e. that singlet and quintuplet phase shifts are equal.

The expression we obtain including data<sup>28-33</sup> up to 13.80 MeV is

$$\frac{d\sigma}{d\Omega} = \frac{0.138359}{E} \left[ 2 \left| F_c(\theta) + F_c(\pi-\theta) + \sum_{\ell=0,2} \frac{2(2\ell+1)P_\ell \Psi_\ell}{\cot\delta_\ell - i} \right|^2 + \left| F_c(\theta) - F_c(\pi-\theta) + \sum_{\ell=1} \frac{2(2\ell+1)P_\ell \Psi_\ell}{\cot\delta_\ell - i} \right|^2 \right]$$

where

$$\Psi_0 = 1, \quad \Psi_1 = (1+i\eta)/(1-i\eta), \quad \Psi_2 = \Psi_1(2+i\eta)/(2-i\eta)$$

and the Coulomb amplitude is

$$F_c = -\frac{\eta}{2} [2/(1-\cos\theta)]^{1+i\eta}$$

with  $\eta = 0.223476/\sqrt{E}$ . The phase shifts are given by

$$\text{tg}\delta_0 = (-2.92914 \cdot 10^{-1} - 8.65496 \cdot 10^{-2} E) E^{1/2}$$

$$\text{tg}\delta_1 = (-4.38663 \cdot 10^{-2} + 2.20396 \cdot 10^{-3} E) E^{3/2}$$

$$\text{tg}\delta_2 = (-7.33607 \cdot 10^{-4} + 2.36004 \cdot 10^{-5} E) E^{5/2}$$

### Deuteron - Triton

In this section,  $E$  denotes the lab energy of the deuteron, the triton being initially at rest.

The cross section for the exothermic D-T reaction  ${}^3\text{H}(d,n){}^4\text{He}$  is well documented<sup>34-40</sup>. The expression that we obtain including data up to 12.3 MeV is

$$\sigma_{d,n} = \left[ 7.18593 \cdot 10^{-1} + \frac{2.74077 \cdot 10^{-1}}{(E - 7.39272 \cdot 10^{-2})^2 + 4.73695 \cdot 10^{-3}} \right] \times \exp(-1.47564/\sqrt{E})/E$$

where again the numerical coefficient in the Gamow factor was treated as a variational parameter.

Below 3.7 MeV (the threshold for deuteron breakup) we assume that the  $(d,n)$  reaction (which is the only inelastic process) occurs in the  $\ell=0$ ,  $J=3/2$  channel. Therefore in this range of energies there is only one inelastic factor

$$\eta_0 = \sqrt{1 - 1.65420 E \sigma_{d,n}}$$

With this assumption, we obtain<sup>41,42</sup> for  $E < 3.7$  MeV

$$\frac{d\sigma}{d\Omega} = \frac{0.0962127}{E} \left[ \left| F_c(\theta) + \sum_{\ell=0}^2 \frac{(2\ell+1)P_\ell \Psi_\ell}{\cot\delta_{\ell 2} - i} \right|^2 + 2 \left| F_c(\theta) + \frac{i}{2} (1-\eta_0) \frac{i - \text{tg}\delta_{04}}{i + \text{tg}\delta_{04}} + \sum_{\ell=1}^2 \frac{(2\ell+1)P_\ell \Psi_\ell}{\cot\delta_{\ell 4} - i} \right|^2 \right]$$

The expressions for  $F_c(\theta)$  and  $\Psi_\ell$  are the same as in the preceding section and the quartet and doublet phase shifts  $\delta_{\ell 4}$  and  $\delta_{\ell 2}$  are given by

$$\text{tg}\delta_{04} = (-9.55679 \cdot 10^{-1} + 2.25676 \cdot 10^{-1} E) E^{1/2}$$

$$\text{tg}\delta_{02} = (-1.38718 + 3.49639 \cdot 10^{-1} E) E^{1/2}$$

$$\text{tg}\delta_{14} = (7.39132 \cdot 10^{-2} - 4.80847 \cdot 10^{-4} E) E^{3/2}$$

$$\text{tg}\delta_{12} = (2.35300 \cdot 10^{-1} - 3.00796 \cdot 10^{-2} E) E^{3/2}$$

$$\text{tg}\delta_{24} = (-2.11482 \cdot 10^{-2} + 2.30548 \cdot 10^{-3} E) E^{5/2}$$

$$\text{tg}\delta_{22} = (-1.04178 \cdot 10^{-2} + 3.59294 \cdot 10^{-3} E) E^{5/2}$$

Above 3.7 MeV<sup>42,43</sup> inelasticity factors have to be introduced for all partial waves and the formula becomes

$$\frac{d\sigma}{d\Omega} = \frac{0.0962127}{E} \left[ 2 \left| F_c + i \sum_{\ell=0}^2 \frac{(2\ell+1)P_\ell \Psi_\ell}{2} \left( 1 - \eta_{\ell 4} \frac{i - \text{tg}\delta_{\ell 4}}{i + \text{tg}\delta_{\ell 4}} \right) \right|^2 + \left| F_c + i \sum_{\ell=0}^2 \frac{(2\ell+1)P_\ell \Psi_\ell}{2} \left( 1 - \eta_{\ell 2} \frac{i - \text{tg}\delta_{\ell 2}}{i + \text{tg}\delta_{\ell 2}} \right) \right|^2 \right]$$

where

$$\eta_{04} = \eta_0 \exp[0.593732(1 - 3.7/E)]$$

and all the other inelasticity factors are given by

$$\eta_{\ell m} = \exp[X_{\ell m}(1 - 3.7/E)]$$

where

$$\begin{aligned} X_{02} &= -1.34428 \cdot 10^{-1} \\ X_{14} &= -4.25545 \cdot 10^{-1} & X_{12} &= -2.41299 \\ X_{24} &= -3.17153 \cdot 10^{-1} & X_{22} &= 2.29534 \cdot 10^{-1} \end{aligned}$$

The phase shifts above threshold are

$$\text{tg}\delta_{04} = [-2.32132 \cdot 10^{-1} + 6.93633 \cdot 10^{-2} (E - 3.7)] (E/3.7)^{1/2}$$

$$\text{tg}\delta_{02} = [-1.79880 \cdot 10^{-1} + 2.16838 \cdot 10^{-2} (E - 3.7)] (E/3.7)^{1/2}$$

$$\text{tg}\delta_{14} = [5.13385 \cdot 10^{-1} - 2.17363 \cdot 10^{-2} (E - 3.7)] (E/3.7)^{3/2}$$

$$\text{tg}\delta_{12} = [8.82557 \cdot 10^{-1} - 6.90601 \cdot 10^{-2} (E - 3.7)] (E/3.7)^{3/2}$$

$$\text{tg}\delta_{24} = [-3.32269 \cdot 10^{-1} - 8.18759 \cdot 10^{-4} (E - 3.7)] (E/3.7)^{5/2}$$

$$\text{tg}\delta_{22} = [7.57325 \cdot 10^{-2} - 1.09782 \cdot 10^{-2} (E - 3.7)] (E/3.7)^{5/2}$$

### Triton - Triton

The total cross section for the T-T reactions up to 1.9 MeV is<sup>44,45</sup>

$$\sigma_{t,2n} = 7.62 \cdot 10^{-2} + 5.58 \cdot 10^{-2} \log_{10} E.$$

There is one single experimental paper<sup>46</sup> on T-T elastic scattering. The expression we obtain is

$$\frac{d\sigma}{d\Omega} = \frac{0.0692965}{E} \left[ \left| F_c(\theta) + F_c(\pi-\theta) + \frac{2}{\cot\delta_0 - i} \right|^2 + 3 \left| F_c(\theta) - F_c(\pi-\theta) \right|^2 \right]$$

where

$$\text{tg}\delta_0 = -5.10253 \cdot 10^{-1} E^{1/2}$$

The expression for  $F_c(\theta)$  is the same as previously, but with  $\eta = 0.273482/\sqrt{E}$ . There was no need of higher waves, because in ref. 46 the maximum triton energy

was 2 MeV, and a single parameter could fit all the data. Clearly, further experiments at higher energies are needed.

#### Helium 4 - Deuteron

In this section, all data refer to the  $^4\text{He}$  lab energy, the deuteron being initially at rest. We have considered only energies up to 3.9 MeV since higher energies are irrelevant for fusion calculations.

The experimental results in alpha-deuteron scattering around 2.1 MeV<sup>47,48</sup> show the existence of a well defined resonance in the  $\ell=2$ ,  $J^P=3^+$  channel. The expression that we obtain including data<sup>48,49</sup> up to 3.9 MeV is

$$\frac{d\sigma}{d\Omega} = \frac{0.155325}{E} \left[ 2 \left| F_c(\theta) + \sum_{\ell=0}^1 \frac{(2\ell+1)P_{\ell}^{\Psi_{\ell}}}{\cot\delta_{\ell}-i} + \left( \frac{2}{\cot(\delta_2+\beta)-i} + \frac{3}{\cot\delta_2-i} \right) P_2^{\Psi_2} \right|^2 + 3 \left| F_c(\theta) + \sum_{\ell=0}^1 \frac{(2\ell+1)P_{\ell}^{\Psi_{\ell}}}{\cot\delta_{\ell}-i} + \left( \frac{3}{\cot(\delta_2+\beta)-i} + \frac{2}{\cot\delta_2-i} \right) P_2^{\Psi_2} \right|^2 + \left| \frac{1}{\cot(\delta_2+\beta)-i} - \frac{1}{\cot\delta_2-i} \right|^2 (25-24.5\sin^2\theta)\sin^2\theta \right]$$

where the expressions for  $F_c(\theta)$  and  $\Psi_{\ell}$  are the same as previously, but with  $\eta=0.630074/\sqrt{E}$ . The phase shifts are given by

$$\begin{aligned} \text{tg}\delta_0 &= (4.13812 \cdot 10^{-2} - 2.03203 \cdot 10^{-1}E)E^{1/2} \\ \text{tg}\delta_1 &= (-1.09999 \cdot 10^{-2} + 3.06920 \cdot 10^{-3}E)E^{3/2} \\ \text{tg}\delta_2 &= (-7.66435 \cdot 10^{-3} + 1.44385 \cdot 10^{-3}E)E^{5/2} \\ \text{tg}\beta &= 3.22039 \cdot 10^{-2} / (2.13624 - E). \end{aligned}$$

#### Helium 4 - Triton

Again,  $E$  is the  $^4\text{He}$  lab energy, the triton being initially at rest, and we considered only energies up to 3.9 MeV.

Data on elastic scattering in this range of energies are very sparse<sup>50,51</sup> (non-existent below 2 MeV), nevertheless to obtain a reasonable fit it was necessary to introduce a  $j$ -dependence. The expression that we obtain is

$$\frac{d\sigma}{d\Omega} = \frac{0.282773}{E} \left[ \left| F_c + \sum_{\ell=0}^2 \left( \frac{\ell+1}{\cot\delta_{\ell+}-i} + \frac{\ell}{\cot\delta_{\ell}-i} \right) P_{\ell}^{\Psi_{\ell}} \right|^2 + \left| \sum_{\ell=1}^2 \left( \frac{1}{\cot\delta_{\ell+}-i} - \frac{1}{\cot\delta_{\ell}-i} \right) \frac{dP_{\ell}}{d\cos\theta} \Psi_{\ell} \right|^2 \sin^2\theta \right]$$

where  $\delta_{\ell\pm}$  denotes the  $j = \ell \pm \frac{1}{2}$  wave, and where the expressions for  $F_c(\theta)$  and  $\Psi_{\ell}$  are the same as previously, but with  $\eta = 0.630074/\sqrt{E}$ .

The phase shifts are given by

$$\begin{aligned} \text{tg}\delta_{0+} &= (-1.037485 + 2.44679 \cdot 10^{-1}E)E^{1/2} \\ \text{tg}\delta_{1+} &= (-1.14880 \cdot 10^{-1} + 1.02002 \cdot 10^{-2}E)E^{3/2} \\ \text{tg}\delta_{1-} &= (-3.32005 \cdot 10^{-1} + 1.04970 \cdot 10^{-1}E)E^{3/2} \\ \text{tg}\delta_{2+} &= -5.05390 \cdot 10^{-3} E^{5/2} \\ \text{tg}\delta_{2-} &= 7.85087 \cdot 10^{-3} E^{5/2} \end{aligned}$$

#### Concluding Remarks

The formulas which we have obtained can be considered as the best interpolation between currently available data. However, we found many other inequivalent sets of phase shifts which reproduced the experimental results almost as well as these ones. Therefore our formulas should be revised when new experimental data becomes available.

#### References

1. A. Horsley, Nucl. Data A4, 321 (1968)
2. M. Holberg, Nucl. Phys. A129, 327 (1969)
3. H.C. Catron, et al., Phys. Rev. 123, 218 (1961)
4. W.D. Allen, et al., Proc. Phys. Soc. A68, 650 (1955)
5. A.J. Elwyn, et al., Phys. Rev. 128, 779 (1962)
6. R.K. Adair, et al., Phys. Rev. 89, 1165 (1953)
7. J.D. Seagrave, et al., Phys. Rev. 105, 1816 (1957)
8. E. Wantuch, Phys. Rev. 84, 169 (1951)
9. J.D. Seagrave, et al., Ann. Phys. 74, 250 (1972)
10. B.E. Bonner, et al., Nucl. Phys. A128, 183 (1969)
11. J.C. Allred, et al., Phys. Rev. 91, 90 (1953)
12. J.D. Seagrave, Phys. Rev. 97, 757 (1955)
13. A.C. Berick, et al., Phys. Rev. 174, 1105 (1968)
14. J.D. Seagrave, et al., Ann. Phys. 74, 250 (1972)
15. J.D. Seagrave, et al., Phys. Rev. 119, 1981 (1960)
16. J.H. Coon, et al., Phys. Rev. 81, 33 (1951)
17. J.M. Kootsey, Nucl. Phys. A113, 65 (1968)
18. Los Alamos Physics and Cryogenics Groups, Nucl. Phys. 12, 291 (1959)
19. V.P. Vertebnyj, Bull. Acad. Sci. USSR, Phys. Ser. 31, 334 (1967)
20. W.A. Wenzel, et al., Phys. Rev. 88, 1149 (1952)
21. R.B. Theus, et al., Nucl. Phys. 80, 273 (1966)
22. N. Ying, et al., Nucl. Phys. A206, 481 (1973)
23. J.R. Smith, et al., Can. J. Phys. 50, 783 (1972)
24. R.L. Schulte, et al., Nucl. Phys. A192, 609 (1972)
25. S.T. Thornton, Nucl. Phys. A136, 25 (1969)
26. F.S. Dietrich, et al., Nucl. Phys. A184, 449 (1972)
27. J.E. Brolley Jr., et al., Phys. Rev. 107, 820 (1957)
28. J.M. Blair, et al., Phys. Rev. 74, 1594 (1948)
29. A.S. Wilson, et al., Nucl. Phys. A126, 193 (1969)
30. J.E. Brolley, et al., Phys. Rev. 117, 1307 (1960)
31. L. Rosen, et al., Phys. Rev. 76, 1283 (1949)
32. L. Rosen, et al., Phys. Rev. 88, 431 (1952)
33. J.C. Allred, et al., Phys. Rev. 76, 1430 (1949)
34. W.R. Arnold, et al., Phys. Rev. 93, 483 (1954)
35. H.V. Argo, et al., Phys. Rev. 87, 612 (1952)
36. S.J. Bame, et al., Phys. Rev. 107, 1616 (1957)
37. J.R. Smith, et al., Nucl. Phys. A187, 433 (1972)
38. M.D. Goldberg, et al., Phys. Rev. 122, 164 (1961)
39. J.E. Brolley Jr., et al., Phys. Rev. 82, 502 (1951)
40. L.E. Stewart, et al., Phys. Rev. 119, 1649 (1960)
41. W.R. Stratton, et al., Phys. Rev. 88, 257 (1952)
42. M. Ivanovich, et al., Nucl. Phys. A100, 441 (1968)
43. J.E. Brolley, et al., Phys. Rev. 117, 1307 (1960)
44. A.M. Govorov, et al., Soviet Phys. JETP 15, 266 (1962)
45. N. Jarmie, et al., Phys. Rev. 111, 1121 (1958)
46. D.M. Holm, et al., Phys. Rev. 101, 1772 (1956)
47. T. Lawritsen, et al., Phys. Rev. 92, 1501 (1953)
48. A. Galonsky, et al., Phys. Rev. 98, 586 (1955)
49. J.M. Blair, et al., Phys. Rev. 75, 1678 (1949)
50. L.S. Chuang, Nucl. Phys. A174, 399 (1971)
51. A. Hemmendinger, Bull. Am. Phys. Soc. 1, 96 (1956)



The neutron emission spectra from <sup>238</sup>U spheres pulsed with 14-MeV neutrons have been measured from the source energy down to 10 keV and have been compared with calculations employing ENDF/B-IV and ENDL cross sections. The low energy spectra (10 keV to 1 MeV) are best described using ENDF/B-IV cross sections while the high energy spectra (2 MeV to 15 MeV) are best described using ENDL cross sections. It is concluded that use of ENDL cross sections should yield the best estimate of tritium breeding and ENDF/B-IV that of Pu breeding in a CTR fusion-fission blanket.

[<sup>238</sup>U Pulsed Sphere Measurements; spectra from 10 keV to 15 MeV compared with calculations; implications for fusion-fission blanket calculations.]

### Introduction

A recent study<sup>1</sup> has shown that the breeding of tritium and Pu in a CTR fusion-fission blanket is quite sensitive to the emission spectra from 14-MeV neutrons on <sup>238</sup>U and other structural materials in the reactor. To have confidence in the breeding calculations, it is essential that the cross sections used in the calculations describe reasonably well the neutron emission spectra from 14-MeV neutrons incident on <sup>238</sup>U. The neutron emission spectra from 0.8 and 2.8 mean-free-paths (m.f.p.) <sup>238</sup>U spheres pulsed with 14-MeV neutrons have been measured from the source energy down to 10 keV. From a comparison of these measurements with calculations, it is concluded that use of ENDL cross sections<sup>2</sup> should yield the best estimate of tritium breeding and ENDF/B-IV that of Pu breeding in a CTR fusion-fission blanket.

### Experimental Method

Figure 1 shows the 0.8 and 2.8 m.f.p. <sup>238</sup>U spheres. A conical insert was machined into the spheres in order to accommodate the low mass target assembly. A tritium loaded titanium target was located at the center of the spherical targets. A solid state silicon detector at 174° with respect to the D<sup>+</sup> beam line monitored the neutron production by counting the associated <sup>4</sup>He particle from the T(d,n)<sup>4</sup>He reaction. For measurements between 2 and 15 MeV, 5.1 cm diameter by 5.1 cm long NE 213 and Pilot B scintillators were used at 120° and 30° respectively. The flight paths were 765 cm at 30° and 977 cm at 120°. The repetition rate for the high energy measurements was 2.5 MHz and the burst width was 4 ns.

For measurements between 10 keV and 1 MeV, a 5.1 cm diameter by 1.9 cm long <sup>6</sup>Li glass scintillator was used at 26° with respect to the deuteron beam line at a flight path of 801 cm. The burst widths were 10 and 100 ns while the repetition rate was 10 KHz. A detailed description of the neutron detector packages and the collimations employed is given in ref. 3.

Standard time-of-flight electronics were used in measuring the emitted spectra. The stop pulses into the time-to-amplitude converter were generated from a capacitive beam pick-off unit. Time calibration of the system and the conversion from counts (cts)/channel to cts/ns (high energy) and cts/μs (low energy) are described in detail in ref. 3. The high energy data are presented as time-of-flight spectra while the low energy data have been converted into energy spectra.

### Experimental Results and Calculations

Figures 2 and 3 show the measured and calculated high energy time-of-flight spectra. The various spectra are identified by the <sup>238</sup>U sphere size, angle of observation and cross section library used. Figures 4, 5 and 6 show the similarly identified low energy spectra.

The high energy spectra are presented as cts (sphere in) per ns per total 14 MeV cts (sphere out). The high energy spectra calculations therefore require that the Pilot B and NE 213 detector efficiencies be folded into the Monte Carlo calculations.

The low energy spectra measurements are presented as neutron/keV/source neutron. The conversion from cts to neutrons requires a knowledge of the <sup>6</sup>Li glass detection efficiency. The detection efficiencies for the <sup>6</sup>Li glass and Pilot B, NE 213 scintillators can be found in ref. 3. The absolute source strength was required for the low energy measurement and it was obtained by calibrating the alpha counter against the 14-MeV flux as measured with the NE 213 and Pilot B scintillators. Reference 4 describes in detail the measurement and data processing of the low energy spectra. In particular, it describes the determination of the time independent background by inserting in good geometry a thick paraffin absorber between the <sup>6</sup>Li detector and <sup>238</sup>U sphere.

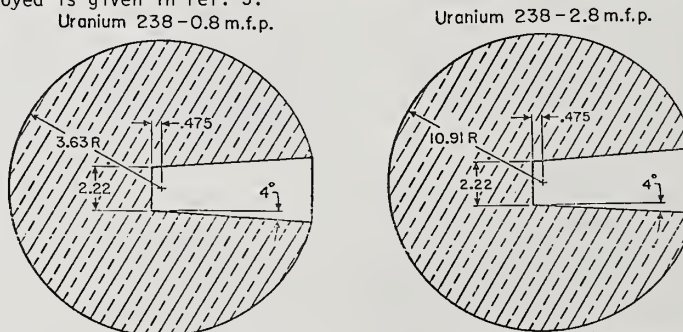


Fig. 1 Schematic drawing of the 0.8 and 2.8 m.f.p. <sup>238</sup>U spheres  
(Dimensions are in centimeters)



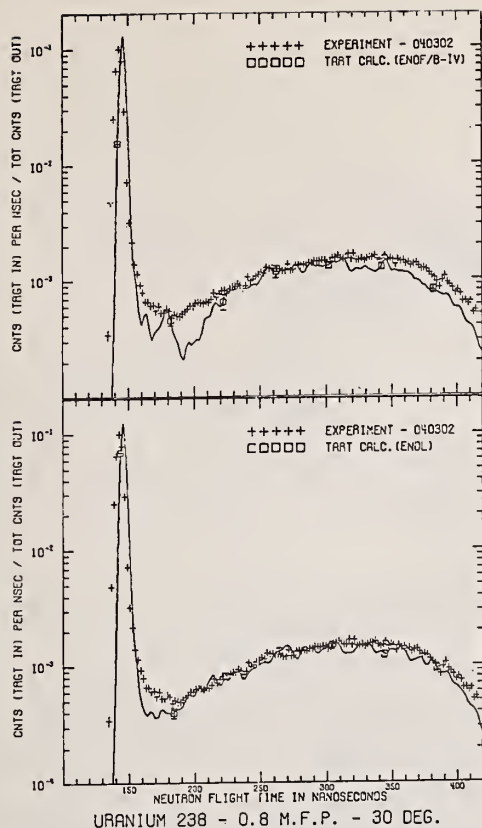


Fig. 2 Comparison between the high energy measurements and calculations for the 0.8 m.f.p.  $^{238}\text{U}$  sphere at  $30^\circ$ .

#### Comparison With Calculations

Table 1 presents a comparison of the measured and calculated integrals for the high energy time-of-flight spectra shown in figs. 2 and 3. The integral above 12 MeV (<164 ns) is a measure of the non-elastic cross section while the integral from 2 to 12 MeV (400 to 164 ns) is a measure of the high energy neutron emission cross section from  $\sigma(n,n')$ ,  $\sigma(n,2n)$ , and  $\bar{\nu}_{sf}$ . Table 1 shows that the ENDF/B-IV non-elastic cross section is correct while that of ENDL appears to be slightly high. In the 2-12 MeV region ENDL gives better agreement with measurements than ENDF/B-IV. The ENDF/B-IV discrepancy for the 2-12 MeV region increases from -16% to -20% in going from 0.8 to 2.8 m.f.p.

Table 1 Comparison of measured<sup>a</sup> and calculated integrals for the  $30^\circ$  high energy emission spectra shown in figs. 2 and 3. 2 and 12 MeV correspond to flight times of 400 and 164 ns, respectively. See figs. 2 and 3 for units on the integrals.

m.f.p.	Measured		ENDF/B-IV		ENDL	
	2-12	>12	2-12	>12	2-12	>12
0.8	0.263	0.644	0.224	0.643	0.243	0.630
2.8	0.324	0.233	0.260	0.232	0.286	0.216

- a. The absolute error on the measured integrals is  $\pm 5\%$ . The error on the ratio of two integrals is  $\pm 3\%$ .
- b. These calculations agree with previous calculations by Howerton.<sup>9</sup>

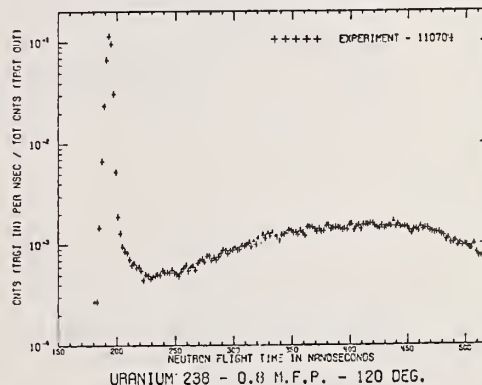
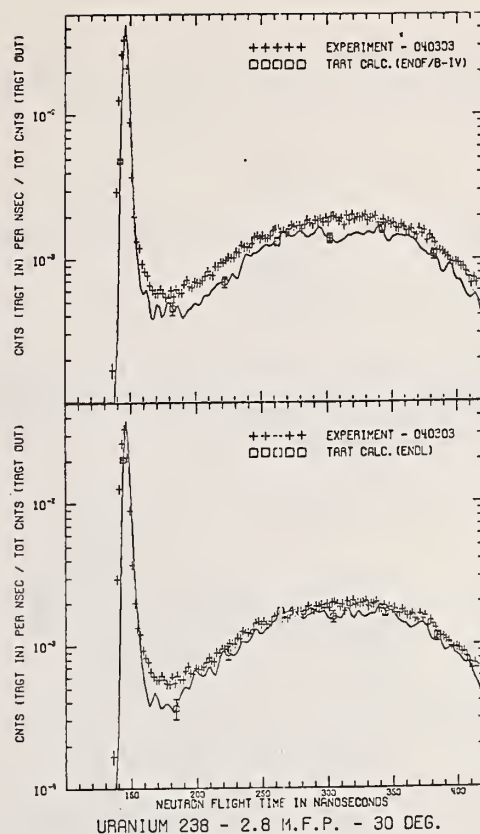


Fig. 3 Comparison between the high energy measurements and calculations for the 2.8 m.f.p. sphere at  $30^\circ$ . The 0.8 m.f.p. data at  $120^\circ$  are presented without calculations.

Table 2 presents the integrals of the 100 ns low energy spectra of figs. 4 and 5 between 10 and 934 keV. Table 2 and figs. 4 and 5 show that the best overall agreement is achieved using ENDF/B-IV cross sections. This agreement is further illustrated by comparison of ENDF/B-IV calculations with the higher resolution 10 ns measurements shown in fig. 6. At 2.8 m.f.p. ENDL yields the correct integral by overestimating the higher energy and underestimating the lower energy neutrons.

Table 2 Comparison of measured<sup>a</sup> and calculated integrals for the emission spectra shown in figs. 4 and 5 between 10 and 934 keV. See figs. 4 and 5 for units.

	0.8 m.f.p. ( $\times 10^{-7}$ )	2.8 m.f.p. ( $\times 10^{-6}$ )
Measured	9.40	3.70
ENDF/B-IV	10.0	3.75
ENDL	8.57	3.65

a. The absolute error on the measured integrals is  $\pm 10\%$  and arises from the uncertainty in the  $^6\text{Li}$  glass efficiency. The error on the ratio of the two measured integrals is  $\pm 5\%$ .

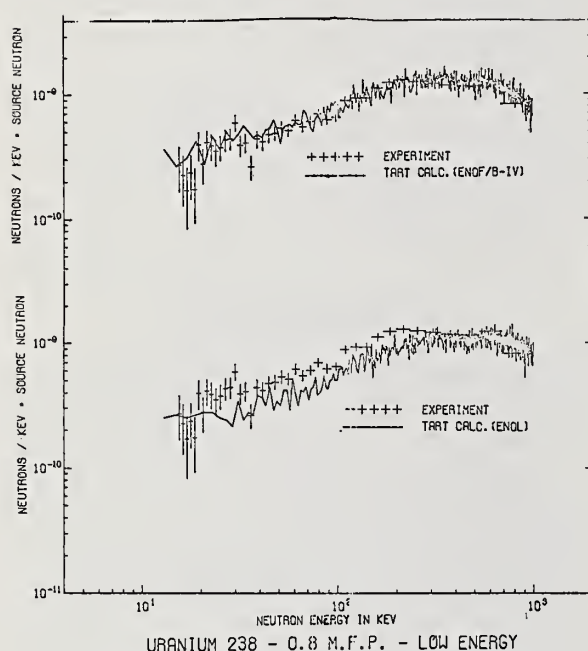


Fig. 4 Comparison between the low energy 100 ns measurements and calculations for the 0.8 m.f.p. sphere.

### Conclusions

Neither library yields satisfactory agreement with both low and high energy spectra. However, ENDL should yield the most reliable estimate of tritium breeding and total fissions in a CTR blanket since it yields the best agreement for the 2.8 m.f.p. high energy spectra and gives the correct number of low energy neutrons for the 2.8 m.f.p. sphere. Agreement with the 2.8 m.f.p. measurements is emphasized since the blanket is fueled with a thick layer of  $^{238}\text{U}$ . Also, because of multiple collisions, the total number of low energy neutrons is more important than exact spectral shape. On the other hand, the breeding of Pu comes mainly from neutron capture below 1 MeV. Since ENDF/B-IV yields the correct number and spectral shape for neutrons between 10 and 934 keV it should yield the most reliable estimate of Pu breeding.

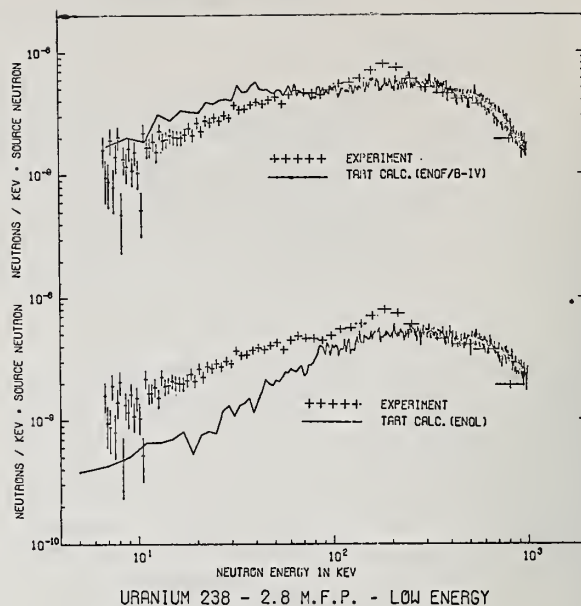


Fig. 5 Comparison between the low energy 100 ns measurements and calculations for the 2.8 m.f.p. sphere.

An earlier calculation<sup>1</sup> of the tritium breeding using ENDL cross sections yielded 1.26 tritons per 14-MeV neutron into the blanket. Since then, ENDL has been revised<sup>6</sup> by decreasing the fission cross section and increasing the  $(n,3n)$  cross section in order to preserve the non-elastic cross section. The predictions shown in figs. 2-5 and tables 1 and 2 were calculated with this latest revised ENDL library. As expected, this revised library yielded a lower tritium breeding ratio of 1.11. The corresponding total fissions using revised ENDL is 0.864, and the Pu breeding using ENDF/B-IV is 2.23.

The present measurements do not cover the energy range between 1 and 2 MeV. Since the various libraries predict percentages from 15 to 25% for neutrons between 1-2 MeV in the sphere calculations, it is clear that these neutrons contribute significantly to total fissions and tritium breeding, and measurements in this energy range would provide additional checks on the various libraries.

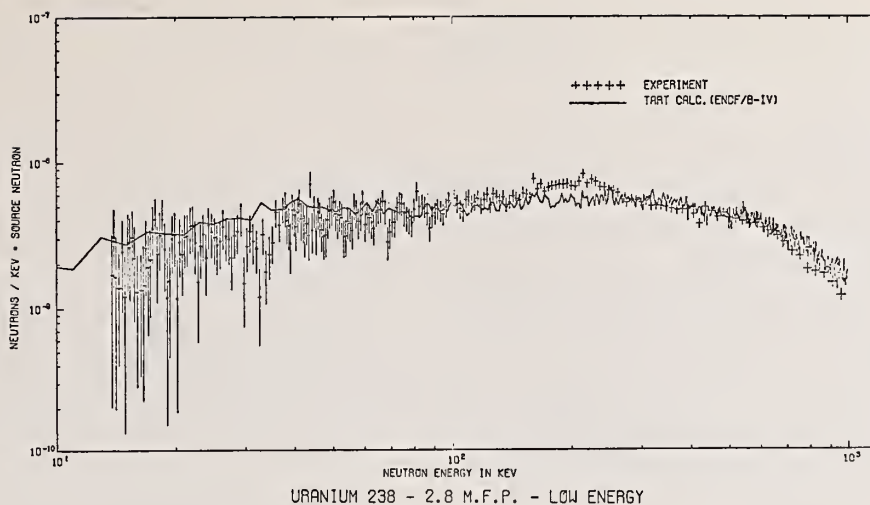


Fig. 6 Comparison between the low energy 10 ns measurements and calculations for the 2.8 m.f.p. sphere.

#### References

1. R. C. Haight and J. D. Lee, Proceedings of the First Topical Meeting on the Technology of Controlled Nuclear Fusion, April 16-18, 1974, San Diego CA (p.271)
  2. R. J. Howerton and M. H. MacGregor, Evaluated Neutron Reaction Data for  $^{238}\text{U}$ , UCRL-51427 (1973) unpublished.
  3. C. Wong et al., Livermore Pulsed Sphere Program: Program Summary Through July 1971, UCRL-51144, Rev. 1, (1972) unpublished.
  4. C. Wong et al., Livermore Pulsed Sphere Program: Low Energy Measurements on Carbon, Iron and Concrete, UCRL-51144, Addendum (1973) unpublished.
  5. R. J. Howerton, Testing of ENDF/B-IV-P Evaluations with SDT-10 Benchmark Pulsed Spheres, UCRL-75693 (Preprint) May 10, 1974.
  6. R. J. Howerton (private communication).
- \*Work performed under the auspices of the Energy Research and Development Administration.



P. J. Persiani and E. M. Pennington  
Argonne National Laboratory 60439  
Y. D. Harker and R. L. Heath  
INEL, Aerojet Nuclear Corp.

Depending on the assumptions made of the neutron cross section behavior in the high-energy region, the captures in  $^{94}\text{Nb}$  have been found to be the major components influencing the afterheat and radioactivity in fusion reactor design problems. Preliminary blanket designs indicate that about 60% of the capture rates in  $^{94}\text{Nb}$  occur above 1 keV and 90% occur above 100 eV. Therefore an important and timely cross section need is an estimate and measurement of the  $^{94}\text{Nb}(n,\gamma)^{95}\text{Nb}$ ,  $^{95m}\text{Nb}$  reaction in the keV-MeV energy region. Nuclear level systematic studies using the two known positive energy resonances, the thermal cross section, the resonance integral and the apparent high-density of the low-lying levels in niobium, have suggested postulating the existence of negative energy levels or level. These considerations involved the postulated negative energy resonances, and assumptions about positive energy resonances above 50 eV and average unresolved parameters based on nuclear systematics. The experimental technique to obtain a measured integrated cross-section in the fast fission spectrum of the Coupled Fast Reactivity Measurements Facility (CFRMF) and the Argonne Fast Source Reactor (AFSR) is investigated with foils of  $^{93}\text{Nb}$  containing 4.1%  $^{94}\text{Nb}$  utilizing Ge(Li) spectrometry.

(fusion; cross-section; resonance-levels; experiment; blanket; afterheat; radioactivity)

### Introduction

An important and timely cross section need is an estimate and measurement of the  $^{94}\text{Nb}(n,\gamma)^{95}\text{Nb}$ ,  $^{95m}\text{Nb}$  cross section in the high-energy  $\sim 1$  MeV region. The significance of this effort is to confirm or not confirm the existence of the afterheat problem usually associated with the niobium structural material.<sup>1,2</sup> It is important to establish this for niobium since it is being used as a merit of performance in selecting candidates for structural materials in fusion power reactors.

The  $^{95}\text{Nb}$  and  $^{95m}\text{Nb}$  afterheat and radioactivity problem results from the assumptions made in Refs. 1 and 2 where the approximation is made that in the absence of cross section data above the thermal energy region, the  $^{94}\text{Nb}(n,\gamma)$  cross section is 15 times greater than the  $^{93}\text{Nb}(n,\gamma)$  over the entire (0.025 eV to 14 MeV) energy region. This factor is based on the ratio of the measured<sup>3-5</sup> 0.025 eV capture cross sections and resonance integrals. The assumptions may be overly pessimistic by an order of magnitude, and if a lower cross section is confirmed then the niobium afterheat and radioactivity problem could be considerably reduced to levels not different from other structural material candidates.

Figures 1 and 2 graphically demonstrate the consequences of reducing the  $^{94}\text{Nb}(n,\gamma)$  reaction rates and subsequently the  $^{95}\text{Nb}$  and  $^{95m}\text{Nb}$  activity, by a factor of ten. The afterheat related activity is directly reduced by approximately the same factor of ten. So that if the measured cross section is found to be much less than  $^{93}\text{Nb}$  in the keV, MeV region, then the contribution to the afterheat and activation levels by  $^{95}\text{Nb}$ ,  $^{95m}\text{Nb}$  can be completely neglected. This means that the major contribution would be from the  $^{92m}\text{Nb}$  and  $^{93m}\text{Nb}$  over the first few days after shutdown and the radioactive level is reduced even further.

In nuclear power plant designs, the near-term (days, weeks, Fig. 1) afterheat and activation levels are most important and will impact directly on the design of many subsystems; particularly the handling of maintenance, transport, and heat transfer intransit operations. The long-term effects (Fig. 2) are controlled by other factors and the change in the activity of  $^{94}\text{Nb}$ , due to reduced burnup, for storage and handling is not as consequential.

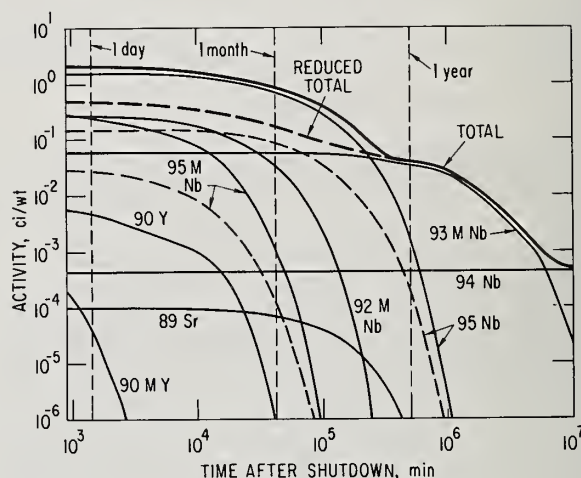


Figure 1. Radioactivity versus time in minutes after shutdown

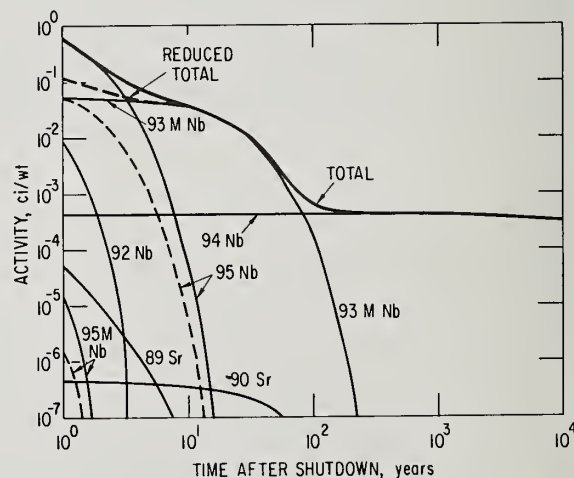


Figure 2. Long term radioactivity after shutdown

<sup>94</sup>Nb(n,γ) Cross Section Structures  
and Sensitivity Calculations

Sensitivity calculations have been attempted<sup>6</sup> in order to estimate the effect on the induced activation due to cross section uncertainties and in particular due to the absence of nuclear data above the 22.6 eV resonance level. However, it is a very difficult procedure to attempt structuring a cross section in an energy region where there is inadequate or an absence of experimental data on resonance parameters, so that to infer a capture cross section for <sup>94</sup>Nb much beyond the wings of the 22.6 eV resonance level could result in large errors. The three cross section structures suggested and used in the sensitivity calculation<sup>6</sup> are speculative and the plausible arguments may not be consistent with nuclear physics systematics. The conclusion of the study was that the afterheat varied within 17% for the range of cross sections constructed.

Negative Energy Level Parameters for <sup>94</sup>Nb(n,γ)

In view of nuclear level systematics, the apparent high-density of the low-lying levels of the <sup>94</sup>Nb isotope suggests the existence of a negative energy level or levels. The introduction of negative energy level resonance parameters along with other positive energy levels lying above the 22.5 eV resonance would readily account for not only the difference between the measured resonance integral of 125b and the computed contribution of 93b from the 11.6 and 22.6 eV resonances; but also the difference between the measured thermal capture cross section of 13.6b and the 4.5b computed from the parameters of the above two levels. Therefore, the high thermal cross section and the high resonance integral for <sup>94</sup>Nb can be accounted for by the low-lying levels <50 eV. These low-lying levels would have a small effect on the magnitude of the capture cross section above 50 or 100 eV.

As a result of this resonance structure, the <sup>94</sup>Nb(n,γ) cross section above 50 or 100 eV could be expected to approach the magnitude of the <sup>93</sup>Nb capture cross section or even lower by a factor of 2 as is now listed in ENDF/B-IV. If this is the case, then the computed capture reaction rate in <sup>94</sup>Nb would be a factor of at least 15 times lower than the capture rates computed for the CTR Nb-structure blankets currently being designed where the approximation is made that the <sup>94</sup>Nb(n,γ) cross section is 15 times greater than the <sup>93</sup>Nb(n,γ) over the entire energy region. This reduced reaction rate is based on a variety of blanket design computations where in general it is found that about 50-60% of the capture reaction rates occur above 1 keV and that 90-98% occur above 100 eV.

In order to study the effect of neutron capture of <sup>94</sup>Nb in a typical CTR blanket, three versions of <sup>94</sup>Nb were prepared in ENDF/B format.<sup>7</sup> Version A is the ENDF/B-IV <sup>94</sup>Nb, Material 238 on Tape 415, with the addition of the elastic scattering angular distributions from ENDF/B-IV <sup>93</sup>Nb and isotropic inelastic angular distributions. Version B, which is described below, differs from Version A in the (n,γ) cross section. In Version C the (n,γ) cross section at all energies is that of ENDF/B-IV <sup>93</sup>Nb multiplied by 13.6/1.15 = 11.83, which is the ratio of the capture cross sections of <sup>94</sup>Nb and <sup>93</sup>Nb at 0.0253 eV.

The capture cross section of ENDF/B-IV <sup>94</sup>Nb (Version A) at energies below 61.649 eV is derived from the contributions of the two positive resonances with the addition of a 1/V background to produce the experimental 0.0253 eV cross section of 13.6 barns. Above 61.649 eV the (n,γ) cross section was computed using the methods of Refs. 8 and 9. For Version B

<sup>94</sup>Nb, the capture cross section up to 61.649 eV is computed from the two positive energy resonances of Version A, along with a negative energy resonance added to give the 0.0253 eV cross section without the use of a background. Parameters for the three resonances are listed in Table I. Above 61.649 eV and

Table I. Resonance Parameters of Version B <sup>94</sup>Nb

E, eV	J	Γ, eV	Γ <sub>n</sub> , eV	Γ <sub>γ</sub> , eV	σ <sub>nγ</sub> (.0253)	R.I., b
					b	
-30.0	6	0.30241	0.11441	0.188	9.11	2.99
11.63	6	0.16786	0.00586	0.162	4.32	89.13
22.63	6	0.21395	0.00095	0.213	0.17	3.93
					13.60	96.05
					total <sup>a</sup>	123.99

<sup>a</sup>The tabulated cross section above 61.649 eV adds 27.94 barns to the infinite dilution capture resonance integral above 0.5 eV to yield a total of 123.99 barns.

below 50 keV the (n,γ) cross section was computed from unresolved resonance parameters using the average level spacings and strength functions derived in Ref. 10, along with the assumption of a 1/(2J+1) dependence for level spacings and a Γ<sub>γ</sub> = 0.188. The Γ<sub>γ</sub> is the average of the experimental values for the two measured positive energy resonances. At 50 keV and above the σ<sub>nγ</sub> values of Version A were used. Of course the cross sections in the lower part of the range above 61.649 eV in either Versions A or B are not very reliable, since the values of the resolved resonance parameters, which are not known experimentally, can affect the cross sections considerably. It would be necessary to have resolved parameters up to a few keV to establish the cross section well.

The capture cross section of Version B is higher than that of Version A in the range from 61.649 eV up to about 10 keV, and lower in the range from about 10 to 50 keV. Version A has a capture resonance integral of 117.4 barns, while the resonance integral of Version B is 124.0 barns. Version C has a 111.9 barn resonance integral. The experimental value is 125 ± 8 barns.<sup>5</sup>

Blanket Computations with the Three Versions of <sup>94</sup>Nb

The three versions of <sup>94</sup>Nb were processed through RIGEL<sup>11</sup> and ETOE-2<sup>12</sup> to produce a binary library in the format required by MC<sup>2</sup>-2.<sup>13</sup> This library was then merged with other materials from the ENDF/B-IV MC<sup>2</sup>-2 library using MERMC2-2<sup>14</sup> to produce a library to be used for running MC<sup>2</sup>-2 problems including <sup>94</sup>Nb. An MC<sup>2</sup>-2 problem was run with <sup>12</sup>C, <sup>6</sup>Li, <sup>7</sup>Li, <sup>93</sup>Nb and the three versions of <sup>94</sup>Nb. Except for carbon, the materials were at low atomic densities to produce essentially infinite dilution cross sections in an 88-group structure with upper energy of 14.19 MeV. The 88-group cross sections were transformed with a service routine<sup>15</sup> into the format required by the discrete ordinates transport code ANISN.<sup>16</sup>

An ANISN S<sub>4</sub> problem was run using the specifications for the benchmark fusion reactor blanket given in Ref. 17. Tables II and IIL, based on Ref. 17, present the specifications for the cylindrical blanket. The isotropic source of neutrons is in group 1 of the multigroup structure.

The output of the first ANISN problem was used to distribute small amounts of <sup>94</sup>Nb in the zones containing



Table II. Configuration of Benchmark Blanket

Zone	Material	Intervals	Outer Radius, cm
1	A	1	150
2	B	1	200
3	C	3	200.5
4	D	6	203.5
5	C	3	204
6	D	10	224
7	D	10	244
8	D	10	264
9	E	15	294
10	D	3	300

Table III. Nuclide Densities for Benchmark Blanket

Material	Constituent	Number Density $10^{24}/\text{cm}^3$
A	Isotropic flat source of neutrons	
B	Vacuum	
C	$^{93}\text{Nb}$	0.05556
D	$^{93}\text{Nb}$	0.003334
	$^6\text{Li}$	0.003234
	$^7\text{Li}$	0.04038
E	Carbon	0.0804

niobium according to  $N^{94} = N_0^{93} \sigma_{ny}^{93} \phi t$ , which holds true for sufficiently short times, since

$$N^{94} = \frac{N_0^{93} \sigma_{ny}^{93} \phi}{(\sigma_{abs}^{94} \phi + \lambda_{g4} - \sigma_{ny}^{93} \phi)} (e^{-\sigma_{ny}^{93} \phi t} - e^{-(\sigma_{abs}^{94} \phi + \lambda_{g4}) t}),$$

where the notation used is conventional. Three more ANISN problems were run using the three versions of  $^{94}\text{Nb}$ . Results from these problems are given in Table IV. In this table the average one-group capture cross section for  $^{94}\text{Nb}$  in each of the zones containing niobium and for the whole blanket are presented for the three versions of  $^{94}\text{Nb}$ . The average  $\sigma_{ny}$  for all three versions increases with increasing zone number because of the progressive softening of the flux spectrum. There is a large increase in going from zone 8 to zone 10 because of the thermalization by the 30-cm thickness of carbon in zone 9. Differences between Versions A and B are not large, but become slightly greater with increasing zone number since the softening of the spectrum yields increasing emphasis to the energy range where  $\sigma_{ny}$  of Versions A and B differ. Version C gives values of the average  $\sigma_{ny}$  which are much greater by a factor of ten than those of Versions A and B in all zones except 10, since  $\sigma_{ny}$  of Version C is much larger than that of Versions A or B except at thermal and near-thermal energies.

Table IV. Average Capture Cross Section of  $^{94}\text{Nb}$ , barns

Zone	Version		
	A	B	C
3	0.1027	0.1042	1.148
4	0.1084	0.1101	1.208
5	0.1143	0.1162	1.268
6	0.1482	0.1578	1.594
7	0.2293	0.2406	2.324
8	0.5271	0.5834	3.728
10	5.977	6.509	7.747
Average	0.1958	0.2066	1.814

Proposed Measurements of  $^{94}\text{Nb}(n,\gamma)$ 

Integral capture cross section measurements are being planned for the fast fission neutron spectra of the Coupled Fast Reactivity Measurement Facility (CFRMF) and the Argonne Fast Source Reactor (AFSR). The integral experiments would check  $\sigma_{ny}$  in the neutron energy range 0.5-1.0 MeV and should help determine the reduction in the activation cross section ratio ( $^{94}\text{Nb}$  to  $^{93}\text{Nb}$ ) at the higher neutron energies. The general features of these facilities are listed in Table V.

Table V. General Features for CFRMF and AFSR

Location	CFRMF	AFSR
	INEL-Aerojet Nuclear Corp.	Argonne
Integral Flux	$1.2 \times 10^{11}$ n/cm <sup>2</sup> -sec	$5 \times 10^{11}$ n/cm <sup>2</sup> -sec
Mean Neutron Energy	700 keV	2.1 MeV
Median Neutron Energy	500 keV	1.3 MeV
90% Energy Range*	16 keV-2.8 MeV	16 keV-4.9 MeV
95% Energy Range**	5 keV-3.85 MeV	5 keV-5.7 MeV

\*Energy range containing 90% of the integrated neutron flux.

\*\*Energy range containing 95% of the integrated neutron flux.

Activation methods will be utilized to arrive at cross section values for the reaction  $^{94}\text{Nb}(n,\gamma)^{95\text{m}}\text{Nb}$  and  $^{94}\text{Nb}(n,\gamma)^{95}\text{Nb}$ . Two samples containing approximately 300  $\mu\text{g}$  of  $^{94}\text{Nb}$  each will be fabricated, one for irradiation in the CFRMF and the other in the AFSR. The fluence for each of these irradiations will be on the order of  $3 \times 10^{16}$  n/cm<sup>2</sup>. After irradiation, the amounts of  $^{95\text{m}}\text{Nb}$  and  $^{95}\text{Nb}$  produced in neutron capture will be determined by Ge(Li)  $\gamma$ -spectrometry using the activity of the 235 keV  $\gamma$ -ray from the decay of  $^{95\text{m}}\text{Nb}$  and the activity of the 765 keV  $\gamma$ -ray from the decay of  $^{95}\text{Nb}$ .

The major difficulty in performing these measurements is the relatively high backgrounds in the  $\gamma$ -spectra arising from the decay of the  $^{94}\text{Nb}$  target material. This background seriously affects the detectability of the much weaker activities from  $^{95\text{m}}\text{Nb}$  and  $^{95}\text{Nb}$ . A test to determine the accuracy of measuring the weaker activities in the presence of the activity from the decay of  $^{94}\text{Nb}$  was organized, whereby the counting conditions expected after an irradiation of 300  $\mu\text{g}$  of  $^{94}\text{Nb}$  in the CFRMF to a fluence  $\sim 10^{16}$  n/cm<sup>2</sup> were simulated. The partial capture cross sections used to estimate these conditions were 200 millibarn/nuclei for  $^{94}\text{Nb}(n,\gamma)^{95}\text{Nb}$  and 100 millibarn/nuclei for  $^{94}\text{Nb}(n,\gamma)^{95\text{m}}\text{Nb}$ . To simulate the activity of the 235 keV  $\gamma$ -ray created in the decay of  $^{95\text{m}}\text{Nb}$ , a 279 keV  $\gamma$ -ray from a  $^{203}\text{Hg}$  source was used and similarly a 834 keV  $\gamma$ -ray from a  $^{54}\text{Mn}$  source was used to simulate the activity of the 765 keV  $\gamma$ -ray created in the decay of  $^{95}\text{Nb}$ . A  $^{94}\text{Nb}$  source was used to produce the high background. The count-rates for the simulated conditions are given in Table VI.



Table VI. Counting Results of Simulated Experiment

Energy	Source	w/o $^{94}\text{Nb}$ bkgd. Activity (counts/sec)	w/ $^{94}\text{Nb}$ bkgd. Activity (counts/sec)
279 keV	$^{203}\text{Hg}$	1.048 ( $\pm 2.4\%$ )	1.022 ( $\pm 3.9\%$ )
702 keV	$^{94}\text{Nb}$	---	145 ( $\pm 1.8\%$ )
834 keV	$^{54}\text{Mn}$	.303 ( $\pm 4.1\%$ )	.280 ( $\pm 18\%$ )
871 keV	$^{94}\text{Nb}$	---	116 ( $\pm 1.8\%$ )

From the error data listed in Table VI, it appears that the counting uncertainties for a single measurement will be  $\sim 4\%$  for determining the activity of  $^{95}\text{mNb}$  and similarly  $\sim 20\%$  for the activity of  $^{95}\text{Nb}$ . When the counting data are reduced to absolute cross sections, it is expected that the cross-section uncertainties will be  $\sim 12\%$  for  $^{94}\text{Nb}(n,\gamma)^{95}\text{mNb}$  and  $\sim 22\%$  for  $^{94}\text{Nb}(n,\gamma)^{95}\text{Nb}$ .

#### Remarks

The first point of this note is to indicate that, in general, sensitivity calculations must always be guided by experiments. Many models may be constructed to fit limited experimental data, with the consequences differing for each of the models.

The second point to make is that in this particular case, the suggested integral measurements of the  $^{94}\text{Nb}(n,\gamma)$  cross section in the keV, MeV spectrum region of the AFSR and the CFRMF would be important experimental points of reference for the theoretical structuring of the cross section. Further, the subsequent sensitivity computations would then be more directly relevant since the analysis would be based on more direct experimental data.

#### References

1. D. Steiner, "The Neutron Induced Activity and Decay Power of the Niobium Structure of a D-T Fusion Reactor Blanket," ORNL-TM-3094, Oak Ridge National Laboratory (August 1970).
2. D. J. Dudziak and R. A. Krakowski, "A Comparative Analysis of D-T Fusion Reactor Radioactivity and Afterheat," Proc. First Topical Meeting on the Technology of Controlled Nuclear Fusion, San Diego, Calif., 1974, pg. 548.
3. G. E. Moore, Ed., "Chemistry Division Annual Progress Report," p. 2, ORNL-4306, Oak Ridge National Lab. (1968).
4. M. R. Serpa, T. E. Young and R. P. Schuman, "Nuclear Technology Branch Annual Progress Report," IN-1317, p. 3 and p. 52, Idaho Nuclear Corp. (1970).

5. S. F. Mughabghab and D. I. Garber, "Neutron Cross Sections: Vol. I, Resonance Parameters," p. 41-6, BNL-325, 3rd ed., Vol. I, Brookhaven National Lab. (1973).
6. D. W. Muir and D. J. Dudziak, "Sensitivity of RTPR Afterheat and Radioactivity to  $^{94}\text{Nb}$  Cross-Section Uncertainty," Trans. Am. Nucl. Soc. 19, 465 (October 19, 1974).
7. M. K. Drake, Ed., "Data Formats and Procedures for the ENDF Neutron Cross Section Library," BNL-50274(T-601), (ENDF102, Vol. I), October 1970.
8. F. Schmittroth and R. E. Schenter, "Fast Neutron Capture Cross Sections for Fission Product Isotopes," HEDL TME 73-63 (ENDF-194), August 1973.
9. F. Schmittroth, "Neutron Capture Calculations for  $E_n = 100$  keV to 4 MeV," HEDL TME 73-79 (ENDF-195), November 1973.
10. A. R. de L. Musgrove, "Interpolative Formulae for Average Nuclear Level Spacing and Total Radiation Width," AAEC/E211, November, 1970.
11. Odelli Ozer, Ed., "Description of the ENDF/B Processing Codes and Retrieval Subroutines," BNL-50300 (ENDF-110), (revised June 1971).
12. C. G. Stenberg, "ETOE-2, A Program for Conversion of ENDF/B to MC<sup>2</sup>-2," Reactor Physics Division Annual Report, July 1, 1970 to June 30, 1971, ANL-7910, pp. 442-445.
13. H. Henryson II and B. J. Toppel, "MC<sup>2</sup>-2: A Code To Calculate Fast Neutron Spectra and Multigroup Cross Sections," ANL-8144, to be issued.
14. E. M. Pennington, Argonne National Laboratory, report to be issued.
15. P. H. Kier, Argonne National Laboratory, private communication.
16. W. W. Engle, Jr., "A Users Manual for ANISN: A One-Dimensional Discrete Ordinate Transport Code with Anisotropic Scattering," K-1693 (March 30, 1967, updated June 6, 1973).
17. D. Steiner, "Analysis of a Bench-Mark Calculation of Tritium Breeding in a Fusion Reactor Blanket: The United States Contribution," ORNL-TM-4177 (April 1973).

PRODUCTION CROSS SECTIONS OF SOME MICRO AND MILLISECOND  
ISOMERS WITH 14.8 MEV NEUTRONS\*

G. N. Salaita and P. K. Eapen<sup>†</sup>  
Department of Physics, Southern Methodist University, Dallas, Tex. 75275

The formation cross sections for the isomeric states in Mg, Al, Y, In, Hf, Tl, Pb, and Bi by the (n,p), (n, $\alpha$ ), and (n,2n) reactions have been measured using the cyclic activation technique and a Ge(Li) detector. The half-lives of the induced isomeric activities were determined using a wide range time-to-pulse height converter and a multichannel analyzer.

$$\left[ \begin{array}{l} \text{NUCLEAR REACTIONS } ^{24}\text{Mg}(n,p), ^{27}\text{Al}(n,\alpha), ^{89}\text{Y}(n,2n), ^{115}\text{In}(n,2n) \\ ^{179}\text{Hf}(n,2n), ^{203,205}\text{Tl}(n,2n), ^{206,207,208}\text{Pb}(n,2n), ^{209}\text{Bi}(n,2n) \\ E \text{ 14.8 MeV; measured } \sigma, T_{1/2}, E_{\gamma}. \end{array} \right]$$

### I. INTRODUCTION

The method, termed cyclic activation involves the efficient utilization of a relatively low-output pulsed source of 14-MeV neutrons and the cumulative counting of induced activities for  $n$  consecutive bombard-wait-count cycles. The method was first suggested by Caldwell et al.<sup>1</sup>, as an experiment for the remote analysis of lunar and planetary surfaces and consequently demonstrated in the analysis of large rock samples using a pulsed neutron generator.<sup>2</sup> Since cycling is electronic rather than mechanical, the method is suitable for the study of activities with half-lives less than one second.

This paper describes the results of measurements of the production cross sections for isomeric states, with half-lives that range from a few tens micro-seconds to about one second, arising from 14.8 MeV neutron reactions using the cyclic activation technique.

The interest in these measurements arose from the lack of agreement in previously reported cross section values and the desire to explore the feasibility of utilizing the isomeric activities for analytical purposes. Another objective of this study was to obtain the isomeric cross-section ratio,  $\sigma_m/\sigma_g$ , and to compare the experimental results with the theoretical data.<sup>3</sup> Absolute gamma counting, which has the advantages of allowing a unique identification of the product nucleus in terms of both the half-life and the characteristic gamma-ray spectrum, was used in this investigation.

### II. EXPERIMENTAL

Pulses of 14.8 MeV neutrons were produced by bombarding a tritiated titanium target with 300 keV magnetically analyzed deuteron beam from a 400 kV Van de Graaff accelerator. A silicon surface barrier detector was used for monitoring the neutron yield by the associated alpha particle technique.

A schematic block diagram of the electronics and experimental arrangement is shown in Figure 1. The samples were high purity powder in thin-wall toroidal containers machined of plexiglas and placed symmetrically about the detector housing with its axis along the direction of the deuteron beam. This geometry is easily reproducible thus eliminating positioning errors.

The activation gamma-ray spectra were measured by a coaxial 43 cm<sup>3</sup> Ge(Li) detector and recorded on a 4096-channel pulse height analyzer. The detector was shielded from the direct neutron beam by a tungsten cone.

The half-lives of short-lived isomeric activities were measured with a time analyzer. The basic unit of the analyzer was a wide range time-to-pulse height converter<sup>4</sup> and a 512-channel analyzer.

Isomeric activities originating from the various isotopes of lead and thallium were separated by proper choice of cyclic timing parameters and energy discrimination. The gamma-ray spectra were obtained by taking a series of pulsed measurements with different time delays between the end of the neutron burst and the start of the analyzer counting gate. Details of the cyclic activation method<sup>2</sup> and measuring technique have been described previously.<sup>5,6</sup>

### III. RESULTS AND DISCUSSIONS

Table 1 lists the results of the isomeric states formation cross sections measurements, together with the half-lives and gamma-ray energies of the products. Also listed are the values of the cross sections available in the literature.

In the present experiment, the isomeric states production cross sections were obtained by using the following relation:

$$\sigma = \frac{D_t}{N\phi\epsilon k} f(\lambda, t_b, t_d, t_c, T, n), \quad (1)$$

where  $D_t$  is the cumulative detector response obtained by summing the responses from all counting intervals during the experiment time,  $\phi$  is the neutron flux at the position of the ring sample during a burst,  $N$  is the total number of relevant nuclei in the sample,  $\epsilon$  is the photopeak efficiency of the detector for the gamma rays observed in the ring geometry, and  $k$  is the absorption correction of the gamma rays produced in the sample. The function  $f$  is derived from the cyclic activation theory<sup>2</sup> and depends on the bombard, wait, and count periods of duration  $t_b$ ,  $t_d$ , and  $t_c$  respectively, and which are repeated with a period  $T$ . It also depends on  $\lambda$ , the decay constant of the

radioactivity produced, and  $n$  the total number of successive bombard-wait-count cycles. The self-absorption factor was calculated from the expression:<sup>7</sup>

$$K = \int_{r_1}^{r_2} e^{-\mu(r-r_1)} \frac{dr}{r} \bigg/ \int_{r_1}^{r_2} \frac{dr}{r}, \quad (2)$$

where  $\mu$  is the total linear absorption coefficient of gamma rays and  $r_1$  and  $r_2$  are the inner and outer radii of the ring sample, respectively.

The error limits quoted in Table 1 arise in the determination of the gamma-ray yield and the neutron flux. The yield involves the photopeak counts, the photopeak efficiency of the detector, the gamma-ray transition probability, the internal conversion correction, and a correction for the self-absorption in the sample. The combined error in these quantities is about 7 per cent. The photopeak efficiency of the detector represents the major error; this efficiency was experimentally determined using standard radioactive sources.<sup>8</sup> The sources were solutions of

<sup>203</sup>Hg (279.15 keV,  $\pm 4$  per cent), <sup>7</sup>Be (477.556 keV,  $\pm 4$  per cent), <sup>137</sup>Cs (661.632 keV,  $\pm 4$  per cent),

<sup>54</sup>Mn (834.861 keV,  $\pm 4$  per cent), and <sup>65</sup>Zn (1115.522 keV,  $\pm 4$  per cent) in thin-wall plexiglas containers having the same dimensions as the ring samples. The data points for the efficiency  $\epsilon$  were analyzed as a function of the gamma-ray energy  $E_\gamma$  (keV) using a

least-squares computer program. The relation obtained by the least-squares fit was

$$\epsilon = aE_\gamma^{-b}, \quad (3)$$

where  $a = 0.0039717$  and  $b = 0.7638$ . The rms deviation of the experimental points from a linear fit in this region is 2.3 per cent.

The neutron flux at the position of the sample was determined from the alpha particle rate and the solid angle subtended by the surface-barrier detector at the target. The geometric calculations were confirmed by activation of copper foils through the Texas convention<sup>9</sup> and also by a standard <sup>241</sup>Am source of known  $\alpha$ -intensity. The error in the neutron flux measurements is estimated to be 5-6 per cent. Errors in timing, weighing of samples, neutron multiple scattering and in background subtraction are estimated at less than 2 per cent each. These errors, when combined quadratically, give a value of about 8-10.

As can be seen from Table 1, for many of the short-lived isomeric activities only one and at most two measurements for the formation cross sections have been reported. Most of the reported measurements were made with beta-counting or with NaI (Tl) detectors. These methods lack the resolution necessary for accurate quantitative analysis of the large number of activities originating from the various isotopes of elements such as lead and thallium. Each cross section and energy value was measured on at least two different occasions and the average value reported in the table.

\*Work sponsored by the Robert A. Welch Foundation, Houston, Texas. Much of the data was obtained with the assistance of S. Sothras and F. Wong.

†Present address: Power Division, United Engineers and Constructors, Philadelphia, PA.

<sup>1</sup>R.L. Caldwell, W.R. Mills, Jr., L.S. Allen, P.R. Bell and R.L. Heath, Science 152, 457 (1966).

<sup>2</sup>W.W. Givens, W.R. Mills and R.L. Caldwell, Nucl. Instr. Meth. 80, 95 (1970).

<sup>3</sup>J.R. Huizenga and R. Vandenbosch, Phys. Rev. 120, 1305 (1960); 120, 1313 (1960).

<sup>4</sup>J. Fischer and A. Lundby, Rev. Sci. Instr. 31, 10 (1960).

<sup>5</sup>G.N. Salaita, Nucl. Phys. A 170, 193 (1971).

<sup>6</sup>G.N. Salaita and P.K. Eapen, J. Inorg. Nucl. Chem. 35, 2139 (1973).

<sup>7</sup>K. Nishimura, K. Okana and S. Kikuchi, Nucl. Phys. 70, 421 (1965).

<sup>8</sup>L. Van Zelst, P. Meyers and J. Oosting, Physica 39,

<sup>9</sup>Proc. of the 1965 Int. Conf. on modern trends in activation analysis, April 19-22, 1965, Texas A. and M. University, College Station, Texas.

<sup>10</sup>E. Monnond, CEA-R-2900, Centre d'Etudes Nucleaires de Grenoble, Decembre, 1965.

<sup>11</sup>J. Karolyi, J. Csikai and G. Peto, Nucl. Phys. A 122, 234 (1968).

<sup>12</sup>R. Prasad, D.C. Sarkar and C.S. Khurana, Nucl. Phys. 88, 349 (1966).

<sup>13</sup>E. Monnand, C. r. hebdom. Séanc. Acad. Sci. Paris Ser. B. 263, 712 (1966).



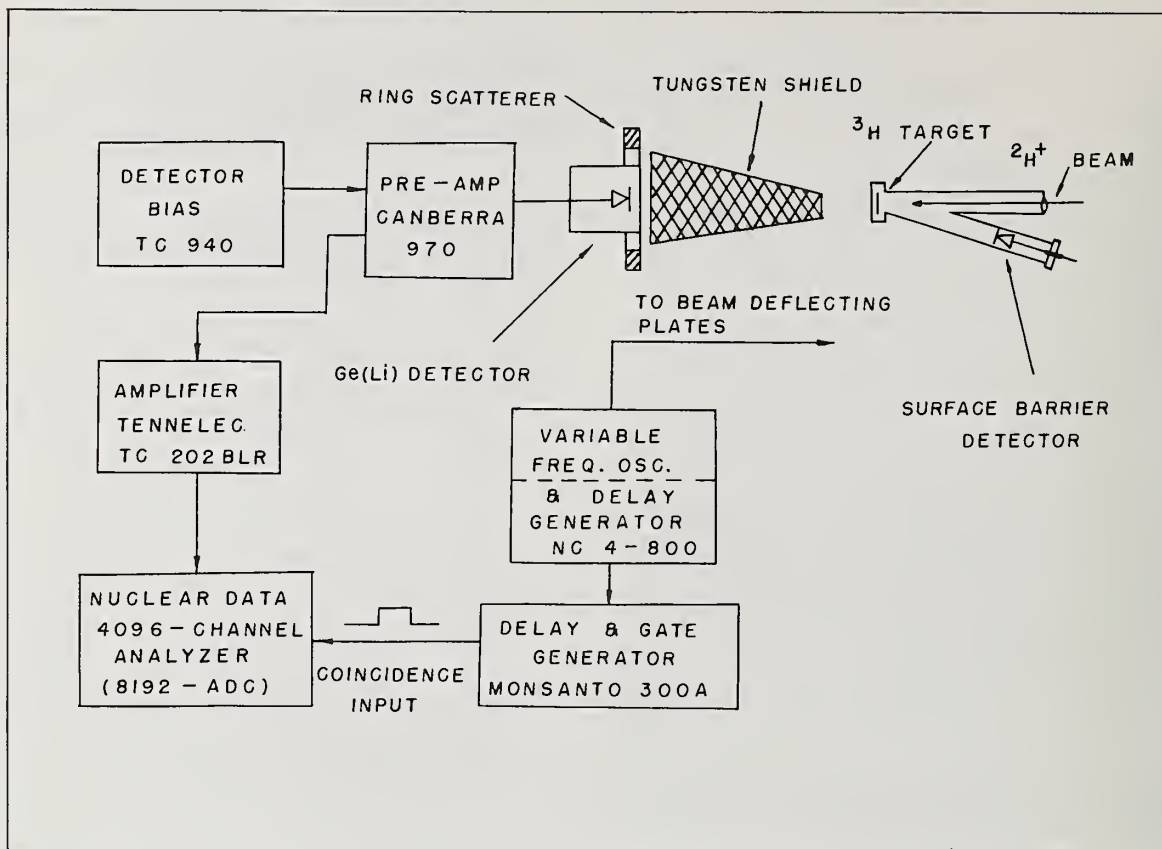


Fig. 1. Block diagram of electronics and experimental arrangement

Table I. Cross Section Measurements for Short-Lived Isomeric Activities

Target	Reactions	$E_{\gamma}$ (keV)	$T_{1/2}$	Cross Section (mb)		
				Present Study	Literature	Ref.
Mg	$^{24}\text{Mg}(n,p)^{24m}\text{Na}$	472.5	19.6±0.5 ms	138±14	48±15	[8]
					100	[10]
Al	$^{27}\text{Al}(n,\alpha)^{24m}\text{Na}$	472.5	19.6±0.5	65±6	33±10	[8]
					60	[10]
$\text{Y}_2\text{O}_3$	$^{89}\text{Y}(n,2n)^{89m}_1\text{Y}$	392.7	320±2 $\mu\text{s}$	96±8	100	[10]
	$^{89}\text{Y}(n,2n)^{86m}_2\text{Y}$	232.2; 442.8	14.6±2 ms	227±18	74±25	[8]
					150	[10]
In	$^{115}\text{In}(n,2n)^{114m}\text{In}$	311.7	42.5±2 ms	703±56	269±90	[8]
					400	[10]
$\text{HfO}_2$	$^{179}\text{Hf}(n,2n)^{178m}\text{Hf}$	214.3; 325.8	4.0 s	1452±116		
	$^{178}\text{Hf}(n,n'\gamma)^{178m}\text{Hf}$	426.5				
$\text{TlCl}$	$^{203}\text{Tl}(n,2n)^{202m}\text{Tl}$	459.6; 490.7	536±15 $\mu\text{s}$	670±54	250	[10]
	$^{205}\text{Tl}(n,2n)^{204m}\text{Tl}$	413.2; 688.2	67±2 $\mu\text{s}$	664±53	700	[10]
Pb	$^{206}\text{Pb}(n,2n)^{205m}\text{Pb}$	284.5; 702.8; 986.0; 1014.3	5.54±0.1 ms	866±69	400	[10]
	$^{207}\text{Pb}(n,2n)^{206m}\text{Pb}$	342.2; 516.4;	125±2 $\mu\text{s}$	1017±92	500	[10]
	$^{206}\text{Pb}(n,n'\gamma)^{206m}\text{Pb}$	537.4; 802.3				
	$^{208}\text{Pb}(n,2n)^{207m}\text{Pb}$	569.6; 1063.5	810±8 ms	1310±116	1340±174	[11]
	$^{207}\text{Pb}(n,n'\gamma)^{207m}\text{Pb}$				990±120	[12]
Bi	$^{209}\text{Bi}(n,2n)^{208m}\text{Bi}$	510.0; 650.5;	2.65±0.14 ms	393±35	118±35	[8]
		920.8			290±30	[13]

# REACTIVITIES FOR TWO-COMPONENT FUSION CALCULATIONS\*

George H. Miley and Harry H. Towner  
Nuclear Engineering Program  
University of Illinois  
Urbana, Illinois 61801

Tables and graphs of fusion reactivities ( $\langle\sigma v\rangle$ ) are readily available for fusion in thermalized (Maxwellian) plasmas using common fuels. However, plans to construct the Two-Component Torus (TCT) have created a need for reactivities to characterize fusion via high-energy beams interacting with low-temperature target plasmas. Such reactivities are derived in the present paper for a variety of fuels including  $D\rightarrow T$ ,  $D\rightarrow^3\text{He}$ ,  $D\rightarrow D$ ,  $T\rightarrow T$ ,  $T\rightarrow^3\text{He}$ , and  $p\rightarrow^{11}\text{B}$ . Some examples of the use of these reactivities in two-component calculations are also described.

(Fusion Reactivities; Two-Component Torus (TCT); Fusion Energy Multiplication; Advanced Fusion Fuels; Fusion Cross Sections; Doppler Effect)

## Introduction

With the steadily increasing research in fusion, a need has developed for a convenient collection of both fusion cross sections and reactivities (i.e.  $\langle\sigma v\rangle$  values). Averaged reactivities are employed in the computation of fusion rates which, for species 1 and 2, are by definition given as  $n_1 n_2 \langle\sigma v\rangle_{1,2}$ . The average indicated must be over the appropriate energy distribution of the reacting species. Until recent years, most of the interest was directed towards fusion in thermalized plasmas that could be accurately represented by a Maxwellian ion distribution function. Thus plots of reactivities averaged over Maxwellian distributions are reasonably available<sup>1,2</sup>, at least for the more common fusion fuels such as D-T, D-D, and D- $^3\text{He}$ . Plans to construct a Two-Component Torus (TCT)<sup>3</sup> have generated a need for reactivities which describe fusion between high-energy beams and a target Maxwellian plasma, the dominant fusion process in the TCT. This requirement motivated the present work.

## Reactivity Calculations

In general, the reactivity is defined as:

$$\langle\sigma v\rangle = \int_{\vec{v}_1} \int_{\vec{v}_2} f_1(\vec{v}_1) f_2(\vec{v}_2) |\vec{v}| \sigma(|\vec{v}|) d\vec{v}_1 d\vec{v}_2 \quad (1)$$

where  $f_1(\vec{v}_1)$  and  $f_2(\vec{v}_2)$  are the velocity distributions of the two fusing species (normalized to unity),  $\vec{v} = \vec{v}_1 - \vec{v}_2$  is the relative velocity of the two species, and  $\sigma(|\vec{v}|)$  is the fusion cross section for the reactants. For the normal Maxwellian plasma with equal ion temperatures, T, this expression reduces to:

$$\langle\sigma v\rangle = \frac{4}{\sqrt{2\pi m_1}} \left( \frac{\mu}{m_1 kT} \right)^{3/2} \int_0^\infty dE E \sigma(E) \exp\left(-\frac{\mu E}{m_1 kT}\right). \quad (2)$$

Here the energy variable, E, is given as  $m_1 v^2/2$  where v is the relative velocity, while the reduced mass of the two fusing ions is given by  $\mu$ . For completeness, we have evaluated this "Maxwellian" reactivity and it is shown in Fig. 1. Since these results are based on the same cross sections that are employed later for beam-target reactivities, this provides a means of

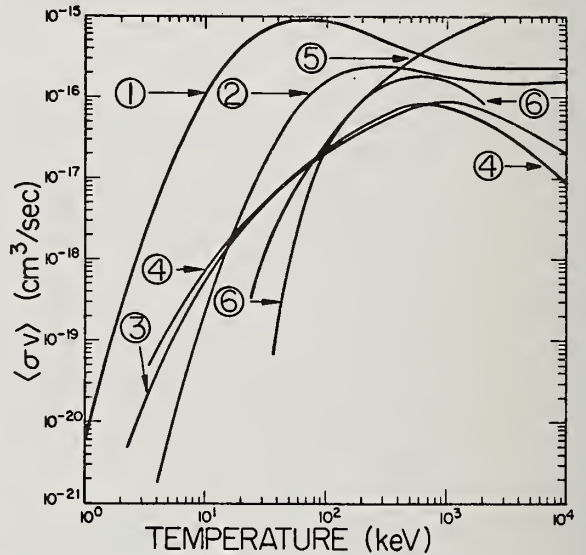


Fig. 1. Reactivities for fusion in a Maxwellian plasma of temperature  $T_i \equiv T$ . Here the curves correspond to: 1.  $T(d,n)^4\text{He}$ ; 2.  $^3\text{He}(d,p)^4\text{He}$ ; 3.  $D(d,p)T$ ; 4.  $T(t,2n)^4\text{He}$ ; 5.  $T(^3\text{He},x)^4\text{He}$  (where  $x=p+n$ , or  $d$ , or  $p$  and  $y = ^4\text{He}$  or  $^5\text{He}$ ); and 6.  $^{11}\text{B}(p,2^4\text{He})^4\text{He}$ .

comparing the present cross section set to that used by others.<sup>1,2</sup> In general, the agreement is good although some slight differences are observed.

The first five reactions shown were evaluated using a fit to experimental cross section data developed by Duane<sup>4</sup>, namely:

$$\sigma(E) = [E\{\exp(A1\sqrt{E})-1\}]^{-1} [A2/\{1+(A3xE-A4)^2\}+A5]. \quad (3)$$

Here E refers to the relative energy of the incident ion in eV and the values of the constants A1 through A5 are tabulated in Refs. 4 and 5. The cross section for the  $p\text{-}^{11}\text{B}$  reaction was obtained by fitting the data of Jarmie and Seagrave<sup>6</sup> in energy segments as described in Ref. 5. These fits, shown in Fig. 2, are thought to be accurate to within a few percent over the energy range involved. All of the cross sections exhibit a characteristic resonance; and compared to the

\* Work performed under auspices of E.R.D.A.



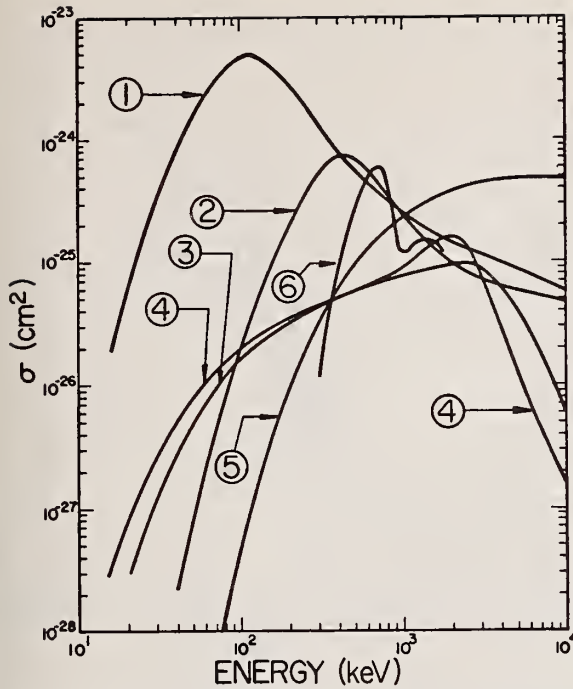


Fig. 2. Fusion cross sections. The curve numbers correspond to reactions listed in Fig. 1.

"standard" D-T cross section, several of the fuels such as p-<sup>11</sup>B and D-<sup>3</sup>He have a narrower resonance width.

While various measurements for the common reactions seem to be in reasonable agreement, there are some noticeable discrepancies in data reported for T-T, T-<sup>3</sup>He, and particularly for p-<sup>11</sup>B. However, the absolute accuracy of the original data used is not certain, so this must be viewed as an unevaluated data set. Tabular presentations from computer print outs of the reactivities and cross section shown in Figs. 1 and 2 are given in Ref. 5 if a more accurate determination is desired.

In the two-component system, fusion occurs as injected high-energy ions slow down in the target plasma. Thus, it is convenient to define an "instantaneous" reactivity corresponding to the reaction between a beam species at velocity  $\vec{v}_0$  and the target plasma at temperature T. As shown later, average fusion rates can then be calculated by integrating the instantaneous reactivity over the slowing down distribution of the injected beam.

In this case, the velocity distribution for the target ions (say species 2) is described by a Maxwellian distribution. That is:

$$f_2(\vec{v}_2) = \frac{\beta^3}{\pi^{3/2}} \exp[-(\beta \vec{v}_2)^2] \quad (4)$$

where  $\beta^2 = m_2/(2T_B)$ . Here the temperature of the target (or background) ions is given by  $T_B$  (in energy units) and their mass as  $m_2$ .

Since the beam is assigned an instantaneous velocity  $\vec{v}_0$ , we have, by definition

$$f_1(\vec{v}_1) = \delta(\vec{v}_1 - \vec{v}_0) \quad (6)$$

where  $\vec{v}_0$  is the velocity of the injected beam particles.

After changing the integration variables in Eq. (1) from  $\vec{v}_1$  and  $\vec{v}_2$  to  $\vec{v}_1$  and  $\vec{v}$ , the instantaneous two-component reactivity becomes:

$$\langle \sigma v \rangle_b = \frac{\beta^3}{\pi^{3/2}} \int_{\vec{v}_1} \delta(\vec{v}_1 - \vec{v}_0) d\vec{v}_1 \int_{\vec{v}} \sigma(|\vec{v}|) |\vec{v}| \times \exp(-\beta^2(v^2 + v_0^2 + 2\vec{v}_1 \cdot \vec{v})) d\vec{v}. \quad (7)$$

Here the subscript b is added to distinguish this reactivity from the previous case for Maxwellian fusion [Eq. (2)]. By using spherical coordinates and letting  $\vec{v}_1$  lie in the z direction, the integration over  $\vec{v}_1$  and  $\phi$  can be completed. Then Eq. (7) simplifies to:

$$\langle \sigma v \rangle_b = \frac{2\beta^3}{\sqrt{\pi}} \int_{v=0}^{\infty} \sigma(v) v^3 \times \int_0^{\pi} \exp(-\beta^2(v^2 + v_0^2 + 2vv_0 \cos \theta)) \sin \theta d\theta dv \quad (8)$$

Finally, performing the  $\theta$  integration, the following form for the beam-target reactivity is obtained:

$$\langle \sigma v \rangle_b = \frac{2\beta}{\sqrt{\pi}} \frac{1}{v_0} \int_{v=0}^{\infty} \sigma(v) v^2 \exp(-\beta^2(v^2 + v_0^2)) \times \sinh(2\beta^2 v_0 v) dv. \quad (9)$$

Results from the numerical evaluation of this reactivity, using the cross sections described earlier, are illustrated in Figs. 3a and 3b. Additional results and tabulations may be found in Ref. 5. The  $\langle \sigma v \rangle_b$  curves display a shape characteristic of the resonance behavior of the fusion cross sections. The width (in energy) of the curves is somewhat larger than for the corresponding cross section per se due to the integration over target velocities. However, these reactivities are much more sharply peaked than the normal Maxwellian reactivities of Fig. 1 since the latter involve a second integration over a broad velocity distribution.

For clarity, curves are only shown for two target plasma temperatures,  $T_1 = 0$  and 50 keV. (Results for intermediate temperatures are given in Ref. 5). As described later the temperature effect on  $\langle \sigma v \rangle_b$  is of importance to energy multiplication calculations, and it can be likened to a Doppler effect, i.e. as  $T_B$  increases, the reactivity curves broaden in energy width. This can be understood physically by observing that in the region below the peak in the cross section, the relative ion velocities, on the average, are below the optimum for a maximum reaction rate. Hence when

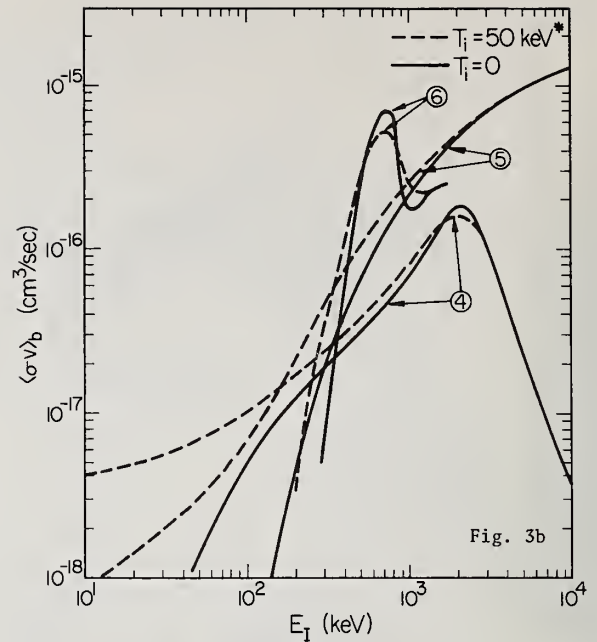
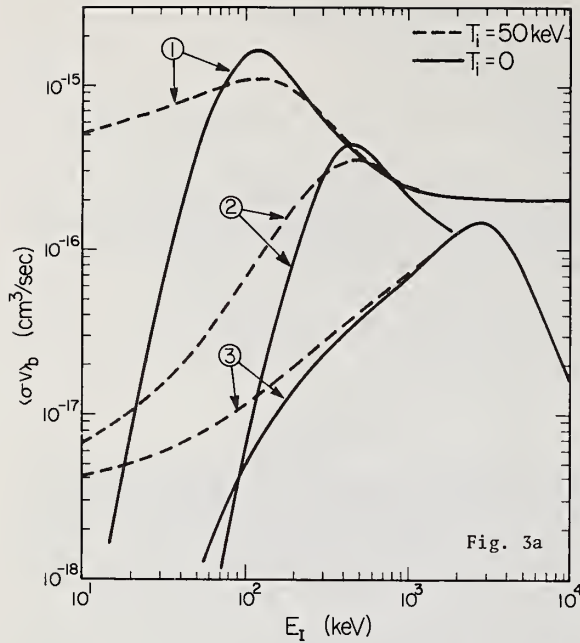


Fig. 3. Instantaneous two-component reactivities. The curve numbers correspond to reactions listed in Fig. 1 except now the first symbol represents the target, e.g.  $T(d,n)^4\text{He}$  indicates D injected into T. (Curves for  $T_i \neq 0$  assume 50 keV except reaction 6 where  $T_i = 100$  keV.)

the target temperature, i.e. velocity increases, the relative ion velocity moves closer to the optimum. Just the reverse effect occurs for energies above the peak.

In the limit where the injection energy is much larger than the background temperature, the relative velocity essentially reduces to the velocity of the injection ion. As a result, the  $\langle \sigma v \rangle_b$  values become temperature independent for large injection energies.

Finally, it should be noted that the maximum values for the two-component reactivities are of the same order of magnitude as that obtained in the usual Maxwellian case. This is important since large power densities are desirable from an economic point of view.

Indeed, Jassby<sup>7</sup> has shown that two-component systems potentially can achieve quite high power densities.

#### Energy Multiplication Calculations

To illustrate the use of these results, the calculation of fusion energy multiplication for two-component operation will be considered. Two types of operation can be envisioned: normal injection into a target plasma or, alternately, injection followed by magnetic compression designed to "clamp" the beam ions at high energies. In the first case the energy multiplication ratio is designated as an F-value while, to distinguish clamping, the term G-value is commonly used in that case. We will briefly consider both.

**F-Value Calculations.** The F-value, defined as the ratio of the total fusion energy produced via beam-target interactions to the energy injected into the plasma, can be written as:

$$F = \frac{n_B Q_f}{E_i} \int_0^{\tau_{SD}} \langle \sigma v \rangle_b dt = \frac{n_B Q_f}{E_i} \int_{E_i}^{E_{th}} \frac{\langle \sigma v \rangle}{|dE/dt|} dE \quad (10)$$

where it is recognized that  $\langle \sigma v \rangle_b$  varies with time, i.e. with the energy of the injected ions as they slow down. Here  $n_B$  is the target ion density,  $Q_f$  is the energy released per fusion reaction, and  $\tau_{SD}$  is the thermalization time, i.e. the time required for an ion injected at energy  $E_i$  to reach the average background plasma energy  $E_{th}$  (for numerical evaluation  $E_{th}$  has arbitrarily been taken as  $2kT_B$ ). The transformation to an energy integration is convenient since it introduces  $|dE/dt|$ , the time rate of energy loss of injected beam ions, which is easily evaluated. This formulation neglects the energy spread or dispersion of the injected ions during slowing, but, as noted later, for most cases this is a reasonable approximation.

F-values calculated in this fashion are shown for  $D \rightarrow T$ , i.e. for deuterium injected into a pure tritium target in Fig. 4. [Here and in subsequent sections the convention  $x \rightarrow y$  indicates that species  $x$  is injected into a target plasma of species  $y$ .]

In evaluating Eq. (10) the Fokker-Planck slowing-down model of Sivukhin<sup>8</sup> was used to represent the energy loss rate  $|dE/dt|$ . The curves shown assume a hot electron background plasma but cold ions ( $T_i \sim 0$ ). As originally discussed by Dawson, et al.<sup>9</sup>, the results for  $D \rightarrow T$  are quite favorable and can be achieved with less demanding confinement times than Maxwellian-fusion plasmas with equivalent energy multiplication. For breakeven operation ( $F = 1$ ), for example, TCT operation



requires  $E_I$  of order of 120 keV at  $T_e \sim 5$  keV. However, to reach the Lawson breakeven point (corresponding to a recirculation of the output power at 33% conversion efficiency and reinjection at 100% efficiency),  $F = 2$  is required making considerably higher electron temperatures necessary. For economic electrical production, an energy multiplication approaching 10 is desirable, necessitating higher background temperatures to achieve additional Maxwellian fusion<sup>10</sup>. Still for near-term experiments or for special purpose reactors where high power densities (regardless of recirculation rates) are the goal<sup>7</sup>, two-component operation appears to be quite attractive.

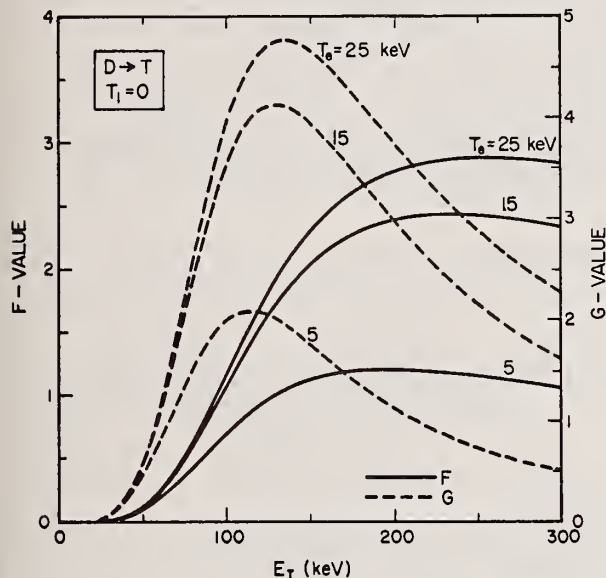


Fig. 4. Energy multiplication for injection of a deuterium beam of energy  $E_I$  into a tritium target plasma of density  $\sim 1 \times 10^{14} \text{ cm}^{-3}$  with electron temperature  $T_e$  and cold ions ( $T_i = 0$ ).

The effect of ion temperature on the F-value has been discussed elsewhere<sup>11</sup> and is illustrated in Fig. 5 for D-T over the range of injection energies expected for early TCT experiments. In this region it is observed that the F-values increase slowly with increasing  $T_i$ . The reason can be explained with reference to Eq. (10). As  $T_i$  increases, the ion drag is reduced, giving a longer thermalization time which is a positive effect. However, the increase in  $\langle \sigma v \rangle_b$  with  $T_i$  for lower energies (cf Figs. 3a and 3b) due to the Doppler effect noted earlier dominates, and the increase in F observed is mainly due to this.

Energy dispersion during thermalization also represents a small correction to the F-value curves of Fig. 5, and an estimate of this effect is shown in Fig. 6. Again a slight increase in F-value is indicated which can be rationalized as follows. To a first approximation the beam dispersion is roughly symmetrical around the average energy. Thus, at energies below the peak in the F-value, the contribution from the high-energy "wing" of the dispersion will outweigh the contribution from the low-energy wing due to the positive slope of the F-value curve in this

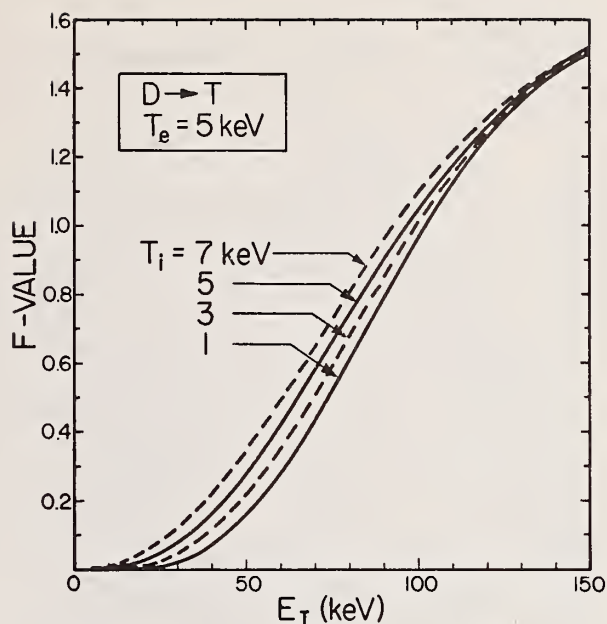


Fig. 5. Illustration of the effect of ion temperature on F-values for D-T.

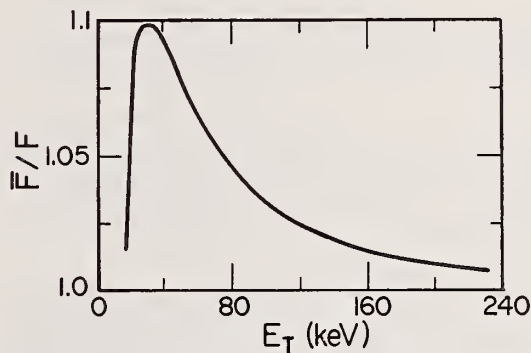


Fig. 6. Ratio of  $\bar{F}$ , the energy multiplication including dispersion, to  $F$ , the value based on the mean energy during slowing. The example shown is for D-T where  $T_e = T_i = 3$  keV at a target density of  $3 \times 10^{13} \text{ cm}^{-3}$ .

region.

In realistic situations, several other corrections must also be included, e.g. small decreases in the F-value are expected due to charge exchange and trapped electron losses under conditions typical of those expected for TCT.

Similar calculations have been carried out for other fuels<sup>11</sup> and the results for D-<sup>3</sup>He shown in Fig. 7 are typical. It is obviously difficult to obtain energy multiplications approaching unity in this case. This is characteristic of non D-T fuels<sup>12</sup>, and although energy breakeven for  $F < 1$  is possible [for example  $F = 0.23$  would provide breakeven with 90% injection and direct conversion efficiencies<sup>13</sup>], attainment of economic operation in this fashion appears as a formidable task. Thus there is a strong incentive to attempt to



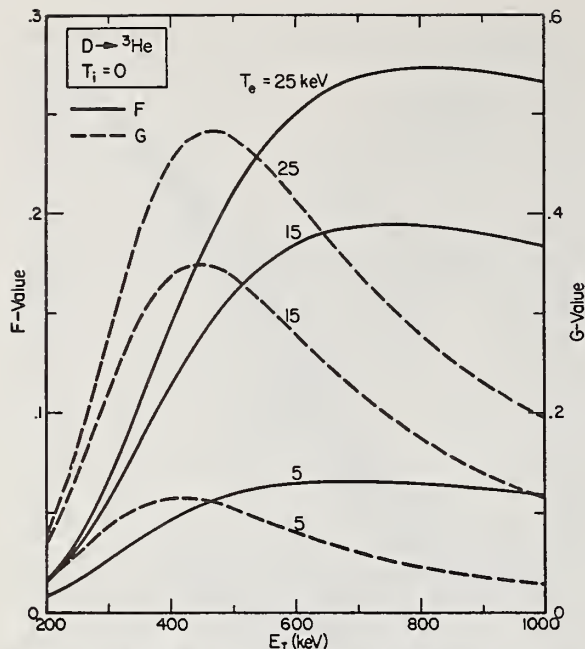


Fig. 7. Energy multiplication for injection of D into pure  $^3\text{He}$  at a target density of  $1 \times 10^{14} \text{ cm}^{-3}$ .

increase the energy multiplication by some technique such as energy clamping<sup>14</sup> or possibly colliding beam techniques<sup>15</sup>.

**Clamping.** In energy clamping magnetic compression or other techniques are employed to supply energy to the beam ions to make up for energy losses due to coulombic drag against the target plasma. In this fashion these ions can be held at high energies, i.e. near the optimum energy for fusion reactions for extended periods of time.

Energy multiplication for the clamped case is defined as the G-value. To illustrate its calculation it is assumed that clamping maintains the high-energy ions for a time long compared to the slowing down time. In that case, the energy associated with injection per se can be neglected compared to the energy required for clamping, and to a good approximation:

$$G \approx \frac{n_B Q_f \langle \sigma v \rangle_b E_I}{|dE/dt|_{E=E_I}} \quad (11)$$

The ions are assumed to be clamped at energy  $E_I$  so both the reactivity and  $|dE/dt|$  are evaluated at that energy.

As seen from Fig. 7, maximum G-values are roughly double the maximum F-values for D-He<sup>3</sup>. Another important advantage of this approach is that the injection energy requirements are almost halved. On the other hand, the large recirculating power associated with clamping must be handled very efficiently to achieve reasonable overall plant performance.

Referring back to Fig. 4, we see that maximum G-values for D-T exceed maximum F-values by factors of order of 1.7. This is somewhat lower than for D-<sup>3</sup>He because the resonance in the fusion cross section for

D-T reactions is less sharply peaked. Even larger factors in  $(G/F)_{\text{max}}$  are obtained for a very sharply peaked cross section such as p-<sup>11</sup>B.

As with normal two component fusion, various small corrections to the G-values shown in the earlier figures should be considered. For example, the effect of the ion temperature is illustrated in Fig. 8 for D-T operation. As might be expected in light of Eq. (11), the temperature effect on the G-value closely follows the Doppler change in  $\langle \sigma v \rangle_b$ . Thus, as in the

case of F-values (Fig. 5), the G-value increases somewhat with increasing  $T_i$  for lower injection energies.

However, now the transition to a negative effect occurs at a somewhat lower injection energy than in the F-value case. This happens because the F-value includes an extra integration over energy [see Eq. (10)]. In that case an ion injected at an energy above the cross-over point in the  $\langle \sigma v \rangle_b$  curve can still provide a net increase in F-values if the positive contribution as the ion slows down through the lower energy region outweighs the initial negative contribution.

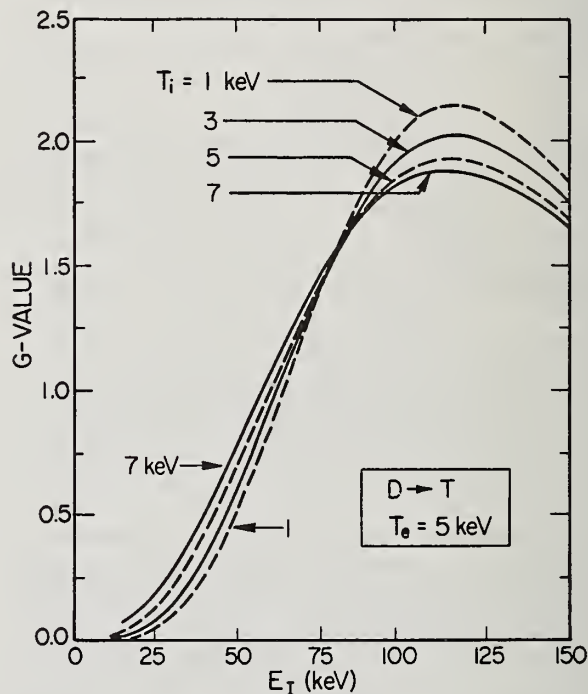


Fig. 8. Illustration of the effect of ion temperature on G-values for D-T.

Ultimately we are interested in obtaining maximum G-values. Unfortunately, in the region of the peak of these curves, the Doppler effect represents a negative contribution. The decrease in G-values is not large however, and, as stressed earlier, various additional small effects must be considered before a final assessment is possible.

### Conclusions

In conclusion, the beam-target plasma reactivities  $\langle \sigma v \rangle_b$  presented in Figs. 3a and 3b have been shown to be extremely useful in two-component fusion calculations. In such cases they replace the conven-

tional Maxwellian reactivities of Fig. 1. Applications of these reactivities to energy multiplication calculations for both normal and clamped two-component operation have been demonstrated and are thought to give reasonably accurate results. However, a number of small corrections such as involved with the ion temperature, energy dispersion and charge exchange during slowing, etc. have been noted that must be included for precision calculations.

Due to space limitations, the reactivities shown here were not complete, but an extensive listing of figures and tables has been included in Ref. 5.

The authors wish to acknowledge the assistance of N. Ivich in compilation of the cross sections and reactivities.

#### References

1. C. F. Barnett, W. B. Gauster, and J. A. Ray, "Atomic and Molecular Collision Cross Sections of Interest in Controlled Thermonuclear Research," ORNL-3113 Rev. Oak Ridge National Laboratory, (1964).
2. S. L. Green, Jr., "Maxwell Averaged Cross Sections For Some Thermonuclear Reactions On Light Isotopes," UCRL-70522, Lawrence Livermore Laboratory, (1967).
3. "TCT - Two Component Torus Joint Conceptual Design Study," Princeton Plasma Physics Laboratory and Westinghouse Electric Corporation, (1974).
4. B. H. Duane, "Fusion Cross Section Theory," in BNWL-1685, Battelle N.W. Laboratories, (1972), p. 57.
5. G. Miley, H. Towner and N. Ivich, "Fusion Cross Sections and Reactivities," AEC Report COO-2218-17, NE Program, Univ. of Illinois, (1974).
6. N. Jarmie and R. Seagrave (eds.), "Charged Particle Cross Sections," LA-2014, Los Alamos Scientific Laboratory, (1957).
7. D. L. Jassby, "Utilization of Fusion Neutrons From Beam-Driven Tokamak Reactors," TM-280, Princeton Plasma Physics Laboratory, (Nov. 1974).
8. D. V. Sivukhin, Reviews of Plasma Physics, (Consultants Bureau, New York, 1966), vol. 4, pp. 93-128.
9. J. M. Dawson, H. P. Furth, F. H. Tenney, Phys. Rev. Lett., 26, 1156 (1971).
10. R. W. Conn, W. A. Houlberg, and J. Kesner, "Parametric Studies of Driven Tokamaks," UWFD-106, Univ. of Wisconsin, (June 1974).
11. H. Towner, G. Miley, D. Jassby, and F. Tenney, Bull. Am. Phys. Soc., Ser. II, 19, 876 (1974).
12. C. Bathke, H. Towner and G. Miley, Trans. Am. Nucl. Soc., 17, 41 (1973).
13. G. Miley and H. H. Towner, "Energy Multiplication in Two-Component Plasmas," in AEC Report COO-2218-18, NE Program, Univ. of Illinois (1974).
14. D. L. Jassby and H. P. Furth, "Two-Energy-Component Fusion Reactors With Sustained Suprathermal-Ion Energy," MATT-1048, Princeton Plasma Physics Laboratory, (May 1974).
15. R. M. Kulsrud and D. L. Jassby, "Neutralized Colliding - Beam Toroidal Fusion Reactors," MATT-1114, Princeton Plasma Physics Laboratory (Jan. 1975).

# APPLICATION OF BONDARENKO FORMALISM TO FUSION REACTORS\*

Patrick D. Soran and Donald J. Dudziak

Theoretical Division  
Los Alamos Scientific Laboratory  
University of California  
Los Alamos, New Mexico 87544

The Bondarenko formalism used to account for resonance self-shielding effects (temperature and composition) in a Reference Theta-Pinch Reactor is reviewed. A material of interest in the RTPR blanket is  $^{93}\text{Nb}$ , which exhibits a large number of capture resonances in the energy region below 800 keV. Although Nb constitutes a small volume fraction of the blanket, its presence significantly affects the nucleonic properties of the RTPR blanket. The effects of self-shielding in  $^{93}\text{Nb}$  on blanket parameters such as breeding ratio, total afterheat, radioactivity, magnet-coil heating and total energy depositions have been studied. Resonance self-shielding of  $^{93}\text{Nb}$ , as compared to unshielded cross sections, will increase tritium breeding by  $\sim 7\%$  in the RTPR blanket, and will decrease blanket radioactivity, total recoverable energy, and magnet-coil heating. Temperature effects change these parameters by less than 2%. The method is not restricted to the RTPR, as a single set of Bondarenko f-factors is suitable for application to a variety of fusion reactor designs.

(Bondarenko; self-shielding; fusion reactors; f-factors;  
Reference Theta-Pinch Reactor; tritium breeding; niobium)

## Introduction

The Bondarenko formalism<sup>1</sup> to account for resonance self-shielding effects was first introduced in 1964. This formalism is generally called the f-factor method. For a given material, the group self-shielding factor,  $f$ , is defined as:

$$f \equiv \frac{\text{resonance - shielded cross section}}{\text{infinite - dilution cross section}} \quad (1)$$

In theory,  $f$  is a function of all the parameters (temperatures, atom densities, and resonance parameters) which define the total macroscopic cross section of the mixture. However, in practice, the f-factors are specified as a function of temperature and a single parameter,  $\sigma_0$ , which represents a conglomerate effect of the remaining parameters of the mixture. The f-factors account for flux depression in the vicinity of resonances. As is shown, the formalism adopts a neutron spectrum which is valid whenever the density of collisions in a given energy range is weakly energy-dependent.

Resonance self-shielding factors (f-factors) can be calculated with a multigroup processing code such as MINX<sup>2</sup> for discrete temperatures (T) and  $\sigma_0$  values. By creating multigroup f-factor tables with parameters T and  $\sigma_0$ , one can provide a general cross-section file which can be used for the analysis of many cases.

## Background

This paper is primarily concerned with the neutronic analysis of the Reference Theta-Pinch Reactor (RTPR).<sup>3</sup> A cutaway perspective view of the RTPR is given in Fig. 1. The RTPR has a minor radius of 0.5m and a major radius of 56m; the blanket is 0.39m thick and the blanket and coils together are 1.42m thick. Natural lithium is the blanket coolant, and blanket neutron multiplication is due primarily to the  $^9\text{Be}(n,2n)$  reaction. The graphite region serves to moderate high-energy neutrons for additional tritium breeding in the  $^6\text{Li}$  region, as well as to protect the implosion and compression coils from neutron and gamma-ray radiation damage.

One material of interest in the RTPR blanket is  $^{93}\text{Nb}$  - the requirements for niobium in the blanket have

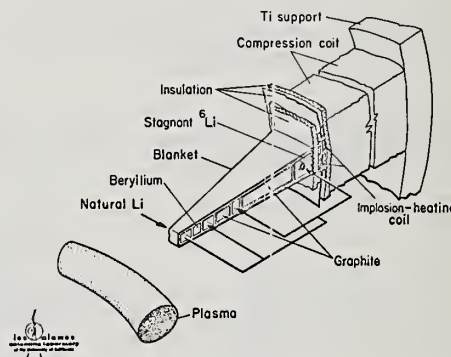


Fig. 1. Cutaway Perspective of Reference Theta-Pinch Reactor.

already been discussed.<sup>4,5</sup> Although niobium constitutes a small volume fraction of the blanket, its presence significantly affects the breeding potential,<sup>6,7</sup> energy deposition, afterheat and radioactivity of the blanket.<sup>8</sup> The reason for niobium's major effect on blanket parameters is the large number of resolved resonances in the energy region below 8 keV. This is explicitly illustrated in Fig. 2. Consequently, it is important to accurately represent the cross-section detail of niobium in a blanket nucleonic analysis.

This paper employs f-factor tables which have been generated by the MINX code using ENDF/B-III data.<sup>9</sup> After determining the proper  $\sigma_0$  in each energy group and the corresponding temperature, self-shielded multigroup data sets were obtained and applied in RTPR blanket nucleonic calculations. Gerstl and Henryson<sup>7</sup> performed similar detailed calculations of the resonance self-shielding in niobium, using the MC2-2 code<sup>10</sup> and  $\sigma_0$  values averaged over the resolved energy region of niobium.

## Calculational Model

The one-dimensional cylindrical model of the RTPR,

\* Work performed under the auspices of the U.S. Atomic Energy Commission



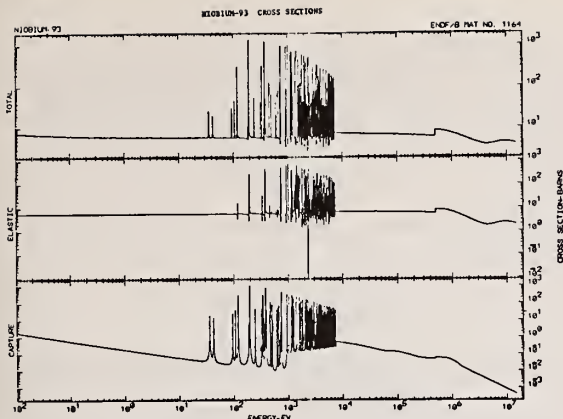


Fig. 2. Niobium-93 Total, Elastic and Capture Cross Sections

as schematically illustrated in Fig. 3, was used for all analyses. Radii are in centimetres, and the definition of the mixture classifications are given in Fig. 4. The concept of a mixture classification is convenient for displaying f-factor and differential results later in this paper. The temperature of the blanket is assumed to be a uniform 1 100 K, since no detailed temperature profile data were available for the original RTPR calculations (unshielded niobium).

All analyses were performed using the LASL CTR Nuclear Analysis System<sup>11</sup> depicted in Fig. 5. As shown in Fig. 5, the neutron transport calculations were

Region	Material	No.	Radius	MIXTURE CLASSIFICATION
Plasma		1	15.0	A
Vacuum		2	49.97	A
Alumina Liner		3	50.0	B
First Wall		4	50.1	B
Li Coolant		5	53.1	C
Nb		6	53.2	C
Be		7	55.7	C
Nb		8	55.8	C
Li Coolant		9	60.3	D
Nb		10	60.4	D
Alumina		11	60.43	D
Nb		12	60.53	D
Graphite		13	64.87	E
Nb		14	64.97	E
Alumina		15	65.0	E
Nb		16	65.1	E
Li Coolant		17	67.6	F
Nb		18	67.7	F
Alumina		19	67.73	F
Nb		20	67.83	F
Graphite		21	82.57	G
Nb		22	82.67	G
Alumina		23	82.7	G
Nb		24	82.8	G
Enriched <sup>6</sup> Li		25	85.2	H
Nb		26	85.3	H
Li Coolant		27	86.3	H
Nb		28	86.4	H
Enriched <sup>6</sup> Li		29	88.8	H
Nb		30	88.9	H
Alumina		31	90.9	H
Impl. Coil		32	92.9	H
Alumina		33	94.9	H
Comp. Coil		34	134.9	H
Ti		35	140.0	H
Alumina		36	142.0	H



Fig. 3. Region Specification for Reference Theta-Pinch Reactor (Mark II Nucleonic Model).

DESCRIPTION	ISOTOPES	MIXTURE CLASSIFICATION
VACUUM	VACUUM	A
ALUMINA (PURE)	O:AL AL	B
NIObIUM WALLS	O:AL Nb	C
LITHIUM COOLANT	<sup>6</sup> Li: <sup>7</sup> Li:O AL:Nb	D
BERYLLIUM	<sup>9</sup> Be:O AL:Nb	E
ALUMINA	O:AL Nb	F
GRAPHITE	C:O AL:Nb	G
ENRICHED <sup>6</sup> Li	<sup>6</sup> Li: <sup>7</sup> Li:O AL:Nb	H

\*EXCLUDES COILS AND T<sub>1</sub> SUPPORTS, ALSO ALL MIXTURES AT 1073 K (800°C) ALTHOUGH CROSS SECTIONS GENERALLY AT 0 K



Fig. 4. Material Specification for Reference Theta-Pinch Reactor (Mark II Nucleonic Model).

performed with the DTF-IV discrete-ordinates code<sup>12</sup> using S<sub>4</sub> angular quadrature in a one-dimensional cylindrical geometry. A uniformly distributed volumetric source of 14.1-MeV neutrons was placed in the plasma region, and a vacuum outer boundary condition was used. Adequacy of the S<sub>4</sub>-P<sub>3</sub> analysis (as compared to S<sub>12</sub>-P<sub>3</sub>) for most integral quantities of interest has been shown previously<sup>13</sup> for a CTR blanket benchmark.

Analysis of the blanket reaction rates (both neutron and gamma) was performed using the TR3 code,<sup>14</sup> as illustrated in Fig. 5. The analysis employs the neutron

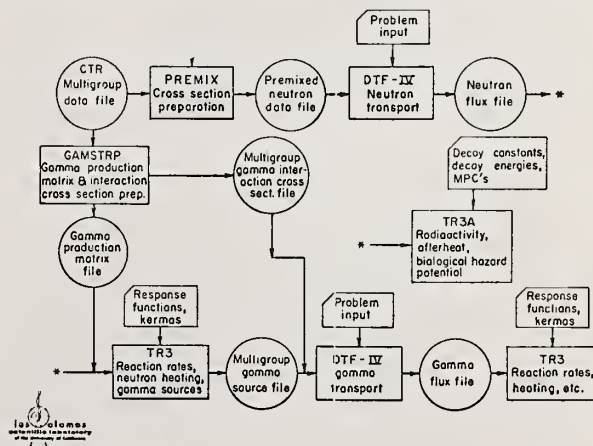


Fig. 5. LASL CTR Nuclear Analysis System.

or gamma-ray flux spatial-spectral distributions computed by the DTF-IV code, and convolutes the calculated fluxes with various response functions to determine reaction rates of interest.

Radioactivity and afterheat are calculated using the TR3A code illustrated in Fig. 5. Neutron or gamma-ray flux files from DTF-IV are employed, along with appropriate decay energies and constants from Ref. 15.

#### Data and Data Processing

The present analysis employs 100-multigroup  $P_3$  cross-section data.<sup>16</sup> Niobium is the only material for which f-factor tables were generated; all other cross sections in the blanket were assumed to be at 0 K and infinite dilution. Other sources of data and data processing are depicted in Fig. 6. The only modification to Fig. 6 is that of an additional code to perform the proper T and  $\sigma_0$  interpolation within the f-factor tables.

Prior to explaining the method of T and  $\sigma_0$  interpolation, it is appropriate to describe how f-factors are generated using the MINX code. One can describe a multigroup (G) resonance self-shielded cross section as

$$\sigma_x^G(\sigma_0, T) \equiv \frac{\int_G dE \sigma_x(E, T) C(E) / (\sigma_t(E, T) + \sigma_0)}{\int_G dE C(E) / (\sigma_t(E, T) + \sigma_0)}, \quad (2)$$

where: E = energy (eV)

T = temperature (K)

C(E) = background neutron spectrum (1/E + D-T peak)

$\sigma_t(E, T)$  = total cross section at energy E and temperature T

$\sigma_0$  = background cross section (at this point discrete values of 1, 10, 100 and 1000)

$\sigma_x(E, T)$  = cross section of type X (generally total, elastic, capture, and possibly fission) at energy E and temperature T.

The infinite-dilution multigroup cross section is calculated using Eq. (2) with  $\sigma_0$  set to infinity, and T set to zero or some other reference temperature. One can see from Eq. (2) that the multigroup cross sections

are being weighted by the reciprocal of the total macroscopic cross section. The f-factor is then defined by Eq. (1). Tables of f-factors are then generated as a function of temperature and  $\sigma_0$  value; in principle, the generation only has to be performed once and the library can then be applied to the analysis of many problems.

The parameter  $\sigma_0$  is the total cross section per atom, that is

$$\sigma_{o,j}^G = \frac{1}{N_j} \sum_{k \neq j} N_k \sigma_{t,k}^G(\sigma_0, T) \quad (3)$$

where:  $\sigma_{o,j}^G$  = the background cross section for isotope j and group G

$N_i$  = number density of isotope i (i = j, k)

$\sigma_{t,k}^G(\sigma_0, T)$  = the total cross section for isotope k at background  $\sigma_0$  and temperature T.

Since the  $\sigma_0$  of each isotope in a material (mixture classification) cannot be obtained until the total cross section is determined, it is necessary to iterate for each energy group to obtain the f-factor and the total cross section. (Segev<sup>17</sup> has suggested a technique for eliminating the iteration process). Having the proper temperature and  $\sigma_0$  value for a material, one can determine the resonance-shielded cross section by interpolation in the f-factor tables. We have assumed that the temperature behavior can be expressed as:

$$f(T) = A + B \ln T \quad (4)$$

and that the  $\sigma_0$  behavior can be computed as:<sup>18</sup>

$$f(\sigma_0) = C \tanh \left[ D(1/\sigma_0 + E) \right] + F \quad (5)$$

The calculated  $\sigma_0$  values and capture f-factors are presented for mixtures D, E and G in Figs. 7 thru 12. We have omitted similar plots for mixtures C and F since they merely represent very thin regions within the blanket, and for mixture H because it lies in a region where the epithermal flux has been reduced by two orders of magnitude. Having obtained the appropriate f-factor for a particular isotope and reaction type in an energy region, the shielded cross section is then determined to be the product of the appropriate f-factor and the infinite-dilution cross section. The shielded transfer matrix is formulated, in this study, by shielding the elastic transfer matrix with the elastic f-factor and adding the shielded matrix to all other transfer processes.

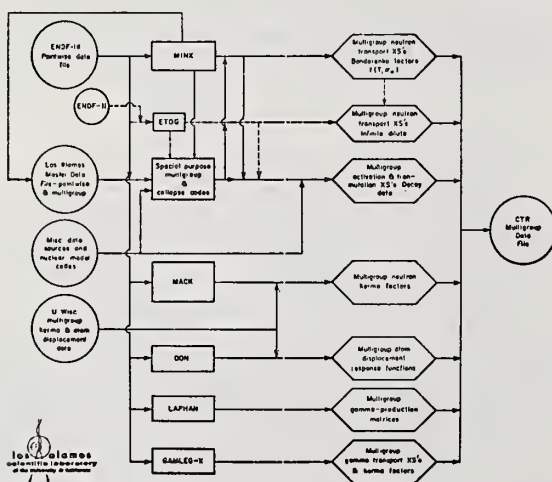


Fig. 6. CTR Multigroup Data Preparation System.

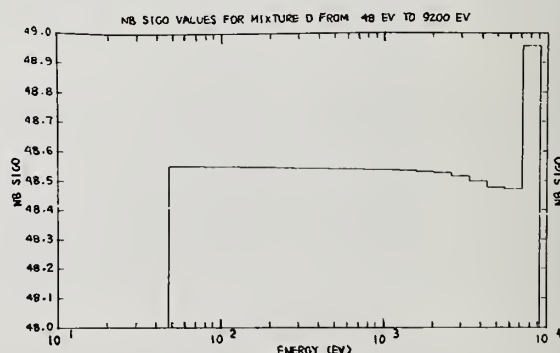


Fig. 7. Background Cross Section for Mixture D.

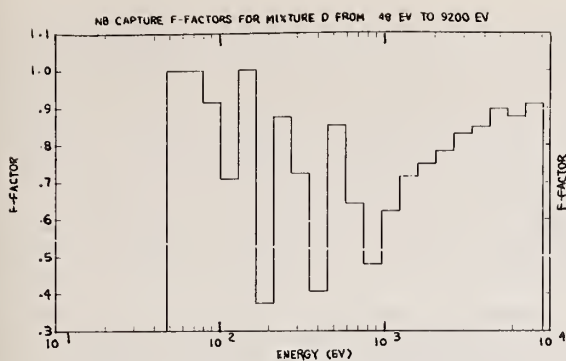


Fig. 8. Capture f-factors for Mixture D.

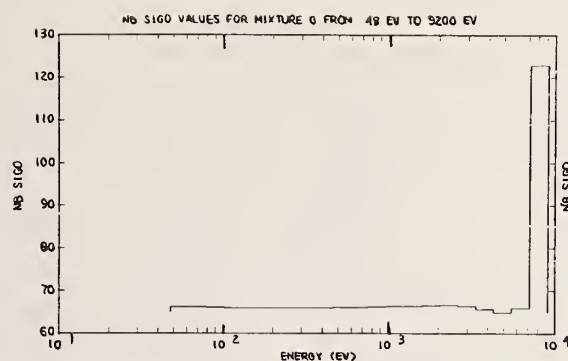


Fig. 11. Background Cross Section for Mixture G.

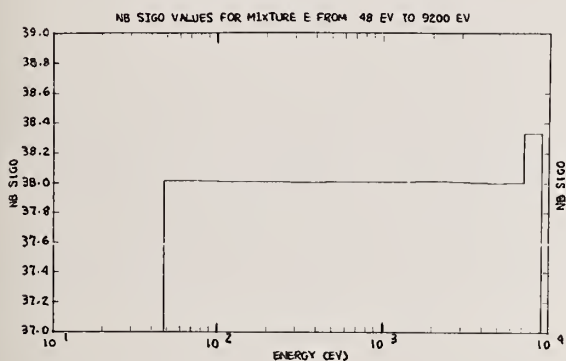


Fig. 9. Background Cross Section for Mixture E.

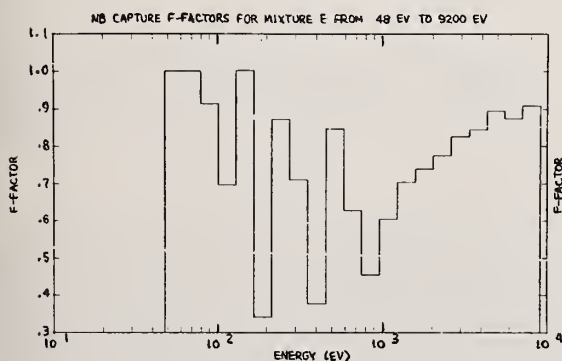


Fig. 10. Capture f-factors for Mixture E.

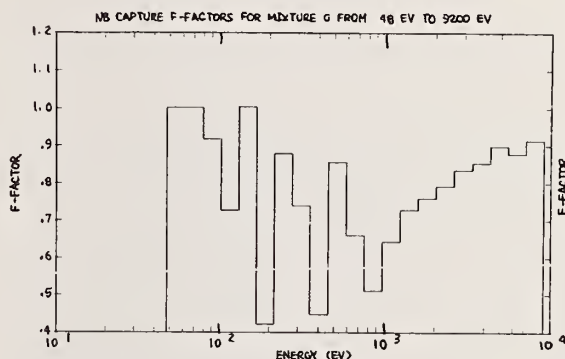


Fig. 12. Capture f-factors for Mixture G.

The use of the Bondarenko formalism creates a new level of data handling, because there has to be a set of microscopic data for each mixture in which self-shielding might occur. Furthermore, additional processing is required to find the proper f-factor corresponding to the mixture temperature and  $\sigma_0$  value (as per Eq. (3)). The latter process is the most time consuming in that the  $\sigma_0$  calculation is iterative and data have to be handled several times. We investigated the consequence of fixing the  $\sigma_0$  value at an estimated average value (in this case at 100) and compared the results of  $f(\sigma_0(\text{calculated}))$  and  $f(\sigma_0 \text{ at } 100)$ . The results of this analysis for mixture D, E and G are graphically illustrated in Figs. 13 through 15. The abscissa of Figs. 13 through 15 ("REL DIFF") is the percentage difference relative to the f-factors using  $\sigma_0$  (calculated).

### Results

Data presented in Table I verify the assumption that resonance self-shielding will increase the tritium breeding ratio by ~7% in the RTPR blanket, as based upon Bell's analysis.<sup>4</sup> The reason for this large change in tritium breeding is clear when one examines the decreased niobium absorption and increased  ${}^6\text{Li}(n,\alpha)$  reaction rates at 1 100 K compared to 0 K, as shown in Table I. Also shown in the table is the decrease of total energy deposited in the blanket and coils, per D-T neutron. This 2.5% decrease from 24.5 to 23.9 MeV may, from an economic point of view, be more significant than the increase in tritium breeding. In fact, the



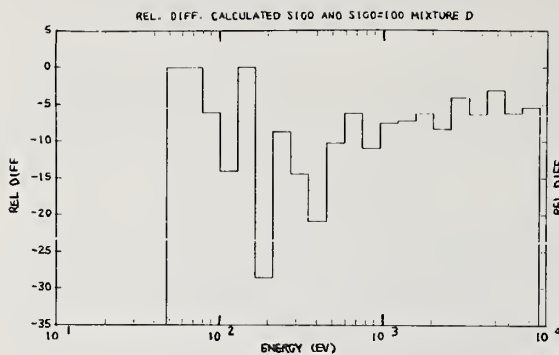


Fig. 13. Relative Difference (%) in Calculated and Estimated f-factors for Mixture D.

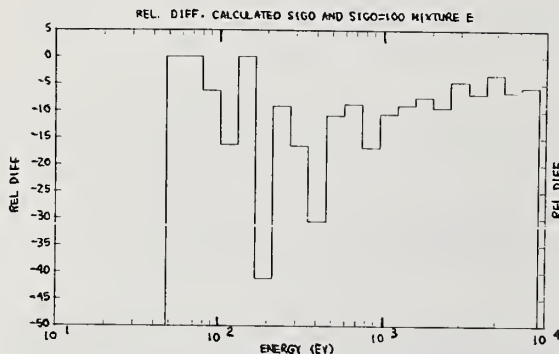


Fig. 14. Relative Difference (%) in Calculated and Estimated f-factors for Mixture E.

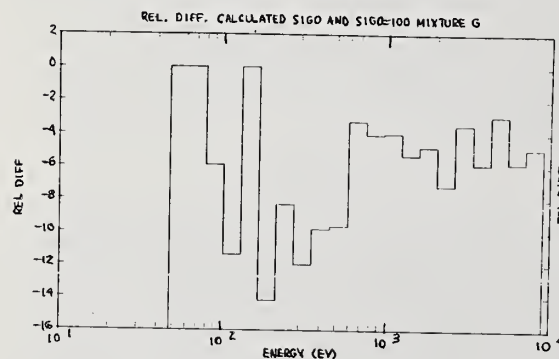


Fig. 15. Relative Difference (%) in Calculated and Estimated f-factors for Mixture G.

two processes are competitive, with the decreased gamma-ray energy from niobium radiative capture only partially compensated for by the relatively low Q-value of the  ${}^6\text{Li}(n,\alpha)$  reaction. Three other important results of resonance self-shielding are illustrated in Table I: 1) the large (11%) decrease in short-term  ${}^{95}\text{Nb}$  radioactivity, 2) the decreased afterheat caused by decreased  ${}^{95}\text{Nb}$  activity, the dominant contributor,<sup>15</sup> and 3) the 14% decrease in coil heating caused by decreased niobium radiative capture gamma-rays. These selected examples illustrate the importance of resonance self-shielding in calculations of blanket integral nucleonic parameters.

In addition, the analysis presented here examined the temperature dependence of these same blanket nucleonic parameters. Results for calculations at 300 K and 1 100 K, both accounting for resonance self-shielding by means of the Bondarenko formalism, are shown in Table I. All differences in integral results were 2% or less, indicating a weak dependence on temperature. Thus, if differences between cold reactor (300 K) and average operating temperature (1 100 K) are <2%, temperature spatial distribution in the blanket will have a second-order effect on self-shielding. There will, however, be temperature effects on atom densities and region dimensions that are not demonstrated in Table I.

Differential results as a consequence of self-shielding have also been examined. We have illustrated two of these results: 1) effects of self-shielding in the total absorption reaction rate as a function of mixture for group 73 (275 to 354 eV), and 2) the neutron spectrum (shielded and unshielded) for group 73 as a function of blanket radius. See Figs. 16 and 17, respectively, and Table II for results where  $\sigma_0 = 100$ .

TABLE I  
SELECTED NUCLEONIC EFFECTS

SELECTED NUCLEONIC EFFECTS IN A RTMR BLANKET  
AS A FUNCTION OF RESONANCE SELF-SHIELDING

TEMPERATURE (K)	%	REFLECTING RATIO	NB ABS.	CU ABS.	${}^6\text{Li}(n,\alpha)\text{T}$	(A) TOTAL NEUTRON ENERGY (MEV)
0		1.024	0.374	9.66-2	0.862	14.60
300	VARIABLE	1.116	0.283	9.70-2	0.953	15.07
1100	VARIABLE	1.095	0.303	9.69-2	0.933	14.98

	(B) TOTAL GAMMA ENERGY (MEV)	(B) GAMMA ENERGY IN CU COILS (MEV)	(C) CI/MT 94 NB	95 NB	(C,D) P/PO(%)
0	9.90	1.65	1.56-3	1.26	1.17
300	8.99	1.43			
1100	8.92	1.42	1.10-3	1.12	1.04

(A) TOTAL NEUTRON ENERGY DEPOSITED IN THE BLANKET AND COILS, PER D-T NEUTRON.

(B) GAMMA ENERGY DEPOSITED PER D-T NEUTRON.

(C) OPERATING TIME IS 20 Y, REPRESENTATIVE OF COIL LIFETIME AND RECYCLED (4 TIMES) NB STRUCTURES, AND SHUTDOWN TIME IS ZERO.

94  $\text{Nb}(n,\gamma)$  CROSS SECTION IS MEDIUM ESTIMATE (CF. REF. (9)).

(D) AFTERHEAT FROM NB AND CU ACTIVATION AT SHUTDOWN AS PERCENTAGE OF OPERATING POWER.



TABLE II

EFFECTS OF RESONANCE SELF-SHIELDING IN ABSORPTION RATES FOR ENERGY GROUP 73(275.4 to 353.6 eV)

Mixture	Region	$\phi\Sigma a$ (shielded)	$\phi\Sigma a$ (unshielded)	Rel Diff %
C	6	3.852-4	4.165-4	7.4
D	7	8.557-4	9.198-4	6.9
E	9	7.686-4	8.407-4	8.6
F	11	5.030-6	5.339-6	5.8
G	13	7.637-4	8.256-4	7.5
H	25	3.552-5	4.013-5	11.5

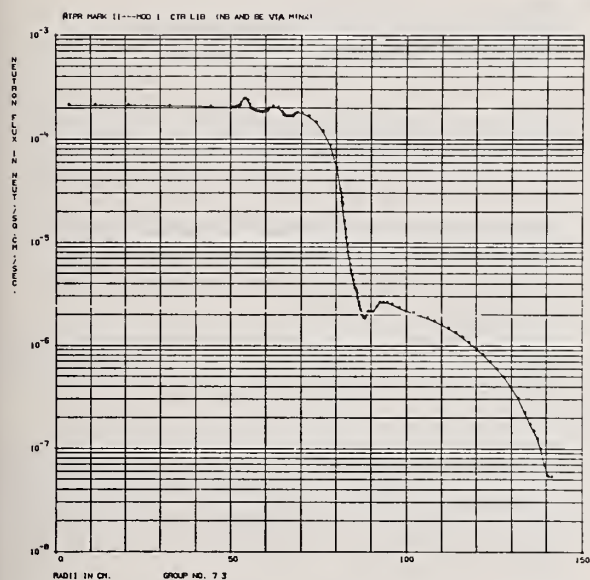


Fig. 16. Shielded Neutron Spectrum in RTPR Blanket for Group 73.

The decrease in the total absorption rate for the shielded case is a consequence of the large decrease in the niobium capture cross section as compared to the small increase in the neutron flux illustrated in Fig. 16.

### Conclusion

In summary, the Bondarenko formalism has been applied to RTPR blanket nucleonic analysis, and it was shown that resonance self-shielding will increase the tritium breeding ratio by ~7%. This is in excellent agreement with other analyses.<sup>4,7</sup> Additionally, niobium self-shielding will decrease blanket short-term radioactivity, total recoverable energy and magnet coil heating. Temperature effects on self-shielding change these parameters by less than 2%.

The Bondarenko formalism is not without its limitations and some of these should be investigated, e.g., strong spatial effects of nearby regions, group-to-group energy transfer of neutrons (i.e. should one use the same shielding factor for transfer of neutrons

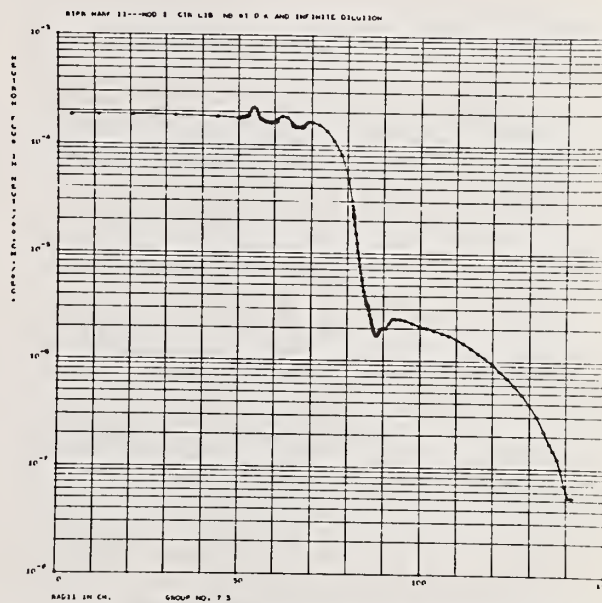


Fig. 17. Unshielded Neutron Spectrum in RTPR Blanket for Group 73.

from group 1 to 1 as from group 1 to 2, etc.), and the possibility of mixture f-factors. However, these are not severe restrictions and the Bondarenko formalism can be a useful tool for future nucleonic analysis of fusion reactors. The generality of the f-factor tables makes them especially suitable for "universal" multi-group data sets, to be applied to a variety of fusion reactor concepts at different laboratories. The only requirement is that the set of  $\sigma_0$  and  $T$  values in the f-factor tables span the expected ranges for these parameters in practical fusion reactor designs.

# REFERENCES

1. I. I. Bondarenko, et al., "Group Constants for Nuclear Reactor Calculators," Consultants Bureau Enterprises, Inc., New York (1964).
2. C. R. Weisbin, P. D. Soran, R. E. MacFarlane, R. J. LaBauve, D. R. Harris and J. S. Hendricks, "MINX - A Multigroup Interpretation of Nuclear Cross Sections from ENDF/B," Los Alamos Scientific Laboratory report, to be published.
3. R. A. Krakowski, F. L. Ribe, T. A. Coultas and A. J. Hatch (eds.), "An Engineering Design Study of a Reference Theta-Pinch Reactor (RTPR)," joint Argonne National Laboratory and Los Alamos Scientific Laboratory report ANL-8019/LA-5336 (1974).
4. G. I. Bell, "Neutron Blanket Calculations for Thermonuclear Reactors, II," Los Alamos Scientific Laboratory report LA-4131-MS (April 1969).
5. J. M. Bunch, F. W. Clinard, Donald J. Dudziak, W. V. Green, and R. A. Krakowski, "An Evaluation of Major Material Problems Anticipated for the Reference Theta-Pinch Reactor (RTPR)," Proc. 5th Symp. on Engrg. Problems of Fusion Research, Princeton, NJ, (Nov. 6-9, 1973).
6. Donald J. Dudziak, "Discrete-Ordinates Neutronic Analysis of a Reference Theta-Pinch Reactor (RTPR)," Proc. Symp. Technology of Controlled Thermonuclear Fusion Exper. and Engrg. Aspects of Fusion Reactors, Austin, TX, p. 884, CONF-721111 (Nov. 20-22, 1972).
7. S. Gerstl and H. Henryson, II., "The Effect of Resonance Self-Shielding in Niobium Structures on Tritium Breeding in CTR Blankets," Trans. Am. Nucl. Soc. 18, 25 (1974).
8. Donald J. Dudziak and R. A. Krakowski, "A Comparative Analysis of D-T Fusion Reactor Radioactivity and Afterheat," Proc. First Top. Mtg. Technology of Controlled Nucl. Fusion, San Diego, CA, CONF-740402 (April 16-18, 1974).
9. M. K. Drake, "Data Formats and Procedures for the ENDF/B Neutron Cross Section Library," Brookhaven National Laboratory report BNL 50274 (T-601), ENDF-102, Vol. 1 (October 1970).
10. B. J. Toppel and H. Henryson, II, "Methodology and Application of the MC<sup>2</sup>-2/SDX Cross Section Capability," Trans. Am. Nucl. Soc. 16, 126 (1973).
11. Donald J. Dudziak, "Fusion Reactor Nuclear Analysis Methods and Applications," Proc. Eighth Symp. on Fusion Technology, Noordwijkerhout, The Netherlands, (June 17-21, 1974).
12. K. D. Lathrop, "DTF-IV, A Fortran-IV Program for Solving the Multigroup Transport Equation with Anisotropic Scattering," Los Alamos Scientific Laboratory report LA-3373 (1965).
13. Donald J. Dudziak, "Neutronic Analysis of CTR Blanket Benchmark by Discrete Ordinates," Trans. Am. Nucl. Soc. 15(2), 630 (1972).
14. Donald J. Dudziak, "TR3, A DTF-IV Post-Processor for Thermonuclear Reactor Nucleonics," unpublished LASL code.
15. Donald J. Dudziak and R. A. Krakowski, "Radioactivity Induced in a Theta-Pinch Fusion Reactor," Nuclear Technology, 25, pp. 32-55 (January 1975).
16. D. W. Muir and R. J. LaBauve, "Neutron Cross Sections for Scyllac Reactor Studies," personal communication (T-2-131, June 1972).
17. M. Segev, "The  $\sigma$ -Ambiguity in the Method of Self-Shielding Factors," Trans. Am. Nucl. Soc. 18, 155 (1974).
18. R. B. Kidman, "An Improved F-Factor Interpolation Scheme for IDX," Tran. Am. Nucl. Soc. 18, 156 (1974).
19. D. W. Muir and Donald J. Dudziak, "Sensitivity of RTPR Afterheat and Radioactivity to <sup>94</sup>Nb Cross Section Uncertainty," Trans. Am. Nucl. Soc., Vol. 19, 465 (1974).



# NEUTRON CROSS-SECTION MEASUREMENTS ON $^{236}\text{U}$

L. Mewissen, F. Poortmans

S. C. K. / C. E. N.

2400 Mol, Belgium

G. Rohr, J. Theobald, H. Weigmann

Central Bureau for Nuclear Measurements

2440 Geel, Belgium

G. Vanpraet

R. U. C. A.

2000 Antwerp, Belgium<sup>+</sup>

Capture, scattering and total cross-section measurements have been performed on  $^{236}\text{U}$ , over an energy range from 30 eV up to 1.8 keV. The neutron width  $\Gamma_n$  could be determined for 97 levels and the capture width  $\Gamma_\gamma$  for 57 among them. The average radiative width is:  $\bar{\Gamma}_\gamma = [23.0 \pm 0.3 \text{ (stat.)} \pm 1.5 \text{ (syst.)}] \text{ meV}$ . For the s-wave strength function we find:  $S_0^\gamma = (1.05 \pm 0.14) 10^{-4}$ .

(NUCLEAR REACTIONS  $^{236}\text{U}(n, n)$ ,  $^{236}\text{U}(n, \gamma)$ ,  $E = 30 - 1800 \text{ eV}$ ; measured  $\sigma_{n, T}$ ,  $\sigma_{n, \gamma}$ ,  $\sigma_{n, n}$ .  $^{237}\text{U}$  resonances deduced  $\Gamma_n$ ,  $\Gamma_\gamma$ . Enriched target.)

## Introduction

The present experiments have been performed with a time-of-flight spectrometer, using the Linac of CBNM pulsed neutron source. Two types of measurements have been done:

a) Carraro and Brusegan<sup>4</sup> did high resolution transmission experiments on a 100 meter flight path, using 57.8 g  $\text{U}_3\text{O}_8$  enriched to 89.4%  $^{236}\text{U}$ . They deduced neutron widths for 185 levels up to 4.1 keV.

b) We did capture, scattering and total cross section measurements up to 1.8 keV, using two different sample thicknesses.

Previous experiments done in other laboratories were limited to the neutron energy range below 415 eV<sup>1, 2, 3</sup>.

## Experimental Details

Note that our transmission experiments were done with a small sample facility ( $\varnothing 11 \text{ mm}$ ) on a 30 m flight path with 5.4 g  $\text{U}_3\text{O}_8$ , enriched to 99.7%  $^{236}\text{U}$ . The experimental details are listed in table 1. The samples were prepared by settling in alcohol and canning under vacuum between two aluminium plates of a thickness of 0.5 mm<sup>5</sup>. The uranium oxide was on loan from the U. S. A. E. C..

In the partial cross section measurements, only the thick sample run (89.4%  $^{236}\text{U}$ ) was analysed. The homogeneity of the thin powder sample (99.7%  $^{236}\text{U}$ ) was not reliable enough, but the run with this sample was very useful to identify the  $^{236}\text{U}$  resonances. The data collection and reduction was done using the CBNM data acquisition system<sup>6</sup>, which consists of different 4096 channel time-of-flight analysers, interfaced with an IBM 1800 computer.

## Data Handling and Analysis

An area analysis of the transmission data was done using a modified version of the Atta-Harvey program<sup>7</sup>.

The scattering cross-section was measured relative to Pb, for which  $\sigma_n = (11.28 \pm 0.6) \text{ barns}$  was assumed<sup>8</sup>. The data were corrected for self-screening and for absorption of the scattered neutrons. For this correction, it was assumed that any second interaction was an absorption. This approximation was not valid for some strong resonances below 500 eV so that for these cases, the resonance parameters  $\Gamma_n$  and  $\Gamma_\gamma$  were deduced from the capture and transmission results only.

The capture experiments were performed on a 60 meter flight path station. The shape of the neutron flux was measured with a  $^{10}\text{B}$  slab viewed by a NaI crystal; the  $^{10}\text{B}(n, \alpha)^7\text{Li}^*$  cross-section is assumed to vary as  $E^{-1/2}$  in the energy range of interest. The absolute calibration of the product detector efficiency times neutron flux was done by observing capture in black resonances of Ag at 5.2, 16.3, 51.4 and 70.9 eV. The resonance analysis was done with a capture area analysis program due to Fröhner and Haddad<sup>9</sup>.

## Results and Discussion

The individual resonance parameters  $\Gamma_n$  and  $\Gamma_\gamma$  are listed in table 2. From the comparison with the results of Carlson et al.<sup>2</sup> we see that:

a) two small levels at 243 eV and 367.8 eV are detected by Carlson but not in any one of our experiments.

b) for about 80 percent of the resonances the  $\Gamma_n$  values of Carlson agree with the present results within

Table 1: Experimental Details

	Transmission	Capture	Scattering
burst width	22 ns	32 ns	32 ns
burst frequency	400 Hz	400 Hz	400 Hz
flight path length	$(31.22 \pm .02) \text{ m}$	$(60.53 \pm .02) \text{ m}$	$(31.10 \pm .02) \text{ m}$
time-of-flight resolution	1.5 - 5.1 ns/m	0.7 - 6.7 ns/m	$\Delta E/E \approx 2 \times 10^{-3}$
sample thicknesses	$7.6 \times 10^{-3} \text{ at/b}$	$2.15 \times 10^{-4} \text{ at/b}$ ; $1.5 \times 10^{-3} \text{ at/b}$	see Capture
total quantity	5.4 g $\text{U}_3\text{O}_8$	5.4 g $\text{U}_3\text{O}_8$ ; 57.8 g $\text{U}_3\text{O}_8$	
enrichment	99.7% $^{236}\text{U}$	99.7% $^{236}\text{U}$ ; 89.4% $^{236}\text{U}$	
detector	$^3\text{He}$ gaseous scintillator	Moxon-Rae	$^3\text{He}$ gaseous scintillators

<sup>+</sup> Work performed at CBNM Geel in the frame of the Euratom-SCK/CEN Mol association contract.

the given error limits. There is a disagreement of about 40% in the neutron widths for two strong resonances at 272.8 and 379.8 eV.

The error on the  $\Gamma_n$ -values which is quoted in table 2 is the sum of two contributions: the statistical error and a normalization error of 5 percent on the capture cross-section measurements.

The following statistical properties have been deduced from the set of resonance parameters:

1) The mean reduced neutron width  $\bar{\Gamma}_n^0$  for the resonances analyzed below 1200 eV is from the present experiments:  $\bar{\Gamma}_n^0 = (2.03 \pm 0.34) \text{ meV}$ . The relative error is given as  $1.4/\sqrt{n}$ ,  $n$  being the number of levels. The degree of freedom of the distribution of the experimental  $\Gamma_n^0$  values has been calculated with the maximum-likelihood method and found to be:  $\nu = (1.5 \pm 0.1)$ . This is an indication that we missed some small resonances. In fact, if we introduce 10 levels with a reduced neutron width  $\Gamma_n^0$ , smaller than 1 percent of the average value  $\bar{\Gamma}_n^0$ , we find  $\nu = 1$ .

2) The mean level spacing  $\bar{D}$ , found from the resonance energies up to 1.2 keV is:  $\bar{D} = (16.1 \pm 0.5) \text{ eV}$  (fractional uncertainty =  $\frac{2}{n}$ ). In order to correct for missed levels one can use the method of Fuketa and Harvey<sup>10</sup>. Some small resonances are not detected because of the finite experimental resolution and the statistical accuracy in the accumulated counts. With a limit of detectability  $\delta(E) = 8 \cdot 10^{-8} \text{ eV}$  we find that:  $\bar{D}_{\text{corr}} = (15.2 \pm 0.5) \text{ eV}$ . Expressed in number of levels it means that 4 small resonances escaped detection in the measured energy range.

We have also examined the possibility that the deviation from  $\nu = 1$  in the experimental  $\Gamma_n^0$ -values came from the fact that some levels were excited by p-wave neutrons. According to reference<sup>11</sup>, among 40 of our smallest  $\Gamma_n$ -values, only three of them might fall in this category.

3) We have calculated the value for the s-wave strength function  $S_0$ , based on 97 levels analyzed below 1.8 keV:  $S_0 = (1.05 \pm 0.14) 10^{-4}$  (fractional uncertainty =  $\frac{1.4}{\sqrt{n}}$ ). This figure is in agreement with the value found by Carlson,  $S_0 = (1.02 \pm 0.4) 10^{-4}$  and with the recent result of Carraro et al.<sup>4</sup>  $S_0 = (1.00 \pm 0.1) 10^{-4}$ .

4) The most important result from our experiments is probably the average radiative width  $\bar{\Gamma}_\gamma$ :  $\bar{\Gamma}_\gamma = [23.0 \pm 0.3 \text{ (stat.)} \pm 1.5 \text{ (syst.)}] \text{ meV}$ .

We have estimated an additional systematic error of about 7 percent on the mean capture width. This error is due to uncertainties in the sample thickness, the flux measurement in the capture experiments, the multiple scattering corrections and the base-line determination in the area analysis. All these sources of possible uncertainties, except the sample thickness, are more or less dependent on neutron energy. In fact, we have noticed a slight increase in the  $\Gamma_\gamma$ -values with increasing energy, what is probably due to one or more of the experimental errors mentioned above.

The mean capture width obtained by Carlson et al.,  $\bar{\Gamma}_\gamma = (23.9 \pm 1.0) \text{ meV}$ , is in good agreement with our result. Carlson et al. do not add a systematic error and their mean value was obtained for 12 resonances.

Comparing the distribution of the experimental  $\Gamma_\gamma$ -values with a chi-square distribution allows us to calculate the number of degrees of freedom for the radiative widths, according to reference<sup>12</sup>. We find  $\nu = 83 \pm 12$ , a typical value for actinides.

### Acknowledgements

The authors wish to thank Dr. Nève de Mévergnies and Dr. K. H. Böckhoff for the continuous interest in this work. They are grateful to Dr. Verdingh for the sample preparations. The support from the data handling and linac operation teams at CBNM and from the electronic and mechanical engineering groups at SCK/CEN and CBNM, is also very much appreciated.

### References

1. J. Harvey, D. Hughes, Phys. Rev. **109**, (1958) 471.
2. A. D. Carlson, S. Friesenhahn, W. Lopez, M. Fricke Nucl. Physics, Vol. **A141** (1970) 577.
3. R. A. Harlan, Report IN-1317, 10 (1970).
4. G. Carraro, A. Brusegan, to be published.
5. V. Verdingh, Nucl. Instr. and Methods **102** (1972) 431.
6. A. De Keyser, S. de Jonge, T. van der Veen, P. ter Meer, Proceedings of the International Symposium on Nuclear Electronics, Paris (1968).
7. W. Kolar, EUR report 4760, e (1972).
8. L. A. Rayburn, E. O. Wallan, Nucl. Physics **61** (1965) 381.
9. F. H. Fröhner, E. Haddad, G. A. Report 5137 (1964).
10. T. Fuketa, J. A. Harvey, Nucl. Instr. and Methods, Vol. **33** (1965) 107.
11. L. M. Bollinger, G. E. Thomas, Phys. Rev. Vol. **171** n° 4 (1968).
12. W. Kolar, J. P. Theobald, J. A. Wartena, Proceedings of the Knoxville Conference (1971).

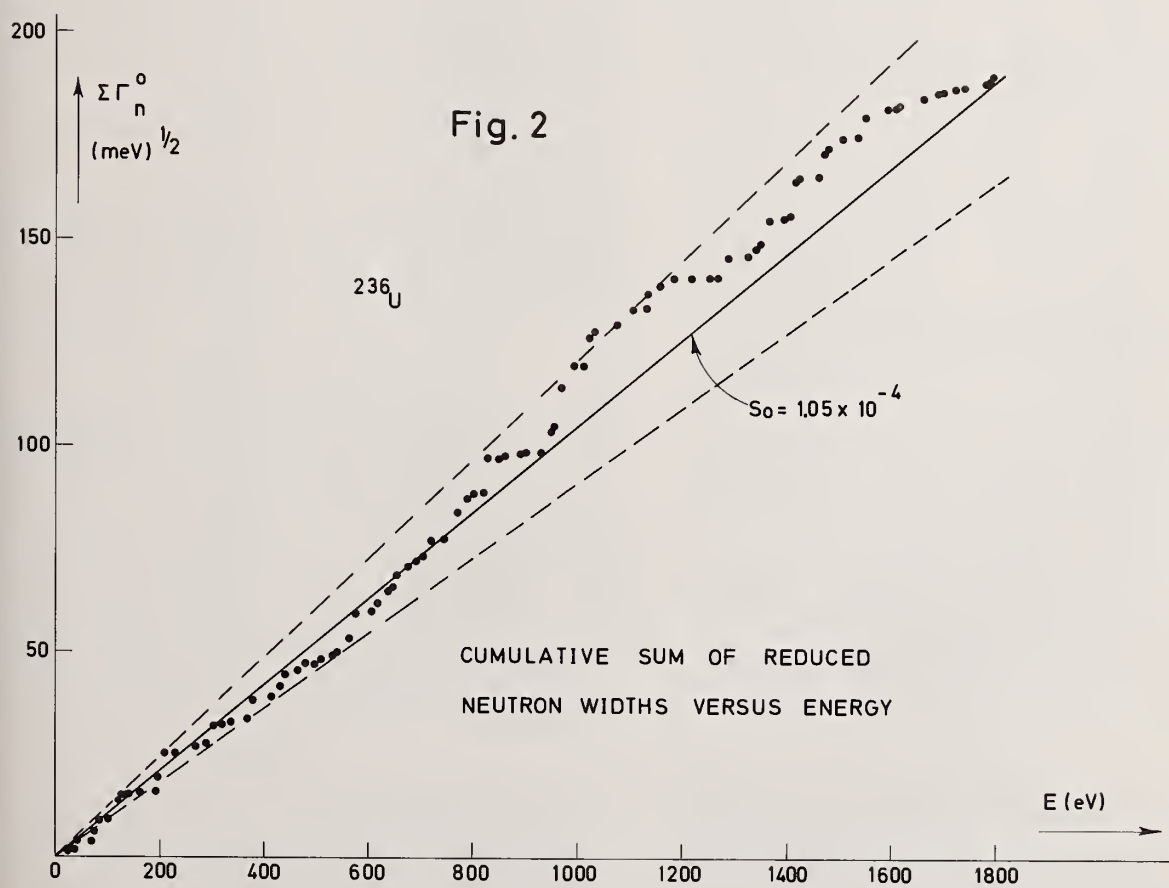
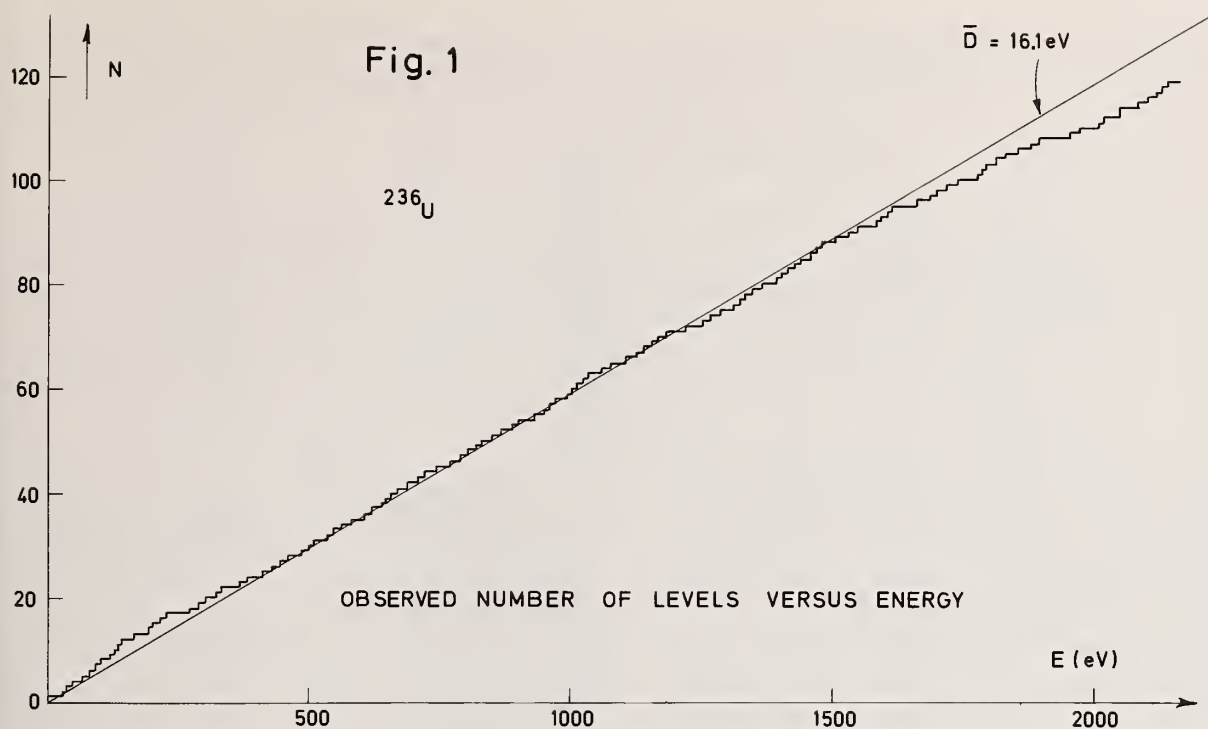




Table 2: Resonance parameters of  $^{236}\text{U}$ 

$E_o$ (eV)	$\Gamma_n$ (meV)	$\Gamma_n^o$ (meV)	$\Gamma_\gamma$ (meV)
5.45 <sup>2</sup>	2.16 $\pm 0.08$	0.925	24.5 $\pm 1.0$
29.7 <sup>2</sup>	0.585 $\pm 0.03$	0.107	
34.12	2.4 $\pm 0.12$	0.411	
43.90	15. $\pm 0.7$	2.26	19.2 $\pm 2$
64.29	0.037 $\pm 0.005$	0.005	
71.47	18.5 $\pm 2.0$	2.19	22. $\pm 2$
86.51	28. $\pm 1.5$	3.01	20. $\pm 1.6$
102.3	0.88 $\pm 0.04$	0.09	
120.9	50. $\pm 2.$	4.55	20. $\pm 1.5$
124.9	17. $\pm 0.5$	1.52	19. $\pm 2.6$
134.4	1.2 $\pm 0.04$	0.10	
137.8	0.57 $\pm 0.03$	0.05	
164.6	2.1 $\pm 0.08$	0.16	
192.8	9.0 $\pm 0.3$	0.65	
194.3	44. $\pm 1.3$	3.16	20. $\pm 1.5$
212.7	85. $\pm 4$	5.83	22.8 $\pm 1.5$
229.6	2. $\pm 0.12$	0.13	
272.8	31. $\pm 1.5$	1.88	23.5 $\pm 1.8$
288.6	11.5 $\pm 1.$	0.68	25. $\pm 8.5$
303.1	77. $\pm 3.$	4.42	22. $\pm 1.5$
320.5	5.4 $\pm 0.3$	0.30	
334.9	6.2 $\pm 0.4$	0.34	
357			
371.2	13.5 $\pm 1.5$	0.70	24. $\pm 4.7$
379.8	91. $\pm 4.$	4.67	22. $\pm 1.5$
415.4	15.7 $\pm 0.6$	0.77	22. $\pm 4.5$
430.9	60. $\pm 2.5$	2.89	22. $\pm 1.5$
440.6	62. $\pm 2.5$	2.95	24. $\pm 1.6$
465.5	13.9 $\pm 0.7$	0.64	18. $\pm 6.2$
478.4	37. $\pm 2.0$	1.69	21. $\pm 1.5$
500.3	2.4 $\pm 0.4$	0.11	
507.1	19. $\pm 1.$	0.84	22. $\pm 3.4$
536.5	30. $\pm 3.$	1.30	22. $\pm 2.4$
542.9	10.3 $\pm 0.5$	0.44	30. $\pm 8.8$
563.8	80. $\pm 4.$	3.37	22. $\pm 1.5$
576.2	142. $\pm 10.$	5.92	26. $\pm 1.8$
607.0	13.3 $\pm 0.7$	0.54	20. $\pm 8.2$
617.8	52. $\pm 5.$	2.09	24. $\pm 1.8$
637.9	78. $\pm 8.$	3.09	24. $\pm 1.7$
647.1	6. $\pm 1.$	0.24	
655.6	96. $\pm 8.$	3.75	23. $\pm 1.9$
673.7	54.5 $\pm 5.$	2.10	24. $\pm 2.4$
691.3	32. $\pm 1.$	1.22	27. $\pm 3.4$
706.1	28.7 $\pm 1.$	1.08	21. $\pm 2.4$
720.7	97. $\pm 3.$	3.61	21. $\pm 1.5$
746.5	20.4 $\pm 1.$	0.75	18. $\pm 2.4$
770.9	181. $\pm 15.$	6.52	22. $\pm 1.5$
789.6	85. $\pm 6.$	3.03	23. $\pm 1.9$
806.5	38.6 $\pm 1.6$	1.36	24. $\pm 2.4$
820.0	9. $\pm 1.$	0.31	
827.4	237. $\pm 20.$	8.24	28. $\pm 2$
848.2	2. $\pm 1.$	0.07	
865.1	17. $\pm 1.$	0.58	19. $\pm 2.6$
888.3	7.5 $\pm 1.$	0.25	

Table 2: Continued

$E_o$ (eV)	$\Gamma_n$ (meV)	$\Gamma_n^o$ (meV)	$\Gamma_\gamma$ (meV)
900.1	4.4 $\pm 1.$	0.15	
930.4	6. $\pm 2.$	0.20	
948.6	162. $\pm 6.$	5.26	24. $\pm 1.9$
955.2	35. $\pm 5.$	1.13	
969.4	300. $\pm 20.$	9.64	23. $\pm 2.3$
998			
994.7	150. $\pm 15.$	4.76	22. $\pm 1.7$
1013	16. $\pm 1.5$	0.50	
1024	237. $\pm 15.$	7.41	26.5 $\pm 2.5$
1032	29.5 $\pm 6.$	0.92	28. $\pm 6.3$
1065	35. $\pm 2.$	1.07	29. $\pm 6.2$
1075	13. $\pm 3$	0.40	
1084			
1098			
1104	122. $\pm 15.$	3.67	25. $\pm 2.3$
1132	11.5 $\pm 2.$	0.34	
1136	120. $\pm 12.$	3.56	21.5 $\pm 2.3$
1157	63. $\pm 6.$	1.85	26. $\pm 2.4$
1166			
1184	57. $\pm 6.$	1.66	25. $\pm 2.4$
1219	5. $\pm 1.5$	0.14	
1254	7. $\pm 2.$	0.20	
1269	5. $\pm 4.$	0.14	
1282			
1291	162. $\pm 16.$	4.51	30.5 $\pm 4.3$
1316			
1324	20. $\pm 4.$	0.55	
1339	67. $\pm 7.$	1.83	24. $\pm 2.8$
1349	51. $\pm 5.$	1.39	32. $\pm 5.3$
1364	212. $\pm 25.$	5.74	29. $\pm 5.2$
1395	12. $\pm 4.$	0.32	
1405	35. $\pm 10.$	0.93	
1414	300. $\pm 60.$	7.98	21. $\pm 4.1$
1426	28. $\pm 6.$	0.74	
1440			
1458	15. $\pm 3.$	0.39	
1470	220. $\pm 30.$	5.74	27. $\pm 4.2$
1477	26. $\pm 5.$	0.68	
1506	105. $\pm 15.$	2.71	26. $\pm 4.2$
1534	13. $\pm 3.$	0.33	
1548	180. $\pm 20.$	4.58	22. $\pm 4.1$
1592	91. $\pm 10.$	2.28	26. $\pm 4.2$
1610	13. $\pm 3.$	0.32	
1614	8. $\pm 2.$	0.20	
1660	85. $\pm 10.$	2.09	28. $\pm 4.2$
1690	48. $\pm 10.$	1.17	26. $\pm 4.3$
1699	15. $\pm 3.$	0.36	
1723	24. $\pm 5.$	0.58	
1738	14. $\pm 3.$	0.34	
1779	45. $\pm 10.$	1.07	
1788	13. $\pm 5.$	0.31	
1794	60. $\pm 15.$	1.42	
1813	26. $\pm 10.$	0.61	

# p-WAVE ASSIGNMENT OF $^{238}\text{U}$ NEUTRON RESONANCES

F. Corvi, G. Rohr, H. Weigmann  
Central Bureau for Nuclear Measurements  
2440 Geel, Belgium  
and  
Comitato Nazionale per l'Energia Nucleare  
Bologna, Italy

A method of p-wave assignment of  $^{238}\text{U}$  resonances is presented, consisting of measuring the fraction of capture  $\gamma$ -rays above 4.3 MeV for neutron resonances in the range 10 - 1600 eV. In this way, 57 resonances showing an enhancement of the high energy  $\gamma$ -ray yield, were identified as p-waves. In addition, a capture cross-section measurement was performed on a  $6.32 \cdot 10^{-3}$  at/barn thick sample in order to obtain the  $g\Gamma_n^1$  values of such small resonances. The derived final estimates of the p-wave strength function  $S_1$  and of the s-wave level spacing  $D_0$  are:  $S_1 = (2.3 \pm 0.5) \cdot 10^{-4}$ ;  $D_0 = (22.4 \pm 1.0) \text{ eV}$ .

(NUCLEAR REACTIONS  $^{238}\text{U}(n, \gamma)$ ,  $E = 10 - 1600 \text{ eV}$ ; measured  $\sigma(E; E_\gamma)$  and  $\sigma_{n\gamma}$   $^{238}\text{U}$  deduced resonances,  $\pi$ ,  $g\Gamma_n$ . Enriched targets.)

## Introduction

A good knowledge of the  $^{238}\text{U}$  resonance parameters and related average quantities is important to the calculation of fast reactor parameters and in particular to the determination of self-shielding factors and Doppler effects. Between the several quantities of interest, the value of the p-wave strength function is perhaps the most uncertain one since there is considerable disagreement between the estimates derived from resolved resonance analysis<sup>1</sup> and from average cross section data<sup>2-4</sup>. As regard to the resonance region, the proposed<sup>1,5</sup> discrimination between s and p-waves was only based up to now on purely probabilistic and statistical arguments, namely: a) Bayes' theorem on conditional probability<sup>5</sup> giving the probability that a resonance of given  $g\Gamma_n$  is excited by p-wave neutrons; b) several statistical tests in order to obtain a complete s-wave energy level set following the Gaussian Orthogonal Ensemble theory for single-population level ordering<sup>6</sup>. Although such methods are very valuable in identifying a certain number of p-wave levels, their total final results are not free from ambiguities. In view of this situation, it was felt desirable to develop an experimental approach giving information on the orbital angular momentum of  $^{238}\text{U}$  resonances. To this end, we tried to exploit the parity-dependence of the high energy part of the  $^{238}\text{U}$  capture  $\gamma$ -ray spectrum.

## Description of the Experiment

From an inspection of the  $^{239}\text{U}$  level scheme<sup>7,8</sup>, one may notice that the first negative parity state lies at 739 keV energy. Therefore all possible dipole transitions ending at states of lower energy, will be M1 for s-wave and E1 for p-wave resonances. More specifically, considering only the energy region within 300 keV from the ground state, there are two levels (at 133 keV and 145 keV) reachable by dipole radiation from all s and p-waves and two additional levels with  $J^\pi = 5/2^+$  (the ground state and the 194 keV state) accessible only to p3/2 resonances. Since the ratio between the E1 and the M1 average strength is known<sup>9</sup> to be about 7, then a measurement of the yield of the primary high energy  $\gamma$ -rays leading to such states will show up, on the average, a considerable enhancement of p-wave resonances.

The experiment was performed on a 50 meter flight path of the Geel linac by measuring the fraction of  $^{238}\text{U}$  capture  $\gamma$ -rays above 4.3 MeV as a function of neutron energy, with two large 7"x6" NaI(Tl) detectors. Their resolution was 8.5% on the  $^{137}\text{Cs}$  line. To limit summing of  $\gamma$ -rays in the crystals, their

entrance window was kept at about 20 cm from the sample centre: moreover, about 9 cm of borated polyethylene were added between sample and detectors in order to absorb scattered neutrons. Two measurements were made: the first one with a  $13.9 \text{ g/cm}^2$  thick  $^{238}\text{U}$  plate (containing 0.4% of  $^{235}\text{U}$ ) of size  $10 \times 10 \text{ cm}$  and inclined  $45^\circ$  as respect to the axis of the neutron beam, the second one with a  $4.64 \text{ g/cm}^2$   $^{238}\text{U}$  disc (with 0.2%  $^{235}\text{U}$ ) of 12 cm diameter placed perpendicular to the neutron beam. Most of the data reported here come from the first measurement which had a better statistics; the second one was used in few cases where a better resolution was needed and also for an accurate absolute determination of the resonance energies.

For normalization purposes, each high energy run was followed by a similar run with the lower threshold set at 1.5 MeV. The ratios  $R = A_{4.3}/A_{1.5}$  were

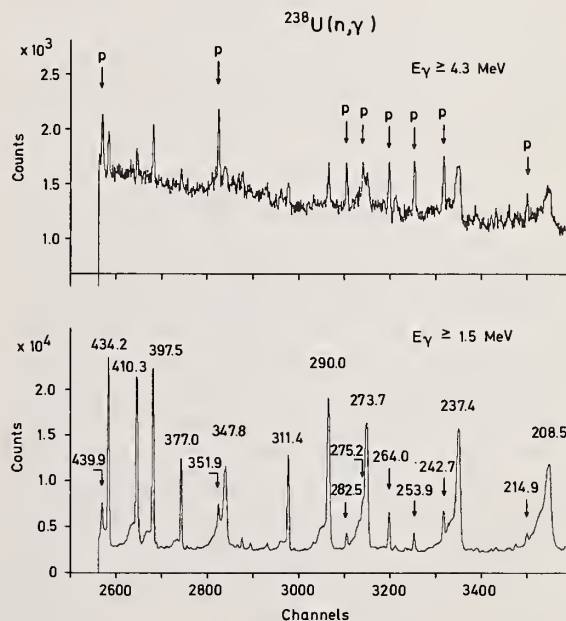


Fig. 1: Time-of-flight spectrum in the range 440-205 eV for the thicker sample runs. All resonances marked with an arrow in the calibration run (lower part) are considerably enhanced in the high-energy run (upper part) with respect to the nearby s-wave resonances

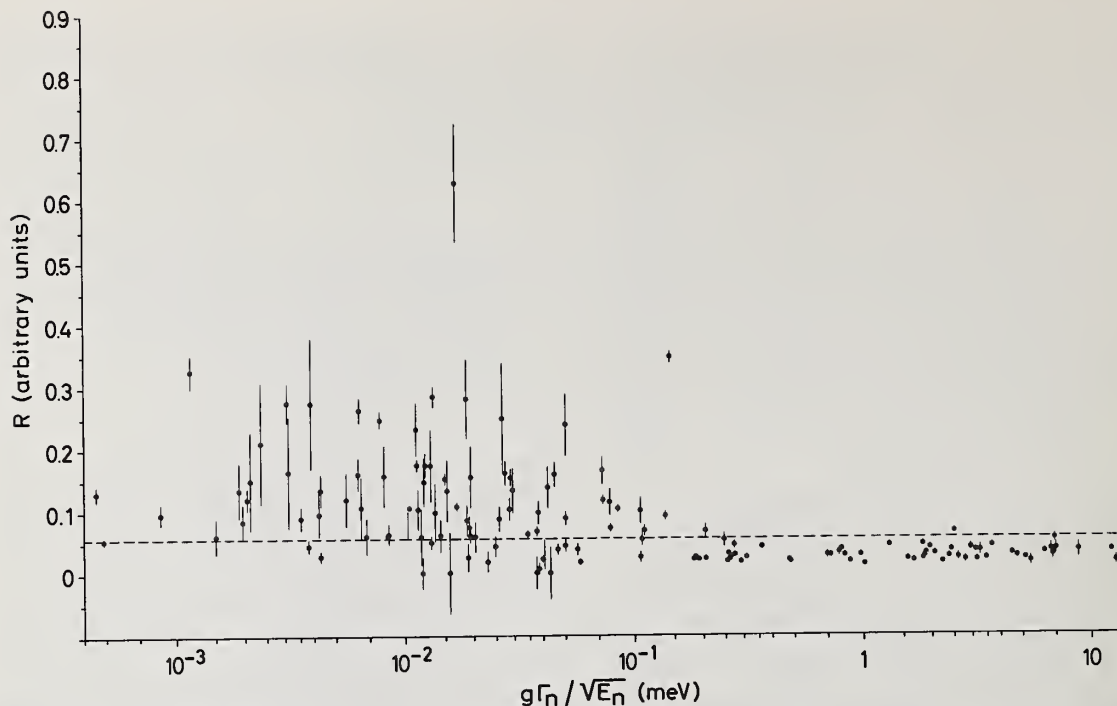


Fig. 2: Plot of R-values against  $g\Gamma_n / \sqrt{E_n}$  for  $^{238}\text{U}$  neutron resonances in the range 10-1600 eV. Values above the dotted line at  $R = 0.055$  are considered to belong to p-waves.

then calculated between the areas of the resonances in the high energy run and the corresponding ones of the calibration run. The magnitude of the parity-dependent effect can be judged from fig. 1, which shows a slice of the time-of-flight spectrum in the range 440 - 205 eV for the two runs with the thicker sample: all resonances marked with an arrow in the lower spectrum are dramatically enhanced in the upper part as compared to the strong s-wave resonances surrounding them.

#### Interpretation of the Results

The ratios  $R$  of resonances in the range 10 - 1600 eV are plotted against  $g\Gamma_n / \sqrt{E_n}$  (eV) in fig. 2: it is readily apparent that high  $R$ -values are found only in relatively weak resonances while all those resonances which are certainly s-waves have low  $R$ -values. This finding strongly supports the basic assumption that p-waves should have an enhanced high-energy spectrum. However, as expected,  $R$ -values exhibit a very large spread due to Porter-Thomas fluctuations of the few transitions considered, so that the  $R$ -values distributions for s and p-waves partly overlap. In order to estimate the confidence level for p-wave assignment as a function of  $R$  and the efficiency of the method used, a more quantitative approach is necessary.

The  $R$ -values given in Fig. 2 have been divided

- 1)  $g\Gamma_n / \sqrt{E_n} > 0.15$  meV and
- 2)  $g\Gamma_n / \sqrt{E_n} < 0.15$  meV.

It is assumed that the first group contains only s-wave resonances while the second group contains mostly p-wave but also a small number of s-wave resonances. The corresponding  $R$ -distributions are presented as histograms in fig. 3. The first group

is fitted with a  $\chi^2$ -function with  $\nu = 2$  degrees of freedom corresponding to the two possible M1 transitions for s-wave resonances. The second group is fitted with a superposition of two  $\chi^2$ -functions with  $\nu = 2$  and  $\nu = 4$  corresponding to the E1 transitions for  $J^\pi = 1/2^-$  and  $J^\pi = 3/2^-$  resonances, respectively. The absence of very small  $R$ -values in the s-wave distribution of fig. 3 can be explained by a  $\gamma$ -ray summing effect in the crystals, which contributes a constant amount estimated to be  $R_c = 0.015$ . Assuming that the same summing effect is present in p-waves, the argument of all  $\chi^2$ -functions can be

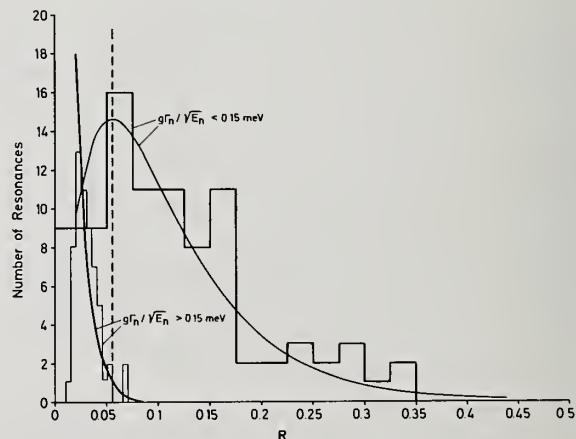


Fig. 3:  $R$ -distributions (histogram) and their fits with  $\chi^2$ -functions for the two different groups of resonances



Table 1: List of resonance parameters for fifty-seven  $^{238}\text{U}$  neutron resonances assigned as p-waves in the present work

$E_0$ (eV)	R	$g \Gamma_n^1$ (meV)
$63.51 \pm 0.10$	$0.10 \pm 0.02$	$3.7 \pm 0.7$
$83.67 \pm 0.10$	$0.32 \pm 0.03$	$3.8 \pm 0.6$
$89.25 \pm 0.10$	$0.106 \pm 0.003$	$31.7 \pm 2.6$
$124.97 \pm 0.12$	$0.12 \pm 0.02$	$4.5 \pm 0.6$
$200.73 \pm 0.10$	$0.090 \pm 0.020$	$4.8 \pm 0.7$
$203.10 \pm 0.10$	$0.085 \pm 0.028$	$2.6 \pm 0.6$
$214.90 \pm 0.10$	$0.28 \pm 0.03$	$3.9 \pm 0.6$
$218.42 \pm 0.10$	$0.14 \pm 0.04$	$2.4 \pm 0.8$
$242.75 \pm 0.10$	$0.18 \pm 0.01$	$12.6 \pm 1.1$
$253.93 \pm 0.10$	$0.25 \pm 0.01$	$8.3 \pm 1.1$
$264.00 \pm 0.10$	$0.11 \pm 0.01$	$17.3 \pm 1.5$
$275.2 \pm 0.2$	$0.061 \pm 0.004$	$8.3 \pm 2.4$
$282.55 \pm 0.15$	$0.26 \pm 0.02$	$6.0 \pm 1.0$
$337.4 \pm 0.2$	$0.16 \pm 0.03$	$5.0 \pm 1.0$
$351.9 \pm 0.2$	$0.29 \pm 0.02$	$10.2 \pm 1.2$
$373.0 \pm 0.3$	$0.15 \pm 0.08$	$1.5 \pm 0.5$
$439.9 \pm 0.2$	$0.15 \pm 0.01$	$9.4 \pm 0.9$
$499.1 \pm 0.3$	$0.31 \pm 0.08$	$2.1 \pm 0.8$
$523.5 \pm 0.2$	$0.18 \pm 0.02$	$6.3 \pm 0.9$
$542.5 \pm 0.14$	$0.14 \pm 0.03$	$2.1 \pm 0.6$
$551.1 \pm 0.4$	$0.16 \pm 0.09$	$1.5 \pm 0.5$
$556.4 \pm 0.3$	$0.07 \pm 0.01$	$18.3 \pm 1.4$
$616.0 \pm 0.3$	$0.11 \pm 0.05$	$2.8 \pm 0.6$
$624.45 \pm 0.20$	$0.064 \pm 0.006$	$14.9 \pm 1.2$
$668.8 \pm 0.3$	$0.16 \pm 0.05$	$3.3 \pm 0.6$
$678.0 \pm 0.2$	$0.14 \pm 0.02$	$11.8 \pm 1.5$
$698.4 \pm 0.3$	$0.15 \pm 0.04$	$4.7 \pm 1.0$
$710.8 \pm 0.4$	$0.16 \pm 0.02$	$17.1 \pm 2.9$
$714.0 \pm 0.3$	$0.23 \pm 0.04$	$4.3 \pm 0.9$

Table 1: (continued)

$E_0$ (eV)	R	$g \Gamma_n^1$ (meV)
$732.8 \pm 0.2$	$0.105 \pm 0.006$	$31.4 \pm 2.7$
$779.6 \pm 0.3$	$0.074 \pm 0.007$	$27.3 \pm 2.5$
$787.5 \pm 0.4$	$0.16 \pm 0.02$	$9.4 \pm 1.0$
$828.9 \pm 0.4$	$0.12 \pm 0.04$	$1.8 \pm 0.6$
$964.7 \pm 0.4$	$0.08 \pm 0.02$	$2.9 \pm 0.7$
$977.6 \pm 0.4$	$0.09 \pm 0.02$	$2.2 \pm 1.0$
$1029.5 \pm 0.3$	$0.12 \pm 0.01$	$19.2 \pm 1.7$
$1047.4 \pm 0.4$	$0.17 \pm 0.06$	$3.4 \pm 0.8$
$1068.1 \pm 0.4$	$0.16 \pm 0.01$	$7.4 \pm 1.6$
$1074.6 \pm 0.4$	$0.10 \pm 0.02$	$7.2 \pm 1.1$
$1082.2 \pm 0.3$	$0.09 \pm 0.01$	$12.5 \pm 1.4$
$1095.6 \pm 0.4$	$0.17 \pm 0.02$	$17.9 \pm 2.2$
$1103.3 \pm 0.3$	$0.12 \pm 0.02$	$19.2 \pm 2.2$
$1131.9 \pm 0.2$	$0.09 \pm 0.01$	$32.7 \pm 3.6$
$1152.9 \pm 0.6$	$0.63 \pm 0.10$	$3.9 \pm 1.2$
$1155.6 \pm 0.3$	$0.25 \pm 0.09$	$6.3 \pm 1.4$
$1220.3 \pm 0.3$	$0.28 \pm 0.06$	$4.1 \pm 1.0$
$1230.5 \pm 0.4$	$0.10 \pm 0.03$	$2.5 \pm 1.0$
$1252.0 \pm 0.3$	$0.09 \pm 0.03$	$4.0 \pm 0.6$
$1277.4 \pm 0.4$	$0.24 \pm 0.05$	$2.7 \pm 1.8$
$1317.7 \pm 0.3$	$0.35 \pm 0.01$	$29.6 \pm 3.0$
$1332.0 \pm 0.3$	$0.10 \pm 0.02$	$7.8 \pm 1.4$
$1387.1 \pm 0.4$	$0.13 \pm 0.05$	$3.0 \pm 0.6$
$1417.5 \pm 0.6$	$0.10 \pm 0.02$	$20.3 \pm 4.1$
$1448.4 \pm 0.6$	$0.14 \pm 0.03$	$7.9 \pm 1.5$
$1511.2 \pm 0.5$	$0.13 \pm 0.04$	$5.3 \pm 0.9$
$1535.6 \pm 0.4$	$0.16 \pm 0.05$	$3.4 \pm 0.7$
$1548.0 \pm 0.5$	$0.07 \pm 0.01$	$19.1 \pm 2.2$

defined as:  $x = \frac{R - 0.015}{R}$ .

The two fits are plotted in fig. 3 as full curves with average values:

- 1)  $\bar{R}_0 = 0.0122$
- 2)  $\bar{R}_1 = 0.0976$ .

The ratio of the average values is 8, in fair agreement with the expected ratio for the E1 and M1 transition strengths<sup>9</sup>.

The vertical dotted line shown in fig. 3 at  $R = 0.055$  is chosen as lower threshold for p-wave selection; in other words, all resonances of the second group with  $R - \Delta R \geq 0.055$  are identified as p-waves.

From the fitting functions of fig. 3, one can estimate a) that an s-wave resonance has a 4% probability of having  $R > 0.055$ .

b) that about 25% of the p-wave resonances have R-values falling below the chosen threshold: this means that the method has a 75% efficiency for p-wave assignment.

In total, 57 resonances were selected as p-waves: their energies and R-values with associated statistical errors are listed in the first two columns of table 1.

#### Neutron Widths of p-Wave Resonances

As for many small resonances which in the present measurement have been detected for the first time, no neutron widths are available in the literature, we have analysed a preliminary measurement of the cap-

ture cross section done in the framework of our  $^{238}\text{U}$  measurement program, to obtain neutron widths for all resonances with  $g \Gamma_n < 10$  meV. This capture cross section measurement was done on a  $2.5 \text{ g/cm}^2$   $^{238}\text{U}$  (0.2% of  $^{235}\text{U}$ ) sample with  $\text{C}_6\text{F}_6$  capture  $\gamma$ -ray detectors, applying the Maier-Leibnitz weighting method to obtain independence of the capture  $\gamma$ -ray cascade. The resonance analysis has been done by an area analysis program containing a Monte Carlo subroutine to calculate the multiple scattering contribution to the resonance area. A renormalization factor has been applied to the data such that the experimental areas for 14 strong s-wave resonances in the range 100 eV to 1700 eV are in agreement with the capture areas calculated with the area analysis code from known resonance parameters<sup>10</sup>. The neutron widths obtained for the resonances assigned as p-wave in the present work, are included in table 1. The effective nuclear radius used was  $R = 8.74 \text{ fm}$ .

The results of the present analysis are generally in good agreement with earlier data<sup>1,11</sup> for resonances with  $\Gamma_n > 0.5 \text{ meV}$ . For smaller resonances, neutron widths obtained here tend to be larger than those of ref.<sup>1</sup>, the discrepancy increasing with decreasing  $\Gamma_n$ .

#### Estimate of $D_0$ and $S_1$

The aim of the present investigation was to obtain an improved value for the p-wave strength function  $S_1$ . In order to arrive at this aim, fits to the neutron width distributions have been done in the way described below.

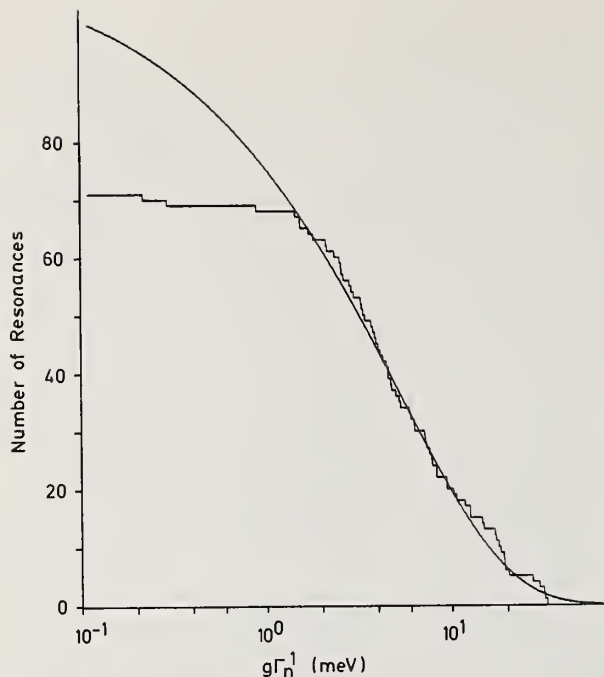


Fig. 4: Histogram of the integral distribution of the reduced neutron widths for the assigned p-wave resonances. The continuous curve represents the fit with a Porter-Thomas distribution.

First, resonances in the range 0 - 1600 eV are subdivided into two groups:

- 1) The group which we call assigned p-wave resonances contains the resonances of table 1 plus resonances below 200 eV which have been assigned p-wave by Bollinger and Thomas<sup>5</sup>. The reasons for including the latter are: a) that the present measurements suffer from disturbance due to <sup>235</sup>U at these low energies and therefore few resonances have been assigned below 200 eV, and b) that the method used in ref. 5 is especially certain at low energies; in fact, except for the 89.25 eV resonance, all their p-wave assignments are based on a probability larger than 98%.
- 2) The second group of resonances contains all the rest, i.e. s-waves plus an unknown number of unassigned p-wave resonances.

Integral neutron width distributions for these two groups are shown in figs. 4 and 5, respectively (staircase functions). The neutron widths used for these distributions are due to the capture area analysis described above for resonances with  $\Gamma_n \leq 10$  meV and to Carraro and Kolar<sup>11</sup> for resonances with  $\Gamma_n > 10$  meV. Fits to these distributions have been done in the following way:

First, the s-wave strength function has been determined assuming that all resonances of fig. 5 are s-wave (the error introduced by including unassigned p-wave levels is very small):

$$S_0 = (1.00 \pm 0.19 - 0.15) \cdot 10^{-4}$$

where the error has been determined according to the description of Liou and Rainwater<sup>12</sup>. Then the s-wave level spacing has been determined such that the best fit is obtained for the part of fig. 5 with  $\Gamma_n^0 > 0.25$  meV. This yields

$$D_0 = (22.4 \pm 1.0) \text{ eV}$$

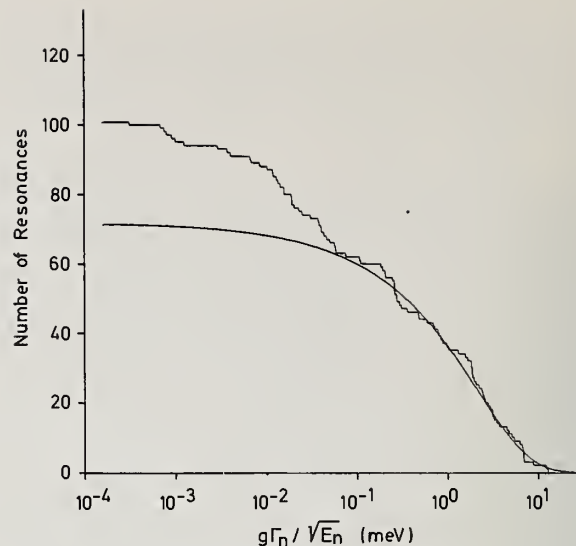


Fig. 5: Histogram of the integral distribution of  $g\Gamma_n / \sqrt{E_n}$  for all resonances except those assigned as p-waves. The continuous curve represents the fit with a Porter-Thomas distribution for  $g\Gamma_n / \sqrt{E_n} > 0.25$  meV.

The bias of 0.25 meV for this fit has been set such that it is above the largest value of  $g\Gamma_n / \sqrt{E_n}$  for any assigned p-wave resonance. Second, a similar procedure has been applied to the distribution of fig. 4, fitting that part of the staircase with  $g\Gamma_n^1 > 2$  meV: since the efficiency of the present method of p-wave assignment is independent of  $g\Gamma_n^1$ , one may assume that the shape of the curve above such a threshold reproduces the real one. Fitting with a Porter-Thomas distribution results in an average reduced width

$$\langle g\Gamma_n^1 \rangle = (5.42 \pm 1.11 - 0.86) \text{ meV}$$

Assuming that the p-wave level spacing  $D_1$  is 1/3 of the s-wave spacing, one obtains for the p-wave strength function:

$$S_1 = \frac{\langle g\Gamma_n^1 \rangle}{3 D_1} = (2.42 \pm 0.5 - 0.4) \cdot 10^{-4}$$

the errors given here for  $\langle g\Gamma_n^1 \rangle$  and  $S_1$  are obtained again according to ref. 12<sup>n</sup> considering the total number of 63 resonances with  $g\Gamma_n^1 > 2$  meV, used for the fit. A further value for the p-wave strength function can be obtained by estimating the influence of the effects which reduce the number of assigned p-wave resonances. The efficiency of the method used for the parity assignment was determined to be 75% and the energy range covered by s-wave resonances is on the average 25%. The p-wave assignment of ref. 5 in the energy range  $E_n < 200$  eV is influenced only by the second effect. Using the parity assignment of Bollinger and Thomas<sup>5</sup> below 200 eV and those of the present work for resonances above 200 eV, one gets the following p-wave strength function

$$S_1 = \frac{1}{3 \Delta E} \left[ \frac{\sum_{E < 200} g\Gamma_n^1}{0.75} + \frac{\sum_{E > 200} g\Gamma_n^1}{(0.75)^2} \right] = (2.16 \pm 0.5 - 0.4) \cdot 10^{-4}$$

Since the two independent estimates agree within the errors, we take their average as a final result

$$S_1 = (2.3 \pm 0.5 \atop - 0.4) \cdot 10^{-4}$$

The increase of the obtained  $S_1$ -value as compared e.g. to the value given by Rahn et al.<sup>1</sup> ( $S_1 = 1.4 \cdot 10^{-4}$ ) is due to both, the assignment of rather strong resonances as p-wave and the larger neutron widths which we obtain for small resonances. Thus, if we apply the same procedure as described for the first estimation of the p-wave strength function, using our p-wave assignments but the neutron widths as given by Rahn et al.<sup>1</sup> (and ignoring resonances which have not been detected in ref.<sup>1</sup>) we obtain a p-wave strength function

$S_1 = 2.02 \cdot 10^{-4}$ . The larger values are in good agreement with those obtained from the analysis of average total cross section measurements<sup>2,3</sup>.

## References

1. F. Rahn et al., Phys. Rev. C6 (1972) 1854.
2. C. A. Uttley, C. M. Newstead and K. M. Diment, Nuclear Data for Reactors 1, 165, IAEA Vienna (1967).
3. J. E. Lynn, Proc. Phys. Soc. 82 (1963) 903.
4. M. C. Moxon, M.Sc. Thesis (1968).
5. L. M. Bollinger and G. E. Thomas, Phys. Rev. 171 (1968) 1293.
6. H. I. Liou, H. S. Camarda and F. J. Rahn, Phys. Rev. C5 (1972) 1002.
7. L. V. Groshev et al., Nucl. Data Tables A5 (1969) 414.
8. L. M. Bollinger and G. E. Thomas, Phys. Rev. C6 (1972) 1322.
9. L. M. Bollinger, Proc. Int. Conf. on photonuclear reactions and applications, Asilomar, 1973, CONF-730301, p. 783.
10. BNL 325, Third Edition, Vol. 1 (1973).
11. G. Carraro and W. Kolar, Proc. Third Conf. on Neutron Cross Sections and Technology, Knoxville, 1971, Vol. 2, p. 701.
12. H. I. Liou and J. Rainwater, Phys. Rev. C6 (1972) 435.



Neutron transmission measurements on natural U samples were performed in the energy region from 20 eV up to 30 keV on a 190-m flight path of the JAERI 120-MeV linac neutron time-of-flight spectrometer. Samples were all metallic slabs with three thicknesses of 0.00725, 0.0144 and 0.0236 atoms/barn, respectively. One of them was cooled down to 77° K to reduce Doppler broadening. The best nominal resolution of the measurements was 0.3 nsec/m. A special attention has been paid to determine the background, because the shape of the background was found to depend on the thickness of the sample in the beam. Resonance parameters  $\Gamma_n^0$  are obtained in the energy region up to about 5 keV with the Atta-Harvey area-analysis program. Results are compared with currently available experimental data.

(Transmission measurements; natural U; 190-m flight path; JAERI linac; three thicknesses; 77°K; background; Resonance parameters  $\Gamma_n^0$  up to 5 keV.)

### Introduction

As is well known,  $^{238}\text{U}$  is one of the most important nuclides in nuclear reactors, particularly as a blanket material of the fast breeder reactor, where the breeding ratio considerably depends on the resonance parameters.

There have been a tremendous amount of measurements made on neutron resonance cross sections of this nuclide. However, most of them are limited to relatively low energy regions, and at higher energies say up to 4 or 5 keV, there are only a few good resolution data sets available.

Garg et al.<sup>1</sup> measured the total cross section of  $^{238}\text{U}$  with high resolution in the region up to 4 keV. Carraro and Kolar<sup>2</sup> of Geel made similar measurements, but they came up with the results surprisingly larger than those of Garg et al. then Rahn et al.<sup>3</sup> of Columbia University made an extensive experiment in which the total and capture cross sections were measured with several thicknesses of the sample. The results showed that their parameters were much closer to the Geel's values.

However, there still remain appreciable systematic differences between these two sets of the parameters, so that the present experiment was undertaken to contribute to solve the discrepancies.

Neutron transmission measurements were made in the energy region from 20 eV to 30 keV with the JAERI 120 MeV linac neutron TOF spectrometer. One of the samples used in the measurements was cooled down to a liquid nitrogen temperature to reduce Doppler broadening. The background was found to depend on the samples used for the measurement, so that a special technique was devised to determine it.

In the next section an experimental procedure is described together with the JAERI linac neutron spectrometer. The data processing of the background determination and the analysis of transmission data are then given. Finally, the results of the analysis are presented in the last section.

### Experimental procedure

#### JAERI linac neutron TOF spectrometer<sup>4</sup>

Since this is the first report to be published on the neutron cross section measurements with the JAERI 120 MeV linac, a general description of the TOF neutron spectrometer is given briefly.

The linac is an s-band machine, and the accelerating waveguides are in five sections, two of which have a length of 2 m each, the remainder being 3 m long each. As for the characteristics of the electron beam for a

maximum peak microwave power of 20 MW fed into each accelerating section, 190 MeV maximum energy with 1 mA peak current, and 100 MeV with 1 A are typically obtained for a pulse width of 100 nsec. The pulse width is variable from 25 nsec to 2 sec with a range of pulse repetition from a single shot to 600 pps.

The neutron producing target is a stack of water-cooled tantalum plates. The main part of neutron moderators is paraffin mixed with boric acid. There are six neutron flight tubes extending from the target, the length of which are 190 m, 52 m, two of 47 m and two 20 m.

The acquisition and reduction of experimental data are performed with a computer system USC-3, the central part of which is a computer (Toshiba ICD-507) with a core memory of 16 K words, a word being 20 bits. Two IBM compatible magnetic tape units and a 64 K words magnetic drum are used as auxiliary memory equipments. Two time-of-flight units are employed in the system, one has a minimum channel width of 25 nsec, the other that of 100 nsec, both operate in a so-called accordion mode.

### Transmission measurements

The transmission measurements were carried out with a neutron detector at the 190 m flight path. Experimental geometry is shown in Fig. 1 together with the block diagram of the electronic circuits. The detector consisted of 7  $^6\text{Li}$ -glass scintillators (NE908,  $\frac{3}{8}$ " dia. x  $\frac{1}{2}$ " thick) mounted on photomultipliers (EMI 9579). Signals from the photomultipliers were mixed and sent through an emitter-follower to a main amplifier in the computer room. The amplitude of the signals was adjusted by a potentiometer through which a high voltage was supplied to each phototube. The detector was surrounded by a neutron shield of paraffin and boric acid, the inner surface of the shield was lined with boron-carbide of 2 cm thick. The neutron flux was monitored with a small  $^6\text{Li}$ -glass scintillator (NE905,  $\frac{1}{2}$ " dia. x  $\frac{1}{8}$ " thick) placed at about 7 m from the target along the 190 m flight tube. The signal from the monitor was fed to a scaler through a time-gate circuit, and sent to the computer. The neutron flight tube was filled with helium to prevent the attenuation of neutron. The tube made of aluminium has mylar windows of 0.075 mm thick each on both ends.

The samples used were natural uranium metal plates with three thicknesses of 0.00725, 0.0144 and 0.0236 atoms/barn, respectively. One of them (0.0144 atoms/barn) was cooled down to a liquid nitrogen temperature with a cryostat mounted on a sample changer. The neutron beam was collimated to have a cross section of 9.5 x 9.5 cm<sup>2</sup> at the sample position when the cryostat was used, and otherwise 10 x 12 cm<sup>2</sup>. The timing channel

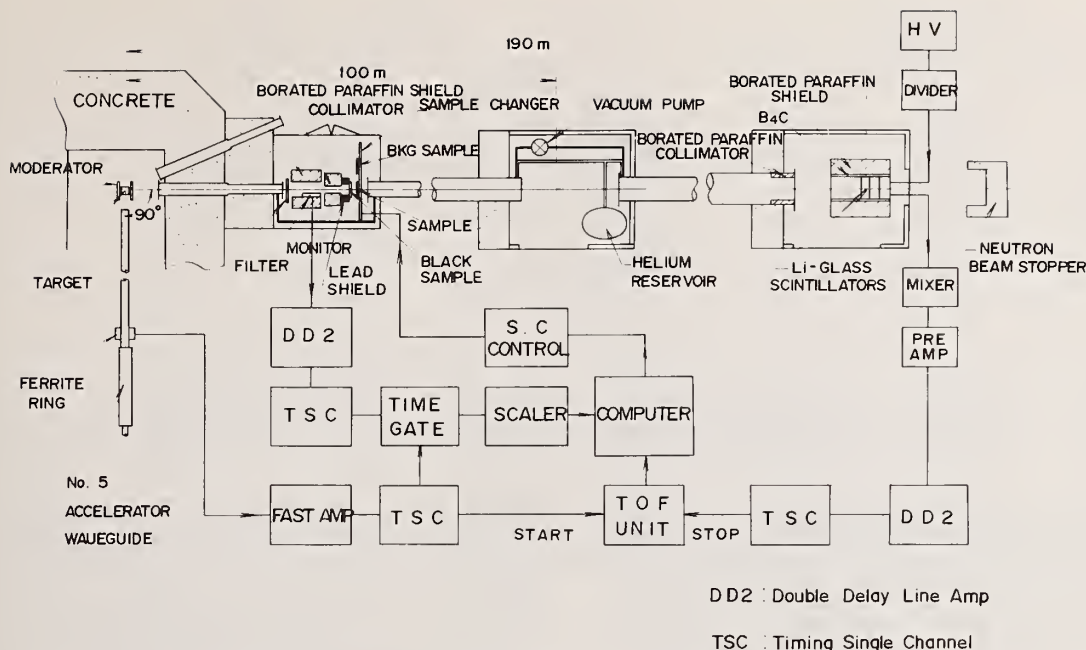


Fig. 1. Experimental arrangement of the target and detector system and the circuit block diagram.

widths used in the measurements were 50 nsec, 100 nsec and 400 nsec, corresponding to the nominal electron beam widths of 62.5 nsec, 125 nsec and 500 nsec, respectively.

As is usually done, cyclic measurements of the neutron spectra were automatically repeated for the configurations that the sample and/or black resonance sample were in or out of the neutron beam. The total number of timing channels used was 8 K for a configuration of the sample and black sample, so the data stored in the core memory had to be transferred onto a magnetic tape before proceeding to the next configuration. Simultaneously the data for individual configuration were summed and stored in the drum. For each configuration in one cycle of the measurement two quantities were always recorded to monitor the measurements, which were a sum counts over a certain time channel region and the time required for the measurement.

The background was measured first with the usual black resonance technique, but it became soon clear that the background depends on the black samples used. Obviously this raised considerable difficulty, since it was hard to find a probe which did not disturb the background. To overcome this difficulty a new technique was devised which consisted of two sets of measurements.

In the first set, the background should be determined accurately, and for this purpose, neutron spectra of the sample in and out of the beam were measured with the black resonance sample (a stack of aluminium and bismuth plates for the high resolution measurements, manganese and cobalt for the low resolution) always in the beam. In addition, neutron spectrum of a 10 mm thick uranium plate, twice as thick as the thickest sample, was also measured with the same black sample.

In the second set, neutron spectra were measured with only the sample in and out of the beam. The backgrounds of these spectra can be determined by making use of the informations obtained in the first set of measurements. Details of the procedure to determine the backgrounds from these two sets of data is described in the next section.

#### Analysis of the data

##### Background determination

For most of the neutron spectra obtained in the first set of measurement, the background seems to be reasonably represented by a curve which smoothly connect black resonances. However, for the thickest sample the neutron counts at strong resonances showed to deviate from the above curve, so that for this spectra the background shape was taken to be those obtained with a 10 mm thick uranium.

In the first set of measurements the backgrounds are determined both for the sample-in and -out spectra. In Fig. 2 the sample-in spectrum is schematically shown, where the following areas can be calculated. The area of a resonance dip (indicated by shaded part A), a resonance transmission area with the background (B.G.) subtracted off (B), and an off-resonance area also without the background (C), for the sample-in spectrum in the second set the corresponding quantities are denoted by the same notations with primes, i.e., A', B' and C'. While A' is known, B' and C' are unknown

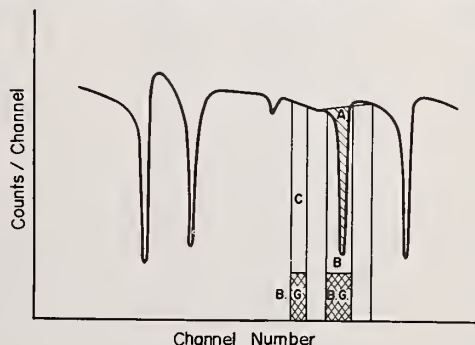


Fig. 2 Schematic neutron time of flight spectrum.



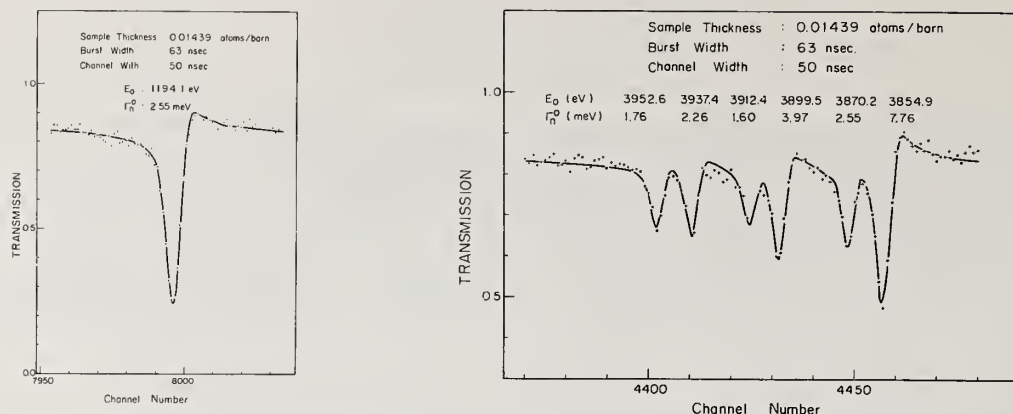


Fig. 3. Examples of results of area analysis. The crosses are plots from experimental data. The solid line represents the calculated transmissions with the resonance parameters indicated.

quantities because in this spectrum the background is not yet determined. Now the following relation should hold,  $A/B = A'/B'$  from which  $B'$  is to be calculated, in other words, the background can be determined. From this  $C'$  is also obtained. Let the corresponding quantities to  $C$  and  $C'$  in the sample-out spectra be denoted by  $D$  and  $D'$ . From the similar argument to the above,  $D'$  is given as  $D' = D/C \times C'$ .

The background values thus determined scatter from resonance to resonance mainly due to statistical fluctuation, however the background can be determined with a suitable accuracy by fitting these values with a smooth curve in case that a sufficient number of resonances is available for the calculation.

#### Resonance analysis

A modified version of the Atta and Harvey area analysis program<sup>5</sup> is used to obtain the resonance parameters of the Breit-Wigner single level formula. For an assumed value of the total width of each resonance, the program calculates a value of the reduced

neutron width  $\Gamma_n^0$  by minimizing the difference between the observed and calculated areas of a transmission dip. A value for the radiation width  $\Gamma_\gamma$  should also be assumed, which was taken to be 24 meV for all resonances. The program iterates until the relation  $\Gamma = \Gamma_n + \Gamma_\gamma$  is satisfied by varying the initially assumed value of  $\Gamma$ . A few typical examples of experimental and calculated transmissions are shown in Fig. 3 (a) and (b). An excellent agreement is seen between the two. These values were obtained for  $R' = 0.96$  fm.

In the energy region above 2.15 keV, only high resolution transmission data are analysed which were deduced from the measurement at the liquid nitrogen temperature. In the region between 20 and 274 eV, the resonance parameters were obtained from low resolution data also measured at 77° K. In the energy range between 274 and 2150 eV, there are three independent sets of parameters for most of the resonances resulted from the transmission data with different thicknesses of the sample. In obtaining a combined result of the parameter for a resonance in this region, a simple arithmetic average was taken over the different sets.

Table 1. Neutron resonance parameters of  $^{238}\text{U}$

$E_0$ (eV)	$\Gamma_n^0$ (meV)	$\Delta\Gamma_n$ (meV)	$E_0$ (eV)	$\Gamma_n^0$ (meV)	$\Delta\Gamma_n$ (meV)	$E_0$ (eV)	$\Gamma_n^0$ (meV)	$\Delta\Gamma_n$ (meV)	$E_0$ (eV)	$\Gamma_n^0$ (meV)	$\Delta\Gamma_n$ (meV)
20.90	2.21	0.22	463.0	0.25	0.02	924.8	0.47	0.06	1443.7	0.38	0.06
36.80	5.59	0.28	477.0	0.18	0.02	936.9	4.95	0.49	1473.6	3.21	0.22
66.15	3.13	0.16	488.2	0.034	0.004	958.2	6.77	0.68	1522.5	6.08	0.36
80.74	0.25	0.02	518.28	2.16	0.06	991.8	12.08	0.84	1565.4	0.13	0.04
89.19	0.009	0.002	535.21	1.97	0.10	1023.0	0.25	0.06	1598.0	9.47	0.76
102.47	7.10	0.43	556.0	0.031	0.009	1054.0	2.74	0.22	1622.6	2.59	0.33
116.85	2.45	0.20	580.0	1.64	0.16	1094.6	0.09	0.02	1638.0	1.14	0.13
145.58	0.084	0.005	594.9	3.49	0.21	1098.2	0.64	0.05	1662.0	5.18	0.47
165.27	0.30	0.02	619.8	1.23	0.06	1108.7	1.10	0.08	1688.0	2.50	0.23
189.70	12.71	0.64	624.1	0.039	0.005	1140.0	6.67	0.40	1709.0	2.09	0.19
208.46	3.65	0.36	628.4	0.23	0.01	1167.0	2.56	0.16	1722.0	0.45	0.07
237.27	1.83	0.18	661.0	4.93	0.49	1177.0	2.10	0.17	1755.5	3.31	0.25
242.65	0.014	0.003	693.0	1.51	0.14	1195.0	2.56	0.15	1782.6	16.5	1.7
263.95	0.019	0.003	708.0	0.78	0.08	1210.7	0.24	0.02	1808.4	0.50	0.09
273.59	1.80	0.08	721.0	0.057	0.009	1245.0	6.83	0.48	1845.5	0.23	0.03
291.00	0.97	0.09	732.3	0.066	0.008	1267.0	0.84	0.05	1902.4	1.09	0.09
311.18	0.053	0.005	765.0	0.26	0.04	1273.0	0.75	0.07	1916.5	1.10	0.16
347.75	4.32	0.22	779.1	0.084	0.014	1298.3	0.08	0.04	1968.6	19.12	1.20
376.90	0.057	0.003	790.9	0.23	0.01	1317.0	0.11	0.02	1974.3	9.61	0.96
397.63	0.30	0.03	821.0	2.51	0.15	1393.0	5.75	0.46	2022.8	4.96	0.50
410.20	1.02	0.06	851.0	2.23	0.18	1405.0	1.95	0.19	2029.8	0.94	0.28
434.00	0.50	0.03	856.2	2.92	0.23	1416.6	0.084	0.015	2088.1	0.59	0.10
439.60	0.021	0.009	866.0	0.19	0.02	1419.5	0.25	0.02	2075.9	0.55	0.07
454.0	0.016	0.005	905.0	1.91	0.15	1427.4	0.81	0.08	2144.6	1.67	0.14



Table 1. (Continued)

$E_0$ (eV)	$\Gamma_n^0$ (meV)	$\Delta\Gamma_n$ (meV)	$E_0$ (eV)	$\Gamma_n^0$ (meV)	$\Delta\Gamma_n$ (meV)	$E_0$ (eV)	$\Gamma_n^0$ (meV)	$\Delta\Gamma_n$ (meV)	$E_0$ (eV)	$\Gamma_n^0$ (meV)	$\Delta\Gamma_n$ (meV)
2152.2	5.33	0.43	2864.1	3.47	0.66	3332.9	1.67	0.18	3939.0	2.26	0.25
2186.0	12.40	0.99	2881.8	10.6	0.8	3355.1	1.93	0.18	3953.9	1.76	0.23
2200.6	2.11	0.25	2896.3	0.31	0.11	3388.3	0.25	0.05	4040.4	1.19	0.20
2258.8	2.11	0.23	2922.1	0.21	0.04	3407.9	3.53	0.34	4063.0	0.22	0.11
2265.9	4.51	0.32	2933.9	0.58	0.08	3435.3	6.37	0.49	4089.4	1.87	0.28
2281.7	3.88	0.31	2955.7	0.29	0.12	3456.3	10.9	0.9	4124.0	0.61	0.17
2314.5	0.31	0.10	3002.4	2.18	0.22	3484.3	1.33	0.16	4167.8	3.31	0.46
2352.8	1.10	0.13	3027.8	2.16	0.17	3560.5	4.21	0.42	4209.4	0.46	0.13
2355.3	1.20	0.14	3058.1	0.57	0.08	3572.7	6.16	0.52	4257.7	0.65	0.17
2391.4	0.51	0.06	3108.8	4.79	0.40	3593.3	0.85	0.13	4299.0	1.98	0.30
2425.7	2.74	0.27	3132.6	0.13	0.03	3628.3	8.59	0.86	4306.0	1.36	0.19
2445.5	4.05	0.29	3148.1	1.50	0.14	3692.0	5.89	0.44	4323.9	0.93	0.20
2454.8	0.39	0.05	3177.8	1.62	0.15	3715.5	1.55	0.19	4375.6	1.90	0.28
2488.4	2.09	0.17	3188.1	1.90	0.16	3733.0	3.44	0.38	4435.0	1.29	0.23
2671.3	4.96	0.40	3204.9	1.57	0.14	3763.6	1.63	0.20	4510.3	8.55	0.85
2695.6	0.54	0.07	3224.9	0.33	0.15	3780.8	6.42	0.55	4542.0	0.92	0.22
2716.5	3.26	0.32	3248.1	0.43	0.09	3856.4	7.76	0.68	4567.2	0.66	0.20
2749.7	0.75	0.09	3278.2	4.64	0.51	3872.1	2.55	0.30	4592.7	0.27	0.11
2761.6	0.28	0.06	3310.3	3.38	0.28	3901.3	3.97	0.40	4630.4	0.27	0.10
2828.4	0.33	0.06	3320.2	2.12	0.23	3913.4	1.60	0.19	4661.7	1.84	0.39

### Results and discussion

Table 1 shows values of  $\Gamma_n^0$  thus obtained for resonances in  $^{238}\text{U}$  in the region between 20 eV and 4.7 keV. There remain several resonances which are not included in the table because of difficulty to obtain a good fit to the transmission data in the analysis. There are many very tiny resonances reported by Rahn et al.<sup>1</sup> which were assumed to be p-wave resonances. In the present experiment these tiny resonances were not seen because even the thickest sample used was much thinner than the thickest one of Rahn et al. All the resonances observed listed in the table are assumed to be due to s-wave neutrons.

The values for the resonance energies listed in the table are those of the reference 6. The quoted errors are resulted from the following: 1) the errors in the transmission values due to counting statistics and background subtraction, 2) the uncertainty of area determination in resonance analysis, 3) other systematic error deduced from the fluctuation between different sets of parameters, this error had to be taken somewhat arbitrarily.

In comparing the present results with other sets of parameters given in Refs. 2 and 3 in the low energy region, it seems no appreciable energy dependent difference exists between three sets of data. There are certainly some resonances for which the parameters of the three sets deviate appreciably from one another, but for other resonances the deviation occurs in the opposite way, so that, on the whole, the agreement seems fairly good. When the energy goes up, however, the situation becomes different, showing that the parameters of Carraro and Kolar<sup>2</sup> are systematically higher than those of Rahn et al., and the present data are about the middle between the two. At high energies a similar tendency continues, but the present parameters are closer to the Geel's values.

### References

1. J.B. Garg, J. Rainwater, J.S. Petersen, W.W. Havens, Jr., Phys. Rev. **134** B985 (1964).
2. G. Carraro, W. Kolar, Second Int. Conf. on Nuclear Data for Reactors, Helsinki (1970) Vol. 1, P. 403. G. Carraro, W. Kolar, Proc. of Third Conf. on Neutron Cross Section and Technology, Knoxville, (1971) Vol. 2, P. 701.
3. F. Rahn, H.S. Camarda, G. Hacken, W.W. Havens, Jr., H.I. Liou, J. Rainwater, M. Slagowitz, S. Wynchank, J. Arbo, C. Ho, Proc. of Third Conf. on Neutron Cross Section and Technology, Knoxville, (1971) Vol. 2, P. 658. F. Rahn, H.S. Camarda, G. Hacken, W.W. Havens, Jr., H.I. Liou, J. Rainwater, M. Slagowitz, S. Wynchank, Phys. Rev. **C6** 1854 (1972).
4. H. Takekoshi et al., to be published in JAERI REPORT.
5. A. Tachibana, T. Iwaki, E. Kimura, A. Asami, Y. Nakajima, T. Fuketa, JAERI-memo 3728 (1969).
6. S.F. Mughabghab, D.I. Garber, Brookhaven National Laboratory Report, BNL-325, Third Edition, Vol. 1 (1973).

E. Melkonian, J. P. Felvinci, and W. W. Havens, Jr.

Columbia University

New York, N.Y. 10027

The levels in  $^{238}\text{U}$  show unusual clusterings of large and small levels as evidenced by runs statistics and sequential correlation of values of  $\Gamma_n^\circ$ . Also,  $\Gamma_n^\circ$  is found to show significant correlation with  $\Gamma_\gamma$ . These effects are interpreted in terms of a model which assumes that excitation states are built upon persistent states of collective vibration and that an entering neutron seeks to form those states involving minimum change of particle motion.

( $^{238}\text{U}$ , resonance levels,  $\Gamma_n^\circ$ ,  $\Gamma_\gamma^\circ$ , collective motion, level densities, correlations)

We have previously reported our observations (1-3) of variations in the fission fragment energy distributions from level to level in the low neutron energy fission of  $^{233}\text{U}$  and  $^{235}\text{U}$ . In addition, we noted that many of the resonance levels, previously assumed to be single, turned out to consist of several levels corresponding to different sets of quantum numbers. In interpreting these results, we were able to form a reasonably consistent model based on two hypotheses: 1) there exist well-defined persistent collective vibrational states of the compound nucleus formed by the addition of a low energy neutron, with its about 6 Mev of binding energy, in contrast to earlier assumptions that the addition of that much energy destroys all correlations between particle motions, and 2) the collective vibrational states most likely to be formed upon the addition of a neutron are those requiring the minimum change of the internal structure of the target nucleus. The sequences of resonance levels, and the corresponding level densities, then correspond to energies left after subtraction of the collective motion energy. Where several collective states with the required quantum numbers, but different energies, exist, the possibility arises that several sequences of levels be present with different level spacings and neutron widths.

Since these ideas are not necessarily restricted to fissile nuclei, we considered other nuclides for similar effects. In particular, we examined  $^{238}\text{U}$  whose properties are important to determining breeding ratios and Doppler effects in fast breeder reactors. Rahn et al.<sup>(4)</sup> (hereafter referred to as I) have determined the resonance parameters of  $^{238}\text{U}$  to 4 Kev and have separated the levels into s-wave and p-wave on the bases of the Dyson-Mehta theory and other statistical tests. Considering only the s-wave levels of I from here on and assuming that the reduced neutron width distribution corresponds to only one Porter-Thomas distribution, one would expect to find various magnitudes of neutron widths distributed randomly with increasing neutron resonance energy. A glance at Fig. (1) based on the table of s-wave parameters of I ap-

pears to show large neutron energy regions with unusually large values of  $\Gamma_n^\circ$  and similar regions devoid of large levels. For a quantitative estimate of this observation, a Wald-Wolfowitz runs statistic test was applied to the s-wave levels of I. The first 120 levels (to 2.4 keV) have a probability of only 0.4% that they were randomly selected from a single Porter-Thomas distribution. The energy region from 1.26 to 2.2 keV (44 levels) has an unusually small number of runs and gives a similar probability of 0.1%. The probability to 3 keV is 1%. Above 3 keV, consistency with the P-T distribution is observed, but this is the energy region where the selection of pure s-wave levels could not be carried out so well. Another type of calculation, that of the correlation coefficient between successive pairs of the reduced neutron widths ( $\Gamma_n^\circ$ ), gives  $0.32 \pm 0.08$  to 2.4 keV, again indicating clustering of levels of similar magnitudes in deviation from the P-T distribution.

The absorption of a neutron by  $^{238}\text{U}$  occurs in the state  $J = 1/2^+$ ,  $K = 1/2$ , denoted by  $(1/2^+, 1/2)$ . Under the present hypotheses the energy levels are not based on the ground state of  $^{239}\text{U}$  but on collective vibrational states. Two such possible Nillson states are  $1/2 + [620]$  at 688 keV, observed by both Sheline et al<sup>5</sup> and Bollinger and Thomas<sup>6</sup>, and  $1/2 + [600]$  calculated to be at about 2 MeV by Gustafson.

Level density calculations based on the residual energy left after subtraction of these values of collective energy give spacings of 20 ev and 200 ev respectively<sup>3</sup>. The 20 ev spacing is close to the measured value of 20.8 ev of  $\langle D \rangle$  for  $^{238}\text{U}$ , while the 200 ev figure is about the spacing of the regions with levels of large  $\Gamma_n^\circ$ . It is assumed that  $\Gamma_n^\circ$  is enhanced for those levels corresponding to the levels built upon the 2 Mev collective state.

Since there appears to be two classes of levels, depending upon coincidence or not with the levels based on the 2 Mev collective state, it becomes possible that  $\Gamma_\gamma$  might be different for the two classes. Figure 2 shows the 71 values of  $\Gamma_\gamma$  given in I for the s-wave

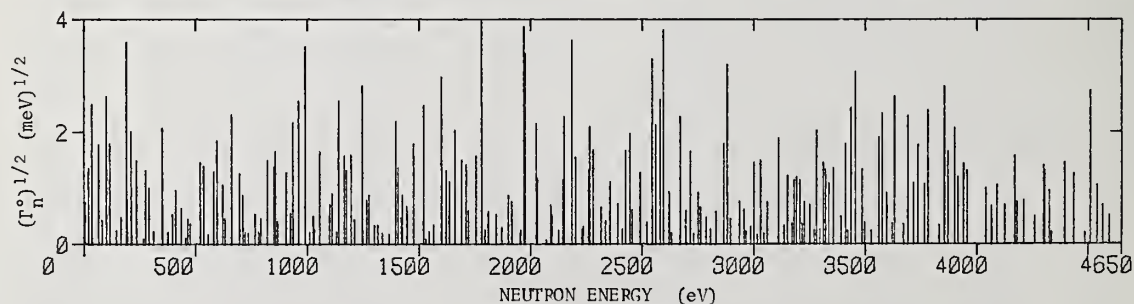


Figure 1. Magnitudes of  $(\Gamma_n^\circ)^{1/2}$  versus level energy, for levels selected as s-wave by Rahn, et al.<sup>4</sup>

levels of  $^{238}\text{U}$  plotted against  $\Gamma_n^0$ . An upward trend is apparent. Calculation of the correlation coefficient gives  $\rho = 0.53 \pm 0.09$ . Removal of levels with large  $\Gamma_\gamma$  or  $\Gamma_n^0$  drops the value of  $\rho$  to  $0.24 \pm 0.15$ , consistent with no or very small correlation. Removal of the same levels and application of the runs statistics as outlined above increases the probability of a single Porter-Thomas family to 20%. The result given is significant statistically, but it assumes that there is no bias in the determination of  $\Gamma_\gamma$ .

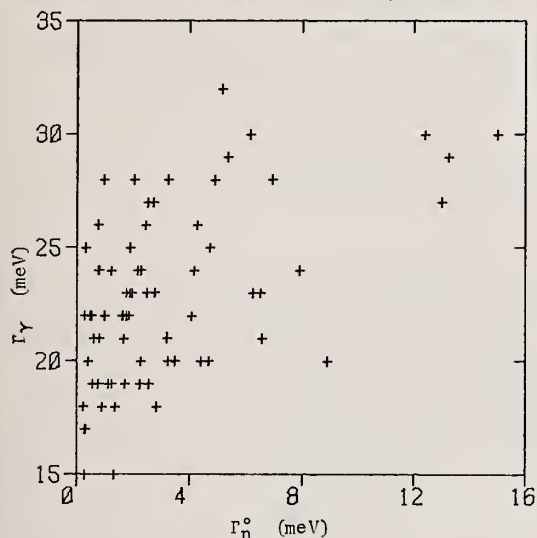


Figure 2.  $\Gamma_\gamma$  versus corresponding values of  $\Gamma_n^0$  for the 71 levels for which  $\Gamma_\gamma$  were given by Rahn, et al.<sup>4</sup>

The effects noted above are statistically significant and lend support to the suggestion of the presence of factors other than those assumed previously. Taken together with the contents of ref. 3, they lend support to the hypotheses presented above.

\* Research supported in part by the U.S.A.E.C.

#### References:

1. E. Melkonian and G.K. Mehta, Physics and Chemistry of Fission, Vol. II, 355 (1965): IAEA, Vienna.
2. J.P. Felvinci and E. Melkonian, Proceedings of the Third Conference of Neutron Cross Sections and Technology. - CONF - 710301, Vol. 2, 855 (1971).
3. J.P. Felvinci and E. Melkonian, Transactions of the ANS, 19, 420, (1974).
4. J.P. Felvinci, E. Melkonian and W.W. Havens, Jr. Paper GB 11, and D. Cacuci, J.P. Felvinci and E. Melkonian, paper EB8, Conference on Nuclear Cross Sections and Technology, (Washington, D.C.) (1975).
5. F. Rahn, H.S. Camarda, G. Hacken, W.W. Havens, Jr., H.I. Liou, J. Rainwater, M. Slagowitz, and S. Wynchank, Phys. Rev. C 6, 1854 (1972).
6. R.K. Sheline, W.N. Shelton, T. Udagawa, E.T. Journey and H.T. Motz. Phys. Rev. 151, 1011 (1966).
7. L.M. Bollinger and C.E. Thomas. Phys. Rev. C 6, 1322 (1972).



H.G.Priesmeyer and U.Harz

Institut für Reine und Angewandte Kernphysik der Universität Kiel

D-2054 Geesthacht, Fed.Rep. of Germany

Fast-chopper time-of-flight transmission measurements have been made using gross fission product samples of different irradiation and cooling histories, in order to find isotopic identifications and parameters of fission product resonances. The covered energy range was from 1 eV to 240 eV with resolutions of 47 ns/m and 94 ns/m. Some prominent fission product resonances have been found and can partly be identified. From the transmission analysis the U 235 content and burnup can be calculated within  $\leq 5\%$ .

( Neutron cross section; gross fission products; time-of-flight; 1-240 eV)

### Introduction

The experiments described in this paper have been made with the fast-chopper time-of-flight spectrometer at the 5 MW FRG1 - research reactor. The results concern the continued measurements on gross fission products, about which we have reported at the Helsinki conference in 1970.[1]. Since then two more gross fission product samples have been produced by irradiating uranium fuel in the 15 MW FRG2 reactor to different burnups. One other GFP sample could be borrowed from RCN, Petten, The Netherlands, and one sample has been made by milling low enrichment irradiated fuel from a nuclear power station in Germany. Changes of the transmission depressions at some resonances during the cooling time are observed. Careful analysis will be necessary to conclude from these changes to isotopic identifications of the resonances.

### GFP - Measurements and Results

Three of the samples contain about 8 g of uranium, enriched to 90% in U 235. They have been irradiated in a thermal neutron flux of about

$10^{13} \text{ n/cm}^2 \text{ s}$ . Burnups are 33%, 47% and 55%. The RCN sample, which was irradiated in a high flux reactor, had a burnup of 77%.

Changes in the transmission during the cooling time are changes of the isotopic concentrations and may yield isotopic assignments from the knowledge of half-lives. For some fission product isotopes the parameters of the prominent resonances are known, so that the transmission may be fitted, when the amount of material in the sample is known. This was the case for the RCN sample, a small part of which had been investigated mass-spectrometrically. For resonances, which clearly decay, the assignment will be relatively easy. Resonances that remain constant, may however belong to a radioactive isotope in decay equilibrium or to a stable or long-lived radioactive nucleus. Resonances that grow with time belong to the latter category and may hope-

fully be identified from the precursors half-lives.

The measurements have been started already within the week after the end of the irradiation in the reactor. Transmissions of the same samples have been compared. There are no changes of the transmission to be seen within the first four months after the irradiation. The statistical accuracy of the transmission points was of the order of 5%, due to the short measuring times. We conclude, that short-lived fission product isotopes, which are in equilibrium during irradiation and decay within a few weeks after shut down, do not contribute prominent resonances to the gross fission product transmission. This may of course as well be due to a low fission yield.

Figure 1 shows transmission curves of 4 different GFP samples, compared to the transmission of a sample of the same fuel before irradiation in the energy range between 45 eV and 3 eV (94 ns/m nominal resolution). It can clearly be seen, that, the higher the burnup is, the fission product resonances grow, while the U 235 resonances become smaller and the U 238 resonances almost remain constant. Among the growing resonances are those of U 236 and for low enrichment fuel, those of the Pu isotopes (cf. Figure 2).

Measurements have been extended to about 240 eV (see Figure 3), but above 50 eV the number of well-resolved resonances decreases. Table 1 contains the energies, at which we observe resonances; the weaker ones are in brackets. Energies, at which there are also resonances in the uranium isotopes, are marked with an asterisk. Nevertheless these resonances are in some cases underlaid by close-by fission product resonances, as can be concluded from the cooling time behaviour.

The analysis of the resonances is very difficult because of the unknown number of isotopes that may contribute. An example is the big resonance at 5.44 eV which may only be fitted reasonably well, when besides U 235, U 236 and U 234 at least the isotopes Tc 99, Pm 147 and Cs 133 are considered. Figure 4 shows a fit of the transmission points

T A B L E 1

between 9.5 eV and 4.7 eV. For the calculation of the solid line the results of a quantitative mass - spectro-metric analysis and the known resonance parameters were used. In this region the transmission is fairly well explained. Assignments for fission product isotopes can be given for the following resonances: at 14.4 eV: Xe 131, at 8.0 eV: Sm 152 and at 5.83 eV: Cs 133. All these isotopes are stable. No assignments for a radioactive nucleus can yet be given. The measurements will be repeated in certain time intervals. Assignments will be counterchecked by calculating and measuring the amounts of isotopes produced. Dilution of the samples and quantitative analysis of the isotopic content will be done only after the measurements with the chopper are completed, since we do not want to set the gaseous fission products free.

It should be mentioned, that we use some resonances with known parameters successfully for a determination of the unknown content of a specific isotope. [2]

Energies of Resonances in the Gross-

Fission-Product	Transmission (eV)		
187.6*	157.0	154.8*	102.03*
70.6	65.6	55.6	(51.1)*
44.3	42.5	(42.1)*	39.3
36.6	(36.2)	34.8*	(34.3)
(33.4)	32.1*	29.6*	27.8
(25.2)	23.3	20.8*	19.5*
18.3	(18.0)	16.6*	16.0*
(15.2)*	14.4	(14.0)*	(13.7)*
12.3*	11.6*	(10.3)	(9.26)*
8.74*	8.00	7.03*	6.64*
6.36*	5.83	5.44*	(5.11)*
4.83*	(4.38)	3.58	

Figure 1:  
Comparison of trans-  
missions of gross-  
fission product samples  
45 eV to 3 eV, 94 ns/m

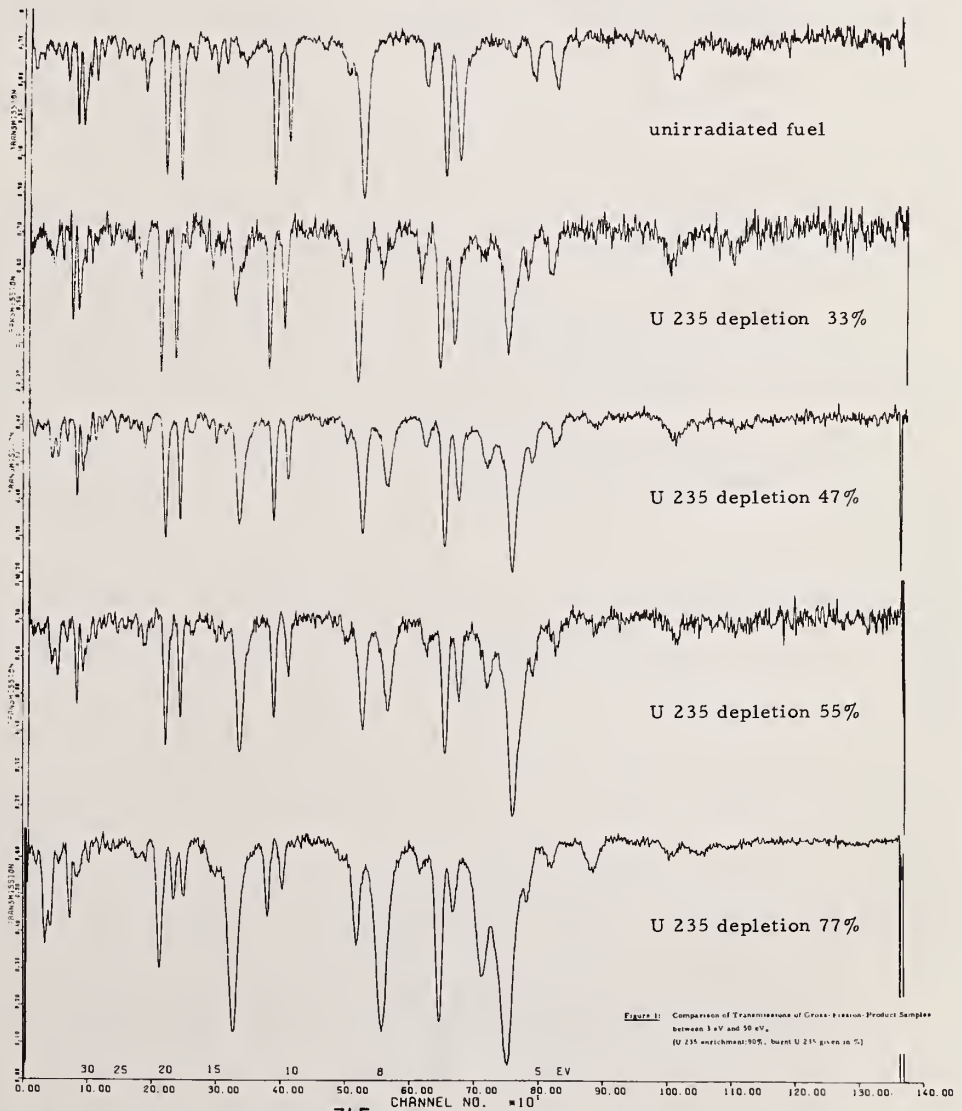
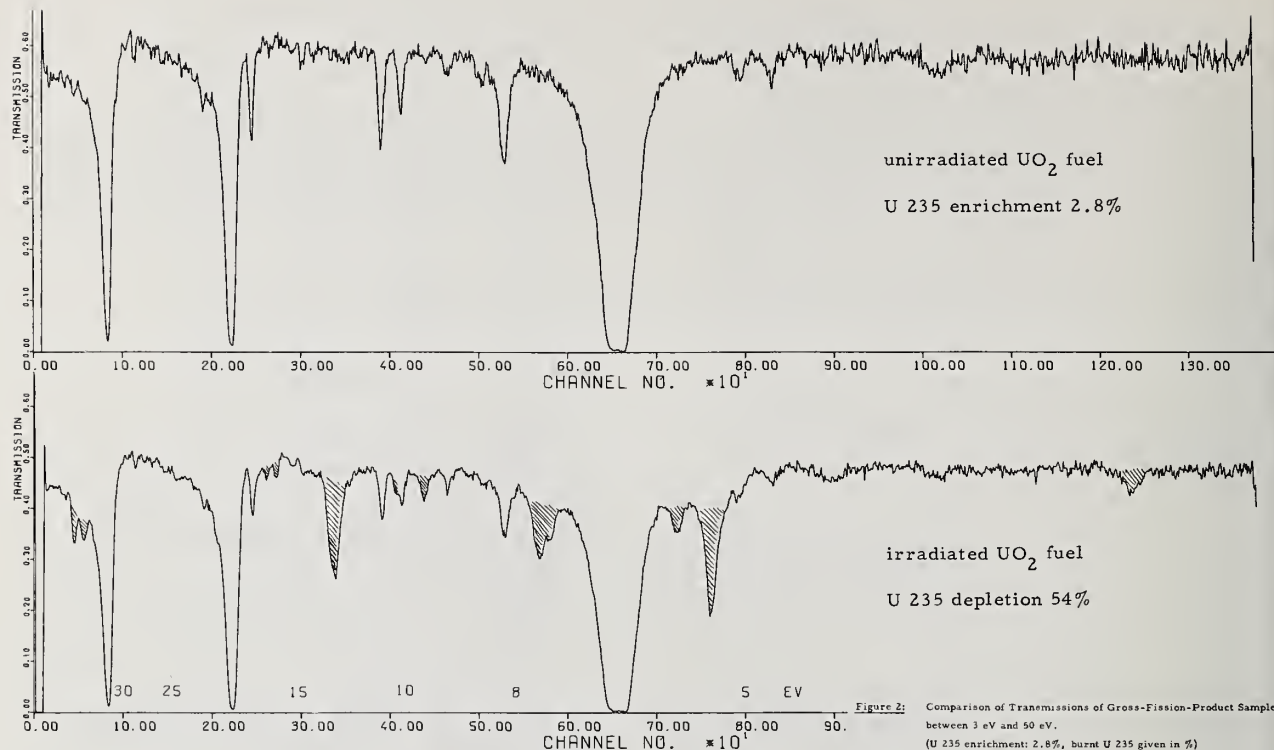
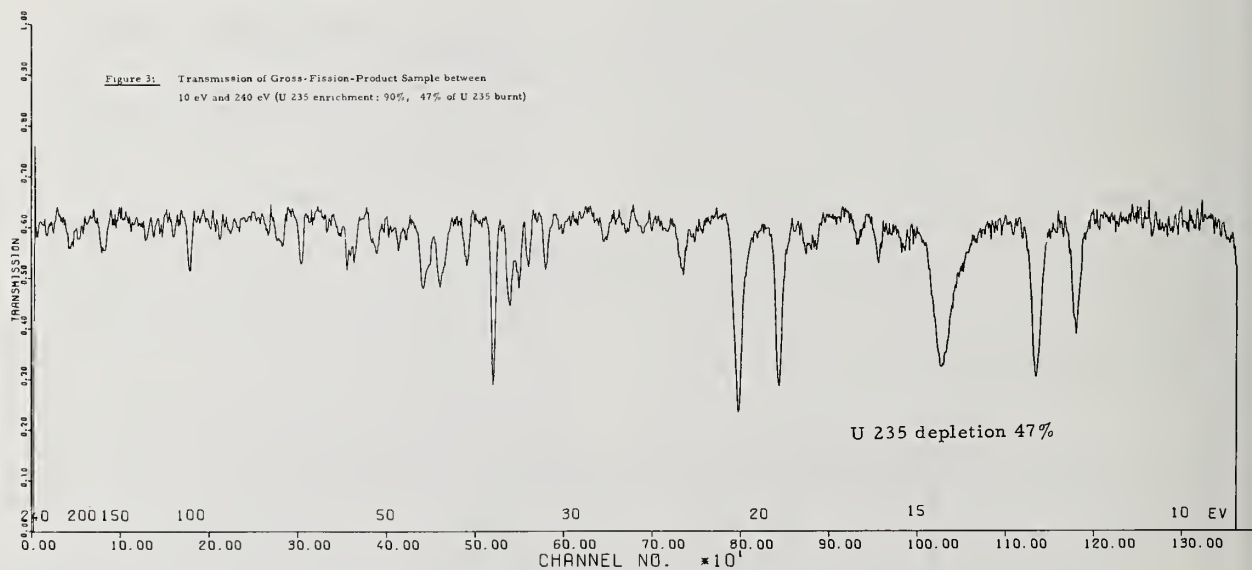


Figure 1: Comparison of Transmissions of Gross-fission Product Samples  
between 3 eV and 50 eV.  
(U 235 enrichment 95%, burnt U 235 given in %)



**Figure 2:** Comparison of GFP - transmissions of unirradiated and irradiated nuclear fuel  
( low U 235 enrichment )



**Figure 3:** Transmission of irradiated nuclear fuel ( 240 eV - 10 eV )



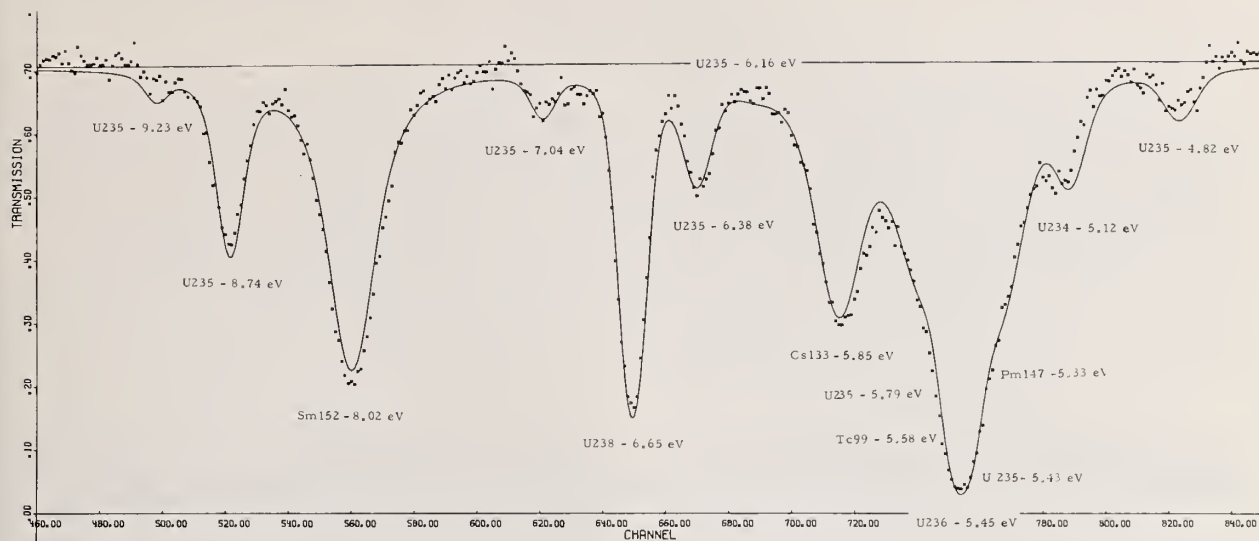


Figure 4: Fitted GFP - transmission between 9.5 eV and 4.8 eV

References:

- [1] H.H.Jung, H.G.Priesmeyer, H.Sulitze Nuclear Data for Reactors, Helsinki 1970  
IAEA STI/PUB/259 p. 679
- [2] H.G.Priesmeyer, U.Harz Isotopic Content Determination in Irradiated Fuel by Neutron  
Transmission Analysis  
(paper presented at KTG-meeting, Stuttgart, Febr. 25-26, 1975 , to be published in  
Atomkernenergie)

# HIGH RESOLUTION TOTAL NEUTRON CROSS-SECTION IN $^{54}\text{Fe}$ AND $^{56}\text{Fe}$ \*

M. S. Pandey and J. B. Garg  
Physics Dept., SUNYA  
Albany, N.Y. 12222  
J. A. Harvey and W. M. Good  
Oak Ridge National Lab.  
Oak Ridge, Tennessee 37830

High resolution neutron total cross-section measurements on  $^{54}\text{Fe}$  and  $^{56}\text{Fe}$  have been made using the ORELA facility and resonance parameters are reported up to an energy of 500 keV. The total cross-section data were analysed by R-matrix multi-level code for broad, interfering s-wave resonances. For narrow and non-interfering s-wave resonances and  $\ell > 0$ -wave resonances transmission data were analysed using Harvey-Atta code of area analysis. From these values of resonance parameters, the values of level density  $\langle D \rangle$  and strength function for s- and p-wave neutron scattering have been determined. Statistical distributions of spacing and reduced neutron widths are presented. A large number of p-wave resonances are observed which have not been reported before.

(Total neutron cross section;  $^{54}\text{Fe}$ ;  $^{56}\text{Fe}$ ; high resolution)

## Introduction

Neutron cross section measurements provide information pertinent to nuclear structure and reactor technology.

From the point of view of nuclear structure and interaction, iron isotopes of even A are important as they are in the immediate neighborhood of 3s giant resonance in the strength function. From the level spacing determination, the effect of ground-state subshell occupation, its dependence on spin and neutron excess effect could be studied. With the improved resolution larger number of  $\ell > 0$  wave interaction resonances are observed, which are most likely p-waves. This provides a more reliable value of p-wave strength function.

The measurements are useful for reactor technology as iron is one of the structural materials used in the fast reactors.

In the energy range of the experiment neutron elastic scattering is by far the dominant process for s-wave interaction. Neutron capture is very small and the threshold for inelastic scattering occurs, in the isotopes in question, above the highest energy of these measurements.

The average level spacings and strength function both for s and p-wave interaction have been determined and statistical distribution for reduced neutron widths are reported.

## Experimental Arrangement

The Oak Ridge Electron Linear Accelerator (ORELA) was used to measure the total cross section in the separated isotope of  $^{54}\text{Fe}$  (isotopic abundance of 97.2% and a sample thickness of  $1.899 \times 10^{-2}$  at/barns) and  $^{56}\text{Fe}$  (natural iron with isotopic abundance of 91.7% and sample thickness of  $2.1787 \times 10^{-1}$  atoms/barn). Measurements on  $^{54}\text{Fe}$  and  $^{56}\text{Fe}$  were made at the flight paths of 78.203 m and 198.733 m respectively.

NE 110 proton-recoil detector was used in both the measurements. The NE 110 scintillator is not sensitive to low-energy

neutrons but is very fast (3.3 nsec decay time constant). The NE 110 detector is equally sensitive to both high energy neutrons as well as  $\gamma$ -rays. To optimise neutron detection sensitivity four different biases were used. This arrangement enables good signal to background ratio and isolates 478 keV  $\gamma$ -rays produced from  $^{10}\text{B}$  in the pyrex of the phototube and 2 MeV  $\gamma$ -rays produced by the neutron capture in hydrogen in the third and the fourth biases respectively.

For  $^{54}\text{Fe}$  1/4" of uranium foil was used to cut off the  $\gamma$ -flash produced at the target producing neutrons.  $^{56}\text{Fe}$  sample was too thick to render much reliance on the peak cross section for its measurement whereas  $^{54}\text{Fe}$  was too thin for cross-section in the valley to be determined reliably.

## Analysis

R-matrix multi-level formalism is used to analyse the cross-section data for mainly s-wave resonances and some p-wave resonances. All the p-wave resonances and non-interfering s-wave resonances are analysed by Harvey-Atta's code of area analysis.

In R-matrix formalism the boundary conditions<sup>†</sup> for eigen-states are real and energy independent so are the corresponding eigenvalues and derived resonance parameters. Experimental data is limited only to a particular energy region so the resonance parameters pertain only to these local resonances. This is recognized and in the R-matrix formalism the reduced R-function is broken in two parts  $R_J(\text{local})$  and  $R_J(\text{residual})$

$$R_J(\text{local}) = \sum \frac{\gamma^2 \lambda J n}{\lambda E_{\lambda J} - E_{1/2} - i\Gamma_{\lambda J} \gamma}$$

$$R_J(\text{residual}) = A_J + B_J (E - E_{1/2})$$

$$A_J = R_J^\infty + \sum \frac{\gamma^2 \lambda J n}{\lambda E_{\lambda J} - E_{1/2}},$$

$$B_J = \sum \frac{\gamma^2 \lambda J n}{\lambda (E_{\lambda J} - E_{1/2})^2}$$

A least square numerical analysis code is used to determine the resonance parameters  $E_{\lambda J}$ ,  $\gamma^2_{\lambda J n}$  and possibly  $\Gamma_{\lambda J \gamma}$ . By fitting the known thermal data on coherent and bound scattering cross sections an estimate of the presence of negative energy state, if any, is made.

Using Harvey-Atta code with resonance-potential scattering interference consideration, some of the s-wave resonances were analysed. The fits are not very reliable because in an attempt to fit the asymmetrical shape, area is either under- or over-estimated.

### Discussion Of The Results

<sup>54</sup>Fe: A large number of p-wave resonances are observed superimposed on clearly distinct broad s-wave resonances. Since the level density is proportional to  $(2J+1)$ ,  $J$  being the compound nuclear level spin, on an average the number of p-wave resonances for the same energy range should be about three times that of the s-wave resonances. The observed values of level density for s- and p-wave neutron interaction is respectively  $(22 \pm 4)$  keV and  $(9 \pm 3)$  keV after making some corrections for the missing levels as determined by neutron width distribution. The values of strength function for s- and p-wave respectively are  $(8.56 \pm 2.6)$  and  $(0.48 \pm 0.13)$  in units of  $10^{-4}$ .

As Bowman et.al.<sup>1</sup> point out the striking feature observed in the case of interfering s-wave resonances is the modification in their shape to the point of almost complete loss of asymmetry. An interesting example is the resonance at 190 keV which is about 40 keV wide and has a surprisingly symmetrical shape. Assignment of this to s-wave interaction is justifiable if we considered the fact that the higher values of cross-sections at the higher energy end of this resonance physically cancelled out all the potential phase shift. This wide resonance, in parallel, affects the region of its lower energy end and is responsible for the lack of asymmetry in s-wave resonances down to an energy of about 90 keV. For this reason, broad resonances, in spite of their apparent symmetrical shape, were assigned to s-wave interaction. The structure of the data becomes more and more complicated beyond 400 keV with broad s-wave resonances superimposed by varied fluctuations of  $\ell > 0$ -wave resonances. The relatively poor fit of the experimental data with the R-matrix theory beyond 300 keV arises from two main reasons (a) the experimental data has been averaged over the energy intervals which include contributions from the p-wave levels. (b) the measured cross-sections at the valley of the resonances have larger uncertainties due to thin sample of <sup>54</sup>Fe used in the measurements which also suffers from poor statistics in this region. On the fluctuating background of this complicated structure, however, p-wave resonances were fitted by area analysis up to 650 keV.

<sup>56</sup>Fe: In comparison to <sup>54</sup>Fe data, <sup>56</sup>Fe data appears less complicated. Even at higher energies the p-wave (or  $\ell > 0$ -wave) resonances were easily assigned as they mostly

appear on the high energy tail of the broad s-wave resonances and do not exhibit the otherwise obvious destructive interference. This combined with the lack of asymmetry and the consideration of peak-cross-section helped the assignment. The widths of the s-wave resonances in <sup>56</sup>Fe are generally smaller in magnitude in comparison to that of <sup>54</sup>Fe. The broadest s-wave resonance in the energy range of the experiment is about 14 keV wide at 380 keV. Evidence of loss of asymmetry is found in the s-wave resonances of <sup>56</sup>Fe also. The s-wave resonance at 380 keV can be considered as an example and an argument similar to that for 192-keV <sup>54</sup>Fe resonance would justify the assignment. The data has been analysed up to 500 keV but an extension up to 600 keV is proposed.  $\langle D \rangle$  for s- and p-wave are respectively  $(25 \pm 5)$  keV and  $6 \pm 2$  keV. The strength function for s and p-wave are respectively  $(2.6 \pm .86) 10^{-4}$  and  $(.25 \pm .04) \times 10^{-4}$ . Evidence of a negative energy state is observed by fitting the thermal cross-section data.

The gap in the ORELA data towards the lower energy range was filled in by the NEVIS data as reported previously by Garg et.al.<sup>2</sup> for shape analysis of the cross-section data by R-matrix for both <sup>54</sup>Fe and <sup>56</sup>Fe.

### Comparison With Previously Reported Results

Results presented here are in good agreement with both ref. 1 and ref. 2. For comparison the values are presented in table I & II. Examining the table we find that Garg et.al. report a s-wave resonance at 102 keV for <sup>54</sup>Fe which we don't observe in <sup>54</sup>Fe. There is, however, a quite prominent p-wave resonance in <sup>56</sup>Fe at 102.6 keV. A s-wave resonance reported by Garg et.al. at 163 keV is not observed by us. With Bowman et.al. we seem to have disagreement on a pair of s-wave resonances at 317 keV and 329.5 keV. From the poor fit of our analysis in this region values of resonance energies cannot be determined very accurately. The resonance at 431 keV observed by Bowman et.al. is not observed by us but we have observed resonances at 426 and 433 keV with good fits to the data.

For non-s-wave resonances agreement is quite good for both <sup>54</sup>Fe and <sup>56</sup>Fe except the fact that we observe a much larger number of resonances.

Garg et.al. as well as Bowman et.al. report a s-wave resonance at 122.0 keV for <sup>56</sup>Fe. From the analysis of the present data we feel confident that it is a p-wave resonance. The width reported by their measurement is consistent with our value.  $\ell = 0$  resonance reported by Bowman et.al. at 164 keV for <sup>56</sup>Fe is not observed in the present data, but we do see a small peak at 164.6 keV in <sup>56</sup>Fe data which appears most likely to be an impurity. We have not analysed it.

### Strength Function

The strength function for  $\ell = 0$  and  $\ell = 1$  for both the isotopes of <sup>54</sup>Fe and <sup>56</sup>Fe is calculated as a function of neutron energy



using the following expressions:

$$S_0 = \frac{\sum g \Gamma_n^0}{E_f - E_i}$$

$$S_1 = \frac{1}{3} \frac{\sum g \Gamma_n^1}{E_f - E_i}$$

with the uncertainties given as:

$$\Delta S_\ell = \sqrt{\frac{2}{N}} S_\ell$$

where N is the number of levels observed.

In both the nuclei the strength function values tend to increase smoothly as the neutron energy increases. For example for p-wave the value of  $S_1$  for  $^{54}\text{Fe}$  is  $(0.44 \pm .12) \times 10^{-4}$  up to 500 keV whereas it is  $(0.56 \pm .16) \times 10^{-4}$  up to 650 keV. Similarly for s wave for  $^{56}\text{Fe}$  the value up to 200 keV is  $(1.88 \pm .94) \times 10^{-4}$  and up to 500 keV it is  $(2.6 \pm .86) \times 10^{-4}$ . From the measurements of Cierjack et.al.<sup>3</sup>, a value of about 3.2 between 500 keV and 1 MeV is determined. This effect of the gradual increase of the strength function vs  $E_n$  is somewhat puzzling, although the values are not completely outside the limits of uncertainties quoted.

#### Neutron Width Distribution

The distribution of neutron reduced width about its mean value has been investigated for s and p-wave levels of  $^{54}\text{Fe}$  and  $^{56}\text{Fe}$ . The combined results of these measurements as shown in the figures 3a and 3b indicated that for s-wave resonances, the neutron width distribution is in good agreement with what is expected from the Porter-Thomas distribution. For the case of p-wave levels, the data shows a lack of small neutron widths (less than  $0.2 \langle \Gamma_n \rangle$ ) but an excess of widths in the interval  $0.2 < x \leq 0.6$  than predicted by the Porter-Thomas distribution. This might indicate that in our analysis we have over-estimated some of the very narrow widths. We intend to re-examine this analysis.

#### Spacing Distribution

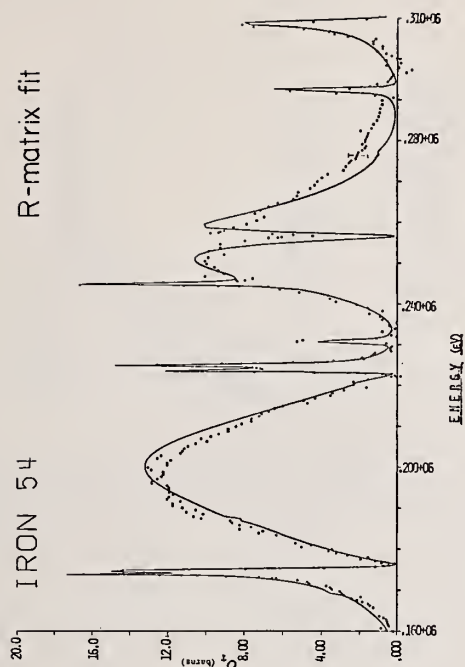
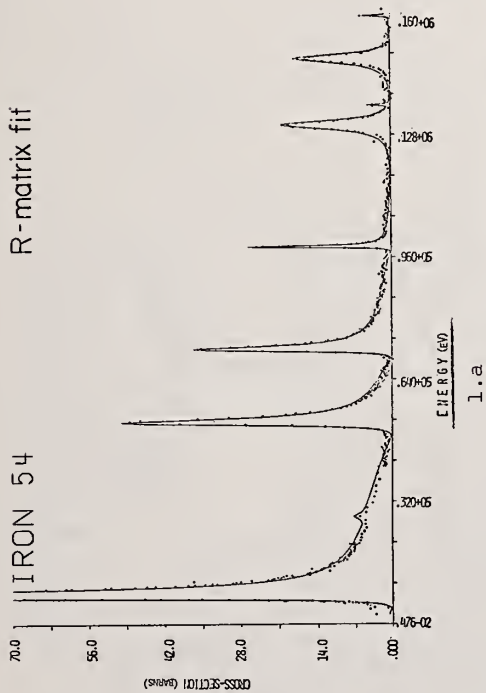
We have also investigated the nearest neighbor spacing distribution of s and p-levels of these nuclei and the results are shown in the figures 4a and 4b. For s-wave levels the agreement is excellent with the Wigner distribution as expected; whereas for p-wave levels, the data agree quite well with the Wigner distribution for a merged series of 2 level sequences with equal level density.

\*Work supported in part by the U.S.A.E.C.

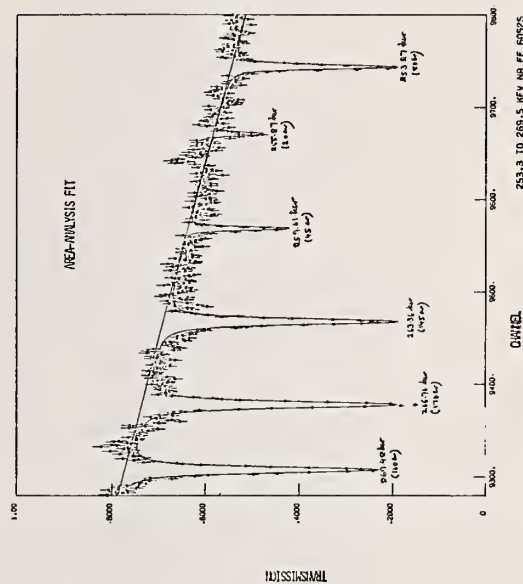
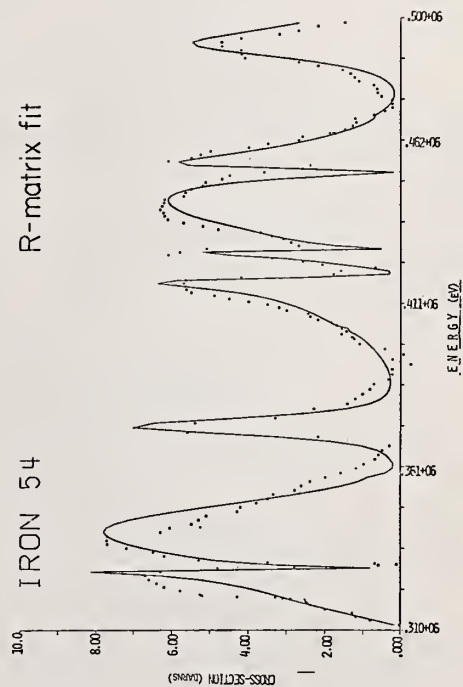
1. C.D. Bowman, E.G. Bilpuch, and H.W. Newson, Annal of Physics 17, 319 (1962).
2. J.B. Garg, J. Rainwater and W.W. Havens, Jr., Phys. Rev. C 3, 2447 (1971).
3. S. Cierjacks, Proc. of International School Neutron Physics, Alushta, USSR (1974).

#### Figure Captions

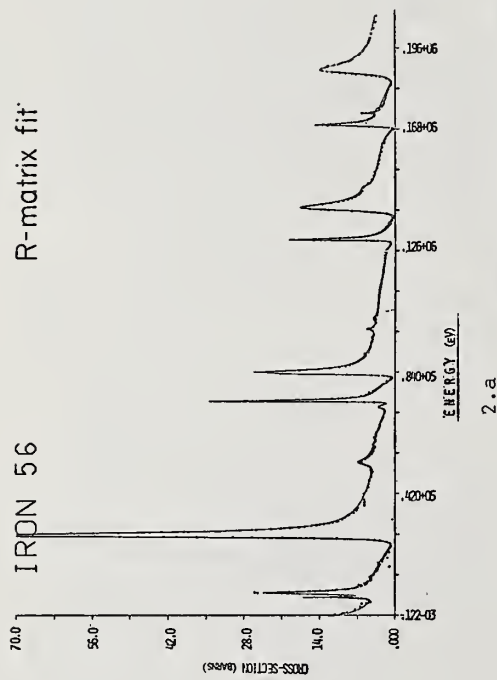
- Fig. 1 & 2: Neutron total cross section data. The solid line is the R-matrix fit to the data.
- Fig. 3: The histogram represents the experimental neutron reduced width distribution. The data has been normalized to the number of levels indicated within the bracket. This number was arrived at by taking into account the missed levels. The comparison is made with the Porter-Thomas distribution for a single sequence and the random distribution of neutron widths.
- Fig. 4: The histogram represents the experimental level spacing distribution. The data has been normalized to the number of levels indicated within the bracket. The comparison is made with the random distribution of spacings, Wigner distribution of single sequence and Wigner distribution of two sequences with equal densities.



Neutron total cross section data. The solid line is the R-matrix fit to the data.

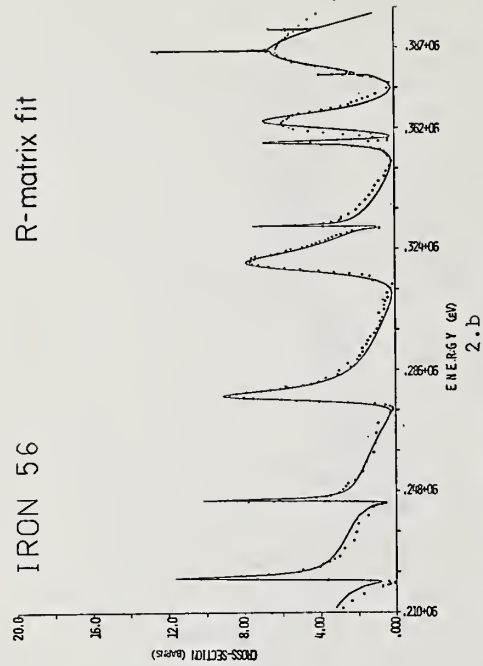


Area analysis fit to transmission  $^{56}\text{Fe}$ .

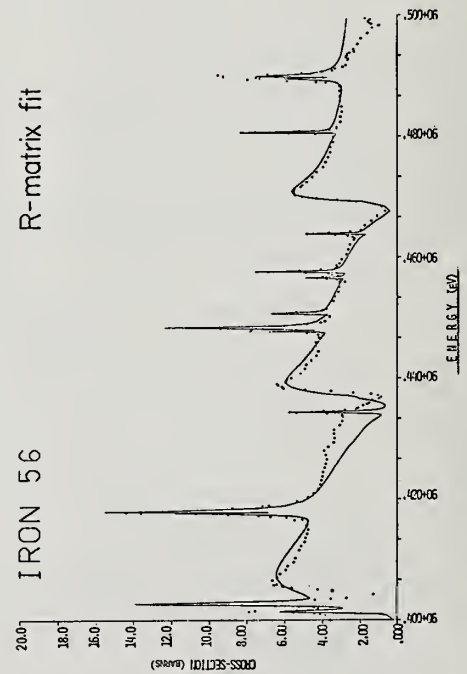


2.a

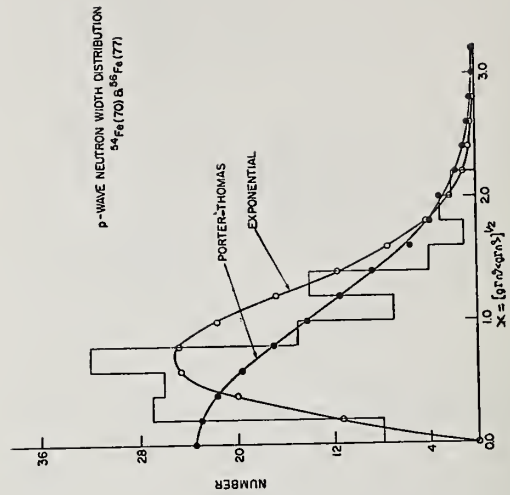
Neutron total cross section data. The solid line is the R-matrix fit to the data.



2.b



2.c



3.a



$^{55}\text{Fe}$ 

\*The uncertainties are determined from fitting the data by R-matrix.

 $^{56}\text{Fe}$ 

\*The uncertainties are estimated from fitting the data by R-matrix.

84.86

THICK SAMPLE TRANSMISSION MEASUREMENT AND RESONANCE ANALYSIS OF  
THE TOTAL NEUTRON CROSS SECTION OF IRON

S. Cierjacks, G. Schmalz, R. Töpke, R.R. Spencer, F. Voss

Institut für Angewandte Kernphysik  
Kernforschungszentrum Karlsruhe, F.R. Germany

New transmission measurements on natural iron samples were performed at the 190 m flight path of the Karlsruhe fast neutron time-of-flight spectrometer, allowing for an improved resolution of 0.015 ns/m. The measurements were carried out in the energy range from 0.5 - 30 MeV using two largely different sample thicknesses. The thick sample results indicate, that the deep s-wave minima are now fully explored in the energy range below the inelastic scattering threshold at about 850 keV. From the highly resolved transmission data resonance parameters were determined by a multilevel R-matrix analysis. The results of the thick sample measurements between 0.5 - 30 MeV and the resonance parameters determined in the range between 500 - 800 keV are presented.

(Fe(n),  $E_n = 0.5-30$  MeV, measured  $\sigma_{nT}(E)$ . Multilevel R-matrix resonance analysis)

### Introduction

Neutron cross sections for iron are of obvious importance for fast breeder reactor calculations. Iron in particular is a major structural material, but also an important shielding material for fast breeders as well as for various types of other nuclear installations. Iron data are of interest in connection with technological problems in thermonuclear research. Currently iron is considered to be a potential constituent of the containment vessel of a hypothetical fusion reactor. The total neutron cross section of iron was measured during the recent years in several laboratories<sup>1-4</sup>. However, application of these data, e.g. for shielding purposes, indicated, that the cross section structure in the many keV- and the a few MeV-range was not known with a sufficient accuracy. In particular poor information about the deep s-wave minima seemed to exist in the range above 100 keV. Therefore, it was the aim of this work to improve the present information about the iron total neutron cross section structure, employing the 190 m flight path of the Karlsruhe fast neutron spectrometer. With the improved resolution of 0.015 ns/m, all s-wave, but also most p- and d-wave resonances could in fact be resolved in the range below 900 keV.

In the a-few hundred keV range iron provides an example of a clean nucleus for an R-matrix single channel description. The ground state spin of the major isotope <sup>56</sup>Fe with an isotopic abundance of 91.66 % is zero and the inelastic channel is not open until 0.845 MeV. Together with the observation that any high resolution data show resolved but closely spaced resonances, a multilevel, single channel R-matrix analysis of the total cross section data can be made.

### Experimental description

The total neutron cross section of iron was measured with the neutron time-of-flight spectrometer at the Karlsruhe Isochronous Cyclotron, a detailed description of which has been given elsewhere<sup>5</sup>. Therefore, in the following only the details pertinent to this measurement will be described briefly. The highly resolved data in the energy range from 0.5-30 MeV were obtained by transmission measurement in good geometry. Neutrons were produced by bombardment of a thick natural uranium target with 45 + 5 MeV deuterons from the internal cyclotron beam. Using a particular deflection-bunching system neutrons are produced in bunches of 1 nsec duration at a repetition rate of 31.02 kHz. Standard time-of-flight techniques were used for data collection. A plastic scintillator (NE 102 A), 25 cm in diameter by 1 cm thick, viewed by two XP 1040 Valvo

photomultiplier tubes, was used for neutron detection. In order to reduce background events, simultaneous registration in both photomultipliers was required by means of a 25 nsec coincidence. The incident neutron beam was monitored by a  $\gamma$ -pulse-shaping detector placed at a second flight path at an angle of 6° to the incident deuteron beam and at a distance of ~11 m from the source.

The time spectrum was analysed in 24,000 channels of 1 ns channel width by a digital time-sorter (LABEN UC-KB) and accumulated with a CDC-3100 on-line computer. The use of a direct input channel and a magnetic disc allowed data accumulation with a detector counting rate of typically 40,000 events/sec. At maximum eight stop events per burst cycle can be accepted by the time analyser, giving little dead time losses. With the flight path of 187.46 meters, an overall spectrometer resolution of 0.015 ns/m was obtained. This corresponds to an energy resolution of 150 eV at 0.5 MeV and of 65 keV at 30 MeV. The scattering samples were slabs of pure Fe-metal (99.87 % Fe), 0.458 at/b and 0.109 at/b thick. Neutron spectra were measured in a typical cycle time of ~500 sec for the sample in place and with sample removed from the beam. Uncertainties due to counting statistics are between 1 % and 3 % at 0.5 MeV and 0.4 % at 15 MeV. Corrections were applied for background and dead time effects. The combined corrections were typically of the order of a few per cent of the open beam counting rate. The correction does not exceed 10 % for the background correction (at 0.5 MeV) and 15 % for the dead time correction (at 5.1  $\mu$ sec). Corrections for in-scattering were less than 0.01% and thus not taken into account.

### R-Matrix multilevel program

Since in the investigated energy range from 0.5 - 0.9 MeV level widths are approaching the level spacings so that level-level interference is important, an appropriate description of the iron resonances is provided by the multilevel R-matrix formulae with one open channel for elastic scattering. This description is exact for <sup>56</sup>Fe at energies below the inelastic threshold at 0.845 keV, assuming that neutron capture is negligible.

For resonance parameter analysis of this type a computer program, FANAL 2, was available at Karlsruhe. Details of this code are given elsewhere<sup>6</sup>. The following essential assumptions are used in this code.

In the single channel case, where the R-matrix reduces to a simple R-function, the usual relation, between the R-function and the collision function  $U_1$  is used



$$U_1 = \exp(2i\phi) \left[ 1 - 2i P_1 (R_1^0 / (1 + L_1^0 R_1^0)) \right]$$

where the  $S_1$ ,  $P_1$  and  $\phi_1$  are the shift factor, the penetration factor and the potential scattering phase shift. The level shift factor is set to zero by choosing the boundary condition  $B_1 = S_1(E)$ . The R-function is splitted as to Lane and Thomas into a slightly energy dependent background term  $R^0$ , and an explicit sum of resonance terms:

$$R_\lambda = R_\lambda^0 + \sum_{\lambda} \gamma_\lambda^2 / (E_\lambda - E)$$

The influence of levels outside the range is accounted for by a power series expansion of the  $R^0$  background component in terms of the medium energy  $E_m$  in the region of analysis

$$R_\lambda^0 = A_\lambda + B_\lambda (E - E_m) + C_\lambda (E - E_m)^2$$

with terms higher than the second order of  $(E - E_m)$  neglected.

On the basis of the above R-matrix formulation the code operates by a  $\chi^2$  minimization, given a particular isotopic composition of the target element and a corresponding set of resonance assignments (l and J-values). With the program the transmission data for two different sample thicknesses can be fitted simultaneously, while weighting is made according to the statistical accuracy of the both data sets. Transmission data with a maximum of 5000 data points can be fitted in one run, if the number of adjustable parameters in the range of analysis does not exceed the limit of fifty.

For inclusion of neutron resonances from higher partial waves, some modifications of the FANAL 2 program were applied, since the program in its standard version was written for the analysis of s-wave resonances only.

#### Cross sections and resonance parameters

Total neutron cross section data are given in the investigated energy range from 0.5-30 MeV. In fig. 1, the data obtained from the thick sample measurements are shown in a double logarithmic plot.

Cross sections variations due to statistical uncertainties are negligible, since the statistical accuracy is better than 1 % over most of the whole energy range; thus lying beyond the point sizes of the data in the plot. An exception is only the narrow range between 0.5-0.7 MeV, where the statistical accuracy ranges between 3-1 %. In order to illustrate the complex cross section behaviour in the a few hundred keV range, fig. 2 shows part of the same results in the range from 0.5-0.9 MeV on a linear scale. It is obvious from these data, that in the several hundred keV range one still deals with separated but closely spaced resonances. This gives the opportunity to extract from the data the major resonance parameters such as resonance energies and widths, by means of an R-matrix multilevel shape fit. In fig. 3 an R-matrix least squares fit to both measured transmission curves simultaneously is presented. Only those resonances which were sufficiently resolved in the measurements are included in the analysis. All resonance structure in the data was treated in terms of  $^{56}\text{Fe}+n$  scattering. Contributions from other isotopes in the natural isotopic composition are only important for  $^{54}\text{Fe}$ , which occurs with 5.8% abundance. Its effect on the transmission was only taken into account by including its potential s-wave scattering cross sections. The resonance parameters obtained for  $^{56}\text{Fe}$  are listed in table 1.

Resonances with sufficiently large peak cross sections to justify a  $J \geq 3/2$  assignment were all treated as p 3/2 resonances. This is expected to give a fairly correct description of resonance energies and resonance widths as long as resonance potential interference is small. Assignments of  $J=(5/2)$  were made in cases in which the peak cross section exceeds

significantly the  $g = 2$  limit. Except for  $J = 1/2$  resonances, which are uniquely identified by this experiment, no l-values are given for all other resonances. This is due to the fact, that the total neutron cross section alone does not permit a clear separation of resonances having the same J-value but belong to different partial waves. For the establishment of unambiguous spin and parity assignment, further investigations are necessary. For this nucleus, in particular, an a few angle elastic scattering experiment appears to be most valuable.

#### Intermediate resonance near 750 keV

An intermediate resonance in the neutron scattering cross section of iron near 750 keV has been suggested from a few previous experiments on total and differential elastic scattering for this nucleus<sup>7,8</sup>. An indication for an intermediate resonance is found in the energy averaged total cross sections shown in fig. 4. In this figure, which shows the Karlsruhe data averaged over 50 keV sliding energy interval, we observe a broad resonance peaking at about 770 keV. If this broad resonance is due to the suggested 2p-1h s-wave doorway state resonance, it is necessary that the intermediate resonance is formed by s-wave fine structure resonances only. Applying in addition the intermediate coupling picture, the total reduced width of the intermediate resonance must be preserved in the sum of the corresponding reduced fine structure width, i.e. a test of the sum rule for the reduced width must be positive. This possibility has been tested and the preliminary result is shown in fig. 5. This diagram compares the summation of the reduced widths of the s-wave fine structure resonances with the width of the intermediate resonance. Considering some uncertainties due to the restricted energy range, fig. 5 shows a remarkably good agreement with a sum rule.

#### Summary

For iron new high resolution total neutron cross section data are given for the energy range between 0.6 - 30 MeV. A satisfactory interpretation of the resonance data in the range from 0.5-0.85 MeV can be obtained with a one channel multilevel R-matrix description. The analysis provides detailed resonance parameters for ~ hundred resonances. Unambiguous l-values from the analysis of the total neutron cross sections can be assigned only for  $J = 1/2$  resonances. A full description of the neutron scattering resonances requires further investigations. For an unambiguous assignment of the spins and parities of the resonances an a-few angle elastic scattering experiment would be sufficient. Such an experiment has recently been performed at the 190 m flight path of the Karlsruhe isochronous cyclotron. The combined interpretation of both high-resolution total neutron cross sections and high resolution a-few angle elastic scattering data is presently under investigation.

#### References

- 1 P. Boscung, J.T. Lindow, E.F. Shrader  
Nucl. Phys. **A161** (1971) 593
- 2 J.A. Harvey, II. Int. School on Neutron Physics, Alushta, Crimea, USSR, 1974,  
J.A. Harvey et al. Report NCSAC-42 (1971) 183
- 3 S. Cierjacks  
Proc. 2nd Int. Conf. on Nuclear Data for Reactors, Helsinki 1970, Vol. II, p. 219 and literature cited therein.
- 4 J.B. Garg, J. Rainwater, W.W. Havens, Jr.  
Phys. Rev. **C3** (1971) 2447



- <sup>5</sup> S. Cierjacks, B. Duelli, P. Forti, D. Kopsch, L. Kropp, M. Lösel, J. Nebe, H. Schweickert, H. Unseld  
Rev. Sci. Instr. 39 (1968) 1279 and  
S. Cierjacks,  
Conf. on Nucl. Structure Study with Neutrons, Buda-  
pest 1972, p. 299
- <sup>6</sup> F.H. Fröhner  
Report KFK 2129 (1975)
- <sup>7</sup> C.D. Bowman, E.G. Bilpuch, H.W. Newson,  
Ann. Physics 17 (1962) 319
- <sup>8</sup> J.E. Monahan, A.J. Elwyn  
Phys. Rev. Letters 20 (1968) 1119

$E_R$ (keV)	$\Gamma_n$ (keV)	$l$	$J$	$E_R$ (keV)	$\Gamma_n$ (keV)	$l$	$J$
500.2	1.22	0	1/2	558.6	1.0		3/2
503.3	0.4	1	1/2	560.82	1.96	0	1/2
511.6	0.46		3/2	561.3	0.2		3/2
513.1	0.26		3/2	565.32	0.06	1	1/2
527.3	0.25	1	1/2	569.12	0.15		3/2
531.8	0.16	1	1/2	575.4	0.06	1	1/2
533.4	0.11	1	1/2	575.87	0.65	0	1/2
535.67	0.18	0	1/2	577.0	1.0		3/2
538.7	0.46		3/2	579.4	0.15		3/2
545.6	0.52		3/2	588.2	0.02	1	1/2
552.27	0.16	1	1/2	590.2	0.1	1	1/2

$E_R$ (keV)	$\Gamma_n$ (keV)	$l$	$J$	$E_R$ (keV)	$\Gamma_n$ (keV)	$l$	$J$
595.0	0.2	1	1/2	716.7	0.8	1	1/2
597.3	0.02	1	1/2	716.8	27.8	0	1/2
603.16	0.15	0	1/2	721.5	1.0	1	1/2
609.77	0.062	0	1/2	727.5	0.75		3/2
613.67	2.47	0	1/2	731.5	0.3	1	1/2
614.5	0.2	1	1/2	737.5	1.0		(5/2)
623.6	0.1	1	1/2	739.2	0.1	1	1/2
626.5	0.07	1	1/2	740.5	0.05	1	1/2
630.8	0.2	1	1/2	742.0	8.9	0	3/2
633.2	0.15	1	1/2	745.4	0.5	1	1/2
637.17	0.41	1	1/2	749.9	1.4		3/2
641.25	0.1	1	1/2	752.97	9.61	0	1/2
643.8	0.1	1	1/2	753.2	0.6	1	1/2
646.33	1.0		(5/2)	755.8	1.5		(5/2)
653.3	0.47	1	1/2	758.9	0.1	1	1/2
655.46	0.78		3/2	760.6	0.02	1	1/2
657.67	0.7		3/2	764.5	0.1	1	1/2
663.1	0.05	1	1/2	766.5	0.8		3/2
665.3	0.2	1	1/2	769.7	6.66	0	1/2
665.72	24.32	0	1/2	770.8	0.5		3/2
670.87	0.21	1	1/2	771.8	0.1	1	1/2
684.8	0.42		3/2	777.6	0.2	1	1/2
689.38	0.35	1	1/2	780.1	0.4		3/2
690.7	0.38	1	1/2	782.5	0.3		3/2
693.18	1.94	0	1/2	785.0	9.14	0	1/2
695.5	1.2		(5/2)	786.0	1.5	1	1/2
702.1	0.08	1	1/2	788.5	1.5		(5/2)
714.1	0.2	1	1/2	793.6	0.3	1	1/2
715.5	0.2	1	1/2	795.3	0.2	1	1/2

Table 1: Resonance parameters for <sup>56</sup>Fe (n,n) between 500 and 800 keV (preliminary)

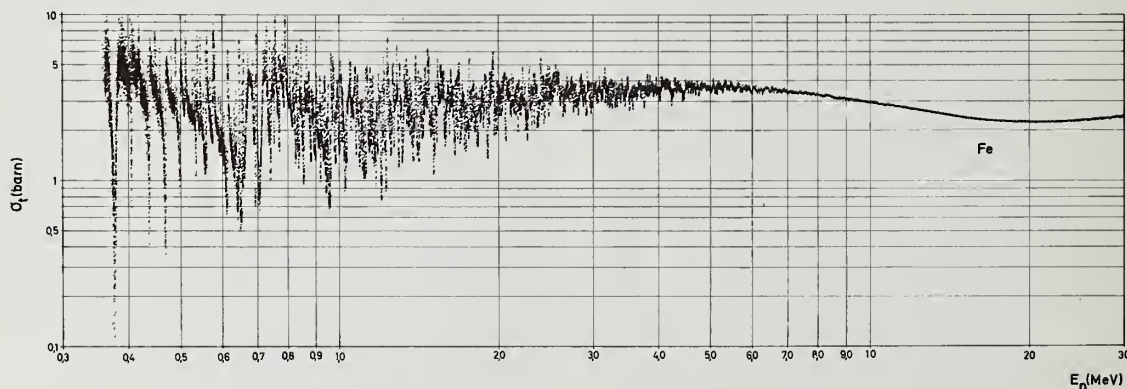


Fig. 1 Total neutron cross section of natural iron between 0.4 - 30 MeV.

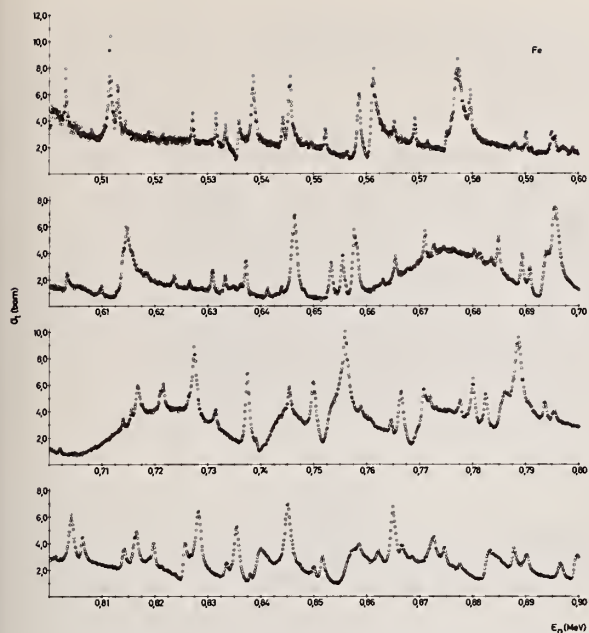


Fig. 2 Total neutron cross section of natural iron between 0.5 - 0.9 MeV

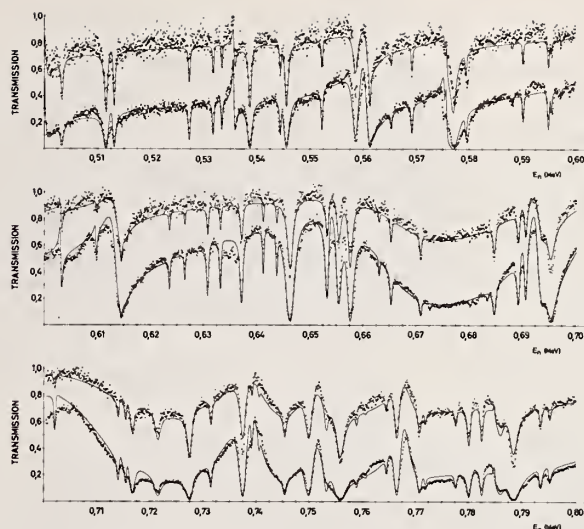


Fig. 3 Transmission data of Fe taken for two different sample thicknesses. The solid curve represents a multilevel least squares fit to both transmission curves simultaneously

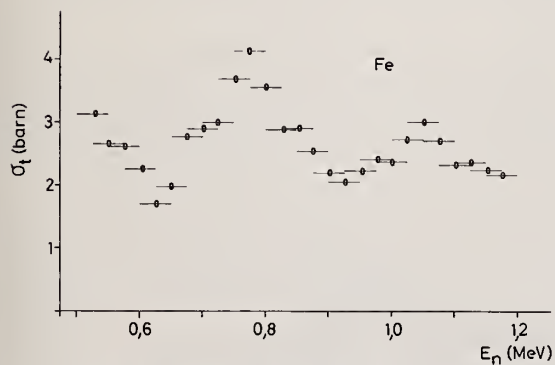


Fig. 4 50 keV average of total neutron cross section of Fe between 0.5 - 1.2 MeV

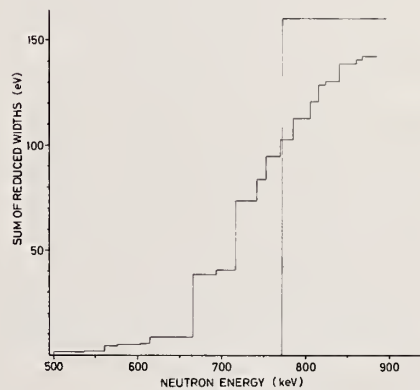


Fig. 5 Check of the sum rule for s-wave fine structure resonances forming the intermediate resonance in the average total cross section of iron near 770 keV (preliminary)

GAMMA-RAY PRODUCTION MEASUREMENTS DUE TO INTERACTIONS OF NEUTRONS  
WITH ELEMENTS REQUIRED FOR NUCLEAR POWER APPLICATIONS AND DESIGN\*  
G. T. Chapman, J. K. Dickens, T. A. Love, G. L. Morgan and E. Newman  
Oak Ridge National Laboratory  
Oak Ridge, Tennessee 37830

For the past three years neutron-induced gamma-ray production cross sections have been made for a variety of elements at the Oak Ridge Electron Linear Accelerator. A large, well shielded, NaI spectrometer was used as the gamma-ray detector and ORELA as the neutron source. The facility provides a consistent data set for neutron energies from 0.7 to 20 MeV and photon energies from 0.3 to 10.5 MeV. Typically the samples are flat plates of the element of  $\approx 0.02$  atoms/barn thickness, although several elements studied required samples in compound form. The data are accumulated in a two-parameter array, gamma-ray pulse height versus neutron time-of-flight. Data reduction was accomplished by binning in desired neutron-energy groups and in fixed photon-energy groups. For each neutron-energy group the data were unfolded using FERD unfolding routine, and the results are in the form of absolute differential cross sections,  $d^2\sigma/d\Omega dE$ , for each photon-energy bin. So far data have been obtained for 20 elements (Li, C, N, O, F, Mg, Al, Si, Ca, Fe, Ni, Cu, Zn, Nb, Ag, Sn, Ta, W, Au, and Pb).

[Cross sections, photon energy, (n,x $\gamma$ )]

### Introduction

There are many applications in the areas weapons effects, fission and fusion reactor shield design, and material selection for which neutron-induced gamma-ray production cross sections are required. For example, accurate cross sections are needed to permit the calculation of radiation fields through and around shields and structural components. In addition data of this type are employed in the calculation of the secondary heating of structural components and control electronics. Finally the cross sections are useful in establishing limits for secondary neutron production from the (n,np) and (n,pn) reactions. The present series of experiments were directed toward obtaining a complete and consistent data set for neutron energies from 700 keV to 20 MeV and for photon energies from 300 keV to 10.5 MeV. Ultimately, the measured cross sections serve as the basis for establishing an evaluated gamma-ray file in the ENDF data compilation.

### Experimental Methods and Data Reduction

For many applications, the detailed information on the deexcitation of each of the individual levels excited in the (n,x $\gamma$ ) reaction is neither required nor desired. Thus, to satisfy the requests<sup>1</sup> for gamma-ray production cross sections a facility has been set up at the Shield Test Station of the Oak Ridge Electron Linear Accelerator (ORELA) to accumulate data for a variety of elements. Basically the system consists of a NaI gamma-ray spectrometer, a computer for data accumulation and storage, and ORELA as the neutron source. A detailed description of the experimental facility, data accumulation, and data reduction techniques has been presented elsewhere<sup>2</sup> and we shall present here only a brief discussion.

Neutrons produced by bremsstrahlung in the tantalum linac target traversed a 47-meter flight path, approximately 40 m of which was maintained under vacuum to both increase the neutron intensity at the target and to reduce the effect of scattering resonances in air on the flux. For most of the data reported here the pulse width was on the order of 10 nsec with some of the data being taken with longer as well as shorter widths. The beam size at the target was limited by collimators to approximately 15-cm dia. Target samples were typically plates of the natural element measuring 30 x 30 cm and about 0.02 atoms/barn thick. Gamma rays from the target were observed in a 12.7 cm dia x 12.7 cm NaI crystal located in a shield and behind collimator made of lead and lithiated paraffin. The detector was shielded from scattered neutrons by a 25 cm thick

slab of lithium hydride placed in front of the detector. The neutron flux at the target was measured by using a NE-213 scintillator counter for energies above 1 MeV and a NE-110 detector below 1 MeV.

Digitized time-of-flight and pulse height signals were presented to a PDP-9 computer which correlated<sup>3</sup> the events and sent the pairs to the ORELA-SEL-810B computer for storage in a 256 x 500 channel PH vs TOF array. The data from individual runs were summed and background subtractions performed. The data were then binned in both neutron and gamma-ray energy intervals. The binned pulse height data were then unfolded with the code FERD<sup>4</sup> using the measured detector response matrix. Corrections were then applied for neutron and gamma-ray attenuation in the target. The final results for the double differential cross section,  $d^2\sigma/d\Omega dE$  vs  $E_\gamma$ , were then made absolute from the knowledge of the neutron flux and the sample thickness. In addition the integrated cross section,  $d\sigma/d\Omega$  vs  $E_n$ , were obtained for those gamma-rays above 0.7 MeV.

### Results and Discussion

In this section we will present a portion of the data which have been accumulated and reduced. The sample elements which are included are N, O, F, Mg, Al, Si, Ca, Fe, Ni, Cu, Zn, Nb, Ag, Sn, Ta, W, Au, and Pb. Table 1 lists the angle at which the experiments were performed and the appropriate references where the tabular data are available. In addition, the data are contained in the NNCSC. The first two figures, Figs. 1 and 2, are isometric representations of the double differential cross section for a light nucleus, aluminum, and a heavy one, tantalum, at  $\theta_\gamma = 125$  deg. The error bars shown do not include the uncertainty in absolute normalization which is estimated to be 10%. The data are shown as a function of incident neutron energy at the center of the neutron energy bin. As might be expected, the light nucleus shows several strong discrete gamma-ray lines whereas the heavy nucleus, because of the higher density of states, is relatively smooth.

To summarize and show the systematics of the data the cross sections for all of the elements studied for particular neutron energy bins are shown in Figs. 3-5. The three energy bins selected are 1.0-1.5 MeV, 5-6 MeV, and of particular interest in CTR work 12-14 MeV. The effect of the onset of the inelastic scattering mechanism is clearly seen by comparing the figures. Also evident is the spectral differences in the region of magic numbers.



The integrated cross section, for gamma-rays having energies greater than 0.7 MeV for most of the elements studied is shown in Fig. 6. The decrease in gamma-ray production cross sections above  $\sim 5$ -8 MeV can be understood in terms of the opening of the  $(n,2n)$  channel. This reaction populates low-lying levels in the residual nucleus with small gamma-ray multiplicities. The second break in the yield discernable in the heavy elements at about  $E_n \sim 15$  MeV is the result of the opening of the  $(n,3n)$  reaction channel. On the average, the gamma-ray production cross sections show a relatively smooth increase as a function of increasing atomic number. Data were also obtained at  $\theta_\gamma = 90$  deg for most of the lighter elements. For all but the very lightest these data are essentially equal to the 125 deg results indicating that to a good approximation the angular distributions are isotropic.

In addition to the nuclei specified above similar studies are scheduled for the elements of V, Cr, and Mo.

#### References

\*Research sponsored primarily by the Defense Nuclear Agency at Oak Ridge National Laboratory, operated by Union Carbide Corporation for the Energy Research and Development Administration.

1. *Compilation of Requests for Nuclear Cross Section Measurements*, LASL Rpt. NCSAC-35 (1971); *RENDA Compilation of EANDC Requests for Neutron Data Measurement*, Eur. Nucl. Energy Agency, O.E.C.D., Paris, Rpt. EANDC-83 "U" (1970).
2. G. L. Morgan, T. A. Love, J. K. Dickens, and F. G. Perey, *Gamma-Ray Production Cross Sections of Tantalum and Carbon for Incident Neutron Energies Between 0.7 and 20.0 MeV*, ORNL-TM-3702 (1972); J. K. Dickens, G. L. Morgan, and F. G. Perey, *Neutron-Induced Gamma-Ray Production in Iron for the Energy Range  $0.8 \leq E_n \leq 20$  MeV*, ORNL-TM-3850 (1972); J. K. Dickens, G. L. Morgan, and F. G. Perey, *Nucl. Sci. Eng.* **50**, 311 (1973).
3. C. E. Burgart and R. M. Freestone, Jr., *Neutron Phys. Div. Ann. Prog. Rpt.*, ORNL-4705, 46 (1971).
4. W. R. Burrus and V. V. Verbinski, *Nucl. Instr. and Meth.* **67**, 181 (1969).

Table 1. ORNL  $(n,xy)$  Measurements 1971-1974.

Element	Angle		Used in Evaluations	Report
	90°	125°		
Li		X	N	TM-4538
C	X	X	Y	TM-3702
N	X	X	Y	ORNL-4864
O	X	X	N	In Preparation
F		X	Y	TM-4538
Mg	X	X	N	TM-4544
Al	X	X	Y	TM-4232
Si	X	X	Y	TM-4389
Ca		X	Y	TM-4252
Fe		X	Y	In Preparation
Ni		X	Y	TM-4379
Cu		X	Y	ORNL-4846
Zn		X	Y	TM-4464
Nb	X		N	In Preparation
Ag		X	Y	In Preparation
Sn		X	Y	TM-4406
Ta	X	X	Y	TM-3702
W		X	Y	ORNL-4847
Au		X	Y	In Preparation
Pb		X	N	TM-4822

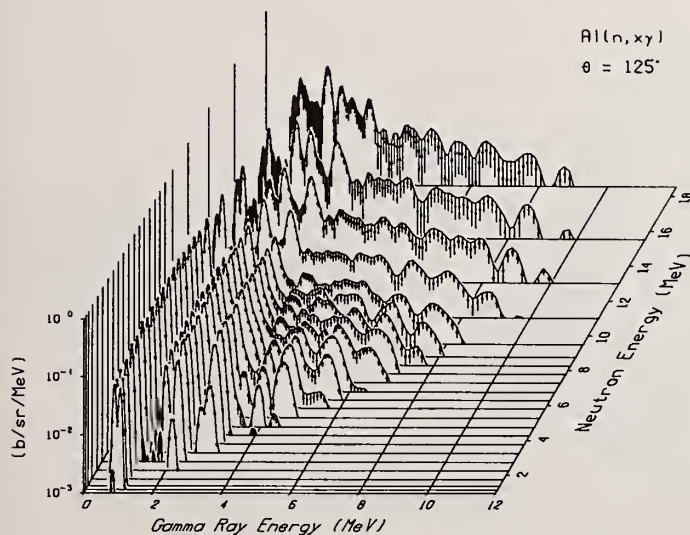


Figure 1. Isometric representation of the  $Al(n,xy)$  cross section at  $\theta_\gamma = 125$  deg. The error bars do not include the uncertainty in absolute normalization which is estimated to be 10%. Note that the solid line in the figure is drawn through the top of the error bars as a guide to the eye.

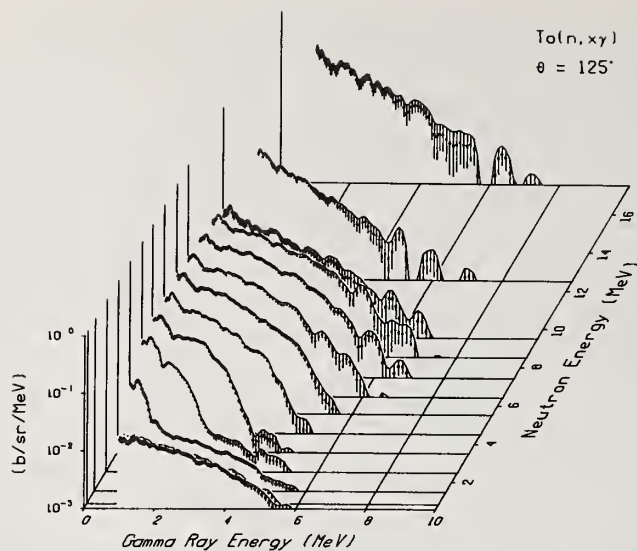


Figure 2. Isometric representation of the  $Ta(n, \gamma)$  cross section at  $\theta = 125^\circ$  deg. The error bars do not include the uncertainty in absolute normalization which is estimated to be 10%. Note that the solid line in the figure is drawn through the top of the error bars as a guide to the eye.

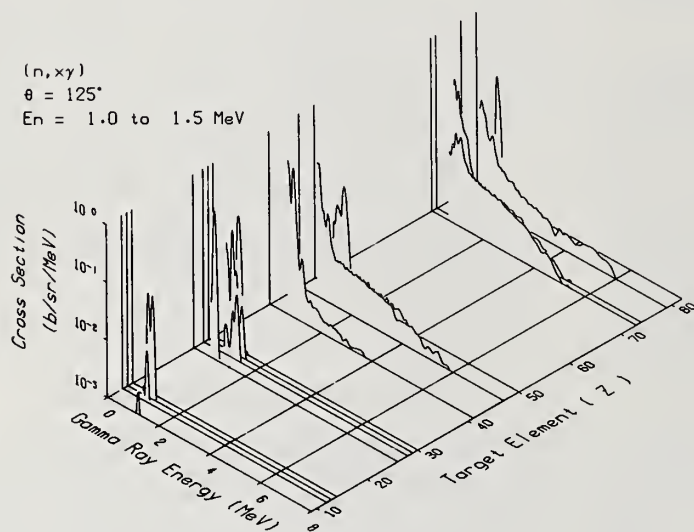


Figure 3. Double differential cross sections for the  $(n, \gamma)$  reaction on the elements studied to date. The curves are lines through the data points for the neutron energy bin 1.0-1.5 MeV.

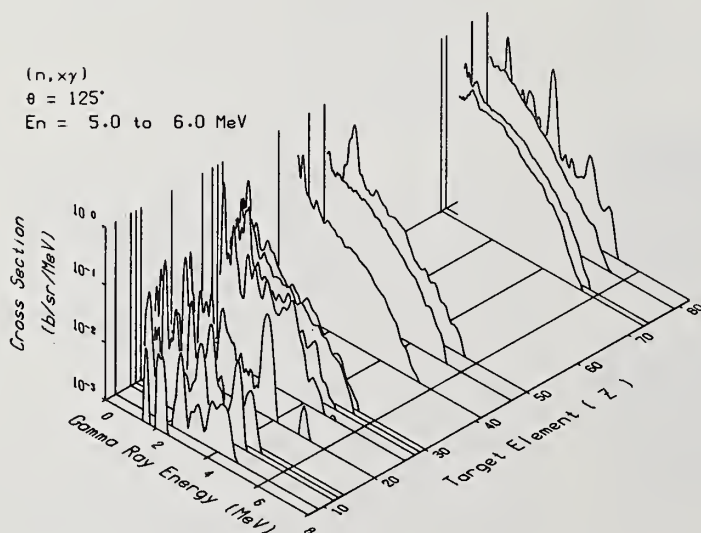


Figure 4. Double differential cross sections for the  $(n, \gamma)$  reaction on the elements studied to date. The curves are lines through the data points for the neutron energy bin 5.0-6.0 MeV.

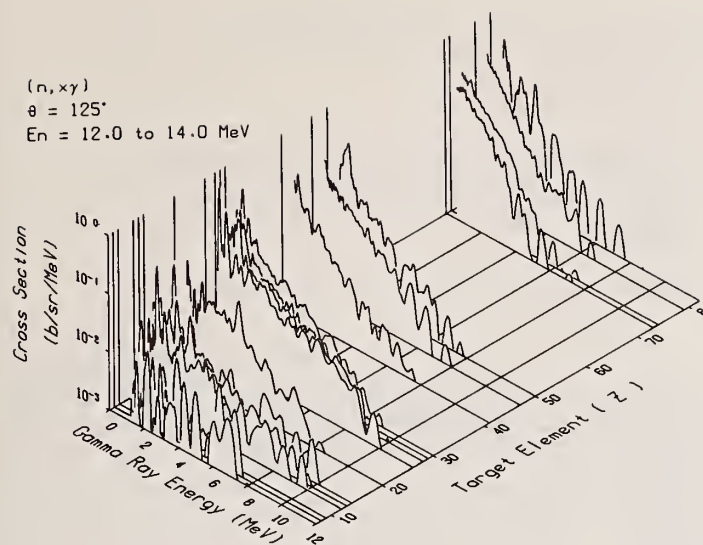


Figure 5. Double differential cross sections for the  $(n, \gamma)$  reaction on the elements studied to date. The curves are lines through the data points for the neutron energy bin 12.0-14.0 MeV.

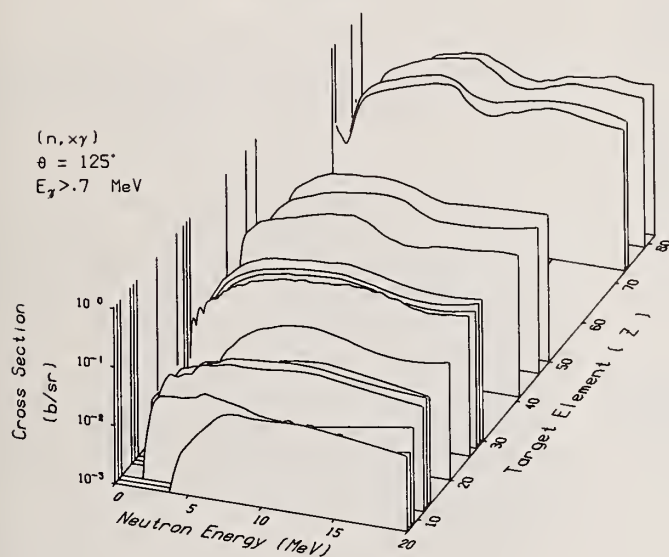


Figure 6. Integrated gamma-ray production cross sections for the  $(n, \gamma)$  reaction for  $E_\gamma$  greater than 0.7 MeV on a variety of target elements.



CROSS SECTIONS FOR THE PRODUCTION OF LOW ENERGY PHOTONS  
BY NEUTRON INTERACTIONS WITH FLUORINE AND TANTALUM\*  
J. K. Dickens, G. L. Morgan, and F. G. Perey  
Oak Ridge National Laboratory  
Oak Ridge, Tennessee 37830

Differential cross sections for the production of low energy photons ( $< 240$  keV) by neutron interactions in fluorine and tantalum have been measured for neutron energies between 0.1 and 20 MeV. Photons were detected at  $92^\circ$  using an intrinsic germanium detector. Incident neutron energies were determined by time-of-flight techniques for a white source spectrum.

(Cross sections, neutron-induced low-energy photons, fluorine, tantalum)

### Introduction

A previous paper at this conference<sup>1</sup> has presented measurements of cross sections for neutron induced gamma radiation in a number of elements. These data, obtained with a NaI detector and covering photon energies as low as 300 keV, are generally adequate for most applications. However, for several nuclides, the cross sections for production of lower energy photons may be quite large and constitute a significant fraction of the total photon production. In particular applications such as neutron-induced heating and ionization, the production of low energy gamma rays, conversion electrons and associated x-rays in these nuclides will be important.

Fluorine in the form of LiF is a possible constituent of a CTR blanket. It occurs as well in insulating material such as teflon. Tantalum is used in reactor control rods, heavy metal shields, and electronic components. We have therefore measured cross sections for the production of 96, 110, and 197 keV gamma rays from fluorine and for the K x-rays and several of the discrete gamma rays from tantalum over the neutron energy range from 0.1 to 20 MeV.

### Experimental Procedure

A schematic diagram of the experimental arrangement is shown in Fig. 1. This is basically the same as used in Ref. 1, except that a Ge detector was used instead of a shielded NaI crystal.

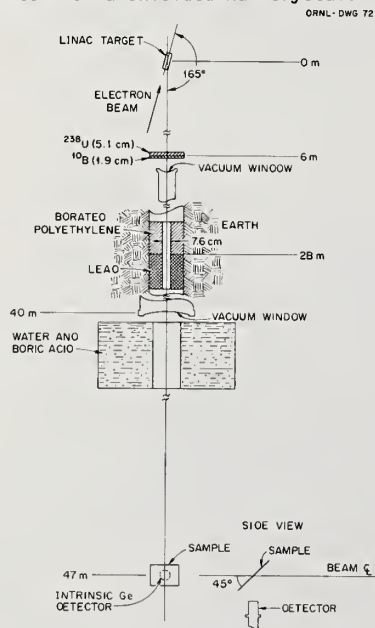


Figure 1.  
Experimental  
Facility Showing  
Neutron  
Source, Colli-  
mators, Sample  
and Detector.

Neutrons were produced at the tantalum target of the Oak Ridge Electron Linear Accelerator (ORELA). The samples consisted of 30 cm x 30 cm sheets of teflon (.0177 molecules/barn) or tantalum (.0007 atoms/b) oriented  $45^\circ$  with respect to the incident beam at a distance of 47 m from the neutron source. The neutron beam was defined by a 7.6-cm-diameter collimator located 28 m from the neutron source. A filter of uranium at 5 m reduced the intensity of the gamma flash. Overlap from adjacent linac bursts was prevented by a filter of  $^{10}\text{B}$ .

The detector, 200 mm<sup>2</sup> intrinsic germanium, was located at  $92^\circ$  with respect to the incident beam. It is important to note that this detector was specially constructed without the usual teflon insulating materials.

For each event occurring in the detector, the pulse of the event and its time of occurrence after the electron burst were recorded. These data were stored in two ways. In the first, the data were placed in a two-parameter array on a fast computer disk (a 2048 channel pulse height spectrum of each of 200 time-of-flight channels). In addition, digital windows were used to select prominent lines (or adjacent regions for background determination) for storage in a series of 1024 channel time-of-flight spectra. This technique permitted retention of all the pulse height information as well as high resolution in the incident neutron energy for dominant lines. Figure 2 shows a typical pulse height spectrum for the teflon sample obtained by integrating the two-parameter data over a range of time-of-flight.

The neutron flux was determined as in Ref. 1 using organic scintillators. The efficiency of the Ge detector was measured using a set of calibrated sources ( $^{241}\text{Am}$ ,  $^{57}\text{Co}$ ,  $^{152}\text{Eu}$ ). Because the low counting rate required a rather close and therefore extended geometry, considerable effort and testing were employed to ensure that the flux weighted efficiency and solid angle were accurately determined.

Backgrounds due to scattered neutrons were checked by acquiring data with a carbon slab (.01 atoms/barn) at the sample position. These were found to be negligible.

Absolute cross sections were derived from either of the two data sets described above by normalizing peak areas to neutron flux, detector efficiency and sample thickness. Corrections were applied for self-absorption in the sample.

### Results

Fluorine. Figures 3 and 4 show the results for the 110, 197, and 96 keV photons from fluorine. Tables of numerical values as well as comparisons with previous data are available elsewhere.<sup>2</sup> It should be

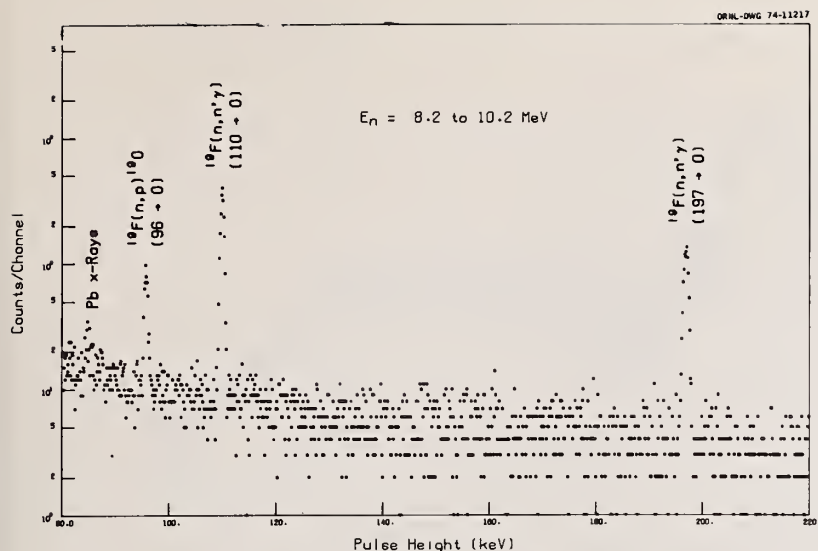


Figure 2. A typical pulse height spectrum from the teflon sample. The lead x-rays originate in the detector collimator.

noted that the 197 keV gamma-ray results from the decay of a level in  $^{19}\text{F}$  having a lifetime of 129 ns. This causes a slewing in the time-of-flight measurement which at neutron energies greater than 5 MeV distorts the energy dependence of the cross section. The dashed curve in Fig. 4 indicates the shape of the cross section after correction for this effect.

**Tantalum.** The total cross section for the production of K-series x-rays in tantalum is shown in Fig. 5. These results were obtained by analyzing each of four lines separately, then summing the differential cross sections and multiplying by  $4\pi$ . Checking the relative intensities of the separate lines with the tabulated values<sup>3</sup> verified the internal consistency of the data.

Figure 6 shows a typical result for one of the several low-energy gamma rays from tantalum. Close examination of the pulse height spectrum shows this line to be two unresolved photons, one from the 136  $\rightarrow$  0 transition, the other from the 619  $\rightarrow$  482 transition. Because the 136 keV level is partially fed by transitions originating at the level of 615 keV, which has a 20  $\mu\text{s}$  lifetime, some time slewing is also present in these data.

### References

\*Research sponsored by the Defense Nuclear Agency at Oak Ridge National Laboratory, operated by the Union Carbide Corporation for the Energy Research and Development Administration.

1. G. T. Chapman, J. K. Dickens, T. A. Love, G. L. Morgan, and E. Newman, preceding paper.
2. J. K. Dickens and G. L. Morgan, Production of Low-Energy Gamma Rays by Neutron Interactions with Fluorine for Incident Neutron Energies between 0.1 and 20 MeV, ORNL-TM-4823 (1975).
3. C. M. Lederer, J. M. Hollander, and I. Perlman, Table of Isotopes, 6th edition, Wiley, New York (1967).

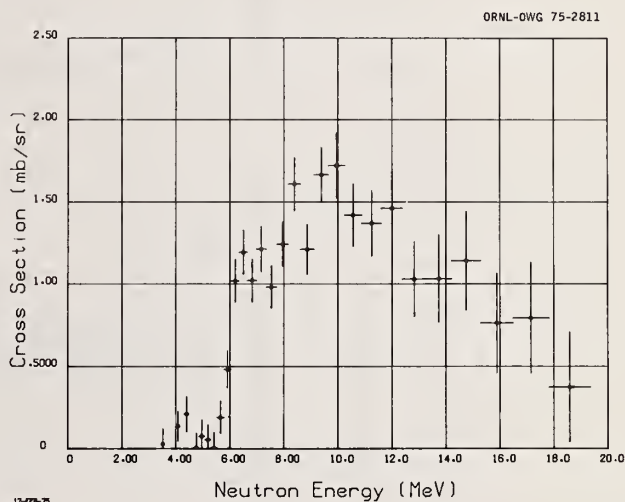


Figure 3. Differential cross section at  $92^\circ$  for the 96 keV gamma ray from the  $^{19}\text{F}(n,p)^{190}$  (96 keV) reaction.

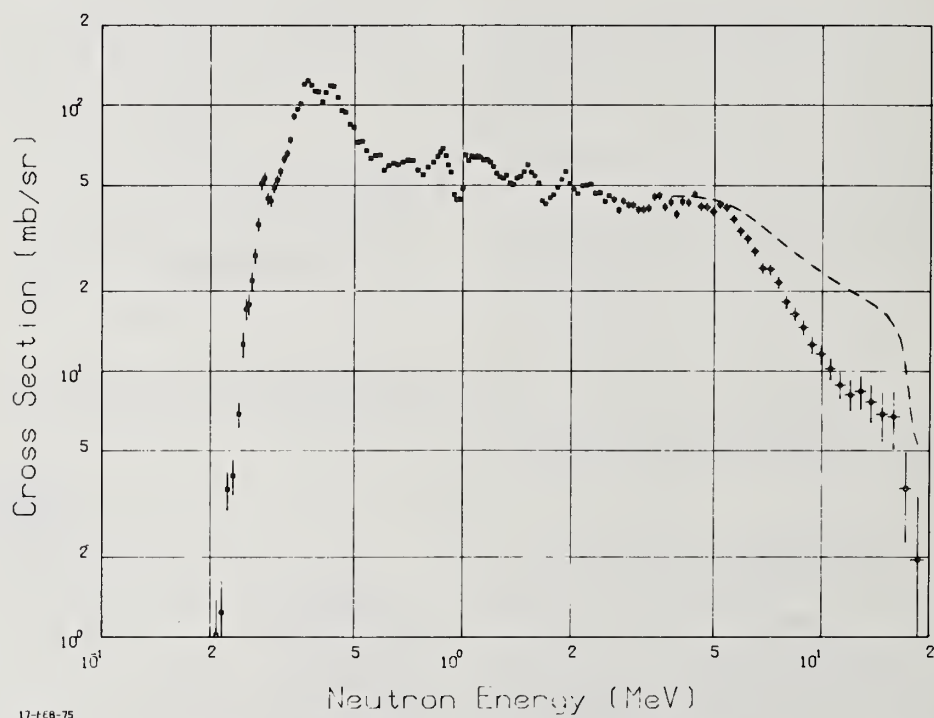
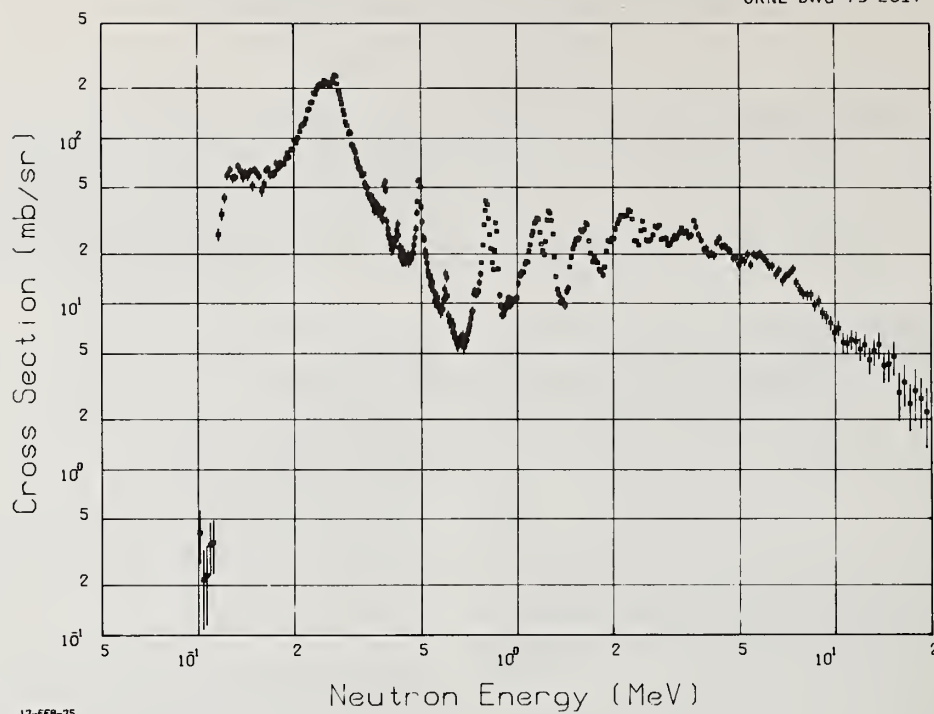


Figure 4. Differential cross section at 92° for the 110 and 197 keV gamma rays from fluorine. The dashed curve is an approximate correction for the 129 ns lifetime of the 197-keV level.



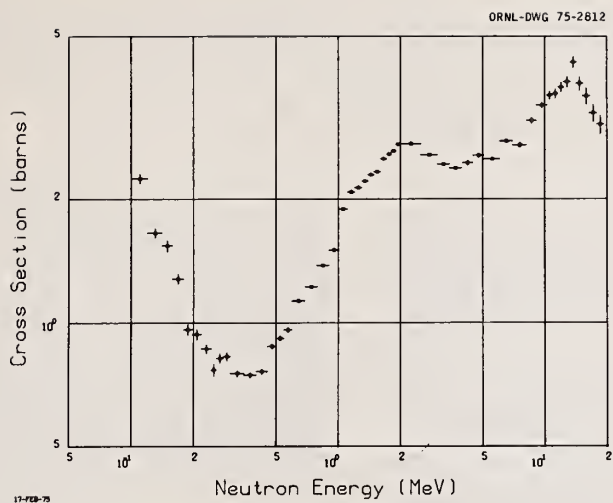


Figure 5. Total K x-ray Production cross section for tantalum.

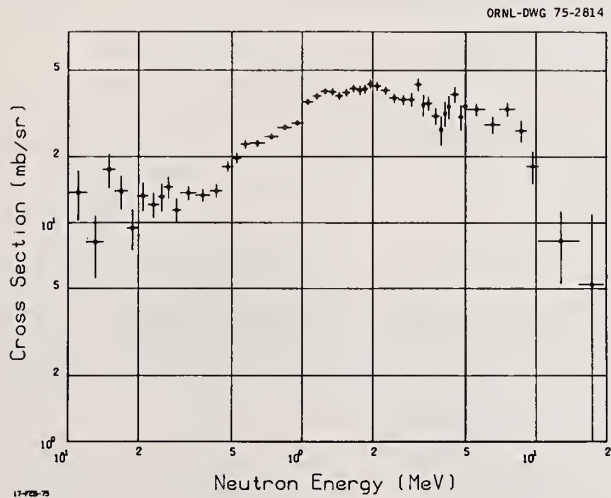


Figure 6. Differential Cross Section at  $92^\circ$  for 136 keV gamma rays from tantalum.

The gamma-ray production cross-section measurement program at IRT is described. Neutrons from epithermal energies to 21 MeV were produced with the IRT Linac, and gamma rays resulting from neutron interactions were detected with a Ge(Li) spectrometer system. Representative results are presented for C, N, Al, Si, and Fe.

$$[\sigma(n, \gamma) \text{ measurements; } E_n \text{ to 21 MeV; } E_\gamma \text{ to 10 MeV}]$$

### Introduction

In 1967 IRT Corporation developed the experimental procedure for measuring neutron-induced gamma-ray production cross sections using a pulsed electron Linac neutron source. Since that time, measurements have been made of the  $\sigma[n, \gamma(E_\gamma)]$  for Fe, W, and  $^{238}\text{U}$ , and of the  $\sigma[n, \gamma(E_\gamma)]$  for C, N, O, Al, Si, Fe, Cu, and Ta, using high gamma-ray energy resolution Ge(Li) detectors. The measurements yielded both high-resolution discrete-energy gamma-ray data, as well as the unfolded continuum-plus-discrete data. The greater sensitivity provided by this technique for measuring gamma-ray production cross sections over a broad neutron energy range is substantiated by its present widespread use.

The use of a pulsed electron Linac neutron source having a continuous distribution of energies allows the  $(n, \gamma)$  and  $(n, \gamma)$  cross sections to be measured simultaneously for neutron energies over a wide and continuous range in a single experimental run. The Linac technique also allows the choice of fine or broad neutron groups, and has the distinct advantage of providing a set of averaged cross sections for a series of contiguous energy intervals spanning the entire neutron energy range of interest for most applications.

This paper describes the program of measurements performed at the IRT Linac. Representative results are presented for many of the materials measured.

### Experimental Method

The facility used in the measurements has been described elsewhere.<sup>1,2</sup> Consequently, only the principal features of the experimental technique are reviewed here. The experimental arrangement is shown schematically in Figure 1. The electron Linac produces pulses of neutrons with a pulse width adjustable from 3 to 100 nsec, and a repetition rate of up to 1000 pps. A Ta-Be target produces a copious yield of high-energy neutrons with a minimum of gamma flash (bremsstrahlung from electrons striking the Ta converter). The neutrons, primarily produced by the  $(\gamma, n)$  reaction in the beryllium converter, traverse a 53-meter evacuated flight path and impinge on a ring-shaped scattering sample in which the gamma-ray producing neutron reactions occur. The scattering sample dimensions were 25 to 28 cm i.d. and 48 to 51 cm o.d., with thicknesses ranging from 0.99 cm for iron to 5.7 cm for the  $\text{D}_2\text{O}$  sample used to measure the oxygen reactions.

The energy (PH) of the gamma rays produced in the samples is measured with a large Ge(Li) detector located on the flight path axis near the sample, and shadow-shielded from the source neutrons and gamma rays with a "keyhole" shaped shadow shield. The corresponding neutron energy is obtained by recording the time-

of-flight (TOF); i.e., the time when the gamma ray is detected in the Ge(Li) detector relative to the Linac burst. During the course of the measurement program, Ge(Li) detectors ranging from 30 cm<sup>3</sup> to 80 cm<sup>3</sup> active volume have been used. The Ge(Li) detector is positioned at an angle of approximately 125° to the incident neutron beam in order to minimize the effect of gamma-ray anisotropy on the determination of the angle-integrated cross sections. Figure 2 presents a typical spectrum of the gamma rays from neutron interactions in copper. The favorable gamma-ray energy resolution is a result of optimizing the Linac conditions, spectrometer electronics, and experimental configuration.

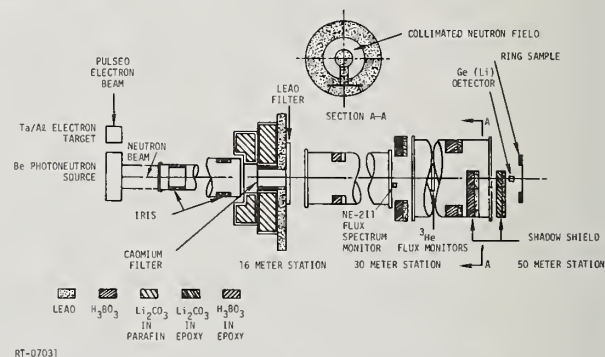


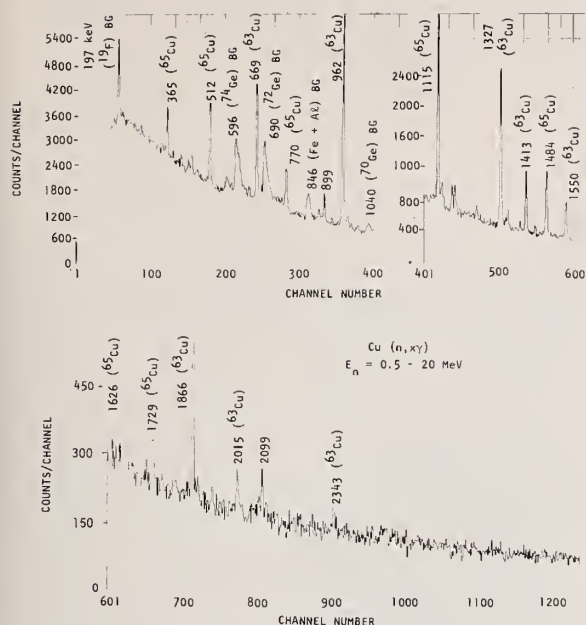
Figure 1. Schematic diagram of the experimental arrangement for the measurement of gamma-ray production cross sections

### Cross-Section Determinations

The two-parameter data are sorted in two ways: (1) the PH data are generated for selected neutron energy intervals (used for broad-group cross-section determination), and (2) TOF spectra are generated for selected gamma-ray peaks (used for the determination of high neutron energy resolution gamma-ray production cross sections).

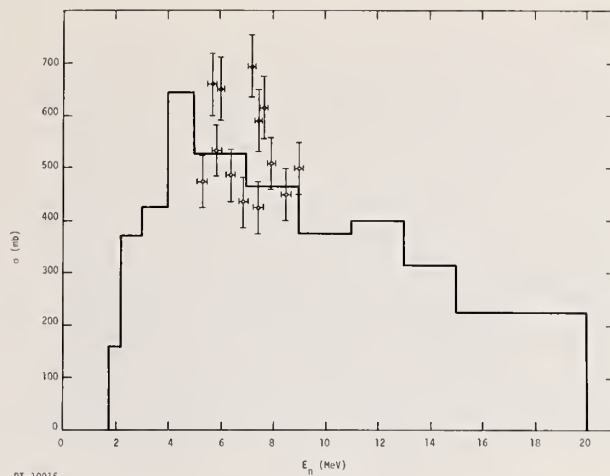
An example of the broad neutron grouped cross sections is presented in Figure 3. The 1.779-MeV gamma ray originates from  $(n, n')$  reactions in  $^{28}\text{Si}$ . Analysis of the silicon measurements is still in progress; thus, these results are preliminary.

A typical high-neutron resolution cross section is shown in Figure 4. The diamond points represent the measured value of the cross section for the production of the 4.44-MeV gamma ray from neutron interactions in carbon. Also shown is a similar measurement<sup>5</sup> made with a NaI detector at the ORNL electron Linac. The two measurements are in excellent agreement. Differences in the inherent neutron energy resolution account for the cross section discrepancies about the major resonances.



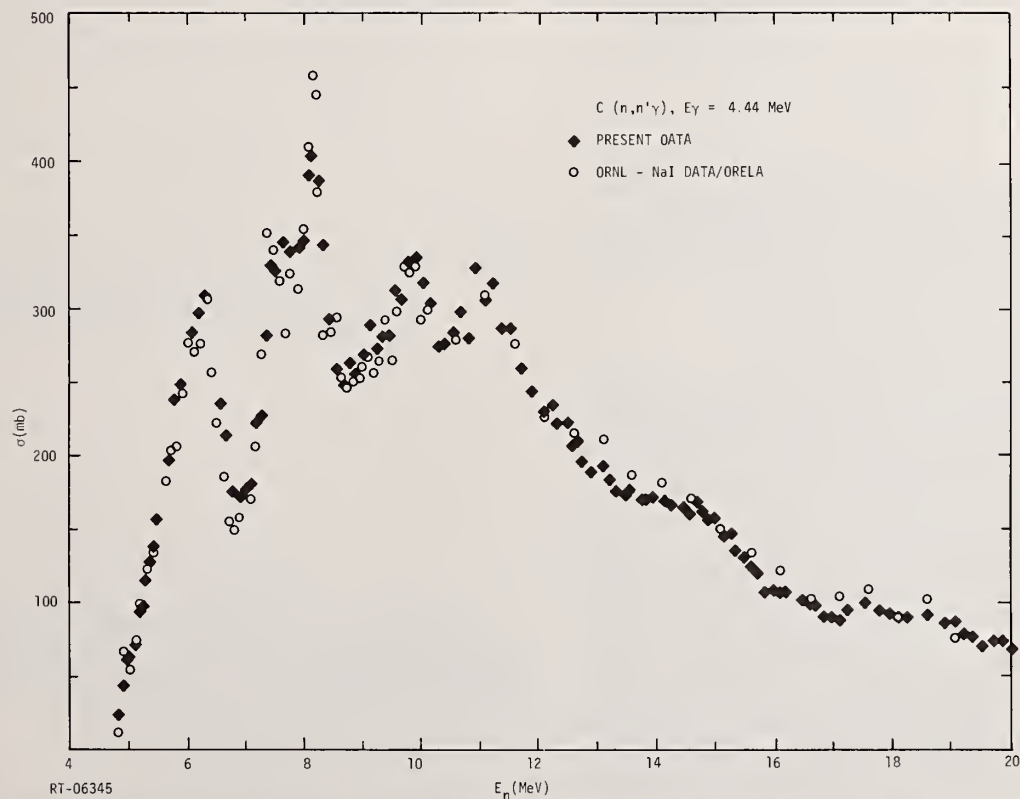
RT-10820

Figure 2. Typical gamma-ray energy spectrum from high-energy neutron interactions in copper



RT-10915

Figure 3. Preliminary results of the cross section for the production of the 1.779-MeV gamma ray from neutron interactions in natural silicon. The histogram represents the present data. Open-circle data are from Ref. 3, and solid circles from Ref. 4.



RT-06345

Figure 4. High neutron resolution cross section for the production of the 4.44-MeV gamma ray from carbon. The ORNL results are from Ref. 5.



Cross sections for the production of discrete gamma rays are obtained from the gamma-ray peak areas by accounting for the detector efficiency, the neutron fluence, sample atomic density, electronic dead time, and for the background contributions. In addition, corrections were made for the  $P_4$  contribution to the gamma-ray anisotropy and for the attenuation and multiple scattering of the neutrons and gamma rays. The sensitivity of the method is illustrated by the cross sections of the 6.444 and 2.499 MeV gamma rays from neutron interactions in nitrogen, shown in Figure 5. Previous measurements of  $\sigma(n, \gamma)$  for the discrete gamma-ray lines from nitrogen and from many of the other elements have not extended above a neutron energy 15 MeV; hence, the present measurements provide important information for the cross-section evaluations between 15 and 20 MeV. Cross sections less than 0.8 mb have been measured.

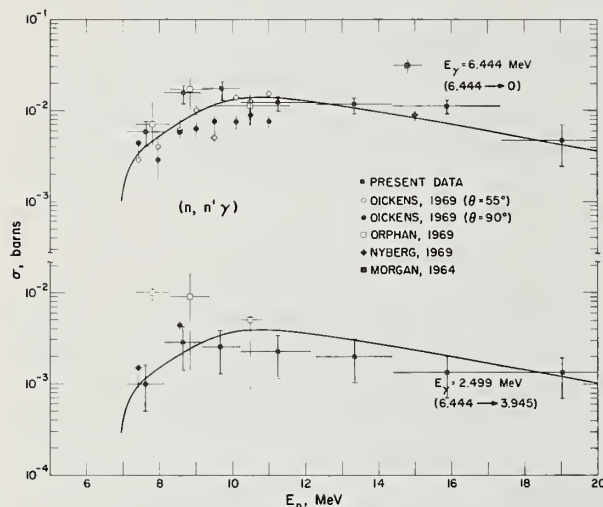
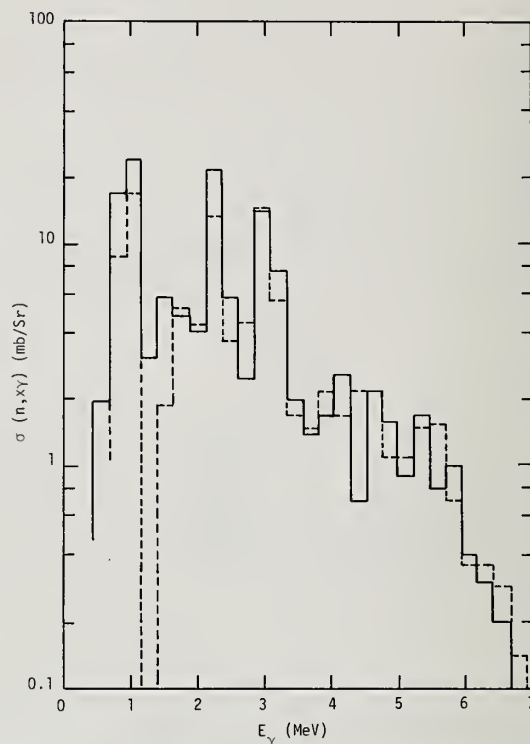


Figure 5. Cross sections for the production of the 6.444 and 2.499 MeV gamma rays from nitrogen. The present data are represented by solid squares. The curve is a recent evaluation. The other experimental data points are given in Ref. 6.

#### Discrete-Plus-Continuum Cross Sections

Frequently the  $\sigma(n, \gamma)$  for discrete lines represents only a fraction of the total gamma-ray production cross section. A significant number of cross sections from weak gamma rays are too small to measure individually, but collectively their sum amounts to a significant fraction of the total  $\sigma(n, \gamma)$ . This component has been determined by unfolding the PH spectra with the MAZE unfolding code.<sup>7</sup> Finite sample response functions used by MAZE are determined from a combination of experimental and calculated spectra. A recent reevaluation of the unfolded aluminum measurements is shown in Figure 6. When unfolding PH spectra, allowance must be made for the Compton scattering of gamma rays with the sample material. Although this correction only reduces the total  $\sigma(n, \gamma)$  for aluminum by 5 to 10%, it is much larger for gamma rays below 2 MeV. The multiple gamma-ray scattering correction for iron and copper is about 10 to 20%; however, the correction is as large as 40% between intense low-energy peaks. The measured spectral  $\sigma(n, \gamma)$  for 6.15 to 7.71 MeV neutrons incident upon iron is given in Figure 7.

Also shown in the figure is a spectral calculation performed with the DEBBIE code.



RT-10902

Figure 6. Total gamma-ray production cross section for 6.2 to 7.7 MeV neutron interactions in aluminum. The present data are represented by the solid curve. The dashed curve is from Ref. 8.

#### Conclusions

In summary, the gamma-ray production cross-section program conducted at the IRT Linac has provided high gamma-ray and neutron energy resolution data, as well as total (continuum-plus-discrete) gamma-ray spectral information for many elements.

#### Acknowledgments

This work is supported by the Defense Nuclear Agency. Appreciation is extended to Dr. P. G. Young of LASL in providing the original drawing for Figure 4.

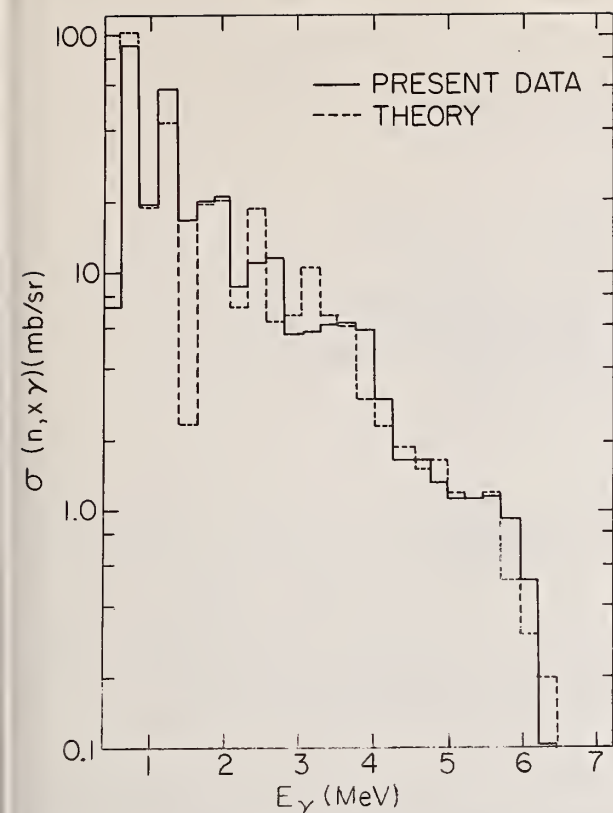


Figure 7. Comparison between measured and calculated differential gamma-ray production cross sections for 6.15 to 7.71 MeV incident neutron interactions in iron

#### References

1. V. J. Orphan, C. G. Hoot, A. D. Carlson, J. John, and J. R. Beyster, Nucl. Instr. Meth. **73**, 1 (1969).
2. V. J. Orphan, C. G. Hoot, and J. John, Nucl. Sci. Eng. **42**, 352 (1970).
3. J. K. Dickens, Phys. Rev. **C2**, 990 (1970).
4. D. M. Drake, et al., Nucl. Phys. **A128**, 209 (1969).
5. G. L. Morgan, T. A. Love, J. K. Dickens, and F. G. Perey, "Gamma-Ray Production Cross Sections of Tantalum and Carbon for Incident Neutron Energies Between 0.07 and 20.0 MeV," ORNL-TM-3702 (1972).
6. P. G. Young and D. G. Foster, Jr., "An Evaluation of the Neutron and Gamma-Ray Production Cross Sections for Nitrogen," LA-4725 (1972).
7. H. Kendrick and S. M. Sperling, "Numerical and Experimental Studies of Spectral Unfolding," RT-10468 (1971).
8. J. K. Dickens, T. A. Love, and G. L. Morgan, ORNL-TM-4232 (1973).

FOURTEEN-MEV, NEUTRON-INDUCED GAMMA-RAY  
PRODUCTION CROSS SECTIONS FOR SEVERAL ELEMENTS\*

E. D. Arthur, D. M. Drake, M. G. Silbert,  
and P. G. Young

Los Alamos Scientific Laboratory, University of California  
Los Alamos, N.M. 87544

A pulsed 14.2 MeV neutron source and a NaI(Tl) gamma-ray spectrometer were used to measure gamma-ray production cross sections for several elements in the range  $A = 12$  to 239. Angular distributions for some of the more prominent gamma ray groups were obtained. Complete gamma-ray production cross sections were measured for all the sample materials, including those in which no clearly separable gamma ray groups appeared.

(Nuclear reaction  $(n, n'\gamma)$ ; measured  $d^2\sigma/d\Omega dE$ ;  $E_n = 14.2$  MeV)

### Introduction

Through the use of a pulsed source of 14.2 MeV neutrons from the  $^2\text{H}(t, n)^4\text{He}$  reaction and a NaI(Tl) gamma-ray spectrometer, we have measured gamma-ray production cross sections for C, Mg, Al, Cr, Fe, Ni, Mo, Nb, Ta, Pt,  $^{235}\text{U}$  and  $^{239}\text{Pu}$ .

### Experimental Arrangement

Figure 1 shows the experimental setup. A chopped (2 MHz) triton beam was accelerated to 2.3 MeV by the Los Alamos Scientific Laboratory Vertical Van de Graff accelerator. The one nanosecond width triton beam pulses were stopped in a deuterium gas target. Neutrons emitted at  $90^\circ$  from the beam with a mean energy of 14.2 MeV interacted with a sample placed 100 mm from the neutron source. The energy of the gamma rays produced from the bombarded samples was measured in a heavily shielded 152 mm x 254 mm NaI(Tl) crystal. A NaI(Tl) anti-Compton shield surrounding the center crystal suppressed background events and helped provide pulse height responses more localized to the photon energy.

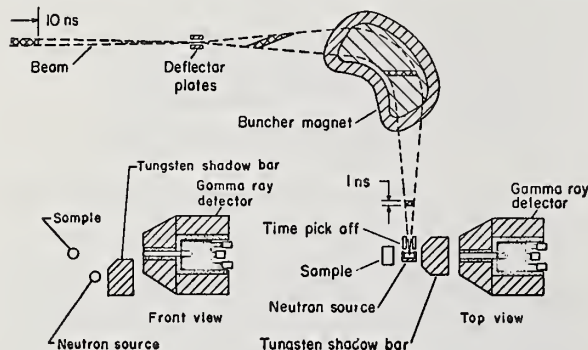


Fig. 1. Experimental arrangement for the measurements of gamma-ray spectra. The detector and sample are about 100 mm above the plane defined by the beam path.

The pulsed neutron beam enabled us to make a time-of-flight (TOF) discrimination of the desired gamma rays from the neutron related and other background events in the crystal. Figure 2 shows the relative time spectrum of NaI(Tl) pulses. Gates 1, 2, and 3 were set to cover, respectively, (a) the time region containing prompt gamma rays directly from the sample;

background; and (c) the time region corresponding to neutron related events in the crystal that were delayed by the neutron TOF.

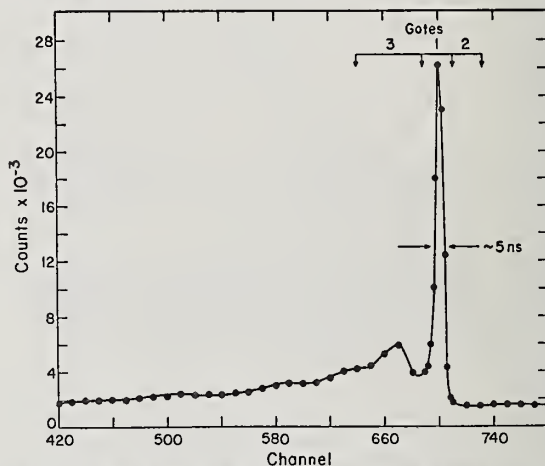


Fig. 2. Time spectrum of pulses in the gamma-ray detector relative to the beam burst pickoff time. Gates 1, 2, and 3 are described in the text.

### Data Reduction

Net photon spectra were obtained after a two step process. First, the background spectrum of Gate 2 was subtracted, properly normalized, from the spectrum of Gate 1. Then a separate net spectrum taken with identical time gates but with no sample in position was subtracted. The pulse height spectra were converted into photon spectra through the use of a computer code<sup>1</sup> which successively stripped off the non-photopeak part of the NaI(Tl) response functions from the net pulse height spectra. The effect of gamma-ray scattering in the samples, which were either cylinders or thin discs, upon the shape of the gamma ray response functions was accounted for in the response function measurements. An example of these scattering effects is shown in Fig. 3 which compares the pulse height spectrum for the 1.27 MeV gamma ray from  $^{22}\text{Na}$  decay for a bare source and for the situation where a 3.2 mm thick iron absorber was placed between the source and detector. Calibrated sources were used over the range from 0.28 to 4.4 MeV to determine the efficiency of the detector.



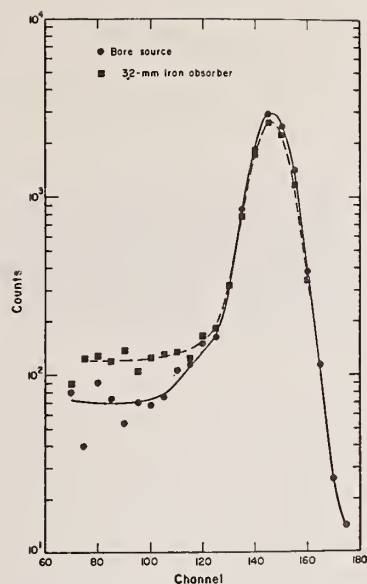


Fig. 3. Gamma-ray pulse height spectrum for the 1.27 MeV  $^{22}\text{Na}$  gamma ray with and without an iron absorber. This figure shows the effect of the gamma-ray production sample in modifying bare source response functions.

The neutron flux was measured at intervals during the experiment with two proton recoil telescopes of different geometrical arrangements. Results obtained from these measurements agreed to within five per cent with neutron flux calculations using the  $^2\text{H}(t,n)^4\text{He}$  cross section together with known target parameters.

Corrections were made for multiple scattering of neutrons in the sample, deadtime, and gamma-ray attenuation in the sample.

### Results

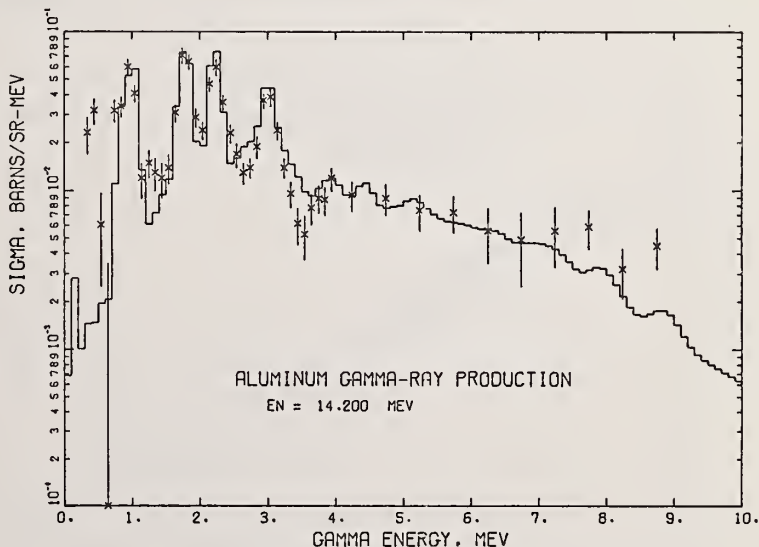
Differential cross sections for gamma ray production as a function of gamma-ray energy in aluminum,

iron, copper, tantalum, and  $^{239}\text{Pu}$  appear in Figures 4 through 8. Small angular variations from the nominal  $120^\circ$  measurements were caused by small geometrical differences for the various samples. The histograms appearing in the figures are from the ENDF/B (Version IV) evaluated datafile. Table 1 lists cross sections for several separated gamma rays; some of the cross sections may include nearby gamma rays. A more complete tabulation of the gamma ray production cross sections measured in this experiment will be published<sup>2</sup>.

Table 1  
DIFFERENTIAL GAMMA-RAY PRODUCTION CROSS SECTIONS FOR PROMINENT GAMMA RAYS

Element	Gamma-Ray Energy (MeV)	Angle	Cross Section (mb/sr)
Carbon	4.4	45	$21.3 \pm 2.8$
		64	$15.0 \pm 2.0$
		90	$11.6 \pm 1.5$
		125	$16.1 \pm 2.1$
Magnesium	1.37	122	$30.3 \pm 3.3$
		90	$27.2 \pm 3.0$
	1.81	122	$8.3 \pm 1.2$
		90	$8.2 \pm 1.2$
Aluminum	2.8	122	$4.2 \pm 0.7$
		90	$6.2 \pm 1.0$
	0.84	122	$5.4 \pm 1.1$
		122	$10.6 \pm 2.1$
	1.8	122	$16.7 \pm 2.5$
	2.2	122	$13.5 \pm 2.0$
Chromium	3.0	122	$8.4 \pm 1.3$
		123	$76.7 \pm 9.2$
Iron	1.33 + 1.44	122	$65.6 \pm 7.0$
		90	$53.2 \pm 5.6$
	0.845	122	$34.0 \pm 4.1$
		90	$27.8 \pm 3.3$

Fig. 4. Differential gamma-ray production cross section for aluminum measured for an angle of 122 degrees. The histogram shown is based on the contents of ENDF/B (Version IV).



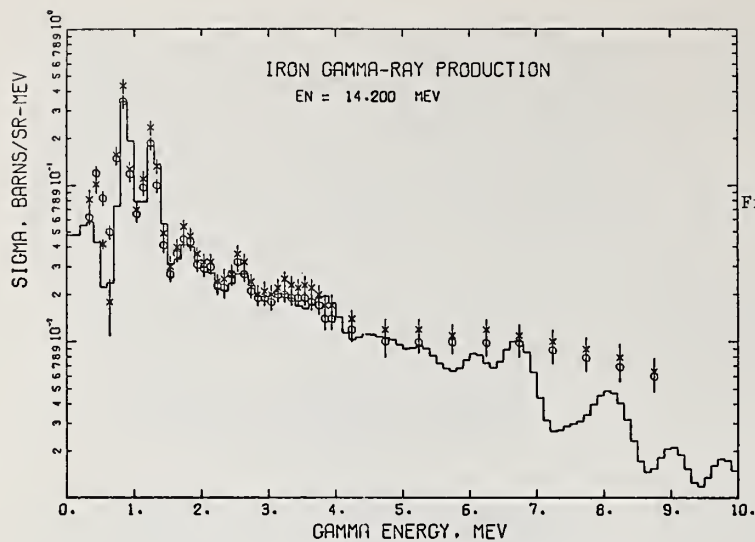


Fig. 5. Differential gamma-ray production cross section for iron with the evaluation from ENDF/B (IV). The  $\circ$  are data taken at  $90^\circ$  while the  $\times$  are data taken at  $122^\circ$ .

Fig. 6. Differential gamma-ray production cross section for copper at  $120^\circ$  with the ENDF/B(IV) evaluation.

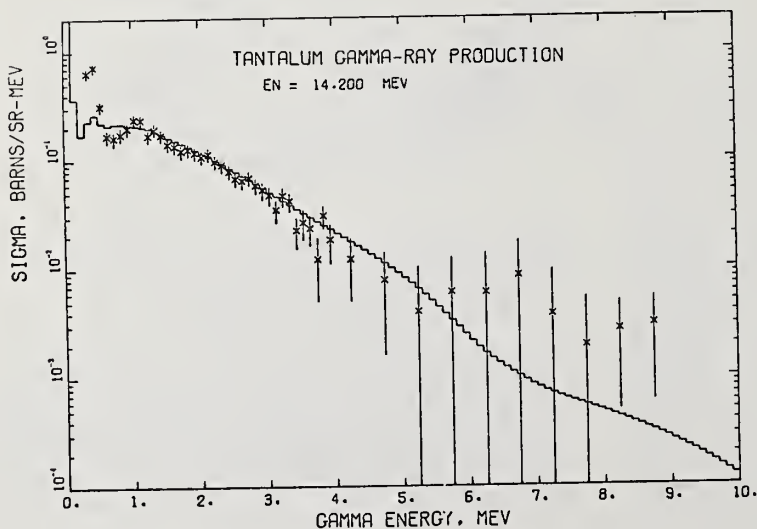
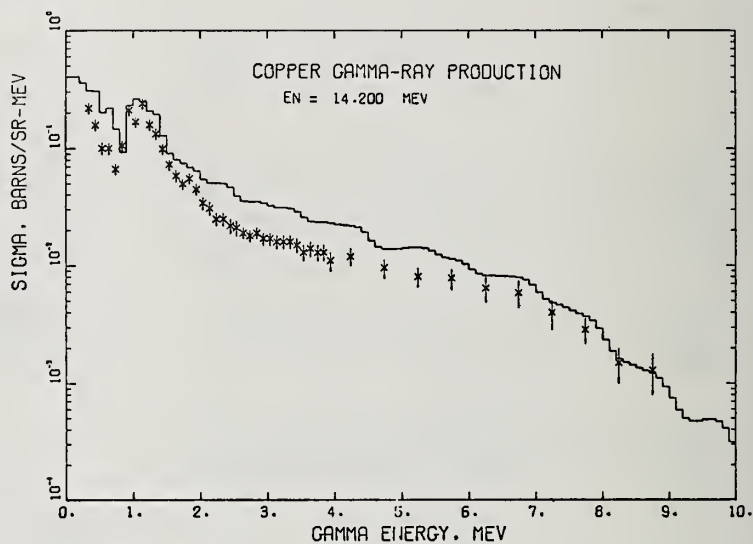
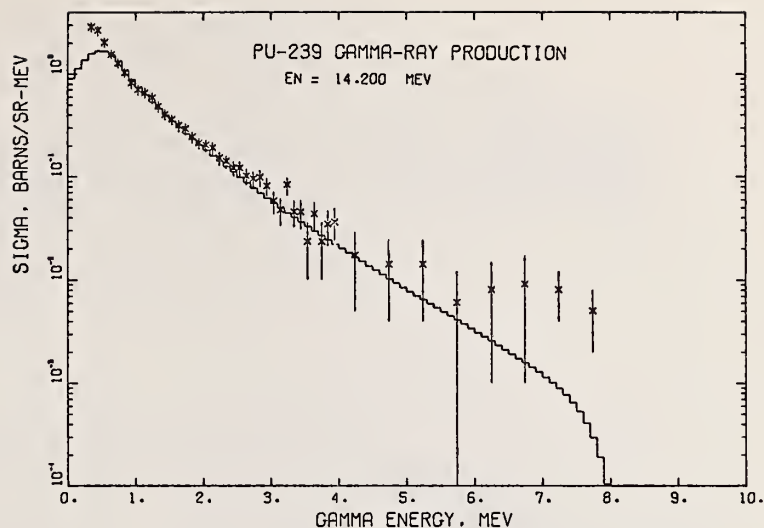


Fig. 7. Differential gamma-ray production cross section measured at  $125^\circ$  for tantalum with the ENDF/B(IV) evaluation.

Fig. 8. Differential gamma ray production cross section at  $120^\circ$  for  $^{239}\text{Pu}$  with the ENDF/B(IV) evaluation.



#### References

1. E. T. Journey, private communication (1974).
2. A preliminary tabulation appears in the Los Alamos Scientific Laboratory report, LA-5662-MS, (1974).

\*Work performed under the auspices of the USAEC.



# THE LOW ENERGY TOTAL CROSS SECTION OF $^{36}\text{Ar}$ \*

S. F. Mughabghab and B. A. Magurno

Brookhaven National Laboratory

Upton, New York 11973

To compare the predictions of the valence model with measured partial radiative widths of Ar-36 an accurate knowledge of the bound-level parameters is required. This is achieved by carrying out a Breit-Wigner parameter fit to the total cross section of Ar-36 measured by Chrien et al and renormalized to the recommended values of the thermal capture and scattering cross sections. The result is as follows:

$$E_0 = -10 \text{ keV}, \Gamma_n^0 = 92.3 \text{ eV}, \Gamma_\gamma = 1.26 \text{ eV}$$

(Parameters of bound level of Ar-36)

## Introduction

The purpose of the present study is to determine the resonance parameters of the s-wave neutron bound state of Ar-36 in the light of recent cross sections measurements. Accurate knowledge of the reduced neutron and total radiative widths is an important requirement for the calculation of the valence capture component in Ar-36. The calculation can then be compared with experimental capture spectra data. This is carried out in a separate contribution<sup>(1)</sup> to this conference.

Previously, Chrien, Jain and Palevsky<sup>(2)</sup> measured the total cross section of Ar-36 in the energy range from 0.1 eV to about 10 keV. From these measurements, the authors<sup>(2)</sup> derived parameters for a bound level on a basis of a scattering radius of  $R' = 4.5$  fermis. Total cross section measurement by Henshaw<sup>(3)</sup> at a neutron energy of 0.076 eV showed that  $\sigma_t = 77 \pm 9$  b. A determination of the thermal capture cross section of Ar-36 by McMurtrie and Crawford<sup>(4)</sup> gave  $\sigma_\gamma = 6.5 \pm 1.0$  b, based on an isotopic abundance of 0.307% for Ar-36. When this value is normalized to an abundance of 0.34% for Ar-36, one obtains  $\sigma_\gamma = 5.9 \pm 0.9$  b. This is in agreement with a value of  $4.8 \pm 0.5$  b reported by Von Wille<sup>(5)</sup>. In addition, a comparison of the thermal capture spectra measured by Von Wille<sup>(5)</sup> and Hardell and Beer<sup>(6)</sup> favors a thermal capture cross section of 5.0 b for Ar-36. Thermal scattering measurements by Krohn and Ringo<sup>(7)</sup> and later by Andriesse et al<sup>(8)</sup> gave  $\sigma_s = 73.7 \pm 0.4$  b and  $74 \pm 2$  b respectively. In this evaluation, thermal capture, scattering, and total cross section values of  $5.0 \pm 0.5$  b,  $73.7 \pm 0.4$  b, and  $78.7 \pm 0.6$  b respectively were adopted for Ar-36. The latter value is utilized to renormalize the total cross section data.<sup>(2)</sup>

## Analysis, Results, and Discussion

To calculate the total cross section of Ar-36, a knowledge of the nuclear scattering radius  $R'$  is an additional requirement. This is achieved by deriving

$R'$  from Ar-40 data by two methods:

(1) A Breit-Wigner multilevel parametric fit of the total cross section of natural argon<sup>(9)</sup> (99.59% Ar-40) gave  $R' = 2.8$  fm.

(2) A coherent scattering amplitude for Ar-40,  $a_{\text{coh}} = 1.83 \pm 0.05$  fm, and use of the relation:

$$a_{\text{coh}} = R' - \sum_j 2.34 \frac{\Gamma_n^0}{E_j}$$

with the aid of the resonance parameters of Ar-40 as reported in BNL-325 (1973) implied  $R' = 2.6$  fm. This is based on the reasonable assumption that bound level contributions in Ar-40 are insignificant. This is essentially justified in view of the good agreement between this result and that derived by method (1).

It is interesting to note that a value of  $R' = 2.6$  is consistent with a minimum in  $R'$  in this mass region as obtained from optical model calculations.

By constraining the thermal capture, scattering, and total cross sections to the adopted values mentioned previously, various combinations for the parameters of the bound level are derived. Fig. 1 shows the calculated Breit-Wigner total cross sections for three such sets illustrated in Table I.

Table I

Set #	$E_0$ (keV)	$\Gamma_n^0$ (eV)	$\Gamma_\gamma$ (eV)
1	- 8	73.82	1.01
2	-10	92.27	1.26
3	-15	138.4	1.9

As described in Fig. 1, the best fit to the experimental data particularly at high neutron energies is achieved for the case of set 2. In addition, with these parameters, the Wescott g factors for capture and scattering were calculated. The results are:

for capture,  $g = 1.0016$

for scattering,  $g = 1.1128$

\*Research supported by U.S. Energy Research and Development Administration.

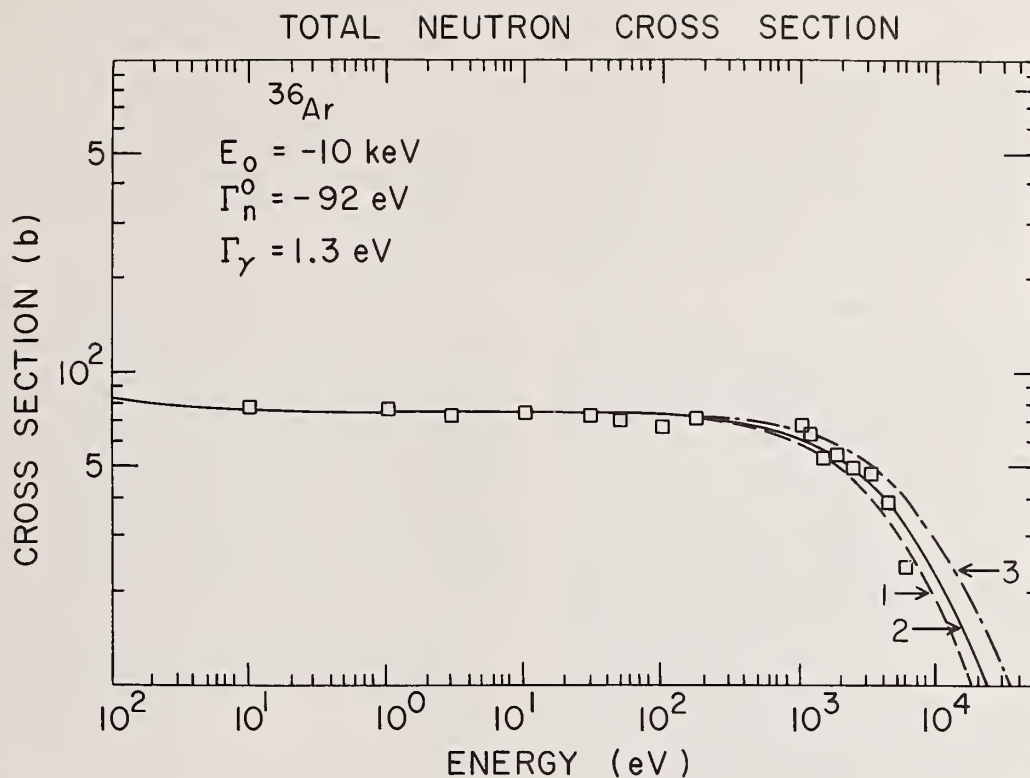


Fig. 1

Comparison of measured and calculated total cross sections of Ar-36

#### References

1. S. F. Mughabghab, contribution to this conference
2. R. E. Chrien, A. P. Jain, and H. Palevsky, Phys. Rev. 125, 275 (1962)
3. D. G. Henshaw, Phys. Rev. 105, 976 (1957)
4. G. E. McMurtrie and D. P. Crawford, Phys. Rev. 77, 840 (1950)
5. P. Von Wille, Atomkernergie 13, 383 (1968) and private communication, 1974
6. R. Hardell and C. Beer, Physica Scripta 1, 85 (1970)
7. V. E. Krohn and G. R. Ringo, Phys. Rev. 148, 1303 (1966)
8. C. D. Andriesse, A. Compagner, A. Hasman, J. J. Van Loef, and F. Zevenbergen, Phys. Letters, 28A, 642 (1969)
9. H. I. Liou, J. Rainwater, G. Hacken, and U. N. Singh, private communication 1974
10. S. F. Mughabghab and D. I. Garber, BNL-325, 3rd edition, volume 1 (1973)

NEUTRON CROSS SECTIONS OF Ni-59  
G. J. Kirouac and H. M. Eiland  
Knolls Atomic Power Laboratory\*  
Schenectady, N. Y. 12301

The thermal cross section and resonance integral for Ni-59 have been measured in integral measurements using the pile oscillator technique. The results are  $\sigma_a$  (2200 m/sec) =  $92 \pm 4$  barns and  $RI = 125 \pm 8$  barns. Separate differential measurements of the neutron total cross section from 0.5 eV to above 2 keV were performed at the RPI linear accelerator. A resonance was observed at 203 eV and analyzed by shape and area methods. Parameters for the resonance have been determined. The integral and differential results were compared and found to be in reasonable agreement.

(Nickel-59, resonance parameters, thermal cross section, resonance integral)

### Introduction

Nickel-rich alloys play an important role as nuclear reactor structural components because of their high strength and corrosion resistance. Within the past five years, several investigators have noted the presence of unexpected large amounts of Ni-60 and helium in highly irradiated nickel. These observations suggested that Ni-59 might have a large absorption cross section, including an  $(n, \alpha)$  component. Later theoretical calculations indicated that the  $(n, \alpha)$  cross section was of unusually large magnitude.<sup>1</sup> Direct measurements of the thermal  $(n, \alpha)^{2,3}$  cross section, the thermal absorption cross section, the resonance integral, and the resonance parameters of Ni-59 have now been performed. This report describes cross section measurements performed on nickel samples containing 4.28 atom percent Ni-59. The thermal absorption cross section and absorption resonance integral were measured by the pile oscillator technique in a small test reactor. The resonance total cross section was measured over the resonance region from 0.5 eV to above 2 keV using the RPI linear electron accelerator as a source of pulsed neutrons.

### Pile Oscillator Measurements

The Ni-59 used in these measurements was obtained from the Oak Ridge National Laboratory Isotope Center. It consisted of 4.57 grams of NiO having the isotopic composition shown in Table I.

Table I

ISOTOPIC COMPOSITION OF NI SAMPLE

Isotope	ORNL-Result Atom Percent	KAPL-Result Atom Percent	Average Atom Percent
Ni-58	$87.06 \pm .10$	$87.63 \pm .20$	$87.35 \pm .29$
Ni-59	$4.31 \pm .05$	$4.24 \pm .05$	$4.28 \pm .05$
Ni-60	$8.30 \pm .08$	$7.87 \pm .09$	$8.09 \pm .21$
Ni-62	$< .05$	$.0066 \pm .0008$	$.007 \pm .001$
Ni-64	$< .05$	$< .00001$	$< .00001$

The two samples used in the pile oscillator measurements were packed in 0.25 in. inside diameter by 2.0 in. long, thin-walled, aluminum capsules. The larger sample consisted of 3.266 grams of NiO (110 mg of Ni-59) which just filled the capsule volume. The smaller sample consisted of 0.512 grams of NiO (17.3 mg Ni-59), and aluminum spacers were used to fill the capsule volume. Compensating "blank" samples of natural NiO were designed to have the same macroscopic scattering cross section, exclusive of Ni-59, as the Ni-59 samples. The geometry and packing density of oxide powder was essentially identical for the Ni-59 and blank samples.

The thermal absorption cross section for Ni-59 was measured relative to cobalt ( $\sigma_a = 37.2 \pm 0.6$  barns) using the pile oscillator technique.<sup>4</sup> For these measurements the small Ni-59 sample was oscillated against the appropriate blank sample on a thirty second cycle. The time dependent response of a standard ionization chamber was digitized and recorded in a multi-channel analyzer operated in multi-scaler mode. Reactor power level was restricted to 100 watts to minimize temperature effects on reactivity. Several 40-cycle runs were completed for the Ni-59 sample and for the cobalt standard. Data from a typical pile oscillator run is shown in Figure 1.

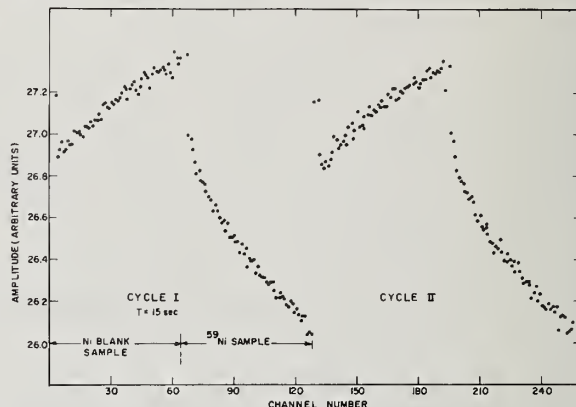


Figure 1. Ionization Chamber Response to Insertion of Ni-59 Sample and Ni Blank Sample into Reactor.

The resonance integral for Ni-59 was measured in a similar manner using the large Ni-59 sample, and a gold standard. The samples were covered by 0.024 in. cadmium. A value of  $1555 \pm 40$  barns was assumed for the gold resonance integral.

### Neutron Total Cross Section Measurements

An energy-dependent measurement of the neutron total cross section of Ni-59 was performed by the time-of-flight technique at the Rensselaer Polytechnic Institute linear electron accelerator. This measurement covered the energy range 0.5 eV to above 2 keV.

Cross section samples were fabricated from the same Ni-59 material used in the pile oscillator measurements. They consisted of 0.25 in. diameter compacts of NiO with sulfur binder. A "thick" sample was made with 1.092 grams of NiO containing  $117 \pm 1$  mg/cm<sup>2</sup> of Ni-59.

\* Operated for the United States Atomic Energy Commission by the General Electric Company, Contract No. W-31-109-Eng.-52.



A "thin" sample was made with 0.248 grams of NiO containing  $26.5 \pm 3$  mg/cm<sup>2</sup> of Ni-59. Blank samples of natural NiO were designed to compensate for the potential scattering of Ni-58 in the Ni-59 samples. All samples contained 0.40 grams of sulfur binder.

Time-of-flight measurements were made using a 0.5 in. thick Li-6 enriched glass scintillation neutron detector at a flight path of 25.1 meters. A survey run on the thick Ni-59 sample was performed with a 100  $\mu$  sec burst width. Between the energy limits 0.5 eV and 2 keV, one Ni-59 resonance was observed at 203 eV. Thereafter the resonance cross section was investigated using a burst width of 0.5  $\mu$ sec. These conditions correspond to an energy resolution of 0.017 eV at 10 eV increasing as  $E^{3/2}$  to 17 eV at 1 keV. The resolution width of 1.5 eV at 200 eV was more than adequate for the broad Ni-59 resonance.

The neutron background was determined by measuring the counting rate under Co and Mn notch filters which were in the beam for about one half of the total measuring time. The resonances in the filters conveniently bracketed the Ni-59 resonance. The background was about 3 percent of the blank sample counting rate in the neighborhood of the resonance. A 120 mg/cm<sup>2</sup> B-10 filter was used to prevent the overlap of neutrons from successive neutron bursts. Raw time-of-flight data showing the Ni-59 resonance in the presence of notch filters is shown in Figure 2. The two Ni-59 samples and their respective blank samples were cycled in the neutron beam by an automatic sample changer on a 30 minute period. Data was accumulated in 6144 time channels using an on-line computer.

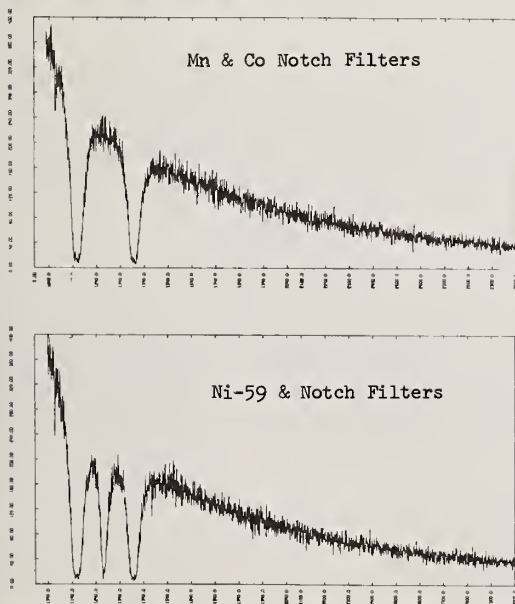


Figure 2. Raw Time-of-Flight Data Obtained for Ni-59.

The Co and Mn filters were removed from the neutron beam for approximately one-half the measuring time in order to insure that data would be available with no possible interference between the notch resonances and the Ni-59 resonance. Thus, four separate measurements were made with the two samples. Although the statistics for individual channels were rather poor (about 7 percent), the area within the Ni-59 resonance contained over 15,000 counts.

## Analysis of Data

### Thermal Absorption and Resonance Integral

The spectra of the response functions obtained in the pile-oscillator measurements were Fourier analyzed by a code written at KAPL<sup>7</sup> to obtain the cosine term coefficients. Corrections are applied within the code to account for any slowly varying drift in reactor power and ionization chamber current. This is accomplished by comparing the spectrum of the  $n$ 'th cycle with that of the  $(n+1)$ 'th cycle. Note that these are stored side-by-side in the analyzer memory and are not summed. If the first spectrum is stored in 128 channels, then the channel-by-channel difference function,  $C(i)-C(i+128)$ , can be computed and fitted to a second order polynomial,  $A+Bi+Ci^2$ . The Coefficients A, B, and C determined the magnitude, slope, and curvature of the ionization current drift. Once the drift corrections have been applied and the cosine coefficients obtained, the unknown thermal cross section or resonance integral can be obtained from the ratio,

$$\sigma_x = \frac{A_x M_s \sigma_s}{A_s M_x} \quad (1)$$

where  $A_x$  and  $A_s$  refer to the cosine term amplitude for the unknown and standard samples respectively. The number of moles of sample or standard are represented by  $M_s$  or  $M_x$ , and the cross sections or resonance integrals are the  $\sigma$ 's.

The following corrections were also required to determine the actual cross section values:

1. A correction for incomplete reactivity matching of matrix materials in the cross section and compensation samples.
2. A self shielding correction for the measurement of the Ni-59 resonance integral relative to Au.
3. A correction for non-1/v behavior of the absorption cross sections.
4. A correction for the deviation of the reactor spectrum from an ideal 1/E slowing down spectrum.

### Resonance Parameters

Transmission data obtained from Ni-59 enriched NiO samples of two different thicknesses were analyzed by both shape and area methods. The shape analysis consists of a three parameter, least squares fit to the Breit-Wigner, single level formula for the total cross section. This procedure yields unique values for the resonance energy,  $E_\lambda$ , the total width,  $\Gamma$ , and the product of the reduced neutron width and spin weighting factor,  $g\Gamma_n^0$ .

Since the ground state spin of Ni-59 is  $3/2^-$ , s-wave neutrons can produce compound resonances with total angular momentum  $J=1^-$  and  $2^-$ . This ambiguity is reflected in a corresponding uncertainty in the spin factor ( $g=0.375$  or  $0.625$ ) and the neutron width,  $\Gamma_n$ . The absorption width can only be obtained by subtracting the neutron width from the total width. Thus, the fundamental lack of knowledge of the compound resonance spin leads to two possible values for the absorption width,  $\Gamma_a$ . However, the fact that the  $(n,\alpha)$  exit channel is dominated by the emission of a 4.75 MeV  $\alpha$ -particle which leaves the residual nucleus Fe-56 in its  $0^+$  ground state, necessitates a  $1^-$  state of the compound nucleus for parity conservation, which corresponds to a value of 0.375 for  $g$ .

It was also possible to use the thermal absorption cross section obtained from the pile oscillator measurements to eliminate one of the absorption widths. It was assumed that the thermal cross section arises from the  $1/\sqrt{E}$  tail of the 203 eV resonance. The assumption was very good since no other Ni-59 resonances were observed below about 2 keV. In this situation, the thermal (2200 m/sec) absorption cross section is related to the resonance by,

$$\sigma_a(2200 \text{ m/sec}) \simeq \frac{6.52 \times 10^5}{\sqrt{E_{\text{thermal}}}} \frac{g \Gamma_n^0 \Gamma_a}{E_\lambda^2} \quad (2)$$

All factors in the formula were uniquely known except the absorption width. Solving for  $\Gamma_a$ , it was found that the thermal cross section was highly consistent with the smaller possible value of  $\Gamma_a$ , and only with that choice. The use of the larger value overpredicted the thermal cross section by more than a factor of two. We conclude that the compound resonance has spin  $J=1^-$ , the  $g$  factor is 0.375 and the absorption width is about 3.5 eV.

Unlike the shape analysis procedure, a resonance area analysis can only provide a functional relationship between the total width,  $\Gamma$ , and the product,  $g\Gamma_n$ . The area under a resonance,  $A_t$ , is proportional to the product  $g\Gamma_n \Gamma^k$ . For thin samples,  $k$  tends to zero so that the area is independent of  $\Gamma$ ; for very thick samples it approaches unity. Since the value of  $g$  is known, the results of the area analyses on multiple sample thicknesses are expressed as a series of curves of  $\Gamma_n$  vs.  $\Gamma$ .

This technique was applied to each of the four sets of data obtained from the two thickness Ni-59 samples. It was found that one of the samples was sufficiently thin that the resonance area was independent of the assumed value of the total width. In this case, the curve traced by the parametric relationship between  $\Gamma_n$  and  $\Gamma$  is very nearly a straight horizontal line. The two data sets for the thick sample provided two additional curves which yielded values of  $\Gamma_n$  and  $\Gamma$  at their points of intersection with the thin-sample curves. The curves are shown in Figure 3.

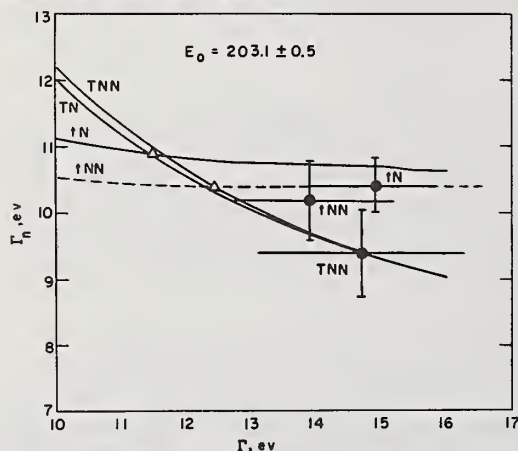


Figure 3. Shape and Area Analysis Results for the 203 eV Ni-59 Resonance. The three points are obtained by shape analysis of the thin sample data with and without the notch filters in place (tN and tNN, respectively) and of the thick sample data (TNN). The curves result from area analyses of the same data sets.

The final results obtained for Ni-59, considering both the shape and area techniques, were five independently determined pairs of  $\Gamma_n$  and  $\Gamma$  values. The shape of the resonance in the thick sample data with the

permanent Co and Mn filters was not analyzed. The wings of the notch resonances overlapped the Ni-59 resonance and made an accurate shape determination impossible.

## Results and Discussion

### Integral Measurements

The pile oscillator measurements gave a value of  $92 \pm 4$  barns for the 2200 m/sec absorption cross section of Ni-59. The sequence of corrections applied to the observed value is illustrated in Table II. The uncertainty quoted for the initial, uncorrected value contains the following five components: uncertainty in the Co standard cross sections, 1.6%; standard deviations of the Ni-59 and cobalt amplitudes, 1.5% and 1.8% respectively; and Co and Ni mass uncertainties 1% and 1.5% respectively. The amplitude uncertainties were obtained from the standard deviation observed for a distribution of four separate measurements.

TABLE II  
THERMAL ABSORPTION CROSS SECTION FOR  $^{59}\text{Ni}$

Correction	$\sigma_{\text{abs}}$ Corrected (barns)	Magnitude of Correction	Uncertainty of Correction	Uncertainty in $\sigma_{\text{abs}}$
Observed	88	--	--	3.4%
Incomplete sample-blank compensation	86	2%	<10%	0.5%
Non-1/v sample and standard cross section	92	7%	~25%	~2.0%
Final result	92	--	--	4.0% $\pm 4$ barns

The result obtained for the Ni-59 resonance integral is shown in Table III. The uncertainty on the uncorrected resonance integral includes the standard Au resonance integral, 2.6%, standard deviation in Ni-59 and Au amplitudes, 1.2% and 3.3% respectively, and the Ni and Au mass uncertainties, 1.5% and 1.0%.

TABLE III  
RESONANCE INTEGRAL FOR  $^{59}\text{Ni}$

Correction	RI Corrected (barns)	Magnitude of Correction	Uncertainty of Correction	Uncertainty in RI
Observed	169 <sup>+</sup>	--	--	4.7%
Au standard Self-shielding	124	27%	~10%	2.7%
$^{59}\text{Ni}$ Self- shielding	141	13%	~20%	2.6%
Incomplete Sample-blank Compensation	138	2.2%	<10%	<0.5%
Non 1/E Reactor Slowing Down Spectrum	125	9%	~25%	2.3%
Final Result	125	--	--	$\pm 8$ barns

<sup>+</sup>Based on Au Resonance Integral of 1550  $\pm 40$  barns.

### Differential Measurements

Resonance parameters derived by shape and area analyses are graphically presented in Figure 3. Included are three points resulting from least square shape fits to the thick and thin sample data. The abbreviations TNN and tNN refer to the data obtained without permanent notch filters for the thick and thin



samples respectively. The TN and tN represent the same results for the data taken with Co and Mn filters always in the neutron beam. Uncertainties in the parameters  $\Gamma$  and  $\Gamma_n$  are shown as horizontal and vertical error bars. These are standard deviations which represent the projection of the statistical uncertainties in the measured transmission onto the resonance parameters.

The  $\Gamma_n$  vs.  $\Gamma$  contours in the figure show the results of multiple sample area analyses. Uncertainties in  $\Gamma_n$  are shown at the points of intersection of the thick and thin sample data. Five separate determinations of  $\Gamma$  and  $\Gamma_n$  are illustrated. These results are summarized in Table IV. The agreement is generally well within the stated uncertainties. Individual values were weighted with their standard deviations and averaged. The evaluated results for  $\Gamma_n$  and  $\Gamma$  then gave the absorption width  $\Gamma_a = 3.4 \pm 1.0$  eV.

TABLE IV

RESONANCE PARAMETERS FOR  $^{59}\text{Ni}$

$E_A = 203.1 \pm .5$  eV    J (resonance spin) =  $1^-$

g (spin weighting factor) = 0.375

Analysis	Run	Sample mg/cm <sup>2</sup>	$\Gamma_n^0$ (eV) <sup>1/2</sup>	$\Gamma$ (eV)	$\Gamma_n$ (eV)
Shape	No filters	26.5	.72 $\pm$ .04	13.9 $\pm$ 1.3	10.2 $\pm$ .6
Shape	Filters	26.5	.73 $\pm$ .03	14.9 $\pm$ 1.0	10.4 $\pm$ .4
Shape	No filters	117.	.66 $\pm$ .05	14.7 $\pm$ 1.6	9.4 $\pm$ .7
Area	No filters	Multiple	.73 $\pm$ .02	12.4 $\pm$ 1.5	10.4 $\pm$ .3
Area	Filters	Multiple	.76 $\pm$ .03	11.5 $\pm$ 2.0	10.8 $\pm$ .3
Wtd. Ave.	--	--	.73 $\pm$ .02	13.9 $\pm$ 1.0	10.5 $\pm$ .3

$\Gamma_a$  (absorption width) =  $\Gamma - \Gamma_n = 3.4 \pm 1.0$  eV.

#### Comparison of Integral and Differential Results

The 2200 m/sec absorption cross section and the resonance integral obtained from the pile oscillator experiments were compared to corresponding quantities calculated directly from the resonance parameters. The final resonance parameters in Table IV were used in the Breit-Wigner, single level formula to predict a thermal absorption cross section of  $93 \pm 27$  barns. The large uncertainty is primarily a reflection of the uncertainty in the absorption width,  $\Gamma_a$ . The predicted value is to be compared with  $92 \pm 4$  barns obtained from the pile oscillator data.

The hypothesis that the thermal cross section can be represented accurately by the  $1/\sqrt{E}$  tail of the 203 eV resonance was tested by assuming another Ni-59 resonance at 2 keV with the same  $\Gamma_n^0$  and  $\Gamma_a$ . This resonance would contribute only 1 barn to the thermal cross section. The calculation justified the use of the integral measurement of the 2200 m/sec cross section to predict a more accurate absorption width for the 203 eV resonance, i.e.  $3.34 \pm 0.15$  eV.

The resonance parameters in Table IV were also utilized to calculate the resonance integral. The isolated resonance integral is given by,

$$RI = 4.097 \times 10^6 \frac{g \Gamma_n \Gamma_a}{E_\lambda^2} \quad (3)$$

To the  $96 \pm 28$  barns must be added a  $41 \pm 2$  barn,  $1/\sqrt{E}$  contribution determined from the thermal cross section. The contribution of unresolved, resonances above 2 keV was also estimated. The calculation yields an estimate of 3 barns for the unresolved resonance contribution to the resonance integral. Thus, the total calculated resonance integral including isolated resonance,  $1/\sqrt{E}$  and unresolved resonance terms, was  $140 \pm 28$  barns. The result is in fair agreement with the directly measured value of  $125 \pm 8$  barns.

#### References

1. G. J. Kirouac, Nucl. Sci. Eng. 46, 427 (1971).
2. H. M. Eiland and G. J. Kirouac, Nucl. Sci. Eng. 53, 1 (1974).
3. R. D. Werner and D. C. Santry, Nucl. Sci. Eng., 56, 98 (1975).
4. F. Feiner, R. T. Frost, and H. Hurwitz, AEC Report, KAPL-1703 (1956).
5. K. Kirlov and E. Johansson, J. Nucl. Energy, Part A, 11, 101 (1960).
6. E. Hellstrand, Reactor Physics in the Resonance and Thermal Regions, Vol. 2, p. 159, MIT Press, Cambridge, Massachusetts, (1966).
7. J. N. Brazos, B. A. Gottschalk, and A. L. Liedel, AEC Report, KAPL-M-6430, Nov., 1964.

#### Acknowledgement

We are grateful to the Oak Ridge National Laboratory Isotope Center for providing the Ni-59 used in this work and to W. O. Haas and E. P. Opalka for performing the mass spectrometric analysis at KAPL.



NEUTRON RESONANCE SPECTROSCOPY AT NEVIS LABORATORIES \*  
G. Hacken, H.I. Liou†, J. Rainwater, U.N. Singh  
Columbia University  
New York, N.Y. 10027

A review of the results of high resolution, high intensity neutron time of flight spectroscopy with the Columbia University Nevis Synchrocyclotron is presented. The review includes a brief description of the experimental facilities and a summary of resonance parameter results.

(Nuclear reactions;  $(n,n)$ ,  $(n,\gamma)$ ,  $E = 1 \text{ eV} - \text{few keV}$ ; measured  $\sigma_t(E)$ ; summary of deduced  $E_0$ ,  $g\Gamma_n$ ,  $\Gamma_\gamma$ ,  $S_0$ ,  $\langle D_0 \rangle$ ; various statistical tests)

### Introduction

Prior to the recent upgrading of the Columbia University Nevis Synchrocyclotron, the Neutron Velocity Spectroscopy (NVS) Group, headed by Prof. J. Rainwater had two major experimental runs. These occurred respectively in 1968 and 1970, and yielded enormous amounts of high quality, high resolution neutron cross section and resonance parameter data, some of which is still being analyzed. The elements studied include medium to heavy elements whose average level spacings  $\langle D \rangle$  are  $\leq 300 \text{ eV}$ , and light elements with spacings in the keV range.<sup>1-16</sup> This report concerns mainly the former, medium to heavy, group. These involve a total of 36 isotopes belonging to the following elements: erbium, samarium, europium, thorium, uranium, ytterbium, tungsten, cadmium, gadolinium, indium, and dysprosium. Results of particular interest to nuclear physics include average total capture widths  $\langle \Gamma_\gamma \rangle$ , average s-level spacings  $\langle D_0 \rangle$ , s- and p-strength functions ( $S_0$  and  $S_1$ ), statistical distributions of nearest neighbor level spacings and of reduced neutron widths, and statistical tests for short and long range order in resonance energy levels (Dyson Mehta Orthogonal Ensemble statistics). The first evidence tending to confirm Dyson's theory concerning level spacings was presented in our erbium paper<sup>1</sup> (H.I. Liou et al). Our subsequent papers on medium to heavy isotopes include orthogonal and two body random matrix<sup>17</sup> tests and results. The s- and p-wave strength function data are of great relevance to the low energy optical models, both spherical and non-spherical.

The between resonance neutron cross sections and the resonance parameters  $E_0$ ,  $g\Gamma_n$  (and  $\Gamma_\gamma$ ,  $l$ ,  $J$  where determined) are of interest to nuclear technology and neutron physics; they allow the actual neutron cross section to be given as a function of energy, i.e., with Doppler and resolution effects unfolded.

### Experimental Characteristics

The 1968 and 1970 NVS runs each included about six weeks of 24 hour-a-day cyclotron operation using the 385 MeV Nevis Proton Synchrocyclotron. (The nearly completed modified version of the Nevis cyclotron will be a  $\sim 575 \text{ MeV}$ , three-fold symmetric magnetic field, sectorized focusing machine.) In both runs, a  $\sim 20 \text{ ns}$  wide proton bunch was deflected into a Pb target inside the cyclotron chamber. Resulting neutrons were moderated by a circulating

water moderator below the Pb target, and these moderated neutrons were collimated to form our neutron beam. The beam traveled mainly through helium filled balloons so that air attenuation was minimized. The main detector for neutron transmission measurements uses a 202.05m flight path. It consists of a boron-10 slab  $\sim 3 \text{ cm}$  thick  $\times 30 \text{ cm} \times 120 \text{ cm}$  area, viewed by banks of NaI detectors to detect the  $\gamma$  rays in the  $(n,\alpha\gamma)$  reaction of neutron capture by boron-10. A side view of the "self indication" detector (neutron capture detector) is shown in Fig. 1. A sample of the element or isotope is suspended in the middle for the detection of resonance capture  $\gamma$  rays using  $\text{Li}_4\text{SiO}_4$  converters and plastic scintillator plates viewed by photomultipliers. Our 202.05m flight path was used for several weeks of running time. The remainder of the time used the 39.536m detector with a sample at the detector and with and without other samples in a transmission position. Transmission measurements were also made at 39.5 meters. Other shorter flight paths were available and were used by the Columbia Nuclear Engineering Group (under Prof. W. Havens and Prof. E. Melkonian) for fission and neutron capture studies. In the following, we limit the discussion to measurements using the 202.05m and 39.536m detector stations.

The cyclotron was run at the rate of 70 proton bunch deflections (bursts) per second, yielding  $> 10^{19}$  evaporation neutrons per second instantaneous at the source.

In 1968, our neutron time of flight raw data were in the form of hundreds of 8192 channel histograms whose channel widths varied in blocks of 512 channels through 1,2,4,8,16,... times 25 ns. In 1970, the histograms had 16000 channels, and the basic unit channel width was 20 ns. The energy range covered for light through heavy elements was 1 eV to hundreds of keV.

### Summary of Results

The following table summarizes our published results on medium and heavy nuclei. The table displays, for each isotope, the number of neutron widths obtained, the number of total radiation widths obtained, the s wave strength function for the isotope, and the average total radiation width deduced from the individually measured ones. Uncertainties are omitted; they can be obtained from the original references.

Isotope	No. of $g\Gamma_n$	No. of $\Gamma_\gamma$	$10^4 S_o$	$\langle \Gamma_\gamma \rangle$ (meV)
Er-166	175	10	1.70	96
Er-167	270	52	1.89	91
Er-168	128	4	1.50	87
Er-170	124		1.54	
Sm-152	91	9	2.2	65
Sm-154	35	3	1.8	79
Eu-151	103	45	3.2	90
Eu-153	78	46	2.3	95
Th-232	302	84	0.84	21
U -238	269	71	1.08	23
Yb-170	22		2.25	
Yb-171	168	37	1.86	76
Yb-172	100	3	1.68	72
Yb-173	166	33	1.60	74
Yb-174	75	2	1.62	83
Yb-176	68		2.29	
W -182	141		2.40	
W -183	93		1.65	
W -184	126		2.35	
W -186	102		2.23	
Cd-110	79	6	0.50	101
Cd-111	98	15	0.38	102
Cd-112	98	5	0.53	102
Cd-113	37	19	0.43	101
Cd-114	54	4	0.70	110
Cd-116	21	1	0.20	
Gd-154	48	25	2.0	88
Gd-158	95	27	1.5	105
Gd-160	56	4	1.8	111
In-113	50	3		75
In-115	233	15	0.26	85
Dy-160	64	9	2.00	108
Dy-161	251	26	1.73	112
Dy-162	142	16	1.88	112
Dy-163	114	39	2.02	113
Dy-164	116	5	1.70	114
Lu-175	446	40	1.83	77

The following table summarizes our light-nucleus results. Here, the experimental upper energy limit exceeds 100 keV, and we list, for each element, the numbers of levels for which  $\Gamma_n$  (or  $ag\Gamma_n$ ),  $I$ , and  $J$  have been determined. Here 'a' is the isotopic abundance and  $g$  is the spin statistical weight.

Element	No. of $\Gamma_n$ or $ag\Gamma_n$	No. of $I$	No. of $J$
Na	7	7	7
K	65	62	25
Ca	31	10	10
Cl	35	23	11
Mg	5	4	4
F	3	3	3
Ar	24	24	9
Al	7	7	7

Papers on the following are in preparation, or have been submitted for publication: Hf-177, Tl, Bi, Ta, La, Ce-140.

#### Comments on Level Parameter Evaluation for Individual Resonances

Studies of resonances can use (a) transmission measurements (total cross section), (b) scattering detector measurements (emphasized by Harwell), (c) measurements using Moxon-Rae capture detectors, or large capture tank detectors to emphasize the neutron capture process. The groups at Saclay and Geel have particularly emphasized that the use of transmission measurements alone, with shape fits, can often yield good results on both  $\Gamma_n$  (or  $g\Gamma_n$ ) and  $\Gamma_\gamma$  for resonances and that care must be taken in interpreting specific scattering or capture measurements due to multiple scattering, etc., in the sample. We have emphasized transmission measurements, and measurements using a capture detector (self-indication station) which is more efficient than a strict Moxon-Rae detector and less efficient than a capture tank detector. For our measurements on  $^{232}\text{Th}$  and  $^{238}\text{U}$ , measurements<sup>3</sup> were also made using a conventional Moxon-Rae detector. It was found that our usual capture (self-indication) detector results agreed very well with those using the Moxon-Rae detector. In particular, by combining the results of transmission and of capture (self-indication) measurements, using a range of sample thicknesses, the preceding table shows that we have been able, in many cases, to determine both  $g\Gamma_n$  and  $\Gamma_\gamma$  for a larger sampling of resonances than previously established. In addition to using our main resonance area analysis, we have also made use of "partial" shape analysis of favorable, usually lower energy levels. In any event, each thickness sample transmission or other area, etc. yields an implied relation between  $\Gamma$  and  $g\Gamma_n$  for the resonance. For a large fraction of all levels near the upper energy end of the region studied, only one (or perhaps two) relation is obtained based on the thickest sample transmission area. In that case, an intersection is established with the curve  $\Gamma \approx \langle \Gamma_\gamma \rangle + g\Gamma_n / \langle g \rangle$  to determine only favored  $g\Gamma_n$ . At lower energies, more ( $\Gamma$  vs  $g\Gamma_n$ ) curves are usually present. If they have an intersection point where their slopes are sufficiently different, the intersection may determine  $g\Gamma_n$  and  $\Gamma$ , yielding  $\Gamma_\gamma \approx \Gamma - g\Gamma_n / \langle g \rangle$ .

Figure 2 for the level in  $^{238}\text{U}$  at 410.2 eV shows a case where 13 different curves are involved, yielding a reasonably limited intersection region. Figure 3 for the  $^{232}\text{Th}$  level at 675.2 eV has 9 independent curves defining the intersection locus. Figure 4 for the  $^{238}\text{U}$  level at 347 eV has 10 curves defining the best intersection. It also shows the ( $\Gamma_n$ ,  $\Gamma_\gamma$ ) selections by groups at LASL, Harwell, Dubna, and Geel from their measurements.

Figures 5-8 show examples of such analysis plots where many curves defined the intersections for the even-even nuclei Cd-112, Yb-172, Sm-152, and Er-166. For odd A nuclei having large  $I$ , the  $J$  of the resonance can usually not be established. Examples are given in Figs. 9 and 10 for levels in Eu-151 and Er-167. Figures 11 and 12 show cases for levels in Yb-171 and Yb-173 where best compound nucleus  $J$  values are established. Such plots were made for each



of the resonances in the preceding table for which  $g\Gamma_n$  values were given.

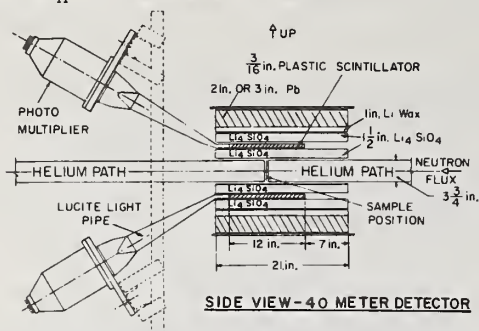


FIG. 1. The 39.57-m self-indication detector. The collimated neutron flux has a smaller area than the  $3\frac{3}{4}$ -in.-vertical by  $9\frac{3}{4}$ -in.-horizontal central aperture through the detector. The sample is positioned at midlength between He-filled boxes having thin Al end windows. Neutron-resonance capture  $\gamma$  rays from the sample produce recoil electrons in the  $\text{Li}_4\text{SiO}_4$  converter which traverse the scintillator plastic.

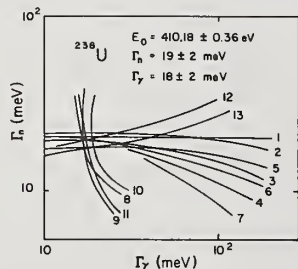


Fig. 2 Analysis plot for the 410 eV level in U-238. Curves 1-7 are for different sample thickness transmission measurements. Curves 8, 9 use a Moxon-Rae detector and curves 10, 11 use our regular 40m capture self-indication detector. Note the quite different slopes of the transmission and the capture detector analyses.

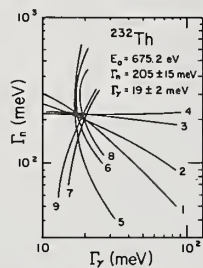


Fig. 3 Similar analysis plot for the 675 eV level in Th-232. Curves 1-4 are from transmission data, curves 5-7 from self-indication data, and curves 8 and 9 from the Moxon-Rae detector data. Similar slope differences appear in the other figures.

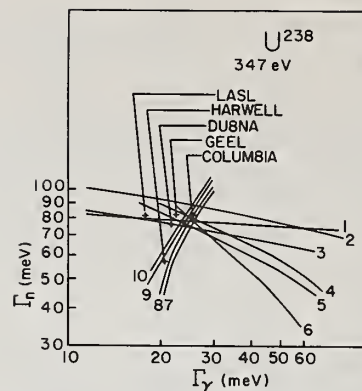


Fig. 4 Level in U-238 at 347 eV

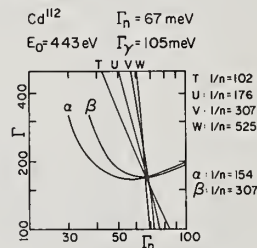


Fig. 5 Level in Cd-112 at 443 eV

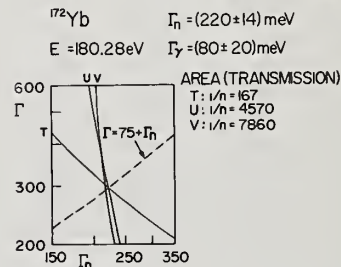


Fig. 6 Level in Yb-172 at 180 eV

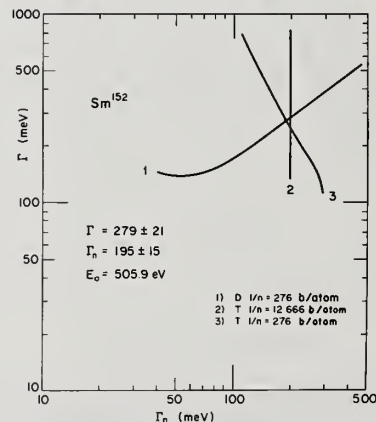


Fig. 7 Level in Sm-152 at 506 eV



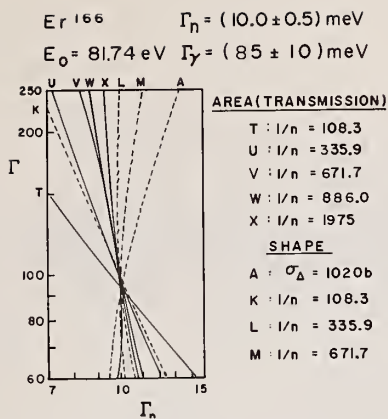


Fig. 8 Level in Er-166 at 82 eV

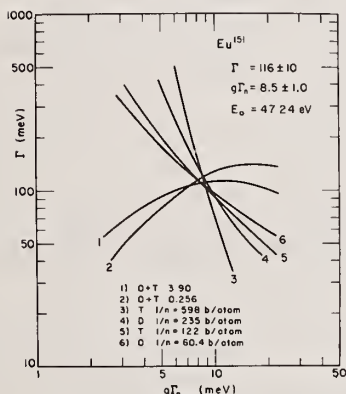


Fig. 9 Level in Eu-151 at 47 eV

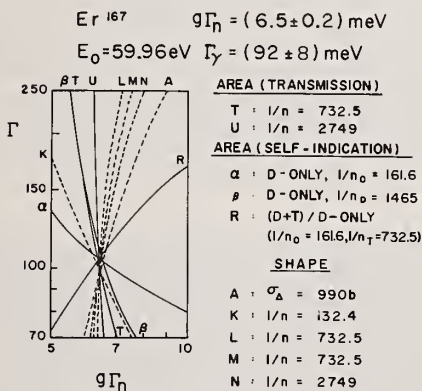


Fig. 10 Level in Er-167 at 60 eV

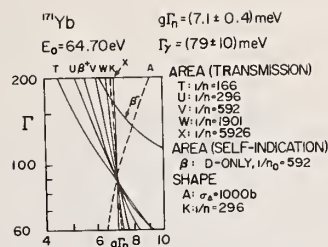


Fig. 11 Level in Yb-171 at 65 eV. J=1 is favored over J=0

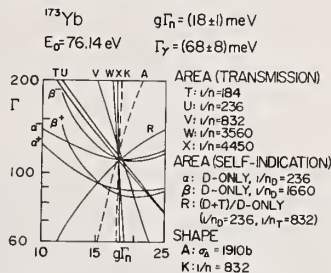


Fig. 12 Level in Yb-173 at 76 eV. J=2 is favored over J=3.

#### References

- 1 H.I. Liou et al, Phys. Rev. C5, 974 (1972), Er.
- 2 F. Rahn et al, Phys. Rev. C6, 251 (1972), Sm, Eu.
- 3 Ibid., 1854, 232<sub>Th</sub>, 238<sub>U</sub>.
- 4 H.I. Liou et al, Phys. Rev. C7, 823 (1973), Yb.
- 5 H.S. Camarda et al, Phys. Rev. C8, 1813 (1973), Yb.
- 6 F. Rahn et al, Phys. Rev. C8, 1827 (1973), Na.
- 7 U.N. Singh et al, Phys. Rev. C8, 1833 (1973), K.
- 8 H.I. Liou et al, Phys. Rev. C10, 709 (1974) Cd.
- 9 G. Hacken et al, Phys. Rev. C10, 1910 (1974), In.
- 10 F. Rahn et al, Phys. Rev. C10, 1904 (1974), Gd.
- 11 U.N. Singh et al, Phys. Rev. C10, 2143 (1974), Ca.
- 12 Ibid., 2138, Cl.
- 13 Ibid., 2150, Mg.
- 14 Ibid., 2147, F.
- 15 H.I. Liou et al, Phys. Rev. C11, 462 (1975) Dy.
- 16 Ibid., 457, Ar.
- 17 S.S.M. Wong, J.B. French, Nucl. Phys. A198, 188 (1972).

\* Research supported by the U.S. Atomic Energy Commission AT(11-1) 2174.

† Present address: Brookhaven National Laboratory, Upton, N.Y. 11973

The E1 and M1 radiative strength functions have been measured for nuclei with atomic mass number near  $A = 140$  and at an excitation energy of approximately 9 MeV using the threshold photoneutron technique. A method was developed for extracting the dipole strength even though the first excited state of the daughter nucleus is near the ground state. The photoneutron spectra were measured at laboratory angles of  $90^\circ$  and  $135^\circ$  and with high resolution (0.5 ns/m) using the time-of-flight spectrometer associated with the Argonne high-current linac. In particular the dipole strengths found in  $^{138}\text{Ba}$  and  $^{140}\text{Ce}$  are discussed. These results are compared with theoretical estimates and with the radiative strengths of nuclei in the mass range  $50 < A < 250$ .

$$\left[ \begin{array}{l} \text{NUCLEAR REACTIONS } ^{138}\text{Ba}(\gamma, n), ^{140}\text{Ce}(\gamma, n); E_x \approx 9 \text{ MeV}; \\ \text{measured } \sigma(E_n, \theta); \text{ deduced } \Sigma \Gamma_{\gamma_0}(\text{M1}) \text{ and } \Sigma \Gamma_{\gamma_0}(\text{E1}) \end{array} \right]$$

### Introduction

Interest in the nuclear mass region near  $A = 140$  has gained impetus from the recent discovery<sup>1</sup> of giant magnetic dipole resonances in Ce, La, and Pr at an excitation energy of 8.7 MeV. Since the neutron binding energy ranges between 7 and 10 MeV for most nuclei near  $A = 140$ , it is expected that the nature of the  $\gamma$ -ray emission from neutron-capture reactions will therefore be predominantly M1. Hence, calculations<sup>2</sup> of the flux of  $\gamma$  rays produced from radiative capture based only on the low-energy "tail" of the E1 giant resonance may grossly underestimate the true flux in this mass region.

In addition, there is considerable theoretical interest in the  $N = 82$  nuclei due to the fact that the  $1h_{11/2}$  neutron orbital is filled and the  $1h_{9/2}$  is vacant. This configuration is analogous to that of the proton orbitals in  $^{208}\text{Pb}$ , where several calculations<sup>3</sup> of the M1 strength have been performed. In addition, the  $1g_{7/2}$  proton orbital is filled in  $^{138}\text{Ba}$  while the  $1g_{7/2}$  orbital is vacant.

For these reasons, we have measured the spectrum of photoneutrons from the  $^{138}\text{Ba}(\gamma, n)^{137}\text{Ba}$  and  $^{140}\text{Ce}(\gamma, n)^{139}\text{Ce}$  reactions at laboratory angles of  $90^\circ$  and  $135^\circ$  and throughout the energy range 10–60 keV. The neutron energies were determined with high resolution (0.5 ns/m) using the time-of-flight spectrometer associated with the Argonne high-current electron linear accelerator. A new method was developed in order to deduce the ground-state radiation widths even though the first excited state of the daughter nucleus is near the ground state. The E1 and M1 photon reduced widths are computed from the present observations and compared with other measurements in the mass range  $A = 55$ –240.

### Experimental Procedure

The Argonne high-current linac provided an intense source of gamma rays for the present photoneutron measurements. The bremsstrahlung is produced by focusing an intense, pulsed electron beam (20 A peak current and 4 ns in duration) onto

a silver converter. The photons emerging from the converter irradiate a sample of  $^{138}\text{Ba}$  or  $^{140}\text{Ce}$ . The remaining electrons are stopped in an aluminum block and provide a start pulse for the neutron time-of-flight spectrometer. The photoneutrons emitted from the  $^{138}\text{Ba}(\gamma, n)$  or  $^{140}\text{Ce}(\gamma, n)$  reactions travel through two separate, well-collimated flight paths which are at angles of  $90^\circ$  and  $135^\circ$  with respect to the electron-beam axis. The neutrons are detected in banks of  $^6\text{Li}$ -glass scintillators located at the end of each flight path. The neutron energies are measured with good resolution (0.5 ns/m) using the time-of-flight spectrometer described in Ref. 4.

The observed time-of-flight spectra for  $^{138}\text{Ba}$  are shown in Fig. 1. The spectra at angles of  $90^\circ$  and  $135^\circ$  were measured simultaneously and throughout the energy range 9–80 keV. However, above 60 keV the resolution of the spectrometer ( $\sim 0.6$  keV) is comparable to the average spacing of the photoneutron resonances in  $^{138}\text{Ba}$ . Hence, only states in the energy interval 9–60 keV were considered in the present analysis. A separate measurement of the spectrum from the  $^{208}\text{Pb}(\gamma, n)^{207}\text{Pb}$  reaction was performed and the radiation widths observed in  $^{138}\text{Ba}$  were determined by a direct comparison of the yields for these levels to that for the 254-keV state in  $^{208}\text{Pb}$ .

In order to extract the ground-state radiation widths from the threshold photoneutron spectra, it is essential to define precisely the energy of the electron beam. In the traditional threshold photoneutron method the electron energy is adjusted so that the photoneutron can decay only to the ground state of the daughter nucleus. However, the first excited states in  $^{137}\text{Ba}$  and  $^{139}\text{Ce}$  are near (281 keV in  $^{137}\text{Ba}$  and 250 keV in  $^{139}\text{Ce}$ ) the ground states. In the present work, no attempt was made to explicitly separate the neutron decay to the ground and first excited states. Instead, the machine endpoint energy was increased in order to include the neutron decay to the first excited state and an analytical technique was used to deduce the ground-state radiative strengths. A detailed discussion of this technique is given in Ref. 5. A schematic diagram of the photoexcitation process is shown in Fig. 2 for  $^{138}\text{Ba}$ . The photoexcitation of  $^{140}\text{Ce}$  is entirely analogous to

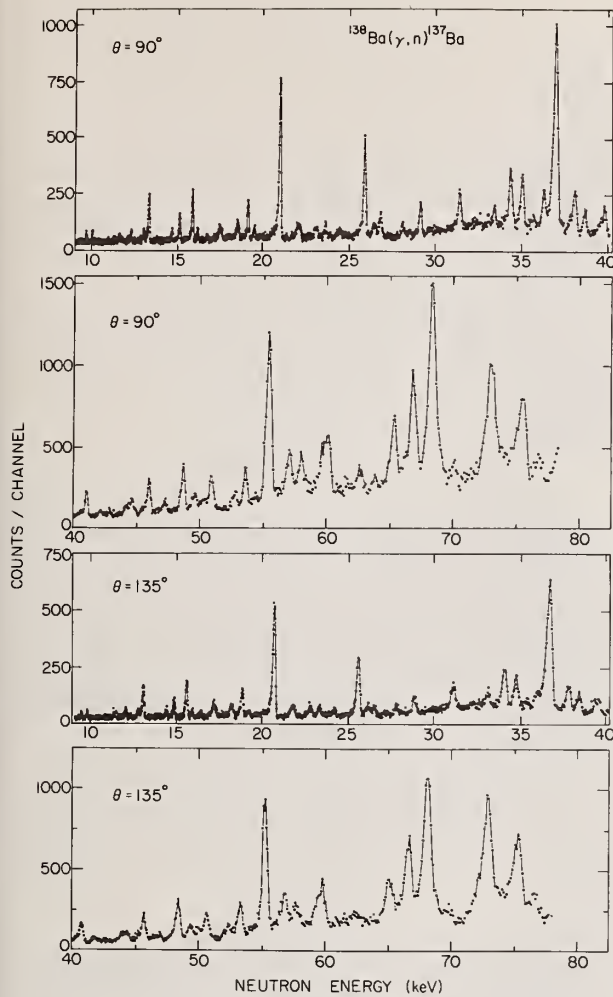


Fig. 1 The observed time-of flight spectra at  $90^\circ$  and  $135^\circ$  for the  $^{138}\text{Ba}(\gamma, n) ^{137}\text{Ba}$  reaction.

the process shown in Fig. 2. In this figure,  $\Gamma_{n0}$ ,  $\Gamma'_{n0}$ , and  $\Gamma'_{n1}$  represent the neutron decay width to the ground state, the width to the ground state from a level higher in excitation energy than the first excited state of the daughter nucleus, and the decay width to the first excited state, respectively. The decay transitions corresponding to  $\Gamma'_{n0}$  are not observed in this measurement, since the neutron energy would be approximately equal to the energy between the ground state and first excited state, and consequently, greater than 281 keV. However, those  $(\gamma, n)$  resonances which neutron decay to the first excited state (corresponding to  $\Gamma'_{n1}$ ) appear in the same energy interval as those ( $\Gamma_{n0}$ ) which decay to the ground state. The strengths of the transitions to the first excited state are diminished compared with the decay strength to the ground state, since  $\Gamma'_{n0} \gg \Gamma'_{n1}$ . The ratio  $r$  of the average photoneutron yield from the first excited state ( $Y_1$ ) to that from the ground state ( $Y_0$ ) is found<sup>5</sup> to be

$$r \equiv Y_1/Y_0 = \frac{\Gamma'_0 \Gamma'_{n1}}{\Gamma_0 \Gamma_{n0}} \frac{(\Gamma_{n0} + \Gamma_Y)}{(\Gamma'_0 + \Gamma'_{n1} + \Gamma_Y)}, \quad (1)$$

where  $\Gamma_Y$  is the total radiative width of the resonance

$$(\Gamma_Y = \sum_i \Gamma_{Yi}),$$

$\Gamma_{Y0}$  is the ground-state radiation width, and the primed widths refer to excitations of higher energy levels. An estimate of the average value of  $r$  was obtained using a Monte Carlo analysis in which sets of the reduced widths of 1000 levels in Eq. (1) were chosen from a Porter-Thomas distribution. In the present case  $r$  was estimated to be approximately 25%. Hence, less than 20% of the total observed strength is due to nonground-state transitions.

The spins and parities of the photoneutron resonances were deduced by measuring the angular distribution of the emitted neutrons. For example, an M1 resonance is expected to decay by neutron emission isotropically to the ground and first excited state of the daughter nucleus. Hence, the angular distribution ratio  $R$  which is defined as the ratio of the observed yield of a given resonance at  $90^\circ$  to that at  $135^\circ$  is expected to be unity for M1 photo-excitation of  $^{138}\text{Ba}$ . For an E1 excitation the most probable values of  $R$  are 0.8 and 1.2 for neutron decay to the ground state and first excited state, respectively. Therefore, a measurement of  $R$  provides a good method for sorting E1 and M1 states in  $^{138}\text{Ba}$ . The power of this method is demonstrated in Fig. 3 for the  $^{138}\text{Ba}(\gamma, n) ^{137}\text{Ba}$  reaction. In Fig. 3 the number of observed resonances is plotted as a function of  $R$  in three energy intervals. The number of M1 states is predominant in the energy interval 9–60 keV. This relatively large number of M1 states indicates that the total M1 radiative strength may also be anomalously large. In addition, the M1 resonances dominate the lower energy interval (9–40 keV). This is due to the fact that the s-wave neutron penetration factor corresponding to M1 excitation is quite large (0.3) compared to the p-wave factor corresponding to E1 excitation (0.02). In the 40–60 keV region the p-wave penetration factor has increased to 0.07 while the s-wave factor has

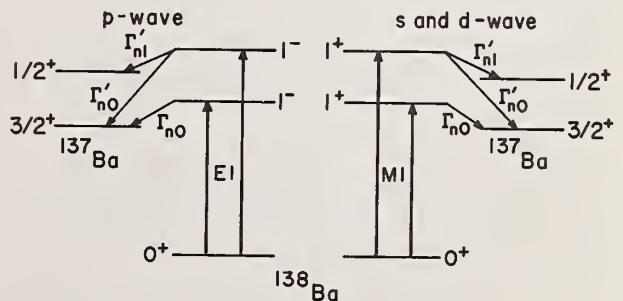


Fig. 2 Photo-excitation process of  $^{138}\text{Ba}$ . The neutrons can decay to the ground and first excited states.



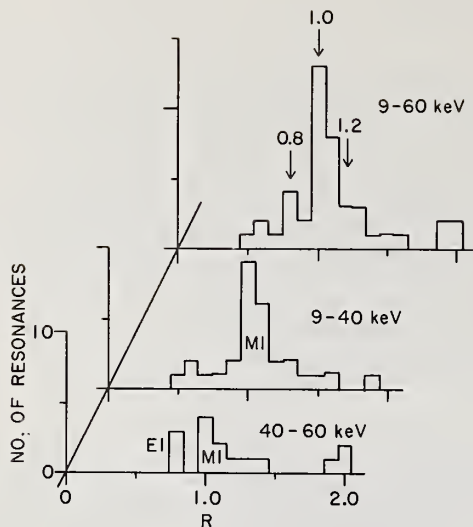


Fig. 3 The number of resonances observed as a function of the angular distribution ratio for  $^{138}\text{Ba}$ .

remained at approximately the same value. Hence, the numbers of observed E1 and M1 states are comparable.

#### Results and Discussion

The analysis described in the preceding section was performed for the  $^{140}\text{Ce}(\gamma, n)^{139}\text{Ce}$  reaction. The number of resonances observed in  $^{140}\text{Ce}$  is plotted as a function of the angular distribution ratio  $R$  in Fig. 4. The number of E1 resonances dominates the energy region 10 to 50 keV, while only three states could possibly be identified as M1 in this energy range. This result is in apparent disagreement with the measurements of Pitthan and Walcher<sup>1</sup> who found a giant M1 resonance in  $^{140}\text{Ce}$  at an excitation of 8.7 MeV. However, there may be no contradiction for two reasons. First, the present measurement was performed at an excitation of 9.05 MeV and, therefore, may be too high in energy to detect the resonance. On the other hand, the state which Pitthan and Walcher observed has a width of approximately 1 MeV and should still have a large strength even at 9 MeV. Secondly, the average resonance spacing for states of  $J = 1$  in  $^{140}\text{Ce}$  may be too large compared with the energy interval of the present measurement (35 keV) to obtain an accurate estimate of the M1 strength. Additional studies are currently underway at Argonne in order to resolve this discrepancy.

The total ground-state M1-radiation width  $\Sigma \Gamma_{\gamma_0}(M1)$  for  $^{138}\text{Ba}$  was found to be 3.0 eV in the energy interval 9–60 keV. The magnetic-dipole average reduced width  $\bar{k}_{M1}$  is computed from the expression<sup>6</sup>

$$\bar{k}_{M1} = \Sigma \Gamma_{\gamma_0}(M1) / (E_{\gamma}^3 \Delta E), \quad (2)$$

where  $E_{\gamma}$  is the photon energy in MeV and  $\Delta E$  is the energy interval in MeV. The value of  $\bar{k}_{M1}$  was found to be  $90 \times 10^{-3}$  for  $^{138}\text{Ba}$ . This value is more than four times the average value<sup>7</sup> of  $\bar{k}_{M1} = 18 \times 10^{-3}$  found for most heavy nuclei. We conclude from this measurement that a giant M1 resonance occurs in  $^{138}\text{Ba}$  at an excitation of 8.6 MeV. The average M1 reduced width was not deduced for  $^{140}\text{Ce}$ , because of the small number of observed M1 states.

In addition, the total ground-state E1-radiation width  $\Sigma \Gamma_{\gamma_0}(E1)$  was found to be 2.1 eV for  $^{138}\text{Ba}$  in the region 9–60 keV and 1.0 eV for  $^{140}\text{Ce}$  in the region 14–50 keV. The expression<sup>6</sup> for the average E1 reduced width is given by

$$\bar{k}_{E1} = \Sigma \Gamma_{\gamma_0}(E1) / (E_{\gamma}^3 A^{2/3} \Delta E), \quad (3)$$

where  $E_{\gamma}$  and  $\Delta E$  are defined in the same manner as in Eq. (2). The average reduced widths were computed [Eq. (3)] to be  $4 \pm 1 \times 10^{-3}$  for  $^{138}\text{Ba}$  and  $2 \pm 1 \times 10^{-3}$  for  $^{140}\text{Ce}$ . These results are in good agreement with other measurements<sup>8</sup> for medium-heavy and heavy nuclei as shown in Fig. 5. The solid curve in Fig. 5 represents the Weisskopf single-particle estimate<sup>8</sup> with the constraint that the E1 strength satisfies the sum rule:

$$\int_0^{\infty} \sigma_a dE = 0.06 \text{ NZ/A MeV-barns},$$

where  $\sigma_a$  is the photon absorption cross section.

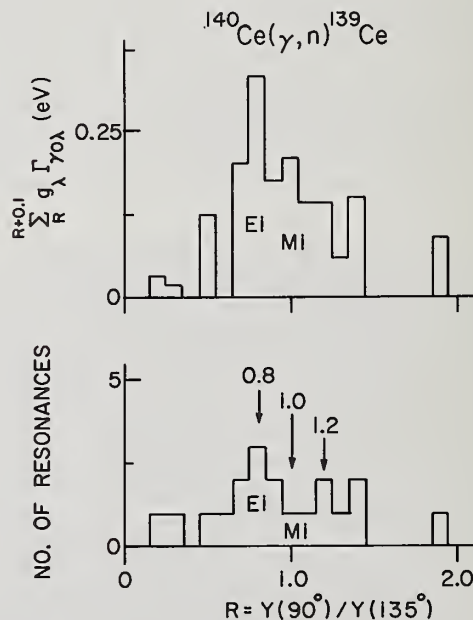


Fig. 4 The observed radiation widths and number of resonances as a function of the angular distribution ratio for  $^{140}\text{Ce}$ .

The dashed curve in this figure represents the Brink-Axel estimate,<sup>9</sup> with  $E_\gamma = 8.0$  MeV. Values of this estimate were generated from the expression

$$\bar{k}_{E1} = (6.1 \times 10^{-9}) E_\gamma^2 A^2. \quad (4)$$

The Axel formulation [Eq. (4)], which is based on the giant-dipole model, consistently overestimates the observed values of the photon reduced width. The single-particle estimate appears to agree with energy and mass-number dependence of the data. However, it is a factor of 3.5 larger<sup>8</sup> than the data. At present there is no reliable model which will predict E1 strength functions near the photoneutron threshold.

### Conclusions

The E1 strengths from the  $^{138}\text{Ba}(\gamma, n)^{137}\text{Ba}$  and  $^{140}\text{Ce}(\gamma, n)^{139}\text{Ce}$  reactions were measured throughout the neutron energy intervals 9–60 keV and 14–50 keV, respectively, using the threshold photoneutron technique. The observed E1 average reduced widths agree with other measurements of heavy nuclei, but disagree with theoretical estimates. In addition, the M1 strength function was measured for the  $^{138}\text{Ba}(\gamma, n)^{137}\text{Ba}$  reaction. The observed M1 reduced width was found to be more than four times the average value ( $k_{M1} = 18 \times 10^{-3}$ ) for most nuclei. We conclude that an M1 giant resonance appears in  $^{138}\text{Ba}$  at an excitation of approximately 8.6 MeV. Neutron-induced gamma-ray production in the 8 to 9-MeV energy range should be enhanced by the presence of giant M1 resonances in this mass region.

### References

<sup>†</sup> Work performed under the auspices of the U.S. Atomic Energy Commission and the Energy Research and Development Administration.

<sup>1</sup> R. Pitthan and Th. Walcher, Phys. Lett. **36B**, 563 (1971).

<sup>2</sup> D. Gardner, Bull. Am. Phys. Soc. **19**, 1017 (1974).

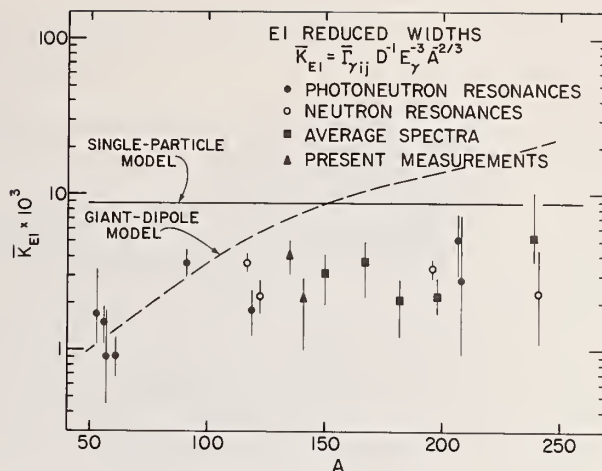


Fig. 5 The E1 photon reduced widths. The present measurements are represented by triangles.

<sup>3</sup> V. Gillet, A. M. Green, and E. A. Sunderson, Nucl. Phys. **88**, 321 (1966); J. Vergados, Phys. Lett. **36B**, 12 (1971); T.-S.H. Lee and S. Pittel, to be published.

<sup>4</sup> H. E. Jackson and E. N. Strait, Phys. Rev. C **4**, 1314 (1971).

<sup>5</sup> R. J. Holt and H. E. Jackson, to be published.

<sup>6</sup> G. A. Bartholomew, Ann. Rev. Nucl. Sci. **11**, 259 (1961).

<sup>7</sup> L. M. Bollinger, in International Symposium on Nuclear Structure, Dubna, 1968 (International Atomic Energy Agency, Vienna, Austria, 1969), p. 317.

<sup>8</sup> H. E. Jackson, in EANDC Topical Conference on Critique of Nuclear Models and Their Validity in Evaluation of Nuclear Data (Tokyo, March 1974), to be published.

<sup>9</sup> P. Axel, Phys. Rev. **126**, 671 (1972).

ANALYZING POWERS OF THE  ${}^6\text{Li}(\vec{n}, t){}^4\text{He}$  REACTION  
Munawar Karim and J. C. Overley  
University of Oregon  
Eugene, Oregon 97403

We have measured analyzing powers for the  ${}^6\text{Li}(\vec{n}, t){}^4\text{He}$  reaction for neutron energies between 0.2 and 1.4 MeV. An energy continuum of neutrons was produced by bombarding a thick lithium metal target with a 3.5-MeV, nanosecond-pulsed proton beam.

The partially polarized neutrons emitted at  $50^\circ$  were incident on an evaporated  ${}^6\text{Li}$  metal target. A silicon surface barrier detector was used to measure triton and  $\alpha$ -particle yields as a function of particle energy. Tritons were distinguished from  $\alpha$  particles with time-of-flight techniques. Yield asymmetries were determined at laboratory angles of  $35^\circ$ ,  $60^\circ$  and  $80^\circ$  with angular resolutions of  $\pm 5^\circ$ . The  $\alpha$ -particle yield asymmetries were converted to backward angle triton asymmetries, providing data at six angles. Analyzing powers as a function of angle were deduced. Although results are tentative, analyzing powers near  $90^\circ$  and 250 keV are negative ( $\sim -0.3$ ) while above 700 keV they are large and positive ( $\sim +0.9$ ) and vary slowly with neutron energy.

(NUCLEAR REACTIONS:  ${}^6\text{Li}(\vec{n}, t){}^4\text{He}$ ,  $E = 0.2\text{--}1.4$  MeV; measured yield asymmetries, deduced analyzing powers  $A(\theta)$ .)

### Introduction

Because of its importance as a neutron flux standard and in neutron detection, the  ${}^6\text{Li}(n, t){}^4\text{He}$  reaction has been extensively studied, both experimentally and theoretically. Differential<sup>1,2</sup> and integrated<sup>3-5</sup> cross sections have been measured. The analyzing power of the reaction has been studied<sup>6</sup> near  $E_n = 250$  keV and  $90^\circ$  but with poor angular resolution. Other  ${}^6\text{Li} + n$  reaction channels have also been studied through total cross section measurements<sup>7,8</sup> and measurements of differential cross sections<sup>9</sup> and analyzing powers<sup>10</sup> for neutron scattering. These results have been synthesized<sup>5,11</sup> through theoretical parameterizations from thermal energies to about 2 MeV.

Despite these efforts some inconsistencies remain. For example, recent measurements<sup>2</sup> of the  ${}^6\text{Li}(n, t){}^4\text{He}$  differential cross sections are at variance with theoretical predictions. The discrepancy is most clearly noted in the behavior of the s-p wave interference term in a Legendre polynomial expansion of the angular distributions in the vicinity of the resonance at  $E_n = 250$  keV.

The analyzing power of the reaction should sensitively depend on the nature of such an interference effect. We have therefore undertaken a measurement of this parameter. Our techniques allow us to determine this quantity over an energy range from 0.2 to 1.4 MeV without repeated flux normalizations. In this paper we report the preliminary results of such an experiment.

### Experimental Method

Fig. 1 depicts the experimental arrangement. The  ${}^7\text{Li}(p, n){}^7\text{Be}$ ,  ${}^7\text{Be}^*$  reactions were used for a source of polarized neutrons. A 3.5-MeV, nanosecond-pulsed proton beam from the University of Oregon's 5 MV Van de Graaff accelerator was allowed to strike a thick metallic lithium target. A neutron energy continuum was produced with a maximum energy at  $50^\circ$  of 1.5 MeV. The beam pulse repetition period was 0.5  $\mu\text{sec}$ , the full-width at half-maximum of the pulse was about 1.2 nsec, and the time averaged beam current was about 5  $\mu\text{A}$ .

The neutrons emitted at  $50^\circ$  with respect to the proton beam were incident on a  ${}^6\text{Li}$  target placed 15 cm from the source. This target was evaporated "in situ" from lithium metal enriched to 96%  ${}^6\text{Li}$ . The substrate was stainless steel 0.4 mm thick. The  ${}^6\text{Li}$  deposit was 184 keV thick to 2-MeV particles. This thickness was determined through a measurement of the maximum energy lost by the  $\alpha$  particles produced by thermal neutrons incident upon the  ${}^6\text{Li}$  layer. The area of the target was defined by a mask to have a diameter of 2.5 cm. Pressure in the target chamber was maintained at less than  $4 \times 10^{-6}$  T and no target deterioration was noticed over a 120 hour interval.

Reaction products were detected with a totally depleted silicon surface barrier detector 200  $\mu\text{m}$  thick. The active diameter of 1.2 cm was defined by a gold collimator. The distance between the target and detector was 11 cm. Energies of the charged fragments were measured, with the energy scale calibrated against the 5.477-MeV particles from  ${}^{241}\text{Am}$ . The neutron continuum can produce tritons and  $\alpha$  particles with the same energy. Since these can be resolved by their differing velocities, a simultaneous measurement of the total (neutron plus particle) flight time was made. The time calibration was determined by introducing known delays.

Data were collected in a two dimensional array of yield as a function of flight time and detected particle energy. The array consisted of 31 rows of flight time channels each of width 1.2 nsec, and 128 columns of energy channels each with a width of 20 keV. The energy channels spanned the range from 1.4 to 4.5 MeV.

Data were obtained at laboratory angles of  $\pm 35^\circ$ ,  $\pm 60^\circ$ , and  $\pm 80^\circ$  with respect to the incident neutron direction. The  ${}^6\text{Li}$  target was maintained parallel to the detector surface for each measurement. False asymmetries due to possible misalignment were minimized by measuring asymmetries on both sides of the proton beam (at neutron emission angles of  $\pm 50^\circ$ ), as indicated in Fig. 1. Data at each angle represents 0.4 C of integrated proton beam current.



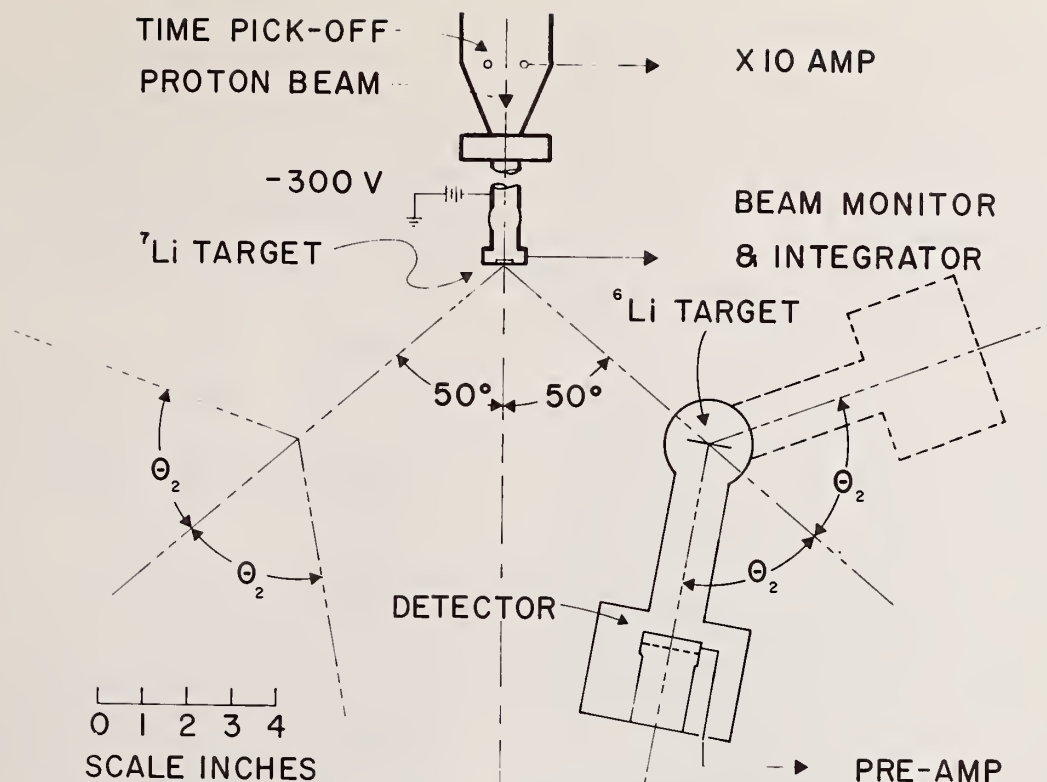


Fig. 1. A plan view of the experimental arrangement, indicating different detector and target configurations.

#### Data Reduction and Results

Procedures for converting two parameter data such as these into differential cross sections have been fully described elsewhere.<sup>2,12</sup> For this presentation, however, we have followed a simplified method, since conversions to cross sections are not necessary. For each reaction product, yield data were projected onto the flight time or particle energy axis by summing counts for a given row of flight time channels or col-

umn of particle energy channels. Asymmetries,  $\epsilon$ , were calculated conventionally:

$$\epsilon = (L - R)/(L + R) \quad (1)$$

where L and R are the integrated number of counts to the left ( $\phi = 0$ ) and right ( $\phi = \pi$ ) of the neutron beam.

The results at neutron emission angles of  $+50^\circ$  and  $-50^\circ$  were averaged, but systematic differences were not statistically significant.

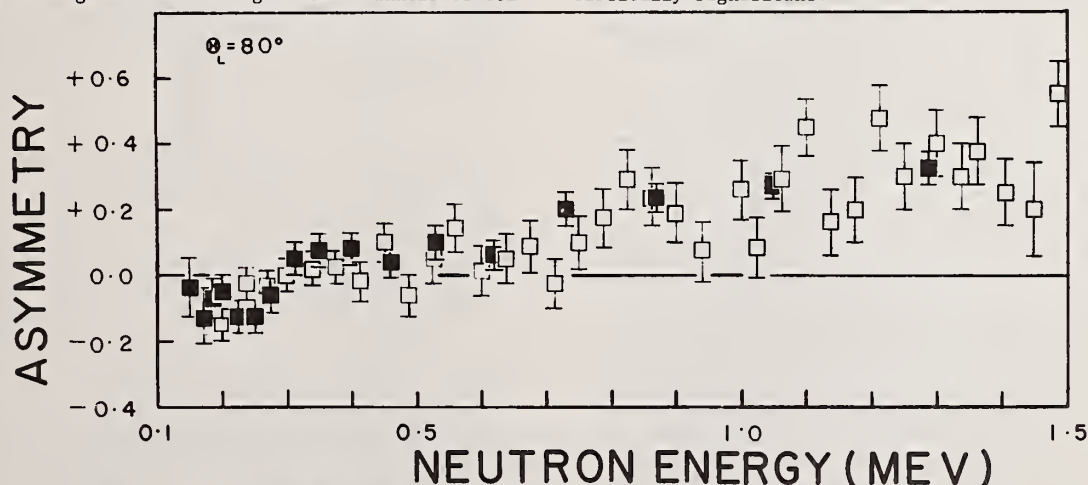


Fig. 2. Triton asymmetries as a function of neutron energy at a laboratory angle of  $80^\circ$ . The solid points result from a projection of counts onto the flight time axis while the open points result from the particle energy projection. Error bars indicate uncertainties due to counting statistics only.

The neutron energy to which the asymmetry is ascribed is calculated from the kinematics, with corrections made for  $^6\text{Li}$  target thickness and finite resolution effects. This calculation, which is also described in refs. (2,12), results in an average neutron energy. The average is obtained with the assumption that all quantities such as cross section, incident neutron spectrum, and  $\alpha$ -particle or triton stopping cross sections vary linearly with energy and angle within the summation range.

The above procedure does not correct for small differences in effective solid angle which result when detector angles are changed. These geometry errors affect the total yield by much less than 1%, however, which is less than the statistical uncertainty.

Fig. 2 shows the asymmetry in the measured triton yield at a laboratory angle of  $80^\circ$  as a function of neutron energy. The error bars represent uncertainties due only to counting statistics. The solid points result from projecting counts onto the flight time axis, while the open points derive from the energy projection. These two sets of points represent the same data summed in different ways.

Data similar to those of Fig. 2 were compiled for tritons and  $\alpha$  particles at each angle. The average neutron energy calculated for each asymmetry varies with angle and particle type. To express the asymmetries at a common set of neutron energies, the average value of the asymmetry over a 50 keV interval was used for energies less than 500 keV. A 100 keV averaging interval was used at higher energies.

Since  $\alpha$ -particle yields are related to triton yields at the supplementary center-of-mass angle,  $\alpha$ -particle asymmetries can be expressed as backward angle triton asymmetries. This has been done and the results compiled as a series of angular distributions.

Fig. 3 shows representative angular dependences of triton asymmetries. The angular resolution is about  $\pm 5^\circ$ . The three backward angle points in each case correspond to asymmetries inferred from  $\alpha$ -particle data. The good agreement near  $90^\circ$  is evidence that false asymmetries are small. For example, if the triton counting rate were too high to the left of the neutron beam due to misalignment, the  $\alpha$ -particle yield would also be too high. Since  $\alpha$ -particle yields to the left correspond to triton yields to the right, effects of misalignment would appear as a discontinuity in asymmetry near  $90^\circ$ .

When the asymmetries are divided by the incident neutron polarization one obtains the analyzing power. The polarizations of neutrons emitted at  $50^\circ$  from the  $^7\text{Li}(p,n)^7\text{Be}$  reaction have been extensively studied and the results compiled by Walter.<sup>13</sup> Neutrons from the  $^7\text{Li}(p,n)^7\text{Be}^*$  reaction are also contained in the continuum and these neutrons are also partially polarized. The yield ratios of the two source reactions were measured and the incident neutron polarizations were corrected for the contribution<sup>13</sup> of the excited state neutrons. Since the yield of first excited state neutrons is relatively small, uncertainties in their polarizations do not contribute significantly to uncertainties in the incident neutron polarization.

The product of the differential reaction cross section and the analyzing power as a function of angle may be expressed as a series in associated Legendre polynomials:

$$A(\theta)\sigma(\theta) = \sum_L C_L p_L^1(\cos\theta_{\text{cm}}) \quad (2)$$

We have used our previously published differential cross sections<sup>2</sup> to produce a weighted least squares fit to the present results. One term, with  $L = 1$ , is adequate to express our results, although at low neutron energies the statistical uncertainties are sufficiently large to make the fit ambiguous.

Fig. 4 shows the energy dependence of  $C_1$ . It is

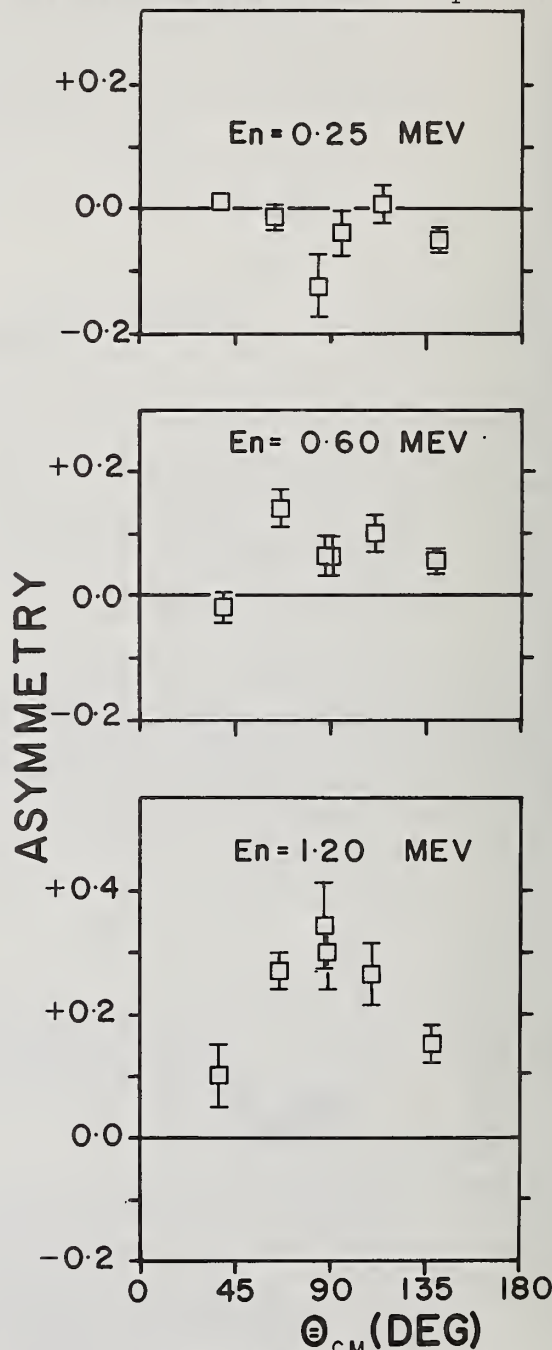


Fig. 3. Triton asymmetries as a function of center-of-mass angle at selected neutron energies. The three backward angle points derive from  $\alpha$ -particle data.

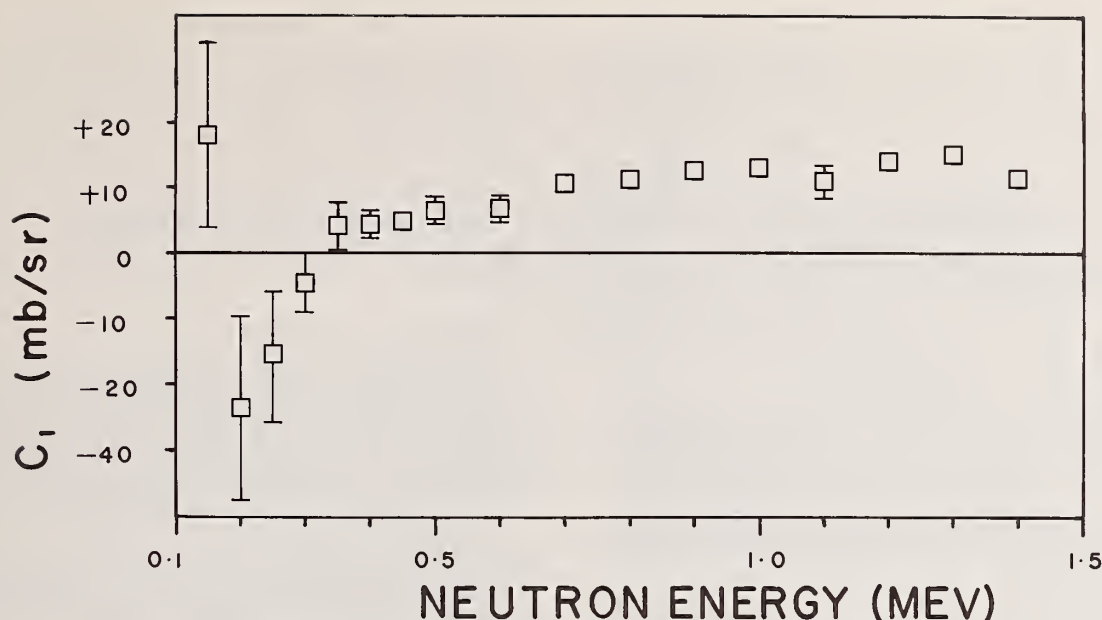


Fig. 4. The coefficient  $C_1$  of the associated Legendre polynomial  $P_1^1$  obtained from a least squares fit to the product of the analyzing power and differential cross section, as a function of laboratory neutron energy.

negative in the vicinity of the resonance at 250 keV and large because of the large differential cross section. It increases smoothly as the energy increases, crossing zero near 300 keV. These results are consistent with previously measured<sup>6</sup> values of  $-0.34 \pm 0.11$  at  $E_n = 260$  keV and  $90^\circ \pm 30^\circ$  and  $-0.10 \pm 0.13$  at  $E_n = 290$  keV and  $90^\circ \pm 45^\circ$ . As energy increases further, the analyzing powers continue to increase, approaching a value of almost 1.0 at about 1.3 MeV. The variation of analyzing power with angle is consistent with s-p wave interference and the energy dependence implies the existence of other broad p-wave states at energies above 1.4 MeV.

#### Discussion

In the region of the resonance at  $E_n = 250$  keV, we find the analyzing power to be about  $-0.3$  near  $90^\circ$ . It increases smoothly as the energy increases, crossing zero near 300 keV. These results are consistent with previously measured<sup>6</sup> values of  $-0.34 \pm 0.11$  at  $E_n = 260$  keV and  $90^\circ \pm 30^\circ$  and  $-0.10 \pm 0.13$  at  $E_n = 290$  keV and  $90^\circ \pm 45^\circ$ . As energy increases further, the analyzing powers continue to increase, approaching a value of almost 1.0 at about 1.3 MeV. The variation of analyzing power with angle is consistent with s-p wave interference and the energy dependence implies the existence of other broad p-wave states at energies above 1.4 MeV.

Many level schemes for the  $^7\text{Li}$  compound nucleus have been suggested. We have not yet examined these possibilities in detail. However, the presence of a broad p-wave state at an excitation energy of 9-10 MeV in  $^7\text{Li}$  seems necessary for R-matrix calculations performed<sup>5</sup> for this reaction. Our result is further evidence that such states contribute significantly to the reaction in the neutron energy range from 0.5 to 1.4 MeV.

Analyzing power data at higher energies would be helpful in locating the excitation energies of such levels. Further work on the inverse reaction, using both polarized and unpolarized triton beams, would be interesting. These data indicate that the neutrons resulting from the triton bombardment of helium would be highly polarized.

Finally, it is intriguing that this reaction may prove its further usefulness by serving as a neutron

polarimeter in the energy range above 0.5 MeV.

We wish to acknowledge the aid of R. M. Sealock and G. Yu in obtaining these data. W. Schulz and J. MacDonald were indispensable in maintaining the equipment. We wish especially to thank Professor H. W. Lefevre for his continuing interest in this work. This work was supported in part by the National Science Foundation.

#### References

1. S. J. Bame and R. L. Cubitt, Phys. Rev. **95**, 117 (1959).
2. J. C. Overley, R. M. Sealock, and D. H. Ehlers, Nucl. Phys. **A221**, 573 (1974).
3. C. A. Uttley, M. G. Sowerby, B. H. Patrick, and E. R. Rae, Neutron Standards and Flux Normalization, Proc. Conf. Argonne, 1971, (National Technical Information Service, Springfield, Va. 1971, CONF-701002), p. 129.
4. S. J. Friesenhahn, V. J. Orphan, A. D. Carlson, M. P. Fricke and W. M. Lopez, USAEC Report INTEL-RT 7011-001 (1974).
5. E. Fort and J. P. Marquette, EANDC(E) 148"U" (Cadarahe, 1972).
6. H. Waffler and G. Walch, Direct Interactions and Nuclear Reaction Mechanisms, (Gordon and Breach, N. Y., 1963) p. 633.
7. J. W. Meadows and J. F. Whalen, Nucl. Sci. Eng. **48**, 221 (1972).
8. C. A. Uttley and K. M. Diment, and reported in ref. 3.
9. R. O. Lane, A. S. Langsdorf, Jr., J. E. Monahan, and A. J. Elwyn, Ann. of Phys. **12**, 135 (1961).
10. R. O. Lane, A. J. Elwyn, and A. Langsdorf, Jr., Phys. Rev. **136**, B1710 (1964).
11. C. Mahaux and G. Robaye, Nucl. Phys. **74**, 161 (1965).
12. J. C. Overley and D. H. Ehlers, Nucl. Instr. **12**, 205 (1973).
13. R. L. Walter, Polarization Phenomena in Nuclear Reactions, (Proc. Conf. H. H. Barschall and W. Haeberli, Eds. University of Wisconsin Press, Madison, Wis. 1970), p. 317.



NEUTRON-ABSORPTION CROSS SECTION OF SODIUM-22  
R. Rundberg, M. F. Elgart, H. L. Finston and E. T. Williams  
Department of Chemistry  
A. H. Bond, Jr., Department of Physics  
Brooklyn College, City University of New York  
Brooklyn, New York 11210

We describe a simple method for determining the neutron-absorption cross sections for radionuclides produced and consumed in a reactor-neutron flux. Data were obtained for  $^{22}\text{Na}$  which through application of Westcott's procedure, yielded the following:  $\sigma_0 = 51.1 \pm 3.1$  Kbarns,  $s_0 = 2.3 \pm 0.1$ , and  $\Sigma' = 100 \pm 10$  Kbarns.

(Thermal; resonance; cross section; sodium-22; neutron; Westcott)

### Introduction

Westcott<sup>1</sup> has published a procedure for determination of the thermal flux and the neutron-absorption cross section of a nuclide in a reactor irradiation. In practice, samples of the nuclide, each with a Cobalt monitor, are simultaneously irradiated with and without cadmium shielding in a flux of reactor neutrons. The effective cross section,  $\hat{\sigma}$ , can be expressed:

$$\hat{\sigma} = \sigma_0 (g + rs), \quad (1)$$

where  $\sigma_0$  is for 2200 m/s neutrons,  $g$  corrects for deviation from  $1/v$  thermal capture,  $r$  is the ratio of epithermal to thermal flux (a reactor parameter) and  $s$  relates the resonance integral,  $\Sigma'$ , to  $\sigma_0$ . The data for  $^{60}\text{Co}$  lead to values for the thermal flux,  $nv_0$ , and  $r$ .

We now apply the Westcott procedure to the case of any nuclide, radioactive or stable, in a reactor irradiation. For a reaction of the general form,



where  $X$  is the target,  $q = 2n, p, d$ , etc.,  $Y$  is the radionuclide whose cross section we wish to measure, and  $u = \gamma, p$ , etc. The rate equation is

$$dN/dt = \sigma(n, q) M \phi(\text{prod}) - \lambda N - \hat{\sigma} nv_0 N, \quad (2)$$

where  $\sigma(n, q)$  is the cross section for production of  $Y$ ,  $\phi(\text{prod})$  is the flux for production,  $M$  is the number of atoms of  $X$ ,  $\lambda$  is the decay constant of  $Y$ ,  $N$  is the number of atoms of  $Y$ , and  $\hat{\sigma}$  is the effective cross section for  $Y$  at the irradiation position used. Since  $\sigma(n, q)$  is typically a few millibarns,  $M$  is assumed constant.

Integrating from  $N = 0$  at  $t = 0$  to  $N = N$ , at  $t = t(\text{irradiation})$ , we obtain:

$$N_1 = M \frac{\sigma(n, q) \phi(\text{prod})}{\lambda + \hat{\sigma} nv_0} \left[ 1 - e^{-(\lambda + \hat{\sigma} nv_0)t} \right] \quad (3)$$

Following irradiation, assuming no absorption of fast neutrons by the cadmium, the ratio of activity in the cadmium-shielded sample to that of the bare sample is given by:

$$R_1 = \frac{N_1^{\text{Cd}}}{N_1^{\text{bare}}} = \frac{\left[ 1 - e^{-(\lambda + \hat{\sigma}^{\text{Cd}} nv_0)t} \right] (\lambda + \hat{\sigma} nv_0)}{\left[ 1 - e^{-(\lambda + \hat{\sigma} nv_0)t} \right] (\lambda + \hat{\sigma}^{\text{Cd}} nv_0)} \quad (4)$$

where  $\hat{\sigma}^{\text{Cd}} = \sigma_0 (r_0/K + rs)$ ,  $K$  is a coefficient depending on the thickness of Cd, and  $r_0 = r(T/T_0)^{1/2}$ .

Equation 4 is not sufficient to give both the  $\sigma_0$  and  $s_0$  ( $s_0 = s(T_0/T)^{1/2}$ ). Both parameters can be determined by irradiating the original sample a second time in a reactor position where  $r$  is sufficiently different to give another independent equation. This is achieved by irradiating first near the core where

the rate of production is adequate to determine the initial activity ratio  $R_1$ . The samples are reirradiated at a second reactor position sufficiently far from the core so that production of  $Y$  is negligible or at least significantly reduced and a second activity ratio,  $R_2$ , is determined. Under these conditions, the following equation can be written:

$$dN/dt = -\lambda N - \hat{\sigma} nv_0 N. \quad (5)$$

This is essentially the same as equation (2) with the production term omitted. Note, however, that  $\hat{\sigma}$  and  $nv_0$  will be different for each irradiation position.

Integrating from  $N = N_1$  at  $t = 0$  to  $N = N_2$  at  $t = t_2$  (duration of the second irradiation) we obtain:

$$N_2 = N_1 e^{-(\lambda + \hat{\sigma} nv_0)t_2}. \quad (6)$$

The ratio,  $R_2$ , is the measured ratio of activity of  $Y$  in the cadmium-wrapped sample to that of the bare sample, and is given by:

$$R_2 = \frac{N_2^{\text{Cd}}}{N_2^{\text{bare}}} = \frac{N_1^{\text{Cd}} e^{-(\lambda + \hat{\sigma}^{\text{Cd}} nv_0)t_2}}{N_1^{\text{bare}} e^{-(\lambda + \hat{\sigma} nv_0)t_2}} \quad (7)$$

or,

$$R_2 = R_1 e^{(\hat{\sigma} - \hat{\sigma}^{\text{Cd}}) nv_0 t_2}. \quad (8)$$

Taking the natural log and rearranging, we obtain:

$$\sigma_0 = \frac{\ln(R_2/R_1)}{(1 - r_0/K) nv_0 t_2} \quad (9)$$

In equations (5) and (9),  $\hat{\sigma}$ ,  $nv_0$ ,  $rs$  and  $r_0$  refer to the second irradiation position and  $g$  is again assumed to equal unity. If we are able to employ a reactor position far enough away from the core so that  $r_0/K$  is negligible (thermal neutrons only), then equation (9) assumes the following form:

$$\sigma_0 = \frac{\ln(R_2/R_1)}{nv_0 t_2} \quad (10)$$

Note that, by itself, the second irradiation corresponds to the usual burnup experiment, however, using the ratio  $R_2/R_1$  improves the reliability of the result. With  $\sigma_0$  known, equation (4) can be solved for  $s_0$ , permitting calculation of the resonance integral;

$$\Sigma' = \sigma_0 s_0 \frac{1}{2} \sqrt{\pi}. \quad (11)$$

It should be noted that the method described above is applicable to any burnup process involving thermal and epithermal neutrons. For example, in the case of  $^{22}\text{Na}$  there is evidence<sup>2</sup> that burnup proceeds primarily via the  $^{22}\text{Na}(n, p)^{22}\text{Ne}$  reaction.

### Experimental Procedure

A preliminary experiment was performed to determine the Westcott parameters and the applicability of the procedure for two irradiation positions in the

HFBR: 5 cm out horizontally from the core (V-14), and in the reflector 50 cm from the core perimeter (V-11). The target materials were  $^{59}\text{Co}$  and  $^{197}\text{Au}$  for which  $\sigma_0$ ,  $\Sigma'$ , and  $s_0$  are known.<sup>3,4</sup> A sample consisted of one segment each of Co-Al and Au-Al wire wrapped together in aluminum foil. The irradiation container was an aluminum tube in which two samples were placed. Two more samples were placed in a cadmium sleeve with walls 0.045" thick, capped with cadmium at both ends, and then force-fitted into the same aluminum tube to ensure good thermal contact. The samples were irradiated simultaneously in the V-14 and V-11 positions for 8 hours.

The activities of  $^{60}\text{Co}$  and  $^{198}\text{Au}$  in the samples were determined by means of gamma-ray spectroscopy using a Ge(Li) detector. Absolute activities were obtained for  $^{60}\text{Co}$  by calibrating the system with an N.B.S.-calibrated  $^{60}\text{Co}$  source. The results are shown in Table I. Next, irradiations were made to determine the cross section of  $^{22}\text{Na}$ , produced by the (n,2n) reaction in  $\text{Na}_2\text{CO}_3$  samples sealed into quartz tubes. The ampoules, each with a segment of Co-Al wire, were individually wrapped in aluminum foil. Duplicate samples were loaded into the irradiation container as described above so that two samples were shielded with cadmium and two were unshielded. The first irradiation, to obtain  $R_1$  (equation (4)), was for 8 days in V-14.

The activities of  $^{22}\text{Na}$  and  $^{60}\text{Co}$  were measured with the Ge(Li) detector system. Since the method depends on a relative measurement, it was not necessary to know either the absolute intensity of the gamma ray or the fraction of decays giving rise to the gamma ray. The gamma-ray spectra were observed over a period of several months and the following ratio is the average of a number of individual measurements:  $R_1 = 4.77 \pm 0.09$ .

Following the determination of  $R_1$ , the samples, each accompanied by a fresh cobalt monitor, were re-irradiated in the same configuration used in the initial irradiation. Due to scheduling difficulties, it was not possible to irradiate in V-11. Therefore the sample was placed in the V-14 thimble, withdrawn to a distance from the core corresponding to that in V-11 and irradiated 10 days. This position was shielded somewhat by the upper control rods in the operating position reducing the thermal flux below that in V-11. After removal of the samples from the reactor, the activity ratio was found:  $R_2 = 7.52 \pm 0.08$ .

## Results

In order for the Westcott convention to be valid, the neutron spectrum to which the sample is exposed must be reasonably well moderated, and have a  $1/E$  distribution above the cadmium cut-off. The energy dependences of the cross sections in the resonance region for  $^{59}\text{Co}$  and  $^{197}\text{Au}$  differ greatly and  $s$  is appreciably different for each. Thus, agreement between the values of  $r_0$  obtained from measurements with the two nuclides at a particular position in the reactor is an indication of the applicability of the Westcott convention there (Table I).

Table I: Westcott parameters in HFBR irradiation positions

	$r_0$ in V-14	$r_0$ in V-11	Cadmium Ratio V-14 V-11	
Au	$0.069 \pm 0.001$	$(4.9 \pm 0.5) \times 10^{-4}$	1.77	112
Co	$0.068 \pm 0.001$	$(4.0 \pm 0.5) \times 10^{-4}$	7.79	1,240

The reactor parameters for the two irradiations in the  $^{22}\text{Na}$  experiment are shown in Table II. As mentioned above, the sample in the second irradiation was exposed to a thermal flux lower than that in V-11. The second irradiation position, 50 cm above the core in V-14, was shielded somewhat by the control rods, which caused an increase in  $r_0$  since the epithermal flux was not appreciably reduced. However, the flux of higher-energy neutrons drops off faster with increasing distance from the core than does the flux of epithermal neutrons having energies just above the cadmium cutoff. Thus, while  $r_0$  was larger than in V-11 due to the control rods, the flux of neutrons above the Q-value for  $^{23}\text{Na}(n,2n)^{22}\text{Na}$ , (-12.4 MeV) was negligible. This is substantiated by the theoretical curves<sup>5</sup> giving the flux versus distance from the core for neutrons in several energy ranges. We would like to emphasize the care with which one must choose the irradiation position to be used and monitor the conditions obtaining there.

Table II: Reactor parameters

Position	$nv_0$ (n/cm <sup>2</sup> -sec)	$r_0$
1: V-14	$(5.02 \pm 0.05) \times 10^{14}$	$0.0903 \pm 0.0002$
2: V-14 <sup>a</sup>	$(0.945 \pm 0.009) \times 10^{13}$	$0.0342 \pm 0.0001$

Note a: See experimental section for explanation

By substituting  $R_1$  and  $R_2$  into equation (10),  $\sigma_0$  was determined. Using  $R_1$  in equation (4), a plot of  $s_0$  versus  $\sigma_0$  was constructed and  $s_0$  was determined graphically.

The errors reported in Tables I, II and III represent statistical uncertainty (67% confidence limit) in the counting data. Most sources of systematic error cancel in the formation of the ratios  $R_1$  and  $R_2$ . The error in  $nv_0$  was 1% which reflects the uncertainty in the activity of the N.B.S. - calibrated  $^{60}\text{Co}$  source.

The extent of depletion of the cadmium shielding during the eight-day irradiation was calculated. The change in the parameter  $K$  due to cadmium burnup was about 10%. The effect on  $r_0$  was around 1% and the value in Table II has been corrected accordingly. The burnup of cadmium in the second irradiation was negligible.

Table III provides a comparison of our results for  $^{22}\text{Na}$  with previously reported work. The values for  $^{22}\text{Na}$  reported by Farinelli and Martini<sup>6</sup> and by Werner and Santry<sup>7</sup> are effective cross sections and, therefore, agreement with the other values is expected to be only approximate. We do not report values for  $\hat{\sigma}$  since the flux and  $r_0$  and hence the value of  $\hat{\sigma}$  for a given nuclide, depend upon the specific irradiation conditions.

Table III: Comparison of previously reported values for  $^{22}\text{Na}$  with this work. All cross sections in barns  $\times 10^{-4}$

Reference	$\sigma_0$	$s_0$	$\Sigma'$
6	$9 \pm 1^a$	-	-
7	$2.83 \pm 0.06^a$	-	-
2	$4 \pm 2$	-	-
8	$3.59 \pm 0.12$	6.02	$19.1 \pm 2.5$
This work	$5.11 \pm 0.31$	$2.3 \pm 0.2$	$10 \pm 1$

Note a: Value reported is actually  $\hat{\sigma}$



The disagreement among the values for  $\sigma_0$  may stem from the possibility that there is a resonance in the absorption cross section for thermal neutrons. The resulting departure of the energy dependence from a  $1/v$  form would invalidate the assumption  $g = 1$  and increase the dependence of the measured cross section on reactor temperature. The possible existence of such a resonance is further suggested<sup>2</sup> by the high values of  $\sigma_0$  which have been measured for  $^{22}\text{Na}$ .

One potential source of error in our results is the possibility that the close proximity of the control rods to position V-14<sup>a</sup> resulted in a hardened<sup>a</sup> Maxwellian neutron spectrum. If the  $^{22}\text{Na}$  cross section is not  $1/v$  below the cadmium cutoff, a hardened spectrum could cause anomalous results. Experiments currently underway to determine the thermal-neutron cross section of  $^{22}\text{Na}$  at two different neutron temperatures should indicate whether such a low-lying resonance exists.

Thus we have demonstrated a simple technique for the determination of neutron-absorption cross sections of radioactive nuclides produced in reactor irradiations. Our method takes advantage of the production of activity by fast neutrons and can be applied to radionuclides produced by  $(n,2n)$ ,  $(n,p)$ , and  $(n,x)$  reactions where production of sufficient activity for a burnup experiment might be difficult or expensive. The method is a general one and can be applied to a number of interesting radionuclides.

#### Acknowledgements

We would like to thank Mr. Jack Floyd of the HFBR for his advice and assistance. We thank Mr. John Stehn of the National Neutron Cross Section Center at Brookhaven National Laboratory for his interest and support. This work was partially supported by the U. S. Atomic Energy Commission under contract No. AT(11-1)-3126.

#### References

1. C. H. Westcott, "Effective Cross Section Values for Well-Moderated Thermal Reactor Spectra", 3rd Edition, Corrected, Chalk River Publication AECL No. 1101, Nov. 1970.
2. R. Eehalt, H. Morinaga, and Y. Shida, Z. Naturforsch., 26a, 590 (1971).
3. C. H. Westcott, W. H. Walker, and T. K. Alexander, "Effective Cross Sections and Cadmium Ratios for the Neutron Spectra of Thermal Reactors", Proc. of the 2nd Int. Conf. on the Peaceful Uses of Atomic Energy, Geneva 1958, Vol. 16, p. 70 United Nations, New York (1959).
4. T. A. Eastwood, Int. Jour. Appl. Rad. and Isotopes, 17, 17 (1966).
5. H. J. C. Kouts, "Neutron Physics of and with the High-Flux Beam Reactor", Brookhaven National Laboratory Report BNL 664, (T-218) March 1961, (Reactor Technology TID-4500, 16th Ed).
6. U. Farinelli and M. Martini, Physica, 29, 1196 (1963).
7. R. D. Werner and D. C. Santry, J. Nuclear Energy, 26, 403 (1972).
8. G. H. E. Sims, J. Inorg. Nucl. Chem., 29, 593 (1967).
9. C.H. Westcott, J. Nucl. Energy, 12, 113 (1960).



The valence and channel neutron model of Lane and Lynn remarkably account for partial radiative widths of neutron resonances in the 3p-giant resonance. In this investigation, evidence is presented for valence neutron capture at and in the neighborhood of the 3s- giant resonance in target nuclei Ar-36 and Fe-54. In addition, the variation of the correlation coefficient  $\rho(\Gamma_{\gamma ij} E_{\gamma}^{-n}, (2J+1) S_{dp})$  with the reduction power factor  $n$  of the  $\gamma$  ray energy is studied.

(Thermal capture spectra; valence capture in  $^{36}\text{Ar}$  and  $^{54}\text{Fe}$ )

### Introduction

A considerable number of recent investigations have been devoted to the study of nonstatistical effects in the neutron capture mechanism in the thermal and resonance region. These nonstatistical effects generally manifest themselves in the observation of enhanced gamma ray transitions to low lying states with large single particle character. The interpretation<sup>(1,2,3)</sup> of the thermal capture data in terms of either of the simple reaction mechanisms described below is one of the interesting aspects of these investigations. Three proposed simple reaction mechanisms<sup>(4,5)</sup> which quantitatively explain these observations are (1) hard sphere capture, (2) channel capture, and (3) valence capture. Other reaction mechanisms such as doorway state formation will not be treated here. The hard sphere or potential capture cross section for an s-wave neutron undergoing a transition to a final p state is expressed by:

$$\sigma_{\gamma}(\text{hard sphere}) = \frac{0.062}{R(E_n)^{\frac{1}{2}}} \left( \frac{Z}{A} \right)^2 \theta_f^2 \frac{(2J_f+1)}{6(2I+1)} \left( \frac{y+3}{y+1} \right)^2 y^2 \quad (1)$$

In this relation,  $\theta_f$  is a reduced dimensionless neutron width of the final state and  $y = k_{NL} R$  where  $k_{NL}$  is the wave number corresponding to the binding energy of the final state. The interesting features of this relation is that the hard sphere partial capture cross section is (i) correlated with the (d,p) spectroscopic factors of the final states and (ii) it follows an  $E_{\gamma}$  energy dependence. Estimates of (1) in the mass region around  $A = 50$  are about 0.3b.<sup>(4)</sup>

The channel capture contribution<sup>(4)</sup> to the radiative width  $\Gamma_{\gamma if}$  of an s-wave resonance with spin  $J$  is given by:

$$\Gamma_{\gamma if} = \Gamma_{in}^0 \theta_f^2 \left( \frac{Z}{A} \right)^2 \frac{y}{R^3} \left( \frac{y+2}{y+1} \right)^2 (2J_f+1) \left\{ \frac{110}{JJ_f} \right\}^2 \text{ in eV} \quad (2)$$

where the last term is the Wigner 6-j symbol. Note that the energy dependence of  $\Gamma_{\gamma if}$  is closely proportional to  $E_{\gamma}^2$ .

The valence capture component for an E1 transition is expressed by:<sup>(5)</sup>

$$\Gamma_{\gamma if}(E1) = \frac{16\pi k^3}{9} \theta_i^2 \theta_f^2 \left( \frac{eZ}{A} I_{if} M_{if} \right)^2 \quad (3)$$

$M_{if}$  and  $I_{if}$  are the angular momentum vector coupling

coefficients and the radial overlap integrals for E1 transitions respectively. It is interesting to note that the limits of integration of  $I_{if}$  are from 0 to  $\infty$ .

For the case of channel capture, the integration was carried out in the external region to arrive at relation (2). In this investigation, the  $\gamma$  ray energy dependence of the radial overlap integrals in (3) was studied for s-wave capture in the mass region 50, using Saxon-Wood potential. The results show that the energy dependence of  $I_{if}$  is not very strong; specifically  $I_{if}^2 \propto E_{\gamma}^{-\frac{1}{4.4}}$ .

### Neutron Capture Mechanism in Ar-36

The  $\gamma$  ray intensities due to thermal neutron capture were measured by Von Wille<sup>(6)</sup> using a highly enriched sample of Ar-36 (99.9%). Hardell and Beer<sup>(7)</sup> using a natural argon sample observed several Ar-36 lines and reported their intensities relative to Ar-40. The Ar-36  $\gamma$  ray intensities were converted here to absolute values with the aid of the thermal capture cross sections of Ar-36 and Ar-40 ( $\sigma_{\gamma} = 0.66\text{b}$ ) and their natural abundances as reported in BNL-325 (1973). As shown in Table I, very good agreement is obtained between the two sets of measurements.

A display of the energy level diagram of Ar-37 and  $\gamma$  ray intensities due to thermal neutron capture is shown in Fig. 1. The (d,p) spectroscopic factor  $S_{dp}$  as indicated in the figure are weighted averages of the most recent data. One notes immediately that the strongest E1 transitions are populating final states with large spectroscopic factors. Analysis of the data show that the  $\gamma$  ray intensities are highly correlated with the (d,p) data,  $(2J-1)S_{dp}$ . When such

significant correlation is established, one seeks to find out whether the reaction mechanism is dominated by hard sphere, channel, or valence capture. The magnitude as well as the  $\gamma$  ray energy dependence of the intensities can shed light on this question. As a result, partial radiative widths are calculated in the framework of the valence neutron model using the parameters of the bound level derived by Mughabghab and Magurno.<sup>(8)</sup> In these calculations, the normalization procedure described by Lane and Mughabghab<sup>(8)</sup> is applied. A comparison between predicted and measured partial radiative widths is described in Fig. 2 which shows good agreement between the two sets. Finally, it is interesting to point out that detailed analysis of the correlation coefficient:

$$\rho(\Gamma_{\gamma ij} E_{\gamma}^{-n}, (2J+1) S_{dp})$$

is optimized for  $n_{\text{max}} = 1.2$ , a result which is not reconciled with channel or valence capture for which  $n_{\text{max}} = 2$  or 3 respectively.

\*Research supported by U.S. Energy Research and Development Administration.

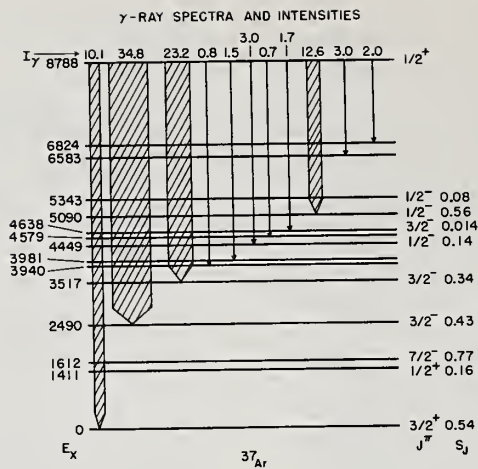


Fig. 1

Energy level diagram and thermal neutron capture  $\gamma$  ray intensities of Ar-37

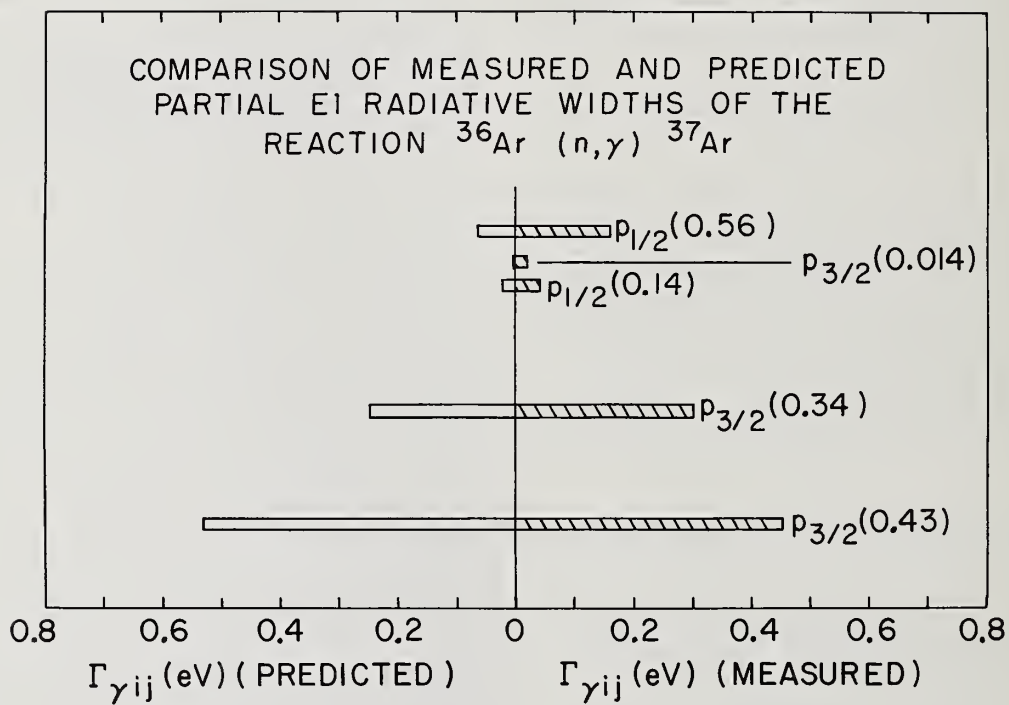


Fig. 2

Comparison of measured and calculated partial radiative widths of  $^{36}\text{Ar} (n, \gamma) ^{37}\text{Ar}$

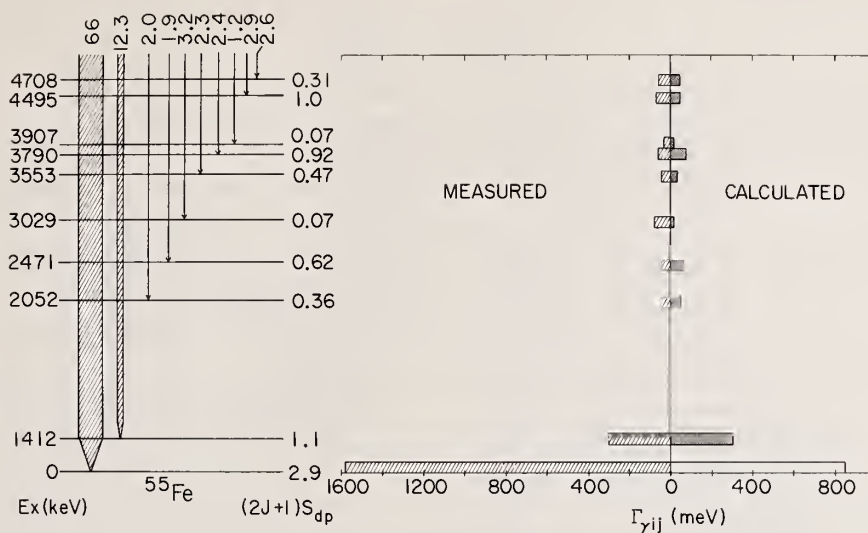


Fig. 3

Energy level diagram and comparison of measured and calculated partial radiative widths of  $^{54}\text{Fe} (n, \gamma) ^{65}\text{Fe}$

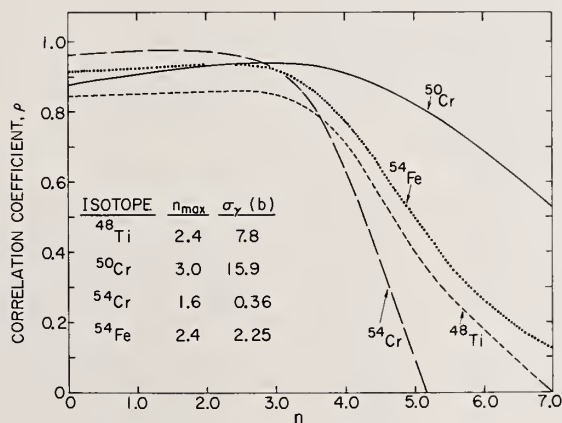


Fig. 4

Study of the variation of the correlation coefficient  $\rho$  with the reduction factor  $n$



Fe-54 is located in the mass region where the 3 s-wave neutron strength function attains a maximum value and where it is expected that the single particle 3s state is located just near the neutron separation energy. In this discussion we report Fe-54 as another candidate for valence capture. Analysis of the thermal cross sections of Fe-54 in terms of positive energy resonances indicates that the thermal capture cross section is accounted for in terms of the 7.8 keV resonance, which information is used to derive a radiative width of 2.4 eV for this resonance. In addition, this indicates that the thermal capture  $\gamma$  ray intensities can be considered as due to capture in the 7.8 keV resonance, neglecting interference effects. The energy level diagram and thermal capture  $\gamma$  ray intensities<sup>(16)</sup> of Fe-55 are described in Fig. 3. The partial radiative widths due to valence capture process are calculated and compared with the experimental values. As shown, the agreement between measured and calculated values is reasonably good. The calculated ground state radiative width is about half the measured value. This could possibly be due to interference effects. As a result, it will be of interest to carry out  $\gamma$  ray spectra measurements due to capture in the 7.8 keV resonance. Finally, the variation of the correlation coefficient with the reduction power factor,  $n$ , is studied. The results illustrated in Fig. 4 show that  $\rho$  is maximized for  $n = 2.4$  in agreement with channel or valence capture. For comparison, similar studies carried out on Ti-48, Cr-50, and Cr-54 are shown in the Fig. 4.

1. J. Kopecky, A. M. J. Spits, and A. M. Lane, Phys. Letters 49B, 323 (1974)
2. S. F. Mughabghab, in Second International Symposium on Neutron Capture Gamma Ray Spectroscopy and Related Topics, Petten, the Netherlands Sept 2-6, (1974)
3. R. E. Chrien in Statistical Properties of Nuclei Ed. J. B. Garg (Plenum Press, New York, 1972) p.233
4. A. M. Lane and J. E. Lynn, Nucl. Phys. 17, 563, 586 (1960)
5. J. E. Lynn, The Theory of Neutron Resonance Reactions, p.333 (Clarendon Press, Oxford, England 1968)
6. Von P. Wille, Atomkernenergie 13, 383 (1968)
7. R. Hardell and C. Beer, Physica Scripta 1, 85 (1970)
8. S. F. Mughabghab and B. A. Magurno, contribution to this conference.
9. A. M. Lane and S. F. Mughabghab, Phys. Rev. C, 10, 412 (1974)
10. J. P. Kopecky, K. Abrahams and F. Stecher-Rasmussen Nucl. Phys. A188, 535 (1972)

Table I  
 $\gamma$  Ray Intensities of  $^{36}\text{Ar}$  ( $n, \gamma$ )  $^{37}\text{Ar}$

$\gamma$ Ray Energy (keV)	$E_x$ (keV)	(6) $I_\gamma$ (photons/100 capture)	(7) $I_\gamma$ (photons/100 capture)
8790.8	0	10.9 $\pm$ 0.8	10.1
6300.2	2491	37.5 $\pm$ 3.0	37.1
5273.5	3517	25.0 $\pm$ 1.5	18.2
4851.8	3939	0.8 $\pm$ 0.1	
4342.3	4449	1.6 $\pm$ 0.2	
4211.6	4579	3.2 $\pm$ 0.2	
4153.0	4638	0.8 $\pm$ 0.1	
3981.4	4810	1.8 $\pm$ 0.2	
3700.2	5091	13.4 $\pm$ 0.9	
2599.6	6191	3.1 $\pm$ 0.5	
2107.5		23.7 $\pm$ 0.1	18.6
1410.6		33.0 $\pm$ 0.5	31.0

J.B. Garg  
 SUNY at Albany  
 Albany, N.Y. 12222

Neutron time of flight transmission measurements were made on several samples of <sup>209</sup>Bi using the Nevis Synchrocyclotron of Columbia University. The resonance parameters are given for 29 levels to 75 keV. Out of the 29 observed levels 10 were  $\ell = 0$  and 19 were  $\ell = 1$  levels. The implied s and p-strength functions are  $10^4 S_0 = (0.60 \pm 0.39)$  and  $10^4 S_1 = (0.19 \pm 0.08) - 0.21$ .

(Nuclear reactions <sup>209</sup>Bi (n,n), (n, $\gamma$ ), E = 500 eV - 75 keV;  
 measured  $\sigma_t(E)$ ; deduced  $E_0$ ,  $\ell$ , J,  $g\Gamma_n$ ,  $S_0$ ,  $S_1$ )

### Introduction

This paper presents the results of high resolution neutron time of flight spectroscopy measurements using the Columbia University Nevis Synchrocyclotron with a 200 m flight path. This is one of a series (Refs. 1-20) of nuclei which have been investigated at Nevis. Our purpose in making these measurements has been to study the behavior of neutron total cross section vs energy for nuclei across the periodic table.

Natural Bismuth is 100% <sup>209</sup>Bi. The ground state spin ( $I^\pi$ ) of <sup>209</sup>Bi is 9/2<sup>-</sup>. Thus, the s-levels have J = 4 or 5 with odd parity and p-levels will have J = 3, 4, 5, 6 and positive parity. <sup>209</sup>Bi nucleus consists of 83 protons and 126 neutrons. Thus, it is a closed neutron shell (magic number N = 126) and very near to a closed proton shell (magic number Z = 82). The level spacing for the observed resonances in <sup>209</sup>Bi is in the keV range. We observed 29 levels (10  $\ell = 0$  levels, 19  $\ell = 1$  levels) to 75 keV.

The main other high resolution measurements on <sup>209</sup>Bi are those of Morgenstern et al<sup>21</sup> (Saclay), 4 keV  $\leq E \leq$  70 keV, and Nichols et al<sup>22</sup> (Duke), 10 keV  $\leq E \leq$  130 keV.

### Results and Discussions

We had two sets of measurements on <sup>209</sup>Bi. First set of measurements used 100 ns channel width and time of flight spectrum was spread over 2000 timing channels. The  $\sigma$  vs E from this set of measurements are plotted in BNL-325.<sup>23</sup> Three samples corresponding to  $1/n = 9.92$ , 50.4, and 228 b/atom were used in the measurements. An example of  $\sigma$  vs E for the s-levels is shown in Fig. 1. The resonance parameters for  $\ell = 0$  levels were obtained using both an area analysis and a shape fit. The latter used a single level analysis including resonance-potential interference effects with corrections for Doppler broadening. The parameters are given in Table I.

Table I. The resonance parameters for  $\ell=0$  levels observed in the neutron interaction with <sup>209</sup>Bi to 75 keV.

$E_0$ (keV)	J	$g\Gamma_n$ (eV)
0.800	5	$2.6 \pm 0.2$
2.312	4	$8.0 \pm 0.4$
5.114	(5)	$3.0 \pm 0.3$
12.15	4	$115 \pm 20$
15.58	4	$55 \pm 10$
27.08		$12 \pm 3$
33.32	4	$110 \pm 20$
45.60	5	$100 \pm 20$
61.80		$40 \pm 8$
69.50		$300 \pm 50$

A second set of measurements used a single sample having  $1/n = 30.31$  b/atom of <sup>209</sup>Bi. The detector channel widths were 40 ns for most of the energy region. The time of flight spectrum was spread over 16,000 timing channels. The parameters for p-levels were obtained on the basis of this set of measurements using the transmission area analysis. In the area analysis corrections were made for Doppler broadening effects and the area under a transmission dip is independent of instrumental energy resolution.  $\ell = 1$  level parameters are given in Table II.

Table II. The  $\ell = 1$  resonance parameters (using the transmission area analysis) to 75 keV

$E_0$ (keV)	$g\Gamma_n$ (eV)
3.348	$0.08 \pm 0.03$
4.455	$0.120 \pm 0.040$
6.524	$0.03 \pm 0.01$
9.018	$0.16 \pm 0.05$
9.153	$0.12 \pm 0.04$
9.762	$0.11 \pm 0.04$
17.45	$0.50 \pm 0.15$
21.05	$2.5 \pm 0.7$
25.28	$9.5 \pm 3.0$
37.25	$6.3 \pm 2.0$
39.19	$1.7 \pm 0.5$
42.44	$7 \pm 2$
44.17	$1.4 \pm 0.4$
51.80	$3.5 \pm 1.0$
52.84	$12 \pm 3$
53.86	$32 \pm 8$
57.60	$5.8 \pm 1.5$
67.07	$0.4 \pm 0.2$
72.60	$12 \pm 4$

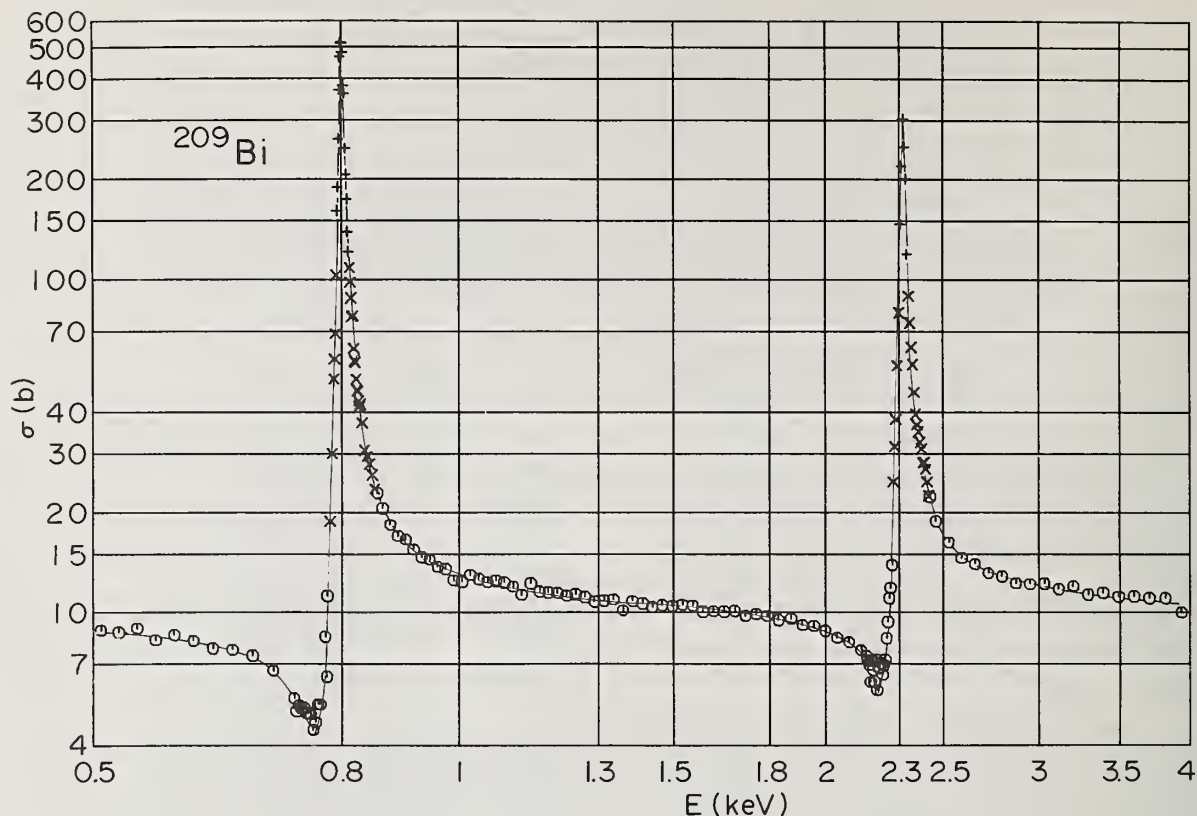


Fig. 1 The neutron total cross section of  $^{209}\text{Bi}$  from 500 eV to 4 keV. The points represent 1 or 3 channel average on or near the resonances and 9 or 27 channel average away from the resonances. The circles represent the thick sample ( $1/n = 9.92$  b/atom), the x's the medium sample ( $1/n = 50.4$  b/atom) and +s the thin sample ( $1/n = 228$  b/atom) values. The curve drawn is only an aid to the eye.

The parameters in Tables I and II imply s- and p-strength functions to be  $10^4 S_0 = (0.60^{+0.39}_{-0.21})$  and  $10^4 S_1 = (0.19^{+0.08}_{-0.05})$ .

#### References

- \* Research supported by the U.S. Atomic Energy Commission AT(11-1) 2174.
- † Present address: Brookhaven National Lab. Upton, N.Y. 11973
- 1 H.I. Liou et al, Phys. Rev. C5, 974 (1972), Er.
- 2 F. Rahn et al, Phys. Rev. C6, 251 (1972), Sm, Eu.
- 3 Ibid., 1854,  $^{232}\text{Th}$ ,  $^{238}\text{U}$ .
- 4 H.I. Liou et al, Phys. Rev. C7, 823 (1973), Yb.
- 5 H.S. Camarda et al, Phys. Rev. C8, 1813 (1973), W.
- 6 F. Rahn et al, Phys. Rev. C8, 1827 (1973), Na.
- 7 U.N. Singh et al, Phys. Rev. C8, 1833 (1973), K.
- 8 H.I. Liou et al, Phys. Rev. C10, 709 (1974), Cd.
- 9 F. Rahn et al, Phys. Rev. C10, 1904 (1974), Gd.
- 10 G. Hacken et al, Phys. Rev. C10, 1910 (1974), In.
- 11 U.N. Singh et al, Phys. Rev. C10, 2138 (1974), Cl.
- 12 Ibid., 2143, Ca.
- 13 Ibid., 2147, F.
- 14 Ibid., 2150, Mg.
- 15 H.I. Liou et al, Phys. Rev. C11, 462 (1975), Dy.
- 16 Ibid., 457, Ar.
- 17 U.N. Singh et al, Phys. Rev. C (to be published),  $^{27}\text{Al}$ .
- 18 H.I. Liou et al, Phys. Rev. C (to be published),  $^{175}\text{Lu}$ .



- 19 H.I. Liou et al, Phys. Rev. C (to be published),  $^{177}\text{Hf}$ .  
20 Ibid., T1.  
21 J. Morgenstern et al, Nucl. Phys. A123, 561 (1969).  
22 P.F. Nichols et al, Annals of Physics (N.Y.) 8, 250 (1959).  
23 Neutron Cross Sections, Brookhaven National Laboratory Report BNL-325, second edition, suppl. no. 2 (1966).

# MEASUREMENT OF NEUTRON CAPTURE CROSS SECTIONS NEAR 24 KeV

N. Yamamuro, T. Doi and T. Hayase

Research Laboratory for Nuclear Reactors, Tokyo Institute of Technology  
Meguro-ku, Tokyo, Japan

and

Y. Fujita, K. Kobayashi and R. C. Block\*

Kyoto University Research Reactor Institute  
Kumatori, Osaka, Japan

Neutron capture cross sections of  $^{93}\text{Nb}$ , Ag,  $^{127}\text{I}$ ,  $^{165}\text{Ho}$ ,  $^{197}\text{Au}$  and  $^{238}\text{U}$  were measured near 24 keV using the Fe-filtered-beam method. A 15-cm thick Fe filter was placed in the neutron time-of-flight beam produced by the KUR 46-MeV electron Linac. Capture  $\gamma$ -rays were detected by two  $\text{C}_6\text{F}_6$  total energy detectors located on a 12-m flight path. Pulse-height weighting was used to determine the relative capture efficiency. The neutron flux was determined with the detector via the  $^{10}\text{B}$  ( $n; \alpha_1 \gamma$ ) reaction and saturated resonance capture in Ag at 5.2 eV. Multiple scattering corrections were applied to the data, resulting in 24 keV capture cross sections of 0.33, 1.10, 0.76, 1.26, 0.68 and 0.50 barns for  $^{93}\text{Nb}$ , Ag,  $^{127}\text{I}$ ,  $^{165}\text{Ho}$ ,  $^{197}\text{Au}$  and  $^{238}\text{U}$ , respectively. Total errors are 5 to 7%, with an estimated systematic error of 4%.

(Neutron Capture Cross Section;  $^{93}\text{Nb}$ , Ag,  $^{127}\text{I}$ ,  $^{165}\text{Ho}$ ,  $^{197}\text{Au}$  and  $^{238}\text{U}$ ; Fe-filtered beam; time-of-flight method;  $\text{C}_6\text{F}_6$  detector; pulse-height weighting)

## Introduction

Although the capture cross sections of materials are important to the design of fission reactors and fusion reactors, the accuracy of these cross sections is not yet satisfactory. For the measurement of capture cross sections in the unresolved region, it is essential to have a low background neutron beam and to know the absolute magnitude of the incident neutron flux and  $\gamma$ -ray intensity emitted from a sample. The saturated capture method is generally used to determine the absolute neutron flux and  $\gamma$ -ray intensity. If a precise absolute "point" cross section is given in the keV region, the relative measurements can be normalized to this "point" cross section to provide an accurate overall determination of the cross section.

Recently it has been shown that if a thick iron filter is inserted into a white-source time-of-flight neutron beam, a low background neutron beam is transmitted with energies corresponding to the cross section minima in iron<sup>1,2</sup>. In particular the band near 24 keV has relatively high transmission and is separated from the other high energy groups. Such well-isolated and low-background beams are ideally suited for precise "point" cross section measurements.

With the aid of the iron-filtered beam, the neutron capture cross sections of In, Ta and depleted U were measured at the RPI 1.25-m dia. liquid scintillation spectrometer and the neutron total cross sections of Be, C and O were determined recently at the KUR Linac<sup>3,4</sup>. In this experiment, the 24-keV neutron capture cross sections of  $^{93}\text{Nb}$ , Ag,  $^{127}\text{I}$ ,  $^{165}\text{Ho}$ ,  $^{197}\text{Au}$  and  $^{238}\text{U}$  have been measured.

## Experimental Method

### Apparatus

The neutrons were generated by a tantalum photo-neutron target with a 5-cm thick  $\text{CH}_2$  moderator irradiated with electrons from the KUR 46-MeV linear accelerator. The accelerator was typically operated with a 0.6  $\mu\text{sec}$  electron pulse width and a 140 Hz repetition rate.

A 5-cm thick iron filter was placed at the entrance to the evacuated flight tube, about 2.5 m from

\* Visiting Professor from Rensselaer Polytechnic Institute.

the neutron source. Another 10-cm thick iron filter was placed at about a 7-m flight distance. The Fe-filtered beam was collimated to 46-mm diameter onto a sample, which was mounted on a 4-position automatic sample changer. The neutron flight path was 11.7 m.

Two 10-cm diameter by 4-cm thick  $\text{C}_6\text{F}_6$  liquid scintillation detectors were located face to face, and a sample was put perpendicularly between them. The detector system was shielded from  $\gamma$ -ray background by a 5-cm thick lead wall.

The scintillation-detector photomultiplier signals were fed into a linear amplifier and the amplified signals were passed to a timing single channel discriminator whose bias was set at about 150 keV. The linear signals and the timing logic signals were recorded with 32 channels x 32 channels two-dimensional mode in a Nuclear Data 4420 Analyzer.

When the data were acquired, ordinarily four samples were mounted and samples were cycled into the neutron beam by the sample changer such that a cycle was repeated every 15 to 20 minutes. The signals for each sample were stored automatically into the corresponding position of memory in the analyzer. Although the beam intensity varied gradually in the course of an experimental run of 10 to 20 hours, it was observed that the neutron flux impinging on the samples was proportional to the preset time of the sample changer within  $\pm 1\%$ .

### Fe-Filtered Beam Shape near 24 KeV

By setting a thick  $^{10}\text{B}$  sample between the  $\text{C}_6\text{F}_6$  detectors, the Fe-filtered beam counting spectrum near 24 keV was measured. As the neutron capture probability of a thick  $^{10}\text{B}$  sample is nearly constant for the 24-keV band of neutrons, the spectrum shown in Fig. 1 illustrates directly the shape of the neutron flux near 24 keV. The ratio of peak count to the background count is about 200. The 'dips' in the spectrum are caused by the Mn impurity in the iron filter.

### Measurements

The incident neutron flux was measured with a  $^{10}\text{B}$  sample (93% enrichment) because the 480-keV  $\gamma$ -rays emitted from the reaction  $^{10}\text{B}(n; \alpha_1 \gamma)$  can be detected with the  $\text{C}_6\text{F}_6$  detector. A thick Ag 'reference' sample

was measured relative to the  $^{10}\text{B}$  sample; capture in this reference sample was then used as the flux monitor for the subsequent measurements.

Fig. 2 shows the time-of-flight spectra for 24-keV neutron capture in Au and  $^{238}\text{U}$  samples. Fig. 3 shows the pulse-height spectrum for Au. The dotted points indicate the spectrum counted and the circular points the weighted spectrum.

Measurements were also performed with a sample of carbon and without any sample. These measurements made it possible to determine the time-dependent background under the 24-keV peak.

### Analysis

#### Principle of Analysis

The probability of neutron capture in a nucleus is usually measured by detection of  $\gamma$ -rays emitted promptly from an excited state of the compound nucleus. The capture detector counting rate integrated over the neutron energy band is given by the equation

$$C = \phi Y \eta, \quad (1)$$

where  $\phi$ ,  $Y$  and  $\eta$  means the integrated neutron flux incident upon a sample, the average capture probability of a sample and the  $\gamma$ -ray detector efficiency, respectively. As is well known, an important characteristic of  $\eta$  is that it must be essentially independent of the  $\gamma$ -ray cascade mode. With the use of the pulse-height weighting technique, it is possible to reduce the detection efficiency to one that is proportional to the total  $\gamma$ -ray energy<sup>5</sup>. Provided that the weighting function of the  $\gamma$ -ray detector is applied to the  $\gamma$ -ray pulse-height spectrum, we can obtain the relation.

$$(CW) \equiv \sum_i C_i W_i \propto \phi Y \{ (BE) + E_n \} \approx \phi Y (BE), \quad (2)$$

where  $W_i$  is the weighting function for the  $i$ -th pulse-height channel,  $(BE)$  is the neutron binding energy of the compound nucleus and  $E_n$  is the incident neutron energy. Here the chance to detect coincidentally two or more  $\gamma$ -rays in the same cascade decay is neglected because this probability is very low.

The neutron flux can be derived from the  $^{10}\text{B}$  count if the neutron capture probability of the sample and the detection efficiency of the  $\text{C}_6\text{F}_6$  detector for 480-keV  $\gamma$ -rays are known. The capture probability of the  $^{10}\text{B}$  sample,  $Y_B$ , can be estimated from the well known  $^{10}\text{B}(n, \alpha)$  cross section, the branching ratio of  $^{10}\text{B}(n; \alpha_1 \gamma)$  to  $^{10}\text{B}(n, \alpha)$  and the calculation of the sample scattering correction. To determine the detection efficiency for 480-keV  $\gamma$ -rays, a comparison between the counting rate of  $\gamma$ -rays from the  $^{10}\text{B}$  sample and that from a standard sample is made at the neutron energy where the standard sample has a black capture resonance. In this experiment the 5.2-eV resonance in  $^{109}\text{Ag}$  was used as the black resonance. To the  $\gamma$ -ray pulse-height spectrum for the resonance neutron absorption in the standard sample, the pulse-height weighting is applied again to reduce the detection efficiency to the neutron binding energy of the compound nucleus,  $^{110}\text{Ag}$ .

Arranging quantities described above, we get a formula for the 24-keV capture probability in a sample,

$$Y = \frac{(CW)}{(CW)_S^r} \cdot \frac{C_B^r}{C_B} \cdot \frac{(BE)_S}{(BE)} \cdot Y_B. \quad (3)$$

where superscript  $r$  means quantities at the black resonance, and subscripts  $S$  and  $B$  mean quantities for the standard sample and for the  $^{10}\text{B}$  sample, respectively. Since the ratios of  $(CW)$  to  $(CW)_S^r$  and  $C_B^r$  to  $C_B$  are included in equation (3), experimental errors and data reduction errors may cancel each other. In addition, it is necessary to take account of the  $\gamma$ -ray self absorption in the samples. The correction of  $\gamma$ -ray self absorption can be also treated as a ratio of a sample to the standard sample.

#### Analysis of Capture Data

The time-dependent background counts under the 24-keV peak are produced by the prompt  $\gamma$ -rays following the capture of neutrons in the collimators and the capture of scattered neutrons in the sample and the surrounding materials. The time-dependent background spectra were measured with a carbon sample and with an open beam. After normalization of the scattering probability, the background was subtracted from the capture spectrum.

The integration of the capture counts was performed over the region, shown in Fig. 1, near the 24-keV peak. This region extends from 19.1 to 27.2 keV and the spectrum-weighted average energy was 23.7 keV. Even if the integral region extends to lower energy, the resultant capture cross sections agree with each other within the statistical uncertainty.

Because all measurements are directly related to capture in  $^{10}\text{B}$ , the  $^{10}\text{B}(n; \alpha_1 \gamma)$  cross section used in the calculation of  $Y_B$  is important. According to the new evaluation of the  $^{10}\text{B}(n, \alpha)$  cross section, it does not vary as  $1/\sqrt{E}$  and falls to a minimum from the  $1/\sqrt{E}$  level in the region of 25 keV. Since we detect the 480-keV  $\gamma$ -ray, the branching ratio of  $^{10}\text{B}(n; \alpha_1 \gamma)$  cross section to the  $^{10}\text{B}(n, \alpha)$  cross section also should be considered. The empirical  $^{10}\text{B}(n, \alpha)$  cross section proposed by Sowerby et al. was used and Hale's calculation and other data were utilized to estimate the  $^{10}\text{B}(n, \alpha)$  cross section.<sup>6,7</sup> As to the  $^{10}\text{B}$  sample scattering correction, an approximate analytical method of calculation similar to Schmitt's analysis was used.<sup>8</sup>

When the 24-keV neutron capture cross section was derived from the capture probability in the samples, the approximate method for the correction of multiple scattering in the sample was used again, since the thickness of samples was sufficiently thin. Even if there is a little error in the scattering correction, the errors may cancel because the same calculation is used twice in the opposite direction.

#### Uncertainty of Data

The statistical error of the capture probability was estimated from the counting statistics of the weighted spectra and the  $^{10}\text{B}$  spectra. These values are shown in Table I.



The systematic errors in the measurement are composed of the following factors:

1. Uncertainty of the weighting function: 2%

To examine the reliability of the weighting function used in this experiment, the hard  $\gamma$ -ray spectrum from the black resonance of 4.9 eV in  $^{197}\text{Au}$  and the soft  $\gamma$ -ray spectra from the black resonances of 5.2 eV in  $^{109}\text{Ag}$  and of 4.3 eV in  $^{181}\text{Ta}$  were measured. The weighting function was applied to all spectra and the average weighting factors thus obtained were divided by each neutron binding energy. As the result of the comparison between them, only a 2% discrepancy remains between the hard spectrum and the soft spectrum.

2. Uncertainty of  $^{10}\text{B}(n; \alpha_1 \gamma)$  cross section: 2%

The uncertainty of the  $^{10}\text{B}(n, \alpha)$  cross section was estimated to be 2% at 10 keV by Sowerby et al. Since the  $^{10}\text{B}(n, \alpha_1 \gamma)$  cross section was about 8% of  $^{10}\text{B}(n; \alpha_1 \gamma)$  cross section, we estimated the error of the  $^{10}\text{B}(n; \alpha_1 \gamma)$  cross section to be 2%.

3. Uncertainty of multiple scattering correction: 2%

Although the approximate analytical method was used to correct the sample scattering effect, the uncertainty of the correction seemed to be small because the thickness of samples was thin and the correction was applied twice in the opposite direction.

4. Uncertainty of  $\gamma$ -ray self-absorption correction in the sample: 2%

The  $\gamma$ -ray self absorption in the sample was calculated by taking the  $\gamma$ -ray attenuation from a place in the sample to the detector into account and averaging it over the region which emitted the prompt  $\gamma$ -rays. Probably the calculation was not accurate, but the ratio of the factors for a sample and for the standard sample was included in the final results. There was about a 2% discrepancy between the correction factors for the  $\gamma$ -ray energy treated as one group and as several groups.

5. Uncertainty of the value of capture probability for the 5.2-eV black Ag resonance: 1%

The value of the saturated capture probability for the 5.2-eV resonance in  $^{109}\text{Ag}$  was calculated by the Monte-Carlo technique. It yielded a value of 0.98 with the relative error of 1%.

Thus the over-all systematic error in this experiment was estimated to be about 4%.

### Results and Discussion

The results of the experiment are presented in Table I. The capture cross sections are the average value over the integrated region; the neutron effective average energy is 23.7 keV. The total errors calculated from the statistical error and the systematic error is 5% except for  $^{238}\text{U}$ . For  $^{238}\text{U}$  the total error is evaluated to be 7%.

The capture cross section of  $^{93}\text{Nb}$ , natural Ag,  $^{127}\text{I}$  and  $^{197}\text{Au}$  obtained in this experiment falls into the 'zone of cross sections' which is formed by many previous measurements. Although two groups of cross sections of  $^{165}\text{Ho}$  are present; our  $^{165}\text{Ho}$  capture cross section agrees with the lower values within the error.

There are three recent high resolution measurements and the other 24-keV measurement of the capture cross section of  $^{238}\text{U}$ .<sup>9,10,11</sup> Table II shows the comparison of the present result to the average values over the energy interval from 20 keV to 30 keV derived from the high resolution measurements and the other 24-keV value. The present cross section lies between them.

### Conclusion

The Fe-filtered beam technique has enabled the 24-keV capture cross sections to be measured with an accuracy of about 5 to 7%. The error can be reduced by accumulating more counts and by improving the pulse-height weighting and the method of corrections. If a high-resolution relative time-of-flight capture measurement is carried out, the 24-keV point cross section can serve as a normalizing value for the continuous energy cross section.

### References

1. K. A. Alfieri, R. C. Block, and P. J. Turinsky, Nucl. Sci. Eng., **51**, 25 (1973).
2. F. Rahn, H. Camarda, G. Hacken, W. W. Havens, Jr., H. Liou, J. Rainwater, M. Slagowitz, and S. Wynchank, Nucl. Sci. Eng., **47**, 372 (1972).
3. R. C. Block, N. N. Kaushal, and R. W. Hockenbury, Nat'l. Topical Meeting on New Devel. in Reactor Phys. and Shielding, CONF-72091, 1107 (1972).
4. R. C. Block, Y. Fujita, K. Kobayashi, and T. Oosaki, Nucl. Sci. Technol., **12**, 1 (1975).
5. R. L. Macklin and J. H. Gibbons, Phys. Rev., **159**, 1007 (1967).
6. M. G. Sowerby, B. H. Patrick, C. A. Uttley, and K. M. Diment, Proc. Symp. Neutron-Standards and Flux Normalization, AEC Symposium Series **23**, 151 (1970).
7. G. M. Hale, P. G. Young, and R. A. Nisley, Trans. American Nucl. Soc. **18**, 327 (1974).
8. H. W. Schmitt "Sample Scattering Corrections in Neutron Beam Experiments", ORNL-2883 (1960).
9. G. de Saussure, E. G. Silver, R. B. Perez, R. Ingle and H. Weaver, Nucl. Sci. Eng., **51**, 385 (1973).
10. M. C. Moxon, "The Neutron Capture Cross Section of  $^{238}\text{U}$  in the Energy Region 0.5 to 100 KeV", AERE-R-6074 U. K. Atomic Energy Authority, Harwell, (1969).
11. S. J. Friesenhahn et al., "Neutron Capture Cross Sections of Molybdenum, Tantalum, and  $^{238}\text{U}$ ", GA-10194, General Atomic (1970).

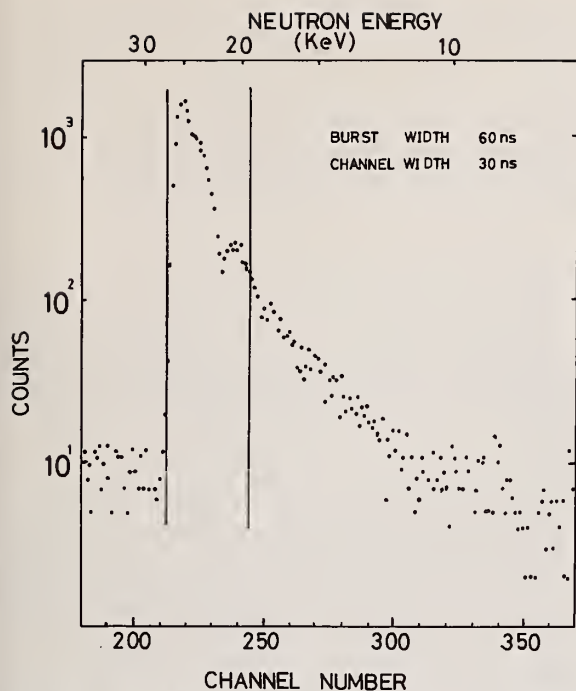


Fig.1 The Fe-filtered beam counting time-of-flight spectrum. Region between two lines represents the interval over which the data are integrated.

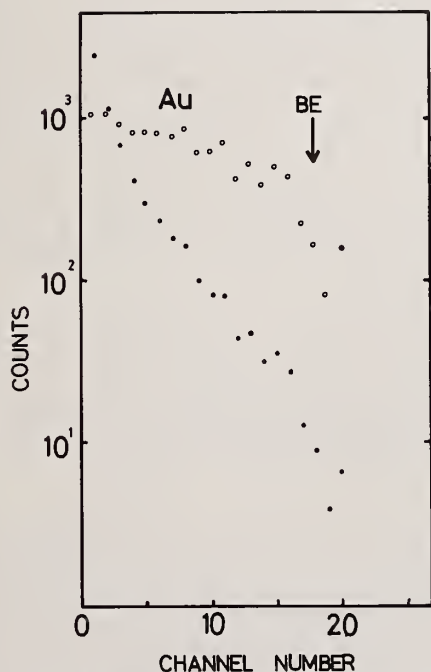


Fig.3 Pulse height spectrum for 24 KeV neutron capture in sample of Au. The dotted points indicate the spectrum counted and the circular points the weighted spectrum.

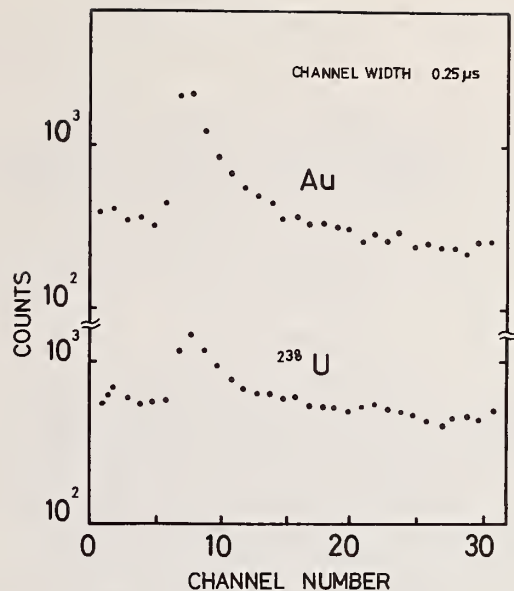


Fig.2 Time-of-flight spectra for 24 KeV neutron capture in samples of Au and  $^{238}\text{U}$ .

Table I  
Sample and 24 KeV Capture Cross Sections

Element	$N$ ( $10^{-3}\text{at/b}$ )	fs* (%)	Statistical Error (%)	$\sigma_{\gamma}$ (b)
$^{93}\text{Nb}$	5.26	7.8	3.0	0.33
Ag	2.98	4.3	2.4	1.10
$^{127}\text{I}^{**}$	4.96	7.1	2.7	0.76
$^{165}\text{Ho}$	6.63	11.6	2.5	1.26
$^{197}\text{Au}$	2.89	6.0	3.3	0.68
$^{238}\text{U}^{***}$	1.30	4.1	6.0	0.50

\* fs means the sample scattering correction.

\*\*  $\text{PbI}_2$  in a Al capsule is used.

\*\*\* Contents of  $^{235}\text{U}$  is <400 ppm.

Table II  
Comparison of  $^{238}\text{U}$  Capture Cross Sections

Energy (KeV)	Capture Cross Section(b)	Authors
20-30	$0.551 \pm 0.03^*$	de Saussure et al. <sup>9</sup>
20-30	$0.462 \pm 0.03^*$	Moxon <sup>10</sup>
20-30	$0.476 \pm 0.03^*$	Friesenhahn et al. <sup>11</sup>
24.3	$0.47 \pm (5\%)^{**}$	Block et al. <sup>3</sup>
23.7	$0.50 \pm (7\%)$	Present

\* The values are quoted from Table VI of de Saussure et al.'s paper.

\*\* The value is normalized to the Au cross section which is assumed to be 0.67b.



# FLUCTUATIONS IN THE NEUTRON STRENGTH FUNCTION

C. M. Newstead

Department of Physics, Nuclear Power Systems Division  
Combustion Engineering, Inc., Windsor, Connecticut, USA 06095

Strength function fluctuations are interpreted in terms of variation of the quasi-particle state density. The anomalous behaviour of the neodymium isotopes is described and an account of the fluctuations of  $S_0$  in the 3S and 4S size resonances is given. Fluctuations of the local strength fluctuations with energy are discussed.

(Neutron strength functions, fluctuations, optical potential, quasi-particles).

## Introduction

In a contribution to the previous conference in the Neutron Cross Sections and Technology series we presented the results of an extensive series of high resolution transmission measurements carried out with the 100, 50 and 25 meter time-of-flight spectrometers of the Saclay Electron Linear Accelerator.<sup>1</sup> In computing the s-wave neutron strength functions  $S_0$  derived from shape analysis of the transmission measurements, we noted striking anomalies in the behaviour with respect to mass number for both the tellurium and neodymium isotopes.

At that time we propose a tentative explanation in terms of a complex Lane potential<sup>2</sup> (complex isospin component of the optical potential). We pointed out however that application of the isospin hypothesis to the neodymium isotopes in particular and the rare earth region in general required rather strong imaginary isospin potential strengths. Our current view is that the striking systematic decrease of the tellurium s-wave neutron strength functions with increasing mass number and hence increasing asymmetry  $e = (N-Z)/A$  is still to be regarded as a manifestation of the complex Lane potential component of the optical potential provided that the Lane potential is accepted to be energy dependent as indeed recent evidence would suggest.<sup>3</sup>

The situation in the rare earth region is of rather a different character. Here the fluctuations in a given isotonic chain are of the oscillatory type rather than of the systematically decreasing variety of the mass 120 region. Indeed recent measurements for the samarium<sup>4,5</sup> and gadolinium isotopes<sup>6</sup> serve to further document the oscillatory nature of the fluctuations in the rare earth region. This suggests that a new mechanism is operative here. In this paper we attempt to demonstrate that the oscillatory fluctuations in the strength function result from variations in the magnitude of the quasi-particle state densities with the several lower order components of the hierarchy of quasi-particle states playing roles of differing importance depending upon the particular mass and excitation energy region. The connection between strength function and quasi-particle density is made via the optical potential by invoking what is variously called the Bloch<sup>7</sup> or Brown-de Dominicis<sup>8</sup> prescription.

The question of strength function fluctuations is closely related to the existence of the deep s- and p-wave strength function minima. At the Budapest conference we presented an analysis of the deep strength function minima in terms of a reduced optical potential strength<sup>9</sup>. In the same paper we pointed out that the optical potential for these low excitation energies can be expected to fluctuate from nuclei to nuclei and gave examples of this behaviour. We suggested that the strength function variations were correlated with changes in the quasi-particle state density. In the present paper we further examine this hypothesis through analysis of the body of highly accurate strength function data which is now available from our own and other work.

## Theory

The strength function analysis to be developed in this paper, rests upon the fundamental concepts regarding simple excitations (doorway and hallway states) proposed in a series of pioneering papers by Feshbach and collaborators<sup>10,11</sup>. The first account of strength function fluctuations was given by Block and Feshbach<sup>10</sup> for the case of even-even spherical nuclei ( $A = 40$  to  $130$ ). They showed how the departure of the measured strength functions from the predictions of the simple optical model could be understood in terms of a modification of the average width in terms of changes in quasi-particle state density.

They assumed that the energy averaged value of the average escape width could be approximated by the product of the optical model strength function  $S_{opt}$  and residual matrix element. Their strength function relation had the form

$$S_0 = (v_0 a^0 + v_1 a^1 + v_2 a^2) S_{opt} \quad (1)$$

where the  $a$ 's are constants to be determined empirically and the  $v$ 's represent the multipole expansion (up to quadrupole) of the doorway state density. Block and Feshbach found that the 3S strength function maxima around  $A = 55$  is associated with the  $L = 0$  monopole, the many large values of  $S_0$  in the region 70 to 80 are connected with the large number of  $L = 1$  and  $L = 2$  transitions possible, while the minima stretching from 90 through 130 is associated with the  $L = 2$  multipole,



indicating that  $a^2$  must be considerably smaller than  $a^1$ . They obtained good qualitative agreement with the strength function fluctuations.

Muller and Rohr<sup>12</sup> extended the Block and Feshbach model to the case of odd nuclei. They proposed the semi-empirical ansatz

$$\bar{a} = (a^*/A^3) \left[ \sum_J (2J+1) \exp(-J(J+1)/2\sigma^2) \right]^{-1} \quad (2)$$

where  $A$  is the target mass number,  $\sigma$  is the spin cut-off parameter,  $J$  is the total angular momentum of the compound system and  $a^*$  is a free parameter used to fit the experimental data. They neglected the multipole expansion and thus wrote the relation for the strength function fluctuations as

$$S_o = v\bar{a} S_{opt} \quad (3)$$

where the density of quasi-particle states  $v$  was determined using BCS theory. An interesting result of their analysis is the observation that the single most dominant factor in the strength function fluctuations is the dependence of the doorway state density on the excitation energy.

Perhaps the simplest demonstration of the fluctuation of doorway state density with excitation energy was given by Le Couteur<sup>13</sup>. He argued that since in a  $2p-1h$  state the excitation energy  $U$  is partitioned between the excitation  $U_1$  of one particle above the Fermi level and the excitation  $U_2$  of another particle above the hole it previously occupied, the number of states within a range  $dU$  of excitation is simply  $(3/4)g^2dU$  where  $g$  is the density of single nucleon states at the Fermi level and the factor  $3/4$  allows for the different identity of neutron and protons. Obtaining an estimate for  $g$  from the well known linear approximation for the Fermi level density parameter  $a$

$$a = (1/8)A \text{ MeV}^{-1} = (\pi/6)^2 g \text{ MeV}^{-1} \quad (4)$$

LeCouteur found that the average spacing of doorway states  $D$  was related to mass number  $A$  and excitation  $U$  by the expression,

$$D = (4/3) (6A/8\pi^2)^{-2} U^{-1} \text{ MeV} = 230 A^{-2} U^{-1} \text{ MeV} \quad (5)$$

Recently Kirouac<sup>14</sup> proposed that the dependence of  $v$  on excitation energy could be simple represented by using the Bethe density distribution. He employed the expression

$$v(E) = (\exp 2(BU)^{1/2})/12\sigma (2)^{1/2} B^{1/4} U^{5/4} \quad (6)$$

and obtained the value of  $B = 7.16 \text{ MeV}^{-1}$  from a fit to  $^{151}\text{Sm}$  and  $^{152}\text{Sm}$  strength functions. Employing this density and the ansatz of Muller and Rohr without multipole expansion for the quasi-particle state density he obtained a good description of the strength function fluctuations in both odd and even nuclei in the 4S region. His treatment neglects shell effects and thus cannot give a description near magic nuclei.

## Analysis of Fluctuations

### 4S Region

As can be seen from figure 1, the behavior of the s-wave strength functions of the neodymium isotopes defy description with the conventional optical model. While it is clear that changes in the optical potential can cause considerable variation of  $S_o$  in this mass region, it is not possible to obtain the peculiar behavior of neodymium strength functions, even with the inclusion of a complex isospin term in the optical potential. Such a term (albeit a strong one) could describe the gross variation in  $S_o$  first noted by Mughabghab and Chrien<sup>15</sup> for the isotopes of Er, Dy, Hf, Yb. However in the case of the neodymium isotopes, the effect of isospin would be to further decrease  $S_o$  for the higher mass isotopes, which is opposite to the effect observed. When this behavior is considered in conjunction with the s-wave strength functions of the isotopes of samarium and gadolinium there emerges a picture of significant fluctuations of the oscillatory type. Application of Kirouac's model to the variations of the neodymium isotopes as well those of samarium and gadolinium gives a good description of the fluctuations as can be seen in figure 2.

### 3S Region

The 3S region affords a good opportunity to study fluctuations because of the large variation in binding energy of neighbouring nuclei. Here we have carried out coupled channel optical model calculations to fit strength functions. The values of the imaginary potential strength  $W$  are given in table 1. We have computed the doorway state density using BCS theory. As can be seen from table 1 there is a remarkable correlation between the magnitude of  $W$  and the doorway state density  $v$ . This is easily understood in terms of the Bloch or Brown-de Dominicis prescription

$$W = \sum_L v_L |(\phi_L^i v_L \phi_L^f)|^2 \quad (7)$$

where  $\phi^i$  and  $\phi^f$  are the wave functions of the initial and final states respectively and  $v$  is the interaction operator.

We are now in the process of carrying out detailed optical model studies of the 4S region. Until this work is complete it is not possible to say if this prescription holds here. Preliminary indications suggest a contradiction between the densities of the Kirouac model and the strength of the imaginary potential. This may be due to neglect of the higher order multipole terms of the density expansion.

### Energy Fluctuation of $S_o$

As can be seen from figures 3 to 5 the local s-wave strength functions of  $^{146}\text{Nd}$ ,  $^{150}\text{Nd}$  and  $^{149}\text{Sm}$  show considerable fluctuation with energy. This may be due to the particular location of the doorway states and the selective excitation of higher components in the hierarchy.

In a study carried out in the 3S region Good et al<sup>16</sup> found a similar energy dependence of the local strength function for the target isotopes <sup>53</sup>Cr, <sup>47</sup>Ti, <sup>57</sup>Fe. They carried out BCS calculations of the density of quasi-particle states as a function of excitation energy. These calculations are illustrated in figure 6 and demonstrate both variation in quasi-particle density from nucleus to nucleus and the manner in which the higher order states exert their influence at

various energies. We believe a similar phenomena takes place in the neodymium and samarium isotopes.

### Conclusion

It has been demonstrated that the anomalous behavior of the s-wave neutron strength functions of the neodymium isotopes can be described in a natural way in terms of a variation of quasi-particle state density. This would appear to be a general phenomena which describes oscillatory fluctuations in both the 3S and 4S regions. Further work concerning the variation of the optical potential strength and its relation to quasi-particle density in both the minima and maxima remains to be done. In this connection it would be most helpful to have accurate measurements of the p-wave neutron strength function for a number of chains of isotopes spanning these regions.

### Acknowledgements

The formative stages of this work were carried out at the Centre d'Etudes Nucleaires de Saclay. It is a pleasure to acknowledge the help and cooperation of the members of the Electron Linear Accelerator Laboratory. The author would particularly like to thank Dr. A.F. Michaudon for helpful discussions and advice. Thanks are also due to Dr. G.J. Kirouac for making available his results prior to publication.

### References

1. C.M. Newstead and H. Tellier, Proc.Third Conf. on Neutron Cross Sections and Technology Knoxville, Vol.2, 680 (1971)
2. A.M. Lane, Phys.Rev.Lett.8,171 (1962); Nucl. Phys. 35, 676 (1962)
3. C.M. Newstead, Proc.Int.Conf. on Nuclear Physics, Munich, Vol.1, 366 (1973) North Holland, Amsterdam 1973

4. G.J. Kirouac and H.M. Eiland, to be published in Phys. Rev.
5. E.N. Karzhavina and A.B. Popov, JINR (Dubna) P3/5655(1971)
6. E.N. Karzhavina and A.B. Popov, and N.N.Fong, JINR (Dubna) P3-3882(1968)
7. C.Bloch, Nucl.Phys. 4 (1957) 503
8. G.E.Brown and C.T. De Dominicis, Proc. Phys. Soc. A72 (1958) 70
9. C.M. Newstead and J.P. Delarochem Proc.Conf. on Nuclear Structure Study with Neutrons, Budapest (1972) paper B7
10. B.Block and H. Feshbach, Ann.Phys.23, 47 (1963)
11. H. Feshbach, A.K. Kerman and R.H. Lemmer, Ann.Phys. 41, 230 (1967)
12. K.N. Muller and G. Rohr, Nucl. Phys. A164, 97 (1971)
13. K.J. Le Couteur, Phys. Lett. 11 (1964) 53
14. G.L. Kirouac, BAPS 19, 1018 (1974) and submitted to Phys. Rev. Lett.
15. S.F. Mughabghab and R.E. Chrien, Phys. Rev C1, 1850 (1970)
16. W.M. Good, D. Paya, R. Wagner and T. Tamura Phys.Rev.151, 912 (1966)

Table 1

Correlation between estimated number of quasi-particle states near neutron separation energy and absorptive potential in 3S region

Target	W MeV	$v$ MeV <sup>-1</sup>
<sup>54</sup> Cr	0.44	3
<sup>52</sup> Cr	0.8	7
<sup>50</sup> Cr	1.12	15
<sup>40</sup> Ca	1.5	(13)
<sup>49</sup> Ti	3.0	55
<sup>45</sup> Sc	6.0	105
<sup>59</sup> Co	13.0	205

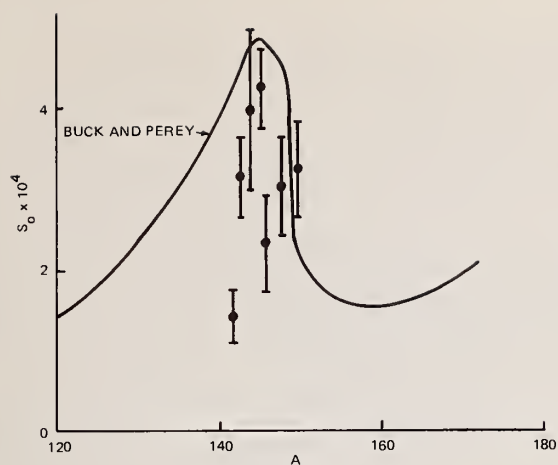


Figure 1

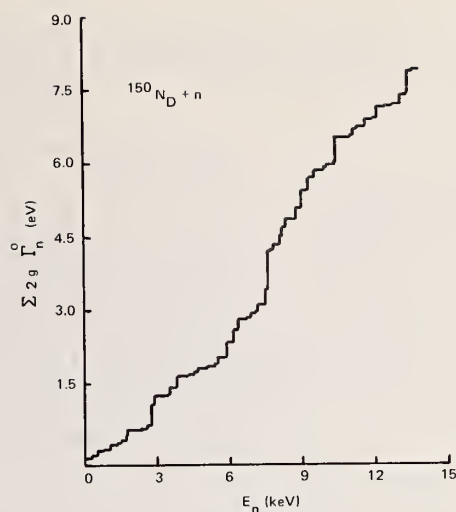


Figure 4

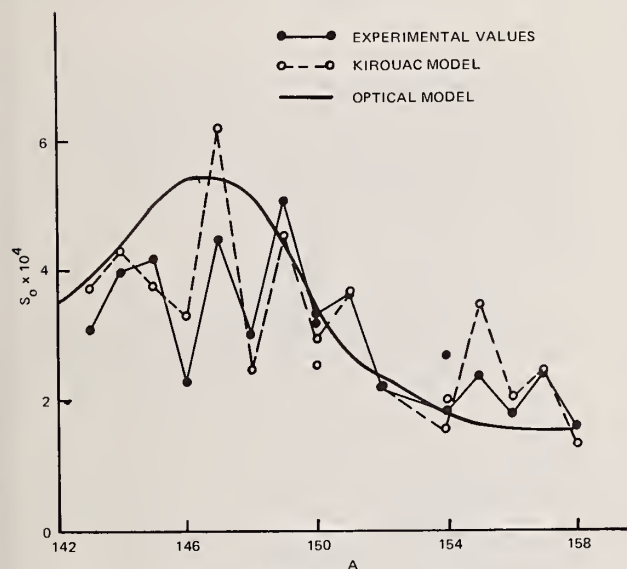


Figure 2

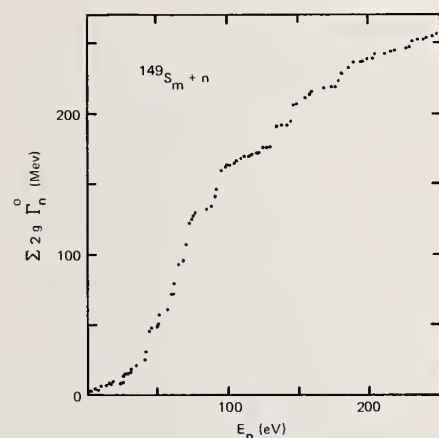


Figure 5

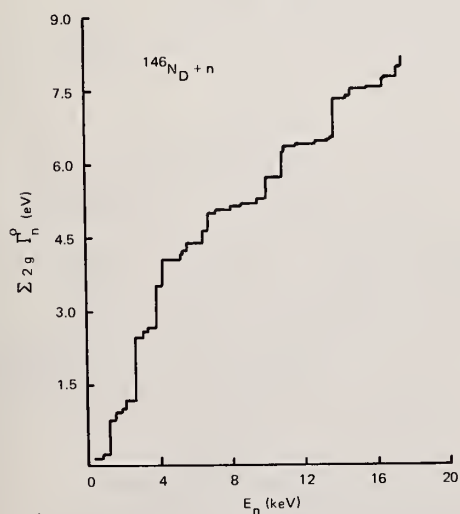


Figure 3

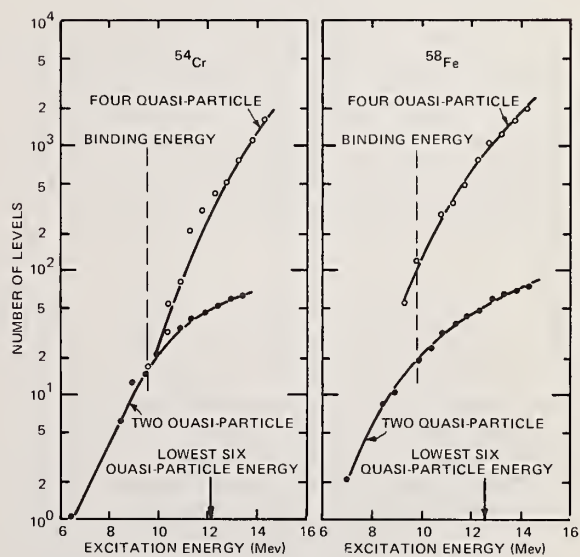


Figure 6



# MEASUREMENTS OF THERMAL NEUTRON CROSS SECTIONS FOR HELIUM PRODUCTION IN $^{59}\text{Ni}$ .

J. McDonald and N. G. Sjöstrand

Department of Reactor Physics, Chalmers University of Technology,  
S-40220 Göteborg, Sweden

The cross section for the reaction  $^{59}\text{Ni} (n, \alpha) ^{56}\text{Fe}$  was measured at three neutron energies from 0.029 to 0.042 eV. The alpha particles were recorded using a Si surface barrier detector. The measurements were made relative to Li-6. Within experimental errors the cross section ratio remained constant for the three energies. Assuming that the  $1/v$  law applies the  $^{59}\text{Ni} (n, \alpha)$  cross section at 0.0253 eV is found to be  $22.2 \pm 1.7$  barn.

( Neutron; cross section; alpha particles; spectrum; nickel; helium )

## Introduction

Helium produced in nuclear transmutations may cause swelling and embrittlement of reactor construction materials<sup>1</sup>. Also in fusion reactors there may arise material problems due to helium production<sup>2</sup>. In stainless steel a two-step transmutation including the  $^{59}\text{Ni} (n, \alpha)$  reaction has been found to contribute substantially to the helium release<sup>3</sup>. It is therefore of interest to accurately determine the large thermal cross section of this reaction. The first direct measurement was reported by Eiland and Kirouac<sup>4</sup>, who observed alpha particle tracks in cellulose-nitrate detectors. The irradiations were performed in a thermal reactor spectrum and the result referred to 2200 m/s neutron speed was  $13.7 \pm 1.2$  barn. Werner and Santry<sup>5</sup> used a monochromatic neutron beam at 0.0551 eV and observed the alpha particles with a silicon surface-barrier detector. Assuming a  $1/v$  dependence of the Ni-59 cross section a value of  $18.0 \pm 1.6$  b was deduced at 2200 m/s.

The measurements to be described here were started before the papers of Eiland and Kirouac<sup>4</sup> and of Werner and Santry<sup>5</sup> were published. In our work a surface barrier detector was used to compare the number of charged particles emitted from a target containing Ni-59 and from reference targets of LiF in identical geometry. The measurements were made with monochromatic neutrons at three different energies.

## Preparation and analyses of targets.

Nickel powder enriched to 99.9 per cent in Ni-58 was irradiated with a thermal neutron fluence of  $2.21 \cdot 10^{21}$  n/cm<sup>2</sup> in the reactor R2. After chemical treatment to remove Co and Fe formed during the irradiation it was found by mass spectrometric analysis that the irradiated material contained  $0.85 \pm 0.01$  atomic per cent Ni-59. A thin circular target ( diameter 14 mm ) of this Ni-58,59 material was prepared by vacuum deposition onto 12  $\mu\text{m}$  thick aluminium. Si-

milar targets were made of Ni-58 and of nickel enriched to 93 per cent in Ni-61. The thicknesses of the Ni deposits were determined by microweighing and X-ray fluorescence. The values deduced were  $1.65 \pm 0.05$   $\mu\text{g}/\text{mm}^2$  for the Ni-58,59,  $1.46 \pm 0.04$  for the Ni-58 and  $0.82 \pm 0.03$   $\mu\text{g}/\text{mm}^2$  for the Ni-61 target.

Three targets of LiF were prepared in a similar way. From microweighing their thicknesses were 1.60, 2.10 and 3.37  $\mu\text{g}/\text{mm}^2$ . The nominal uncertainties in these values were 8 per cent, but in view of the facts that they were prepared at different times and that their specific yield of tritons ( see next section ) under the same experimental conditions were always consistent to within 3 per cent, a value of  $2.10 \pm 0.13$   $\mu\text{g}/\text{mm}^2$  ( i.e. a 6 per cent uncertainty ) has been adopted for the thickness of the target used in the main measurements. Mass spectrometry was used to check that the Li-6 content in the LiF material was the natural one.

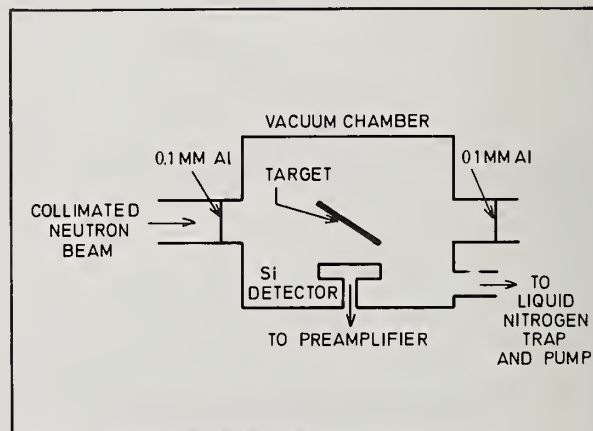


Fig. 1. Schematic view of the experimental arrangement.

## Experimental arrangement

A schematic view of the apparatus is shown in Fig. 1. The neutron beam was obtained from a double crystal monochromator attached to the R2 reactor at Studsvik, and provided thermal neutrons free from gamma radiation and fast neutrons. Energies of 0.0290, 0.0345 and 0.0421 eV were used for the measurements reported here. Each of the targets described in the previous section was mounted on 30  $\mu\text{m}$  thick Al attached to special holders, which could be easily and reproducibly placed in the vacuum chamber in such a way that the target was rigidly held at  $45^\circ$  in the beam. A silicon surface barrier detector (active area 114  $\text{mm}^2$ ) was mounted in the chamber at right angles to the beam and with its centre 10 mm from the target centre. A photographic test showed that the neutron beam covered the complete target area without directly impinging on the holders or the detector itself.

Energy calibration of the detection system was performed using alpha particles from thin sources of Am-241, Pu-239, U-234 and U-235. A resolution (FWHM) of 33 keV was observed for 5.15 MeV alpha particles. The calibration was extended to lower energies using the tritons and alpha particles from the  $^6\text{Li} (n, \alpha) \text{T}$  reaction. A typical spectrum from this reaction is shown in Fig. 2. Such spectra were taken for all three of the LiF targets. Despite the broadening of the alpha peaks due to the target thickness it was possible to observe that the numbers of alpha particles and tritons from a particular target were equal to within the counting statistics.

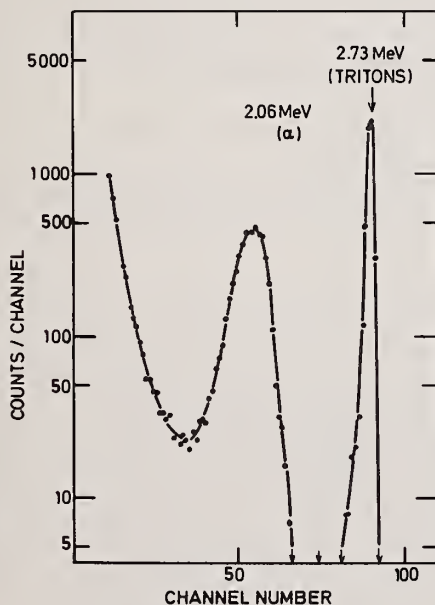


Fig. 2. Spectrum recorded from a 20 min exposure of a 1.6  $\mu\text{g}/\text{mm}^2$  thick LiF target to a beam of 0.0345 eV neutrons. (No background subtraction has been made).

At 50 MW reactor power the beam flux at the target position was of the order of  $10^5$  neutrons per second.

## Measurements

A typical spectrum recorded with the target containing Ni-59 is shown in Fig. 3. The peak at  $4.75 \pm 0.01$  MeV can be assigned to alpha particles from the  $^{59}\text{Ni} (n, \alpha) ^{56}\text{Fe}$  reaction. The energy agrees well with that expected for alpha emission to the ground state of Fe-56. This peak did not appear when targets of pure Al, Ni-58 (cf. the spectrum in Fig. 4), or Ni-61 were used, nor when the enriched target itself was reversed so that the backing material prevented charged particles from reaching the detector.

In order to determine the  $^{59}\text{Ni} (n, \alpha)$  cross section the following procedure was adopted. Firstly, the spectrum from the 2.10  $\mu\text{g}/\text{mm}^2$  LiF target was recorded for 20 min, giving about 7000 counts in the triton peak. The Ni-59 target was then studied for a period of about 25 h. Intermediate runs with the LiF target served to improve the triton counting statistics. They also gave checks on the constancy of the neutron flux and on the reproducibility of the target positioning. The complete procedure was repeated several times for each of the three neutron energies.

Table 1 gives details of the measurements. The ratio of the required cross section to that of Li-6 could be deduced directly from the known target thicknesses and the measured counting rates for the 4.75 MeV alpha particles and the 2.73 MeV tritons. The average ratios obtained together with the experimental errors are quoted in table 1. These errors include the effects of counting statistics, any small reactor power variations during the measurement periods and possible slight al-

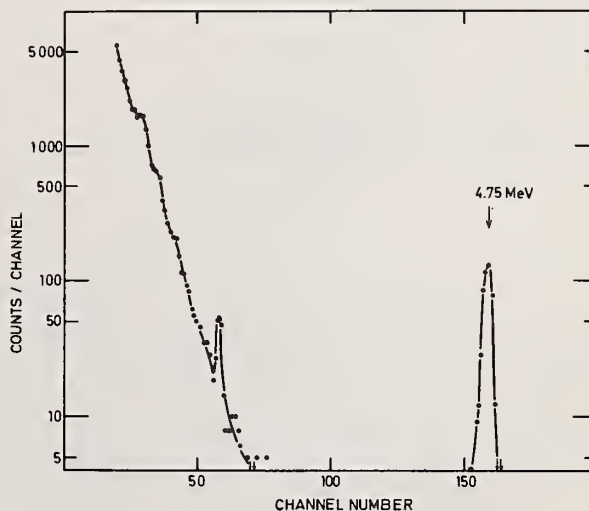


Fig. 3. Spectrum from a 25 hour run with 0.0345 eV neutrons on the target containing 0.85 per cent Ni-59.

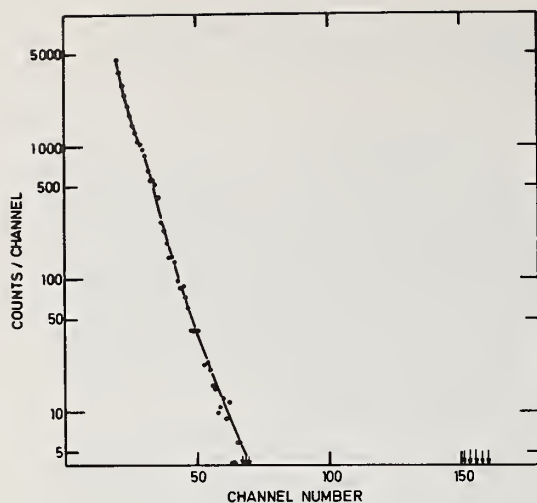


Fig. 4. Spectrum from a 25 hour run with the Ni-58 target.

terations in the target positioning. Furthermore, since different electronics and in some cases a different detector bias were used for several of the runs, any systematic effects due to these changes are also included. However, the spread of individual ratios from the mean values indicated that the largest contribution to the uncertainty arises from the statistics in counting alpha particles.

The mean ratios for each neutron energy were equal to within the errors, suggesting that the  $^{59}\text{Ni}(n,\alpha)$  cross section follows the  $1/v$  law in this region. If this is the case, then the value deduced for the 2200 m/s (0.0253 eV) cross section for this reaction is  $22.2 \pm 1.7$  b relative to 940 b for Li-6. The overall error has been estimated from the following contributions:

- 2 per cent from the cross section ratio measurements;
- 6 and 3 per cent from the uncertainties in the thicknesses of the LiF and Ni targets, respectively;

2 per cent from the uncertainty in the atomic percentage of Ni-59.

Since the Q-value for the  $(n,p)$  reaction in Ni-59 is also positive, the data were examined for evidence of proton emission. In fact, in all of the spectra taken with the Ni-59 target two extra peaks of  $1.82 \pm 0.07$  MeV and  $0.9 \pm 0.2$  MeV were observed (see Fig. 3). These peaks were too narrow to be due to alpha particles. The energy of 1.82 MeV is in agreement with that expected for proton emission from the Ni-60 compound nucleus to the ground state of Co-59. Assuming that this assignment is correct a cross section of  $5 \pm 2$  barn at 2200 m/s can be deduced for this reaction. The origin of the lower energy (and more intense) peak is at present obscure and requires further investigation.

In a subsidiary study the spectrum from Ni-61 was collected for 48 h. No evidence of charged particle emission was found. From the absence of significant counts in the region of 3.34 MeV it was deduced that the  $^{61}\text{Ni}(n,\alpha)$  cross section is less than 2 mb. This result disagrees with the value  $45 \pm 20$  mb suggested from earlier work<sup>6</sup> using alpha track detection.

#### References

1. F. W. Wiffen and E. E. Bloom, Nucl. Techn. **25**, 113 (1975)
2. W. F. Vogelsang, G. L. Kulcinski, R. G. Lott and T. Y. Sung, Nucl. Techn. **22**, 379 (1974)
3. J. Weitman, N. Däverhög and S. Farvolden, Trans. Am. Nucl. Soc. **13**, 557 (1970)
4. H. M. Eiland and G. J. Kirouac, Nucl. Sci. Eng. **53**, 1 (1974)
5. R. D. Werner and D. C. Santry, Nucl. Sci. Eng. **56**, 98 (1975)
6. F. Münnich, Zeitschr. Phys. **153**, 106 (1958)

Table 1. Experimental results.

Neutron energy (eV)	Number of individual measurements with target containing Ni-59	Total measuring time with Ni target (h)	Total number of 4.75 MeV alpha particles registered	Deduced average value for the ratio of the $^{59}\text{Ni}(n,\alpha)$ cross section to that of Li-6
0.0290	5	130	1870	$(2.37 \pm 0.07) \cdot 10^{-2}$
0.0345	7	162	3340	$(2.36 \pm 0.04) \cdot 10^{-2}$
0.0421	3	69	1072	$(2.37 \pm 0.08) \cdot 10^{-2}$

Note. The average value is the mean of the ratios obtained from the individual runs at the given energy. The uncertainties quoted are those arising from random errors only.



Darrell M. Drake and Lynn R. Veaser  
Los Alamos Scientific Laboratory  
Los Alamos, New Mexico 87544

Manfred Drosch  
University of Vienna, Austria

Gary Jensen  
Brigham Young University  
Provo, Utah 84601

Neutron-induced differential gamma-ray production cross sections for the 0.847-MeV gamma ray from iron have been measured using a pulsed  ${}^3\text{H}(p,n){}^3\text{He}$  neutron source and a NaI spectrometer. Background caused by break-up neutrons and Compton-scattered gamma rays was suppressed by placing the sample about one meter from the neutron source and using time-of-flight to select only pulses caused by the monoenergetic  ${}^3\text{H}(p,n){}^3\text{He}$  neutrons.

(Nuclear reactions;  $\text{Fe}(n,\gamma)$ ; measured  $\sigma(\theta)$  for  $E_\gamma = 0.847$  MeV;  
 $E_n = 8.5, 10.0, 12.2, 14.2$  MeV;  $\theta = 90^\circ, 75^\circ, 55^\circ, 35^\circ$ )

### Introduction

The neutron-induced gamma-ray production cross section for iron has been measured using the reaction

${}^3\text{H}(p,n){}^3\text{He}$  as a source of pulsed, monoenergetic neutrons. We report here the differential cross section for producing the 0.847-MeV gamma transition arising from inelastic scattering of neutrons from natural iron. The experimental arrangement, which has been used extensively for other gamma-ray production experiments with neutrons of 8 MeV and below, is shown in Fig. 1. The sample is located about 0.1 m from the neutron source, with the gamma-ray detector a meter or more away from the sample so that time-of-flight techniques can be used to help eliminate background.

For neutrons with energies above 8 MeV two sources of background arise which make it necessary to change the experimental arrangement. These background sources are 1) gamma rays that are produced in the target beam stop and are then Compton-scattered by the sample into the detector, and 2) gamma rays that are produced in

the sample by neutrons from the  ${}^3\text{H}(p,n){}^2\text{H}$  reaction.

Because the flight times both of the gamma rays and of the break-up neutrons from target to the sample are small, these background pulses tend to be in the same time bin as the gamma rays one wishes to measure,

i.e. those produced by the monoenergetic,  ${}^3\text{H}(p,n){}^3\text{He}$  source neutrons. Neither of these backgrounds is easy to subtract in a straightforward way. Figure 2 shows two pulse-height spectra (normalized to the same number of incident neutrons) for gamma rays counted as being in the prompt gamma-ray peak of the time-of-flight spectrum. The incident proton energy for these spectra was 10 MeV. The gas cell had a  ${}^{58}\text{Ni}$  beam stop to reduce the neutrons from the  $(p,n)$  reactions. Compton-scattered gamma rays appear in the  $90^\circ$  spectrum as a sudden increase of pulses below 0.5 MeV. At  $35^\circ$  the Compton-scattered gamma rays extend to much higher energies in the spectrum. For incident protons of 15 MeV, these Compton-scattered gamma rays dominate the spectra.

In order to separate these sources of background from the gamma rays produced by the monoenergetic

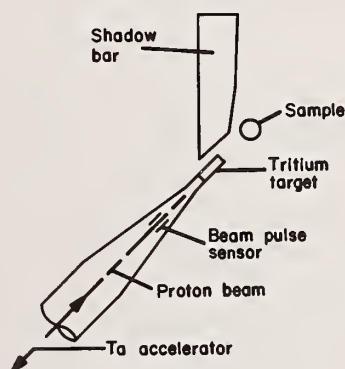
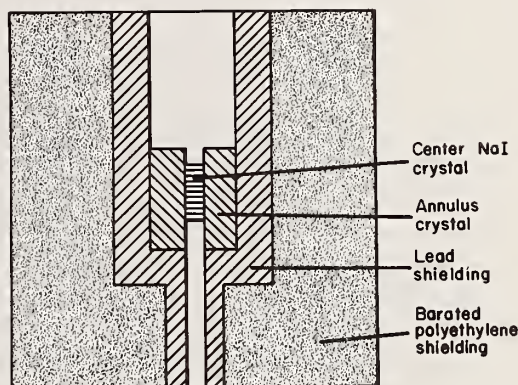


Fig. 1 - Experimental arrangement for measuring neutron-induced gamma-ray production cross sections using the  ${}^3\text{H}(p,n){}^3\text{He}$  reaction with neutrons below 8 MeV. The sample-to-detector distance in this arrangement was about 0.1 meters. For neutrons above 8 MeV, as in the present experiment, the sample-to-source distance was increased to almost one meter, with appropriate adjustments in shadow bar and detector positions.

\*Work done under the auspices of the U.S. Energy Research and Development Administration.

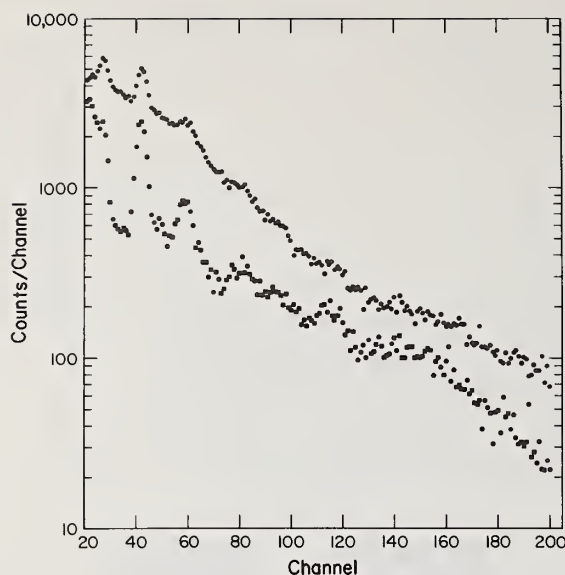


Fig. 2 - Pulse height spectra at 35° and 90° for prompt rays from the interaction of 9 MeV neutrons with iron. These spectra also include gamma rays produced in the beam stop that are Compton-scattered into the detector by the iron sample, as well as gamma rays produced in the sample by secondary neutron sources such as

${}^3\text{H}(\text{p},\text{np}){}^2\text{H}$  and neutrons from the beam stop and entrance foil of the gas target. The incident proton energy for this figure was 10 MeV, the sample was 0.1 m from the

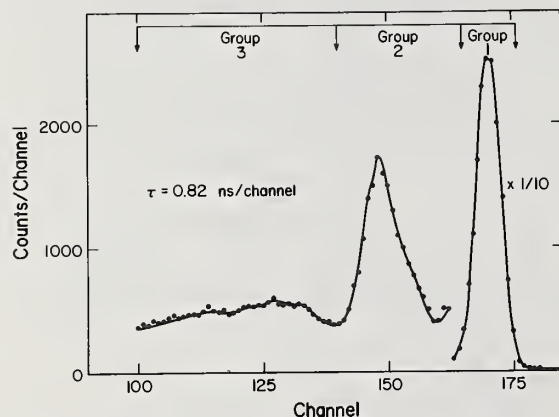


Fig. 3 - The time spectrum of pulses from the gamma-ray detector for sample-to-source distance of 0.94 m. This spectrum is for 11-MeV incident protons, with the gamma-ray detector at 55°. Group 1 is primarily composed of gamma rays produced in the beam stop that are Compton-scattered in the iron sample. Group 2 is primarily composed of gamma rays produced in the sample by the monoenergetic neutrons from the  ${}^3\text{H}(\text{p},\text{n}){}^3\text{He}$  reaction. Group 3 contains gamma rays produced in the gamma-ray detector by scattered neutrons, as well as gamma rays produced in the sample by slower neutrons from secondary sources.

neutrons, we increased the source-to-sample distance to almost one meter. With this longer distance from target to sample, the "prompt" gamma-ray peak can be separated into three distinct peaks in the gamma-ray detector time spectrum as seen in Fig. 3. The earliest peak (Group 1) is due to the Compton-scattered gamma rays; the next, Group 2, is due to gamma rays produced in the sample by the monoenergetic group of source neutrons; and the third peak is a mixture of gamma rays produced in the NaI crystal by scattered neutrons and gamma rays produced in the sample by the slower break-up neutrons. By choosing the appropriate time bins, one can collect spectra of gamma rays induced only by the monoenergetic source neutrons.

The gamma-ray spectrometer was a 60 x 150-mm NaI crystal centered in a NaI annulus inside a large shield-collimator. The efficiency of the detector system was measured with calibrated radioactive gamma-ray sources.

Data were obtained for neutrons from the  ${}^3\text{H}(\text{p},\text{n}){}^3\text{He}$  reaction at energies of 8.5, 10.0, 12.2, and 14.2 MeV. The neutron flux was measured with a proton recoil telescope. The sample was a 32 by 32-mm cylinder of natural iron.

Figure 4 shows the prompt pulse height spectrum from iron at 55° for incident neutrons of 10 MeV. Table 1 gives the cross sections measured in this experiment for the 0.847-MeV gamma ray. Corrections have been made for dead time (< 2%), beam heating in the gas target (< 5%), and gamma-ray attenuation (< 40%), but not for neutron attenuation and multiple scattering. Literature values for the 0.847-MeV gamma ray for 14.2-MeV neutrons are plentiful and cover a wide range (from about 30 to 80 mb/sr). However, the values quoted in Table 1 agree fairly well with those of Refs. 1 and 2.

For the 0.847-MeV gamma ray produced by 8.5-, 10.0-, and 12.2-MeV neutrons, the 55° value of Table 1 agrees with white neutron source measurements of Refs. 3 and 4.

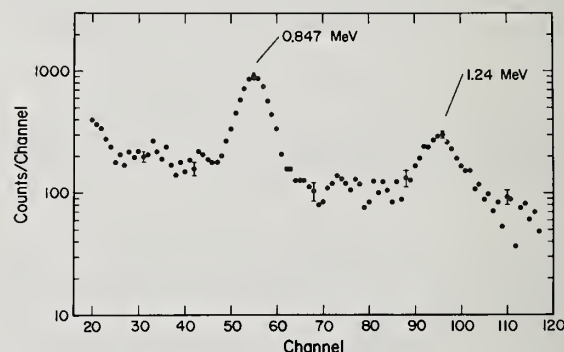


Fig. 4 - Pulse height spectrum at 55° for 10-MeV neutrons incident on iron. About one hour of beam time was required to collect this spectrum and there are approximately 4000 counts in the 0.847-MeV peak. The usual time-independent background has been subtracted.

Table 1 Neutron induced cross sections for the production of the 0.847 MeV gamma ray from iron

Detector angle	90°	75°	55°	35°
Incident neutron energy (MeV)	Cross Section (mb/sr)			
8.5	77.5 ± 9.3	79.7 ± 9.6	85.8 ± 10.3	91.6 ± 11.0
10.0	68.4 ± 8.2	74.6 ± 8.9	83.0 ± 10.0	84.5 ± 10.2
12.2	62.4 ± 7.5	64.7 ± 7.8	66.1 ± 7.9	
14.2	49.2 ± 5.9	52.6 ± 6.3	54.9 ± 6.6	

Elemental differential cross sections for production of the 0.847 MeV gamma ray by neutrons incident in an iron sample with energies of 8.5, 10.0, 12.2 and 14.2 MeV.

#### References

1. Abbondanno, Giacomich, Lagonegro, and Pauli, "Gamma Rays Resulting from Nonelastic Processes of 14.2-MeV Neutrons with Sodium, Magnesium, Silicon, Sulphur, Titanium, Chromium and Iron", J. Nucl. Energy 27, 227-239 (1973).
2. Grenier, Centre d'Etudes de Bruyeres-le-Chatel, "Sections Efficaces de Production de Rayonnement Gamma Pour le Magnesium, le Silicium, le Calcium, le Scandium, le Chrome, le Nickel, et le fer Naturel Avec des Neutrons de 14.1 MeV", presented at the National Soviet Conf. on Neutron Physics, Kiev, May 28-June 1, 1973.
3. Dickens, Morgan, Perey, "Neutron-Induced Gamma-Ray Production in Iron for the Energy Range  $0.8 < E_n < 20$  MeV", Nucl. Sci. Eng. 50, 311-336 (1973)
4. Orphan and Hoot, "Gamma-Ray Production Cross Sections for Iron and Aluminum", Gulf Radiation Technology report Gulf-RT-A10743 (1971).



# HIGH ENERGY $\gamma$ -RAY TRANSITIONS OF $^{56}\text{Fe}$ RESONANCES IN THE ENERGY RANGE 7-70 keV

H. Beer, R.R. Spencer and F. Käppeler  
 Institut für Angewandte Kernphysik  
 Kernforschungszentrum Karlsruhe

High energy  $\gamma$ -ray transitions to low lying states in  $^{57}\text{Fe}$  following neutron capture in  $^{56}\text{Fe}$  were investigated for individual resonances in the energy region 7-70 keV at the Karlsruhe 3 MV pulsed Van-de-Graaff-accelerator by means of a 50 cc Ge(Li)-detector. As a result relative partial radiation widths for 5 transitions of 4 resonances were determined.

(nuclear reaction  $^{56}\text{Fe}(n,\gamma)$ ;  $E_n = 7-70$  keV;  $\gamma$ -transitions in  $^{57}\text{Fe}$  of  $^{56}\text{Fe}$  resonances; relative partial radiation widths; natural iron target)

## Introduction

Thermal capture  $\gamma$ -ray spectra of isotopes in the mass range  $A = 40-70$  are frequently characterized by strong high energy E1 transitions to low lying states in contrast to the expectations of the statistical model of compound nucleus formation. In addition, for a large number of nuclei in this mass region correlations between  $(n,\gamma)$  and  $(d,p)$  strengths have been found exhibiting the existence of a single particle capture mechanism. As thermal capture is often caused by the tails of nearby resonances it is not surprising that keV neutron capture shows similar effects<sup>1</sup> which can be investigated much better due to the well-defined initial resonance states. The occurrence of strong high energy transitions in the keV capture  $\gamma$ -ray spectra of individual  $^{58}\text{Ni}$  and  $^{60}\text{Ni}$  resonances has been demonstrated recently<sup>2</sup>.

As elements in the mass range  $A = 40-70$ , especially Cr, Fe and Ni, are contained in the structural materials of fast breeder reactors, high energy  $\gamma$ -rays from keV neutron capture are of particular interest for reactor shielding calculations.

In the present investigation high energy  $\gamma$ -ray transitions in  $^{57}\text{Fe}$  following neutron capture from  $^{56}\text{Fe}$  resonances were measured in the energy range 7-70 keV. So far, in this energy region no neutron capture  $\gamma$ -ray lines for single  $^{56}\text{Fe}$  resonances have been observed. At lower energies the p-wave resonance at 1.17 keV has been investigated<sup>3</sup>. Strong transitions to the ground state and first excited state have been obtained which were identified as M1 transitions. From the similarity of the p-wave resonance and the thermal  $\gamma$ -ray spectrum it was concluded that M1 and E1 radiation is of comparable strength.

## Experimental Technique

The present measurement was carried out at the Karlsruhe 3 MV pulsed Van-de-Graaff-accelerator using the time-of-flight technique. Neutrons from 7 to 70 keV were produced via the  $^7\text{Li}(p,n)^7\text{Be}$  reaction just above the reaction threshold. The reaction kinematics and a paraffin collimator guaranteed a clean collimation so that the neutron beam was restricted to fall within the sample area. The sample was a disk of 6 cm dia. x 0.25 cm thickness of 56.5 g natural iron. The 50 cc Ge(Li)-detector (2.1 keV FWHM for  $^{60}\text{Co}$ ) was located 9 cm from the center of the sample. It was shielded against the  $\gamma$ -flash from the accelerator target and from room background by 10 cm lead and against neutrons scattered in the sample by  $^6\text{Li}$ -loaded paraffin of 4 cm thickness. The accelerator provided proton bursts of 1 ns width and a repetition rate of 2.5 MHz. A time resolution of 10 ns/m has been obtained using a flight path of 0.44 m. As a neutron flux mea-

suring device a  $^{235}\text{U}$  gas scintillation chamber was used as described in Ref.<sup>4</sup>. The chamber was arranged between collimator and iron sample. The  $^{235}\text{U}$  foil at a flight path of 24 cm was a  $121 \mu\text{g}/\text{cm}^2$  layer of uranium acetate sprayed onto a thin plastic film<sup>5</sup>. The detected high energy  $\gamma$ -rays between 4 and 8 MeV from capture events in iron were recorded in a two-dimensional array of 32 time versus 1024 pulse height channels. In an additional 1024 channel time-of-flight spectrum the  $^{235}\text{U}$  fission events were accumulated.

## Results and Discussion

For the determination of the  $\gamma$ -ray line intensities of individual resonances the appropriate time-of-flight channels were added together. The time-independent background due to thermal capture events and room background was subtracted. The resulting  $\gamma$ -spectra of the investigated resonances are shown in Fig. 1. From the observed  $\gamma$ -ray transitions the peak areas  $A$  were determined. These are related to the partial radiation widths  $\Gamma_{\gamma p}$  by the equation:

$$2\pi^2 \lambda^2 g \frac{\Gamma_{\gamma p} \Gamma_n}{\Gamma} = \frac{A}{\phi N \epsilon} \cdot \frac{1}{1-MS} \cdot \frac{1}{1-f} K \quad (1)$$

where  $\Gamma_n$  and  $\Gamma$  are the neutron and total widths,  $\lambda$  is the neutron wave length,  $g = 2J+1/2(2I+1)$  the statistical spin factor with  $J$  the compound state spin and  $I$  the target spin,  $N$  the number of atoms,  $\phi$  the neutron flux,  $\epsilon$  the Ge(Li)-detector efficiency,  $MS$  the correction for multiple scattering and self absorption,  $f$  the fraction of absorbed  $\gamma$ -rays in the sample and  $K$  the ratio of the total and differential cross section at  $90^\circ$ .

The corrections  $MS$  were computed by the Fortran IV code TACASI<sup>6</sup>. In case of the broad s-wave resonance at 27.48 keV this correction starts to become extremely large for samples which are considerably larger than the one used in this work. As the efficiency  $\epsilon$  for the Ge(Li)-detector was not yet determined relative partial radiation widths have been calculated. In Table 1 the results for the observed five transitions of four resonances are summarized. An estimated uncertainty of 25 % for the multiple scattering correction and a statistical uncertainty between 4 and 6 % resulted in a total uncertainty of the relative partial radiation widths  $\Gamma_{\gamma p}$  between 5 and 18 %. For comparison the total radiation widths of Fröhner and Ernst<sup>7</sup> are included in Table 1. For the s-wave resonance at 27.48 keV the ground state transition was found to be considerably stronger than the transition to the first excited state. This ratio is significantly different from that observed in thermal neutron capture<sup>8</sup>. The resonances at 34.18 keV and 59.09 keV show strong ground state transitions. This excludes higher partial waves than  $l = 1$  because of the spin determination of these resonances by Jackson and

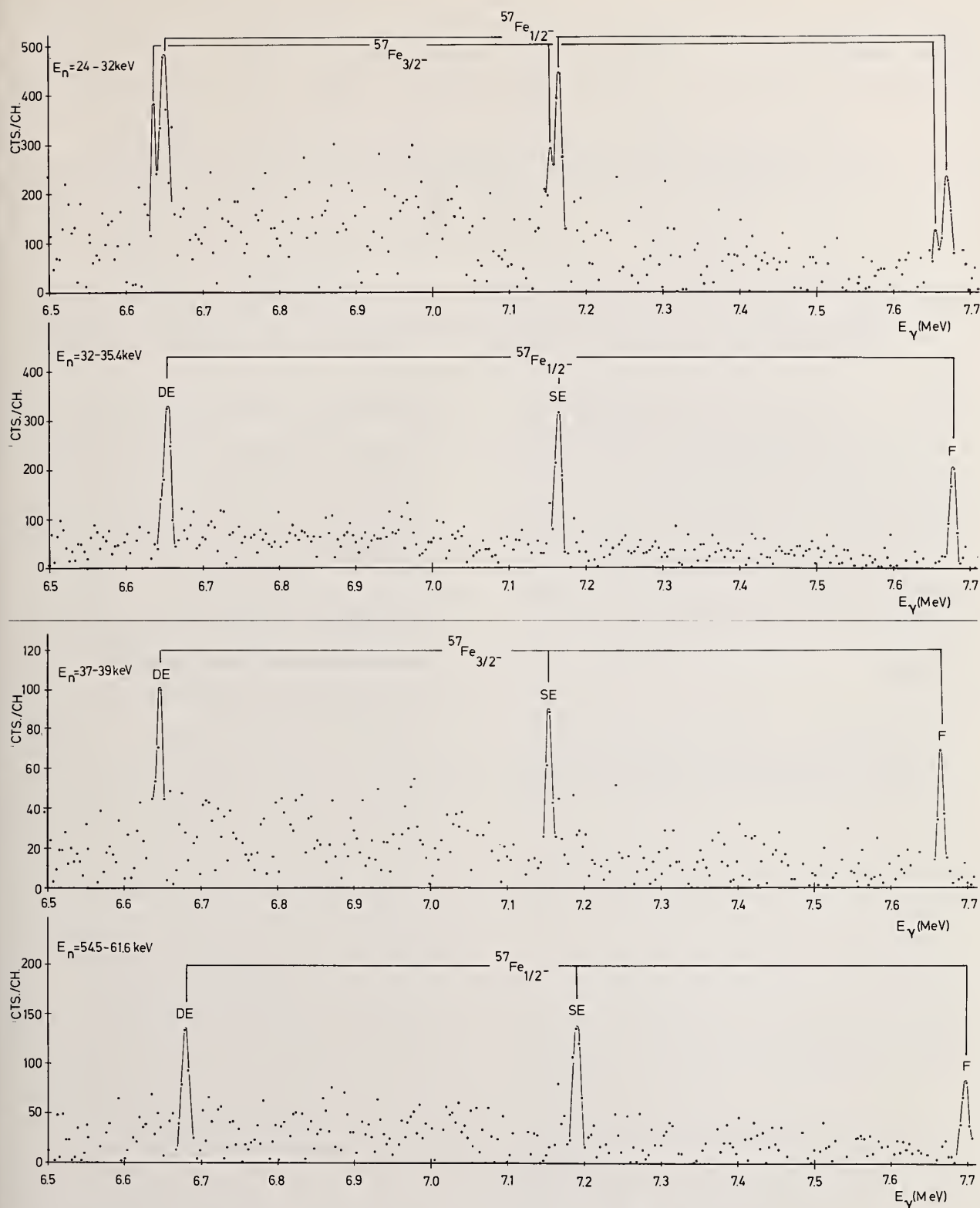


Fig. 1 Measured  $\gamma$ -ray spectra from various neutron capture resonances in  $^{56}\text{Fe}$ . From above:  
a) s-wave resonances at 27.48 keV neutron energy; b) p-wave resonance at 34.18 keV neutron energy;  
c) p-wave resonance at 38.33 keV neutron energy; d) p-wave resonance at 59.09 keV neutron energy.  
The full energy peak and the single and double escape peaks are observed for each transition and the respective final states in  $^{57}\text{Fe}$  are indicated.

Target Nucleus	Resonances Energy (keV)	$J_i$	$\Gamma_\gamma$ (eV)	$g\Gamma_\gamma\Gamma_n/\Gamma$ (eV)	$E_f$ (MeV)	$J_f$	$g\Gamma_\gamma\Gamma_p\Gamma_n/\Gamma$ (eV)	MS %
$^{56}\text{Fe}$	27.48	$\frac{1}{2}^+$	1.21		0 0.014	$\frac{1}{2}^-$ $\frac{3}{2}^-$	0.39 0.08	68
	34.18	$\frac{1}{2}^-$		0.54	0	$\frac{1}{2}^-$	1*	14
	38.33	$\frac{1}{2}^-$ or $\frac{3}{2}^-$		0.31	0.014	$\frac{3}{2}^-$	0.48	11
	59.09	$\frac{1}{2}^-$		0.60	0	$\frac{1}{2}^-$	0.40	11

Table 1. Numerical results for the observed high energy  $\gamma$ -transitions; relative partial radiation widths (\*) normalized to 1 eV.

Strait<sup>9</sup> ( $J_i$  in Table 1). For the resonance at 38.33 keV no ground state transition but a strong transition to the first excited state has been observed. According to the total capture cross section<sup>7</sup> 10 resonances with  $\ell > 0$  are located in the investigated neutron energy range. As Zuhr and Min<sup>10</sup> reported that there is essentially no d-wave contribution in  $^{56}\text{Fe}$  below 400 keV all 10 resonances with  $\ell > 0$  can be interpreted as p-wave resonances. Although their total radiation widths are very similar only in three cases strong transitions to the ground state or the first excited state were found. The strength of these M1 transitions may be explained by a Porter-Thomas-fluctuation or by a single particle effect due to configurations near the closed shell at 28.

#### References

- (1) H. BEER and R.R. SPENCER, Nucl. Phys. A 240 (1975) (to be published).
- (2) H. BEER, R.R. SPENCER and F. KÄPPELER, 2<sup>nd</sup> Int. Symp. on Neutr. Capture  $\gamma$ -ray Spectroscopy, Petten 1974, (to be published).
- (3) R.E. CHRIEN, M.R. BHAT, O.A. WASSON, Phys. Rev. C1 (1970) 973.
- (4) F. KÄPPELER, Neutron Standards Reference Data, IAEA, Vienna (1974) 213.
- (5) V. VERDINGH and K.F. LAUER, Nucl. Instr. Meth. 21 (1963) 161.
- (6) F.H. FRÖHNER, General Atomic Report GA-6906 (1966).
- (7) F.H. FRÖHNER and A. ERNST (to be published).
- (8) L.V. GROSHEV, A.M. DEMIDOV, G.A. KOTELNIKOV and V.N. LUTSENKO, Nucl. Phys. 58 (1964) 465.
- (9) H.E. JACKSON and E.N. STRAIT, Phys. Rev. C4 (1971) 1314.
- (10) R.A. ZUHR and K. MIN, Nucl. Phys. A 237 (1975) 29.



A. Ackermann, B. Anders, M. Bormann and W. Scobel

University of Hamburg, Hamburg, Germany

The excitation functions of the reaction  $^{12}\text{C}(n,2n)^{11}\text{C}$  for incident neutron energies from 23 to 34 MeV and of  $^{238}\text{U}(n,2n)^{237}\text{U}$  from 13 to 18 MeV have been measured with activation techniques. The results are compared with existing data and interpreted with the statistical model approach. The calculations performed for  $^{238}\text{U}$  include fission competition and preequilibrium contributions to account for an enhanced (n,2n) yield at projectile energies above 15 MeV.

(Nuclear reactions  $^{12}\text{C}(n,2n)$ ,  $E = 23\text{--}34$  MeV;  $^{238}\text{U}(n,2n)$ ,  $E = 13\text{--}18$  MeV; measured  $\sigma(E)$ ; statistical model calculations)

### Introduction

For most target nuclei in the mass region from  $A=20$  up to  $A=210$  the (n,2n) reaction for projectile energies of 10–25 MeV has been shown to proceed via compound

nucleus formation<sup>1</sup> and the excitation functions often can be described satisfactorily within the framework of the statistical theory of nuclear reactions. Recent compilations of cross section data for neutron induced reactions<sup>2,3</sup> have taken advantage of this behaviour and used statistical model calculations as a guide for interpolation and extrapolation of (n,2n) data.

It is the purpose of this paper to check to what extent the assumption of a dominating evaporation mechanism for (n,2n) reactions can be maintained for very light and very heavy target nuclei.

For light target nuclei it is questionable that all requirements for a successful application of the statistical theory can be fulfilled. In order to compensate for the main deficiencies due to insufficient

level overlap in the compound system we have chosen the reaction  $^{12}\text{C}(n,2n)^{11}\text{C}$  which is strongly endothermic. So far, only the excitation function of Brill et al.<sup>4</sup> with an accuracy of  $\pm 30\%$  has been published.

Heavy compound systems excited to moderate excitation energies decay predominantly by either fission or by neutron evaporation; accordingly the competition between these two models has to be incorporated into the statistical model formalism. This requires knowledge on the ratio of the fission width  $\Gamma_f$  to the neutron decay width  $\Gamma_n$ . Using the formula of Bohr and Wheeler<sup>5</sup>,  $\Gamma_f$  may be calculated from the level density of the compound system stretched to the saddle point deformation. The result depends strongly on the excess of the level density parameter  $a_f$  over the value of  $a$  for the nondeformed nucleus, which is not precisely known<sup>6</sup>. Instead, the calculations can be performed with fission width  $\Gamma_f$  determined experimentally. We have used this method to analyze the excitation function of the reaction  $^{238}\text{U}(n,2n)^{237}\text{U}$  from 6 to 19 MeV, composed of the data of Knight et al.<sup>7</sup> and our data.

### Experimental Procedure

Both excitation functions have been determined by activation techniques.

$^{238}\text{U}(n,2n)^{237}\text{U}$  ( $Q = -6.14$  MeV)

The  $\text{UO}_2$  samples were irradiated for 72 hours with neutrons between 13 and 18 MeV, which were produced in the reaction  $^3\text{H}(d,n)^4\text{He}$  with the deuteron beam of our 2 MV Van de Graaff and a Tritium Titanium target. The

neutron flux was measured and monitored with two proton recoil detectors, each consisting of a  $1.5'' \times 1''$  stilbene crystal. The n- $\gamma$  discrimination technique applied and the method of flux evaluation from the proton recoil spectra are described elsewhere<sup>8,9</sup>. The variations of the neutron flux as a function of time were accounted for.

The residual nucleus  $^{237}\text{U}$  decays with a half life of 6.75 days by  $\beta$  emission and subsequent  $\gamma$  decay. The experimental problem is to identify this activity in presence of an intensive  $\gamma$  background resulting from the decay chain starting from  $^{235}, ^{238}\text{U}$  and the fission fragments. The identification of the isotope  $^{237}\text{U}$  could best be performed with the 208 keV  $\gamma$ -line that appears in the decay scheme with a 23% probability. The  $\gamma$ -detection was achieved with a Ge(Li) detector. Its efficiency was determined experimentally by comparison with a  $^{22}\text{Na}$  calibration source and a  $^{90m}\text{Y}$  source, produced in the reaction  $^{89}\text{Y}(d,p)^{90m}\text{Y}$ , that emits  $\gamma$ -lines at 203 and 480 keV with a precisely known branching ratio<sup>10</sup>.

$^{12}\text{C}(n,2n)^{11}\text{C}$  ( $Q = -18.72$  MeV)

A self supporting Titanium foil of  $4 \text{ mg/cm}^2$  thickness, which contained adsorbed Tritium, was bombarded with 6–16 MeV deuterons from the Hamburg Isochronous Cyclotron to produce monoenergetic neutrons with energies from 23 to 35 MeV from the  $^3\text{H}(d,n)^4\text{He}$  reaction. The continuous background of neutrons from breakup processes and (d,n) reactions with the Titanium isotopes does not reach the  $^{12}\text{C}(n,2n)^{11}\text{C}$  threshold. The neutron flux was measured as described above with the modifications due to the higher neutron energy<sup>11</sup>.

A circular sample of natural Carbon was irradiated with neutrons under  $0^\circ$  with respect to the deuteron beam axis for about 1 hour. The reaction leads to the  $\beta^+$  emitting nucleus  $^{11}\text{C}$  with a half life of 20.3 min. The sample was covered with 1 mm lead after irradiation and the annihilation radiation was determined with a  $\gamma\gamma$ -coincidence spectrometer consisting of two  $3'' \phi \times 3''$  NaJ crystals, whose efficiency was computed and checked with calibration sources.

The estimated total errors for both excitation functions include contributions from the detector efficiencies, the neutron flux determination, counting statistics, background subtraction, multiple scattering, neutron flux attenuation and self absorption of  $\gamma$  radiation in the sample and amount to 8–11%. The total errors in the projectile energies are due to target thickness and reaction kinematics and vary from 80 to 210 keV for the  $^{238}\text{U}(n,2n)^{237}\text{U}$  reaction and from 350 to 440 keV for  $^{12}\text{C}(n,2n)^{11}\text{C}$ .

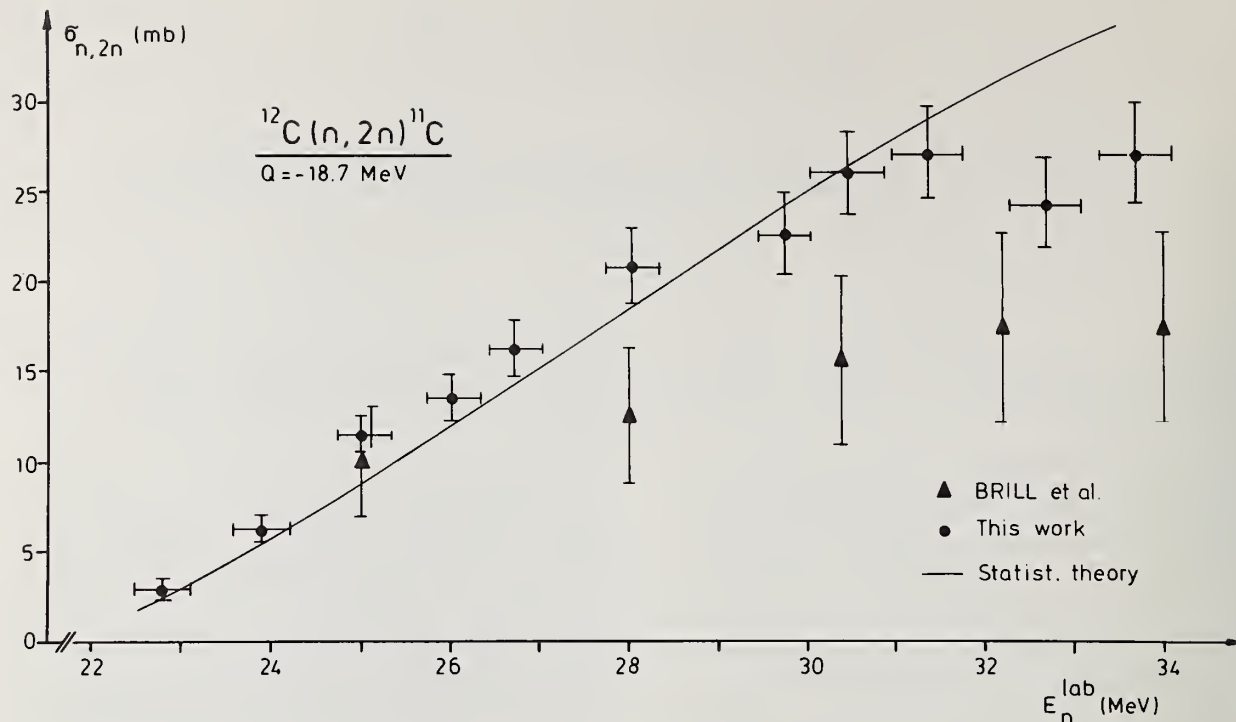


Fig. 1 Experimental and calculated excitation functions of the reaction  $^{12}\text{C}(n, 2n)^{11}\text{C}$ .

#### Results and Discussion

##### $^{12}\text{C}(n, 2n)^{11}\text{C}$

Our experimental results are shown in fig. 1 together with the data of Brill et al.<sup>4</sup>. The systematic difference between these two data sets is believed to be due to uncertainties in the neutron flux determination of the work cited. We have confirmed our method of neutron flux determination in this energy range with measurements of the  $^3\text{H}(d, n)^4\text{He}$  angular distributions<sup>11</sup>.

Statistical model calculations have been performed with the code of Uhl<sup>12</sup>, which takes into account the energy and angular momentum conservation for sequential evaporation. The competing decay modes are neutron, proton, alpha and gamma emission. The low lying levels of the residual nuclei reached are explicitly included in this formalism with their excitation energies, spins and parities. The continuum is described with the level density formulas of the back-shifted Fermi gas model<sup>13</sup>. The level density parameters used for the residual nuclei follow the mass dependence  $a = A/8.5 \text{ MeV}^{-1}$  with the exemption of  $^{12}\text{C}$  ( $a = 1.2 \text{ MeV}^{-1}$ ) and  $^{11}\text{B}$  ( $a = 1.03 \text{ MeV}^{-1}$ ). For the energy shift parameter  $\Delta$  values of  $+0.6 \text{ MeV}$  for even even nuclei,  $-2.0 \text{ MeV}$  for odd odd nuclei and  $-0.65 \text{ MeV}$  for odd mass nuclei were taken, respectively<sup>13</sup>. The spin cut off parameter  $\sigma$  was calculated from the rigid body moment of inertia. The level distance calculated from these parameters for  $^{13}\text{C}^*$  is in the order of  $40 \text{ keV}$  at  $30 \text{ MeV}$  excitation energy, i.e. small compared with the uncertainty of the projectile energy.

The transmission coefficients and reaction cross sections were calculated with optical model parameter sets from Watson et al.<sup>14</sup> for protons and neutrons and from David et al.<sup>15</sup> for alpha particles. Absorption cross sections for radiation were taken from Axel<sup>16</sup>. The result is shown in fig. 1. The agreement with the experimental data is satisfying and may indicate, that the compound system  $^{13}\text{C}^*$  is formed in the reaction under study. Further investigation of this compound system with the reactions  $^{11}\text{B}(d, 2n)^{11}\text{C}$  and  $^9\text{Be}(\alpha, 2n)^{11}\text{C}$  is in process.

##### $^{238}\text{U}(n, 2n)^{237}\text{U}$

The experimental results are given in fig. 2 together with the data of Knight et al.<sup>7</sup>. Some more experimental points between 13 and 15 MeV neutron energy are known<sup>3</sup> which on the average agree well with our data.

The curves given in fig. 2 refer to calculations which were performed under the following assumptions: Starting with an interaction given by the reaction cross section  $\sigma_R$ , the system will undergo preequilibrium nucleon emission with a probability  $\sigma_{\text{PRE}}/\sigma_R$  or equilibrate towards the compound system  $^{239}\text{U}^*$ . For the moment we will not take into account fission competition, so that the compound system may decay by  $n$ ,  $p$ ,  $\alpha$  or  $\gamma$  emission, see fig. 3. The cross section for the formation of  $^{237}\text{U}$  by sequential evaporation of two neutrons is denoted by  $\sigma_{n, 2n}^{\text{CN}}$ . If the neutron preequilibrium emission branch is followed, the system may

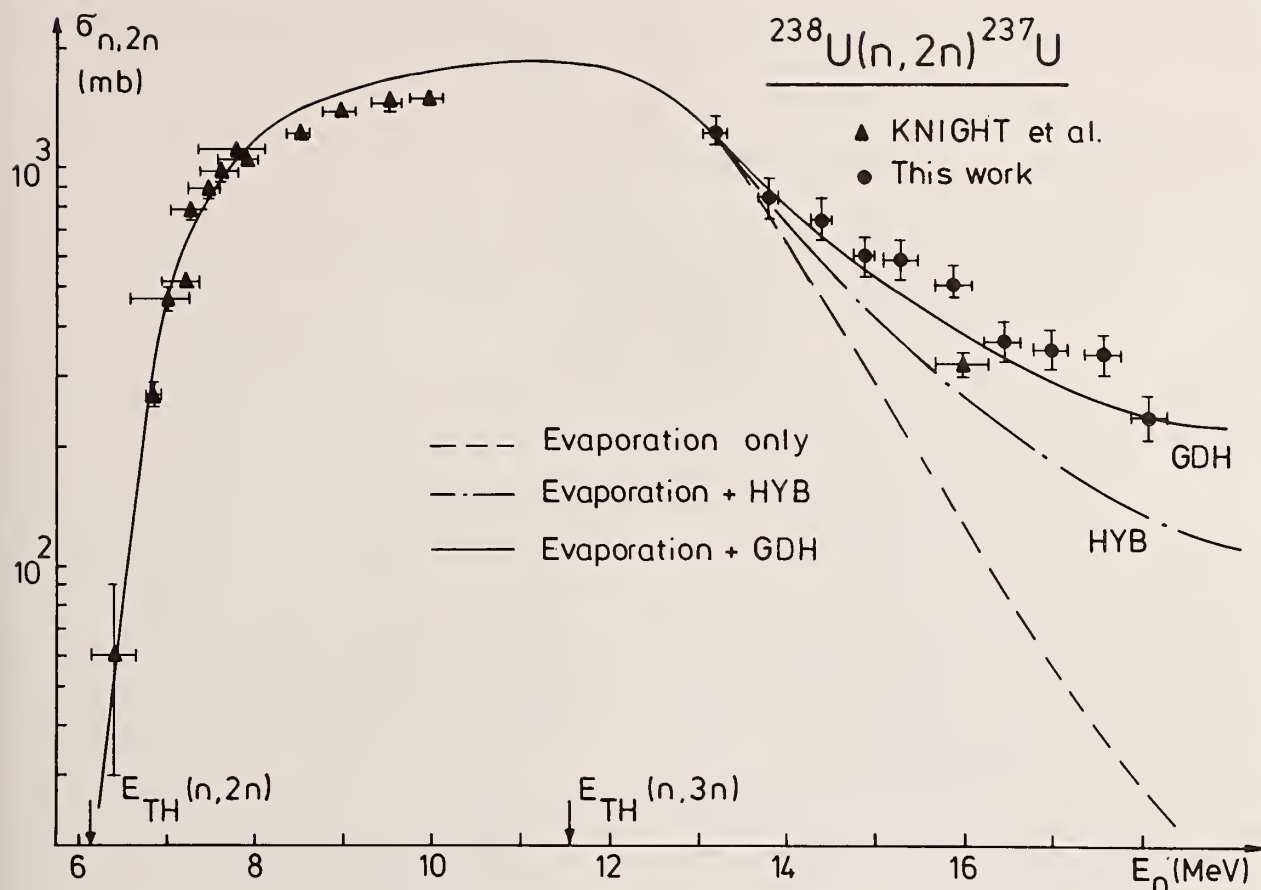


Fig. 2 Experimental and calculated excitation functions of  $^{238}\text{U}(n,2n)^{237}\text{U}$ .

either emit a second preequilibrium neutron:  $\sigma_{n,2n}^{\text{PRE}}$ , or will develop towards the compound nucleus  $^{238}\text{U}^*$  and contribute with  $\sigma_{n,2n}^{\text{PRE}}$  to the  $(n,2n)$  reaction by evaporation of a second neutron. These contributions were calculated simultaneously with a code combining evaporation in the Weißkopf-Ewing model and preequilibrium emission in the hybrid model<sup>17</sup> (HYB) or the geometry dependent hybrid model<sup>18</sup> (GDH). The parameters for the compound part were chosen from a compilation<sup>19</sup>, the transmission coefficients and reaction cross sections were calculated as described above with parameters from refs. 16, 20. The preequilibrium calculation was started with a 1 hole, 2 particle (1.3 neutrons, 0.7 protons) configuration.

Fission competition was accounted for by introducing  $T_n / (T_n + T_f)^{-1}$  as a depletion factor for each neutron evaporation step<sup>21</sup>. In a good approximation the angular momentum dependence of this ratio may be neglected<sup>22</sup>. The total  $(n,2n)$  cross section thus is given by

$$\sigma_{n,2n}^{\text{tot}} = \sigma_{n,2n}^{\text{PRE}} + \sigma_{n,2n}^{\text{PRE}} \left( \frac{T_n}{T_n + T_f} \right) {}^{238}\text{U} \quad (1)$$

$$+ \sigma_{n,2n}^{\text{CN}} \left( 1 - \frac{\sigma_{\text{PRE}}}{\sigma_{\text{R}}} \right) \left( \frac{T_n}{T_n + T_f} \right) {}^{238}\text{U} \left( \frac{T_n}{T_n + T_f} \right) {}^{238}\text{U}$$

For  $T_n / T_f$  a constant value of 5 was taken for  $^{239}\text{U}$  and 4 for  $^{238}\text{U}$  from refs. 21, 23.

First the calculation was performed without preequilibrium contributions. The result is given by the dashed line in fig. 2. The experimental data are reproduced fairly well up to the  $(n,3n)$  threshold; at higher energies this ansatz overestimates the  $(n,3n)$  and 3<sup>rd</sup> chance fission competition. The curve in fig. 2 denoted HYB was calculated according to eq. (1) with the hybrid model and the parameter  $k=1$  for the mean free path of nucleons in nuclear matter<sup>17</sup>. The corresponding branching ratios  $\sigma_{\text{PRE}} / \sigma_{\text{R}}$  are given in fig. 4. The results are improved, but still show a discrepancy at high energies.

A more realistic mean free path for nucleons in the nuclear well can be achieved<sup>17</sup> by an increase of the parameter  $k$ . Fig. 4 shows, that  $k=2$  leads to results similar to those of the geometry dependent calculation, which was performed with intranuclear transition rates deduced from an imaginary optical potential<sup>18</sup>. The results of eq. (1) for the GDH model are shown in fig. 2, too. The significant contribution at high energies comes from the second term in eq. (1). The good agreement may be interpreted as an indication for substantial preequilibrium contributions in the reaction under study above 15 MeV projectile energy.



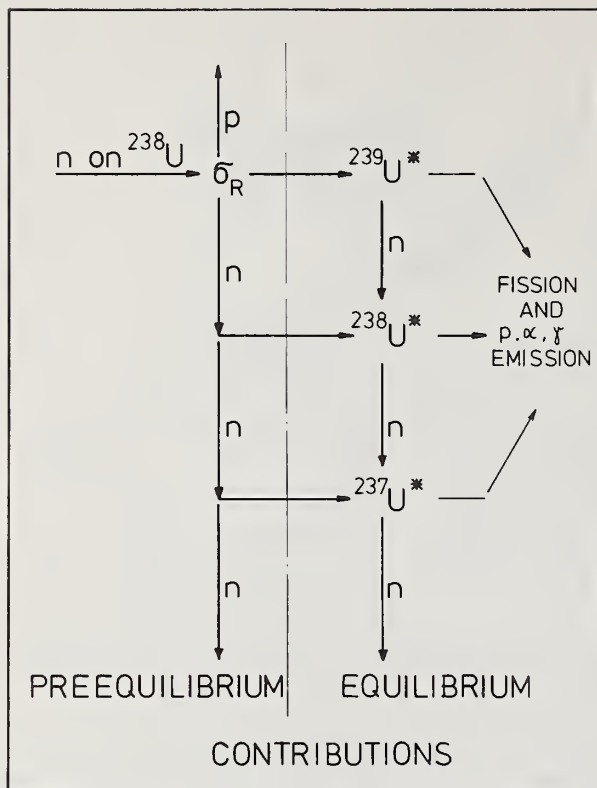


Fig. 3 Diagram illustrating the branching of the compound nucleus formation and decay corresponding to eq. (1)

#### Acknowledgement

One of us (W. S.) wishes to thank M. Blann for many helpful discussions and supplying the programs for preequilibrium model calculations.

#### References

- 1 M. Bormann, H.H. Bissem, E. Magiera and R. Warne-münde, Nucl. Phys. A157(1970)481
- 2 W.E. Alley and R.M. Lesser, Nucl. Data A11(1973) 621
- 3 M. Bormann, H. Neuert and W. Scobel, Handbook on Nuclear Activation Cross-Sections (IAEA, Vienna) (1974)p. 87
- 4 O.D. Brill, N.A. Vlasov, S.P. Kalinin and L.S. Sokolov, Sov. Phys.-Doklady 6(1961)24
- 5 N. Bohr and J.A. Wheeler, Phys. Rev. 56(1939)426
- 6 C.J. Bishop, I. Halpern, R.W. Shaw, jr. and R. Vandenbosch, Nucl. Phys. A198(1972)161
- 7 J.D. Knight, R.K. Smith and B. Warren, Phys. Rev. 112(1958)259
- 8 M. Bormann, R. Kühn, K. Schäfer and U. Seebeck, Nucl. Instr. & Meth. 88(1970)245
- 9 M. Bormann, V. Schröder, W. Scobel and L. Wilde, Nucl. Instr. & Meth. 98(1972)613
- 10 A. Hauser, Nucl. Instr. & Meth. 107(1973)187

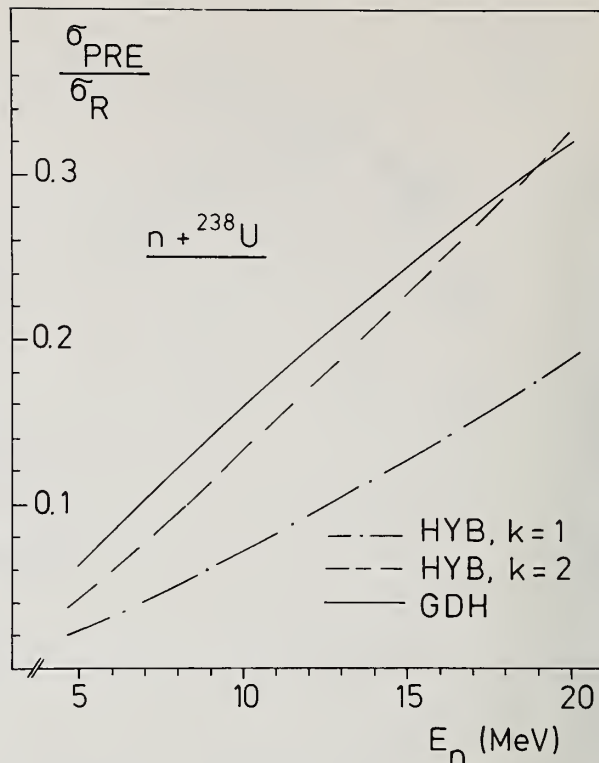


Fig. 4 Fraction of the  $n+^{238}\text{U}$  interaction which leads to preequilibrium emission prior to a formation of the compound system  $^{239}\text{U}^*$ .

- 11 E. Magiera, M. Bormann, W. Scobel and P. Heiß, to be published (1975)
- 12 M. Uhl, Nucl. Phys. A184(1972)253
- 13 H. Vonach and M. Hille, Nucl. Phys. A127(1969)289
- 14 B.A. Watson, P.P. Singh and R.E. Segel, Phys. Rev. 182(1969)977
- 15 P. David, J. Debrus, H. Mommsen and A. Riccato, Nucl. Phys. A182(1972)234
- 16 P. Axel, Phys. Rev. 126(1962)671
- 17 M. Blann and A. Mignerey, Nucl. Phys. A186(1972)245
- 18 M. Blann, Nucl. Phys. A213(1973)570
- 19 U. Facchini and E. Saetta-Menichella, Energia Nucleare 15(1968)54
- 20 F.D. Becchetti and G.W. Greenlees, Phys. Rev. 182 (1969)1190
- 21 H.L. Hahn, Nucl. Phys. A185(1972)241
- 22 H. Freiesleben, H.C. Britt and J.R. Huizenga in "Proc. of the Third Intern. Atomic Energy Symp. on Phys. and Chem. of Fission", Rochester, 1973, p. 447
- 23 R. Vandenbosch, J.R. Huizenga, Nuclear Fission, Academic Press, New York (1973) ch. VII

# INCOHERENT NEUTRON SCATTERING CROSS-SECTIONS AS DETERMINED BY DIFFUSE NEUTRON SCATTERING TECHNIQUES

W. Schmatz, G. Bauer and M. Löwenhaupt  
Institut für Festkörperforschung der KFA Jülich,  
517 Jülich, Federal Republic of Germany

A discussion is given of the way in which small incoherent scattering cross-sections can be obtained as a by-product of point defect scattering studies. A table with  $\sigma_{inc}$ -values for ten elements is given.

(Incoherent neutron scattering; diffuse neutron scattering; point defects)

Incoherent neutron scattering cross-sections are very important in defect scattering studies. We know that a perfect single crystal made from a monoisotopic element with zero nuclear spin has practically no elastic scattering except at Bragg positions. Such a crystal is favourable as a host material for defects to be studied by diffuse neutron scattering between the Bragg peaks. However for most elements spin- or isotope-incoherence produces elastic diffuse scattering. The corresponding cross-section  $d\sigma/d\Omega$  per atom for a crystal containing  $\nu$  different elements is given by (see e.g. <sup>1</sup>, <sup>2</sup> or <sup>3</sup>)

$$d\sigma/d\Omega = \sum_{\nu=1}^{\nu_0} c_{\nu} \cdot \sigma_{inc,\nu} \cdot e^{-2W_{\nu}} / 4\pi$$

where  $c_{\nu}$  is the atomic fraction,  $\sigma_{inc,\nu}$  the incoherent scattering cross-section and  $\exp(-2W_{\nu})$  the averaged Debye-Waller factor of the element  $\nu$ .  $\sigma_{inc,\nu}$  of course is independent of the particular crystal investigated. The simple form above holds only if the spin and isotope distribution is completely random. Proper definitions have to be made if the natural isotopic composition is changed or if the nuclear spins are partially ordered.

Within the last decade diffuse neutron scattering has been applied with increasing success to the study of lattice distortions around point defects (see e.g. <sup>4</sup>, <sup>5</sup> and <sup>6</sup>). Such studies are reasonable only at small concentrations and are then only possible if the contributions from spin- and isotope incoherence are small. Therefore the point defect studies have been accompanied by occasional determinations of incoherent scattering cross-sections. The data obtained so far have never been presented comprehensively, although some

values have been published in journals, others have been included in reviews and in diploma and thesis works. Therefore this conference is taken as an occasion to present them all together including some new values.

Two techniques have been applied so far: In one case, the sample was cooled to low temperatures to avoid phonon absorption and sufficiently long wavelength were used to avoid phonon creation and Bragg scattering. In the second case the elastic diffuse scattering was separated by a time-of-flight method. Both methods have been described in detail in a recent experimental review <sup>6</sup>. The absolute values of  $\sigma_{inc}$  were obtained by calibration with vanadium standards. A  $\sigma_{inc}$ -value for vanadium of  $(5.01 \pm 0.03)$  barn was used <sup>7</sup>. Corrections for absorption in the sample and the standard were always applied.

The results for ten elements are given in table 1. The errors quoted are experimental and include calibration uncertainties. All samples were of high chemical purity and except in the cases of Bi and Be no uncertainties arise from scattering due to unknown impurities. For Bi and Be the enormous sensitivity to hydrogen - an atomic fraction of  $10^{-4}$  gives 8 mbarn - may have introduced errors. The Be-samples were not chemically analysed for hydrogen and the Bi-samples were not analysed throughout. However the values given for Bi and Be are at least upper limits. The value given for Pb is a proper average of the values in <sup>8</sup> and <sup>9</sup> according to the discussion in <sup>9</sup>. The incoherent scattering cross-section of Al has been measured with three different experimental arrangements and with material (Al 99.999) from at least two different manufac-

Table 1. Incoherent Scattering Cross-Sections

Element	$\sigma_{inc}$ (mbarn)	References
Be	$< 4 \pm 1$	10
Al	$10.5 \pm 0.6$	10, 11, 12, 13, 14, 15
Si	$15 \pm 1.3$	11
Cu	$590 \pm 40$	11
Nb	$6.3 \pm 0.6$	15
Ag	$520 \pm 50$	unpublished
Nd	$11000 \pm 2000$	unpublished
Au	$500 \pm 50$	unpublished
Pb	$2 \pm 1$	8, 9
Bi	$< 10 \pm 2$	10, 8

Table 2.  $\sigma_{inc}$ -values for Al

$10 \pm 1$	Ref. 10
$11.4 \pm 1.2$	Ref. 11, 12 and 13
$9 \pm 1$	Ref. 14
$10.5 \pm 0.6$	Ref. 15

tures. The good agreement for the values (table 2) demonstrates the reliability of the method. The large uncertainty in the value for Nd is mainly due to the uncertainties in removing the quasielastic paramagnetic scattering of the  $Nd^{++}$ -ion.

The continuation of the point defect studies can be expected to yield additional incoherent scattering cross-sections and we are also prepared to measure such values for other investigators upon request.

#### References

1. Marshall, W., and Lovesey, S.W. (1971). In "Theory of Thermal Neutron Scattering" (W. Marshall and P.H. Wilkinson, eds.). Oxford Univ. Press (Clarendon), London and New York;
2. Gurevich, I.I., and Tarasov, L.V. (1968). "Low-Energy Neutron Physics Translation" (R.I. Sharp and S. Choment, eds.), North-Holland Publ., Amsterdam;
3. Turchin, V.F. (1965). "Slow Neutrons," Israel Prog. Scientific Translations;
4. Schmatz, W. (1970). In "Vacancies and Interstitials in Metals" (A. Seeger et al., eds.), North-Holland Publ., Amsterdam;
5. Schmatz, W., Treatise on Materials Science and Technology, ed. H. Hermans, Academic Press New York, Vol. 2 (1973);
6. Bauer, G., Seitz, E. and Just, W., J. Appl. Cryst. (1975), 8, in press;
7. Hughes, D.J., and Schwartz, R.B. (1958). "Neutron Cross Sections," 2nd ed. BNL-325 Suppl. Ser. up to 1972;
8. Scherm, R., (1968). Nukleonik 12, 4;
9. Schumacher, H., Schmatz, W. und Seitz, E., phys. stat. sol. (a), 20, 109 (1973);
10. Scherm, R., and Schmatz, W., (1964). Z. Naturforsch. A 19, 354;
11. Niklaus, J.-P., Simson, R., Triftshäuser, W., and Schmatz, W. (1966). Z. Phys. 190, 295;
12. Niklaus, J.-P., Simson, R., Schmatz, W. and Wenzl, H. (1968). Z. Angew. Phys. 24, 313;
13. Simson, R., (1964). Diploma work, Technische Hochschule München;
14. Simson, R., (1968). Dissertation, Technische Hochschule München;
15. Bauer, G., (1975). Dissertation, Universität Bochum.

1. Marshall, W., and Lovesey, S.W. (1971). In "Theory of Thermal Neutron Scattering" (W. Marshall and P.H. Wilkinson, eds.).



CROSS SECTION AND METHOD UNCERTAINTIES: THE APPLICATION OF SENSITIVITY ANALYSIS  
TO STUDY THEIR RELATIONSHIP IN CALCULATIONAL BENCHMARK PROBLEMS\*

C. R. Weisbin, E. M. Oblow, J. Ching, J. E. White  
R. Q. Wright, and J. Drischler

Oak Ridge National Laboratory  
Oak Ridge, Tennessee 37830

Sensitivity analysis is applied to the study of an air transport benchmark calculation to quantify and distinguish between cross-section and method uncertainties. The boundary detector response was converged with respect to spatial and angular mesh size,  $P_k$  expansion of the scattering kernel, and the number and location of energy grid boundaries. The uncertainty in the detector response due to uncertainties in nuclear data is 17.0% (one standard deviation, not including uncertainties in energy and angular distribution) based upon the ENDF/B-IV "error files" including correlations in energy and reaction type. Differences of approximately 6% can be attributed exclusively to differences in processing multigroup transfer matrices.

(Air transport; benchmark; sensitivity; profiles; uncertainties)

## I. Introduction

The complete ORNL cross section sensitivity and uncertainty analysis system (FORSS)<sup>1</sup> has been applied to estimate the overall uncertainty and the contribution of individual components in several calculational benchmark transport problems. Only relatively simplified geometries were considered so that uncertainties due to spatial modelling were considerably reduced. Since the availability of evaluated uncertainties and their correlations in energy and reaction type is limited in ENDF/B-IV but do exist for N and O, this paper describes the analysis of an air transport benchmark problem including the estimation of the effects of uncertainties in nuclear data.

Cross-section sensitivity studies of radiation transport in air have been underway for several years. The most recent and complete analysis is that of Bartine *et al*<sup>2</sup> which includes preliminary estimates of the uncertainty in cross section over broad energy ranges based on simplified assumptions about data correlations. The present work extends this type of analysis by incorporating the final, and very detailed, ENDF/B-IV uncertainty files including covariance as a function of energy and reaction type. It then attempts to go further by quantifying other types of uncertainties introduced in the analysis procedure.

Section II presents the problem characteristics pointing out the differences between the specifications used in ref. 2 and those for the present study. Section III describes the sensitivity methodology<sup>2,3</sup> used in conjunction with the point-energy discrete ordinates technique<sup>4</sup> to attempt to converge<sup>5</sup> the results with respect to the energy grid used. Section IV reviews the formulation for processing large multigroup covariance matrices<sup>6</sup> with special emphasis placed on display techniques and bulk data management schemes. Differences due to divergent cross-section processing techniques<sup>7</sup> are treated, in Section V, by successive runs with different processed sets and with projections based upon sensitivity theory. Section VI presents the results of folding covariance matrices with sensitivity profiles to estimate uncertainties due to nuclear data. The effects of using different transport methods are assessed only briefly in Section VII by comparing the results from Discrete Ordinates and Moments Method techniques. Section VIII summarizes the results and conclusions of the entire study.

## II. Benchmark Problem Definition

The source geometry approximates a point source at the center of a sphere of air of radius  $r_0$ . A uniformly distributed, isotropic source is contained within a region, characterized by radius  $r_s$ , sufficiently small with respect to the dimension of the transport media,  $r_0$ . A detector with a flat energy response,  $\Sigma_D = 1.0 \text{ cm}^{-1}$ , is distributed in a zone from  $r_D$  to  $r_0$ . The geometry is shown in Fig. 1.

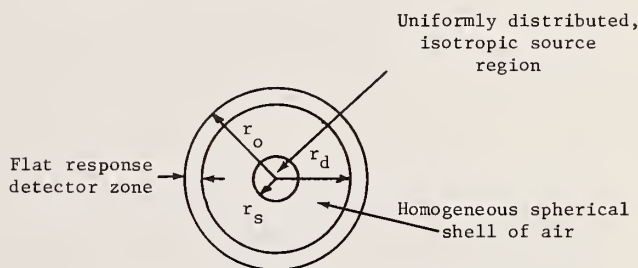


Fig. 1. Geometric Model Employed

$$r_D = 1990 \text{ m}$$

$$r_s = 12.5 \text{ m}$$

$$r_0 = 2000 \text{ m}$$

$$\rho_{14N} = 4.25 \times 10^{-5} \text{ (atoms/barn-cm)}$$

$$\rho_{16O} = 1.13 \times 10^{-5} \text{ (atoms/barn-cm)}$$

In order to standardize the source description in a form which is both general for fission and fusion devices and useful for recalculation with other methods and group structures, an analytic representation was chosen. The source spectrum was obtained by superposition of a Gaussian energy distribution around 14 MeV and a Watt fission spectrum peaked around 1 MeV. More precisely, the source spectrum was represented analytically in terms of a Gaussian

$$G(E) = G_0 e^{-\frac{1}{2}[(E-E_0)/(\Delta E)]^2} \quad (1)$$

and a Watt fission spectrum

$$F(E) = F_0 e^{-E/\alpha} \sinh[(\beta E)^{1/2}] \quad (2)$$

\*Research performed by Union Carbide Nuclear Division under contract with the United States Energy Research and Development Administration.

where  $E$  is the neutron energy in MeV,  $E_0 = 14$  MeV,  $\Delta E = 1$  MeV,  $\alpha = 1$  MeV,  $\beta = 2$  MeV<sup>-1</sup>,  $G(E)$  and  $F(E)$  are in units of source neutrons/sec-MeV-cm<sup>3</sup>, and the constants  $G_0$  and  $F_0$  are determined by normalizing the total source strength to unity over the energy range of interest with half of the neutrons coming from each of the distributions. That is

$$\int_E \int_{r_s} G(E) dE dV = \int_E \int_{r_s} F(E) dE dV = 0.5 \quad (3)$$

A graph of the source spectrum is presented in Fig. 2. The transport characteristics of the media are illustrated in Fig. 3 which presents the macroscopic total cross section for air between 100 keV and 15 MeV. The quantity of interest is the flux everywhere in the system and, in particular the response of a flat detector of unit cross section in the zone at 2000 meters.

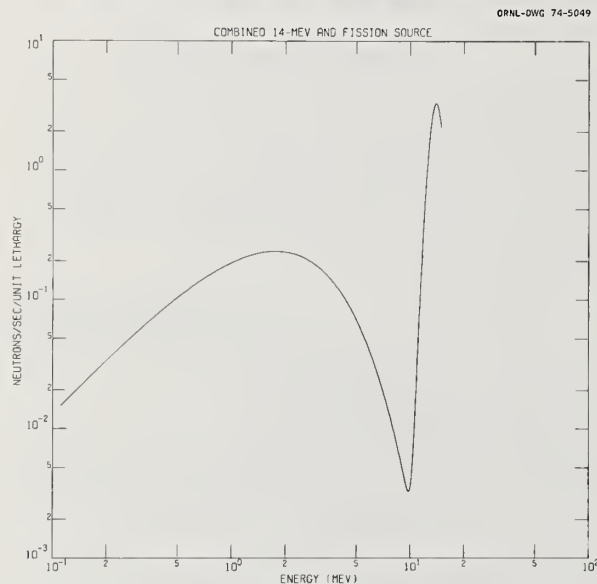


Fig. 2. Air Transport Benchmark Source Spectrum

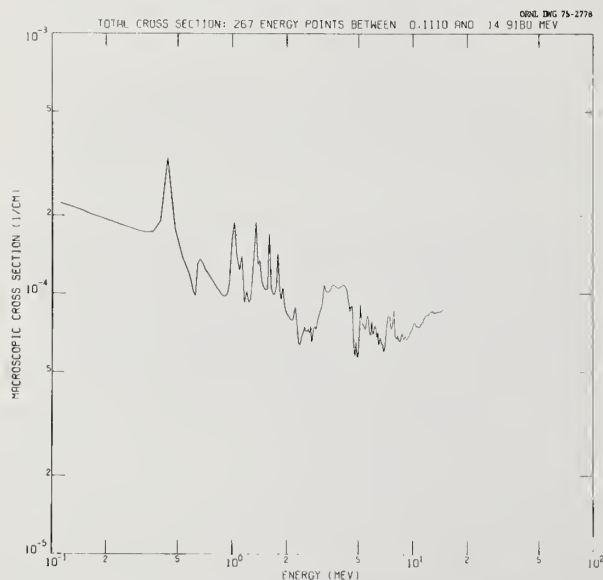


Fig. 3. Macroscopic Total Cross Section for Air Between 100 keV and 15 MeV.

The problem specifications presented above differ significantly in several important respects from the problem analyzed in ref. 2. In the earlier work, the quantity of interest was the total (neutron and gamma ray) tissue dose at 2000 meters from a prototypical thermonuclear source. This work focuses primarily on total integrated boundary flux (i.e., the response of the flat detector) arising from a hypothetical 14-MeV Gaussian source with an equal fission component. The number densities in ref. 2 were  $3.664 \times 10^{-5}$  for N and  $9.74 \times 10^{-6}$  for O, markedly different from those taken for this work and presented in Fig. 1. Finally, the problem was solved earlier in a 101-33 coupled neutron and gamma-ray energy group structure, using ENDF/B-III MAT 1133, Mod 3 for <sup>14</sup>N and MAT 1134, Mod 1 for <sup>16</sup>O. This work finalized on a 266-group optimized structure, selected using MAT 4133 Mod 3 and MAT 4134 Mod 1 while the complete uncertainty analysis using this multigroup structure was based on cross-section sets from ENDF/B IV, MAT 1275 for <sup>14</sup>N and MAT 1276 for <sup>16</sup>O.

### III. Energy Grid Selection and Converged Solutions

The key element in the creation of a fine-energy structure solution to the benchmark problem was the selection of a fine-structure energy grid. The point-energy processing code MOMANS<sup>4</sup> and a point-energy version of the SWANLAKE<sup>8</sup> sensitivity code was used for this purpose. The great speed and flexibility in generating processed neutron cross sections and sensitivity results on a pointwise energy grid make it possible to converge transport results as a function of the number and location of energy boundaries.

The convergence procedure is described as follows. First, an integral flux parameter was chosen for the problem defined in Section II above, the result of interest was the total boundary detector response. The response at the outer boundary in a shielding situation was found to usually ensure equal or better convergence of the total flux versus distance throughout the rest of the shield system. Next, a fine point-energy solution of the benchmark problem was obtained using a point energy grid. These results were then analyzed with the point-energy sensitivity code to select an initial few-point energy grid (~40 points) to begin convergence tests. This initial grid was chosen by constructing a cumulative probability function for the sensitivity profile as a function of energy and then selecting energy boundaries invoking an equal total importance criteria.<sup>5</sup> That is, the group boundaries are selected so that the reaction rate, biased by an importance function, is divided equally among the energy groups. In the terminology of sensitivity theory, each energy group is chosen to be equally sensitive in absolute magnitude to all the multigroup cross-section data. Hence, any error introduced in subsequent approximations of the weighting flux in the multigroup averaging process would be spread more uniformly over the entire energy range. This initial grid is not equally spaced in lethargy as was the starting grid.

The second phase of the benchmark calculation consisted of convergence tests to ensure high accuracy of the final flux results within the limitations of computer storage and run time. Thus, the few point grid (41 points) was used as energy boundaries and successive multigroup runs were made with ANISN to attempt to converge the solution with respect to spatial and angular mesh interval size and  $P_0$  expansion of the scattering kernel. When 1% or better convergence was achieved on this scale, additional energy boundaries (in multiples of the number in the original few-point grid) were added uniformly and point discrete ordinates calculations performed to try to converge the results in energy. This latter procedure was carried out until either 1% con-



vergence was achieved or cross-section core storage requirements were exceeded. Finally, the optimized energy bounds were used as the multigroup structure for computation of forward and adjoint fluxes for use in the analysis presented in subsequent sections.

With the following notation:

- $P_L$  - Legendre expansion of the scattering kernel  
 $S_N$  - Discrete angles at which the angular flux is calculated  
 $I_m$  - Spatial intervals used in problem solution  
 $J_k$  - Number of energy groups employed for solution  
 $E$  - Relative error given by

$$\frac{F(\text{run of interest}) - F(\text{best converged run})}{F(\text{best converged run})} \times 100$$

$F$  - Boundary detector response

(or mathematically)

$$\int_{111 \text{ keV}}^{15 \text{ MeV}} \int_{r_d}^{r_o} \phi_o(E, r) dE dV$$

and the initial problem parameters set as  $P_3$ ,  $S_{16}$ ,  $I_{82}$ ,  $J_{40}$ , Tables I through IV indicates the type of convergence achieved.

Table I.  $P_L$  Convergence for Legendre Expansion of Scattering Kernel

$P_L$	$P_1$	$P_2$	$P_3$	$P_5$
$F$	2.490	2.760	2.774	2.772
$E(\%)$	-10.17	-0.43	-0.07	0

Table II.  $S_N$  Convergence for Angular Flux Quadrature

$S_N$	$S_8$	$S_{12}$	$S_{16}$	$S_{20}$	$S_{24}$
$F$	2.503	2.714	2.774	2.831	2.861
$E(\%)$	-12.51	-5.14	-3.04	-1.02	0

Table III.  $I_m$  Convergence for Spatial Intervals

$I_m$	$I_{43}$	$I_{82}$	$I_{121}$	$I_{201}$	$I_{281}$
$F$	2.557	2.774	2.855	2.900	2.910
$E$	-12.13	-4.67	-1.89	-0.34	0

Table IV.  $J_k$  Convergence for Number of Energy Groups (Number Points -1)

$J_k$	$J_{40}$	$J_{78}$	$J_{116}$	$J_{154}$	$J_{192}$	$J_{266}$
$F$	2.774	2.493	2.305	2.452	2.481	2.454
$E$	13.04	1.59	-6.07	-0.08	1.10	0

The final results of the convergence test indicated that good convergence of the response ( $<5\%$ ) could be achieved with the following parameter set:  $P_3$ ,  $S_{24}$ ,  $I_{201}$ , and  $J_{266}$ . The convergence of the final set of problem parameters was examined by reducing the specifications jointly ( $P_2$ ,  $S_{20}$ ,  $I_{121}$ ,  $J_{192}$ ) and observing the convergence to within 1%. The numerical values for the energy group bounds and spatial intervals are not given here due to space limitations; they can be found in ref. 15. Figures 4 and 5 illustrate the converged scalar flux spectrum at 2000 meters and the adjoint spectrum at the center of the sphere.

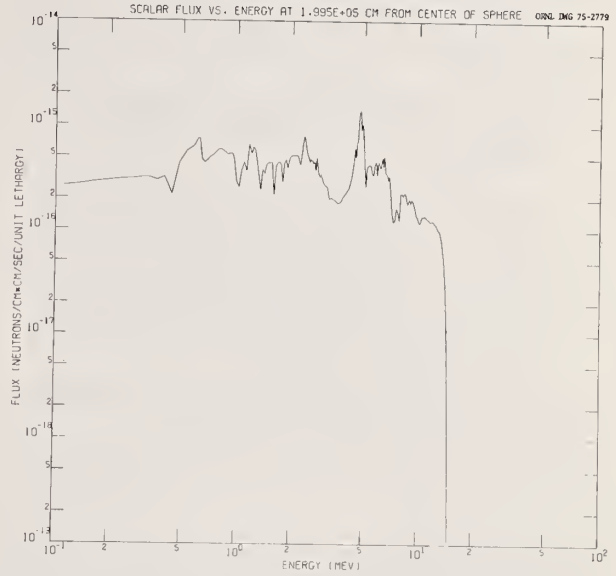


Fig. 4. Total Scalar Flux Spectrum at 2000 Meters - Air Transport Benchmark Problem.

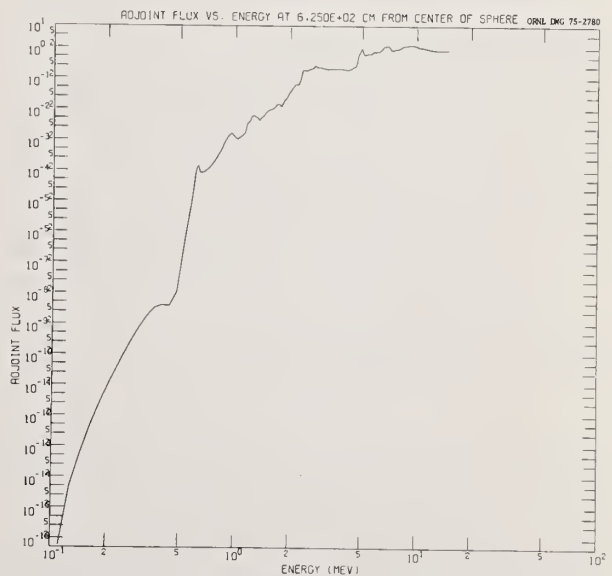


Fig. 5. Adjoint Spectrum at the Center of the Sphere - Air Transport Benchmark Problem



#### IV. Processing Uncertainty Files

##### A. Formulation of Multigroup Covariance Matrices

Only recently have standard formats and procedures been established within the ENDF/B system<sup>10</sup> for the processing of evaluated and correlated energy-dependent uncertainty information into a multigroup covariance matrix formulation. These covariance matrices were established to permit systematic sensitivity investigations<sup>11,12</sup> to determine, in a credible fashion, what cross-section measurements, evaluation, or processing methods most need further refinement.

Some of the guiding principles behind the formulation of uncertainty files for microscopic cross sections are designed to:

1. Provide a unique format for the estimated uncertainties which is flexible, but not unwieldy.
2. Permit the information to be processed at the same time as the cross-section data without imposing an undue burden on cross-section processing codes.
3. Promote the use of the file by implementation of a format to which experimental uncertainties could be readily translated.

With this in mind, the types of covariance representations permitted<sup>10</sup> in ENDF/B-IV include:

LB=0 absolute components only correlated over each  $E_k$  interval

$$\text{Cov}(X_i, Y_j) = \sum_k P_{j;k}^{i;k} F_{XY,k} \quad (4)$$

LB=1 fractional components only correlated over each  $E_k$  interval

$$\text{Cov}(X_i, Y_j) = \sum_k P_{j;k}^{i;k} F_{XY,k} X_i Y_j \quad (5)$$

LB=2 fractional components correlated over all  $E_k$  intervals

$$\text{Cov}(X_i, Y_j) = \sum_{k,l} P_{j;k}^{i;k} F_{XY,k} F_{XY,l} X_i Y_j \quad (6)$$

LB=3 fractional components correlated between  $E_k$  and  $E_l$  intervals

$$\text{Cov}(X_i, Y_j) = \sum_{k,l} P_{j;l}^{i;k} F_{X,k} F_{Y,l} X_i Y_j \quad (7)$$

where  $X_i$  and  $Y_j$  represent cross sections  $X$  and  $Y$  evaluated at energies  $i$  and  $j$ , respectively, the  $F$ 's ( $F_{XY,k}$ ,  $F_{XY,k'}$ ,  $F_{X,k}$ , and  $F_{Y,l}$ ) represent uncertainty coefficients, taken directly from the ENDF/B file, describing the correlation between cross sections  $X$  and  $Y$  for a specific energy interval. These fractional components are defined with respect to assumed normal distribution of cross-section uncertainties; furthermore, multiple sections (e.g.,  $F_{XY,k}^n$ ) may be provided

to identify specific types of experimental uncertainties associated with the complete covariance matrix. The  $F_{XY,k}$  and  $F_{XY,k'}$  are taken from a single table of energy-dependent correlation information for reactions  $X$  and  $Y$ . The  $F_{X,k}$  and  $F_{Y,l}$  indicates that the covariance data for these reactions are taken from two independent tables, one for  $X$  and one for  $Y$ . The  $P_{j,k}^{i,k'}$  is zero except for the case when energy  $i$  is contained within energy interval  $k$  and energy  $j$  is contained within energy interval  $k'$ .  $\text{Cov}(X_i, Y_j)$  is then the covariance between cross section  $X$  and energy  $i$  and cross section  $Y$  at energy  $j$ . There is a fifth law (LB=4), but since it can be described as combinations of the first four, no data has yet been cast in this form for ENDF/B-IV.

This type of formulation (sums of quantities separable in  $X$  and  $Y$ ) has the very desirable characteristic that if one assumes a flux model uncorrelated to the cross sections of interest, the multigroup covariance matrices are reduced to combinations of single integrals involving group fluxes and cross sections which can be calculated easily. In particular, for

LB=0,

$$\text{Cov}(X_G, Y_H) = \frac{\sum_n \sum_k F_{XY,k}^n \phi_{G,k}^n \phi_{H,k}^n}{\phi_G \phi_H}$$

LB=1,

$$\text{Cov}(X_G, Y_H) = \frac{\sum_n \sum_k F_{XY,k}^n \phi_{G,k}^n X_{G,k}^n \phi_{H,k}^n Y_{H,k}^n}{\phi_G \phi_H}$$

LB=2,

$$\text{Cov}(X_G, Y_H) = \sum_n \left[ \left( \sum_k F_{XY,k}^n \phi_{G,k}^n X_{G,k}^n \right) \times \left( \sum_{k'} F_{Y,k'}^n \phi_{H,k'}^n Y_{H,k'}^n \right) \right] / \phi_G \phi_H \quad (10)$$

LB=3

$$\text{Cov}(X_G, Y_H) = \sum_n \left[ \left( \sum_k F_{X,k}^n \phi_{G,k}^n X_{G,k}^n \right) \left( \sum_{k'} F_{Y,k'}^n \phi_{H,k'}^n Y_{H,k'}^n \right) \right] / \phi_G \phi_H \quad (11)$$

The derivation of Eqs. (8-11) are fully described in ref. 10; the notation used here is:

$\text{Cov}(X_G, Y_H)$  = Multigroup covariance between reaction X group G as it relates to reaction Y, group H.

$\phi_G$  = Multigroup flux for user group G.

$X_{G,k}^n$  = Multigroup cross section for reaction X for a super-group (G,k) constructed from the union of energy bounds for interval k (taken from subsection n) and those which were user input.  $\phi_{G,k}^n$  is the flux for this group.

## B. Implementation

The PUFF processing system<sup>13</sup> based on the MINX<sup>14</sup> multigroup processing code was developed specifically to read the ENDF/B-IV "error" files and construct multigroup covariance matrices according to Eqs. (8-11). For detailed programming considerations, the reader is referred to Appendix A of ref. 15.

The salient features are noted below:

1. Multigroup cross sections and fluxes are computed for a group structure which is the union between the user group structure and all energies used in the error file description for all the reactions and materials of interest. This supergroup structure obviously can get very large quite rapidly as the size of the problem considered and the level of detail available in the files expand.
2. The large number of fluxes and cross sections required have been appropriately labelled for subsequent automated retrieval. (Note that most processing codes normally do not preserve group flux values.)
3. All programming reflects variable dimensioning storage allocation.
4. All new coding is transparent to the MINX user not interested in processing error files. There is a single input flag which is 0/1; no error processing required/process errors. All other input is identical to a normal multigroup processing run. It should also be noted that with just a single additional input flag, the error processing input is quite user-oriented.

## C. Results for Processed Uncertainty Files

Several quantities related to uncertainties in multigroup cross sections have been derived from the pointwise ENDF/B "error" file. Clearly, of interest, is the covariance matrix

$$\text{Cov}(X_G, Y_H) = \langle (X_G - \bar{X}_G) (Y_H - \bar{Y}_H) \rangle \quad (12)$$

for reaction X, group G as it relates to reaction Y group H, and the associated quantity, the relative covariance matrix.

$$\text{Rel Cov}(X_G, Y_H) = \text{Cov}(X_G, Y_H) / X_G Y_H \quad (13)$$

In this notation, the standard deviation is given by:

$$\text{Std. Dev}(X_G) = \sqrt{\text{Cov}(X_G, X_G)} \quad (14)$$

and the analogous relative quantity, the relative standard deviation, is

$$\text{Rel Std. Dev}(X_G) = \frac{\text{Std. Dev}(X_G)}{X_G} \quad (15)$$

It is reasonable to expect that the covariance matrix of energy-dependent cross sections is strongly diagonal, i.e., the magnitude of the matrix elements tend to be small for groups G and H significantly displaced from each other in energy. However, the greater number of off-diagonal terms makes it difficult to say, a priori, that only the diagonal elements need be considered.

The correlation matrix is a quantity constructed by dividing the relative covariance matrix for  $X_G$  and  $Y_H$  by the respective relative standard deviations.

$$\text{Corr}(X_G, Y_H) = \frac{\langle (X_G - \bar{X}_G) (Y_H - \bar{Y}_H) \rangle}{\sqrt{\langle (X_G - \bar{X}_G)^2 \rangle \langle (Y_H - \bar{Y}_H)^2 \rangle}} \quad (16)$$

The correlation matrix is bounded by unity, i.e.,

$$|\text{Corr}(X_G, Y_H)| \leq 1 \quad (17)$$

When  $\text{Corr}(X_G, Y_H) = 0$ , the group cross sections are said to be totally uncorrelated; when  $|\text{Corr}(X_G, Y_H)| = 1$ , the group cross sections are termed fully correlated.

Figures 6 through 8 illustrate some of the processed correlation matrices and standard deviations obtained for nitrogen and oxygen. Appendix B of ref. 15 presents a complete set of correlation matrices (and standard deviations) for all energies and reaction types for N and O. These graphs are given in 22 groups for clarity of presentation. The actual matrices used in the section on results correspond to the problem described in this paper (266 groups). Figure 6 presents the correlation matrix for elastic scattering (reaction 2) as a function of energy as well as the standard deviation for  $^{14}\text{N}$ . Several points are immediately noteworthy. First, the standard deviation has not appreciably changed from its description in ref. 2 (this is true for all reactions for N and O); the cross section is reasonably well known at lower energies ( $\sim 3\%$ ) and only slightly less so at higher energies ( $\sim 5-8\%$ ). The cross section is not fully correlated, as assumed in ref. 2 (with only the limited information available at that time) and there is some structure clearly evident. Above 1 MeV, the correlation matrix tends to become more diagonal with increasing energy; at lower energies ( $< 600$  eV) the full correlation assumption appears valid.

Figure 7 illustrates the same type of behavior exhibited in the  $(n, \alpha)$  cross section. Where the standard deviation curve goes outside the plot frame, the uncertainty has become inordinately large. This typically is the case for a reaction near threshold. The standard deviation is of the order of (20-30%) and is not fully correlated. It is the diagonal elements that are primarily important for the descrip-



tion of the inelastic (reaction 4), capture (reaction 102), and (n,p) (reaction 103) cross sections above 600 eV. Below this energy, both capture and (n,p) are fully correlated functions of energy. Figure 8 illustrates the correlation matrix as a function of energy for cross section covariance. The "deep" hole indicates the anti-correlation between elastic and (n, $\alpha$ ) below 10 MeV (to preserve the total cross section, if the elastic cross section increases, the (n, $\alpha$ ) would decrease etc.). The "grand canyon" has significant structure and is not uniformly -1 across the entire energy range as assumed in ref. 2.

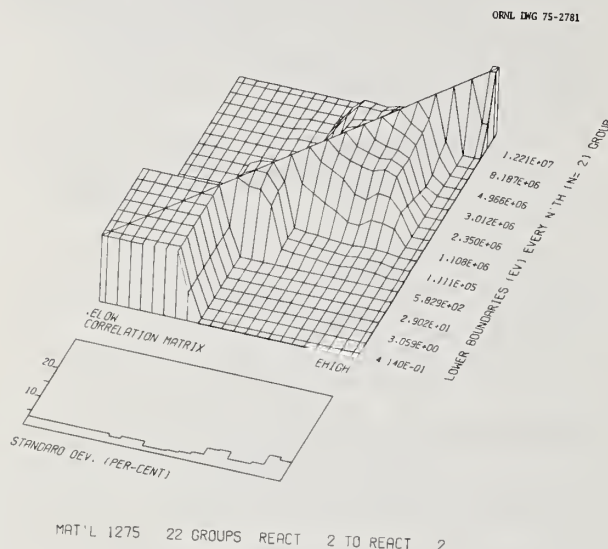


Fig. 6. Correlation Matrix and Standard Deviation for the Elastic Scattering Cross Section

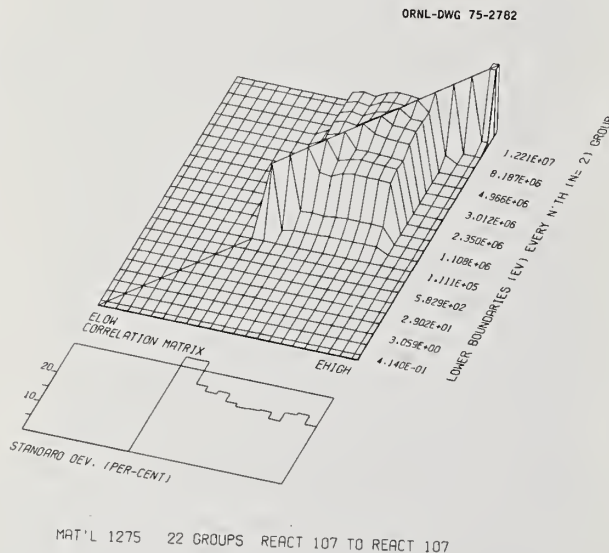


Fig. 7. Correlation Matrix and Standard Deviation for the (n, $\alpha$ ) Cross Section

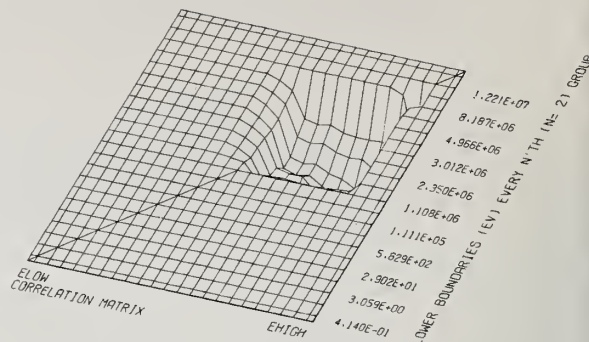


Fig. 8. Correlation Matrix as a Function of Energy Between the Elastic and (n, $\alpha$ ) Cross Section

The process of folding these covariance matrices with sensitivity profiles is described in Section VI.

#### V. Uncertainties Introduced in the Averaging of Multigroup Cross Section

The neutron multigroup cross sections used in the energy grid selection phase of the study were processed using the XLACS module of the AMPX system<sup>17</sup> while those used in the final analysis of the 266-group benchmark were obtained with the MINX<sup>14</sup> code. Both programs are available at ORNL and the choice was made primarily for expediency. However this, and more fundamental interest, does raise the question of consistency and validity of different multigroup processing techniques. Significant differences due to a wide variety of distinct physical approximations in flux modeling and methods of numerically group averaging have already been reported for fast reactor situations.<sup>7</sup>

To investigate the potential impact of cross-section processing methods uncertainties, the benchmark was repeated using MINX (M) multigroup data, XLACS (X) multigroup data, and pointwise cross sections used in conjunction with the point-ANISN (PA) technique.<sup>4</sup> The integrated boundary fluxes obtained were .925 (PA), .835 (M), and .784 (X) neut/sec. The volume of the detector zone is that corresponding to the last of the 201 spatial intervals. The point-ANISN results are expected to be on the high side because the points on the chosen grid emphasize minima in the total cross section and do not use averages of  $\sigma_T$ . This approach tends to increase the response for deep penetration problems compared with that obtained using multigroup methods. Approximately, six percent differences in the integrated boundary flux can be attributed exclusively to differences in multigroup processing techniques. Using a linear perturbation theory estimate,  $\Delta R/R$  is estimated by:



$$(\Delta R/R)_X = \sum_{X,G} P_{X,G} (\Delta \sigma/\sigma)_{X,G} \quad (18)$$

$$(\Delta R/R) = \sum_X (\Delta R/R)_X \quad (19)$$

$P_{X,G}$  = relative sensitivity coefficient,  
reaction X group G

$(\Delta \sigma/\sigma)_{X,G}$  = relative difference in multigroup  
cross sections for reaction X, group G

$(\Delta R/R)_X$  = projected change in response due to  
a change in multigroup cross section  
type X

We find that essentially all the 6% difference comes in the processing of multigroup transfer matrices. Differences arising from processing integrated cross section (e.g.,  $\sigma_{el}$ ,  $\sigma_{in}$ ) lead to changes in response which are less than .2% most of this coming from the linearization approximation in MINX.

#### VI. Folding Nuclear Data Covariance Matrices with Sensitivity Profiles

The 266-group forward and adjoint fluxes computed in section III have been combined to generate sensitivity profiles<sup>2</sup> for all important reaction cross sections in air. A complete set of illustrations can be found in ref. (15); one of the most important, the profile for (n, $\alpha$ ), is presented in Fig. 9. The complete set of profiles were then folded with the relative covariance matrices generated in section IV according to the following equation:

$$\left(\frac{\Delta R}{R}\right)^2 = \sum_{X,Y,G,H} P_{X,G} \text{Rel. Cov. } (X_G, Y_H) P_{Y,H} \quad (20)$$

with the following definitions

$P_{X,G}$  - relative sensitivity profile for reaction X,  
group G

$\left(\frac{\Delta R}{R}\right)^2$  - relative variance due to nuclear data uncertainties in integrated reaction cross sections

Tables V and VI present the results of this folding process. The summation has been partitioned in thirds to distinguish the contribution from a given reaction Z, how it correlates with all other reactions, and the contributions from all terms not involving reactions Z. The individual reactions are enumerated below:

Reaction Number	Reaction Type
2	$\sigma_{el}$
4	$\sigma_{in}$
102	$\sigma_{n,\gamma}$
103	$\sigma_{n,p}$
107	$\sigma_{n,\alpha}$

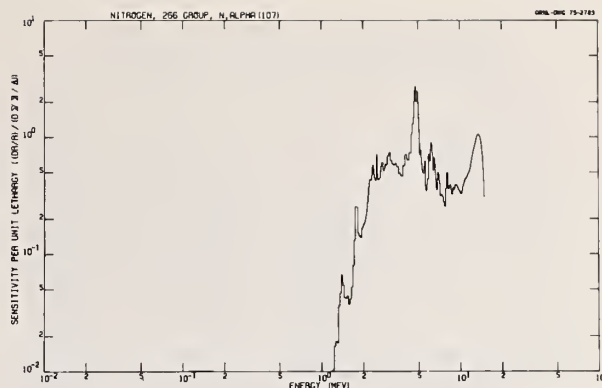


Fig. 9. Sensitivity Scattering for (n, $\alpha$ ) Scattering Cross Section

Table V. Components to the Variance of the Integrated Boundary Fluence due to Nuclear Data Uncertainties in <sup>14</sup>N (MAT 1275)

Variance Component	ENDF/B IV	Uncorrelated	Fully Correlated
React 2 + 2	4.518+1	1.038+0	2.182+2
React 2 + others	-2.147+2	-5.506+0	2.168+3
All react 2	-1.696+2	-4.468+0	2.386+3
Not react 2	4.532+2	1.326+1	5.387+3
React 4 + 4	7.805+1	4.835+0	5.211+2
React 4 + others	-5.294+1	-3.807+0	2.983+3
All react 4	2.512+1	1.028+0	3.504+3
Not react 4	2.585+2	7.761+0	4.269+3
React 102 + 102	4.675-4	2.657-5	4.664-3
React 102 + others	0	0	1.203+1
All react 102	4.675-4	2.657-5	1.204+1
Not react 102	2.836+2	8.789+0	7.761+3
React 103 + 103	1.916+1	9.377-1	1.578+2
React 103 + others	-1.368+1	-6.514-1	1.899+3
All react 103	5.486+0	2.863-1	2.057+3
Not react 103	2.781+2	8.502+0	5.716+3
React 107 + 107	3.812+2	9.379+0	1.439+3
React 107 + others	-1.985+2	-4.838+0	3.811+3
All react 107	1.826+2	4.541+0	5.250+3
Not react 107	1.010+2	4.247+0	2.523+3
Relative standard deviation <sup>14</sup> N cross section uncertainties (%)	1.684+1	2.964+0	8.816+1

Table VI. Components to the Variance of the Integrated Boundary Fluence due to Nuclear Data Uncertainties in  $^{16}\text{O}$  (MAT 1276)

Variance Component	ENDF/B IV	Uncorrelated	Fully Correlated
React 2 $\rightarrow$ 2	1.723+0	7.356-2	1.365+1
React 2 $\rightarrow$ others	-2.473+0	-2.080-1	7.410+1
All react 2	-7.502-1	-1.344-1	8.775+1
Not react 2	5.385+0	4.319-1	1.006+2
React 4 $\rightarrow$ 4	3.490+0	3.435-1	3.224+1
React 4 $\rightarrow$ others	-2.275+0	-2.119-1	9.136+1
All react 4	1.215+1	1.317-1	1.236+2
Not react 4	3.420+0	1.858-1	6.471+1
React 103 $\rightarrow$ 103	4.179-2	5.016-3	2.438-1
React 103 $\rightarrow$ others	-4.248-2	-3.833-3	1.306+1
All react 103	-6.889-4	1.184-3	1.331+1
Not react 103	4.635+0	2.963-1	1.750+2
React 107 $\rightarrow$ 107	2.427+0	1.222-1	1.487+1
React 107 $\rightarrow$ others	-1.304+0	-6.997-2	7.609-1
All react 107	1.123+0	5.223-2	9.097+1
Not react 107	3.512+0	2.453-1	9.734+1
Relative standard deviation from $^{16}\text{O}$ cross section uncertainties (%)	2.152+0	5.455-1	1.372+1

Since covariance matrices for all the integrated reaction cross sections (including those quantities served) were explicitly given in the ENDF/B-IV file, we have chosen to consider each of the partials as the independent reaction cross section; thus, the total cross section appears only implicitly in Tables V and VI.

Assuming no correlation between the N and O uncertainty files, the relative standard deviation due to all integrated reaction cross section uncertainties is 17.0%. The importance of the  $^{14}\text{N}$  (n, $\alpha$ ) cross section is clearly evident, as it was in earlier studies. Just as clear is the relative unimportance of  $^{16}\text{O}$  cross sections. The  $^{14}\text{N}$  elastic cross section is anti-correlated with other reactions diminishing the contribution to the variance from the uncertainties in the elastic scattering cross section considered by itself. As a function of energy, the "Uncorrelated" case corresponds to no correlation between cross sections in different energy groups; correlation between reactions for a given energy group is still included. "Fully Correlated" corresponds to the case of unity everywhere in the correlation matrix. These latter two cases are included simply to give the reader a feeling for the sensitivity of the estimated overall uncertainty due to two extreme kinds of correlation evaluation.

#### VII. Comparison of Transport Methods

The point and multigroup discrete ordinates results obtained above have been compared to fluxes calculated using the moments method technique. This latter procedure was one of the earliest methods applied to deep penetration radiation transport problems in simplified geometry of uniform composition. Modern moments method<sup>18</sup> and flux reconstruction<sup>19</sup> programs are very fast (the 267 energy point air problem, including cross section preparation, runs in less than three minutes on the ORNL 360/91) and compute the infinite medium spectrum, the age, higher moments (up to 20,0), and the flux at all spatial and energy points in the system including all cross section detail.

We have found that the total integrated fluxes agrees to within 1% at all space points out to 1000 meters. At 1500 meters, differences of the order of 7% are observed. The fluxes right at the boundary cannot be easily compared since the moments technique applies only to infinite media. However, for higher energy groups (e.g., 12.2-14.9 MeV), where the angular flux is primarily outward directed, the two techniques give fluxes at 2000 meters which at 11 agree to within 7%. Finally, detailed comparisons of flux spectra at individual space points were inconclusive due to non-physical structure in the moments method fluxes at specific energy points due primarily to failure of a particular reconstruction scheme. In general, however, the moments method spectra agree well with the benchmark results. The agreement is spatial behavior, with the flux averaged over broad energy bins is also good.

#### VIII. Conclusions

Sensitivity analysis is applied to the study of an air transport benchmark calculation to quantify and distinguish between cross section and method uncertainties. The boundary detector response was converged with respect to spatial and angular mesh size,  $P_L$  expansion of the scattering kernel, and the number and location of energy grid boundaries. The uncertainty in the detector response due to uncertainties in nuclear data is 17.0% (one standard deviation, not including uncertainties in energy and angular distribution) based upon the ENDF/B-IV "error files". Differences of approximately 6% can be attributed exclusively to differences in processing multigroup transfer matrices.

#### Reference

- <sup>1</sup>E. G. Silver, E. M. Oblo, J. M. Kallfelz, C. R. Weisbin, D. E. Bartine, G. F. Flanagan, and F. R. Mynatt, "Generalized Reactor Sensitivity Program at ORNL," Trans. Am. Nucl. Soc. **18**, 341 (June 1974).
- <sup>2</sup>D. E. Bartine, E. M. Oblo, and F. R. Mynatt, "Radiation Transport Cross-Section Sensitivity Analysis - A General Approach Illustrated for a Thermonuclear Source in Air," Nucl. Sci. Eng., **55**, 147-167 (1974).
- <sup>3</sup>E. M. Oblo, D. E. Bartine, and F. R. Mynatt, "General Sensitivity Theory for Radiation Transport," ORNL-TM-4110 (March 1973).
- <sup>4</sup>J. Ching, H. Goldstein, and E. M. Oblo, "Application of a Discrete-Energy Discrete-Ordinates Technique to the Study of Neutron Transport in Iron," ORNL-TM-4235 (December 1974).
- <sup>5</sup>E. Oblo, J. Ching, and J. Drischler, "Selection of Group Energy Boundaries Using Sensitivity Theory," Trans. Am. Nucl. Soc. **17**, 547 (1973).
- <sup>6</sup>F. G. Perey, G. deSaussure, and R. B. Perez, "Estimated Data Covariance Files for Evaluated Cross Sections - Examples for  $^{235}\text{U}$  and  $^{238}\text{U}$ ," Proceedings of ANS Topical - Advanced Reactors: Physics, Design, and Economics, September, 1974, to be published.
- <sup>7</sup>C. R. Weisbin, N. M. Greene, H. Henryson, II, R. J. LaBauve, C. Durston, D. E. Cullen, and R. B. Kidman, "Fast Reactor Cross-Section Processing Codes - Is There a Dollars Worth of Difference Between Them?" Proceedings of ANS Topical - Advanced Reactors: Physics, Design, and Economics, September, 1974, to be published.

<sup>8</sup>D. E. Bartine, F. R. Mynatt, and E. M. Oblow, "SWANLAKE, A Computer Code Utilizing ANISN Radiation Transport Calculations for Cross-Section Sensitivity Analysis," ORNL-TM-3809 (May 1973).

<sup>9</sup>W. W. Engle, Jr., "A Users Manual for ANISN, A One-Dimensional Discrete Ordinates Transport Code with Anisotropic Scattering," K-1693, Computing Technology Center, Oak Ridge Gaseous Diffusion Plant (1967).

<sup>10</sup>F. Perey, Format Modifications 73-7, minutes of the CSEWG meeting, December 1973 (enclosures 6 and 12).

<sup>11</sup>F. G. Perey, "The Estimated Data Covariance Files of ENDF/B - Their Uses," minutes of the CSEWG meeting, June 17-19, 1974 (enclosure 10).

<sup>12</sup>H. Henryson, II *et al.*, "Variational Sensitivity Analysis - Theory and Application," Proceedings of ANS Topical - Advanced Reactors: Physics, Design, and Economics, September, 1974, to be published.

<sup>13</sup>C. R. Weisbin, "PUFF, An ENDF/B-IV Error File Processing Code," ORNL Quarterly Report to the Defense Nuclear Agency (April 1974).

<sup>14</sup>C. R. Weisbin, P. D. Soran, R. E. MacFarlane, D. R. Harris, R. J. LaBauve, J. S. Hendricks, and J. E. White, "MINX, A Multigroup Interpretation of Nuclear Cross Sections from ENDF/B," Los Alamos Scientific Laboratory (to be published); see also, Trans. Am. Nucl. Soc., 16, 127 (1973).

<sup>15</sup>C. R. Weisbin, E. M. Oblow, J. Ching, J. E. White, R. Q. Wright, and J. Drischler, "Cross Section and Method Uncertainties: The Application of Sensitivity Analysis to Study Their Relationship in Computational Benchmark Problems," Oak Ridge National Laboratory report ORNL-TM-4847 (to be published).

<sup>16</sup>F. G. Perey, "Tedium Isotopes for MF=33," correspondence to the Error Quantity Subcommittee of the CSEWG (May 29, 1974).

<sup>17</sup>N. M. Greene and F. R. Mynatt, "The AMPX Modular Code System for Generating Coupled Neutron-Gamma Multigroup Cross-Section Sets," Trans. Am. Nucl. Soc., 15, 568 (1972); see also N. M. Greene *et al.*, "AMPX: A Modular Code System for Generating Coupled Multigroup Neutron-Gamma Libraries from ENDF/B," ORNL-TM-3706 (to be published).

<sup>18</sup>C. R. Weisbin, H. Goldstein, and L. J. Lidofsky, Trans. Am. Nucl. Soc., 12, 402 (1969); see also "A New Moments Solution to the Neutron Transport Equation," NYO-268, Pegram Nuclear Physics Lab. (1969).

<sup>19</sup>P. D. Soran, "Reconstruction of Neutron Spatial Distribution from Spatial Moments," Columbia University Doctoral Thesis, 1971.

#### Acknowledgments

The authors take great pleasure in acknowledging the efforts of D. K. Trubey in making the moments method technique operational and getting appropriate solutions for this problem. F. G. Perey and P. G. Young made significant contributions in the review and application of the ENDF/B-IV error files. Virginia Glidewell and Susan Pierce deserve many thanks for preparing the manuscript in the appropriate format and having it available ahead of schedule.



## BENCHMARK EXPERIMENTS FOR NUCLEAR DATA

E. M. Bohn Argonne National Laboratory Argonne, Illinois 60439	R. E. Maerker Oak Ridge National Laboratory Oak Ridge, Tennessee 37830	F. J. McCrosson Savannah River Laboratory Aiken, South Carolina 29801
R. J. LaBauve Los Alamos Scientific Laboratory Los Alamos, New Mexico 87544	B. A. Magurno Brookhaven National Laboratory Upton, New York 11973	R. E. Schenter Hanford Engineering Dev. Laboratory Richland, Washington 99352

Benchmark experiments offer the most direct method for validation of nuclear data. Benchmark experiments for several areas of application of nuclear data have been specified by CSEWG. These experiments are surveyed and tests of recent versions of ENDF/B are presented.

(Benchmark experiments; thermal reactor testing; fast reader testing; shielding; dosimetry; fission products)

Introduction

Benchmark experiments provide the reference for the validation of basic nuclear data. The validation process can be described very simply as the comparison of calculations utilizing a set of evaluated nuclear data, with the results of measurements in a benchmark experiment. In order for an experiment to be classified as a benchmark, it must satisfy a basic criterion; the measurements must be performed in a system that facilitates simple calculational modelling and the results of the measurements must be reliably established and documented. Five general areas of application for nuclear cross sections have been identified for benchmark testing by the Cross Section Evaluation Work Group (CSEWG): thermal and fast nuclear reactors, shielding, dosimetry and fission product properties. For each of these areas of application, specifications for benchmark experiments have been developed by CSEWG and a program has been established to test the evolving versions of the evaluated nuclear data file, ENDF/B. In this paper, a general survey of benchmark experiments is given for each of the areas of application and representative results of benchmark testing with the most recent versions of ENDF/B are presented.

Thermal Reactor Benchmark Experiments

Thermal reactor benchmark testing is concerned with establishing the merit of ENDF/B cross sections for the analysis of thermal reactor systems. The integral experiments used in the testing are designed to analyze each of the phenomena identified in the familiar four-factor formula,  $k = \eta f p \epsilon$ . The experiments are simple, clean and well-documented to minimize the complexity of the analysis and provide the clearest test of the cross sections. Personnel from six organizations participated in Version III thermal data testing, thus blending a diversity of calculational methods: Floyd Wheeler (ANC); Jud Hardy (BAPL); D. S. Craig and M. Hughes (ORNL); Don Mathews (GGA); Lester Petrie (ORNL); and R. L. Reed and F. J. McCrosson (SRL).

For brevity, only the testing of the cross sections in uranium systems is described below. The results of plutonium systems are summarized in Ref. 1.

CSEWG benchmark experiments ORNL-1, 2, 3, 4, and 10 in Table I refer to experiments by R. Gwin and D. W. Magnuson<sup>2,3</sup> in which critical compositions were determined for homogeneous aqueous solutions of <sup>235</sup>U (uranyl nitrate). The hydrogen-to-<sup>235</sup>U atom ratio varied from 1000 to 2000. The solutions were contained in thin walled, unreflected spheres of aluminum or stainless steel. These experiments are useful for testing H<sub>2</sub>O fast scattering data, the <sup>235</sup>U fission spectrum, thermal capture and fission of <sup>235</sup>U, and thermal absorption of hydrogen.

The results of criticality calculations for these experiments are presented in Table I. The GGA and SRL calculations used  $S_N$  methods, whereas the BAPL calculations were  $P_3$  epithermally and double  $P_1$  thermally with Marshak boundary conditions. The sets of calculations agree fairly well with perhaps a bias of +0.2 to +0.3% in  $k_{eff}$  demonstrated by GGA. Taken collectively, the BAPL, GGA, and SRL results appear to indicate ENDF/B-III underpredicts  $k_{eff}$  by about 0.4%. This underprediction has been attributed in part to an underestimation of  $\nu_{sf}$  for <sup>235</sup>U at thermal energies. Also shown in Table I are ENDF/B-IV data testing results obtained at SRL. These results indicate that there is a small improvement in the prediction of criticality for the ORNL spheres in going from Version III to Version IV. The observed increase in  $k_{eff}$  is primarily the result of a 0.7% increase in the ENDF/B-IV <sup>235</sup>U thermal values for  $\nu_{sf}$ . Fast leakage is increased somewhat using ENDF/B-IV because the effective nuclear temperature for the <sup>235</sup>U fission spectrum is 1.30 MeV in Version III and 1.323 MeV in Version IV.

TABLE I  
Calculations of  $k_{eff}$  for Thermal Benchmark Experiments

Benchmark	Description	$k_{eff}$ (ENDF/B-III)						$k_{eff}$ (ENDF/B-IV)
		ANC	BAPL	CRNL	GGA	ORNL	SRL	SRL
ORNL	Unref. spheres of uranyl nitrate sol.							
-1	H <sub>2</sub> O-235=1378; R=34.595 cm		0.9965		0.9999		0.9973	0.9996
-2	H <sub>2</sub> O-235=1177; R=34.595 cm		0.9963		0.9995			
-3	H <sub>2</sub> O-235=1033; R=34.595 cm		0.9933		0.9963			
-4	H <sub>2</sub> O-235=971; R=34.595 cm		0.9947		0.9980		0.9958	0.9976
-10	H <sub>2</sub> O-235=1835; R=61.011 cm		0.9931		0.9956		0.9935	0.9951
TRX	H <sub>2</sub> O moderated U lattices							
-1	Mod/Fuel = 2.35	0.9741	0.9872	0.9908	0.9791	0.985	0.9766	0.9975
-2	Mod/Fuel = 4.02	0.9823	0.9913	0.9876	0.9924	0.998	0.9859	0.9941
MIT	O <sub>2</sub> O moderated U lattices							
-1	Mod/Fuel = 20.74			0.9801	0.9898	0.984	0.9735	0.9883
-2	Mod/Fuel = 25.88			0.9804	0.9925	0.974	0.9752	0.9888
-3	Mod/Fuel = 34.59			0.9826	0.9996	0.975	0.9788	0.9911

Benchmark experiments TRX-1 and 2 in Table I correspond to lattice measurements by J. Hardy, Jr., D. Klein and J. J. Volpe.<sup>4</sup> These lattices are light water moderated and contain slightly enriched (1.3%) uranium rods with diameters of 0.4915 cm. Benchmarks MIT-1, 2, and 3 correspond to D<sub>2</sub>O-moderated lattices of natural uranium rods with diameters of 2.565 cm.<sup>5</sup> In contrast to the uranyl nitrate spheres discussed above, the lattice experiments include a large amount of <sup>238</sup>U and introduce geometric complexities more typical of commercial reactors. In addition to material bucklings, the TRX and MIT series of experiments determined several important activation parameters:

- $\rho^{28}$  = The ratio of epithermal-to-thermal  $^{238}\text{U}$  captures  
 $\delta^{25}$  = The ratio of epithermal-to-thermal  $^{235}\text{U}$  fissions  
 $\delta^{28}$  = The ratio of  $^{238}\text{U}$  fission to  $^{235}\text{U}$  fissions

These benchmark experiments directly test the thermal and epithermal cross sections for  $^{238}\text{U}$  capture and  $^{235}\text{U}$  fissions and the  $^{238}\text{U}$  fast fission cross section. They are sensitive to  $^{238}\text{U}$  inelastic scattering, the  $^{235}\text{U}$  fission spectrum, and the moderator cross sections.

The calculated values of  $k_{\text{eff}}$  reported by the laboratories for the lattices differ by as much as 1%. Part of this large variation may be attributed to the multiplicity of calculational methods used. Some laboratories used Monte Carlo, others the  $S_N$  approximation, and others integral transport theory. All the laboratories used detailed resonance treatments to account for resonance self-shielding, but again, there were variations in the methods and approximations. Differences can arise in the initial step of processing the ENDF/B point-wise data to multigroup form, but some of the laboratories were able to compare multigroup edits to eliminate this possibility. Taken collectively, the results obtained with ENDF/B-III very significantly under predict  $k_{\text{eff}}$ .

The SRL results in Table I indicate that ENDF/B-IV yields a 1.0% increase in  $k_{\text{eff}}$  for the TRX lattices and a 1.4% increase for the MIT lattices. These increases significantly improve the prediction of  $k_{\text{eff}}$ , particularly when they are applied to the average ENDF/B-III  $k_{\text{eff}}$  as determined by all the participating laboratories.

The calculated values of  $\rho^{28}$  in Table II correspond to a thermal cutoff energy of 0.625 eV. The ENDF/B-III values are about 10% higher than experiment. This suggests epithermal  $^{238}\text{U}$  neutron capture is being overpredicted by about 10%. This overprediction of epithermal  $^{238}\text{U}$  capture largely accounts for the 1.5 to 2.0% underprediction of  $k_{\text{eff}}$  for the benchmark lattices. The ENDF/B-IV results for  $\rho^{28}$  are about 3% lower than the ENDF/B-III results obtained at SRL.

TABLE II  
Ratio of Epithermal-to-Thermal  $^{238}\text{U}$  Captures<sup>a</sup>

Bench- Mark	$\rho^{28}$ (ENDF/B-III)						$\rho^{28}$ (ENDF/B-IV)	
	Exp	ANC	BAPL	CRNL	GGA	ORNL	SRL	SRL
TRX-1	1.311 $\pm 0.020$	1.438	1.422	1.419	1.416	1.44	1.454	1.417
TRX-2	0.830 $\pm 0.015$	0.906	0.899	0.874	0.877	0.91	0.890	0.868
MIT-1	0.498 $\pm 0.008$	-	-	0.5319	0.534	0.535	0.5683	0.5464
MIT-2	0.394 $\pm 0.002$	-	-	0.4365	0.435	0.430	0.4659	0.4483
MIT-3	0.305 $\pm 0.004$	-	-	0.3400	0.334	0.346	0.3624	0.3490

<sup>a</sup>Thermal cutoff energy = 0.625 eV.

Finally, it will be noted that the results for  $\delta^{25}$  and  $\delta^{28}$  for the lattices did not reveal deficiencies in the ENDF/B-III or ENDF/B-IV data. The first of these parameters tests the epithermal  $^{235}\text{U}$  fission cross section, while the second tests not only the  $^{238}\text{U}$  fast fission cross section, but also the  $^{238}\text{U}$  inelastic cross section and the  $^{235}\text{U}$  and  $^{238}\text{U}$  fission neutron spectra.

## Fast Reactor Benchmark Experiments

The prototypical designs of commercial breeder reactors employ a (Pu-U) $\text{O}_2$  fuel with a fertile-to-fissile atom ratio in the range 4:1 to 8:1 and are cooled with liquid sodium. Hence, the most important nuclear data for fast reactors includes the fission properties and capture cross section of plutonium and uranium, the moderating properties of uranium, oxygen, sodium and stainless steel isotopes, and, the capture cross section of sodium and stainless steel. The approximate uncertainty in these data and the accuracy desired for efficient breeder reactor design are listed in Table III. As is apparent from Table III, fast reactor design is most sensitive to the neutron production properties of the heavy metals and to the capture cross section of  $^{238}\text{U}$ . For most of the important nuclear data, the current uncertainty in the data is significantly larger than desired, and, it is for this reason that benchmark testing of fast reactor nuclear data serves a very useful purpose.

TABLE III

### NUCLEAR DATA IMPORTANT FOR FAST REACTORS

Nuclear Data	Approximate Uncertainty in Data <sup>(a)</sup>	Desired Accuracy <sup>(b)</sup>
$^{239}\text{Pu}(n,f)$	$\sim 5-10\%$	$< 1\%$
$^{239}\text{Pu}(n,\gamma)$	$\sim 10-15\%$	$< 7\%$
$^{238}\text{U}(n,f)$	$\sim 10\%$	$< 5\%$
$^{238}\text{U}(n,\gamma)$	$\sim 10-15\%$	$< 2\%$
$^{238}\text{U}(n,n')$ INEL	$\sim 10-15\%$	$< 8\%$
$^{16}\text{O}(n,n')$ EL	$\sim 5\%$	$< 10\%$
$^{23}\text{Na}(n,n')$ EL	$\sim 5\%$	$< 25\%$
$^{23}\text{Na}(n,\gamma)$	$\sim 20\%$	$< 40\%$
Stainless Steel(n, $\gamma$ )	$\sim 30\%$	$< 20\%$
Stainless Steel(n,n')	$\sim 10-20\%$	$< 20\%$
$\nu_{\text{TOT}}$ ; Pu,U	$\sim 2-3\%$	$< 1\%$
$\nu_{\text{DELAYED}}$ ; Pu,U	$\sim 5-15\%$	$< 3\%$
$\chi(E)$ ; Pu,U	$\sim 5\%$ in $\bar{E}$	

<sup>a</sup>See References 6-10.

<sup>b</sup>See References 11, 12.

A list of fast reactor benchmark experiments currently specified by CSEWG is given in Table IV. The benchmarks cover a range of compositions and geometry. The list includes the easy-to-calculate, small, single

TABLE IV

### FAST REACTOR BENCHMARK EXPERIMENTS<sup>a</sup>

Benchmark Reactor	Laboratory	Comments
JEZEREL	LASL	Bare sphere of Pu
VERA-11A	AWRE(UK)	Small Pu-C assembly
ZPR3-48	ANL	Small Pu-C assembly
ZEBRA-3	AEW(UK)	U-Pu metal assembly
GODIVA	LASL	Bare sphere of enriched U
VERA-1B	AWRE(UK)	Enriched U and C assembly
ZPR3-6F	ANL	U assembly, 1:1 fertile/fissile
ZPR3-11	ANL	U assembly, 7:1 fertile/fissile
ZPR3-12	ANL	U-C assembly
ZEBRA-2	AEW(UK)	U-C assembly
ZPPR-2	ANL	(Pu-U) $\text{O}_2$ Commercial breeder
ZPR6-7	ANL	(Pu-U) $\text{O}_2$ Breeder benchmark
ZPR3-56B	ANL	(Pu-U) $\text{O}_2$ FTR assembly
SEFOR	GE	(Pu-U) $\text{O}_2$ Doppler benchmark
ZPR6-6A	ANL	U $\text{O}_2$ benchmark

<sup>a</sup>See ENDF-202, CSEWG Benchmark Specifications, November, 1974.



composition metal spheres of plutonium and uranium (Jezebel and Godiya), early uranium oxide and carbide lattices or assemblies, and, most recently, large (Pu-U)<sub>2</sub>O<sub>2</sub> assemblies typical of current breeder reactor design (ZPR6-7, ZPPR-2, SEFOR). This series of benchmarks affords the testing of nuclear data over a range of neutron spectra important for fast reactor design. The metal spheres provide integral tests of nuclear data in a fission spectrum ( $\sim 100$  keV to 10 MeV) while the large, dilute oxide assemblies provide tests in a relatively softer spectrum ( $\sim 1$  keV to 10 MeV).

In order to serve as a benchmark, the experiment must be amenable to simple calculational modelling; uncertainties introduced in modelling must not be allowed to mask the errors that may be contained in the nuclear data. In this sense, the single composition spheres are especially useful. Calculational modelling becomes more complex as the materials in a composition increases and as the experiment attempts to more closely simulate breeder reactor designs. A good benchmark experiment must compromise these requirements, and, perhaps the most successful compromise to date is represented by the ZPR6-7 assembly.

ZPR6-7 was a zero-power critical assembly constructed by loading platelets of fuel, coolant and structural materials into a large stainless steel matrix. The matrix loading pattern is shown in Fig. 1; the loading pattern is symmetric about the Pu-U metal fuel plate and includes platelets of Fe<sub>2</sub>O<sub>3</sub>, U<sub>3</sub>O<sub>8</sub> and sodium canned in stainless steel. This "unit-cell" loading pattern was repeated throughout the core region of the matrix to produce a large uniform composition loading. The core was surrounded with a thick depleted uranium metal reflector and the critical assembly matrix loading, appearing cylindrical in shape, is shown in Fig. 2.

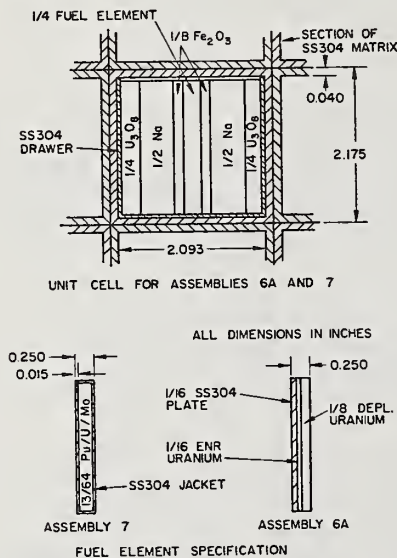


Fig. 1. Cross Section of Unit-Cell Showing Matrix and Plate Loaded Drawer, ZPR-6 Assemblies 6A and 7. ANL Neg. No. 116-888.

The measurements in these benchmark experiments that are most often used to test nuclear data are criticality, reaction rate ratios and reactivity coefficients. The measurements are integral in nature. The typical imprecision in these measurements is  $\pm 0.2$ - $0.5\%$  for criticality,  $\pm 2\%$  for reaction rate

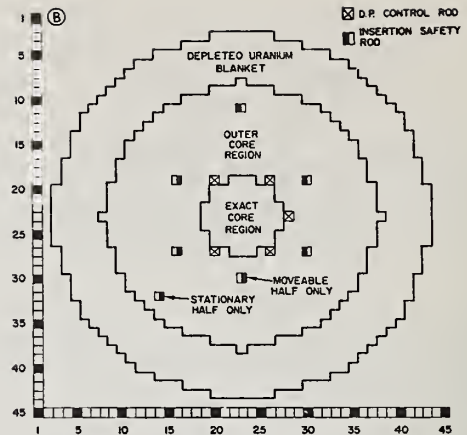


Fig. 2. Radial Cross Section for 96.2 Th Excess Reactivity, As-Built ZPR-6 Assembly 7. ANL Neg. No. 116-889.

ratios and  $\pm 5\%$  for reactivity coefficients. These estimates of imprecision do not include possible systematic errors.

Some results of benchmark tests with the most recent versions of ENDF/B are presented in Table V. (The HEDL results have been extracted from the comprehensive data testing by Hardie et al.<sup>13</sup>) Computations with two sets of cross section processing codes are listed; the ETOX/IDX code in use at HEDL<sup>16,17</sup> and the MC<sup>2</sup> code in use at ANL.<sup>18</sup> Comparing calculated-to-experimental ratios obtained with ENDF/B versions III and IV, there appears to be little change in the predictability of integral measurements with the exception of the <sup>238</sup>U fission rate ratios ( $f^{28}/f^{49}$ ,  $f^{25}$ ) and reactivity worths ( $\rho^{28}$ ). The improvement in the calculated <sup>238</sup>U parameters can be attributed to the difference between Version-III and Version-IV <sup>238</sup>U cross sections; the <sup>238</sup>U fission cross section increased  $\sim 1.5\%$  while the capture cross section decreased  $\sim 3$ - $10\%$  below 1 MeV.<sup>19</sup> The <sup>238</sup>U capture cross section impacts very significantly upon the calculated spectra in fast reactors (and hence reaction rates in general) and accounts for a large portion ( $\sim 35\%$ ) of the neutron absorption in a fast reactor.

TABLE V

Fast Reactor Benchmark Tests; Calculated-to-Experimental Ratios for Some Important Parameters

Benchmark Experiment	Parameter	ETOX/IDX Calculations (HEDL) <sup>a</sup>		MC <sup>2</sup> -1 Calculations (ANL) <sup>b</sup>		MC <sup>2</sup> -2 Calculations (ANL) <sup>c</sup>	
		ENDF/B-III	ENDF/B-IV	ENDF/B-III	ENDF/B-III	ENDF/B-IV	ENDF/B-IV
ZPR 6-7	k	0.9926	0.9917	0.992	0.987	0.986	
	$c^{28}/f^{49}$	1.095	1.088	1.09	1.111	1.095	
	$f^{28}/f^{49}$	0.928	0.951	0.99	0.916	0.952	
	$\rho^{49}$	1.23	1.22	1.27	1.27	1.25	
	$\rho^{28}$	1.09	1.02	1.16	1.11	1.05	
ZPR 6-6A	k	0.9988	0.9967	0.992	-	-	
	$c^{28}/f^{25}$	1.022	1.017	1.03	-	-	
	$f^{28}/f^{25}$	0.900	0.926	0.90	-	-	
ZPR 3-48	k <sup>d</sup>	0.9997	1.0015	0.993	-	-	
	$c^{28}/f^{25}$	0.976	0.963	0.94	-	-	
	$f^{28}/f^{25}$	0.977	1.026	0.96	-	-	

<sup>a</sup>Ref. 13. Results corrected to equivalent, 2-0, heterogeneous reactor systems for calculation of k.

<sup>b</sup>Ref. 14. Results corrected to equivalent, 2-0, heterogeneous reactor systems for calculation of k.

<sup>c</sup>Ref. 15. Results computed for a homogeneous spherical reactor model, corrected to equivalent 2-0 heterogeneous model by adding 0.0184.

<sup>d</sup>A recent change in the benchmark specifications for ZPR 3-48 accounts for the higher k value computed with ENDF/B-IV.



There have also been significant changes in the important fission cross section; the  $^{235}\text{U}$  and  $^{239}\text{Pu}$  cross sections have been increased 2-7% above 3 MeV and generally lowered (~1-10%) over the lower energy ranges. These changes along with modifications to other important data (i.e.,  $\nu$ ) have combined to yield very little change in calculated criticality. These results serve to indicate one of the outstanding difficulties in the validation of evaluated cross section sets by a limited set of integral measurements. Many pieces of nuclear data contribute importantly to the calculation of a fast reactor and it is very possible to observe simultaneous modifications to sets of nuclear data which impact only slightly on some calculated integral parameters (e.g.,  $k$ ) while affecting others more sensitively. For this reason, it becomes more important to consider these sensitive parameters as the evolution and refinement of a nuclear data set continues.

Comparing calculated results obtained with different cross section processing codes in Table V indicates another difficult aspect of fast reactor benchmark testing. The processing codes employ many approximations and algorithms in the generation of a broad energy group cross section set from the basic evaluated data. Where these approximations and algorithms differ, benchmark testing results will also differ as is the case comparing the MC<sup>2</sup>-II<sup>(15)</sup> and ETOX/IDX<sup>13</sup> Version-IV calculations. While the difference is only small for the central spectral parameters listed, there is a large difference in  $k$ . This difference, in part, may be attributed to the treatment of neutron emission spectra in the codes. Recent modifications to the MC<sup>2</sup> code that are present in the current MC<sup>2</sup>-II version include the capability for isotope-dependent fission neutron spectra and improvements in the treatment of inelastic scattering matrices and unresolved resonance region capture.<sup>15</sup> Finally, it is noted that in general, a comprehensive listing of data testing results would demonstrate that  $k$  is calculated too low, the capture rate in  $^{238}\text{U}$  is calculated too high relative to  $^{239}\text{Pu}$  fission and reactivity worths are overpredicted. Thus considerable latitude exists for modification and improvement in fast reactor nuclear data.

### Shielding Benchmark Experiments

For shielding benchmarks, the important parameters being tested include neutron total cross sections in the MeV range (the ORNL "broomstick" series of experiments), secondary gamma-ray production cross sections at both thermal-neutron energies and averaged over neutron energies in the MeV range (ORNL secondary gamma-ray experiments), and neutron cross sections in the range 8-14 MeV (the LLL pulsed sphere experiments). Table VI presents a list of the experiments so far adopted by the CSEWG shielding subcommittee as shielding benchmarks. They are all integral experiments in the sense that they do not determine unique cross sections defined for a particular neutron and/or gamma-ray energy.

A good benchmark experiment must have a well-defined source having a known spatial, energy, and angular distribution. It should use detectors which have known response functions. The experimental results should be reduced to fluxes, average cross sections, or similar units independent of the detector. The experiment should be calculable in one- or at most two-dimensional geometry, since the transport calculations are both expensive and time consuming. Further, the integrity of a benchmark experiment must be verified by either another experiment that measures the

same quantities or by an accurate calculation of the experiment before the benchmark is adopted.

TABLE VI

List of Shielding Benchmarks

Experiment	Laboratory	Reference <sup>a</sup>	Quantity Measured
Iron Broomstick (8, 12 in.)	ORNL	SOT1(ENOF-166)	$\bar{\sigma}_T$ (1-8 MeV)
Oxygen Broomstick (5 ft LOX)	ORNL	SOT2(ENOF-167)	$\bar{\sigma}_T$ (2-8 MeV)
Nitrogen Broomstick (3 ft LN)	ORNL	SOT3(ENOF-168)	$\bar{\sigma}_T$ (1-10 MeV)
Sodium Broomstick (2 ft solid)	ORNL	SOT4(ENOF-169)	$\bar{\sigma}_T$ (1-11 MeV)
Stainless Steel Broomstick (8 in.)	ORNL	SOT5(ENOF-170)	$\bar{\sigma}_T$ (1-7 MeV)
Gamma-Ray Production from Thermal Capture in Iron, Stainless Steel, Nitrogen, and Sodium.	ORNL	SOT6(ENOF-176)	$\bar{\sigma}_n$ (1-11 MeV in 0.5 MeV wide gamma-ray bins)
Gamma-Ray Production Averaged over a Neutron Spectrum in the Range 1-8 MeV from Iron, Stainless Steel, Oxygen, and Sodium	ORNL	SOT7(ENOF-177)	$\bar{\sigma}_n$ (1-6 MeV in 0.5 MeV wide gamma-ray bins)
ZPPR/FTR-2 Shield Experiment	ANL	SOT8(LA-5288)	TLO heating rates neutron spectra foil activation
Neutron Measurements through a Mock-up of the FFTF Radial Shield	AI	SDT9(ENOF-181)	Neutron fluxes
Pulsed Sphere Neutron Measurements	LLL	SOT10(UCRL-51144)	Neutron fluxes (8-14 MeV)
Neutron Transport through Thick Shields of Iron and Stainless Steel	ORNL	SDT11(ENOF-188)	Neutron fluxes Bonner ball counting rates
Neutron Transport through Thick Shields of Sodium	ORNL	SDT12(ENOF-189)	Neutron fluxes Bonner ball counting rates

<sup>a</sup>See ENOF-202, CSEWG Benchmark Specifications, November 1974.

An example of a shielding benchmark is the ORNL "broomstick" type shown in Fig. 3. Long, small diameter cylindrical samples of materials were placed in a collimated neutron beam and transmitted neutron spectra were obtained using an NE-213 spectrometer. The detector was placed in "good" geometry so that only uncollided neutrons were observed. The measurements can determine an average cross section for energies in the MeV range behind very thick samples. Thus the accuracy of minima in the total cross section can be checked, since the minima dominate the transmitted flux in the broomstick experiments. These minima are of the utmost importance in shielding.

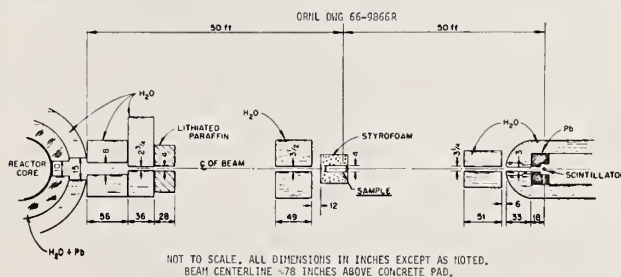


Fig. 3. Schematic of Experimental Arrangement for a "Broomstick" Shielding Experiment.

Figure 4 shows a comparison of the measured fluxes transmitted through 8 and 12 in. of iron (denoted by the hatched area) with calculated fluxes using ENDF/III (triangles) and ENDF/IV (circles). The calculated uncollided fluxes have been smoothed with the energy resolution function of the NE-213 spectrometer system. The hatched area represents the 63% confidence limits of the unfolded measurement. The comparison shows that Version-IV is considerably better than Version-III from 0.8 to 2.5 MeV. The two versions are identical beyond 2.5 MeV, however, and discrepancies still exist between the measured and calculated data from 2.5 to 5 MeV. Behind 12 in. of iron the Version-III average cross

sections are about 10% higher than the measured values in the range 1-2.5 MeV, while the Version-IV average cross sections are about 4% higher.

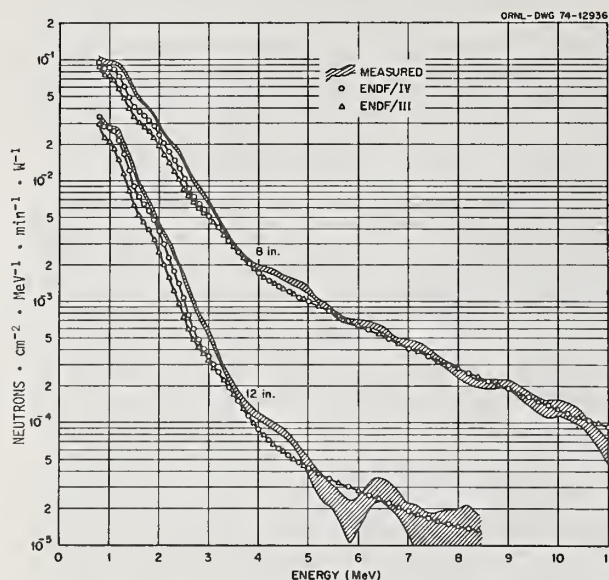


Fig. 4. Measured and Calculated Neutron Flux Transmitted Through an Iron "Broomstick".

Results of comparing calculations using ENDF/IV with the remaining broomstick experiments indicate that oxygen, nitrogen, and stainless steel average cross sections check to within about 2% in the vicinity of the minima but that sodium is uniformly about 6% too low in ENDF/IV.

The ORNL measurements of neutron induced secondary gamma rays, SDT6 and SDT7, were also accomplished in a very simple one-dimensional geometry. Analysis of the results shows that the gamma-ray production cross sections from thermal-neutron capture using ENDF/IV usually agree with the results of SDT6 within the accuracy of the experiment ( $\pm 15\%$ ). The average gamma-ray production cross sections from neutrons in the range 1-6 MeV usually agree with the results of SDT7 within the accuracy of the experiment ( $\pm 30\%$ ).

Version-IV data have not been checked against any of the remaining benchmarks except for the pulsed sphere experiment (SDT10) and the thick sodium experiment (SDT12). Much better agreement in the neutron spectrum is found using ENDF/IV than ENDF/III for SDT10. Comparison with SDT12 shows an overprediction of the neutron spectrum above 1 MeV by about 20% through 5 ft of sodium and 30% through 10 ft. The neutron spectrum between 100 keV and 1 MeV is overpredicted by 5% through 5 ft, 40% through 10 ft, and 60% through 12.5 ft of sodium. Fluxes below 1 keV are underpredicted by 10% through 10 ft and 12.5 ft, and by 25% through 15 ft.

In general, calculations using Version-IV agree with the benchmarks as well as or better than calculations using Version-III. For some materials, notably chromium, nickel and manganese, no gamma-ray production data existed in Version-III. For others, such as sodium, Versions-III and -IV were almost identical, differing only in the extension to 20 MeV.

Future benchmarks are envisioned from existing measurements on additional materials and/or additional thicknesses in the broomstick series, additional materials in the two gamma-ray production experiments, an extension of the iron transport experiment to include existing neutron spectra through 2 and 3 ft of iron, and an existing photon interaction experiment.

### Benchmark Experiments for Dosimetry

A special set of evaluated neutron cross sections designated as the Dosimetry file, has been established as an aid to the Interlaboratory Reaction Rate Program (ILRR). The program is just recently and very completely described in Ref. 20. Dosimetry is primarily concerned with the characterization of reactor spectra by a set of reaction rate indices.

A dosimetry benchmark experiment consists of reaction rate measurements in a well defined neutron spectrum. Five benchmark tests have been specified by CSEWG and they include reaction rate measurements in a thermal spectrum, a fission spectrum, the relatively hard spectra of the  $\Sigma\Sigma$  and CFRMF facilities, and measurements of resonance integrals. The results of the reaction rate measurements are reported as spectrum averaged cross sections; i.e.,

$$\hat{\sigma} = \frac{\int_{10^{-5} \text{ eV}}^{20 \text{ MeV}} \sigma(E) \phi(E) dE}{\int_{10^{-5} \text{ eV}}^{20 \text{ MeV}} \phi(E) dE}$$

The 26 isotopes and 36 reactions for which dosimetry data is available are given in Table VII.<sup>21</sup> The data covers a broad range of reaction types and spectral indices.

The dosimetry data is tested very simply by computing the spectrum averaged cross section for a given spectrum, or the resonance integral as defined by

$$I = \int_{E_c}^{20 \text{ MeV}} \sigma(E) \frac{dE}{E}$$

The results of benchmark tests using ENDF/B-IV and measurements in three spectra are given in Table VII. All calculations were performed at BNL. These tests indicate acceptable agreement for a few reactions but there does exist a wide range of disagreement, especially for some of the important reactions. Of the integral spectrum reactions used as broad energy range indices, only  $^{115}\text{In}$  shows some degree of agreement.  $^{238}\text{U}(n,\gamma)$  is underpredicted by  $\sim 13\%$  in both  $\Sigma\Sigma$  and CFRMF and  $^{197}\text{Au}(n,\gamma)$  is underpredicted by  $\sim 30\%$  in  $\Sigma\Sigma$ . For the important fission cross sections,  $^{235}\text{U}(n,f)$  is computed  $\sim 3\%$  low in CFRMF while  $^{239}\text{Pu}(n,f)$  is consistently computed a few percent low in all three spectra. The threshold fission reactions are used as high energy spectral indices. Both  $^{232}\text{Th}(n,f)$  and  $^{238}\text{U}(n,f)$  are consistently calculated low with the greatest disagreement ( $\sim 10-12\%$ ) in the fission spectrum. For the low energy absorbers, the standard cross section,  $^{10}\text{B}(n,\alpha)$  and  $^6\text{Li}(n,\alpha)$  disagree by 5 and 10%, respectively, with the measurements in CFRMF.

The need for improvement in the dosimetry file is evident. Additional measurements of microscopic cross sections, especially threshold reactions and heavy element capture, are necessary. The measurement and specification of "standard" neutron spectra are also required. Benchmark measurements in spectra that have been specified or measured with the latest spectroscopy methods would be useful.



TABLE VII

Dosimetry Benchmark Tests Using ENDF/B-IV.<sup>21</sup>

Reaction	$\hat{\sigma}(\Sigma)$ Dosimetry File (mb)	$\hat{\sigma}(\Sigma)^{(a)}$ (mb)	$\hat{\sigma}(\text{CRFMF})$ Dosimetry File (mb)	$\hat{\sigma}(\text{CFRMF})^{(b)}$ (mb)	$\hat{\sigma}_f(T = 1.29)$ Dosimetry File (mb)	$\hat{\sigma}_f(T = 1.32)$ Dosimetry File (mb)	$\hat{\sigma}_f^{(c)}$ (mb)
<sup>6</sup> Li(n, total He)	924.1		998.1	900 ± 39	486.9	486.0	
<sup>10</sup> B(n, total He)	1605.0		1843.6	1940 ± 60	515.2	512.3	
<sup>23</sup> Na(n,γ)	1.392		1.842		0.295	0.291	
<sup>27</sup> Al(n,p)	1.047	1.033 ± 0.103	0.917	0.931 ± 0.033	3.926	4.222	4.0 ± 0.4
<sup>27</sup> Al(n,α)	0.208	0.182 ± 0.005	0.156	0.172 ± 0.053	0.709	0.801	0.73 ± 0.02
<sup>32</sup> S(n,p)	16.32		13.90		61.32	63.87	69 ± 2
<sup>45</sup> Sc(n,γ)	18.79		20.06	25.0 ± 0.009	5.982	5.879	
<sup>46</sup> Ti(n,p)	2.523		2.195	2.78 ± 0.097	9.503	10.24	12.3 ± 0.3
<sup>47</sup> Ti(n,np)	5 × 10 <sup>-4</sup>		0.0				
<sup>47</sup> Ti(n,p)	5.712		4.78	4.44 ± 0.02	20.62	21.40	20.0 ± 2.0
<sup>48</sup> Ti(n,np)	5 × 10 <sup>-4</sup>		0.0				
<sup>48</sup> Ti(n,p)	0.0510		0.034	0.073 ± 0.003	0.171	0.194	0.32 ± 0.02
<sup>55</sup> Mn(n,2n)	0.080		0.0	18.6 ± 0.58	0.302	0.367	0.25 ± 0.01
<sup>54</sup> Fe(n,p)	19.56		16.85		74.04	77.67	82.5 ± 2.0
<sup>56</sup> Fe(n,p)	0.296	0.273 ± 0.008	0.238		1.033	1.145	1.07 ± 0.06
<sup>58</sup> Fe(n,γ)	5.093		6.13	6.52 ± 0.22	1.709	1.695	
<sup>59</sup> Co(n,2n)	0.056		0.0		0.215	0.262	
<sup>59</sup> Co(n,γ)	55.60		89.88	97.6 ± 3.6	6.517	6.433	
<sup>59</sup> Co(n,α)	0.043		0.033		0.149	0.168	0.156 ± 0.006
<sup>58</sup> Ni(n,2n)	6.88 × 10 <sup>-4</sup>		0.0		3.9 × 10 <sup>-3</sup>	4.9 × 10 <sup>-3</sup>	
<sup>58</sup> Ni(n,p)	26.23	28.8 ± 0.7	22.26	25.6 ± 0.8	97.21	101.5	113 ± 3
<sup>60</sup> Ni(n,p)	0.683		0.569		2.413	2.658	
<sup>63</sup> Cu(n,γ)	41.53	40.0 ± 2.0	48.63	48.4 ± 2.6	11.15	11.01	10.1 ± 1.5
<sup>63</sup> Cu(n,α)	0.104		0.080		0.354	0.396	0.50 ± 0.05
<sup>85</sup> Cu(n,2n)	0.102		0.0		0.383	0.464	
<sup>115</sup> In(n,n')	54.37	58.6 ± 1.2	44.033	53 ± 3	163.9	166.8	188 ± 4
<sup>115</sup> In(n,γ)	276.97	261 ± 9	301.4	300 ± 11	138.4	136.6	146 ± 5
<sup>127</sup> I(n,2n)	0.393		0.068		1.379	1.368	1.09 ± 0.05
<sup>197</sup> Au(n,γ)	331.41	442 ± 8	414.87	452 ± 14	86.35	84.92	88 ± 5
<sup>232</sup> Th(n,f)	19.77	21.0 ± 1.3	16.08		67.25	69.01	83.0 ± 3.5
<sup>232</sup> Th(n,γ)	261.37		286.26		105.4	103.8	
<sup>235</sup> U(n,f)	1598.3	1589 ± 55	1588.0	1659 ± 53	1243.2	1243.2	1250 (REF)
<sup>238</sup> U(n,f)	86.46	87.4 ± 3.1	70.04	81.0 ± 0.3	288.9	295.4	328 ± 10
<sup>238</sup> U(n,γ)	223.16	194 ± 8	231.76	196 ± 11	76.79	75.60	
<sup>237</sup> Np(n,f)	625.52	634 ± 22	551.01	591 ± 21	1313.2	1322.8	1370 ± 75
<sup>239</sup> Pu(n,f)	1753.3	1875 ± 66	1771.4	1930 ± 60	1780.1	1782.4	1859 ± 60

<sup>a</sup>Measured results; see Ref. 8 of Ref. 21.<sup>b</sup>Measured results; see Ref. 11 of Ref. 21.<sup>c</sup>Measured results in a fission spectrum; see Ref. 12 of Ref. 21.Benchmark Experiments for Fission Product Data

The fission product file of ENDF/B-IV contains cross sections and decay data for 824 nuclides. In addition, fission yield data is given for six fissionable nuclides. The cross section and decay parameters (half lives,  $\beta$  and  $\gamma$  energies, branching, etc.) constitute a collection of about 300000 data entries and the fission yields, 13000 entries. The objectives of benchmark testing should be to infer the accuracy of this extensive set of data and, if possible, to indicate where readjustment of the data may be made according to differential measurements or theoretical calculation uncertainty tolerances. This should be done at least for the more important fission product nuclide contributors (in general, isotopes with large cumulative yields).

Integral experiments which have been made and should be considered for use as "Benchmarks" include the following four areas:

- fission product absorption
- decay heat following "burst" or long time exposure fission
- delayed and prompt neutron yields
- $\beta$  and  $\gamma$  spectra production.

Reactivity measurements have been made at the STEK<sup>22</sup> and CFRMF<sup>23</sup> facilities for individual important fission product nuclides in fast reactor spectra. At the STEK facility experiments were made in several fast assemblies (STEK-500, 1000, 2000, 3000, 4000) for about 80 individual fission product nuclides and 4 "lumped" fission product sets. In addition, at CFRMF direct capture measurements<sup>24,25</sup> were performed for several important fission product nuclides. At Bettis Laboratories absorption measurements have been completed for samples of <sup>233</sup>U, natural uranium, <sup>238</sup>U and natural thorium. Irradiations were made in high-flux facilities in different thermal neutron spectra and for different durations including exposure to more than 90% depletion in fissile material and more than 30,000



MWd/tonne in fertile material.<sup>26</sup> A number of resonant integral measurements have been made in the past and a good recent source which evaluates these measurements and their uncertainties is BNL-325 (June, 1973).<sup>27</sup>

Tobias<sup>28</sup> and Perry et al<sup>29</sup> have reviewed previous (before 1973) integral measurements of decay heat following both "burst" and long time exposure fission. These include beta, gamma, and total decay energy experiments. Perry et al<sup>29</sup> propose after-heat functions based on these experiments for thermal-neutron fission of <sup>235</sup>U for the decay time interval of 1 sec. to  $5 \times 10^5$  sec. Recently reported decay heat measurements include the calorimetric experiments of Lott et al<sup>30</sup> for <sup>235</sup>U and high thermal neutron flux ( $>10^{14}$  n/cm<sup>2</sup> - sec) experiments by Gunst et al<sup>31</sup> for samples of <sup>235</sup>U, <sup>233</sup>U, <sup>239</sup>Pu and <sup>232</sup>Th.

Delayed neutron yield experiments have been reviewed by Cox et al<sup>32</sup> and this work was used as a basis for the ENDF/B-IV evaluation. Prompt neutron yield evaluations, on ENDF/B-IV for example, can serve as integral tests of the direct fission yields.

An example of an integral experiment which constitutes a sensitive measure of fission yields and gamma emission for about thirty fission product nuclides is delayed photoneutron production from Be and D.<sup>33</sup> Harris<sup>34</sup> has analyzed integral measurements of this type.

The ENDF/B-IV fission product file was just recently released (January 1975) so that there is currently a large effort in making comparison calculations with integral experiments. Decay heat and gamma spectra calculations have been reported at this conference by Schenter and Schmittroth<sup>35</sup> and Stamatelatos and England.<sup>36</sup>

Due to the extensive size of the data to be tested and the numerous applications for which fission product data is needed there continues to be several integral experiments in progress which should, when completed, be candidates for benchmark testing. These include continued reactivity and capture measurements at the CFRMF, calorimetric experiments at LASL and Berkeley laboratories, and beta and gamma decay heat measurements at ORNL. A comprehensive status of world wide activities related to fission product data is given in the review papers and the to-be-published summary of the "IAEA Panel on FPND" held in Bologna, Italy, November 1973.

#### References

1. F. J. McCrosson, "Thermal Data Testing of ENDF/B-III and Prognosis for ENDF/B-IV." Trans. Amer. Nucl. Soc. 18, 352 (1974).
2. R. Gwin and D. W. Magnuson, "The Measurement of Eta and Other Nuclear Properties of <sup>233</sup>U and <sup>235</sup>U in Critical Aqueous Solutions." Nucl. Sci. Eng. 12, 364 (1962).
3. A. Staub, D. R. Harris, and M. Goldsmith, "Analysis of a Set of Critical Homogeneous U-H<sub>2</sub>O Spheres." Nucl. Sci. Eng. 34, 263 (1968).
4. J. Hardy, Jr., D. Klein, and J. J. Volpe, "A Study of Physics Parameters in Several H<sub>2</sub>O-Moderated Lattices of Slightly Enriched and Natural Uranium." Nucl. Sci. Eng. 40, 101 (1970).
5. T. J. Thompson, et al, "Heavy Water Lattice Project Final Report." MIT-2344-12 (1967).
6. M. G. Sowerby, B. H. Patrick and D. S. Mather, "A Detailed Report on the Simultaneous Evaluation of the Fission Cross-Sections of U-235, Pu-239 and U-238 and the U-238 Capture Cross-Section in the Energy Range 100 eV to 20 MeV." AERE-R-7273, 1973.
7. W. P. Poenitz, "Recent Experimental Data for Heavy Nuclei." Nuclear Data for Reactors, Vol. II, IAEA, 1970.
8. G. deSaussure and R. B. Perez, "Present Status of Cross Section Data of the Fissile and Fertile Isotopes for Fast Reactors." Conf. on Advanced Reactors; Physics, Design and Economics, Atlanta, Ga., 1974.
9. M. Segev, S. Yiftah, V. Gor and L. Gitter, "Comparative Analysis of Neutron Data Files as a Sensitivity Study." Nucl. Sci. Eng. 55, 1974.
10. R. D. McKnight, L. G. LeSage and J. M. Christenson, "Sensitivity Studies of the Effects of Nuclear Data Uncertainties for the Higher Plutonium Isotopes Upon Fast Reactor Design." ibid Ref. 8.
11. H. H. Hummel and W. M. Stacey, Jr., "Sensitivity of a Fast Critical Assembly to Uncertainties in Input Data Determined by Perturbation Theory." Nuc. Sci. Eng. 54, 1974.
12. E. M. Bohn, "The Central Worth Discrepancy in Three Fast Reactor Benchmark Critical Assemblies." ANL-75-14, 1975.
13. R. W. Hardie, R. E. Schenter and R. E. Wilson. "An Analysis of Selected Fast Critical Assemblies Using ENDF/B-IV." (to be published in Nuc. Sci. Eng, 1975).
14. B. A. Zolotar, E. M. Bohn and K. D. Dance, "Benchmark Tests and Comparisons Using ENDF/B Version-III Data." Trans. Am. Nucl. Soc. 15(2), (1972).
15. Private communication from H. Henryson, Argonne National Laboratory, 1975.
16. R. E. Schenter, J. L. Baker and R. B. Kidman, "ETOX, A Code to Calculate Group Constants for Nuclear Reactor Calculations." BNWL-1002, Battelle Northwest Laboratory (1969).
17. R. W. Hardie and W. W. Little, Jr., "1DX, A One-Dimensional Diffusion Code for Generating Effective Nuclear Cross Sections." BNWL-954, Battelle Northwest Laboratory (1969).
18. B. J. Toppel, A. M. Rago and D. M. O'Shea, "MC<sup>2</sup> - A Code to Calculate Multigroup Cross Sections." ANL-7318, Argonne National Laboratory (1967).
19. Private communication from R. D. McKnight, "Review of ENDF/B Version 4 Nuclear Data." ZPR-TM-191, (1975).
20. Nuclear Technology, February 1975.
21. B. A. Magurno and O. Ozu, "ENDF/B File for Dosimetry Applications." Nuc. Tech., February 1975.
22. H. Gruppelaar, et al., "Evaluation, Uncertainty Estimation and Adjustment of Capture Cross Sections for Fission Product Nuclei." Conf. on Nuclear Cross Sections and Technology, Washington, D. C., March 3-7, 1975.

23. J. W. Rogers, et al., "Comparison of Measured and Calculated Reactivities in CFRMF." Conf. on Nuclear Cross Sections and Technology, Washington, D. C., March 3-7, 1975.
24. R. A. Anderl, et al., "Integral Capture Cross-Section Measurements in CFRMF for LMFBR Control Materials." Conf. on Nuclear Cross Sections and Technology, Washington, D. C., March 3-7, 1975.
25. Y. D. Harker and E. H. Turk, "The Use of CFRMF Integral Data in Cross Section Evaluations." Conf. at Kiamesha Lake, N.Y., CONF-720901, Book 2, p. 613, (1972).
26. S. B. Gunst, et al., "Measurements and Calculations of Heavy Isotopes in Irradiated Fuels and of  $^{233}\text{U}$  Fission-Product Poisoning." WAPD-TM-1182 (July 1974).
27. S. F. Mughabghab and B. I. Garber, "Neutron Cross Sections, Vol. 1, Resonance Parameters." BNL-325 (June 1973).
28. A. Tobias, J. Nucl. Energy, 27, 725 (1973).
29. A. M. Perry, et al., "Fission-Product Afterheat - A Review of Experiments Pertinent to the Thermal-Neutron Fission of  $^{235}\text{U}$ ," ORNL-TM-4197 (October 1973).
30. P. M. Lott, et al., "Mesures Calorimetriques De La Puissance Emise Par Les Produits De Fission De U-235 Pour Des Temps De Refroidissement Comprise Entre 70 Secondes Et  $7.10^6$  Secondes." B.I.S.T. Commissariat A L'Energie Atomique, No. 181 (Mai 1973). (French)
31. S. B. Gunst, et al., "Decay Heating Measurements and Calculations for Irradiated  $^{235}\text{U}$ ,  $^{233}\text{U}$ ,  $^{239}\text{Pu}$ , and  $^{232}\text{Th}$ ." WAPD-TM-1183 (July 1974).
32. S. A. Cox, "Delayed Neutron Data -- Review and Evaluation." ANL/NDM-5, April 1974.
33. T. R. England and D. R. Harris, Trans. Am. Nucl. Soc., 18, 331 (1974).
34. D. R. Harris, Naval Reactor Physics Handbook, Vol. 1, TID-7630, A. Radkowsky, Editor, p. 1103-1122 (1964).
35. R. E. Schenter and F. Schmittroth, "Radioactive Decay Heat Analyses." Conf. on Nuclear Cross Sections and Technology, Washington, D. C., March 3-7, 1975.
36. M. G. Stamatelatos and T. R. England, "Fission Product Gamma-Ray and Photoneutron Spectra." Conf. on Nuclear Cross Sections and Technology, Washington, D. C., March 3-7, 1975.



# ESTIMATED UNCERTAINTIES IN NUCLEAR DATA -- AN APPROACH\*

F. G. Perey

Oak Ridge National Laboratory  
Oak Ridge, Tennessee 37830

The need to communicate estimated uncertainties in evaluated nuclear data to be used in the assessment of their adequacy in applications has been recognized in the ENDF/B system. Starting with ENDF/B-IV, the data files contain formatted data describing the estimated covariances of some of the microscopic cross sections in such a form that they can be processed by computer codes to generate covariance matrices of quantities used in solving neutron transport problems such as group cross sections. The basic concepts behind the representation of such quantities will be described and the work done so far in the representation and manipulation of such quantities will be discussed. Problem areas not yet addressed in ENDF/B-IV but under study will be discussed.

(Evaluations, estimated uncertainties, correlations, covariances, data adequacy, neutron transport)

## Introduction

By definition nuclear technologies are those for which the design, operation and analysis of some systems are dependent upon the values of some nuclear properties which we shall refer to as basic microscopic nuclear data. Each technology develops its appropriate tools and methods which use as input either the basic microscopic data directly or some quantities which we will refer to as basic data, which can in principle at least be obtained by suitable manipulations of the basic microscopic data. We are not trying to make a subtle semantic distinction regarding microscopic data, but for the purposes of this talk we will say that basic data are any physical quantities which have a meaning and value independent of the applications in which they are used as opposed to some application-dependent parameters. Each technology can be said to require an appropriate basic data base. The question of adequacy of a basic data base for a technology is a very important one and the main purpose of conferences such as this one is to bring together the providers, whether they be measurers and/or evaluators, and the users of the basic data in order to discuss the areas of needs and inadequacies for various nuclear technologies. The purpose of this paper is to report the progress made recently within CSEWG (the U.S. Cross Section Evaluation Working Group) to communicate the degree of confidence we have in the basic nuclear data so that the question of adequacy of the data for any specific applications can be addressed realistically and quantitatively for any specific use. These efforts have been limited so far to the area of the evaluated neutron cross sections contained in the ENDF/B files and therefore will be of interest mostly for problems involving neutron transport such as fission and fusion reactor work. There is a general feeling that the time and costs involved to bring the accuracy of the basic data to such a level that they contribute a totally negligible fraction of the uncertainties in applications would be so large that we cannot adopt these as operational goals for much of the basic nuclear data. For a number of nuclear technologies, for instance fast reactors, the present goals concerning accuracy in the basic data are formulated in terms of contributing no more than a certain targeted uncertainty in some important parameters. The tools we will describe will therefore be of assistance in determining for which basic nuclear data we have met the goals and where to apply most effectively our limited resources to meet them.

We shall first discuss how we presently address the question of nuclear data adequacy. Then we shall present an interpretation of the evaluated data files which would allow us to address the question of adequacy in a logical and realistic manner. We shall

finally describe the progress made to date in ENDF/B and what remains to be done.

## Data Adequacy

We all realize that adequacy in data must always be addressed in terms of specific applications. We shall say that data are adequate for a specific application when the desired quantities can be realistically predicted to a preassigned degree of confidence. Operationally it does the practitioner of a technology little good to know that he can calculate only results which he already knows through measurements or observations except as a check on his methods. It is only when the required degree of confidence with which one can predict all of the needed behavior of unbuilt systems is achieved that the data can be said to have adequate accuracy for the systems in question. This definition of adequacy in nuclear data does not say anything about how accurate some of the results must be since sometimes no great accuracy may be needed in these results, nor does it say anything either about how accurate any specific data must be since the results may have little sensitivity to the specific data in question. It is fair to say that what is important is the overall accuracy of a calculated result and that we must include any contribution from inadequacies in the methods used to perform the calculations. It is to the extent that the nuclear data contribute a significant fraction of the total uncertainties that data uncertainties are relevant; otherwise we must talk about uncertainties in methods.

The traditional method of testing the adequacy of data and calculational methods for some applications is to perform integral experiments on simpler and less expensive systems which have some of the attributes of the desired final system and to compare the results of predictions for these integral experiments with observations. As far as usefulness for testing data and methods which apply to the final system, this technique is valid only for those results which have in the integral experiments very similar sensitivity to data and methods as the final system. It is our inability to perform integral experiments which have exactly the same sensitivity to data and methods for all parameters and properties of interest in the final system which limits the usefulness of this method. We are therefore forced to proceed toward the final system by a series of jumps which is expensive if we cannot perform large extrapolations from one experiment to the next.

Whenever disagreement occurs between calculations and observations for these integral measurements the situation is handled in one of two ways. In the U.S., or at least within CSEWG, where all evaluations in ENDF/B are based upon microscopic data measurements,



the sensitivity of the discrepant results to specific cross sections is determined and the evaluations which contribute the most to the results are scrutinized to discover any possible mistakes, and a few important ones have been detected this way. The methods used in the computation are also scrutinized for inadequacies, and often different computational methods are used to ascertain if the disagreement is a method deficiency. If the discrepancies in the results still persist and are sensitive to some partial cross sections which were evaluated on the basis of discrepant data, a special task force of measurers of microscopic data and evaluators is convened for the purpose of establishing within which limits the experimental data constrain the evaluation, which is then adjusted, within these limits, to reduce or remove the discrepancy in the results. I must emphasize that this adjustment procedure is performed on only one or two of the partial cross sections of the ENDF/B set and that experimental programs are always in progress to remove any apparent discrepancies in microscopic data for important cross sections. Since the ENDF/B evaluations are based entirely upon microscopic data, they are applicable to many applications and therefore submitted to many tests<sup>1</sup> which have a wide variety of sensitivity to the data. One of the serious deficiencies of ENDF/B, as far as I am concerned, is that it is not possible to predict from the files what confidence limits to attach to the results of any calculations due to uncertainties in the data. The question of adequacy at the moment is only subjective and based on experience at calculating systems having closely the same sensitivity to data. For new applications or those which require evaluations which were performed for a special purpose, there is at present no way for the user to estimate the adequacy of the data.

Several groups,<sup>2-5</sup> outside the U.S. have exploited the results of integral experiments in a way different than we do in CSEWG. Evaluations based on microscopic data are used to generate some group cross sections which are then adjusted in a least square sense to produce a best fit to the observed quantities, thereby yielding an adjusted set. If one starts from the best estimates based on microscopic data, one must make violence to the microscopic data. However, since the justification of the method is based on the fact that one is using the nuclear data information from the integral measurements, this is permissible and valid; but one must be careful to weigh properly the changes in the cross sections with the sensitivities of the various group cross sections for the result being fitted and the known uncertainties and correlations in the microscopic data in order to produce a valid answer. Some of the advantages and disadvantages of this method are obvious. Deficiencies in methods used in the calculations are reflected in data adjustment; since the adjustment procedure is usually performed on very few groups, these may be large. However, this may not be too serious if one limits the use of the adjusted set to applications having very nearly the same sensitivity to data and method uncertainties. Although limited in their range of applicability, these adjusted data sets contain in principle for some specific applications a greater amount of information than the set they originated from. It is not my purpose here to discuss in detail the merits of these methods, but it is evident that in order for them to be successful and contain more valid input than the set they originated from it is essential that the proper estimated covariances in the initial group cross section sets be used.

#### Probabilistic Interpretation of Evaluations in ENDF/B

It is evident from our discussion so far that in order to properly address the question of adequacy in

nuclear data, whether for new applications or in areas where we have results of integral measurements to whatever use those results are put, we must develop a probabilistic interpretation of evaluations.

It is generally admitted that what the data in the files represent is in some sense, or intended to be, the most likely values of the microscopic data; and what we are looking for is a way of attaching confidence limits to these most likely values. We must find a suitable probability distribution to associate with our evaluations. It is evident that we can only base this probability distribution on what we know, that is the information at our disposal, to establish the evaluated data. It is also clear that what we want to define are quantities which can be used to answer in some quantitative way the legitimate questions of the users of our files. What we mean is that we must develop an appropriate framework which will allow for the manipulations of the quantities we put in the files without any ambiguities. To start with we must assume that there is no freedom associated with the numbers placed in the files as most likely values. Given exactly the "information" we had and exactly our "understanding" of this information, we had to come up with the exact numbers we put in the files as most probable values. However, we feel that even though we had no freedom in principle in adjusting the most probable values, in view of the type of information we had and our understanding of it, "small departures" from the values being put in the files are not too unlikely but larger departures are less likely. This feeling comes from the fact that we realize that our "particular set of information" used is not unique in some sense, and if we had been given an "equivalent set of information" the numbers we would have come up with as most probable values may well not have been exactly the same numbers we now have in the files. This is due to the nature of the information we use. For every "equivalent set of information" we would have come up with specific values which are not necessarily the same; and we envisage a whole distribution of such most probable values, one associated with each set and all equally likely. We therefore see that it is possible because of the "nature of the information" available, "our understanding" of it to communicate more than just most probable values and arrive at the concept of a complete distribution of most probable values, all equally likely, based upon the idea of "equivalent data sets." Having established this concept of "distribution of equally likely most probable values" we need to select an appropriate method to communicate it so that it can be safely manipulated. We recognize that we face a standard problem of the theory of variates which can be completely specified. We therefore make the following interpretations and assumptions: the numerical values of the data put in the files represent the most likely values of this distribution; the distribution of these most probable values is assumed to follow the normal distribution law. Since cross sections are bounded, they cannot strictly follow a normal distribution law; but this is a subtlety which we shall ignore in view of the convenience of using a normal distribution law. Having selected the normal distribution law and specified the most probable values, our probability distributions are completely defined if we provide the covariances of these distributions.

It is worthwhile to remark at this stage that we could have selected other quantities to put in the files to achieve similar results. For some applications these quantities may have been more immediately useful. However, since our aim in ENDF/B is to generate application independent evaluated microscopic data files, the above choice is the most fundamental one and is not tied to any specific applications. If for some



applications it is more useful to work with other quantities, these can always be obtained from the information put in the files.

Within CSEWG the following broad guidelines have been adopted to guide work on the estimated data covariance files of ENDF/B:

1) The estimated data covariance information put in the files shall pertain to the evaluated microscopic quantities in the "data" files. It will represent the estimated distribution of all equally likely evaluations based on equivalent microscopic data bases. The numerical values of the "data" in the files shall be identified as the most likely values of those equally likely evaluations. The ensemble of equally likely evaluations described by an ENDF/B evaluation is assumed to have a normal distribution law. The estimated data covariance files shall represent the variances and/or covariances of the distributions.

2) The method of representation of the estimated variances and covariances in the files shall follow as closely as possible the one used by experimentalists and evaluators to arrive at estimated data uncertainties and correlations from the analysis of experiments yielding microscopic data so as to build upon a previous body of experience.

3) It shall be possible by simple methods to obtain from the files the estimated variance of any evaluated microscopic quantity and the estimated covariance of any two such quantities.

4) Simple methods shall be given to propagate the estimated microscopic data covariances in the files to obtain realistic covariances of quantities generated by processing codes which access the "data" in order to prepare quantities used in applications for which the data are intended. For microscopic cross sections this will be interpreted to mean group cross sections used in transport applications. Since great precision is not required in the processing of these quantities, approximate methods shall be used whenever this speeds up and simplifies the processing. However, the approximate methods should yield accuracies consistent with our anticipated knowledge of such quantities in the near future.

5) The major aim of the estimated data covariance files in ENDF/B is to provide a substantial improvement in our past methods of handling and communicating microscopic data uncertainties and their correlations so as to allow a realistic assessment of their adequacy for various applications in which the data are used.

#### The Estimated Data Covariance Files of ENDF/B

We shall now describe some of the work done for ENDF/B-IV and the status of uncertainty representation. Before we go into some of the details, we should briefly review the general format of ENDF/B.

Cross section data are represented in different ways on the ENDF/B data tapes. Evaluations for each nuclide or element are kept separate and assigned a specific material number called a MAT. Each MAT is then divided into a number of files identified by MF values, each MF value containing information of a different type. In one file, denoted by MF=2, is entered the information concerning resolved and unresolved resonance parameters. File MF=3 contains integrated continuum cross sections as a function of energies; these are often referred to as smooth cross sections, defined by a table of pairs of (energy, cross section) values with different interpolation schemes to obtain the values of the cross sections between entry points. In file MF=3 each different partial cross section is identified by a MT value. Files MF=4 and 5 are reserved for angular and energy distributions information, respectively; these are in the form of normalized

probability distributions associated with the data in file MF=3. A similar set of files denoted by MF values of 12, 13, 14 and 15 is reserved for gamma-ray production cross sections. Because a major format change, which would require modifications to all processing codes presently accessing ENDF/B, was not judged essential at this stage to enter the estimated data covariances on the tape, separate files, i.e. new MF values, were allocated for the data presently formatted. For new types of nuclear data, those previously not handled on the tapes, a more logical way of handling the evaluated microscopic data and their estimated covariances is being implemented. With ENDF/B-IV, due to the early stage of development of the system and the desire to proceed systematically in order to gain experience, the only type of covariance data being handled is for files MF=3 and 13, the smooth cross sections as a function of energy. The covariance files have been assigned MF values of 33 and 43, respectively, obtained by adding 30 to the corresponding data files. Unfortunately this division is arbitrary and has led to these files being referred to as "error files"; this practice is very objectionable because it is completely misleading, and if a name is to be attached to them they should be called estimated data covariance files or covariance files for short. This point may appear to be a fine semantic one to many of you, but labeling them by the name "error file" will likely promote their misuse by some less technically sophisticated users.

The decision to proceed first in ENDF/B-IV with the smooth cross-section covariance files was influenced by the fact that most of the data on the tape are in that form and that the shielding community appeared to be the first one to be able to generate and use the information.<sup>6</sup> For reactor applications where sensitivity studies are in progress, it is essential to treat the resolved and unresolved resonance energy region, and this will be done for ENDF/B-IV; the approach taken will be outlined later for the resolved resonance region.

We shall now describe the covariance files for the smooth cross sections, MF=33. Let  $X_i$  and  $Y_j$  stand for cross section type X and Y at energies  $E_i$  and  $E_j$ , respectively; then we wish to describe the quantities:

$$\text{Cov}(X_i, Y_j) \equiv \langle (X_i - \bar{X}_i)(Y_j - \bar{Y}_j) \rangle, \quad (1)$$

where  $\bar{X}_i$  and  $\bar{Y}_j$  are the most probable values found in file MF=3 and the expectation value, denoted by the angle brackets  $\langle \rangle$ , is taken over the ensemble of all equally likely evaluations based on equivalent data sets. The values of  $X_i$  and  $Y_j$  are to be taken from each equally likely evaluation and stand for any two cross sections. For instance X and Y may be in a single MT, in which case we may say that we are dealing with the covariance of an energy-dependent cross section. X and Y may be from two different MT values within a single MAT, and we are then dealing with the covariances of two different cross sections of the same nuclide. It is well known that such correlations in uncertainties exist, if only because all partial cross sections must add up to the total cross sections. These covariances are very important, but in the past have been treated as being either zero, i.e. uncertainties fully uncorrelated, or having their maximum value, uncertainties fully correlated. We need also to consider the case where X and Y are two different types of cross sections, MT values, of two different nuclides, MAT values. This is so because many cross section ratios are known very accurately, and to make use of these measurements we must perform the evaluations of these nuclides simultaneously. Finally we must consider the question of correlations introduced by

uncertainties in common standards and methods used by the measurers to establish the shapes and/or the absolute magnitudes of the cross sections. The question of covariances introduced by standard cross sections and how to handle them practically in ENDF/B has been treated in detail. Although the thought of all these covariances between the evaluated data boggles the mind, and if we were to represent them all we would be faced with a gigantic task. We must develop a practical system which in principle can accommodate all of the important aspects of uncertainties and correlations in order to obtain a realistic estimate of the adequacy of the data. In practice we will not represent all these covariances, but only those which are important enough to affect the results -- only for the nuclides and cross sections for which the efforts are justified and when their absence from the files would lead to duplication of efforts or other inefficient use of limited resources.

The covariance  $\text{Cov}(X_i, Y_j)$  is first expanded as a sum of independent components  $\text{Cov}^n(X_i, Y_j)$ :

$$\text{Cov}(X_i, Y_j) = \sum_n \text{Cov}^n(X_i, Y_j) \quad (2)$$

Each component  $\text{Cov}^n(X_i, Y_j)$  represents elements which are correlated over some energy ranges of  $X(E)$  and  $Y(E)$ . This method follows very closely the way estimated uncertainties are analyzed in experiments. Each component represents a contribution to the variance due to separate factors affecting the experimental data and/or the methods of data reduction such as: background subtraction, detector efficiencies, sample thickness, flux determination, multiple scattering corrections, etc. Very often experimentalists combine many of these factors together to report an overall estimated uncertainty in the data. This practice is adequate when a single cross section is reported, but very inadequate to represent the uncertainties when the measurement spans a range of energies, since then one must phrase the uncertainties in terms of shapes and magnitudes as well. The elements represented in  $\text{Cov}^n(X_i, Y_j)$  are directly identifiable with the various individual factors composing the uncertainties in the data. The task of evaluators would be very much simplified if the experimentalists reported more in detail how these various elements are correlated and over what energy ranges, whether the evaluator is creating covariance files or not, since the knowledge of these elements is essential for properly combining several data sets to arrive at the most likely cross sections. An extensive analysis of the different kinds of elements required to handle the description of covariances has been made,<sup>8</sup> but we shall only give here the results of this analysis and not bother with the technicalities of formats on the ENDF/B tape.<sup>9</sup>

Let the energy range of  $X(E)$  and  $Y(E)$  be broken up into nonoverlapping consecutive energy intervals, which we identify with the value of the lowest energy in each interval  $E_k^n$ , and associate with each energy interval an element  $E_{xy,k}^n$ , thereby creating an  $(E_k^n, F_{xy,k}^n)$  table of values.

Let  $S_i^k$  be an operator, where the subscript  $i$  refers to the energy  $E_i$ , and the superscript  $k$  refers to the  $k^{\text{th}}$  interval of a table. This operator  $S_i^k$  is defined to be unity when the energy  $E_i$  is within the energy interval  $E_k^n$  of the table and zero otherwise.

With each component  $\text{Cov}^n(X_i, Y_j)$  is associated a table of elements  $(E_k^n, F_{xy,k}^n)$  and depending upon the value of a flag, LB, associated with it the following

three types of components are defined:

- 1) LB=0, absolute elements correlated only within each  $E_k^n$  interval

$$\text{Cov}^n(X_i, Y_j) \equiv \sum_k S_i^k S_j^k F_{xy,k}^n \quad (3)$$

- 2) LB=1, fractional elements correlated only within each  $E_k^n$  interval

$$\text{Cov}^n(X_i, Y_j) \equiv \sum_k S_i^k S_j^k F_{xy,k}^n \bar{X}_i \bar{Y}_j \quad (4)$$

- 3) LB=2, fractional elements correlated over all  $E_k^n$  intervals

$$\text{Cov}^n(X_i, Y_j) \equiv \sum_{k,k'} S_i^{k,k'} S_j^{k,k'} F_{xy,k}^n F_{xy,k'}^n \bar{X}_i \bar{Y}_j \quad (5)$$

The complete formalism allows for any number of such tables to be associated with a single component allowing a wide variety of correlation patterns to be represented. In ENDF/B-IV the formats allow for up to two such tables for some values of LB. Let  $(E_k^n, F_{x,k}^n)$  be the table associated with  $X(E)$  and  $(E_\ell^n, F_{y,\ell}^n)$  with  $Y(E)$ , then we also have:

- 4) LB=3, fractional elements correlated between the  $E_k^n$  and  $E_\ell^n$  intervals

$$\text{Cov}^n(X_i, Y_j) \equiv \sum_{k,\ell} S_i^k S_j^\ell F_{x,k}^n F_{y,\ell}^n \bar{X}_i \bar{Y}_j \quad (6)$$

Although several other combinations are presently defined, they are only used to achieve a compact representation and basically involve only combinations of the above components.

There are several advantages to this formalism:

- 1) It gives the covariance information of the microscopic cross sections in a very compact form.
- 2) Because it parallels very closely the method used by experimentalists to analyze the estimated uncertainties in their data, it should facilitate greatly the preparation of these files in many instances and promote more accurate and complete communications between experimentalists and evaluators.
- 3) Group cross-section processing codes can easily be adapted to generate the covariance matrices of group cross sections. The introduction of the operators  $S_i^k$  guarantees that double integrals need not be performed,<sup>8</sup> a proof we will not give here. The computation reduces itself to very simple group cross section collapsing schemes using the various elements read directly from the files as "weights." Already stand alone codes exist for processing the information<sup>10</sup> and standard processing codes have been adapted to routinely process the data.<sup>11</sup>

We shall now give those simple collapsing schemes for covariances of two group cross sections. Let  $X_G$  and  $Y_H$  be the group cross sections for reaction  $X$  group  $G$  and reaction  $Y$  group  $H$ . Let  $\phi_G$  and  $\phi_H$  be the flux in groups  $G$  and  $H$ , respectively. Let  $X_{G,k}^n$  stand for the group cross section of  $X$  over the energy range which is the union of  $G$  and the  $k^{\text{th}}$  energy interval in the table associated with the component  $n$  and  $\phi_{G,k}^n$  be the flux in this group. Then depending upon the value of LB associated with the  $n^{\text{th}}$  component, the following formulae apply for

LB=0

$$\phi_G \phi_H \text{Cov}^n(X_G, Y_H) = \sum_k F_{xy,k}^n \phi_{G,k}^n \phi_{H,k}^n \quad (7)$$



LB=1

$$\phi_G \phi_H \text{Cov}^n(x_G, y_H) = \sum_k F_{xy,k}^n \phi_{G,k}^n x_{G,k}^n \phi_{H,k}^n y_{H,k}^n, \quad (8)$$

LB=2

$$\phi_G \phi_H \text{Cov}^n(x_G, y_H) = \left( \sum_k F_{xy,k}^n \phi_{G,k}^n x_{G,k}^n \right) \left( \sum_{k'} F_{xy,k'}^n \phi_{H,k'}^n y_{H,k'}^n \right), \quad (9)$$

LB=3

$$\phi_G \phi_H \text{Cov}^n(x_G, y_H) = \left( \sum_k F_{x,k}^n \phi_{G,k}^n x_{G,k}^n \right) \left( \sum_{\ell} F_{y,\ell}^n \phi_{H,\ell}^n y_{H,\ell}^n \right). \quad (10)$$

With ENDF/B-IV complete covariance files were generated for all important cross sections of N and O in file MF=3<sup>12</sup> and for all partial cross section for C. In the case of air transport of neutrons, these files have already been used in sensitivity studies.<sup>6</sup>

For reactor applications it is very important to extend the formulation to treat the resonance region, both resolved and unresolved. Recent investigations have been made of the treatment of data covariances in the resolved resonance region.<sup>13</sup> It appears that it is quite possible to use a simple method which will yield adequate covariance matrix elements for group cross sections, taking into account self-shielding and Doppler effects, for both fast and thermal reactors. The method will be submitted to CSEWG at its next meeting for consideration for ENDF/B. We shall now briefly describe the elements of the proposed method without going into the details.

Neutron cross sections in the resolved resonance region are characterized by an energy dependence which is best described in terms of a slowly varying component upon which is superimposed isolated relatively sharp resonances. An analysis of the nature of data uncertainties in the resolved resonance region reveals that for most experiments one may represent them by means of components of the covariance of the cross sections which fall into three separate classes:

- 1) Those which affect only our knowledge of the resonance behavior of each individual resonance.
- 2) Those which affect only our knowledge of the "smooth cross sections" between the resonances.
- 3) Those which affect in a similar way our knowledge of both the smooth and the resonant part of the cross sections.

The factors responsible for the first class of components are those which affect our knowledge of the individual parameters of single resonances. They represent our inability to determine very precisely all the parameters of the resonance from the observed peaks or dips in the experimental data. These uncertainties can be expressed, and often are, in terms of variances and covariances of the parameters of the resonance.

The factors responsible for the second class of components are those which affect only our knowledge of the magnitude of the cross sections between the resonances, such as experimental background subtraction, sensitivity of the detectors to scattered neutrons in a capture measurement, etc. They are most often expressed in terms of an absolute value independent of the magnitude of the cross sections; these components represent uncertainties which are strongly correlated over large energy ranges.

In the final class fall components which arise out of factors which affect the magnitude of the experimentally "observed yield" for the cross sections. These are factors such as sample thickness, flux determination, solid angles, detector efficiencies, etc. They produce an uncertainty which is strongly correlated as a function of energy, proportional to the cross sections and are the major sources of correlation between yields of different resonances. They are often reported in terms of a fractional uncertainty fully correlated over broad energy ranges of the measurements. They are almost never reported in terms of variance components of the resonance parameters and never as covariances of parameters of different resonances.

The above discussion suggests that we represent the data covariances in the resolved resonance region in the following fashion. Components of the first class as variances and covariances of the resonance parameters of each resonance and components of the second and third class in the same manner we handled the covariances of the smooth cross sections in the higher energy region.

We shall now indicate how we propose to treat the propagation of the covariances in the microscopic data to obtain covariances of group cross sections. The covariance components of the second and third class shall be treated just as for the smooth cross sections. This is an approximation since in the higher energy region we did not treat self-shielding, but this will be somewhat taken into account by the fact that we will use self-shielded cross sections which incorporate Doppler effects also. Because these components do not show variations over the resonances, i.e. they are long-range correlations, this approximation will be adequate. The variances and covariances of the resonance parameters represent large variations in the covariances of the cross sections over energy ranges comparable to the widths of the resonances; therefore we must treat carefully self-shielding and Doppler effects for them. In order to develop fast approximate formulae to determine their effect on the covariances of group cross sections, we consider two different cases. In the first one a single resonance contributes significantly to several energy groups; this is the case in the low region for thermal applications and we shall not detail the treatment here. The second one, of greatest interest for fast reactors, is the one where we assume that most of the contribution of a given resonance is in a single group. We will consider each resonance separately, which is adequate since we have taken care of correlations between resonances by separate components, and we are concerned here only with the components of the covariance of the cross section expressed as variances and covariances of the parameters of a single resonance. As is well known,<sup>14</sup> the contribution to the group cross section of a resonance  $i$ , taking into account self-shielding and Doppler effects, is proportional to:

$$A_Y^i f^i(\theta^i, \beta^i) \quad (11)$$

where  $A_Y^i$  is the resonance area for capture of the  $i^{\text{th}}$  resonance and the arguments of the  $f$  function are:

$$\theta^i \equiv \frac{\Gamma^i}{\Delta^i}, \quad (12)$$

with  $\Gamma^i$  the total width of the resonance and  $\Delta^i$  its Doppler width; and

$$\beta^i \equiv \frac{-i}{\sigma_b^i} \frac{1}{\sigma_o^i}, \quad (13)$$

with  $\bar{\sigma}_b^i$  the total cross section of the medium, excluding the contribution of the  $i^{\text{th}}$  resonance, in the neighborhood of the resonance and  $\sigma_0^i$  the peak total cross section of the resonance in the absence of self-shielding and Doppler effects.

If we denote by  $y_k^i$  the parameters of the resonance, then the fractional change of the contributions of the  $i^{\text{th}}$  resonance to the group cross section is:

$$\frac{d G_Y^i}{G_Y^i} = \frac{d A_Y^i}{A_Y^i} + \frac{d f^i}{f^i} \quad (14)$$

If we now make use of the appropriate closed form expressions for  $A_Y^i$  and  $f^i$  in terms of the  $g_k^i$ , it is easy to obtain explicit formulae for  $dA_Y^i$  and  $df^i$  in terms of the  $dy_k^i$ 's. After some straightforward manipulation, one obtains for instance the contribution of the resonance to the fractional variance of the group cross section due to the covariances in the parameters as:

$$\langle \left( \frac{d G_Y^i}{G_Y^i} \right)^2 \rangle = \sum_{k,l} \left( \frac{1}{A_Y^i} \frac{\partial A_Y^i}{\partial y_k^i} + \frac{1}{f^i} \frac{\partial f^i}{\partial y_k^i} \right) \left( \frac{1}{A_Y^i} \frac{\partial A_Y^i}{\partial y_l^i} + \frac{1}{f^i} \frac{\partial f^i}{\partial y_l^i} \right) \langle dy_k^i \cdot dy_l^i \rangle, \quad (15)$$

where  $\langle dy_k^i \cdot dy_l^i \rangle$  are the covariance matrix elements of the resonance parameters for the  $i^{\text{th}}$  resonance. One may similarly obtain the contribution of the resonance to the fractional covariance of two group cross sections, capture and fission for instance, due to the covariances in the parameters. To obtain the contribution of all the resonances within a group, one needs only to sum the contribution of each resonance.

Although approximate, the method we have just outlined should have the required accuracy for the processing of estimated data covariances in the resolved resonance region.

#### Future Work

In order to complete the treatment of estimated data covariances of integrated cross sections we have to address the problems of the unresolved resonance region, which we plan to do in the near future. Several approaches have been looked at and some appear promising, but we have not pushed them far enough to make specific recommendations to CSEWG yet.

The next areas of the files to be addressed will have to be the angular and energy distributions since these are very important in some applications. Until we have considered all major areas of uncertainties in the basic data, we shall not be able to make confident objective conclusions regarding the adequacy of the data for predictive purposes. In areas where we have considerable experience with integral measurements which have similar sensitivities to data and methods, we should always be able to make *a posteriori* statements as to the adequacy of the data, but we should be always cautious since many of the agreements may be fortuitous due to correlations in the data.

#### Acknowledgements

I wish to thank many of the people within CSEWG who have made this work possible. In particular the members of the Codes and Formats Subcommittee, who have allowed this experimentation in communicating the quality of the data in ENDF/B prior to the development

of a completely tested system. Also P. G. Young for having used the system for oxygen and nitrogen, thereby allowing it to be tested in a real and important problem -- air transport. My thanks also go to many of my colleagues at ORNL for their encouragements and critical discussions, in particular F. C. Maienschein, R. W. Peelle, G. de Saussure and the members of the Transport and Sensitivity Studies Group under F. R. Mynatt. Finally my thanks to Jan Gentry for having successfully gotten this manuscript out under trying conditions.

#### References

1. E. M. Bohn, R. J. LaBauve, R. E. Maerker, B. A. Magurno, F. J. McCrosson and R. E. Schenter, "Benchmark Experiments for Nuclear Data," this conference.
2. A. Pazy, G. Rakavy, Y. Reiss and Y. Yeivin, "Use of Integral Measurements as Supplementary Data in Nuclear Cross Section Evaluation," ANL-7320, p. 270 (1966).
3. J. L. Rowlands and J. D. MacDougall, "The Use of Integral Measurements to Adjust Cross Sections and Predict Reactor Properties," Proceedings BNES Int. Conf. on the Physics of Fast Reactor Operation and Design, London (1969).
4. H. Mitani and H. Kuroi, J. of Nucl. Sci. and Tech. 9, 383 (1972) and 9, 642 (1972).
5. J. Y. Barre and J. Bouchard, "After Phenix, What is the Importance of Nuclear Data Programs for Fast Breeder Reactor Development?", this conference.
6. C. R. Weisbin, E. M. Oblow, J. Ching, J. E. White, R. Q. Wright, and J. Drischler, "Cross Section and Method Uncertainties: The Application of Sensitivity Analysis to Study their Relationship in Computational Benchmark Problems," this conference.
7. R. W. Peelle, "Uncertainties and Correlations in Evaluated Data Sets Induced by Use of Standard Cross Sections," this conference.
8. F. G. Perey, "Minutes of the Spring and Fall 1973 Meetings of the Cross Section Evaluation Working Group, and F. G. Perey, to be published.
9. F. G. Perey, "ENDF/B Format Modification 73-7," CSEWG (December 1973).
10. F. G. Perey, ORNL (1974).
11. C. R. Weisbin, "PUFF, An ENDF/B-IV Covariance File Processing Code," ORNL Quarterly Report to the Defense Nuclear Agency (April 1974).
12. P. G. Young, Los Alamos Scientific Laboratory.
13. F. G. Perey, to be published.
14. L. Dresner, "Resonance Absorption in Nuclear Reactors," Pergamon Press, 1960.

\*Research performed at Oak Ridge National Laboratory, operated by Union Carbide Corporation for the Energy Research and Development Administration.



N. M. Greene

Union Carbide Corporation - Nuclear Division  
Oak Ridge, Tennessee 37830

The features of three code systems that produce multigroup neutron data are contrasted. This includes the ETOE-2/MC<sup>2</sup>-2/SDX, MINX/SPHINX and AMPX code packages. These systems all contain a fairly extensive set of processing capabilities with the current evaluated nuclear data files -- ENDF/B. They were designed with different goals and applications in mind. This paper discusses some of their differences and the implications for particular situations.

(Computer codes; multi-group data; Survey)

### Introduction

During its (sometime short) life, a set of cross section data goes through four distinct phases.

There is the initial phase, when the data are obtained through a laboratory measurement or model calculation. The second phase involves the introduction of the data into the body of existing data. This phase produces a "cross section evaluation" and includes much value judgment on type of experiment, sophistication of equipment, adequacy of nuclear model, credibility of experimenter, etc. The third phase is encountered when the data are processed. Few applications require cross section data in the forms commonly used to define an evaluation, and the data must be manipulated and massaged to fit the myriad of situations which need cross sections. The fourth phase is the "user phase." This is the payoff phase. A set of cross sections is of little value unless it can be used in criticality studies, shielding analyses, or safety studies, etc.

Each of the four phases has its own set of problems which prevents an absolute determination of a set of "answers." The third phase is particularly prone to yield a widely varying set of results. This "processing phase" is the subject of this paper. In particular, the paper discusses three processing schemes that produce multigroup neutron cross sections with particular emphasis on features which lead to variations in their results.

In the United States, the ENDF/B<sup>1</sup> system is the standard means of disseminating the latest basic neutron and gamma cross section data. At present, three large processing codes maintain a fairly complete processing capability with the ever-expanding ENDF/B formats. These are the ETOE-2/MC<sup>2</sup>-2/SDX<sup>2</sup> codes, the MINX<sup>3</sup>/SPHINX<sup>4</sup> codes, and the AMPX<sup>5</sup> system. These include among their most recent predecessors such codes as: MC<sup>2</sup><sup>6</sup>, ETOX<sup>7</sup>, IDX<sup>8</sup>, ETOG<sup>9</sup>, SUPERTOG<sup>10</sup>, FLANGE-II<sup>11</sup>, ENDRUN<sup>12</sup>, and GAM-II<sup>13</sup>. This paper will limit itself to a discussion of treatments that are used in the three newer "systems".

In the multigroup scheme, basic data must be processed into tables of "effective cross sections" in a user selected energy structure. These cross sections should relate to the multigroup form of the Boltzmann transport or diffusion equations to allow the calculation of reasonable values for neutron fluxes which are then used to determine reaction rates of one form or another.

ETOE-2/MC<sup>2</sup>-2/SDX, MINX/SPHINX, and AMPX perform many analogous operations in preparing these constants. They all "weight" point data to obtain group averages; they all Doppler broaden resonance data; they all have provisions for processing resolved and unresolved parameter data; they all calculate group-to-group transfer matrices for elastic, inelastic, and n<sub>2</sub>n processes; all can do resonance self-shielding calculations; all have provisions for doing one dimensional multigroup calculations whose fluxes can be used to "collapse" multigroup data. A user would very likely find that if he delved into the interior of either of the three codes, most processed numbers would be well converged as far as the physical method employed in the code. However, when he compares any two of the systems, there is very marked disagreement. Such a comparison was the topic of a recent paper<sup>14</sup>. This study commonly observed differences of ten and twenty percent on individual cross sections; and many observations were made of quantities differing by factors. However, the "payoff" numbers -- the k-effectives, and region reaction rates -- were in much better accord. An earlier study<sup>15</sup> observed similar differences.

How do these systems attack ENDF/B data, and why do they produce different values? What are the obvious advantages and disadvantages of their attacks?

### System Differences

To examine the situation, the following topics will be discussed:

1. General Philosophy
2. Working Data Base
3. Resolved Resonances
4. Unresolved Resonances
5. Doppler Broadening
6. Weighting Spectrum (Non-resonance Region)
7. Transfer Matrices
8. Thermal Data Processing
9. Multigroup Collapse
10. Integration Techniques
11. Resonance Self Shielding
12. Fission Spectrum
13. Computer System
14. Unique Features

#### 1. General Philosophy

It is impossible to discuss all the intents and goals of the three systems under study. All have been described in numerous publications and papers. However, the following statements hopefully cover major intents.

ETOE-2/MC<sup>2</sup>-2/SDX. ETOE-2 is a preprocessor for the MC<sup>2</sup>-2 and SDX codes. Among its many functions is to process resonance data for "light" ( $A \leq 100$ ) elements and to convert ENDF/B formats to the types of formats used in the other codes, which do not process

\*Research performed by Union Carbide Corporation under contract with the U. S. Energy Research and Development Administration.



ENDF/B libraries directly. MC<sup>2</sup>-2 is a very detailed treatment designed to produce cross sections for fast reactor analysis. It will also handle many criticality applications and is being extended to produce constants suitable for shielding studies. The most unique feature of the code is the use of a very detailed (~2000 groups)  $B_1$  calculation to determine a weighting function for obtaining multigroup cross sections in the 100-200 group range. SDX is a code that starts with multigroup libraries produced by MC<sup>2</sup>-2 (or elsewhere) and uses these in a one dimensional diffusion calculation which can collapse to coarser group structures. In the words of its developers: "At its most rigorous, the SDX calculation is more rigorous, yet significantly more economical, than the most rigorous previously existing fast neutron multigroup cross section preparation capability . . . . the simplest SDX calculation . . . . should be an improvement upon the self-shielding factor schemes because of the more accurate resonance cross section treatment."<sup>2</sup>

MINX/SPHINX. MINX was initiated in early 1972 by the AEC-DRDT to provide an upgraded and efficient method for obtaining multigroup constants to use in LMFB design studies. It also includes many treatments especially applicable for shielding problems. It produces Bondarenko factors (narrow resonance approximation) for use in self shielding calculations. A unique goal is the attempt to assign a "processing error" to any number it calculates. A version has been extended to allow processing of the ENDF/B error files. SPHINX forms the other half of this team. The IDX code served as the basis of SPHINX, which has had extensive revision to the routines used to perform self shielding calculations based on Bondarenko factors. Work is presently being done to allow a one dimensional transport calculation to augment the diffusion theory calculation now provided. The ANISN<sup>16</sup> code will be modified for this task.

AMPX. AMPX is a modular code system which presently contains ~30 separate codes dealing with the production and use of multigroup cross sections. It will produce both multigroup neutron and gamma cross sections. Its basic modules were originally developed for shielding and soft spectrum reactor analysis; e.g., water and molten salt reactors, although it has been extended to allow preparing constants for fast reactors. Its most distinguishing features are the modular approach, the ability to prepare coupled neutron-gamma cross sections (including self-shielding effects), and the internal use of very general formats for its cross section libraries.

## 2. Working Data Base

All three systems accept their basic data from ENDF/B; yet, there are subtle differences which ultimately show up in multigroup values. In ETOE-2/MC<sup>2</sup>-2/SDX and MINX/SPHINX, ENDF/B libraries must be pre-processed before the stage that produces multigroup data is reached. The most obvious disadvantage is the lag-time before multigroup processing, especially if the processed data must be merged with previously existing libraries. Another disadvantage is that the "preprocessing" creates a new evaluation which possibly can neglect details important in some applications. The advantages are equally obvious. Preprocessing allows one to make multigroup processing schemes simpler and more economical, especially since the preprocessed library can be reused.

ETOE-2/MC<sup>2</sup>-2/SDX. MC<sup>2</sup>-2/SDX do not read ENDF/B libraries. ETOE-2 reformats some ENDF/B data; it processes other data into ultrafine group form ( $\Delta u \sim$

.008) using flatweighting on the premise that cross sections are nearly composition independent on this scale; nuclides with masses less than ~100 are pre-processed into "smooth" data; three of the formats describing secondary energy distributions are pre-processed into tabulated distributions; also, processing is done to calculate parameters which will be used in MC<sup>2</sup>-2 to determine scattering distributions.

MINX/SPHINX. The initial part of MINX converts ENDF/B cross sections and resonance parameter data to tabular cross section sets which are linear in energy. The process allows the user to specify a tolerance for the fit. The use of this scheme<sup>17</sup> in the resonance region is, in our opinion, much more superior to many schemes used to "fit" the resolved resonance range because, in large part, these other schemes are based on "cut and try" and can produce erroneous fits. The linearization has two major advantages. First, the routines which produce multigroup values are simplified, because they need not consider the 5 interpolation schemes provided in ENDF/B. Secondly, the numerical Doppler broadening routines used elsewhere in MINX expect data in this form. The primary disadvantage is that it generally takes more points to represent a function in this manner. The linearized libraries are written in ENDF/B formats using the BCD mode. This mode is required to interact properly with "paging" techniques in MINX discussed later.

AMPX. ENDF/B libraries are processed directly in this system, even to the point of allowing several libraries in any combination of modes (BCD or binary) to be used in a single run. The primary advantages are the elimination of the intermediate library and the convenience of processing. It should be emphasized, however, that this "direct processing" involves many of the same "fittings" as do the two previous schemes; e.g., resonance arrays are constructed from resonance parameters, evaporation spectra must be fit, etc.

## 3. Resolved Resonances

ENDF/B provides for resolved resonances to be represented in 5 ways:

1. Single Level Breit Wigner parameters (SLBW)
2. Multilevel Breit Wigner parameters (MLBW)
3. Adler-Adler parameters (A-A)
4. Reich-Moore parameters (R-M)
5. Tabulated points

In some cases, the parameters will be augmented by "background" tabulations.

The systems differ considerably in "fitting" resonances. ETOE-2/MC<sup>2</sup>-2/SDX handle all forms above, with no Doppler broadening in the latter case. MINX/SPHINX handle forms 1, 2, 3, and 5 and uses numerical Doppler broadening. AMPX has provisions for forms 1, 2, and 5. A module is provided which employs numerical Doppler broadening routines. In ETOE-2/MC<sup>2</sup>-2/SDX, form 4 is generally processed by creating an equivalent Adler-Adler set and background file per the prescriptions of Perez and deSaussure<sup>18</sup>. Form 2 is also transformed to Adler-Adler form for processing.

ETOE-2/MC<sup>2</sup>-2/SDX. ETOE-2 does resonance processing for the lighter ( $A \leq 100$ ) elements in the ultrafine group ( $\Delta u \sim 0.008$ ) range. A tabular array is formed for these elements and flat weighting is used to process to the ultrafine group level. MC<sup>2</sup>-2 and SDX share many sections of coding in their resolved

treatment, except that SDX has additional options that are more approximate, yet very much more economical. The treatment is based on the narrow resonance approximation and involves the calculation of  $J^*$  integrals. These include a term for each resonance along with interference terms due to neighboring resonances. Typically, four resonances on either side contribute to the interference term. For broad resonances, contributions for a resonance are distributed at the ultrafine group level; otherwise, a single group receives the whole contribution. The  $J^*$  integrals ultimately are used to obtain "effective" averages at the ultrafine group level in MC<sup>2</sup>-2 or intermediate group level in SDX.

For low energy applications where the narrow resonance approximation may be invalid, a general integral transport calculation is provided based on the RABBLE<sup>19</sup> code. This code is used in the 1-300 eV range and calculates in micro groups ( $\Delta u \sim 0.0002$ ). Resonance parameters are used to form arrays of cross sections versus energy which are flat weighted to the micro group level.

MINX/SPHINX. MINX constructs linearized arrays in energy for the resolved resonance range to a tolerance that is specified by the user. These values are then processed through the numerical Doppler broadening routines, after which tables of Bondarenko factors at several  $\sigma_0$ 's are calculated by averaging in a selected energy group structure.

AMPX. Resonance parameters can be processed in the NPTXS, XLACS, and NITAWL modules of AMPX. NPTXS produces point cross section arrays from resonance parameters. The mesh scheme for constructing a resonance is based on a ratio determined from the SLBW formula for  $\sigma_T$ . Points are included such that the ratio of cross section value from point to point is some ratio; e.g., 0.95. In XLACS, resonances are constructed using the same scheme; in addition, it must construct "background" values which are consistent with the Nordheim Integral Treatment<sup>20</sup>. The NITAWL module also reconstructs resonances based on equal lethargy spacings. Each resonance receives between four to five hundred points within four or five practical widths of the peak of a resonance. As compared to the "ratio mesh" of XLACS, this is a very inefficient mesh that is required because the commonly programmed form of the Nordheim treatment requires the constant lethargy spacing.

#### 4. Unresolved Resonances

As contrasted with the resolved region, there is more accord between the three systems in this region than in any other. All three use methods derived from a treatment originally developed in MC<sup>2</sup>. The primary difference is in the fact that MC<sup>2</sup>-2/SDX include a "same-sequence" overlap term<sup>21</sup> that is ignored by MINX/SPHINX and AMPX. It has been shown<sup>22</sup> that the effect of this term is negligible on k-effective calculations ( $> 0.1\%$ ), but can have a significant impact on Doppler coefficients. Another difference is in the  $\sigma_0$  used to account for the "other materials" in a mixture containing the nuclide. MC<sup>2</sup>-2/SDX determine "point values" with realistic variation throughout the unresolved region. MINX calculates at several values of  $\sigma_0$  in the process of obtaining Bondarenko factors. These "tables" are used in an iterative interpolation treatment in SPHINX where mixture dependent  $\sigma_0$ 's are determined. The XLACS module of AMPX has tables of  $\sigma_0$ 's for several "fast reactor" nuclides that are used to determine a variable  $\sigma_0$ , but no iteration is possible.

#### 5. Doppler Broadening

For Doppler broadening resolved resonances, one can choose between 2 techniques in the three systems:

1.  $\psi$  and  $\chi$  methods<sup>6</sup>
2. the  $\sigma'$  method<sup>23</sup>

The first method uses analytic expressions to evaluate rather complicated integrals encountered in Doppler broadening and is by far the faster. The second method is the most general and includes an integral neglected in the other method. It handles tabulated data and, as one might expect, takes more time than the other method - typically factors of two to ten times longer, depending on points.

ETOE-2/MC<sup>2</sup>-2/SDX.  $\psi$  and  $\chi$  techniques are employed throughout.

MINX/SPHINX. The  $\sigma'$  method is used in MINX.

AMPX. NPTXS uses  $\sigma'$ ; XLACS and NITAWL use  $\psi$  and  $\chi$  techniques.

#### 6. Weighting Spectrum

Significant differences occur in the formulation of the weighting spectrum used to collapse from point or ultrafine group data down to a tractable number of groups (25-300).

ETOE-2/MC<sup>2</sup>-2/SDX. MC<sup>2</sup>-2 calculates a spectrum in the ultrafine group mode using  $B_n$  theory. It includes inelastic and n2n scattering explicitly and is the most "correct" treatment used by any of the codes discussed (outside of the resolved resonance region) to obtain a weighting spectrum.

MINX/SPHINX. MINX allows several of the more commonly used "analytic" weighting forms to be used. These are impressed on the Bondarenko  $1/\sigma_T + \sigma_0$  weighting used throughout the code.

AMPX. AMPX generally uses the simple "analytic" forms for weighting. In addition, it has available pre-determined spectra which fit several shielding applications, such as air transport, concrete transport, SS304 transport, etc. These are based on simpler approximations, such as narrow resonance.

The principal advantage of the MC<sup>2</sup>-2 method is its correctness, and conversely, its disadvantage is the time required to calculate the spectrum. The advantage of the other schemes is that they reduce the complexity of the problem and are adequate for many applications. In most applications, the "resonance region" weighting is much more important than elsewhere and additional treatments are provided in all 3 systems to account for this. (It should be mentioned that MINX and the modules in AMPX allow arbitrary spectra to be read which circumvents the problem of "correctness" if a proper weighting function is predetermined).

#### 7. Transfer Matrices

Aside from resonance processing, the most time-consuming part of multigroup cross section preparation is in making transfer arrays. In ENDF/B libraries, this involves elastic scattering, up to 40 levels of discrete inelastic scattering, a variety of "inelastic" processes which have reaction products other than gammas, several n2n reactions, n3n's, and n4n's. Each of these processes must be



calculated independently. In addition, thermal matrices can be determined.

ETOE-2/MC<sup>2</sup>-2/SDX. ETOE-2 prepares Legendre coefficients in the CMS system to pass to MC<sup>2</sup>-2 for use in determining elastic scattering matrices. MC<sup>2</sup>-2 calculates functions that give the scattering from energy points to ultrafine groups.<sup>24</sup> These functions are then weighted over a flat spectrum in source energy to obtain ultrafine group to ultrafine group transfers. These, in turn, are flux weighted to produce intermediate group matrices. P<sub>0</sub> and P<sub>1</sub> matrices are determined. P<sub>0</sub> inelastic matrices are determined which contain a "transport-like" approximation to account for anisotropic behavior in the CMS system.

MINX/SPHINX. MINX determines anisotropic matrices<sup>25</sup> to arbitrary order for all the processes mentioned above, except thermal scattering. It treats all forms of ENDF/B angular and energy distribution data in Files 4 and 5. Adaptive Simpson's integration routines are used which ensure convergence of all terms to a user specified tolerance. For "evaporation" treatments, analytic techniques are used which are very accurate and efficient.

AMPX. AMPX determines anisotropic matrices<sup>26</sup> for elastic, discrete level inelastic, and thermal scattering. Other processes are generally treated as isotropic in the laboratory system.

For shielding applications, the production of P<sub>0</sub> matrices higher than the P<sub>1</sub> is required for analyses of a highly differential nature. Anisotropic matrices for "inelastic" processes are almost never required for other than "cross section measuring" experiment analyses; however, if one approximates higher order flux moments by the scalar flux, anisotropic matrices cost little extra in time. A few of the very light elements, notably deuterium, have strong anisotropic behavior associated with "evaporation" processes. The MINX code will produce anisotropic matrices for these evaporation processes; the other processing codes produce isotropic matrices.

## 8. Thermal Data Processing

Accurate thermal calculations require thermal scattering matrices which include upscatter terms.

The AMPX system is the only one of the three which calculate these parameters. The treatments it uses have been extensively used in the past for light water reactor calculations. However, the treatments are very dependent on group structure and mass. Failure to take these matters into account can lead to inaccurate thermal matrices and cause spurious calculational results. Since the treatments were largely developed before the advent of the latest, high speed computers, it is likely that the deficiencies noted will be corrected in the future.

## 9. Multigroup Collapse

All three systems recognize the utility of the retention and use of libraries in the 100-200 group range for use in design calculations, which may not require the full rigor available in the system.

ETOE-2/MC<sup>2</sup>-2/SDX. SDX has a one dimensional diffusion theory calculation available for producing fluxes for use in collapsing libraries to a range (10-50 groups) which is desirable for subsequent nuclear analysis involving two and three dimensional techniques.

MINX/SPHINX. SPHINX also uses diffusion theory to collapse cross sections, although, a transport option is being developed.

AMPX. AMPX has both diffusion and transport theory available in its XSDRNP module to collapse cross sections.

## 10. Integration Techniques

All three systems contain multi-dimensional integrations involving cross sections, fluxes, probabilities, etc. Many different integration techniques are used, including Gaussian quadrature, analytic methods, Simpson's rule, adaptive Simpson's method, trapezoidal rule, etc. These introduce variations in multigroup constants.

As an example, consider the elastic matrix calculations performed in MC<sup>2</sup>-2, MINX, and the XLACS module of AMPX.

All three codes start with the same basic expression:

MC<sup>2</sup>-2 uses a Gaussian integration over angle to obtain point-to-ultrafine group values<sup>24</sup>. Then, trapezoidal integrations are used to obtain ultrafine group to ultrafine group numbers. The angular integration is analytic through P<sub>1</sub> and uses Gaussian quadrature elsewhere.

MINX uses analytic expressions<sup>25</sup> over angle to obtain point-to-group values (note that it is operating in the 50-300 group range) and then uses an adaptive Simpson's technique to obtain group-to-group values.

XLACS turns the process<sup>26</sup> inside out by doing the angular integration last. The integrations of cross section times fluxes are analytic and treat all combinations of the products of the 5 different ENDF/B interpolation types.

As so it is throughout the codes.

## 11. Resonance Self Shielding

In many applications, one of the most important considerations in preparing multigroup data is in the treatment of the "self-shielding" effects of large resolved resonances. This area, in particular, spotlights some of the major differences in philosophy and heritage in the three systems.

ETOE-2/MC<sup>2</sup>-2/SDX. Most processing relies on the narrow resonance approximation which has been demonstrated to be adequate for many applications, in particular fast reactor studies. Within the framework of the narrow resonance approximation, the treatments are quite correct. The calculations are performed on a very detailed scale and allow for treating resonance overlaps, even between resolved and unresolved resonances. For those applications where the narrow resonance approximation is clearly inadequate, an integral transport treatment is available which overrides values produced by the narrow resonance treatments. Multiregion systems containing arbitrary mixtures can be modeled in one dimensional slab or cylindrical geometries. The calculation is performed in the 1-300 eV range in a variable microgroup lethargy structure ( $\Delta u \approx 0.0002$ ). Inelastic and n<sub>2n</sub> downscattering sources are explicitly included.

MINX/SPHINX. This system relies solely on the Bondarenko (narrow resonance) approach. The primary



advantage of this approach is the economy and simplicity of the treatment, once the factors are obtained. It is quite adequate for most fast reactor design applications. The primary disadvantage relative to the MC<sup>2</sup>-2/SDX type narrow resonance approach is that the shielding of one nuclide on another or one resonance on another is applied on the fine group scale and can lead to erroneous "overlap" corrections.<sup>27</sup>

**AMPX.** The NITAWL module of AMPX relies primarily on the Nordheim Integral Treatment for resonance self shielding. This method was developed for water reactor applications and, as programmed, assumes completely isolated resonances in a pseudo two region integral transport calculation. A narrow resonance approximation is also available which allows one nuclide to "shield" another through tabulations of group cross sections built into the coding. This, of course, suffers from the same deficiency as does the Bondarenko approach. The ROLAIDS module of AMPX is an integral transport resonance treatment. This module will calculate self shielded resonance cross sections for any of the simple one dimensional geometries -- slabs, spheres, and cylinders -- and allows an arbitrary number of regions, each containing an arbitrary mixture of elements. The energy spacing of cross sections is completely arbitrary. Typical calculations cover the 1 eV-15 keV range. No provisions are made at present for the inclusion of downscattering sources from inelastic and n<sub>2</sub>n scattering.

#### 12. Fission Spectrum

Differences even exist on the manner in which fission spectra are determined. As presently programmed, all the systems calculate one dimensional fission spectrum arrays for fissionable nuclides.

MC<sup>2</sup>-2 uses a built-in expression. The user can input a "temperature" to satisfy different systems. In SPHINX, a single fission spectrum, normally selected from the multigroup library, is used for a one dimensional calculation. In the XSDRNP module of AMPX, the fission spectrum used is zone dependent and is weighted over the production rate of each nuclide in a zone.

Generally, one nuclide will dominate the "correct" fission spectrum, so that these differences are of little significance except to further cloud cross section comparisons.

#### 13. Computer System

This area is a very important consideration for any potential user of a code system. Generally, it is a very expensive and time-consuming task to convert a large computer code from one type of computer to another.

**ETOE-2/MC<sup>2</sup>-2/SDX.** This system was developed on an IBM system, and a CDC version is operational at Los Alamos.

**MINX/SPHINX.** Versions of the two codes in this system are operational on IBM 360 and CDC-6600 systems.

**AMPX.** Versions of this system are operational on IBM-360, CDC-6600, and UNIVAC-1108 systems.

In certain processes, the difference in significance on various computers leads to calculational differences. Single precision arithmetic on an IBM machine is good for 6 1/2 to 7 significant digits.

On a CDC machine, single precision arithmetic is good to 12 digits.

#### 14. Unique Programming Techniques

Each of the three systems has its list of fortes in which it claims superiority over the other two.

**ETOE-2/MC<sup>2</sup>-2/SDX.** The calculation of a weighting function on the ultrafine group scale and the very complete narrow resonance options are beyond the capabilities of the other two systems. A "same-sequence" overlap term is included in its unresolved treatment that is neglected in the other systems.

**MINX/SPHINX.** MINX attempts to determine errors in processing -- a feature not treated elsewhere. It processes ENDF/B error information. It uses "paging techniques" which allow one to use small core computers to process "large array" data. This has its disadvantages, however, since it requires BCD ENDF/B libraries and produces input/output bound jobs in some situations, especially on an IBM machine.

**AMPX.** The ability to process a large number of ENDF/B libraries, the neutron to gamma coupling, the thermal processing, one dimensional transport theory, and free form input schemes are among salient features of AMPX.

#### Conclusions

With all the differences noted above, it is futile to expect that any complex problem would show agreement among the systems on other than "integrated" results. Even when one gets good agreement on k-effectives and reaction rates, the more complicated parameters, such as material "worths" and Doppler coefficients will probably have significant disagreement because they are very sensitive to the areas where the systems are most different. Fast reactor Doppler coefficients, for example, are very sensitive to what goes on in the low keV region where effects like overlaps on both resolved<sup>27</sup> and unresolved<sup>22</sup> resonances can become important. Shielding studies require transport calculations with good representations for anisotropic processes. Most water moderated systems are poorly represented by narrow resonance approximations. Any problem has its own set of unique sensitivities that require different levels of approximation for different processes. With the guidance of the cross section sensitivity programs such as are being pursued at Argonne<sup>28</sup> and Oak Ridge<sup>29</sup>, among others, one can begin to make intelligent decisions as to the adequacy or inadequacy of particular approximations.

The three systems are in fairly advanced states of development. Because of the differences in procedures and techniques noted above, any benchmarking effort must be restricted to comparing specific algorithms, rather than a more global comparison. For example, the two integral transport codes can be benchmarked against each other and against simpler treatments for resonance self shielding. The various treatments of inelastic scattering can be compared, etc., etc.

A question of a more elemental nature concerns weighting. Can one produce "properly" weighted cross sections when he uses values already weighted over an approximate spectrum to arrive at a new weighting spectrum? (Note that even MC<sup>2</sup>-2 suffers from this effect since its cross sections are flat weighted at the ultrafine group level.)

Many other questions on weighting remain unanswered. Greenspan<sup>30</sup> suggests, with calculational support, that the flux weighting techniques commonly used in the resonance region can overpredict the reactivity worths of U-238 and Pu-239 by as much as 30%. He recommends that cross section processing codes be modified to produce constants physically "consistent" with particular applications; e.g., constants used in reactivity worth calculations employing adjoint techniques should use "adjoint" weighted values. To this author's knowledge, no system is available that properly addresses this type of effect. A study by Kier and Zolotar<sup>31</sup> that investigated the same "weighting" effects suggests that the overprediction is more like 2%.

For deep penetration problems, Ginsberg and Becker<sup>31</sup> have demonstrated that the use of the scalar flux to weight higher moments of the cross sections can lead to constants which give improper results for some problems and group structures.

Some of these effects are circumvented by the procedures used in the three systems, but in many cases, a lack of resources combined with large commitments on more urgent problems causes many of these avenues for disagreement to remain unexplored.

With modular programming techniques, it is possible to build a single system which combines virtually all of the features used in the three systems. A user would then be able to make intelligent decisions as to the approximations required for a particular problem. All areas would potentially benefit from technical improvements to all other areas in the system. This system should not have ten paths for producing inelastic scattering matrices -- or ten separate "complete" codes. It should of necessity be limited to techniques which have strong theoretical support and which have a decided superiority over other similar treatments.

In truth, there remains an overwhelming amount of work before this ideal state can be reached, especially towards tailoring codes to different machines with different core sizes and peripheral equipment. But the trend is in this direction. MC<sup>2</sup>-2 and SDX share many of the same modules for resonance processing. A version of MINX has been interfaced into the AMPX system. All of the systems are committed to operating on more than one computer system. Perhaps . . . . . ?

#### Acknowledgements

The author gratefully acknowledges the comments of Chuck Weisbin, Herb Henryson, Jim Lucius, and Lester Petrie concerning this paper. Many thanks also to Beckie Eddlemon who very patiently waded through my rough drafts.

#### References

1. M. K. Drake, (ed.), "Data Formats and Procedures for the ENDF Neutron Cross Section Library," BNL-50279 (October 1970).
2. H. Henryson, II, B. J. Toppel, and C. G. Stenberg, "ETOE-2/MC<sup>2</sup>-2/SDX Multigroup Neutron Cross-Section Processing," presented at the Seminar on Codes for Nuclear Data Processing held at NEA-CPL, CONF-731207-1, Ispra, December 5-7, 1973; see also B. J. Toppel and H. Henryson, II, "Methodology and Application of the MC<sup>2</sup>-2/SDX Cross-Section Capability," Trans. Am. Nucl. Soc., 16, 126 (1973); see also H. Henryson, II and B. J. Toppel, "MC<sup>2</sup>-2--A Code to Calculate Fast Neutron Spectra and Multigroup Cross Sections, ANL-8144 (to be published).

3. C. R. Weisbin, P. D. Soran, D. R. Harris, R. J. LaBauve, and J. S. Hendricks, "MINX - A Multigroup Interpretation of Nuclear X-Sections," Trans. Am. Nucl. Soc. 16, 127 (June 1973); see also C. R. Weisbin, P. D. Soran, R. E. MacFarlane, D. R. Harris, R. J. LaBauve, J. S. Hendricks, and J. E. White, "MINX, A Multigroup Interpretation of Nuclear Cross Sections from ENDF/B," Los Alamos Scientific Laboratory, report to be published; see also D. R. Harris, R. J. LaBauve, R. E. MacFarlane, and P. D. Soran, Los Alamos Scientific Laboratory, and C. R. Weisbin and J. E. White, Oak Ridge National Laboratory, "MINX, A Modular Code System for Processing Multigroup Cross Sections from Nuclear Data in ENDF/B Format," LA-UR-1766, presented at the Seminar on Codes for Nuclear Data Processing held at NEA-CPL, CONF-731207-1, Ispra, December 5-7, 1973.
4. N. C. Paik, C. Durston, W. Davis, and M. B. Yarbrough, "Physics Evaluations and Applications - Quarterly Progress Report for Period Ending January 31, 1974," WARD-XS-3045-5 (March 1974).
5. N. M. Greene and F. R. Mynatt, "The AMPX Modular Code System for Generating Coupled Neutron-Gamma Multigroup Cross-Section Sets," Trans. Am. Nucl. Soc. 15, 568 (1972); see also N. M. Greene et al., "AMPX: A Modular Code System for Generating Coupled Multigroup Neutron-Gamma Libraries from ENDF/B," ORNL-TM-3706 (to be published).
6. B. J. Toppel, A. L. Rago, and D. M. O'Shea, "MC<sup>2</sup>, A Code to Calculate Multigroup Cross Sections," ANL-7318 (June 1967).
7. R. E. Schenter, J. L. Baker, and R. B. Kidman, "ETOX - A Code to Calculate Group Constants for Nuclear Reactor Calculations," BNWL-1002 (1969).
8. R. W. Hardie and W. W. Little, Jr., "IDX, A One-Dimensional Diffusion Code for Generating Effective Nuclear Cross Sections," BNWL-954 (March 1969).
9. D. E. Kusner, R. A. Dannels, and S. Kellman, "ETOG-1, A Fortran IV Program to Process Data from the ENDF/B File to the MUFT, GAM, and ANISN Formats," WCAP-3845-1 (1969).
10. R. Q. Wright, J. L. Lucius, N. M. Greene, and C. W. Craven, Jr., "SUPERTO: A Program to Generate Fine Group Constants and P<sub>n</sub> Scattering Matrices from ENDF/B," ORNL-TM-2679 (Sept. 1969).
11. H. C. Honeck and D. R. Finch, "FLANGE-II, A Code to Process Thermal Neutron Data from an ENDF/B Tape," DP-1278 (1971).
12. B. A. Hutchins, C. L. Cowan, M. D. Kelley, and J. E. Turner, "ENDRUN-II, A Computer Code to Generate a Generalized Multigroup Data File from ENDF/B," GEAP-13704 (1971).
13. G. D. Joanou and J. S. Dudek, "GAM-II-A B<sub>3</sub> Code for the Calculation of Fast-Neutron Spectra and Associated Multigroup Constants," GA-4265, (Sept. 1963).
14. C. R. Weisbin, N. M. Greene, H. Henryson, II, R. J. LaBauve, C. Durston, D. E. Cullen, and R. B. Kidman, "Fast Reactor Cross Section Processing Codes - Is There a Dollars Worth of Difference Between Them?" Proceedings of the ANS Topical -- Advanced Reactors: Physics, Design and Economics, (Sept. 1974), to be published.
15. R. B. Kidman, "A Comparison of Two Fast Reactor Cross Section Codes," HEDL-TME 72-57 (February 1972).
16. W. W. Engle, Jr., "A Users Manual for ANISN," K-1693, (March 1967).
17. Odelli Ozer, "RESEND: A Program to Pre-process ENDF/B Materials with Resonance Files into Pointwise Form," BNL-17134, (November 1973).
18. G. deSaussure and R. B. Perez, "POLLA, A FORTRAN Program to Convert R-Matrix-Type Multilevel Resonance Parameters for Fissile Nuclei into Equivalent Kapur-Peierls-Type Parameters," ORNL-TM-2599, (1969).



19. P. H. Kier and A. A. Rabba, "RABBLE, A Program for Computation of Resonance Absorption in Multi-region Reactor Cells," ANL-7326 (1967).
20. L. W. Nordheim, "The Theory of Resonance Absorption," Proceedings of Symposia in Applied Mathematics, Vol. XI, p. 58, Garrett Birkhoff and Eugene P. Wigner, (eds.), American Mathematical Society (1961).
21. R. N. Hwang, "Efficient Methods for the Treatment of Resonance Cross Sections," Nucl. Sci. Eng., 52, pp. 157-175, (1973).
22. H. Henryson, II, private communication.
23. D. E. Cullen, O. Ozer, and C. R. Weisbin, "Exact Doppler Broadening of Evaluated Neutron Cross Sections," Trans. Am. Nucl. Soc. 16, 320 (1973).
24. E. Gelbard and H. Henryson, II, "An Efficient Calculation of Legendre Moments of Multigroup Elastic Scattering Transfer Matrices, Trans. Am. Nucl. Soc., Vol. 17, p. 263 (1973).
25. C. R. Weisbin, P. D. Soran, J. S. Hendricks, "A New Procedure for the Determination of Neutron Multigroup Transfer Matrices," Nucl. Sci. Eng., 55, pp. 329-341, (1974).
26. N. M. Greene, "Anisotropic Inelastic Scattering Matrices from ENDF Data," Trans. Am. Nucl. Soc., Vol. 17, p. 549 (1973).
27. I. Broeders-Siep, "Contribution to the Mutual Resonance Shielding of  $U^{238}$  and  $Pu^{239}$ ," KFK-1890, (February 1974).
28. H. Henryson, II, H. Hummel, R. Hwang, W. M. Stacey, Jr., and B. J. Toppel, "Sensitivity of Integral Neutronics Properties of LMFBR Assemblies to Cross-Section Preparation Methods and Data Uncertainties Using the ETOE-2/MC<sup>2</sup>-2/SDX Code System," proceedings of the ANS Topical - Advanced Reactors: Physics, Design, and Economics, (Sept. 1974), to be published.
29. E. G. Silver, E. M. Oblow, J. M. Kallfelz, C. R. Weisbin, D. E. Bartine, G. F. Flanagan, and F. R. Mynatt, "Generalized Reactor Sensitivity Program at ORNL," Trans. Am. Nucl. Soc., 18 (June 1974).
30. E. Greenspan, "On the Calculation of Reactivity Worths in Fission Reactors," MATT-944, Plasma Physics Laboratory, (Dec. 1972).
31. P. H. Kier and B. A. Zolotar, "On Fine Structure Effects in Central Worth Calculations," Trans. Am. Nucl. Soc., 18, p. 310, (1974).
32. A. Ginsberg and M. Becker, "Models for Anisotropic Weighting Spectra," Trans. Am. Nucl. Soc., 14, No. 1, p. 368, (1971).



Cross sections for the (n,2n) and (n,3n) reactions have been measured for several nuclides between 6 and 15 MeV using a large liquid scintillator to count the neutrons directly. Measurements were made relative to fission cross section of  $^{238}\text{U}$  for  $^{56}\text{Fe}$ ,  $^{59}\text{Co}$ ,  $^{76}\text{Se}$ ,  $^{78}\text{Se}$ ,  $^{80}\text{Se}$ ,  $^{82}\text{Se}$ ,  $^{89}\text{Y}$ ,  $^{93}\text{Nb}$ ,  $^{103}\text{Rh}$ ,  $^{169}\text{Tm}$ ,  $^{175}\text{Lu}$ ,  $^{181}\text{Ta}$ ,  $^{197}\text{Au}$ ,  $^{209}\text{Bi}$ ,  $^{238}\text{U}$ , and for the natural elements Pt and W. The relative accuracy was generally in the range 5 to 10 %. The present results are compared with previous measurements.

(Nuclear reactions  $^{56}\text{Fe}$ ,  $^{59}\text{Co}$ ,  $^{76,78,80,82}\text{Se}$ ,  $^{89}\text{Y}$ ,  $^{93}\text{Nb}$ ,  $^{103}\text{Rh}$ ,  $^{169}\text{Tm}$ ,  $^{175}\text{Lu}$ ,  $^{181}\text{Ta}$ , W, Pt,  $^{197}\text{Au}$ ,  $^{209}\text{Bi}$ ,  $^{238}\text{U}$ (n,2n) ;  $^{238}\text{U}$ (n,3n) ;  $E_n = 8 - 15$  MeV ; measured  $\sigma(E_n)$ ).

## Introduction

The activation technique generally used to measure (n,2n) and (n,3n) cross sections depends on the determination, after neutron bombardment, of the activity produced in a sample and is therefore limited to nuclides which leave a suitably active residual isotope.

The large scintillator method used in the present experiment depends on the detection of the emitted neutrons and thus can be used for any nuclide, provided that several grams of material are available for a sample. The present work uses essentially the same technique as Mather and Pain<sup>1</sup>. The main difference is the energy range covered which was from threshold to 15 MeV in the present work, as compared to the energies of 12.4 and 14.3 MeV for Mather's measurements.

## Experimental Method

A description of the principle of the method and details of the experimental set up and of corrections are given elsewhere<sup>2</sup>. The experiment relies on two properties of the neutron detector, a large loaded liquid scintillator : its high neutron efficiency and the relatively long lifetime in the scintillator for neutrons before capture. This gives identification of an (n,2n) event by two separate pulses in the scintillator within the 30  $\mu\text{s}$  following the event.

### Detection of (n,2n) and (n,3n) events (fig. 1)

About 10 to 15 grams of the sample to be measured are placed at the center of the scintillator and irradiated by a collimated neutron beam. Neutrons are produced by the  $\text{D(d,n)}^3\text{He}$  reaction, using a gaseous target and the 14 MeV tandem Van de Graaff accelerator pulsed at a frequency of 2.5 MHz (pulse width  $\sim 2$  ns). An electrostatic beam sweeper is used to keep only three bursts each 60  $\mu\text{s}$ .

After each group of three bursts, a 30  $\mu\text{s}$  counting gate is opened on the output of the liquid scintillator. The number of gates containing 0, 1, 2, ... pulses are recorded during a run. These data are corrected for the two sources of background in the scintillator :

- The natural background, measured for the same number of counting gates with the accelerator beam off.
- The accelerator dependant background, measured with the beam on and the sample out for the same number of incident neutrons.

The data are also corrected for the detection dead time (120 ns), for the detector efficiency ( $\sim 75\%$ ), and for the possibility of two (n,n') or (n,n) events occurring in the same counting gate, being then indistinguishable from a (n,2n) event.

These corrections give the number of gates containing 2 or 3 neutrons, i.e. the number of (n,2n) and (n,3n) events, for non fissionable materials.

In the case of fissionable materials, it is necessary to subtract the fission events of neutron multiplicity 2 or 3. The total number of fissions can be calculated from the higher measured multiplicities ( $\geq 4$ ) using fission multiplicity distributions previously determined with a fission chamber<sup>3</sup>. These distributions and the calculated number of fissions thus enable one to deduce the number of fission events of multiplicity 2 or 3.

### (n,2n) and (n,3n) cross section determinations

A relative incident neutron flux measurement allows the (n,2n) and (n,3n) cross-sections to be normalized on a reference cross section.

In the case of fissionable materials, (n,2n) and (n,3n) cross sections can be directly obtained relative to fission cross section, since the number of fission events occurring during the measurement is also determined. Because of the lack of accurately determined (n,2n) cross sections, a fission cross section was also chosen as reference for non fissionable materials, the fission cross section of  $^{238}\text{U}$ .

### Relative flux measurement (fig. 1)

The flux monitor consists of a small liquid scintillator located 1.5 meter behind the sample, in the collimated neutron beam. Monoenergetic incident neutrons in the energy range 6-15 MeV are produced using the  $\text{D(d,n)}^3\text{He}$  reaction. With the pulsing system adopted, it is possible, by the time-of-flight technique, to separate the monoenergetic neutrons, the only neutrons which induce (n,2n) or (n,3n) reactions, from deuteron break-up neutrons as well as from neutrons induced by (d,n) reactions on the target materials. This technique provides very precise relative flux measurement for (n,2n) and (n,3n) reactions.

A relative determination of the efficiency of the monitor versus neutron energy, using the results of a Monte-Carlo code calculation, allows, in the case of  $^{238}\text{U}$ , an accurate determination of the apparent fission cross section and of the fission neutron multiplicities. This calibration is necessary since, in contrast to (n,2n) or (n,3n) events, fission events may be induced by the secondary neutrons.

## Results

### Standards

The large liquid scintillator efficiency was determined using a  $^{252}\text{Cf}$  source and assuming a value of  $\bar{\nu} = 3.732 \pm 0.000$  for the average number of prompt neutrons emitted per spontaneous fission.

The standard fission cross section of  $^{238}\text{U}$  used for the normalization of the results was taken from the evaluation of Sowerby et al.<sup>4</sup>.

## Error derivation

The errors quoted are standard errors derived by quadratic addition of the statistical errors of the experimental data and the errors of the corrections. The uncertainties of the standards,  $\bar{\nu}$  for  $^{252}\text{Cf}$  and the fission cross section of  $^{238}\text{U}$ , have not been included.

## (n,2n) and (n,3n) cross sections

The final (n,2n) cross sections for 17 non fissionable materials between threshold and 15 MeV are given in table I. Also listed are the (n,2n) and (n,3n) cross sections of  $^{238}\text{U}$  and the fission cross section of  $^{238}\text{U}$  used as a standard.

(n,2n) cross sections of  $^{56}\text{Fe}$  and  $^{175}\text{Lu}$  were derived from measurements on the natural elements, using the results of the calculations by Pearlstein<sup>47</sup> to subtract the contribution of the other isotopes. Enriched isotopes were used for the measurements on selenium. The calculations of Pearlstein were, here also, used in order to correct for the contribution of the non measured  $^{74}\text{Se}$  and  $^{77}\text{Se}$  isotopes present in small amount in the samples.

## Discussion

The present measurements are compared to previously published results in figure 2. The values of Ashby et al.<sup>5</sup> at 14.1 MeV for  $^{56}\text{Fe}$ ,  $^{209}\text{Bi}$ ,  $^{197}\text{Au}$ ,  $^{181}\text{Ta}$  and the values of Mather et al.<sup>1</sup> at 12.4 and 14.3 MeV for  $^{89}\text{Y}$ ,  $^{93}\text{Nb}$ ,  $^{103}\text{Rh}$ ,  $^{169}\text{Tm}$ ,  $^{197}\text{Au}$  and  $^{238}\text{U}$ , also obtained with the large liquid scintillator method, are in relatively good agreement with the present results. By contrast, results obtained by the activation technique are generally more scattered, partly due to the variety of standards used for detector calibration and for flux determination.

Nevertheless, the agreement between the results obtained by the two techniques is rather good for  $^{56}\text{Fe}$ ,  $^{76}\text{Se}$ ,  $^{82}\text{Se}$ ,  $^{89}\text{Y}$  (ref. 45),  $^{197}\text{Au}$ ,  $^{209}\text{Bi}$  and  $^{238}\text{U}$ .

The lack of agreement between the two techniques for  $^{103}\text{Rh}$ ,  $^{175}\text{Lu}$ ,  $^{181}\text{Ta}$  is probably due to the measurement in the activation method of only one isomer for each of the nuclei  $^{102}\text{Rh}$ ,  $^{174}\text{Lu}$  and  $^{180}\text{Ta}$ ; whereas the large liquid scintillator method has the advantage of measuring the total (n,2n) cross sections.

In the case of  $^{93}\text{Nb}$ , earlier measurements of the (n,2n) cross section by the activation method have not been plotted in the figure, since they are now proved<sup>46</sup> to be measurements of only the 10.15 days isomeric state of  $^{92}\text{Nb}$ .

For  $^{169}\text{Tm}$ , although two activation measurements are approximately a factor 2 lower, a recent compilation<sup>46</sup> of experimental data has proved the consistency of the results obtained by the two techniques.

In the case of  $^{59}\text{Co}$ , results of activation measurements are too widely scattered for a valuable comparison to be possible.

Results for the 4 measured isotopes of Se are compared in fig.2. Such measurements are useful for studying the dependence of (n,2n) cross sections on the number of neutrons for isotopes of a given element and should help in calculating more precise (n,2n) cross sections.

## Conclusion

The major experimental difficulty encountered in the present work was the presence of secondary neutrons accompanying the monoenergetic neutrons of the  $\text{D(d,n)}^3\text{He}$  reaction used to produce incident neutrons. However this difficulty was overcome by the use of pulsed beam which allowed one to measure the incident neutron spectrum and at the same time to maintain a sufficiently high neutron flux.

As far as we know, the present results are the only ones to cover the entire energy range from threshold to 15 MeV. They show the value of the large liquid scintillator method for providing (n,2n) and (n,3n) cross sections over a large energy range.

## References

1. D S Mather et al., AWRE Report 047/69 (1969)  
AWRE Report 072/72 (1972)
2. J Frehaut, G Mosinski, Rapport CEA-R-4627 (1974)
3. M Soleilhac et al., J. Nucl. Energy 23 (1969) 257
4. M G Sowerby et al., AERE Report R7273 (1973)
5. V J Ashby et al., Phys. Rev. 111 (1958) 616
6. R Wenusch et al., Nucl. Sci. Abstracts 17(1963)3475
7. P Hille et al., Data taken in Nucl. Phys. 65 (1965) 257
8. N Flerov et al., Atomnaya Energiya 5 (1958) 657
9. L Rosen, L Stewart, Phys. Rev. 107 (1957) 824
10. E Feicht, H. Vonach, Nukleonik 10 (1967) 58
11. V Lebedev, Data taken in ref. 10
12. A Adam et al., Nucl. Phys. 49 (1963) 489
13. S Okumura, Nucl. Phys. A93 (1967) 74
14. Gabbard, Data taken in Euratom Report EUR 122.e (1963)
15. E Veigold, R N Glover, Nucl. Phys. 32 (1962) 106
16. A Paulsen, H Liskien, J. Nucl. Energy 19 (1965) 907
17. P Decowski et al., Nucl. Phys. A112 (1968) 513
18. M Bormann et al., J. Phys. Radium 22 (1961) 602
19. J Cabé et al., Euratom Report EANDC 49 (1963) 82
20. B Granger et al., Euratom Report EANDC 49 (1963) 83
21. W Dilg et al., Nucl. Phys. A118 (1968) 9
22. D R Nethaway, Nucl. Phys. A190 (1972) 635
23. R G Wille, R W Fink, Phys. Rev. 118 (1960) 242
24. D G Vallis, AWRE Report 076/66 (1966)
25. R Rieder, H Munzer, Acta Phys. Austria 23 (1966) 42
26. H A Tewes et al., UC34-WASH (1960) 1028
27. R J Prestwood, B P Bayhurst, Phys. Rev. 121 (1961) 1438
28. H K Vonach et al., EANDC E 89 "U" (1968) 37
29. A K Hankla et al., Bull. Am. Phys. Soc. 13 (1968) 1421
30. S K Mangal et al., Nucl. Phys. 69 (1965) 158
31. J Karolyi et al., Nucl. Phys. A122 (1968) 234
32. R Vos et al., Bull. Am. Phys. Soc. 18 (1973) 775
33. A Poularikas et al., J. Inorg. Nucl. Chem. 13 (1960) 196
34. M Bormann et al., Nucl. Phys. A115 (1968) 309
35. J D Knight et al., Phys. Rev. 112 (1958) 259
36. E R Graves et al., Data taken in ref. 35
37. J A Phillips, AERE NP/R 2033 (1956)
38. A Daroczy et al., Proc. Conf. on Neutron Physics, Kiev 1 (1971) 228
39. G P Antropopov et al., Atomnaya Energiya 5 (1958) 456
40. J L Perkin et al., J. Nucl. Energy 14 (1961) 69



41. P V Rao, R W Fink, Phys. Rev. 154 (1967) 1023  
 42. S S Hasan et al., Nucl. Phys. A181 (1972) 101  
 43. W Lu and al., Phys. Rev. 1C (1970) 350  
 44. A Paulsen, R Wiedera, Z. Physik 238 (1970) 23

45. C Philis, Rapport CEA-R-4636 (1975)  
 46. C Philis, P G Young, to be published as Rapport CEA  
 47. S Pearlstein, Nuclear Data B, Section A, 3 (1967) 3

$E_n$ MeV	$\Delta E_n$ keV	$\sigma_f$ mb	$\sigma(n, 2n)$ , mb									
		$^{238}\text{U}$		$^{56}\text{Fe}$	$^{59}\text{Co}$	$^{76}\text{Se}$	$^{78}\text{Se}$	$^{80}\text{Se}$	$^{82}\text{Se}$	$^{89}\text{Y}$	$^{93}\text{Nb}$	$^{103}\text{Rh}$
9.44	115	960									$56 \pm 21$	
9.93	110	952							$109 \pm 6$		$404 \pm 27$	$103 \pm 13$
10.42	100	948						$65 \pm 5$	$325 \pm 16$		$607 \pm 39$	$361 \pm 24$
10.91	95	952			$19 \pm 6$		$17 \pm 5$	$257 \pm 14$	$518 \pm 26$		$800 \pm 45$	$593 \pm 31$
11.40	90	957			$127 \pm 10$		$148 \pm 9$	$457 \pm 24$	$689 \pm 36$		$947 \pm 54$	$837 \pm 48$
11.88	85	965		$39 \pm 8$	$232 \pm 15$	$116 \pm 12$	$352 \pm 21$	$635 \pm 36$	$814 \pm 44$	$53 \pm 8$	$1133 \pm 65$	$1011 \pm 58$
12.36	85	978		$108 \pm 10$	$368 \pm 24$	$252 \pm 24$	$522 \pm 38$	$844 \pm 61$	$970 \pm 68$	$215 \pm 12$	$1215 \pm 65$	$1194 \pm 64$
12.85	80	999		$220 \pm 16$	$508 \pm 30$	$434 \pm 36$	$693 \pm 50$	$936 \pm 67$	$1044 \pm 73$	$450 \pm 21$	$1286 \pm 71$	$1257 \pm 69$
13.33	75	1031		$326 \pm 23$	$601 \pm 37$	$607 \pm 48$	$828 \pm 60$	$1036 \pm 73$	$1147 \pm 80$	$668 \pm 41$	$1380 \pm 72$	$1314 \pm 68$
13.80	75	1086		$415 \pm 26$	$711 \pm 41$	$743 \pm 56$	$970 \pm 69$	$1137 \pm 81$	$1132 \pm 80$	$846 \pm 35$	$1300 \pm 70$	$1364 \pm 72$
14.28	70	1163		$413 \pm 29$	$626 \pm 46$	$798 \pm 60$	$971 \pm 70$	$1109 \pm 79$	$1134 \pm 81$	$837 \pm 61$	$1358 \pm 98$	$1396 \pm 101$
14.76	65	1216		$521 \pm 36$	$742 \pm 53$	$873 \pm 65$	$1018 \pm 74$	$1136 \pm 82$	$1172 \pm 84$	$981 \pm 71$	$1444 \pm 104$	$1458 \pm 105$

$E_n$ MeV	$\Delta E_n$ keV	$\sigma_f$ mb	$\sigma(n, 2n)$ , mb									$\sigma(n, 3n)$ mb
		$^{238}\text{U}$	$^{169}\text{Tm}$	$^{175}\text{Lu}$	$^{181}\text{Ta}$	$^{197}\text{Au}$	$^{209}\text{Bi}$	Nat. Pt	Nat. W	$^{238}\text{U}$	$^{238}\text{U}$	
7.93	150	952					$131 \pm 15$	$208 \pm 26$	$238 \pm 27$	$1081 \pm 110$		
8.44	140	962	$68 \pm 34$	$180 \pm 37$	$310 \pm 28$	$44 \pm 22$	$382 \pm 36$	$404 \pm 36$	$690 \pm 46$	$1178 \pm 113$		
8.94	125	964	$377 \pm 27$	$686 \pm 50$	$808 \pm 47$	$288 \pm 20$	$810 \pm 51$	$614 \pm 48$	$1032 \pm 55$	$1313 \pm 113$		
9.44	120	960	$978 \pm 87$	$1220 \pm 110$	$1382 \pm 112$	$738 \pm 65$	$1191 \pm 98$	$1059 \pm 74$	$1510 \pm 99$	$1361 \pm 139$		
9.93	110	952	$1232 \pm 69$	$1482 \pm 83$	$1560 \pm 84$	$1027 \pm 57$	$1563 \pm 86$	$1338 \pm 78$	$1729 \pm 101$	$1378 \pm 114$		
10.42	100	948	$1567 \pm 87$	$1709 \pm 96$	$1795 \pm 97$	$1378 \pm 75$	$1837 \pm 100$	$1505 \pm 88$	$1755 \pm 101$	$1407 \pm 92$		
10.91	95	952	$1661 \pm 107$	$1872 \pm 125$	$1850 \pm 115$	$1589 \pm 101$	$1948 \pm 124$	$1619 \pm 85$	$1800 \pm 94$	$1389 \pm 142$		
11.40	90	957	$1715 \pm 79$	$1802 \pm 105$	$1860 \pm 103$	$1691 \pm 76$	$1936 \pm 110$	$1794 \pm 101$	$2014 \pm 113$	$1478 \pm 111$		
11.88	85	965	$1799 \pm 96$	$1878 \pm 103$	$1877 \pm 96$	$1816 \pm 94$	$1935 \pm 101$	$1953 \pm 111$	$2011 \pm 114$	$1360 \pm 125$	$-4 \pm 46$	
12.36	85	978	$1953 \pm 84$	$2060 \pm 120$	$2051 \pm 113$	$2012 \pm 83$	$2131 \pm 119$	$2028 \pm 108$	$2087 \pm 112$	$1449 \pm 113$	$109 \pm 43$	
12.85	80	999	$2093 \pm 86$	$2101 \pm 124$	$2143 \pm 117$	$2166 \pm 87$	$2125 \pm 121$	$2062 \pm 113$	$2124 \pm 117$	$1374 \pm 105$	$209 \pm 68$	
13.33	75	1031	$2131 \pm 123$	$2134 \pm 109$	$2137 \pm 119$	$2197 \pm 123$	$2165 \pm 122$	$2070 \pm 107$	$2206 \pm 114$	$1207 \pm 109$	$337 \pm 60$	
13.80	75	1086	$2172 \pm 88$	$2195 \pm 115$	$2219 \pm 119$	$2287 \pm 90$	$2350 \pm 130$	$2094 \pm 111$	$2122 \pm 112$	$906 \pm 115$	$507 \pm 91$	
14.28	70	1163	$1916 \pm 139$	$2071 \pm 151$	$2101 \pm 151$	$2037 \pm 147$	$2144 \pm 155$	$2124 \pm 158$	$2146 \pm 154$	$908 \pm 184$	$502 \pm 116$	
14.76	65	1216	$2053 \pm 147$	$2252 \pm 161$	$2229 \pm 159$	$2215 \pm 158$	$2348 \pm 168$	$2221 \pm 164$	$2269 \pm 177$	$749 \pm 182$	$647 \pm 128$	

Table I. Experimental results for the (n,2n) cross section of  $^{56}\text{Fe}$ ,  $^{59}\text{Co}$ ,  $^{76}\text{Se}$ ,  $^{78}\text{Se}$ ,  $^{80}\text{Se}$ ,  $^{82}\text{Se}$ ,  $^{89}\text{Y}$ ,  $^{93}\text{Nb}$ ,  $^{103}\text{Rh}$ ,  $^{169}\text{Tm}$ ,  $^{175}\text{Lu}$ ,  $^{181}\text{Ta}$ ,  $^{197}\text{Au}$ ,  $^{209}\text{Bi}$ , Pt, W,  $^{238}\text{U}$ , and for the (n,3n) cross section of  $^{238}\text{U}$ . Cross sections are normalized on the fission cross section of  $^{238}\text{U}$  as evaluated by Sowerby et al<sup>4</sup>.

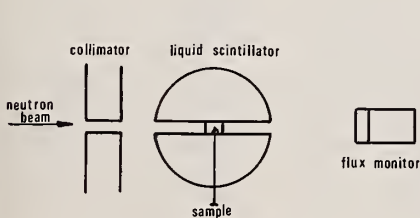


fig. 1a Experimental set up

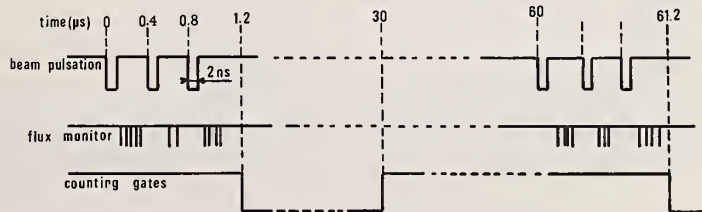


fig. 1b Time sequence of gated data collection



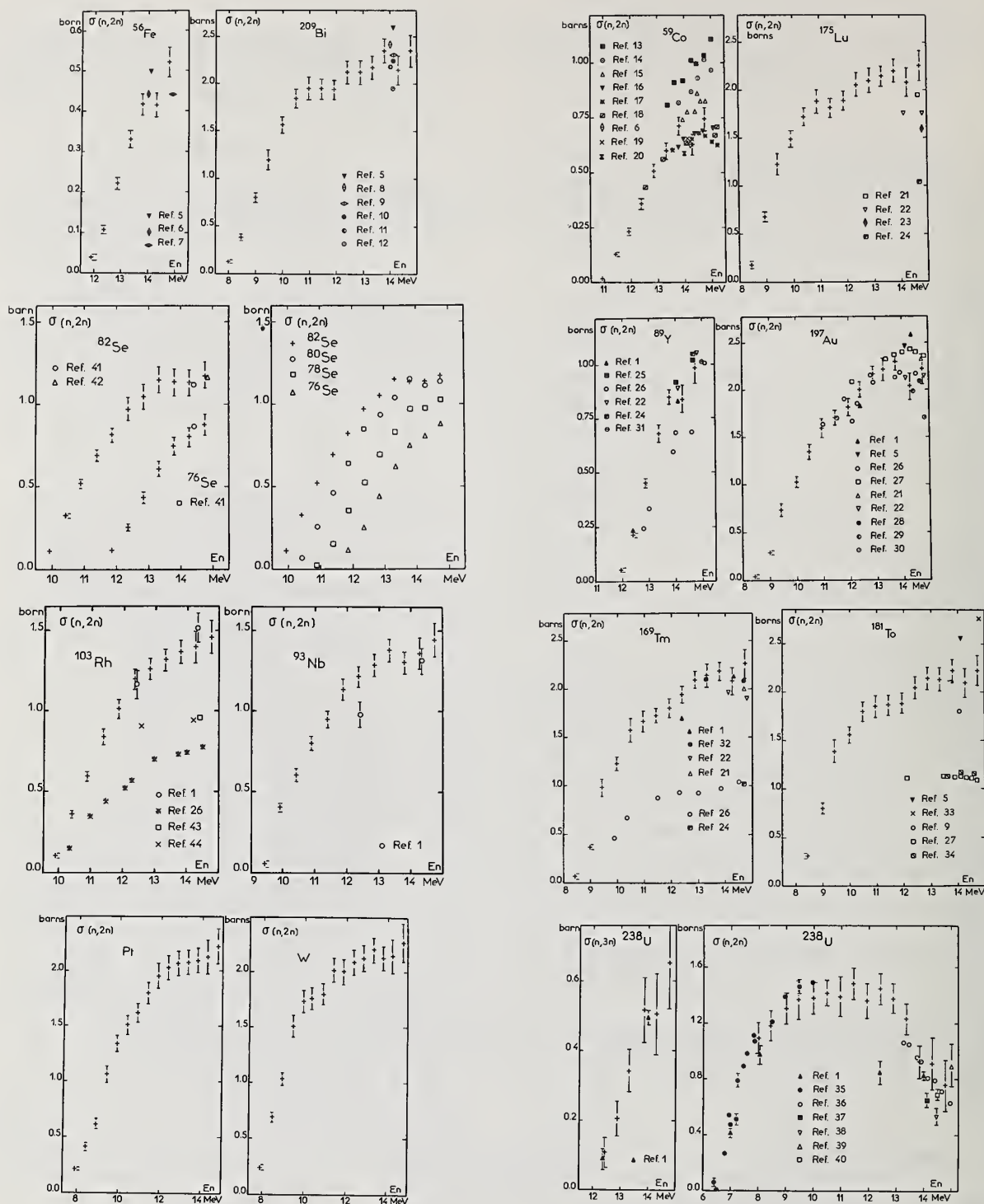


Fig. 2. Values of (n,2n) and (n,3n) cross sections obtained in the present experiment, (+) symbols, plotted against incident neutron energy and compared with previously published results.

EXCITATION CURVE FOR THE PRODUCTION OF  $^{115}\text{In}^m$  BY NEUTRON INELASTIC SCATTERING

D.C. Santry and J.P. Butler  
Atomic Energy of Canada Limited  
Chalk River, Ontario, Canada

Cross sections for the reaction  $^{115}\text{In}(n,n')^{115}\text{In}^m$  have been measured by the activation method from a threshold energy of 0.335 MeV to 14.74 MeV. Cross sections at energies below 5.3 MeV were based on neutron flux measurements determined with a calibrated neutron long counter, while at higher energies measurements were made relative to the known cross section for the  $^{32}\text{S}(n,p)^{32}\text{P}$  reaction. An effective cross section for a  $^{235}\text{U}$  fission neutron spectrum calculated from the measured excitation curve is  $173 \pm 9$  mb.

(Neutron elastic scattering;  $^{115}\text{In}^m$ ; excitation curve; 0.335-14.7 MeV)

### Introduction

As a continuation of our previous studies to provide a set of precise fast-neutron excitation curves for threshold detectors, this paper describes measurements of the  $^{115}\text{In}^m$  production cross section from threshold energies to 14.7 MeV.

Because of its low effective threshold, indium is considered an important fast neutron flux monitor, especially for measuring low energy perturbations in nuclear reactor neutron spectra.

Table 1 lists some of the more important fast neutron induced reactions which can occur with natural indium (4.28%  $^{113}\text{In}$ , 95.72%  $^{115}\text{In}$ ). The multiplicity of neutron reactions with indium complicates its use as a neutron threshold detector. However, by measuring several of these products after a reactor irradiation, it should be possible to characterize the thermal, epithermal and fast neutron contributions.

Table 1 Fast Neutron Reactions Observed With Indium

Reaction	Q Value (MeV)	Half-Life of Product	$\gamma$ -Ray Analyzed (keV)
$^{115}\text{In}(n,n')^{115}\text{In}^m$	-0.335	4.49h	335
$(n,v)^{116}\text{In}$		54.2 min	417, 1097, 1293
$(n,p)^{115}\text{Cd} \rightarrow ^{115}\text{In}^m$	-0.670	2.23d	335
$(n,\alpha)^{112}\text{Ag}$	2.67	3.13h	617
$(n,2n)^{114}\text{In}^m$	-9.03	50 d	192
$^{113}\text{In}(n,n')^{113}\text{In}^m$	-0.392	99.4 min.	392
$(n,v)^{114}\text{In}^m$		50 d	192
$(n,2n)^{112}\text{In}^m$	-9.58	20.0 min.	155
$(n,2n)^{112}\text{In}$	-9.43	14.4 min.	615

### Experimental

A complete description of the techniques and equipment used was given recently in our paper on fast neutron cross sections for the  $^{103}\text{Rh}(n,n')^{103}\text{Rh}^m$  reaction.<sup>1</sup>

### Neutron Irradiations

Monoenergetic neutrons were obtained using the reactions and accelerators listed in Table 2.

Table 2 Reactions used to produce monoenergetic neutrons

Neutron energy (MeV)	Reaction	Target	Accelerator
0.122 to 0.455	$^7\text{Li}(p,n)^7\text{He}$	LiF	2 MV Van de Graaff
0.145 to 6.00	$\text{T}(p,n)^3\text{He}$	TiF	{ 2 MV Van de Graaff Tandem Van de Graaff
5.00 to 13.58	$\text{D}(d,n)^3\text{He}$	$\text{D}_2$ gas	Tandem Van de Graaff
13.58 to 14.74	$\text{T}(d,n)^4\text{He}$	Ti-T	Texas Nuclear Neutron Generator

Disks of indium metal 4.76 mm in diameter and 0.5 mm in thickness were sandwiched between disks of pressed sulfur of the same diameter. The samples were

placed 1.4 cm from the irradiation cell at an angle of  $0^\circ$  to the 3.2 mm diameter proton or deuteron beam. For  $\text{T}(d,n)$  irradiations, samples were also positioned at angles of 50, 75, 105 and  $140^\circ$ . Irradiation times varied from 30 min to 4 hours. The effect of background neutrons produced by beams stopping in apertures, windows and target backing materials was measured by irradiating samples in the absence of deuterium or tritium in the irradiation cell.

### Neutron Flux Monitoring

A neutron long counter, similar to that described by McTaggart<sup>2</sup>, was used to monitor the neutron flux during all irradiations. By using a computer program, saturation radioactivity values were corrected for any changes in neutron intensity with time.

At neutron energies below 5.3 MeV, the long counter was also used to determine absolute values for the neutron flux. A long counter is well suited for flux determinations since it is directional, has a high efficiency and a nearly flat response which varied only by 10% over the neutron energy range used. At neutron energies above 5.5 MeV corrections to the long counter for background neutrons become large and uncertain. For this reason flux measurements at energies above 4.8 MeV were based on the activation of sulfur samples and the known cross section for the  $^{32}\text{S}(n,p)^{32}\text{P}$  reaction.<sup>3,4</sup>

### Activity Measurements

The irradiated sulfur samples were ignited to produce weightless sources of 14.22 day  $^{32}\text{P}$  which were beta counted with an overall efficiency of  $49.2 \pm 0.8\%$ .<sup>4</sup>

A 76 mm x 76 mm NaI(Tl) gamma-ray spectrometer was used to measure the radioactivity in irradiated indium disks. By following the radioactive decay of every sample it was possible to confirm the identity of the observed activities and to obtain the best counting statistics possible with the limited amount of radioactivity present. The  $^{115}\text{In}^m$  was determined from the intensity of the 335 keV gamma ray after the 21 min  $^{112}\text{In}^m$  had decayed. The intensity was corrected for the presence of 54 min  $^{116}\text{In}$  and for 2.3 day  $^{115}\text{Cd}$  which decays to  $^{115}\text{In}^m$ . It was not always possible to resolve the 392 keV photopeak of 99.4 min  $^{113}\text{In}^m$  from  $^{115}\text{In}^m$ . For a few selected irradiations, samples were analyzed with a 17 cm<sup>3</sup> Ge(Li) high resolution gamma-ray spectrometer to determine correction factors for the small amount of  $^{113}\text{In}^m$  present.

Using a value of  $0.459 \pm 0.001$  for the number of gamma-ray emissions per disintegration<sup>5</sup>, the NaI(Tl) detector counting efficiency for  $^{115}\text{In}^m$  was  $9.12 \pm 0.1\%$ .

## Results

Cross sections for the  $^{115}\text{In}(n,n')^{115}\text{In}^m$  reaction were calculated from measured activities in irradiated indium disks and the neutron flux as measured either with a neutron long counter or  $^{32}\text{S}$  activity produced by the  $^{32}\text{S}(n,p)$  reaction. The results are plotted in Figures 1 and 2 as a function of neutron energy. The excitation curve rises rapidly from its observed

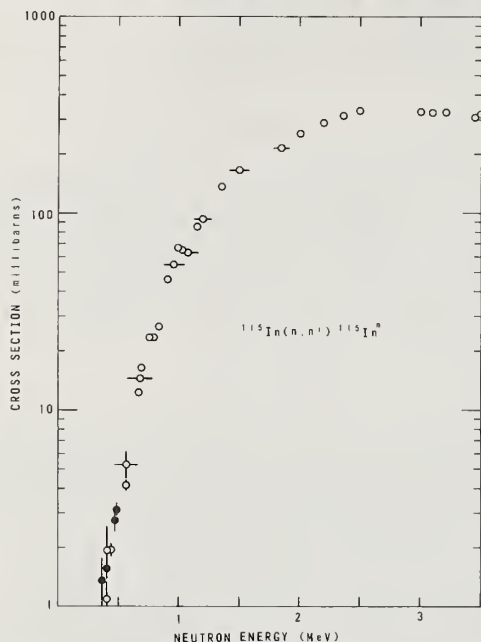


Figure 1 Measured  $^{115}\text{In}(n,n')^{115}\text{In}^m$  cross sections. Neutron source ( $^7\text{Li} + p$ ) ●, ( $\text{T} + p$ ) O.

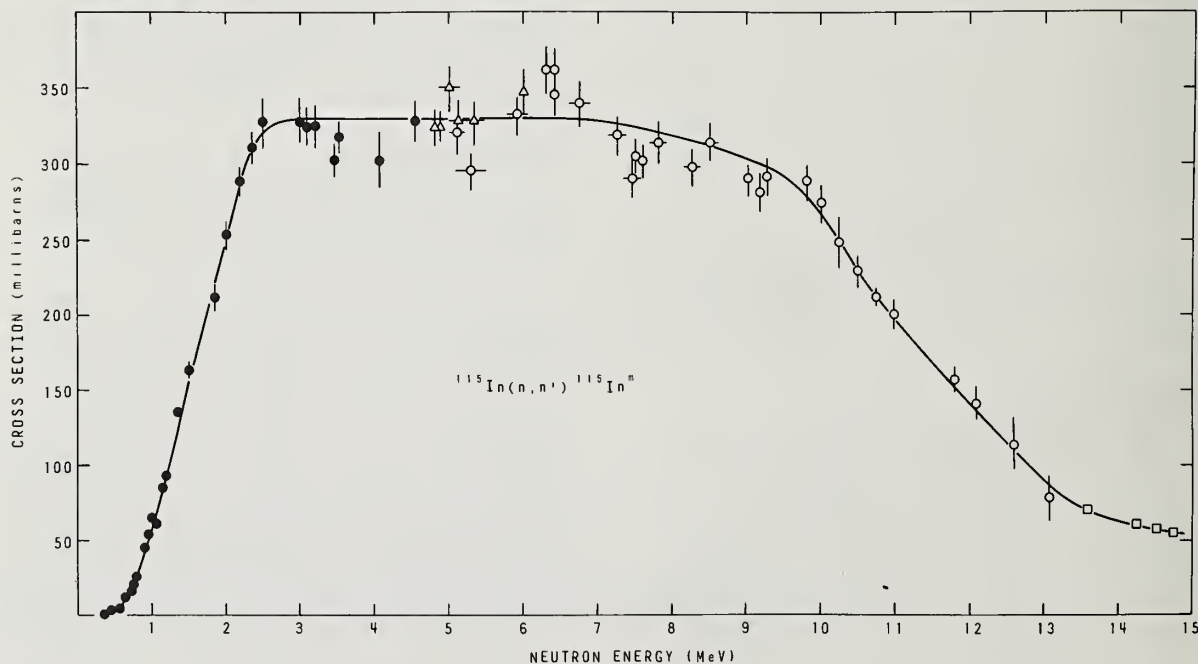


Figure 2 Excitation curve for the  $^{115}\text{In}(n,n')^{115}\text{In}^m$  reaction. Neutron long counter flux measurements for ( $^7\text{Li} + p$ ) and ( $\text{T} + p$ ) neutrons ●,  $^{32}\text{S}(n,p)$  flux measurements for ( $\text{T} + p$ ) neutrons Δ, ( $\text{D} + \text{D}$ ) neutrons O, and ( $\text{D} + \text{T}$ ) neutrons □.

threshold and reaches a maximum value of  $330 \pm 12$  mb at 2.5 MeV, then remains nearly constant until 8.0 MeV. Above this energy the cross section decreases slowly with energy and has a value of  $57.7 \pm 2.3$  mb at 14.5 MeV. Continuity in the shape of the cross section curve was obtained where neutrons were produced by different reactions.

In the energy region 4.8 to 5.1 MeV, 8 irradiations were performed and cross sections were calculated relative to both the neutron long counter and sulfur monitors. The average values agreed to within 2%. It should be emphasized that fluxes measured with the long counter were in no way normalized to the  $^{32}\text{S}(n,p)$  measurements.

Errors in the measured cross sections are 5 to 6% except near the reaction threshold energy, where radioactivity levels are low, and from 12 to 13 MeV, where larger corrections are required for extraneous neutron production. Errors in neutron flux measurements with the long counter are estimated at 3 to 5% and have been included. Where  $^{115}\text{In}^m$  cross sections are given relative to  $^{32}\text{S}(n,p)$  values, possible errors of 6% in the latter have not been included. The average neutron energy spread due to neutron source thickness and geometrical effects, varied from  $\pm 30$  keV at lower energies to  $\pm 110$  keV at higher energies. Neutron energies plotted are average values with 68% of the neutrons having energies within the range indicated.

Cross section values measured over limited energy regions by Menlove<sup>6</sup> and Grench<sup>7</sup> are in agreement with values presented here. The present study provides a complete excitation curve with smaller experimental errors.



An effective cross section value for  $^{115}\text{In}(n,n')$   $^{115}\text{In}^m$  for a  $^{235}\text{U}$  fission neutron spectrum was calculated from

$$\bar{\sigma} = \int_0^{\infty} N(E) dE,$$

where  $\sigma$  values were obtained at 0.2 MeV intervals from a smooth curve drawn through our experimental cross section values. Using a neutron distribution suggested by Cranberg et al;<sup>8</sup>

$$N(E) = k \exp (-1.036) \sinh (2.29E)^{\frac{1}{2}}$$

where  $E$  is the neutron energy and  $k$  is a normalization factor, the calculated  $\bar{\sigma}$  was  $173 \pm 9$  mb. The response curve for  $\text{In}$  and a fission spectrum, as shown in Figure 3, reaches a maximum at 2.2 MeV. Our calculated value appears to be in agreement with measured fission average cross sections for  $^{115}\text{In}^m$  as summarized by Kobayashi.<sup>9</sup>

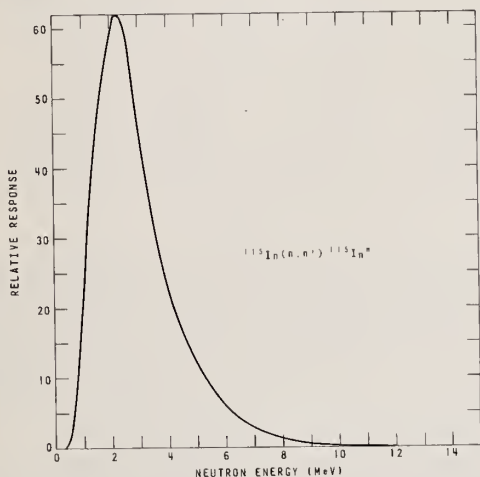


Figure 3 Response curve for  $^{115}\text{In}^m$  production with a  $^{235}\text{U}$  fission neutron spectrum.

The present study suggests that indium can be used to monitor fast neutrons but due to ancillary reactions does require careful radioactivity analysis. Unless experimental conditions require indium for other reasons, rhodium is to be preferred as a low threshold fast neutron monitor. The  $^{103}\text{Rh}(n,n')^{103}\text{Rh}^m$  reaction has an effective cross section for a fission neutron spectrum of  $724 \pm 43$  mb and a peak response at 1.12 MeV.<sup>1</sup> The absence of interfering reactions makes the analysis of  $^{103}\text{Rh}^m$  much easier.

#### References

1. D.C. Santry and J.P. Butler, Can. J. Phys. 52, 1421 (1974).
2. M.H. McTaggart. United Kingdom Atomic Energy Weapons Research Establishment, AWRE Rep. NR/A-1/59.
3. L. Allen, Jr., W.A. Biggers, R.J. Prestwood and R.K. Smith, Phys. Rev. 107, 1363 (1957).
4. D.C. Santry and J.P. Butler, Can. J. Chem. 41, 123 (1963).
5. H.H. Hansen, E. de Roost, W. van der Eijk and R. Vaninbroukx, Z. Physik. 269, 155 (1974).
6. H.O. Menlove, K.L. Coop and H.A. Grench, Phys. Rev. 163, 1308 (1967).
7. H.A. Grench and H.O. Menlove, Phys. Rev. 165, 1298 (1968).
8. L. Cranberg, G. Frye, N. Nereson and L. Rosen, Phys. Rev. 103, 662 (1956).
9. K. Kobayashi, I. Kimura, H. Gotoh and H. Yagi, J. Nucl. Energy 27, 741 (1973).

INELASTIC NEUTRON EXCITATION OF THE GROUND  
STATE ROTATIONAL BAND OF  $^{238}\text{U}$ \*

P. Guenther and A. Smith  
Argonne National Laboratory  
Argonne, Illinois 60939

Cross sections for the neutron excitation of the  $2+(45\text{ keV})$ ,  $4+(148\text{ keV})$  and  $6+(308\text{ keV})$  states in  $^{238}\text{U}$  were measured to incident energies of  $\sim 3.0\text{ MeV}$ . The experimental resolution was sufficient to resolve these components throughout the measured energy range. Particular attention was given to energies near threshold and in the few MeV range where direct reaction contributions were appreciable. The experimental results were compared with theoretical estimates based upon statistical and coupled-channel models deduced from comprehensive studies of neutron scattering from heavy-rotational-deformed nuclei. An evaluated inelastic scattering data set was derived from the present experimental and calculational results and previously reported experimental values and compared with respective values from the ENDF-IV file.

(Nuclear reaction  $^{238}\text{U}(n,n)$  and  $^{238}\text{U}(n,n')$ ,  $E = 0.3\text{--}3.0\text{ MeV}$ ,  $\sigma(\theta, E)$ ,  
 $\theta_{\text{lab}} = 20^\circ$  to  $160^\circ$ ).

### Introduction

The inelastic neutron excitation of the ground-state rotational band of  $^{238}\text{U}$  is of applied interest<sup>1</sup>. At a few hundred keV the respective cross sections are large and strongly contribute to energy transfer within fast-reactor systems. Experimental determination of these cross sections at low energies is difficult. Measured values are discrepant by nearly a factor of two and some of the experimental values display a curious energy dependence<sup>2-6</sup>. At energies above  $\sim 1.0\text{ MeV}$  inelastic neutron scattering from  $^{238}\text{U}$  is a complex and uncertain composite of a number of components<sup>3,7,8</sup>. As a consequence, experimental values have large uncertainties and evaluations are deduced to a considerable extent from non-elastic cross sections derived from measured total and elastic-scattering values. This procedure is uncertain as above  $\sim 1.0\text{ MeV}$  most measured "elastic" cross sections include substantial inelastic contributions due to the excitation of the first few states. The "true" elastic scattering is not clear with consequent uncertainties in the non-elastic cross section.

Of physical interest are the relative strengths of the compound-nucleus and direct-reaction mechanisms in the neutron excitation of collective, low-lying states of rotational nuclei such as  $^{238}\text{U}$ <sup>9,10</sup>. Calculations including the direct-reaction mechanism have led to varying results, some indicating large ( $\sim \frac{1}{2}b$ ) cross sections for the excitation of the  $2+(45\text{ keV})$  state of  $^{238}\text{U}$  at several MeV. Further, calculations indicate sharply anisotropic inelastic neutron emission. The calculations generally assume that the collective deformation involved in the neutron interaction is identical to that observed in charge-particle experiments (e.g. charged-particle scattering, coulomb excitation, etc.). This assumption is not necessarily true. Only recently has it become possible to test these calculational results and associated reaction mechanisms in the few MeV range<sup>6,8</sup>.

Here we address the above basic and applied issues with experiment and calculation giving primary attention to the inelastic neutron excitation of the  $2+(45\text{ keV})$ ,  $4+(148\text{ keV})$  and  $6+(308\text{ keV})$  states of  $^{238}\text{U}$  to incident neutron energies of  $3.0\text{ MeV}$ .

### Experimental Methods

The measurements were made using monoenergetic time-of-flight techniques and a 10-angle detector system<sup>11</sup>. The  $^7\text{Li}(p,n)^7\text{Be}$  reaction was used as a neutron source with a burst duration of  $\sim 1\text{ ns}$ <sup>12</sup>. The incident neutron energy spread at the samples was  $10\text{--}15\text{ keV}$ . Differential cross section values

were determined at up to  $\sim 50$  scattering angles distributed between  $\sim 20\text{--}160^\circ$ . At each period every detector was independently calibrated using one of the following two methods. 1) For  $E \sim 0.4\text{ MeV}$  neutron scattering from carbon was observed at an angle such that the scattered neutron energy exactly corresponded to that due to the excitation of the  $2+(45\text{ keV})$  state of uranium. The detector sensitivity and thence the uranium cross section was determined relative to the known differential carbon cross section<sup>13</sup>. This method was not sensitive to the relative detector energy dependence in a region where it may be rapidly changing, 2) Above  $E \sim 0.4\text{ MeV}$  the relative sensitivity of each detector was determined by observing the scattering of neutrons from carbon or hydrogen at a number of incident energies and the relative distributions were then experimentally normalized at a few selected energies using known carbon and hydrogen cross sections<sup>13,14</sup>.

All of the measured results were corrected for incident beam attenuation, angular resolution, fission neutron and multiple-event perturbations using analytical and Monte-Carlo computational procedures applied to both the scattering samples and the reference standards<sup>15</sup>.

The major experimental problem was the separation of the prominent  $2+(45\text{ keV})$  uranium inelastic neutron group from the elastic contribution. Scattered neutron flight paths ranged up to 12 meters and provided velocity resolutions of  $\sim 0.2\text{ nsec/m}$ . The resolution of the two prominent components was generally very good below  $\sim 1.5\text{ MeV}$  but decreased with increasing energy, resulting in strongly overlapping distributions at  $\sim 3.0\text{ MeV}$ . These resolutions are illustrated by the representative time distributions shown in Fig. 1. At higher energies and forward scattering angles the  $^{238}\text{U}$  elastic component can be several orders of magnitude more intense than the  $2+(45\text{ keV})$  inelastic contribution. The latter could not be resolved at such angles and energies and, as a consequence, the high resolution measurements above  $2.0\text{ MeV}$  were limited to single scattering angles generally in the range  $110$  to  $120^\circ$ . Concurrent and well resolved studies of similar inelastic processes in  $^{186}\text{W}$  provided an understanding of the inelastic neutron angular distributions essential for extrapolating the single-angle uranium results to angle-integrated inelastic cross sections. In addition, the  $^{186}\text{W}$  measurements defined the experimental resolution function. The latter was well described by a simple Gaussian whose parameters were determined from the  $^{186}\text{W}$  results by a least-square fitting procedure. The resulting Gaussian width was then used as a constraint in the subsequent least-

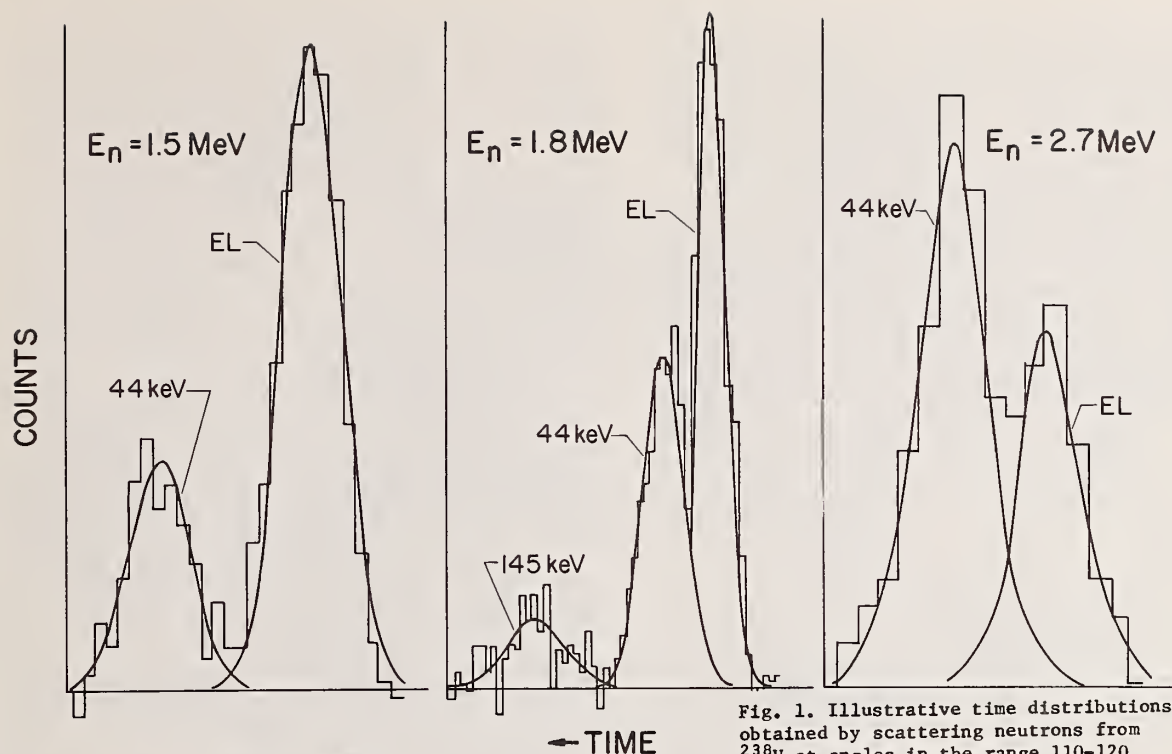


Fig. 1. Illustrative time distributions obtained by scattering neutrons from  $^{238}\text{U}$  at angles in the range 110-120 degs.

square fitting of the observed  $^{238}\text{U}$  time distributions. Some results of such fits are illustrated by the curves of Fig. 1. Generally, the relative contributions from the components contributing to the observed distributions were determined from the Gaussian parameters. The results were supported by subjective graphical analysis.

#### Experimental Results and Interpretation

The differential cross sections for elastic and/or inelastic scattering from the ground-state rotational band of  $^{186}\text{W}$  ( $0^+(0\text{ keV})$ ,  $2^+(125\text{ keV})$ ,  $4^+(396\text{ keV})$ ) were well resolved to 3.0 MeV at a number of scattering angles. These results, illustrated in Fig. 2, provided the foundation for a coupled-channel model subsequently used for the energy-angle extrapolation of the more difficult  $^{238}\text{U}$  measurements. Scattering from these two nuclei is similar with large contributions from direct and compound-nucleus reaction processes.

The potential parameters used here are those of LaGrange given by<sup>16</sup>

$$\begin{aligned} V_{\text{real}} &= 47.5 - 0.3 \cdot E(\text{MeV}), \quad r_0 = 1.24 \text{ f}, \quad a = 0.62 \text{ f} \\ W_{\text{imag.}} &= 2.7 + 0.4 \cdot E(\text{MeV}), \quad r_0 = 1.26 \text{ f}, \quad b = 0.58 \text{ f} \end{aligned} \quad (1)$$

where  $V$  is a Saxon form,  $W$  a Saxon derivative and the direct-reaction potential is equal to  $V$ . LaGrange has shown that this potential gives a good description of total cross sections in the rare-earth and actinide regions and gives a reasonable representation of the scattered neutron distributions of  $^{238}\text{U}$ <sup>16</sup>. The calculational results are sensitive to the quadrupole deformation ( $\beta_2$ ). Comparison of the present  $^{186}\text{W}$  experimental and calculational results indicated a  $\beta_2 = 0.20$ - $0.21$ , about 10% smaller than deduced from charged-particle studies<sup>17</sup>. The  $^{238}\text{U}$  calculations employed a  $\beta_2 = 0.216$  as given by Möller<sup>18</sup>. The above model gave a reasonable description of the observed  $^{186}\text{W}$  scattering cross sections as illustrated in Fig. 2. Particularly, the prominent excitation of the

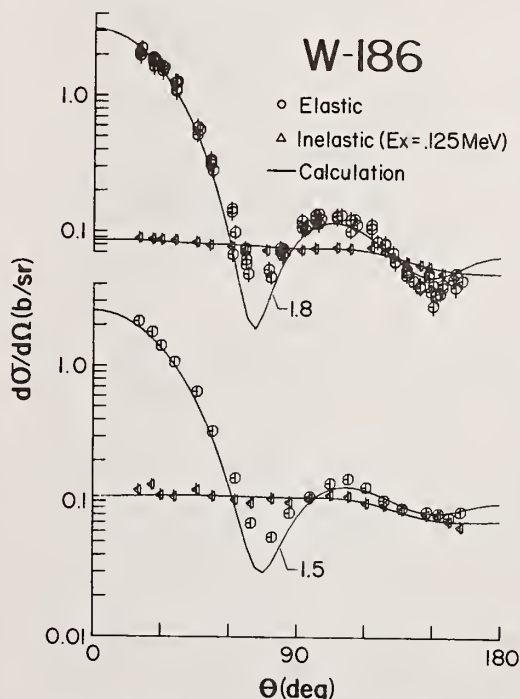


Fig. 2. Illustrative elastic and inelastic neutron scattering cross sections of  $^{186}\text{W}$ .

first excited state ( $2^+$ , 125 keV) is well described over a wide angular range. The general features of the elastic distributions are also reasonably represented. However, the calculations under-predict the first diffraction minimum by appreciable amounts.



A number of other potential choices have led to the same type of discrepancy including some derived from extensive parameter searches<sup>19</sup>. This shortfall is only evident with unusually good resolutions, such as in these <sup>186</sup>W examples. It may be of a basic nature. In <sup>238</sup>U the discrepancy is masked as the elastic and first-inelastic components are not generally resolved and the above potential is more descriptive of the observed scattered neutron distributions as illustrated in Fig. 3. The calculated distributions deviate from the observed <sup>238</sup>U distributions at large scattering angles and the effect becomes more pronounced as the energy increases (similar discrepancies are evident in the original work of LaGrange<sup>16</sup>). Despite these various calculational problems, the comparisons of Fig. 2 (<sup>186</sup>W) and Fig. 3 (<sup>238</sup>U) give reasonable confidence to the use of the above model

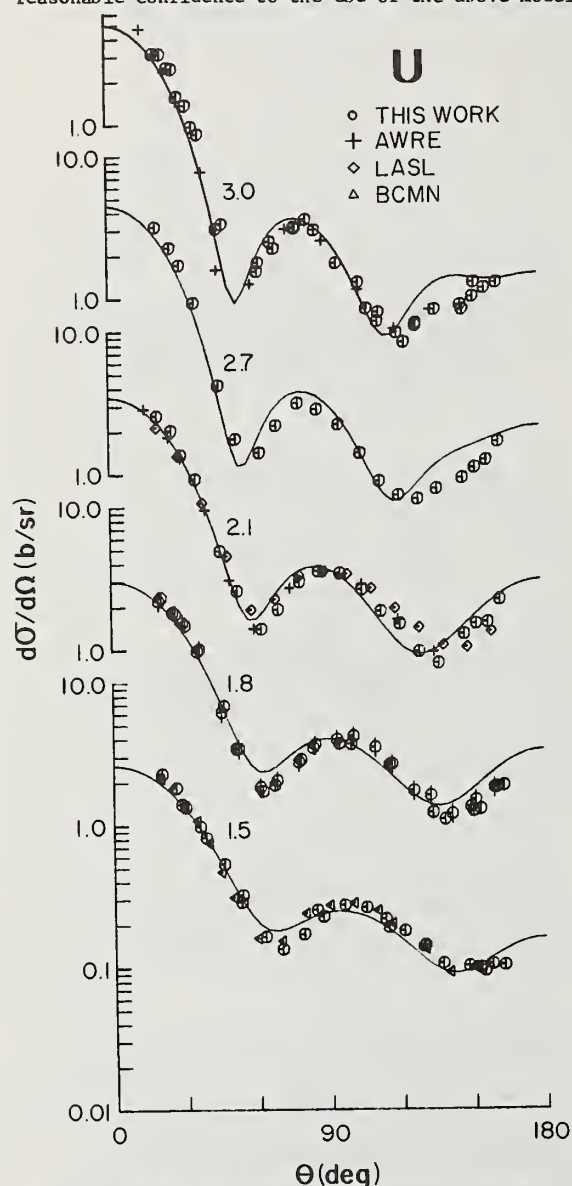


Fig. 3. Illustrative comparisons of measured and calculated scattered neutron distributions for <sup>238</sup>U. The results of the present measurements are indicated by circular data points. Previously reported values as noted in the Fig. are defined in primary ref.7 and 8.

for the relative angle-energy extrapolation of the measured <sup>238</sup>U inelastic cross sections.

The relevant inelastic excitation cross sections of <sup>238</sup>U were measured over a period of more than five years using different detection systems and calibrations. Below ~ 1.0 MeV the angle-integrated cross sections were determined by least-square fitting a Legendre polynomial series to the observed angular distributions. Above ~ 1.0 MeV the angle-integrated values were obtained from a fit of the relative angular distributions determined with the above model to measured values at one or several scattering angles. The cross section uncertainties varied from less than 10% to more than 20% depending upon the particular measurement region. The results for the 2+(45 keV), 4+(148 keV) and 6+(308 keV) states of <sup>238</sup>U are summarized in Fig. 4.

The prominent <sup>238</sup>U inelastic component is associated with the 2+(45 keV) state. The present results are consistent with those previously reported from this laboratory<sup>2</sup>, and with those reported by Marcella et al.<sup>6</sup> in the energy range 1.0-2.7 MeV and with the values of Cranberg<sup>5</sup>. The values of Barnard et al.<sup>3</sup> tend to be slightly higher than those of the present work in the region 0.5-1.0 MeV and the later values of Barnard et al.<sup>4</sup> are much larger. The latter values show structure that is difficult to explain though there is possibly some trace of a similar effect in the present work.

The present results for the excitation of the 4+(148 keV) state in <sup>238</sup>U are consistent with those previously reported from this laboratory<sup>2</sup> and with those of Barnard et al.<sup>3</sup>, Barnard et al.<sup>4</sup>, Cranberg<sup>5</sup> and Marcella et al.<sup>6</sup>.

The excitation of the 6+(308 keV) state is weak and as a consequence the measured cross sections are relatively uncertain. The present results are consistent with those reported by Cranberg<sup>5</sup> near 1.0 MeV but imply lower values near 0.5 MeV.

Despite ambiguities and parameter uncertainties, the above model reasonably describes the present <sup>238</sup>U inelastic scattering results as illustrated by the curves in Fig. 4. The direct excitation of the 2+ state rises to nearly 1/2 b at 3.0 MeV. The direct excitation of the 4+ state is much smaller and essentially negligible for the 6+ state. Only the ground- and first-excited states are strongly coupled. Below ~ 1.0 MeV compound nucleus processes are dominant. The present calculational results were obtained using the above potential and the Hauser-Feshbach formula corrected for width fluctuation and correlation effects (correlation parameter  $Q=0.5$ )<sup>20</sup>. The exact physical nature of these correction factors is a matter of some debate<sup>21</sup>. However, the energy dependent shapes of the calculated results from threshold to ~ 1.0 MeV is not particularly sensitive to either these correction factors or the exact choice of potential parameters. Thus the calculations based upon the present experimental values in the region 0.5-1.0 MeV reasonably extrapolate the cross sections to threshold. These shapes are rooted in compound-nucleus theory. The calculational extrapolations toward threshold imply that some previous experimental measurements are systematically in error with respect to magnitude and/or energy-shape. Above ~ 1.0 MeV the compound-nucleus calculations become increasingly uncertain due to unknown channel competition. The present calculations introduced a number of speculative channels corresponding to excitations of greater than 1.0 MeV. The calculational results were consistent with measurements and essentially all due to direct reactions at 3.0 MeV.

#### Comparisons with ENDF/B-IV<sup>22</sup>

The above measured and calculated inelastic

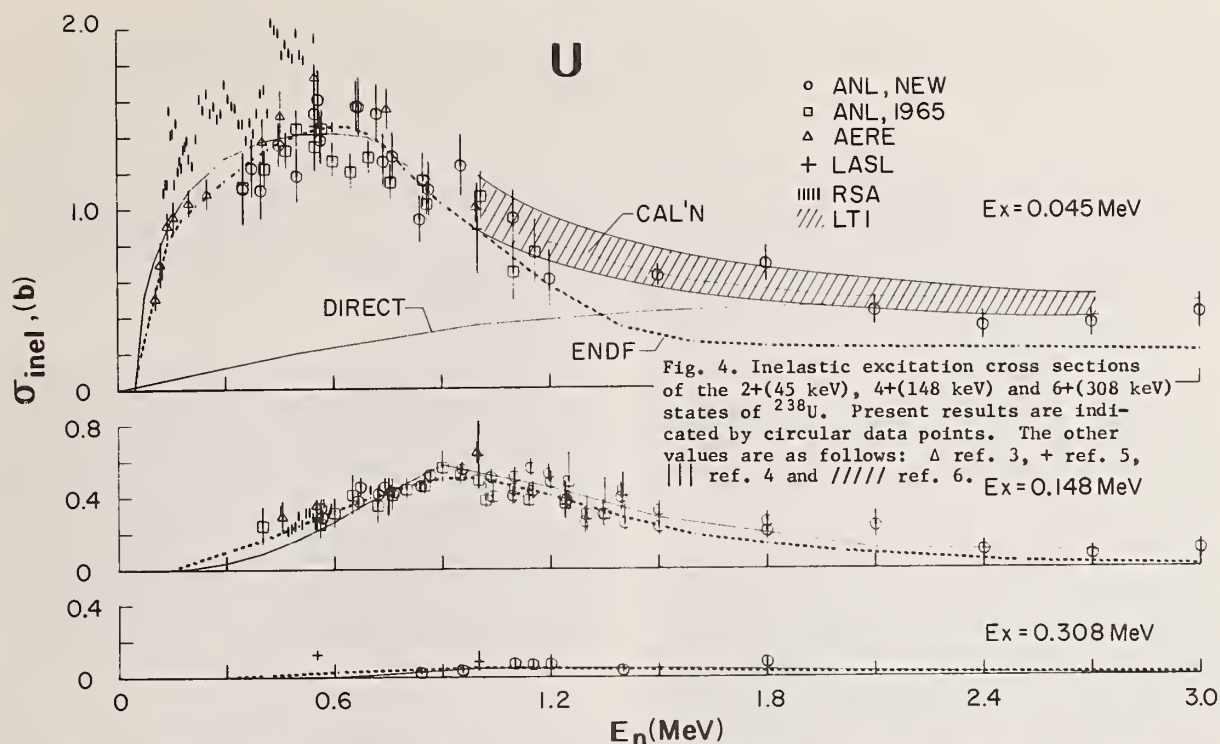


Fig. 4. Inelastic excitation cross sections of the 2+(45 keV), 4+(148 keV) and 6+(308 keV) states of  $^{238}\text{U}$ . Present results are indicated by circular data points. The other values are as follows:  $\Delta$  ref. 3, + ref. 5, ||| ref. 4 and ///// ref. 6.  $E_x = 0.148 \text{ MeV}$

scattering cross sections of  $^{238}\text{U}$  are compared with those of ENDF/B-IV in Fig. 4. For the 2+(45 keV) state the present experimental and calculational results are relatively consistent with those given in ENDF/B-IV below  $\sim 1.0 \text{ MeV}$ . However, the energy dependence of the present results is markedly different than that of ENDF/B-IV. Moreover, if the normalization of the present results in the range 0.5–1.0 MeV is revised upwards by 10–20%, as may be indicated by some previously reported values<sup>3,4</sup>, the present shape leads to cross sections in the region from threshold to 0.6 MeV much larger than given in ENDF/B-IV. The present measurements and those reported previously from this laboratory<sup>2</sup> do not support such an upward normalization. Above approximately 1.0 MeV the present cross sections for the excitation of the 2+(45 keV) state are larger than those given by ENDF/B-IV by as much as a factor of two due to strong direct-reaction contributions. Generally we suggest that the evaluations for the excitation of the 2+ state follow the calculations based upon the present experiments shown in Fig. 4. The excitations of the 4+(148 keV) state are relatively smaller than those of the 2+ state and the present results are reasonably consistent with those given in ENDF/B-IV, excepting possibly higher energies where direct contributions are again major factors and near threshold. The cross sections for the excitation of the 6+(308 keV) state are small and of minor applied importance. However, the values of the present work are consistent with those of ENDF/B-IV.

#### References

\* This work supported by ERDA.

1. For example, USNDC-6 Compilation of Requests for Nuclear Cross Section Measurements, National Tech. Inf. Service, (1973).
2. A. Smith, Nucl. Phys. **47** 633 (1963).
3. E. Barnard et al., Nucl. Phys. **80** 46 (1966).
4. E. Barnard et al., Proc. of 2nd. Int. Conf. on Nucl. Data for Reactors, IAEA Press, Vienna (1971), Vol. 2, p-103.

5. L. Cranberg, Los Alamos Scientific Lab. Report, LA-2177(1959), See also L. Cranberg and J. Levin, Phys. Rev. **109** 2063 (1958).
6. T. Marcella et al., Bull. Am. Phys. Soc. **19** No.-4, 575 (1974).
7. A. Smith, Comments on the Inelastic Neutron Scattering Cross Section of  $^{238}\text{U}$ , Argonne National Lab. Memorandum (1973), unpublished.
8. A. Smith, Inelastic Neutron Scattering Cross Sections of  $^{238}\text{U}$ , Argonne National Lab. Memorandum (1974), unpublished.
9. B. Mottelson and S. Nilsson, K. Danske Vidensk. Selsk. mat.-fys. Skr. **1**, No-8, (1959).
10. D. Chase and L. Wilets, Bull. Am. Phys. Soc., **2** 72 (1957).
11. A. Smith et al., Nucl. Inst. and Methods, **50** 277 (1967).
12. H. Newson and J. Gibbons, Fast Neutron Physics part-2, Ed. J. Marion and J. Fowler, Interscience Pub. New York, (1963).
13. A. Langsdorf et al., Argonne National Lab. Report, ANL-5567 Rev., (1961).
14. H. Hopkins and G. Breit, Nucl. Data, **A9** 137 (1971).
15. A. Smith and P. Guenther, Priv. Communication (1973).
16. Ch. LaGrange, Critique of Nuclear Models and Their Validity in the Evaluation of Nuclear Data, EANDC Topical Discussion, Tokyo (1974).
17. P. Stelson and L. Grodzins, Nucl. Data, **1A** No.-1 (1965).
18. P. Moller, Nucl. Phys., **A192** 529 (1972).
19. D. Lister et al., Phys. Rev., **162** 1077 (1967); See also, P. Guenther et al., Models, Measurements and Evaluation, EANDC Topical Discussion, Tokyo (1974).
20. P. Moldauer, Phys. Rev., **135** B642, (1964).
21. P. Moldauer, Bull. Am. Phys. Soc., **19** 988 (1974).
22. Evaluated Nuclear Data File-B, version IV, ENDF/B-IV, National Neutron Cross Section Center, Brookhaven National Lab. (1974).



Measurements have been made of the differential elastic and inelastic scattering cross sections, at 28 angles each, for 9, 9.21, 9.6, 10, 10.25, 10.74, 11, 11.22, 11.79, 12, 13, 14, 14.5, and 15 MeV neutrons incident upon natural carbon. The measurements were made with the TUNL FN tandem accelerator and a high-precision goniometer time-of-flight spectrometer. Monte Carlo simulation has been used to correct the differential cross sections for multiple scattering. Absolute uncertainties are typically 5%. These data partially fill the 9-15 MeV gap in the C elastic and inelastic scattering data set required for the CTR program.

[NUCLEAR REACTIONS C(n,n), C(n,n'), E = 9-15 MeV; measured  $\sigma(E_n, \theta)$ ]

### Introduction

Detailed knowledge of the energy-dependent differential cross sections for the scattering of fast neutrons by carbon is required for accurate calculations of neutron transport in the blanket and shield of prototype fusion reactors.

### Experimental Apparatus

Differential cross-section experiments were performed using the TUNL neutron time-of-flight (TOF) facility which is shown in Fig. 1. The details of the facility are described in BB12 of the conference proceedings; thus, only a brief description will be given here. The TUNL FN tandem accelerator provided a beam of deuterons which was preacceleration pulsed and bunched into bursts with a time dispersion of approximately 1.5 nsec. The average beam current at the target was about 2  $\mu$ A at a pulse repetition rate of 2 MHz. Neutrons were produced via the D(d,n)<sup>3</sup>He reaction in a deuterium gas cell. The gas cell was a thin-wall stainless steel, tantalum-lined cylinder 3.0 cm in length and isolated from the accelerator vacuum system by a 3.5  $\mu$ m thick molybdenum foil. The cell contained deuterium gas at a pressure of 2 atm.

Figure 2 illustrates the scattering geometry. The 99.98%-pure carbon sample was a right circular cylinder with 1.9 cm diam. and 2.54 cm height. The sample was suspended with its axis vertical and located a distance of 9.3 cm from the center of the gas cell. The neutron detector was an 8.9 cm diam x 5.08 cm thick NE 218 scintillator which was coupled to a Phillips 58DVP phototube and could be positioned at distances of 1.5 to 4.0 m from the scatterer. The detector was housed in a 7300 kg shield composed of Cu, paraffin, and Li<sub>2</sub>CO<sub>3</sub>. The detector was also shielded from direct neutrons from the source by a tungsten shadow bar 62 cm long. A second neutron detector was housed in a cylindrical copper shield which was suspended above the scattering plane. This detector viewed the primary neutron source directly and served the purpose of normalizing the neutron fluence for the carbon and polyethylene scatterers throughout the course of the experiment.

A block diagram of the electronics is shown in Fig. 3. Fast timing signals from the main and monitor detectors and the beam pulse pick-off were converted to logic signals by constant-fraction pulse-height discriminators. The time difference between the detector pulses and the delayed pick-off pulses, as measured by time-to-amplitude converters (TAC), determined the flight times of the neutrons. The linear signals from both detectors were used for lower-level discrimination to reject pulses with amplitudes smaller than a predetermined value

and for pulse-shape discrimination (PSD) to reject detected  $\gamma$  rays from the time spectra. The PSD, TOF, and routing pulses were fed through a computer interface to four ADC's. The experimental information was stored and processed by an on-line computer (DDP-224) for on-line display and analysis. Neutron TOF, gamma TOF, and PSD cross-over timing spectra were stored and displayed for both the monitor and main detector systems. The TOF spectra could be displayed simultaneously for on-line diagnostic purposes. The computer also provided for on-line calculations of peak yields, background subtraction, TOF energy calculations, kinematic energy calculations, plus a host of other calculations and diagnostics.

### Experimental Procedure

In order to obtain absolute cross sections, comparisons must be made of the scattering from the nuclei in question and some standard. The accuracy with which this comparison can be made is a major source of uncertainty in the determination of differential cross sections. The principal source of this uncertainty arises because the neutrons scattered from the standard usually have an energy much different from those scattered by the nuclei being studied, and hence, the comparison depends on the relative efficiency of the neutron detector at widely separated neutron energies. This relative efficiency has been difficult to measure in the past with an accuracy better than  $\pm 5\%$ .

Measurements of the <sup>2</sup>H(d,n)<sup>3</sup>He cross-section angular distributions at a number of bombarding energies between 2 and 10 MeV have provided a technique for measuring the energy dependence of the neutron detector efficiency with improved accuracy. The relative efficiency of the neutron detector used in the work reported here was determined by measuring the angular distributions of neutrons from the <sup>2</sup>H(d,n)<sup>3</sup>He reaction at deuteron bombarding energies of 4.0, 6.2, 9, and 10 MeV. These are energies for which the absolute cross sections are quoted with errors of 1-3%. The scattering geometry, PSD, and neutron energy thresholds of the main and monitor detectors were maintained in the same geometrical and electronic configurations during the efficiency and scattering cross section measurements. The PSD electronics was tested and maintained with the continuous neutron and gamma ray spectra generated by a Pu-Be source, while the energy thresholds were placed on the Compton edge which resulted from <sup>137</sup>Cs gamma rays interacting in the scintillators. The relative efficiency of the main detector was determined for neutrons with energies between 2.0 and 13 MeV. The efficiency curve exhibited systematic structure between 7 and 9 MeV when calculated from the absolute cross sections of Schulte, *et al.*<sup>1)</sup>, and lesser systematic structure between 11 and 13 MeV when calculated from the absolute cross sections of Thornton<sup>2)</sup>. This structure was also observed by experimenters in another TUNL group. A series of n-p scattering experiments which overlapped the above energy

\*Partially supported by USAEC

<sup>†</sup>Visiting scientist from Tübingen U.

<sup>††</sup>Visiting scientist from Frankfurt U.

<sup>\*\*</sup>Visiting scientist from Tulane U.



regions were performed to determine the relative efficiency over the 6-9 and 10-13 MeV regions. No systematic structure was observed in the relative efficiency curve by this time-consuming method. The experimental uncertainty on each data point was  $\pm 1-3\%$ , and the fitted curve (Fig. 4) through the points defined the energy dependence of the efficiency to better than  $\pm 2\%$ .

For the scattering cross-section measurements, the cylindrical sample was suspended with its axis aligned with the center of rotation of the detector-collimator system and perpendicular to the reaction plane. The position of the sample was carefully monitored by observation with a leveling telescope. Neutron TOF spectra were obtained with the sample in place and with the sample removed for a fixed number of monitor counts. In addition, sample-in gas-out spectra were taken to complete the background subtraction process. During the course of an angular-distribution measurement, the energy thresholds and PSD of the main and monitor detectors were periodically checked. The course of a measurement proceeded from the forward to the backward angles in  $10^\circ$  increments and then reversed to obtain the  $5^\circ$  incremental angles. This technique served as an additional monitor of the experimental stability. The differential cross sections measured in this experiment were normalized to the accurately known n-p scattering differential cross sections of Hopkins and Breit<sup>3)</sup>. This was accomplished by measuring the number of neutrons scattered by a thin polyethylene  $(\text{CH}_2)_n$  scatterer at a laboratory angle sufficient to give separations of the carbon elastic and inelastic and n-p scattering peaks. At energies  $> 13$  MeV it was necessary to perform an additional scattering experiment on a cylindrical carbon scatterer (containing the same number of C nuclei as the polyethylene) so as to correct for overlap of the n-p and C scattering peaks. One of these time spectra with background subtracted is shown in Fig. 5. The well-defined but kinematically broadened n-p scattering peak is seen to be clearly separated from the two peaks resulting from elastic and inelastic scattering by carbon. One polyethylene scattering spectrum was obtained near the beginning of an angular distribution and the second near the end. The normalization constants derived after correcting the yields for dead time in the counting electronics were always found to be consistent with the counting statistics. Additional uncertainties in sample flux-attenuation calculations and n-p scattering cross-section values increase the over-all uncertainty in normalization to 2-3%.

In addition to providing normalization, the polyethylene scattering spectra provided a means of verifying the scattering angle of the neutron detector. The relative positions of the n-p, the carbon elastic, and inelastic scattering peaks depend very sensitively on scattering angle; consequently, comparison of TOF and kinematic peak positions allowed the average scattering angle, with respect to the incident neutron beam, to be determined to within  $\pm 0.3^\circ$ .

#### Data Corrections

The measurements were corrected for background, dead time in the electronic counting systems, and for the effects of finite geometry. The finite sample size and source size corrections were performed using Monte Carlo simulation techniques. The Monte Carlo calculations were performed with an IBM S/370-135 computer using a modified version of the Oak Ridge code. The calculations corrected for the anisotropy of the flux from the primary neutron source, finite source size, angular resolution, multiple scattering, and attenuation in the carbon and polyethylene scatterers. The first two corrections for source anisotropy and size affect the normalization, and depend upon the relative sizes of the scattering sample and the polyethylene sample used to obtain the normalization. The normal-

ization correction factors due to this effect were calculated with the Monte Carlo code to be 1.01.

The remaining finite sample effects which may alter the shape of an angular distribution were also obtained by Monte Carlo calculations. The code simulated the effects of the finite source, detector, and sample geometry and, by iteration, found a single scattering angular distribution which would provide a calculated laboratory angular distribution in agreement with the measured distribution. Sufficient neutron histories were run so that uncertainties in the calculated cross sections due to Monte Carlo statistics were  $< \pm 1\%$  and the calculations stopped when the calculated cross sections were within  $\pm 1\%$  of the least-squares fit to the measured cross sections. A typical Monte Carlo calculation involving 20,000 (forced collision) neutron histories in each of 3 iterations typically required 18 min of computer time. This particular code executes twice as fast on the IBM S/370-135 as on a CDC 6600.

#### Experimental Results

Measurements were made of the differential elastic and inelastic scattering cross sections of natural carbon at 28-30 angles each (in  $5^\circ$  increments) over the angular range  $25-160^\circ$  for incident neutron energies of 9.0, 9.21, 9.60, 10.0, 10.25, 10.74, 11.0, 11.22, 11.79, 12.0, 13.0, 14.0, 14.5, and 15 MeV. These energies were selected in order to probe the structure in the total cross section of carbon. Particular care was taken to probe the minima of the angular distributions in  $2.5^\circ$  increments for a number of cases. The results are displayed in Figs. 6 and 7. The curves through the experimental points are the least-squares fit (LSF) to a sum of Legendre polynomials. The polynomial coefficients and their uncertainties were computed using the LSF technique described by Cziffra and Moravcsik<sup>4)</sup>. The calculations were terminated: (1) when the uncertainty in the highest-order coefficient exceeded the coefficient, (2) when chi-square divided by the number of degrees of freedom reaches a minimum, and (3) when the inclusion of the next higher-order polynomial does not change the integrated cross section by more than its uncertainty. The experimental uncertainties associated with each data point are a propagated combination of relative and normalization errors. The internal consistency of the data sets is illustrated by the completeness with which the polynomial fits intersect nearly all of the data points. The extrapolated zero degrees elastic scattering cross sections are  $> \sigma_{\text{wick}}$  for all energies. Extrapolations of the Legendre polynomial fit to zero degrees agrees to within 1-7% with the recent small angle scattering performed at the USA-BRL at  $E_n=9.5, 11, \text{ and } 14 \text{ MeV}$ <sup>5)</sup>. However, the 7% disagreement emphasizes the need for more detailed small angle scattering measurements over the entire energy range of this experiment.

#### References

1. R.L. Schulte, M. Cosack, A.W. Obst, and J.L. Weil, Nucl. Phys. **A192**, 609 (1972).
2. S.T. Thornton, Nucl. Phys. **A136**, 25 (1969).
3. J.C. Hopkins and G. Breit, Nucl. Data Tables **A9**, 137 (1971).
4. P. Cziffra and M.J. Moravcsik, UCRL-8523, 1959 (unpublished).
5. C.E. Hollandsworth and W.P. Bucher, private communication.

# Cyclo-Graaff Laboratory

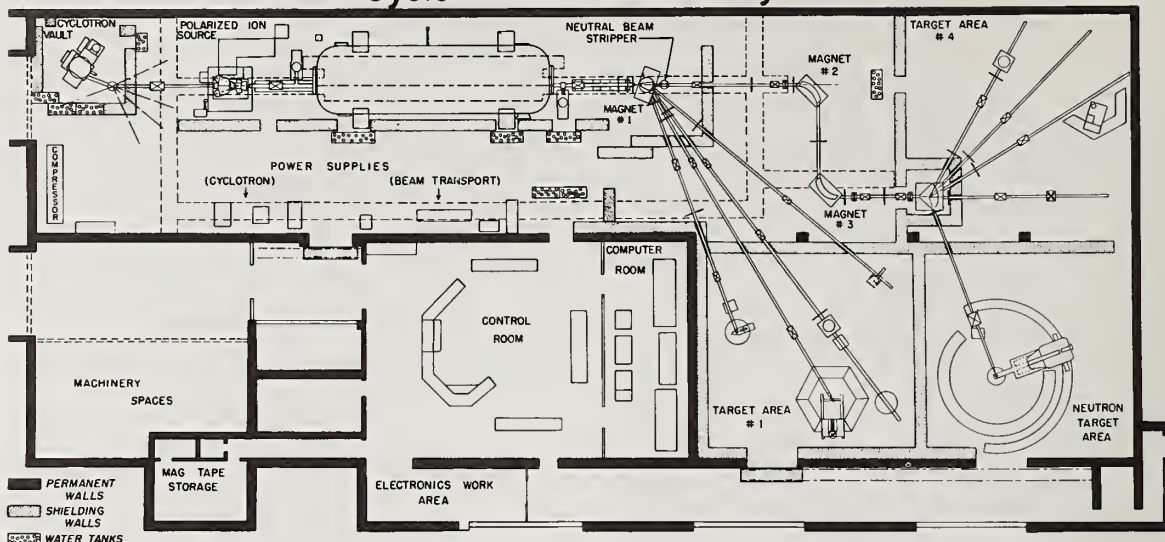


Fig. 1 Plan view of the Cyclo-Graaff Laboratory.

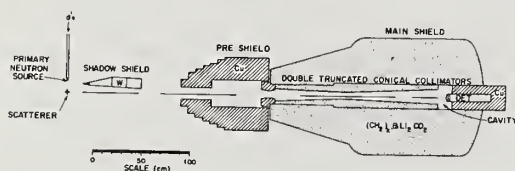


Fig. 2 The experimental scattering geometry used in the differential cross section measurements.

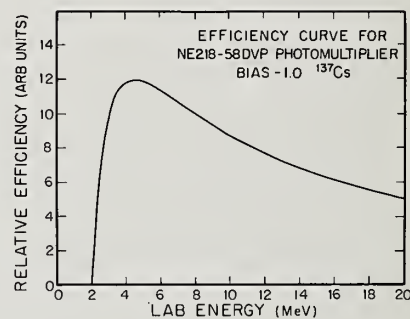


Fig. 4 Relative efficiency curve of the main neutron detector. The curve is an empirical fit to the experimental data.

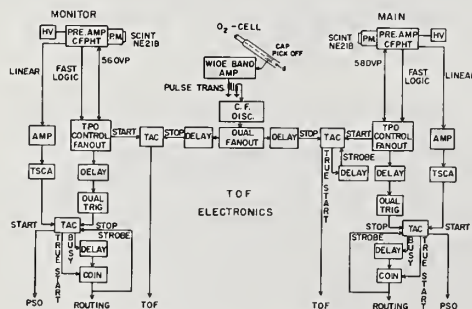


Fig. 3 Block diagram of the experimental electronics.

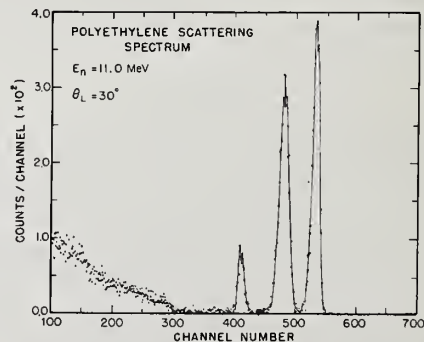


Fig. 5 Neutron TOF spectra showing 11 MeV neutrons scattered from a 5 mm dia. polyethylene cylinder.

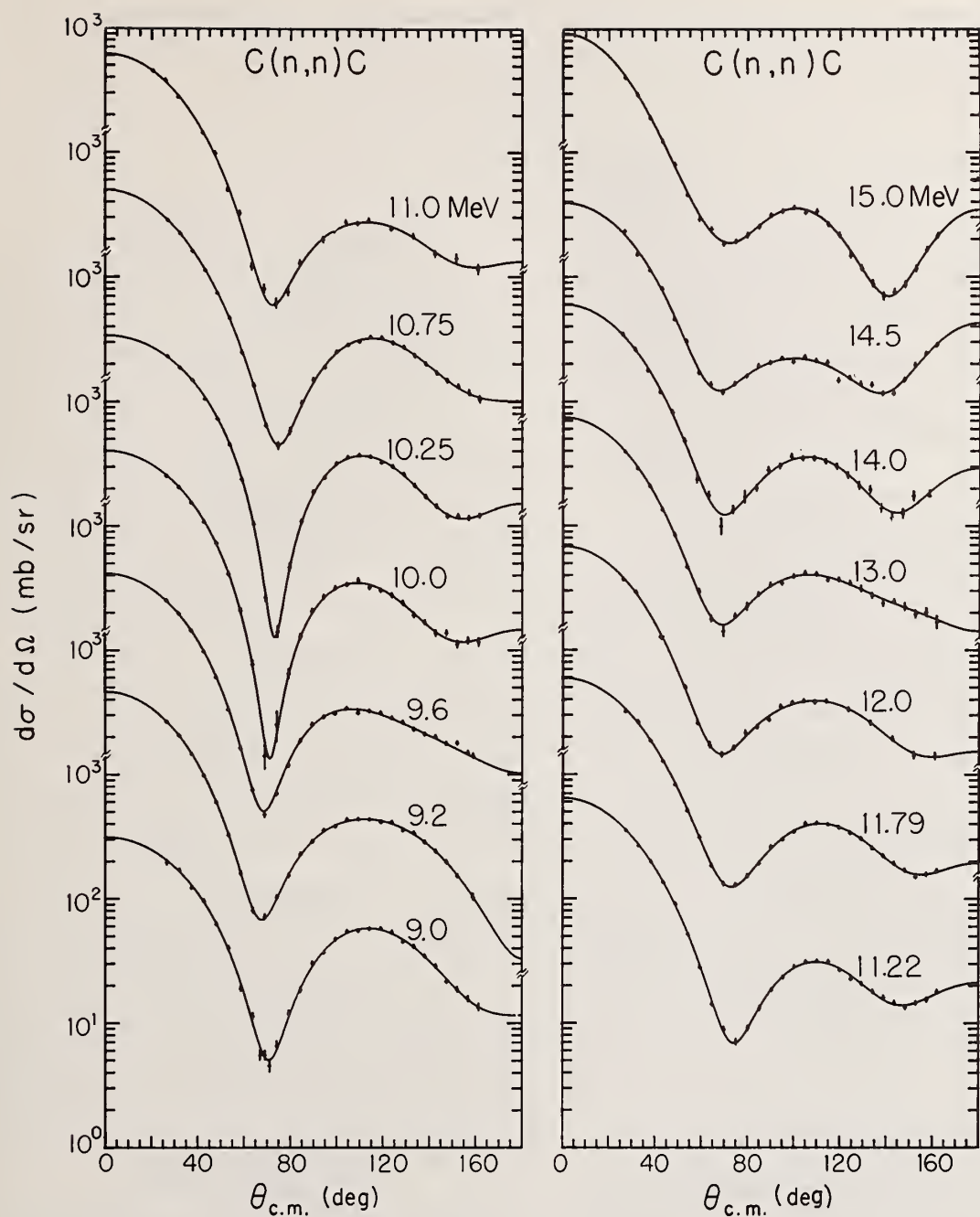


Fig. 6. The angular distribution for the elastic scattering of 9-15 MeV neutrons from carbon.



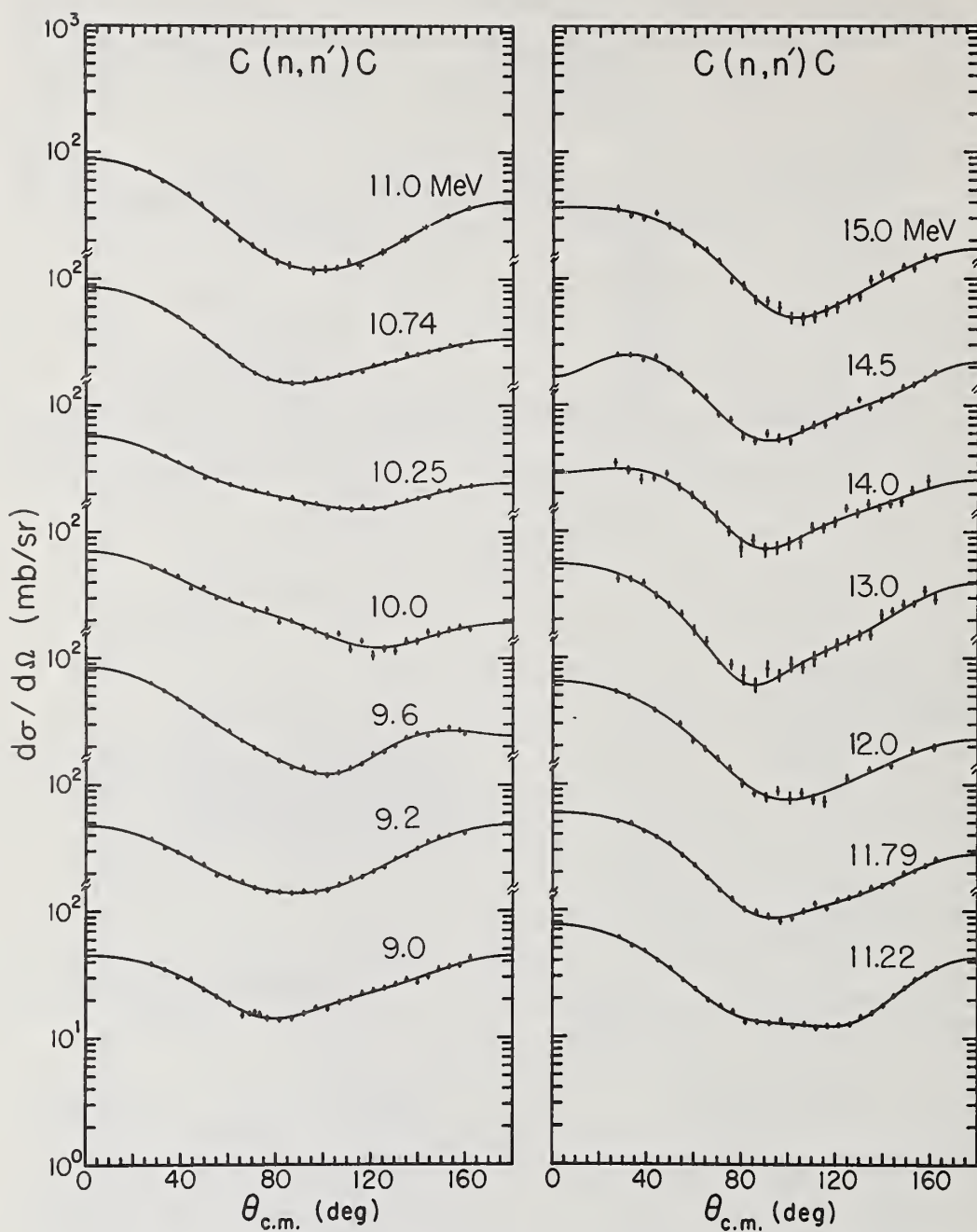


Fig. 7. The angular distribution for the inelastic scattering ( $Q = -4.43$  MeV) of 9-15 MeV neutrons from carbon.

Fast neutron inelastic scattering cross sections have been measured for the elements Al, Ti, V, Mn, Fe, Ni, Nb, Pb and Bi by the time-of-flight technique. The measurements were made in the energy range of 2 to 4.5 MeV in steps of 0.25 MeV and at a scattering angle of  $125^\circ$ . The experimental results are compared to the excitation functions calculated on the basis of the Hauser-Feshbach formalism and corrected for the effects of the level width fluctuations.

(Neutrons, Inelastic-Scattering, MeV Range 2 to 4.5, Measurements, Time-of-flight, Hauser-Feshbach)

### 1. Introduction

The accurate knowledge of cross sections for neutron inelastic scattering is important in many fields of nuclear science and technology. In fast reactors inelastic scattering processes largely determine the neutron spectrum, but also in thermal reactors inelastic scattering contributes substantially to the slowing down of neutrons. For the efficient design of neutron shields for all kinds of reactors and also for many types of accelerators one has to know the cross sections for inelastic neutron scattering and the spectrum of the gamma radiation resulting from the subsequent de-excitation of levels. Uncertainties in these cross sections will directly affect the safety and economy of reactors. Accordingly, neutron inelastic cross sections are frequently requested for reactor core and shielding calculations<sup>1</sup>. A study of the list of neutron inelastic cross sections available at present<sup>2</sup> shows clearly that there are still large regions, both in energy and mass number, for which there exist no or few experimental data.

In those cases where no experimental data are available or the existing data are uncertain, calculations of the cross sections based on well established theories will constitute a good basis for the evaluation of the requested cross sections. However, to check the reliability of the models for cross section predictions and in order to estimate the confidence level of the calculated data a systematic study of the inelastic scattering process based on experimental information for a rather large number of elements and over a wide range of energy is necessary.

The present investigation was undertaken to perform a systematic study of neutron inelastic scattering cross sections for a number of elements between Al and Bi over a wide energy range. Neutron inelastic scattering processes have been observed in the elements: Al, Ti, V, Mn, Fe, Ni, Nb, Pb,  $Pb_r$  (radiogenic lead) and Bi in the energy region from 2 to 4.5 MeV at energy steps of 250 KeV. Scattering samples of natural isotopic abundance were used. The experimental results have been compared with those calculated using the Hauser-Feshbach<sup>3</sup> formalism properly corrected for the level width fluctuation and resonance interference effects according to Moldauer<sup>4</sup>.

### Experimental Techniques

The inelastic scattering measurements were performed using the Studsvik 6 MV Van de Graaff accelerator. By using a klystron bunching system in the top terminal of the accelerator pulses shorter than 2 ns at a repetition rate of 1 MHz could be obtained. A neutron time-of-flight spectrometer, with a flight path of 300 cm, was used to record the neutron inelastic scattering spectra. This spectrometer used a neutron detector consisting of a fast organic scintillator with a diameter of 10 cm and a thickness of 5 cm, viewed by a fast photomultiplier.

Neutrons for the scattering measurements were produced by the T(p,n) reaction using a gas target with a length of 3.0 cm. The target cell was filled with tritium gas to a pressure of about 1 atmosphere. The total energy spread of the neutron beam was  $\pm 50$  KeV in the energy range of this work. The scattering samples consisted of cylinders of 5 cm height, 2.5 cm outer diameter and 0.95 cm inner diameter. The target flux was monitored by a direction sensitive neutron long counter positioned at a distance of 300 cm from the target and at an angle of  $72^\circ$  relative to the direction of the charged particle beam. The experimental set up of the present measurements is explained more fully elsewhere<sup>5</sup>.

The inelastic neutron scattering measurements were performed at energies between 2.0 and 4.5 MeV, in steps of 0.25 MeV. The cross sections were measured at only one scattering angle of  $125^\circ$ . This has been shown to be sufficient since the neutron inelastic scattering angular distribution functions are either isotropic or only slightly anisotropic but symmetric around  $90^\circ$  in the C.M. system. To check this, neutron inelastic angular distributions were studied at 3.02 MeV neutron energy and at five different angles;  $30^\circ$ ,  $60^\circ$ ,  $90^\circ$ ,  $125^\circ$  and  $150^\circ$ <sup>5</sup>. The angular distribution functions could be well described by second order Legendre polynomial expansion. Then the total inelastic cross sections were found by multiplying  $4\pi$  by differential cross sections at  $125^\circ$ .

The inelastic cross sections were determined relative to the well known n-p cross sections which has been compiled by Horsley<sup>6</sup>. Thus scattering from hydrogen in the form of a polythene sample was measured for each incident neutron energy at a scattering angle of  $30^\circ$ . The size of the polythene sample was 3 cm in height, 0.95 cm outer diameter and 0.65 cm inner diameter. The method of data analysis and the measurements of neutron detector efficiency curve are discussed in detail elsewhere<sup>5</sup>. The experimental cross sections have been corrected for the effects of the neutron source anisotropy, attenuation of the neutron flux in the scatterer, finite geometry of target-scatterer system and the multiple scattering of neutrons, using Monte Carlo techniques<sup>7</sup>.

### Theoretical Analysis

The inelastic scattering process is mainly characterized by compound nucleus formation in the neutron energy range of the present investigation, i.e. 2.0 to 4.50 MeV. According to the Hauser-Feshbach (H-F)<sup>3</sup> formalism, the angular distributions and the total inelastic scattering cross sections can be calculated provided that the transmission coefficients and the level characteristics (such as spins and parities) of the target nuclei are known. According to Moldauer<sup>4</sup>, the H-F cross section formula must be corrected for the effects of level width fluctuations and resonance interference. Thus a "corrected" transmission coefficient has been

\* Work has been performed at AB. Atomenergi, Studsvik during author's stay in Sweden.



introduced which is a function of a parameter  $Q$ . This parameter which takes into account the resonance interference contribution is depended on the properties of the compound nucleus. In the limit of strongly overlapping resonances its value goes to zero while in the case of isolated resonances  $Q$  approaches unity.

The transmission coefficients used to calculate the neutron inelastic cross sections were obtained from optical model calculations using a local optical potential and a set of generalized optical model parameters. These parameters are derived by Holmqvist and Wiedling<sup>8</sup> on the basis of more than 100 neutron elastic scattering angular distributions measured at Studsvik. These generalized parameters were found to be independent of incident neutron energy but were a function of mass number. The usefulness of these parameters has been further investigated by Etemad<sup>9</sup> who has compared the calculated neutron elastic scattering cross sections for 12 elements, in the energy range of 1.5 to 8.5 MeV, with the available measured cross sections. The neutron inelastic cross sections were calculated on the basis of H-F formalism with and without Moldauer corrections. In the former case calculations were performed for the two limiting cases of  $Q$  equal to zero and one. Information on the properties of the energy levels of the studied elements, used in H-F calculations, is given in a previous report<sup>5</sup>.

### Results

The results of the present neutron inelastic scattering measurements are shown in Figs. 1-9 where the total (integrated) inelastic cross sections are plotted against incident neutron energy. The numerical values of the cross sections are given in a previous report<sup>5</sup>. Included in the figures are also cross sections measured by other experimenters. The results of the theoretical calculations are given by three curves in the Figs. 1-9. The solid curves represent the H-F calculations while the dashed and dashed-dotted curves are those corrected for the level width fluctuations and resonance interference effects with the value of  $Q$  taken to be zero and one, respectively. For the elements Al, V, Fe and Nb, the available experimental data in the literature were adequate to compare the experimental results with the theoretical predictions from threshold to 4.5 MeV. In such cases, comparisons have also been made with the excitation functions recommended by the evaluated nuclear data file ENDF/B-III (dotted curves).

All cross sections given in this work are determined for 100% of the individual isotopes except in the case of element Ti. For this element, the integrated cross sections are given per atom of the natural Ti. The total errors of the inelastic cross sections measured in this work are shown in the figures representing the excitation functions and they are in general of the order of 10-15%.

### Discussions

Since it will be too lengthy, for this report, to discuss the results of the present work in detail, the discussions will be limited to some general remarks. The results of this work are, however, discussed more fully elsewhere<sup>5</sup>.

An overall comparison of the experimental and theoretical results reported in this work indicates that the calculation of neutron inelastic scattering cross sections based on Hauser-Feshbach formalism and properly corrected for the level width fluctuation and resonance interference effects will in general give a good description of these cross sections. At low energies where there are few channels open for the decay of the compound nucleus the corrections according to the Moldauer theory are more important and can not be

neglected. At higher energies where inelastic transitions to many states of the target nucleus will be energetically possible these corrections are small and pure H-F calculations seem to be adequate. The results of the cross section calculations according to Moldauer theory indicate that the excitation functions calculated with the parameter  $Q$  equal to zero agree better with the measured excitation functions.

This type of calculations is very sensitive to the level properties of the target nucleus. Accordingly, proper knowledge of the level energies and their spins and parities is necessary for realistic calculations. Some of the discrepancies between experimental and calculated cross sections in this work can be due to the lack of such information.

### Acknowledgement

The present work has been performed at the Neutron Physics Section of AB. Atomenergi, Studsvik, during author's stay in Sweden. The author wishes to express his appreciation for the support and assistance he received from the AB. Atomenergi, Studsvik.

### References

1. WRENDA 73, INDC(SEC) - 32/U
2. CINDA 74, LAEA, Vienna, 1974.
3. HAUSER, W. and FESHBACH, H., Phys. Rev. 87 (1952) 366.
4. MOLDAUER, P.A., Phys. Rev. 135B (1964) 642.
5. ETEMAD, M.A., AB. Atomenergi, Studsvik, Sweden, Report AE-481, 1973.
6. HORSLEY, A., Nuclear Data A2 (1966) 243.
7. HOLMQVIST, B., et al., Arkiv Fysik 34 (1967) 481.
8. HOLMQVIST, B. and WIEDLING, T., AB. Atomenergi, Studsvik, Sweden, Report AE-430, 1971.
9. ETEMAD, M.A., AB. Atomenergi, Studsvik, Sweden, Report AE-485, 1975.
10. CHIEN, J.P. and SMITH, A.B., Nucl. Sci. Eng. 26 (1966) 500.
11. TOWLE, J.H. and GILBOY, W.B., Nucl. Phys. 39 (1962) 300.
12. HOLMQVIST, et al., Nucl. Phys. A146 (1970) 321.
13. TOWLE, J.H., Nucl. Phys. A117 (1968) 657.
14. SMITH, A.B., et al., Phys. Rev. C1 (1970) 581.
15. BARROWS, A.W. et al., Nucl. Phys. A107 (1968) 153.
16. HOPKINS, J.C. and SILBERT, M.G., Nucl. Sci. Eng. 19 (1964) 431.
17. GILBOY, W.B. and TOWLE, J.H., Nucl. Phys. 64 (1965) 130.
18. MONTAGUE, J.H. and PAUL, E.B., Nucl. Phys. 30 (1962) 93.
19. BARNARD, E. et al., Nucl. Phys. A118 (1968) 321; (PEL-180).
20. ROGERS, V.C., et al., Nucl. Sci. Eng. 45 (1971) 297.
21. TOWLE, J.H., et al., Nuclear Data for Reactors, Paris 17-21 October, 1966. Conf. Proc. IAEA, Vienna, 1967. Vol. 1, p. 367.
22. COLES, R.E., AWRE - 0 - 66/71, 1971.
23. CRANBERG, L. et al., Phys. Rev. 159 (1967) 969.
24. TANAKA, S. et al., Nucl. Phys. A179 (1972) 513.



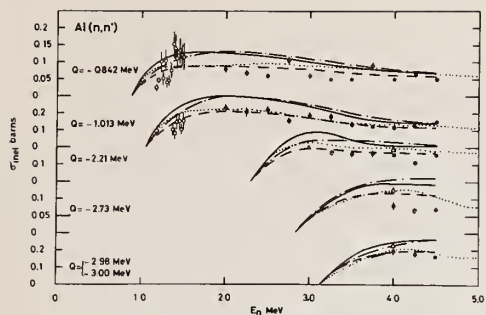


Fig. 1 Excitation functions for Al.

(●) Present measurement,  
 (○) Ref. 10 (△) Ref. 11  
 (—) H - F (---) Q = 0  
 (-.-) Q = 1 (.....) ENDF/B-III

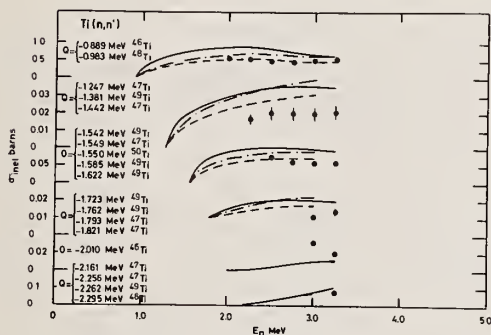


Fig. 2 Excitation functions for Ti.

(●) Present measurement,  
 (—) H - F, (---) Q = 0,  
 (-.-) Q = 1

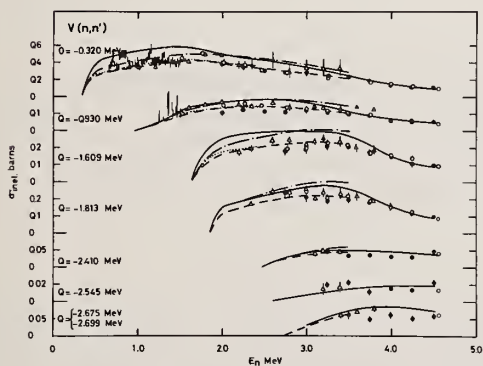


Fig. 3 Excitation functions for V.

(●) Present measurement,  
 (○) Ref. 12, (△) Ref. 13,  
 (□) Ref. 14, (—) H - F,  
 (---) Q = 0, (-.-) Q = 1,  
 (.....) ENDF/B-III

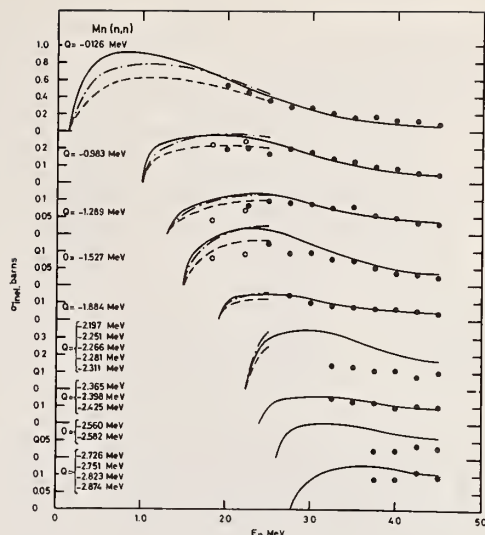


Fig. 4 Excitation functions for Mn.

(●) Present measurement,  
 (○) Ref. 15, (—) H - F,  
 (---) Q = 0, (-.-) Q = 1

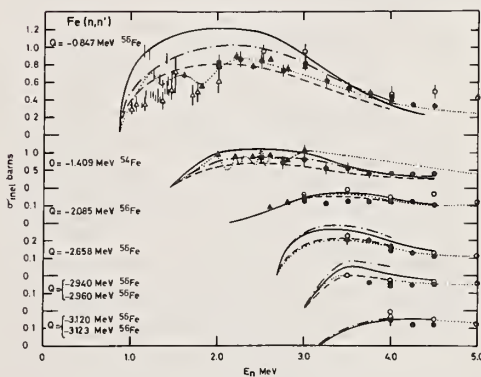


Fig. 5 Excitation functions for Fe.

(●) Present measurement,  
 (○) Ref. 16, (△) Ref. 17,  
 (□) Ref. 18, (◇) Ref. 19,  
 (—) H - F, (---) Q = 0,  
 (-.-) Q = 1, (.....) ENDF/B-III

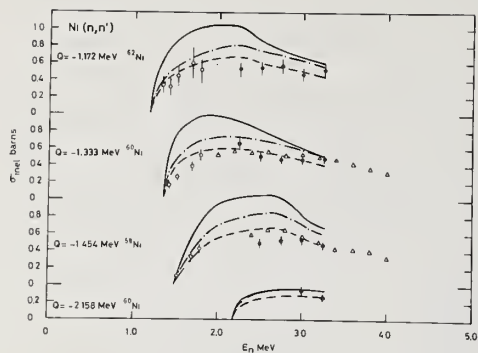


Fig. 6 Excitation functions for Ni.

(●) Present measurements,  
(○) Ref. 20, (△) Ref. 21,  
(—) H - F, (---) Q = 0,  
(-.-) Q = 1

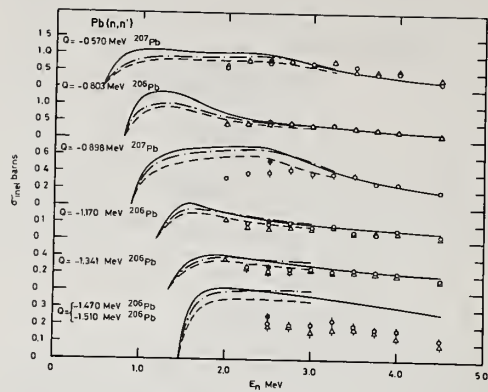


Fig. 8 Excitation functions for Pb.

(○) Present measurement - Pb sample  
(△) Present measurement - Pb<sub>r</sub> sample  
(●) Ref. 23, (—) H - F,  
(---) Q = 0, (-.-) Q = 1

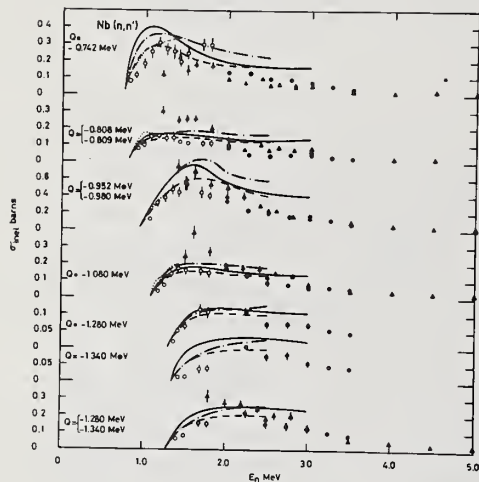


Fig. 7 Excitation functions for Nb.

(●) Present measurement,  
(○) Ref. 20, (▲) Ref. 22,  
(—) H - F, (---) Q = 0,  
(-.-) Q = 1, (.....) ENDF/B-III

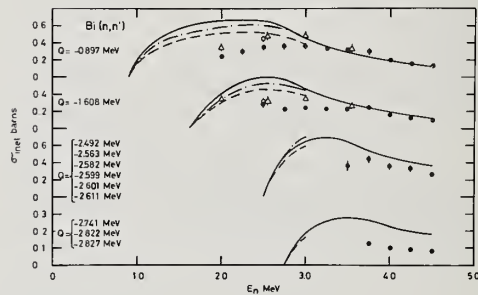


Fig. 9 Excitation functions for Bi.

(●) Present measurement,  
(○) Ref. 23, (△) Ref. 24,  
(—) H - F, (---) Q = 0,  
(-.-) Q = 1

Photoneutrons from the target of the Yale LINAC were polarized by elastic scattering from a cylinder of graphite. The polarized neutrons were observed at angles of  $50^\circ$  and  $130^\circ$  and their energies determined with a time-of-flight resolution of  $0.75 \text{ ns.m}^{-1}$ . The absolute polarization of the neutrons was measured in a true double-scattering experiment; this polarized source then was used to measure the analyzing powers of the reactions  ${}^4\text{He}(\vec{n},n)$ ,  ${}^6\text{Li}(\vec{n},n)$ ,  ${}^9\text{Be}(\vec{n},n)$ , and  ${}^{16}\text{O}(\vec{n},n)$  over wide ranges of energy and angle. These reactions are of interest from three viewpoints i) the design of fission and fusion power reactors ii) absolute neutron standards and iii) fundamental theory. General, multi-level R-function analyses and phase-shift analyses of the observed analyzing powers were made in all cases. Differential and total cross sections were predicted and compared with currently available measurements.

(NUCLEAR REACTIONS:  ${}^4\text{He}(\vec{n},n)$ ;  ${}^6\text{Li}(\vec{n},n)$ ;  ${}^9\text{Be}(\vec{n},n)$ ;  ${}^{12}\text{C}(\vec{n},n)$  and  ${}^{16}\text{O}(\vec{n},n)$ ;  $E=2$  to  $5 \text{ MeV}$ ;  $\theta_{\text{lab}}=20^\circ$  to  $150^\circ$ ; measured  $\vec{p}(E,\theta)$  absolutely for  ${}^{12}\text{C}(n,\vec{n})$  reaction then determined  $A(E,\theta)$  for other reactions; R-function and phase-shift analyses.)

### Introduction

In this paper, we present the results obtained at the Yale Electron Accelerator Laboratory in an extensive program of studies of the polarization of fast neutrons elastically scattered from selected light nuclei. The objectives of the work are the measurement of absolute values of the neutron polarizations over wide ranges of energy and angle, the interpretation of the results in terms of the R-matrix theory of nuclear reactions and the determination of definitive sets of phase-shifts. It is possible not only to shed light on those results deduced from earlier analyses of total and differential cross sections but also to uncover new information concerning those states that do not make themselves felt in the more conventional work.

The importance of polarization measurements stems from the fact that polarization is a consequence of interference effects between the various amplitudes associated with a particular reaction. In the case of neutron-nucleus scattering, such effects can arise in a number of ways, for example: i) in the make-up of the hard-sphere scattering at energies where many different partial wave amplitudes are allowed, ii) from the interference between certain resonance and hard-sphere scattering, iii) from resonance-resonance interference and iv) from interference due to distant levels (which may be interpreted in terms of an optical model).

We have taken the results of our analyses of the polarization data and have predicted the total and differential cross sections. In all cases, good agreement with published work is obtained. This approach is the inverse of that taken in those analyses prior to this work.

The reactions that we have studied are of interest from both pure and applied points of view.

### Experimental Method

The basic method used in these studies involves the polarization of an initially unpolarized flux of neutrons by elastic scattering from a suitable light nucleus (in this case,  ${}^{12}\text{C}$ ). The state of polarization of the flux scattered at a given angle is measured using a true double-scattering method in which the polarized flux is scattered again from an identical  ${}^{12}\text{C}$  target at an identical scattering angle.

The left-right asymmetry in the doubly scattered flux is measured and, after taking into account the (known) energy-loss at the first scattering, the results are analyzed to give the absolute polarization  $\vec{p}$  of the flux.<sup>1</sup> Having established the polarization of the source, the analyzing powers of other nuclei can be obtained simply by replacing the second scatterer with an appropriate target.<sup>2,3</sup>

The initial flux of unpolarized neutrons is generated via the  $(\gamma,n)$  reaction in a heavy nucleus and therefore the primary spectrum is Maxwellian with a maximum intensity at an energy of about  $1 \text{ MeV}$ . The intensity decreases rapidly at energies above  $5 \text{ MeV}$ ; this is a necessary feature in making measurements of polarization that results from elastic scattering of neutrons in light nuclei.<sup>1</sup> The pulsed nature of the LINAC makes it possible to measure the neutron energies with good resolution (typically  $0.7 \text{ ns.m}^{-1}$ ). We have also developed a generalized neutron spin-precession method that is well-suited for use with such a continuous energy spectrum of neutrons; this method greatly reduces the systematic errors that would otherwise occur in the experiment.<sup>4</sup>

Photoneutrons from a Pb-U target are generated by bombardment with  $50 \text{ MeV}$  electrons at a rate of  $270 \text{ ns}^{-1}$ . The pulse width is typically  $20 \text{ ns}$  and the peak current  $5$  to  $10 \text{ A}$ . In order to measure the  $\vec{n}$ - ${}^{12}\text{C}$  polarization absolutely, a fraction of the photoneutrons is scattered from a flat plate of graphite  $15 \text{ cm}$  long x  $7.5 \text{ cm}$  wide x  $1.5 \text{ cm}$  thick placed at a reaction angle of  $50^\circ$ . The angular resolution of the arrangement is  $\pm 7^\circ$ . The polarized neutrons travel along a  $27\text{-m}$  flight path (passing through the solenoid) and scatter from a second graphite plate (identical to the first) into two plastic scintillators (each  $12.5 \text{ cm}$  dia x  $15 \text{ cm}$  thick) which are placed at  $\pm 50^\circ$ . These detectors each subtend an angle of  $\pm 7^\circ$  at the second target. The neutron time-of-flight spectra are stored in an on-line computer; the channel widths are typically  $6 \text{ ns}$ . At  $2 \text{ MeV}$ , the overall resolution is about  $50 \text{ keV}$ .

Having determined the "point" polarization of the  ${}^{12}\text{C}(n,\vec{n})$  reaction, the experiment is repeated using cylinders of graphite, each  $10 \text{ cm}$  dia x  $1 \text{ cm}$  thick, in place of the thin plates. The flux of polarized neutrons incident on the second scatterer is in excess of  $0.5 \times 10^6$  neutrons/ $100 \text{ cm}^2\text{-hour}$  between  $2$  and  $5 \text{ MeV}$ . At a reaction angle of  $50^\circ$ , the source polarization in the range  $2.1$  to  $3.4 \text{ MeV}$  is greater than  $50\%$  (negative) and from  $4.4$  to  $5 \text{ MeV}$ , it increases from  $30\%$  to  $50\%$  (positive).

A typical layout of the experiment when used to measure the analyzing power of a light nucleus is shown in Fig. 1. Here, the first reaction angle is  $130^\circ$  (chosen to increase the source polarization

\*Work supported by U.S.A.E.C.

†Now at A.N.U. Canberra, Australia.

††Now at A.N.L. Argonne, Ill. U.S.A.



between 1 and 2MeV) and the analyzer under study is a liquid oxygen target, viewed by an array of scintillation counters:

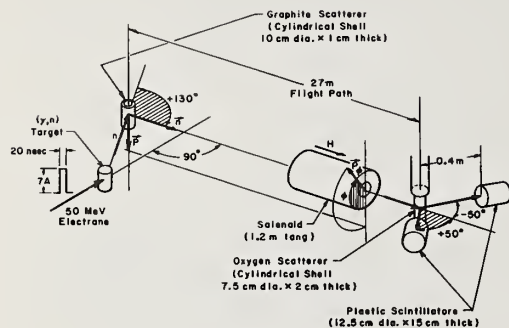


Figure 1.

Arrangement for measuring the analyzing power in  $\bar{n}$ - $^{16}\text{O}$  scattering in the energy range 1 to 4MeV.

The essential points in obtaining the analyzing power when using the generalized spin-precession solenoid are:

The integrated magnetic field required to precess a neutron of measured energy  $E_n$  through  $180^\circ$  is

$$\int H \cdot dl = 2.37 \times 10^5 \times \sqrt{E_n(\text{MeV})} \text{ Oe-cm}$$

and the angle of precession,  $\phi$ , of a non-relativistic neutron of measured energy  $E_\phi$  is

$$\phi = \pi \sqrt{E_n/E_\phi}$$

The product of the polarization  $p$  of the source and the analyzing power  $A$  of the second scatterer is

$$pA = \pm(1-R_\pm)/(R_\pm - \cos\phi)$$

where + and - refer to the right and left detector, respectively and

$$R_\pm = [N_\pm(H)/N_\pm(0)] [C(0)/C(H)]$$

where  $N_\pm(H)$  and  $C(H)$  are the corresponding detector count rates and monitor count rate with the field on and  $N_\pm(0)$  and  $C(0)$  the corresponding rates with the field off. It is now straightforward to deduce  $pA$  independently of the monitor rates. Details of the method are given in Ref. 4. The advantages of this method are well-illustrated in Fig. 2 which shows the time-of-flight spectra of neutrons (doubly-scattered from  $^{12}\text{C}$ ) observed in the left detector ( $-50^\circ$ ) with and without the magnetic field:

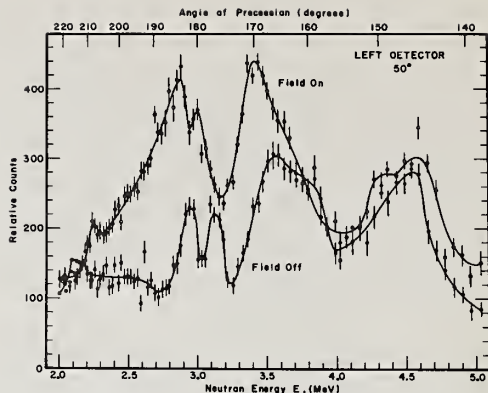


Figure 2.

Spectra of neutrons observed in a single detector at  $-50^\circ$  in a  $^{12}\text{C}$  double-scattering experiment, with and without the solenoidal field on. The field is set to precess a 3MeV neutron through  $180^\circ$ . The precisely determined angles of precession are also given.

The neutron energy-loss that occurs at the first ( $^{12}\text{C}$ ) scatterer can be put to advantage in those cases where it is necessary to reduce the number of high energy neutrons that are generated above the threshold for inelastic scattering. This method was successfully used in the studies of  $\bar{n}$ - $^6\text{Li}$  and  $\bar{n}$ - $^9\text{Be}$  scattering (primary reaction angle equal to  $130^\circ$ ).

#### Phase-shift and R-matrix Analyses

The measured polarizations were analyzed using iterative grid search techniques to give definitive sets of phase-shifts and R-matrix parameters. The inclusion of partial waves higher than d-waves did not alter the quality of the fits significantly. Expressions for the differential cross section, polarization and total cross section used are:

$$\sigma(\theta) = (1/k^2) \sum_{L=0}^{\infty} B_L P_L(\cos\theta)$$

$$\sigma(\theta)p(\theta) = (1/k^2) \sum_{L=1}^{\infty} C_L P_L^1(\cos\theta)$$

$$\sigma_T = (4\pi/k^2) \sum_{L=0}^{\infty} [L \sin^2 \delta_L^- + (L+1) \sin^2 \delta_L^+]$$

where  $P_L(\cos\theta)$  and  $P_L^1(\cos\theta)$  are the Legendre and associated Legendre polynomials. Values for the expression  $B_L$  and  $C_L$  in terms of phase-shifts have been derived by Blatt and Biedenharn and Simon and Welton.<sup>5,6</sup>

The elastic scattering of neutrons from spin-zero nuclei is the simplest application of R-matrix theory.<sup>7</sup> Only one channel is open so that

$$R_{1J} = \sum_{\lambda} \gamma_{\lambda 1J}^2 / (E_{\lambda 1J} - E)$$

where  $\gamma_{\lambda 1J}^2$  and  $E_{\lambda 1J}$  are the reduced widths and energies and the states are denoted by  $\lambda$ , and, also

$$R_{1J} = (f_1 - B_{1J})^{-1}; f_1(E) = a u_1^{-1}(a) (du_1/dr)_a$$

where  $a$  is the channel radius,  $u_1$  is the radial part of the wave function and  $B_{1J}$  is the boundary condition. The collision function  $U_{1J}$  can be expressed in terms of a single, real phase-shift,  $\delta_{1J}$  thus

$$U_{1J} = \exp(2i\delta_{1J})$$

The phase-shifts are related to the R-function as follows

$$\delta_{1J} = -\phi_1 + \arctan \left\{ P_1 R_{1J} / [1 - R_{1J}(S_1 - B_{1J})] \right\}$$

where  $S_1$ ,  $P_1$  and  $\phi_1$  are the well-known shift function, penetrability, and hard-sphere phase-shift. We define the resonance energy  $E_R$  as the energy at which the resonant phase-shift is an odd integral multiple of  $\pi/2$ . The width of the resonance is

$$\Gamma_{\lambda 1J} = 2P_{1J} \gamma_{\lambda 1J}^2$$

Distant levels are taken into account using the method given in Ref. 8, i.e.

$$R_{1J}^{\infty} = R_{01J} + R_{1J}^E$$

A fit was made to the polarization measurements by minimizing the quantity

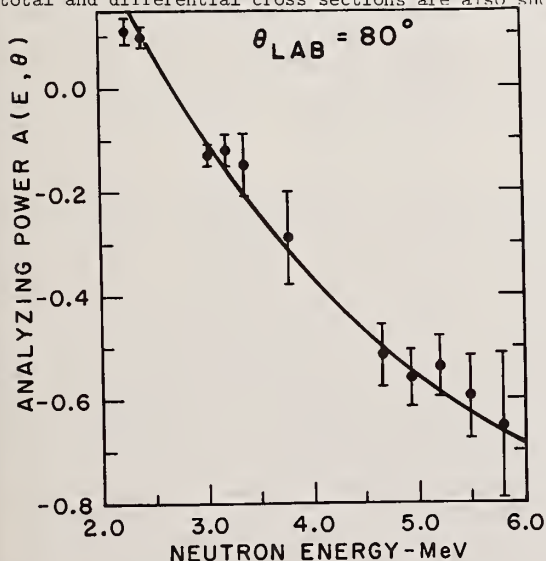
$$S = \sum_{j=1}^M \sum_{i=1}^N \frac{[P_{\text{cal}}(\theta_i, E_j) - P_{\text{exp}}(\theta_i, E_j)]^2}{[\Delta P(\theta_i, E_j)]^2}$$

where  $N$  is the number of angles (between 4 and 9, depending on the experiment) and  $M$  is the total number of energy points used. The optimum R-matrix parameters derived from this procedure, were used to predict the differential and total cross sections, and additional polarizations throughout the entire energy range up to about 5 MeV.

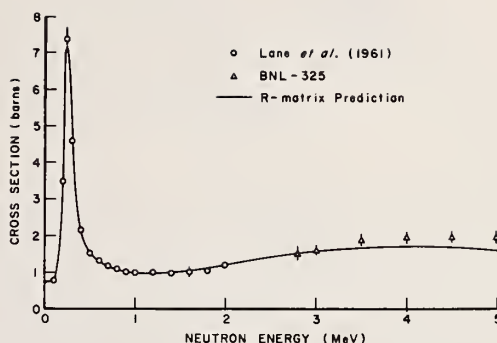
Details of the analysis of the polarization data in the case of  $\bar{n}$ - $^6\text{Li}$  scattering are given in a recent paper.<sup>3</sup> This is a complex problem because the target nucleus no longer has spin zero and the  $(n, \alpha)$  channel must be properly taken into account.

### Results

Typical examples of our measured polarizations (or analyzing powers) and various R-function fits are shown in the following figures. Some predicted total and differential cross sections are also shown:



The measured (absolute) analyzing power for the reaction  $^6\text{Li}(\bar{n}, n)$  at  $\theta_{\text{lab}} = 80^\circ$  in the energy range 2 to 6 MeV. The curve is in good agreement with the predictions of Ref. 9.



The Neutron Total Cross Section of  $^6\text{Li}$   
Figure 4.

The neutron total cross section of  $^6\text{Li}$  predicted from an R-matrix fit to the measured (absolute) analyzing power. The calculation also predicts the  $(n, \alpha)$  cross section using the Thomas approximation for the R-matrix. The points shown above are taken from Refs. 10.

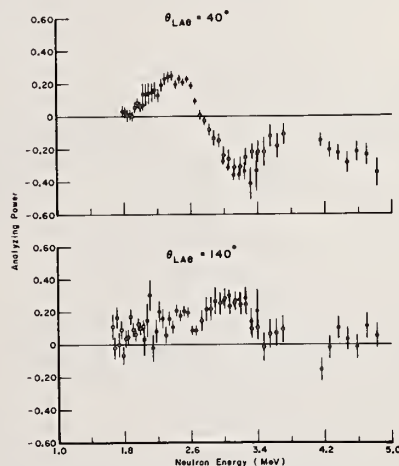


Figure 5.

The measured (absolute) analyzing power for the reaction  $^6\text{Li}(\bar{n}, n)$  at  $\theta_{\text{lab}} = 40^\circ$  and  $140^\circ$  in the energy range 1.6 to 4.8 MeV. The open and closed circles refer to measurements made with the primary reaction angle of the source equal to  $130^\circ$  and  $50^\circ$  respectively.

## Conclusions

The power of this new method of measuring absolute neutron polarizations in light nuclei has now been amply demonstrated. The results have been analyzed within the framework of standard R-matrix theory and have been incorporated into the existing body of data on these nuclei to give information of unprecedented completeness for neutron-induced reactions.

## References

1. R. J. Holt, F. W. K. Firk, R. Nath and H. L. Schultz, Phys. Rev. Lett. **28**, 114(1972) and Nucl. Phys. **A213**, 147(1973).
2. G. T. Hickey, F. W. K. Firk, R. J. Holt and R. Nath, Nucl. Phys. **A225**, 470(1974).
3. R. J. Holt, F. W. K. Firk, G. T. Hickey and R. Nath, Nucl. Phys. **A237**, 111(1975).
4. R. Nath, F. W. K. Firk, R. J. Holt and H. L. Schultz, Nucl. Instr. **98**, 385(1972).
5. J. Blatt and L. Biedenharn, Rev. Mod. Phys. **24**, 258(1952).
6. A. Simon and T. Welton, Phys. Rev. **90**, 1036(1953).
7. A. M. Lane and R. G. Thomas, Rev. Mod. Phys. **30**, 257(1958).
8. F. W. K. Firk, J. E. Lynn and M. C. Moxon, Proc. Phys. Soc. **82**, 477(1963).
9. R. L. Walter and T. Stambach, Nucl. Phys. **A180**, 225(1972).
10. R. O. Lane, A. J. Elwyn and A. Langsdorf, Jr., Phys. Rev. **136**, B1710(1964) and BNL-325(1958).
11. R. B. Schwartz, R. A. Schrack, and H. T. Heaton, II, "MeV Total Neutron Cross Sections" National Bureau of Standards, (1974).

## Appendix

The following R-matrix parameters were obtained in a preliminary fit to our measured analyzing power of the  $^{16}\text{O}(\bar{n},n)$  reaction. The total neutron cross section data given in Ref. 11 were also used in the fitting procedure. Interaction radius =  $1.4(A+1) = 4.3\text{fm}$

1 J S	$E_{1JJS}$ (MeV)	$\gamma_{1JJS}^2$ (MeV)	$R_{1JJS}^\infty$	$B_{1JJS}$
0 1 1	-0.885	0.4	0	0
0 2 2	-0.555	0.4	0	0
1 0 2	0.7	2.4	0.4	-0.7
1 1 1	-	-	0.4	0
1 2 1	2.75	0.2	0	-0.4
1 1 2	-	-	0.2	0
1 2 2	2.75	1.0	0	-0.4
1 3 2	-	-	0.2	0
2 1 1	-	-	-	0
2 2 1	-	-	-	0
2 3 1	0.63	0.6	0	-1.9
2 0 2	-	-	-	0
2 1 2	-	-	-	0
2 2 2	-	-	-	0
2 3 2	-	-	-	0
2 4 2	2.71	0.8	0	-1.4

The narrow state at 0.82MeV was ignored in the overall fit.

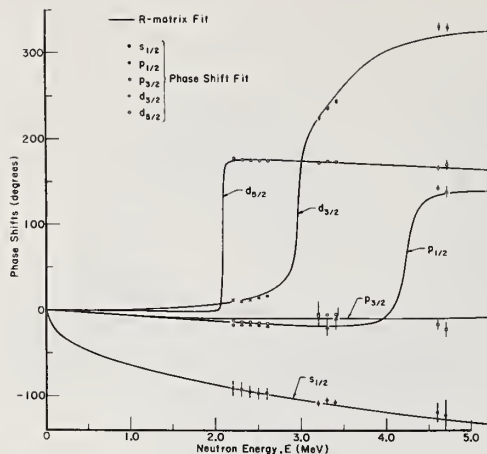


Figure 6.

A phase-shift analysis of the measured absolute polarization for the reaction  $^{12}\text{C}(n,\bar{n})$  the source polarization, together with the phase-shifts derived from the R-matrix fit.

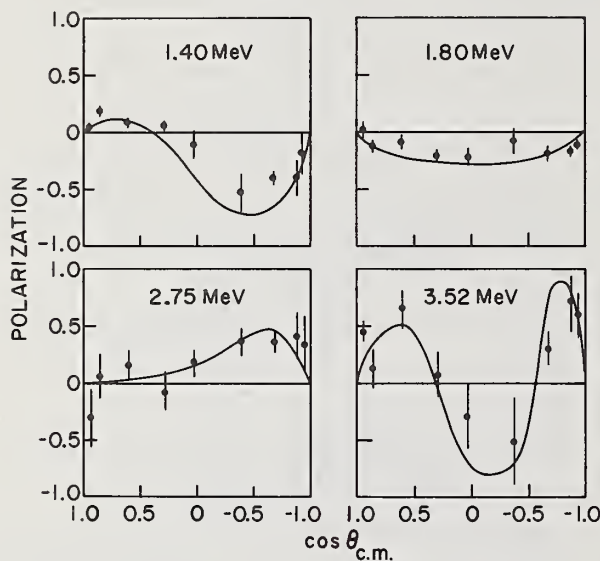


Figure 7.

Four typical R-function fits to the measured analyzing power for the reaction  $^{16}\text{O}(\bar{n},n)$ . Measurements of this kind were made as a continuous function of energy between 1 and 5MeV.



# INELASTIC SCATTERING OF FAST NEUTRONS FROM $^{103}\text{Rh}$

D. Reitmann, E. Barnard, D.T.L. Jones and J.G. Malan

Atomic Energy Board

Pelindaba, South Africa

Cross sections for elastic and inelastic scattering of fast neutrons from  $^{103}\text{Rh}$  were measured at energies up to 1500 keV. Additional information about the level scheme followed from  $(n,n'\gamma)$  measurements. The effective cross section for excitation of the isomeric state at 40 keV was derived from these results and compared with activation measurements and theoretical results.

(Rhodium-103; inelastic scattering; fast neutrons; isomeric state; level scheme; optical model)

## Introduction

Excitation of the 40 keV isomeric state in  $^{103}\text{Rh}$  by inelastic neutron scattering has attractive properties for selective fast-flux monitoring. The half-life of 57 minutes is convenient; the cross section rises rapidly from threshold and becomes nearly constant at high energies. Accurate measurement of the activation cross section, however, requires careful calibration of the incident-neutron flux and large corrections for absorption of the 20 keV K X-rays. These difficulties are probably responsible for the paucity of experimental data and the discrepancies between existing results.

The shape of the excitation curve and the nature of the known level scheme indicate that, towards higher energies, several excited states decay to the 40 keV level so that their inelastic scattering cross sections contribute to the activation cross section. These individual cross sections have not previously been measured, and it was considered useful to compare existing activation cross sections with those deduced from inelastic scattering cross sections and improved knowledge of the decay scheme. Apart from their applied importance, fast-neutron interactions with a nucleus in the mass range where both s-wave and p-wave strength functions exhibit large anomalies, are also theoretically interesting.

## Experiment

Accurate measurement of the inelastic neutron scattering cross sections for individual levels is best done by time-of-flight. Corrections for multiple scattering and flux attenuation in the scattering sample require knowledge of the elastic scattering cross sections and angular distributions as a function of incident-neutron energy. These data are also essential for establishing optical-model parameters for theoretical interpretation. High-resolution gamma spectroscopy complements these measurements by providing information on the decay scheme, the behaviour of cross sections near their thresholds and the relative cross sections for levels which cannot be resolved by neutron time-of-flight.

In the present experiment, a 3 MV pulsed Van de Graaff accelerator and the  $^7\text{Li}(p,n)^7\text{Be}$  reaction were used as a neutron source of well-defined energy. Proton pulses were of approximately 1 ns duration, the repetition rate was 3 MHz and the Li targets were about 20 keV thick for most of the measurements. The scatterer was a hollow right cylinder of 99.9% pure rhodium metal, 2.5 cm high and 2.5 cm in outside diameter, with a wall thickness of 2 mm. This cylinder was suspended 10 to 15 cm from the neutron source. Neutrons were detected in a conventional plastic scintillator at flight paths of about 2 m, and gamma rays in a 40 cm<sup>3</sup> Ge(Li) detector placed 45 cm from the scatterer. Suitable shadow wedges, collimation and shielding protected the detectors against neutrons coming directly from the source.

### Elastic scattering

Angular distributions for elastic scattering were measured at 15° intervals between 30° and 150° to the beam direction, and at 100 keV intervals between 600 and 1300 keV. The elastic peaks in the time-of-flight spectra could not be resolved from those due to inelastic scattering from the 40 and 93 keV levels, and small corrections for these effects were applied. All cross sections were measured relative to the known cross section for elastic scattering from carbon.

The carbon scatterer had the same outside dimensions as the rhodium, but a wall thickness of only 1 mm.

### Inelastic scattering

Observation of inelastically scattered neutrons from the 40 and 93 keV levels is extremely difficult, due to their very small cross sections and the inevitable "tail" of the strong elastic peak. It was, however, possible to resolve these three peaks at incident energies of 550 and 600 keV by using a thin (8 keV) Li target and employing a suitable Zr scatterer to obtain the shape of a pure elastic peak.

Inelastically scattered neutrons from known levels at 295, 357, 537, 651, 803, 848, 881, 920, 1107 and 1277 keV were clearly seen and resolved at incident energies up to 1500 keV. A level at 607 keV was also observed and has since been included in the published level schemes in Nuclear Data Sheets.<sup>1</sup> Additional unknown levels were observed at about 1040, 1200, 1250 and 1290 keV, and confirmed by the  $(n,n'\gamma)$  results. Effects due to the second neutron group from the  $^7\text{Li}(p,n)^7\text{Be}^*$  reaction were carefully compensated for by subtracting a time-of-flight spectrum obtained at the appropriate lower energy and reduced incident flux. Cross sections, measured relative to carbon elastic scattering, were corrected for flux attenuation and multiple scattering. The fact that all these measurements were made at 125° obviated the need for corrections for anisotropic inelastic scattering.

### $(n,n'\gamma)$ measurements

The gamma rays from inelastic neutron scattering were detected in a 40 cm<sup>3</sup> Ge(Li) detector. Time gating reduced the effects due to neutrons striking the detector and to gamma rays from the target. Background corrections were obtained from runs with a Zr scatterer which has very few excited states in the energy range employed here. Accurate gamma energies were measured at a scattering angle of 90°, whereas intensities were measured at 55° and corrected for absorption and detector efficiency.

Gamma angular distributions were also measured at 550 and 1400 keV incident-neutron energy. These were mostly very slightly anisotropic and, especially for low-energy transitions, obviously not symmetric around 90°. This effect was explained by the fact that most low-energy gamma rays are detected from the side of the sample facing the detector. The scatterer, however, is exposed to a higher neutron flux on the target side than the far side (due both to flux attenuation and the inverse square law). This leads to an apparent relative enhancement in large-angle scattering, an effect which has hitherto usually been ignored in  $(n,n'\gamma)$  measurements. The magnitude of the distortion depends on the geometry, sample size and thickness, the total neutron cross section and the gamma absorption cross section. It was possible to simulate the effect by computer calculation, and angular distributions were suitably corrected. Conventional  $\chi^2$  analyses with spin, parity and mixing ratio as variable parameters, indicated that the experimental accuracy was in most cases insufficient to determine these parameters uniquely.

Gamma-gamma coincidence measurements with two 40 cm<sup>3</sup> Ge(Li) detectors were only successful for the strongest transitions and contributed to the construction of the decay scheme.

## Results

Elastic scattering data were corrected for flux attenuation and multiple scattering, and were fitted to a Legendre polynomial expansion of the form

$$\frac{d\sigma_e(\theta)}{d\Omega} = \frac{\sigma_e}{4\pi} \left\{ 1 + \sum_{i=1}^4 \omega_i P_i(\theta) \right\} \quad (1)$$

These results are presented in Fig. 1, where error bars on the cross sections reflect statistical errors, plus an 8% uncertainty allowed for detector efficiency and flux normalization uncertainties. Errors on the polynomial coefficients, as derived from the least-squares fitting procedure, are smaller than the circles representing the results.

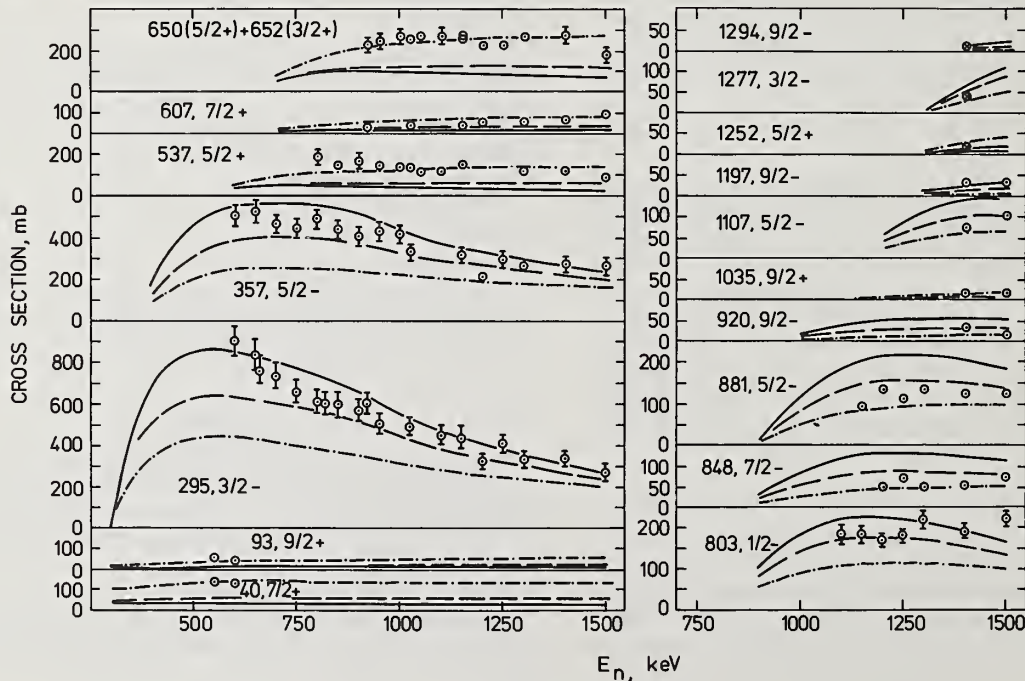
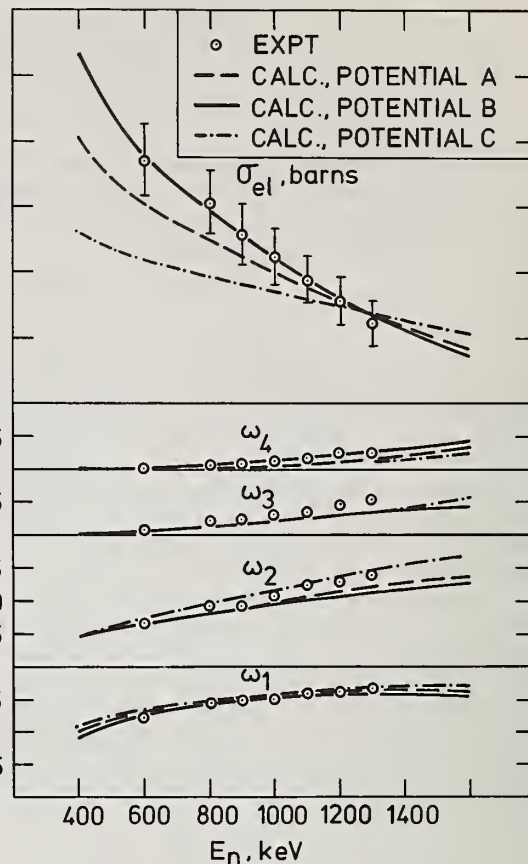
Fig. 1

Elastic scattering cross sections and Legendre polynomial coefficients [Eq. (1)] for  $^{103}\text{Rh}$ . Curves were derived from optical-model and Hauser-Feshbach calculations with different potential parameters.

Experimental values for the cross sections for inelastic scattering from various levels in  $^{103}\text{Rh}$  are plotted in Fig. 2. Error bars once again include statistical errors, as well as an 8% uncertainty in absolute normalization and are plotted whenever they extend beyond the circles. Results for the three highest levels, which could not be properly resolved in the neutron time-of-flight spectra, were derived from the corresponding gamma-ray intensities measured at an incident-neutron energy of 1400 keV. These data are plotted as encircled crosses. The known doublet at about 651 keV could, of course, not be resolved in the time-of-flight experiments, and the combined cross section is plotted in Fig. 2.

Fig. 2

Inelastic scattering cross sections for various levels in  $^{103}\text{Rh}$  as determined by neutron time-of-flight measurements. The curves result from Hauser-Feshbach calculations with potential A (dashed line), potential B (solid line) and potential C (dot-dashed line).





[illegible]

The level scheme for  $^{103}\text{Rh}$  as derived from the present experiment. Levels and transitions marked with an asterisk are here reported for the first time, although transitions marked b) have also been seen by Sayer et al.<sup>3</sup> Levels and transitions marked a) were too low in energy to be observed in the present experiment.

The cross section for excitation of the isomeric state could thus be obtained by simply adding up the measured cross sections for inelastic scattering from all positive parity levels. Experimental results for all these levels could, however, not be obtained at all incident energies. The 40 and 93 keV levels could not be resolved at incident energies above 600 keV. However, their contribution to the activation cross section at high energies is only about 30 % and theoretical extrapolation was considered sufficiently reliable. Missing data points for the higher positive parity states are to be blamed on either the poor efficiency of the neutron detector at low energies (due to the slow channel bias) or poor statistics. Missing data points were obtained by interpolation in the cases of the 537 and 607 keV levels, and theoretical values were used for the levels at 1035 and 1252 keV which contribute less than 10 % to the activation cross section even at the highest incident energies.

$^{103}\text{Rh}(n,n')^{103}\text{Rh}^*$

CROSS SECTION, mb

$E_n$ , keV

• SANTRY AND BUTLER  
 □ KIMURA ET AL.  
 ○ PRESENT EXPT.  
 --- CALC., POTENTIAL A  
 ——— CALC., POTENTIAL B  
 - · - · - CALC., POTENTIAL C

*Cross sections for the excitation of the 40 keV isomeric state in  $^{103}\text{Rh}$  as determined by various experiments and calculated from three different potentials.*

Theoretical values for elastic and inelastic scattering cross sections were obtained with the computer program PELINSCA<sup>6</sup> which allows one to perform conventional optical-model and Hauser-Feshbach calculations as well as "variable enhancement" corrections as suggested by Tepel *et al*.<sup>7</sup> These corrections were employed here instead of the level width fluctuation corrections proposed by Moldauer.<sup>8</sup>

Introduction of the variable enhancement correction improved the fit to the experimental elastic scattering cross sections by about 4 %, reduced the theoretical cross sections for inelastic scattering from negative parity states slightly and made little difference to the results for positive parity levels. These results are plotted as dashed curves (Potential A) in Figs. 1, 2 and 4.

881



However, this potential badly underestimates excitation of the known positive parity levels.

Agreement for low-lying positive parity levels with known spins required increasing the well depths to  $V = 49.7$  and  $W = 15$  MeV (Potential C). This potential also improves the fit to the shape of the elastic angular distributions somewhat, but fits the cross sections for elastic scattering and inelastic scattering from negative parity levels very poorly.

The results obtained with potential B were used to establish spins for negative parity levels, whereas spins of positive parity levels were derived from potential C. It seems doubtful that any single set of optical-model potential parameters will be able to reproduce all experimental results.

### Discussion

Rhodium lies in the mass range where the s-wave strength function has a minimum and the p-wave strength function a maximum. This implies that transmission coefficients for neutrons with  $\ell = 0$  are unusually small, and those for  $\ell = 1$  unusually large. Since the ground state has  $J^\pi = \frac{1}{2}^-$ , excitation of a final state with positive parity requires, to lowest order in  $\ell$ , a p-wave in and an s-wave out or vice versa, whereas negative parity states can be excited via a strong p-wave in both entrance and exit channels. This explains why the negative parity levels are excited much more strongly than the others.

The additional fact that the cross sections for excitation of positive and negative parity states apparently require different potentials probably bears a relationship to the particular sensitivity of s-wave and p-wave strengths in this mass range. Any change in the potential well depth will increase the s-wave transmission coefficients while decreasing those for p-waves, or vice versa. This is reflected in the behaviour of different potentials mentioned earlier. This phenomenon was also recently observed by Camarda<sup>11</sup> who found that no single potential would fit both s-wave and p-wave strength functions in this mass range. Proper theoretical treatment of  $^{103}\text{Rh}$  might then require an  $\ell$ -dependent optical-model potential.

An alternative explanation would be that the positive parity states in  $^{103}\text{Rh}$  are different in character from the negative parity states, a suggestion which is supported by the observation that all strong gamma transitions conserve parity. It is then conceivable that different optical-model potentials might be required to produce the proper transmission coefficients for all partial waves leading to final states with different parities. This hypothesis was tested by calculating complete sets of transmission coefficients with potentials B and C, and combining them in such a way that transmission coefficients for all outgoing

partial waves leading to positive parity final states were taken from potential C, whereas those for ingoing waves and outgoing waves leading to negative parity states were taken from potential B. Shape elastic scattering cross sections were calculated with potential B. As should be expected, experimental results for elastic scattering as well as inelastic scattering from negative parity levels, were well reproduced, whereas the excitation of positive parity levels was underestimated, though not as badly as with the original potentials A or B. Further increasing the real and imaginary well depths for the positive parity partial waves improved results for these levels at slight cost to the negative parity states, indicating the need for adjusting the "negative parity" potential as well. The search is being continued but the indications are that two potentials will be found which, together, will explain all experimental results. This would then constitute a strong indication that the excited states of different parity in  $^{103}\text{Rh}$  are different in character.

### Conclusions

Remarkable agreement was obtained between the cross sections for excitation of the isomeric state in  $^{103}\text{Rh}$ , as measured by activation, and those derived from microscopic measurements of inelastic neutron scattering from individual excited states. Comparison with theory implies interesting differences between the nature of excited states of different parity.

### References

1. Nuclear Data Sheets 13, 337(1974)
2. J.L. Black, W.J. Caelli and R.B. Watson, Nucl. Phys. A125, 545(1969)
3. R.O. Sayer, J.K. Temperley and D. Eccleshall, Nucl. Phys. A179, 122(1972)
4. D.C. Santry and J.P. Butler, Can. J. Phys. 52, 1421(1974)
5. I. Kimura, K. Kobayashi and T. Shibata, J. Nucl. Sci. & Techn. 6, 485(1969)
6. C.A. Engelbrecht, H. Fiedeldey and J.W. Tepel, S.A. Atomic Energy Board report PEL-202(1974)
7. J.W. Tepel, H.M. Hofmann, and H.A. Weidenmüller, Phys. Lett. 49B, 1(1974)
8. P.A. Moldauer, Phys. Rev. 123, 968(1961), Phys. Rev. 135, B642(1964)
9. C.A. Engelbrecht and H. Fiedeldey, Ann. Phys. 42, 262(1967); H. Fiedeldey and C.A. Engelbrecht, Nucl. Phys. A128, 673(1969)
10. A.B. Smith, P.T. Guenther and J.F. Whalen, Argonne National Laboratory report ANL/NDM-7(1974)
11. H.S. Camarda, Phys. Rev. C9, 28(1974)

## A SUMMARY\*

W. E. Kinney and F. G. Perey  
Oak Ridge National Laboratory  
Oak Ridge, Tennessee 37830

The ORNL program to measure neutron elastic and inelastic scattering cross sections for 26 nuclides from C to  $^{238}\text{U}$  in the 4–8.5 MeV energy range is summarized. Data acquisition and reduction techniques are reviewed and typical results given. The nuclides investigated are tabulated.

(Neutron, scattering, cross section, elastic, inelastic, differential)

### Introduction

A program to measure neutron elastic and inelastic scattering cross sections in the 4–8.5 MeV incident neutron energy range was started in 1965 at the ORNL Van de Graaff facility. The program concluded with the publication of the final report in June, 1974, bringing to 26 the number of nuclides investigated. The data acquisition and reduction techniques employed in the program are first discussed. Typical results are given and the results summarized.

### Data Acquisition

Conventional time-of-flight techniques were used in the data acquisition. Neutrons were produced by the  $\text{D(d,n)}^3\text{He}$  reaction on both the 3.0 and 5.5 MeV Van de Graaffs. The deuteron beam was pulsed at 2 MHz and bunched to  $\sim 1.5$  nsec. Deuterium was circulated at  $\sim 1.5$  atm pressure in one of several gas cells from 1 to 4 cm in length and diameter  $\sim 1.5$  cm. Energy resolutions varied from  $\pm 0.03$  to  $\pm 0.17$  MeV depending on the cell length and incident deuteron energy.

The scattering samples, nominally  $\sim 1$  mole of material in the form of solid right circular cylinders, were suspended 10–30 cm from the gas cell. The diameters were  $\sim 1/3$  total mean-free-path to prevent multiple scattering from becoming excessive. The scattered neutrons were detected in NE-213 liquid scintillators optically coupled to XP-1040 photomultipliers. The scintillators were 12.5 cm in diameter. Both 2.5 and 5.0 cm thicknesses were used. A single detector was used in earlier work. Later, three detectors with an angular separation of  $\sim 7^\circ$  were employed. The detectors were mounted on a coordinate system with flight path variable to  $\sim 6$  m and angle to  $\sim 150^\circ$ . Three paraffin shields were employed: a fore shield to attenuate source neutrons, an intermediate shield to decrease the contribution of room and air scattering in the source vicinity, and a detector shield. The source neutron production was monitored by a separate time-of-flight system using a 5 cm diameter by 2.5 cm thick NE-213 detector viewed by a 56-AVP photomultiplier placed  $\sim 4$  m from the gas cell at an angle of  $\sim 55^\circ$ .

Standard electronics supplied the flight time and pulse height for each event to a PDP-7 computer which up-dated the spectra. The electronic bias was set at  $\sim 700$  keV to ensure good pulse shape discrimination against  $\gamma$ -rays. Detector efficiencies were measured by (n,p) scattering from a 6 mm diameter polyethylene sample and also the  $\text{D(d,n)}^3\text{He}$  neutron production at  $0^\circ$ <sup>1</sup>.

When sufficient data were accumulated at a desired experimental configuration (generally to achieve better than 3% statistics in the elastic peak), the data were written on magnetic tape for later processing.

### Data Reduction

Neutron peak areas were first extracted from the monitor spectra on the PDP-7 with the aid of a light pen. The monitor areas, time-of-flight spectra, and geometric parameters were then sent to an

IBM/360 computer where sample-out spectra were normalized to sample-in by the ratios of their monitor areas and subtracted from the sample-in spectra. The resulting spectra were converted from counts vs time-of-flight spectra to center-of-mass cross section vs energy spectra. The energy spectra were then smoothed and written on magnetic tape for further processing by the PDP-7. Figure 1 shows the initial time-of-flight spectrum with its converted energy spectrum for  $^{54}\text{Fe}$  at an incident neutron energy of 6 MeV at  $90^\circ$ .

Peak areas were extracted from the energy spectra on the PDP-7 with the aid of its light pen. Generally, three areas corresponding to best, low, and high estimates of the background were extracted for each peak. The high and low estimates were treated as 95% confidence limits in including stripping uncertainties with other uncertainties in the error analysis. The peak areas and continuum information, if any, were written on magnetic tape for final processing by the IBM/360.

Finite sample corrections were made according to semi-analytic recipes<sup>2</sup>. Corrections to elastic data were typically 5–10% at forward angles and 40–80% in the first minimum. Anisotropic results were fit by least squares to a Legendre series to obtain angle-integrated cross sections.

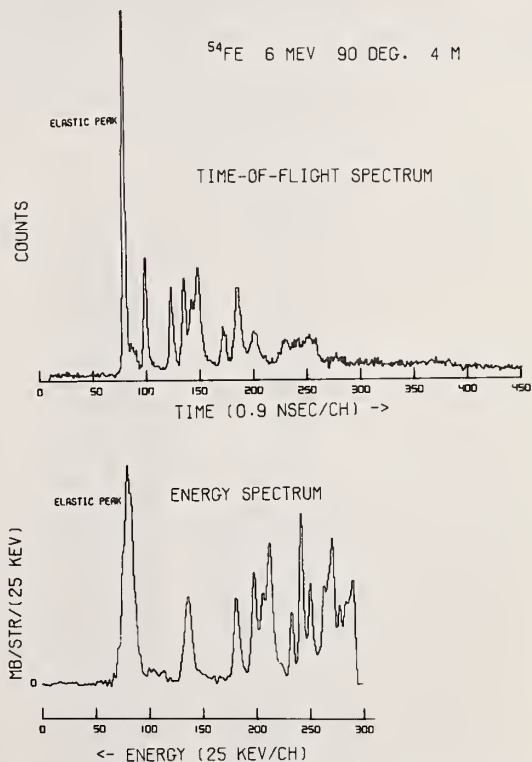


Fig. 1. A typical time-of-flight spectrum for  $^{54}\text{Fe}$  with its transformed energy spectrum. The sample-out spectrum has not been subtracted from the time-of-flight spectrum and the energy spectrum has been offset. The energy spectrum terminates at  $\sim 1$  MeV scattered neutron energy— $\sim$  channel 350 in the time-of-flight spectrum.

\*Research performed at Oak Ridge National Laboratory operated by Union Carbide Corporation for the Energy Research and Development Administration.



The nuclides studied are summarized in Table I, below. Most were chosen to satisfy, at least partially, requests to NCSAG.

Elastic scattering differential cross sections were measured for all samples except  $^{206}\text{Pb}$  and  $^{207}\text{Pb}$  since their elastic scattering cross sections are expected to be essentially the same as those for  $^{208}\text{Pb}$ . The data were reported in both graphical and tabular form and were compared with the results of others and with the then-current ENDF/B evaluations. A typical graphical presentation of elastic scattering data is shown in Figure 2 where data for natural nickel and  $^{60}\text{Ni}$  are compared. The curves are Legendre fits to the natural nickel results. The degree of agreement among the data is gratifying and lends confidence to the reproducibility achievable with our data acquisition and reduction techniques. It is to be noted that the 6.44–8.56 MeV  $^{60}\text{Ni}$  data were taken roughly a year earlier than the other data and were reduced by different experimentalists.

Differential cross sections for inelastic scattering to discrete levels or groups of levels in the residual nucleus (the predominant isotope in the case of natural samples) were measured for all samples except  $^{238}\text{U}$ . Comparisons were made with the results of others but no other data existed for 12 of the samples. Comparisons with then-current ENDF/B evaluations, when available, were also made.

Level densities and spacings are such for 14 of the nuclides investigated that, with our experimental energy resolutions, maxima in the inelastic scattering cross sections could not be uniquely identified with the excitation of specific groups of levels for excitation energies above a few MeV. In these cases, the data were reduced as inelastic scattering to a continuum. Considerable structure indicating preferential excitation of some levels was found in the continua for all nuclides lighter than W thus casting doubt on the adequacy of treating continuum inelastic scattering by a simple evaporation model in those cases. An example of continuum structure is shown in Figure 3 where data for  $^{60}\text{Ni}$  are given.

Table I  
Summary of Results

Element or Isotope	Maximum Inelastic Discrete Level $E_x$ , MeV	ORNL Report
C	4.43	4441 (12/69)
N	5.10	4805 (2/74)
O	6.131	4780 (4/72)
Na	5.78 + continuum	4518 (8/70)
Mg	6.00	4550 (6/70)
Al	5.825	4516 (10/70)
Si	6.887	4517 (7/70)
S	6.76	4539 (6/70)
Ca	6.58	4519 (4/70)
Ti	3.86 + continuum	4810 (10/73)
V	3.08 + continuum	4551 (10/70)
Cr, $^{52}\text{Cr}$	3.49 + continuum	4806 (1/74)
$^{54}\text{Fe}$	4.58 + continuum	4907 (2/74)
Fe	4.116 + continuum	4515 (6/70)
Co	2.585 + continuum	4549 (6/70)
Ni, $^{60}\text{Ni}$	4.613 + continuum	4523 (4/70)
		4807 (1/74)
$^{63}\text{Cu}$ , $^{65}\text{Cu}$	1.72 + continuum	4908 (2/74)
Y	3.87 + continuum	4552 (12/70)
W	continuum	4803 (5/73)
$^{206}\text{Pb}$	2.634 + continuum	4909 (6/74)
$^{207}\text{Pb}$	4.386 + continuum	"
$^{208}\text{Pb}$	5.254 + continuum	"
$^{238}\text{U}$	—	4804 (6/73)

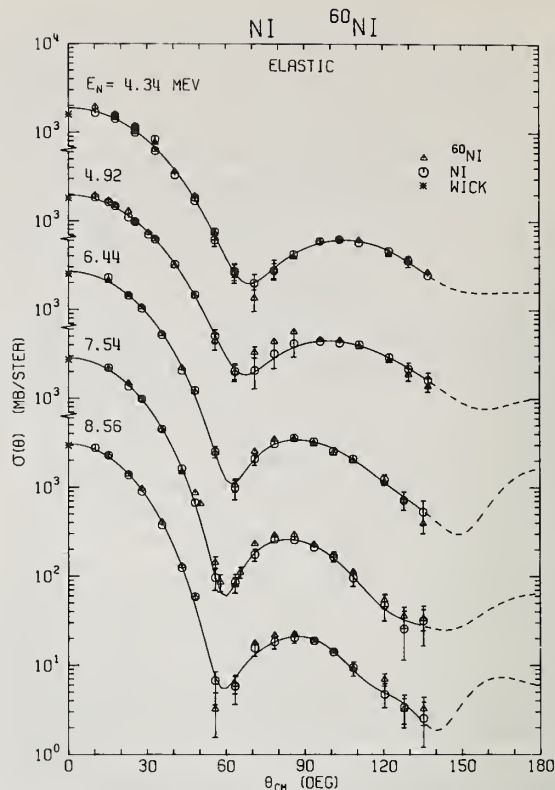


Fig. 2. Our natural nickel and  $^{60}\text{Ni}$  elastic differential elastic scattering cross sections with Legendre fits to the natural nickel data. WICK is Wick's Limit.

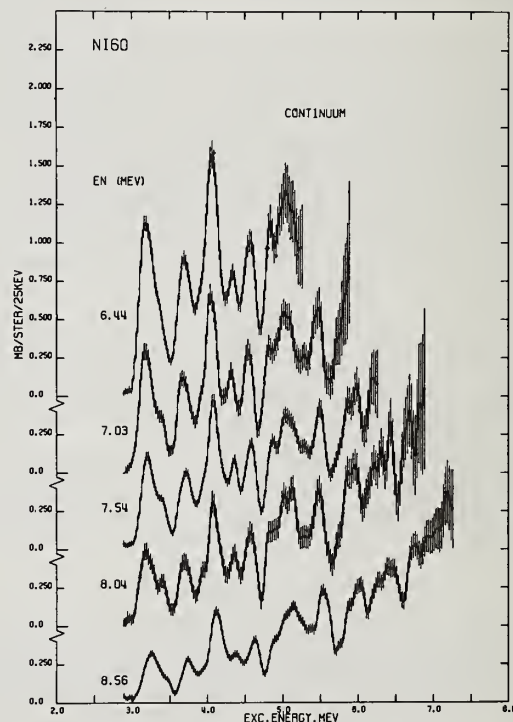


Fig. 3.  $^{60}\text{Ni}$  angle-averaged cross sections for inelastic scattering to the continuum as a function of excitation energy for incident neutron energies,  $E_N$ , from 6.44 to 8.56 MeV. The structure is typical of that found in the continua for nuclides lighter than W.



Our differential cross sections were integrated over angle by fitting anisotropic angular distributions to a Legendre series or by averaging distributions which were isotropic within experimental uncertainties. The angle-integrated data were plotted vs incident neutron energy and compared with the results of others and with then-current ENDF/B evaluations. Typical of these results is Figure 4 where  $^{52}\text{Cr}$  and natural

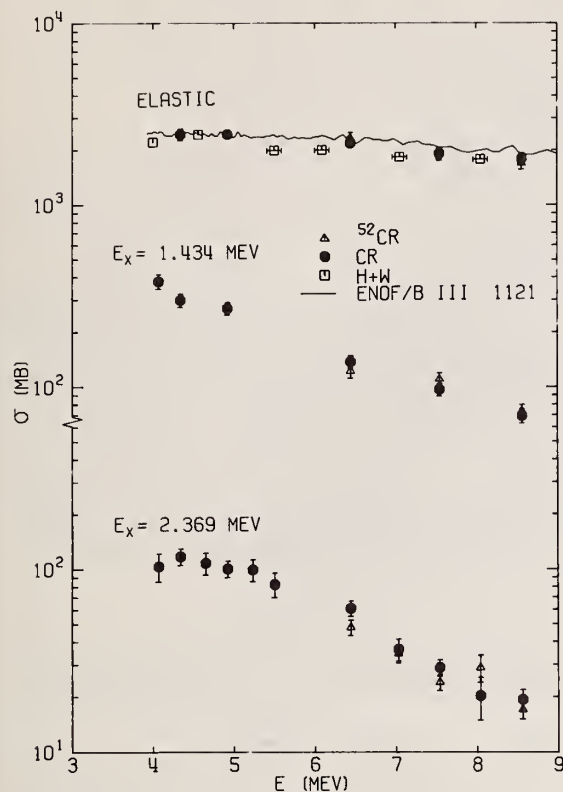


Fig. 4. Natural chromium and  $^{52}\text{Cr}$  angle-integrated elastic scattering cross sections and cross sections for inelastic scattering to levels in  $^{52}\text{Cr}$  per atom of natural chromium as a function of incident neutron energy,  $E$ . Results of Holmqvist and Wiedling (H + W)<sup>3</sup> and the ENDF/B III 1121 curve are also shown.

chromium data are compared with the results of Holmqvist and Wiedling<sup>3</sup> and with the ENDF/B III 1121 evaluation.

Our data were generally in agreement or consistent with the results of others in our opinion. We considered eight of the then-current ENDF/B evaluations to be an adequate-to-good representation of neutron elastic and inelastic scattering data in the 4–9 MeV energy range while nine were found to be deficient in some respects. All the materials for which evaluations existed have been re-evaluated.

### Summary of Results

Table I summarizes the nuclides investigated. The second column lists the maximum excitation energy for which inelastic scattering to discrete levels was extracted and also whether inelastic scattering to a continuum was included. The ORNL report number and date of publication are given in column 3. All results have been sent to the National Neutron Cross Section Center for inclusion in CSISRS.

### Acknowledgement

This program reflects the work of many. We gratefully acknowledge the contributions of J. W. McConnell, A. M. Marusak, J. A. Biggerstaff, M. V. Harlow, C. O. LeRigoleur, J. K. Dickens, P. H. Stelson, E. Hungerford, C. M. Perey, and the staff of the ORNL Van de Graaff Laboratory.

### References

1. W. E. Kinney, "Neutron Elastic and Inelastic Scattering from  $^{56}\text{Fe}$  from 4.60 to 7.55 MeV", ORNL-TM-2052, January, 1968
2. W. E. Kinney, *Nucl. Instr. and Methods*, 83, 15 (1970)
3. B. Holmqvist and T. Wiedling, "Neutron Elastic Scattering Cross Sections: Experimental Data and Optical Model Cross Section Calculations", AE-366, Aktiebolaget Atomenergi (1969)

# DIFFERENTIAL ELASTIC SCATTERING CROSS SECTIONS OF SULPHUR FOR 14.8 MEV NEUTRONS BY SURFACE OF REVOLUTION TECHNIQUE\*

A.M.Ghose, A. Chatterjee and S.Nath,  
Bose Institute,  
Calcutta-700009, India.

A new technique has been developed for the absolute measurements of differential elastic scattering cross sections of nuclei for fast neutrons. The method is based on constant angle scatterers shaped in the form of a surface of revolution around the source to detector line as axis. Inelastically scattered neutrons have been discriminated by the multiple bias technique applied to recoil proton plastic detectors. The results obtained for sulphur for 14.8 MeV neutrons will be presented.

(Differential elastic scattering cross section ; fast neutrons; scattering geometry; uniform sensitivity neutron counter)

## Introduction

In the present paper an absolute method suitable for the measurement of differential elastic scattering cross sections of fast neutrons over a wide range of energy will be presented. In this investigation emphasis has been placed on the general adaptability of the method rather than on the results obtained by using it. The two important features of the method are geometry of the experimental set up and the effectively uniformly sensitive fast neutron detector which can yet discriminate elastically scattered neutrons from inelastically scattered ones.

## Experimental Arrangement

The experimental arrangement used in the present investigation is shown in Fig.1. "14" MeV neutrons are generated by the T-d reaction at the target T. The scatterer is distributed in the shape of a surface of revolution obtained by rotating the arc of a circle passing through the centres of T and the detector D, which consists of a small spherical recoil proton plastic scintillator.

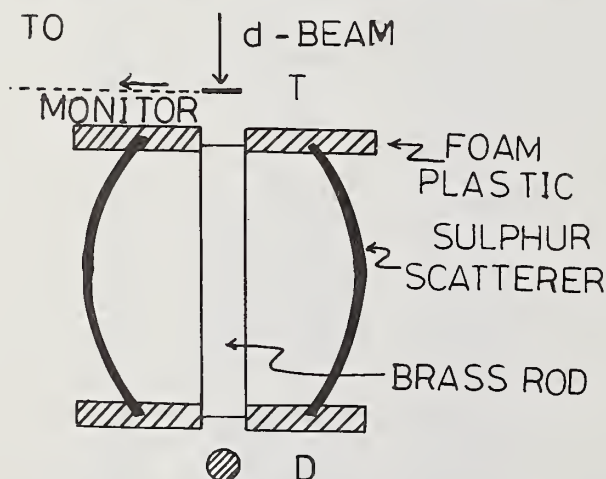


Fig. 1. Experimental Arrangement.

\*Work performed under PL-480 project supported by National Bureau of Standards, U.S.A.

The direct beam from the source to the detector is eliminated by a properly shaped beam stopper. Conventional adequately fast and stable electronics has been used. The beam was continuously monitored by a suitably biased proton recoil counter placed at right angles to the deuteron beam incident on S. Sulphur has been chosen as the target material since it is proposed to extend the investigations to develop a double scattering fast neutron polarimeter following the design discussed elsewhere<sup>1</sup>.

## Calculations

In Fig.2, the no. of neutrons emitted by the source per sec. into the elementary

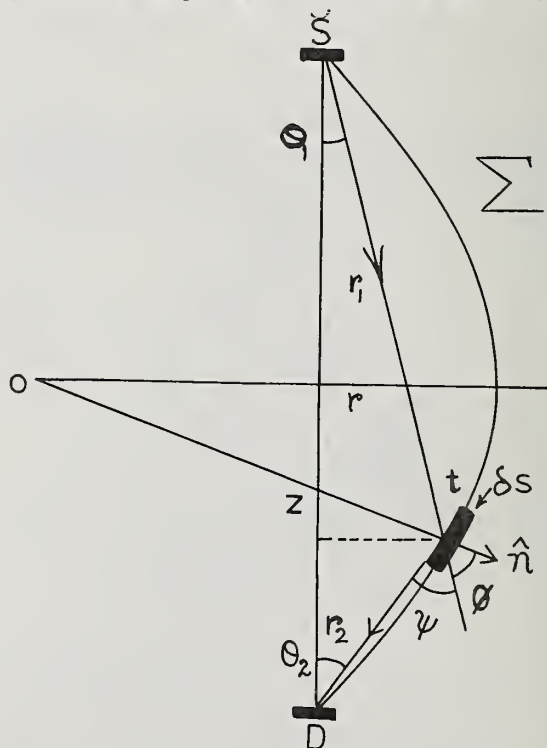


Fig.2. Scattering Geometry.

solid angle  $\delta\Omega$ , around the angle  $\theta$ , and reaching the detector sphere of radius  $a$  after being elastically scattered by an element  $\delta s$  of the scattering surface through an angle  $\psi$  is given by<sup>2</sup>

$$dN = N_0 \cdot \frac{2\pi r \delta s \cos\phi}{4\pi r^2} \cdot \frac{d\sigma_s(\psi)}{d\Omega} \cdot \frac{1}{\sigma_t} \cdot (1 - e^{-\nu t \sigma_t \sec\phi}) \quad \dots (1)$$

where  $N_0$  is the number neutrons emitted per sec. by the source,  $\nu$  is the number of scattering nuclei per c.c. of  $\Sigma$ ,  $t$  is the radial thickness of the absorber and  $\sigma_t$  and  $\frac{d\sigma_s(\psi)}{d\Omega}$  are the total and differential elastic scattering cross sections involved. Since larger superficial distribution of scatterers allows one to use small values of  $t$  without unduly sacrificing the counting rate, eqn.(1) can be readily approximated to

$$dN = \frac{\pi a^2 \nu N_0 t}{2} \cdot \frac{d\sigma_s(\psi)}{d\Omega} \cdot \sec\psi \tan^4\psi f(x, \psi) dx$$

where

$$f(x, \psi) = \frac{(1-x)(\sqrt{1+(1-x^2)\tan^2\psi} - 1)}{1+(1+x)\tan^2\psi - \sqrt{1+(1-x^2)\tan^2\psi}} \cdot \frac{1}{[1+(1-x)\tan^2\psi - \sqrt{1+(1-x^2)\tan^2\psi}]^{3/2}} \cdot \frac{1}{(\sec^2\psi - x^2 \tan^2\psi)^{1/2}} \quad \dots (2)$$

where  $x = z/l$  (Fig.2). The counting rate registered by the detector is thus

$$N = \epsilon \cdot \frac{\pi a^2 \nu N_0 t}{2^{3/2} l^2} \left( \frac{d\sigma_s(\psi)}{d\Omega} \right) \cdot \tan^4\psi \sec\psi \cdot \int_{-f}^{+f} f(x, \psi) dx$$

where the mean detection efficiency  $\epsilon$  is assumed to be independent over the spectrum of elastically scattered neutrons (including distortion caused by multiple scattering, if any and other effects) while it is zero for neutrons of significantly lower energies. The limits  $f$  of  $\int$  are kept low to avoid undesirable geometrical complications.

If the detector is exposed to the direct beam with both the stopper and the scatterer removed, the counting rate registered by D will become

$$n = \epsilon N_0 \frac{\pi a^2}{l^2} \quad \dots (3)$$

Hence

$$\frac{d\sigma_s(\psi)}{d\Omega} = \frac{N}{n} \cdot \frac{\cot^4\psi \cos\psi}{\int_{-f}^{+f} f(x, \psi) dx} \quad \dots (4)$$

Eqn.(4) enables us to calculate the differential scattering cross section from the observed ratios of counting rates and the geometry of the arrangement.

### Detection Procedure

In the derivation of the above equations we have assumed that the detector responds with uniform efficiency to elastically scattered and primary neutrons but is totally insensitive to inelastically scattered ones. Unfortunately the response of recoil proton detectors deviate far from this ideal behaviour as can be seen from Fig.3 which shows typical relative efficiency characteristics of a spherical plastic scintillator exposed

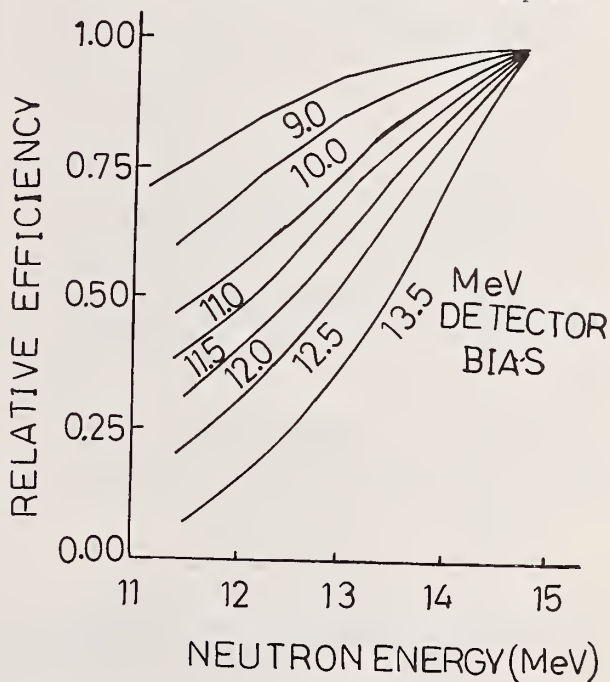


Fig.3. Relative efficiency of biased proton recoil neutron counters.

to fast neutrons. However, one can devise an effectively uniform sensitivity counter by following the procedure given below<sup>3</sup>.

The fractional deviation of the relative efficiency  $\epsilon(E, b)$  of a detector for neutrons of energy  $E$  MeV when the nominal detector bias is set at  $b$  MeV is given by

$$\delta(E, E_n, b) = 1 - \frac{\epsilon(E, b)}{\epsilon(E_n, b)} \quad \dots (4a)$$

where  $E_n$  MeV is the energy of the primary neutrons. When the bias is changed to  $b'$  MeV, the corresponding fractional deviation changes to



$$\delta'(E, E_n, b') = 1 - \frac{\epsilon(E, b')}{\epsilon(E_n, b')} \quad \dots(4b)$$

The ratio  $m$  of  $\delta$  to  $\delta'$ , the scale factor which transforms response function given in Fig.3 corresponding to bias  $b$  to that corresponding to  $b'$ , is given by

$$m(E, E_n, b, b') = 1 - \frac{\epsilon(E, b)}{\epsilon(E_n, b)} \bigg/ 1 - \frac{\epsilon(E, b')}{\epsilon(E_n, b')} \quad \dots(4c)$$

It has been shown by Chatterjee and Ghose<sup>4</sup> that the factor  $m$  is constant over a wide

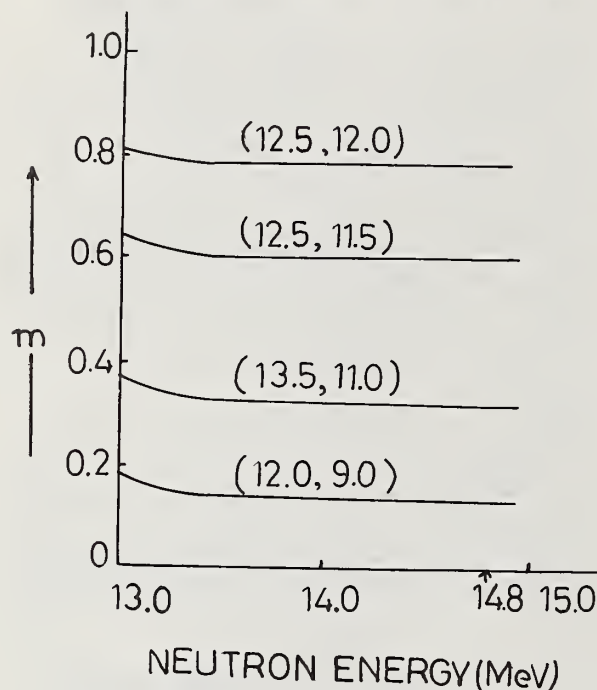


Fig.4. The scaling factor  $m$ .

range of  $E$  (Fig.4). This fact enables one to relate cross sections  $\sigma$  and  $\sigma'$  measured at biases  $b$  and  $b'$  without correction for non-uniformity, to the corrected cross section  $\sigma_0$  through the equation

$$\sigma_0 = \frac{\sigma - m\sigma'}{1 - m} \quad \dots(5)$$

Since  $m$  is independent of  $E$  over a large range of energy, application of eqn.(5) requires no knowledge whatsoever of the spectrum of the elastically scattered neutrons.

## Results and Discussion

In Fig.5 we have presented the results obtained by us as well as the experimental values measured by different workers<sup>5</sup>. It

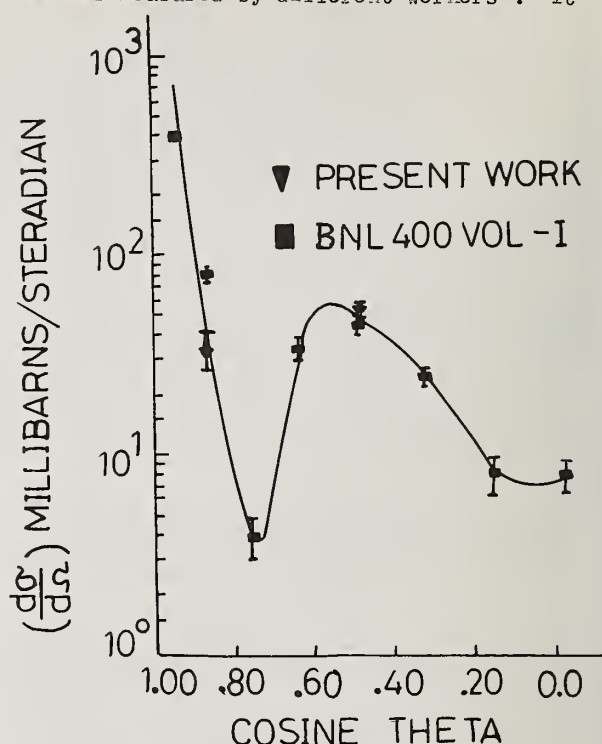


Fig.5. Differential elastic scattering cross sections of sulphur for 14.8 MeV neutrons.

would be seen that the present technique is of reasonable accuracy and since its validity is determined only by geometrical factors and accurately measured n-p scattering cross sections, it has a potential to be employed over a wide range of neutron energies.

## Acknowledgement

The authors wish to thank Prof.S.M. Sircar, Director, Bose Institute for his kind interest in this work. Thanks are due also to Mr. B.Ghosh, D.Mitra and B.Bhaskar and Miss B.Pal for their co-operation in this work. One of us (S.Nath) is acknowledging the receipt of a Fellowship from C.S.I.R., India.

## References

1. A.M. Ghose Proc. International Symp. Radiation Physics, Calcutta, 1974 (in press).
2. R.Potenza and A.Rubino Nucl. Instr. Methods 25, 77 (1963).
3. A. Chatterjee and A.M.Ghose Nucl. Instr. Methods 49, 101 (1967).
4. A. Chatterjee and A.M.Ghose Trans.Bose Res. Inst. 29, 35 (1966).
5. BNL 400 Vol.1, 3rd Edition.

DIFFERENTIAL CROSS SECTIONS FOR CARBON NEUTRON  
ELASTIC AND INELASTIC SCATTERING FROM 8.0 TO 14.5 MeV.  
G. Haouat, J. Lachkar, Y. Patin, J. Sigaud, F. Coçu  
Service de Physique Nucléaire - Centre d'Etudes de Bruyères-le-Châtel  
B.P. n° 61 - 92120 Montrouge, France.

Differential elastic and inelastic cross sections for fast neutrons scattered by carbon have been measured between 8.0 and 14.5 MeV. No other results on  $^{12}\text{C}$  seem to have been reported, at this time, between 9 and 14 MeV. A complete and consistent set of data for carbon, including total, elastic and inelastic,  $(n,\alpha)$  and  $(n,n'\alpha)$  cross sections, is now available for energies below 14.5 MeV.

(Carbon-neutron elastic and inelastic scattering- $E_n=8.0-14.5$  MeV-Angular distributions-Excitation functions)

### Introduction

A detailed knowledge of differential cross sections for fast neutrons scattered by carbon is required for engineering applications, mainly for neutron transport calculations in shielding materials.

During these last years, elastic and inelastic scattering measurements have been made, some of them below a neutron energy of  $9\text{ MeV}^{1-3}$ , the others above  $14\text{ MeV}^{4,5}$ . No experimental contribution seems to have been reported, yet, between 9 and 14 MeV. Our measurements were made for incident energies from 8.0 to 14.5 MeV. Angular distributions and excitation functions for the elastic and inelastic (1st excited level) scattering by carbon are presented and compared with the evaluated values of ENDF/B. The consistency of our data with those of total,  $(n,\alpha)$  and  $(n,n'\alpha)$  cross sections<sup>6-10</sup> has been attempted and is discussed.

### Experimental procedure

The differential cross section measurements were performed using the neutron time-of-flight facility of the Centre d'Etudes de Bruyères-le-Châtel. The experimental set-up has been extensively described in prior reports<sup>11</sup>; therefore only a few experimental details of this study will be given here.

The incident neutrons were produced from the  $\text{D(d,n)}^3\text{He}$  reaction using a deuterium gas target. A pulsed deuteron beam was provided with the tandem Van de Graaff accelerator. The monoenergetic neutron energies between 8.0 and 14.5 MeV correspond to the incident deuteron energies from 5.1 to 11.6 MeV respectively. In this range, the deuteron break-up reaction, whose threshold is 4.45 MeV, gives rise to an undesirable neutron flux having a wide energy spectrum. However, the energy difference between the monoenergetic neutrons and those coming from the break-up reaction is large enough to enable scattering measurements for the ground state and the first excited (4.439 MeV) level in  $^{12}\text{C}$ . The upper levels have excitation energies higher than 7.66 MeV; moreover the inelastic scattering leaving the residual  $^{12}\text{C}$  nucleus in these excited states contributes to the  $(n,n'\alpha)$  reaction which gives rise to continuous energy distributions of the emitted neutrons.

The sample was a cylinder of pure carbon with 25 mm diameter and 30 mm height. It was suspended 15 cm from the center of the gas cell for the runs with detection angles greater than  $20^\circ$ . For the measurements at  $10^\circ$ , the cell-to-sample distance was increased up to 24.5 cm to improve the shielding of the detectors from direct neutrons.

The scattered neutrons were detected by four detectors, each of them composed of a NE 213 liquid scintillator mounted on a fast photomultiplier (XP 1040).

The primary neutron beam was monitored by counting the number of protons produced by the  $\text{D(d,p)}\text{T}$  reaction from the target. Those protons were detected by two diodes, each at  $90^\circ$  with respect to the beam axis, through windows in the gas target holder. In

addition, an auxiliary liquid scintillator set at  $55^\circ$  to the incident beam was used. All the monitor indications were consistent within 0.3 %. The neutron flux was determined using the  $n\text{-p}$  scattering cross-section near  $0^\circ$  as a standard. It was measured with a proton recoil counter telescope having the same solid angle as that of the sample. The overall accuracy of the flux measurements was about 5 %.

The measurements were made using standard time-of-flight techniques and  $n\text{-}\gamma$  pulse shape discrimination. Flight-path lengths varied from 5 to 7 m, detector angles ranged from  $10^\circ$  to  $160^\circ$ . During the experiment, the linear pulse height from the time-to-amplitude converter was recorded simultaneously with the linear output of the photomultiplier which is proportional to the recoil-proton energy. The energy dependence of the neutron-detector efficiency was measured using the same recording method. In the data reduction process, the time-of-flight spectra were extracted off line for two neutron energy thresholds of 1.5 and 2.5 MeV respectively. The deduced cross-sections for the two thresholds were in agreement within their statistical uncertainties.

Measurements were corrected for finite sample effects (neutron flux attenuation, multiple scattering and finite angular resolution) using an analytic method<sup>12</sup>. The overall accuracy was varying between 5 and 20 %.

### Results and discussion

Differential cross sections for neutron elastic and inelastic scattering by the first excited level in  $^{12}\text{C}$  were obtained at 14 incident neutron energies between 8.0 and 14.5 MeV in steps of 0.5 MeV. These measurements confirm and complete earlier ones at 8.5, 9.0, 10.0 and 11.0 MeV neutron energies<sup>13</sup>. The incident neutron energy spread was constant over the whole range and equal approximately to 60 keV. The angular distributions were measured between  $10^\circ$  and  $160^\circ$  in steps of  $10^\circ$ . Our data, expressed in the center-of-mass system, are plotted in fig. 1 and at the neutron energies  $E_n=8.5, 9.0, 14.0$  and  $14.5$  MeV they are compared to previously reported data<sup>1-5</sup>. The overall agreement is good. The solid lines, in fig. 1, are the result of a least-squares fit to a Legendre polynomial expansion. The zero-order coefficients were used to deduce the integrated cross sections. Their variations as a function of neutron energy are given in fig. 2 and 3 with the evaluated excitation functions. For the elastic scattering, the comparison of our data with the evaluated curves shows significant disagreements by about 7 to 15 %. The recommended values seem too high at about 11.0 and 12.0 MeV and systematically low between 12.5 and 14.5 MeV. For the inelastic scattering to the first excited level in  $^{12}\text{C}$ , the disagreement is even more pronounced: relative differences by more than 50 % can be seen mainly between 9.5 and 14.0 MeV.

The integrated cross sections for neutron inelastic scattering have been compared with the gamma-ray production cross sections for the  $^{12}\text{C}(n,\gamma)$



reaction. These measurements have been made by Morgan et al.<sup>14</sup> from the threshold up to 20 MeV neutron energy, at angles of 90° and 125°. Our values are found to be in good agreement with the data of Morgan at 125° (when multiplied by 4  $\pi$ ). We may then deduce that the four-order coefficient in the Legendre polynomial expansion of the 4.43 MeV  $\gamma$ -ray angular distribution is low in the whole energy range.

The consistency of our data with those from total,  $(n,\alpha)$  and  $(n,n'3\alpha)$  cross sections<sup>6-10</sup> was attempted. It was checked by doing the sum of the partial cross sections and comparing it to the total cross section. The  $(n,\alpha)$  cross section has been measured at 14.0 and 14.1 MeV<sup>8,9</sup>. At lower energies the data have been deduced from the experimental values of the measured  $^9\text{Be}(\alpha,n)^{12}\text{C}$  cross sections using the reciprocity theorem<sup>7</sup>. Between 12.5 and 14.5 MeV only two measurements for the  $^{12}\text{C}(n,n'3\alpha)$  reaction have been reported with large uncertainties. To prevent from the lack of information below 12.5 MeV we assumed that the  $(n,n'3\alpha)$  reaction has no significant contribution to the total cross section up to 10 MeV and that between 10 and 12 MeV the cross section may be estimated from the non elastic data of Mc Gregor and Booth<sup>15</sup>. Using our measurements and these data, the sum of the partial cross sections is consistent, within the uncertainties, with the measured total cross section<sup>6</sup>.

From all these measurements we propose a complete and consistent set of data on the neutron scattering by carbon in the range from 8.0 to 14.5 MeV. These data are compared to the recent evaluated values and show significant discrepancies. Moreover it appears, in addition to the disagreements mentioned above, that the evaluated  $(n,n'3\alpha)$  cross section is, near 12 MeV, too low. Such a conclusion has been deduced from an integral experiment on carbon carried out by Cramer and Oblo<sup>16</sup>.

## References

1. F.G. Perey and W.E. Kinney, O.R.N.L. 4441 (1969)
2. D.E. Velkley, J.D. Brandenberger, D.W. Glasgow, M.T. McEllistrem, J.C. Manthuruthil and C.P. Poirier, Phys. Rev. C7 (1973) 1736
3. D.J. Garber, L.G. Strömberger, M.D. Goldberg, D.E. Cullen and V.M. May, B.N.L. Report 400. Third Ed. E.A.N.D.C. (US) 138 "U" (1970)
4. R.L. Clarke and W.G. Cross, Nucl. Phys. 53(1964)177
5. R. Bouchez, J. Duclos, P. Perrin, Nucl. Phys. 43 (1963) 628
6. S. Cierjacks, P. Forti, D. Kopsh, L. Kropp, J. Nehe and H. Ansel, E.A.N.D.C. (E) 111 "U" report (1968) (K.F.K. 1000)
7. R.B. Schwartz, R.A. Schnack and H.T. Heaton, National Bureau of Standard EANDC (US) 143 "U" (1967)164
8. D.G. Foster and D.W. Glasgow, Phys. Rev. C3 (1971) 576
9. A.W. Obst, T.B. Grandy and J.L. Weil, Phys. Rev. C5 (1972) 738
10. E.R. Graves and R.W. Davis, Phys. Rev. 97 (1955) 1205
11. H. Kitazawa and N. Yamamuro, J. Phys. Soc. Jap. 26 (1969) 600
12. L.M. Frye Jr and L. Rosen and L. Stewart, Phys. Rev. 99 (1955) 1375
13. G. Haouat, J. Lachkar, Y. Patin, J. Sigaud and F. Coçu, C.E.A. Report R-4641 (1975)
14. W.E. Kinney, Nucl. Inst. Meth. 83 (1970) 15
15. G. Haouat and F. Coçu, Neutronaya Fisika Vol. 3 (1974) 233 - CEA-CONF 2869
16. G.L. Morgan, T.A. Love, J.K. Dickens, F.G. Perey, ORNL-TM-3702 (1972)
17. M.H. Mc Gregor and R. Booth, Phys. Rev. 112 (1958) 486
18. S.N. Cramer and E.M. Oblo, ORNL TM 4494 (1974)



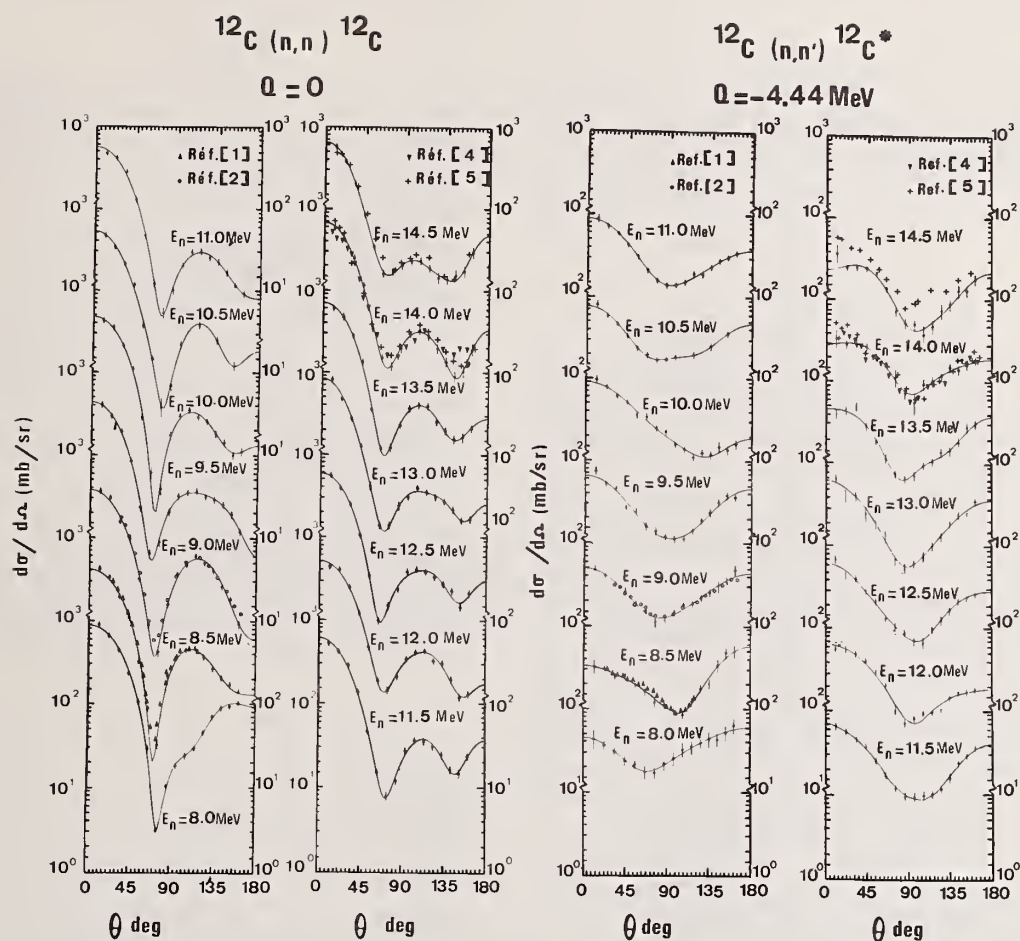


Fig. 1 : Angular distributions for elastic and inelastic (1<sup>st</sup> level) neutron scattering by carbon between 8.0 and 14.5 MeV. The solid lines are a least-squares fit of the data to a Legendre polynomial expansion.

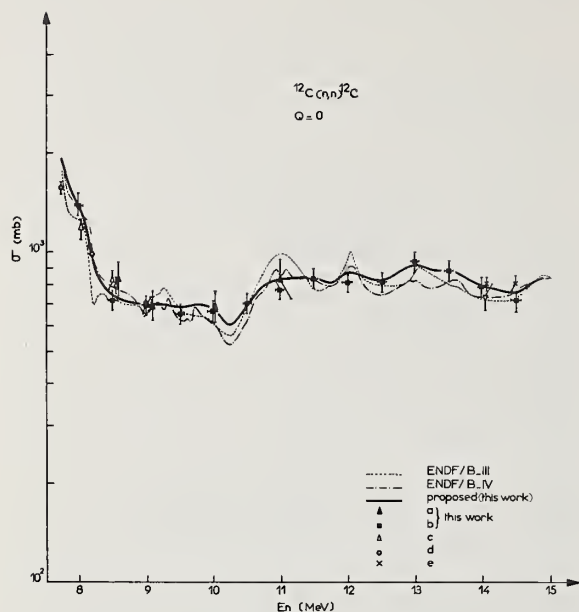


Fig. 2 : Excitation functions for neutron elastic scattering by carbon.

a : G. Haouat et al.<sup>13</sup>      d : D.E. Velkley et al.<sup>2</sup>  
 b : G. Haouat et al.<sup>11</sup>      e : R. Bouchez et al.<sup>5</sup>  
 c : W.E. Kinney et al.<sup>1</sup>

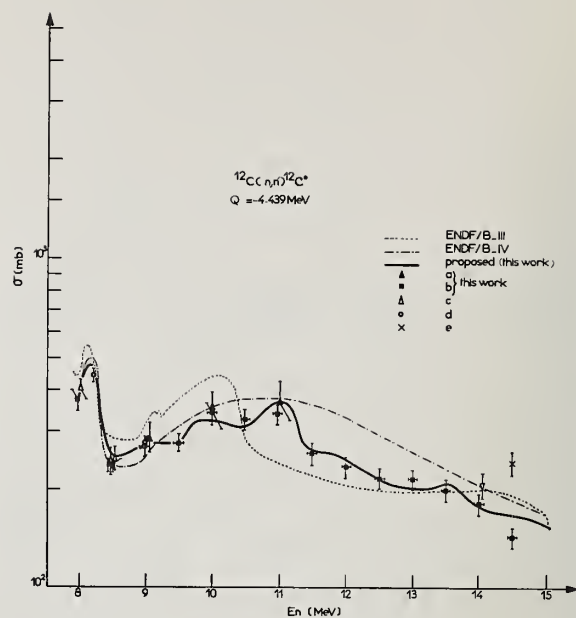


Fig. 3 : Excitation functions for neutron inelastic scattering to the first excited level (4.439 MeV) of  $^{12}\text{C}$ .

a : G. Haouat et al.<sup>13</sup>      d : D.E. Velkley et al.<sup>2</sup>  
 b : G. Haouat et al.<sup>11</sup>      e : R. Bouchez et al.<sup>5</sup>  
 c : W.E. Kinney et al.<sup>1</sup>

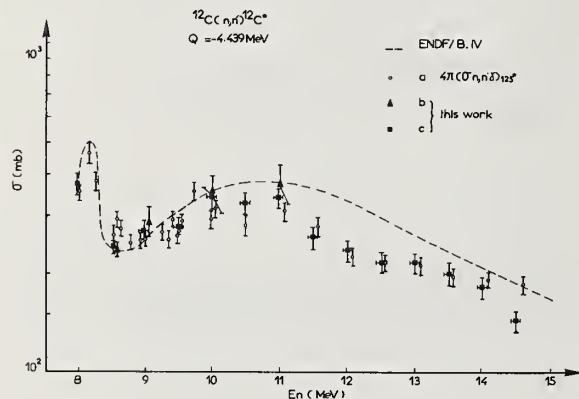


Fig. 4 : Cross sections for neutron inelastic scattering to the first excited level (4.439 MeV) of  $^{12}\text{C}$  between 8.0 and 14.5 MeV.

a :  $(n,n'\gamma)$  measurement of G.L. Morgan et al.<sup>14</sup>  
 b :  $(n,n')$  measurement of G. Haouat et al.<sup>13</sup>  
 c :  $(n,n')$  measurement of G. Haouat et al.<sup>11</sup>

J. Sigaud, Y. Patin, M.T. McEllistrem<sup>†</sup>, G. Haouat and J. Lachkar  
Service de Physique Nucléaire - Centre d'Etudes de Bruyères-le-Châtel  
B.P. n° 61 - 92120 Montrouge, France.

The energy levels and the decay schemes of  $^{76}\text{Se}$ ,  $^{78}\text{Se}$ ,  $^{80}\text{Se}$ ,  $^{82}\text{Se}$  and  $^{76}\text{Ge}$  have been studied through the measurements of  $(n,n'\gamma)$  differential cross sections. Gamma-ray excitation functions have been measured between 2.0- and 4.1-MeV incident neutron energy, and angular distributions have been observed for all of these isotopes.

( $^{76,78,80,82}\text{Se}$ ,  $^{76}\text{Ge}$  ;  $(n,n'\gamma)$  reaction ;  $E_n=2.0-4.1$  MeV ;  $E_\gamma$  ;  $\sigma(E_\gamma,0)$  ; level schemes)

### Introduction

Besides the applied interest in providing neutron data, there are several reasons for measuring the gamma ray production cross sections for even-A Se and Ge isotopes. At first, these isotopes have neutron numbers between 42 and 48, that is just below the closed shell at  $N=50$ . Then, the spectroscopy of the low lying states in even-A isotopes may give some information about their structures. Secondly, the level schemes of  $^{76}\text{Ge}$ ,  $^{76}\text{Se}$ ,  $^{78}\text{Se}$  and, in particular,  $^{80}\text{Se}$  and  $^{82}\text{Se}$  are not well known. The energy levels and their decay schemes have been investigated by coulomb excitation<sup>1</sup> and mainly by means of the  $\beta$  decay from As or Br for the Se isotopes<sup>2-5</sup> and from Ga for Ge isotope<sup>6</sup>. No previous work on these isotopes using the  $(n,n'\gamma)$  techniques seems to have been reported yet. In the present study, a lot of new information has been obtained from the analysis of the excitation functions of the gamma rays following the inelastic scattering of neutrons between 2.0 and 4.1 MeV. We have completed these results by measuring the angular distributions of the main gamma rays at 3.0-MeV incident neutron energy. More complete level schemes are then proposed for the five isotopes. These measurements supplement the neutron scattering data obtained by direct neutron detection reported elsewhere in this meeting. In this paper we present only our results for  $^{76}\text{Se}$  and  $^{82}\text{Se}$ .

### Experimental procedures and data reduction

The  $T(p,n)^3\text{He}$  reaction was used to produce the neutron beam in the 2.0- to 4.1-MeV energy range. The incident protons were accelerated by the tandem Van de Graaff accelerator of the Centre d'Etudes de Bruyères-le-Châtel. The beam was pulsed with a burst width of 1 nsec and a repetition rate of 2.5 MHz. The average current was 2  $\mu\text{A}$ .

A 3-cm long gas target with two entrance nickel foils (each, 4.4-mg/cm<sup>2</sup> thick) was used. The description of this tritium gas cell has been presented in detail in a previous report<sup>7</sup>.

Each Selenium sample was in a form of metallic powder with an isotopic enrichment greater than 90%. The container for each sample was a polyethylene can of diameter 25 mm and length 50 mm.

During a run, the sample was placed at 0° with respect to the incident proton beam and 6.65 cm from the center of the tritium cell.

The apparatus and the experimental techniques have been discussed in detail in previous reports<sup>8,9</sup>, and will be described only briefly here.

Photons following the inelastic scattering of neutrons by the sample were detected by an anti-compton spectrometer composed of a central Ge(Li) detector and a Na I (Tl) annulus. A pulsed beam time-of-flight detection mode was used to eliminate background caused by prompt neutrons striking the detector. In the present work a 100-cm<sup>3</sup> gamma ray detector was used in the gamma ray spectrometer instead of the 30-cm<sup>3</sup> and 67-cm<sup>3</sup>

detectors used previously. The flight path between the sample and the Ge(Li) detectors was 1.2 m. The time resolution of the Ge(Li) detector was 6 nsec for gamma-rays energies greater than 200 keV. The absolute value of the gamma-ray production cross sections has been given by reference to the 846.8-keV gamma-ray production cross section of  $^{56}\text{Fe}$ , reported by Dickens et al.<sup>10</sup> The overall uncertainties of the measured cross sections vary between 10 to 25 %.

### Results and discussion

Neutron-induced gamma-ray production measurements were undertaken for 11 energies in the range from 2.0 to 4.1 MeV at 55°, in steps of 0.2 MeV, the overall energy spread. These steps were small enough to remove ambiguities in the assignment of energies to the levels found in this work. No other measurements seem to have been reported yet. As an example, the excitation functions for both  $^{82}\text{Se}$  and  $^{76}\text{Se}$  and the deduced level schemes proposed for those isotopes are given respectively in tables I and II and figures 1 and 2. Detailed discussions of new assignments are beyond the scope of this paper, but new results of this study have been emphasized by an asterisk (\*) (figures 1 and 2).

The level schemes proposed for each isotope are a large extension of those deduced from the  $\beta$  decay of As or Br and of Ga. The analysis of the proposed level schemes shows that more levels are excited in the  $^{76}\text{Se}$ ,  $^{78}\text{Se}$  and  $^{80}\text{Se}$  than in the  $^{82}\text{Se}$ . This is proved by comparing the gamma-ray production cross sections for the first level at 4.1-MeV incident-neutron energy : the values for  $^{76}\text{Se}$ ,  $^{78}\text{Se}$  and  $^{80}\text{Se}$  are quite the same : about 135 mb/sr at 55° ; whereas for  $^{82}\text{Se}$  the value is 110 mb/sr at 55°.

Angular distributions of the main gamma rays were obtained for each isotope for a neutron energy of 3.0 MeV.

All of these measured cross sections are being compared to predictions of the Hauser-Feshbach formalism with width fluctuation corrections included. New results of this study will be given in subsequent papers.

### References

1. J. Barrette, M. Barrette, G. Lamoureux, S. Monaro and S. Marzika, Nucl. Phys. A235 (1974) 154.
2. D.K. McMillan and B.D. Pate, Nucl. Phys. A174 (1971) 604.  
G. Funel, C. Ythier, Compt. Rend., Ser. B ; 272 (1971) 158.
3. D.K. McMillan and B.D. Pate, Nucl. Phys. A140 (1970) 529.  
J. Lehman, N. Vanuffelen and J. Vervier, J. Physique 33 (1972) 465.  
P.F. Hinrichsen, G. Kennedy and T. Paradellis, Nucl. Phys. A212 (1973) 365.
4. D.K. McMillan and B.D. Pate, Nucl. Phys. A174 (1971) 593.

<sup>†</sup>Present address: University of Kentucky, Lexington, Ky.



5. J. Van Klinken, L.M. Taff, H.T. Dijkstra, A.H. de Haan, M. Hanson, B.K.S. Koene, J.W. Maring, J.J. Schuurman and F.B. Yano, Nucl. Phys. A157 (1970) 385.
6. D.C. Camp and B.P. Foster, Nucl. Phys. A177 (1971) 401.
7. G. Haouat and S. Seguin, Note CEA-N-1739 (1974).
8. J. Chardine, G. Haouat, C. Humeau, J. Lachkar and J. Sigaud, Rapport CEA-R-3747 (1969).
9. J. Lachkar, J. Sigaud, Y. Patin and G. Haouat, Nucl. Sci. Eng. 55 (1974) 168.
10. J.K. Dickens, G.L. Morgan and F.G. Perey, Nucl. Sci. Eng. 50 (1973) 311.

$^{82}\text{Se}$		$(d\sigma/d\Omega)_{55^\circ} \text{ (mb/sr)}$									
		$E_n \text{ (MeV)}$									
Energy	Transitions	2.5	2.7	2.9	3.1	3.3	3.5	3.7	3.9	4.1	
343.6	2894.6 $\rightarrow$ 2551.0					w	0.8 $\pm$ 0.2	1.7 $\pm$ 0.3	2.9 $\pm$ 0.6	2.2 $\pm$ 0.4	
654.8	654.8 $\rightarrow$ 0	100.6 $\pm$ 10.1	102.3 $\pm$ 10.2	110.7 $\pm$ 11.0	107.1 $\pm$ 10.7	123.3 $\pm$ 12.3	120.3 $\pm$ 12.0	111.8 $\pm$ 11.2	110.7 $\pm$ 11.1	113.3 $\pm$ 11.3	
755.7	1410.5 $\rightarrow$ 654.8	10.3 $\pm$ 1.0	10.6 $\pm$ 1.1	9.0 $\pm$ 0.9	7.7 $\pm$ 0.8	7.5 $\pm$ 0.8	6.2 $\pm$ 0.6	5.4 $\pm$ 0.6	4.3 $\pm$ 0.4	4.0 $\pm$ 0.4	
818.3 816.4	2551.0 $\rightarrow$ 1732.1 2551.0 $\rightarrow$ 1734.6		0.4 $\pm$ 0.1	3.6 $\pm$ 0.7	3.5 $\pm$ 0.7	4.9 $\pm$ 1.0	4.4 $\pm$ 0.9	4.5 $\pm$ 0.9	5.4 $\pm$ 1.0	4.3 $\pm$ 0.9	
1079.8 1077.3	1734.6 $\rightarrow$ 654.8 1732.1 $\rightarrow$ 654.8	22.7 $\pm$ 2.3	22.7 $\pm$ 2.3	25.2 $\pm$ 2.5	22.3 $\pm$ 2.2	28.2 $\pm$ 2.8	26.2 $\pm$ 2.6	24.8 $\pm$ 2.5	26.3 $\pm$ 2.6	27.8 $\pm$ 2.8	
1113.3	2847.9 $\rightarrow$ 1734.6				2.5 $\pm$ 0.5	6.0 $\pm$ 0.9	6.0 $\pm$ 0.9	5.8 $\pm$ 0.9	5.4 $\pm$ 0.8	5.1 $\pm$ 0.8	
1369.1	3101.8 $\rightarrow$ 1732.1 or 3103.7 $\rightarrow$ 1734.6					1.8 $\pm$ 0.4	2.8 $\pm$ 0.6	4.2 $\pm$ 0.8	4.6 $\pm$ 0.9	4.9 $\pm$ 1.0	
1385.4	3117.5 $\rightarrow$ 1732.1						w	0.9 $\pm$ 0.2	0.8 $\pm$ 0.2	w	
1507.0	3237.6 $\rightarrow$ 1732.1								w	0.8 $\pm$ 0.3	
1553.3	3287.9 $\rightarrow$ 1734.6						w	1.0 $\pm$ 0.3	2.2 $\pm$ 0.6	2.7 $\pm$ 0.7	
1594.6	3326.7 $\rightarrow$ 1732.1							1.4 $\pm$ 0.4	1.0 $\pm$ 0.3	1.6 $\pm$ 0.3	
1732.1	1732.1 $\rightarrow$ 0	24.2 $\pm$ 2.4	23.4 $\pm$ 2.3	25.7 $\pm$ 2.6	20.9 $\pm$ 2.1	24.8 $\pm$ 2.5	23.3 $\pm$ 2.3	21.5 $\pm$ 2.2	19.9 $\pm$ 2.0	19.7 $\pm$ 2.0	
1826.0 1827.0	3558.2 $\rightarrow$ 1732.1 3237.6 $\rightarrow$ 1410.5							w	w	2.3 $\pm$ 0.8	
1860.8	2515.6 $\rightarrow$ 654.8		1.4 $\pm$ 0.3	2.4 $\pm$ 0.5	3.4 $\pm$ 0.7	4.2 $\pm$ 0.8	4.2 $\pm$ 0.8	2.5 $\pm$ 0.5	2.6 $\pm$ 0.5	1.4 $\pm$ 0.3	
1896.3	2551.0 $\rightarrow$ 654.8		0.7 $\pm$ 0.2	3.2 $\pm$ 0.6	3.3 $\pm$ 0.7	4.8 $\pm$ 1.0	4.5 $\pm$ 0.9	5.2 $\pm$ 1.0	4.6 $\pm$ 0.9	4.5 $\pm$ 0.9	
1931.7	3558.2 $\rightarrow$ 1734.6								w	1.2 $\pm$ 0.3	
1972.1	2626.9 $\rightarrow$ 654.8		0.5 $\pm$ 0.2	5.0 $\pm$ 1.0	9.2 $\pm$ 1.4	13.1 $\pm$ 2.0	13.2 $\pm$ 2.0	9.5 $\pm$ 1.4	8.4 $\pm$ 1.3	8.1 $\pm$ 1.2	
2327.2	2981.7 $\rightarrow$ 654.8				w	1.8 $\pm$ 0.4	2.3 $\pm$ 0.5	2.3 $\pm$ 0.5	2.1 $\pm$ 0.4	2.3 $\pm$ 0.5	
2355.2	3010.2 $\rightarrow$ 654.8				w	3.9 $\pm$ 0.8	5.4 $\pm$ 1.1	5.1 $\pm$ 1.0	5.3 $\pm$ 1.0	4.2 $\pm$ 0.8	
2379.9	3034.7 $\rightarrow$ 654.8					0.7 $\pm$ 0.2	1.8 $\pm$ 0.4	1.9 $\pm$ 0.4	1.7 $\pm$ 0.3	1.9 $\pm$ 0.4	
2447.0	3101.8 $\rightarrow$ 654.8						1.3 $\pm$ 0.3	1.7 $\pm$ 0.3	1.9 $\pm$ 0.4	1.4 $\pm$ 0.3	
2462.7	3117.5 $\rightarrow$ 654.8						0.7 $\pm$ 0.2	1.1 $\pm$ 0.3	w	w	
2583.1	3237.6 $\rightarrow$ 654.8						0.8 $\pm$ 0.2	2.2 $\pm$ 0.4	3.1 $\pm$ 0.6	3.1 $\pm$ 0.6	
2672.0	3326.7 $\rightarrow$ 654.8						w	1.0 $\pm$ 0.3	2.2 $\pm$ 0.6	1.7 $\pm$ 0.4	
2688.9	3343.1 $\rightarrow$ 654.8							0.7 $\pm$ 0.2	1.0 $\pm$ 0.3	0.8 $\pm$ 0.2	
2721.0	3375.8 $\rightarrow$ 654.8							1.2 $\pm$ 0.2	2.2 $\pm$ 0.4	3.0 $\pm$ 0.6	
2743.6	3398.2 $\rightarrow$ 654.8							1.1 $\pm$ 0.2	1.2 $\pm$ 0.2	1.8 $\pm$ 0.4	
2902.8	3558.2 $\rightarrow$ 654.8							w	1.5 $\pm$ 0.4	1.3 $\pm$ 0.3	
2981.4	2981.4 $\rightarrow$ 0				w	2.0 $\pm$ 0.4	2.4 $\pm$ 0.5	2.3 $\pm$ 0.5	2.7 $\pm$ 0.5	2.6 $\pm$ 0.5	
3011	3663.3 $\rightarrow$ 654.8								w	1.8 $\pm$ 0.5	
3034.4	3034.7 $\rightarrow$ 0					2.1 $\pm$ 0.4	2.4 $\pm$ 0.5	3.2 $\pm$ 0.6	3.2 $\pm$ 0.6	2.4 $\pm$ 0.5	
3101.8 3103.7	3101.8 $\rightarrow$ 0 3103.7 $\rightarrow$ 0					0.6 $\pm$ 0.2	1.7 $\pm$ 0.3	2.1 $\pm$ 0.4	2.7 $\pm$ 0.5	3.3 $\pm$ 0.7	
3244.8	3244.8 $\rightarrow$ 0						1.3 $\pm$ 0.3	2.4 $\pm$ 0.5	2.5 $\pm$ 0.5	2.6 $\pm$ 0.5	
3342.5	3342.5 $\rightarrow$ 0						w	1.5 $\pm$ 0.3	1.8 $\pm$ 0.4	2.1 $\pm$ 0.5	
3398.2	3398.2 $\rightarrow$ 0							w	w	1.0 $\pm$ 0.3	

Table I  
Differential cross section measured at 55 deg for the main gamma transitions from the  $^{82}\text{Se}$  (n,n' $\gamma$ ) reaction. (Energies are given in keV).

$^{76}\text{Se}$		$(d\sigma/d\Omega)_{55^\circ}$ (mb/sr)											
		$E_n$ (MeV)											
Energy	Transitions	2.0	2.2	2.5	2.7	2.9	3.1	3.3	3.5	3.7	3.9	4.1	
238.8	2027.0 $\rightarrow$ 1788.5	$1.0 \pm 0.3$	$1.5 \pm 0.4$	$0.4 \pm 0.1$	$0.6 \pm 0.2$	$0.6 \pm 0.2$	$1.3 \pm 0.3$	$0.5 \pm 0.2$	$1.0 \pm 0.3$	$0.9 \pm 0.2$	w		
339	2128.1 $\rightarrow$ 1788.5			$0.9 \pm 0.2$	$1.5 \pm 0.4$	$1.7 \pm 0.4$	$1.6 \pm 0.4$	$1.4 \pm 0.4$	$1.7 \pm 0.4$	w	w	w	
472.9	1689.8 $\rightarrow$ 1216.7	$2.0 \pm 0.3$	$2.3 \pm 0.4$	$2.8 \pm 0.6$	$3.6 \pm 0.7$	$4.3 \pm 0.9$	$4.2 \pm 0.8$	$4.6 \pm 0.9$	$4.4 \pm 0.9$	$4.2 \pm 0.8$	$4.2 \pm 0.8$	$3.6 \pm 0.7$	
559.5	559.5 $\rightarrow$ 0	$128.8 \pm 12.9$	$106.2 \pm 10.6$	$99.5 \pm 10.0$	$132.5 \pm 13.3$	$165.5 \pm 16.6$	$140.8 \pm 14.1$	$139.6 \pm 14.0$	$141.9 \pm 14.2$	$143.5 \pm 14.4$	$125.6 \pm 12.6$	$130.2 \pm 13.0$	
571.7	1788.5 $\rightarrow$ 1216.7	$1.4 \pm 0.3$	$2.5 \pm 0.5$	$3.3 \pm 0.7$	$3.7 \pm 0.7$	$4.2 \pm 0.8$	$3.7 \pm 0.7$	$2.3 \pm 0.5$	$2.2 \pm 0.4$	$2.2 \pm 0.4$	$2.0 \pm 0.4$	$1.7 \pm 0.3$	
656.9	1216.7 $\rightarrow$ 559.5	$23.1 \pm 2.3$	$21.9 \pm 2.2$	$19.3 \pm 1.9$	$25.8 \pm 2.6$	$26.1 \pm 2.6$	$27.2 \pm 2.7$	$28.3 \pm 2.8$	$30.5 \pm 3.1$	$30.1 \pm 3.0$	$25.4 \pm 2.5$	$26.7 \pm 2.7$	
666.0	1788.5 $\rightarrow$ 1123.0	$1.5 \pm 0.3$	$2.6 \pm 0.5$	$2.0 \pm 0.4$	$3.7 \pm 0.7$	$3.7 \pm 0.7$	$4.1 \pm 0.8$	$4.3 \pm 0.8$	$4.9 \pm 0.9$	$4.1 \pm 0.8$	$2.6 \pm 0.5$	$2.1 \pm 0.4$	
726.8	2515.3 $\rightarrow$ 1788.5				$1.4 \pm 0.2$	$2.4 \pm 0.4$	$3.3 \pm 0.5$	$3.7 \pm 0.6$	$3.7 \pm 0.6$	$2.3 \pm 0.3$	$3.3 \pm 0.5$	$2.2 \pm 0.3$	
772.1	1331.6 $\rightarrow$ 559.5	$8.7 \pm 0.9$	$9.5 \pm 1.0$	$9.5 \pm 1.0$	$13.2 \pm 1.3$	$14.4 \pm 1.4$	$15.6 \pm 1.6$	$17.6 \pm 1.8$	$18.5 \pm 1.9$	$19.6 \pm 2.0$	$19.4 \pm 1.9$	$20.2 \pm 2.0$	
798.0	2487.4 $\rightarrow$ 1689.8					w	$1.2 \pm 0.3$	$1.1 \pm 0.3$	$1.1 \pm 0.3$			w	
810.5	2027.0 $\rightarrow$ 1216.7		$1.1 \pm 0.2$	$2.2 \pm 0.3$	$3.2 \pm 0.5$	$3.5 \pm 0.5$	$3.7 \pm 0.6$	$3.0 \pm 0.5$	$3.0 \pm 0.5$	$3.3 \pm 0.5$	$3.9 \pm 0.6$	$3.6 \pm 0.5$	
930.9	2620 $\rightarrow$ 1689.8				w	w	$0.5 \pm 0.2$	$0.8 \pm 0.3$	w	w	w	$1.4 \pm 0.4$	
954.7	2171.2 $\rightarrow$ 1216.7				$0.6 \pm 0.2$	w	w	w					
1130.5	1689.8 $\rightarrow$ 559.5	$5.0 \pm 0.5$	$6.6 \pm 0.7$	$6.8 \pm 0.7$	$9.9 \pm 1.0$	$10.5 \pm 1.1$	$10.3 \pm 1.0$	$11.2 \pm 1.1$	$11.9 \pm 1.2$	$12.6 \pm 1.3$	$11.0 \pm 1.1$	$10.4 \pm 1.0$	
1155.6	2487.4 $\rightarrow$ 1331.6				$0.5 \pm 0.1$	$1.1 \pm 0.2$	$1.6 \pm 0.3$	$1.8 \pm 0.3$	$1.3 \pm 0.3$	$1.2 \pm 0.2$	$1.0 \pm 0.2$		
1216.9	1216.7 $\rightarrow$ 0	$12.2 \pm 1.2$	$13.1 \pm 1.3$	$10.3 \pm 1.0$	$17.3 \pm 1.7$	$19.8 \pm 2.0$	$20.7 \pm 2.1$	$22.0 \pm 2.2$	$22.0 \pm 2.2$	$22.7 \pm 2.3$	$22.2 \pm 2.2$	$21.5 \pm 2.2$	
1229.6	1788.5 $\rightarrow$ 559.5	$3.8 \pm 0.5$	$7.2 \pm 0.7$	$6.6 \pm 0.7$	$10.4 \pm 1.0$	$11.0 \pm 1.1$	$10.3 \pm 1.0$	$9.4 \pm 0.9$	$9.2 \pm 0.9$	$8.7 \pm 0.9$	$7.2 \pm 0.8$	$6.9 \pm 0.8$	
1270	2487.4 $\rightarrow$ 1216.7				w	w	$0.7 \pm 0.2$	w			$1.1 \pm 0.3$		
1287.7	2620 $\rightarrow$ 1331.6					w	$1.2 \pm 0.3$	w	$2.9 \pm 0.6$	$2.5 \pm 0.5$	$3.2 \pm 0.6$	$2.0 \pm 0.4$	
1440.1	2657.0 $\rightarrow$ 1216.7					$0.4 \pm 0.1$	$0.9 \pm 0.2$	$0.8 \pm 0.2$	$0.4 \pm 0.1$	w	$1.0 \pm 0.3$	w	
1454.2	2671.0 $\rightarrow$ 1216.7					w	$1.0 \pm 0.3$	$0.8 \pm 0.2$	$1.1 \pm 0.3$	$0.9 \pm 0.2$	$0.8 \pm 0.2$	$0.9 \pm 0.2$	
1473.9	2805 $\rightarrow$ 1331.6						$1.2 \pm 0.2$	$1.7 \pm 0.3$	$1.5 \pm 0.3$	$2.0 \pm 0.4$	$2.3 \pm 0.5$	$1.9 \pm 0.4$	
1531.3	2654 $\rightarrow$ 1123					w	$0.7 \pm 0.2$	$0.6 \pm 0.2$	$0.7 \pm 0.2$	$1.5 \pm 0.4$	$1.3 \pm 0.4$	$1.1 \pm 0.3$	
1568.8	2128.1 $\rightarrow$ 559.5	$0.4 \pm 0.1$	$2.7 \pm 0.5$	$4.7 \pm 1.2$	$4.9 \pm 1.2$	$4.3 \pm 1.1$	$3.6 \pm 0.9$	$3.7 \pm 0.9$	$3.3 \pm 0.8$	$2.6 \pm 0.7$	$2.6 \pm 0.7$	$2.6 \pm 0.7$	
1588	2805 $\rightarrow$ 1216.7					w	w	$1.6 \pm 0.4$	$1.3 \pm 0.3$	$1.2 \pm 0.3$	$1.1 \pm 0.3$	$1.1 \pm 0.3$	
1600.1	2817.0 $\rightarrow$ 1216.7					$0.5 \pm 0.2$	$2.3 \pm 0.7$	$4.0 \pm 1.2$	$3.5 \pm 1.1$	$3.1 \pm 0.9$	$2.3 \pm 0.7$	$2.7 \pm 0.8$	
1611.7	2171.2 $\rightarrow$ 559.5		$1.4 \pm 0.3$	$2.5 \pm 0.5$	$2.8 \pm 0.6$	$2.9 \pm 0.6$	$2.5 \pm 0.5$	$2.2 \pm 0.4$	$1.5 \pm 0.3$	$1.1 \pm 0.2$	$0.8 \pm 0.2$		
1653.3	2870.2 $\rightarrow$ 1216.7							$1.2 \pm 0.5$	$0.9 \pm 0.3$	$0.7 \pm 0.2$	w	w	
1788.3	1788.5 $\rightarrow$ 0	$1.1 \pm 0.2$	$1.8 \pm 0.3$	$1.6 \pm 0.3$	$2.5 \pm 0.5$	$2.8 \pm 0.4$	$2.6 \pm 0.5$	$2.6 \pm 0.5$	$2.0 \pm 0.4$	$2.4 \pm 0.5$	$1.9 \pm 0.4$	$2.5 \pm 0.5$	
1956.3	2515.3 $\rightarrow$ 559.5				$0.9 \pm 0.2$	$1.8 \pm 0.4$	$2.1 \pm 0.4$	$2.3 \pm 0.5$	$2.4 \pm 0.5$	$2.6 \pm 0.5$	$2.3 \pm 0.5$	$2.4 \pm 0.5$	
2046.6	2606.1 $\rightarrow$ 559.5				$0.3 \pm 0.1$	$1.2 \pm 0.3$	$1.5 \pm 0.4$	$1.5 \pm 0.4$	$1.0 \pm 0.3$	$1.7 \pm 0.4$	$1.0 \pm 0.3$	$1.5 \pm 0.4$	
2097.7	2657.0 $\rightarrow$ 559.5					$1.3 \pm 0.3$	$1.8 \pm 0.4$	$2.0 \pm 0.4$	$1.9 \pm 0.4$	$2.1 \pm 0.4$	$1.7 \pm 0.3$	$1.5 \pm 0.3$	
2111.7	2671.0 $\rightarrow$ 559.5					$1.3 \pm 0.2$	$2.4 \pm 0.4$	$2.2 \pm 0.3$	$3.0 \pm 0.5$	$3.1 \pm 0.5$	$3.0 \pm 0.5$	$3.1 \pm 0.5$	
2128.1	2128.1 $\rightarrow$ 0			$0.4 \pm 0.1$	$1.9 \pm 0.5$	$0.9 \pm 0.2$	$1.1 \pm 0.3$	$0.8 \pm 0.2$	$0.5 \pm 0.1$	$1.2 \pm 0.3$	$0.9 \pm 0.2$	$0.8 \pm 0.2$	
2258.0	2817.0 $\rightarrow$ 559.5					w	$1.0 \pm 0.2$	$1.2 \pm 0.2$	$1.6 \pm 0.3$	$1.8 \pm 0.4$	$1.6 \pm 0.3$	$2.5 \pm 0.5$	
2310.9	2870.2 $\rightarrow$ 559.5						$1.0 \pm 0.2$	$1.8 \pm 0.4$	$1.8 \pm 0.4$	$1.6 \pm 0.3$	$1.8 \pm 0.4$	$1.3 \pm 0.3$	
2392.0	2951.3 $\rightarrow$ 559.5					w	$0.4 \pm 0.1$	$0.8 \pm 0.2$	$0.8 \pm 0.2$	$1.3 \pm 0.3$	$1.3 \pm 0.3$	$0.9 \pm 0.2$	
2450.5	3010.0 $\rightarrow$ 559.5						w	$1.2 \pm 0.2$	$1.9 \pm 0.4$	$1.7 \pm 0.3$	$1.9 \pm 0.4$	$2.1 \pm 0.4$	
2525.3	3084.5 $\rightarrow$ 559.5							$1.0 \pm 0.2$	$1.5 \pm 0.3$	$2.0 \pm 0.4$	$2.1 \pm 0.4$	$2.1 \pm 0.4$	
2547.0	3106.5 $\rightarrow$ 559.5							$0.5 \pm 0.1$	$0.8 \pm 0.2$	$1.1 \pm 0.3$	$1.0 \pm 0.3$	$1.1 \pm 0.3$	
2654	2654 $\rightarrow$ 0							w	$1.6 \pm 0.3$	$3.0 \pm 0.6$	$3.4 \pm 0.7$	$2.8 \pm 0.6$	
2656.8	2657.0 $\rightarrow$ 0												
2738.2	3297.7 $\rightarrow$ 559.5									w	$1.3 \pm 0.4$	$0.9 \pm 0.3$	
2794.7	3354.2 $\rightarrow$ 559.5									w	$1.0 \pm 0.3$	$0.7 \pm 0.2$	
2905.6	3465.2 $\rightarrow$ 559.5									w	$1.4 \pm 0.3$	$1.7 \pm 0.4$	
2951.0	2951.3 $\rightarrow$ 0						$0.4 \pm 0.1$	$0.9 \pm 0.3$	$1.5 \pm 0.4$	$2.0 \pm 0.5$	$1.7 \pm 0.4$	$1.7 \pm 0.4$	
3098.3	3657.8 $\rightarrow$ 559.5										w	$1.2 \pm 0.3$	
3530.0	3530.0 $\rightarrow$ 0										w	$0.9 \pm 0.3$	

Table II

Differential cross section measured at 55 deg for the main gamma transitions from the  $^{76}\text{Se}$  (n,n' $\gamma$ ) reaction. (Energies are given in keV).

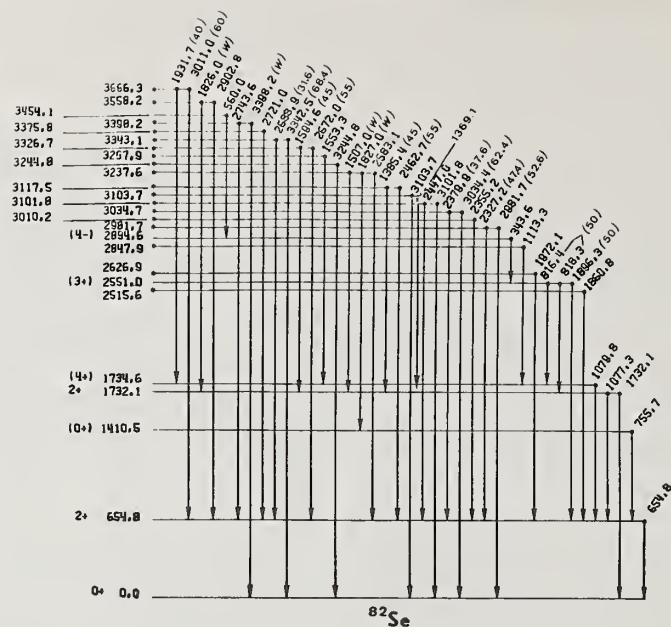
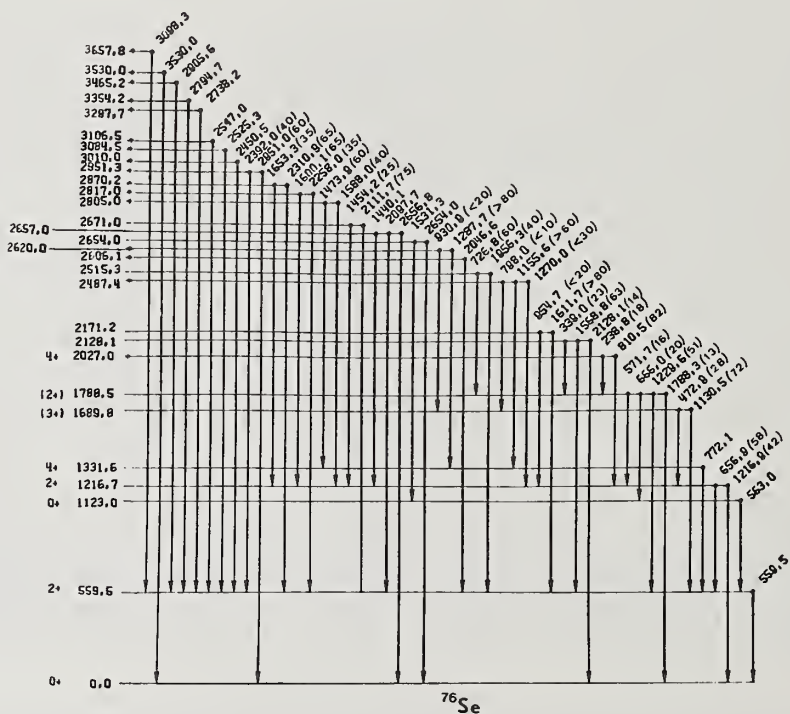


Figure 1. Proposed level scheme of  $^{82}\text{Se}$ . The levels noted with an asterisk have least one characteristic determined from these measurements.





Differential cross sections for neutron elastic and inelastic scattering from  $^{76}\text{Se}$ ,  $^{78}\text{Se}$ ,  $^{80}\text{Se}$  and  $^{82}\text{Se}$ , have been measured at 8-MeV incident neutron energy and from  $^{76}\text{Se}$  and  $^{82}\text{Se}$  at 6- and 10-MeV incident energies. The differences observed in the elastic scattering cross sections are interpretable as the effects of isospin term in the scattering potentials. A full analysis of the elastic scattering data are presented.

(Nuclear Reactions  $^{76,78,80,82}\text{Se}(n,n)$ ,  $(n,n')$ ,  $E=6-10$  MeV ; measured  $\sigma(\theta)$  ; deduced optical-model parameters ; Enriched targets).

### Introduction

In recent years, a large quantity of accurate elastic scattering data for protons on medium to heavy nuclei have been collected. They have been used to deduce various sets of proton-nucleus optical model parameters<sup>1,2</sup>. For neutrons, elastic scattering data are less numerous and accurate than for protons. Also, most of the measurements have been made at low neutron energies where the compound elastic contribution cannot be neglected. In addition to this lack of data, many features of the optical model seem to be still unclear for neutrons, namely the energy and the isospin dependence of the parameters<sup>2</sup>. In order to improve the understanding of neutron-nucleus scattering we have undertaken the study of elastic and inelastic scattering of neutrons from the enriched isotopes  $^{76}\text{Se}$ ,  $^{78}\text{Se}$ ,  $^{80}\text{Se}$ ,  $^{82}\text{Se}$  over the neutron-energy range 6 to 10 MeV.

There are several reasons why a study of these Se isotopes is of particular interest. Firstly, for the four separated Se isotopes, the isospin dependence of the optical model parameters can be investigated over a relatively large range of the  $N-Z$  asymmetry term

(0.105-0.184). Secondly, these isotopes have neutron numbers between 42 and 48, that is just below the closed shell at  $N = 50$ . In this mass region, Lane et al.<sup>3</sup> have pointed out that some shell effects may induce a strong decrease in the magnitude of the imaginary part of the optical potential. Finally, this element is in a region of spherical nuclei where the deformation effects are low and therefore where the optical model gives a good description of the shape elastic scattering.

### Experimental procedure

Differential cross section measurements were performed using the neutron time-of-flight facility of the Centre d'Etudes de Bruyères-le-Châtel. The experimental set-up is extensively described elsewhere<sup>4</sup> and therefore only a brief description will be given here.

The  $D(d,n)^3\text{He}$  reaction was used to produce the incident neutrons at 8-MeV energy and at 6- and 10- MeV energies, the incident neutrons were produced from the  $T(p,n)^3\text{He}$  reaction. Deuterons or protons were accelerated by the tandem Van de Graaff accelerator. The beam was pulsed and bunched so that 1 ns bursts at a frequency of 2.5 MHz were available. The average beam currents were approximately  $3\ \mu\text{A}$  both for deuterons and for protons.

The samples were powders of metallic isotopically enriched Se isotopes, weighing about 50 g each, on loan from U.S.S.R. They were contained in polyethylene cans of diameter 25 mm and height 50 mm. The cell-to-sample distance was about 12 cm.

Scattered neutrons were detected independently by four detectors. Each of them was composed of a NE213 liquid scintillator, 12.7 cm in diam by 5 cm thick, mounted on a fast photomultiplier (XP1040). Each detec-

<sup>a</sup> Present address: University of Kentucky, Lexington, Ky.

tor was housed in a heavy shield of polyethylene and lead behind a 1.5 m-long collimator of paraffin loaded with lithium and boron. Four 70 cm-long iron shadow bars with tungsten tips reduced the background caused by direct neutrons coming from the target. To prevent from gamma events, we employed pulse-shape discrimination. The flight-path length was 8 m for the three incident neutron energies. The measurements were made using standard time-of-flight techniques. In the data reduction process, the time-of-flight spectra were sorted off line for neutron-energy thresholds of 1.5 MeV at 6- and 8-MeV neutron energies and of 2.5 MeV at 10- MeV energy.

The energy dependence of the neutron-detector efficiency was measured by two independent methods. In the first one, we counted directly monoenergetic neutrons from the target produced by the  $D(d,n)^3\text{He}$  reaction. In the second one, a  $(n-p)$  scattering experiment was performed using a polyethylene sample (1 cm-diam. by 4 cm-height).

An auxiliary liquid scintillator with  $n-\gamma$  discrimination was used, with the time-of-flight method, for monitoring the primary neutron beam. The neutron flux was measured with a proton recoil counter telescope, placed at  $0^\circ$ , which had the same solid angle as that of the sample.

The measurements were corrected for finite sample effects using both an analytic method and a monte-carlo method ; the corrected values were consistent within 3 per cent. The overall accuracy of the measurements ranged from 5 to 20 %.

### Results and discussion

Differential cross sections for neutron elastic and inelastic scattering from  $^{76}\text{Se}$ ,  $^{78}\text{Se}$ ,  $^{80}\text{Se}$  and  $^{82}\text{Se}$  were measured at 8-MeV incident neutron energy and from  $^{76}\text{Se}$  and  $^{82}\text{Se}$  at 6- and 10- MeV incident energies. Measurements were completed over the angular range from  $20^\circ$  to  $150^\circ$  at 16 to 24 angles in either  $5^\circ$  or  $10^\circ$  steps, with  $5^\circ$  steps taken at the minima of the cross section curves. Incident neutron-energy spreads were between 180 keV at 6- and 10- MeV neutron energies and 300 keV at 8 MeV. They were small enough to ensure good separation at the first excited level but large enough to allow energy-averaged measurements. The elastic scattering data at 6, 8, and 10 MeV are shown in figs.1,2,3 respectively. It is seen that, at each of these energies, the large angle scattering increases with the neutron number of the isotope. On the other hand, the inelastic cross sections to the first  $2^+$  levels (not shown here) were observed to be exactly the same for  $^{76}\text{Se}$  and  $^{82}\text{Se}$  at 6- MeV incident energy and very similar for all four isotopes at 8 MeV. The observed likeness of the inelastic scattering to the first excited levels in all the isotopes may reflect the fact that the four isotopes have similar deformabilities. Since this effect was observed at 6- and 8- MeV energies, we may assume that channel coupling has a very small contribution to the elastic and inelastic scattering.

The pronounced differences observed in the elastic scattering cross sections are then directly interpretable as the effect of isospin term in the scattering potentials. These effects have been studied, here, by  $\chi^2$  fitting of the optical model parameters to the shape elastic angular distributions. For this purpose, we have subtracted from the differential cross sections the compound elastic contribution. This last contribution has been calculated on the basis of the  $(n,n'\gamma)$  reaction studies for selenium isotopes reported elsewhere in these proceedings.

In the analysis of the optical model parameters, we have adopted fixed shapes of the potentials and placed some constraints upon the parameters. The real potential was assumed to be of the Saxon-Woods shape, and the imaginary and the spin-orbit potentials are taken to be of the Saxon-Woods derivative shapes. Moreover, we have chosen to fix values for the geometrical parameters as follows :

$$\text{Radii : } R = R_S = R_{I_S} = R_0 A^{1/3} \text{ fm.} \quad R_0 = 1.25 \text{ fm.}$$

$$\text{Diffusiveness : } a = a_{I_S} = 0.67 \text{ fm.}$$

The adopted value for the radii is that which is the most frequently used<sup>1</sup>. On the other hand, Holmqvist and Wiedling<sup>5</sup> have shown that the real diffusiveness parameter is essentially mass independent and equal to  $0.66 \pm 0.01$  fm. With this fixed geometry we avoided some correlated ambiguities, such as the well-known  $VR^n$  one ( $V$  being the real potential depth).

The imaginary diffusiveness  $a_S$  was not kept constant. Previous systematic studies of fast neutron elastic scattering have yielded many very different values for  $a_S$  ranging from 0.44 to 0.67.<sup>1,2,3,5-8</sup>

Theoretical considerations predict energy and isospin dependence for both the real and imaginary potentials. The first dependence is a consequence of the non-locality of the nuclear forces<sup>9</sup>. The second is based on the expectation that the optical potential contains an isovector term leading to a dependence on symmetry number  $\frac{N-Z}{A}$ .<sup>10</sup>

The neutron real and imaginary potentials were assumed to be of the form :

$$V = V_0 - \alpha E - \frac{N-Z}{A} V_1$$

$$W_S = W_0 - \alpha_S E - \frac{N-Z}{A} W_1$$

where  $E$  is the incident laboratory neutron energy  $V_0, \alpha, V_1, W_0, \alpha_S$  and  $W_1$  constants to be determined. The spin-orbit potential depth was supposed real and without any dependence.

The optical-model code SPI was used to fit, with search routine, the experimental data. Optimum parameters were obtained by performing series of subsearches on groups of less than six parameters. The main features revealed in the present analysis are as follows :

- The strength of the real potential  $V_0$  was determined to an accuracy of less than 1 MeV; its value : 49.0 is consistent with those obtained for adjacent nuclei and the same value of  $R$ .

- A linear variation of the real potential with the neutron energy  $E$  was assumed. In most cases the  $\alpha$  coefficient has been kept fix and equal to the common value of 0.32. When this parameter was let free, good overall fits to the data were obtained for  $\alpha$  from 0.25 to 0.34. The value of 0.32 has been adopted.

- The real part of the isospin potential  $V_1$  was found equal to  $9.3 \pm 1.8$  MeV. This value is considerably lower than those obtained by Becchetti and Greenlees<sup>2</sup> (24 MeV), and Dukarevich et al.<sup>7</sup> ( $17 \pm 2$  MeV) but consistent within the uncertainties with that reported by Holmqvist and Wiedling<sup>5</sup> ( $13 \pm 6$  MeV).

- The completeness of the experimental data

mainly at backward angles has allowed an accurate determination of the spin-orbit potential strength. The deduced value,  $6.0 \pm 1.5$  MeV, is very close to that reported by Becchetti and Greenlees<sup>2</sup> (6.2 MeV) although the values of  $R_{I_S}$  are different in the two sets of optical-model parameters.

- For  $a_S$  varying from 0.44 to 0.67 fm, we have deduced the optimized values for  $W_0$  and  $W_1$  along with the corresponding  $\chi^2$  values. The results are presented in fig. 4. The other parameters have been either kept fixed or found nearly constant. The quality of the fit to the data is almost the same for  $a_S$  between 0.49 and 0.67 fm. In this range,  $W_0$  varies with  $a_S$  so that  $W_0 a_S$  is nearly constant. Moreover, in the whole range for  $a_S$ , the ratio  $W_1/W_0$  remains approximately constant and equal to about 3.2. The deduced values for  $W_0$  are in good agreement with those previously reported particularly with that of ref.<sup>2</sup> ( $W_0 = 13$  MeV with  $a_S = 0.58$  fm). The physical meaning of these features will be discussed in the conclusion.

- No evidence for any definite energy dependence of the absorption potential  $W$  has been found ( $\alpha_S = 0$ ). The fitting procedures indicated either a constancy of  $W$  with  $E$  as it was previously proposed by Rosen et al.<sup>11</sup> or a slight increase of  $W$  with  $E$  qualitatively consistent with that used by Mani et al.<sup>12</sup>.

In the adjustment procedures no imaginary volume potential was used at 6- and 8- MeV neutron energies; good overall fits to the data were obtained for volume absorption potential strength of 0.95 MeV for 10-MeV data.

### Conclusion

All the optical-model parameters deduced from this study are consistent with those from previous systematic studies except for one of them, the isospin dependent imaginary potential  $W_1$ . In conjunction with an absorption roughly proportional to the product  $W_0 a_S$ , we have deduced the constancy of the ratio  $\frac{W_1}{W_0}$  over a large range for  $a_S$ . This constant (3.2) is anomalously high in comparison to that reported by Becchetti and Greenlees<sup>2</sup> (0.92) or by Dukarevich et al.<sup>7</sup> (1.8). This disagreement may be apparent and due to the neutron numbers of the Se isotopes which are close to the magic number  $N=50$ . It may be argued, as it was expected by Lane et al.<sup>3</sup>, that  $W$  has not only a smooth dependence on  $N$  and  $Z$  but also a strong decrease near magic numbers. This hypothesis has been previously established by two experiments for the doubly closed shells at  $A = 40$  and  $A = 208$ . Holmqvist and Wiedling<sup>5</sup> have reported that the magnitude of  $W$  for Ca, found in their study, deviates from the linear dependence of  $W$  versus  $\frac{N-Z}{A}$  as they observed for other elements. On the other hand, Vonach et al.<sup>13</sup> have presented some evidence for a minimum in  $W$  near the doubly closed shell at  $A = 208$ . We may then conclude that the large deduced value of  $W_1$ , inducing a low value of  $W$ , reflects the influence of the neutron shell closure at  $N = 50$  on neutron optical-model absorption.

### References

1. C.M.Perey and F.G.Perey, Nucl. Data Tables **10** (1972) 539
2. F.D. Becchetti and G.W. Greenlees, Phys. Rev. **182** (1969) 1190
3. A.M. Lane, J.E. Lynn, E. Melkonian and E.R. Rae, Phys. Rev. Lett. **2** (1959) 424
4. G. Haouat, J. Lachkar, J. Sigaud, Y. Patin, F. Coçu, CEA-Report R-4641 (1975)
5. B. Holmqvist and T. Wiedling, Nucl. Phys. **A188** (1972) 24



6. D. Wilmore and P.E. Hodgson, Nucl. Phys. 55 (1964) 673
7. Yu. V. Dukarevich, A.N. Dyumin and D.M. Kaminker, Nucl. Phys. A92 (1967) 433
8. C.M. Newstead, J. Delaroche, B. Cauvin, Proc. Conf. Int. on Statistical Properties of Nuclei, Albany (1971) 367
9. F.G. Perey and B. Buck, Nucl. Phys. 32 (1962) 353
10. A.M. Lane, Rev. Mod. Phys. 29 (1957) 193 and Nucl. Phys. 35 (1962) 676
11. L. Rosen, J.G. Beery, A.S. Goldhaber and E.H. Auerbach, Ann. Phys. 34 (1966) 96
12. G.S. Mani, M.A. Melkanoff, I. Iori, CEA Report R-2380 (1963)
13. W.G. Vonach, A.B. Smith and P.A. Moldauer, Phys. Lett. 11 (1964) 331

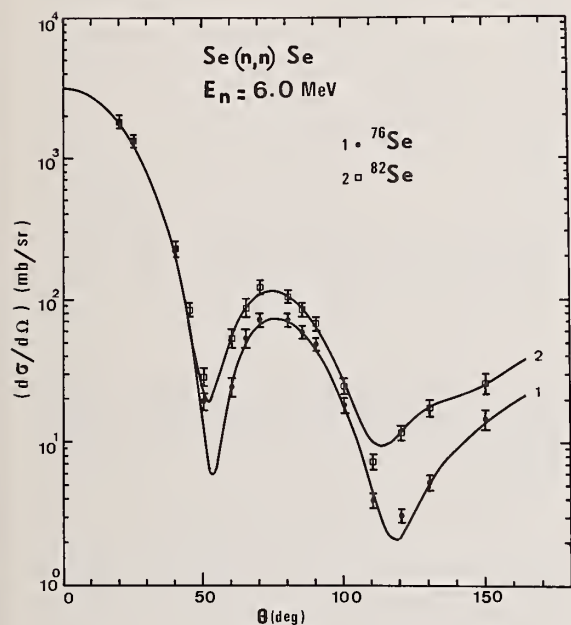


Fig. 1

Elastic scattering angular distributions at 6.0-MeV incident neutron energy for  $^{76}\text{Se}$  and  $^{82}\text{Se}$ . The solid lines are the results of optical model calculations as described in the text.

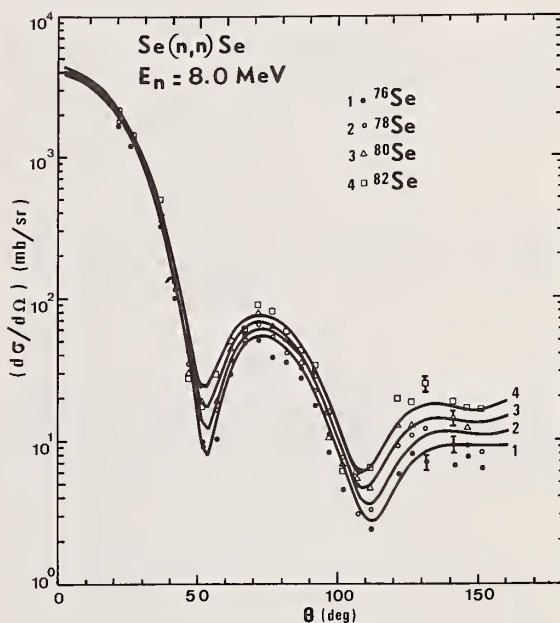


Fig. 2

Elastic scattering angular distributions at 8.0-MeV incident neutron energy for  $^{76}\text{Se}$ ,  $^{78}\text{Se}$ ,  $^{80}\text{Se}$  and  $^{82}\text{Se}$ . The solid lines are the results of optical model calculations as described in the text.



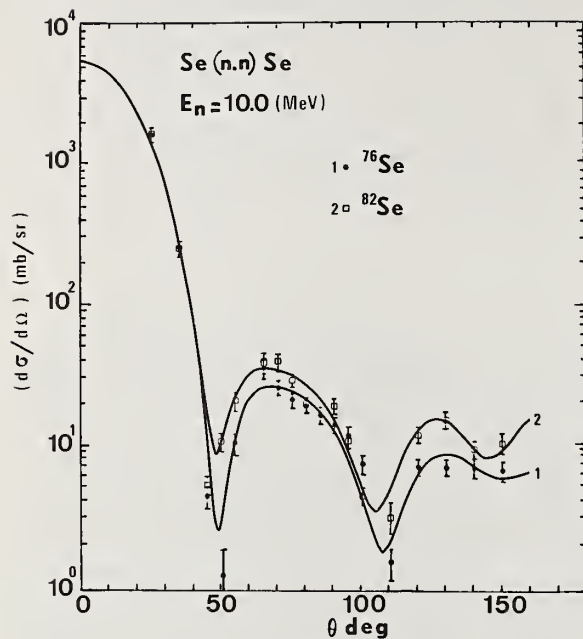


Fig. 3  
Elastic scattering angular distributions at 10.0-MeV incident neutron energy for  $^{76}\text{Se}$  and  $^{82}\text{Se}$ . The solid lines are the results of optical model calculations as described in the text.

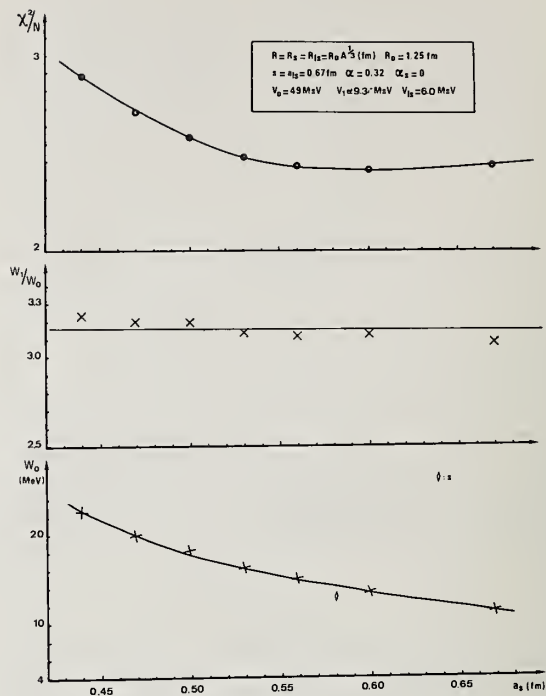


Fig. 4  
Variation with the imaginary diffusiveness  $a_s$  of the imaginary potential  $W_0$ , the ratio  $W_1/W_0$  and the corresponding  $\chi^2/N$  values.

FAST NEUTRON CAPTURE AND ACTIVATION CROSS SECTIONS  
W. P. Poenitz  
Argonne National Laboratory  
9700 South Cass Avenue, Argonne, Illinois 60439, U.S.A.

Fast neutron capture cross sections were measured in the energy interval from 0.02 to 0.7 MeV using white source neutron time-of-flight techniques and from 0.3 to 3.0 MeV using monoenergetic neutrons. Target materials were Co, Ni, Zn, Cu, Nb, Ho, Ta, Au and  $^{238}\text{U}$ . A 1300 l liquid scintillator was used as a capture  $\gamma$ -ray detector. Flat efficiency neutron detectors and/or the standard capture cross section of Au were used for the neutron flux determination. Fast neutron capture and activation cross sections were calculated in terms of the statistical model. The Hauser-Feshbach formalism and a gamma cascade model previously described<sup>1</sup> were used.

(Fast neutron capture, Co, Ni, Cu, Zn, Nb, Ho, Ta, Au,  $^{238}\text{U}$ , theory and experiment).

### Introduction

Fast neutron capture and activation cross sections are of considerable interest to fission and fusion reactor evaluators in connection with neutron absorption losses,  $\gamma$ -ray production and after-heat problems. These important applications have led to a large number of measurements, applying a variety of experimental techniques. In the present measurements, a large liquid scintillator<sup>2</sup> was used for the detection of the prompt capture  $\gamma$ -rays. The neutron flux was measured with a Grey Neutron Detector<sup>3</sup> and most of the cross section values were normalized with the standard capture cross section of Au. Measurements for elemental samples of Co, Ni, Zn, Cu, Nb, Ho, Ta, Au and  $^{238}\text{U}$  were carried out in various energy ranges depending on the specific interest in a material.

The basic formalism for the theoretical calculation of fast neutron capture cross sections in terms of the statistical model was developed more than two decades ago<sup>4-5</sup>. This formalism was applied in many systematic calculations of capture cross sections<sup>6-10</sup>. The agreement between different theoretical results and between theoretical and experimental values was not always satisfactory. Discrepancies up to a factor of 2 were found<sup>8-10</sup>. Other theoretical calculations resulted in a relatively good description of the experimental values<sup>7-10</sup>. There are many publications dealing with the calculation of activation cross sections at thermal neutron energy, however, only a few concerning the calculation of fast neutron activation cross sections<sup>11-13</sup>. In view of the difficulties to measure most of the important activation and capture cross sections of fission product nuclei, further study of fast neutron activation and capture cross sections appears desirable.

### Experimental Techniques

The  $^7\text{Li}(p,n)^7\text{Be}$  reaction was utilized as a neutron source. A pulsed and bunched proton beam was accelerated by the Argonne Tandem-Dynamitron. The repetition rates were 0.5, 1 or 2 MHz and the pulse width was 1-2 nsec. The targets consisted of metallic lithium with thicknesses between 0.04 and 0.1 MeV for the production of "monoenergetic" neutrons and about 0.5 MeV for white-spectrum measurements. A 4 $\pi$  neutron shield surrounding the source was used in order to reduce the  $\gamma$ -ray and neutron background of the detectors. A conical opening in the shield provided a collimated neutron beam.

The capture  $\gamma$ -ray detector was a 1300-liter iron tank filled with a liquid scintillator. The scintillation light was viewed by twelve AVP 57 multipliers. The time resolution of the detector was 3-4 nsec and the  $\gamma$ -energy resolution was 26 per-

cent for  $^{60}\text{Co}$  (FWHM). The threshold for the detection of  $\gamma$ -rays was set in the range 0.8-3.0 MeV in order to eliminate the detection of  $(n,n'\gamma)$  and  $(n,\gamma n')$  processes. The tank was shielded by 10-20 cm of lead, 60 cm of concrete and partially by 2-4 cm of low-background iron.

The samples consisted of metallic discs with a diameter of 8.9 cm. With exception of the Ho sample, which contained 2 percent Er, all samples were at least 99.5 percent pure. The samples were placed in the flight-path 2.5 m from the source. This was sufficient to separate by time-of-flight the low-energy neutron group of the source reaction up to 2.5 MeV primary neutron energy.

The Grey Neutron Detector<sup>3</sup> was used as a neutron monitor for measurements with monoenergetic neutrons. However, some absolute values for the capture cross section of Au were obtained by using the Black Neutron Detector<sup>14</sup>. A 1 mm-thick lithium glass detector was used as a neutron flux monitor in the white spectra measurements.

The data were recorded with an on-line computer system. The time-of-flight spectra from the capture  $\gamma$ -ray detector and from the Li-glass detector were recorded as well as the energy spectrum coincident with the neutron peak in the time-of-flight channel. A corresponding energy spectrum coincident with an equally spaced interval adjacent to the neutron peak was utilized for background subtraction.

Corrections were applied for the capture of neutrons scattered elastically or inelastically within the sample, the efficiencies for the capture and the neutron detector, scattering of neutrons in air, and the neutron flux attenuation in the samples. The dominant uncertainty is due to the extrapolation of the capture  $\gamma$ -ray energy spectra to zero pulse height. This uncertainty limits the accuracy of the present measurements to 7 percent at best.

In the case of some low energy resonance cross section measurements of Ni, only an average correction was applied for the capture of scattered neutrons. The statistics and background contribute in this case appreciably to the uncertainty of the data.

### Experimental Results

#### Low Energy Measurements for Ni and $^{238}\text{U}$

The capture cross sections of Ni and  $^{238}\text{U}$  are of interest as structural and as fertile materials in reactor design. These cross sections were measured in the lower keV range relative to the capture cross section of Au using a white spectra neutron source. The data are shown in Figs. 1 and 2. The  $^{238}\text{U}$  data were averaged over 4, 10 and 20 keV intervals, eliminating most of the structure which exists in both the  $^{238}\text{U}$  capture and the Au

reference cross sections. The Ni capture cross section has many very narrow resonances and hence the widths observed in the measurements are given by the experimental resolution. In order to improve the statistics of the results the data were further averaged with a resolution of about 3 nsec/m.

#### Intermediate Energy Range

The white spectra measurements on Ni revealed some structure at several hundred keV. Thus, the white spectra measurements were extended to the 0.35-0.75 MeV range. Neighboring elements were included in these measurements. Fig. 3 shows the data obtained for Co, Ni, Cu and Zn. Ni shows a very pronounced structure with fluctuations exceeding 30 percent above 0.5 MeV. Also shown in this figure are data for the total cross section of Co and Ni. These data were obtained from an evaluated data file<sup>15</sup> and averaged with the same resolution as those for the capture cross section. The structure obtained for the capture cross sections is very similar to that of the total cross sections, however, differences in the amplitudes at some energies are apparent.

#### MeV Energy Range

Measurements with monoenergetic neutrons were

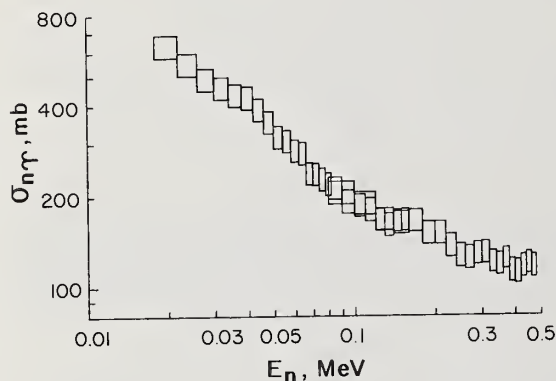


Fig. 1. Capture Cross Section of  $^{238}\text{U}$ .

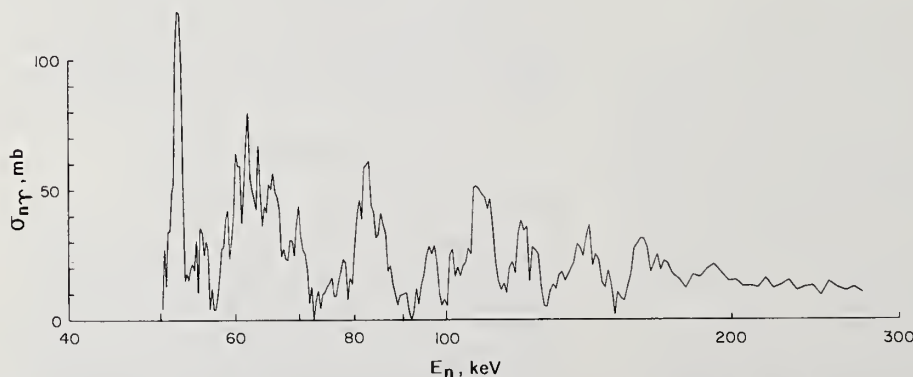


Fig. 2. Capture Cross Section of Ni obtained with white neutron source measurements.

carried out between 0.3 and 3.0 MeV for Ni, Cu, Zn, Nb, Mo, Ta, Au, and  $^{238}\text{U}$ . The results are shown in Fig. 4. The size of the symbols shows the uncertainty of the measurement. All values were normalized at 0.5 MeV to a capture cross section of 138 mb for Au which was obtained in an evaluation of a consistent set of data for several standard cross sections<sup>16</sup>.

#### Model Calculations

In the energy range of the present measurements, the statistical theory should apply and the neutron capture or activation cross section were derived from

$$\sigma_1(E) = \frac{1}{2(2I+1)} \frac{\pi}{k^2} \sum_{l=0}^{\infty} \sum_{j=|l-\frac{1}{2}|}^{l+\frac{1}{2}} T_n(lj, E) \cdot \frac{\sum_{j=|j-I|}^{j+I} (2J+1) T_c(J, E) \cdot R \cdot B_i(J, E)}{T_Y(J, E) + \sum_n T_n(l', j', E, E_m)}.$$

The sum in the denominator is over all neutron exit channels.  $R$  is a correction for replacing the average over the ratios in above formula with the ratio of the averages.  $T_c$  and  $T_n$  are given by  $2\pi\langle\Gamma\rangle/\langle D \rangle$  where a difference is made between the total radiation width  $\langle\Gamma\rangle$  and the capture width  $\langle\Gamma\rangle$ . The  $B_i(J, E)$  are the probabilities for the occupation of a low lying level by the  $\gamma$ -cascades. Thus, if  $i$  denotes an isomeric state,  $\sigma_i$  is the appropriate activation cross section. The total capture cross section is obtained for setting all  $B_i=1$ . All other notations in above formula are as commonly used.

Following the experimental situation and a previously used model<sup>1</sup>, both the target and the compound nucleus are assumed to consist of discrete low lying levels with known spin energy and parity and at higher energies of a level continuum described by a level density formula. The fermi-gas model with modifications for shell and pairing energy was used in the present calculations.

Partial  $\gamma$ -radiation widths obtained from the single-particle model by Weisskopf<sup>17</sup> were commonly used in the calculation of total radiation widths and  $\gamma$ -cascade behavior. However, Axel<sup>18</sup>, derived a different expression for the  $\gamma$ -width from the inverse cross section,  $\sigma_Y$ , thus suggesting the giant resonance energy dependence for the partial widths.



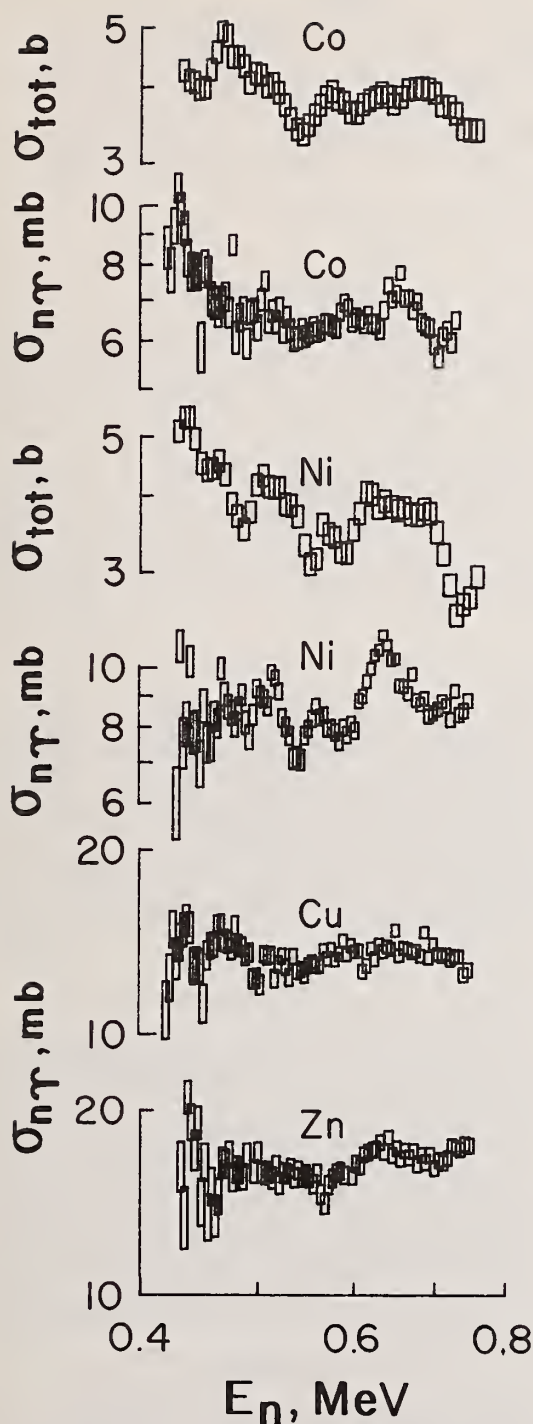


Fig. 3. Total and Capture Cross Sections of Co, Ni, Cu and Zn.

The neutron transmission coefficients for the discrete levels were calculated with the optical model code ABACUS<sup>19</sup>. Neutron transmission coefficients to levels in the continuum of the target nucleus were calculated with the assumption of a completely absorbing nucleus.

Gamma and capture transmission coefficients were calculated by summing over all transitions to discrete levels and integrating over the level density in the continuum. Weisskopf, Axel and Pigmy resonance transitions were used optionally.

The calculation of the low level occupation probabilities was carried out with a  $\gamma$ -cascade model previously described<sup>1</sup>. However, the Axel and Pigmy resonance transition probabilities were included as an option to the single-particle transition probabilities.

Model calculations are discussed here for the capture and activation of <sup>181</sup>Ta. Ta is of specific interest as a test example for the present calculations because the daughter nucleus, <sup>182</sup>Ta, has an isomeric state with a high spin value (10<sup>-</sup>) and thus a very small activation cross section for this isomeric state. Experimental values for the activation cross section exist up to 1.6 MeV<sup>20</sup>.

Capture cross sections are very insensitive to the neutron transmission coefficients. As a result, the difference between spherical model and deformed model calculations result in negligible differences for Ta<sup>9</sup>. Brzosko et al.<sup>21</sup> calculated  $\gamma$ -ray spectra and fast neutron capture cross sections for a number of elements including Ta using the Axel transition probabilities. They suggested that Ta requires a Pigmy resonance contribution as well as all the other considered elements, though the  $\gamma$ -ray spectrum does not show the anomalous bump in the 5-6 MeV range.

Fig. 5 shows the results from the present calculations in comparison with the present experimental results for the capture cross section and the measurements by Cox<sup>20</sup> for the isomeric state. All curves labeled with A are for parameters in the level density formulas and transition probabilities applicable to a wide range of nuclei. The only normalization used is the value for  $\langle \Gamma \rangle / \langle D \rangle$  which was obtained from experimental values in the eV-energy range<sup>22</sup>. The improvement obtained for the capture cross section by using Axel instead of Weisskopf is similar as recently reported by Gardner<sup>23</sup>, however, the difference between the inclusion or exclusion of 1 percent Pigmy resonance is much smaller than obtained by Brzosko et al.<sup>21</sup>. The most satisfactory result of the present calculations is the good agreement obtained for the isomeric cross section which is about two orders of magnitude smaller than the capture cross section. Inclusion of quadrupole radiation in the  $\gamma$ -ray cascades changes the isomeric cross section very little, however, increasing the spin cut-off factor in the level density formula to a value desirable for a deformed nucleus<sup>24</sup> improves the agreement for the capture cross section but increases the isomeric cross section excessively.

#### Conclusions

Experimental measurements of fast neutron capture cross sections on stable nuclei provide a basis for the calculation of capture and activation cross sections. The agreement obtained for calculated cross sections gives confidence in calculations for unstable isotopes which are difficult to measure. An example is <sup>94</sup>Nb in which results were recently reported<sup>13</sup>.

Acknowledgment. This work was supported by the U.S. Energy Research and Development Agency.

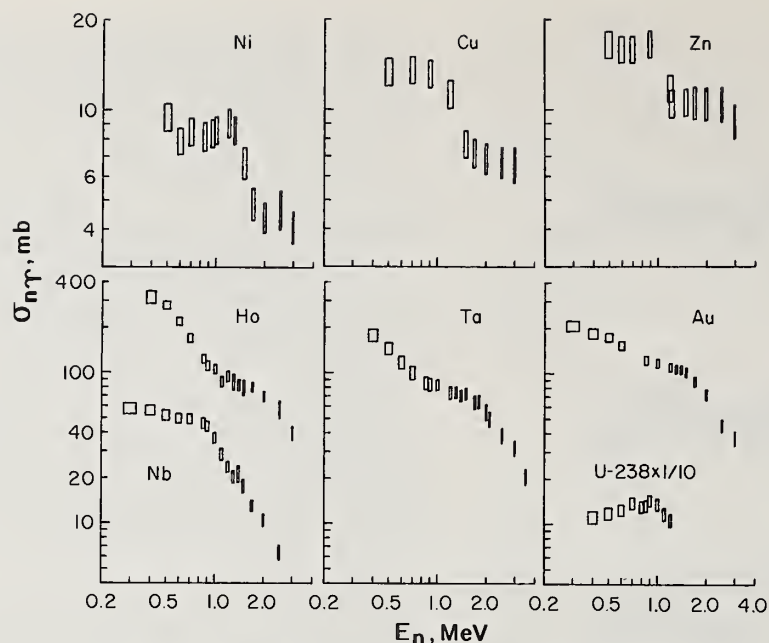


Fig. 4. Results obtained with monoenergetic neutrons.

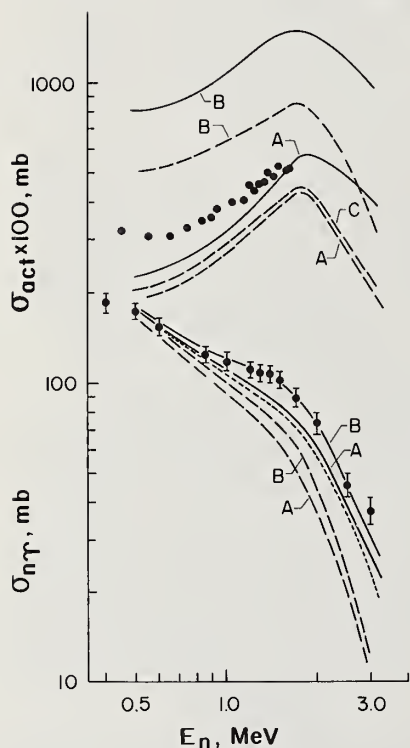


Fig. 5. Comparison of experimental values and theoretical calculations. All solid curves were obtained with Axel and 1 percent Pigmy resonance transitions, the dotted curve is for Axel only, and all dashed curves are for Weisskopf. Curves labeled B assume larger spin cut-off factors, curve C includes 2 percent quadrupole transition.

#### References

1. W. P. Poenitz, *Z. f. Physik* **197**, 262 (1966).
2. F. Reines et al., *Rev. Sci. Instr.* **25**, 1061 (1954).
3. W. P. Poenitz, *Nucl. Instr. Methods* **58**, 39 (1968).
4. B. Margolis, *Phys. Rev.* **88**, 327 (1952).
5. A. M. Lane, J. E. Lynn, *Proc. Phys. Soc.* **A70**, 557 (1957).
6. V. Benzi and M. V. Bortolani, *Conf. on Nucl. Data*, Vol. I, 537, IAEA (1967).
7. V. Benzi et al., *Comitato Nazionale Energia Nucleare*, RT/ I(69)44 (1969).
8. J. L. Cook, *Conf. on Nucl. Data*, Vol. I, 549, IAEA (1967).
9. M. P. Fricke et al., *Conf. on Nucl. Data*, Vol. II, 281, IAEA (1970).
10. F. Schmittroth, *hanford Eng. Dev. Lab.*, ENDF-195 (1973).
11. J. Csikai et al., *Nucl. Phys.* **41**, 316 (1963).
12. H. A. Grench et al., *Nucl. Phys.* **A94**, 157 (1966).
13. W. P. Poenitz, *Argonne National Laboratory*, ANL/NDM-8 (1974).
14. W. P. Poenitz, *Nucl. Instr. Methods* **109**, 413 (1973).
15. A. B. Smith, *Argonne National Laboratory*, ANL/NDM-1 and priv. com. (1974).
16. W. P. Poenitz, *Conf. on Neutron Standards*, USAEC CONF-701002 (1970).
17. J. M. Blatt, V. F. Weisskopf, *Theoretical Nuclear Physics*, John Wiley & Sons, N.Y. (1952).
18. P. Axel, *Phys. Rev.* **126**, 671 (1962).
19. E. H. Auerbach, *Brookhaven National Laboratory*, BNL-765 (1962).
20. S. A. Cox, *Phys. Rev.* **133**, B378 (1964).
21. J. S. Brzosko et al., *Can. J. Physics* **47**, 2849 (1969).
22. S. F. Mughabghab, D. I. Garber, *Brookhaven National Laboratory*, BNL-325, 3rd Ed. (1973).
23. D. G. Gardner, *Bull. Am. Phys. Soc.*, Vol. 19, No. 9, 1017 (1974).



# FISSION PRODUCT CAPTURE CROSS SECTIONS IN THE KEV REGION\*

R. W. Hockenbury, H. R. Knox<sup>†</sup> and N. N. Kaushal<sup>††</sup>

Rensselaer Polytechnic Institute

Troy, N. Y. 12181

Capture cross section measurements have been made on  $^{105}\text{Pd}$ ,  $^{151,153}\text{Eu}$  and  $^{103}\text{Rh}$  from 20 eV to 200 keV. Capture data in the resolved resonance region are combined with our own transmission data to obtain a consistent capture normalization. For these experiments, the statistical uncertainty of the normalization is  $\pm 4\%$  for  $^{151}\text{Eu}$ ,  $^{153}\text{Eu}$  and  $^{105}\text{Pd}$ , and  $\pm 8\%$  for  $^{103}\text{Rh}$ . The statistical uncertainty of the keV capture cross section point data is about  $\pm 4\%$ . The information derived from these measurements is the measured keV capture cross section and the average s and p wave parameters  $\bar{\Gamma}_\gamma$ ,  $S^0$  and  $S^1$ .

(Capture cross sections; average  $\bar{\Gamma}_\gamma$ ,  $D$ ,  $S^0$  and  $S^1$ .)

## Introduction

The significance of fission products in the LMFBR is determined by the product of their keV capture cross section and abundance.<sup>1</sup> The most significant isotope on this basis is  $^{105}\text{Pd}$ . The fifth isotope on such a list is  $^{103}\text{Rh}$ . The isotopes  $^{151}\text{Eu}$  and  $^{153}\text{Eu}$  are considered as possible control materials because of their relatively high keV capture cross section and the fact that their use avoids the production of  $^4\text{He}$  as in the case of  $^{10}\text{B}$  control material. The capture cross sections of these four isotopes have been measured from 6 to 200 keV.

## Samples

The  $^{105}\text{Pd}$  sample was a metallic powder weighing 5.787 grams with an isotopic purity of 94.5 atom % and a thickness of 0.00213 atoms/barn. The  $^{103}\text{Rh}$  sample was a foil of 0.00204 atoms/barn thickness. The  $^{151,153}\text{Eu}$  samples were oxide powders of 96.8 and 98.8 atom % purity and with thicknesses of 0.00199 and 0.00206 atoms/barn respectively. The samples were sealed in thin Al cells and a blank Al cell was used for correction for capture in the Al.

## Experiment

Capture measurements were made on the four isotopes from 20 eV to about 200 keV. A 1.25m liquid scintillator was used at a 25.6m flight path. The RPI LINAC was run at 500 pps and 0.100  $\mu\text{sec}$ . pulse width. Neutron flux and transmission measurements were made using a conventional  $^{10}\text{B}$ -NaI detector at 28.3m. Resonance filters of S, Al, Na and Co were left in the beam at all times to determine the time-dependent background. Because of their high thermal capture cross sections (especially  $^{151}\text{Eu}$ ), special  $^{10}\text{B}$  liners were used to prevent thermalized neutrons from scattering back into the samples.

## Analysis

The capture and flux data were reduced to relative capture cross sections by conventional methods correcting for deadtime, background, relative efficiency of the flux detector and capture in the Al cell. Contributions due to impurity isotopes were either performed or found to be negligible, depending on the

sample. The capture cross section at energy  $E_i$ , in time-of-flight channel  $i$  is generally written as:

$$\sigma_c(E_i) = \frac{N_\gamma(E_i)}{\omega\phi(E_i)N} \quad (1)$$

where:

$N_\gamma(E_i)$  = net capture events in channel  $i$   
 $N$  = atoms/barn of the isotope  
 $\omega\phi(E_i)$  = product of detector efficiency and absolute flux (in neutrons/channel) at  $E_i$

For these samples, the self-shielding correction was equal to or less than 2%. Since the capture cross sections are relatively large for these four isotopes, statistically good data can be acquired and the absolute normalization thus takes on a more significant part in the overall precision.

## Normalization

Capture data can be normalized in several ways: (1) saturated resonances where the resonance peak counting rate at  $E_0$  is equal to the product  $\omega\phi(E_0)$ , (2) cross calibration to another sample (ratio measurement) and (3) normalization to transmission data of selected resonances with  $\Gamma_n \ll \bar{\Gamma}_\gamma$ . The third method has been fully described<sup>2</sup> and has several advantages over the first two methods. Since both capture and transmission experiments are performed in the same laboratory, a more consistent measurement results. This consistency extends to that between the resolved resonance data and the keV region as well as between capture and total cross section results in the resonance region alone. This has the advantage then of helping to tie the average s-wave parameters ( $\bar{\Gamma}_\gamma, S^0$ ) to the keV capture cross section and of determining limits on the p-wave parameters ( $\bar{\Gamma}_\gamma, S^1$ ). The basic statistical accuracy of the normalization is controlled by that of the transmission data since the corresponding capture data have a statistical uncertainty less than one per cent.

Briefly, resonances in both the capture and transmission data with  $g\Gamma_n \ll \bar{\Gamma}_\gamma$  are selected. For thin samples, the transmission



data give  $g\Gamma_n$  directly using the Harvey-Atta code.<sup>3</sup> The capture area,  $A_\gamma$ , for the same resonance is then calculated using a Monte Carlo code<sup>4</sup> and an assumed radiation width. Since  $g\Gamma_n \ll \Gamma_\gamma$ , the calculated area is insensitive to the assumed radiation width. Then the calculated capture area is used in the following manner to determine  $\mu\phi(E_0)$ :

$$\int N_\gamma(E_i) dE = \mu\phi(E_i) \int N_c E_i dE \quad (2)$$

$$\int N_\gamma(E_i) dE = \mu\phi(E_i) A_\gamma \quad (3)$$

$$\text{and} \quad \mu\phi(E_0) = \frac{\sum_i N_\gamma(E_i) \Delta E_i}{A_\gamma} \quad (4)$$

where

$A_\gamma$  = calculated capture area

$\sum_i$  = sum over the resonance

$\Delta E_i$  = energy increment in channel  $i$

Table 1 lists each resonance and  $g\Gamma_n$  used in the absolute normalization.

The principal contribution to the uncertainty in absolute normalization is due to the uncertainty in  $g\Gamma_n$  from the transmission data. These values are given in a later section for each isotope.

#### KeV Data

The statistical precision of the keV results is composed of the relative flux  $\pm 2\%$ , the capture data (averaged to  $\pm 3\%$ ), and possible systematic errors ( $\pm 5\%$ ).

#### Results

The capture cross sections are shown in Figures 1-4 after averaging over various energy groups. Also shown in each figure are the average capture cross sections as calculated by Lane and Lynn's formalism.<sup>5</sup> The s and p wave contributions are shown in order to illustrate their relative importance for each isotope in this energy region. The d wave contribution is very small in this region and also less well known than the others. The first step in the calculations consisted of using a set of average parameters ( $\Gamma_\gamma, D, R, S^0$  and  $S^1$ ) from an evaluation. Then depending on the comparison of this calculated result to the experimental result, the second and third steps were to vary the appropriate individual parameters necessary to improve the fit. For example, below 50 keV, if  $\Gamma_\gamma \gg \Gamma_n$ , and if the s-wave part dominates, the s-wave strength function should be varied. None of the calculated results are claimed to be completely adequate representations of the experimental data. In fact, the principal point to be made here is that the various average parameters found by the authors were generally inadequate and emphasize the fact that there is presently no substitute for experimental data.

The standard deviation of the averaged

data in the keV region is about  $\pm 4\%$  for all the measurements, not including possible systematics. The individual isotopes are briefly discussed in the following sections.

For  $^{105}\text{Pd}$  the estimated uncertainty in absolute normalization is  $\pm 4\%$ . The average parameters shown in Figure 1 give a calculated capture cross section which lies slightly below the data. Increasing  $S^0$  and  $S^1$  would improve the fit. The p-wave contribution is most important above about 20 keV thus enhancing the sensitivity to  $\Gamma_\gamma$  and  $S^1$ .

The standard deviation of the absolute normalization of  $^{151}\text{Eu}$  is  $\pm 2\%$  again mostly due to the uncertainty in  $g\Gamma_n$ . The calculated capture cross section in Fig. 2 is slightly low below 20 keV and high above 40 keV. The p-wave part is small below 20 keV and becomes significant above that energy thus the calculation is more sensitive to  $\Gamma_\gamma$  and  $S^0$ . The data of Czirr<sup>6</sup> are in good agreement with our results in the overlap range 7-12 keV.

The comments pertaining to  $^{151}\text{Eu}$  on uncertainty also apply to  $^{153}\text{Eu}$ . The relative importance of the p-wave part of the capture cross section is similar to that for  $^{151}\text{Eu}$ . Comparison of Fig. 2 and 3 shows that the  $^{151}\text{Eu}$  cross section is significantly greater than that of  $^{153}\text{Eu}$ .

The  $\pm 8\%$  uncertainty in absolute normalization of  $^{103}\text{Rh}$  is the largest of the four isotopes. However, there is excellent agreement with data reviewed by Carlson<sup>7</sup> in this energy region. As is evident in Fig. 4, the average parameters do not give a good fit to the data. Further improvement can only be made by drastically reducing the average radiation width and/or  $S^1$ .

#### Conclusions

Experimental capture cross sections in the keV region provide valuable checks on the averaged resonance parameters used for calculations. The sensitivity of the calculation to each parameter is dependent on the nucleus and the energy. The maximum use of keV capture data is obtained when the s-wave average radiation width, level spacing and strength function are well known since the p wave parameter fit is then less ambiguous. The s wave parameters do not appear to be firmly established for these four nuclei. Until they are, the p wave parameters remain somewhat uncertain.

Table 1

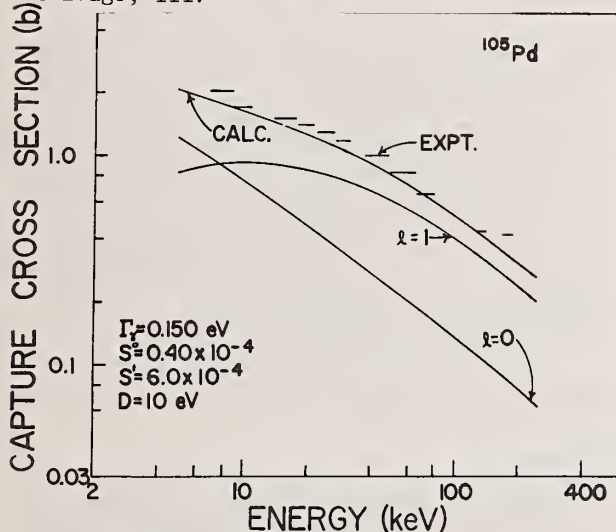
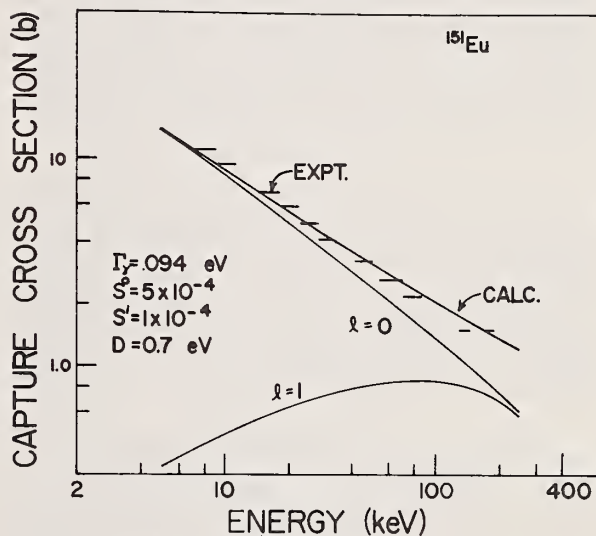
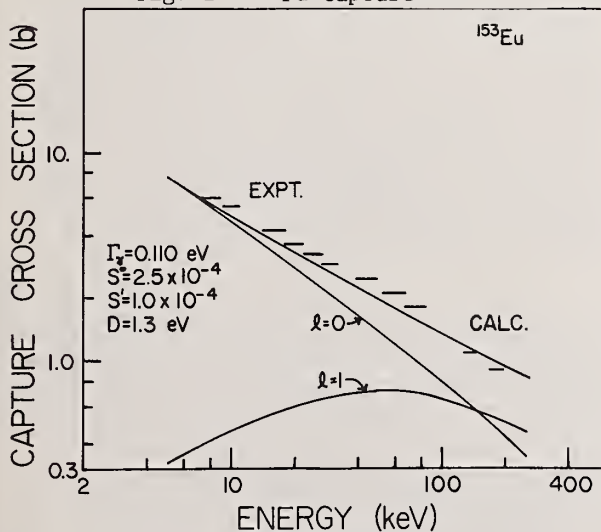
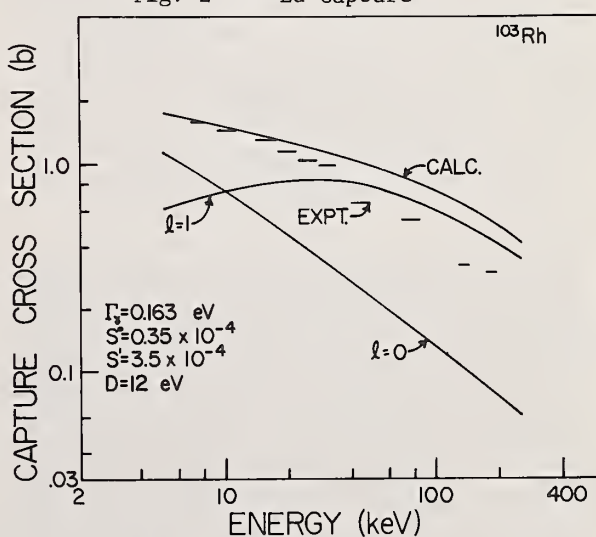
Resonances for Normalization

	$E_0$ (eV)	$2g\Gamma_n$ (meV)
$^{105}\text{Pd}$	55.2	6.9
$^{151}\text{Eu}$	31.6	1.84
$^{153}\text{Eu}$	31.3	2.28
$^{103}\text{Rh}$	187.3	54

\* Work Supported by U.S.A.E.C. Contract AT(11-1)-3058.

+ Now at Texas A. & M. Univ., College Station, Texas 77843

++ Now with Project Management Corporation, Chicago, Ill.

Fig. 1  $^{105}\text{Pu}$  CaptureFig. 2  $^{151}\text{Eu}$  CaptureFig. 3  $^{153}\text{Eu}$  CaptureFig. 4  $^{103}\text{Rh}$  Capture

## References

1. R. E. Schenter, private communication.
2. R. W. Hockenbury, W. R. Moyer and R. C. Block, Nucl. Eng., **49**, 153 (1972).
3. S. E. Atta and J. A. Harvey, "Numerical Analysis of Resonances," ORNL-3205, Oak Ridge National Laboratory (1964).
4. J. G. Sullivan, G. F. Warner, R. C. Block and R. W. Hockenbury, "A Monte Carlo Code for Neutron Capture Experiments," RPI-328-155, Rensselaer Polytechnic Institute (1969)(unpublished).
5. A. M. Lane and J. E. Lynn, Proc. Phys. Soc., **A70**, 557 (1957).
6. J. B. Czirr, UCRL-50804, Lawrence Radiation Laboratory, Feb. 12, 1970.
7. A. D. Carlson, Neutron Standards and Flux Normalization, Proc. Symposium at Argonne National Laboratory, Oct. 21, 1970.



Integral capture-cross sections for separated isotopes of Eu and Ta are reported for measurements in the Coupled Fast Reactivity Measurements Facility (CFRMF). These cross sections along with that measured in the CFRMF for  $^{10}\text{B}(n,\alpha)$  provide an absolute standard for evaluating the relative reactivity worth of  $\text{Eu}_2\text{O}_3$ ,  $\text{B}_4\text{C}$  and Ta in neutron fields typical of an LMFBR core. Based on these measurements and for neutron fields characterized by the  $^{235}\text{U}:^{238}\text{U}$  reaction rate spectral index ranging from 23 to 50, the infinitely dilute relative worth of  $\text{Eu}_2\text{O}_3$  has been estimated to be 25% to 40% higher than that for  $\text{B}_4\text{C}$  and 80% to 100% higher than that for Ta.

(CFRMF Reactor, fast reactors, control materials, neutron reactions, capture cross sections, europium oxides, boron carbides, tantalum)

### Introduction

The major emphasis of this paper concerns the basic nuclear data required for the evaluation of  $\text{Eu}_2\text{O}_3$ ,  $\text{B}_4\text{C}$  and Ta as control element materials for the LMFBR. For some time  $\text{B}_4\text{C}$  and Ta were considered as reference control materials for the fast breeder reactors; however, the merits of  $\text{Eu}_2\text{O}_3$  as a potentially superior neutron absorber have since been recognized<sup>1,2</sup>. The relative merits of the three materials in terms of reactivity worth, nature of the reaction products, burn-up and decay heat has been summarized by Spenke<sup>1</sup>.

To more reliably assess the relative reactivity worth and long term stability and the decay heat rates for these materials, measurements are needed for differential cross-sections and integral capture cross sections in fast and intermediate neutron fields.<sup>2</sup> This work provides integral capture cross sections measured for separated isotopes of the above control materials in the Coupled Fast Reactivity Measurements Facility<sup>3</sup> (CFRMF) at the INEL which apply directly to the evaluation of control materials.

In this paper the measurements of the integral capture cross sections for the reactions  $^{151}\text{Eu}(n,\gamma)$ ,  $^{152\text{m}}_2\text{Eu}$ ,  $^{151}\text{Eu}(n,\gamma)^{152\text{m}}_2\text{Eu}$ ,  $^{151}\text{Eu}(n,\gamma)^{152\text{g}}\text{Eu}$ ,  $^{181}\text{Ta}(n,\gamma)^{182\text{m}}\text{Ta}$  and  $^{181}\text{Ta}(n,\gamma)^{182\text{g}}\text{Ta}$  are described in detail. These cross sections, along with that measured in the CFRMF by Farrar<sup>4</sup> for the  $^{10}\text{B}(n,\alpha)$  reaction are used as an absolute standard for estimating the relative worth of  $\text{Eu}_2\text{O}_3$ , natural  $\text{B}_4\text{C}$  and Ta in different neutron fields. In neutron fields characterized by the  $^{235}\text{U}:^{238}\text{U}$  reaction rate spectral index ranging from 23.3 to 50, the per unit volume relative reactivity of  $\text{Eu}_2\text{O}_3$  has been estimated to be 25% to 40% higher than that for  $\text{B}_4\text{C}$  and 80% to 100% higher than that for Ta.

### Integral Capture Cross Section Measurements

#### Neutron Field

The CFRMF, described in detail in a previous publication<sup>3</sup>, is a zoned core critical facility with a fast neutron spectrum zone in the center of a water moderated thermal "driver" zone and with flux levels up to  $\sim 10^{11}$  n/(cm<sup>2</sup> sec). The neutron energy spectrum at the center of the CFRMF has been extensively studied by proton-recoil spectrometry, multi-foil dosimetry, Li-6 spectrometry and calculations employing resonance absorption, transport theory and Monte Carlo multigroup techniques.<sup>3</sup> General features characterizing the central neutron energy spectrum are indicated in column 1

of Table I. These features were derived from a 68 group representation of the CFRMF central flux as calculated by transport theory (1D,  $S_8$ , P1).

#### Experiment

A summary of some of the experimental details pertinent to the irradiation of the europium and tantalum samples is given in Table II. To remove any possible rare-earth contamination, the europium samples were purified by ion exchange column separation of the enriched materials obtained from Oak Ridge Isotope Sales. Samples Eu-1 and Eu-2 were used for the measurement of the cross sections for the reactions  $^{151}\text{Eu}(n,\gamma)^{152\text{m}}_2\text{Eu}$  and  $^{151}\text{Eu}(n,\gamma)^{152\text{g}}\text{Eu}$ , sample Eu-3 for the  $^{151}\text{Eu}(n,\gamma)^{152\text{m}}_2\text{Eu}$  reaction, and all three tantalum samples for the reactions  $^{181}\text{Ta}(n,\gamma)^{182\text{m}}\text{Ta}$  and  $^{181}\text{Ta}(n,\gamma)^{182\text{g}}\text{Ta}$ . Gold monitor foils (0.0127 cm thick) accompanied each sample during the irradiation to provide for a power normalization to an absolute flux level.

Standard Ge(Li) gamma spectrometry was used to measure the europium, tantalum and gold activities following the irradiations.

#### Analysis

Central to the analysis of the data for each irradiated sample and monitor foils were the analysis of the gamma ray spectra for the gamma peaks characteristic of the desired reaction products with computations of peak areas<sup>5</sup> and reaction rates. The half-lives<sup>6</sup>, gamma ray lines and branching ratios (from reference 7 for Eu and 8 for Ta) used in the reaction rate computations are listed in Table III. These computations gave several estimates of the sample or gold foil reaction rates as determined by the number of characteristic gamma peaks used and the number of spectra recorded. A best estimate of the sample reaction rate was computed as the unweighted average of the individual determinations, with the square of the uncertainty given by the sum of the residuals squared divided by  $N(N-1)$ .

Corrections for resonance self shielding, estimated to be negligible for the  $\text{Eu}_2\text{O}_3$  samples and approximately  $\sim 1\%$  to  $\sim 2\%$  for the tantalum foils were not applied to the reaction rates. Corrections for gamma absorption in the  $\text{Eu}_2\text{O}_3$  samples were determined to be negligible, however, it was necessary to correct the tantalum reaction rates for gamma absorption. Uncertainties in the branching ratios and in the half-lives were not considered in the assessment of the uncertainty in the reaction rate. Their contribution is expected to not

\* Work performed under the auspices of the Energy Research and Development Administration.

<sup>†</sup> Retired.

<sup>††</sup> Presently employed with the Allied Chemical Corporation, INEL, Idaho Falls, Idaho 83401.



be as significant as that contributed by the uncertainty in the absolute flux level to the uncertainty in the absolute cross section.

The absolute spectral-averaged cross section for the reaction was computed as the best estimate of the sample reaction rate divided by the absolute integral flux corresponding to a constant power level during the irradiation. The absolute flux level was determined by normalizing the gold foil reaction rate for the sample to a gold foil reaction rate determined as part of the Interlaboratory LMFBR Reaction Rate (ILRR) program<sup>9</sup> for which the absolute flux level was established with an uncertainty of  $\pm 8\%$ .

## Results

The results of the reaction rate and cross-section calculations are summarized in Table IV. From these results the total capture cross sections for  $^{151}\text{Eu}$  and for natural Eu (47.8%  $^{151}\text{Eu}$ , 52.2%  $^{153}\text{Eu}$ ) are  $2.59 \pm 0.15$  barns/atom and  $2.03 \pm 0.19$  barns/atom, respectively.

### Reactivity Calculations

In the following discussion concerning reactivity worth, the integral capture cross sections of  $^{151}\text{Eu}$ ,  $^{153}\text{Eu}$ ,  $^{181}\text{Ta}$  and  $^{10}\text{B}$ , as measured in the CFRMF, are used as an absolute standard for computing infinitely dilute relative reactivities of  $\text{Eu}_2\text{O}_3$ ,  $\text{B}_4\text{C}$  and Ta in the neutron field of the CFRMF. They are also used to obtain reasonable estimates of the integral cross sections and relative reactivities for these materials in other neutron fields.

### Computational Method

Reactivity calculations were made with a multi-group diffusion approximation formulation of the following first order perturbation theory expression:<sup>10</sup>

$$\rho = -\frac{1}{K} \cdot \langle \phi \rangle \cdot \bar{\Sigma}_a \cdot \langle \phi_a^+ \rangle$$

where

$K$  = product of the eigenvalue for the unperturbed reactor and the normalization integral

$\langle \phi \rangle$  = the space and lethargy - averaged flux in the sample

$$= \frac{\iiint \phi(r, u, \Omega) d^3r d\Omega du}{\iiint d^3r d\Omega du}$$

$\langle \phi_a^+ \rangle$  = the absorption-weighted adjoint in the sample

$$= \frac{\iiint \phi_a^+(r, u, \Omega) \Sigma_a(r, u) \phi(r, u, \Omega) d^3r d\Omega du}{\iiint \phi(r, u, \Omega) \Sigma_a(r, u) d^3r d\Omega du}$$

$\bar{\Sigma}_a$  = the macroscopic spectral-averaged absorption cross section for the sample.

### Application to $\text{Eu}_2\text{O}_3$ , $\text{B}_4\text{C}$ and Ta

The neutron fields used here were the CFRMF and assemblies<sup>11</sup> designated ECEL-17, ECEL-17FS, LMFBR-17 and LMFBR-17FS. Real and adjoint fluxes in a 68 group structure were used for all assemblies. General features derived from the 68 group central real fluxes for each assembly are summarized in Table I.

Infinitely dilute differential capture cross sections for  $^{151}\text{Eu}$ ,  $^{153}\text{Eu}$ ,  $^{181}\text{Ta}$  and  $^{10}\text{B}$  were generated from ENDF/B-III data using ETOP and PHROG processing codes. In addition, the cross sections for  $^{198}\text{Au}(n, \gamma)$ ,  $^{235}\text{U}(n, f)$  and  $^{238}\text{U}(n, f)$  were generated to provide a comparison of the calculated spectral-averaged cross

sections against standard dosimetry materials and to permit a computation of the spectral index for each neutron field.

Atomic densities used to compute the macroscopic cross sections were  $2.72 \times 10^{22}$  atoms ( $\text{Eu}$ )/ $\text{cm}^3$  for  $\text{Eu}_2\text{O}_3$ ,  $2.343 \times 10^{22}$  atoms ( $^{10}\text{B}$ )/ $\text{cm}^3$  for  $\text{B}_4\text{C}$  and  $2.983 \times 10^{22}$  atoms ( $\text{Ta}$ )/ $\text{cm}^3$  for tantalum. These atomic densities assume material densities of  $7.95 \text{ gm/cm}^3$  for  $\text{Eu}_2\text{O}_3$ ,  $2.51 \text{ gm/cm}^3$  for  $\text{B}_4\text{C}$  and  $16.6 \text{ gm/cm}^3$  for tantalum.

The pertinent steps in the calculation of the relative reactivities for the control materials in the selected neutron fields is illustrated in figures 1, 2 and 3. The relative cross sections in figure 1 indicate the change in relative value of the spectral-averaged cross sections for a material as the neutron spectral shape is changed. Assuming the energy dependence of the cross sections to be well represented by the differential cross sections from ENDF/B-III, the relative cross sections plotted in figure 1 multiplied by the integral cross sections measured for these materials in the CFRMF provide reasonable estimates of the absolute integral cross sections in the selected neutron fields. These estimates multiplied by the appropriate atomic densities are illustrated in figure 2 relative to the macroscopic cross section for  $\text{Eu}_2\text{O}_3$  in each field.

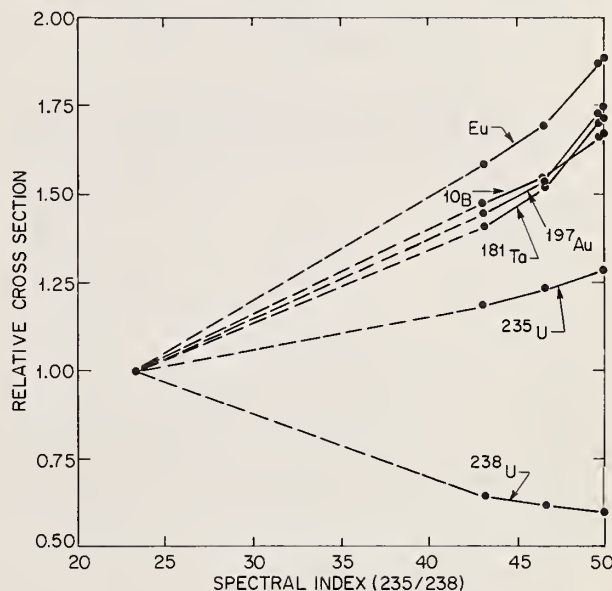


Fig. 1. Calculated integral cross sections for each neutron field (closed circles) relative to the values for the CFRMF.

Using the 68 group real and adjoint fluxes for each assembly, the macroscopic differential cross sections from ENDF/B-III and the relative macroscopic spectral averaged cross sections from figure 2, the relative reactivities per unit volume were computed by the method discussed above and are illustrated in figure 3. The results in figure 3 seem to indicate a considerable increase in the relative reactivity of  $\text{B}_4\text{C}$  as the neutron spectrum hardens. The magnitude of this effect was found to be related to the slope of the adjoint flux. For the CFRMF, the adjoint flux is relatively steep changing by 75% over the 95% energy range of the real flux, whereas for ECEL-17, the variation is only 4% and for LMFBR-17, 35%. The values for the symbol X and the open circle in figure 3 indicate the relative reactivities calculated using the CFRMF real flux and

the ECEL-17 and LMFBR-17 adjoints respectively. Similar computations for Ta reduced the relative reactivity in the CFRMF by only 4% from the value indicated in figure 3.

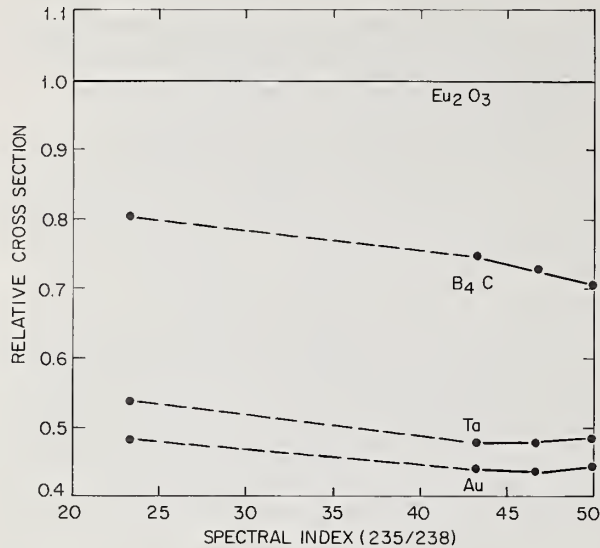


Fig. 2. Estimated macroscopic integral cross sections for each material relative to that for  $\text{Eu}_2\text{O}_3$  in each neutron field (closed circles).

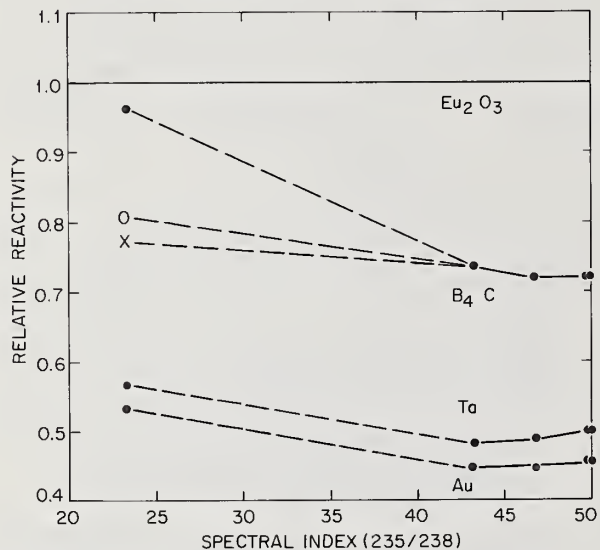


Fig. 3. Reactivity per unit volume for each material relative to that for  $\text{Eu}_2\text{O}_3$  in each neutron field. Closed circles are values obtained using the corresponding real and adjoint fluxes for each field. The symbol X and the open circle are the values obtained for the CFRMF with the normal adjoint replaced by that for ECEL-17 and LMFBR-17, respectively.

Table V gives a comparison of the relative reactivities for  $\text{Eu}_2\text{O}_3$ , natural  $\text{B}_4\text{C}$  and Ta as reported here and derived from measured specific reactivities.<sup>1,11</sup> There appears to be good agreement in the  $\text{Eu}_2\text{O}_3$ - $\text{B}_4\text{C}$

relative comparisons as indicated by columns B-E. However, the relative value for Ta as derived from a measurement in the ECEL-17 is considerably higher than the other relative values. Spenke<sup>1</sup> indicated that the value for Ta, as measured in the SNEAK facility, is probably low because of self-shielding.

### Conclusions

Absolute integral capture cross sections, measured for  $^{151}\text{Eu}$ ,  $^{153}\text{Eu}$ ,  $^{181}\text{Ta}$  and  $^{10}\text{B}$  in the CFRMF, provide an absolute standard for normalizing the model-dependent calculations of the differential cross sections, for evaluating the relative reactivity worth of  $\text{Eu}_2\text{O}_3$ ,  $\text{B}_4\text{C}$  and Ta in neutron fields typical of an LMFBR core and for estimating burnup and decay heating rates. The results of reactivity calculations here demonstrate that the infinitely dilute relative reactivity per unit volume for  $\text{Eu}_2\text{O}_3$  is 25% to 40% higher than  $\text{B}_4\text{C}$  and 80% to 100% higher than tantalum in neutron fields characterized by the  $^{235}\text{U}$ - $^{238}\text{U}$  reaction rate spectral index ranging from 23 to 50. To evaluate the long term worth of  $\text{Eu}_2\text{O}_3$  and to permit realistic calculations of the decay heating rates, measurements of the integral capture cross sections for  $^{152}\text{Eu}$ ,  $^{154}\text{Eu}$ ,  $^{152}\text{Sm}$ ,  $^{152}\text{Gd}$  and  $^{154}\text{Gd}$  are needed. Experiments to measure these cross sections in EBR-II are planned.

### References

1. H. Spenke, *Atomwirtschaft* **17**, 161 (1972).
2. A. E. Pasto, "Europium Oxide as a Potential LMFBR Control Material", ORNL-TM-4226 (September, 1973).
3. J. W. Rogers, D. A. Millsap and Y. D. Harker, *Nuclear Technology* **25**, 330 (1975).
4. Harry Farrar IV, W. N. McElroy and E. P. Lippincott, *Nuclear Technology* **25**, 305 (1975).
5. R. G. Helmer and M. H. Putnam, "Gauss V - A Computer Program for the Analysis of Gamma-Ray Spectra from Ge(Li) Spectrometers", USAEC report ANCR-1043 (January, 1972).
6. Chart of the Nuclides, Eleventh Edition, October, 1972. KAPL, General Electric Company.
7. A. Tobias, "Data for the Calculation of Gamma Radiation Spectra and Beta Heating from Fission Products (Revision 3)", Central Electricity Generating Board Report RD/B/M2669, CNDC (73) P4, (June, 1973).
8. C. M. Lederer, J. M. Hollander, and I. Perlman, *Table of Isotopes*, 6th Edition, John Wiley and Sons, New York (1967).
9. J. W. Rogers, *Nuclear Technology Division Annual Progress Report for Period Ending June 30, 1973*, USAEC Report ANCR-1129 (1973) p. 106.
10. W. K. Foell, *Small Sample Reactivity Measurements in Nuclear Reactors*, Monograph Series on Nuclear Science and Technology, American Nuclear Society, (1972).
11. R. J. Tuttle and T. H. Springer, *Nuclear Science and Engineering* **49**, 468 (1972).

TABLE I

General Features of Selected Neutron Fields

Neutron Field	CFRMF	ECEL-17	ECEL-17FS	LMFBR-17	LMFBR-17FS
Mean Energy <sup>a</sup>	700	470	450	420	420
Median Energy <sup>a</sup>	360	170	150	136	135
90% Range <sup>a,b</sup>	12.2-2800	4.3-2000	3.7-1940	3.2-1970	3.2-1970
95% Range <sup>a,c</sup>	3.5-3800	1.8-2900	1.5-2850	1.2-2840	1.1-2840
Spectral Index <sup>d</sup>	23.3	43.1	46.6	49.8	49.9

<sup>a</sup>Energy in keV.<sup>b</sup>Energy range containing 90% of the integrated neutron flux.<sup>c</sup>Energy range containing 95% of the integrated neutron flux.<sup>d</sup>Spectral Index = Ratio of Calculated Reaction Rates for <sup>235</sup>U to <sup>238</sup>U. Measured value for CFRMF is 20.5.

TABLE III

Nuclear Data for Reaction Rate Calculations

Isotope	Half-Life	E <sub>γ</sub> (keV)	B.R. <sup>a</sup>
<sup>152m</sup> Eu	96 m	89.85	0.74
<sup>152m</sup> Eu	9.3 h	841.45 963.27	0.125 0.103
<sup>152g</sup> Eu	13.2 y	778.75 1085.77 1112.07 1408.16	0.125 0.105 0.129 0.215
<sup>154</sup> Eu	8.6 y	723.34 1004.76 1274.43	0.198 0.174 0.347
<sup>182m</sup> Ta	15.9 m	147.11 171.89 318.59	0.40 0.40 0.05
<sup>182g</sup> Ta	115 d	100.11 152.40 222.11 1121.27 1221.38	0.14 0.07 0.08 0.34 0.27
<sup>198</sup> Au	2.696 d	411.79	0.95

<sup>a</sup>B.R. = Gamma-ray branching ratio

TABLE II

Summary of Experimental Details

Sample Tag	Isotope	Enrichment (%)	Form	Mass (mg)	Irradiation Time (hr)	Total Neutron Fluence (m/cm <sup>2</sup> )
Eu-1	151	96.83	Eu <sub>2</sub> O <sub>3</sub> <sup>a</sup>	15.33	287.5	1.2x10 <sup>17</sup>
Eu-2	153	98.76	Eu <sub>2</sub> O <sub>3</sub> <sup>a</sup>	14.87	287.5	1.2x10 <sup>17</sup>
Eu-3	151	96.83	Eu <sub>2</sub> O <sub>3</sub> <sup>c</sup>	5.49	0.5	2.2x10 <sup>14</sup>
Ta-1	181	99.988	Metal <sup>b</sup>	141.73	2.0	8.8x10 <sup>14</sup>
Ta-2	181	99.988	Metal <sup>b</sup>	141.93	2.0	8.8x10 <sup>14</sup>
Ta-3	181	99.988	Metal <sup>b</sup>	142.05	2.0	8.8x10 <sup>14</sup>

<sup>a</sup>Powder encapsulated in quartz ampule.<sup>b</sup>Metal foils were 0.0127 cm thick by 1 cm diameter.<sup>c</sup>Encapsulated in high density poly container with 5 mil wall thickness.

TABLE IV

Summary of Cross Section Measurements

Reaction	Reaction Rate [Reactions/(sec atom)] (x10 <sup>13</sup> )	Cross Section (barns/atom)
<sup>151</sup> Eu(n,γ) <sup>152m</sup> Eu	(2.64±0.10)x10 <sup>-3</sup>	(2.1±0.2)x10 <sup>-3</sup>
<sup>151</sup> Eu(n,γ) <sup>152m</sup> Eu	1.284±0.020	1.07±0.09
<sup>151</sup> Eu(n,γ) <sup>152g</sup> Eu	2.803±0.024	1.52±0.12
<sup>153</sup> Eu(n,γ) <sup>154</sup> Eu	1.782±0.008	1.51±0.12
<sup>181</sup> Ta(n,γ) <sup>182m</sup> Ta	(9.41±0.20)x10 <sup>-4</sup>	(8.1±0.7)x10 <sup>-4</sup>
<sup>181</sup> Ta(n,γ) <sup>182g</sup> Ta	0.657±0.009	0.54±0.04
<sup>10</sup> B(n,α) <sup>7</sup> Li		1.90±0.07 <sup>a</sup>

<sup>a</sup>Reported by Farrar *et al.*<sup>4</sup>

TABLE V

Comparison of Relative Reactivities

Material	Relative Reactivity <sup>a</sup>				
	A <sup>b</sup>	B <sup>c</sup>	C <sup>d</sup>	D <sup>e</sup>	E <sup>f</sup>
Eu <sub>2</sub> O <sub>3</sub>	1.0	1.0	1.0	1.0	1.0
B <sub>4</sub> C	0.961	0.776	0.735	0.775	0.770
Ta	0.567	0.542	0.481	0.684	0.424

<sup>a</sup>Reactivity per unit volume.<sup>b</sup>As calculated here for the CFRMF.<sup>c</sup>As calculated here for the CFRMF using the adjoint for ECEL-17.<sup>d</sup>As calculated here for the ECEL-17.<sup>e</sup>Derived from measured specific reactivities reported in reference 11.<sup>f</sup>Derived from measured specific reactivities reported in reference 1.



R. C. Greenwood  
INEL, Aerojet Nuclear Co., Idaho Falls, Idaho 83401  
and  
R. E. Chrien and K. Rimawi  
Brookhaven National Laboratory  
Upton, New York 11973

Essentially monoenergetic neutrons with keV energies can be obtained from a reactor by using suitable filters. To date, prompt  $\gamma$ -ray spectra have been measured using 24-, 2-, and 1-keV neutrons, obtained through Fe+Al+S, Sc+Ti and  $^6\text{Li}$  filters, respectively. Two features of these data are of note to reactor shielding. First, the radiative capture spectra from higher Z nuclei usually result from an average over many resonance states. Hence statistical fluctuations in the primary  $\gamma$ -ray intensities, to which the corresponding thermal neutron capture spectra are subject, are averaged out. Second, such data provide information on the dependence of radiative capture spectra on neutron energy. The data shows that at 24 keV there is a significant p-wave contribution to these spectra, even for those mass regions where the ratio of the p-to-s wave strength function is close to a minima. This occurs because the smallness of the relative penetrability at 24 keV,  $0.04 < (kR)^2 < 0.08$  for  $100 < A < 240$ , is compensated for by the branching ratio  $\Gamma_\gamma/\Gamma$  which is now much larger for p-wave than for s-wave resonances.

(Neutron capture gamma-rays;  $^6\text{Li}$  filter; Iron filter; Mn(n, $\gamma$ );  $^{154}\text{Gd}$ (n, $\gamma$ );  $^{156}\text{Gd}$ (n, $\gamma$ ))

In order to assess  $\gamma$ -ray production in a fast reactor, and thereby estimate the shielding requirements, it is necessary to know how the prompt  $\gamma$ -ray spectrum varies with neutron capture energy. These prompt capture  $\gamma$ -rays will constitute much of the "hard" component of the reactor photon spectrum and will therefore have the most stringent shielding requirements. Reliable prediction of the neutron energy dependence of the capture  $\gamma$ -ray spectrum requires an understanding of the reaction mechanisms involved. Of crucial importance are (1) the magnitude of the contributions from neutron capture with  $l > 0$ , and (2) whether there are appreciable departures from the statistical model of compound nucleus states. Either of these effects can significantly alter the photon spectrum from that obtained from thermal neutron capture.

Nuclear research reactors can be used as a source of keV neutrons, with sufficient intensities to allow detailed studies of reaction mechanisms over a wide range of neutron energies. The simplest experimental scheme for doing this is to insert a thick filter of a material having a  $1/v$  neutron cross section dependence into an external beam channel of a reactor. The resulting filtered neutron beam will, assuming a  $1/E$  flux distribution for the source neutrons, have the following neutron energy distribution

$$\phi(E_n) \propto \frac{1}{E_n} \exp(-k/E_n^{1/2}) \quad (1)$$

where k is a constant. A  $^6\text{Li}$  filter whose thickness is such as to peak the neutron energy distribution at  $\sim 1$  keV has been installed in the H1 channel of the High Flux Beam Reactor at Brookhaven National Laboratory.<sup>1</sup> The flux properties of this facility are summarized in Table 1. As can be seen from this table

a major disadvantage of this type of filter is that there also exists an appreciable flux of higher energy ( $> 2$  keV) background neutrons. This, of course, is to be expected since in eq. 1 when  $E \gg k^2$ ,  $\phi(E) \propto 1/E$ ; that is, identical to the unfiltered neutron energy distribution. In practical terms then this means that the external beam contains a large flux of high energy neutrons, for which it is difficult to shield the Ge(Li)  $\gamma$ -ray detector from, and appreciable radiation damage of the Ge(Li) detector can occur.

A recently developed, and for most applications a more satisfactory, method of obtaining external beams of keV-energy neutrons from a reactor is to use thick filters of materials which have "deep" interference minima in their total neutron interaction cross sections. By use of suitable combinations of two or more different materials in the filter it is usually possible to suppress the transmission of neutrons with energies corresponding to all but one of these minima. In this manner an intense beam of essentially monoenergetic neutrons, with energies corresponding to that of the selected transmission minima is obtained. In the first such facility developed, a beam of 1.95 keV neutrons was obtained through a thick Sc filter located in a beam channel of the Materials Testing Reactor.<sup>2</sup> The use of this facility for neutron capture  $\gamma$ -ray spectroscopy has been described in ref. 3. Subsequently, a 24 keV neutron beam was developed on the MTR using a filter combination of Fe+Al+S.<sup>4</sup> A versatile 24-keV filtered neutron beam facility, in which varying lengths of Fe and Al can be used, has subsequently been installed in the H1 channel of the HFBR.<sup>1</sup> Figure 1 shows the 24-keV flux profile for two filter combinations containing 9- and 27-in of Fe.

TABLE 1. Filter Parameters. Fluxes and backgrounds for filter combinations available at the Tailored-Beam Facility.

Filter	Available Flux (n/cm <sup>2</sup> /sec)	Thermal (n/cm <sup>2</sup> /sec)	Backgrounds	
			Fast (n/cm <sup>2</sup> /sec) >50 keV	$\gamma$ 's (mr/hr)
23.76 cm Fe				
+35.56 cm Al	$1.0 \times 10^6$	300	$1.4 \times 10^3$	6
+ 5.08 cm S				
11.3 cm $^6\text{Li}_2\text{CO}_3$	$1.5 \times 10^6$	500	$3 \times 10^6$	1700
+10.5 cm Pb	( $500 < E_n < 2000$ eV)			

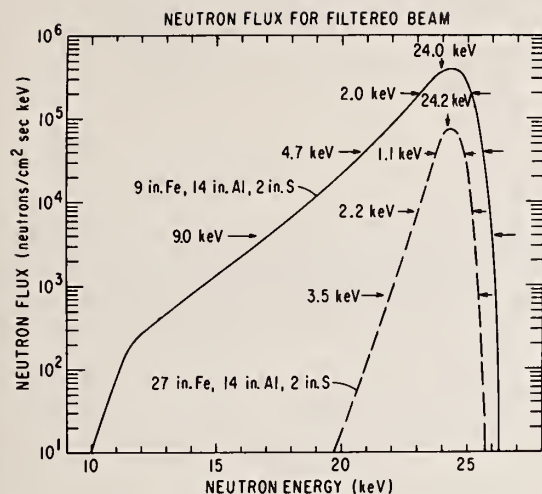


Fig. 1. Calculated flux through Fe+Al+S filters containing 9- and 27-in Fe.

Thus, the 24-keV neutron energy distribution will have a FWHM of 1.1-2.0 keV depending upon the thickness of the Fe in the filter. The purity of the 24-keV neutron beam has been measured with a hydrogen-filled

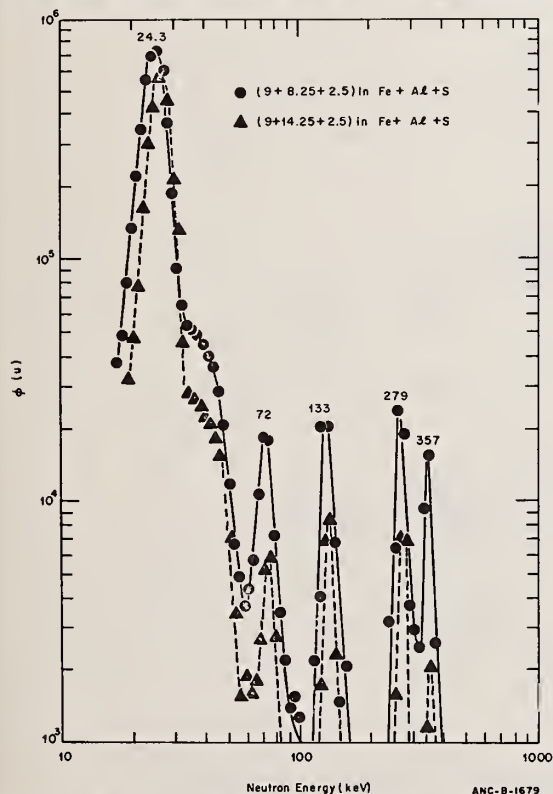


Fig. 2. Fast neutron spectra transmitted through Fe+Al+S filter arrangements as measured with a hydrogen filled proportional counter. The two curves illustrate the effectiveness of Al in reducing the high-energy neutron components relative to that of the 24-keV neutron group.

proportional counter. Neutron spectra were obtained from these data by differentiation, using a code developed by Bennett, *et al.*<sup>5</sup> An example of these data is given in Fig. 2, which illustrates the effectiveness of the Al in reducing the leakage through the higher energy Fe "windows." For the 9-in Fe plus 14-in Al filter the higher energy neutron components are  $\sim 1.9\%$  of the 24-keV neutron flux. The background from thermal neutrons and reactor produced  $\gamma$  rays are also low, as can be seen from Table 1.

Advantages of filtered neutron beams from reactor sources for studying neutron capture reaction mechanisms in the keV-neutron region can briefly be summarized as:

1. There are several neutron energies which are available using filtered neutron beams.
2. High fluxes ( $> 10^6$  neutrons/cm<sup>2</sup>.sec) of essentially monoenergetic neutrons can be obtained.
3. Because of the finite energy spread inherent in the filtered neutrons, the primary capture  $\gamma$ -ray transitions (i.e. those de-exciting the capturing state) generally result from the decay of many compound nucleus states, and the normal statistical fluctuations in their intensities tend to be averaged out.
4. The resultant energy shift of the primary  $\gamma$ -ray transitions compared to the energies measured in thermal-neutron capture provide a unique discrimination between primary and secondary transitions.

An example of the significant variation in the capture spectra obtained with thermal, 1- and 24-keV neutrons is illustrated in Fig. 3 for Mn. The Fe-filter spectrum is dominated by the 23.7 keV resonance while the <sup>6</sup>Li-filter spectrum is influenced by the 337-, 1098- and 2375-eV resonances.

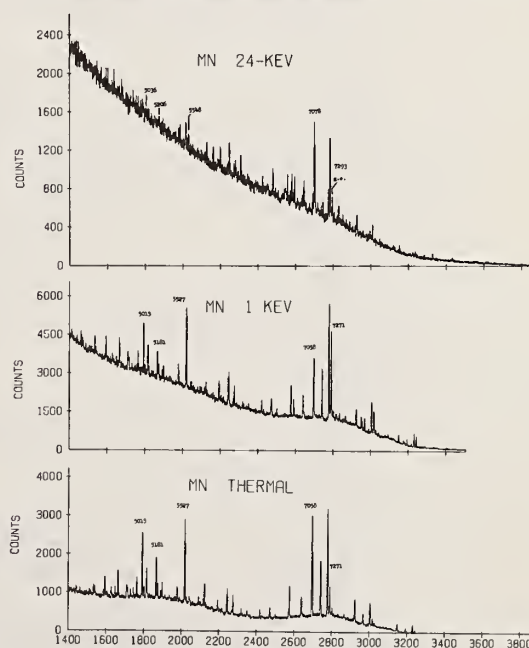


Fig. 3. Manganese prompt  $\gamma$ -ray spectra from capture of thermal, 1- and 24-keV neutrons.

The 24-keV neutron beam facility has proven to be particularly valuable in assessing both, the importance of p-wave capture (compared to s-wave capture) in this

neutron energy region and, the changes in the photon spectrum which can be attributed to p-wave capture. Initial measurements have centered on the Gd isotopes; principally because of the paucity of information on the prompt  $\gamma$  rays resulting from neutron capture in the even-mass Gd isotopes, and some anticipated interesting nuclear structure effects to be found from these data. In this mass region the s-wave strength function is at near a maximum while the p-wave strength function is near a minimum. Even so, in the photon spectrum resulting from capture of 24-keV neutrons in  $^{154}\text{Gd}$ , which represents then an average over  $\sim 130$  resonance states thereby averaging out the statistical fluctuations in the primary  $\gamma$ -ray transition intensities, and which is shown in Fig. 4, final states with  $I^\pi = 1/2^+$ ,  $3/2^+$  and  $5/2^+$  are populated with comparable intensities to those having  $I^\pi = 1/2^-$  and  $3/2^-$ . (This is illustrated quantitatively in the plot of reduced transition intensities shown in Fig. 5.) This is in contrast to the situation expected for s-wave capture alone where the E1 transitions to negative parity states would be expected to have intensities 5-10 times greater than the M1 transitions to the positive parity states, and final states with  $I^\pi = 5/2^+$  would be even more weakly populated. Thus we conclude that in  $^{154}\text{Gd}$ ,  $\ell=0$  and  $\ell=1$  neutron capture are comparable at 24 keV. This observation is consistent with our expectation. Although the relative

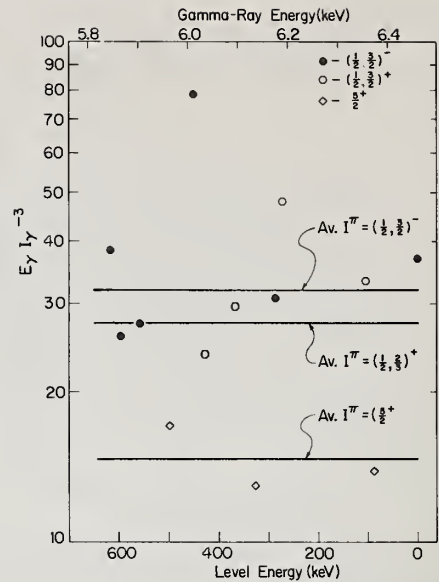


Fig. 5. Plot of reduced transition intensities ( $I_\gamma E_\gamma^{-3}$ ) for primary  $\gamma$  rays from capture of 24-keV neutrons in  $^{154}\text{Gd}$ .

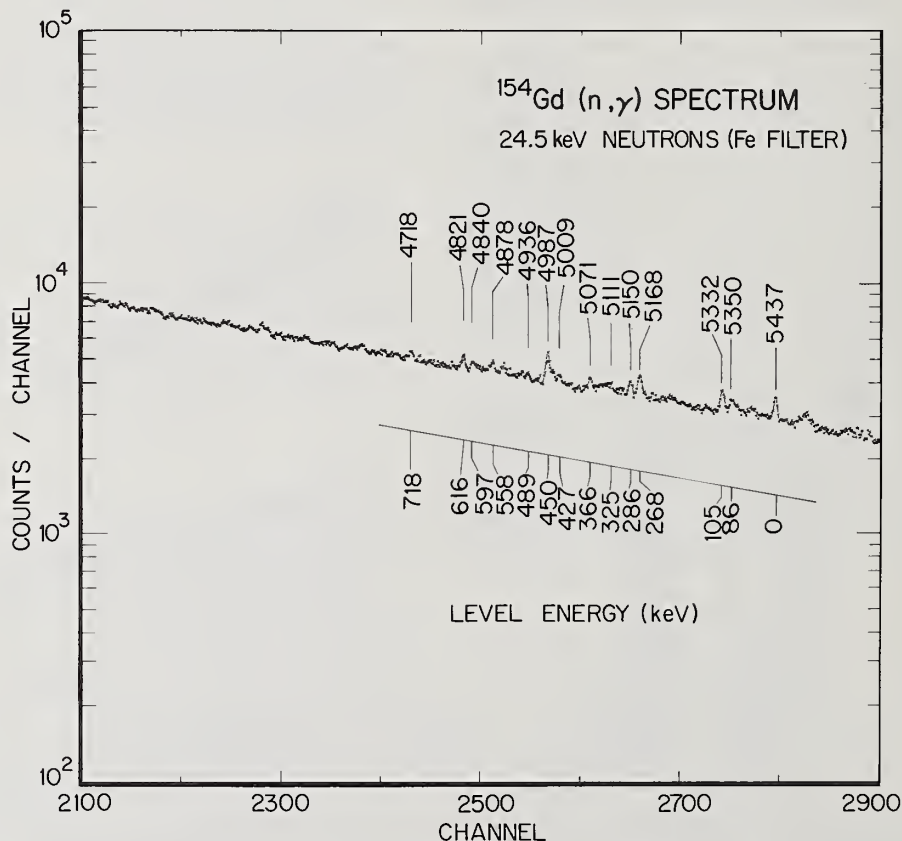


Fig. 4. High-energy portion of the spectrum of  $\gamma$ -rays from 24-keV neutron capture in  $^{154}\text{Gd}$ .



penetrabilities between  $\ell=0$  and  $\ell=1$  neutrons at 24 keV are only  $0.04 < (kR)^2 < 0.08$  for  $100 < A < 240$ , they are compensated somewhat by the branching ratio  $\Gamma_\gamma/\Gamma$  which is often much larger for  $\ell=1$  resonances. The expression for the ratio of p- to s-wave capture, ignoring the fluctuation correlation factor is

$$\frac{\langle \sigma_{\gamma}^1 \rangle}{\langle \sigma_{\gamma}^0 \rangle} \sim \frac{3S_1}{S_0} \frac{\langle \Gamma^0(I) \rangle}{\langle \Gamma^1(I) \rangle} (kR)^2 \quad (2)$$

In the case of 24-keV neutron capture in  $^{154}\text{Gd}$  this ratio is  $\sim 0.5$ , assuming values of  $S_0 = 2.0 \times 10^{-4}$  and  $S_1 = 1.0 \times 10^{-4}$ . In considering the relative p- to s-wave capture ratio as a function of neutron energy,  $E_n$ , we can note from eq. 2 that

$$\frac{\langle \sigma_{\gamma}^0 \rangle}{\langle \sigma_{\gamma}^1 \rangle} \propto E_n \quad \text{when } \langle \Gamma_n^0(I) \rangle \ll \langle \Gamma_\gamma \rangle$$

and that

$$\frac{\langle \sigma_{\gamma}^1 \rangle}{\langle \sigma_{\gamma}^0 \rangle} \propto E_n^{3/2} \quad \text{when } \langle \Gamma_n^0(I) \rangle \gg \langle \Gamma_\gamma \rangle.$$

A final example of the importance of p-wave capture at 24 keV is provided by the data on  $^{156}\text{Gd}(n, \gamma)$  reaction, where the photon spectra resulting from 1- and 24-keV neutron capture are compared in Fig. 6.

Using the above estimate for the relative p- to s-wave capture cross sections with values of  $S_0 = 1.8 \times 10^{-4}$  and  $S_1 = 1.0 \times 10^{-4}$  we calculate that  $\sigma_1/\sigma_0$  are  $\sim 1.0$  and  $0.2$  for 24- and 1-keV neutron capture, respectively. The relative contribution of p-wave capture to the two spectra shown in Fig. 6 is dramatically illustrated by the 5297 keV peak which results from a primary transition to a final state in  $^{157}\text{Gd}$  having  $I^\pi = 5/2^+$ .

#### References

\*Work supported by the Energy Research and Development Administration.

- 1 R. E. Chrien, K. Rimawi, O. A. Wasson and R. C. Greenwood, "Proc. Second International Symposium on Neutron Capture Gamma Ray Spectroscopy and Related Topics, Petten, The Netherlands, 1974", to be published.
- 2 O. D. Simpson and L. G. Miller, Nucl. Instr. Meth. **61**, 245 (1968); and AEC Report No. IN-1218, 1968.
- 3 R. C. Greenwood, R. A. Harlan, R. G. Helmer and C. W. Reich, "Proc. International Symposium on Neutron Capture Gamma-Ray Spectroscopy, Studsvik, Sweden, 1969" (IAEA, Vienna, 1969), p. 607.
- 4 B. W. Howes, R. M. Brugger, J. W. Rogers, R. P. Schuman, F. B. Simpson and O. D. Simpson, AEC Report No. IN-1308, 1969.
- 5 E. F. Bennett, R. Gold and I. K. Olson, Argonne National Laboratory Report ANL-7394 (1957).

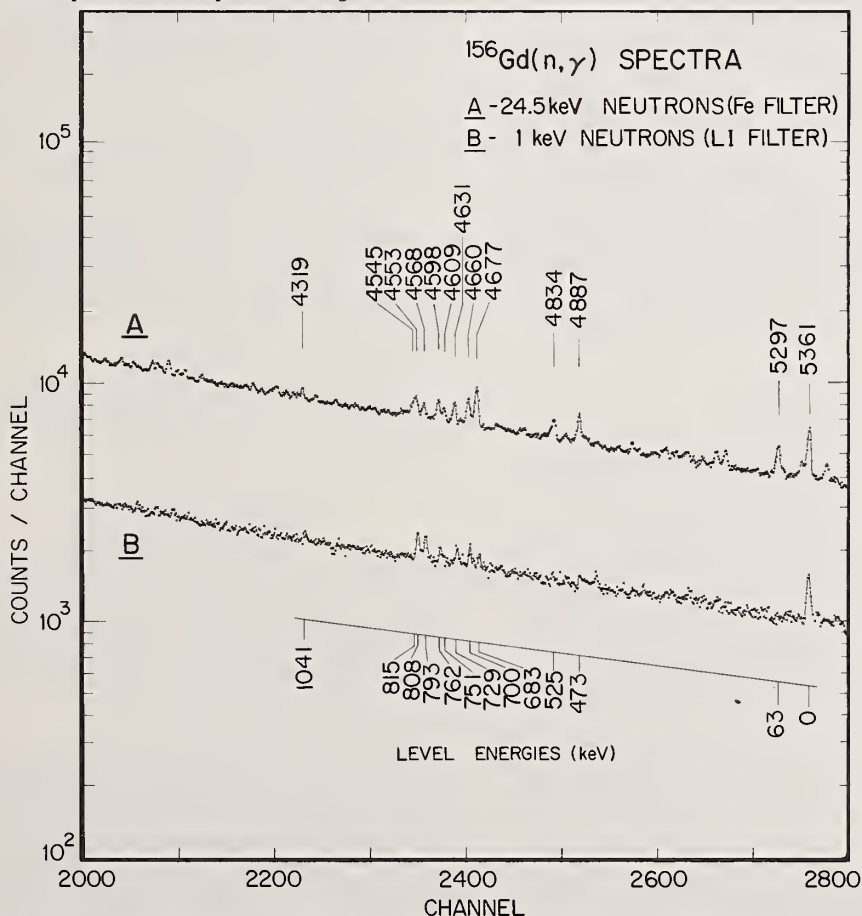


Fig. 6. Comparison of the high-energy  $\gamma$ -ray spectra from capture of 24- and 1-keV neutrons in  $^{156}\text{Gd}$ .

MEASUREMENT OF THE  $\gamma$ -RAY PRODUCTION CROSS SECTIONS FROM INELASTIC NEUTRON SCATTERING  
IN SOME CHROMIUM AND NICKEL ISOTOPES BETWEEN 0,5 AND 10 MeV

F. Voss, S. Cierjacks, D. Erbe, G. Schmalz  
Institut für Angewandte Kernphysik  
Kernforschungszentrum Karlsruhe, F.R., Germany

At the Karlsruhe fast neutron time-of-flight spectrometer the investigation of  $\gamma$ -ray production cross sections of technologically important materials has been continued with the elements Cr and Ni. The excitation functions for the  $\gamma$ -ray production cross sections in inelastic neutron scattering have been measured at  $125^\circ$  from threshold to 10 MeV. The Karlsruhe cyclotron was used to produce a pulsed beam of neutrons having a continuous energy spectrum between 0,5 and 30 MeV. The incident neutron energy was determined by the time of flight technique. The energy resolution ranged from 2,2 keV at 1 MeV to 70 keV at 10 MeV. Neutron flux determination was accomplished by use of a calibrated proton recoil detector. Preliminary results are shown for the  $\gamma$ -ray energies 1434 keV in  $^{52}\text{Cr}$ , 1454 keV in  $^{58}\text{Ni}$  and 1333 keV in  $^{60}\text{Ni}$  and compared with the results of other authors.

( $^{52}\text{Cr}$ ,  $^{58}\text{Ni}$ ,  $^{60}\text{Ni}$  (n,n' $\gamma$ ) experimental results of  $\gamma$ -ray production cross sections,  $E_n=0,5-10$  MeV)

### Introduction

Apart from the need of inelastic neutron scattering cross sections for fission reactor shielding calculations such cross sections and the corresponding  $\gamma$ -ray spectra are required to calculate the heat generation in the blanket and the shield of thermonuclear reactors. In particular, chromium and nickel are potential constituents of the containment vessel and potential useful structural materials. Thus new measurements of high-resolution  $\gamma$ -ray production cross sections for these materials have been performed with the fast neutron time-of-flight spectrometer at the Karlsruhe isochronous cyclotron. Total cross sections were obtained by multiplying the differential cross sections measured at  $125^\circ$  by  $4\pi$ . The following  $\gamma$ -ray transitions were investigated: 781 keV in  $^{50}\text{Cr}$ , 648, 935, 1332, 1434, 1531, 1728 keV in  $^{52}\text{Cr}$ , 1005, 1454 keV in  $^{58}\text{Ni}$  and 467, 826, 1173, 1333 keV in  $^{60}\text{Ni}$ . As an example of these measurements results are presented for the production of the 1434 keV  $\gamma$ -rays in  $^{52}\text{Cr}$ , 1454 keV  $\gamma$ -rays in  $^{58}\text{Ni}$  and 1333 keV  $\gamma$ -rays in  $^{60}\text{Ni}$  between threshold and 4,5 MeV. They are compared with other available data.

### Experimental Method

The experimental device consisting of a  $\gamma$ -ray spectrometer used in conjunction with the Karlsruhe fast neutron time-of-flight spectrometer<sup>1</sup> has been described previously<sup>2,3</sup>. Therefore, only a brief description of the experimental conditions will be given here. A schematic graph of the experimental arrangement is shown in fig. 1. The Karlsruhe cyclotron was used to provide a pulsed beam of neutrons having a continuous energy spectrum ranging from 0,5 to 30 MeV. Neutron bursts of 1,5 nsec width with a repetition rate of 100 kHz were produced by bombarding a thick natural uranium target with the internal beam of deuterons at an average energy of approximately 45 MeV.

A ring-shaped scattering sample was placed at a distance of 57,90 m from the neutron source, having an inner diameter of 120 mm, an outer diameter of 254 mm and a thickness of 6,7 mm and 9,4 mm for Cr and Ni, respectively.

A  $42\text{ cm}^3$  Ge(Li)-detector was used to measure the  $\gamma$ -ray energies and the corresponding neutron energy by the usual time-of-flight technique. For each event

the energy information and time information were digitized in a fast ADC (LABEN FC-4096) and a time analyzer (LABEN TIME-SORTER UC-KB), respectively. The average angle of observation with regard to the incident neutron beam was  $125^\circ$  with an angular resolution of  $\pm 20^\circ$ . This angle was chosen because the Legendre polynomial  $P_2$  is zero at  $125^\circ$  and higher order terms in the angular distribution are usually small, so that the total  $\gamma$ -ray production cross sections can be obtained by multiplying the differential cross sections at  $125^\circ$  by  $4\pi$ . The absolute photopeak efficiency of the Ge(Li)-detector between 0,5 and 2 MeV was determined with a set of calibrated  $\gamma$ -sources. Measurements were carried out at 35 positions in the scattering plane. The average efficiency was obtained by numerical integration over the total area of the scatterer.

A scintillation counter was used to measure the neutron flux during the "sample out" periods. Its efficiency was calculated by a Monte-Carlo-program. All data were processed with a CDC-3100 on-line computer where the time-of-flight spectra of the interesting  $\gamma$ -lines and of suitably chosen regions for background subtraction were accumulated.

The overall time resolution obtained in this experiment was  $\leq 4,5$  ns corresponding to a neutron energy resolution of  $\leq 2,2$  keV at 1 MeV and 70 keV at 10 MeV.

### Results and Comparison

Fig. 2 shows typical  $\gamma$ -ray spectra obtained in the interaction of fast neutrons with Cr (upper curve) and Ni (lower curve). Only photopeaks which can be attributed to  $\gamma$ -rays following inelastic neutron scattering have been assigned. The energies were taken from published decay schemes<sup>4-8</sup>. Together with the energies the corresponding isotopes and the initial and final levels of the  $\gamma$ -radiation are given.

The next three figures show preliminary results for the  $\gamma$ -ray transitions from the first excited to the ground state in  $^{52}\text{Cr}$ ,  $^{58}\text{Ni}$ , and  $^{60}\text{Ni}$ . The error bars represent only statistical errors. The uncertainties of the flux determination (8 %) and of the efficiency (3 %) of the Ge(Li)-detector are not included. Corrections for multiple scattering of neutrons, flux attenuation and  $\gamma$ -ray attenuation in the sample have not yet been applied. The first two effects are of

the same order of magnitude (10-20 %) but of opposite sign so that they tend to cancel each other. The correction for  $\gamma$ -ray attenuation (20-25 %) will shift all cross sections to higher values.

In fig. 3 our  $\gamma$ -ray production cross sections for the 1434 keV transition in  $^{52}\text{Cr}$  are compared with other measurements. The results of Broder et al.<sup>9</sup> are systematically higher. A smaller deviation in the same direction is found for the two recent data points of Grenier et al.<sup>10</sup> at 3.8 and 4.2 MeV. Included in this figure there are data of Coles<sup>11</sup> which we obtained from their published differential cross sections at 100° by multiplying them by  $4\pi$ . They tend to be a little bit lower especially above 3 MeV which might be due to the different average angles.

The results for the 1454 keV  $\gamma$ -ray of  $^{58}\text{Ni}$  are shown in fig. 4. Again there is a discrepancy for the cross sections of Broder et al.<sup>9</sup> and of Grenier et al.<sup>10</sup>. Good agreement is found with the five data points between 1.4 and 2 MeV and two data points at 2.6 MeV measured by Nishimura et al.<sup>12</sup>. The same holds for the (n,n')-cross sections of Rogers et al.<sup>13</sup> between 1.5 and 1.8 MeV which can be directly compared since at these energies the  $\gamma$ -ray production cross sections contain no contribution from higher levels. The values of Konobeevskij et al.<sup>14</sup> below 1.7 MeV are considerably higher. This discrepancy may be due to a shift in the energy scale.

A similar situation as before is found for the 1333 keV  $\gamma$ -ray in  $^{60}\text{Ni}$  as shown in fig. 5. We see again large discrepancies for the data of Broder et al.<sup>9</sup> and of Konobeevskij et al.<sup>14</sup> and a smaller discrepancy for these of Grenier et al.<sup>10</sup>. The agreement with the inelastic scattering cross sections of Rogers et al.<sup>13</sup> is fairly good except for the value at 1.8 MeV.

In summary, most of the recently published data tend to be higher than the present preliminary results when averaged over the rapid fluctuations which are still present at 4.5 MeV. This deviation can qualitatively be understood in view of the not yet applied corrections mentioned above.

## References

- <sup>1</sup> S. Cierjacks, B. Duelli, P. Forti, D. Kopsch, L. Kropp, M. Lösel, J. Nebe, H. Schweickert, H. Unseld; *Rev. Sci. Instr.* **39** (1968) 1279
- <sup>2</sup> F. Voss, S. Cierjacks, L. Kropp; *Proc. of the 3<sup>rd</sup> Conf. on Neutron Cross Sections and Technology*, 1971, Knoxville, Tennessee, KFK 1494 (1971)
- <sup>3</sup> F. Voss; *Thesis, Karlsruhe* 1972; KFK 1611 (1972)
- <sup>4</sup> S.W. Sprague, R.G. Arns, B.J. Brunner, S.E. Caldwell, C.M. Rosza; *Phys. Rev.* **C4** (1971) 2074
- <sup>5</sup> T.P.G. Carola, J.G. Tamboer; *Nucl. Phys.* **A185** (1972) 81
- <sup>6</sup> L.E. Carlson, D.A. Hutcheon, A.G. Robertson, D.F.H. Start, E.K. Waburton, J.J. Weaver *Nucl. Phys.* **A162** (1971) 35
- <sup>7</sup> D.M. van Patter, R.N. Horoshko, H.L. Scott, P.F. Hinrichsen; *Nucl. Phys.* **A137** (1969) 353
- <sup>8</sup> D.M. van Patter, F. Rauch; *Nucl. Phys.* **A191** (1972) 245
- <sup>9</sup> D.L. Broder, V.E. Kolesov, A.I. Lashuk, I.P. Sadokhin, A.G. Dovbenko; *Atom. Energ.* **16** (1964) 103, transl. *Sov. J. Atom. Energ.* **16** (1964) 113
- <sup>10</sup> G. Grenier, B. Duchemin, D. Parisot; *CEA-R-4634* (1974)
- <sup>11</sup> R.F. Coles; *AWRE O 41/71* (1971)
- <sup>12</sup> K. Nishimura, K. Okano, K. Kikuchi; *Nucl. Phys.* **70** (1965) 421
- <sup>13</sup> V.C. Rogers, L.F. Peghian, F.M. Clikeman; *Nucl. Sci. Eng.* **45** (1971) 297
- <sup>14</sup> E.S. Konobeevskij, R.M. Musaelyan, V.I. Popov, I.V. Surkova; *Isv. Akad. Nauk SSSR, Ser. fis.* **35** (1971) 2345



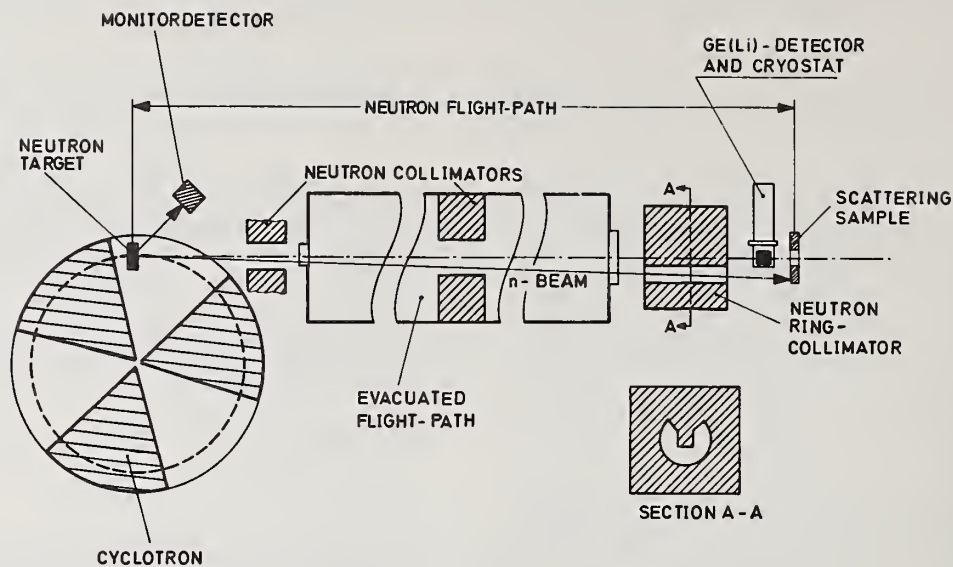


Fig. 1 Experimental arrangement.

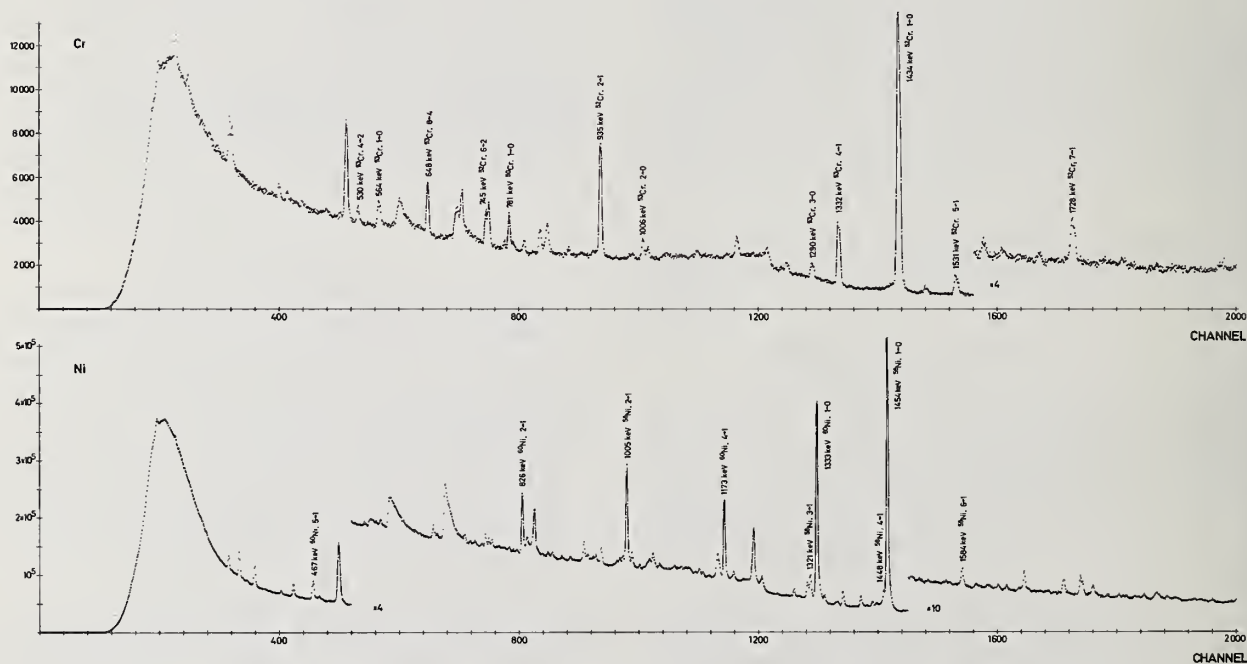


Fig. 2  $\gamma$ -ray spectra for the interaction of fast neutrons with chromium and nickel, respectively.

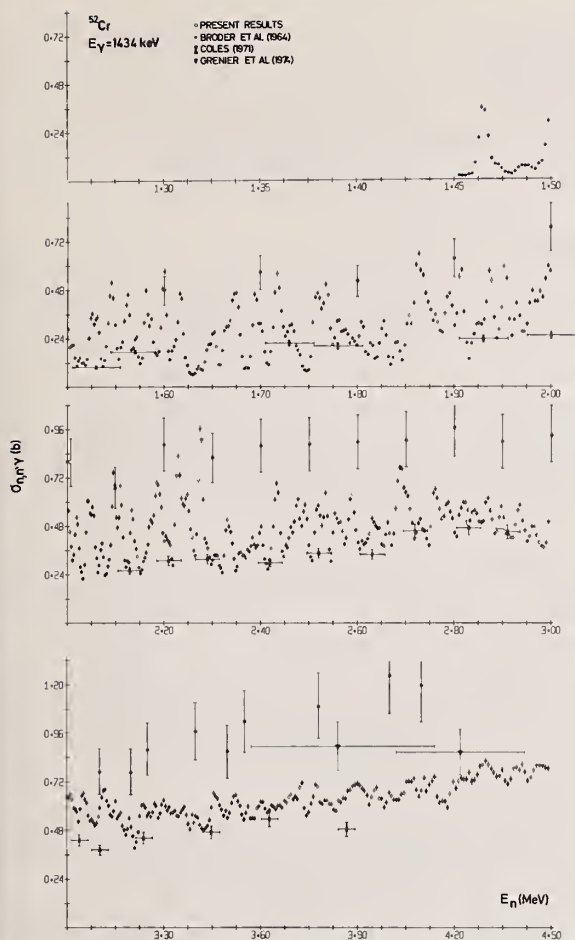


Fig. 3 Cross section for the production of the 1434 keV  $\gamma$ -ray from inelastic neutron scattering in  $^{52}\text{Cr}$ .

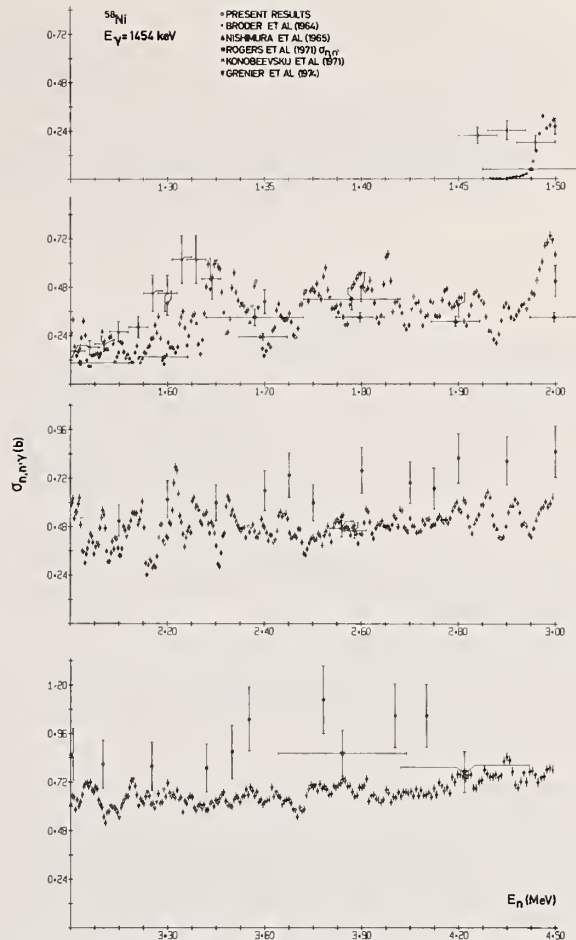


Fig. 4 Cross section for the production of the 1454 keV  $\gamma$ -ray from inelastic neutron scattering in  $^{58}\text{Ni}$ .

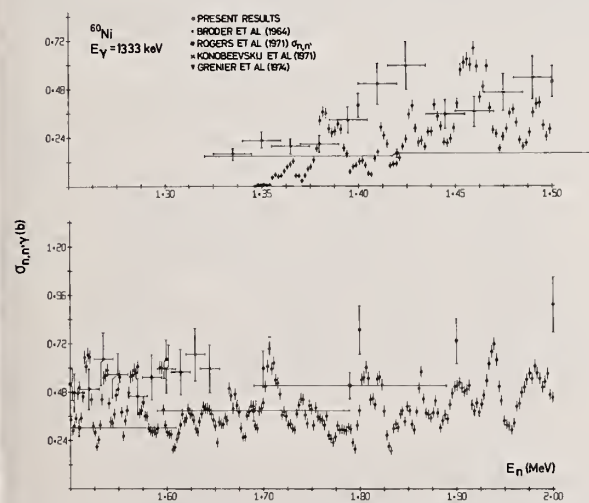


Fig. 5 Cross section for the production of the 1333 keV  $\gamma$ -ray from inelastic neutron scattering in  $^{60}\text{Ni}$ .

K. Rimawi and R. E. Chrien  
Brookhaven National Laboratory  
Upton, New York 11973

Using high-resolution detection techniques, intensities of specific activation lines from  $^{197}\text{Au}(n,\gamma)^{238}\text{U}(n,\gamma)^{127}\text{I}(n,\gamma)$ , and  $^{115}\text{In}(n,\gamma)$  {54 min + 2.2 sec} were recorded, using the BNL HFBR iron-filtered neutron beam. From a comparison with the reaction  $^{10}\text{B}(n,\alpha\gamma)$ , cross sections at 24.3 keV were determined.

(24.3 keV neutron activation cross sections, relative  $^{10}\text{B}$  standard)

## I. Introduction

The measurement of the neutron capture cross section leading to the population of a ground state unstable against beta decay, or an isomeric state in the product nucleus, is a simple one in principle. A large number of such measurements have been conducted, using a variety of methods, which cover a wide range of neutron energies impinging on different target nuclides.

These measurements have suffered, however, from the difficulties of using a proper standard for normalization of the neutron flux and the sometimes large self shielding and multiple scattering effects that have to be accounted for.

In the present experiment we report the results of such measurements on four different nuclei using the activation method and counting intensities for selected strong gamma rays emitted in the decay of the product nuclei or their daughters.

The cross sections studied were those of In-115, I-127, Au-197 and U-238. Two main points dictated the selection of the nuclei to be used. U-238 was studied because of the importance of this cross section in reactor calculations. The other three were studied since they are widely used as standards in capture measurements.

## II. Experiment

The availability of a strong neutron beam ( $\sim 10^7$  n/sec) allows the use of thin targets to obtain adequate counting statistics. This reduces multiple scattering effects considerably. The neutron beam was derived from the High Flux Beam Reactor at Brookhaven through a filter composed of 9 inches of iron, 14 inches of aluminum and 2 inches of sulfur. A sheet of cadmium, 0.8 mm thick, was placed at the exit opening of the neutron collimator, which has a square cross section area of 1" x 1".

The neutron beam energy profile derived from such a filter is shown in Fig. 1. The flux is seen to peak at about 24.25 keV and to have a full width at half maximum of 2 keV. The beam is free of thermal neutron as well as gamma contamination. The fast neutron component is measured at  $1.4 \times 10^{-3}$  of the total flux, while the  $\gamma$  background is less than 0.1 mR/hr.

Because of this distribution in the neutron flux, one has to keep in mind that the cross sections reported here are averaged over the energy interval covered by the neutron beam and weighted by the transmitted flux distribution. The samples and a standard of similar area were placed in the beam, at  $45^\circ$  with the direction of incidence of the neutron beam. Samples either were larger than the beam cross section, which was  $1.25'' \times 1.25''$  at the sample position, and thus intercepted the full neutron beam, or smaller than the beam size and thus were immersed completely in the neutron beam.

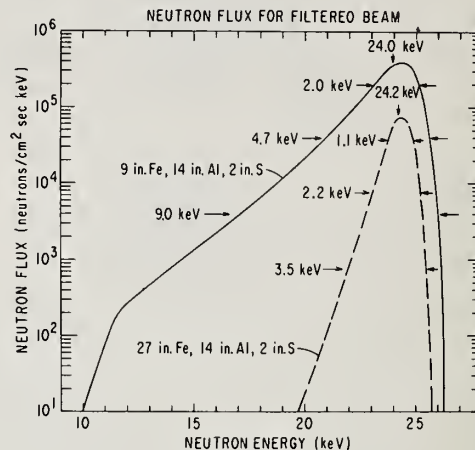


Fig. 1. Energy distribution of the iron-filtered flux. The 9" filter was used for these measurements.

The sample was viewed by a  $12\text{ cm}^3$  germanium detector whose axis was  $90^\circ$  with the neutron beam. The detector viewed the sample through a two inch  $^6\text{LiH}$  neutron shield. Gamma spectra were accumulated both during the irradiation of the sample and the subsequent decay after the beam was turned off.

The detector efficiency was determined, for the same geometry, using a series of sources with  $\gamma$ -cascades overlapping the region of interest. The portion of the efficiency curve pertinent to these measurements is shown in Fig. 2, which includes the effect of geometry and shielding.

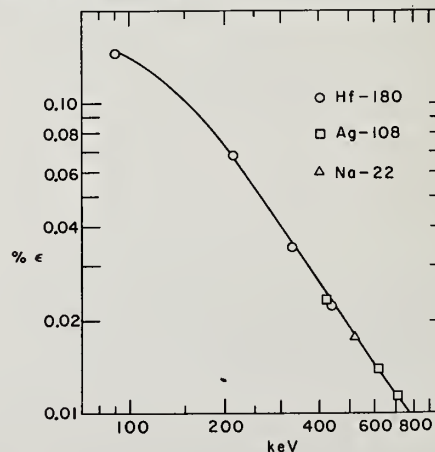


Fig. 2. The efficiency curve for the GeLi detector.



As mentioned above one of the largest sources of uncertainty in activation measurements is the value for the standard cross section used in the experiment. For a standard the  $^{10}\text{B}(n,\alpha\gamma)^7\text{Li}$  reaction was selected since this cross section is well established. A total cross section of 5.9175 barns and a partial  $(n,\alpha\gamma)$  cross section of 3.4875 barns as derived from INDEF B-III tabulations, were used.<sup>1</sup>

Boron samples were made of boron powder between two glass plates. The glass was checked for boron content and was determined to be boron-free. The sample was chemically and isotopically analyzed for boron and  $^{10}\text{B}$  content. It was found to be 93.14% boron of which 92.818% was boron-10. This sample was used for measuring the gold activation cross section.

Once a value for the gold cross section was established it was used in turn in conjunction with the other three samples as a standard. This was done to avoid the tendency toward settling exhibited by the powder samples, as well as the problem of water absorption and the effects of sample holder walls.

The branching ratios for the different gamma rays emitted in the decay process were taken from the Table of Isotopes compilation.<sup>2</sup>

Typical counting statistics in the experiment ranged from 0.5% for gold to 2.4% for uranium. Errors in sample thickness and non-uniformities were less than 2.0%. Relative detector efficiency error estimates ranged from negligible (for  $^{115}\text{In}$ ) to 7% for U-238, while errors in half-lives and branching ratios were in the range of 1.0 to 3.0%. Absorption corrections for neutrons and  $\gamma$ -rays were typically less than 5%, except for U-238 where absorption corrections of up to 12% for the low energy  $\gamma$ -rays had to be applied.

### III. Results

#### $^{197}\text{Au}(n,\gamma)^{198}\text{Au}$

The sample consisted of a gold sheet  $1.48 \times 10^{-3}$  atoms/barn thick combined with a boron sample which was  $3.24 \times 10^{-3}$  atoms/barn thick. We measured the intensity of the 412 keV line, following Au-198 beta decay against the 478 keV gamma ray emitted in the  $^{10}\text{B}(n,\alpha\gamma)^7\text{Li}$  process. The sample was irradiated for a period of 61 hours while the gamma ray spectrum was being recorded. Spectra were also recorded during the decay of  $^{198}\text{Au}$  for a period of 129 hours.

A third spectrum was obtained with a carbon scatterer in the beam and was used to obtain the beam-dependent room background contribution to the 478 keV boron line. The beam independent room background, which arises from the capture in boron of slow neutrons present on the experimental floor of the reactor, was estimated from the beam-off run while the sample was in place in front of the detector. This correction amounted to approximately 4%.

Using the above-mentioned values for the boron cross section and correcting for the neutron and gamma ray attenuation in the sample, one obtains a cross section of  $630 \pm 17$  mb, exclusive of error in the  $^{10}\text{B}$  standard.

#### $^{238}\text{U}(n,\gamma)^{239}\text{U}$

The strongest gamma ray emitted in the decay of  $^{239}\text{U}$  has an energy of 75 keV. It is difficult to utilize this line in an activation measurement due to the large background expected at this energy in addition to the large variation in detector efficiency

relative to the 478 keV boron line energy or the alternative 412 keV gold line energy which we use as standards. However, the daughter nucleus  $^{239}\text{Np}$  decays, emitting in the process a large number of higher energy gamma rays, representing transitions in the daughter nucleus Pu-239. Figure 3 shows the portion of the spectrum of interest to this experiment. The 228 keV and the 278 keV lines are the strongest useable lines in the spectrum.

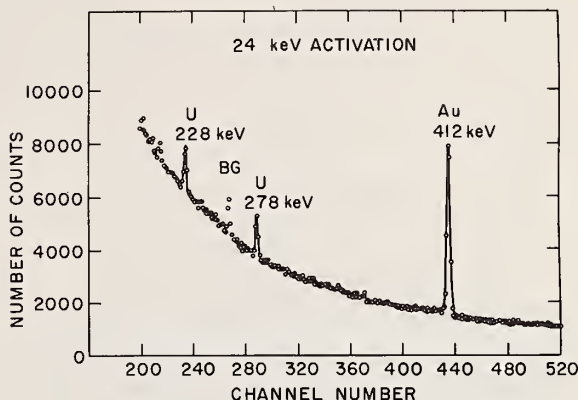


Fig. 3. A portion of the gold-uranium spectrum.

Two separate measurements were carried out. The first measured the uranium cross section relative to that of boron-10. The second used gold as a standard. The uranium samples in both experiments were  $4.7 \times 10^{-4}$  atoms/barn thick. The boron sample was the same used in conjunction in the gold measurement. The sample was irradiated for 65.5 hours. The decay spectrum was accumulated for 46.5 hours.

In the second measurement the sample was made small enough to be entirely covered by the neutron beam. The gold sample was  $6.13 \times 10^{-4}$  atoms/barn thick. The samples were irradiated for a period of 55 hours. The decay run was 84 hours. The two measurements agreed within statistical errors. The cross section averaged over the two measurements was found to be  $475 \pm 36$  mb.

#### $^{115}\text{In}(n,\gamma)^{116\text{m}}\text{In}(54.0 \text{ min} + 2.2 \text{ sec})$

The cross section for populating the 60 keV isomeric state in In-116 was determined by counting the 417 keV gamma ray relative to the 412 keV gold line. Figure 4 shows that portion of the spectrum relevant to this experiment. Three separate measurements were taken with different sample sizes and thicknesses. Gold was used as a standard in all three measurements. The thickest gold sample was  $1.45 \times 10^{-3}$  atoms/barn thick, while the In samples were less than  $4.85 \times 10^{-4}$  atoms/barn thick. The runs were typically about 20 hours irradiation time and a few hours decay time. A cross section of  $469 \pm 28$  mb was obtained from the average of three measurements.

#### $^{127}\text{I}(n,\gamma)^{128\text{I}}$

Iodine was obtained in powder form and packaged between glass plates. The 441 keV gamma ray emitted in the decay of  $^{128}\text{I}$  was used to measure the activation cross section.

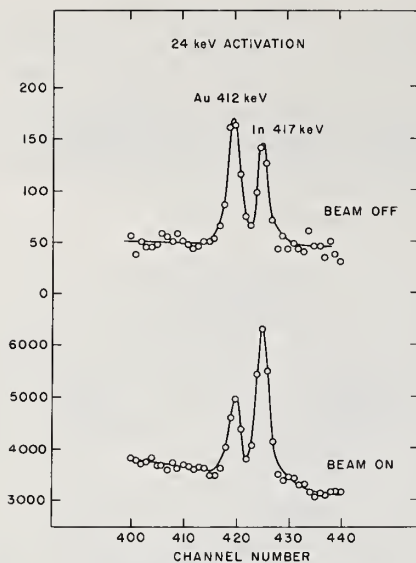


Fig. 4. A portion of the gold-indium spectra.

Two measurements were carried out; one relating to the cross section of gold, and the second relative to the cross section of In. The I samples were  $4.80 \times 10^{-3}$  atoms/barn thick while the gold was  $1.54 \times 10^{-3}$  atom/barn and the indium was  $5.84 \times 10^{-4}$  atoms/barn thick. The runs consisted of a 22 hour irradiation time for the gold-reference run and two hour irradiations for the In-reference run. Decay times of a few half lives were taken. An average cross section of  $722 \pm 47$  mb was obtained when averaging the two runs.

#### IV. Discussion of Results

##### $^{197}\text{Au}$

The present result of  $630 \pm 17$  mb is in good agreement with the results of Macklin<sup>3</sup> at Oak Ridge. Macklin has measured the Au capture cross section relative to a  $^6\text{Li}$  flux monitor. When this cross section, measured in 250 eV intervals, is folded into the spectral distribution of the 24 keV Fe-filtered beam, a value of 622 mb is obtained. The agreement between the two methods is excellent.

##### $^{238}\text{U}$

The interpolated value for  $^{238}\text{U}(n,\gamma)$  at 24.3 keV in the ENDF/B IV evaluation<sup>4</sup> is 487 mb. The present value of  $475 \pm 36$  mb is in good agreement with this evaluation.

##### $^{127}\text{I}$

Activation results with a Sb-Be source from Robertson<sup>5</sup> yield a value of  $832 \pm 26$  mb, while the corrected sphere transmission results of Schmitt and Cook<sup>5</sup> yield  $768 \pm 90$  mb. The same data as interpreted by Bogart and Semler<sup>6</sup> yield  $800 \pm 80$  mb. The present result of  $722 \pm 47$  mb is significantly lower than the Sb-Be measurement, but in agreement with the transmission measurements.

##### $^{115}\text{In}$ (54 min + 2.2 sec)

This activity can be accurately measured by the

present technique since the daughter  $^{116}\text{Sn}$  contains a  $\gamma$ -ray at 417 keV, close to 412 keV Au standard. The present value of  $469 \pm 28$  mb is lower than the value of  $580 \pm 40$  reported by Chaubey and Seghal, who used an Sb-Be source. Their value is, however, based on  $\sigma_{\text{act}}(\text{I}) = 820$  mb at 24 keV. Renormalized to the value measured here, the Chaubey and Seghal result would be  $511 \pm 35$  mb, in reasonable agreement with our measurement.

#### References

- \*Work supported by the Energy Research and Development Administration.
- 1M. K. Drake, ENDF/B III Cross Section Measurement Standards, ENDF-179, BNL 17188.
- 2C. M. Lederer, J. M. Hollander, and I. Perlman, "Table of Isotopes" 6th Ed. John Wiley and Sons, N. Y. 1967.
- 3R. L. Macklin, private communication.
- 4ENDF/B Summary Documentation, ENDF-201, BNL 17541 (Version IV revisions in Press).
- 5J. C. Robertson, Nucl. Phys. **71**, 417-425 (1965).
- 6D. Bogart and T. T. Semler, Conf. on Neutron Cross Section Technology, March 22-24, 1966, USAEC Conf. 660303, Book 1 page 502.
- 7A. K. Chaubey and M. L. Seghal, Nucl. Phys. **66** 267 (1965).

#### Note Added in Proof:

Two recent evaluations of branching ratios appeared shortly after the above results were obtained. These were the evaluations for the intensities of the 228 and 278 keV transitions following beta decay of  $^{239}\text{Np}$  by R. G. Helmer and R. C. Greenwood, in Nuclear Technology **25** p. 258, Feb. 1975, in which the following intensities were reported: 228 keV (11.3 $\pm$ 2%) and 278 keV (14.3 $\pm$ 2%). Furthermore Carlson, Talbert, and Raman have re-evaluated the nuclear data sheets for A=116 in Nuclear Data Sheets **14**, 247 (1975), and give a branching ratio of 32% for the 417 keV  $\gamma$ -ray following  $^{116}\text{In}$  (54.0 min) decay. These values result in significant changes for  $^{238}\text{U}$  and  $^{115}\text{In}$  cross sections, and a change in the  $^{127}\text{I}$  cross section, since one of measurements of this quantity were made relative to indium. The corrected values are as follows:  $^{238}\text{U}$ ,  $500 \pm 38$  mb;  $^{115}\text{In}$  (54.0 min + 2.2 sec)  $528 \pm 32$  mb; and  $^{127}\text{I}$ ,  $767 \pm 50$  mb. These corrections do not alter the conclusions of the present paper, except to improve significantly the agreement with previous measurements of indium and iodine cross sections.



D. M. Drake and E. D. Arthur  
Los Alamos Scientific Laboratory  
Los Alamos, New Mexico 87544

I. Bergqvist  
University of Lund  
Lund, Sweden

D. K. McDaniels and Philip Varghese\*\*  
University of Oregon  
Eugene, Oregon 97403

The spectrum of gamma rays emitted by  $^{209}\text{Pb}$  from 11-MeV neutron capture has been measured with a Ge(Li) detector. Although the statistical quality of the data is poor, it seems apparent that two-particle, one-hole states, as well as single-particle states, play a prominent role in fast neutron capture in  $^{208}\text{Pb}$ .

(Nuclear reactions  $^{208}\text{Pb}(n,\gamma)^{209}\text{Pb}$   $E_n = 11.2$  MeV; measured capture gamma rays resolution approximately 80 keV)

An earlier measurement<sup>1</sup> of the  $\gamma$ -ray spectrum following radiative capture of fast neutrons by  $^{208}\text{Pb}$  using a pulsed beam of neutrons from 6 to 15 MeV and a large NaI spectrometer seemed to agree with the primary predictions of various semidirect capture theories,<sup>2</sup> i.e., strong transitions to single-particle states and giant resonance-type excitation functions. However, theoretical fits to results of a similar experiment,<sup>3</sup>

$^{40}\text{Ca}(n,\gamma)^{41}\text{Ca}$ , were unsatisfactory either in magnitude or shape.

In order to test whether a different type of coupling between the incident particle and the vibration mode of the nucleus could be used to better fit the

$^{208}\text{Pb}$  data, calculations were made<sup>4</sup> using two different models, one emphasizing a surface-type interaction and the other a volume interaction. Although the fits to the experimental cross sections were not greatly affected, these calculations showed that the relative strengths of two single-particle states,  $3d_{5/2}$  and  $1j_{15/2}$  (separated by about 150 keV), differ by about a factor of three, depending on whether surface or volume coupling is used.

Using volume coupling the predicted cross section for the  $3d_{5/2}$  state is about 3.4 times larger for neutrons of 11.2 MeV than that predicted by the surface coupling, while the difference in the predicted values of the  $1j_{15/2}$  cross section is only a few percent. The resolution of the NaI spectrometer in Ref. 1 was not sufficient to separate transitions to these states.

In order to distinguish between these two coupling terms we have used a Ge(Li) detector to measure the capture gamma-ray spectrum with 11.2-MeV incident neutrons.

The experimental arrangement is much the same as that of Ref. 1, except that the Ge(Li) detector replaced the NaI detector. The spectral resolution is determined primarily by two factors: the finite energy spread of the neutron source,  $^3\text{H}(p,n)^3\text{He}$ , due to energy loss of the protons in the tritium gas, and

the kinematic energy spread caused by the finite solid angle subtended by the sample.

In order to obtain sufficient resolution to separate these two states, we had to fill the target cell with about one third the amount of tritium used in Ref. 1, and move the sample about 1.5 times farther away from the neutron source. Both these procedures reduce the counting rate and along with the low efficiency of the Ge(Li) detector and the small capture cross section, contribute to data with poor statistical quality.

Figure 1 shows the net spectrum (sample-out spectrum subtracted) for a 50-hr run. The solid lines are drawn with approximate experimental resolution to indicate where known single-particle states<sup>5,6</sup> should appear. The heights of these peaks indicate rough correspondence to the calculated relative intensities, corrected for spectroscopic factors and efficiency, predicted by the surface coupling semidirect model.

The pair of states,  $d_{5/2}$  and  $j_{15/2}$ , appear twice, once as a single escape and once as double escape peaks. Either pair seems to indicate that their strengths are about equal, and that the surface form of interaction may be preferred over the volume form.

The states labeled A and B appear to be two-particle, one-hole states, matching well with the two-particle, one-hole states found in the  $^{210}\text{Pb}(d,p)^{209}\text{Pb}$  reaction,<sup>5</sup>  $(g_{9/2})^2(p_{3/2})^{-1}$  and  $(g_{9/2})^2(p_{1/2})^{-1}$ .

The semidirect model of radiative capture contains only single-particle final states, and it was speculated in Ref. 2 that the poor fit to the  $^{40}\text{Ca}(n,\gamma)^{41}\text{Ca}$  could be caused by two-particle, one-hole states such as found in  $^{40}\text{Ca}(d,p)^{41}\text{Ca}$ .<sup>7</sup>

If these spectra are confirmed by future experiments that are more statistically significant, it will be necessary to include two-particle, one-hole states, as well as single-particle states in semidirect capture calculations.

\*Work done under the auspices of the U.S. Energy Research and Development Administration.

\*\*Work partially supported by a grant from the National Science Foundation.



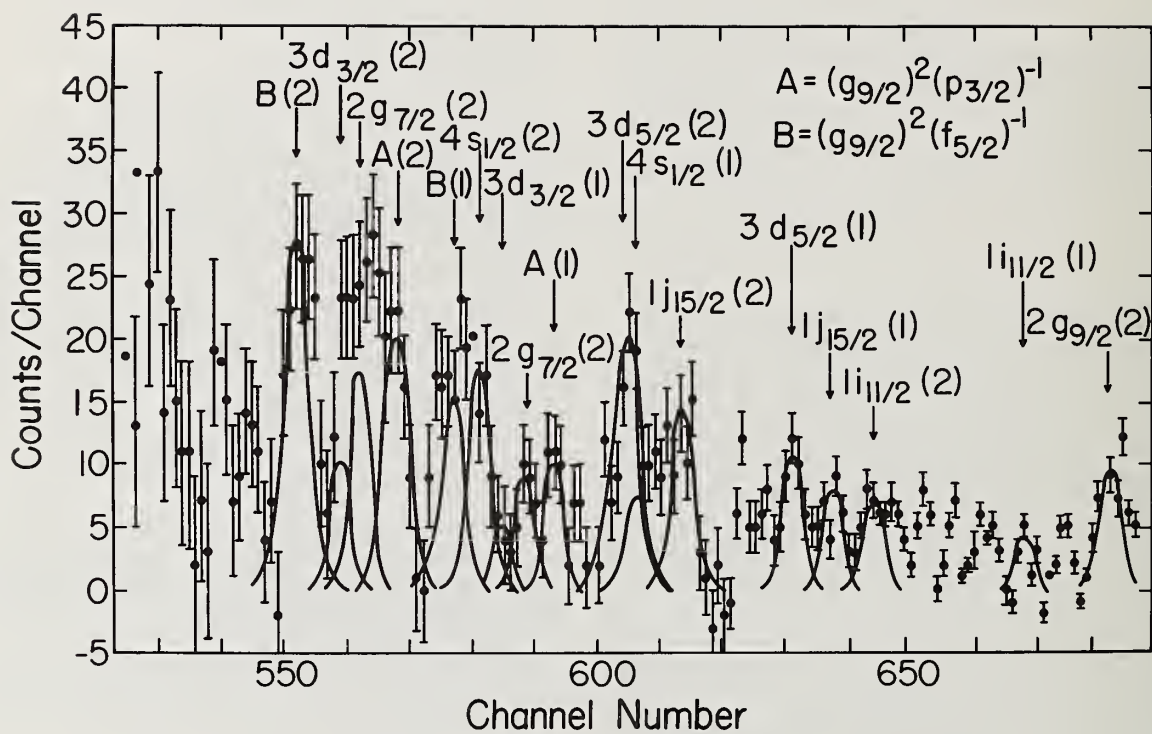


Fig. 1 Net gamma-ray height spectrum for  $^{208}\text{Pb} + 11.2\text{-MeV}$  neutrons. Single-particle state transitions are identified with (1) and (2) indicating single and double escape peaks. A and B are tentatively identified as 2-particle, 1-hole states.

## References

1. I. Bergqvist, D. M. Drake, and D. K. McDaniels, Nucl. Phys. A191, 641 (1972).
2. C. F. Clement, A. M. Lane, and J. R. Rook, Nucl. Phys. 66, 273 (1965); G. E. Brown, Nucl. Phys. 57, 339 (1964); A. A. Lushnibov and D. F. Zaretsky, Nucl. Phys. 66, 35 (1965).
3. I. Bergqvist, D. M. Drake, and D. K. McDaniels, Nucl. Phys. A231, 29 (1974).
4. G. Longo and F. Saporetti, Nucl. Phys. A119, 530 (1973).
5. G. Igo, P. D. Barnes, E. R. Flynn, and D. Armstrong, Phys. Rev. 177, 1831 (1969).
6. G. Igo, E. R. Flynn, B. J. Dropesky, and P. D. Barnes, Phys. Rev. C3, 1831 (1971).
7. T. A. Belate, A. Sperduto, and W. W. Buechner, Phys. Rev. 139, 380 (1965).

K. Rimawi and R. E. Chrien  
Brookhaven National Laboratory  
Upton, New York 11973

The characteristics of neutron capture  $\gamma$ -ray spectra near  $E_n = 24.3$  keV are discussed. The E-1 transitions following the capture of p-wave neutrons show a marked preference for populating low-lying states with an s or d single-particle character. This preference introduces a significant correlation between partial (n, $\gamma$ ) cross sections and the neutron reduced widths for final states as measured in the (d,p) reaction.

(Neutron capture  $\gamma$ -rays;  $E_n = 24.3$  keV; width correlations)

For s-wave capture in heavy nuclides, the behavior of the partial cross sections for radiative transitions to discrete final states is seen to follow reasonably well the predictions of a statistical decay model; namely that the partial widths  $\Gamma_{\gamma lf}$  follow an approximately Porter-Thomas distribution and that correlations between partial widths are small and negligible.

The situation for p-wave capture near the 3p giant neutron resonance is markedly different. In this region the low-lying states have a predominantly  $\ell=0$  and  $\ell=2$  character; the strengths of  $\gamma$ -rays feeding these states are correlated with the single particle reduced widths of these states as measured by the (d,p) reaction. Recent summaries of the experimental evidence have been given in a number of review papers.<sup>1,2</sup>

The iron filter has been used to examine a series of nuclides near the 3p resonance:  $^{92}\text{Mo}$ ,  $^{94}\text{Mo}$ ,  $^{96}\text{Mo}$ ,  $^{98}\text{Mo}$ ,  $^{93}\text{Nb}$  and  $^{89}\text{Y}$ . Examples of these spectra are shown in Figs. 1 and 2. Figure 1 illustrates the capture spectrum for  $^{92}\text{Mo}$  at 24.3 keV. The spectrum

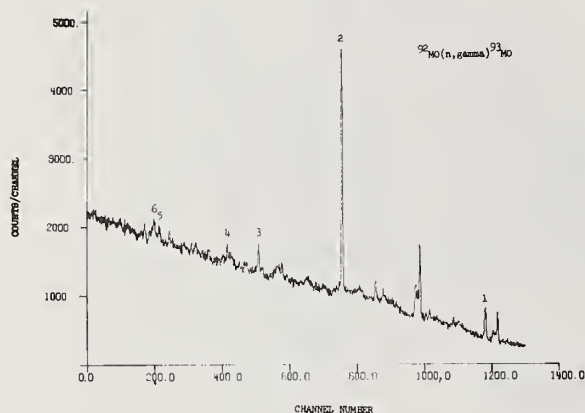


Fig. 1. A portion of the capture spectrum for 24.3 keV neutrons on  $^{92}\text{Mo}$ .

is dominated by a strong transition to the s-1/2 level in  $^{93}\text{Mo}$  at 941 keV. Figure 2 illustrates p-wave capture in  $^{93}\text{Nb}$ . Consistent with the high level density of  $^{94}\text{Nb}$ , we see a much more complex spectrum. Nevertheless we can observe, qualitatively that all six states of the ground state configuration  $\pi(g_9/2)^3$ , are populated strongly, including the  $2^+$  state at 334 keV, and the  $7^+$  state at 79 keV.

A striking pattern for these radiative transitions is noted when we compare the average (n, $\gamma$ ) strengths to the (d,p) reduced widths in these nuclides. Figures 3-6 illustrate the patterns for the Mo isotopes while Fig. 7 shows the result for Nb. In each of these cases a significant correlation

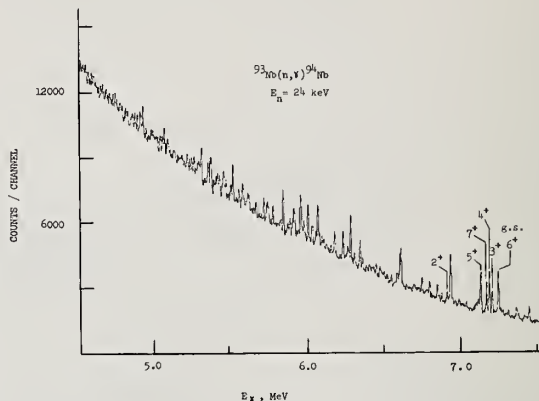


Fig. 2. A portion of the capture spectrum for 24.3 keV neutrons on  $^{93}\text{Nb}$ .

(shown on the figure) is obtained, ranging from  $\rho = 0.97$  for  $^{98}\text{Mo}$  to 0.47 for  $^{93}\text{Nb}$ . The results for  $^{89}\text{Y}$ , for which our analysis is not complete, also shows qualitatively a strong population of the  $\ell=2$  single particle states.

We have estimated the partial cross sections for these reactions by measuring the incident flux via the  $^{10}\text{B}(n,\alpha\gamma)^7\text{Li}$  reaction. Some of the partial cross sections are comparatively large, especially to the s-1/2 states of the Mo isotopes. We obtain, for example, 12.3 mb for the transition to the 941 keV  $1/2^+$  level of  $^{93}\text{Mo}$ , and 8.2 mb to the  $1/2^+$  ground state of  $^{99}\text{Mo}$ .

The interpretation of these cross sections in terms of photon strength functions is somewhat more complicated at high energies, where  $\Gamma_n > \Gamma_\gamma$ , than is the case in the low energy region. Neglecting an s-wave contribution followed by M-1 radiation, we can write

$$\langle \sigma(n,\gamma) \rangle_p = \frac{2\pi^2 \lambda^2 k^2 R^2}{1 + k^2 R^2} \sqrt{E_n} S^1 \sum_{J,J'} \frac{\Gamma_\gamma(J)}{\Gamma(J)} f_J$$

where  $S^1$  denotes the p-wave strength function and  $f_J$  the resonance fluctuation factor, and the other symbols have their usual meaning. The summations are over spin and channel spin. By rewriting this expression, we obtain

$$\langle \sigma(n,\gamma) \rangle_p = C E_\gamma^3 \sum_{J,J'} f_J / \bar{\Gamma}(J)$$



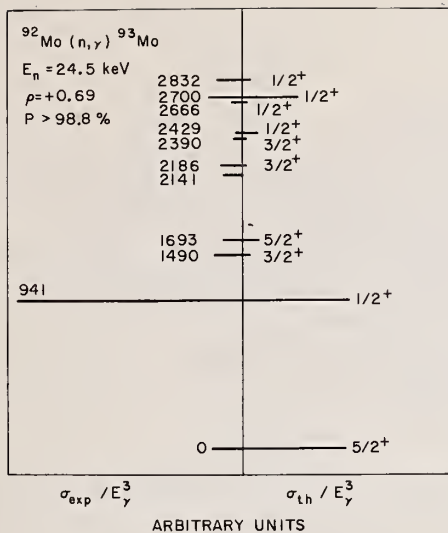


Fig. 3.  $^{93}\text{Mo}$

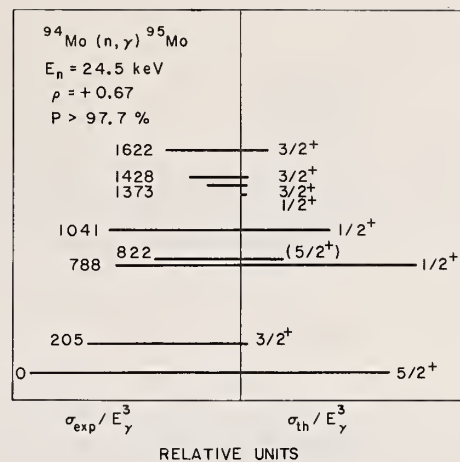


Fig. 4.  $^{94}\text{Mo}$

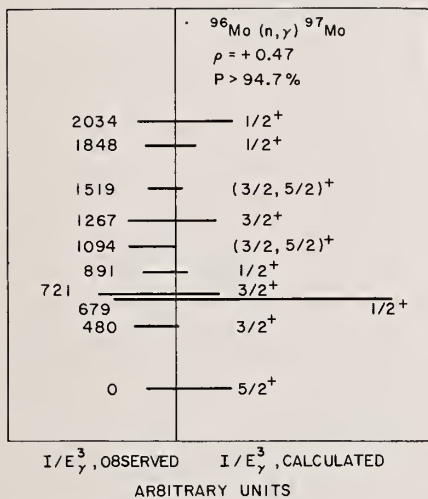


Fig. 5.  $^{96}\text{Mo}$

Partial cross sections for (n,γ) cross sections on Mo isotopes compared to (d,p) stripping widths.

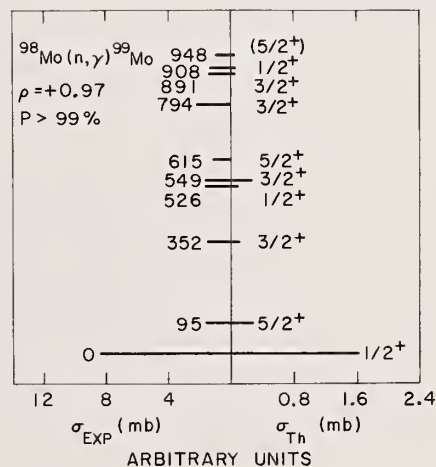


Fig. 6.  $^{98}\text{Mo}$

$$\text{with } C = 2\pi^2 \chi^2 \left( \frac{k^2 R^2}{1 + k^2 R^2} \right) \sqrt{E_n} \frac{D_0}{2(2I+1)} S^1 A^{2/3} k_{E1}$$

$$k_{E1} = \bar{\Gamma}_\gamma / E_\gamma A^{2/3} D$$

The value of  $k_{E1}$  to be inserted in the above expression depends on the model assumed for photon interactions with the nucleus. If we wish to take account of the effect of the giant E-1 resonance, we use the expression for  $k_{E1}$  given by Bollinger:<sup>3</sup>

$$k_{E1} = 2.5 E_\gamma^2 A^2 \times 10^{-15} \text{ MeV}^{-3}.$$

The calculated cross sections from this model fall generally below the observed cross sections; in  $^{92}\text{Mo}$  for example the measured cross sections are, on average, a factor of 1.5 higher than the prediction. Similarly the application of a simple valence model does not account for the observed cross sections. We know also from previous measurements<sup>4,5</sup> that the

valence model cannot account for the observed correlations in  $^{92}\text{Mo}$  and  $^{93}\text{Nb}$ .

It is evident, therefore, that the enhanced and correlated transitions occurring in this mass region indicate the presence of doorway states in the reaction mechanism, and imply the existence of intermediate structure in the p-wave capture cross sections of these nuclides.

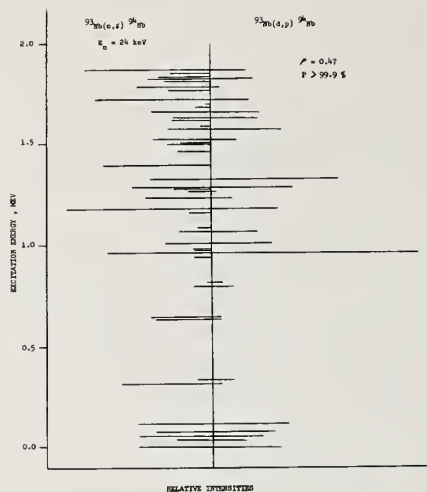


Fig. 7. Partial cross sections for  $^{93}\text{Nb}(n,\gamma)$  compared to  $(d,p)$  stripping widths.

## References

- \*Work supported by the Energy Research and Development Administration.
- <sup>1</sup>A. M. Lane in Proceedings of the Second International Symposium on Neutron Capture  $\gamma$ -Ray Spectroscopy and Related Topics, Petten, the Netherlands, Sept. 2-6, 1974, to be published.
  - <sup>2</sup>R. E. Chrien in Nuclear Structure Study with Neutrons, Plenum Press, London and New York 1974, p. 101.
  - <sup>3</sup>L. M. Bollinger, Proceedings of the Intl. Conf. on Photonuclear Reactions and Applications, Conf. #730301, (1973), p. 783.
  - <sup>4</sup>O. A. Wasson and G. G. Slaughter, Phys. Rev. **C8**, 297 (1973).
  - <sup>5</sup>R. E. Chrien, K. Rimawi, and J. B. Garg, Phys. Rev. **3C**, 2054 (1971).

F. H. Fröhner

Institut für Angewandte Kernphysik  
Kernforschungszentrum Karlsruhe

Previously reported neutron capture data were analyzed up to 150 keV for  $^{56}\text{Fe}$ ,  $^{58}\text{Ni}$  and  $^{60}\text{Ni}$ , and up to 30 keV for  $^{61}\text{Ni}$  with a newly developed multilevel shape analysis code with the aim to improve and extend older area analysis results, to check whether the reported correlations between neutron and radiation widths are not produced e.g. by neglect of multi-level effects in the older self-shielding and multiple-scattering calculations and to search for channel effects such as asymmetric peak shapes.

NUCLEAR REACTIONS  $^{56}\text{Fe}$ ,  $^{58,60,61}\text{Ni}(n,\gamma)$ ,  $E = 6\text{--}150$  keV, deduced  $\Gamma_\gamma$ , width correlations. Shape analysis.

### Introduction

Resonance capture of keV neutrons by medium-weight nuclei has been studied systematically at the Karlsruhe 3 MV Van de Graaff accelerator for a number of years, mainly for fast-breeder and also for astrophysics applications.<sup>1-3</sup> Capture yields and resonance parameters for  $^{47}\text{Ti}$ ,  $^{56}\text{Fe}$ ,  $^{58}\text{Ni}$ ,  $^{60}\text{Ni}$  and  $^{61}\text{Ni}$  were first reported in 1970.<sup>1</sup> The radiation widths presented at that time were new and could not be compared to other authors' results except for the 28 keV resonance of  $^{56}\text{Fe}$  where agreement was good.<sup>4-6</sup> When our results on  $^{60}\text{Ni}$  were confirmed by Stieglitz et al.<sup>7</sup>, however, it became clear that the apparent positive correlation between neutron widths and radiation widths observed for  $^{60}\text{Ni}$  (and for several chromium isotopes<sup>7,8</sup>) had to be taken seriously. In view of the great difficulties, however, which affect capture cross section measurements on these nuclei with their very much (100 or 1000 times) higher scattering cross section there remained some suspicion that the correlations might have been introduced by some experimental or data analysis error. Although the groups at KFK and at RPI had worked with different accelerators, hence on different flight time scales, and had employed different flux determination methods, there was a number of similarities: both used the time-of-flight technique, large liquid scintillators for capture gamma ray detection, and single-level area analysis. It was argued<sup>9</sup> that underestimation of rapid capture of resonance-scattered neutrons in the vicinity of the capture sample or the neglect of level-level interference effects in the very large self-shielding and multiple-scattering corrections could be sources of error. The present paper contains at least a partial answer to these arguments.

### Data Reduction

The data acquisition equipment, the sample specifications and the reduction of raw data were described earlier<sup>1</sup>. The experimental conditions are summarized in Table 1.

Table 1 - Experimental Conditions

Source reaction	$^7\text{Li}(p,n)$ , white neutron spectrum
Accelerator	pulsed 3 MV Van de Graaff pulse length : 1 ns repetition rate : 250 kHz
Flight path	2.05 m
Reference reaction	$^{197}\text{Au}(n,\gamma)$

Capture yields were measured with enriched samples relative to gold. The reference cross section used was that

determined by Kompe.<sup>10</sup> The small (few percent) time-dependent background caused by capture of scattered neutrons in the detector was determined with a pure scatterer (graphite) with matched scattering properties. Both pulse-height and flight-time information was recorded.

In addition to the usual background subtraction the following corrections were applied to the data :

- (1) Spectrum fractions above the detector threshold of 3 MeV gamma ray energy were determined for each time channel with the help of average pulse height data extending down to 0.5 MeV.
- (2) Intrinsic detector efficiencies  $\epsilon_i$  for the various target nuclei were obtained by estimation of cascade escape probabilities for the 800 l scintillator tank for various cascade modes. Table 2 shows the ratios  $\epsilon_i/\epsilon_i^{\text{Au}}$  obtained for strong, moderately strong and negligible high-energy transitions. The observed pulse-height distributions for individual resonances (examples are given in<sup>1</sup>) were divided into three categories - peaked, intermediate and flat - and the corresponding efficiency ratios from Table 2 were then applied to the detection efficiency used in the shape analysis (see below). This admittedly crude procedure is assumed to eliminate most of the effect of intrinsic efficiency fluctuations caused by cascade mode variations from level to level.

Table 2 - Binding Energies and Estimates of Intrinsic Efficiency Ratios for KFK 800 l Scintillation Detector

Reaction	Neutron Binding Energy (MeV)	$\epsilon_i/\epsilon_i^{\text{Au}}$ estimated for contributions from high-energy transitions of		
		50 %	10 %	0 %
$^{56}\text{Fe} + n$	7.646	0.81	0.91	0.98
$^{58}\text{Ni} + n$	8.999	0.79	0.90	0.97
$^{60}\text{Ni} + n$	7.819	0.81	0.91	0.98
$^{61}\text{Ni} + n$	10.596	0.77	0.89	0.95
$^{197}\text{Au} + n$	6.512	1	1	1

- (3) Capture of scattered neutrons in the vicinity of the sample is only partially corrected for by subtraction of the graphite scatterer counts because scattering is smooth for carbon (and the gold reference sample) but has resonance structure for the capture sample. It is true that capture of scattered neutrons after moderation in the tank should exhibit no time correlation with the resonances of the capture sample. Due to the detector bias and the boron poisoning of the scintilla-



tor this background is small anyway, as confirmed by the quite flat count rate distribution observed with the graphite sample. Rapid capture of unmoderated resonance-scattered neutrons in the vicinity of the sample, however, retains appreciable time correlation with the resonances. A detailed calculation based on the dimensions and cross sections of the bronze sample containers and the aluminum through-tube of the tank showed that non-negligible corrections were required for a few broad s-wave resonances: 12% at 27.6 keV, 14% at 83 keV for  $^{56}\text{Fe}$ , 13% at 15.4 keV for  $^{58}\text{Ni}$  and 12% at 12.3 keV for  $^{60}\text{Ni}$ .

The uncertainties of the capture yields due to the principal error sources are summarized in Table 3.

Table 3 - Estimated capture yield uncertainties	
Reference cross section	3-8%
Spectrum fraction	3-8%
Intrinsic efficiency	4-7%
Scattered-neutron background	1-5%
Total, including statistics	10-20%

#### Capture Shape Analysis

In order to make the resonance analysis more efficient and reliable, especially with respect to

- interpretation of incompletely resolved resonance multiplets and
- inclusion of multi-level effects in the self-shielding and multiple-scattering calculations

an automatic shape-fitting program for capture yield data was written. This code, FANAC,<sup>11</sup> is designed in close analogy to the well-tested FANAL program<sup>12</sup> that has been in use at Karlsruhe since 1970 for multi-level shape analysis of neutron transmission data. Cross sections are calculated with conventional multi-level R matrix formulae, narrow peaks are Doppler broadened. First-collision yields are obtained analytically from the capture and total cross sections, multiple-collision capture yields by Monte Carlo simulation including careful bookkeeping of energy changes and time delays during multiple-collision events. Calculated yields are resolution-broadened and then compared to the measured data. An efficiency factor associated with each resonance allows for variations of detector sensitivity from level to level. Data from several experimental runs, e. g. with different resolution or sample thickness, can be fitted simultaneously.

#### Results

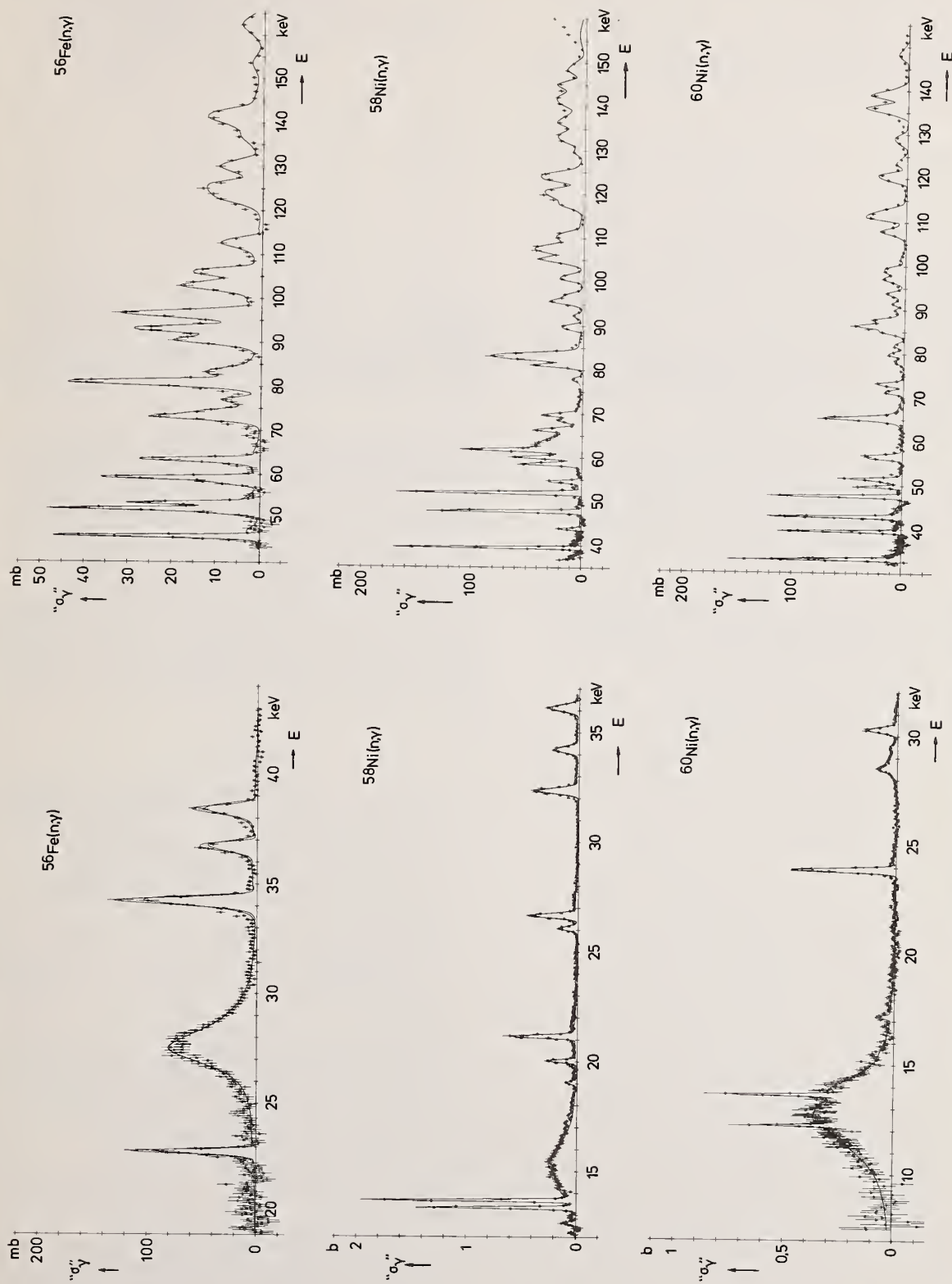
Figs. 1-4 show the capture yield data reported earlier.<sup>1</sup> The fits obtained with the FANAC program are represented by solid lines, they are seen to be reasonably good. The fact that the pedestals caused by multiple-collision capture on the high-energy side of isolated narrow resonances (compare e. g.  $^{58}\text{Ni}$ ) are well reproduced lends credibility to the multiple scattering calculations. The goodness-of-fit criterion  $\sqrt{(\chi^2/\nu)} \approx 1$  ( $\chi^2$ : sum of least squares,  $\nu$ : degree of freedom, i. e. number of data points minus number of adjusted parameters) was satisfied in all cases;

values between 0.9 and 1.6 were obtained which indicated that the assumptions underlying the fits - formalism, error estimates, instrumental resolution specifications etc. - and the resulting parameters were consistent.

The parametrization obtained forms a reliable basis for the calculation of quantities such as capture cross section averages, resonance integrals, Maxwellian averages for stellar temperatures, group constants etc. It should be understood, however, that above about 70 keV for the even isotopes and above 20 keV for  $^{61}\text{Ni}$  a number of new levels had to be introduced to fit some of the peaks. Except for  $^{56}\text{Fe}$ , where high-resolution transmission data<sup>13-15</sup> showing even quite narrow (p- and d-wave) resonances allowed verification, a certain ambiguity exists as to the reality of these newly introduced levels for the other isotopes. In other words, although the parameters represent the data well for practical applications, and are free of the effects of self-shielding and multiple scattering, one must exercise caution in drawing level-statistical conclusions about level spacings, average widths etc. for the higher energies.

Full lists of the parameters found will be published elsewhere. The results on s-wave resonances that are relevant to the width correlation discussion are listed in Table 4 together with earlier results obtained by area analysis.

Table 4a - Parameters of s-wave resonances for even isotopes					
Target nucleus	$E_0$ (keV)	$\Gamma_n$ (eV)	$\Gamma_\gamma$ (eV)		
			area RPI <sup>6,7</sup>	area KFK <sup>1,2</sup>	shape KFK
$^{56}\text{Fe}$	27.6 $\pm$ 2	1400 $\pm$ 70	1.44 $\pm$ .14	1.4 $\pm$ .2	1.18 $\pm$ 15
	73.8 $\pm$ 5	540 $\pm$ 40			.62 $\pm$ 15
	83.2 $\pm$ 3	960 $\pm$ 80		.9 $\pm$ .3	.55 $\pm$ .22
	129.8 $\pm$ 4	500 $\pm$ 50			1.12 $\pm$ .16
	140.7 $\pm$ 5	2370 $\pm$ 200			1.20 $\pm$ .35
$^{58}\text{Ni}$	15.4 $\pm$ .1	1200 $\pm$ 30		2.1 $\pm$ .7	1.42 $\pm$ .18
	63.0 $\pm$ .2	3600 $\pm$ 200		3.2 $\pm$ .8	2.3 $\pm$ .3
	107.6 $\pm$ .3	1400 $\pm$ 300		3.3 $\pm$ .8	3.8 $\pm$ .9
	124.0 $\pm$ .5	700 $\pm$ 250		3.0 $\pm$ .6	3.5 $\pm$ .6
$^{60}\text{Ni}$	12.3 $\pm$ .1	2660 $\pm$ 100	3.30 $\pm$ .30	3.3 $\pm$ .4	2.65 $\pm$ .28
	28.6 $\pm$ .1	800 $\pm$ 50	1.1 $\pm$ .1	1.2 $\pm$ .3	.6 $\pm$ .15
	42.9 $\pm$ .1	120 $\pm$ 30	1.73 $\pm$ .30	1.0 $\pm$ .2	.92 $\pm$ .18
	65.4 $\pm$ .2	500 $\pm$ 150	2.43 $\pm$ .25	1.8 $\pm$ .3	1.79 $\pm$ .26
	86.3 $\pm$ .2	330 $\pm$ 25		1.5 $\pm$ .3	1.51 $\pm$ .30
	97.2 $\pm$ .3	1000 $\pm$ 200		1.0 $\pm$ .3	1.13 $\pm$ .20
	108.0 $\pm$ .3	700 $\pm$ 100		1.1 $\pm$ .3	1.35 $\pm$ .20
	155.4 $\pm$ .5	440 $\pm$ 50		.8 $\pm$ .3	.85 $\pm$ .17
	161.7 $\pm$ .5	1400 $\pm$ 200		1.8 $\pm$ .5	1.9 $\pm$ .4



Figs. 1-3 - Experimental capture data (point symbols with error bars) and multi-level R matrix fits (solid lines). Enriched samples: 99.7%  $^{56}\text{Fe}$ , .00992 nuclei/b; 99.9%  $^{58}\text{Ni}$ , .01057 nuclei/b; 99.8%  $^{60}\text{Ni}$ , .01022 nuclei/b.

Some of the preliminary area analysis results<sup>1</sup> turned out to be inaccurate, especially those for incompletely resolved multiplets (<sup>56</sup>Fe: 83.2 keV; <sup>58</sup>Ni: 63.0 and 107.6 keV; <sup>60</sup>Ni: 28.6 keV; <sup>61</sup>Ni: 17.99, 28.35 and 29.3 keV) and those affected by background from rapid capture of resonance-scattered neutrons (<sup>56</sup>Fe: 27.6 and 83.2 keV; <sup>58</sup>Ni: 15.4 and 63.0 keV; <sup>60</sup>Ni: 12.3 keV). The effect of level-level interference on the self-shielding and multiple-collision calculations was less obvious.

The detailed shape fits allow the following conclusions:

(1) The neutron widths required for the fitting procedure were taken from KFK transmission work where possible<sup>13,16</sup> or from standard sources<sup>17</sup>. In a few cases the latter values were incompatible with the capture yield data and had to be modified. Thus the recommended neutron width of the 27.6 keV level of <sup>56</sup>Fe, 1600±50 eV, was evidently too large to fit the measured capture peak and had to be replaced by 1400±50 eV, which by the way is also in better agreement with the single-level equation  $\Gamma = (E_+ - E_-) \sin 2kR'$  ( $E_+$ : peak energy,  $E_-$ : energy of the interference minimum,  $R'$ : effective channel radius) and available  $R'$  and total cross section data.

(2) On the other hand, the shape of the <sup>60</sup>Ni resonance at 12.3 keV could be very well fitted without any channel capture contribution. Recent claims that the shape of this capture peak cannot be explained without a channel capture contribution<sup>18</sup> are not supported by the present results.

(3) The same is true for suggestions that the apparent residual capture cross section between resonance peaks is due to significant potential capture. The detailed calculations show that it is mainly due to resonance capture of scattered neutrons.

The width correlations obtained with the shape analysis results are shown in Table 5.

Target nucleus	E <sub>O</sub> (keV)	J	$\Gamma_n$ (eV)	$\Gamma_\gamma$ (eV)	
				area KFK <sup>1</sup>	shape KFK
<sup>61</sup> Ni	7.15±.02	1	74±8	2.5±.5	2.55±.35
	7.58±.02	2	177±16	2.3±.6	2.23±.35
	8.75±.02	2	6±2	2.6±.8	2.31±.60
	12.67±.03	2	75±4	1.7±.4	1.72±.25
	13.68±.05	2	61±4	1.6±.4	1.65±.25
	14.06±.05	1	17±4	3.1±.5	3.20±.45
	16.61±.10	1	817±16	2.2±.4	2.07±.30
	17.99±.10	1	177±8	1.6±.5	1.4 ±.4
	18.97±.10	2	69±4	.9±.3	.78±.11
	24.73±.07	1	129±10	1.4±.3	1.41±.20
	28.35±.07	2	5±4	3.0±1.0	2.2 ±.8
	29.3 ±.1	1	409 ±22	2.4±.4	1.6 ±.3

Table 5 - Width correlation coefficients calculated from shape analysis results.

Target nucleus	J	Sample size	$\frac{\text{cov}\{\Gamma_n^0, \Gamma_\gamma\}}{\sqrt{\text{var}\{\Gamma_n^0\} \cdot \text{var}\{\Gamma_\gamma\}}}$
<sup>56</sup> Fe	1/2	5	+0.55±0.65
<sup>58</sup> Ni	1/2	4	-0.74±0.77
<sup>60</sup> Ni	1/2	9	+0.71±0.26
<sup>61</sup> Ni	1	6	-0.19±0.37
	2	6	+0.10±0.51

The errors of the correlation coefficients include the influence of the width uncertainties as well as the uncertainty due to the limited size of the statistical sample. The only statistically significant non-zero correlation between reduced neutron and radiation widths is obtained for <sup>60</sup>Ni where it turns out to be almost exclusively due to the broad level at 12.3 keV.

It appears that before non-random phenomena such as width correlations can really be established in a quantitative way one must improve the resolution of both transmission and capture data so that p- and d-wave satellites sitting on top of broad s-wave peaks can be more clearly identified and their capture contributions more reliably subtracted. The words spoken after presentation of the data on which the shape analysis reported here was based are still true - at least the second part: " - there are so many resonances that it would seem to be a semi-infinite set and it may be that not all of them will ever be parameterized. What will probably happen is that (...) other resonances will be found which have affected the parameters already determined ..." <sup>19</sup>

#### References

1. A. Ernst, F. H. Fröhner and D. Kompe, Proc. 2nd Int. Conf. on Nuclear Data for Reactors, Helsinki, 1970, vol. 1, p. 633;
2. F. H. Fröhner, cf. Report KFK-2046, 1975;
3. H. Beer, Astron. and Astrophys. **13**(1974)197;
4. M. C. Moxon, Proc. Int. Conf. on the Study of Nucl. Structure with Neutrons, Antwerp, 1965, paper 88;
5. R. L. Macklin, P. J. Pasma and J. H. Gibbons, Phys. Rev. **136**(1964)B695;
6. R. W. Hockenbury, Z. M. Bartolome, J. R. Tatarczuk, W. R. Moyer and R. C. Block, Phys. Rev. **178**(1969)592;
7. R. G. Stieglitz, R. W. Hockenbury and R. C. Block, Nucl. Phys. **A163**(1971)592;
8. H. Beer and R. R. Spencer, Report KFK-2046, 1974;
9. Panel on keV Capture of the Structural Materials Cr, Fe, Ni, Karlsruhe, 1973, Report KFK-2046;
10. D. Kompe, Nucl. Phys. **A133**(1969)513;
11. F. H. Fröhner, Report KFK-2145; 1975;
12. F. H. Fröhner, Report KFK-2129, 1975;
13. G. Rohr, E. Friedland and J. Nebe, Proc. 1st Int. Conf. on Nuclear Data for Reactors, Paris, 1966, vol. 1, p. 137;
14. J. A. Harvey, private communication;
15. N. J. Pattenden, data files of the NEA Centre de Compilation de Données Neutroniques, Saclay;
16. M. Cho, F. H. Fröhner, M. Kazerouni, K.-N. Müller and G. Rohr, Proc. 2nd Int. Conf. on Nuclear Data for Reactors, Helsinki, 1970, vol. 1, p. 619;



17. S. F. Mughabghab, D. I. Garber, BNL 325, 3rd ed., 1973, vol. 1;
18. M. Lubert, N. C. Francis and R. C. Block, Nucl. Phys. A230(1974)83;
19. W. W. Havens Jr., Proc. 2nd Int. Conf. on Nucl. Data for Reactors, Helsinki, 1970, vol. 2, p. 926.

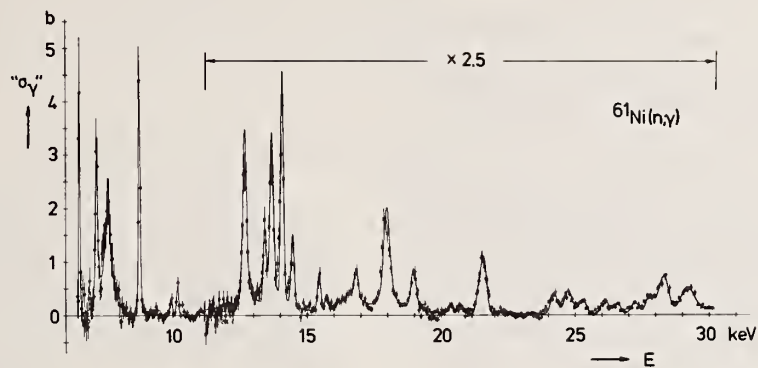


Fig. 4 - Experimental capture data (point symbols with error bars) and multi-level R matrix fit (solid line). Enriched sample, 91.8%  $^{61}\text{Ni}$ , 0.00460 nuclei/b.

$\gamma$ -RAY PRODUCTION CROSS SECTIONS FOR NEUTRON INELASTIC SCATTERING  
FROM Cr, Ni,  $^{92}\text{Zr}$ , AND  $^{94}\text{Zr}$  FROM 3 TO 6 MeV  
G. Tessler and S. S. Glickstein  
Bettis Atomic Power Laboratory  
West Mifflin, Pennsylvania 15122

Cross sections for  $\gamma$ -ray production by neutron inelastic scattering from Cr, Ni,  $^{92}\text{Zr}$ , and  $^{94}\text{Zr}$  have been measured for incident neutrons in the energy range 3-6 MeV. The  $\gamma$ -rays were detected with a 55 cm<sup>3</sup> coaxial Ge(Li) anti-Compton spectrometer located at 55° to the incident neutron direction. Background associated with neutrons scattering from the samples into the Ge(Li) detector was suppressed by the pulsed beam time-of-flight technique. Assignment of  $\gamma$ -rays to transitions from specific energy levels of the isotopes of Cr, Ni, and Zr has been made using  $\gamma$ -ray energies determined from this work and energies and level schemes reported in the literature. Many of the observed  $\gamma$ -rays could not be assigned to known levels.

(Nuclear Reactions;  $(n, n'\gamma)$ ;  $\gamma$ -Production;  $E_n = 3\text{-}6$  MeV; Cr, Ni, Zr)

Cross sections for  $\gamma$ -ray production by neutron inelastic scattering from Cr, Ni,  $^{92}\text{Zr}$ , and  $^{94}\text{Zr}$  have been measured for incident neutrons in the energy range 3-6 MeV. The experimental arrangement is shown on Fig. 1. A 5 MHz pulsed deuteron beam from the Bettis 3 MV Van de Graaff accelerator passed through a 0.000254 cm Havar foil (Havar is a high tensile strength cobalt-base alloy supplied by the Precision Metals Division of Hamilton Watch Company, Lancaster, Penna.) into a deuterium gas cell 2.235 cm long maintained at 1 atm by a continuous flow of deuterium gas. Neutrons were produced by the  $\text{D(d,n)}^3\text{He}$  reaction. The spread in neutron energy due to deuteron energy loss in the gas target was 385 keV at an average neutron energy of 3.3 MeV and 110 keV at an average neutron energy of 5.6 MeV. The scattering samples were in the form of right circular cylinders whose centers were located 5.715 cm from the near end of the gas target. The Ni and Cr samples were 2.54 cm in diameter by 2.54 cm high, the  $^{92}\text{Zr}$  sample 2.002 cm x 2.002 cm and the  $^{94}\text{Zr}$  sample 0.986 cm x 1.976 cm. The  $^{92}\text{Zr}$  sample was 95.13% enriched and the  $^{94}\text{Zr}$  sample was 96.10% enriched.  $\gamma$ -rays were detected at 55° to the incident deuteron beam direction with an anti-Compton spectrometer consisting of a 55-cm<sup>3</sup> coaxial Ge(Li) detector inside a 20.32-cm-outer diameter x 6.32-cm-inner diameter x 15.24-cm-long NaI(Tl) annulus. The spectrometer was placed inside a massive shield as shown on Fig. 1. Background associated with neutrons scattering from the samples into the Ge(Li) detector was suppressed using the pulsed beam time-of-flight technique. The front face of the Ge(Li) detector was 99 cm from the center of the samples.

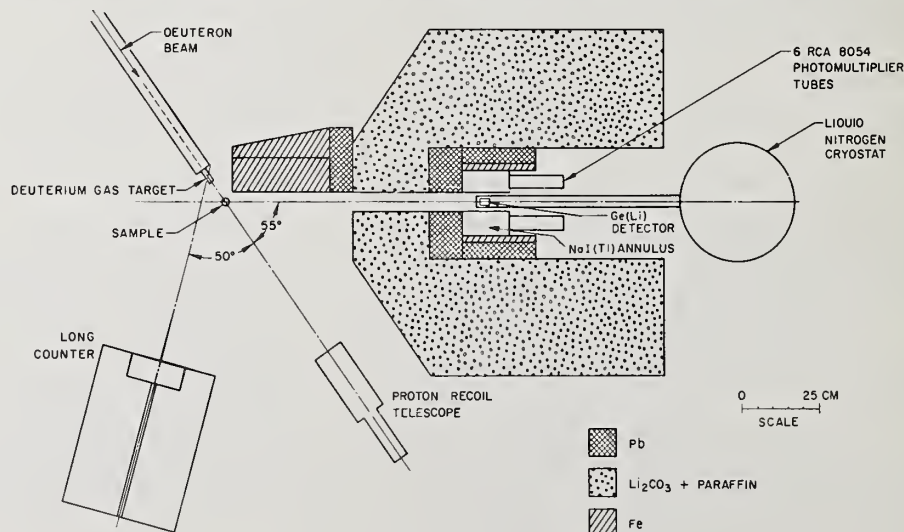
A spectrum obtained with the Cr scattering sample is shown on Fig. 2. In the analysis of the data, a  $\gamma$ -ray present in more than one sample spectrum is assumed to be part of the background unless it is known from other work to originate in the sample. An example of this is the 1332 keV  $\gamma$ -ray which is present in both the Ni and Cr spectra. In the Ni spectrum this  $\gamma$ -ray originates from the first excited state of  $^{60}\text{Ni}$  while for Cr the  $\gamma$ -ray is from a transition between the 2768 and 1434 keV levels in  $^{52}\text{Cr}$ .

The extraction of peak areas from the measured  $\gamma$ -ray spectra was carried out using the computer program SAMPO<sup>1</sup>. The full energy peak efficiency of the Ge(Li) detector was measured using calibrated point sources. The Monte Carlo program O5R<sup>2</sup> was used to calculate a geometry correction arising from the distribution of the source throughout the volume of the scattering sample and the effect of self-shielding of the  $\gamma$ -rays by the sample.

The neutron flux at the sample was monitored with both a Hansen and McKibben type long counter<sup>3</sup> located at 50° to the deuteron beam direction and a simplified proton-recoil telescope of the Los Alamos design<sup>4</sup> located directly behind the scattering sample 46.99 cm from the front face of the gas target. Due to severe background in the long counter at incident deuteron energies above 2 MeV, the proton-recoil telescope was used to determine the neutron flux.

The telescope data yields the number of neutrons incident on the scattering sample per steradian at 0° to the deuteron beam direction. The average flux in the sample, taking account of the sample-source geometry and angular distribution of neutrons from the

Figure 1.  
Experimental  
Arrangement



source was calculated using the Monte Carlo program O5R<sup>2</sup>. No correction has been made for multiple scattering or beam attenuation in the sample. It is assumed that the flux increase due to multiple scattering is cancelled by the flux decrease due to beam attenuation in the sample. Results of previous calculations<sup>5,6</sup> for <sup>90</sup>Zr, <sup>92</sup>Zr and <sup>94</sup>Zr indicate that this assumption is approximately correct (within 3%) away from the threshold of a level where the excitation cross section is slowly varying with energy.

### Results

γ-ray production cross sections measured at 55° to the incident deuteron beam direction were converted into total cross sections by multiplying by 4π. The isotropy assumption was checked where possible using the angular distribution coefficients compiled by Mathur et al.<sup>7</sup>. For levels whose J<sup>π</sup> are known and assuming direct excitation (no transitions to these levels from higher lying ones), corrections of up to 5 percent are possible. In most cases the correction is less than 2 percent. However, since the contribution to the angular distribution caused by a level being excited by the decay of a higher lying level could not be calculated, no correction to the isotropy assumption has been made.

Major sources of uncertainty in the cross sections are listed in Table I. The uncertainty in the neutron flux arises primarily from the analysis of the proton-recoil telescope spectra where difficulties were encountered in determining the background. The total estimated uncertainty does not include contributions from the omission of the corrections for anisotropy, multiple scattering, and flux attenuation.

Table I. Estimated Uncertainties

Neutron Flux	15%
Ge(Li) Detector Efficiency	4%
Counting Statistics	0.5-30%
SAMPO Analysis	5%
Omission of Correction for Multiple Scattering and Flux Attenuation	* 0-3%
Omission of Anisotropy Correction	* 0-5%
Total Estimated Uncertainty	16-36%

\*Not included in total estimated uncertainty.

The γ-ray production cross sections are tabulated in Tables II-V. The energy level giving rise to a particular γ-ray is indicated when known. Ambiguities in the assignments due to differences between the observed γ-ray energy and the value obtained from the decay schemes are indicated by placing brackets around the energy of the level. Sources of the decay schemes used for making the assignments are Nuclear Data Sheets<sup>8</sup> for Cr, Nuclear Data Sheets<sup>9</sup> for Ni, Nuclear Data Sheets<sup>10</sup> for <sup>92</sup>Zr, J. G. Beery<sup>11</sup>, Ball, Auble and Roos<sup>12</sup>, and Tessler and Glickstein<sup>13</sup> for <sup>94</sup>Zr.

### Acknowledgments

We wish to thank Dr. A. V. Dralle for his assistance with the calculations requiring the use of O5R. The assistance of Messrs. W. J. McDonald, S. J. Hogya, A. J. Vergona, and E. J. Charney in acquiring the data and Mrs. C. R. Ursiny and D. A. Iannuzzi in analyzing the data is gratefully acknowledged.

Figure 2.

Cr (n, n'γ) γ-ray Spectrum.  
Unlabeled peaks appear in the background.  
Energies are in KeV.

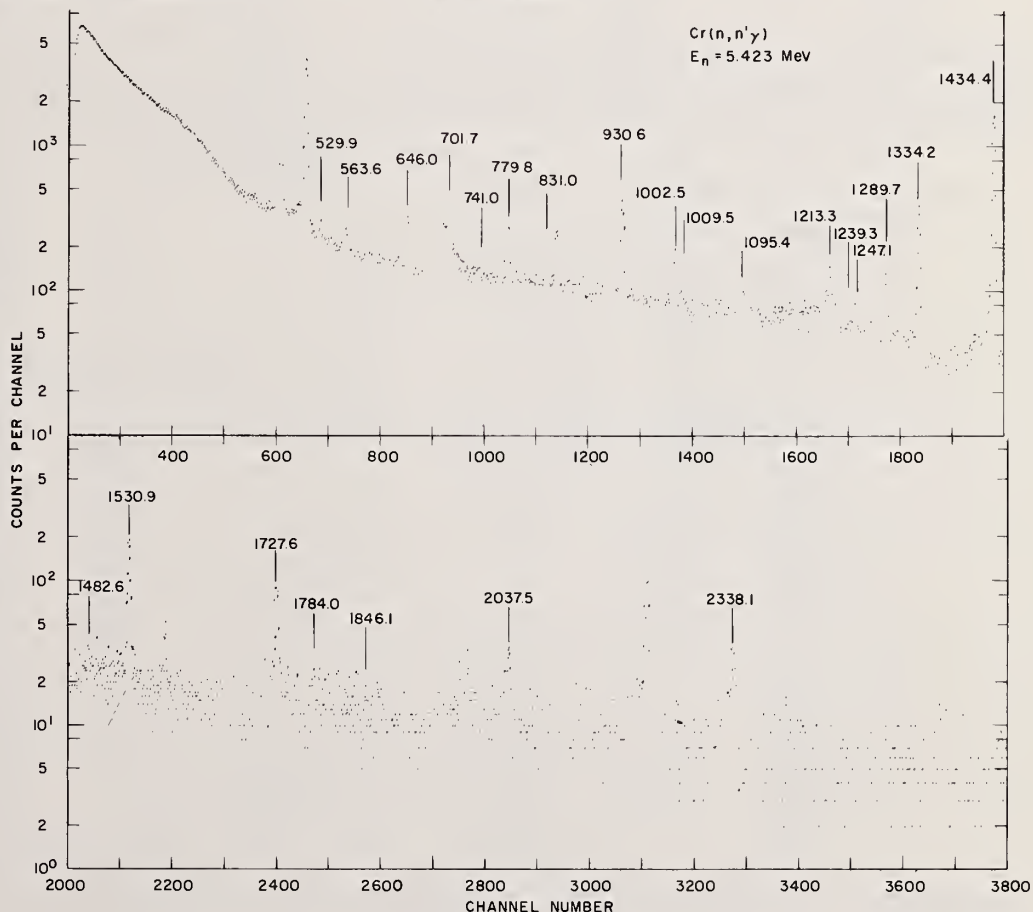




Table II.  $\gamma$ -ray production cross sections for Cr. Bracketed ( ) numbers indicate ambiguity due to differences between the observed  $\gamma$ -ray energy and the value obtained from the decay scheme.

Isotope	$\gamma$ -Ray (keV)	Level <sup>a</sup> (keV)	Cross Section (mb)				
			Neutron Energy (MeV)				
			3.43	4.216	4.845	5.423	5.97
50	779.8	783.1	906.0 $\pm$ 152.2	962.8 $\pm$ 157.9	888.4 $\pm$ 143.0	982.7 $\pm$ 158.2	956.3 $\pm$ 154.9
	1095.4	1879	128.7 $\pm$ 38.5	234.6 $\pm$ 42.9	289.9 $\pm$ 48.1	245.3 $\pm$ 41.2	266.6 $\pm$ 45.3
52	1434.4 <sup>b</sup>	1434.19	861.2 $\pm$ 137.8	961.0 $\pm$ 153.8	996.1 $\pm$ 159.4	1147.0 $\pm$ 183.5	1014.0 $\pm$ 162.2
	930.6 <sup>b</sup>	(2369.8)	90.6 $\pm$ 14.9	98.8 $\pm$ 16.0	137.2 $\pm$ 22.0	158.8 $\pm$ 25.4	148.1 $\pm$ 23.7
	1213.3	2647	52.7 $\pm$ 9.0	52.2 $\pm$ 8.6	38.9 $\pm$ 6.3	35.8 $\pm$ 5.8	23.4 $\pm$ 3.9
	1334.2	2768	48.7 $\pm$ 8.4	142.7 $\pm$ 23.0	184.7 $\pm$ 29.6	238.5 $\pm$ 38.2	195.8 $\pm$ 31.3
	1530.9	2965.0	124.3 $\pm$ 20.5	137.4 $\pm$ 22.3	124.9 $\pm$ 20.0	138.2 $\pm$ 22.1	105.3 $\pm$ 17.0
	741.0 <sup>c</sup>	(3113.8)	6.2 $\pm$ 1.3	5.8 $\pm$ 1.1	10.9 $\pm$ 1.8	11.9 $\pm$ 2.0	11.8 $\pm$ 2.0
	1727.6	3162.0	60.4 $\pm$ 10.4	114.9 $\pm$ 18.7	104.9 $\pm$ 16.9	91.9 $\pm$ 14.8	73.0 $\pm$ 11.8
	646.0	3414	6.1 $\pm$ 1.3	25.8 $\pm$ 4.3	39.1 $\pm$ 6.3	49.8 $\pm$ 8.0	46.7 $\pm$ 7.5
	2037.5	3472	0	17.4 $\pm$ 3.3	24.4 $\pm$ 4.1	35.0 $\pm$ 5.7	28.1 $\pm$ 4.7
	1247.1	3616.6, 4015	0	5.0 $\pm$ 1.2	10.0 $\pm$ 1.7	13.6 $\pm$ 2.3	10.6 $\pm$ 1.9
	2338.1	3771	0	39.9 $\pm$ 6.9	42.2 $\pm$ 6.9	46.7 $\pm$ 7.6	33.6 $\pm$ 5.7
	563.6	564.1	165.8 $\pm$ 29.2	144.1 $\pm$ 24.4	134.0 $\pm$ 21.8	143.1 $\pm$ 23.3	153.4 $\pm$ 25.2
	1009.5	1006	98.9 $\pm$ 20.0	105.1 $\pm$ 19.2	84.2 $\pm$ 14.2	97.9 $\pm$ 16.7	85.3 $\pm$ 14.8
53	1289.7	1287	343.3 $\pm$ 60.4	364.1 $\pm$ 61.2	361.8 $\pm$ 58.6	383.2 $\pm$ 62.1	371.5 $\pm$ 60.9
	529.9	1539	109.1 $\pm$ 20.0	92.3 $\pm$ 16.1	118.1 $\pm$ 19.3	127.7 $\pm$ 20.8	98.7 $\pm$ 16.5
54	831.0	834.825	1119.0 $\pm$ 192.5	1042.0 $\pm$ 175.1	1082.0 $\pm$ 175.2	1352.0 $\pm$ 217.7	1299.0 $\pm$ 211.7
	1784.0	2619.52	114.1 $\pm$ 54.8	279.0 $\pm$ 75.1	139.5 $\pm$ 30.0	160.6 $\pm$ 36.0	-
Nat.	701.7		15.9 $\pm$ 2.9	45.9 $\pm$ 7.5	55.5 $\pm$ 8.9	74.6 $\pm$ 11.9	64.2 $\pm$ 10.3
	1002.5		37.2 $\pm$ 6.3	30.7 $\pm$ 5.1	33.2 $\pm$ 5.4	39.6 $\pm$ 6.4	37.9 $\pm$ 6.2
	1239.3		9.2 $\pm$ 1.9	7.4 $\pm$ 1.4	6.1 $\pm$ 1.1	6.5 $\pm$ 1.1	4.3 $\pm$ 0.8
	1482.1		4.6 $\pm$ 1.4	5.5 $\pm$ 1.5	3.6 $\pm$ 0.7	3.6 $\pm$ 0.7	4.3 $\pm$ 0.9
	1846.1		0	3.9 $\pm$ 1.3	3.2 $\pm$ 0.7	3.6 $\pm$ 0.8	-
a) Reference 8			b) 2369.8 $\rightarrow$ 1434.19 = 935.6		c) 3113.8 $\rightarrow$ 2369.8 = 744		

Table III.  $\gamma$ -ray production cross sections for Ni. Bracketed ( ) numbers indicate ambiguity due to differences between the observed  $\gamma$ -ray energy and the value obtained from the decay scheme.

Isotope	$\gamma$ -Ray (keV)	Level <sup>a</sup> (keV)	Cross Section (mb)			
			Neutron Energy (MeV)			
			3.43	4.216	4.845	5.423
58	1453.8	1454.0	892.4 $\pm$ 142.8	734.4 $\pm$ 117.5	738.4 $\pm$ 118.1	741.5 $\pm$ 118.6
	1321.1	2775.3	125.6 $\pm$ 21.0	102.8 $\pm$ 16.9	96.1 $\pm$ 15.5	85.0 $\pm$ 13.6
	1447.6	2901.7	116.0 $\pm$ 19.6	96.9 $\pm$ 16.0	74.1 $\pm$ 11.9	92.2 $\pm$ 14.8
	1583.4	3037.3	35.1 $\pm$ 6.6	52.6 $\pm$ 8.9	37.9 $\pm$ 6.2	35.3 $\pm$ 5.7
	1809.5	3263.5	12.0 $\pm$ 2.7	25.1 $\pm$ 4.6	18.7 $\pm$ 3.2	23.9 $\pm$ 3.9
	2076.4	3530.9	0	19.3 $\pm$ 3.7	16.8 $\pm$ 2.9	14.3 $\pm$ 2.4
60	1332.6	1332.5	1205.5 $\pm$ 194.1	1174.6 $\pm$ 187.9	1206.9 $\pm$ 193.1	1261.5 $\pm$ 201.8
	821.8 <sup>b</sup>	(2158)	305.7 $\pm$ 64.2	270.1 $\pm$ 43.5	269.7 $\pm$ 43.2	254.9 $\pm$ 40.8
	956.6 <sup>c</sup>	(2286)	26.6 $\pm$ 9.6	106.7 $\pm$ 17.9	114.0 $\pm$ 18.5	114.1 $\pm$ 18.4
	468.0	2625	74.8 $\pm$ 12.9	86.4 $\pm$ 14.3	82.4 $\pm$ 13.3	89.2 $\pm$ 14.3
	1293.0	2625	47.3 $\pm$ 9.9	49.6 $\pm$ 9.1	51.3 $\pm$ 8.6	44.5 $\pm$ 7.3
	1790.9	3123	8.2 $\pm$ 3.9	67.5 $\pm$ 13.1	62.0 $\pm$ 11.0	46.8 $\pm$ 7.9
	641.4 <sup>d</sup>	(3270)	11.1 $\pm$ 3.1	15.9 $\pm$ 3.3	12.5 $\pm$ 2.2	11.7 $\pm$ 2.0
	1937.6	3270	0	39.8 $\pm$ 8.3	21.5 $\pm$ 4.2	20.1 $\pm$ 3.6
	1984.6	3316	0	23.2 $\pm$ 5.1	22.5 $\pm$ 4.1	25.5 $\pm$ 4.5
	2060.7	3392	0	30.1 $\pm$ 6.4	58.4 $\pm$ 9.9	61.3 $\pm$ 10.1
62	1171.0	1172	1758.4 $\pm$ 297.2	1880.6 $\pm$ 306.5	2209.4 $\pm$ 353.5	2320.2 $\pm$ 371.2
Nat.	366.9		22.0 $\pm$ 3.7	30.0 $\pm$ 4.9	31.4 $\pm$ 5.0	35.6 $\pm$ 5.7
	433.6		7.0 $\pm$ 1.4	12.2 $\pm$ 2.1	15.6 $\pm$ 2.5	16.9 $\pm$ 2.7
	989.2		5.9 $\pm$ 2.5	10.1 $\pm$ 1.9	7.6 $\pm$ 1.3	7.7 $\pm$ 1.3
	1001.0		63.8 $\pm$ 10.7	105.6 $\pm$ 17.1	123.9 $\pm$ 19.8	133.8 $\pm$ 21.4
	1009.2		10.3 $\pm$ 2.1	6.8 $\pm$ 1.3	5.6 $\pm$ 1.0	7.5 $\pm$ 1.3
	1159.5		4.7 $\pm$ 1.4	15.2 $\pm$ 2.8	18.8 $\pm$ 3.1	21.3 $\pm$ 3.5
	1163.2		7.3 $\pm$ 1.6	10.4 $\pm$ 2.0	12.7 $\pm$ 2.1	15.9 $\pm$ 2.6
	1605.1		0	3.2 $\pm$ 0.8	4.7 $\pm$ 0.9	5.5 $\pm$ 1.0
	1786.6		13.6 $\pm$ 4.7	9.4 $\pm$ 1.9	12.9 $\pm$ 2.2	13.4 $\pm$ 2.2
a) Reference 9			b) 2158 $\rightarrow$ 1332.5 = 825.5		c) 2286 $\rightarrow$ 1332.5 = 953.5	
			d) 3270 $\rightarrow$ 2625 = 645			

# References

1. J. T. Routti and S. G. Prussin, Nucl. Instr. Methods **72**, 125 (1969).
2. D. C. Irving, R. M. Freestone, Jr., and F. M. Kam, O5R, A General Purpose Monte Carlo Transport Code, ORNL-3622 (Feb. 1965).
3. W. D. Allen, in Fast Neutron Physics, Part I, edited by J. B. Marion and J. L. Fowler (Interscience Publishers, Inc., New York, 1960), p. 362.
4. S. J. Bame, Jr., E. Haddad, J. E. Perry, Jr., and R. K. Smith, Rev. Sci. Instr. **28**, 997 (1957).
5. G. Tessler, S. S. Glickstein and E. E. Carroll, Jr., Phys. Rev. **C2**, 2390 (1970).
6. S. S. Glickstein, G. Tessler, and M. Goldsmith, Phys. Rev. **C4**, 1818 (1971).
7. S. C. Mathur, P. S. Buchanan, I. L. Morgan, Texas Nuclear Corp. Report, No. ORO-2791-21, 1966.
8. Nucl. Data Sheets **B3**, No. 5, 6, April 1970.
9. Nucl. Data Sheets **B2**, No. 5, March 1968; **B3**, No. 3-4, January 1970.
10. Nucl. Data Sheets **B7**, No. 4, April 1972.
11. J. G. Beery, "A Study of the (t,p) Reaction on <sup>90</sup>92, <sup>94</sup>96Zr and <sup>122</sup>124Sn," LA-3958, June 1968.
12. J. B. Ball, R. L. Auble, and P. G. Roos, Phys. Rev. **C4**, 196 (1971).
13. G. Tessler and S. S. Glickstein, Phys. Rev. **C6**, 1430 (1972).

Table IV.  $\gamma$ -ray production cross sections for <sup>92</sup>Zr, Bracketed ( ) numbers indicate ambiguity due to differences between the observed  $\gamma$ -ray energy and the value obtained from the decay scheme

$\gamma$ -Ray (keV)	Level <sup>a</sup> (keV)	Cross Section (mb)			
		Neutron Energy (MeV)			
		3.43	4.216	4.845	5.423
934.5	934.46	1623 $\pm$ 260	1598 $\pm$ 256	1544 $\pm$ 247	1569 $\pm$ 251
448.5	1383.0	106.3 $\pm$ 17.2	84.1 $\pm$ 13.6	63.9 $\pm$ 10.3	66.2 $\pm$ 10.7
561.1	1495.6	401.9 $\pm$ 64.3	469.6 $\pm$ 75.1	540.6 $\pm$ 86.5	574.9 $\pm$ 92.0
912.8	1847.3	195.5 $\pm$ 31.7	152.6 $\pm$ 24.7	129.0 $\pm$ 20.8	119.4 $\pm$ 19.2
1847.3	1847.3	99.5 $\pm$ 16.9	63.4 $\pm$ 10.8	62.6 $\pm$ 10.3	64.7 $\pm$ 10.6
1132.4	2066.9	270.7 $\pm$ 43.9	196.2 $\pm$ 31.8	150.4 $\pm$ 24.2	124.2 $\pm$ 20.0
492.6	2339.9	15.6 $\pm$ 2.8	17.3 $\pm$ 3.0	11.9 $\pm$ 2.0	9.9 $\pm$ 1.7
844.3	2339.9	60.6 $\pm$ 10.2	52.4 $\pm$ 8.8	43.3 $\pm$ 7.1	47.5 $\pm$ 7.7
1405.4	2339.9	112.2 $\pm$ 18.8	107.2 $\pm$ 17.7	114.5 $\pm$ 18.4	105.1 $\pm$ 16.9
780.0		23.7 $\pm$ 4.3	29.8 $\pm$ 5.2	21.6 $\pm$ 3.6	20.4 $\pm$ 3.4
902.9 <sup>b</sup>	(3.24 MeV)	80.3 $\pm$ 13.5	85.3 $\pm$ 14.0	80.3 $\pm$ 12.9	76.1 $\pm$ 12.3
918.6	( <sup>84</sup> Zr)	21.0 $\pm$ 4.0	20.1 $\pm$ 3.6	15.6 $\pm$ 2.7	15.9 $\pm$ 2.7
972.3	2819.6	76.8 $\pm$ 12.9	44.1 $\pm$ 7.5	30.0 $\pm$ 5.0	23.9 $\pm$ 4.0
990.5		63.5 $\pm$ 10.7	91.4 $\pm$ 15.0	109.6 $\pm$ 17.6	115.2 $\pm$ 18.5
995.8		8.0 $\pm$ 2.1	10.7 $\pm$ 2.1	13.6 $\pm$ 2.4	11.2 $\pm$ 1.9
1238.3		17.5 $\pm$ 3.5	12.9 $\pm$ 2.7	17.7 $\pm$ 3.0	18.3 $\pm$ 3.1
1248.3		12.1 $\pm$ 2.6	15.6 $\pm$ 3.2	21.4 $\pm$ 3.6	21.2 $\pm$ 3.6
1369.6		43.0 $\pm$ 7.7	45.7 $\pm$ 7.9	42.2 $\pm$ 7.0	38.9 $\pm$ 6.4
1413.9 <sup>c</sup>	(3263.9)	30.2 $\pm$ 5.7	26.0 $\pm$ 4.8	16.4 $\pm$ 2.9	15.4 $\pm$ 2.7
1463.3		29.7 $\pm$ 5.6	42.6 $\pm$ 7.5	46.7 $\pm$ 7.7	51.7 $\pm$ 8.5
1696.0		5.8 $\pm$ 1.7	14.6 $\pm$ 3.0	18.4 $\pm$ 3.3	20.3 $\pm$ 3.5
1711.9		7.9 $\pm$ 3.2	12.5 $\pm$ 3.4	9.3 $\pm$ 1.9	9.2 $\pm$ 1.8
1975.3		38.8 $\pm$ 7.4	21.1 $\pm$ 4.2	18.2 $\pm$ 3.3	25.6 $\pm$ 4.4
2105.6	3040.1	23.8 $\pm$ 5.0	22.9 $\pm$ 4.6	23.9 $\pm$ 4.2	26.6 $\pm$ 4.5
2612.4		15.6 $\pm$ 5.5	12.4 $\pm$ 3.1	18.5 $\pm$ 3.4	16.4 $\pm$ 3.3
2866.7		0	10.0 $\pm$ 2.8	15.0 $\pm$ 2.9	14.2 $\pm$ 2.8

a) Reference 10

b)  $3240 \rightarrow 2339.9 = 900.1$

c)  $3263.9 \rightarrow 1847.3 = 1416.6$

Table V.  $\gamma$ -ray production cross sections for <sup>94</sup>Zr

$\gamma$ -Ray (keV)	Level <sup>a</sup> (keV)	Cross Section (mb)			
		Neutron Energy (MeV)			
		3.43	4.216	4.845	5.423
920	920	1553 $\pm$ 253	1541 $\pm$ 247	1585 $\pm$ 254	1554 $\pm$ 249
380	1300	94.9 $\pm$ 17.5	64.4 $\pm$ 10.8	56.4 $\pm$ 9.2	55.5 $\pm$ 9.2
550.2	1471	254.2 $\pm$ 43.5	369.8 $\pm$ 59.5	407.9 $\pm$ 65.3	474.0 $\pm$ 75.8
752.9	1675	166.4 $\pm$ 30.8	101.5 $\pm$ 17.2	98.8 $\pm$ 16.3	96.2 $\pm$ 16.1
1674.6	1675	227.4 $\pm$ 45.0	172.1 $\pm$ 29.3	143.0 $\pm$ 24.0	159.1 $\pm$ 27.0
1142.0	2060	170.1 $\pm$ 33.2	174.3 $\pm$ 29.5	193.9 $\pm$ 31.8	181.6 $\pm$ 30.0
1237.1	2154	145.4 $\pm$ 29.5	120.6 $\pm$ 20.6	90.2 $\pm$ 15.2	68.0 $\pm$ 12.0
1416	2336 <sup>b</sup>	67.6 $\pm$ 17.0	118.8 $\pm$ 20.7	109.9 $\pm$ 18.5	113.5 $\pm$ 19.3
441.5		24.2 $\pm$ 6.0	23.3 $\pm$ 4.6	37.8 $\pm$ 7.3	42.8 $\pm$ 7.3
570.2		0	0	9.2 $\pm$ 2.0	12.6 $\pm$ 2.5
787.0		0	11.0 $\pm$ 4.7	12.5 $\pm$ 3.5	25.3 $\pm$ 4.8
1138.5	2.61	62.9 $\pm$ 15.3	66.5 $\pm$ 11.8	77.6 $\pm$ 13.1	103.1 $\pm$ 17.5
1593.0		90.0 $\pm$ 21.6	52.0 $\pm$ 10.5	53.5 $\pm$ 10.4	41.6 $\pm$ 8.1
1782.3		66.0 $\pm$ 17.8	55.0 $\pm$ 11.2	66.5 $\pm$ 11.8	61.9 $\pm$ 11.5
1813.8		61.7 $\pm$ 17.2	60.4 $\pm$ 11.8	54.8 $\pm$ 10.0	43.4 $\pm$ 8.5

a) References 11, 12

b) Reference 13



# SCATTERING OF NEUTRONS BY NITROGEN AND OXYGEN FROM 5.0 TO 9.3 MeV

D. L. Bernard

University of Southwestern Louisiana  
Lafayette, Louisiana 70501

and

M. C. Taylor

Columbia Scientific Industries Corporation  
Austin, Texas 78762

Angular distributions of neutrons scattered elastically and inelastically from nitrogen-14 and oxygen-16 have been measured at neutron energies of 5.04, 6.25 and 9.29 MeV. Neutron flux attenuation and multiple scattering corrections were made using a modified version of an existing computer code. Special consideration was given in the modification of the code to developing an angular resolution function to treat the effects on multiple scattering corrections due to the solid angle subtended by the scattering sample at the neutron producing target. Graphs and tabulated results are presented as center of mass differential scattering cross sections versus the cosine of the center of mass scattering angle.

(Differential cross sections; neutron cross sections; neutron time-of-flight spectroscopy; angular distributions)

## Introduction

Neutron scattering cross-sections for elements such as nitrogen and oxygen have important applications in the area of neutron transport calculations with air as the transport medium. Furthermore, such applications require accurate cross-section values to obtain meaningful results.

Several research groups have devoted considerable efforts to measuring neutron scattering data with oxygen and nitrogen scatterers. Particular efforts have been made at ORNL by J. L. Fowler, et al.<sup>1</sup> and Dickens and Perey<sup>2</sup> and Perey and Kinney<sup>3</sup>, the latter group being primarily concerned with the nitrogen nonelastic discrepancy below 9 MeV. Gamma-ray production cross-sections for nitrogen have been measured by V. J. Orphan et al.<sup>4</sup>

A fast neutron spectrometer system was built for determining neutron differential cross-sections with several scatterers including oxygen and nitrogen. However, only the oxygen and nitrogen data are presented here. Neutron bombarding energies at which data were measured are 5.04 MeV, 6.25 MeV and 9.29 MeV. Data were also measured at 10.0 MeV; however, due to the abnormally high gamma ray background yields, the gamma rejection electronics did not function as desired, thus making the accuracy of these data points questionable.

The differential scattering cross-sections were determined by normalizing the measured angular distributions to known n-p cross-sections at the appropriate incident neutron energies. The cross-sections were then corrected for neutron flux attenuation and multiple scattering in the samples using an analytical computer code modified with target-detector angular resolution functions.

## Experimental Method

The Tandem Van de Graaff of the University of Texas Center for Nuclear Studies was used as the basic accelerator system. A pulsed negative ion source was designed and assembled onto a 100 keV Cockroft-Walton accelerator built by Columbia Scientific Industries and University of Texas personnel. The resulting injector system provided a pulsed beam of protons to be accelerated to the desired energy by the Tandem accelerator.

A low background neutron producing target was developed and used in conjunction with a neutron

detector, shield assembly, angular distribution goniometer, and automatic scattering sample changer. Details of the design of the Van de Graaff pulsed beam facility used in this work are presented elsewhere<sup>5</sup>. Only a brief description will be given here including pertinent instrumental developments made since the last publication.

## The Pulsed Ion Source

A McKibben<sup>6</sup> type direct extraction negative ion source was designed and assembled on a 100 keV Cockroft-Walton accelerator. Power for the ion source extraction high voltage as well as that of the 100 keV for acceleration was transported by a specially fabricated insulated coaxial cable. All isolation transformers and power supplies were placed in oil filled containers at ground potential. This allowed for removal of considerable weight from the terminal of the Cockroft-Walton injector. Furthermore, confined quarters for the injector did not allow use of a large air insulated terminal in relation to standard designs. Consequently, high voltage safety in the region of the injector terminal was enhanced by this arrangement.

Negative ions from the injector were chopped into bursts of 25 nanosecond duration by R. F. sweeping the beam across a slit. The chopped beam then entered a klystron buncher which compressed the bursts. The 100 keV pulsed-bunched beam then entered the tandem accelerator. Neutron spectra were measured by conventional methods of fast neutron time-of-flight electronics. From the measured full-width-half-maximum (FWHM) of the  $T(p,n)^3\text{He}$  neutron group produced at the target end of the beam tube, beam pulse widths of 1 to 2 nanoseconds were verified. Average beam currents of 0.5 microampere to 1.0 microampere with peak currents of 0.3 milliamperes were obtained.

## The Neutron Producing Target

Considerable effort was put into developing a monoenergetic primary neutron beam. Only one beam collimator was used in the beam tube within the target room area in order to minimize target room background. This was fabricated with isotopically pure Silicon-28, as the (p,n) threshold of Silicon-28 is about 15 MeV. The beam was stopped in a tritium gas cell at the end of which was a 20 mil Silicon-28 disc. The gas cell was 3 cm long and pressurized at 1 atmosphere. The entrance foil of the gas cell was made of 1/10 mil Havar.



## Neutron Detector and Shield Assembly

The neutron detector consisted of a 58AVP photo-multiplier optically coupled to an NE218 liquid scintillator 12.5 cm diameter by 15.2 cm long. With this type of scintillator, pulse shape discrimination could be employed to reject gamma rays. The detector was housed in 2.54 cm thick lead rings. Surrounding the lead rings was a  $\text{LiCO}_3$ -paraffin shield. The collimator throat of the shield was made of research-grade graphite. The detector-shield assembly was located on a mobile angular distribution carriage which permitted measuring neutron flight paths of 3.5 meters. Figure 1 shows schematically the arrangement of neutron producing target, sample holder and angular distribution carriage. A layer of  $\text{LiCO}_3$ -paraffin blocks lined the wall nearest the tritium gas cell to minimize the occurrence of neutron reactions with the concrete material of the wall.

In addition to the main neutron detector, a stationary neutron detector was used to monitor the primary neutron beam. Neutron time-of-flight electronics was also used with this detector.

The best time resolution obtained with the main detector was 2.5 nanoseconds due in large part to the relatively large thickness of the scintillator. Time resolutions of 1.25 to 1.50 nanoseconds were obtained consistently with the monitor detector which used a 2 cm thick scintillator, and this represents more realistically the neutron beam resolution.

## Angular Distribution Measurement

Angular distributions of neutrons elastically scattered from oxygen-16 ( $\text{H}_2\text{O}$  sample) were measured for 5.04 and 6.25 MeV incident neutron energies. The oxygen differential cross-sections as a function of the cosine of the scattering angle in the center-of-mass system of coordinates are plotted in Figure 2. The solid curve represents data corrected for flux attenuation and multiple scattering. The points with error bars represent uncorrected data. Both data points and curve have been corrected for detector efficiency. The corrected data are presented in Table I.

The presence of hydrogen in the sample permitted absolute differential cross-section determinations using known n-p cross-sections<sup>7</sup>. The scatterer used for these measurements consisted of distilled water in a thin walled polyethylene cylindrical container 2.54 cm diameter by 3.81 cm long. An empty polyethylene container of the same dimensions was used for measuring background spectra.

Figure 3 shows elastic and inelastic neutron scattering angular distributions for 6.25 MeV neutrons incident on hydrazine ( $\text{NH}_2\text{NH}_2$ ). The hydrazine was contained in a thin walled polyethylene cylinder 3.81 cm diameter by 5.08 cm long. The container was epoxy sealed to minimize exposure of hygroscopic hydrazine to room air. The angular distributions were normalized to the n-p differential cross sections at this energy and were corrected for detector efficiency. The solid curve represents the differential cross-sections corrected for flux attenuation and multiple scattering within the sample. The corrected data including experimental errors are tabulated in Tables 2 and 3.

The same hydrazine sample was used to measure neutron angular distributions at 9.29 MeV incident energies. Figure 3 shows the differential cross sections and the cross sections (curve) corrected for

flux attenuation and multiple scattering. The cross sections and their experimental errors are tabulated in Tables 4 and 5.

## Data Corrections

### Flux Attenuation and Multiple Scattering Corrections

Flux attenuation corrections were made using the method of Levin<sup>8</sup>. They ranged from 10% to 12% for scattering yields from oxygen and nitrogen.

Multiple scattering corrections were made using a method originally developed by Blok and Jonker<sup>9</sup> and applied to neutron scattering by Walt and Barschall<sup>10</sup>, Meier et al.<sup>11</sup>, Wills et al.<sup>12</sup>, J. D. Reber and J. D. Brandenberger<sup>13</sup> and W. Galati<sup>14</sup>. The method was modified by including an angular resolution function for deconvoluting the data to remove effects of the finite width of the scatterer and neutron detector. These corrections were generally between 10% and 15%. Occasionally, there were angles at which a 60% correction was required.

Flux attenuation and multiple scattering corrections were incorporated into a computer code and run on the University of Southwestern Louisiana Univac 70/46 computer.

## References

1. J. L. Fowler, C. H. Johnson, F. X. Hass and R. M. Feezel, Proceedings of the Third Conference on Neutron Cross Sections and Technology, Knoxville.
2. J. K. Dickens and F. G. Perey, Nucl. Science and Eng. **36**, 280 (1969).
3. F. G. Perey and W. E. Kinney, Nucl. Science and Eng. **46**, 428 (1971).
4. V. J. Orphan, C. G. Hoot, and V. V. Verbinshi, Trans. Amer. Nucl. Soc. **16**, 348 (June, 1973).
5. D. L. Bernard, et al., IEEE Trans. Nucl. Sci. **NS-18**, 90 (1971).
6. G. P. Lawrence, R. K. Beauchamp, and J. L. McKibben, Nucl. Instr. and Meth. **32** (1965) 357.
7. J. C. Hopkins and G. Breit, Nucl. Data, Sect. A: 137-45 (Mar., 1971).
8. L. Cranberg and J. S. Levin, LASL Report No. LA-2177, Jan. 1959 (see Appendix II by J. S. Levin).
9. J. Blok and C. C. Jonker, Physica **18**, 809 (1952).
10. M. Walt and H. H. Barschall, Phys. Rev. **93**, 1062 (1954).
11. R. W. Meier, P. Scherrer, and A. Trumphy, Helv. Phys. Acta. **27**, 577 (1954).
12. J. E. Wills, et al., Phys. Rev. **109**, 891 (1958).
13. J. D. Reber and J. D. Brandenberger, Phys. Rev. **103**, 1077 (1967).
14. W. Galati, Ph.D. Dissertation, University of Kentucky, 1969 (unpublished).

Table I. Differential cross sections of neutrons elastically scattered from oxygen-16 at 5.05 MeV and 6.25 MeV bombarding energies. The errors are rms absolute errors consisting of systematic and statistical uncertainties. The uncertainty in scattering angle is estimated to be  $\pm 0.5^\circ$ . The scattering angle,  $\cos\theta$  and  $\sigma(\theta)$  are in the center of mass system. All cross sections are in mb/steradian and have been corrected for sample attenuation, multiple scattering and detector efficiency.

$\theta$ (degrees)	$\cos\theta$	$E_n=5.04$ MeV $\sigma(\theta) \pm \Delta\sigma(\theta)$	$E_n=6.25$ MeV $\sigma(\theta) \pm \Delta\sigma(\theta)$
21.2	0.932	717.8 $\pm$ 70.5	3429.4 $\pm$ 150.2
31.8	0.849	580.6 $\pm$ 56.5	1608.5 $\pm$ 80.1
42.3	0.739	324.1 $\pm$ 26.6	1000.6 $\pm$ 50.0
52.8	0.605	98.3 $\pm$ 9.2	340.2 $\pm$ 17.5
63.1	0.452	88.8 $\pm$ 8.2	14.1 $\pm$ 1.0
73.4	0.285	80.6 $\pm$ 7.9	10.1 $\pm$ 1.0
83.6	0.112	43.9 $\pm$ 4.2	27.2 $\pm$ 2.7
93.6	-0.063	36.5 $\pm$ 3.6	177.3 $\pm$ 8.5
103.6	-0.235	81.2 $\pm$ 7.9	260.9 $\pm$ 13.0
113.4	-0.397	112.9 $\pm$ 10.6	222.9 $\pm$ 10.5
123.1	-0.547	117.9 $\pm$ 10.2	150.4 $\pm$ 7.5
132.8	-0.679	100.5 $\pm$ 9.8	134.1 $\pm$ 6.5
142.3	-0.792	105.4 $\pm$ 9.6	14.6 $\pm$ 1.0
151.8	-0.881	112.0 $\pm$ 10.1	88.0 $\pm$ 4.5

Table 2. Differential cross sections of neutrons elastically scattered from nitrogen-14 at 6.25 MeV bombarding energy. See caption of Table I.

$\theta$ (degrees)	$\cos\theta$	$\sigma(\theta) \pm \Delta\sigma(\theta)$
21.2	0.932	827.9 $\pm$ 40.2
31.8	0.849	408.4 $\pm$ 40.8
42.3	0.739	49.4 $\pm$ 2.9
52.8	0.605	129.1 $\pm$ 7.2
63.1	0.452	157.8 $\pm$ 11.6
73.4	0.286	99.1 $\pm$ 5.6
83.6	0.112	73.9 $\pm$ 2.9
93.6	-0.063	69.6 $\pm$ 4.2
103.6	-0.235	66.4 $\pm$ 3.9
113.4	-0.397	75.1 $\pm$ 6.0
123.1	-0.547	50.4 $\pm$ 3.0
138.8	-0.679	51.5 $\pm$ 4.0
142.3	-0.792	95.9 $\pm$ 9.0
151.8	-0.881	31.1 $\pm$ 3.1

Table 3. Differential cross sections of neutrons inelastically scattered from nitrogen-14 at 6.25 MeV bombarding energy. See caption of Table I.

$Q = -2.311$ MeV			$Q = -3.945$ MeV		
$\theta$ (deg.)	$\cos\theta$	$\sigma(\theta) \pm \Delta\sigma(\theta)$	$\theta$ (deg.)	$\cos\theta$	$\sigma(\theta) \pm \Delta\sigma(\theta)$
43.3	0.728	37.1 $\pm$ 2.5	44.7	0.711	6.9 $\pm$ 0.4
53.9	0.728	5.5 $\pm$ 0.3	55.6	0.566	1.1 $\pm$ 0.2
64.4	0.431	3.2 $\pm$ 0.3	66.3	0.402	7.7 $\pm$ 0.4
74.8	0.262	8.1 $\pm$ 0.5	76.8	0.228	6.4 $\pm$ 0.4
85.1	0.086	2.2 $\pm$ 0.2	87.2	0.049	0.5 $\pm$ 0.2
95.1	-0.089	4.7 $\pm$ 0.4	97.3	-0.127	3.6 $\pm$ 0.2
105.1	-0.259	11.4 $\pm$ 0.5	107.2	-0.295	10.8 $\pm$ 1.0
114.8	-0.419	6.4 $\pm$ 0.3	116.8	-0.451	8.3 $\pm$ 0.9
124.4	-0.566	1.5 $\pm$ 0.2	126.3	-0.592	1.3 $\pm$ 0.2
133.9	-0.694	14.9 $\pm$ 1.5	135.6	-0.714	4.8 $\pm$ 0.3
143.3	-0.802	5.4 $\pm$ 0.5	144.7	-0.816	4.3 $\pm$ 0.4
152.6	-0.888	9.8 $\pm$ 0.9	153.6	-0.896	9.4 $\pm$ 0.9

Table 4. Differential cross sections of neutrons elastically scattered from nitrogen-14 at 9.29 MeV bombarding energy. See caption of Table I.

$\theta$ (degree)	$\cos\theta$	$\sigma(\theta) \pm \Delta\sigma(\theta)$
42.6	0.736	185.0 $\pm$ 15.2
53.1	0.600	51.0 $\pm$ 3.1
73.8	0.279	18.5 $\pm$ 1.5
83.9	0.105	10.8 $\pm$ 1.0
94.1	-0.072	60.2 $\pm$ 4.5
103.9	-0.242	83.0 $\pm$ 5.2
113.8	-0.404	27.4 $\pm$ 2.5
123.5	-0.552	18.0 $\pm$ 1.5

Table 5. Differential cross sections of neutrons inelastically scattered from nitrogen-14 at 9.29 MeV bombarding energy. See caption of Table 1.

$Q = -2.311$ MeV			$Q = -3.945$ MeV		
$\theta$ (deg.)	$\cos\theta$	$\sigma(\theta) \pm \Delta\sigma(\theta)$	$\theta$ (deg.)	$\cos\theta$	$\sigma(\theta) \pm \Delta\sigma(\theta)$
43.1	0.730	20.0 $\pm$ 1.2	43.5	0.725	26.0 $\pm$ 1.2
53.6	0.592	13.3 $\pm$ 1.0	54.2	0.585	14.0 $\pm$ 1.4
74.5	0.267	6.0 $\pm$ 0.6	75.1	0.257	2.2 $\pm$ 1.0
84.7	0.092	16.0 $\pm$ 1.6	85.4	0.081	3.0 $\pm$ 1.0
94.8	-0.084	33.1 $\pm$ 2.9	95.4	-0.095	7.2 $\pm$ 0.5
104.7	-0.254	32.2 $\pm$ 3.0	105.4	-0.265	10.8 $\pm$ 1.0
114.5	-0.415	0.7 $\pm$ 0.5	115.1	-0.424	1.6 $\pm$ 1.0
124.2	-0.561	2.0 $\pm$ 1.0	124.7	-0.569	1.0 $\pm$ 0.5

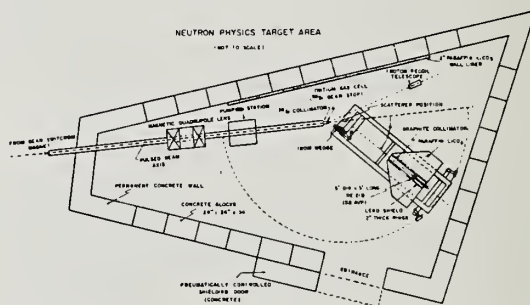


Figure 1. A schematic diagram of the arrangement of apparatus in the Tandem accelerator target room used for neutron cross section measurements.

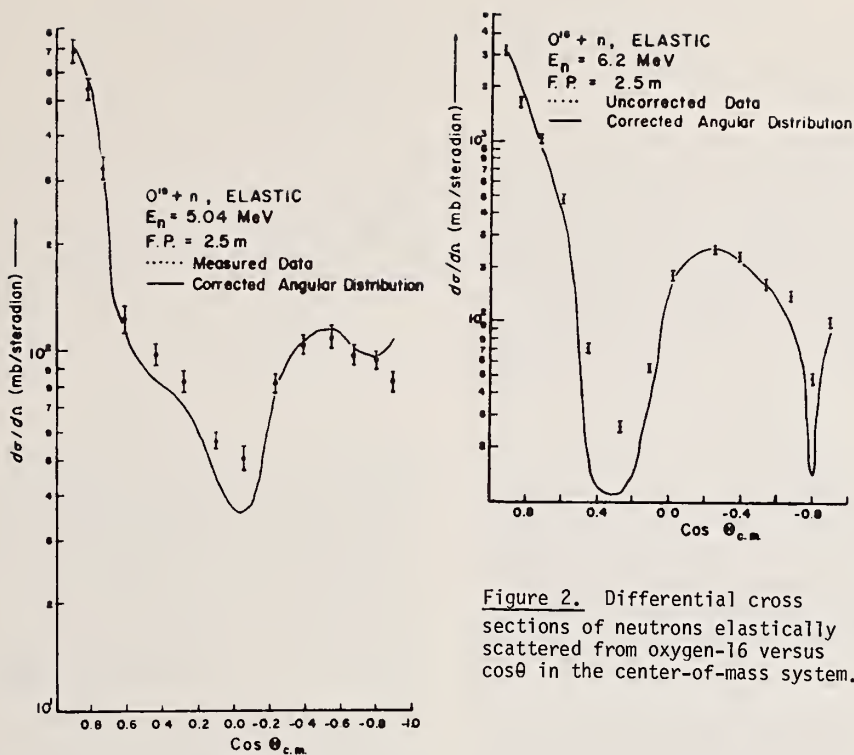
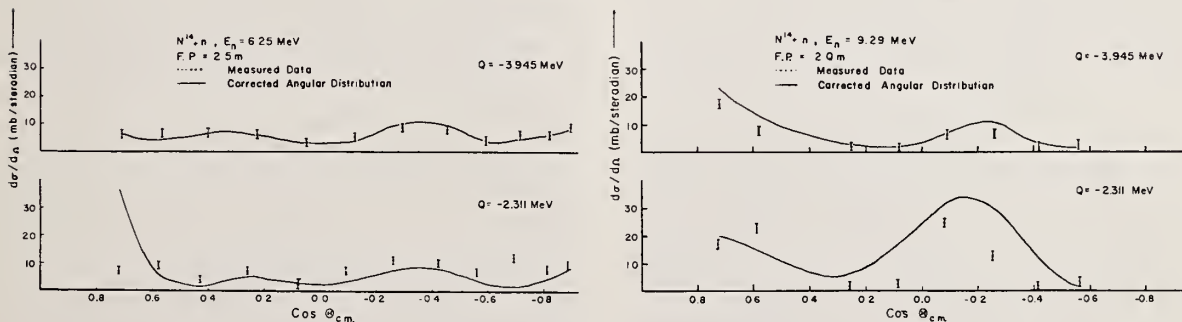
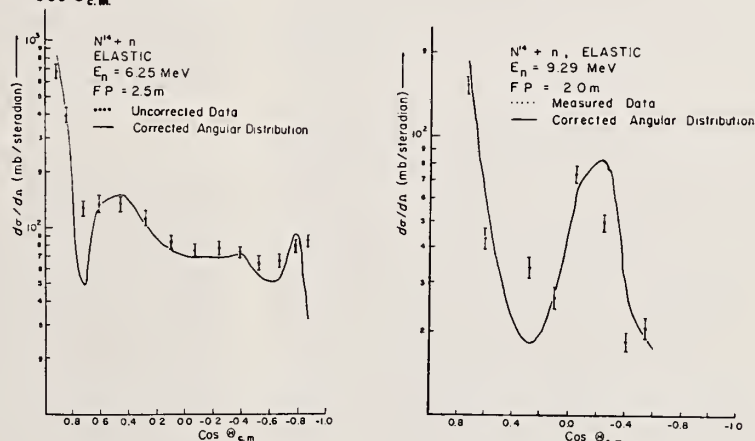


Figure 2. Differential cross sections of neutrons elastically scattered from oxygen-16 versus  $\cos\theta$  in the center-of-mass system.

Figure 3. Differential cross sections of neutrons scattered from nitrogen-14 versus  $\cos\theta$  in the center-of-mass system.





Deformation effects in neutron scattering from isotopically enriched  $\text{Sm}_2\text{O}_3$  samples have been studied at an incident neutron energy of 7 MeV where a maximum of the deformation effects was observed in total cross section measurements on the same isotopes.

Differential cross sections for elastic scattering and inelastic scattering (first  $2^+$  state) were measured for  $^{148}\text{Sm}$  and  $^{150}\text{Sm}$  and for  $^{146}\text{Nd}$ , which was included in this study to aid in separating isospin effects from deformation effects. Cross sections for the sum of elastic and inelastic scattering (first  $2^+$  state) were determined for  $^{152}\text{Sm}$  and  $^{154}\text{Sm}$ .

Experimental cross sections are compared to the results of non-spherical optical-potential coupled-channel calculations.

(NUCLEAR REACTIONS  $^{146}\text{Nd}(n,n)$ ,  $(n,n')$ ,  $^{148,150}\text{Sm}(n,n)$ ,  $(n,n')$ ,  $^{152,154}\text{Sm}(n,n+n')$ ,  $E = 7.0$  MeV ; measured  $\sigma(\theta)$  ; calculated  $\sigma(\theta)$ .)

## Introduction

The results of several recent experiments suggest that the effect of nuclear deformation on fast neutron elastic and inelastic scattering may be appreciable. Holmqvist *et al.* have measured the angular distribution of neutrons elastically scattered from the deformed nucleus  $^{181}\text{Ta}$  between 2.5 and 8.0 MeV neutron energy.<sup>1</sup> The angular distribution at angles greater than about  $60^\circ$  was observed to be considerably damped, as compared to optical model fits to the data using a spherical potential.

Angular distributions computed using a non-spherical potential were found to provide significantly better fits to the data. Tanaka *et al.* have performed somewhat similar studies on natural isotopic mixtures of each of the elements Er and Gd over the neutron energy range 1.5 to 3.5 MeV.<sup>2</sup>

From the results of coupled channel calculations, i.e., by Tamura<sup>3</sup>, it is expected that nuclear deformation would have a strong effect on neutron inelastic scattering from both dynamically deformed and permanently deformed nuclei, that is, vibrational and rotational nuclei. As an extreme example, in the DWBA the direct part of the inelastic scattering is proportional to the square of the deformation parameter. Using a vibrational optical model, Fu and Perey have obtained good fits to inelastic scattering data on Pb for 14 MeV incident neutrons.<sup>4</sup> Also, Belovitzk *et al.*<sup>5</sup> have studied the excitation by 14 MeV neutrons of the low-lying octupole states of the isotopes  $^{206,207,208}\text{Pb}$ . In this latter work reasonable agreement between the experimental data and the results of calculations based on DWBA theory was found. We are not aware of any published cross sections on neutron inelastic scattering, separated from the elastic scattering, for heavy, permanently deformed nuclei at incident neutron energies where direct excitation of the rotational levels predominates.

In the present work, deformation effects in neutron scattering were investigated by scattering 7 MeV neutrons from the isotopes  $^{148}\text{Sm}$ ,  $^{150}\text{Sm}$ ,  $^{152}\text{Sm}$ , and  $^{154}\text{Sm}$ . The Sm isotopes are desirable nuclei for studying the effects of nuclear deformation because they span the region near  $N = 88$  where the nuclear deformation changes rapidly. In this regard the nucleus  $^{150}\text{Sm}$  is of special interest because of its role as a transitional nucleus between vibrational and rotational nuclei. The nucleus  $^{146}\text{Nd}$  was included in these investigations, also, in order to separate possible isospin effects from deformation effects. The Sm and Nd samples were isotopically enriched and were available only in the form of oxides.

Differential cross sections for elastic scattering and inelastic scattering to the first  $2^+$  state were measured for the nuclei  $^{146}\text{Nd}$ ,  $^{148}\text{Sm}$ ,  $^{150}\text{Sm}$  ;

whereas for  $^{152}\text{Sm}$  and  $^{154}\text{Sm}$ , cross sections for the sum of elastic and inelastic scattering (first  $2^+$  state) were determined. Measurements were performed over the angular range  $20^\circ$  to  $145^\circ$  ; however, inelastically scattered neutrons were not observed directly at forward angles because of appreciable elastic scattering from oxygen.

An incident energy of 7 MeV was chosen for the present study primarily because, as shown in fig. 1, measurements<sup>6</sup> and calculations<sup>7</sup> of total cross section differences for the Sm isotopes suggest that at this energy the deformation effects in neutron scattering may be maximum. Calculations using a range of deformation parameters indicate that the energy of this maximum does not depend appreciably on nuclear shape.<sup>7</sup> This incident energy is believed to be sufficiently high that compound elastic scattering effects are unimportant for these nuclei.

## Experimental Method

The differential cross section measurements were performed using the neutron time-of-flight facility of the Centre d'Etudes de Bruyères-le-Châtel, which has been described in detail elsewhere.<sup>8</sup> Briefly, proton bursts of repetition rate 2.5 MHz and width 1 nsec (FWHM) were accelerated by the Bruyères tandem accelerator. Monoenergetic 7-MeV neutrons were produced by bombarding tritium, contained in a 3-cm long gas target at a pressure of about 1.5 atm, with this pulsed proton beam. Neutrons were scattered by cylindrical samples located at  $0^\circ$  with respect to the incident proton beam and 11.3 cm from the center of the gas target. The scattered neutrons were detected by an array of four detectors placed at  $20^\circ$  intervals, each detector consisting of a 12.5-cm diameter, 5-cm thick NE-213 liquid scintillator which was optically coupled to an XP-1040 photomultiplier tube. Pulse-shape discrimination was utilized to reject  $\gamma$ -ray induced events in the scintillators. The data acquisition system which was employed permitted off-line adjustment of the energy threshold for neutron detection. Only scintillation pulses which corresponded to neutron energies greater than 1.5 MeV were utilized in the present work.

Each neutron detector was housed in a shield consisting of polyethylene and lead and was placed behind a 1.5 m collimator composed of paraffin loaded with lithium and boron. Four 70-cm long Fe shadow bars with W tips were positioned near the gas target in order to reduce background caused by direct neutrons. The flight path from the sample to each detector was 8 m. For this flight path the energy spreads and time spreads of the experiment were such that the overall energy spread at each neutron detector was less than 150 keV. With this spread, kinematic



separation of the oxygen scattering was sufficient to observe the inelastic scattering to first excited states for  $^{146}\text{Nd}$  and  $^{148,150}\text{Sm}$  at angles  $\geq 90^\circ$ .

Detector efficiencies were determined by scattering neutrons from a 1-cm diameter 4-cm high polyethylene sample and by counting directly monoenergetic neutrons from the  $\text{D(d,n)}$  reaction.<sup>9</sup> The incident neutron flux was measured using a proton-recoil counter telescope.

The number of incident neutrons from the gas target was monitored by an auxiliary NE-213 liquid scintillation detector placed at  $55^\circ$  to the incident proton beam and about 10 m from the gas target.

All samples were contained in air-tight thin-walled polyethylene cans about 2.2 cm in diameter and 5 cm high. The Sm samples,  $^{148,150,152,154}\text{Sm}$ , consisted of powdered  $\text{Sm}_2\text{O}_3$  and ranged in mass from 40.8 g ( $^{154}\text{Sm}_2\text{O}_3$ ) to 68.6 g ( $^{148}\text{Sm}_2\text{O}_3$ ). The isotopic enrichment of each sample was greater than 96 % except for  $^{150}\text{Sm}$ , for which the enrichment was 87.4 %. The  $^{146}\text{Nd}_2\text{O}_3$  sample had a mass of 63.6 g and an enrichment of 94.5 %.

Background peaks in the TOF spectrum caused by the carbon of the polyethylene can and the oxygen of the oxide samples were subtracted with the aid of an empty can and an  $\text{H}_2\text{O}$  sample, respectively.

Cross sections were corrected for neutron flux attenuation in the sample, multiple scattering, and geometrical effects using the analytic method described by Kinney.<sup>10</sup>

### Results and Discussion

Some of the results from a preliminary analysis of the data are given in figs. 2, 3 and 4.

The measured differential cross sections for elastic scattering are presented in fig. 2 for each of the nuclei  $^{146}\text{Nd}$ ,  $^{148}\text{Sm}$ , and  $^{150}\text{Sm}$ . The uncertainty of each datum has been estimated to be about the size of the data point or smaller, except at  $35^\circ$  where the statistical uncertainty is about 12 % because the  $^{160}\text{Sc}$  scattering is relatively large at that angle. It is observed that the three angular distributions are very similar. Quantitative comparisons were made by making a Legendre fit to each distribution. The Legendre curves for  $^{148}\text{Sm}$  and  $^{150}\text{Sm}$  for example, were found to differ by at most about 10 % over the angular range of the measurements. Also shown in this figure is the result of a coupled channel calculation for  $^{148}\text{Sm}$ , which was assumed to be a vibrational nucleus with a quadrupole deformability,  $\beta_2$ , of 0.13. The deformed-potential optical-model parameters which were used for this calculation were determined by fitting total cross section data,<sup>11</sup> strength function data, and potential scattering at low energies. These parameters are similar to parameter set 2 of ref. 7. It is seen that the agreement between the experimental and calculated cross sections for  $^{148}\text{Sm}$  is remarkably good, even though no attempt has been made to fit the present data.

The cross section data for  $^{152}\text{Sm}$  and  $^{154}\text{Sm}$  are given in fig. 3. For each of these nuclei, the cross sections for the sum of elastic scattering plus inelastic scattering to the first excited state are shown. Here, also, the experimental uncertainties are about the size of the data points or smaller, except at  $35^\circ$ . It is observed that the angular distributions for these two nuclei are very similar, except for small differences at the  $40^\circ$  and  $80^\circ$  minima and at angles greater than  $120^\circ$ . The calculated curve for  $^{154}\text{Sm}$  given in this figure represents the sum of cross sections for elastic plus inelastic (first  $2^+$  state) scattering. This coupled-channel calculation differed from the one for  $^{148}\text{Sm}$  in that: 1)  $^{154}\text{Sm}$  was assumed to be a rotational nucleus, 2) the real part of the optical potential was about 1 % smaller in magnitude

for  $^{154}\text{Sm}$  because of the inclusion of an isospin term in the optical potential, and 3) the quadrupole deformation was taken to be 0.22. The parameters used for the  $^{148}\text{Sm}$  and  $^{154}\text{Sm}$  calculations provide a very good fit to total cross section difference measurements<sup>11</sup> over the energy range 1 to 15 MeV. These parameters have not been adjusted in order to improve the fit to the  $^{154}\text{Sm}$  data of the present work. Again, it is seen that there is good agreement between the calculated curve and the data.

Figure 4 shows a comparison of elastic scattering angular distributions between the vibrational nucleus  $^{148}\text{Sm}$  and the rotational nucleus  $^{154}\text{Sm}$ . For  $^{148}\text{Sm}$ , the cross section data and calculated curve presented here are identical to those given in fig. 2. The elastic cross sections for  $^{154}\text{Sm}$  were obtained by subtracting the computed inelastic ( $2^+$ ) cross sections from the experimental ( $0^+ + 2^+$ ) cross sections. The  $^{154}\text{Sm}$  calculated curve in this figure represents, of course, only elastic scattering.

No inelastic cross sections will be presented in the present report, primarily because of space limitations. It suffices to say at this time that at backward angles the inelastic cross sections for scattering to the first  $2^+$  state are similar for  $^{146}\text{Nd}$  and  $^{148}\text{Sm}$  and significantly larger for  $^{150}\text{Sm}$  as compared to the two lighter nuclei.

It was possible for each of the nuclei studied to compare the  $0^\circ$  differential cross section, determined by means of a Legendre fit, with Wick's limit, since measured total cross section values are available at 7.0 MeV for these Sm isotopes<sup>11</sup> and the  $^{146}\text{Nd}$  nucleus.<sup>12</sup> The differences ranged from 16 % for  $^{148}\text{Sm}$  to - 6 % for  $^{154}\text{Sm}$  with a standard deviation of 4 %. This standard deviation is well within the range expected on the basis of the estimated uncertainties for the present work and for the total cross section measurements.

The elastic differential cross sections for  $^{148}\text{Sm}$  and the elastic plus inelastic differential cross sections for  $^{154}\text{Sm}$  of the present work at 7.0 MeV have been compared to the results of recent measurements on these nuclei at 6.25 MeV neutron energy which were performed at the TOF facility of the University of Kentucky.<sup>13</sup> For each isotope the angular distributions at the two energies were observed to be in good qualitative agreement. Coupled-channel calculations indicated that the small quantitative differences which were present were a consequence of the different energies which were employed.

The work of Holmqvist et al.<sup>1</sup> on  $^{181}\text{Ta}$  suggests that the major effect of nuclear deformation on the elastic scattering of neutrons is to increase considerably the cross sections at the minima of the elastic angular distributions. However, the data and the calculated curves presented in fig. 4 indicate that for the Sm isotopes the effect of an increased quadrupole deformation parameter is to lower the elastic scattering angular distribution at back angles.

The reason for this apparent difference in deformation effects between Ta and Sm is not clear at the present time. Holmqvist et al. assumed that inelastic scattering to the 6 keV state of  $^{181}\text{Ta}$ , which of course was not experimentally resolved, was negligible. However, the 6.25 MeV study<sup>13</sup> of Sm, the present work, and coupled-channel calculations<sup>3</sup> for the scattering of 17.5 MeV neutrons by  $^{156}\text{Gd}$  all indicate that for even-A deformed rare earth nuclei, inelastic scattering to the first excited state is larger than elastic scattering at most back angles. Thus, contrary to their assumption<sup>1</sup>, it is likely that inelastic scattering to the 6 keV state of  $^{181}\text{Ta}$  is relatively very large, also.

### Acknowledgements

It is a pleasure to thank Dr. A. Michaudon for his support and encouragement, Jean Sol and his group for dehydrating and compacting samples, and the USAEC for the loan of the samples.

### References

- + present address : University of Ky., Lexington, Ky.
- ++ On leave from West. Mich. Univ., Kalamazoo, Mich.
1. B. Holmqvist, T. Wiedling, V. Benzi, L. Zuffi, Nucl. Phys. **A150**, 105 (1970).
2. S. Tamaka, Y. Tomita, Y. Yamanouti, K. Ideno, Nuclear Structure Study with Neutrons (Plenum Press N.Y., 1974) p. 148.
3. T. Tamura, Rev. Mod. Phys. **37**, 679 (1965).
4. C.Y. Fu and F.G. Perey, ORNL - 47 (1972).
5. G. Belovitzk, L. Kolesnikova, I. Frank, Nuclear Structure Study with Neutrons (Plenum Press, N.Y., 1974) p. 166.
6. Shamu, Bernstein, Blondin, Ramirez, Rochau, Phys. Lett. **45B**, 241 (1973).
7. Ch. Lagrange, Lett. J. de Phys. **35**, 111 (1974).
8. Haouat, Lachkar, Patin, Sigaud, Coçu, C.E.A. R-4641 (1975).
9. H. Liskien and A. Paulsen, Nucl. Data Tables **11**, 569 (1973).
10. W.E. Kinney, Nucl. Inst. Meth. **83**, 15 (1970).
11. R. Shamu, E. Bernstein, J. Ramirez, Bull. Am. Phys. Soc. **19**, 103 (1974).
12. E. Bernstein and R. Shamu, private communication.
13. Burrows, Dawson, Glasgow, Hardie, Lagrange, McDaniel, Shamu, private communication.

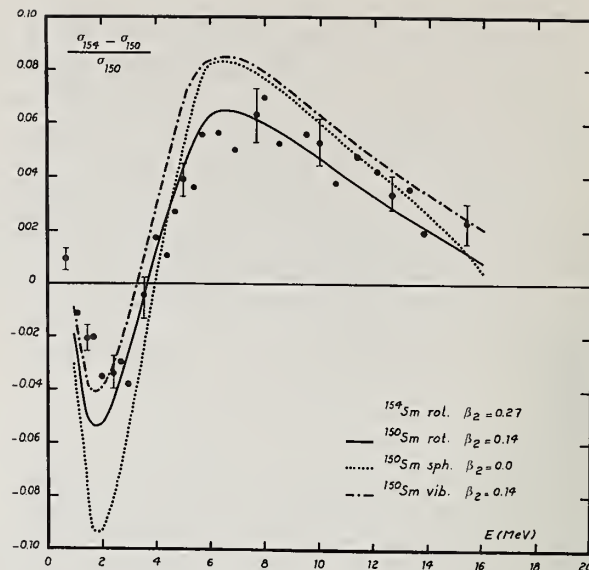


Fig. 1. Variation with neutron energy of the relative difference between the total cross sections<sup>6</sup> of <sup>154</sup>Sm and <sup>150</sup>Sm. The curves are the results of coupled-channel calculations<sup>7</sup>.



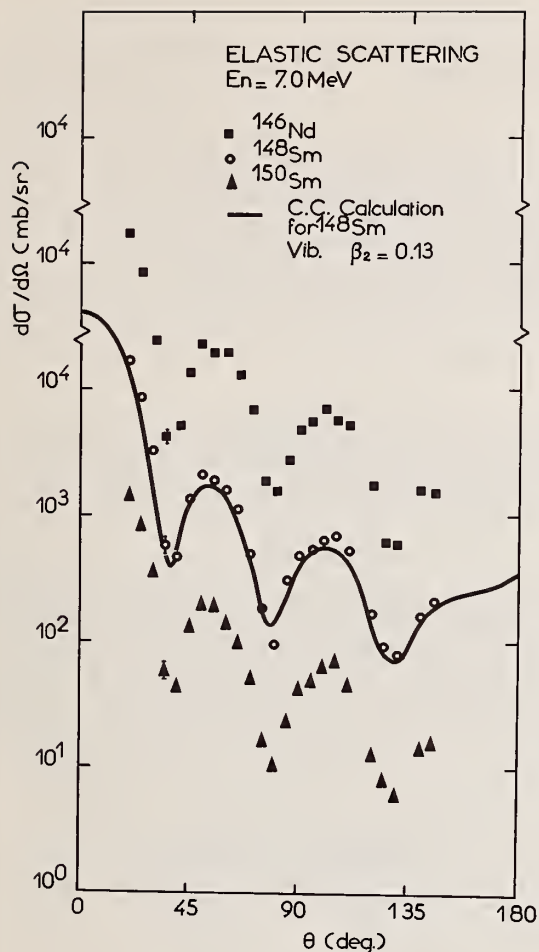


Fig. 2 (above) Elastic scattering angular distributions for  $^{146}\text{Nd}$ ,  $^{148}\text{Sm}$  and  $^{150}\text{Sm}$  at 7.0 MeV incident neutron energy. The solid line is the result of a coupled-channel calculation for  $^{148}\text{Sm}$ .

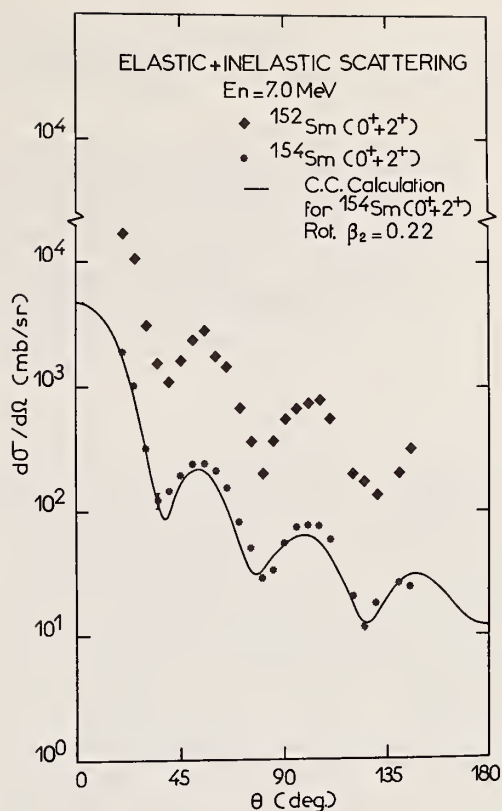


Fig. 3 (topright) Angular distributions for the sum of elastic and inelastic (first  $2^+$  state) cross sections for  $^{152}\text{Sm}$  and  $^{154}\text{Sm}$  at 7.0 MeV incident neutron energy. The solid line represents the calculated cross sections for elastic and inelastic (first  $2^+$  state) scattering by  $^{154}\text{Sm}$ .

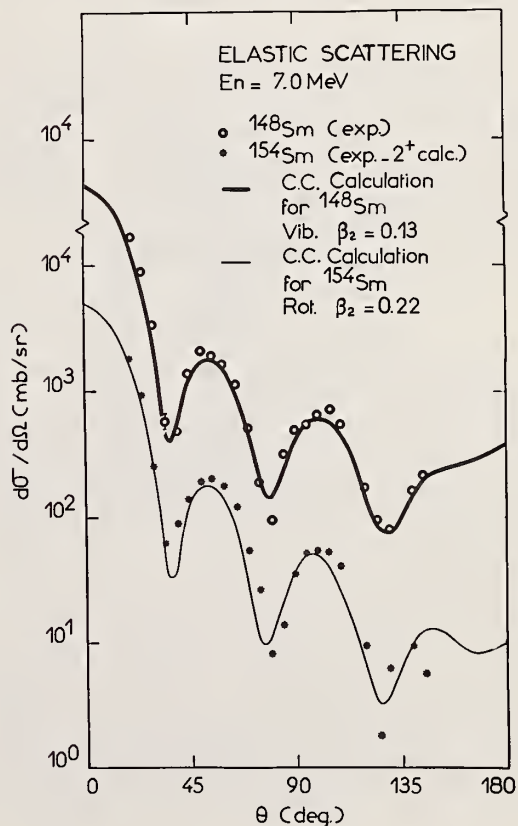


Fig. 4 (bottom right) Comparison of elastic scattering angular distributions between  $^{148}\text{Sm}$  (vibrational nucleus) and  $^{154}\text{Sm}$  (rotational nucleus). The data points for  $^{154}\text{Sm}$  represent the difference between the experimental ( $0^+ + 2^+$ ) and the computed inelastic ( $2^+$ ) cross sections. The solid lines are calculated elastic angular distributions.

By the application of a new technique, absolute cross sections for the small-angle elastic scattering of neutrons by U have been accurately determined at various energies in the range 7-14-MeV. The data show less strong forward-peaking at small angles than previously reported results. In addition, measurements of the small-angle scattering by Pb were also carried out over the same energy range; and the results, while in conflict with some previous reported measurements, are, apart from normalization, in excellent agreement with optical model calculations based on the energy independent, non-local potential of Perey and Buck.

(Fast Neutrons; Scattering; Pb; U; Small Angles)

### Introduction

There have been many conflicting measurements<sup>1-5</sup> of the scattering of fast neutrons through small angles by heavy nuclei. Several important questions of a fundamental nature, which concern the strength of the electric dipole moment of the neutron, the nature of the fission process, and the possible existence of long-range nuclear forces, have been raised by reported anomalies in the scattering at small angles, and these questions still remain to be clearly resolved. One reason for this conflict of results is that, even though measurements at small angles are difficult, a higher precision is required. Another problem lies in the interpretation of existing data, which in general is available only at isolated energies and with large uncertainties in the normalizations. As a result many investigators have relied, in the interpretation of their data, on specialized nuclear models which fit only the shape of angular distribution data at a single energy.

It is the purpose of this paper to present results which contribute to the resolution of the above problem. Absolute measurements of the elastic scattering of neutrons by Pb and <sup>238</sup>U were carried out to high accuracy for angles in the interval 3 to 15 degrees and over the range of energies from 7 to 14 MeV. This energy range spans a large body of existing data and, in addition, is sufficiently wide to provide a good test for optical model predictions of differential scattering cross sections at small angles.

### Experimental Technique

A detailed description of the experimental arrangement for the U measurements (shown in figure 1) has been reported elsewhere<sup>6</sup>. Basically, it can be characterized as a four-fold shielded detector configuration that involves shielding (collimating channels) along the entire beam path(s) from scatterer to detector. The distinguishing difference between the conventional shielded-detector geometry and the configuration applied here is that with the latter the transverse dimensions of the collimating channels are small compared to those of the scattering sample, and the scattering is therefore defined by the acceptance profiles of the channels rather than the size of the scatterer. The main advantages of this technique are high counting rates and the near elimination of background due to air scattering. For the U measurements, as well as for other small-angle measurements at this laboratory, Pb was used as a standard of reference at each measured point. The absolute cross sections for Pb were, in turn, determined by a set of auxiliary

measurements which were carried out in a ring-type geometry. Corrections for air scattering are important at small angles in ring geometry and were found to be most accurately determined by analytical means.

### Measurements

Both time-of-flight and pulse-shape discrimination techniques were employed in the measurements. Deuterons from the BRL Tandem Van de Graaff were pulsed at a repetition rate of 2MHz and bunched to 1.5 nsec FWHM. The energy spreads of neutrons produced by means of the d(D,N)<sup>3</sup>He reaction in a gas cell were typically 120 and 260 KeV for neutron energies of 14.0 and 7.0 MeV, respectively. Over each angular distribution measurement the deuteron energy was adjusted to compensate for slight changes in the neutron emission angle and thereby yield a constant neutron energy. The high counting rates inherent in each of the scattering geometries permitted the use of relatively thin scattering samples (75% transparency), and thus the greater uncertainties inherent in large multiple scattering corrections were avoided.

Correction to the data were made for multiple scattering, air scattering, finite geometry and other effects.<sup>6</sup> In calculating the effects of both multiple scattering (by Monte Carlo techniques) and air scattering, constraints due to neutron flight time requirements were imposed. The error flag assigned to each data point includes that due to counting statistics (0.5 to 2.5%), uncertainties in the corrections, and other experimental uncertainties such as in the detector efficiency and in the transmission of the scatterer.

### Results

In Figure 2 the data, less Schwinger scattering, is displayed in the C.M. system. These data are well represented (see curves of Figure 2) by the functional relationship

$$\ln \sigma(\theta, E) = A(E) + B(E)\mu + C(E)\mu^2 \quad (1)$$

where  $\mu = 1 - \cos\theta$ ,  $A(E)$  is a polynomial of 4th order in  $E$ , and  $B(E)$  and  $C(E)$  are quadratic in  $E$ . It was verified that the form of the angular dependence of Equation (1) is sufficiently general so as not to preclude good fits (i.e.,  $< 0.5\%$ ) to a variety of optical model calculations over the range 0-15°. The percent deviations of Equation (1) from both the data and Wick Limits are plotted in Figure 3 for Pb. For U, the arrows in Figure 2 indicate Wick Limits.

The present data can be clearly compared with those of other workers at neighboring energies by the curves generated from Equation (1). It is seen that the present results for both Pb and U disagree with the data of references 1 and 2 on which were based reports of anomalous scattering. The shape of the angular distribution of Adam et al<sup>3</sup> at 14.7 MeV for U, which indicates some anomalous peaking around 5°, is only in fair agreement with the corresponding curve. While good statistical agreement is obtained with the data of Benenson et al<sup>4</sup> for Pb, we do not support their claim that the optical model parameters of Rosen et al<sup>7</sup> best describe the data (see figure 4). The 14.1 MeV cross sections for Pb and U which were measured over the angular range 5-150° by Coon et al<sup>8</sup> are in excellent agreement with our measurements.

### Conclusions

In Figure 4 it is seen that the present data strongly disagree with the optical model predictions of Rosen et al.<sup>7</sup> However, the parameters of Fu and Perey<sup>9</sup>, which are based on the energy independent, non-local optical model potential of Perey and Buck<sup>10</sup>, are apart from normalization, in excellent agreement; i.e. the shapes of the angular distributions agree to within ±2% (see Figure 5). For U, similar agreement is obtained with the theoretical calculations of Palla<sup>11</sup> which take into account the nuclear deformation. It is concluded that, to within ±2%, no anomalies exist in the scattering of 7-14 MeV neutrons by Pb or U.

### References

1. G.V. Anikin and I.I. Kotukhov, *Yad. Fiz.* **12** 1121 (1970) [*Sov. J. Nucl. Phys.* **12** 614 (1971)].
2. Yu. V. Dukarevich and A.N. Dyumin, *Zh. Eksp. Teor. Fiz.* **44** 130 (1963) [*Sov. Phys. - JEPT* **17** 87 (1973)].
3. A. Adam et al., *Acta. Phys.* **25** 261 (1968).
4. R. E. Benenson et al., *Nucl. Phys.* **A212** 147 (1973).
5. For other references to small-angle scattering results see N.S. Lebedeva and V.M. Morozov, *Atomnaya Energiya* **28** 310 (1970).
6. W. Bucher et al., *Nucl. Inst. and Meth.* **111**, 237 (1973).
7. L. Rosen et al., *Ann. of Phys.* **34** 96 (1965).
8. J.H. Coon et al., *Phys. Rev.* **111** 250 (1958).
9. C.Y. Fu and F.G. Perey, *Ornl-4765*, Oak Ridge National Lab. (1972).
10. F. Perey and B. Buck, *Nucl. Phys.* **32** 353 (1962).
11. G. Palla, *Phys. Lett.* **35B** 477 (1971).

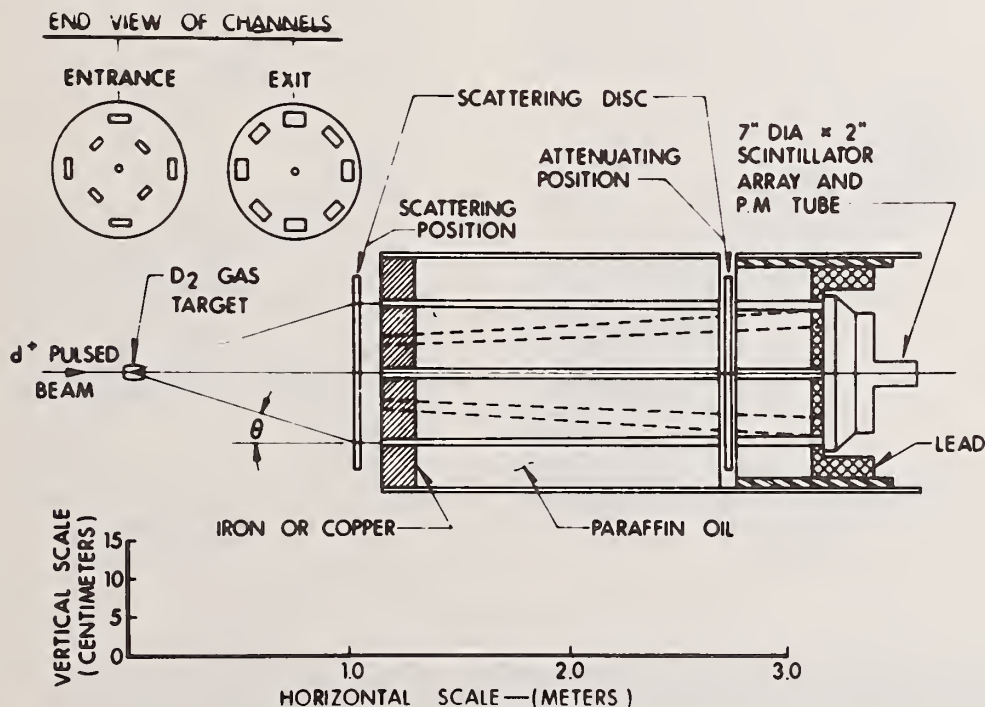


FIG. 1. Schematic diagram of experimental arrangement showing 3 of 9 channels. Note expanded vertical scale.



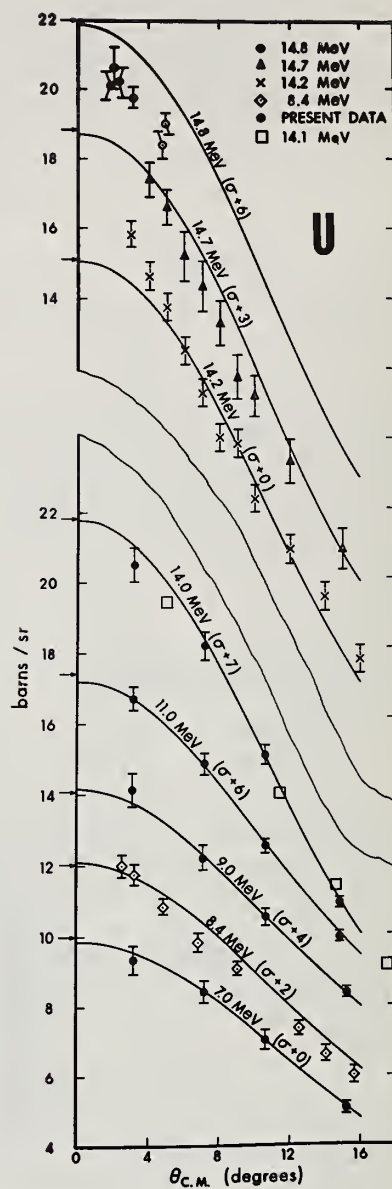
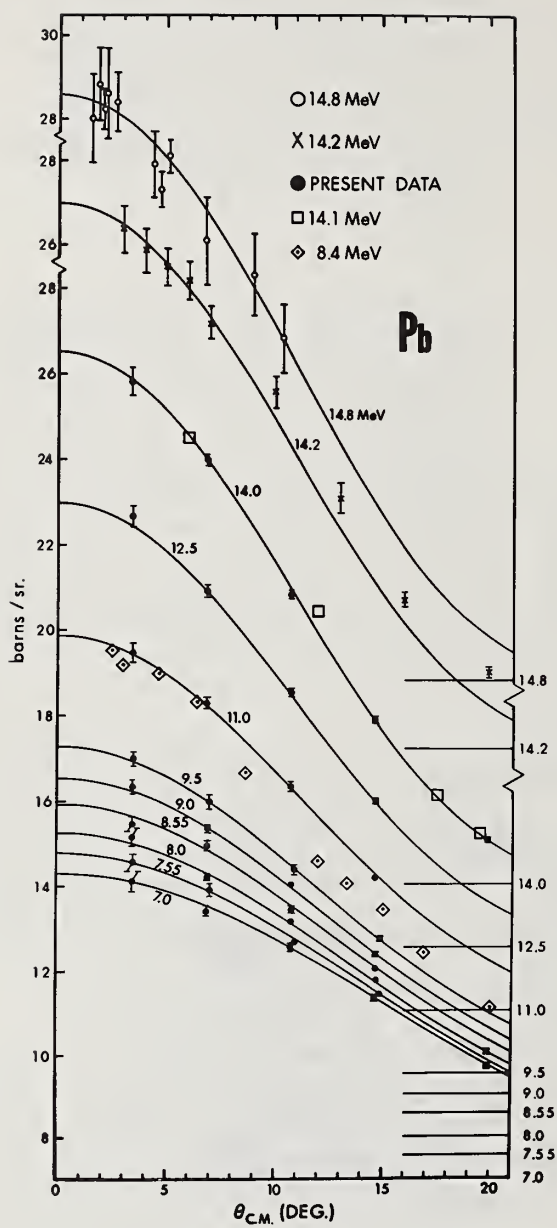


FIG. 2. Neutron scattering from Pb and U. The data at 8.4, 14.1, 14.2, 14.7, and 14.8 are from refs. 1, 8, 2, 3, and 4, respectively. The scale for the Pb cross sections is displaced by the amount  $E(\text{MeV})$  in b/sr.; the displacements for U are as indicated on each curve.

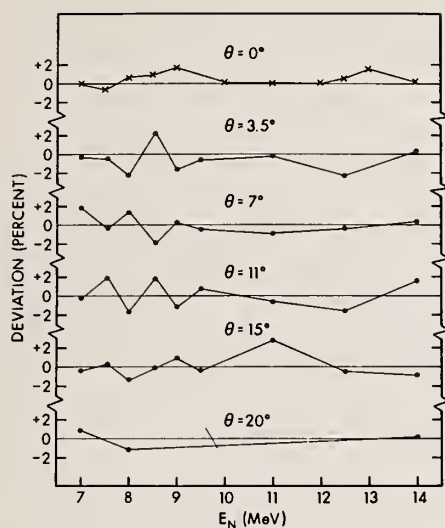


FIG. 3. Percent deviations of Eq. (1) from the data points and, at zero degrees, from the energy-averaged Wick Limit values.

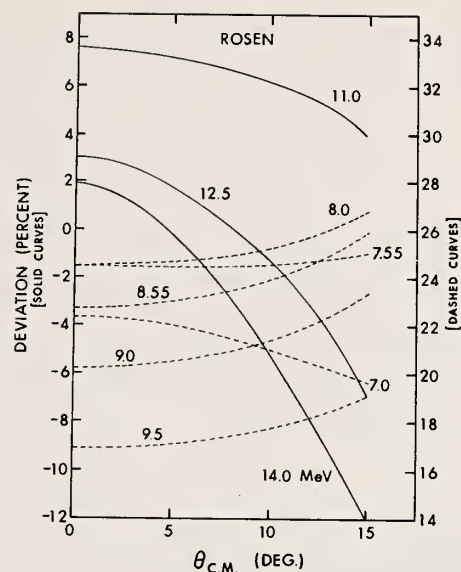


FIG. 4. Percent deviations of predictions of optical Model of Rosen et al.<sup>7</sup> from present data.

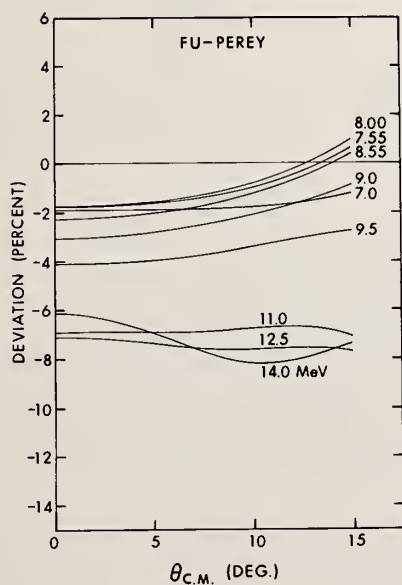


FIG. 5. Percent deviations of predictions of optical model of Fu and Perey<sup>9</sup> from present data.

ELASTIC AND INELASTIC DIFFERENTIAL NEUTRON SCATTERING CROSS SECTIONS FOR  $^{238}\text{U}$  FROM 0.9 - 2.7 MeV\*  
 J. J. Egan, G. H. R. Kegel, G. P. Couchell, A. Mittler, B. K. Barnes, W. A. Schier, D. J. Pullen, P. Harihar,  
 T. V. Marcella, N. B. Sullivan, and E. Sheldon  
 Lowell Technological Institute  
 Lowell, Massachusetts 01854,  
 and  
 A. Prince,  
 Brookhaven National Laboratory  
 Upton, Long Island, New York 11973

Differential cross sections have been measured via the time-of-flight method for neutrons scattered at  $90^\circ$  from the ground and first two excited states, at 45 and 148 keV, of  $^{238}\text{U}$  in the bombarding energy range 0.9 to 2.7 MeV. The  $^7\text{Li}(p,n)^7\text{Be}$  reaction was the neutron source. The LTI 5.5 MeV Van de Graaff accelerator in conjunction with a Mobley bunching system generated proton pulses with durations as short as 320 picoseconds (fwhm). The excellent timing characteristics of this system enabled the three states in  $^{238}\text{U}$  to be resolved up to 2.7 MeV. Above 1.5 MeV the present results for the  $2^+$  state at 45 keV are 2 to 2.5 times larger than the ENDF/IV cross sections. However, the present results are in good agreement with theoretical calculations which incorporate both direct interaction and compound nucleus contributions to the cross sections.

(NUCLEAR REACTIONS  $^{238}\text{U}(n,n)$ ,  $(n,n')$ ,  $E = 0.9 - 2.7$  MeV; measured  $\sigma(E_n, 90^\circ)$  for ground, 45, 148 keV states. Time-of-flight. Compared with calculated excitation functions.)

### Introduction

The purpose of this paper is to report measurements of the differential neutron scattering cross sections for the ground and first two excited states, at 45 keV ( $2^+$ ) and 148 keV ( $4^+$ ), in  $^{238}\text{U}$  for bombarding energies up to 2.7 MeV. Previously published data on the  $2^+$  state have been subject to large uncertainties in the region above 1.1 MeV due to the inability to resolve this state from the ground state. The  $4^+$  state has been resolved only up to 1.5 MeV. Estimates of the level cross sections at higher energies have been obtained from theoretical calculations and from analysis of data on the combined neutron groups.

In the present work these levels have been resolved up to 2.7 MeV. The differential cross sections at  $90^\circ$  will be presented and compared with theoretical calculations which include contributions from direct interaction and compound nucleus mechanisms.

### Experimental Methods

The data were taken at the Lowell Technological Institute Van de Graaff accelerator laboratory. The 5.5 MV type CN machine with terminal pulsing and Mobley bunching system routinely produces proton pulses of 320 ps at a 5 MHz repetition rate. We have recently achieved pulse widths as short as 280 ps, as determined by the full width at half maximum of the prompt gamma-ray peak in a time-of-flight spectrum measured by a scintillation detector with premium timing characteristics.

The scattering data were taken using the time-of-flight technique with the  $^7\text{Li}(p,n)^7\text{Be}$  reaction as the neutron source. The scattered neutron groups due to incident neutrons which leave  $^7\text{Be}$  in its first excited state were not in the time region of interest, and hence presented no problem in these measurements. Before each data point was taken, a new target was made in place in the proton beam by an evaporator system incorporated in the target assembly. Target thickness was monitored during the evaporation process by the main neutron detector, which will be described later.

Figure 1 depicts the experimental arrangement. The scattering sample was a circular disk of depleted uranium 0.25-in. thick by 1.5-in. diameter. For measurements at  $90^\circ$  the plane of the disk was oriented at  $45^\circ$  to the beam direction in order to minimize

the spread in flight times arising from neutrons scattering from different parts of the sample.

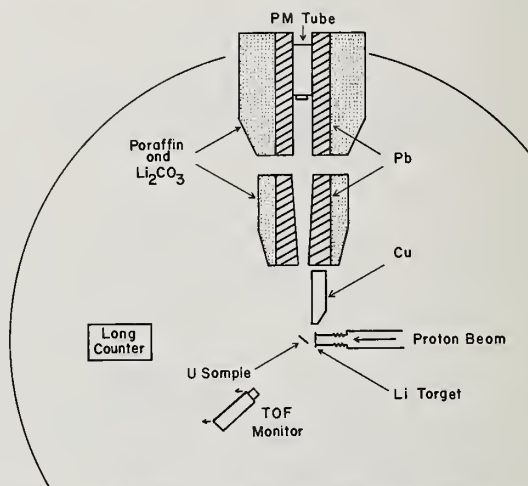


Fig. 1. Schematic diagram of the experimental arrangement.

The main neutron detector consisted of a 0.25-in. thick by 4.5-in. diameter NE102 plastic scintillator mounted on an RCA 8854 photomultiplier tube. The detector is shielded by two massive shields containing a paraffin and lithium carbonate mixture. The shields are lined with thick lead annuli. A massive copper shadow bar intercepts the direct target neutrons. The flight path for this experiment was 2.82 m.

The normalization of the data was accomplished by monitoring the prompt gamma rays produced by proton induced reactions in  $^7\text{Li}$  with the time-of-flight (TOF) monitor detector, which consists of a 0.25-in. thick by 1.5-in. diameter Pilot U plastic scintillator mounted on an RCA C31024 photomultiplier tube. This detector has extremely good time resolution. It was also used to monitor the proton beam pulse width.

An on-line computer system sampled the gamma-ray peak width in the TOF monitor spectrum at two minute intervals and automatically inhibited data acquisition whenever the beam pulse width became larger than a



predetermined value (usually this was set at 350 ps). A standard long counter calibrated against a recoil proton telescope served as an auxiliary monitor.

The associated electronic system consisted of commercially available NIM modules with the addition of a "walk" correction circuit which subtracted a fraction of the linear signal of the main neutron detector from the output of the time-to-amplitude converter (TAC) in order to minimize time jitter due to signals of different sizes at the TAC input. The electronic system was adjusted for optimum time resolution before each data point was taken.

Efficiency curves for the main detector were taken before and after each data point. These were obtained by measuring the  ${}^7\text{Li}(p,n){}^7\text{Be}$  angular distribution and normalizing to the known relative cross section. The absolute efficiency was not needed because we removed the sample and brought the main detector to  $0^\circ$  (we also moved the target to the sample position, and the TOF monitor back an equal distance) in order to measure the incident flux. Hence the incident and scattered flux were measured with the same detector.

Figures 2 and 3 show the time-of-flight spectra of the scattered neutrons at 0.9 and 2.0 MeV respectively. The run times for these spectra were approximately 48 hours. The excellent resolution at 2 MeV attests to the good long term stability of our system. The full width at half maximum of the elastic neutron group is 0.8 ns for the spectrum at 2.0 MeV.

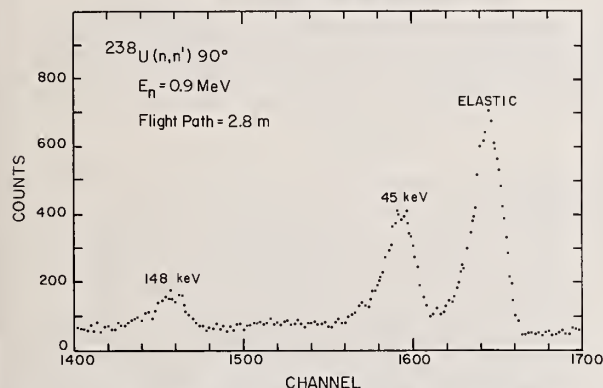


Fig. 2. The time-of-flight spectrum for 0.9 MeV incident neutrons scattered from  ${}^{238}\text{U}$  at  $90^\circ$ .

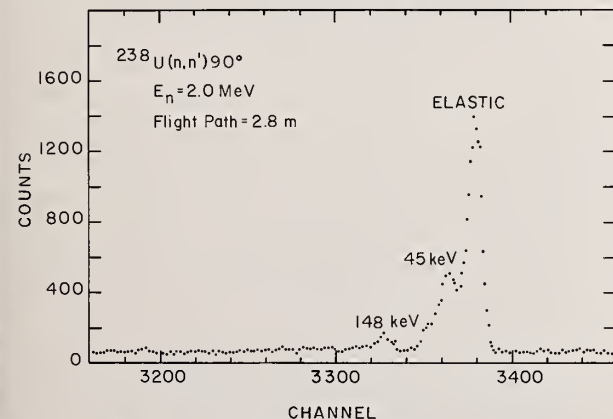


Fig. 3. The time-of-flight spectrum for 2.0 MeV incident neutrons scattered from  ${}^{238}\text{U}$  at  $90^\circ$ .

## Results and Analysis

The results of the experiment are shown on Figs. 4, 5, and 6. Figure 4 shows the elastic differential cross section at  $90^\circ$ . Figures 5 and 6 show the inelastic differential cross sections for the 45 and 148 keV levels respectively. The solid curves represent theoretical calculations and the dashed curve is the ENDF/IV evaluation for comparison. The upper solid curve is the sum of the direct and compound nucleus curves. The data shown in these figures have been corrected for neutron attenuation and multiple scattering using the Monte Carlo code MCN.<sup>1</sup>

As early as 1970, Prince<sup>2</sup> indicated that previous estimates of the inelastic cross sections above 1.5 MeV may be too low due to a direct excitation of the rotational levels by inelastic scattering. Indeed some earlier cross section compilations<sup>3</sup> list the inelastic cross sections as zero for both the  $2^+$  and  $4^+$  states above 1.5 and 1.8 MeV respectively. Prince's 1970 calculation indicated that the direct interaction contributes significantly to the cross sections and becomes the dominant component above 1.5 MeV.

The elastic scattering data in Fig. 4 agree with the ENDF/IV evaluation up to 1.5 MeV and are somewhat lower than ENDF/IV at higher energies. Presumably this is due to the inability to separate out the 45 keV state in earlier experiments. The calculations underestimate the cross section somewhat in the 1.5 to 2.0 MeV region. At other energies there is good agreement between data and theory.

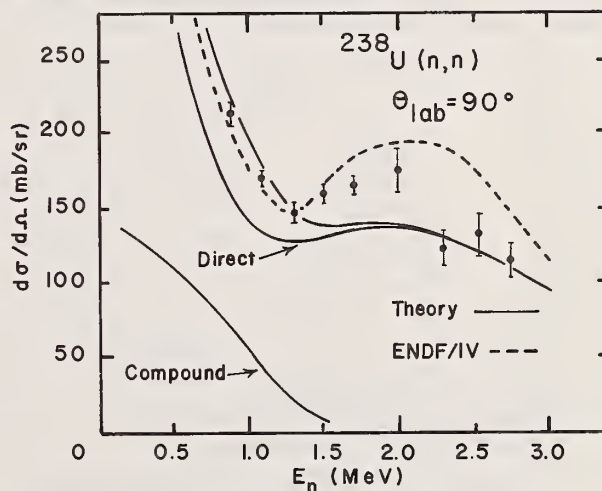


Fig. 4 The lab differential elastic neutron scattering cross section at  $90^\circ$  for  ${}^{238}\text{U}$ . The upper solid curve is the sum of the compound nucleus plus direct interaction theoretical calculations.

The data for the  $2^+$  state at 45 keV in Fig. 5 are a factor of 3 times higher than ENDF/IV above 2 MeV. The theoretical calculations are slightly low in this region, but the overall agreement with the theory is not unreasonable.

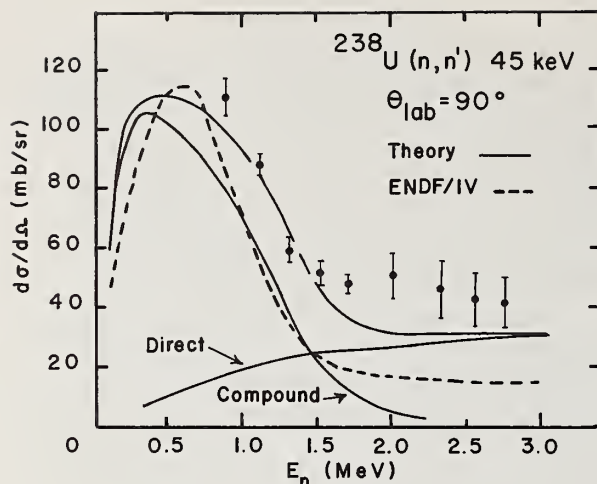


Fig. 5. The lab differential inelastic scattering cross section at  $90^\circ$  for the  $2^+$  45 keV state in  $^{238}\text{U}$ . The upper solid curve is the sum of the compound nucleus plus direct interaction theoretical calculations.

The data for the  $4^+$  state at 148 keV in Fig. 6 are significantly higher than ENDF/IV, especially above 2 MeV. The theoretical calculations are consistently high, but again the agreement between the data and the calculations is reasonable.

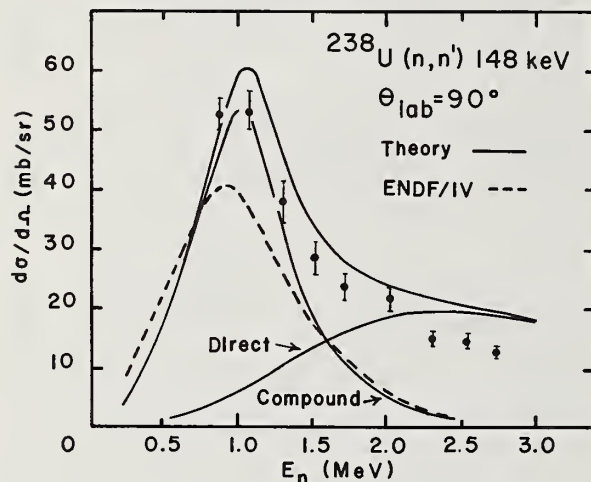


Fig. 6. The lab differential inelastic scattering cross section at  $90^\circ$  for the  $4^+$  148 keV state in  $^{238}\text{U}$ . The upper solid curve is the sum of the compound nucleus plus direct interaction theoretical calculations.

The theoretical calculations shown were accomplished using the coupled channel code JUPITOR-1<sup>4</sup> for the direct interaction contribution, and the code COMNUC-3 for the compound nucleus contribution. The JUPITOR calculations coupled the  $0^+$ ,  $2^+$ , and  $4^+$  levels using a non-spherical energy dependent optical model potential with spin-orbit coupling. The COMNUC Hauser-Feshbach calculations were made using transmission coefficients obtained from a spherical optical potential. These compound nucleus calculations included as possible exit channels compound elastic scattering,

inelastic scattering to discrete as well as continuum levels, radiative capture ( $n,\gamma$ ), and fission ( $n,f$ ). New compound nucleus calculations are currently in progress using transmission coefficients obtained from the non-spherical optical potential used in the JUPITOR calculations. Indications are that these new calculations will increase the compound nucleus cross section by about ten percent.

The ENDF/IV compilation lists the angular distributions for inelastic scattering to the  $2^+$  and  $4^+$  states as isotropic. The theoretical calculations indicate that these angular distributions are not isotropic. We are currently making measurements of these angular distributions in order to check the predictions of the theory. In light of this, one must exercise caution in determining  $\sigma_{n,n'}$ , the integrated cross section, from our  $90^\circ$  measurements. Simply multiplying our results by  $4\pi$  may lead to gross errors.

In conclusion, our data confirm the theoretical prediction that the inelastic cross sections for the 45 and 148 keV states are much more significant at energies above 1.5 MeV than ENDF/IV and previous cross section compilations indicate. And, of theoretical interest, the contribution to inelastic scattering due to direct interaction becomes very important at energies above 1.5 MeV for the first two excited states of  $^{238}\text{U}$ .

#### Acknowledgement

The authors wish to thank G. D. Turner and Charles Forest of the Los Alamos Scientific Laboratory for performing the Monte Carlo calculations used in the finite sample corrections.

#### References

\*This work supported in part by the National Science Foundation.

1. E. D. Cashwell, J. R. Neergaard, W. M. Taylor, and G. D. Turner, LASL Report LA-4751 (1972).
2. A. Prince, *Nuclear Data for Reactors Vol. II* (International Atomic Energy Agency, Vienna 1970) p. 825.
3. I. Langer, J. J. Schmidt, D. Woll, KFK Report KFK-750, EUR 3715e, EANDC (E)-88 "u" p. 605 (1968).
4. T. Tamura, ORNL Report ORNL 4152 (1967).

ABSOLUTE MEASUREMENTS OF NEUTRON RADIATIVE CAPTURE CROSS SECTIONS  
FOR  $\text{Na}^{23}$ ,  $\text{Cr}$ ,  $\text{Mn}^{55}$ ,  $\text{Fe}$ ,  $\text{Ni}$ ,  $\text{Rh}^{103}$ ,  $\text{Ta}$ ,  $\text{U}^{238}$  IN THE keV ENERGY RANGE

C. LE RIGOLEUR, A. ARNAUD, J. TASTE

C.E.N. CADARACHE

13.115 Saint-Paul-lez-Durance (France)

The absolute measurements of several neutron radiative capture cross sections in the keV energy range are presented. The total energy weighting technique was used. Absolute neutron flux were done. Special care was given to the correction arising from the neutron sensitivity of the gamma detector.

(Absolute radiative capture cross sections - keV energy range -  
 $\text{Na}^{23}$ ,  $\text{Cr}$ ,  $\text{Mn}^{55}$ ,  $\text{Fe}$ ,  $\text{Ni}$ ,  $\text{Rh}^{103}$ ,  $\text{Ta}$ ,  $\text{U}^{238}$ )

### Experiment

The capture gamma ray detector was used with fast time of flight technique and with the total energy weighting technique in order to make the detection efficiency for a capture independant of the gamma ray cascade. This efficiency was absolutely determined.

The neutron flux was measured with a  $\text{B}^{10}\text{Ina}$  (Tl) detector or with a  $\text{Li}^6$  glass scintillator. The absolute efficiency of these detectors was determined from a standard detector.

Details on total energy weighting technique, experimental set-up and neutron flux detectors are given in Ref. 1-2-3-4.

The usual corrections for neutron scattering and self-shielding, gamma attenuation in the sample, non linearity of the weighting function ... have been applied. Special care was given to the correction arising from the neutron sensitivity of the gamma detector. Neutron scattered by the sample may be captured by the gamma detector. This time dependant background depends of the mass and thickness of the sample, angular distribution of scattered neutrons, energy and shape of the incident neutron flux. To cope with this serious problem we have first calculated the time probability that a neutron scattered at angle  $\theta$  and energy E be captured by the gamma detector. Then and for each experimental run we have calculated the capture yield arising from neutrons scattered by the sample. We have assumed an isotropic angular distribution

in the center of mass system. Multiple scattering in the sample was taken into account. These calculations were checked experimentally measuring the gamma detector response using a carbon sample.

For iron this correction is very large. There is a large resonance scattering cross section at 27.7 keV and an important resonance capture cross section in fluorine at 27.07 keV.

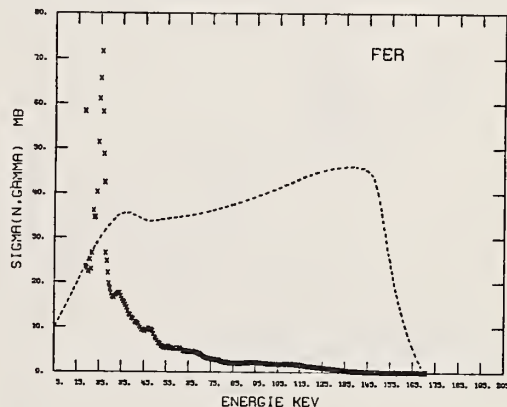


Fig. 1.

\*\* Contribution of scattered neutrons in the capture detector for iron sample.  
-- Incident neutron flux.

On Fig. 1. is shown the calculated contribution of scattered neutron. This contribution has the same order of magnitude than the capture yield from the iron sample

### Results $^{23}\text{Na}$ (20 - 160 keV)

The metallic sodium sample were sealed in Al containers with two thin windows (.1 mm and .03 mm). The background from the aluminum

.../...



This work				CAPTURE CROSS SECTION MEASUREMENTS		Other measurements on Na		
En LAB (keV)	Atom/Barn	$\lambda \gamma \pm \Delta \lambda \gamma$ BARN x eV	$\sigma \frac{\Gamma_n \Gamma_\gamma}{eV}$	$\lambda \gamma \pm \Delta \lambda \gamma$ BARN x eV	En LAB (keV)	$\sigma \frac{\Gamma_n \Gamma_\gamma}{eV}$	En LAB (keV)	
35.45	0.01599	38.41 $\pm$ 1.50	0.3048	35.8 $\pm$ 4 (a) - 2	35.0 (b)	0.394 $\pm$ 0.048(b)	Total Cross section measurements.  35.39 (c)	
35.39	0.01963	36.51 $\pm$ 2.24	0.306					
35.38	0.03225	39.50 $\pm$ 2.16	0.313					
35.30	0.03707	38.66 $\pm$ 1.60	0.307					
35.38 $\pm$ 0.19		38.77 $\pm$ 1.5	0.307 $\pm$ 0.012					
53.62	0.01599	38.51 $\pm$ 2.5	0.4607	34.16 $\pm$ 4 (a) - 2	52.2 (b)	$\frac{\Gamma_n}{\Gamma_\gamma} = 700 \text{ eV}$ $\sigma \frac{\Gamma_n}{\Gamma_\gamma} = 0.987(b)$	53.15 (d)	
53.26	0.01963	34.89 $\pm$ 5.0	0.4169					
53.33	0.03225	39.54 $\pm$ 3.2	0.4730					
53.36	0.03707	38.05 $\pm$ 3.9	0.4547					
53.39 $\pm$ 0.35		37.74 $\pm$ 2.5	0.4513 $\pm$ 0.030					
118.32	0.01963	32.118 $\pm$ 1.55	0.852		114.7 (b)	1.50 $\pm$ 0.37(b)	117.61 (e)	
117.88	0.03707	33.245 $\pm$ 1.58	0.882					
118.10 $\pm$ 1.2		32.68 $\pm$ 1.50	0.867 $\pm$ 0.040					
132.95	0.01963	10.045 $\pm$ 1.2	0.299					
132.70	0.03707	10.48 $\pm$ 1.2	0.312					
132.8 $\pm$ 1.4		10.26 $\pm$ 1.2	0.305 $\pm$ 0.035		129.5 (b)	0.29 $\pm$ 0.07(b)		
144.06	0.01963	11.57 $\pm$ 0.85	0.406					
144.08	0.03707	8.55 $\pm$ 0.6	0.276					
144.07 $\pm$ 1.6		10.06 $\pm$ 2.0	0.341 $\pm$ 0.064					
					139.1 (b)	0.71 $\pm$ 0.18(b)		

TABLE I

a) Capture cross section measurements by activation  
(Le Rigoleur et al - ref 5-6)

b) Capture cross section measurements with a large liquid  
scintillator detector at RPI (R. W. Hockenbury et al - ref 7)

c) Transmission measurements at Saclay (P. Ribon et al - ref 8)

d) Transmission measurements at Columbia University  
(F. Rahn et al - ref 9)

containers, important at 119.8 and 145 keV, was determined with an empty can. The results are shown in table I. There are large discrepancies between our results and those of R.P.I.

Cr, Ni (15 - 65 keV)

Fe (15 - 165 keV)

Only one sample thickness was used for Cr (0.0182 atom/barn) and Ni (0.0185 atom/barn) but two for Fe (0.00824 and 0.0166 atom/barn).

Our data are shown on Fig. 2-3-4 and complete the results already published (Ref. 3-4).

Up to now no detail comparison has been done with other data.

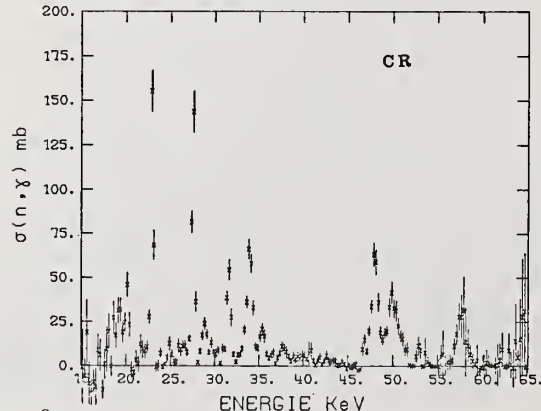


Fig. 2.

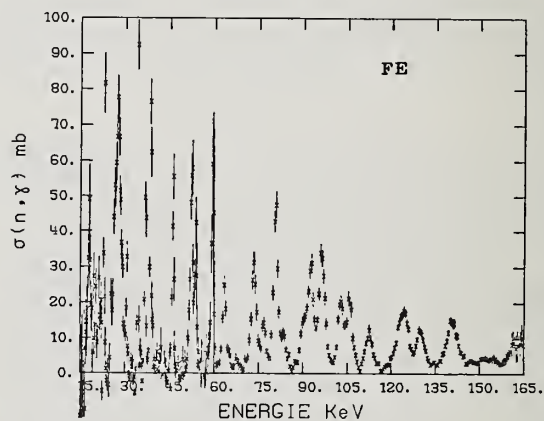


Fig. 3.

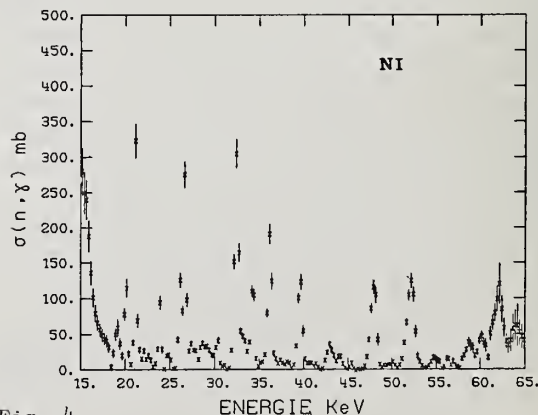


Fig. 4.

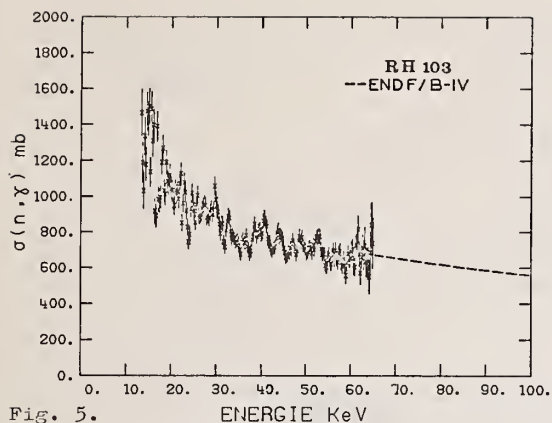


Fig. 5.

Rh<sup>103</sup> (15 - 350 keV)

The thickness of the metallic sample was 0.0062 atom/barn and its diameter 20 mm. Our data are shown on Fig. 5-6. Below 65 keV our data are in good agreement with ENDF/B-IV but are 20-25 % lower above 100 keV. On Fig. 7. is also shown an evaluation (Ref. 12.) which has been completed recently and the agreement with our data is better. We must notice that our data were not taken into account in this last evaluation.

Ta (10 - 160 keV)

The thickness of the metallic sample was 0.00463 atom/barn and its diameter 25 mm. Our data are shown on Fig. 8-9. Below 30 keV our data are in rather good agreement with ENDF/B-IV but 20-25 % higher above.

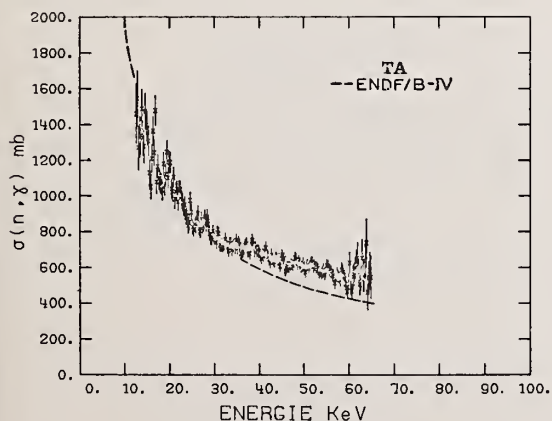


Fig. 8

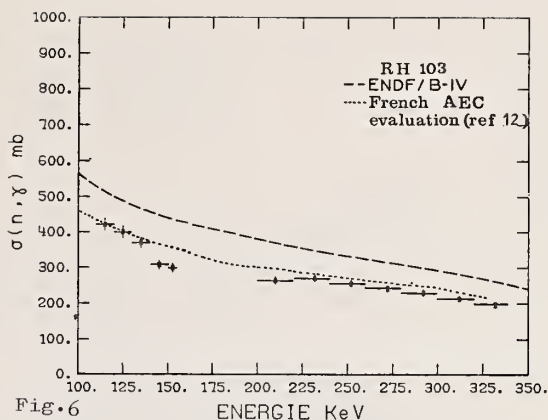


Fig.6

Mn<sup>55</sup> (15 - 500 keV) (Fig. 7.)

Two metallic samples were used in these measurements (0.0113 and 0.0198 atom/barn). Our data averaged over 10 keV below 100 keV and 20 keV above agree with the results of SPITZ et al (Ref. 10.) obtained with the time of flight technique but are 25 % lower than those of STUPEGIA obtained by the activation technique (Ref. 11.).

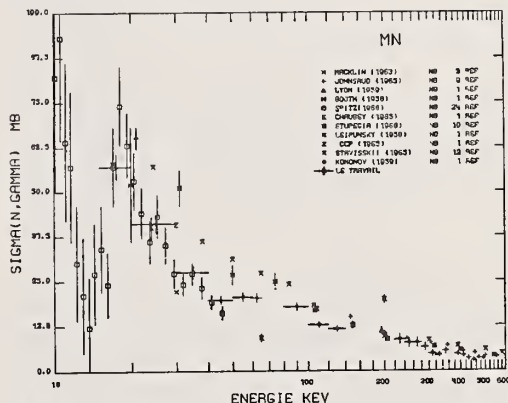


Fig. 7

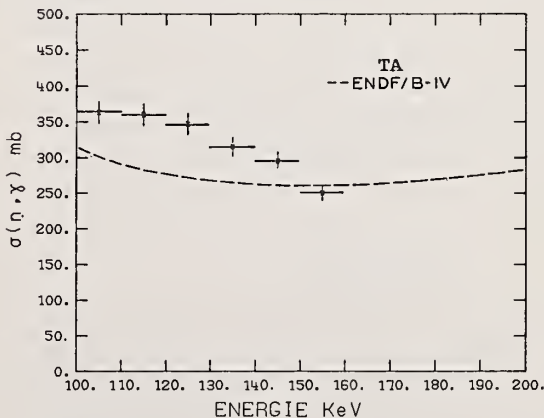


Fig. 9

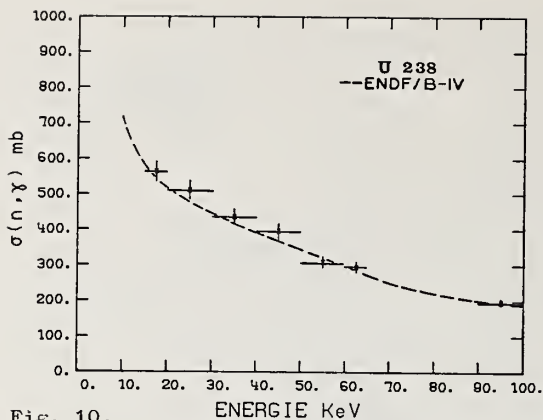


Fig. 10.

$^{238}\text{U}$  (15 keV - 550 keV)

We used a metallic sample (410 ppm of  $^{235}\text{U}$ ). The thickness of the sample was 0.003388 atom/barn and its diameter 16.2 mm. Because of the rather poor statistic we have averaged our results over 10 keV below 100 keV and 20 keV above 100 keV. Our data are shown on Fig. 10 and 11. Below 100 keV our data are 6-8 % below those of ORELA, between 10 % and 20 % higher than those of MOXON and agree within  $\pm 5$  % with those of FRIESNHAHN. Between 120 keV and 250 keV our results are smaller than any other measurements. If we compare with the data of RYVES our results are 15 % smaller at 160 keV, 6 % smaller at 238 keV, but in better agreement around 500 keV.

All these authors are referenced in Ref. 13. Consequently our results are in a rather good agreement with ENDF/B-IV below 100 keV and above 300 keV. Between 100 and 300 keV they are up to 15 % smaller. The gamma absorption correction in the sample is very high 18 % and the associated error on the cross section is estimated to 3 %. Additional work must be done on this correction and new experiments are planned in the 200 keV range. Consequently our data on  $^{238}\text{U}$  are preliminary data.

#### Conclusions

The present measurements are believed to give absolute capture cross sections within 4-8 % (1 standard deviation and all errors added quadratically). For some elements the ENDF/B-IV evaluated data are not in our expe-

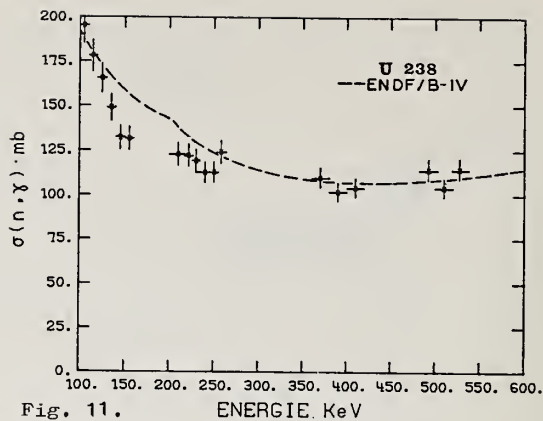


Fig. 11.

rimental error bars.

#### References

- 1) R.L. MACKLIN and J.H. GIBBONS  
Phys. Rev. 159 (1967) 1007.
- 2) C. LE RIGOLEUR, A. ARNAUD  
Proceedings of a meeting hold at Karlsruhe  
KFK 2046 - NEACRP U-61 - NEANDC U-98
- 3) C. LE RIGOLEUR et al - CEA N-1661
- 4) C. LE RIGOLEUR et al - CEA N-1662
- 5) C. LE RIGOLEUR et al - Journal of Nuclear  
Energy - A/B - 1966 - Vol 20, p. 67 to 73
- 6) EANDC (E) 140U for renormalization of  
Ref. 5
- 7) R.W. HOCKENBURY et al - Phys. Rev. -  
178-4, 1746 (1969)
- 8) P. RIBON et al  
Conf. PARIS CN 23/72, 1966
- 9) F. RAHN et al  
Phys. Rev. 8 - 1827 (1973)
- 10) L.M. SPITZ et al  
Nuclear Physics A 121 (1968) 655 - 672
- 11) D.C. STUPEGIA et al  
Journal of Nuclear Energy  
Vol 22 - N° 5 - p 267 (1968)
- 12) P. RIBON et al - to be published
- 13) G. DE SAUSSURE and R.B. PEREZ  
Atlanta meeting - to be published.



# CAPTURE CROSS SECTION OF $^{197}\text{Au}$ BETWEEN 10 keV AND 500 keV

E. FORT, C. LE RIGOLEUR

C.E.N. - CADARACHE

13115 SAINT-PAUL-LEZ-DURANCE (France)

This reference capture cross-section has been measured by two different absolute methods ; prompts  $\gamma$  measurements, activation method. The results obtained are in good agreement between themselves and with POENITZ's recommendation.

(Absolute values, Monte Carlo calculations for corrections, fluctuations, total energy weighting technique,  $4\pi(3\gamma)$  detector).

## I. Time of flight method

(C. LE RIGOLEUR, A. ARNAUD, J. TASTE).

The experimental technique used is presented in another communication at this conference (Ref. 1). The thickness of the sample was 0.002911 or 0.005831 atom/barn and its diameter 2.5 cm.

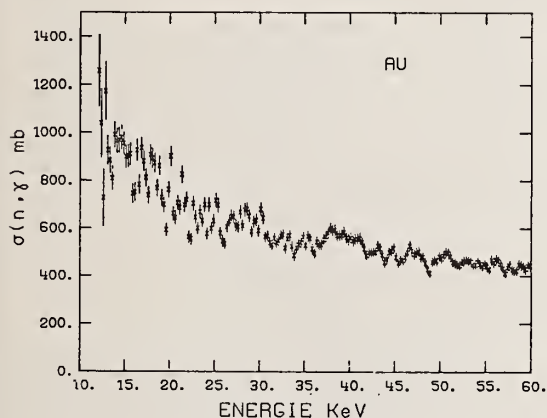


Fig. 1.

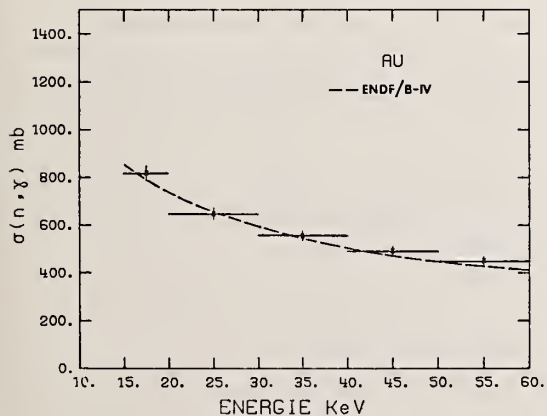


Fig. 3.

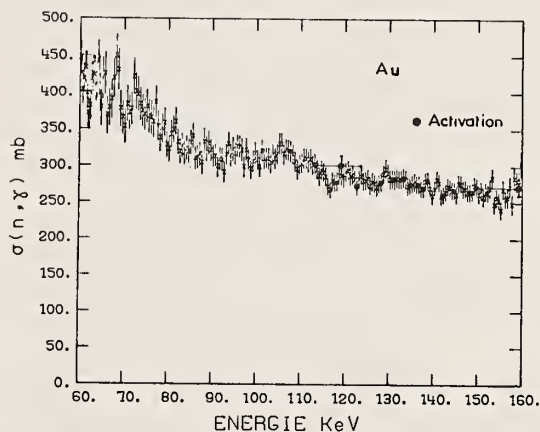


Fig. 2.

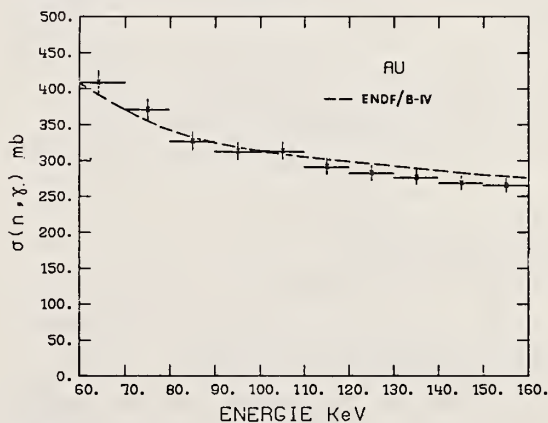


Fig. 4.

These absolute measurements cover the energy range between 10 and 160 keV. They are shown on Fig. 1-2. The averaged results over 10 keV are represented on Fig. 3 and 4. These data complete those already published between 70 and 550 keV (Ref. 2). The two sets of data are in good agreement between 70 and 115 keV. At higher energy the new results are 1-2 % .../..

lower, except in the 130-140 keV range where they are 5 % lower. In the first set of data the neutron flux was measured with a  $B^{10}INa$  (Tl) detector and with a  $Li^6$  glass scintillator in the second. Each detector efficiency is known within 2.5 % and this could explain the above discrepancy. The overall agreement with ENDF/B IV is good.

Rather large fluctuations in the capture cross section appear below 100 keV. One may be worried about the effect of these fluctuations on measurements with bad energy resolution (i.e. activation technique near  $Li^7$  (p, n) threshold). In order to check this point we have averaged our values over experimental neutron spectrum from the  $Li^7$  (p, n) reaction near threshold. The results are shown on Table I with those of MACKLIN (Ref. 3). Within 1 % the averaged cross section does not depend of the neutron energy resolution around 30 keV.

Our averaged cross sections are 3 % higher than those of MACKLIN. With the known uncertainties added quadratically our results are estimated about 3.5 % (1  $\sigma$ ).

GOLD CAPTURE CROSS SECTION AVERAGED  
OVER  $^7Li$  (p, n) SOURCE YIELD.

$\Delta E_p$ (KeV)	$E_n$ (KeV) - Range	This work (mb)	R.L. Macklin et al (mb) Ref 3
0.5	23.3 36.2	593 $\pm$ 21	576.7
1	20.9 40.0	591 $\pm$ 21	570.6
2	17.7 44.7	590 $\pm$ 21	570.0
4	13.7 51.9	590 $\pm$ 21	571.3

Table I.

## II. Activation method

(E. FORT, J.P. BRUNET)

In this method we used two techniques depending on the sample activity :

- $\beta$ -or  $\gamma$  counting. The activity was normalized on the saturated activity of a sample of same geometry irradiated with thermal neutrons.
- $\beta$ - $\gamma$  coincidences counting. This technique gives absolute values.

### II-1. Experimental set-up

Neutrons were produced by means of  $^7Li$  (p, n)  $^7Be$  reaction with targets of 10-15 keV thicknesses. The spot of the beam on the

target was 0.5 cm in diameter. A very simple "beam scanner" could give at any time an approximate form of the charge distribution in the proton beam.

Gold samples were disks of 1.6 cm in diameter and 0.005 cm thick placed at 0° with respect of the proton beam. The distance from the target were  $r_1 = 5$  cm (sample 1) and  $r_2 = 10$  cm (sample 2). The neutron detector placed on the same axis was the standard flat response detector of Cadarache, described elsewhere (4). The neutron flux is recorded on a time multiscale basis.

### II-2. Experimental data analysis

The activity of the sample 1 ( $A_1$ ) was determined by measuring  $\beta$ - $\gamma$  coincidences, while the sample 2 ( $A_2$ ) was measured in a relative way by  $\beta$ -or  $\gamma$  counting, as mentioned before. ( $A_1$  and  $A_2$  are values at the end of the irradiation). The measured activity  $A$  is a function of the distance  $r$  from the neutron target such as :

$$A = \frac{K}{r^2} + b \quad \text{where } b \text{ is the constant background.}$$

Taking into account that  $r_2 = 2r_1$  the part of the activity due to irradiation by direct neutrons for the sample 1 is :

$$A_{ct} = \frac{4}{3} (A_1 - A_2)$$

The capture cross section  $\sigma(n, \gamma)$  has the following expression :

$$\sigma_{n\gamma} = \frac{\epsilon \times A_{ct}}{N \times R_{\omega} \times \sum_i \frac{n_i}{\Delta t} (1 - e^{-\lambda \Delta t}) e^{-\lambda(t_f - t_i)} \times \prod_j F_{c_j}}$$

Where :

- $N$  - atom number per  $cm^2$  of the sample
- $R_{\omega}$  - ratio of the solid angles of the gold sample and the sensitive volume of the neutron detector viewed from the neutron target
- $\epsilon$  - efficiency of the neutron detector
- $n_i$  - counting rate of the flux detector during  $\Delta t$  at  $t_i$
- $F_{c_j}$  - correction factor  $F_c$  for the  $j$  effect.

### II-3. Corrections

The basic experimental data are corrected for :

.../...

- neutron scattering by air
- "Target effect"

The incident flux  $N_n(E)$  is contaminated by neutrons scattered by the backing at energies  $E' < E$ , distributed according to a spectrum  $n_d(E')$ . The corresponding correction factor can be written as :

$$1 + \frac{\int_{\Delta E'} n_d(E) \sigma(E) dE}{\int_{\Delta E} N_n(E) \sigma(E) dE}$$


---


$$1 + \frac{\int_{\Delta E'} n_d(E) dE}{\int_{\Delta E} N_n(E) dE}$$

It was calculated from the  $\sigma(E)$  capture cross-section given by VAUGHN and GRENN (8) for gold and from the spectrum  $n_d(E)$  calculated by FILIPPI (5) using a Monte Carlo method.

- Influence of the finite dimensions of the proton beam. This correction, concerning solid angle calculation, has been calculated by a Monte Carlo method using the data of the "beam scanner".
- Multiple scattering inside the sample. TASTE calculated this correction by a Monte Carlo method (6)
- Transmission by the samples.

The neutron flux is detected after transmission through the samples.

The values of this correction factors are given in the table II.

#### II-4. Errors

The values of cross section are given with an error (standard deviation) calculated by the following formula :

$$\frac{\Delta \sigma}{\sigma} = \left( \frac{\Delta \epsilon}{\epsilon} + \frac{\Delta N}{N} + \frac{\Delta R_w}{R_w} + \sum_j \frac{\Delta F_j^i}{F_j^i} + \frac{\Delta A_{ct}}{A_{ct}} \right)^{1/2}$$

Considering the errors concerning  $\lambda$ ,  $n_i$ , and all time measurements negligible.

$$\Delta A_{ct} = \frac{4}{3} \left( t_1^2 \sigma_{A_1}^2 + t_1'^2 \sigma_{A_2}^2 \right)^{1/2}$$

$t_1$  and  $t_1'$  are student's factors depending on the degree of freedom and confidence level (68.3 %).

#### II-5. Results

The results (we obtain) are mean values corresponding to large neutron spectra. These neutron spectra are calculated by a Monte Carlo method. The given energies are averaged over the spectra.

Our cross section values (see the table II) are generally in good agreement with those obtained by LE RIGOLEUR and al (2), (See Fig. 2, 5, 6, 7).

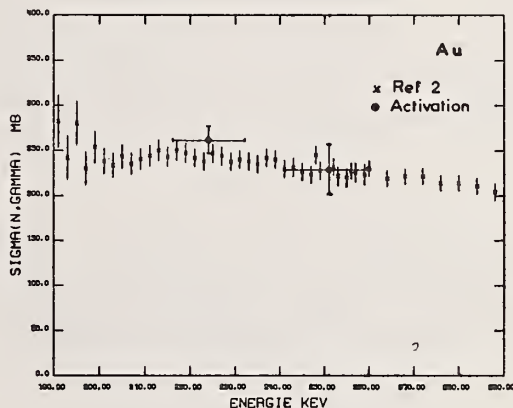


Fig. 5.

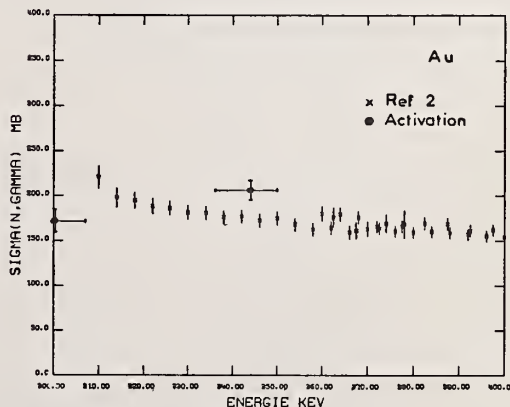


Fig. 6.



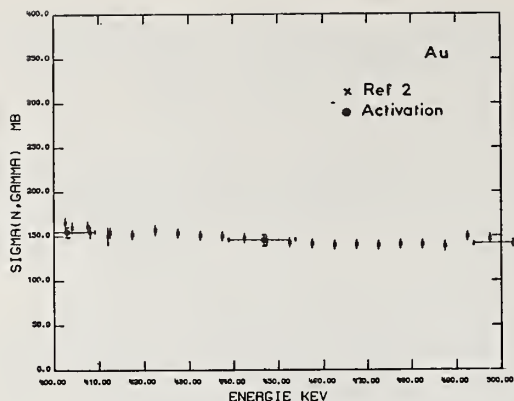


Fig. 7.

En keV	$\Delta$ half width at half max keV	Contribution of neutron background %	Correction Factors					$\sigma$ Barn	$\frac{\Delta\sigma}{\sigma}$ %
			Air Scattering b	Target effect	Finite dimensions of the beam	Multiple scattering	Transmission		
119	- 7 + 4	1.13	1.064	1.039	0.9995	1.007	1.007	0.301	4.25
139	- 10 + 8.5	2.58	1.057	1.018	1.	1.007	1.005	0.272	4.2
224	- 8 + 4	1.	1.052	1.032	0.991	1.006	1.005	0.265	7.2
251	- 10 + 9	1.9	1.048	1.02	1.	1.006	1.005	0.235	9.4
300	- 8 + 7	1.	1.05	1.016	0.99	1.0051	1.005	0.177	6.2
344	- 8 + 6	2.	1.054	1.006	0.99	1.0055	1.005	0.209	5.9
403	- 8 + 6	3.8	1.061	1.12	1.	1.007	1.005	0.156	5.1
447	- 8 + 7	0	1.10	1.012	0.985	1.0064	1.005	0.146	5.8
503	- 9 + 7	0	1.055	1.028	0.9995	1.0064	1.005	0.140	5.2

Table II.

### III. Conclusion

The recent data of LE RIGOLEUR and al, MACKLIN and al, FORT and BRUNET obtained by different methods support the recommended curve of POENITZ (7).

The fluctuations observed both by LE RIGOLEUR and MACKLIN should not affect the quality of standard of the gold capture cross section. As a reference, average values of this cross section have to be used.

- (1) C. LE RIGOLEUR, A. ARNAUD, J. TASTE  
This conference.
- (2) C. LE RIGOLEUR, A. ARNAUD, J. TASTE  
Mesure de la section efficace de capture radiative des neutrons par l'Or entre 75 keV et 550 keV - C.E.A. N 1662.
- (3) R.L. MACKLIN, J. HALPERIN, R.R. WINTERS  
To be published.
- (4) J.L. LEROY and al  
Conference proceedings - Helsinki 1970  
Communication CN 26/70.
- (5) G. FILIPPI  
Rapport C.E.A. - DPRMA/SECPR/71/12.
- (6) J. TASTE  
Note C.E.A. (To be published).
- (7) W. P. POENITZ  
Neutron standards and flux normalization  
AEC Symposium - Series 23, 320 to 325  
(August 1971).
- (8) F.J. VAUGHN, H.A. GRENCHE  
Neutron cross section and technology  
Proceedings Conference Knoxville (1971)  
1, CONF - 710301, USAEC, OAK-RIDGE (1971)  
430.

SELF SHIELDING FACTOR MEASUREMENTS FOR NATURAL IRON  
AND Na<sup>23</sup> BETWEEN 24 keV AND 160 keV AT 300° K

A. ARNAUD - C. LE RIGOLEUR - J.P. MARQUETTE

C.E.N. CADARACHE

13115 SAINT-PAUL-LEZ-DURANCE (FRANCE)

We present experimental values of the multigroup capture cross section and self shielding factor for natural iron and Na<sup>23</sup> between 24 keV and 160 keV. The capture rate is measured with a shielded neutron flux  $\phi = \phi_0 \exp(-n \sigma_T X)$  after transmission through a sample of iron or Na<sup>23</sup>, at room temperature. The self shielding factors at the non zero dilution are obtained by analytical calculation.

(Multigroup capture cross section - Self shielding factor - 24 keV - 160 keV - Fe - Na<sup>23</sup>).

# I - Introduction

Multigroup capture cross section ( $\tilde{\sigma}_{ci}$ ) and self shielding factor ( $f_{ci}$ ) for an energy group (i) and a dilution ( $\sigma_p$ ) can be defined as :

$$\tilde{\sigma}_{ci} = \frac{\int_{E_i}^{E_{i+1}} \frac{\sigma_c}{\sigma_T + \sigma_p} dE}{\int_{E_i}^{E_{i+1}} \frac{1}{\sigma_T + \sigma_p} dE} \quad (1)$$

$$f_{ci}(\sigma_p) = \frac{\tilde{\sigma}_{ci}(\sigma_p)}{\tilde{\sigma}_{ci}(\sigma_p \rightarrow \infty)} = \frac{\tilde{\sigma}_{ci}(\sigma_p)}{\langle \sigma_c \rangle_i}$$

$\sigma_T$  and  $\sigma_c$  are the microscopic total and capture cross section ;  $\langle \sigma_c \rangle_i$  is the mean value of  $\sigma_c$  over the energy group (i), or  $\tilde{\sigma}_{ci}$  when  $\sigma_p \rightarrow \infty$ .

# II - Principle of the method

## II-1. Zero dilution ( $\sigma_p = 0$ )

The experimental method used gives  $\tilde{\sigma}_{ci}$  and  $f_{ci}$  for  $\sigma_p = 0$ . A sample of a thickness (x) is exposed to a shielded neutron flux  $\phi = \phi_0 \exp(-n \sigma_T X)$  obtained by transmission through a sample of the same material and of thickness X. For an energy group (i) the capture rate of the sample (x) and the neutron flux transmitted by the sample X are expressed as :

$$T_{ci}(E_i, X) = \int_{E_i}^{E_{i+1}} N \phi_0 \exp(-n \sigma_T(E) X) \sigma_c(E) dE \quad (2)$$

$$\phi_i(E_i, X) = \int_{E_i}^{E_{i+1}} \phi_0 \exp(-n \sigma_T(E) X) dE$$

N is the total number of atoms in the sample (x), n is the atom number/cm<sup>3</sup> for the samples x and X.

For X = 0, the incident flux on the sample x is not self shielded and then we determine  $\sigma_c(E)$  and  $\langle \sigma_c \rangle_i(E_i)$ . As the experiments are carried out with different thicknesses of sample X we calculate the integrals :

$$S_{Tc}(E_i) = \int_0^\infty T_{ci}(E_i, X) dX$$

$$= \frac{N}{n} \int_{E_i}^{E_{i+1}} \frac{\sigma_c(E)}{\sigma_T(E)} dE \quad (3)$$

$$S_{\phi i}(E_i) = \int_0^\infty \phi_i(E_i, X) dX$$

$$= \frac{1}{n} \int_{E_i}^{E_{i+1}} \frac{1}{\sigma_T(E)} dE$$

We deduced :

$$\tilde{\sigma}_{ci}(E_i, \sigma_p = 0) = \frac{1}{N} \frac{S_{Tc}(E_i)}{S_{\phi i}(E_i)} \quad (4)$$

$$f_{ci}(E_i, \sigma_p = 0) = \frac{\tilde{\sigma}_{ci}(E_i, \sigma_p = 0)}{\langle \sigma_c \rangle_i}$$

## II-2. Non zero dilution ( $\sigma_p \neq 0$ )

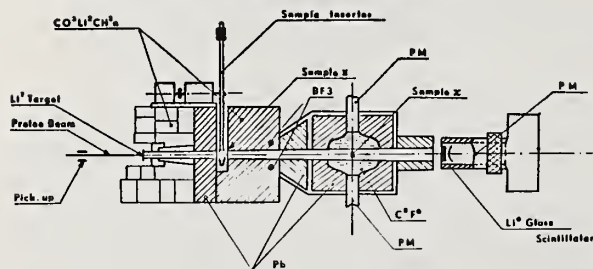
The self shielding factors at the non  
.../..

zero dilution are obtained with an analytical calculation, multiplying  $T_{ci}(E_i, X)$  and  $\phi_i(E_i, X)$  by  $\exp(-n\sigma_p X)$ .

### II-3. Capture rate measurement

The total energy weighting technique has been applied to measure absolute capture rate. This way, the efficiency of the detector is independant of the gamma ray cascade (Ref. 1.)

### III - Experimental set up



We used the fast time of flight method. The experimental set up consists mainly of the apparatus used for measuring microscopic capture cross sections (Ref. 2). A  $Li^7$  target produce a pulsed neutron flux (1.75 MHz, 1.2 ns) with a broad energy spectrum (up to 160 keV). The neutrons at  $0^\circ$  are collimated by  $HLi^6$ ,  $Li_2CO_3$  plus paraffin, and lead. The samples of different thicknesses are placed on a rotating wheel. Every sample is exposed during a short time (10 minutes) in comparison with the two weeks run. So that, each sample X receives the same shape neutron flux. The flux intensity is monitored both by the integrated current of the proton beam and by an INa scintillator used to detect the 478 keV gamma ray from the  $Li^7(p, p') Li^7$  reaction. The sample x ( $e = 2$  mm,  $\phi = 25$  mm) is exposed at the center of the prompt gamma ray detector at 85 cm from the target ( $C_6F_6$  scintillator associated with 2 P.M.). The experimental resolution is 1.8 ns. The neutron flux is measured with a  $Li^6$  glass scintillator at 136 cm from the target. The efficiency of this detector has been measured by comparison with a flat detector of well known efficiency (Ref. 2). The experimental resolution is 1.5 ns. The data are stored in a on line computer.

### IV - Corrections (Ref. 3)

Several corrections are applied for different effects :

- multiple neutron scattering and resonance self shielding in the sample x.
- gamma attenuation in the sample x and non linearity of the weighting function (Corrections connected with the capture gamma ray spectrum)
- neutron sensitivity of the gamma ray detector (Fluor capture resonance at 27 keV, 49 keV, and 97 keV).
- effects of the Al container for  $Na^{23}$
- neutron scattering by air.

Considering the keV range (24-160) we do not introduce correction for inelastic scattering.

According with the good collimation of the neutron flux we consider the transmitted flux expressed by  $\phi = \phi_0 \exp(-n\sigma_T X)$ . So, no correction for multiple scattering in the sample X is introduced.

### V - Results

#### V-1. Capture infinite diluted cross section

The numerical values are presented in another communication at this conference. (Ref. 6). The accuracy of the measurement is about 6 %. The energy resolution is 0.5 % at 20 keV, 1 % at 100 keV, and 1.3 % at 160 keV.

#### V-2. Multigroup capture cross section and self shielding factor.

Natural iron : Tables I, II, III and IV give the results for 4 energy groups (numbers 11, 10, 9, 8) used in the Cadarache multigroup cross section set.

IRON									
ENERGY GROUP 11 ( 24.75 KEV - 40.75 KEV)									
DILUTION (BARN)	AVERAGE CROSS SECTION (BARN)	RELATIVE ERROR	SELF SHIELDING CROSS SECTION (BARN)	RELATIVE ERROR	SELF SHIELDING FACTOR	RELATIVE ERROR	RELATIVE ERROR	RELATIVE ERROR	RELATIVE ERROR
0.0000E+00	2.2951E+021	0.57	1.1200E+001	1.03	1.4806E+000	0.97			
1.0000E+001	2.2951E+021	0.53	1.1716E+001	0.93	1.5105E+000	0.81			
2.0000E+001	2.2951E+021	0.57	1.2130E+001	0.84	1.5285E+000	0.70			
5.0000E+001	2.2951E+021	0.53	1.1744E+001	0.70	1.5685E+000	0.52			
1.0000E+002	2.2951E+021	0.53	1.1405E+001	0.65	1.6145E+000	0.45			
2.0000E+002	2.2951E+021	0.53	1.1536E+001	0.56	1.6781E+000	0.47			
5.0000E+002	2.2951E+021	0.53	1.1822E+001	0.71	1.7451E+000	0.53			
1.0000E+003	2.2951E+021	0.57	1.1936E+001	0.73	1.8629E+000	0.56			
2.0000E+003	2.2951E+021	0.57	1.2121E+001	0.73	1.9244E+000	0.56			
5.0000E+003	2.2951E+021	0.53	1.2266E+001	0.72	1.9700E+000	0.53			
1.0000E+004	2.2951E+021	0.53	1.2265E+001	0.72	1.9870E+000	0.53			

Table 1.

.../...



ENERGY GROUP 10 ( 60.75 KEV - 67.25 KEV)							Iron
DILUTION (BARN)	AVERAGE CROSS SECTION (BARN)	RELATIVE ERROR	SELF SHIELDING CROSS SECTION (BARN)	RELATIVE ERROR	SELF SHIELDING FACTOR	RELATIVE ERROR	
+0000E 000	+97700E-032	+053	+44716E-002	+091	+45854E 000	+079	
+13000E 001	+99700E-032	+053	+48371E-002	+031	+45357E 000	+066	
+20000E 001	+99700E-032	+053	+50505E-002	+074	+53657E 000	+059	
+50300E 001	+97700E-032	+353	+55190E-002	+064	+55356E 000	+044	
+10000E 002	+97700E-032	+053	+60353E-002	+059	+60535E 000	+036	
+23000E 002	+97700E-032	+053	+66982E-002	+059	+67190E 000	+036	
+50000E 002	+97700E-032	+053	+77515E-002	+062	+77849E 000	+041	
+10000E 003	+97700E-032	+053	+85637E-002	+053	+85894E 000	+043	
+20000E 003	+97700E-032	+053	+21723E-002	+064	+91996E 000	+043	
+50000E 003	+97700E-032	+053	+96142E-002	+063	+96429E 000	+043	
+13000E 004	+99700E-032	+053	+57733E-002	+063	+98033E 000	+043	

Table 2.

ENERGY GROUP 9 ( 67.25 KEV - 110.75 KEV)							Iron
DILUTION (BARN)	AVERAGE CROSS SECTION (BARN)	RELATIVE ERROR	SELF SHIELDING CROSS SECTION (BARN)	RELATIVE ERROR	SELF SHIELDING FACTOR	RELATIVE ERROR	
+0000E 000	+12500E-031	+049	+14509E-002	+082	+54767E 000	+067	
+13000E 001	+12500E-031	+049	+73857E-002	+075	+59043E 000	+059	
+20000E 001	+12500E-031	+049	+77304E-002	+071	+62199E 000	+054	
+50000E 001	+12500E-031	+049	+53372E-002	+065	+68244E 000	+045	
+13000E 002	+12500E-031	+049	+82147E-002	+061	+73665E 000	+039	
+20000E 002	+12500E-031	+049	+90195E-002	+059	+79299E 000	+036	
+50000E 002	+12500E-031	+049	+10494E-001	+060	+86882E 000	+038	
+10000E 003	+12500E-031	+049	+11498E-001	+061	+91915E 000	+040	
+20000E 003	+12500E-031	+349	+11915E-001	+061	+95244E 000	+040	
+50000E 003	+12500E-031	+049	+12191E-001	+061	+97455E 000	+040	
+10000E 004	+12500E-031	+049	+12287E-001	+061	+98225E 000	+040	

Table 3.

ENERGY GROUP 8 (113.75 KEV - 163.25 KEV)							Iron
DILUTION (BARN)	AVERAGE CROSS SECTION (BARN)	RELATIVE ERROR	SELF SHIELDING CROSS SECTION (BARN)	RELATIVE ERROR	SELF SHIELDING FACTOR	RELATIVE ERROR	
+0000E 000	+64219E-032	+048	+34023E-002	+071	+53444E 000	+054	
+13000E 001	+64219E-032	+048	+37652E-002	+064	+58647E 000	+044	
+20000E 001	+64219E-032	+048	+39995E-002	+061	+62271E 000	+039	
+50000E 001	+64219E-032	+048	+44377E-002	+056	+69394E 000	+031	
+13000E 002	+64219E-032	+048	+48075E-002	+054	+74863E 000	+028	
+23000E 002	+64219E-032	+048	+52104E-002	+055	+81136E 000	+029	
+50000E 002	+64219E-032	+048	+57219E-002	+087	+89101E 000	+032	
+13000E 003	+64219E-032	+048	+60165E-002	+058	+93685E 000	+034	
+20000E 003	+64219E-032	+048	+61996E-002	+058	+96543E 000	+034	
+50000E 003	+64219E-032	+048	+63194E-002	+058	+98406E 000	+034	
+10000E 004	+64219E-032	+048	+63610E-002	+058	+99052E 000	+034	

Table 4.

Usually, the self shielding factors are calculated using the resonance parameter sets from ENDF/B-II and III (Ref. 4) and evaluated data (Ref. 4 and 5). Often, the differences between these results are very large.

We do not know others experimental results. We get a good agreement for the 9<sup>th</sup> energy group, higher values for the 11<sup>th</sup> and smaller values for the 8<sup>th</sup>. The difference is more important for the 10<sup>th</sup> energy group, the calculated values present a weak shielding effect and experimentally we get a stronger one.

Na<sup>23</sup>

Only 4 experimental points and low thicknesses X are used in the integral calculation of the capture rate and the neutron flux. So, we consider the results as preliminary results. Except the resonances at 35 keV, 53 keV, 118 keV, 132 keV, and 144 keV, the microscopic capture cross section is very small in the keV range. The experimental self shielding factor are given only for these resonances (Table V for the 53 keV resonance).

ENERGY GROUP 2 ( 49.50 KEV - 57.50 KEV)							Na <sup>23</sup>
DILUTION (BARN)	AVERAGE CROSS SECTION (BARN)	RELATIVE ERROR	SELF SHIELDING CROSS SECTION (BARN)	RELATIVE ERROR	SELF SHIELDING FACTOR	RELATIVE ERROR	
+0000E 000	+47133E-032	+064	+15447E-002	+131	+33645E 000	+127	
+13000E 001	+47100E-002	+066	+17173E-002	+127	+36460E 000	+123	
+50000E 001	+47100E-002	+066	+21522E-002	+114	+45694E 000	+109	
+20000E 001	+47100E-002	+066	+18392E-002	+123	+39048E 000	+119	
+10000E 002	+47100E-002	+066	+25446E-002	+133	+54071E 000	+097	
+20000E 002	+47100E-002	+066	+30594E-002	+089	+64954E 000	+083	
+50000E 002	+47100E-002	+066	+37523E-002	+074	+79667E 000	+066	
+13000E 003	+47130E-002	+066	+41549E-002	+068	+88215E 000	+060	
+20000E 003	+47100E-002	+066	+44181E-002	+066	+93802E 000	+057	
+50000E 003	+47130E-002	+066	+46035E-002	+065	+97739E 000	+056	
+13000E 004	+47100E-002	+064	+46704E-002	+065	+99168E 000	+056	

Table 5.

## References

- 1) C. LE RIGOLEUR-- Note EEA N-1661
- 2) C. LE RIGOLEUR et al - Proceeding of a meeting hold at Karlsruhe.  
KFK 2046/NEACRP - U-61/NEANDC - U-98
- 3) C. LE RIGOLEUR - To be published.
- 4) M. TAKANO et al - Proceeding of a meeting hold at Karlsruhe.  
KFK 2048/NEACRP - U-61/NEANDC - U-98
- 5) P. RIBON - Private communication.
- 6) C. LE RIGOLEUR - This conference.

E. P. Wigner:

I am very grateful for the invitation to this conference. We all learned a great deal about nuclear physics and about nuclear reactors - and even about subjects outside the area of these. If I have any criticism it is that we were not exposed to more what I would call crazy ideas. Only two occur to me. The first of these is the fast breeder reactor, slow blanket proposal advanced by Tang and by Otterville and also considered by General Atomics. This is a very attractive idea. The other one is a suggestion made by McNally to devise fusion reactors without  $H^3$ . This is an interesting suggestion, well worth looking into.

One may group the papers we heard into five classes: 1, pure nuclear physics; 2, reactors and breeders; 3, determination of the nuclear constants for these; 4, estimation of the accuracy desirable for these constants, that is the sensitivity of the efficiency of reactors to errors in these constants; and 5, general questions. I'll give a brief and extremely incomplete review of what I learned about these five subjects.

1. Nuclear Physics. Here, a dream of mine came true: in the case of the reaction  $Li^6 + n^2 \rightarrow He^4 + H^3$  all three cross sections, that is two scattering and one reaction cross section, and even angular distributions, have been measured. Hale reported on this and he used R matrix theory for his interpretation to obtain a coherent set of data, reinforcing each other. This gives, in my opinion, a more firm support for a particular datum than the repetition of the measurement of this would give. Such a repetition may well be subject to the same type of errors as was the original measurement.

Another discussion which gave me a great deal of pleasure was Michaudon's review of the fission theories. These theories are on the side of the spectrum opposite to that of R matrix theory, replete with imaginative approximations and guesses. It would be difficult to give a brief review of the theories Michaudon discussed. There were many other interesting papers, many, the ones on the neutron cross section of Fe not excepted, but I will not go into further detail on them.

The decay of the radioactivity of the totality of fission products presents a mystery which was not discussed and about which it would be good to know more. Starting at a few seconds after the fission burst, the decay follows a  $t^{-1.2}$  law. However, after a few months, the decay becomes much faster, faster than even the second power of  $t$ , that is  $t^{-2}$ . In order to explain this one has to assume that very low energy differences between the isobars are very unlikely. This is hard to swallow and I do not know any explanation for the increased time dependence after around 3 months.

2. Reactors and Breeders. We heard a great deal about reactors and breeders. What I missed badly were thermal breeders even though the foundation for these, the  $\eta$  of  $U^{233}$ , was amply discussed. With some of the information about fast breeders I was not entirely happy. Dr. Barre told me about the expected doubling time of the Phenix breeders. The new one, better than the present one, will have a doubling time of about 30 years, the shortest that

they expect from later models is between 15 and 20 years. If we had enough breeders now, this would be ample but if we hope to replace oil by nuclear energy in the near future 20, or even 15, years are far too long doubling times. Part of the reason for the rather long doubling time is the aim at a high thermal efficiency, over 40 percent. My crazy idea is to be satisfied with a lower efficiency but aim at a shorter doubling time. Separation of core and blanket, and even the use of a metallic core, would work strongly in this direction. I learned from Dr. Avery's talk about some of the disadvantages of this but also about some advantages. The reactivity temperature coefficient would threaten to become positive if one goes too far in the direction indicated. On the other hand, the cavitation of the coolant would reduce the reactivity. Also, if the criticality is achieved with the minimum, or almost minimum, material, there is less danger of supercriticality. I could go on praising this but I realize that it is, in the present atmosphere, a crazy idea. I like it, as I also like thermal breeders.

Dr. Barre, in his address, advocated less reliance on theory and calculations, more on integral experiments. Those of us who were involved in the planning of the early reactors, were a bit shaken. On the other hand, we must admit that if a hammer or a drill are to be designed, we all use Dr. Barre's method and our hammers and drills are better than our reactors. Nevertheless, there is a difference. We can make 50 tries to make a better drill and if we do, we can sell 50,000 of them. We can not afford to try out 50 reactors - and we can not sell 50,000 even of the best ones. I hope Dr. Barre will contradict me.

3. Nuclear Constants for Reactors. The progress about which we learned in this area is truly astounding and represents again a dream of mine come true. The uncertainty in the values of  $\eta$  and  $\nu$ , the average numbers of neutrons emitted per neutron absorbed and per fission, has been decreased for all reactor used fissionable elements, with the exception of  $^{241}Pu$ , to one quarter of a percent. Incidentally, the thermal  $\eta$  of  $^{233}U$  turned out to be 2.26 and perhaps even a shade higher, assuring the possibility of thermal breeders at least theoretically. However, this is far from being the only constant more precisely determined which is of importance for reactors breeders, or for fusion. As was mentioned before, practically all  $\eta$  and  $\nu$  of relevance are now known with high accuracy, and the neutron cross sections for many materials which can be expected to be in reactors are more accurately known and the same applies to the principal cross sections for the fusion process. Enumerating the new data would add little to what we have heard and I will desist.

4. Sensitivity to Errors. This was, at least for me, a new subject. It concerned the determination of the effect of an error in a nuclear constant on the functioning and efficiency of a reactor in which the material in question is to be used. Some of the conclusions were truly surprising. Thus, we learned from Uotinen that a 1 percent error in the power peaking would imply a one million dollar per year loss in the operation of a single reactor. It may, of course, reduce the power output of the reactor by almost 1 percent. A similar error in the fission product cross sections - this is even more surprising - might cost \$200,000 per year. Naturally, the most important information which the error sensitivity studies provide is the specification of the nuclear constants which are most important to determine accurately.



5. General Questions is the last subject I'll discuss. One of these is the safety of reactors, discussed in particular by Dr. Taylor. I wish I had the time to repeat all that he said - maybe I could even add a few words. Another important question concerns the radiation from nuclear explosions and, again, I was glad to hear this discussed - we must not forget this danger or close our minds to its existence even if it is extremely unlikely. However, I will not repeat what we learned in these regards but close my report with the expression of appreciation to the organizers of the conference and the many very helpful participants.

J. L. Fowler:

For several years now I have been involved with the Nuclear Physics Commission of the International Union of Pure and Applied Physics, and this is the first I.U.P.A.P. conference I have known which justifies the Applied Physics part of the name. In the world's energy crisis, it is high time nuclear physicists recognize the technological needs of energy research.

It is gratifying that so many have attended this conference. Last fall I had estimated, on the basis of papers submitted to the Division of Nuclear Physics meetings of the APS that during the last several years less than 10 percent of nuclear physicists were concerned with the energy crisis. I had expected, therefore, the order of 150 people might attend this meeting. The fact that the attendance is more than twice that number indicates to me one of two things: either my original estimate of 10 percent was wrong or in recent months more than 10 percent of Nuclear Physicists have become concerned with research in energy. I believe the latter is the explanation, that there has been a growing awareness of the energy problem during the past year, and that more physicists want to do something about it.

My primary assignment for this panel is to cover nuclear instrumentation. First, let me comment on neutron techniques. We have heard during the last several days of a number of innovations in neutron instrumentation which are improving the quality of neutron data. The many-pronged attack on the problem of neutron standards for flux measurements at the National Bureau of Standards, described in a number of contributed papers and summarized by A. D. Carlson, should certainly be welcomed by the neutron physics community. Efforts in refining techniques and apparatus to measure neutron cross sections in a number of laboratories are producing neutron data which, if they are not completely satisfying the requirements of the nuclear-based technology, are at least closing the gap toward meeting these requirements. Particularly impressive was the type of apparatus H. Liskien described for identifying charged particle reaction products from fast neutron reactions and for measuring their angular distributions. He described experiments being done in Basel, Switzerland. A contributed paper (BB 13) by F. P. Brady, N. S. P. King, W. W. McNaughton, J. F. Harrison and B. E. Bonner discussed similar apparatus. This type of instrumentation should go far in filling the gap in fast neutron cross section data which we learned at this conference are needed for prediction of radiation damage and also for medical use of fast neutrons in radiotherapy.

Having made these complimentary remarks on recent neutron instrumentation discussed at this conference, I shall now spend a few minutes criticizing our general philosophy with regard to instrumentation. As neutron physicists, we think on much too small a scale; we are not radical enough - not bold enough in our plans. After all, neutron physics is that branch of nuclear physics most pertinent to energy in the near future. Yet our colleagues who work with charged particle reactions have analyzing magnets, position sensitive detectors, and the like, which amount to almost as large an investment as their accelerators. The only really major neutron experiment I heard about at this conference was the polarization experiment of G. A. Keyworth, C. E. Olsen, J. D. Moses, J. W. T. Dabbs and N. W. Hill. Here was apparatus for an important experiment designed on a grand scale - a million-dollar scale. I don't suggest that we should all go home and design million-dollar equipment - we wouldn't get away with it. But we should, I think, recognize the importance of neutron physics to energy and break out of the rut of thinking in terms of research "on the cheap". It is time for radical new approaches to neutron physics. We should think big!

Let me now turn to the approximately 10 percent of the papers in this conference concerned with applications of nuclear physics to medicine, to industry, and to space. As nuclear physicists, we should be proud of the impact nuclear physics is having in medicine. The medical instrumentation we heard about, such as the "Biomedical Application of Short-Lived Positron Emitting Isotopes" (FB 1), by P. Meyer, E. Behrin, N. R. Frank, R. Holub and C. E. McJilton is impressive. I think we should all be excited by the promise for the medical use of fast neutrons in radiotherapy described by D. K. Bewley (GA 2).

We learned in this conference that the uses of nuclear techniques in chemical analysis and in monitoring industrial processes are greatly improving the efficiency of manufacturing processes resulting in significant savings in energy consumption. More effort of nuclear physicists could have great impact in these fields.

As an enthusiastic follower of space exploration, I was particularly interested in several contributed papers and the invited paper by R. C. Reedy (GA 4) on mapping the moon and other bodies in the solar system by  $\gamma$ -ray spectroscopy.

I regret that we didn't have more papers on the applications of nuclear physics to other fields and to industry. Perhaps in the next such conference this very important aspect of nuclear physics will be discussed in more detail.

B. Rose:

No one will expect me to approach the matter of reviewing the conference with the breadth of view shown by Dr. Wigner. I shall therefore proceed immediately to discussion of the sessions which Bill Havens asked me to review.

The sessions allocated to me were two on standards of cross sections and flux, FA and DB, and two inordinately long sessions, HB and IB, with 29 and 26 papers, respectively. Thank God for the French postal strike.



It is clearly impossible to deal with the latter two sessions in anything other than the most general terms. A great deal of the work was the bread and butter work of this field and I am not using that expression in the pejorative sense. It seemed to me all to be highly relevant either to the problem of supplying important cross sections or to the understanding of the basic physics behind neutron interactions - to important cross-checking of the work of other laboratories, or producing massive new comprehensive compilations.

There were several things that caught my fancy - ranging from the work reported from Kiel University (HB 6) on the transmission of bulk fission products and the Chalmers University (HB 25) work on the direct measurement of the  $(n,\alpha)$  and  $(n,p)$  cross sections of Ni 59 to the enormous body of work from Oak Ridge on the gamma production cross section, the new technique employed by the Geel-Bologna group (HB 3) for the separation of s and p wave resonances in  $^{238}\text{U}$  and the large  $(n,2n)$  programme at Bruyeres-le-Chatel.

Turning now to the problems of standards, clearly Dr. Lemmel's paper (EA 2) on the third IAEA evaluation of the thermal parameters of the fissile isotopes was an important one, which in retrospect stood up very well to the determined sabotage by Dr. Leonard (EA 1).

As usual, some questions seem to be resolved, or partly so, and new ones appear and the general conclusion that attention should be turned for example to the g factor, cross sections below the thermal range, and perhaps some studies of the low energy end of the so-called Maxwellian energy distribution in thermal neutron spectra seem well worth pursuing. At least it offers something different from the sempiternal re-examination of ancient  $\bar{\nu}$  experiments. I wonder whether evaluations of this type, when so much of the effort has to be devoted to attempts to reconcile conflicting experiments, do not run into the old danger of "optional stopping" - that is you continue looking very hard for corrections until finally your conflicting numbers are in agreement - and then stop looking for any others. In this situation it seems likely that the only way forward is by carrying out a new series of experiments designed to minimize the corrections which have been turned up in the evaluations. Undoubtedly this would not be very exciting work but it would be extremely important and best carried out in my view in a very thorough international collaboration on the lines of that in progress in neutron flux measurement.

Dr. Leonard (EA 1), apart from adding a few new experimental proposals - for example a systematic study of coherent scattering amplitudes - laid bare his bleeding evaluator's heart and exposed the perennial evaluation problem of the correct relative weighing to be given to those experiments which are published with so much information that it is possible to criticise them in great detail and possibly downgrade their accuracy as a result - and those which give insufficient detail for this detailed criticism but which should probably be downgraded for that very reason--but by how much? I suppose we all know that evaluation is almost as much an art form as a science and all we can do is to wish Dr. Leonard luck and tell him to get on with it.

It is of course extremely good to have differential experiments subjected to this degree of criticism and their inadequacies exposed. However, I suspect

double standards are being adopted in the following sense. As Dr. Kouts said in the first session, one of the most important reasons for doing differential measurements is to be able to compare the results of integral experiments with theoretical calculations based on differential data. But if the integral experiments themselves are not subjected to the same degree of detailed criticism we are not able to make a valid comparison and not able to understand the deficiencies of the calculational techniques employed.

The papers of Dr. Carlson and Dr. Hale - and other papers elsewhere - revealed in a great deal of gory detail the present unhappy situation over the  $^6\text{Li}(n,\alpha)$  cross section over the resonance and beyond. On this matter I want to emphasize certain points - some of which have already been made at the meeting.

(1)  $^6\text{Li}(n,\alpha)$  is clearly not a good reference cross section beyond the  $1/v$  region - not only because it has a fairly rapid energy variation but clearly because it has so far proved extremely difficult to measure - and therefore any instrument incorporating it must be used with the greatest possible care. The latter argument may become invalidated over the next year or so, of course, if the difficulties are all found to be in one of the competing experiments, but past experience suggests otherwise.

(2) However, if one is forced to use it as a standard in this region I personally would find it very difficult to accept as a reference standard the cross section value at the resonance peak, and its error, derived from an R-matrix analysis in which the greatest statistical weight came from the  $\alpha$ -t differential cross section. It was interesting to listen to arguments about the lowest peak total cross section that the R-matrix analysis would allow - and bets were laid on the highest value of the peak  $n,\alpha$  cross section - but none of these numbers mean anything, even in R-matrix analysis terms, until the results of the full error analysis are known - and perhaps the  $^6\text{Li}(n,\gamma)$  reaction is put into the analysis (its amplitude is  $\sim 1/2$  percent of the  $^6\text{Li}(n,\alpha)$  at thermal energies so it could presumably affect cross sections by 1 percent or so).

However, even then, I personally am sufficiently a sceptic about parametric fits (even with the best theoretical pedigree) that I should find it difficult to accept standard values for the  $^6\text{Li}(n,\alpha)$  cross section any more precise than the direct experimental measurement of that quantity. This comment, I believe, applies also for example to a remark made in connection with the  $\text{C}^{12}$  differential scattering cross section for use as a standard below about 2 MeV - namely that the R-matrix fit was so good to the data above 2 MeV, and to the polarization, that it could be used to predict the values of differential scattering below 2 MeV. I just don't believe it for a real precision standard. This is clearly the year of the R-matrix but it is not the millenium.

(3) The next point I wanted to make is that it is disturbing to find that large quantities of data, highly relevant to the study of this problem, have been lying around on tape unanalyzed, while new experiments on the same topic are being mounted elsewhere.

And if anyone thinks I am getting at Jack Harvey - they are right - but not only at him. In response to a recent request from Hank Motz for some

relevant information from Harwell - the elastic differential neutron scattering data from  $^6\text{Li}$  - I was ashamed to discover that, though it had certainly been worked out about five years ago, it had neither been published nor sent to the data centers.

This is a manifestation of a quite serious problem and I suspect that before we start any new experiments at Harwell it may be a wise move to write around and find out if it has already been carried out years ago and either not worked up or not reported. It might be quicker and cheaper for example, to send someone to OR to work up the data than to mount a whole new experiment. It is clearly impracticable to declare a two-year moratorium on all experimental work but maybe there should be less emphasis on keeping the accelerators running and more on getting the data published.

There was for me one surprising omission from the meeting - namely a progress report on the international comparison of methods of flux measurement that has been going on for a year or two. This is a topic quite central to the meeting's interest and I for one would have been interested in the chance of hearing an account of its progress.

Finally, I should like to comment on slidesmanship - to use the term of a distinguished fellow countryman. There is nothing that turns off an audience more than a speaker projecting a slide and saying "You won't be able to read this but . . .". I was many times on the front row and the speaker was far too often dead right, even at that range.

The second personal point is that coloured slides are in general an unmitigated nuisance. I have referred to the full horror of the colours chosen by a speaker from a certain laboratory but at least one didn't need to put the lights down to see them. For many others we saw the lights had to be turned down (and too often that meant turned off) and therefore it was virtually impossible to take notes.

Finally, if all the range of colours used on the slides are really necessary, then they contain too much information for the audience to take in.

On this matter, I go along with Henry Ford - you can have any colour so long as it is black and white.

J. J. Schmidt:

Let me start with a few general impressions before reviewing individually the sessions attributed to me.

First I agree with Professor Wigner's statement that this conference did not show strikingly new highlights and crazy inventions. In my opinion its value lay in bringing together much solid systematic work and detailed improvements in use, measurement, testing, evaluation and theory of nuclear data.

Second I feel that the field of nuclear data has gained in momentum by changing motivation and direction and broadening its applications and by getting more widely needed and acknowledged.

Certainly this is part of the consequences of the growth of national nuclear industries, of the energy crisis and of the growing public concern with nuclear safety and environmental protection. This all

brought to light the importance of build-up, burn-out and decay data of the wealth of fission product and actinide nuclides needed e.g., for all stages of the nuclear fuel cycle starting from cooling of reactor decay heat after shutdown and ending with the waste management. Environmental safety considerations are behind the increased attention to, and the sophisticated treatment of a large variety of shielding problems with the associated large amounts of more and more detailed nuclear data needed particularly in the MeV range.

Furthermore, for the first time in the series of US Conferences on nuclear data, a whole session has been devoted to nuclear data for fusion, although the most imminent and urgent data problems for fusion seem at present to lie in certain atomic and ionic data. Another rather short session, which I found extremely interesting, has been devoted to nuclear data for medical diagnostics and therapy.

In both fusion and medical applications of nuclear data the requirements seem slowly to become more clear and defined. Both fusion and medicine shift the interest in nuclear data to higher MeV energies with largely unknown charged particle nuclear reaction data, partial reaction cross sections and energy and angular distribution of secondary particles.

A further strong impression from several different sessions relates to the application of nuclear theory and models to the interpretation and prediction of nuclear data which have gained in reliability, particularly in the MeV range through more detailed descriptions of the nuclear reaction and decay processes.

Certainly, because of our unsatisfactory knowledge of nuclear forces, nuclear theory must always be parameterized when applied to nuclear data calculations, and needs fitting to some experimental data to derive numerical values for these parameters. Much of this, however, can nowadays be systematized, so that one can expect from a theoretical calculation a reasonable accuracy compared to experimental capability and compared to the requirements. This has made nuclear theory a powerful additional tool, - sometimes more economic than a difficult experiment, sometimes almost the only means for nuclear data prediction, - particularly in cases of survey or exploratory studies over large ranges of reactions and nuclides; this has been demonstrated at a number of occasions throughout the conference.

Having on the one hand more sophisticated theories applied, there have been on the other hand several demonstrations that fairly simple models, which take major nuclear features into account such as conservation of quantum numbers and others are apt to describe a wide variety of data. Here I refer for example to Felvinci's (EB 8) refined level density model, Kirov's (HB 14) and Newstead's (HB 23) analysis of strength function systematics and Pearlstein's (EB 7) statistical theory model. They may find application by project-oriented data users and evaluators who cannot spend much time on data problems.

The current opening of the interest in nuclear data from reactors proper to the whole nuclear fuel cycle and the growing applications of radiations and radioisotopes in medicine and many other areas underline the growing applied importance of reliable structure and decay data compilations for nuclides covering almost the whole atomic weight range. An impressive



amount of work in this direction has been demonstrated at this conference both on the more fundamentally oriented side such as by the Oak Ridge Nuclear Data Project (NDP) and on the application oriented side such as by the US fission product task force. It was particularly gratifying to learn from B. Ewbank's talk (EB 1) that the Oak Ridge NDP which covers the whole field of nuclear structure and decay as well as associate atomic data has constructed a computer file of its data from which repackagings of data can be done for many different uses. This could in the future promise much saving of duplicate compilation work under the condition that the basic data files were currently being kept well up-to-date. Incidentally, I was astonished that in spite of the immense variety of applications of activation analysis methods, almost no paper was delivered on this subject.

In a number of reports reference was made to completed or ongoing research in laboratories in smaller countries. Unfortunately only rather few of the smaller countries were represented at this conference, a fact which may partly be attributed to financial shortcomings. I am sure that people from those laboratories would have been much interested in participating in this conference to share their ideas and results with their colleagues in the larger countries and learn more about the importance of nuclear data in the context of scientific and technological progress and development.

A final general observation relates to the role of sensitivity studies and benchmark testing of microscopic nuclear data, for subjects on which we have much heard during this conference.

The sensitivity equations connect the requirements of the data user in reactor technology, fusion research, biomedicine and other fields with the accuracy requirements in nuclear data and thus represent probably the only sensible means, provided that sensitivity coefficients and error correlations are realistically defined, of determining nuclear data accuracy requirements which can legitimately be transmitted to nuclear data measurers. Ideally all nuclear data requests which appear in national or international nuclear data request lists should be based on such sensitivity studies. To give a typical example: the contributions from the USSR to the 1975 world request list for nuclear data (WRENDA 75) prepared by L. N. Usachev and M. N. Nikolaev from FEI Obninsk, which could not be reported at this conference, are totally based on sensitivity calculations for given accuracy requirements regarding the prediction of  $K_{\text{eff}}$  and breeding ratios of fast breeder reactors.

A second importance of sensitivity studies lies in the fact, that for given nuclear data uncertainties one can read from the sensitivity equations the resulting uncertainties in design parameters and see immediately how far off the desirable or admissible design tolerances one still is. This illustrates the importance of assigning error limits (including systematic error estimates) to evaluated data; this was in detail demonstrated for example in the papers reported by R. W. Peelle (CB 4) and F. G. Perey (IA 3).

The important role of benchmark experiments in the testing of microscopic nuclear data was solidified at this conference by many contributions including reports on several ongoing large cooperative projects which concern neutron data for thermal and fast reactors, for reactor dosimetry, a large variety of shielding problems and other applications. I shall shortly come back to this subject.

Let me now make some additional remarks on details of the sessions I have been given to review, in the hope that because of the large number of papers reported, the reviewer will be forgiven if he is unable to mention every name and paper and if instead he tries to highlight a few selected impressions and suggestions.

#### Sessions CB + IA. Benchmarks and Sensitivities

1. Each adjustment of microscopic data to integral experiment should try to preserve the nuclear physics features inherent in the data to be adjusted--such as for example the decrease of one cross section with the onset of a competing other reaction, or, as in the case of calculated and adjusted cross section curves, transmission and level density parameters and their energy dependence over a larger energy range. An excellent example of this kind appeared to me to be the systematic evaluation and adjustment of fission product neutron cross sections as reported by H. Gruppelaar (CB 2).

2. From R. W. Peelle's (CB 4) paper on uncertainties and corrections in evaluated data sets induced by the use of standard cross sections, I learned that when constructing a covariance uncertainty file to be attached to an ENDF file, there will arise a problem, namely to coordinate evaluators at different places, so that the error assignments to individual data and thus the uncertainty files are consistent among each other.

3. Benchmark experiments as reported serve normally two purposes: to test microscopic data by their integral counterpart and to adjust microscopic data so that the integral measurements are better reproduced and power reactor predictions more reliable. The discrepancies between the leakage spectra from iron spheres as measured by Johnson et al. (BB 1) from the University of Illinois and calculations with ENDF/B-III data may, however, not so easily be resolved by an adjustment of the 14 MeV inelastic scattering spectrum of iron, but by more detailed investigations of the precompound emission of neutrons, as e.g. demonstrated in a paper submitted on this very subject in another session by H. Jahn (EB 13).

4. I was strongly impressed by the refinement in benchmark testing applied to a large variety of nuclear data for thermal and fast reactors, shielding, dosimetry and fission product properties, and by the degree of sophistication of theoretical methods e.g. in the ORNL cross section sensitivity and uncertainty analysis system (FORSS), this all forming part of a large comprehensive programme between many laboratories in the U. S. as was reported by C. R. Weisbin et al. (IA 1) and E. M. Bohn et al. (IA 2) this morning. I would express the equally strong hope that these large efforts lead to a better understanding and definition of the still outstanding nuclear data needs particularly for the large variety of shielding applications. In this context the review paper delivered by N. M. Greene (IA 4) well illustrated the large sophisticated amount of data handling which has today to go in the conversion of basic ENDF/B data to multigroup etc. data systems used as input to large transport theory computer codes.

5. The intense European efforts complementing those in the U. S. and described by M. Mattes (CB 5) in shielding experiments and sensitivity studies, illustrated the need for a detailed theoretical description of secondary processes and for a comprehensive computerized library of standardized nuclear input data



such as optical model transmission coefficients, nuclear masses, level densities,  $\gamma$ -ray schemes and branching ratios, level schemes, etc. It seems advisable and now possible, that such a library for multiple consistent international use be developed in future on the basis of e.g. the Wapstra/Cove mass tables, the basic data file of the Oak Ridge Nuclear Data Project and other data libraries.

6. The paper delivered by W. N. McElroy (CB 7) seemed to me to indicate a considerable improvement in reliability of spectra unfolding from integral measurements of neutron dosimetry cross sections, although at present a testing of the data to better than about 5 - 10 percent seems still not possible. Also there seems to be a discrepancy persistent in the microscopically measured  $^{235}\text{U}$  fission spectrum and that deduced from fast measurements. According to Grundl's (DB 6) evaluation reported at this conference the first yields an average energy of 1.97 MeV, the foil spectrum data 2.05 MeV, as the foils produce a harder spectrum in the MeV range. As McElroy pointed out, the source of these and other discrepancies may not lie in the (ENDF/B-IV) data, but in inaccuracies in the specification of the benchmark spectra. I should add that also the IAEA Nuclear Data Section is continuing to be very interested in a solution of these discrepancies, including the accurate definition and comparison of benchmark spectra and the derivation of an internally consistent set of benchmark tested microscopic neutron cross sections for reactor dosimetry. It is planning to hold a consultants meeting on integral cross section measurements in standard neutron files for reactor neutron dosimetry in 1976.

7. The very impressive and voluminous afterheat calculations of fission produced  $\gamma$ -ray and photoneutron spectra reported by M. G. Stamatelatos (CB 10) illustrated the first use of the comprehensive ENDF/B-IV fission product yield and decay data files. As an interesting detail result, they revealed a constancy of the photoneutron yield for between 10 and 200 hours following reactor shut-down indicating the possibility of sourceless start-ups. A comparison of the calculated spectra with experiment seems not yet to have been done and would be highly desirable, to test the reliability of the calculations as well as of the input data used.

#### Session EB. Evaluation and Calculation of Cross Sections of Non-Fissionable Materials

1. Probably due to an increasing interest of nuclear theorists in nuclear data evaluation problems and a better interaction between nuclear theorists and nuclear data evaluators, a number of contributions to this session, e.g. by D. Larson (EB 3), A. Asami et al. (HB 4), C. Y. Fu (EB 6), G. Longo et al. (EB 11), H. Jahn et al. (EB 13), M. Mattes (CB 5) and others, showed that evaluation by using refined nuclear models and theories has gained in physical quality and, by more detailed description of secondary, tertiary, etc. reactions and of energy spectra of the emitted particles, also in reliability.

2. By adding to the simple evaporation model, which covers only the compound part of the reactions, direct and precompound terms, an impressive improvement in the understanding and description of experimental data could be achieved. From the contributions to this conference I would conclude three needs for further work; first the extension of the quasi-particle models to higher incident particle energies so as to cover data needs e.g. for medical purposes, second to develop,

as H. Feshbach and co-workers have already stated, a more fundamental understanding of the approximations used in precompound calculations such as those introduced by M. Blann et al. The third need would be to review comprehensively the present status of nuclear theories and models used in nuclear data evaluation with regard to the range of their validity, and their predictive power and reliability particularly for difficult-to-measure cross sections like those of fission product and actinide nuclei.

3. In this context I may mention that the IAEA Nuclear Data Section in cooperation with the International Center for Theoretical Physics (ICTP), in Trieste will convene a meeting of application-minded nuclear theorists and data evaluators at Trieste from 8-12 December this year with the double objective to review the status of nuclear theories and models used in evaluation and to delimit areas for further development and better fundamental understanding of current theories and models. As the outcome of this meeting and further efforts in this direction will be of particular value to laboratories in developing countries who cannot afford large evaluation programs, a considerable interest of these countries can be anticipated in participating in such development work, for example in workshops held at the ICTP in Trieste.

4. I should not leave this session without mentioning the excellent results of the continuous cooperative efforts particularly between Oak Ridge and Lucas Heights in high resolution measurements of keV neutron capture  $\gamma$ -ray spectra in many isotopes as reported by B. J. Allen (EB 16) at this meeting which complements the well-known efforts going on at Brookhaven, Chalk River and other places. On the fundamental side, they are more and more able to define validity and limitations of the valence neutron model.

Speaking for other type uses of such  $\gamma$ -spectral data, e.g. for shielding, it seems to me more and more imperative to develop concerted efforts to compile all this data in computer-readable form.

#### Session HA. Fusion

1. Don Steiner's (HA 1) introductory talk on nuclear data needs for fusion reactor design well illustrated the slowly increasing trend to more detailed and more realistic nuclear data requirements for the various application areas within the current DT fusion reactor research, particularly if supported by those sensitivity studies as reported by S. A. W. Gerstl (HA 5), while J. Rand McNally's talk (HA 7) clearly pointed to the need not to forget the investigation of more exotic fusion reactions such as DD,  $^6\text{LiD}$  and others, part of which have the advantage of reduced radioactivity hazards.

2. Regarding the highest priority need which Steiner mentioned, namely an evaluation of the  $\text{T(d,n)}^3\text{He}$  reaction cross sections, I would like to draw the attention to the thorough recent evaluation by H. Liskien published in ADNDT and to the recent work by L. Stewart et al. who also considered more recent Soviet measurements. All further evaluation work on this reaction should in my opinion start from these two comprehensive reviews. I should also like to underline the importance of the experimentally difficult-to-approach low keV part of this reaction which is not well known and is of importance during the ignition phase. Furthermore I believe that both Steiner's and McNally's suggestions of establishing

an evaluated nuclear data library for charged particle nuclear reactions - as many as 80 should be considered - particularly needed for further exploratory fusion studies should be taken seriously, as demanding quite a lot of work, which may be internationally shared e.g. between centers in the USA and in the USSR such as the Nuclear Data Center at the Kurchatov Institute in Moscow.

3. In this context D. G. Gardner's (HA 2) approach to contribute to satisfying CTR nuclear data needs by nuclear model calculations, seems to me important. Nuclear models should rather rapidly be able to predict to uncertainties of, say, typically 20 - 30 percent and often better, unknown cross sections needed in CTR exploratory studies. This approach would be more economic than a-priori measurements of the massive amount of all needed quantities, would allow a better definition of the design importance and priority of the individual reactions, and would permit the concentration of experimental efforts to the more important data. Similarly helpful in exploratory studies should be such 14 MeV cross section systematics as developed and excellently reported by S. J. Quaim (HA 4).

4. T. A. Tombrello (HA 3) reminded us of the similarity of the nuclear reactions occurring in the sun and in stellar dimensions to those in a fusion reactor and thus of the similarity of fusion and astrophysics problems, particularly for plasma processes in the sun corona. By this latter remark I would like to recall the fact that the realizability of fusion is, at present at least, not so much bound to a better understanding of the nuclear reactions involved, but to the better knowledge and technical domination of the much more ample atomic, molecular and ionic reactions connected with plasma impurities which, by detracting fusion heat, may even endanger the feasibility of fusion altogether.

5. Quaim's paper (HA 4) brought me to think still about another problem. He underlined the importance of neutron reactions on structural materials producing  $^3\text{He}$  and  $^3\text{H}$  for fundamental as well as fusion purposes. Although only of the order of microbarns, such cross sections might create an additional problem of tritium generation in fusion reactor materials.

6. The call by J. Rand McNally (HA 7) and other concerned with advanced fusion reactor fuels and designs for better charged particle data is being taken up by several laboratories, who performed, and reported on fairly extensive studies of charged particle nuclear reactions such as reactions of protons, deuterons,  $^3\text{He}$  and  $\alpha$ -particles with  $^6\text{Li}$  in the MeV range. I refer here to work presented by A. J. Elwyn et al. (HA 9) and C. R. Gould et al. (HA 10).

7. The  $^6\text{Li}(n,\alpha)$  reaction has been studied over the range 2 - 10 MeV by C. M. Bartle (HA 8), in a range where the cross action was hitherto barely known from experiment, and where it is very important for the tritium breeding. Only the evaluation by E. Pendlebury from Aldermaston existed since 1964. It was gratifying to see how well Pendlebury's more-than-10-years-ago interpolation was now reproduced by Bartle's experimental data. They also seem to rule out the far lower values measured recently by Clements and Rickard.

Although the new data seem to be very accurate, of the order of three percent, I would nevertheless doubt the conjecture of Don Steiner, that the tritium breeding can be calculated at present to 1 percent accuracy. Over the whole energy range of interest to tritium breeding the  $^6\text{Li}(n,\alpha)$  data seem not yet established to the reliability required for such accurate prediction.

8. In competition to the current DT fusion design studies are those considering fusion-fission hybrid systems, of which blanket aspects were reported in papers by B. Leonard et al. (HA 6) and K. C. Wong et al. (FA 14). I would like to draw the attention here to the need emanating from these studies for a better knowledge of neutron emission spectra from  $^{238}\text{U}$  and structural materials where pulsed sphere measurements such as performed at Livermore, in addition to microscopic measurements and theoretical estimates, may give an answer to the outstanding data problems.

Finally, also on behalf of all the participants from outside the USA, I would like to express my deep gratitude for the excellent assistance and hospitality extended to us by the organizers of this conference.



# LIST OF REGISTRANTS

Abdou, Mohamed  
Argonne National Laboratory  
Building 208  
Argonne, Illinois 60439

Adams, Richard J.  
National Research Co. of Canada  
Montreal Road  
Ottawa, Ontario K1A 0R6  
Canada

Ahluwalia, Harjit S.  
University of New Mexico  
3509 Brussels Court, N.E.  
Albuquerque, New Mexico 87111

Alberts, Wolfgang G.  
Physikalisch-Techn. Bundesanst.  
Bundesallee 100  
D-3300 Braunschweig  
Germany

Alfonse, William A., Jr.  
General Electric - Tempo  
777 - 14th Street, N. W.  
Washington, D. C. 20005

Allen, Barry J.  
AAEC Research Establishment  
Lucas Heights 2232  
N.S.W., Australia

Alsmiller, R. G., Jr.  
Oak Ridge National Laboratory  
P. O. Box X  
Oak Ridge, Tennessee 37830

Alvar, Kenneth R.  
University of Wisconsin  
Engineering Research Bldg.  
Madison, Wisconsin 53706

Anderl, Robert A.  
Aerojet Nuclear Company  
550 2nd Street  
Idaho Falls, Idaho 83401

Arthur, Edward D.  
Los Alamos Scientific Laboratory  
T-2 MS455  
Los Alamos, New Mexico 87544

Asami, Akira  
Japan Atomic Energy Res. Inst.  
Tokai-Mura, Naka-Gun  
Ibaraki-Ken, Japan

Auchampaugh, George F.  
Los Alamos Scientific Laboratory  
P. O. Box 1663  
Los Alamos, New Mexico 87544

Avery, Robert  
Reactor Analysis & Safety Division  
Argonne National Laboratory  
9700 South Cass Avenue  
Argonne, Illinois 60439

Baker, R. W.  
1464 E. Glenwood  
Springfield, Missouri 65804

Barre, Jean Yves  
Commissariat a l'Energie Atomique  
SECPR-CEN CADARACHE  
Boite Postale No 1  
Saint Paul Les Durance  
France 13115

Barschall, Henry H.  
University of Wisconsin  
Engineering Research Bldg.  
Madison, Wisconsin 53706

Bartle, C. Murray  
c/o Dept. of Nuclear Physics  
Australian National University  
Canberra, ACT 2600  
Australia

Bassel, Robert H.  
Naval Research Laboratory  
Code 6660  
Washington, D. C. 20375

Bauer, Gunter S.  
Oak Ridge National Laboratory  
P. O. Box X  
Oak Ridge, Tennessee 37830

Behrens, James W.  
Lawrence Livermore Laboratory  
University of California  
P. O. Box 808  
Livermore, California 94550

Benjamin, Richard W.  
Savannah River Laboratory-duPont  
Reactor Physics Division  
Aiken, South Carolina 29841

Bentley, Richard F.  
Los Alamos Scientific Laboratory  
Box 1663  
Los Alamos, New Mexico 87544

Bernard, Davy L.  
Univ. of Southwestern Louisiana  
P. O. Box 4210, USL Station  
Lafayette, Louisiana 70501

Bewley, David K.  
Hammersmith Hospital  
Medical Research Council  
Ducane Road, London W12 0HS  
United Kingdom

Bhat, M. R.  
Brookhaven National Laboratory  
Upton, Long Island  
New York 11973

Blewer, Robert S.  
Sandia Laboratories  
P. O. Box 5800  
Albuquerque, New Mexico 87115

Block, Robert C.  
Rensselaer Polytechnic Institute  
Troy, New York 12181

Blons, Jacques  
C.E.N. - Saclay  
91190 Gif sur Yvette  
France

Bockhoff, Karl H.  
Euratom, CBNM, Steenweg naar Retie  
2440 GEEL, Belgium

Bohn, Edward M.  
Argonne National Laboratory  
9700 S. Cass Avenue  
Argonne, Illinois 60439

Bowman, Charles D.  
Center for Radiation Research  
National Bureau of Standards  
Washington, D. C. 20234

Boyce, James R.  
Computer Sciences Corporation  
3333 Weeping Willow Ct., Apt. 11  
Silver Spring, Maryland 20906

Brady, F. Paul  
Department of Physics  
University of California  
Davis, California 95616

Bucher, William P.  
B.R.L. Aberdeen Proving Ground  
919 Cromwell Bridge Road  
Baltimore, Maryland 21204

Bunker, Stephen N.  
Simulation Physics, Inc.  
41 B Street  
Burlington, Massachusetts 01803

Carlson, Allan D.  
Center for Radiation Research  
National Bureau of Standards  
Washington, D. C. 20234

Carlson, Gary W.  
Lawrence Livermore Laboratory  
University of California  
P. O. Box 808 L-24  
Livermore, California 94550

Carter, Robert E.  
AFRRI-DNA  
Bethesda, Maryland 20014

Caswell, Randall S.  
Center for Radiation Research  
National Bureau of Standards  
Washington, D. C. 20234

Chatterjee, Arun Kumar  
Bose Institute, Calcutta-9  
India

Chrien, Robert E.  
Brookhaven National Laboratory  
Upton, Long Island  
New York 11973



Clark, Ronald G.  
Federal Energy Administration  
5805 Cherrywood Lane, Apt. 202  
Greenbelt, Maryland 20770

Coates, Michael S.  
United Kingdom Atomic Energy Auth.  
A.E.R.E. Harwell, Oxfordshire  
OX11 0RA England

Corvi, Francesco  
BCMN Euratom  
B-2440 GEEL  
Belgium

Cowan, Charles L.  
General Electric  
598 Elvis Drive  
San Jose, California 95123

Cox, John M.  
Ohio University  
Athens, Ohio 45701

Coyne, J. Joseph  
Center for Radiation Research  
National Bureau of Standards  
Washington, D. C. 20234

Cross, William G.  
Atomic Energy of Canada, Ltd.  
Chalk River Nuclear Laboratories  
Chalk River, Ontario  
Canada K0J-1P0

Cullen, Dermott E.  
Lawrence Livermore Laboratory  
1182 Burgundy Way  
Livermore, California 94550

Czirr, J. Bart  
Lawrence Livermore Laboratory  
P. O. Box 808  
Livermore, California 94550

Dabbs, John W. T.  
Oak Ridge National Laboratory  
P. O. Box X  
Oak Ridge, Tennessee 37830

Dabby, Danny  
Monroeville Nuclear Center  
Box 355  
Pittsburgh, Pennsylvania 15230

Davey, William G.  
Los Alamos Scientific Laboratory  
P. O. Box 1663  
Los Alamos, New Mexico 87544

Delucchi, Arnaldo A.  
Lawrence Livermore Laboratory  
P. O. Box 808  
Livermore, California 94554

Derrien, H.  
D.P.R.M.A. C.E.N. SACLAY  
BP N° 2, GIF/YVETTE  
91190 France

deSaussure, Gerard  
Oak Ridge National Laboratory  
Bldg. 6010  
Oak Ridge, Tennessee 37830

Devillers, Christian  
DPRMA/SERMA SACLAY  
BP N° 2, 91190 GIF Sur Yvette  
France

Dickens, Kirk  
Oak Ridge National Laboratory  
P. O. Box X  
Oak Ridge, Tennessee 37830

Didier, Daniel J.  
C.E.A.  
BP N° 61  
92120 Montrouge  
France

DiFilippo, Felix C.  
Oak Ridge National Laboratory  
P. O. Box X  
Oak Ridge, Tennessee 37830

Divadeenam, M.  
Brookhaven National Laboratory  
Upton, Long Island  
New York 11973

Diven, Ben C.  
Los Alamos Scientific Laboratory  
Box 1663  
Los Alamos, New Mexico 87544

Donoghue, Timothy R.  
Ohio State University  
Physics Department  
Columbus, Ohio 43210

Dorning, Jack  
Nuclear Engineering Lab.  
University of Illinois  
Urbana, Illinois 61801

Drake, Darrell M.  
Los Alamos Scientific Laboratory  
P. O. Box 1663  
Los Alamos, New Mexico 87544

Durston, Colin  
Argonne National Laboratory  
9700 S. Cass Avenue  
Argonne, Illinois 60439

Dyer, Clive S.  
Code 682, NASA  
Goddard Space Flight Center  
Greenbelt, Maryland 20771

Eapen, P. K.  
United Eng. & Constructors  
1401 Arch Street (10F)  
Philadelphia, Pennsylvania 19105

Egan, James J.  
Dept. of Physics & Applied Physics  
Lowell Technological Institute  
Lowell, Massachusetts 01854

Eiland, Henry M.  
KAPL  
P. O. Box 1072  
Schenectady, New York 12301

Eisenhauer, Charles M.  
Center for Radiation Research  
National Bureau of Standards  
Washington, D. C. 20234

Elwyn, Alexander J.  
Physics Division, D203  
Argonne National Laboratory  
Argonne, Illinois 60137

England, T. R.  
Los Alamos Scientific Laboratory  
P. O. Box 1663  
Los Alamos, New Mexico 87544

Epperson, Dennis H.  
Physics Department  
Duke University  
Durham, North Carolina 27706

Erdal, Bruce R.  
Los Alamos Scientific Laboratory  
CNC-11, MS514  
Los Alamos, New Mexico 87544

Etemad, Mohammad-Ali  
Atomic Energy Organization of Iran  
Nuclear Research Centre  
P. O. Box 2989  
Tehran, Iran

Evans, John E.  
Lockheed Palo Alto Research Lab.  
615 Joandra Court  
Los Altos, California 94022

Ewbank, W. Bruce  
Oak Ridge National Laboratory  
P. O. Box X  
Oak Ridge, Tennessee 37830

Extermann, Richard C.  
The Cooper Union  
Physics Department  
51 Astor Place  
New York, New York 10003

Fabry, Albert M.  
CEN-SCK Mol  
270 Boeretang  
2400 Mol, Belgium

Fahri, Domanic  
University of Ankara-Turkey  
Fen Fakultesi  
Ankara, Turkey

Farrar, Harry IV  
Atomics International  
P. O. Box 309  
Canoga Park, California 91304

Feiner, Frank  
GE - KAPL  
P. O. Box 1072  
Schenectady, New York 12301

Felvinci, John P.  
Columbia University  
Engineering Terrace Building  
520 W. 120th Street  
New York, New York 10027

Ferguson, James M.  
Lawrence Livermore Laboratory  
Box 808  
Livermore, California 94550

Finch, Donald R.  
Savannah River Laboratory  
Aiken, South Carolina 29841

Fleming, Ronald F.  
National Bureau of Standards  
19167 Stedwick Drive  
Gaithersburg, Maryland 20760

Forman, Leon  
Los Alamos Scientific Laboratory  
P. O. Box 1663  
Los Alamos, New Mexico 87544

Fowler, Joseph L.  
Oak Ridge National Laboratory  
P. O. Box X  
Oak Ridge, Tennessee 37830

Friesenhahn, Stanley J.  
IRT Corporation  
P. O. Box 80817  
San Diego, California 92138

Fritts, Martin J.  
Science Applications, Inc.  
1651 Old Meadow Road  
McLean, Virginia 22101

Fu, Chia-Yao  
Oak Ridge National Laboratory  
Neutron Physics Division,  
P. O. Box X  
Oak Ridge, Tennessee 37830

Fuller, Everett G.  
Center for Radiation Research  
National Bureau of Standards  
Washington, D.C. 20234

Gabbard, Fletcher  
Department of Physics & Astronomy  
University of Kentucky  
Lexington, Kentucky 40506

Garber, Donald I.  
Brookhaven National Laboratory  
Bldg. 197  
Upton, Long Island  
New York 11793

Gardner, Donald G.  
Lawrence Livermore Laboratory  
P. O. Box 808  
Livermore, California 94550

Garg, Jagadish B.  
Nuclear Accelerator Laboratory  
State University of New York  
1400 Washington Avenue  
Albany, New York 12303

Gay, Rodney R.  
E.P.R.I.  
1058 California Avenue  
Palo Alto, California 94306

Gayther, Derek B.  
A.E.R.E. Harwell, Didcot  
Oxfordshire OX11 0RA  
England

Gerstl, Sig. A.W.  
Los Alamos Scientific Laboratory  
T-1, MS.269  
Los Alamos, New Mexico 87544

Ghose, Ananda M.  
Head, Dept. of Physics  
Bose Institute  
93/1 A.P.C. Road  
Calcutta 9, India

Gilliam, David M.  
Center for Radiation Research  
National Bureau of Standards  
Washington, D. C. 20234

Glasgow, Dale W.  
Physics Department  
Duke University  
Durham, North Carolina 27706

Glickstein, Stanley S.  
Bettis Atomic Power Lab.  
P. O. Box 79  
West Mifflin, Pennsylvania 15122

Goishi, Wataru  
Lawrence Livermore Laboratory  
L-234, P. O. Box 808  
Livermore, California 94550

Goldberg, Eugene  
Lawrence Livermore Laboratory  
P. O. Box 808, L-24  
Livermore, California 94550

Goldman, David T.  
Institute for Basic Standards  
National Bureau of Standards  
Washington, D.C. 20234

Goldsmith, Mark  
Westinghouse  
6627 Forest Glen Road  
Pittsburgh, Pennsylvania 15217

Goldstein, Herbert  
Columbia University  
144-19 68th Road  
Flushing, New York 11367

Gould, Christopher R.  
Physics Department  
North Carolina State University  
Raleigh, North Carolina 27607

Greene, N. Maurice  
Oak Ridge National Laboratory  
P. O. Box X, Bldg. 6025  
Oak Ridge, Tennessee 37830

Greenwood, Lawrence R.  
Argonne National Laboratory  
9700 S. Cass Avenue  
Argonne, Illinois 60439

Greenwood, Reginald C.  
Physics Department  
Brookhaven National Laboratory  
Upton, Long Island  
New York 11973

Grundl, James A.  
Center for Radiation Research  
National Bureau of Standards  
Washington, D.C. 20234

Gruppelaar, Harm  
Reactor Centrum Nederland  
Physics Department  
Westerduinweg 3, PETTEN (N.N.)  
The Netherlands

Hacken, George  
Nevis Labs, Columbia University  
P. O. Box 137  
Irvington, New York 10533

Hale, Gerald M.  
Los Alamos Scientific Laboratory  
Group T-2  
Los Alamos, New Mexico 87544

Hansen, Gordon E.  
Los Alamos Scientific Laboratory  
P. O. Box 1663  
Los Alamos, New Mexico 87544

Harris, Donald R.  
Los Alamos Scientific Laboratory  
P. O. Box 1663  
Los Alamos, New Mexico 87544

Harvey, Jack A.  
Oak Ridge National Laboratory  
P. O. Box X  
Oak Ridge, Tennessee 37830

Havens, William W.  
Columbia University  
520 West 120th Street  
New York, New York 10027

Heath, Russell L.  
Idaho National Eng. Laboratory  
550 2nd Street  
Idaho Falls, Idaho 83401

Heaton, H.T., II  
Center for Radiation Research  
National Bureau of Standards  
Washington, D. C. 20234

Helmer, Richard G.  
Aerojet Nuclear Company  
550 2nd Street  
Idaho Falls, Idaho 83401

Hemmig, Philip P.  
US Energy Research & Development Admin.  
Div. of Reactor Research & Development  
Washington, D.C. 20545

Hennelly, Edward J.  
I. E. DuPont  
Savannah River Laboratory  
Aiken, South Carolina 29801

Henryson, Herbert II  
Argonne National Laboratory  
9700 S. Cass Avenue  
Argonne, Illinois 60439

Hill, Nathaniel W.  
Oak Ridge National Laboratory  
P. O. Box X  
Oak Ridge, Tennessee 37830

Hines, John J.  
Argonne National Laboratory  
9700 S. Cass Avenue  
Argonne, Illinois 60439

Hjaerne, Leif  
Ministry of Industry  
AKA-Utredningen  
Humlegatan, 1A  
21127 Malmö  
Sweden

Hockenbury, Robert W.  
Rensselaer Polytechnic Institute  
Department of Nuclear Engineering  
Troy, New York 12181

Hogue, Henry H.  
Physics Department  
Duke University  
Durham, North Carolina 27706

Holden, Norman E.  
Brookhaven National Laboratory  
NNCSC, Bldg. 197  
Upton, Long Island  
New York 11973

Hollandsworth, Clinton E.  
AMSL, BRL  
Aberdeen Proving Ground  
Maryland 21005

Holmgren, Harry D.  
Department of Physics  
University of Maryland  
College Park, Maryland 20742

Holt, Roy J.  
Argonne National Laboratory  
9700 S. Cass Avenue  
Argonne, Illinois 60439

Horen, Daniel J.  
Oak Ridge National Laboratory  
P. O. Box X  
Oak Ridge, Tennessee 37830

Hunter, Raymond E.  
Los Alamos Scientific Laboratory  
111 Shirlane Place  
Los Alamos, New Mexico 87544

Huynh, Vinh Dinh  
Bureau International des Poids  
et Mesures  
Pavillon de Bretenil  
F-92310 Sèvres  
France

Hwang, Richard N.  
Applied Physics Division  
Argonne National Laboratory  
Argonne, Illinois 60439

Jackson, Harold E., Jr.  
Argonne National Laboratory  
Physics Division  
Argonne, Illinois 60439

Jahn, Helmut  
University of Karlsruhe  
75 Karlsruhe 1-Waldstadt  
19 Erasmusstr.  
Germany

Johansson, Per-Ivar  
AB Atomenergi, Studsvik, Fack  
S-611 01 Mykoping, Sweden

Johnson, Richard H.  
214 NEL  
University of Illinois  
Urbana, Illinois 61801

Kaeppler, Franz  
Gesellschaft fuer Kernforschung  
IAK  
D 7500 Karlsruhe, Postfach 3640  
Germany

Kammerdiener, John L.  
Los Alamos Scientific Laboratory  
TD-2, P. O. Box 1663  
Los Alamos, New Mexico 87550

Kanda, Keiji  
Kyoto University,  
Research Reactor Inst.  
Kumatori, Sennan  
Osaka, Japan

Keyworth, George A.  
Los Alamos Scientific Laboratory  
MS 422, P. O. Box 1663  
Los Alamos, New Mexico 87544

Kinney, William E.  
Neutron Physics Division  
Oak Ridge National Laboratory  
Post Office Box X  
Oak Ridge, Tennessee 37830

Kinsey, Bernard B.  
Department of Physics  
University of Texas  
Austin, Texas 78712

Kinsey, Robert R.  
Brookhaven National Laboratory  
197C  
Upton, New York 11973

Kirouac, George J.  
Knolls Atomic Power Laboratory  
Schenectady, New York 12301

Kmetyk, Lubomyra N.  
Cooper Union  
Physics Department  
Cooper Square  
New York, New York 10003

Knoll, Glenn F.  
2266 GGBL  
University of Michigan  
Ann Arbor, Michigan 48105

Knox, Harold D.  
Accelerator Laboratory  
Ohio University  
Athens, Ohio 45701

Ku, Long-Poe  
292 B Engineering Terrace  
S.W. Mudd Building  
Columbia University  
New York, New York 10027

LaBauve, Raphael V.  
Los Alamos Scientific Laboratory  
P. O. Box 1663  
Los Alamos, New Mexico 87544

Lachkar, Jean C.  
Service de Physique Nucleaire  
Centre d'Etudes de Bruyeres-le-chatel  
B.P. n° 61 - Montrouge 92120  
France

Lamaze, George P.  
Center for Radiation Research  
National Bureau of Standards  
Washington, D. C. 20234

Lane, Raymond O.  
John E. Edwards Accelerator Laboratory  
Ohio University  
Athens, Ohio, 45701

Lanier, Robert G.  
P. O. Box 808  
Livermore, California 94550

Larson, Duane C.  
Neutron Physics Division, Building 6010  
Post Office Box X  
Oak Ridge, Tennessee 37830

LeRigoleur, Claude  
CEN Cadarache  
B.P. No. 1  
13115 St. Paul lez Durance  
France

Lemmel, Hans-Dietrick  
A-1011  
Vienna, Box 590  
Austria

Leiss, James E.  
Center for Radiation Research  
National Bureau of Standards  
Washington, D. C. 20234

Leonard, Bowen, R., Jr.  
Battelle-Northwest  
P.O. Box 999  
Richland, Washington 99352

Lesca, Luigi L.  
Centre de Compilation de Donnees  
Neutroniques  
B.P. 9 (Batiment 45)  
Gif Sur Yvette, France 91190

Lindner, Manfred  
Lawrence Livermore Laboratory  
P. O. Box 808  
Livermore, California 94550

Liskien, Horst O.  
CBNM Geel Europ. Comm.  
Retie Belgium

Liou, Horng-ing  
Department of Physics  
Brookhaven National Laboratory  
Upton, Long Island, New York 11973

Lubitz, Cecil R.  
Knolls Atomic Power Laboratory G2-316  
Schenectady, New York 12301



Macklin, Richard L.  
Union Carbide Nuclear  
225 Outer Drive  
Oak Ridge, Tennessee 37830

Maeck, William J.  
Allied Chemical  
550 - 2nd Street  
Idaho Falls, Idaho 83401

Magurno, Benjamin A.  
Brookhaven National Laboratory  
T-197 Upton  
New York 11973

Mahna, Kashmiri C.  
Public Service Electric and Gas Co.  
80 Park Place, Room 3333  
Newark, New Jersey 07052

Maienschein, Fred C.  
Oak Ridge National Laboratory  
P. O. Box X  
Oak Ridge, Tennessee 37830

Malik, S. S.  
University of Rhode Island  
Physics Department  
Kingston, Rhode Island 02881

Mann, Fredrick M.  
California Institute of Technology  
Kellogg Lab. 106-38  
Caltech  
Pasadena, California 91125

Mann, Lloyd G.  
Lawrence Livermore Laboratory  
P. O. Box 808  
Livermore, California 94550

Maskewitz, Betty F.  
Oak Ridge National Laboratory  
P. O. Box X  
Oak Ridge, Tennessee 37830

Mathews, Donald R.  
General Atomic Company  
P. O. Box 81608  
San Diego, California 92138

Mattes, Margarete  
Institut für Kernenergetik  
D 7000 Stuttgart -80  
Pfaffenwaldring 31  
Germany

Matthes, W.  
Euratom  
CCR Euratom  
Ispra, Italy

Maxson, Donald R.  
Brown University  
Physics Department  
526 Barus-Holley Building  
Providence, Rhode Island 02912

May, Victoria M.  
Brookhaven National Laboratory  
T-197  
Upton, New York 11973

Medvedev, Petter I.  
U.S.S.R. Embassy  
1125 - 16th Street, N.W.  
Washington, D. C. 20036

Meier, Michael  
Center for Radiation Research  
National Bureau of Standards  
Washington, D. C. 20234

Meinke, W. Wayne  
KMS Fusion  
P. O. Box 1567  
Ann Arbor, Michigan 48106

Mewissen, W. Louis  
CEN-SCK Mol  
200 Boeretang  
B2400 Mol, Belgium

Meyer, Paul  
Lawrence Livermore Laboratory  
P. O. Box 808 L-221  
Livermore, California 94550

Michaudon, André F.  
Service De Physique Nucleaire  
Centre D'Etudes de Bruyeres-Le-Chatel  
B. P. N° 61  
Montrouge 92120  
FRANCE

Mignelo, Emilio  
Institute di Fisica, Corso Itacia  
Catania, Italy

Mikado, Tomohisa  
Center for Radiation Reserach  
National Bureau of Standards  
Washington, D. C. 20234

Mittler, Art  
Department of Physics  
University of Lowell  
Lowell, Massachusetts 01854

Momota, Teruo, T.  
Department of Nuclear Engineering  
Tohoku University  
Sendai, Japan

Moore, Michael S.  
Los Alamos Scientific Laboratory  
P. O. Box 1663  
MS 808 P-11  
Los Alamos, New Mexico 87544

Morrison, Gilbert W.  
Oak Ridge National Laboratory  
P. O. Box X  
Building 6002  
Oak Ridge, Tennessee 37830

Moses, John D.  
Los Alamos Scientific Laboratory  
P. O. Box 1663  
Los Alamos, New Mexico 87544

Motz, Henry T.  
Los Alamos Scientific Laboratory  
Mail Stop 434, P. O. Box 1663  
Los Alamos, New Mexico 87544

Mughabghal, Soid F.  
Brookhaven National Laboratory  
Upton, Long Island  
New York 11973

Muir, Douglas W.  
Los Alamos Scientific Laboratory  
P. O. Box 1663 M.S. 455  
Los Alamos, New Mexico, 87544

McEllistrem, Marcus T.  
Department of Physics & Astronomy  
University of Kentucky  
Lexington, Kentucky 40506

McElroy, William N.  
P. O. Box 1970  
Richland, Washington 99352

MacFarlane, Robert E.  
Los Alamos Scientific Laboratory  
P. O. Box 1663  
Los Alamos, New Mexico 87544

McGarry, Emmert D.  
Harry Diamond Laboratories  
2800 Powder Mill Road  
Adelphi, Maryland 20783  
Attn: DORF/290

McKnight, Richard D.  
Argonne National Laboratory  
9700 South Cass Avenue D-316  
Argonne, Illinois 60439

McNally, J. Rand, Jr.  
Oak Ridge National Laboratory  
P. O. Box Y,  
Building 9201-2  
Oak Ridge, Tennessee 37830

Nagel, Michael Z.  
General Atomic Company  
P. O. Box 81608  
San Diego, California 92138

Nagle, Richard J.  
Lawrence Livermore Laboratory  
P. O. Box 808  
Livermore, California 94550

Namenson, Arthur I.  
Naval Research Laboratory  
Washington, D. C. 20375

Nath, Ravinder  
Yale University  
Physics Department  
New Haven, Connecticut 06520

Nelson, Charles E.  
University of Chicago  
FMI Box 420  
950 E 59th Street  
Chicago, Illinois 60637

Nelson, John W.  
Physics Department  
Florida State University  
Tallahassee, Florida 32206

Nethaway, David R.  
Lawrence Livermore Laboratory  
Livermore, California 94550

Newman, Eugene  
Neutron Physics Division  
Bldg. 6010  
P. O. Box X  
Oak Ridge National Laboratory  
Oak Ridge, Tennessee 37830

Newson, H. W.  
TUNL  
Duke University  
Durham, North Carolina 27705

Newstead, Charles M.  
Physics Dept., C-E  
15 Woodland Avenue, Apt. 15F  
Bloomfield, Connecticut 06002

Niiler, Andrus  
USA-Ballistics Research Lab.  
Aberdeen Proving Ground  
Maryland 21005

Ohlsen, Gerald G.  
Los Alamos Scientific Laboratory  
P-9, MS456  
Los Alamos, New Mexico 87544

Olsen, David K  
Oak Ridge National Laboratory  
Bldg. 6010  
Oak Ridge, Tennessee 37830

Overly, Jack C.  
Physics Department  
University of Oregon  
Eugene, Oregon 97403

Orphan, Victor J.  
Science Applications, Inc.  
1138 Eolus Avenue  
Leucadia, California 92024

Ottewitte, Eric H.  
Swiss Federal Inst. for Reactor  
Research  
Wurenlingen, Switzerland CH5303

Ozer, Odelli  
Electric Power Research Institute  
P. O. Box 10412  
Palo Alto, California 94304

Padgett, Doran W.  
Office of Naval Research  
3801 N. 36th Road  
Arlington, Virginia 22207

Paik, N. C.  
Westinghouse ARD  
Waltz Mill Site  
Madison, Pennsylvania 15663

Pandey, Madhu S.  
Physics Dept., SUNY-Albany  
1400 Washington Avenue  
Albany, New York 12222

Pannetier, Raymond  
C.E.A. France  
B.P. 27  
Villineuve St. Georges 96  
France

Pearlstein, Sol  
Brookhaven National Laboratory  
Bldg. 197  
Upton, New York 11973

Peelle, Robert W.  
Oak Ridge National Laboratory  
P. O. Box X, Bldg. 6010  
Oak Ridge, Tennessee 37830

Pennington, Edwin M.  
Argonne National Laboratory  
9700 S. Cass Avenue  
Argonne, Illinois 60439

Peres, Asher  
Technion (Physics)  
Haifa, Israel

Perey, Francis G.  
Oak Ridge National Laboratory  
P. O. Box X  
Oak Ridge, Tennessee 37830

Perez, Rafael B.  
Oak Ridge National Laboratory  
Bldg. 6010  
Oak Ridge, Tennessee 37830

Persiani, Paul J.  
Argonne National Laboratory  
9700 S. Cass Avenue  
Argonne, Illinois 60439

Petersen, Edward L.  
Naval Research Laboratory  
Code 6611  
Washington, D. C. 20375

Poenitz, Wolfgang P.  
Argonne National Laboratory  
9700 S. Cass Avenue  
Argonne, Illinois 60439

Prabulos, Joseph J.  
Combustion Engineering, Inc.  
50 Hildurcrest Drive  
Simsbury, Connecticut 06070

Prael, Richard E.  
Applied Physics Division  
Bldg. 208-A101A  
Argonne National Laboratory  
Argonne, Illinois 60439

Priesmeyer, Hans G.  
Institut fuer Kernphysik  
D-2054 Geesthacht  
Reaktor Station  
Fed. Rep. of Germany

Prince, Augustus  
Brookhaven National Laboratory  
Upton, New York 11973

Qaim, Syed M.  
Nuclear Research Centre  
D-517 Juelich  
West Germany

Ragan, Charles E., III  
Los Alamos Scientific Laboratory  
P. O. Box 1663  
Los Alamos, New Mexico 87544

Rahn, Frank J.  
EPRI  
Box 10412  
Palo Alto, California 94304

Raman, S.  
Oak Ridge National Laboratory  
P. O. Box X  
Oak Ridge, Tennessee 37830

Raymund, Mahlon  
Westinghouse Electric Corp.  
P. O. Box 355  
Pittsburgh, Pennsylvania 15230

Reed, John H.  
Science Applications, Inc.  
1200 Prospect Street  
P. O. Box 2351  
LaJolla, California 92037

Reed, Raymond L.  
E. I. DuPont  
Savannah River Laboratory  
Aiken, South Carolina 29801

Reeder, Paul L.  
Battelle-Northwest Laboratory  
P. O. Box 999  
Richland, Washington 99352

Reedy, Robert C.  
Los Alamos Scientific Laboratory  
CNC-11 Mail Stop 514  
Los Alamos, New Mexico 87544

Reich, Charles W.  
Aerojet Nuclear Company  
550 Second Street  
Idaho Falls, Idaho 83401

Reitmann, Daniel  
S.A. Atomic Energy Board  
Private Bag X256  
Pretoria, South Africa

Reynolds, J. Terrence  
Knolls Atomic Power Laboratory  
River Road  
Schenectady, New York 12301

Rimawi, Kavim  
Brookhaven National Laboratory  
118 Longbranch Circle  
Liverpool, New York 13088

Ritter, Enloe T.  
Division of Physical Research  
Energy Research & Development Admin.  
Washington, D. C. 20545

Robertson, James Craig  
Department of Nuclear Engineering  
University of Michigan  
Ann Arbor, Michigan 48105

Robertson, James S.  
Mayo Clinic, Hilton C66  
Rochester, Minnesota 55901

Rogers, Vern  
IRT Corporation  
P. O. Box 80817  
San Diego, California 92138

Rohr, Gert  
Euratom, CBNM  
Steenweg naar Retie  
2440 Geel, Belgium

Rose, Basil  
A.E.R.E. Harwell, Didcot  
Oxfordshire OX11 0RA  
England

Rose, Philip F.  
Brookhaven National Laboratory  
Bldg. 197  
Upton, New York 11973

Rothenstein, Wolfgang  
NNCSC, Brookhaven National Lab.  
Upton, L.I., New York 11973

Roussin, Robert W.  
ORNL - RSIC  
P. O. Box X  
Oak Ridge, Tennessee 37830

Rundberg, Robert S.  
Chemistry Department  
Brooklyn College of CUNY  
Brooklyn, New York 11210

Russell, Gary J.  
Los Alamos Scientific Laboratory  
P. O. Box 1663  
P-11 MS 808  
Los Alamos, New Mexico 87544

Saccenti, John C.  
U.S. Army Ballistic Res. Lab.  
Building E-5695  
Aberdeen Proving Ground  
Maryland 21005

Salaita, George N.  
Physics Department  
Southern Methodist University  
Dallas, Texas 75275

Salvatores, Massimo  
CSN Casaccia - CNEN  
St. Provin. Anguillarese KM 1+300  
Rome 00060  
Italy

Santry, Dallas C.  
Chalk River Nuclear Laboratories  
Chalk River  
Ontario, Canada

Saporetti, Franco  
Centro di Calcolo - CNEN  
Via Mazzini, 2 - Bologna  
Italy

Schanzler, Ludwig  
3042 Munster  
P. O. Box 342  
West Germany

Schenter, Robert E.  
Westinghouse Hanford Co.  
P. O. Box 1970  
Richland, Washington 99352

Schmidt, Josef J.  
IAEA Nuclear Data Section  
P. O. Box 590  
A-1010 Vienna  
Austria

Schmitt, Andre  
CEN Cadarache  
B.P. N° 1  
13115 Saint Paul  
67 Durance  
France

Schofield, Anton  
C.C.D.N.  
B.P. 9  
91190 GIF/YVETTE  
France

Scholtyssek, Werner J.  
GFK, 75 Karlsruhe  
Webrstr. 5  
IASR/SNEAK  
Germany

Schrack, Roald A.  
Center for Radiation Research  
National Bureau of Standards  
Washington, D. C. 20234

Schroder, Ivan G.  
Center for Radiation Research  
National Bureau of Standards  
Washington, D. C. 20234

Scobel, Wolfgang  
Universitat Hamburg  
2 Hamburg 50, Luruper Chaussee 149  
Germany

Seamon, Robert E.  
Los Alamos Scientific Laboratory  
Group TD-6, Mail Stop 226  
P. O. Box 1663  
Los Alamos, New Mexico 87544

Sheahan, Thomas P.  
Industrial Nucleonics  
650 Acuerman Road  
Columbus, Ohio 43202

Sheldon, Eric  
Department of Physics  
Lowell Technological Institute  
Lowell, Massachusetts 01854

Shin, Iwasaki  
Department of Nuclear Engineering  
Tohoku University  
Sendai, Japan

Shneiderov, Anatol J.  
The Polycultural Institution of  
America, IPI  
1673 Columbia Road, Apt. 309  
Washington, D. C. 20009

Sidhu, Gernam S.  
Lawrence Livermore Laboratory  
P. O. Box 808  
Livermore, California 94550

Sigaud, Jean P.  
Service de Physique Nucleaire  
Centre D'Etudes de Bruyeres-le-Chateau  
B.P. n° 61 - Montrouge 92120  
France

Singh, Udit N.  
Nevis Laboratories  
P. O. Box 137  
Irvington, New York 10533

Sjöstrand, Nils G.  
Dept. of Reactor Physics  
Chalmers University of Technology  
S-40220 Göteborg  
Sweden

Smith, Alan B.  
D-316 Argonne National Laboratory  
Argonne, Illinois 60439

Smith, J. Richard  
Aerojet Nuclear Company  
550 2nd Street  
Idaho Falls, Idaho 83401

Spencer, Robert R.  
Oak Ridge National Laboratory  
P. O. Box X, Bldg. 6010  
Oak Ridge, Tennessee 37830

Spiegel, Valentine  
Center for Radiation Research  
National Bureau of Standards  
Washington, D. C. 20234

Spitzer, Howard  
McDonnell-Douglas Astronautics Company  
A3-206-AAN1-11-2  
5301 Bolsa Avenue  
Huntington Beach, California 92647

Stamatelatos, Michael G.  
Los Alamos Scientific Laboratory  
Los Alamos, New Mexico 87544

Stehn, John R.  
Brookhaven National Laboratory  
Upton, New York 11973

Steiner, Don  
Oak Ridge National Laboratory  
P. O. Box Y  
Oak Ridge, Tennessee 37830

Stephany, William P.  
University of Michigan  
2254 G.G. Brown Lab.  
North Campus  
Ann Arbor, Michigan 48105

Stewart, Leona  
Los Alamos Scientific Laboratory  
Los Alamos, New Mexico 87544

Sugiyama, Kazusuke  
Department of Nuclear Engineering  
Tohoku University  
Aoba, Sendai, Japan 980

Sullivan, N. B.  
Physics Department  
Lowell Technological Institute  
Lowell, Massachusetts 01854

Tang, Lun Han  
Physics Department  
University of Detroit  
Detroit, Michigan 48221



Taylor, M. C.  
Columbia Scientific Ind. Corp.  
P. O. Box 6190  
Austin, Texas 78762

Taylor, Theodore B.  
International Research &  
Technology Corp.  
1501 Wilson Boulevard  
Arlington, Virginia 22209

Tessler, George  
Bettis Atomic Power Lab.  
Box 79  
West Mifflin, Pennsylvania 15122

Thompson, Gail I.  
Brookhaven National Laboratory  
Bldg 197-C, Dept. of App'ld Sci.  
Upton, New York 11973

Tilbury, Roy S.  
Sloan-Kettering Institute  
410 East 68th Street  
New York, New York 10021

Tombrello, Thomas A.  
106-38  
Calif. Inst. of Technology  
Pasadena, California 91125

Toppel, Bert J.  
Argonne National Laboratory  
9700 S. Cass Avenue  
Argonne, Illinois 60439

Towner, Harry H.  
205 Nuclear Engr. Laboratory  
University of Illinois  
Urbana, Illinois 61801

Uilo, John T.  
Bettis Atomic Power Lab.  
P. O. Box 79  
West Mifflin, Pennsylvania 15122

Uotinen, Vic O.  
Babcock & Wilcox  
9102 Oakland Circle  
Lynchburg, Virginia 24502

Vagelatos, Nicholas  
Reactor Building  
National Bureau of Standards  
Washington, D. C. 20234

Vanpraet, Georges J.  
State University Antwerp  
Groenenborgerlaan, 171  
B-2020 Antwerp  
Belgium

Velarde, Guillermo  
Junta de Energia Nuclear of Spain  
Avda. Complutense.  
Madrid -3. Spain

Viola, Vic  
Department of Chemistry  
University of Maryland  
College Park, Maryland 20742

Voigt, Adolf F.  
Ames Laboratory, ERDA  
Iowa State University  
Ames, Iowa 50010

Wachter, John W.  
Oak Ridge National Laboratory  
Bldg. 4500N/228  
P. O. Box X  
Oak Ridge, Tennessee 37830

Wasson, Oren A.  
Center for Radiation Research  
National Bureau of Standards  
Washington, D. C. 20234

Wehring, Bernard W.  
Nuclear Engineering Lab.  
University of Illinois  
Urbana, Illinois 61801

Weisbin, Charles R.  
Oak Ridge National Laboratory  
P. O. Box X  
Oak Ridge, Tennessee 37830

Werntz, Carl W.  
Physics Department  
Catholic University  
Washington, D. C. 20064

Westfall, Robert M.  
Oak Ridge National Laboratory  
Bldg. 6025 X-10  
Oak Ridge, Tennessee 37830

Weston, Lawrence W.  
Oak Ridge National Laboratory  
P. O. Box X, Bldg. 6010  
Oak Ridge, Tennessee 37830

White, Roger M.  
Physics Department  
Ohio University  
Athens, Ohio 45701

Wiedling, Tor  
AB Atomenergi, Studsvik, Fack  
S-611 01 Nyköping  
Sweden

Wigner, Eugene P.  
Princeton University  
Jadwin Hall, P. O. Box 708  
Princeton, New Jersey 08540

Wilhelmy, Jerry B.  
CNC-11, MS 514  
Los Alamos Scientific Laboratory  
Los Alamos, New Mexico 87544

Williams, Evan T.  
Chemistry Department  
Brooklyn College of CUNY  
Brooklyn, New York 11210

Wong, Calvin  
Lawrence Livermore Laboratory  
P. O. Box 808  
Livermore, California 94550

Wright, R. Q.  
Oak Ridge National Laboratory  
P. O. Box X  
Oak Ridge, Tennessee 37830

Yamamoto, Toru  
Department of Nuclear Engineering  
Tohoku University  
Sendai, Japan

Yamamuro, Nobuhiro  
Tokyo Institute of Technology  
Ohokayama, Meguro-ku  
Tokyo 152 Japan

Young, Phillip G.  
Los Alamos Scientific Laboratory  
Mail Stop 455  
P. O. Box 1663  
Los Alamos, New Mexico 87544

Young, Robert C.  
Aerojet Nuclear Company  
550 - 2nd Street (CSC)  
Idaho Falls, Idaho 83401

# AUTHOR INDEX

- Abramson, D. -- p. 367  
 Abulaffio, Carla -- p. 701  
 Ackermann, A. -- p. 819  
 Adams, J. M. -- p. 631  
 Adams, R. J. -- p. 409  
 Ahluwalia, H. S. -- p. 512  
 Akseleson, R. -- p. 484  
 Albert, T. E. -- p. 459  
 Alberts, W. G. -- p. 273  
 Allen, B. J. -- p. 360  
 Alsmiller, R. G., Jr. -- p. 533  
 Anderl, R. A. -- pp. 401, 908  
 Anders, B. -- p. 819  
 Anderson, J. D. -- p. 704  
 Ando, M. -- p. 184  
 Armini, A. J. -- p. 509  
 Arnaud, A. -- pp. 953, 961  
 Arthur, E. D. -- pp. 476, 770, 923  
 Asami, A. -- p. 738  
 Auchampaugh, G. F. -- p. 560  
 Avery, R. -- p. 45
- Bandl, R. -E. -- p. 549  
 Banks, N. E. -- p. 436  
 Barnard, E. -- p. 879  
 Barnes, B. K. -- p. 950  
 Barre, J. Y. -- p. 51  
 Bartle, C. M. -- p. 688  
 Bauer, G. -- p. 823  
 Bauer, R. W. -- p. 591  
 Bean, E. -- p. 93  
 Beer, H. -- p. 816  
 Behrens, J. W. -- p. 591  
 Behrin, E. -- p. 469  
 Bemis, C. E. -- p. 81  
 Benjamin, R. W. -- p. 224  
 Bentley, R. F. -- p. 476  
 Bergqvist, I. -- p. 923  
 Bernard, D. L. -- pp. 496, 938  
 Berreth, J. R. -- p. 908  
 Beverly, W. B. -- p. 436  
 Bewley, D. K. -- p. 527  
 Bigler, R. E. -- p. 520  
 Bilpuch, E. G. -- pp. 99, 866  
 Blachot, J. -- p. 29  
 Blewer, R. S. -- p. 488  
 Block, R. C. -- pp. 93, 802  
 Blons, J. -- p. 642  
 Bluet, J. C. -- p. 367  
 Bohn, E. M. -- p. 834  
 Boldeman, J. W. -- p. 360  
 Bond, A. H. -- p. 792  
 Bond, J. E. -- p. 875  
 Bonner, B. E. -- p. 103  
 Bonsignore, P. -- p. 607  
 Bormann, M. -- p. 819  
 Bortfeldt, J. -- p. 273  
 Bouchard, J. -- p. 51  
 Bowman, C. E. -- p. 119  
 Boyce, J. R. -- pp. 99, 697, 866  
 Brady, F. P. -- p. 103  
 Britt, H. C. -- p. 218  
 Broeders, C. H. M. -- p. 350  
 Broeders, I. -- p. 350  
 Brotz, P. -- p. 277  
 Bryan, D. E. -- p. 161  
 Buccino, S. G. -- p. 866  
 Bucher, W. -- p. 946  
 Bunker, S. N. -- p. 509  
 Butler, J. P. -- p. 859
- Cacuci, D. -- p. 335  
 Carlson, A. D. -- p. 232  
 Carlson, A. D. -- pp. 75, 293  
 Carlson, G. W. -- p. 591  
 Carre, C. -- p. 516  
 Casella, V. R. -- p. 492  
 Cerbone, R. -- p. 444  
 Chapman, G. T. -- p. 758  
 Chatterjee, A. -- p. 886  
 Chaudat, J. P. -- p. 51  
 Ching, J. -- p. 825  
 Cho, B. Y. -- p. 500  
 Chrien, R. E. -- pp. 139, 912, 920, 926  
 Christenson, J. M. -- p. 385  
 Chuang, L. S. -- p. 426  
 Cierjacks, S. -- pp. 277, 754, 916  
 Clark, R. G. -- p. 504  
 Clement, J. C. -- pp. 99, 866  
 Coates, M. S. -- p. 568  
 Cocu, F. -- pp. 889, 897, 942  
 Cookson, J. A. -- p. 66  
 Cops, F. -- p. 258  
 Corvi, F. -- pp. 599, 733  
 Costello, D. G. -- p. 766  
 Couchat, Ph. -- p. 516  
 Couchell, G. P. -- p. 950  
 Cramer, D. S. -- p. 93  
 Cullen, D. E. -- pp. 392, 419  
 Czirr, J. B. -- pp. 546, 615
- Dabbs, J. W. T. -- pp. 81, 222, 576  
 Dabby, D. -- p. 415  
 Davis, M. C. -- p. 112  
 Dekker, J. W. M. -- p. 165  
 De Leeuw, G. -- p. 258  
 De Leeuw, S. -- pp. 240, 258  
 De Leeuw-Giert, G. -- p. 240  
 Derrien, H. -- p. 637  
 Deruytter, A. J. -- p. 603  
 De Saussure, G. -- pp. 371, 623  
 De Tourreil, R. -- p. 29  
 Devillers, C. -- p. 29  
 Dickens, J. K. -- pp. 758, 762  
 Doi, T. -- p. 802  
 Dorning, J. J. -- pp. 62, 169  
 Dragt, J. B. -- p. 165  
 Drake, D. M. -- pp. 476, 770, 813, 923  
 Drischler, J. -- p. 825  
 Drosch, Manfred -- p. 813  
 Dudziak, D. J. -- pp. 674, 722  
 Dyer, C. S. -- p. 480
- Eapen, P. K. -- p. 712  
 Egan, J. J. -- p. 950  
 Eiland, H. M. -- p. 776  
 Eisenhauer, C. -- pp. 250, 254, 258, 266, 270  
 Elgart, M. F. -- p. 792  
 Elwyn, A. J. -- p. 692  
 Engdahl, J. C. -- p. 112  
 England, T. R. -- p. 193  
 Epperson, D. E. -- pp. 99, 866  
 Erbe, D. -- p. 916  
 Erdal, B. R. -- p. 492  
 Etemad, M. A. -- p. 871  
 Ewbank, W. B. -- p. 309
- Fabry, A. -- pp. 254, 258
- Fardeau, P. -- p. 367  
 Farrar, H., IV -- p. 375  
 Fehsenfeld, P. -- p. 258  
 Felvinci, J. P. -- pp. 335, 580, 742  
 Fiche, C. -- p. 29  
 Finston, H. L. -- p. 792  
 Firk, F. W. K. -- p. 875  
 Fluharty, R. G. -- p. 476  
 Fort, E. -- p. 957  
 Fowler, J. L. -- pp. 66, 965  
 Frank, R. -- p. 469  
 Frehaut, J. -- p. 855  
 Fricke, M. P. -- p. 232  
 Friesenhahn, S. J. -- pp. 161, 232, 766  
 Fritts, M. J. -- p. 69  
 Froehner, F. H. -- p. 929  
 Fu, C. Y. -- p. 328  
 Fujita, Y. -- p. 802  
 Fuketa, T. -- p. 738
- Gabbard, F. -- p. 108  
 Gardner, Donald G. -- p. 651  
 Garg, J. B. -- pp. 748, 799  
 Gavron, A. -- p. 218  
 Gay, R. -- p. 587  
 Gayther, D. B. -- pp. 564, 568  
 Gerstl, S. A. W. -- p. 674  
 Ghose, A. M. -- p. 886  
 Giacobbe, P. -- p. 599  
 Gilliam, D. M. -- pp. 259, 266, 270, 635  
 Glasgow, D. W. -- pp. 99, 866  
 Glendinning, S. G. -- p. 866  
 Glickstein, S. S. -- p. 934  
 Gober, W. E. -- p. 161  
 Goel, B. -- p. 313  
 Goldsmith, M. -- pp. 553, 557  
 Goldstein, H. -- p. 440  
 Good, W. M. -- p. 748  
 Gorrell, T. C. -- p. 224  
 Gould, C. R. -- pp. 99, 697, 866  
 Grant, P. M. -- p. 492  
 Green, D. -- p. 97  
 Greene, N. M. -- p. 848  
 Greenwood, R. C. -- pp. 324, 912  
 Groschel, D. -- p. 277  
 Grundl, J. A. -- pp. 250, 254, 258, 266, 270  
 Gruppelaar, H. -- p. 165  
 Guenther, P. -- p. 862  
 Gunther, E. -- p. 273  
 Gwin, R. -- p. 627
- Hacken, G. -- pp. 780, 799  
 Hagiwara, M. -- p. 611  
 Haight, R. C. -- p. 704  
 Hale, G. M. -- p. 302  
 Hansen, C. J. -- p. 69  
 Hansen, L. F. -- p. 704  
 Haouat, G. -- pp. 889, 893, 897, 942  
 Harihar, P. -- p. 950  
 Harker, Y. D. -- pp. 708, 908  
 Harris, L., Jr. -- p. 161  
 Harrison, J. F. -- p. 103  
 Harvey, J. A. -- pp. 244, 748  
 Harz, U. -- p. 744  
 Havens, W. W., Jr. -- pp. 1, 580, 742

- Hayase, T. -- p. 802  
 Hayashi, Shu A. -- p. 184  
 Heath, R. L. -- p. 708  
 Heaton, H. T., II -- pp. 97, 266, 270  
 Heer, W. -- p. 464  
 Hehn, G. -- p. 177  
 Helmer, R. G. -- pp. 14, 324  
 Hennelly, E. J. -- p. 214  
 Henryson, H., II -- p. 451  
 Hickey, G. T. -- p. 875  
 Hill, N. W. -- pp. 81, 244, 576  
 Ho, J. Le -- p. 516  
 Hockenbury, R. W. -- pp. 93, 584, 905  
 Hogue, H. H. -- pp. 99, 866  
 Holland, R. E. -- p. 622  
 Hollandsworth, C. E. -- p. 946  
 Holmqvist, B. -- p. 572  
 Holt, R. J. -- pp. 246, 784, 875  
 Holub, R. -- p. 469  
 Hoot, C. G. -- p. 766  
 Hussain, M. -- p. 66  
  
 Igarasi, S. -- p. 320  
 Iijima, S. -- p. 320  
 Ingle, R. W. -- p. 627  
 Iwasaki, S. -- p. 611  
  
 Jackson, H. E. -- p. 784  
 Jahn, H. -- p. 350  
 Janssen, A. J. -- p. 165  
 Jeki, L. -- p. 572  
 Jenquin, U. P. -- p. 680  
 Jensen, Gary -- p. 813  
 Jermann, M. -- p. 464  
 Johansson, P. I. -- pp. 572, 631  
 Johnson, R. H. -- pp. 62, 169  
 Jones, D. T. L. -- pp. 879  
 Joyce, J. M. -- p. 697  
  
 Kanazawa, S. -- p. 184  
 Kappeler, F. -- pp. 549, 620, 816  
 Karim, Munawar -- p. 788  
 Kaushal, N. N. -- pp. 584, 905  
 Hawai, M. -- p. 320  
 Kee, C. W. -- p. 455  
 Kegel, G. H. R. -- p. 950  
 Kenny, M. J. -- p. 360  
 Keyworth, G. A. -- p. 576  
 Kikuchi, Y. -- p. 320  
 Kimura, I. -- p. 184  
 King, N. S. P. -- p. 103  
 Kinney, W. E. -- p. 883  
 Kirouac, G. J. -- pp. 338, 776  
 Knauf, K. -- p. 273  
 Knoll, G. F. -- pp. 236, 635  
 Knox, H. -- p. 905  
 Kobayashi, K. -- pp. 184, 802  
 Komoto, T. -- p. 704  
 Konechny, E. -- p. 218  
 Kouts, H. J. C. -- p. 3  
 Ku, L. P. -- p. 440  
 Kusters, H. -- p. 313  
  
 LaBauve, R. J. -- p. 834  
 Lachkar, J. -- pp. 889, 893, 897, 942  
 Lagrange, Ch. -- p. 942  
  
 Lamaze, G. P. -- pp. 73, 75, 106  
 Lanzano, G. -- p. 607  
 Larson, D. -- p. 317  
 Laughlin, J. S. -- p. 520  
 Laumer, H. -- p. 108  
 Lemmel, H. D. -- p. 286  
 Leonard, B. R., Jr. -- pp. 281, 680  
 Le Rigoleur, C. -- pp. 953, 957, 961  
 LeSage, L. G. -- p. 385  
 Lessor, D. L. -- p. 680  
 Leugers, B. -- p. 277  
 Liou, H. I. -- pp. 780, 799  
 Lippincott, E. P. -- p. 375  
 Liskien, H. -- p. 156  
 Lisowski, P. W. -- p. 866  
 Loewenhaupt, M. -- p. 823  
 Lokan, K. H. -- p. 409  
 Longo, G. -- p. 346  
 Lopez, W. M. -- p. 232  
 Love, T. A. -- p. 758  
 Lucas, B. -- p. 637  
 Lucas, C. W., Jr. -- p. 472  
 Lurie, N. A. -- p. 161  
 Lutz, D. C. -- p. 398  
 Lynch, F. J. -- p. 692  
  
 Mack, G. -- pp. 99, 866  
 Macklin, R. L. -- p. 360  
 Maack, W. J. -- p. 378  
 Maerker, R. E. -- p. 834  
 Magurno, B. A. -- pp. 357, 774, 834  
 Maki, K. -- p. 320  
 Malan, J. G. -- p. 879  
 Mann, F. M. -- p. 354  
 Marcella, T. V. -- p. 950  
 Marcesse, J. -- p. 516  
 Marquette, J. P. -- p. 961  
 Maskewitz, B. F. -- p. 363  
 Matsunobu, H. -- p. 320  
 Mattes, M. -- p. 177  
 Matthes, W. -- p. 177  
 Matzke, M. -- p. 273  
 Mazur, C. -- p. 642  
 McCombie, C. -- p. 464  
 McCrosson, F. J. -- pp. 224, 834  
 McDaniels, D. K. -- p. 923  
 McDonald, J. -- p. 810  
 McEllistrem, M. T. -- pp. 893, 897, 942  
 McElroy, W. N. -- pp. 189, 375  
 McGarry, E. D. -- pp. 89, 116, 240  
 McJilton, C. E. -- p. 469  
 McKnight, R. D. -- p. 385  
 McNally, J. Rand, Jr. -- p. 683  
 McNaughton, M. W. -- p. 103  
 Meier, M. M. -- pp. 73, 75  
 Melkonian, E. -- pp. 335, 580, 742  
 Methews, G. J. -- p. 504  
 Mewissen, L. -- p. 729  
 Meyer, P. -- p. 469  
 Michaudon, A. -- p. 202  
 Migneco, E. -- pp. 597, 607  
 Miley, G. H. -- p. 716  
 Mittler, A. -- p. 950  
 Mizumoto, M. -- p. 664  
 Monahan, J. E. -- p. 692  
 Moore, M. S. -- p. 129  
  
 Mooring, F. P. -- p. 692  
 Morgan, G. L. -- pp. 758, 762  
 Morrison, G. W. -- p. 455  
 Moses, J. D. -- p. 576  
 Mosinski, G. -- p. 855  
 Muir, D. W. -- p. 674  
 Mughabghab, S. F. -- pp. 357, 774, 795  
 Musgrove, A. R. -- p. 360  
  
 Nagel, M. -- p. 444  
 Nakagawa, M. -- p. 184  
 Nakagawa, T. -- p. 320  
 Nakajima, Y. -- p. 738  
 Nath, R. -- p. 875  
 Nath, S. -- p. 886  
 Nelson, J. W. -- p. 484  
 Nestor, C. W., Jr. -- p. 222  
 Newman, D. F. -- p. 680  
 Newman, E. -- p. 758  
 Newson, H. W. -- pp. 99, 866  
 Newstead, C. M. -- p. 806  
 Nicks, R. -- p. 560  
 Niiler, A. -- p. 436  
 Nimai, B. -- p. 29  
 Nishihara, H. -- p. 184  
 Nisle, R. G. -- p. 908  
 Nissimov, H. -- p. 389  
 Noel, J. P. -- p. 29  
  
 Oblow, E. M. -- p. 825  
 O'Brien, H. A., Jr. -- p. 492  
 Olsen, C. E. -- p. 576  
 Orphan, V. J. -- pp. 232, 766  
 Ottewitte, E. H. -- p. 464  
 Overley, J. C. -- p. 788  
 Ozer, Odelli -- p. 419  
  
 Paik, N. C. -- p. 39  
 Pandey, M. S. -- p. 748  
 Patin, Y. -- pp. 889, 893, 897, 942  
 Pattenden, N. J. -- p. 568  
 Paya, D. -- p. 642  
 Pe, Hla -- p. 360  
 Pearlstein, S. -- p. 332  
 Peelle, R. W. -- p. 173  
 Pennington, E. M. -- p. 708  
 Peres, Asher -- p. 701  
 Perey, F. G. -- pp. 762, 842, 883  
 Perez, R. B. -- pp. 371, 623  
 Persiani, P. J. -- p. 708  
 Peterson, R. J. -- p. 69  
 Pinter, M. -- p. 258  
 Poenitz, W. P. -- p. 901  
 Poortmans, F. -- p. 729  
 Prael, R. E. -- pp. 447, 451  
 Priesmeyer, H. G. -- p. 744  
 Prince, A. -- p. 950  
 Pullen, D. J. -- p. 950  
 Purser, F. O. -- pp. 99, 866  
  
 Qaim, S. J. -- p. 664  
 Quaadvliet, W. H. J. -- p. 258  
  
 Rainwater, J. -- pp. 780, 799  
 Raman, S. -- pp. 81, 222  
 Rassl, G. -- p. 273  
 Reeder, P. L. -- p. 401  
 Reedy, Robert C. -- p. 540  
 Reich, Charles W. -- p. 14



- Reitmann, D. -- p. 879  
Rhodes, J. R. -- p. 496  
Richmond, R. -- p. 464  
Rief, H. -- p. 177  
Rimawi, K. -- pp. 912, 920, 926  
Robertson, J. C. -- p. 112  
Robertson, J. D. -- p. 7  
Roche, C. T. -- p. 504  
Rogers, V. C. -- p. 766  
Rohr, G. -- pp. 729, 733  
Rose, B. -- p. 965  
Roughton, N. A. -- p. 69  
Roussin, R. W. -- p. 363  
Rundberg, R. -- p. 792  
Russell, G. J. -- p. 476
- Saccenti, J. C. -- p. 431  
Salaita, G. N. -- p. 712  
Sanislo, A. J. -- p. 584  
Sano, K. -- p. 611  
Santry, D. C. -- p. 859  
Saporetti, F. -- p. 346  
Sato, S. -- p. 611  
Schanzler, L. -- p. 161  
Schenter, R. E. -- pp. 21, 834  
Schier, W. A. -- p. 950  
Schmalz, G. -- pp. 754, 916  
Schmatz, W. -- p. 823  
Schmidt, J. J. -- p. 967  
Schmittroth, F. -- p. 21  
Scholtyssek, W. -- p. 258  
Schouky, I. -- p. 277  
Schrack, R. A. -- pp. 97, 106  
Schroder, I. G. -- pp. 89, 116, 240  
Schultz, H. L. -- p. 875  
Schwartz, R. B. -- pp. 66, 89  
Scobel, W. -- p. 819  
Seeger, P. A. -- p. 476  
Sekharan, K. K. -- p. 108  
Seltzer, S. M. -- p. 480  
Seth, S. -- p. 464  
Shamu, R. E. -- p. 942  
Sheahen, T. P. -- p. 500  
Sheldon, E. -- p. 950  
Sher, R. -- p. 587  
Sidhu, G. S. -- pp. 546, 615  
Siegel, V. -- p. 273  
Sigaud, J. -- pp. 889, 893, 897, 942  
Silbert, M. G. -- p. 770  
Simmons, G. L. -- p. 459  
Singh, U. N. -- pp. 780, 799  
Sjostrand, N. G. -- p. 810  
Slovacek, R. E. -- p. 93  
Smith, A. B. -- pp. 246, 862  
Smith, J. R. -- p. 262  
Sommer, W. F. -- p. 476  
Soran, P. D. -- p. 722  
Spencer, R. R. -- pp. 620, 754, 816  
Spiegel, V., Jr. -- p. 266  
Stamatelatos, M. G. -- p. 193  
Steiner, D. -- p. 646  
Steinman, D. -- p. 161  
Stelzer, K. -- pp. 99, 866  
Stephany, W. P. -- p. 236  
Stewart, K. B. -- p. 680  
Sugiyama, K. -- pp. 342, 611  
Sugiyama, S. -- p. 83
- Sullivan, N. B. -- p. 950  
Switkowski, Z. E. -- p. 354
- Takekoshi, H. -- p. 738  
Tang, L. H. -- p. 422  
Taste, J. -- p. 953  
Taylor, M. C. -- pp. 496, 938  
Taylor, T. B. -- p. 199  
Tessler, G. -- p. 934  
Theobald, J. -- p. 729  
Tilbury, R. S. -- p. 520  
Todd, J. H. -- pp. 229, 623  
Tombrello, T. A. -- p. 659  
Tomimasu, T. -- p. 83  
Topke, R. -- p. 754  
Towner, H. H. -- p. 716  
Trombka, J. I. -- p. 480  
Trubey, D. K. -- p. 363  
Tulenko, J. S. -- p. 7  
Turk, E. H. -- p. 908
- Ullo, J. J. -- pp. 553, 557  
Uotinen, V. O. -- p. 7  
Uttley, C. A. -- p. 66
- Van der Kamp, H. A. J. -- p. 258  
Vandervelde, V. D. -- p. 224  
Vanpraet, G. -- p. 729  
Varghese, Philip -- p. 923  
Veaser, L. R. -- pp. 476, 813  
Verbinski, V. V. -- p. 766  
Viola, V. E., Jr. -- p. 504  
Voss, F. -- pp. 754, 916
- Wagemans, C. -- p. 603  
Wagschal, J. J. -- pp. 389, 405  
Walz, K. F. -- p. 273  
Wartena, J. A. -- pp. 597, 607  
Wasson, O. A. -- pp. 73, 78, 106  
Weaver, H. -- p. 627  
Weber, J. -- p. 218  
Wehring, B. W. -- pp. 62, 169  
Weigmann, H. -- pp. 597, 607, 729, 733  
Weisbin, C. R. -- pp. 392, 419, 455, 825  
Weller, F. -- p. 313  
Werntz, C. -- p. 472  
Weston, L. W. -- pp. 229, 560, 627  
Whalen, J. F. -- p. 246  
White, J. E. -- pp. 392, 825  
Whittaker, J. K. -- p. 106  
Wiedling, T. -- p. 572  
Wigner, E. P. -- p. 964  
Wilhelmy, J. B. -- p. 218  
Williams, E. T. -- p. 792  
Winchester, J. W. -- p. 484  
Wong, C. -- p. 704  
Wong, K. C. -- p. 426  
Wood, W. M. -- p. 748  
Woolson, W. A. -- p. 431  
Wright, J. F. -- p. 401  
Wright, R. Q. -- pp. 392, 825  
Wydler, P. -- p. 464
- Ya'ari, A. -- p. 405  
Yamamoto, S. -- p. 184  
Yamamoto, T. -- p. 342  
Yamamuro, N. -- p. 802  
Yana, K. -- p. 611
- Yeivin, Y. -- p. 405  
Young, J. C. -- p. 161  
Young, P. G. -- pp. 149, 770  
Youngblood, J. -- p. 946
- Zaidins, C. S. -- p. 69  
Zeitz, L. -- p. 520

ELEMENT S A	QUANTITY	TYPE	ENERGY		DOCUMENTATION			LAB	COMMENTS
			MIN	MAX	REF	VOL	PAGE DATE		
H 001	DIFF ELASTIC	REVM-CONF	14+7		75WASH		293 375	NBS CARLSON, GRPH CALC CFD EXP	
H PLE	SCATTERING	EXPT-CONF	10+6	15+7	75WASH		169 375	UI JOHNSON+GRPH, LEAKAGE N/252CF SOURC N	
D 002	ELASTIC SCAT	THEO-CONF		14+7	75WASH		700 375	HFA ABULAFFIO+ FORMULAS FOR PLASMA CALC	
T 003	ELASTIC SCAT	THEO-CONF		14+7	75WASH		700 375	HFA ABULAFFIO+ FORMULAS FOR PLASMA CALC	
HE 003	N, PROTON	REVM-CONF	10+2	10+7	75WASH		293 375	NBS CARLSON, GRPHS EVAL CFD EXP	
LI	INELST GAMMA	EXPT-CONF	70+5	20+7	75WASH		757 375	ORL CHAPMAN+TUF, G-RAY PROD CS	
LI 006	TOTAL XSECT	EXPT-CONF	10+1	10+7	75WASH		244 375	ORL HARVEY+TBL, GRPH, 11, 0+0, 1B(E=246KEV)	
LI 006	TOTAL XSECT	THEO-CONF	10+4	10+6	75WASH		302 375	LAS HALE, R-MATR CALC, GRPH	
LI 006	N, TRITON	REVM-CONF	50+5	20+6	75WASH		156 375	GEL LISKIEN, GRPH DISCREPANCY RECENT MEAS	
LI 006	N, TRITON	EXPT-CONF	10+3	15+6	75WASH		232 375	IRT FRIESENHANN+GRPH CFD ENDF, OTHER EXP	
LI 006	N, TRITON	EXPT-CONF	96+5		75WASH		236 375	MHG STEPHANY+CS=356MB+-12PCT, NA=BE SOURC	
LI 006	N, TRITON	EXPT-CONF	25+4		75WASH		240 375	NBS SCHRODER+ANG ANISOTROPY =1.80+-0.06	
LI 006	N, TRITON	REVM-CONF	10+2	20+6	75WASH		293 375	NBS CARLSON, GRPHS EXP CFD ENDF-3 EVAL,	
LI 006	N, TRITON	THEO-CONF	10+4	10+6	75WASH		302 375	LAS HALE, R-MATR ANAL GRPH TOT + ANG DIST	
LI 006	N, TRITON	REVM-CONF	14+7		75WASH		663 375	JUL GAIM, REVIEW EXPTS CFD CALC	
LI 006	N, TRITON	EXPT-CONF	22+6	97+6	75WASH		687 375	WIS BARTLE, TBL, GRPHS CS, ANG DIST TRITON	
LI 006	N, TRITON	EXPT-CONF	15+5	15+6	75WASH		787 375	ORE KARIM+ GRPHS MEAS YIELD ASYMMETRIES	
BE 009	SCATTERING	EXPT-CONF	10+6	15+7	75WASH		169 375	UI JOHNSON+GRPH, LEAKAGE N/252CF SOURC N	
BE 009	SCATTERING	EXPT-CONF	-3		75WASH		822 375	JUL SCHMATZ+INCON SC LT 4+-1 MB, REL VA	
R 010	DIFF ELASTIC	THEO-CONF	38+5	85+5	75WASH		302 375	LAS HALE, R-MATR ANAL GRPH 2 ES CFD EXP	
R 010	POLARIZATION	THEO-CONF	38+5	85+5	75WASH		302 375	LAS HALE, R-MATR ANAL GRPH 2 ES CFD EXP	
B 010	N, ALPHA REAC	EXPT-CONF	10+3	15+6	75WASH		232 375	IRT FRIESENHANN+GRPH CFD ENDF, OTHER EXP	
R 010	N, ALPHA REAC	REVM-CONF	10+3	10+6	75WASH		293 375	NBS CARLSON, GRPHS EXP CFD ENDF=3 EVAL,	
B 010	N, ALPHA REAC	THEO-CONF	10+3	10+6	75WASH		302 375	LAS HALE, R-MATR ANAL GRPH TOT + ANG DIST	
C 012	TOTAL XSECT	EXPT-CONF	15+6	50+6	75WASH		246 375	ANL HOLT+R-MATR ANAL, EXP CFD OTHER EXP	
C 012	TOTAL XSECT	REVM-CONF	10+3	10+6	75WASH		293 375	NBS CARLSON, GRPH EVAL CFD EXP0	
C 012	DIFF ELASTIC	EXPT-CONF	82+6	15+7	75WASH		99 375	DKE GLASGOW+ GRPHS ANG DIST, ABS ACC 8PCT	
C 012	DIFF ELASTIC	EXPT-CONF	18+6	40+6	75WASH		246 375	ANL HOLT+ GRPHS 20-160DEGS, R-MATR ANAL	
C 012	DIFF ELASTIC	EXPT-CONF	90+6	15+7	75WASH		865 375	DKE PURSER+ TOF, GRPHS 14ES + 20 ANGLES	
C 012	DIFF ELASTIC	EXPT-CONF	20+6	50+6	75WASH		874 375	YAL FIRK+ FAST NEUT POL BY GRAPHITE	
C 012	DIFF ELASTIC	EXPT-CONF	80+6	15+7	75WASH		888 375	BRC HAQUAT+ GRPHS, CFD ENDF4, OTHER EXPTS	
C 012	POLARIZATION	EXPT-CONF	20+6	50+6	75WASH		874 375	YAL FIRK+ FAST NEUT POL BY GRAPHITE	
C 012	DIFF INELAST	EXPT-CONF	82+6	15+7	75WASH		99 375	DKE GLASGOW+ GRPHS ALL LVLS AT GIVEN ANG	
C 012	DIFF INELAST	EXPT-CONF	90+6	15+7	75WASH		865 375	DKE PURSER+ TOF, GRPHS 14ES + 20 ANGLES	
C 012	DIFF INELAST	EXPT-CONF	80+6	15+7	75WASH		888 375	BRC HAQUAT+ GRPHS, CFD ENDF4, OTHER EXPTS	

ELEMENT S A	QUANTITY	TYPE	ENERGY		DOCUMENTATION			LAB	COMMENTS
			MIN	MAX	REF	VOL	PAGE		
-----									
C 012	INELST GAMMA	EXPT-CONF	70+5	20+7	75WASH			757 375 ORL	CHAPMAN+TOF.
C 012	INELST GAMMA	EXPT-CONF	14+7		75WASH			769 375 LAS	ARTHUR+DOUBLE DIFF. CS.
C 012	N2N REACTION	EXPT-CONF	23+7	34+7	75WASH			818 375 HAM	ACKERMANN+ACT,GRPH CFD STAT THEORY
C 012	N, DEUTERON	EXPT-CONF	56+7		75WASH			103 375 DAV	BRADY+ GRPH COUNTS VS CHANNEL,1 ANG
N 014	DIFF ELASTIC	EXPT-CONF	50+6	93+6	75WASH			937 375 SWL	BERNARD+ TBL,GRPH,MEASD AT 3 ENS
N 014	DIFF INELAST	EXPT-CONF	50+6	93+6	75WASH			937 375 SWL	BERNARD+ TBL,GRPH,MEASD AT 3 ENS
N 014	SCATTERING	EXPT-CONF	20+6	20+7	75WASH			161 375 IRT	HARRIS+ GRPH SCAT NEUT 125 DEGS
N 014	INELST GAMMA	THEO-CONF	40+6	20+7	75WASH			149 375 LAS	YOUNG,GRPH PROD CS 4.9+1.6MEV GAMMAS
N 014	INELST GAMMA	EXPT-CONF	20+6	20+7	75WASH			161 375 IRT	HARRIS+ GRPH SCAT G AT 125 DEGS
N 014	INELST GAMMA	EXPT-CONF	70+5	20+7	75WASH			757 375 ORL	CHAPMAN+TOF.
N 014	INELST GAMMA	EXPT-CONF	TR	20+7	75WASH			765 375 IRT	ROGERS+GRPH.
N 014	N, TRITON	REVW-CONF	14+7		75WASH			663 375 JUL	QAIM, REVIEW EXPTS CFD CALC
N 014	N,ALPHA REAC	EXPT-CONF	FISS		75WASH			375 375 HEO	LIPPINCOTT+ TBL MEAS CFD ENDF4
O 016	DIFF ELASTIC	EXPT-CONF	50+6	93+6	75WASH			937 375 SWL	BERNARD+ TBL,GRPH,MEASD AT 3 ENS
O 016	DIFF INELAST	EXPT-CONF	50+6	93+6	75WASH			937 375 SWL	BERNARD+ TBL,GRPH,MEASD AT 3 ENS
O 016	INELST GAMMA	EXPT-CONF	70+5	20+7	75WASH			757 375 ORL	CHAPMAN+TOF.
F 019	INELST GAMMA	EXPT-CONF	70+5	20+7	75WASH			757 375 ORL	CHAPMAN+TOF.
F 019	INELST GAMMA	EXPT-CONF	10+5	20+7	75WASH			761 375 ORL	DICKENS+ORELA,GRPH.
F 019	NONEL GAMMAS	THEO-CONF	14+7	17+7	75WASH			328 375 ORL	FU, H-F CALC CFD EXP
NA 022	N. GAMMA	EXPT-CONF	25-2		75WASH			791 375 BLN	RUNDBERG+ HFBR,WESTCOTT PROCEDURE
NA 022	RES INT CAPT	EXPT-CONF	50-1		75WASH			791 375 BLN	RUNDBERG+ HFBR,WESTCOTT PROCEDURE
NA 023	N. GAMMA	EXPT-CONF	20+4	16+5	75WASH			952 375 CAD	LERIGOLEUK+ TBL, EO,GWN(WG/WT)
MG	INELST GAMMA	EXPT-CONF	70+5	20+7	75WASH			757 375 ORL	CHAPMAN+TOF.
MG	INELST GAMMA	EXPT-CONF	14+7		75WASH			769 375 LAS	ARTHUR+DOUBLE DIFF. CS.
AL 027	DIFF INELAST	EXPT-CONF	20+6	45+6	75WASH			870 375 IRT	ETEMAD,GRPD,125DEGS,CFD OPT MOL CALC
AL 027	SCATTERING	EXPT-CONF	-3		75WASH			822 375 JUL	SCHMATTZ+INCOH SC=10.5+-0.6MB,REL VA
AL 027	INELST GAMMA	THEO-CONF	12+7	14+7	75WASH			149 375 LAS	YOUNG,GRPH E SPECT AT 125 DEGS
AL 027	INELST GAMMA	EXPT-CONF	70+5	20+7	75WASH			757 375 ORL	CHAPMAN+TOF,GRPH.
AL 027	INELST GAMMA	EXPT-CONF	TR	20+7	75WASH			765 375 IRT	ROGERS+GRPH.
AL 027	INELST GAMMA	EXPT-CONF	14+7		75WASH			769 375 LAS	ARTHUR+DOUBLE DIFF. CS,GRPH.
AL 027	N2N REACTION	THEO-CONF	14+7	19+7	75WASH			650 375 LRL	GARDNER,CFD EXPT DATA,GRPH.
AL 027	N, PHOTON	EXPT-CONF	FISS		75WASH			189 375 HEO	MCELROY,235U THERM FISS SPECT AVG CS
AL 027	N,ALPHA REAC	EXPT-CONF	FISS		75WASH			189 375 HEO	MCELROY,235U THERM FISS SPECT AVG CS
AL 027	N,ALPHA REAC	EXPT-CONF	FISS		75WASH			273 375 PTB	ALBERTS+252CF SOURCE,SPECTRUM AVG.
AL 027	N,ALPHA REAC	EXPT-CONF	FISS		75WASH			375 375 HEO	LIPPINCOTT+ TBL MEAS CFD ENDF4



ELEMENT S A	QUANTITY	TYPE	ENERGY		DOCUMENTATION			LAB	COMMENTS
			MIN	MAX	REF	VOL	PAGE		
AL 027	N, ALPHA REAC	EXPT-CONF	15+7		75WASH	711	375	SMU SALAITA+SHORT-LIVED ISOMER PROD. TBL.	
AL 027	RESON PARAMS	EXPT-CONF	50+3	50+5	75WASH	360	375	ORL ALLEN+ AV RES PAR, WG, STF, D	
SI	INELST GAMMA	EXPT-CONF	70+5	20+7	75WASH	757	375	ORL CHAPMAN+TOP,	
SI	INELST GAMMA	EXPT-CONF TR		20+7	75WASH	765	375	IRT ROGERS+GRPH.	
SI	SCATTERING	EXPT-CONF	-3		75WASH	822	375	JUL SCHMATZ+INOCH SC LT 20+-3 MB REL VA	
SI	NONEL GAMMAS	THEO-CONF	95+6	10+7	75WASH	317	375	ORL LARSON, GRPH CALC CS VS EG CFD EXP	
SI	NEUT EMISSN	THEO-CONF	16+7		75WASH	317	375	ORL LARSON, GRPH SIN+(N,NP)+(N,NA)-ENDF4	
SI	N, PROTON	THEO-CONF	16+7		75WASH	317	375	ORL LARSON, GRPH (N,PG)+(N,NP) FOR ENDF4	
SI	N, ALPHA REAC	THEO-CONF	16+7		75WASH	317	375	ORL LARSON, GRPH (N,AG)+(N,NA) FOR ENDF4	
SI	RESON PARAMS	EXPT-CONF	10+4	50+5	75WASH	360	375	ORL ALLEN+ AV RES PAR, WG	
SI 028	N, GAMMA	EXPT-CONF	10+4	50+5	75WASH	360	375	ORL ALLEN+ TBL GP AV CS	
S	DIFF ELASTIC	EXPT-CONF	15+7		75WASH	885	375	BOS GHOSE+ GRPH, CS BY SURFACE OF REVOL.	
AR 036	TOTAL XSECT	EVAL-CONF	-1+4	10+4	75WASH	773	375	BNL MUGHABGHAB+RES PARAM FIT, GRAPH	
AR 036	N, GAMMA	THEO-CONF THR			75WASH	794	375	BNL MUGHABGHAB, VALENCE NEUT S-WAVE CAPT	
AR 036	RESON PARAMS	EVAL-CONF	-1+4		75WASH	773	375	BNL MUGHABGHAB+TBL, HNO=92.27EV, WG=1.26EV	
CA	INELST GAMMA	EXPT-CONF	70+5	20+7	75WASH	757	375	ORL CHAPMAN+TOP,	
CA 040	NONEL GAMMAS	THEO-CONF	17+7	20+7	75WASH	328	375	ORL FU, H-F CALC CFD EXP	
CA 040	N, ALPHA REAC	THEO-CONF	30+6	15+7	75WASH	650	375	LRL GARDNER, GRAPH CALC CFD LASL MEAS	
CA 040	RESON PARAMS	EXPT-CONF	25+3	20+5	75WASH	360	375	ORL ALLEN+ AV RES PAR, WG, STF, D	
SC 045	TOTAL XSECT	EVAL-CONF THR		+5	75WASH	357	375	BNL MAGURNO+ B-W FIT BOUND LEVEL.	
SC 045	RESON PARAMS	EVAL-CONF	-3+3	12+4	75WASH	357	375	BNL MAGURNO+SPINS, BOUND LEVEL PARAMETERS	
TI	DIFF INELAST	EXPT-CONF	20+6	45+6	75WASH	870	375	IRN ETEMAD, GRPO, 125DEGS, CFD OPT MDL CALC	
TI	N, ALPHA REAC	EXPT-CONF FISS			75WASH	375	375	HED LIPPINCOTT+ TBL MEAS CFD ENOF4	
TI 046	N, PROTON	EXPT-CONF FISS			75WASH	273	375	PTB ALBERTS+252CF SOURCE, SPECTRUM AVG.	
V 051	DIFF INELAST	EXPT-CONF	20+6	45+6	75WASH	870	375	IRN ETEMAD, GRPD, 125DEGS, CFD OPT MDL CALC	
V 051	N, ALPHA REAC	THEO-CONF	14+7		75WASH	332	375	BNL PEARLSTEIN, LSQ FIT OPT MOD CFD EXP	
V 051	N, ALPHA REAC	EXPT-CONF FISS			75WASH	375	375	HED LIPPINCOTT+ TBL MEAS CFD ENOF4	
CR	ELASTIC SCAT	REVW-CONF	40+6	86+6	75WASH	882	375	ORL KINNEY+ GRPH, ANGLE AVG	
CR	N, GAMMA	EVAL-CONF	23+1	14+6	75WASH	367	375	CAD ABRAMSON+ GRPHS, TBL REC GP AV CS	
CR	N, GAMMA	EXPT-CONF	15+4	65+4	75WASH	992	375	CAD LERIGOLEUR+ GRPH	
CR	INELST GAMMA	EXPT-CONF	14+7		75WASH	769	375	LAS ARTHUR+DOUBLE DIFF, CS	
CR	INELST GAMMA	EXPT-CONF	50+5	10+7	75WASH	915	375	KFK VOSS+GAMMA PROO CS, INELAST SCATT	
CR	N, ALPHA REAC	EXPT-CONF FISS			75WASH	375	375	HED LIPPINCOTT+ TBL MEAS CFD ENOF4	
CR 050	INELST GAMMA	EXPT-CONF	34+6	60+6	75WASH	933	375	BET TESSLER+ TBL, GAMMA PROO CS	
CR 052	ELASTIC SCAT	REVW-CONF	60+6	86+6	75WASH	882	375	ORL KINNEY+ GRPH, ANGLE AVG	

ELEMENT S A	QUANTITY	TYPE	ENERGY		DOCUMENTATION			LAB	COMMENTS
			MIN	MAX	REF	VOL	PAGE		
CR 052	DIFF INELAST	REVM=CONF	60+6	86+6	75WASH	882	375	DRL KINNEY+	GRPH, LEVEL EXCITATION
CR 052	INELST GAMMA	EXPT=CONF	34+6	60+6	75WASH	933	375	BET TESSLER+	TBL, GAMMA PROD CS
CR 052	RESON PARAMS	EXPT=CONF	25+3	20+5	75WASH	360	375	ORL ALLEN+	AV RES PAR, WG, STP, D
CR 053	INELST GAMMA	EXPT=CONF	34+6	60+6	75WASH	933	375	BET TESSLER+	TBL, GAMMA PROD CS
CR 053	RESON PARAMS	EVAL=CONF	36+3	54+4	75WASH	367	375	CAD ABRAMSDN+	E0, J, WN, WG CPO EXP+ENOF4
CR 054	INELST GAMMA	EXPT=CONF	34+6	60+6	75WASH	933	375	BET TESSLER+	TBL, GAMMA PROD CS
MN 055	DIFF INELAST	EXPT=CONF	20+6	45+6	75WASH	870	375	IRN ETEMAO,	GRPD, 125DEG9, CPO OPT MOL CALC
MN 055	N, GAMMA	EXPT=CONF	15+4	50+5	75WASH	952	375	CAD LERIGOLEUR+	GRPH CPO OTHER EXPTS
MN 055	SPECT N, GAMM	EXPT=CONF	THR	24+4	75WASH	911	375	ANG GREENWOOD+	GRPH, E=THR, 1KEV, 24KEV
FE	TOTAL XSECT	EXPT=CONF	50+5	30+7	75WASH	753	375	KFK CIERJACKS+	GRAPHS, DEEP MINIMA
FE	DIFF INELAST	EXPT=CONF	85+6	14+7	75WASH	812	375	LAS ORAKE+TDF,	MEAS AT 4 ENB, TBL, GRPH.
FE	DIFF INELAST	EXPT=CONF	20+6	45+6	75WASH	870	375	IRN ETEMAO,	GRPD, 125DEG9, CPO OPT MOL CALC
FE	SCATTERING	EXPT=CONF	10+6	15+7	75WASH	169	375	UI JOHNSON+	GRPH, LEAKAGE N/252CF SOURC N
FE	N, GAMMA	EXPT=CONF	15+4	17+5	75WASH	952	375	CAO LERIGOLEUR+	GRPH
FE	INELST GAMMA	EXPT=CONF	70+5	20+7	75WASH	757	375	ORL CHAPMAN+TDF,	
FE	INELST GAMMA	EXPT=CONF	TR	20+7	75WASH	765	375	IRT ROGERS+GRPH,	
FE	INELST GAMMA	EXPT=CONF	TR	20+7	75WASH	765	375	IRT ROGERS+GRPH,	
FE	INELST GAMMA	EXPT=CONF	14+7		75WASH	769	375	LAS ARTHUR+DOUBLE	DIFF, CS, GRPH.
FE	N, ALPHA REAC	EXPT=CONF	FISS		75WASH	375	375	WED LIPPINCOTT+	TBL MEAS CPO ENOF4
FE	RESON PARAMS	EXPT=CONF	50+5	80+5	75WASH	753	375	KFK CIERJACKS+R=	MAT FIT, TBL, EO, WN, L, J
FE 054	TOTAL XSECT	EXPT=CONF	48+3	50+5	75WASH	747	375	ALB PANDEY+TBL,	ED, GWN CPO OTHER EXPT
FE 054	N, GAMMA	THEO=CONF	THR		75WASH	794	375	BNL HUGHABGHAB,	VALENCE NEUT S-WAVE CAPT
FE 054	N, PHOTON	EXPT=CONF	FISS		75WASH	189	375	WED MCELROY, 235U	THERM FISS SPECT AVG CS
FE 054	N, PHOTON	EXPT=CONF	FISS		75WASH	273	375	PTB ALBERTS+252CF	SOURCE, SPECTRUM AVG.
FE 054	RESON PARAMS	EXPT=CONF	76+3	65+5	75WASH	747	375	ALB PANDEY+	E0, GWN, TBL, CPO OTHER EXPT
FE 054	STRNGTH FUNC	EXPT=CONF		65+5	75WASH	747	375	ALB PANDEY+	S1=(0.56+-0.16)E-04
FE 056	TOTAL XSECT	EXPT=CONF	12+4	50+5	75WASH	748	365	ALB PANDEY+	R MATRIX ANAL
FE 056	TOT INELASTI	THEO=CONF	15+7		75WASH	350	375	KFK JAHN+DIRECT+EVAP+PREEQUIL	CPO EXP
FE 056	DIFF INELAST	THEO=CONF	15+7		75WASH	350	375	KFK JAHN+PLANE WAVE	BORN APPROX CPO EXP
FE 056	N, GAMMA	EXPT=CONF	70+4	70+5	75WASH	815	375	KFK BEER+	GRPH, G-RAY TRANS.
FE 056	N, GAMMA	EXPT=CONF	60+3	15+5	75WASH	928	375	KFK FROEHNER,	GRPH, WG WIDTH CORRELATION
FE 056	INELST GAMMA	EVAL=CONF	90+5	20+7	75WASH	149	375	LAS YOUNG,	REVM MEAS, GRPHS
FE 056	N2N REACTION	EXPT=CONF	12+7	15+7	75WASH	854	375	BRO FREHAUT+	TBL, GRPH, REL 238U(N, F)
FE 056	NEUT EMISSN	THEO=CONF	15+7		75WASH	328	375	ORL FU,	H-F CALC CPO EXP
FE 056	N, PHOTON	EXPT=CONF	FISS		75WASH	189	375	WED MCELROY, 235U	THERM FISS SPECT AVG CS

ELEMENT S A	QUANTITY	TYPE	ENERGY		DOCUMENTATION REF VOL PAGE DATE	LAB	COMMENTS
			MIN	MAX			
FE 056	N, PHOTON	EXPT-CONF	FISS		75WASH	273 375	PTB ALBERTS+292CF SOURCE, SPECTRUM AVG.
FE 056	N, PHOTON	THEO-CONF	14+7		75WASH	332 375	BNL PEARLSTEIN, LSQ FIT OPT MOD CFO ENDF
FE 056	RESON PARAMS	EXPT-CONF	27+5	59+5	75WASH	815 375	KFK BEER+ TBL 4 RES, G-RAY TRANS.
FE 056	RESON PARAMS	EXPT-CONF	28+4	14+5	75WASH	928 375	KFK FROEHNER, EO, WN, WG, AREA + SHAPE ANAL
FE 056	RESON PARAMS	EXPT-CONF	-2+3	50+5	75WASH	747 375	ALB PANOEY+TBL, EO, GWN CFO OTHER EXPT
FE 056	STRNGTH FUNC	EXPT-CONF		50+5	75WASH	747 375	ALB PANOEY+ $80 = (2.6 + -0.86)E-04$
CO 059	TOTAL XSECT	EXPT-CONF	40+5	80+5	75WASH	900 375	ANL POENITZ, GRAPH
CO 059	OIFF INELAST	THEO-CONF	40+6	90+7	75WASH	354 375	CAL MANN+PARAMETRIZED STAT MODEL FIT
CO 059	N, GAMMA	EXPT-CONF	40+5	80+5	75WASH	900 375	ANL POENITZ, GRAPH
CO 059	N2N REACTION	EXPT-CONF	11+7	15+7	75WASH	854 375	BRC FREHAUT+ TBL, GRPH, REL 238U(N,P)
CO 059	N, PHOTON	THEO-CONF	40+6	18+7	75WASH	354 375	CAL MANN+PARAMETRIZED STAT MODEL FIT
CO 059	N, ALPHA REAC	THEO-CONF	50+6	18+7	75WASH	354 375	CAL MANN+ H-P STAT CALC CFO EXP
NI	TOTAL XSECT	EXPT-CONF	40+5	80+5	75WASH	900 375	ANL POENITZ, GRAPH
NI	OIFF ELASTIC	REVW-CONF	43+6	86+6	75WASH	882 375	ORL KINNEY+ GRPH, 5 ENERGIES
NI	OIFF INELAST	EXPT-CONF	20+6	45+6	75WASH	870 375	IRN ETENAD, GRPO, 1250EGS, CFO OPT MDL CALC
NI	N, GAMMA	EXPT-CONF	50+4	80+5	75WASH	900 375	ANL POENITZ, GRAPH
NI	N, GAMMA	EXPT-CONF	15+4	65+4	75WASH	952 375	CAD LERIGOLEUR+ GRPH
NI	INELST GAMMA	EXPT-CONF	70+5	20+7	75WASH	757 375	ORL CHAPMAN+TOP,
NI	INELST GAMMA	EXPT-CONF	14+7		75WASH	769 375	LAS ARTHUR+OUBLE OIFF, CS
NI	INELST GAMMA	EXPT-CONF	50+5	10+7	75WASH	915 375	KFK VOSS+GAMMA PROD CS, INELAST SCATT
NI	N2N REACTION	EXPT-CONF	79+6	15+7	75WASH	854 375	BRC FREHAUT+ TBL, GRPH, REL 238U(N,P)
NI	N, ALPHA REAC	EXPT-CONF	FISS		75WASH	375 375	WEO LIPPINCOTT+ TBL MEAS CFO ENOF4
NI 058	N, GAMMA	EXPT-CONF	60+3	15+5	75WASH	928 375	KFK FROEHNER, GRPH, WG WIDTH CORRELATION
NI 058	INELST GAMMA	EXPT-CONF	34+6	54+6	75WASH	933 375	BET TESSLER+ TBL, GAMMA PROD CS
NI 058	N, PHOTON	EXPT-CONF	FISS		75WASH	189 375	WED MCELROY, 235U THERM FISS SPECT AVG CS
NI 058	RESON PARAMS	EXPT-CONF	15+4	12+5	75WASH	928 375	KFK FROEHNER, EO, WN, WG, AREA + SHAPE ANAL
NI 059	TOTAL XSECT	EXPT-CONF	50+1	20+3	75WASH	775 375	KAP KIROUAC+ GRPH RAW DATA, 203 EV RES.
NI 059	ABSORPTION	EXPT-CONF	25-2		75WASH	775 375	KAP KIROUAC+ SIG = $92 + -4$ B, TBL
NI 059	RES INT ABS	EXPT-CONF	50+1		75WASH	775 375	KAP KIROUAC+ RES INT = $125 + -8$ B
NI 059	N, ALPHA REAC	EXPT-CONF	29-2	42-2	75WASH	809 375	OTH McDONALD+ TBL, GRPH, REL 6LI REACTION
NI 059	RESON PARAMS	EXPT-CONF	20+2		75WASH	775 375	KAP KIROUAC+ TBL, WT, WA, WN, G, EO=203, EV
NI 060	OIFF ELASTIC	REVW-CONF	43+6	86+6	75WASH	882 375	ORL KINNEY+ GRPH, 5 ENERGIES
NI 060	TOT INELAST	REVW-CONF	64+6	86+6	75WASH	882 375	ORL KINNEY+ GRPH, 5 ENERGIES, ANGLE AVG
NI 060	N, GAMMA	EXPT-CONF	60+3	15+5	75WASH	928 375	KFK FROEHNER, GRPH, WG WIDTH CORRELATION
NI 060	INELST GAMMA	EXPT-CONF	34+6	54+6	75WASH	933 375	BET TESSLER+ TBL, GAMMA PROD CS



ELEMENT S A	QUANTITY	TYPE	ENERGY		DOCUMENTATION			LAB	COMMENTS
			MIN	MAX	REF	VOL	PAGE		
NI 060	RESON PARAMS	EXPT-CONF	12+4	16+5	75WASH			928 375 KFK FROEHNER, EO, WN, WG, AREA + SHAPE ANAL	
NI 061	N, GAMMA	EXPT-CONF	60+3	30+4	75WASH			928 375 KFK FROEHNER, GRPH, WG WIDTH CORRELATION	
NI 061	RESON PARAMS	EXPT-CONF	42+3	29+4	75WASH			928 375 KFK FROEHNER, EO, WN, WG, AREA + SHAPE ANAL	
NI 062	INELST GAMMA	EXPT-CONF	34+6	54+6	75WASH			933 375 BET TESSLER+ IBL, GAMMA PROD CS	
CU	SCATTERING	EXPT-CONF	-3		75WASH			822 375 JUL SCHMATE+INCON SC=590+-40MB, REL VA	
CU	N, GAMMA	EXPT-CONF	40+5	80+5	75WASH			900 375 ANL POENITE, GRAPH	
CU	INELST GAMMA	EXPT-CONF	70+5	20+7	75WASH			757 375 ORL CHAPMAN+TOP,	
CU	INELST GAMMA	EXPT-CONF	14+7		75WASH			769 375 LAS ARTHUR+DOUBLE OIFF, CS, GRPH.	
CU	N, ALPHA REAC	EXPT-CONF	FISS		75WASH			375 375 HED LIPPINCOTT+ TBL MEAS CPO ENDF4	
CU 063	N, ALPHA REAC	EXPT-CONF	FISS		75WASH			375 375 HED LIPPINCOTT+ TBL MEAS CPO ENDF4	
ZN	N, GAMMA	EXPT-CONF	40+5	80+5	75WASH			900 375 ANL POENITE, GRAPH	
ZN	INELST GAMMA	EXPT-CONF	70+5	20+7	75WASH			757 375 ORL CHAPMAN+TOP,	
ZN 068	N, ALPHA REAC	THEO-CONF	14+7		75WASH			332 375 BNL PEARLSTEIN, LSQ FIT OPT MOD CPO EXP	
SE 076	DIFF ELASTIC	EXPT-CONF	60+6	10+7	75WASH			896 375 BRC LACHKAR+ IOF, GRAPHS	
SE 076	INELST GAMMA	EXPT-CONF	20+6	41+6	75WASH			892 375 BRC SIGAUD+ TBL, GAMMA TRANS, LEVEL SCHEME	
SE 076	N2N REACTION	EXPT-CONF	12+7	15+7	75WASH			854 375 BRC FREHAUT+ IBL, GRPH, REL 238U(N,F)	
SE 078	OIFF ELASTIC	EXPT-CONF	80+6		75WASH			896 375 BRC LACHKAR+ IOF, GRAPHS	
SE 078	N2N REACTION	EXPT-CONF	11+7	15+7	75WASH			854 375 BRC FREHAUT+ IBL, GRPH, REL 238U(N,F)	
SE 080	OIFF ELASTIC	EXPT-CONF	80+6		75WASH			896 375 BRC LACHKAR+ IOF, GRAPHS	
SE 080	N2N REACTION	EXPT-CONF	10+7	15+7	75WASH			854 375 BRC FREHAUT+ IBL, GRPH, REL 238U(N,F)	
SE 082	OIFF ELASTIC	EXPT-CONF	60+6	10+7	75WASH			896 375 BRC LACHKAR+ IOF, GRAPHS	
SE 082	INELST GAMMA	EXPT-CONF	25+6	41+6	75WASH			892 375 BRC SIGAUD+ TBL, GAMMA TRANS, LEVEL SCHEME	
SE 082	N2N REACTION	EXPT-CONF	10+7	15+7	75WASH			854 375 BRC FREHAUT+ IBL, GRPH, REL 238U(N,F)	
BR 079	N, ALPHA REAC	THEO-CONF	14+7		75WASH			332 375 BNL PEARLSTEIN, LSQ FIT OPT MOD CPO EXP	
BR 081	N, ALPHA REAC	THEO-CONF	14+7		75WASH			332 375 BNL PEARLSTEIN, LSQ FIT OPT MOD CPO EXP	
SR 090	N, GAMMA	EVAL-CONF	THR		75WASH			320 375 JAE IGARASI+ IBL REC VALUE	
SR 090	RES INT CAPT	EVAL-CONF	NDG		75WASH			320 375 JAE IGARASI+ OPT MOD CALC, TBL REC VALUE	
Y 089	N, GAMMA	THEO-CONF	50+6	15+7	75WASH			346 375 BOL LONGO+LVLS LT 4,5MEV IN Y90, CPO EXP	
Y 089	N2N REACTION	EXPT-CONF	15+7		75WASH			711 375 SMU SALAITA+SHORT-LIVED ISOMER PROD, TBL.	
Y 089	N2N REACTION	EXPT-CONF	12+7	15+7	75WASH			854 375 BRC FREHAUT+ IBL, GRPH, REL 238U(N,F)	
ER	N, ALPHA REAC	EXPT-CONF	FISS		75WASH			375 375 HED LIPPINCOTT+ TBL MEAS CPO ENDF4	
ER 090	RESON PARAMS	EXPT-CONF	25+3	15+5	75WASH			360 375 ORL ALLEN+ AV RES PAR, WG, STF, D	
ER 092	INELST GAMMA	EXPT-CONF	34+6	54+6	75WASH			933 375 BET TESSLER+ IBL, GAMMA PROD CS	
ER 093	N, GAMMA	EVAL-CONF	THR		75WASH			320 375 JAE IGARASI+ IBL REC VALUE	
ER 093	RES INT CAPT	EVAL-CONF	NDG		75WASH			320 375 JAE IGARASI+ CALC FROM RES PAR, FIT THR	

ELEMENT S A	QUANTITY	TYPE	ENERGY		DOCUMENTATION			LAB	COMMENTS
			MIN	MAX	REF	VOL	PAGE		
ER 094	INELST GAMMA	EXPT-CONF	34+6	54+6	75WASH			933 375	BET TESSLER+ TBL GAMMA PROD CS
NB 093	DIFF INELAST	EXPT-CONF	20+6	45+6	75WASH			870 375	IRN ETEMAD, GRPO, 1250EGS, CFD OPT MDL CALC
NB 093	SCATTERING	EXPT-CONF	10+6	15+7	75WASH			169 375	UI JOHNSON+GRPH, LEAKAGE N/252CF SOURC N
NB 093	SCATTERING	EXPT-CONF	-3		75WASH			822 375	JUL SCHMAPE+INCOH SC=6.3+-0.6MB, REL VA
NB 093	N, GAMMA	EXPT-CONF	24+4		75WASH			801 375	KYO YAMAMURO+N, FLUX=B10(N, AG), CS=0.33B
NB 093	SPECT N, GAMM	EXPT-CONF	24+4		75WASH			925 375	BNL RIMAWI+ PARTIAL CS CFO THEORY
NB 093	INELST GAMMA	EVAL-CONF	THR		75WASH			149 375	LAS YOUNG, MEAS CFO ENDF-4
NB 093	INELST GAMMA	EVAL-CONF	14+7		75WASH			149 375	LAS YOUNG, MEAS CFO ENDF AT 125 OEGS,
NB 093	INELST GAMMA	EXPT-CONF	70+5	20+7	75WASH			757 375	ORL CHAPMAN+TQF,
NB 093	INELST GAMMA	EXPT-CONF	14+7		75WASH			769 375	LAS ARTHUR+DOUBLE OIFF, CS,
NB 093	N2N REACTION	EXPT-CONF	94+6	15+7	75WASH			854 375	ORC FREHAUT+ TBL, GRPH, REL 238U(N, F)
NB 093	N, PHOTON	THEO-CONF	40+6	18+7	75WASH			650 375	LRL GARONER, PHOTON PROD, (N, P+NP+PN+2NP)
NB 093	N, ALPHA REAC	EXPT-CONF	FISS		75WASH			375 375	HEO LIPPINCOTT+ TBL MEAS CFO ENDF4
NB 093	N, ALPHA REAC	THEO-CONF	40+6	18+7	75WASH			650 375	LRL GARONER, GRAPH ALPHA PRDO, (N, A+AN+NA)
MO	INELST GAMMA	EVAL-CONF	14+7		75WASH			149 375	LAS YOUNG, MEAS CFO ENDF AT 90 + 125 OEGS
MO	INELST GAMMA	EXPT-CONF	14+7		75WASH			769 375	LAS ARTHUR+DOUBLE OIFF, CS,
MO	N, ALPHA REAC	EXPT-CONF	FISS		75WASH			375 375	HEO LIPPINCOTT+ TBL MEAS CFO ENDF4
MO 092	SPECT N, GAMM	EXPT-CONF	24+4		75WASH			925 375	BNL RIMAWI+ PARTIAL CS CFO THEORY
MO 094	SPECT N, GAMM	EXPT-CONF	24+4		75WASH			925 375	BNL RIMAWI+ PARTIAL CS CFO THEORY
MO 095	N, GAMMA	EVAL-CONF	THR		75WASH			320 375	JAE IGARASI+ TBL REC VALUE
MO 095	RES INT CAPT	EVAL-CONF	NOG		75WASH			320 375	JAE IGARASI+ TBL REC VALUE
MO 096	SPECT N, GAMM	EXPT-CONF	24+4		75WASH			925 375	BNL RIMAWI+ PARTIAL CS CFO THEORY
MO 097	N, GAMMA	EVAL-CONF	THR		75WASH			320 375	JAE IGARASI+ TBL REC VALUE
MO 097	RES INT CAPT	EVAL-CONF	NDG		75WASH			320 375	JAE IGARASI+ TBL REC VALUE
MO 098	SPECT N, GAMM	EXPT-CONF	24+4		75WASH			925 375	BNL RIMAWI+ PARTIAL CS CFO THEORY
TC 099	N, GAMMA	EVAL-CONF	10-2	10+7	75WASH			320 375	JAE IGARASI+ GRPH CALC CFO EXPT VALUES
TC 099	RES INT CAPT	EVAL-CONF	NOG		75WASH			320 375	JAE IGARASI+ TBL REC VALUE
RU 101	N, GAMMA	EVAL-CONF	10-3	10+7	75WASH			165 375	RCN GRUPPELAAR+RCN=2 DATA LIBRARY
RU 101	N, GAMMA	EVAL-CONF	THR		75WASH			320 375	JAE IGARASI+ TBL REC VALUE
RU 101	RES INT CAPT	EVAL-CONF	NOG		75WASH			320 375	JAE IGARASI+ TBL REC VALUE
RU 102	N, GAMMA	EVAL-CONF	10-3	10+7	75WASH			165 375	RCN GRUPPELAAR+RCN=2 DATA LIBRARY
RU 102	N, GAMMA	EVAL-CONF	THR		75WASH			320 375	JAE IGARASI+ TBL REC VALUE
RU 102	RES INT CAPT	EVAL-CONF	NDG		75WASH			320 375	JAE IGARASI+ TBL REC VALUE
RU 104	N, GAMMA	EVAL-CONF	10-3	10+7	75WASH			165 375	RCN GRUPPELAAR+RCN=2 DATA LIBRARY
RU 104	N, GAMMA	EVAL-CONF	THR		75WASH			320 375	JAE IGARASI+ TBL REC VALUE

ELEMENT S A	QUANTITY	TYPE	ENERGY		DOCUMENTATION			LAB	COMMENTS
			MIN	MAX	REF	VOL	PAGE		
RU 104	RES INT CAPT	EVAL-CONF	NDG		75WASH		320 375	JAE IGARASI+	TBL REC VALUE
RU 106	N, GAMMA	EVAL-CONF	THR		75WASH		320 375	JAE IGARASI+	TBL REC VALUE
RU 106	RES INT CAPT	EVAL-CONF	NDG		75WASH		320 375	JAE IGARASI+	TBL REC VALUE
RH 103	DIFF ELASTIC	EXPT-CONF	60+5	15+6	75WASH		878 375	PEL REITMANN+	GRAPHS, EXCITED LEVELS
RH 103	DIFF INELAST	EXPT-CONF	60+5	15+6	75WASH		878 375	PEL REITMANN+	GRAPHS, EXCITED LEVELS
RH 103	N, GAMMA	EVAL-CONF	THR		75WASH		320 375	JAE IGARASI+	TBL REC VALUE
RH 103	N, GAMMA	EXPT-CONF	20+1	20+5	75WASH		904 375	RPI HOCKENBURY+	GRPH CFD CALC
RH 103	N, GAMMA	EXPT-CONF	15+4	35+5	75WASH		952 375	CAD LERIGOLEUR+	GRPH, CFD ENDF4, RIBON EVAL
RH 103	RES INT CAPT	EVAL-CONF	NDG		75WASH		320 375	JAE IGARASI+	TBL REC VALUE
RH 103	N2N REACTION	EXPT-CONF	10+7	15+7	75WASH		854 375	BRC FREHAUT+	TBL, GRPH, REL 238U(N,F)
RH 103	RESON PARAMS	EXPT-CONF	NDG		75WASH		904 375	RPI HOCKENBURY+	AVG WG, D
RH 103	STRNGTH FUNC	EXPT-CONF	NDG		75WASH		904 375	RPI HOCKENBURY+	AVG S0, S1
PD 105	N, GAMMA	EVAL-CONF	THR		75WASH		320 375	JAE IGARASI+	TBL REC VALUE
PD 105	N, GAMMA	EXPT-CONF	20+1	20+5	75WASH		904 375	RPI HOCKENBURY+	GRPH CFD CALC
PD 105	RES INT CAPT	EVAL-CONF	NDG		75WASH		320 375	JAE IGARASI+	TBL REC VALUE
PD 105	RESON PARAMS	EXPT-CONF	NDG		75WASH		904 375	RPI HOCKENBURY+	AVG WG, D
PD 105	STRNGTH FUNC	EXPT-CONF	NDG		75WASH		904 375	RPI HOCKENBURY+	AVG S0, S1
PD 107	N, GAMMA	EVAL-CONF	THR		75WASH		320 375	JAE IGARASI+	TBL REC VALUE
PD 107	RES INT CAPT	EVAL-CONF	NDG		75WASH		320 375	JAE IGARASI+	TBL REC VALUE
AG	SCATTERING	EXPT-CONF	63		75WASH		822 375	JUL SCHMATE+	INCOH, CS REV VANADIUM
AG	N, GAMMA	EXPT-CONF	24+4		75WASH		801 375	KTO YAMAMURO+	N, FLUX=B10(N, AG), CS=1.108
AG	INELST GAMMA	EXPT-CONF	70+5	20+7	75WASH		757 375	ORL CHAPMAN+	TOF,
AG 109	N, GAMMA	EVAL-CONF	THR		75WASH		320 375	JAE IGARASI+	TBL REC VALUE
AG 109	RES INT CAPT	EVAL-CONF	NDG		75WASH		320 375	JAE IGARASI+	TBL REC VALUE
CD 110	RESON PARAMS	REVM-CONF	NDG		75WASH		779 375	COL HACKEN+	TBL AVG WG, STF, NUMBER GWN, WG
CD 110	STRNGTH FUNC	REVM-CONF	NDG		75WASH		779 375	COL HACKEN+	NEVIS TOF S-WAVE STF
CD 111	RESON PARAMS	REVM-CONF	NDG		75WASH		779 375	COL HACKEN+	TBL AVG WG, STF, NUMBER GWN, WG
CD 111	STRNGTH FUNC	REVM-CONF	NDG		75WASH		779 375	COL HACKEN+	NEVIS TOF S-WAVE STF
CD 112	RESON PARAMS	REVM-CONF	NDG		75WASH		779 375	COL HACKEN+	TBL AVG WG, STF, NUMBER GWN, WG
CD 112	STRNGTH FUNC	REVM-CONF	NDG		75WASH		779 375	COL HACKEN+	NEVIS TOF S-WAVE STF
CD 113	RESON PARAMS	REVM-CONF	NDG		75WASH		779 375	COL HACKEN+	TBL AVG WG, STF, NUMBER GWN, WG
CD 113	STRNGTH FUNC	REVM-CONF	NDG		75WASH		779 375	COL HACKEN+	NEVIS TOF S-WAVE STF
CD 114	RESON PARAMS	REVM-CONF	NDG		75WASH		779 375	COL HACKEN+	TBL AVG WG, STF, NUMBER GWN, WG
CD 114	STRNGTH FUNC	REVM-CONF	NDG		75WASH		779 375	COL HACKEN+	NEVIS TOF S-WAVE STF
CD 116	RESON PARAMS	REVM-CONF	NDG		75WASH		779 375	COL HACKEN+	TBL AVG WG, STF, NUMBER GWN, WG



ELEMENT S A	QUANTITY	TYPE	ENERGY		DOCUMENTATION			LAB	COMMENTS
			MIN	MAX	REF	VOL	PAGE		
CD 116	STRNGTH FUNC	REVM-CONF	NDG		75WASH		779 375	COL HACKEN+	NEVIS TDF S-WAVE STF
IN 113	RESON PARAMS	REVM-CONF	NDG		75WASH		779 375	COL HACKEN+	TBL AVG WG,STF,NUMBER GWN,WG
IN 113	TOT INELASTI	EXPT-CONF	FISS		75WASH		189 375	WED MCELROY,	FISS SPECT AV CS TO M-STATE
IN 115	TOT INELASTI	EXPT-CONF	FISS		75WASH		254 375	MOL FABRY+INTEG	CS REL U238NF=.620+-0.019
IN 115	TOT INELASTI	THEO-CONF	25+5	16+7	75WASH		650 375	LRL GARDNER,	TO MS STATE,CFD EXPT,GRPH.
IN 115	TOT INELASTI	EXPT-CONF	34+5	15+7	75WASH		858 375	CRC SANTRY+EXCITATION	CURVE PROD IN=115H
IN 115	N, GAMMA	EXPT-CONF	24+4		75WASH		919 375	BNL RIMAWI+	CS=469+-28MB,CFD OTHER EXPT
IN 115	N2N REACTION	EXPT-CONF	15+7		75WASH		711 375	SHU SALAITA+SHORT-LIVED	ISOMER PROD,TBL.
IN 115	RESON PARAMS	REVM-CONF	NDG		75WASH		779 375	COL HACKEN+	TBL AVG WG,STF,NUMBER GWN,WG
IN 115	STRNGTH FUNC	REVM-CONF	NOG		75WASH		779 375	COL HACKEN+	NEVIS TOF S-WAVE STF
SN	INELST GAMMA	EXPT-CONF	70+5	20+7	75WASH		757 375	ORL CHAPMAN+TOF,	
I 127	N, GAMMA	EVAL-CONF	10+3	10+7	75WASH		165 375	RCN GRUPPELAAR+RCN-2	DATA LIBRARY
I 127	N, GAMMA	EXPT-CONF	24+4		75WASH		801 375	KTO YAMAMURD+N,FLUX=810(N,AG),	CS=0.76B
I 127	N, GAMMA	EXPT-CONF	24+4		75WASH		919 375	BNL RIMAWI+	CS=722+-47MB,CFD OTHER EXPT
I 129	N, GAMMA	EVAL-CONF	THR		75WASH		320 375	JAE IGARASI+	TBL REC VALUE
I 129	RES INT CAPT	EVAL-CONF	NDG		75WASH		320 375	JAE IGARASI+	TBL REC VALUE
XE 131	N, GAMMA	EVAL-CONF	THR		75WASH		320 375	JAE IGARASI+	TBL REC VALUE
XE 131	RES INT CAPT	EVAL-CONF	NDG		75WASH		320 375	JAE IGARASI+	TBL REC VALUE
CS 133	N, GAMMA	EVAL-CONF	THR		75WASH		320 375	JAE IGARASI+	TBL REC VALUE
CS 133	RES INT CAPT	EVAL-CONF	NDG		75WASH		320 375	JAE IGARASI+	TBL REC VALUE
CS 133	N, GAMMA	EVAL-CONF	THR		75WASH		320 375	JAE IGARASI+	TBL REC VALUE
CS 135	RES INT CAPT	EVAL-CONF	NDG		75WASH		320 375	JAE IGARASI+	TBL REC VALUE
CS 137	N, GAMMA	EVAL-CONF	THR		75WASH		320 375	JAE IGARASI+	TBL REC VALUE
CS 137	RES INT CAPT	EVAL-CONF	NOG		75WASH		320 375	JAE IGARASI+	TBL REC VALUE
BA 138	RESON PARAMS	EXPT-CONF	25+3	90+4	75WASH		360 375	ORL ALLEN+	AV RES PAR,WG,STF,D
CE 140	N, GAMMA	THEO-CONF	50+6	15+7	75WASH		346 375	BOL LONGO+CE141	LVLS LT 3.5MEV,CFD EXP
CE 140	SPECT N,GAMM	THEO-CONF	99+6	11+7	75WASH		346 375	BOL LONGO+2	EN,G SPECT 9-19MEV CFD EXP
CE 144	N, GAMMA	EVAL-CONF	THR		75WASH		320 375	JAE IGARASI+	TBL REC VALUE
CE 144	RES INT CAPT	EVAL-CONF	NDG		75WASH		320 375	JAE IGARASI+	TBL REC VALUE
ND	SCATTERING	EXPT-CONF	-3		75WASH		822 375	JUL SCHMATZ+	INCOH,CS REV VANADIUM
ND 143	N, GAMMA	EVAL-CONF	THR		75WASH		320 375	JAE IGARASI+	TBL REC VALUE
ND 143	RES INT CAPT	EVAL-CONF	NDG		75WASH		320 375	JAE IGARASI+	TBL REC VALUE
ND 144	N, GAMMA	EVAL-CONF	THR		75WASH		320 375	JAE IGARASI+	TBL REC VALUE
ND 144	RES INT CAPT	EVAL-CONF	NDG		75WASH		320 375	JAE IGARASI+	TBL REC VALUE
ND 145	N, GAMMA	EVAL-CONF	THR		75WASH		320 375	JAE IGARASI+	TBL REC VALUE

7-MY-75

ELEMENT S A	QUANTITY	TYPE	ENERGY		DOCUMENTATION			LAB	COMMENTS
			MIN	MAX	REF	VOL	PAGE DATE		
ND 145	RES INT CAPT EVAL=CONF	NDG			75WASH	320	375	JAE IGARASI+ IBL REC VALUE	
ND 145	N, ALPHA REAC EXPT=CONF	44+0 17+3	75WASH			93	375	RPI BLOCK+ GRPH COUNTS VS CHANNEL	
ND 146	DIFF ELASTIC EXPT=CONF	70+6	75WASH			941	375	BRC MCELLISTREM+ DEFORM EFFECTS	
PM 147	N, GAMMA EVAL=CONF	THR	75WASH			320	375	JAE IGARASI+ IBL REC VALUE	
PM 147	RES INT CAPT EVAL=CONF	NDG	75WASH			320	375	JAE IGARASI+ IBL REC VALUE	
SM 147	N, GAMMA EVAL=CONF	THR	75WASH			320	375	JAE IGARASI+ IBL REC VALUE	
SM 147	RES INT CAPT EVAL=CONF	NDG	75WASH			320	375	JAE IGARASI+ IBL REC VALUE	
SM 148	DIFF ELASTIC EXPT=CONF	70+6	75WASH			941	375	BRC MCELLISTREM+ DEFORM EFFECTS	
SM 149	N, GAMMA EVAL=CONF	THR	75WASH			320	375	JAE IGARASI+ IBL REC VALUE	
SM 149	RES INT CAPT EVAL=CONF	NDG	75WASH			320	375	JAE IGARASI+ IBL REC VALUE	
SM 150	DIFF ELASTIC EXPT=CONF	70+6	75WASH			941	375	BRC MCELLISTREM+ DEFORM EFFECTS	
SM 151	N, GAMMA EVAL=CONF	THR	75WASH			320	375	JAE IGARASI+ IBL REC VALUE	
SM 151	RES INT CAPT EVAL=CONF	NDG	75WASH			320	375	JAE IGARASI+ IBL REC VALUE	
SM 152	DIFF ELASTIC EXPT=CONF	70+6	75WASH			941	375	BRC MCELLISTREM+ DEFORM EFFECTS	
SM 152	RESON PARAMS REVW=CONF	NDG	75WASH			779	375	COL HACKEN+ TBL AVG WG,STF,NUMBER GWN,WG	
SM 152	STRNGTH FUNC REVW=CONF	NDG	75WASH			779	375	COL HACKEN+ NEVIS TOF S-WAVE STF	
SM 152	LVL DENSITY THEO=CONF	THR	75WASH			335	375	COL FELVINCI+MOD ERICSON CALC CFD EXP	
SM 154	DIFF ELASTIC EXPT=CONF	70+6	75WASH			941	375	BRC MCELLISTREM+ DEFORM EFFECTS	
SM 154	RESON PARAMS REVW=CONF	NDG	75WASH			779	375	COL HACKEN+ TBL AVG WG,STF,NUMBER GWN,WG	
SM 154	STRNGTH FUNC REVW=CONF	NDG	75WASH			779	375	COL HACKEN+ NEVIS TOF S-WAVE STF	
EU 151	N, GAMMA EXPT=CONF	20+1 20+5	75WASH			904	375	RPI HOCKENBURY+GRPH CFD CALC	
EU 151	RESON PARAMS REVW=CONF	NDG	75WASH			779	375	COL HACKEN+ TBL AVG WG,STF,NUMBER GWN,WG	
EU 151	RESON PARAMS EXPT=CONF	NDG	75WASH			904	375	RPI HOCKENBURY+ AVG WG,D	
EU 151	STRNGTH FUNC REVW=CONF	NDG	75WASH			779	375	COL HACKEN+ NEVIS TOF S-WAVE STF	
EU 151	STRNGTH FUNC EXPT=CONF	NDG	75WASH			904	375	RPI HOCKENBURY+ AVG S0,S1	
EU 153	N, GAMMA EVAL=CONF	THR	75WASH			320	375	JAE IGARASI+ IBL REC VALUE	
EU 153	N, GAMMA EXPT=CONF	20+1 20+5	75WASH			904	375	RPI HOCKENBURY+GRPH CFD CALC	
EU 153	RES INT CAPT EVAL=CONF	NDG	75WASH			320	375	JAE IGARASI+ IBL REC VALUE	
EU 153	RESON PARAMS REVW=CONF	NDG	75WASH			779	375	COL HACKEN+ TBL AVG WG,STF,NUMBER GWN,WG	
EU 153	RESON PARAMS EXPT=CONF	NDG	75WASH			904	375	RPI HOCKENBURY+ AVG WG,D	
EU 153	STRNGTH FUNC REVW=CONF	NDG	75WASH			779	375	COL HACKEN+ NEVIS TOF S-WAVE STF	
EU 153	STRNGTH FUNC EXPT=CONF	NDG	75WASH			904	375	RPI HOCKENBURY+ AVG S0,S1	
EU 155	N, GAMMA EVAL=CONF	THR	75WASH			320	375	JAE IGARASI+ IBL REC VALUE	
EU 155	RES INT CAPT EVAL=CONF	NDG	75WASH			320	375	JAE IGARASI+ IBL REC VALUE	
GD 154	SPECT N,GAMM EXPT=CONF	24+4	75WASH			911	375	ANC GREENWOOD+ GRPH COUNTS VS CHANNEL	

ELEMENT S A	QUANTITY	TYPE	ENERGY		DOCUMENTATION			LAB	COMMENTS
			MIN	MAX	REF	VOL	PAGE DATE		
GD 154	RESON PARAMS	REVM-CONF	NDG			75WASH	779 375	COL HACKEN+ TBL AVG WG,STF,NUMBER GWN,WG	
GD 154	STRNGTH FUNC	REVM-CONF	NDG			75WASH	779 375	COL HACKEN+ NEVIS TOP S-WAVE STF	
GD 154	LVL DENSITY	THEO-CONF	THR			75WASH	335 375	COL FELVINCI+MOD ERICSON CALC CFD EXP	
GD 156	SPECT N,GAMM	EXPT-CONF	10+3 24+4			75WASH	911 375	ANC GREENWOOD+ GRPH COUNTS VS CHANNEL	
GD 158	RESON PARAMS	REVM-CONF	NDG			75WASH	779 375	COL HACKEN+ TBL AVG WG,STF,NUMBER GWN,WG	
GD 158	STRNGTH FUNC	REVM-CONF	NDG			75WASH	779 375	COL HACKEN+ NEVIS TOP S-WAVE STF	
GD 158	LVL DENSITY	THEO-CONF	THR			75WASH	335 375	COL FELVINCI+MOD ERICSON CALC CFD EXP	
GD 160	RESON PARAMS	REVM-CONF	NDG			75WASH	779 375	COL HACKEN+ TBL AVG WG,STF,NUMBER GWN,WG	
GD 160	STRNGTH FUNC	REVM-CONF	NDG			75WASH	779 375	COL HACKEN+ NEVIS TOP S-WAVE STF	
DY 160	RESON PARAMS	REVM-CONF	NDG			75WASH	779 375	COL HACKEN+ TBL AVG WG,STF,NUMBER GWN,WG	
DY 160	STRNGTH FUNC	REVM-CONF	NDG			75WASH	779 375	COL HACKEN+ NEVIS TOP S-WAVE STF	
DY 161	RESON PARAMS	REVM-CONF	NDG			75WASH	779 375	COL HACKEN+ TBL AVG WG,STF,NUMBER GWN,WG	
DY 161	STRNGTH FUNC	REVM-CONF	NDG			75WASH	779 375	COL HACKEN+ NEVIS TOP S-WAVE STF	
DY 162	RESON PARAMS	REVM-CONF	NDG			75WASH	779 375	COL HACKEN+ TBL AVG WG,STF,NUMBER GWN,WG	
DY 162	STRNGTH FUNC	REVM-CONF	NDG			75WASH	779 375	COL HACKEN+ NEVIS TOP S-WAVE STF	
DY 163	RESON PARAMS	REVM-CONF	NDG			75WASH	779 375	COL HACKEN+ TBL AVG WG,STF,NUMBER GWN,WG	
DY 163	STRNGTH FUNC	REVM-CONF	NDG			75WASH	779 375	COL HACKEN+ NEVIS TOP S-WAVE STF	
DY 164	RESON PARAMS	REVM-CONF	NDG			75WASH	779 375	COL HACKEN+ TBL AVG WG,STF,NUMBER GWN,WG	
DY 164	STRNGTH FUNC	REVM-CONF	NDG			75WASH	779 375	COL HACKEN+ NEVIS TOP S-WAVE STF	
HO 165	N, GAMMA	EXPT-CONF	24+4			75WASH	881 375	KTO YAMAMURO+N,FLUX=B10(N,AG),CS=1.268	
ER 164	LVL DENSITY	THEO-CONF	THR			75WASH	335 375	COL FELVINCI+MOD ERICSON CALC CFD EXP	
ER 166	RESON PARAMS	REVM-CONF	NDG			75WASH	779 375	COL HACKEN+ TBL AV WG,STF,NUMBER GWN,WG	
ER 166	STRNGTH FUNC	REVM-CONF	NDG			75WASH	779 375	COL HACKEN+ NEVIS TOP S-WAVE STF	
ER 166	LVL DENSITY	THEO-CONF	THR			75WASH	335 375	COL FELVINCI+MOD ERICSON CALC CFD EXP	
ER 167	RESON PARAMS	REVM-CONF	NDG			75WASH	779 375	COL HACKEN+ TBL AV WG,STF,NUMBER GWN,WG	
ER 167	STRNGTH FUNC	REVM-CONF	NDG			75WASH	779 375	COL HACKEN+ NEVIS TOP S-WAVE STF	
ER 168	RESON PARAMS	REVM-CONF	NDG			75WASH	779 375	COL HACKEN+ TBL AV WG,STF,NUMBER GWN,WG	
ER 168	STRNGTH FUNC	REVM-CONF	NDG			75WASH	779 375	COL HACKEN+ NEVIS TOP S-WAVE STF	
ER 168	LVL DENSITY	THEO-CONF	THR			75WASH	335 375	COL FELVINCI+MOD ERICSON CALC CFD EXP	
ER 170	RESON PARAMS	REVM-CONF	NDG			75WASH	779 375	COL HACKEN+ TBL AV WG,STF,NUMBER GWN,WG	
ER 170	STRNGTH FUNC	REVM-CONF	NDG			75WASH	779 375	COL HACKEN+ NEVIS TOP S-WAVE STF	
TM 169	TOT INELASTI	THEO-CONF	80+6 20+7			75WASH	650 375	LRL GARDNER,GRAPH CALC	
TM 169	N2N REACTION	THEO-CONF	80+6 20+7			75WASH	650 375	LRL GARDNER,CFO LLL EXPT,GRPH.	
TM 169	N2N REACTION	EXPT-CONF	84+6 15+7			75WASH	854 375	BRC FREHAUT+ TBL,GRPH,REL 238U(N,F)	
TM 169	N3N REACTION	THEO-CONF	15+7 20+7			75WASH	650 375	LRL GARDNER,GRAPH CALC CFD LLL EXPT	



ELEMENT S A	QUANTITY	TYPE	ENERGY		DOCUMENTATION			LAB	COMMENTS
			MIN	MAX	REF	VOL	PAGE	DATE	
YB 170	RESON PARAMS	REVIEW-CONF	NDG		75WASH		779 375	COL HACKEN+	TBL AVG WG,STF,NUMBER GWN,WG
YB 170	STRNGTH FUNC	REVIEW-CONF	NDG		75WASH		779 375	COL HACKEN+	NEVIS TOF S-WAVE STF
YB 171	RESON PARAMS	REVIEW-CONF	NDG		75WASH		779 375	COL HACKEN+	TBL AVG WG,STF,NUMBER GWN,WG
YB 171	STRNGTH FUNC	REVIEW-CONF	NDG		75WASH		779 375	COL HACKEN+	NEVIS TOF S-WAVE STF
YB 172	RESON PARAMS	REVIEW-CONF	NDG		75WASH		779 375	COL HACKEN+	TBL AVG WG,STF,NUMBER GWN,WG
YB 172	STRNGTH FUNC	REVIEW-CONF	NOG		75WASH		779 375	COL HACKEN+	NEVIS TOF S-WAVE STF
YB 172	LVL DENSITY	THEO-CONF	THR		75WASH		335 375	COL FELVINCI+MOD	ERICSON CALC CFD EXP
YB 173	RESON PARAMS	REVIEW-CONF	NOG		75WASH		779 375	COL HACKEN+	TBL AVG WG,STF,NUMBER GWN,WG
YB 173	STRNGTH FUNC	REVIEW-CONF	NOG		75WASH		779 375	COL HACKEN+	NEVIS TOF S-WAVE STF
YB 174	RESON PARAMS	REVIEW-CONF	NDG		75WASH		779 375	COL HACKEN+	TBL AVG WG,STF,NUMBER GWN,WG
YB 174	STRNGTH FUNC	REVIEW-CONF	NDG		75WASH		779 375	COL HACKEN+	NEVIS TOF S-WAVE STF
YB 175	RESON PARAMS	REVIEW-CONF	NDG		75WASH		779 375	COL HACKEN+	TBL AVG WG,STF,NUMBER GWN,WG
YB 176	STRNGTH FUNC	REVIEW-CONF	NOG		75WASH		779 375	COL HACKEN+	NEVIS TOF S-WAVE STF
LU 175	N2N REACTION	EXPT-CONF	84+6	15+7	75WASH		854 375	BRC FREHAUT+	TBL,GRPH,REL 238U(N,F)
LU 175	RESON PARAMS	REVIEW-CONF	NOG		75WASH		779 375	COL HACKEN+	TBL AVG WG,STF,NUMBER GWN,WG
LU 175	STRNGTH FUNC	REVIEW-CONF	NDG		75WASH		779 375	COL HACKEN+	NEVIS TOF S-WAVE STF
WF 179	N2N REACTION	EXPT-CONF	15+7		75WASH		711 375	SMU SALAITA+SHORT-LIVED	ISOMER PROD,TBL,
TA 181	N, GAMMA	EXPT-CONF	10+4	16+5	75WASH		952 375	CAD LERIGOLEUR+	GRPH CFD ENDF=4
TA 181	SPECI N,GAMM	EVAL-CONF	THR		75WASH		149 375	LAS YOUNG, GA MEAS	CFD CALC
TA 181	INELST GAMMA	EVAL-CONF	14+7		75WASH		149 375	LAS YOUNG,ORELA MEAS	CFD ENDF AT 125 DEG
TA 181	INELST GAMMA	THEO-CONF	10+5	20+7	75WASH		650 375	LRL GARDNER,CFD ORNL	EXPT,GRPH,
TA 181	INELST GAMMA	EXPT-CONF	70+5	20+7	75WASH		757 375	ORL CHAPMAN+TOF,	GRPH,
TA 181	INELST GAMMA	EXPT-CONF	10+5	20+7	75WASH		761 375	ORL OICKENS+ORELA,	GRPH,
TA 181	INELST GAMMA	EXPT-CONF	14+7		75WASH		769 375	LAS ARTHUR+DOUBLE	DIFF, CS,GRPH,
TA 181	N2N REACTION	EXPT-CONF	84+6	15+7	75WASH		854 375	BRC FREHAUT+	TBL,GRPH,REL 238U(N,F)
W	INELST GAMMA	EVAL-CONF	10+6	15+6	75WASH		149 375	LAS YOUNG,ORELA MEAS	CFD ENDF AT 125 DEG
W	INELST GAMMA	EVAL-CONF	12+7	14+7	75WASH		149 375	LAS YOUNG,ORELA MEAS	CFD ENDF AT 125 DEG
W	INELST GAMMA	EXPT-CONF	70+5	20+7	75WASH		757 375	ORL CHAPMAN+TOF,	
W	N2N REACTION	EXPT-CONF	79+6	15+7	75WASH		854 375	BRC FREHAUT+	TBL,GRPH,REL 238U(N,F)
W 182	RESON PARAMS	REVIEW-CONF	NDG		75WASH		779 375	COL HACKEN+	TBL STF,NUMBER GWN
W 182	STRNGTH FUNC	REVIEW-CONF	NOG		75WASH		779 375	COL HACKEN+	NEVIS TOF S-WAVE STF
W 182	LVL DENSITY	THEO-CONF	THR		75WASH		335 375	COL FELVINCI+MOD	ERICSON CALC CFD EXP
W 183	RESON PARAMS	REVIEW-CONF	NOG		75WASH		779 375	COL HACKEN+	TBL STF,NUMBER GWN
W 183	STRNGTH FUNC	REVIEW-CONF	NDG		75WASH		779 375	COL HACKEN+	NEVIS TOF S-WAVE STF
W 184	RESON PARAMS	REVIEW-CONF	NOG		75WASH		779 375	COL HACKEN+	TBL STF,NUMBER GWN

ELEMENT S A	QUANTITY	TYPE	ENERGY		DOCUMENTATION			LAB	COMMENTS
			MIN	MAX	REF	VOL	PAGE	DATE	
W 184	STRNGTH FUNC	REVW=CONF	NDG		75WASH	779	375	COL HACKEN+ NEVIS TOF 8-WAVE STF	
W 184	LVL DENSITY	THEO=CONF	THR		75WASH	335	375	COL FELVINCI+MOD ERICSON CALC CFD EXP	
W 186	RESON PARAMS	REVW=CONF	NDG		75WASH	779	375	COL HACKEN+ TBL STF,NUMBER GWN	
W 186	STRNGTH FUNC	REVW=CONF	NDG		75WASH	779	375	COL HACKEN+ NEVIS TOF 8-WAVE STF	
PT	INELST GAMMA	EXPT=CONF	14+7		75WASH	769	375	LAS ARTHUR+OBYBLE DIFF, CS'	
PT	N2N REACTION	EXPT=CONF	79+6	15+7	75WASH	854	375	BRC FREHAUT+ TBL,GRPH,REL 238U(N,F)	
AU 197	N, GAMMA	EXPT=CONF	FISS		75WASH	189	375	HED MCELROY,235U THERM FISS SPECT AVG CS	
AU 197	N, GAMMA	EXPT=CONF	FISS		75WASH	254	375	MOL FABRY+INTEG CS REL U238NF=,287+-,014	
AU 197	N, GAMMA	REVW=CONF	10+3	10+6	75WASH	293	375	NBS CARLSON, GRPHS EXP CFD ENDF=4 EVAL.	
AU 197	N, GAMMA	THEO=CONF	10+3	60+5	75WASH	650	375	LRL GARDNER,CEO ORNL + LLL EXPT,GRPH,	
AU 197	N, GAMMA	EXPT=CONF	24+4		75WASH	801	375	KTO YAMAMURO+N,FLUX=810(N,AG),CS=0,688	
AU 197	N, GAMMA	EXPT=CONF	24+4		75WASH	919	375	BNL RIMAWI+ CS=630+-17MB,CFO OTHER EXPT	
AU 197	N, GAMMA	EXPT=CONF	10+4	50+5	75WASH	956	375	CAD FORT+TBL,GRPHS CFD ENDF=4,OTHER EXPT	
AU 197	SPECT N,GAMM	THEO=CONF	THR		75WASH	650	375	LRL GARDNER,CEO ORPHAN OATA,GRPH,	
AU 197	INELST GAMMA	THEO=CONF	40+6	65+6	75WASH	650	375	LRL GARDNER,GRAPH GAMMA PROO	
AU 197	INELST GAMMA	EXPT=CONF	70+5	20+7	75WASH	757	375	ORL CHAPMAN+TOP,	
AU 197	SCATTERING	EXPT=CONF	=3		75WASH	822	375	JUL SCHMATZ+INCOH SC LT 500+-50MB REL VA	
AU 197	N2N REACTION	EXPT=CONF	84+6	15+7	75WASH	854	375	BRC FREHAUT+ TBL,GRPH,REL 238U(N,F)	
AU 197	N,ALPHA REAC	EXPT=CONF	FISS		75WASH	375	375	HED LIPPINCOTT+ TBL MEAS CFD ENDF4	
TL 203	N2N REACTION	EXPT=CONF	15+7		75WASH	711	375	SMU SALAITA+SHORT-LIVED ISOMER PROD,TBL.	
TL 205	N2N REACTION	EXPT=CONF	15+7		75WASH	711	375	SMU SALAITA+SHORT-LIVED ISOMER PROD,TBL.	
PB	DIFF ELASTIC	EXPT=CONF	70+6	14+7	75WASH	945	375	BRL BUCHER+ GRAPHS CFD OPTICAL MODEL	
PB	DIFF INELAST	EXPT=CONF	20+6	45+6	75WASH	870	375	IRN ETEMAO,GRPO,1250EGS,CFO OPT MDL CALC	
PB	SCATTERING	EXPT=CONF	-3		75WASH	822	375	JUL SCHMATZ+INCOH SC=2.0+-1.0MB,REL VA	
PB	INELST GAMMA	EXPT=CONF	70+5	20+7	75WASH	757	375	ORL CHAPMAN+TOP,	
PB 206	N2N REACTION	EXPT=CONF	15+7		75WASH	711	375	SMU SALAITA+SHORT-LIVED ISOMER PROD,TBL.	
PB 207	N2N REACTION	EXPT=CONF	15+7		75WASH	711	375	SMU SALAITA+SHORT-LIVED ISOMER PROD,TBL.	
PB 208	N, GAMMA	THEO=CONF	50+6	15+7	75WASH	346	375	BOL LONGO+GRPH CALC CFD EXP	
PB 208	SPECT N,GAMM	THEO=CONF	11+7	13+7	75WASH	346	375	BOL LONGO+2 EN,G SPECT 10-18MEV CFD EXP	
PB 208	SPECT N,GAMM	EXPT=CONF	11+7		75WASH	922	375	LAS ORAKE+ GRPH COUNTS VS CHANNEL	
PB 208	N2N REACTION	EXPT=CONF	15+7		75WASH	711	375	SMU SALAITA+SHORT-LIVED ISOMER PROD,TBL.	
BI 209	TOTAL XSECT	EXPT=CONF	50+2	75+4	75WASH	798	375	COL SINGH+ NEVIS TOF GRPH	
BI 209	DIFF INELAST	EXPT=CONF	20+6	45+6	75WASH	870	375	IRN ETEMAO,GRPO,1250EGS,CFO OPT MDL CALC	
BI 209	SCATTERING	EXPT=CONF	-3		75WASH	822	375	JUL SCHMATZ+INCOH SC LT 10+-2MB,REL VA	
BI 209	N2N REACTION	EXPT=CONF	15+7		75WASH	711	375	SMU SALAITA+SHORT-LIVED ISOMER PROD,TBL.	

ELEMENT S A	QUANTITY	TYPE	ENERGY		DOCUMENTATION			LAB	COMMENTS
			MIN	MAX	REF	VOL	PAGE		
BI 209	N2N REACTION	EXPT-CONF	79+6	15+7	75WASH	854	375	BRO FREHAUT+	TBL GRPH,REL 238U(N,P)
BI 209	RESON PARAMS	EXPT-CONF	80+2	73+4	75WASH	798	375	COL SINGH+	TBL E0,GWN FOR S+P RES,NEVIS
BI 209	STRNGTH FUNC	EXPT-CONF	80+2	73+4	75WASH	798	375	COL SINGH+	NEVIS,S+P-WAVE STF
TH 232	FISSION	EXPT-CONF	70+2	26+2	75WASH	93	375	RPI BLOCK+ND	STRUCT,AV NF LT 15+~101-9EV
TH 232	FISSION	EXPT-CONF	FISS		75WASH	189	375	HEO MCELROY,	235U THERM FISS SPECT AVG CS
TH 232	FISSION	EXPT-CONF	60+6		75WASH	641	375	SAC BLONS+STRUCTURE,	REL TD U235.
TH 232	NUBAR,(NU)	THEO-CONF	40+5	15+7	75WASH	342	375	TOM YAMAMOTO+	STAT MODEL CALC CFO EXPT,
TH 232	FISS YIELD	THEO-CONF	40+5	15+7	75WASH	342	375	TOM YAMAMOTO+	STAT MODEL CALC CFO EXPT,
TH 232	RESON PARAMS	REVW-CONF	NOG		75WASH	779	375	COL HACKEN+	TBL AVG WG,STF,NUMBER GWN,WG
TH 232	STRNGTH FUNC	REVW-CONF	NOG		75WASH	779	375	COL HACKEN+	NEVIS TDF S-WAVE STF
TH 232	LVL DENSITY	THEO-CONF	THR		75WASH	335	375	COL FELVINCI+MOD	ERICSON CALC CFO EXP
PA 231	FISSION	THEO-CONF	+5	63+6	75WASH	218	375	LAS WILHELMY+CALC	USING TH232(ME3,TF)
PA 231	NUBAR,(NU)	THEO-CONF	40+5	15+7	75WASH	342	375	TOM YAMAMOTO+	STAT MODEL CALC CFO EXPT,
PA 231	FISS YIELD	THEO-CONF	40+5	15+7	75WASH	342	375	TOM YAMAMOTO+	STAT MODEL CALC CFO EXPT,
U 232	FISSION	THEO-CONF	30+6	50+6	75WASH	129	375	LAS MOORE,'GRPH	R MATR STAT CALC CFO EXP
U 233	TOTAL XSECT	EVAL-CONF	25+2		75WASH	286	375	IAE LEMMEL,	TBL LSQ ANAL CFO OTHER EVAL
U 233	ELASTIC SCAT	EVAL-CONF	25+2		75WASH	286	375	IAE LEMMEL,	TBL LSQ ANAL CFO OTHER EVAL
U 233	ABSORPTION	EVAL-CONF	25+2		75WASH	286	375	IAE LEMMEL,	TBL LSQ ANAL CFO OTHER EVAL
U 233	N, GAMMA	EVAL-CONF	25+2		75WASH	286	375	IAE LEMMEL,	TBL LSQ ANAL CFO OTHER EVAL
U 233	FISSION	THEO-CONF	30+6	50+6	75WASH	129	375	LAS MOORE,'GRPH	R MATR STAT CALC CFO EXP
U 233	FISSION	EVAL-CONF	25+2		75WASH	286	375	IAE LEMMEL,	TBL LSQ ANAL CFO OTHER EVAL
U 233	FISSION	EXPT-CONF	10+3	30+7	75WASH	591	375	LRL BEHRENS+REL	235U,GRPH,CFO OTHER EXPT
U 233	ALPHA	EVAL-CONF	25+2		75WASH	286	375	IAE LEMMEL,	TBL LSQ ANAL CFO OTHER EVAL
U 233	ETA	EVAL-CONF	25+2		75WASH	286	375	IAE LEMMEL,	TBL LSQ ANAL CFO OTHER EVAL
U 233	ETA	EVAL-CONF	25+2		75WASH	553	375	BET ULLD+M+C	ANAL SMITH EXP,SYST ERRORS
U 233	ETA	EVAL-CONF	THR		75WASH	557	375	BET GOLDSMITH+MONTE-CARLO	ANAL,ORNL EXPT
U 233	NUBAR,(NU)	EVAL-CONF	25+2		75WASH	286	375	IAE LEMMEL,	TBL LSQ ANAL,CFO OTHER EVAL.
U 233	NUBAR,(NU)	THEO-CONF	THR	15+7	75WASH	342	375	TOM YAMAMOTO+	STAT MODEL CALC CFO EXPT,
U 233	F NEUT DELAY	EVAL-CONF	25+2		75WASH	286	375	IAE LEMMEL,	TBL LSQ ANAL,CFO OTHER EVAL.
U 233	FISS YIELD	THEO-CONF	THR	15+7	75WASH	342	375	TOM YAMAMOTO+	STAT MODEL CALC CFO EXPT,
U 233	FISS YIELD	EXPT-CONF	FAST		75WASH	378	375	ACC MAECK,	FISS YIELDS OF 58 MASSES
U 234	FISSION	THEO-CONF	30+6	50+6	75WASH	129	375	LAS MOORE,GRPH	R MATR STAT CALC CFO EXP
U 234	FISSION	EXPT-CONF	10+3	30+7	75WASH	591	375	LRL BEHRENS+REL	235U,GRPH,CFO OTHER EXPT
U 234	LVL DENSITY	THEO-CONF	THR		75WASH	335	375	COL FELVINCI+MOD	ERICSON CALC CFO EXP
U 235	TOTAL XSECT	EVAL-CONF	25+2		75WASH	286	375	IAE LEMMEL,	TBL LSQ ANAL,CFO OTHER EVAL.



ELEMENT S A	QUANTITY	TYPE	ENERGY		DOCUMENTATION			LAB	COMMENTS
			MIN	MAX	REF	VOL	PAGE	DATE	
U 235	TOTAL XSECT	THEO=CONF	10+3	20+6	75WASH	650	375	LRL GARDNER,CFO ENOF + ENOL,GRPH.	
U 235	ELASTIC SCAT	EVAL=CONF	25-2		75WASH	286	375	IAE LEMMEL, TBL LSQ ANAL,CFO OTHER EVAL.	
U 235	ELASTIC SCAT	THEO=CONF	10+3	10+7	75WASH	650	375	LRL GARDNER,CFO ENOF + ENOL,GRPH.	
U 235	DIFF ELASTIC	THEO=CONF	20+5	50+5	75WASH	650	375	LRL GARDNER,CFO ENOF + ENOL,GRPH.	
U 235	TOT INELASTI	THEO=CONF	10+4	30+6	75WASH	650	375	LRL GARDNER,CFO ENOF + ENOL,GRPH.	
U 235	ABSORPTION	EVAL=CONF	25-2		75WASH	286	375	IAE LEMMEL, TBL LSQ ANAL,CFO OTHER EVAL.	
U 235	N, GAMMA	EVAL=CONF	3	12-1	75WASH	281	375	BNW LEONARD,GRPH LEAST SQ EVAL CFO EXP	
U 235	N, GAMMA	EVAL=CONF	25-2		75WASH	286	375	IAE LEMMEL, TBL LSQ ANAL,CFO OTHER EVAL.	
U 235	N, GAMMA	THEO=CONF	10+3	10+7	75WASH	650	375	LRL GARDNER,CFO ENOF + ENOL,GRPH.	
U 235	INELST GAMMA	EXPT=CONF	14+7		75WASH	769	375	LAS ARTHUR+OUBLE DIFF, CS.	
U 235	FISSION	THEO=CONF	20+4	25+7	75WASH	129	375	LAS MOORE,GRPH R MATR STAT CALC CFO EXP	
U 235	FISSION	EXPT=CONF	FISS		75WASH	189	375	WED MCCLROY,235U THERM FISS SPECT AVG CS	
U 235	FISSION	EXPT=CONF	FISS		75WASH	254	375	MOL FABRY+INTEG CS REL U238NF= 3.94+-0.08	
U 235	FISSION	EXPT=CONF	FISS		75WASH	266	375	NBS HEATON+252CF SOURC,CS=1204+-29 MB	
U 235	FISSION	EXPT=CONF	FISS		75WASH	270	375	NBS GILLIAM+252CF SOURC,REL 238U,PU,NP	
U 235	FISSION	EVAL=CONF	3	35-2	75WASH	281	375	BNW LEONARD,GRPH LEAST SQ EVAL CFO EXP	
U 235	FISSION	EVAL=CONF	25-2		75WASH	286	375	IAE LEMMEL, TBL LSQ ANAL,CFO OTHER EVAL.	
U 235	FISSION	REVW=CONF	10+5	20+7	75WASH	293	375	NBS CARLSON, GRPHS EXP CFO ENOF=3 EVAL	
U 235	FISSION	EXPT=CONF	10+2	10+6	75WASH	546	375	LRL CZIRRA MEAS CS REL 6LI(N,A),TBL,GRPH	
U 235	FISSION	EXPT=CONF	60+5	22+7	75WASH	568	375	HAR COATES+U238/U235 FISS CS RATIO	
U 235	FISSION	EXPT=CONF	15+1	15+2	75WASH	576	375	LAS KEYWORTH+SPINS,POL SOURCE + TARGET	
U 235	FISSION	EXPT=CONF	10+0	39+1	75WASH	580	375	COL FELVINCI+ LOW LYING RES,SPINS	
U 235	FISSION	EXPT=CONF	78+2	20+5	75WASH	606	375	CAT MIGNECO+STRUCTURE EFFECTS,GRPHS.	
U 235	FISSION	EXPT=CONF	80+5	20+7	75WASH	615	375	LRL SIOHU+TABLE,GRAPH,REL TO N-P SCATT.	
U 235	FISSION	EXPT=CONF	96+5		75WASH	634	375	MHC GILLIAM+CS=1.218+-2.1PCT,NA=BE NEUTS	
U 235	FISSION	THEO=CONF	10+3	20+6	75WASH	650	375	LRL GARDNER,CFO ENOF + ENOL,GRPH.	
U 235	ALPHA	EVAL=CONF	25-2		75WASH	286	375	IAE LEMMEL, TBL LSQ ANAL,CFO OTHER EVAL.	
U 235	ALPHA	EXPT=CONF	15+2	32+4	75WASH	599	375	GEL CORVI+TBL,GRPH,STAT ERROR LT +-5PCT.	
U 235	ETA	EVAL=CONF	3	10-1	75WASH	281	375	BNW LEONARD,GRPH LEAST SQ EVAL CFO EXP	
U 235	ETA	EVAL=CONF	25-2		75WASH	286	375	IAE LEMMEL, TBL LSQ ANAL,CFO OTHER EVAL.	
U 235	ETA	EVAL=CONF	25-2		75WASH	553	375	BET ULLO+M=C ANAL SMITH EXP,SYST ERRORS	
U 235	ETA	EVAL=CONF	THR		75WASH	557	375	BET GOLDSMITH+MONTE-CARLO ANAL,ORNL EXPT	
U 235	NUBAR,(NU)	EVAL=CONF	25-2		75WASH	286	375	IAE LEMMEL, TBL LSQ ANAL,CFO OTHER EVAL.	
U 235	NUBAR,(NU)	THEO=CONF	THR	15+7	75WASH	342	375	TOH YAMAMOTO+ STAT MODEL CALC CFO EXPT.	
U 235	NUBAR,(NU)	EXPT=CONF	20+5	14+6	75WASH	549	375	KFK KAPPELER+GRPH 22 PTS,AV E RES=3.3PCT	

ELEMENT S A	QUANTITY	TYPE	ENERGY		DOCUMENTATION			LAB	COMMENTS
			MIN	MAX	REF	VOL	PAGE	DATE	
U 235	F NEUT DELAY EVAL=CONF	25-2			75WASH			286 375	IAE LEMMEL, TBL LSG ANAL,CFO OTHER EVAL.
U 235	SPECT FISS N EXPT=CONF	THR			75WASH			189 375	HED MCELROY, GRPH, SAND-2
U 235	SPECT FISS N EVAL=CONF	THR			75WASH			250 375	NBS GRUNDL+EV, MEAS, E AV=1.97+-0.014 MEV
U 235	SPECT FISS N EXPT=CONF	10+5	21+6		75WASH			572 375	AE JOHANSSON+ANG OIST, SHAPE FIT TO WATT
U 235	SPECT FISS N EXPT=CONF	52+5			75WASH			630 375	AE JOHANSSON+TOF, AERE+STUDSVIK EXP, GRPH
U 235	SPECT FISS G THEO=CONF	THR			75WASH			193 375	LAS STAMATELAKIS+GRPHS G SPECT, CINDER
U 235	FISS YIELD	THEO=CONF	THR	15+7	75WASH			342 375	TOH YAMAMOTO+ STAT MODEL CALC CFO EXPT.
U 235	FISS YIELD	EXPT=CONF	FAST		75WASH			378 375	ACC MAECK, FISS YIELDS OF 58 MASSES
U 235	FISS YIELD	EXPT=CONF	THR		75WASH			401 375	BNW REEOER+ TBL INO, CUM YLDS RB, CS, BR
U 235	RESON PARAMS	EXPT=CONF	15+1	23+1	75WASH			576 375	LAS KEYWORTH+SPIN ASSIGNMENTS
U 235	RESON PARAMS	EXPT=CONF	10+0	39+1	75WASH			580 375	COL FELVINCIA+ LOW LYING RES, SPINS
U 236	TOTAL XSECT	EXPT=CONF	30+1	18+3	75WASH			728 375	MOL MEWISSEN+IBL, RES PAR
U 236	SCATTERING	EXPT=CONF	30+1	18+3	75WASH			728 375	MOL MEWISSEN+MEAS, REL PB SCAT=11.288
U 236	N, GAMMA	REVW=CONF	10+3	10+6	75WASH			202 375	BRC MICHAUDON, CALC CFO MEAS
U 236	N, GAMMA	EXPT=CONF	30+1	18+3	75WASH			728 375	MOL MEWISSEN+MEAS, REL 10B(N, AG)
U 236	FISSION	THEO=CONF	30+6	50+6	75WASH			129 375	LAS MOORE, GRPH R MATR STAT CALC CFO EXP
U 236	FISSION	REVW=CONF	10+3	10+6	75WASH			202 375	BRC MICHAUDON, CALC CFO MEAS
U 236	FISSION	EXPT=CONF	10+5	30+7	75WASH			591 375	LRL BEHRENS+REL 235U, GRPH, CFO OTHER EXPT
U 236	RESON PARAMS	EXPT=CONF	34+1	18+3	75WASH			728 375	MOL MEWISSEN+IBL, EO, WN, WNO, WG
U 236	STRNGTH FUNC	EXPT=CONF		18+3	75WASH			728 375	MOL MEWISSEN+S0=(1.05+-0.14)E-4
U 236	LVL DENSITY	THEO=CONF	THR		75WASH			335 375	COL FELVINCIA+ MOD ERICSON CALC CFO EXP
U 237	FISSION	THEO=CONF	30+6	50+6	75WASH			129 375	LAS MOORE, GRPH R MATR STAT CALC CFO EXP
U 238	DIFF ELASTIC	EXPT=CONF	70+6	14+7	75WASH			945 375	BRL BUCHER+ GRAPHS CFO OPTICAL MODEL
U 238	DIFF ELASTIC	EXPT=CONF	90+5	27+6	75WASH			949 375	LTI EGAN+ TOF, GRAPHS CFO ENFD, THEORY
U 238	TOT INELASTI	EVAL=CONF	45+4	15+7	75WASH			313 375	KFK GOEL+ KEDAK-3 LIBRARY, GRPH CFO EXPT.
U 238	TOT INELASTI	EXPT=CONF	30+5	30+6	75WASH			861 375	ANL GUENTHER+GRND ST ROT BANDS EXCITED
U 238	DIFF INELAST	EXPT=CONF	90+5	27+6	75WASH			949 375	LTI EGAN+ TOF, GRAPHS CFO ENFD, THEORY
U 238	N, GAMMA	THEO=CONF	50+4	50+6	75WASH			129 375	LAS MOORE, GRPH R MATR STAT CALC CFO ENFD
U 238	N, GAMMA	EVAL=CONF	40+3	10+5	75WASH			313 375	KFK GOEL+ KEDAK-3 LIBRARY, GRPH CFO EXPT.
U 238	N, GAMMA	EXPT=CONF	20+4	56+5	75WASH			619 375	ORL SPENCER+TBL, SHAPE REL 235U NF +AU NG
U 238	N, GAMMA	EXPT=CONF	50+3	10+5	75WASH			622 375	ORL PEREZ+ STAT MODEL TESTS
U 238	N, GAMMA	EXPT=CONF	10+1	16+3	75WASH			732 375	GEL CORVIA+ GRPH, COUNTS VS CHANNEL
U 238	N, GAMMA	EXPT=CONF	24+4		75WASH			801 375	KTO YAMAMURO+N, FLUX=B10(N, AG), CS=0.508
U 238	N, GAMMA	EXPT=CONF	20+4	50+5	75WASH			900 375	ANL POENITZ, GRAPH
U 238	N, GAMMA	EXPT=CONF	24+4		75WASH			919 375	BNL RIMAWI+ CS=475+-36MB, CFO OTHER EXPT



ELEMENT S A	QUANTITY	TYPE	ENERGY		DOCUMENTATION			LAB	COMMENTS
			MIN	MAX	REF	VOL	PAGE		
U 238	N, GAMMA	EXPT-CONF	15+4	55+5	75WASH	952	375	CAD LERIGOLEUR+ GRPH CPO ENOF=4	
U 238	INELST GAMMA	EVAL-CONF THR			75WASH	149	375	LAS YOUNG, MEAS CPO ENDF-4	
U 238	N2N REACTION	EXPT-CONF	13+7	18+7	75WASH	818	375	HAM ACKERMANN+ACT, GRPH CPO STAT THEORY	
U 238	N2N REACTION	EXPT-CONF	79+6	15+7	75WASH	854	375	BRC FREHAUT+ TBL, GRPH, REL 238U(N,F)	
U 238	N3N REACTION	EXPT-CONF	12+7	15+7	75WASH	854	375	BRC FREHAUT+ TBL, GRPH, REL 238U(N,F)	
U 238	FISSION	EXPT-CONF	15+0	35+4	75WASH	93	375	RPI BLOCK+ SUBTR FISSION, GRPH COUNTS VS E	
U 238	FISSION	THEO-CONF	30+6	50+6	75WASH	129	375	LAS MOORE, GRPH R MATR STAT CALC CPO EXP	
U 238	FISSION	EXPT-CONF FISSION			75WASH	189	375	HEO MCLEROY, 235U THERM FISSION SPECT AVG CS	
U 238	FISSION	EXPT-CONF FISSION			75WASH	254	375	MOL FABRY+INTEG CS, MOL STANOARO N FIELD	
U 238	FISSION	EXPT-CONF FISSION			75WASH	270	375	NBS GILLIAM+252CF SOURC, REL 235U, PU, NP	
U 238	FISSION	REVM-CONF	90+5	20+7	75WASH	293	375	NBS CARLSON, GRPH CS CPO U235, NP237	
U 238	FISSION	EVAL-CONF	10+6	15+7	75WASH	313	375	KFK GOEL+ KEDAK-3 LIBRARY, GRPH CPO EXPT.	
U 238	FISSION	EXPT-CONF	60+5	22+7	75WASH	568	375	HAR COATES+U238/U235 FISSION CS RATIO	
U 238	FISSION	EXPT-CONF	10+5	30+7	75WASH	591	375	LRL BEHRENS+REL 235U, GRPH, CPO OTHER EXPT	
U 238	FISSION	EXPT-CONF	65+2	13+3	75WASH	597	375	GEL WARTENA+RES DATA, TOF, GRPH	
U 238	FISSION	EXPT-CONF		60+6	75WASH	641	375	SAC BLONS+STRUCTURE, REL TO U235,	
U 238	NUBAR, (NU)	THEO-CONF	40+5	15+7	75WASH	342	375	TOH YAMAMOTO+ STAT MODEL CALC CPO EXPT,	
U 238	SPECT FISSION N	EXPT-CONF	21+6		75WASH	572	375	AE JOHANSSON+ ANG DIST PROMPT NEUTRONS	
U 238	SPECT FISSION N	EXPT-CONF	14+7		75WASH	703	375	LRL WONG+ GRPHS EMISSION SPECTRA	
U 238	SPECT FISSION G	THEO-CONF FAST			75WASH	193	375	LAS STAMATELAKOS+GRPHS G SPECT, CINDER	
U 238	FISSION YIELD	EXPT-CONF FAST			75WASH	378	375	ACC MAECK, FISSION YIELDS OF 98 MASSES	
U 238	RESON PARAMS	EXPT-CONF	67+0	37+1	75WASH	93	375	RPI BLOCK+ E0, WF, SUBTR GPS AT 700+1200EV	
U 238	RESON PARAMS	EXPT-CONF	66+2	13+3	75WASH	597	375	GEL WARTENA+ TOF, TBL E0, WF	
U 238	RESON PARAMS	EXPT-CONF	64+1	15+3	75WASH	732	375	GEL CORVI+ TBL E0, GWN, P-WAVE ASSIGN,	
U 238	RESON PARAMS	EXPT-CONF	21+1	47+3	75WASH	737	375	JAE NAKAJIMA+ TBL E0, WNO CPO EXPT	
U 238	RESON PARAMS	REVM-CONF NDG			75WASH	779	375	COL HACKEN+ TBL AVG WG, STF, NUMBER GWN, WG	
U 238	STRNGTH FUNC	EXPT-CONF	10+1	16+3	75WASH	732	375	GEL CORVI+ S0, S1, 00	
U 238	STRNGTH FUNC	REVM-CONF NDG			75WASH	779	375	COL HACKEN+ NEVIS TOF S-WAVE STF	
U 238	LVL DENSITY	THEO-CONF THR			75WASH	335	375	COL FELVINGI+MOD ERICSON CALC CPO EXP	
U 238	LVL DENSITY	EXPT-CONF	10+1	16+3	75WASH	732	375	GEL CORVI+ 00 = 22.4 +/- 1.0 EV	
U 238	PHOTO-FISSION	EXPT-CONF		60+7	75WASH	610	375	TOH IWASAKI+TBL, GRPHS, DELAYED N-SPECT,	
U 239	FISSION	THEO-CONF	30+6	50+6	75WASH	129	375	LAS MOORE, GRPH R MATR STAT CALC CPO EXP	
NP 232	FISSION	THEO-CONF	+5	30+6	75WASH	218	375	LAS WILHELMY+ CALC USING U233(HE3, TF)	
NP 233	FISSION	THEO-CONF	+5	39+6	75WASH	218	375	LAS WILHELMY+ CALC USING U234(HE3, TF)	
NP 234	FISSION	THEO-CONF	+5	62+6	75WASH	218	375	LAS WILHELMY+ CALC USING U235(HE3, TF)	



ELEMENT S A	QUANTITY	TYPE	ENERGY		DOCUMENTATION			LAB	COMMENTS
			MIN	MAX	REF	VOL	PAGE		
NP 235	FISSION	THEO=CONF	+5	66+6	75WASH			218 375	LAS WILHELMY+ CALC USING U235(HE3,DF)
NP 236	FISSION	THEO=CONF	+5	43+6	75WASH			218 375	LAS WILHELMY+ CALC USING U237(HE3,TF)
NP 237	FISSION	EXPT=CONF	FISS		75WASH			189 375	HED MCCLROY, 235U THERM FISS SPECT AVG CS
NP 237	FISSION	REVW=CONF	25+1	55+1	75WASH			202 375	BRC MICHAUDON, RVW EXP SUBTR FISS DATA
NP 237	FISSION	THEO=CONF	+5	77+6	75WASH			218 375	LAS WILHELMY+ CALC USING U238(HE3,TF)
NP 237	FISSION	EXPT=CONF	FISS		75WASH			254 375	MOL FABRY+INTEG CS REL U238NF= 4.35+- .13
NP 237	FISSION	EXPT=CONF	FISS		75WASH			270 375	NBS GILLIAM+252CF SOURC.REL U235,238,PU
NP 237	FISSION	REVW=CONF	10+5	20+7	75WASH			293 375	NBS CARLSON, GRPH CS CFO U235,U238
NP 237	NUBAR, (NU)	THEO=CONF	40+5	15+7	75WASH			342 375	TOM YAMAMOTO+ STAT MODEL CALC CFO EXPT.
NP 238	FISSION	THEO=CONF	+5	52+6	75WASH			218 375	LAS WILHELMY+ CALC USING U238(HE3,DF)
PU 238	N, GAMMA	REVW=CONF	10+3	10+6	75WASH			202 375	BRC MICHAUDON, CALC CFO MEAS
PU 238	FISSION	THEO=CONF	30+6	50+6	75WASH			129 375	LAS MOORE, GRPH R MATR STAT CALC CFO EXP
PU 238	FISSION	REVW=CONF	10+3	10+6	75WASH			202 375	BRC MICHAUDON, CALC CFO MEAS
PU 239	TOTAL XSECT	EVAL=CONF	25-2		75WASH			286 375	IAE LEMMEL, TBL LSQ ANAL, CFO OTHER EVAL.
PU 239	TOTAL XSECT	EVAL=CONF	10+5	15+7	75WASH			313 375	KFK GOEL+ KEDAK-3 LIBRARY, GRPH CFO EXPT.
PU 239	ELASTIC SCAT	EVAL=CONF	25-2		75WASH			286 375	IAE LEMMEL, TBL LSQ ANAL, CFO OTHER EVAL.
PU 239	ABSORPTION	EVAL=CONF	25-2		75WASH			286 375	IAE LEMMEL, TBL LSQ ANAL, CFO OTHER EVAL.
PU 239	N, GAMMA	EVAL=CONF	25+2		75WASH			286 375	IAE LEMMEL, TBL LSQ ANAL, CFO OTHER EVAL.
PU 239	N, GAMMA	EXPT=CONF	20-2	20+5	75WASH			626 375	ORL GWIN+ TABLE, NORM TO 2200M/S
PU 239	INELST GAMMA	EXPT=CONF	14+7		75WASH			769 375	LAS ARTHUR+DOUBLE DIFF, CS, GRPH.
PU 239	FISSION	THEO=CONF	30+6	50+6	75WASH			129 375	LAS MOORE, GRPH R MATR STAT CALC CFO EXP
PU 239	FISSION	EXPT=CONF	FISS		75WASH			189 375	HED MCCLROY, 235U THERM FISS SPECT AVG CS
PU 239	FISSION	EXPT=CONF	FISS		75WASH			254 375	MOL FABRY+INTEG CS REL U238NF= 5.93+- .13
PU 239	FISSION	EXPT=CONF	FISS		75WASH			270 375	NBS GILLIAM+252CF SOURC.REL U235,238,NP
PU 239	FISSION	EVAL=CONF	25-2		75WASH			286 375	IAE LEMMEL, TBL LSQ ANAL, CFO OTHER EVAL.
PU 239	FISSION	EVAL=CONF	10+3	10+4	75WASH			313 375	KFK GOEL+ KEDAK-3 LIBRARY, GRPH CFO EXPT.
PU 239	FISSION	EXPT=CONF	10+3	10+6	75WASH			564 375	WAR GAYTHER, TBL S, GRPH S, CFO EVAL SIG
PU 239	FISSION	EXPT=CONF	20-2	20+5	75WASH			626 375	ORL GWIN+ TABLE, NORM TO 2200M/S
PU 239	ALPHA	EVAL=CONF	25+2		75WASH			286 375	IAE LEMMEL, TBL LSQ ANAL, CFO OTHER EVAL.
PU 239	ALPHA	EVAL=CONF	30+4	10+6	75WASH			313 375	KFK GOEL+ KEDAK-3 LIBRARY, GRPH CFO EXPT.
PU 239	ALPHA	EXPT=CONF	10+2	20+5	75WASH			626 375	ORL GWIN+ CFO 2 EXPT, AVG DIFF 6PCT
PU 239	ETA	EVAL=CONF	25-2		75WASH			286 375	IAE LEMMEL, TBL LSQ ANAL, CFO OTHER EVAL.
PU 239	NUBAR, (NU)	REVW=CONF	+0	10+2	75WASH			202 375	BRC MICHAUDON, GRPH NUBAR VS E FOR J=1+
PU 239	NUBAR, (NU)	EVAL=CONF	25-2		75WASH			286 375	IAE LEMMEL, TBL LSQ ANAL, CFO OTHER EVAL.
PU 239	NUBAR, (NU)	THEO=CONF	THR	15+7	75WASH			342 375	TOM YAMAMOTO+ STAT MODEL CALC CFO EXPT.

ELEMENT S A	QUANTITY	TYPE	ENERGY		DOCUMENTATION REF VOL PAGE DATE	LAB	COMMENTS
			MIN	MAX			
PU 239	F NEUT DELAY	EVAL=CONF	25-2		75WASH	286 375	IAE LEMMEL, TBL LSQ ANAL CFO OTHER EVAL.
PU 239	SPECT FISS N	EXPT=CONF	10+5	21+6	75WASH	572 375	AE JOHANSSON+ SHAPE FIT TO WATT DISTR.
PU 239	FISS YIELD	THEO=CONF	THR	15+7	75WASH	342 375	TOH YAMAMOTO+ STAT MODEL CALC CFO EXPT.
PU 239	FISS YIELD	EXPT=CONF	FAST		75WASH	378 375	ACC MAECK, FISS YIELDS OF 59 MASSES
PU 240	N, GAMMA	REVM=CONF	10+3	10+6	75WASH	282 375	BRC MICHAUDON, CALC CFO MEAS
PU 240	N, GAMMA	EXPT=CONF	25-2	35+5	75WASH	229 375	ORL WESTON+ CFO ENDF, REL 108(NA)+6L1(NA)
PU 240	FISSION	THEO=CONF	30+6	50+6	75WASH	129 375	LAS MOORE, GRPH R MATR STAT CALC CFO EXP
PU 240	FISSION	REVM=CONF	10+3	10+6	75WASH	282 375	BRC MICHAUDON, CALC CFO MEAS
PU 240	FISSION	EXPT=CONF	61+2	29+3	75WASH	560 375	ORL AUCHAMPAUGH+SUBTR FISS, GRPH, RES PAR
PU 240	RESON PARAMS	EXPT=CONF	61+2	29+3	75WASH	560 375	ORL AUCHAMPAUGH+SUBTR FISS, TBL WF, WNO, EO
PU 240	LVL DENSITY	THEO=CONF	THR		75WASH	335 375	COL FELVINCI+ MOD ERICSON CALC CFO EXP
PU 241	TOTAL XSECT	EVAL=CONF	25-2		75WASH	286 375	IAE LEMMEL, TBL LSQ ANAL CFO OTHER EVAL.
PU 241	ELASTIC SCAT	EVAL=CONF	25-2		75WASH	286 375	IAE LEMMEL, TBL LSQ ANAL CFO OTHER EVAL.
PU 241	ABSORPTION	EVAL=CONF	25-2		75WASH	286 375	IAE LEMMEL, TBL LSQ ANAL CFO OTHER EVAL.
PU 241	N, GAMMA	EVAL=CONF	25-2		75WASH	286 375	IAE LEMMEL, TBL LSQ ANAL CFO OTHER EVAL.
PU 241	FISSION	THEO=CONF	30+6	50+6	75WASH	129 375	LAS MOORE, GRPH R MATR STAT CALC CFO EXP
PU 241	FISSION	EVAL=CONF	25-2		75WASH	286 375	IAE LEMMEL, TBL LSQ ANAL CFO OTHER EVAL.
PU 241	ALPHA	EVAL=CONF	25-2		75WASH	286 375	IAE LEMMEL, TBL LSQ ANAL CFO OTHER EVAL.
PU 241	ETA	EVAL=CONF	25-2		75WASH	286 375	IAE LEMMEL, TBL LSQ ANAL CFO OTHER EVAL.
PU 241	NUBAR, (NU)	EVAL=CONF	25-2		75WASH	286 375	IAE LEMMEL, TBL LSQ ANAL CFO OTHER EVAL.
PU 241	NUBAR, (NU)	THEO=CONF	THR	15+7	75WASH	342 375	TOH YAMAMOTO+ STAT MODEL CALC CFO EXPT.
PU 241	F NEUT DELAY	EVAL=CONF	25-2		75WASH	286 375	IAE LEMMEL, TBL LSQ ANAL CFO OTHER EVAL.
PU 241	FISS YIELD	THEO=CONF	THR	15+7	75WASH	342 375	TOH YAMAMOTO+ STAT MODEL CALC CFO EXPT.
PU 242	N, GAMMA	EVAL=CONF	25-2		75WASH	224 375	SRL BENJAMIN+ TBL BEST FIT TRANSPU PROD.
PU 242	N, GAMMA	EXPT=CONF	20+2	70+4	75WASH	584 375	RPI HOCKENBURY+ TABLE, GRAPH
PU 242	RES INT CAPT	EVAL=CONF	63-1		75WASH	224 375	SRL BENJAMIN+ TBL BEST FIT TRANSPU PROD.
PU 242	FISSION	THEO=CONF	30+6	50+6	75WASH	129 375	LAS MOORE, GRPH R MATR STAT CALC CFO EXP
PU 242	FISSION	EVAL=CONF	25-2		75WASH	224 375	SRL BENJAMIN+ TBL BEST FIT TRANSPU PROD.
PU 242	RES INT FISS	EVAL=CONF	63-1		75WASH	224 375	SRL BENJAMIN+ TBL BEST FIT TRANSPU PROD.
PU 242	RESON PARAMS	EXPT=CONF	21+2	38+2	75WASH	584 375	RPI HOCKENBURY+ TABL EO, WN
PU 242	STRNGTH FUNC	EXPT=CONF	23-2		75WASH	584 375	RPI HOCKENBURY+S0=1.16E-04.
PU 243	N, GAMMA	EVAL=CONF	25-2		75WASH	224 375	SRL BENJAMIN+ TBL BEST FIT TRANSPU PROD.
PU 243	RES INT CAPT	EVAL=CONF	63-1		75WASH	224 375	SRL BENJAMIN+ TBL BEST FIT TRANSPU PROD.
PU 243	FISSION	THEO=CONF	30+6	50+6	75WASH	129 375	LAS MOORE, GRPH R MATR STAT CALC CFO EXP
PU 243	FISSION	EVAL=CONF	25-2		75WASH	224 375	SRL BENJAMIN+ TBL BEST FIT TRANSPU PROD.



ELEMENT S A	QUANTITY	TYPE	ENERGY		DOCUMENTATION			LAB	COMMENTS
			MIN	MAX	REF	VOL	PAGE		
PU 243	RES INT FISS	EVAL-CONF	63-1		75WASH		224 375	SRL BENJAMIN+	TBL BEST FIT TRANSPU PROD.
PU 244	FISSION	THEO-CONF	30+6	50+6	75WASH		129 375	LAS MOORE,GRPH R MATR	STAT CALC CFD EXP
AM 241	TOTAL XSECT	EXPT-CONF	80-1	10+3	75WASH		636 375	SAC DERRIEN+SHAPE	ANALYSIS TO 150 EV
AM 241	ABSORPTION	EXPT-CONF	25-2	35+5	75WASH		229 375	ORL WESTON+ CFD ENDF,REL	10B(NA)+6LI(NA)
AM 241	FISSION	THEO-CONF	+5	67+6	75WASH		218 375	LAS WILHELMY+ CALC	USING PU242(HE3,TF)
AM 241	FISSION	EXPT-CONF	80-1	15+2	75WASH		636 375	SAC DERRIEN+TBL,EO,WF	
AM 241	RESON PARAMS	EXPT-CONF	31-1	15+2	75WASH		636 375	SAC DERRIEN+TBL,EO,2GWN,WG	
AM 241	STRNGTH FUNC	EXPT-CONF		50+1	75WASH		636 375	SAC DERRIEN+80=0.75E-04.	
AM 241	STRNGTH FUNC	EXPT-CONF		15+2	75WASH		636 375	SAC DERRIEN+80=0.94E-04.	
AM 242	FISSION	THEO-CONF	+5	46+6	75WASH		218 375	LAS WILHELMY+242M	CALC,PU242(HE3,DF)
AM 243	N, GAMMA	EVAL-CONF	25-2		75WASH		224 375	SRL BENJAMIN+	TBL BEST FIT TRANSPU PROD.
AM 243	RES INT CAPT	EVAL-CONF	63-1		75WASH		224 375	SRL BENJAMIN+	TBL BEST FIT TRANSPU PROD.
AM 243	FISSION	EVAL-CONF	25-2		75WASH		224 375	SRL BENJAMIN+	TBL BEST FIT TRANSPU PROD.
AM 243	RES INT FISS	EVAL-CONF	63-1		75WASH		224 375	SRL BENJAMIN+	TBL BEST FIT TRANSPU PROD.
CM 244	N, GAMMA	EVAL-CONF	25-2		75WASH		224 375	SRL BENJAMIN+	TBL BEST FIT TRANSPU PROD.
CM 244	RES INT CAPT	EVAL-CONF	63-1		75WASH		224 375	SRL BENJAMIN+	TBL BEST FIT TRANSPU PROD.
CM 244	FISSION	EVAL-CONF	25-2		75WASH		224 375	SRL BENJAMIN+	TBL BEST FIT TRANSPU PROD.
CM 244	RES INT FISS	EVAL-CONF	63-1		75WASH		224 375	SRL BENJAMIN+	TBL BEST FIT TRANSPU PROD.
CM 245	N, GAMMA	EVAL-CONF	25-2		75WASH		224 375	SRL BENJAMIN+	TBL BEST FIT TRANSPU PROD.
CM 245	RES INT CAPT	EVAL-CONF	63-1		75WASH		224 375	SRL BENJAMIN+	TBL BEST FIT TRANSPU PROD.
CM 245	FISSION	EXPT-CONF	25-2	20+1	75WASH		81 375	ORL DABBS+ TBL RES,DET	FISS REL ALPHA
CM 245	FISSION	EVAL-CONF	25-2		75WASH		224 375	SRL BENJAMIN+	TBL BEST FIT TRANSPU PROD.
CM 245	RES INT FISS	EVAL-CONF	63-1		75WASH		224 375	SRL BENJAMIN+	TBL BEST FIT TRANSPU PROD.
CM 245	RESON PARAMS	EXPT-CONF	98-1	16+1	75WASH		81 375	ORL DABBS+ TBL EO,REL	HEIGHTS
CM 246	N, GAMMA	EVAL-CONF	25-2		75WASH		224 375	SRL BENJAMIN+	TBL BEST FIT TRANSPU PROD.
CM 246	RES INT CAPT	EVAL-CONF	63-1		75WASH		224 375	SRL BENJAMIN+	TBL BEST FIT TRANSPU PROD.
CM 246	FISSION	EVAL-CONF	25-2		75WASH		224 375	SRL BENJAMIN+	TBL BEST FIT TRANSPU PROD.
CM 246	RES INT FISS	EVAL-CONF	63-1		75WASH		224 375	SRL BENJAMIN+	TBL BEST FIT TRANSPU PROD.
CM 247	N, GAMMA	EVAL-CONF	25-2		75WASH		224 375	SRL BENJAMIN+	TBL BEST FIT TRANSPU PROD.
CM 247	RES INT CAPT	EVAL-CONF	63-1		75WASH		224 375	SRL BENJAMIN+	TBL BEST FIT TRANSPU PROD.
CM 247	FISSION	EVAL-CONF	25-2		75WASH		224 375	SRL BENJAMIN+	TBL BEST FIT TRANSPU PROD.
CM 247	RES INT FISS	EVAL-CONF	63-1		75WASH		224 375	SRL BENJAMIN+	TBL BEST FIT TRANSPU PROD.
CM 248	N, GAMMA	EVAL-CONF	25-2		75WASH		224 375	SRL BENJAMIN+	TBL BEST FIT TRANSPU PROD.
CM 248	RES INT CAPT	EVAL-CONF	63-1		75WASH		224 375	SRL BENJAMIN+	TBL BEST FIT TRANSPU PROD.
CM 248	FISSION	EVAL-CONF	25-2		75WASH		224 375	SRL BENJAMIN+	TBL BEST FIT TRANSPU PROD.



ELEMENT S A	QUANTITY	TYPE	ENERGY		DOCUMENTATION			LAB	COMMENTS
			MIN	MAX	REF	VOL	PAGE		
CM 248	RES INT FISS	EVAL=CONF	63-1		75WASH	224	375	SRL BENJAMIN+	TBL BEST FIT TRANSPU PROD.
BK 249	N, GAMMA	EVAL=CONF	25-2		75WASH	224	375	SRL BENJAMIN+	TBL BEST FIT TRANSPU PROD.
BK 249	RES INT CAPT	EVAL=CONF	63-1		75WASH	224	375	SRL BENJAMIN+	TBL BEST FIT TRANSPU PROD.
BK 249	FISSION	EVAL=CONF	25-2		75WASH	224	375	SRL BENJAMIN+	TBL BEST FIT TRANSPU PROD.
BK 249	RES INT FISS	EVAL=CONF	63-1		75WASH	224	375	SRL BENJAMIN+	TBL BEST FIT TRANSPU PROD.
CF 249	N, GAMMA	EVAL=CONF	25-2		75WASH	224	375	SRL BENJAMIN+	TBL BEST FIT TRANSPU PROD.
CF 249	RES INT CAPT	EVAL=CONF	63-1		75WASH	224	375	SRL BENJAMIN+	TBL BEST FIT TRANSPU PROD.
CF 249	FISSION	EVAL=CONF	25-2		75WASH	224	375	SRL BENJAMIN+	TBL BEST FIT TRANSPU PROD.
CF 249	RES INT FISS	EVAL=CONF	63-1		75WASH	224	375	SRL BENJAMIN+	TBL BEST FIT TRANSPU PROD.
CF 250	N, GAMMA	EVAL=CONF	25-2		75WASH	224	375	SRL BENJAMIN+	TBL BEST FIT TRANSPU PROD.
CF 250	RES INT CAPT	EVAL=CONF	63-1		75WASH	224	375	SRL BENJAMIN+	TBL BEST FIT TRANSPU PROD.
CF 250	FISSION	EVAL=CONF	25-2		75WASH	224	375	SRL BENJAMIN+	TBL BEST FIT TRANSPU PROD.
CF 250	RES INT FISS	EVAL=CONF	63-1		75WASH	224	375	SRL BENJAMIN+	TBL BEST FIT TRANSPU PROD.
CF 251	N, GAMMA	EVAL=CONF	25-2		75WASH	224	375	SRL BENJAMIN+	TBL BEST FIT TRANSPU PROD.
CF 251	RES INT CAPT	EVAL=CONF	63-1		75WASH	224	375	SRL BENJAMIN+	TBL BEST FIT TRANSPU PROD.
CF 251	FISSION	EVAL=CONF	25-2		75WASH	224	375	SRL BENJAMIN+	TBL BEST FIT TRANSPU PROD.
CF 251	RES INT FISS	EVAL=CONF	63-1		75WASH	224	375	SRL BENJAMIN+	TBL BEST FIT TRANSPU PROD.
CF 252	N, GAMMA	EVAL=CONF	25-2		75WASH	224	375	SRL BENJAMIN+	TBL BEST FIT TRANSPU PROD.
CF 252	RES INT CAPT	EVAL=CONF	63-1		75WASH	224	375	SRL BENJAMIN+	TBL BEST FIT TRANSPU PROD.
CF 252	FISSION	EVAL=CONF	25-2		75WASH	224	375	SRL BENJAMIN+	TBL BEST FIT TRANSPU PROD.
CF 252	RES INT FISS	EVAL=CONF	63-1		75WASH	224	375	SRL BENJAMIN+	TBL BEST FIT TRANSPU PROD.
CF 252	ETA	EXPT=CONF	SPON		75WASH	262	375	ANC SMITH,MN=BATH,CFO MONTE CARLO CALC	
CF 252	NUBAR,(NU)	EXPT=CONF	SPON		75WASH	262	375	ANC SMITH,MN=BATH,CFO MONTE CARLO CALC	
CF 252	NUBAR,(NU)	EVAL=CONF	25-2		75WASH	286	375	IAE LEMMEL, TBL LSQ ANAL CFO OTHER EVAL.	
CF 252	F NEUT DELAY	EVAL=CONF	25-2		75WASH	286	375	IAE LEMMEL, TBL LSQ ANAL CFO OTHER EVAL.	
CF 252	SPECT FISS N	EXPT=CONF	SPON		75WASH	62	375	UI JOHNSON+ GRPH,FITS MAXW T=1.43MEV	
CF 252	SPECT FISS N	EVAL=CONF	SPON		75WASH	250	375	NBS GRUNOL=EVLM,MEAS,E AV=2.13+-0.027 MEV	
CF 253	N, GAMMA	EVAL=CONF	25-2		75WASH	224	375	SRL BENJAMIN+	TBL BEST FIT TRANSPU PROD.
CF 253	RES INT CAPT	EVAL=CONF	63-1		75WASH	224	375	SRL BENJAMIN+	TBL BEST FIT TRANSPU PROD.
CF 253	FISSION	EVAL=CONF	25-2		75WASH	224	375	SRL BENJAMIN+	TBL BEST FIT TRANSPU PROD.
CF 253	RES INT FISS	EVAL=CONF	63-1		75WASH	224	375	SRL BENJAMIN+	TBL BEST FIT TRANSPU PROD.
ES 253	N, GAMMA	EVAL=CONF	25-2		75WASH	224	375	SRL BENJAMIN+	TBL BEST FIT TRANSPU PROD.
ES 253	RES INT CAPT	EVAL=CONF	63-1		75WASH	224	375	SRL BENJAMIN+	TBL BEST FIT TRANSPU PROD.
ES 253	FISSION	EVAL=CONF	25-2		75WASH	224	375	SRL BENJAMIN+	TBL BEST FIT TRANSPU PROD.
ES 253	RES INT FISS	EVAL=CONF	63-1		75WASH	224	375	SRL BENJAMIN+	TBL BEST FIT TRANSPU PROD.

7-MY-75

ELEMENT S A	QUANTITY	TYPE	ENERGY		DOCUMENTATION			LAB	COMMENTS
			MIN	MAX	REF	VOL	PAGE		
FP ROD	TOTAL XSECT	EXPT-CONF	10+0	24+2	75WASH	743	375	KIL	PRIESMEYER+ GRAPH
FP ROD	RESON PARAMS	EXPT-CONF	36+0	19+2	75WASH	743	375	KIL	PRIESMEYER+ TABLE
MANY	TOT INELASTI	REVM-CONF	14+7		75WASH	663	375	JUL	QAIM, GRAPH SYSTEMATICS
MANY	N, GAMMA	REVM-CONF	14+7		75WASH	663	375	JUL	QAIM, GRAPH SYSTEMATICS
MANY	N2N REACTION	REVM-CONF	14+7		75WASH	663	375	JUL	QAIM, GRAPH SYSTEMATICS
MANY	N, PROTON	REVM-CONF	14+7		75WASH	663	375	JUL	QAIM, GRAPH SYSTEMATICS
MANY	N, TRITON	REVM-CONF	14+7		75WASH	663	375	JUL	QAIM, GRAPH SYSTEMATICS
MANY	N,HE3 REACTN	REVM-CONF	14+7		75WASH	663	375	JUL	QAIM, GRAPH SYSTEMATICS
MANY	N,ALPHA REAC	REVM-CONF	14+7		75WASH	663	375	JUL	QAIM, GRAPH SYSTEMATICS
MANY	STRNGTH FUNC	THEO-CONF	NDG		75WASH	338	375	KAP	KIROUAC,CALC FLUCTUATIONS CFD EXP
MANY	STRNGTH FUNC	THEO-CONF	NDG		75WASH	805	375	CBE	NEWSTEAD,FLUCTUATIONS IN STF.

U.S. DEPT. OF COMM. BIBLIOGRAPHIC DATA SHEET		1. PUBLICATION OR REPORT NO. NBS SP-425, Vol. II	2. Gov't Accession No.	3. Recipient's Accession No.
4. TITLE AND SUBTITLE  Proceedings of the Conference on Nuclear Cross Sections and Technology, March 3-7, 1975			5. Publication Date  October 1975	
			6. Performing Organization Code	
7. AUTHOR(S) Editors: R.A. Schrack and C.D. Bowman			8. Performing Organ. Report No.	
9. PERFORMING ORGANIZATION NAME AND ADDRESS  NATIONAL BUREAU OF STANDARDS DEPARTMENT OF COMMERCE WASHINGTON, D.C. 20234			10. Project/Task/Work Unit No.	
			11. Contract/Grant No.	
12. Sponsoring Organization Name and Complete Address (Street, City, State, ZIP)  Energy Research Development Administration			13. Type of Report & Period Covered Final	
			14. Sponsoring Agency Code	
15. SUPPLEMENTARY NOTES  Library of Congress Catalog Card Number: 75-619216				
16. ABSTRACT (A 200-word or less factual summary of most significant information. If document includes a significant bibliography or literature survey, mention it here.)  These preceedings are the compilation of 217 papers presented at the Conference on Nuclear Cross Sections and Technology held in Washington, D.C. on March 3-7, 1975. The Conference summarized the present status of nuclear cross sections and technology and discussed future cross sections needs. Special emphasis is placed on reactor technology and biomedical applications of nuclear science and the measurement of standard cross sections.				
17. KEY WORDS (six to twelve entries; alphabetical order; capitalize only the first letter of the first key word unless a proper name; separated by semicolons)  Biomedical; Conference; Cross section; nuclear; standards; technology.				
18. AVAILABILITY  <input checked="" type="checkbox"/> Unlimited  <input type="checkbox"/> For Official Distribution. Do Not Release to NTIS  <input checked="" type="checkbox"/> Order From Sup. of Doc., U.S. Government Printing Office Washington, D.C. 20402, SD Cat. No. C13 .10:425/vol. II  <input type="checkbox"/> Order From National Technical Information Service (NTIS) Springfield, Virginia 22151			19. SECURITY CLASS (THIS REPORT)  UNCLASSIFIED X	21. NO. OF PAGES  Vol. II  553
			20. SECURITY CLASS (THIS PAGE)  UNCLASSIFIED X	22. Price











